NORTHWESTERN UNIVERSITY

Two-Dimensional Polymers: Syntheses, Properties, and Applications

A DISSERTATION

SUBMITTED TO THE GRADUATE SCHOOL
IN PARTIAL FULFILLMENT OF THE REQUIREMENTS

for the degree

DOCTOR OF PHILOSOPHY

Field of Chemistry

By
Austin Michael Evans

EVANSTON, ILLINOIS

March 2021

ABSTRACT

Two-Dimensional Polymers: Syntheses, Properties, and Applications

Austin M. Evans

Discrete molecules, linear and branched polymers, and disordered cross-linked networks are well studied objects of chemical synthesis. However, two-dimensional polymers (2DPs) have been long missing from this continuum of molecular architectures, both in chemical synthesis and in Nature. Recently, new polymerization strategies and characterization methods have enabled the unambiguous realization of covalently linked macromolecular sheets. However, the controlled polymerization of these planar macromolecules and evaluation of their fundamental properties has only just begun. In this dissertation, I will begin by discussing controlled colloidal polymerization strategies, which have enabled the synthesis of single-crystalline 2DPs and high-quality 2DP films. Next, I will explore the unique combination of optical, electronic, magnetic, mechanical, and thermal properties that arise as a consequence of the structure of layered 2DPs. Finally, I end by describing the application potential of 2DPs, which is augmented by several proof-of-principle demonstrations. Taken together, this Dissertation will demonstrate how a robust understanding of 2D polymerization enables the exploration of the fundamental properties and application relevance of macromolecular sheets.

ACKNOWLEDGMENTS

As I began to prepare my thesis, I quickly became sentimental remembering the remarkable people that have guided me through my life and scientific endeavors. Without those mentioned below, and countless others, I would certainly not be the man and scientist I am today.

First and foremost, I would like to thank my thesis advisor, Professor William R. Dichtel. Will and I first met face-to-face in a BBQ restaurant near my hometown in Oklahoma. I remember leaving that meeting appreciating that Will had a unique combination of scientific intellect and genuine care for his students. Over the past several years, I have come to realize that my initial assessment fell far short of how remarkable Will is. I am fortunate to have been mentored by him and hope that someday I will more fully embody Will's traits as a scientist and mentor.

I am also enormously indebted to several others that mentored me during my thesis work. First, I would like to thank Professor Seth Marder (Georgia Institute of Technology) who has profoundly impacted how I approach scientific research. Working with Professor Marder and his team has refined my training in careful scientific inquiry in ways that are sure to benefit me for the rest of my career. I am specifically grateful to Professor Marder for his guidance in how to master a scientific subject while remaining humble in the boundaries of my knowledge. Next, I would like to thank Professor Jean-Luc Brédas (University of Arizona). Professor Brédas' computational chemistry expertise has been critically important to many of the efforts I have pursued as a graduate student. Through our joint works, Professor Brédas has repeatedly given profound feedback in the most constructive manner I have ever received. I hope that someday I will be able to mirror this style, which has been enormously valuable in my training. I have also benefited enormously from

mentorship by Professor Mark Hersam (Northwestern University) over the past several years. Professor Hersam is world-class mentor and group leader. I hope to his highly effective management style as I progress through my scientific career. I would also like to thank Professor J. Fraser Stoddart (Northwestern University, Tianjin University, University of New South Wales). I have been fortunate to work with his team through several different endeavors, through which I have benefited from his professional guidance. I look up enormously to his incredible scientific contributions but am also highly impressed by how he uses his prominence to serve as an effective steward for the scientific community. As I progress through the next stages of my professional life, I hope to serve as a mentor to others as those mentioned above have served as a mentor to me.

I must also thank the incredible people who fostered my development as an undergraduate. First, I would like to recognize Professor Justin M. Chalker for his transformative mentorship early in my scientific career. The training I received from Professor Chalker set me down on a path towards scientific research that has been a source of profound joy for me over the past several years. I also thank Professor Gordon Purser for his tireless mentorship as an undergraduate. Without Professor Purser, I likely would not have started my journey into academia and so I am greatly appreciative to the time and energy he invested in me. I hope that someday I will be able to impact young students as deeply as he has impacted me. I would also like to thank my scientific mentors at Ludwig-Maximilians-Universität München, Professor Thomas Bein, Professor Dana Medina, and Dr. Torben Sick. Each of these scientists invested an undeserved amount of time in my early training, which was critical to the development of skills I have relied on since.

In addition, I would like to thank the large number of collaborators I have been lucky to work with over the past few years including: Professor Michael Crommie (University of California,

Berkeley), Professor Nathan Gianneschi (Northwestern University), Professor Omar Farha (Northwestern University), Professor Lin Chen (Northwestern University, Argonne National Laboratory), Professor Richard Schaller (Northwestern University, Argonne National Laboratory), Professor Danna Freedman (Northwestern University), Professor F. Dean Toste (University of California, Berkeley), Professor Feng Wang (University of California, Berkeley), Professor Daniel C. Ralph (Cornell University), Professor Scott E. Denmark (University of Illinois, Urbana-Champaign), Professor Karl Börjesson (University of Gothenburg), Professor Garry Rumbles (National Renewable Energy Laboratory and University of Colorado, Boulder), Professor Gonçalo Bernardes (Cambridge University), Professor Patrick Hopkins (University of Virginia), Professor Ashutosh Giri (University of Rhode Island), Professor Andrew Livingston (Imperial College London), Professor François-Xavier Coudert (Université Paris Sciences et Lettres and Centre National de la Recherche Scientifique), Professor Alex Adronov (McMaster University), Professor Gleb Yushin (Georgia Institute of Technology), Dr. Catherine Mulzer (Dupont), Dr. Matthew Ryder (Oak Ridge National Laboratory), Dr. Tijana Rajh (Argonne National Laboratory), Dr. Lei Sun (Argonne National Laboratory), Dr. Massimiliano Delferro (Argonne National Laboratory), Dr. Martin Fuchs (Brookhaven National Laboratory), Dr. Xiaobing Zuo (Argonne National Laboratory), Dr. Andrey Yakovenko (Argonne National Laboratory), Dr. Steven Weigand (Argonne National Laboratory), and all of their amazing teams. All of these researchers have made a notable impact in my scientific training, which I will always treasure.

Of the many scientists I have had the pleasure of working with over the past several years, I must acknowledge several who have made particularly substantive impacts on my training. First, I

appreciate the dedication my thesis committee (Professor Julia Kalow, Professor Regan Thomson, and Professor Chad Mirkin) have shown to my development as a young scientist. I am fortunate to have such well-rounded mentors and role models. I would like to thank Dr. Samik Jhulki and Dr. Cameron Feriante for their tireless efforts in fundamental and applied understanding in two-dimensional polymerization. I also acknowledge Dr. Haoyuan Li, Dr. Hong Li, Dr. Matthew Ryder, and Sangni Xun all of whom have used their expertise in computational techniques to advance our collective understanding. I also thank Nathan Bradshaw for his efforts in processing two-dimensional polymers, which is essential for their continued development. Finally, I would like to thank Kelsey Collins for glovebox training and the honorary junior magnetochemist badge she has given me over the past several years. Most importantly, I would like to thank all of those noted above for their friendship over the past several years.

I would also like to note the phenomenal people I have had the pleasure of working with in the Dichtel Research Group. First, I would like to thank Tory Helgeson, who is vital to all activities in the Dichtel Group and without whom I would have been helpless. As I joined the Dichtel Group, my colleagues Dr. Ryan Bisbey, Dr. Edon Vitaku, Dr. Amanda Corcos, Dr. Anton Chavez, and Professor Brian Smith all took an interest in my training, which was crucial for my early development. In addition to those mentioned above, I am fortunate to have had such a great group of friends and colleagues to grow alongside throughout graduate school, including Dr. Max Klemes, Dr. Diego Sanchez, Rachel Snyder, Rebecca Li, Nathan Flanders, and Daylan Sheppard.

I would also like to acknowledge the next generation of Dichtelians who I expect will continue to foster the culture that supported me throughout my graduate studies. In particular, I would like to thank my great friend, tennis competitor, best man, and partner-in-science, Michael Strauss for the

great memories over the past few years. I would also like to thank Ioannina and Calla Castano for constantly indulging my half-baked ideas and teaching me about popular culture. Also, I acknowledge Dr. Benjamin Elling for the many helpful scientific and nonscientific discussions we have shared over the past several years. I'm lucky to have worked with these and so many other talented scientists over the past several years. Going forward, I am certain the next generations of Dichtelians will continue the camaraderie that has been formative to my time as a graduate student.

I must also thank my family who has consistently supported me throughout my studies. Without the guidance, love, and support of my mother, stepfather, and sister I would certainly not be the man I am today. I would also like to specifically thank my grandfather, Professor Michael L. Evans, who fostered my early interest in science. By indulging my early scientific curiosity, he sent me down a career path that I have found deeply rewarding. To my entire family, thank you for always being there for me.

Finally, I would like to thank my wife, Dr. Madelyn Stalzer, who is by far my most meaningful discovery during my time at Northwestern. Our relationship makes me a better person and inspires me both in- and out of the lab. In addition to Madelyn, I am also thankful to the entire Stalzer clan, who I am fortunate to have recently added to my family.

To anyone I may have forgotten and those listed above, thank you for the memories.

DEDICATION

This thesis is dedicated to my grandparents, Michael and Linda Evans and Edson “Bill” Lewis and Joanne Lewis, who nurtured my early scientific interests.

TABLE OF CONTENTS

LIST OF DISPLAY ITEMS

Chapter 1 : Two-Dimensional Polymers and Polymerizations

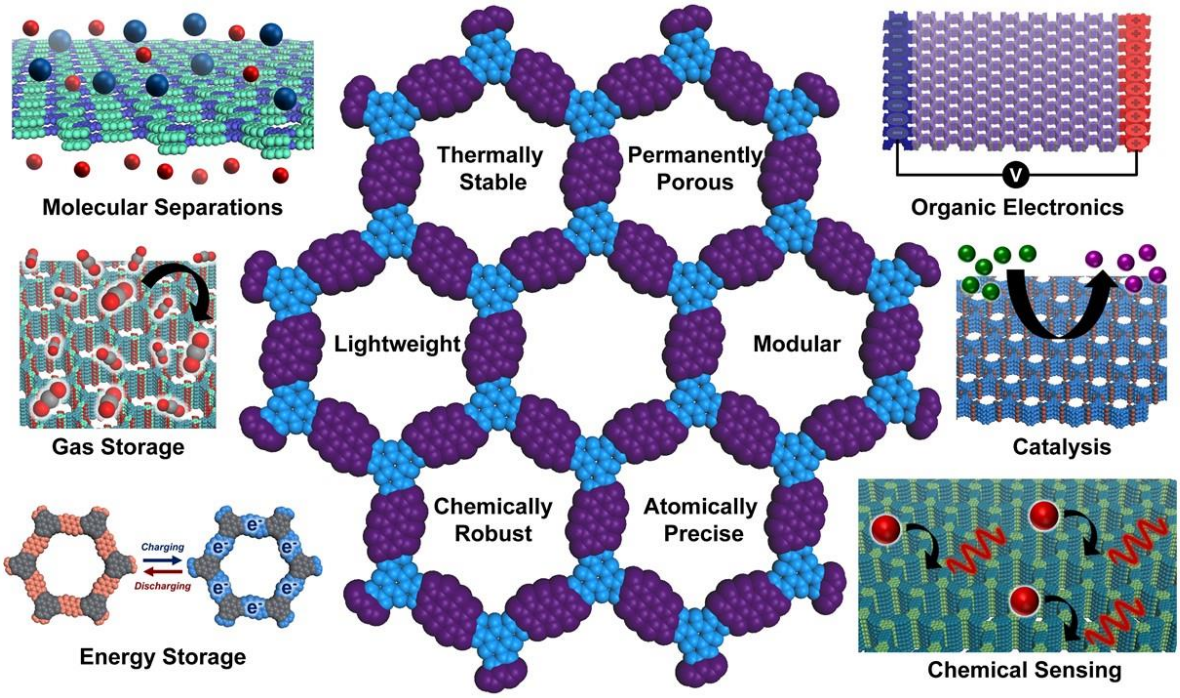

Figure 1.1 The properties and potential applications of two-dimensional polymers.

1.1 Preface

In 1920, Hermann Staudinger postulated the existence of high-molecular weight species, which he termed *Makromolekülen*.[1] After a century of research and development, macromolecules have become one of the most technologically important classes of materials. [2-8] Synthetic polymers now permeate every facet of human existence and are integrated into coatings,[9-12] building materials,[13, 14] textiles,[15] and electronic devices.[16-18] Nature also uses polymers to encode and replicate information,[19] to catalyze and regulate chemical reactions,[19-22] to convert and store chemical energy,[20, 23, 24] and for structural support and motility.[25] Two structural paradigms have dominated the first 100 years of synthetic polymerization: topologically linear chains, such as thermoplastics,

and amorphous, cross-linked networks, such as thermoset resins or hydrogels.[26] Across this continuum between perfectly linear macromolecules and cross-linked networks, branches and loops give rise to many other architectures, such as dendrimers,[27, 28] star polymers,[29, 30] cyclic polymers,[31, 32] and polymer brushes,[33-35] to name a few.[26] However, long missing from these topologies, both in Nature and in synthetic polymer chemistry, are sheet-like macromolecules whose covalent bonds are confined to two orthogonal directions. The controlled synthesis, fundamental properties, and applications of these two-dimensional polymers (2DPs) are the subject of this Dissertation.

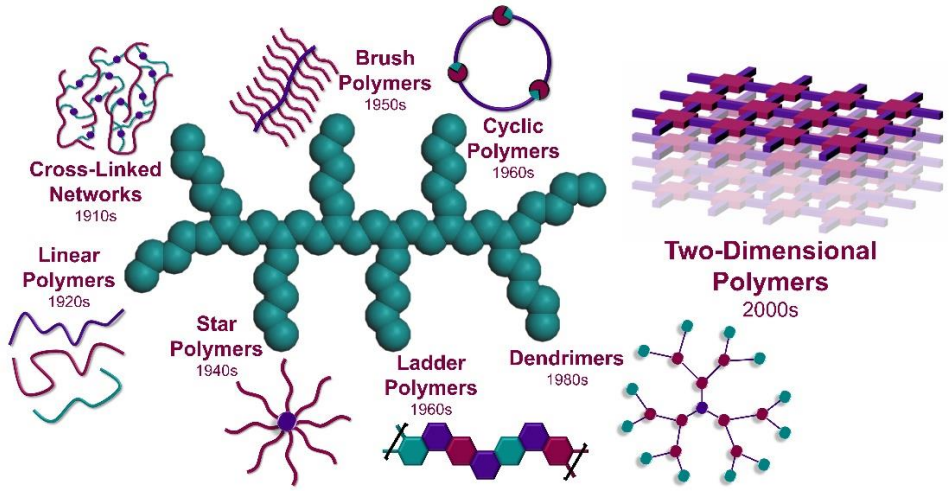

Figure 1.2. General classes of synthetically realized polymer architectures and the decade that they were first produced through artificial (i.e. not biological) means. Structures are organized by date of first synthesis, from linear strands and cross-linked networks (left) to more complex architectures including dendrimers and cyclic macromolecules (right).

1.2 A Brief History of Two-Dimensional Polymerization

As early as 1935, chemists speculated that the same approaches used to polymerize linear strands and cross-linked networks could also be used to prepare macromolecular sheets. For example, an early report by Gee and Rideal explored the polymerization of immiscible functionalized β-eleostearic acids at air-water interfaces.[36] Soon after, Talmud and coworkers used the term two-dimensional polymerization to describe a similar interfacial cross-linking of stearic aldehydes and polyfunctional amines.[37] These interfacial reactions between polyfunctional species were speculated to produce "two-dimensional polymers", although these reactions almost certainly produced irregularly cross-linked polymer films instead. Despite this early interest in 2D polymerization, the synthetic and analytical toolkit available at the time were insufficient to unambiguously realize this goal. These early reports hinted that linear polymerization strategies, which mostly use untemplated and irreversible bond-forming reactions, are generally not suitable for the polymerization of large-area macromolecular sheets. Ultimately, these challenges led to an interlude in the development of 2D polymerization. Recognizing this challenge, Roald Hoffmann famously noted in 1993 that, "Organic chemists are masterful at exercising control in zero dimensions. One subculture of organic chemists has learned to exercise control in one dimension. These are polymer chemists, the chain builders… But in two or three dimensions, it's a synthetic wasteland."[38]

In the early 2000s, interest in 2DPs was reinvigorated by the revelation that topologically planar materials, such as graphene or transition-metal dichalcogenides, exhibit unique properties as a consequence of their atomically thin structures.[39, 40] The bottom-up preparation of inorganic 2D materials demonstrated that chemists could produce chemical structures confined to an atomic

plane. However, inorganic 2D materials differ from 2DPs because they do not retain the structure of their molecular precursors and typically rely on extreme synthetic conditions not compatible with molecular organic species. Nonetheless, these successes inspired organic chemists to revisit and ultimately realize the successful synthesis of 2DPs from designed monomers for the first time.[41] Over the past fifteen years, the number and complexity of successfully synthesized 2DPs has increased substantially to include over 500 distinct chemical structures prepared through several complementary synthetic approaches. Due to their unique dimensionality and structural regularity, 2DPs exhibit combinations of properties not available in other materials. For this reason, 2DPs have already been explored for diverse applications including gas storage, molecular separations, and organic electronics. Many other intriguing 2DP properties are now emerging as high-quality samples become more widely available, such that the application landscape for 2DPs is likely to expand in the coming years.

Although the goal of polymerizing macromolecular sheets has undoubtedly been achieved, the available polymerization techniques are by no means fully developed or even understood. As such, significant opportunities and challenges remain in 2D polymerization including: the production of large area macromolecular sheets with minimal defects, morphological control at all length scales, property engineering through structural and chemical design, and ultimately device integration and assessment. These developments can only be achieved by advancing the fundamental mechanistic understanding of various 2D polymerization methods. Similarly, existing characterization methods and new tools must also be developed to definitely analyze macromolecular sheets. When realized, these advances will enable 2DPs to be implemented in real devices and technologies that leverage their unique properties.

1.3 Two-Dimensional Polymerization from Many Synthetic Traditions

The irreversible bond-forming reactions established for linear polymerizations, in the absence of molecular preorganization or templation, are largely unamenable to the production of large-area macromolecular sheets. Largely, this restriction originates from the enormous entropic penalty incurred by polymerizing monomers into a 2D monolayer. If these entropic penalties lead to even a small number of intersheet defects, an amorphous network is more likely to be obtained than a topologically planar molecular sheet. This fundamental limitation hindered the development of 2D polymerization for many years and led some researchers to speculate that 2DPs might be a synthetic impossibility. However, developments in areas outside of traditional polymer science, such as supramolecular chemistry,[42-54] coordination networks,[48, 55-64] two-dimensional materials,[39, 65-74] and crystal engineering,[62, 75-82] have led to the coevolution of 2D polymerization approaches that would have been challenging to envision from controlled linear or network polymerizations. As such, contemporary 2D polymerization strategies largely emerge and continue to draw inspiration from many synthetic traditions.

In 2005, Yaghi and coworkers polymerized and subsequently characterized the formation of 2DPs for the first time.[41] The authors speculated that by using reversible condensation reactions between aromatic boronic acids and polyfunctional catechols, structural defects were annealed during the production of these layered, periodic, macromolecular sheets. This strategy takes clear inspiration from the chemistries used to prepare crystalline, porous coordination polymers— often known as metal-organic frameworks (MOFs).[59] The structural similarity and traditions that produced these 2DPs led researchers to name these macromolecular sheets 2D covalent organic frameworks (2D

COFs). Since these early reports, the term COF has been used widely to describe hundreds of 2DP structures, which at the outset were speculated to require reversible bond-forming chemistries.[83-85] However, as the COF subfield has matured, irreversible reactions have provided polycrystalline, layered 2DPs with sufficiently large domains for characterization by powder X-ray diffraction (PXRD).[86] It is therefore conceivable that solution-based, irreversible- and reversible-chemistries take advantage of self-templated formation, which blurs the distinction between 2DPs prepared this way and those produced through strategies that rely on explicit monomer preorganization.

Separately, researchers have shown that 2D polymerization at an interface can take advantage of many different bond-forming strategies.[87-89] As such, 2DPs have been prepared by confining and then polymerizing monomer species at air-liquid, liquid-liquid, and liquid-solid interfaces. Within the rich field of interfacial polymerization, solvent-free polymerizations confined to a solid interface under vacuum have also been explored and continue to draw inspiration from the formation of inorganic 2D materials on metal substrates.[90] These approaches are advantageous because polymerization confined to an interface limits the entropic penalty paid when forming 2D macromolecules.[90] Moreover, in some cases the underlying substrate can template or catalyze bond formation, either of which can be important to drive successful 2D polymerization. For this reason, some reactions, especially catalyzed carbon-carbon bond-forming processes, are amenable to on-surface polymerization but have yet to be demonstrated in solution.

The most recently developed approach to prepare 2DPs is topochemical polymerization, where monomers are preorganized through crystallization.[91-93] The resulting lamellar monomer crystals are isolated and subsequently irradiated with light to trigger bond-forming processes. This topochemical process has produced the largest and highest quality 2DPs reported to date, which in

some cases have been characterized by single-crystal X-ray diffraction.[94] Although the number of monomers that crystallize into structures amenable for topochemical 2D polymerization is limited, this strategy has unambiguously demonstrated that monolayer 2DPs with large lateral dimensions can be experimentally realized.

As will be described in greater detail below, these 2D polymerization strategies have been developed independently, each with their own mechanisms of formation and design considerations. However, a unifying element of all 2D polymerizations is the use of polyfunctional monomers that are constrained to react within the molecular plane, whether polymerization occurs in the solid-state following monomer preorganization, in solution under reversible bond-forming conditions, or confined to various interfaces. As these dominant polymerization strategies have matured, the differences among the 2DPs produced by these methods are less distinct. We consider this to be not unlike linear polymerization, which operates by many methods and mechanisms ranging from addition polymerization, to chain-growth processes,[95] to the templated synthesis of biopolymers[96, 97] – all of which produce fundamentally linear macromolecules regardless of whether they are obtained as solution-stable isolated strands, self-assembled double helices, or entangled solid-state structures. Likewise, all 2D polymerization strategies fundamentally produce macromolecular sheets, whether isolated as single layers or probed as multilayer assemblies. As such, we refer to all these material classes as 2DPs though in this Dissertation we sometimes use other terms such as covalent organic frameworks (COFs), covalent triazine frameworks (CTFs), covalent organic networks, covalent organic nanosheets (CONs), covalent organic monolayers (COMs), and the many other acronyms that have proliferated in the literature.

1.4 Two-Dimensional Polymer Terminology and Definitions

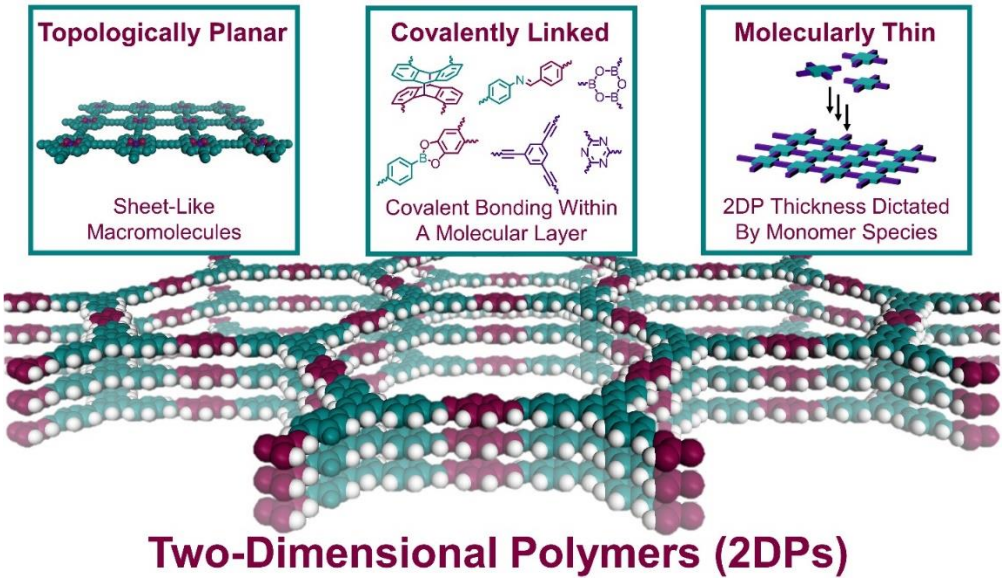

Figure 1.3. Defining features of 2DPs. 2DPs are topologically planar sheets, linked entirely through covalent bonds, with fundamental thicknesses consistent with their monomer species.

To discuss the emerging field of 2D polymerization, we must first set out criterion for 2DPs to be classified as such. The term 'two-dimensional polymer' has been used in many reports from different periods, with varying definitions and disqualifications. To mitigate any inconsistencies regarding the use of this term in this Review, we use the following criteria (**Figure 1.3**) for the assignment of the 2DP label:

1. Planar — 2DPs are topologically planar.
2. Covalently linked — 2DPs are linked entirely through covalent bonds within a molecular sheet.

3. Molecularly thin — Individual 2DP sheets will have thicknesses consistent with their monomer species. Layered 2DPs will have interlayer spacings consistent with their monomer species and noncovalent interlayer interactions.

Notably, several other definitions of 2DPs have also been proposed. For instance, a previously proposed 2DP definition used the defining features above but also impose the constraint that 2DPs must be obtained as single layers.[98] This constraint is unnecessary because even multilayered 2DPs are fundamentally composed of macromolecular sheets. As a more established comparison, it is indisputable that entangled polyethylene films and double-stranded DNA are both fundamentally linear strands, even though in these cases they exist in assembled states. Moreover, while exfoliation of multilayer 2DPs is a developing frontier in polymer science, the top-down preparation of monolayer 2DPs from multilayer assemblies is likely to become commonplace in the coming years. For these reasons, we discuss macromolecular polymer sheets, regardless of how they are obtained, as 2DPs.

Another area of considerable debate among previously proposed definitions is whether 2DPs must be, by definition, crystalline. We posit that this is not a stringent requirement, as topologically 2D macromolecular sheets with irregular cross-links are possible. However, the structural characterization of 2DP sheets is more easily performed with crystalline materials and has so far not been unambiguously demonstrated in amorphous systems. For this reason, we do not discuss amorphous, crosslinked materials that have been polymerized at interfaces and reported as 2DPs. Furthermore, we explicitly note other classes of materials that will not be discussed in this Review. First, we will not consider 2D coordination polymers or 2D MOFs.[99] Second, we will not consider recently synthesized interwoven structures as 2DPs, as they are still fundamentally linear covalent

strands.[100] Third, while some 2D allotropes and compounds, such as graphene, graphite, or hexagonal boron nitride, meet the criteria for 2D polymers, they are not rationally synthesized from monomers whose structures are preserved as 2D macromolecular sheets. Furthermore, their formation and properties have been reviewed extensively elsewhere.[39, 40, 65, 67-73, 101] Finally, we note that bifunctional monomers polymerized at interfaces cannot produce 2DPs, as these materials have no lateral repeat unit and are thus not topologically 2D.

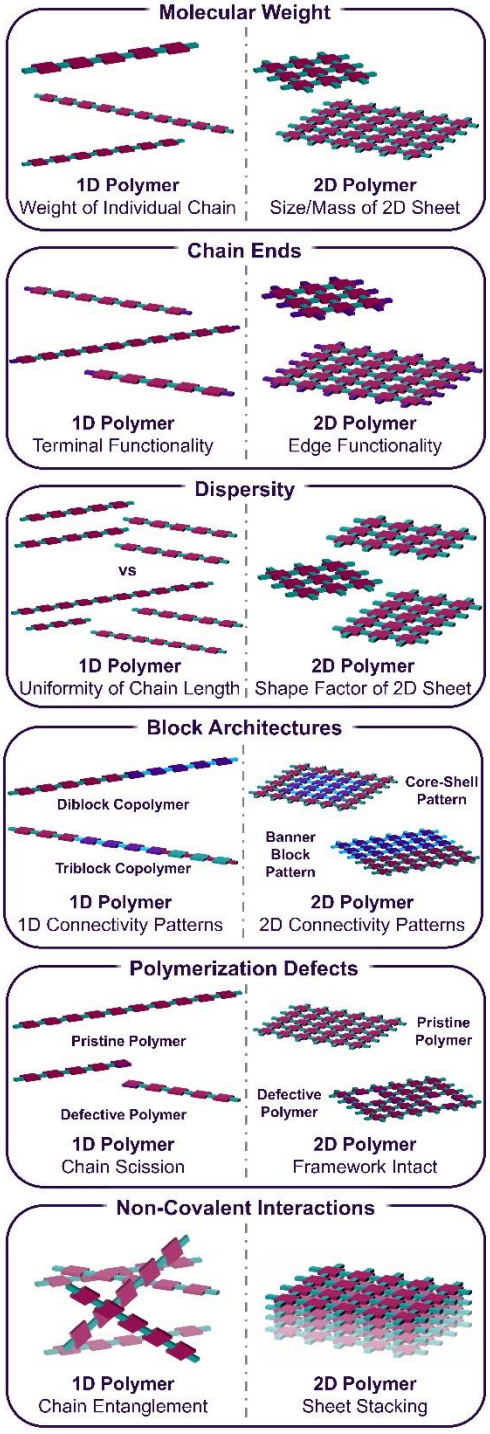

Figure 1.4. The emerging vocabulary used to describe 2DPs and the relationship of select terms to more defined concepts in linear polymerization.

Last, we note that the vocabulary used to discuss 2D polymerization is not well developed. Toward better describing 2DPs, we draw inspiration from the rigorously agreed-upon language of linear polymers (**Figure 1.4**). A one-dimensional polymer sample represents an ensemble of topologically linear macromolecules of varying composition, and a 2DP sample represents an ensemble of macromolecular sheets, each of which is also chemically distinct. The molecular weight of a 1D polymer sample is calculated from the masses of each strand and has a distribution associated with differing degrees of polymerization. Molecular masses can be estimated for many 2DPs by considering their dimensions and chemical structure. These sheets thus also have an associated dispersity that is often uncharacterized. However, characterization of the mass or size of a single-molecular sheet is sometimes complicated by their isolation as insoluble polycrystalline samples, similar to the difficulty in estimating the size of entangled, poorly soluble linear polymers. The challenge of isolating single sheets and the periodicity of 2DPs has led many to describe macromolecular sheet size by the average lateral crystallographic domain size, as this parameter can sometimes calculated from X-ray diffraction patterns or microscopy of the products. We find these the molecular weight and crystallographic domain size to be complementary descriptors of 2DP size.

Other terms used to describe linear polymer structures have more obvious differences within 2DPs. For example, linear polymer chain ends correspond to edge functionality in macromolecular sheets. Similarly, as bond breakage in a 1D polymer leads to chain scission, broken chemical bonds in the center of a 2D sheet typically introduce defects while leaving the overall 2D structure largely intact. While linear block polymers have been explored extensively, block 2DPs have not yet been experimentally realized. However, it is conceivable that many block architectures could be

prepared in the 2D limit, with opportunities to explore their assembly and phase separation. There are also descriptors that may need to be entirely redefined for 2DPs. For instance, non-covalent interactions, whether due to crystallization or chain entanglement, strongly impact the properties of linear polymer strands. Likewise, the non-covalent interactions related to tacticity, multilayer stacking, or interpenetrations likely influence the properties of 2DPs. While all of these defining features will critically impact 2DP properties, characterization of these attributes represents a forefront challenge in 2D polymerization. As the field of 2D polymerization matures, we suspect that the tools and language used to characterize 2DPs will mature as well.

1.5 Solution-Phase Two-Dimensional Polymerization

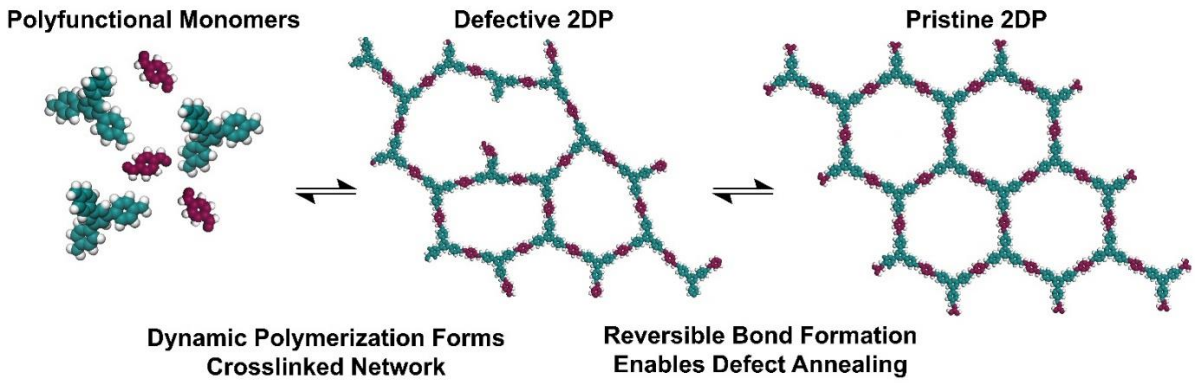

Figure 1.5. General strategy of dynamic bond-forming reactions.

The solution-phase synthesis of macromolecules enables chemists to tune polymerization conditions (e.g. solvent, catalysts, temperature), ultimately manifesting in a suite of chemically and structurally diverse polymer architectures. Similarly, solution-phase polymerization has

proven to be the most synthetically general approach to the preparation of 2DPs, with hundreds of chemically distinct 2DPs prepared to-date.[83, 84, 102-106] Inspired by the realization that dynamic coordination bonds allow for the synthesis of crystalline coordination polymers, Yaghi and coworkers developed a dynamic polymerization strategy for the solution-phase synthesis of 2DPs.[55, 59, 107-110] All early solution-based 2D polymerizations used reversible chemistries[42, 43, 46, 111-113] and long reaction times that were speculated to produce 2DPs as the thermodynamic product of these syntheses (**Figure 1.5**). Recent mechanistic investigations have revealed that an interplay of reversible and irreversible processes is likely operative in solution-based 2D polymerizations, which are more complex than simple defect annealing. Using synthetic designs based off of this mechanistic understanding, several researchers have produced large-area 2DPs through dynamic polymerization chemistries. As solution-based 2D polymerization has developed, researchers have found that solution-based irreversible chemistries can also produce layered, crystalline, aggregated 2DPs, as characterized by powder X-ray diffraction. These materials indicate that monomer rigidity and/or undesigned templation effects can give rise to crystalline layers with lateral dimensions on the scale of tens of nanometers. These chemistries greatly broaden the scope of solution-based 2D polymerization but will likely require additional monomer preorganization strategies to produce larger sheets. Below, we will focus our discussion on the mechanisms of dynamic covalent chemistries, which have been investigated in depth.

1.6. Dynamic Covalent Chemistries

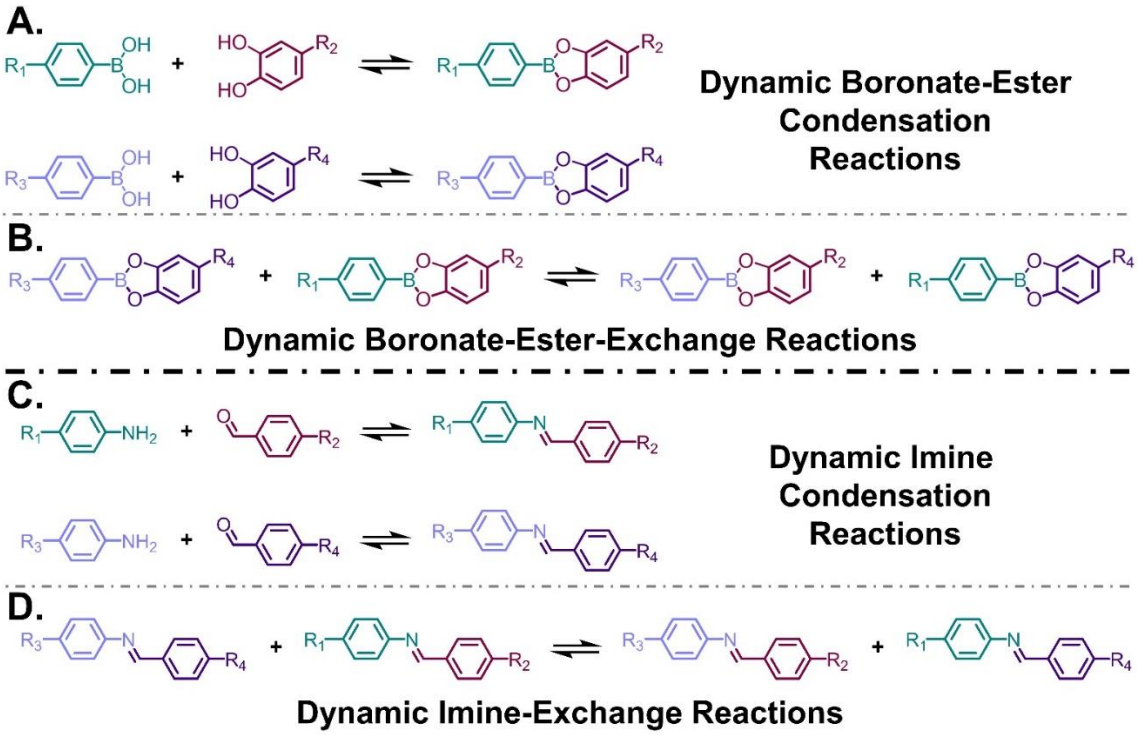

Figure 1.6. (A) Dynamic condensation reactions between boronic acids and catechols to produce boronate-esters and **(B)** exchange reactions between different boronate-ester molecules. **(C)** Dynamic condensation reactions between amines and aldehydes to produce imines and **(D)** exchange reactions between different imine molecules.

Model reactions have enhanced the understanding of the dynamic reactions used to polymerize 2D nets. For example, when different imine- or boronate ester-containing compounds are placed under polymerization-relevant conditions, their components undergo exchange (**Figure 1.6**).[46, 111, 114-116] This finding suggests that these bonds might also exchange during 2D polymerization, which could anneal structural defects. This understanding is consistent with the observation that the addition of

species that increase the dynamicity of covalent bonds leads to more crystalline 2DPs, as assessed by X-ray diffraction and N_2 sorption measurements. For example, adding methanol, which facilitates boronate-ester exchange, to the polymerization of boronate-ester-linked 2DPs leads to more-crystalline polycrystalline powders.[117-121] In two later studies, Bein and coworkers found that synthesizing 2DPs in the presence of monofunctional pinacol or boronic acid components increased the crystallinity of their 2DPs.[122, 123] These components presumably assist in defect annealing. These findings are consistent with those of Dichtel and coworkers, who showed that protecting the amine monomers used in imine condensation as benzophenone imines yielded higher-quality 2DPs.[124] In this case, the produced benzophenone may also promote transimination reactivity in the 2DP. However, in both cases, the addition of competitive dynamic bond-forming species slowed 2D polymerization. It is therefore not trivial to determine the thermodynamic and kinetic effects of these species on 2D polymerization. Moreover, these 2DPs all precipitate during their synthesis, which introduces an irreversible process, thereby making definitive assignments of the effect of modulating species a challenge.[121]

Irreversible aggregation of multilayered, polycrystalline powders precludes continued solution-phase growth. To address the challenge of irreversible aggregation, Dichtel and coworkers developed a colloidal synthetic approach that removed this confounding factor.[125] Nitrile cosolvents in boronic-acid-based 2D polymerizations provide stable colloidal suspensions instead of aggregated powders, which allowed researchers to investigate the operative 2D polymerization mechanisms in the absence of an irreversible thermodynamic trap. First, they observed that 2D polymerization in the presence of high monomer concentrations produced primarily newly nucleated, small 2D polymer domains.[126] However, when monomer concentrations were kept

sufficiently low, the nucleation of polymer domains was not observed and instead, existing polymer domains grew substantially. This observation led to the finding that the growth of existing polymer domains could be favored under conditions where monomers are slowly added via syringe pump to seed particles. Ultimately, controlling these nucleation and growth processes yielded solution-polymerized 2DPs as micron-sized single crystals.

The realization that large-area 2DPs could be grown under controlled nucleation conditions led Dichtel and coworkers to reconsider the effects of monofunctional modulating species on colloidal 2D polymerization.[125, 127] Addition of a monofunctional catechol to colloidal boronate-ester polymerizations revealed several considerations not discussed in earlier reports. First, they found that a modulating species slowed nucleation. This restricted nucleation allowed growth to proceed faster than that accessible by slow monomer addition via syringe pump. Growth in the presence of a modulating species occurred primarily in the out-of-plane direction, as assessed by TEM imaging, suggesting that the monofunctional catechol modulators capped dangling bonds along the periphery of the 2DP sheets.

Taken together, these findings highlight that there are several challenges associated with developing controlled 2D polymerizations in solution. First, precipitation of agglomerated 2DPs prevents their continued growth and obfuscates a mechanistic understanding of their polymerization. Second, isolating agglomerated powders makes it challenging to assign the extent of growth in the in-plane or out-of-plane direction. Third, the complex interplay between nucleation, growth, and molecular-scale reactivity and reversibility is not trivially impacted by changes to the polymerization conditions. Despite these challenges, these studies collectively

demonstrate that, to some degree, 2D polymerizations benefit from the dynamic exchange of covalent bonds.

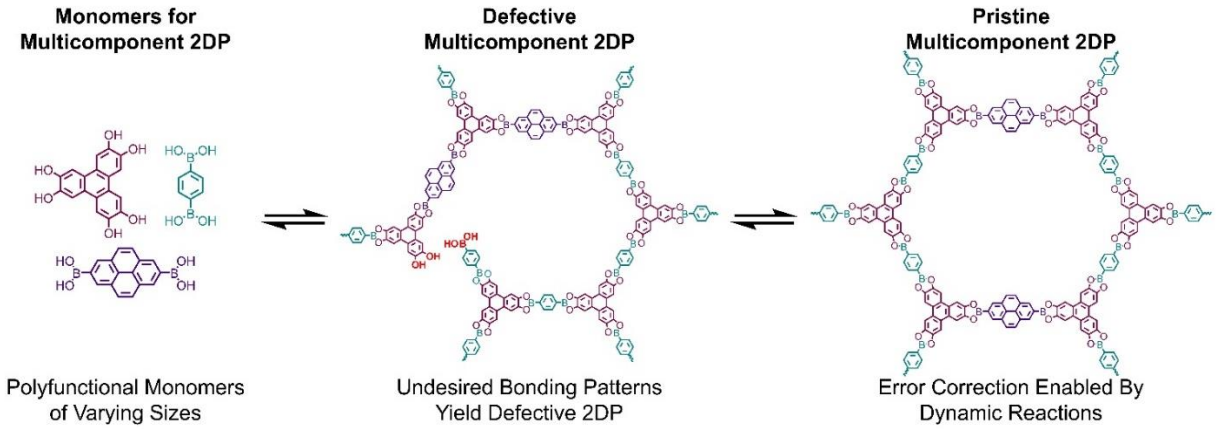

Figure 1.7. Simultaneous reaction of several monomer species and representative defective structures that are speculated to be annealed by dynamic error correction.

As additional evidence for dynamic rearrangement, researchers have found that multicomponent 2DPs prepared by the simultaneous reaction of more than two monomers can self-sort to produce crystalline, intermixed 2DPs.[85] For example, Jiang and coworkers found that polymerizing multiple boronic acids with a polyfunctional catecholate produces a single intermixed 2DP structure **(Figure 1.7**).[128] The preparation of an intermixed structure indirectly suggests that dynamic error correction occurs during this 2D polymerization, as it is unlikely that a perfectly 1:1 intermixed structure occurs initially. However, interplane templating interactions likely reinforce this self-sorting, which may also contribute to the synthesis of a preferred structure.

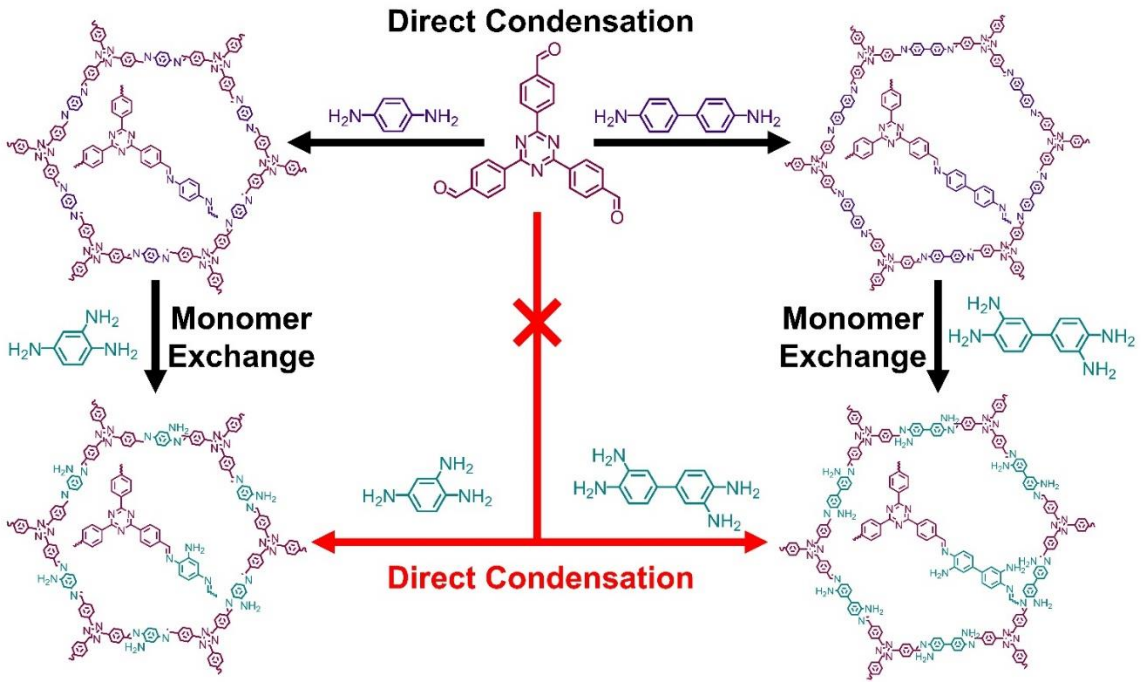

Figure 1.8. Monomer exchange reactions used to generate 2DPs that cannot be prepared *via* direct synthesis.[129]

The introduction of monomer species to pre-polymerized 2DPs can also result in molecular exchange, which demonstrates that the chemistries used to polymerize these networks are reversible.[129-132] For instance, Yan and coworkers polymerized imine-linked 2DPs by condensation of polyfunctional-amine and -aldehyde precursors (**Figure 1.8**).[129] Then, in a second step, they exposed this imine-linked 2DP to a chemically different, though structurally similar amine monomer. Under optimized conditions, the authors observed near complete exchange of the introduced amine monomer for the starting amine species, as characterized by elemental analysis. Similarly, Zhao and coworkers showed how 2DPs could be exchanged to yield topologically unique imine-linked 2DPs with three unique pore shapes.[132] These reports demonstrate that 2DPs

polymerized through imine bonds are at least partially dynamic, which allows for their rearrangement. However, it is currently unclear whether these processes occur by a true exchange mechanism or through a depolymerization-repolymerization pathway. Of note, ligand exchange in MOFs are known to proceed through a continuum of exchange and repolymerization mechanisms,[133-139] which we suspect is also the case of monomer exchange processes in covalent 2DPs. Recently, Dichtel and coworkers showed that imine-linked 2DPs could have one of their monomer components exchanged to produce a more thermodynamically stable β-ketoenamine-linked 2DP.[130] The crystallinity and surface area of 2DPs prepared *via* this approach were of significantly higher quality than those of β-ketoenamine-linked 2DPs prepared by any other method. This suggests that the original imine-linked structure assists the formation of the resultant β-ketoenamine-linked 2DP. Taken together, these findings demonstrate that solution-synthesized 2DPs are dynamic in the presence of reactive species in solution and that original structures can template structures produced through exchange reactions.

While these reports indicate that established dynamic polymerizations are indeed reversible, more recent explorations have reexamined the necessity of dynamicity in solution-based 2D polymerization. For example, imidization has recently been used to prepare crystalline 2DPs,[140-143] even though this chemistry is potentially irreversible under the conditions studied. Despite this irreversibility, these materials exhibit crystalline domain sizes on the order of tens of nanometers, which are sufficient to provide powder X-ray diffraction patterns. However, irreversible bond formation is likely to limit the formation of larger crystallites in the absence of other templation or monomer preorganization effects. Overall, structural rigidity, polymerization efficiency, and reversibility are all important factors for successful 2D polymerization. For these reasons, we

suspect that in-depth mechanistic investigations into the extent and kinetics of dynamicity will inform the optimization of solution-based 2D polymerization generally.

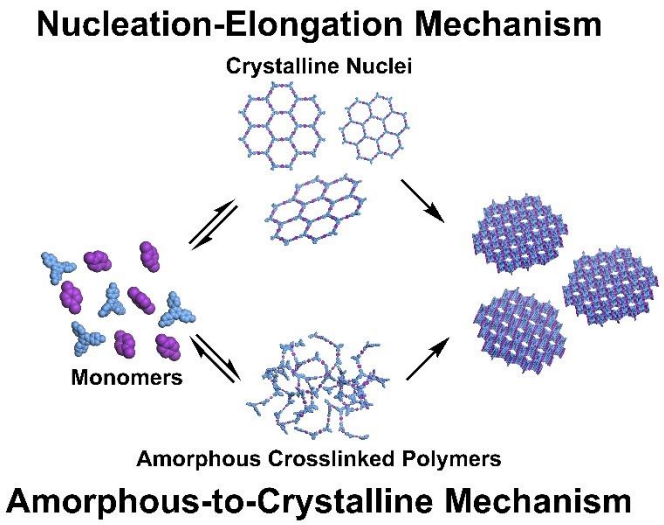

Figure 1.9. General mechanistic proposals for solution-based 2D polymerization.

1.7. Nucleation-Elongation Two-Dimensional Polymerization Mechanisms

Dynamic 2D polymerizations sometimes proceed through a nucleation-elongation mechanism, wherein initially formed crystalline species grow *via* continued polymerization (**Figure 1.10**).[117-120, 126, 127] When this mechanism is operative, structural defects are thought to be few and transiently removed by dynamic error correction. Dichtel and coworkers observed this behavior in boronate-ester-linked 2DPs, which were found to crystallize and precipitate with rates consistent with a nucleation-elongation mechanism even before these processes were intentionally controlled.[121] As indirect evidence that dynamicity was pertinent to this reactivity, they also found that the average crystallite size increased when controlled amounts of water were added to the polymerization mixture. In this same report, the precipitation of 2DP species greatly reduced

subsequent dynamicity and limited continued polymerization. Separate computational works by Brédas,[118] Grünwald,[117] and their coworkers found that a nucleation-elongation mechanism was operative in the formation of boronate-ester-linked 2DPs.[117, 118, 144] Moreover, they found that interlayer interactions were the primary driving force for 2DP growth, which was corroborated by investigations into the stacking of boronate-ester-linked macrocycles into 1D arrays.[145] Both Brédas' and Grünwald's computational investigations also found that defects embedded deep within the structures were challenging to anneal. Taken together, these results indicate that slow growth, in the absence of precipitation, could be used to prepare large-area single-crystalline sheets.

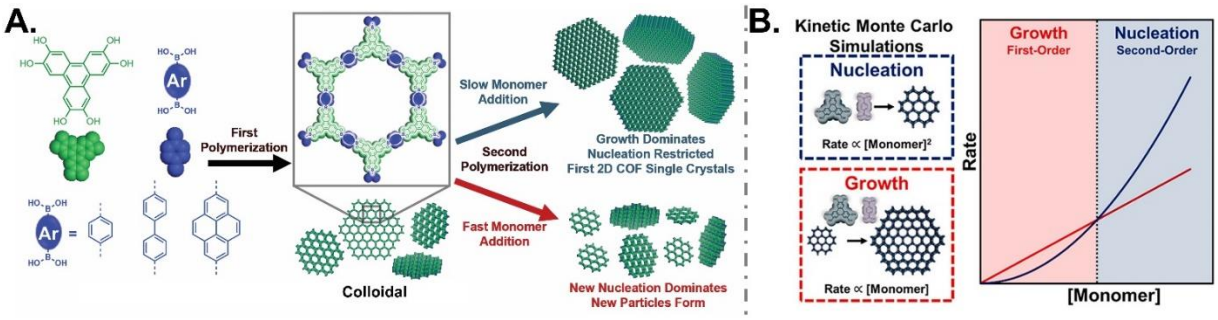

Figure 1.10. (A) Controlled growth and nucleation behavior in the presence of slow versus fast monomer addition to polymerized colloidal 2DP seeds.[126] **(B)** The two different regimes for nucleation and growth processes as a function of monomer concentration.

Soon after, Dichtel and coworkers realized that the precipitation of boronate-ester-linked 2DPs could be avoided by the inclusion of nitrile cosolvents in the reaction mixture.[125] By subverting irreversible crystalline aggregation, the authors were able to temporally resolve nucleation and growth processes in 2D polymerization for the first time.[126] This mechanistic understanding

enabled the first syntheses of isolable micron-sized 2DPs prepared through solution-based approaches (**Figure 1.10**). Additionally, because these crystalline 2DPs were stabilized as colloidal suspensions, the dynamics of the nucleation and growth processes were monitored using *in situ* X-ray diffraction.[144] By combining Monte Carlo simulations with experimental X-ray diffraction investigations, they showed that nucleation and growth are second- and first-order with respect to monomer concentration, respectively. Importantly, the observed rates led to the conclusion that slow monomer addition is likely to be impractically slow for growing crystals above the micron size regime since the polymerization of millimeter-sized 2DPs by this method would require growth times on the order of millions of years.[144] The realization that direct slow growth approaches were impractically slow in boron-based polymerizations led to the development of modulated-growth approaches, wherein monofunctional catechol additives prevented nucleation and allowed for more rapid polymerization.[127] As discussed above, it appears that the modulating species restricts growth in the in-plane direction and instead promotes growth in the out-of-plane direction. Though it is likely that other 2DP systems or combined synthetic strategies may enable rapid lateral growth through modulated approaches. Even so, nucleation-elongation is found to be a highly desirable mechanism for the preparation of high-quality 2DPs. However, the boron-based 2DPs that readily form by this mechanism rapidly nucleate, even at low monomer concentrations, which complicates their growth to arbitrarily large sizes. Taken together, controlled 2D polymerization approaches remain in their infancy. Therefore, we expect that strategies to polymerize a variety of 2DPs with practical rates will be of substantial interest as the field of solution-phase 2D polymerization continues to mature.

1.8. Amorphous-to-Crystalline Transitions

As theories regarding nucleation-elongation mechanisms in boron-based 2DPs were being developed, researchers observed that nitrogen-based 2DPs appeared to polymerize differently. Specifically, early mechanistic studies of imine-linked 2DP formation reported that polymerization of monomer species occurred rapidly to produce an initially amorphous, cross-linked gel.[146] It was then observed that this amorphous network polymer transiently reorganized through reversible transimination reactions to produce a thermodynamically preferred crystalline 2DP. Several follow-up reports also isolated amorphous low-surface-area networks that became more crystalline with higher surface areas after multiday reaction times.[147, 148] This slow transition was then expedited from days to minutes by replacing a traditional Brønsted acid catalyst with a more active Lewis acid catalyst.[148, 149] Furthermore, amorphous-to-crystalline transitions were observed in imine-linked macrocycles that were designed as 2DP analogues.[150] Similar to the investigations of nucleation-elongation mechanisms described above, the irreversible precipitation of 2DPs from solution makes the evaluation of dynamic processes in amorphous-to-crystalline transitions challenging. Recently, it was found that imine-linked 2DPs could be prepared as stable colloidal suspensions in acetonitrile.[151] By studying the polymerization of monomer species to 2DPs *via in situ* small- and wide-angle X-ray scattering, it was observed that growth proceeded by a slightly faster rate than crystallization.[151] These differential rates led the authors to conclude that amorphous particles were formed initially and then slowly crystallized over the course of the reaction. This conclusion was found to agree with other observations of transient amorphous phases in nitrogen-based 2DPs.[119, 146, 152-158]

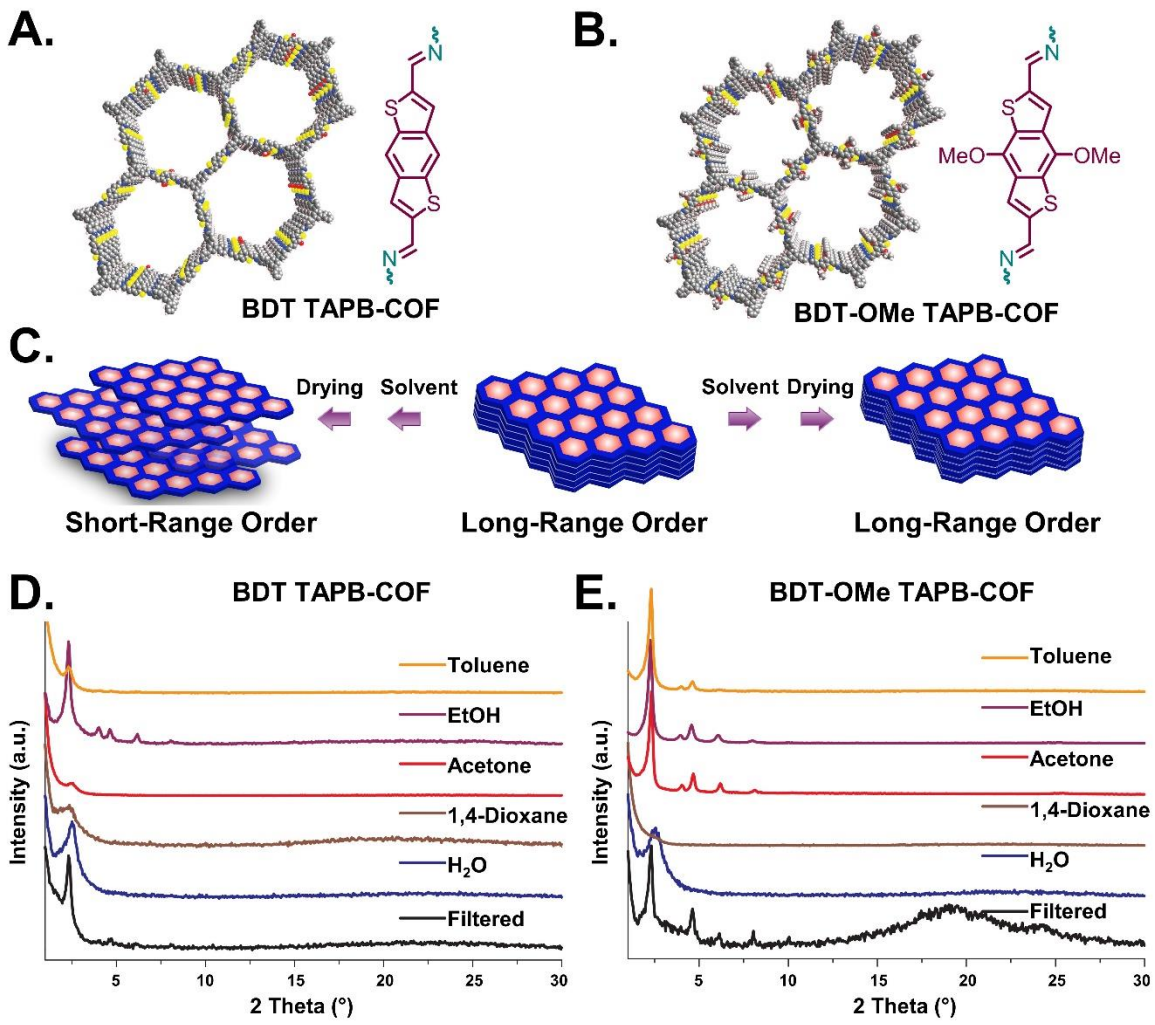

Figure 1.11. Chemical structure of the 2DPs known as **(A)** BDT TAPB COF and **(B)** BDT-OMe TAPB COF. **(C)** Transient reorganization of the 2DP layers during isolation and activation. X-ray diffraction patterns of either **(D)** BDT TAPB COF or **(E)** BDT-OMe TAPB COF that was immersed in a variety of solvents and then vacuum activated.[159]

Recently, Marder,[160] Bein,[159] and their coworkers have found that workup protocols used widely in 2DP syntheses can damage the isolated polymer structure, including the 2DPs that have been

studied extensively for their formation mechanisms (**Figure 1.11**). Both studies noted that by avoiding damaging workup conditions, high-quality 2DPs could be isolated more rapidly than initially reported. A subsequent report found that a 2DP, TAPB-PDA COF, previously reported to proceed through an amorphous-to-crystalline mechanism initially polymerized as few-layer disorganized 2DP sheets, when activated using gentler conditions. These species then slowly reorganized to produce well-layered stacks of 2DP sheets, which were more robust to conventional activation procedures. These results demonstrate that careful isolation of these early species may be critical to the preparation and exfoliation of few-layer 2DPs, which remains an important frontier in 2D polymerization. These reports demonstrate the enormous value of *in situ* characterization techniques and that great care must be taken when generating mechanistic conclusions by analysis of isolated products, especially those subjected to extensive workup protocols. Further development of *in situ* 2D polymerization monitoring techniques are likely to provide additional mechanistic insight and improved synthetic control. We speculate that a combination of mechanisms is active in all dynamic 2D polymerizations, the extent of which depends greatly on the polymerization conditions and polymer system studied. As an array of monomer systems and synthetic conditions has not been routinely studied for their mechanistic behavior, broad conclusions about the polymerization mechanism remain elusive.[83-85]

1.9. Interlayer Interactions

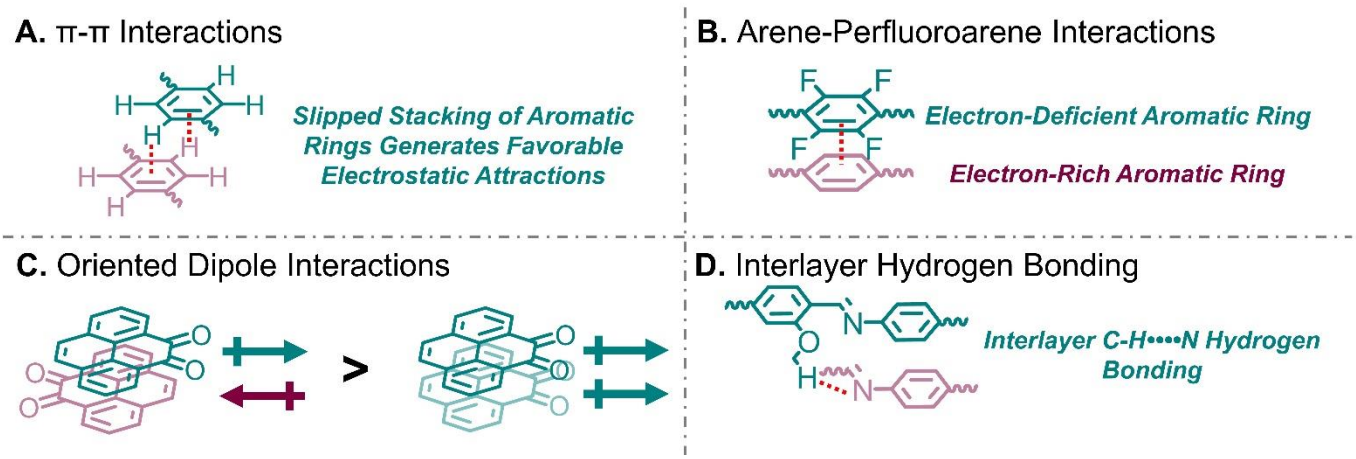

Figure 1.12. Interlayer interactions in 2DP sheets. **(A)** π-π interactions, **(B)** arene-perfluoroarene interactions, **(C)** dipolar interactions, and **(D)** hydrogen bonding.

Researchers have recently shown that noncovalent interlayer interactions greatly impact the dynamics of solution-based 2D polymerization and the resultant polymer quality (**Figure 1.12**). For example, Bein and coworkers showed how the self-assembly of tetraphenylethylene, pyrene, and dibenzochrysene monomers produces particularly crystalline 2DPs.[161-163] In these reports, the authors suggest that monomer self-assembly in adjacent 2DP layers limits the number of defects formed in the network, thereby increasing the fidelity of 2D polymerization. Importantly, these 2DPs were also observed to be more robust to withstanding workup procedures, which may be a result of their strong interlayer interactions further facilitating their isolation as high crystallinity and porous polycrystalline powders. Similar strategies aimed at enhancing 2DP quality through dipole interactions,[164, 165] hydrogen bonding,[166-170] arene-perfluoroarene interactions,[171, 172] and π-π interactions[162, 163, 173, 174] have all produced crystalline 2DP networks. However, competing

conclusions have been reached regarding whether 2DP stacking interactions should be increased or decreased to enhance 2DP crystallinity and porosity. As in all other aspects of 2D polymerization, a balance of factors is required to synthesize highly crystalline materials. For example, if interlayer interactions are too strong then defects will not be efficiently annealed from the structure. However, if they are too weak then defects become more prevalent since there is limited thermodynamic preference for a well-ordered material. Moreover, stronger interlayer interactions will likely prefer a 2DP system to form by desirable nucleation-elongation mechanisms, but this will likely be accompanied by diminished error correction capacity. These possibilities make manipulation of 2DP interlayer interactions and important frontier in 2DP synthesis.

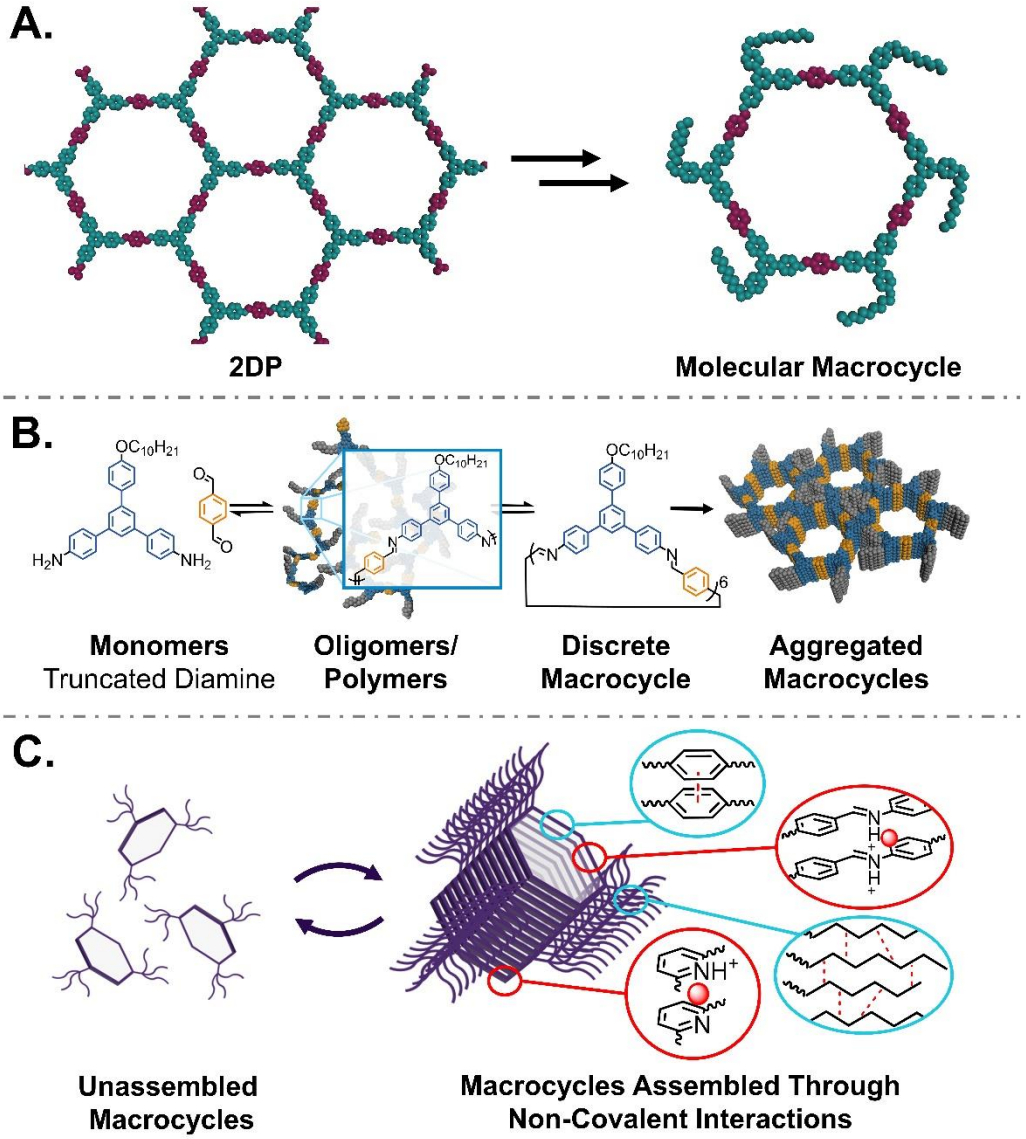

Figure 1.13. (A) Representative 2DP and its corresponding molecular macrocyclic analogue that is produced by truncating the polyfunctional node to restrict in-plane polymerizaton. **(B)** Mechanistic analysis of macrocycle polymerization that provides through an amorphous intermediate.[150] **(C)** Interlayer interactions in macrocycles that are assembled into one-dimensional nanotubes.

Evaluation of the mechanisms of solution-phase 2D polymerization is a complex endeavor because it involves a combination of in-plane covalent polymerization and out-of-plane noncovalent assembly. To circumvent the challenges associated with characterizing these processes simultaneously, researchers have studied molecular macrocyclic species as structural analogues of 2DPs (**Figure 1.13A**).[145, 150, 175-177] The first report with this paradigm found that boronate ester-linked macrocyclic assemblies became larger in the presence of a monofunctional modulating catechol. This behavior is analogous to the formation of boronate ester-linked 2DP formation. This result indirectly suggests that interlayer interactions may drive nucleation-elongation behavior, as has been found in several computational studies. By contrast, imine-linked macrocycles first formed as oligomers, which later transformed into the 2DP-inspired analogues (**Figure 1.13B**). This is reminiscent of an amorphous-to-crystalline transition that has been observed in nitrogen-based 2DPs, though the oligomers found here are mostly small (>10 repeat units) and soluble. Precipitation is driven in this case by interlayer forces that form small tubular aggregates *via* π-π interactions in their neutral state or high-aspect-ratio nanotubes in their protonated state.[150, 175-177] The formation of extremely robust ionic assemblies was also supported by molecular mechanic simulations,[177] which suggest that cohesive forces are on the order of the strength of C-C bonds at least. Going forward, we expect that using molecular and macrocyclic analogues to unravel molecular and interlayer interactions in 2DPs will be a productive area of research. Comparative observations between 2DPs and their macrocyclic analogues leads us to speculate that interlayer interactions are an important thermodynamic driving force of solution-phase 2D polymerization (**Figure 1.13C**). As such, structural engineering of 2DPs through interlayer supramolecular

interactions represents a new approach to managing solution-based 2D polymerization. For a more expansive exploration of stacking in 2DPs we direct readers to a recent review on this topic.[178]

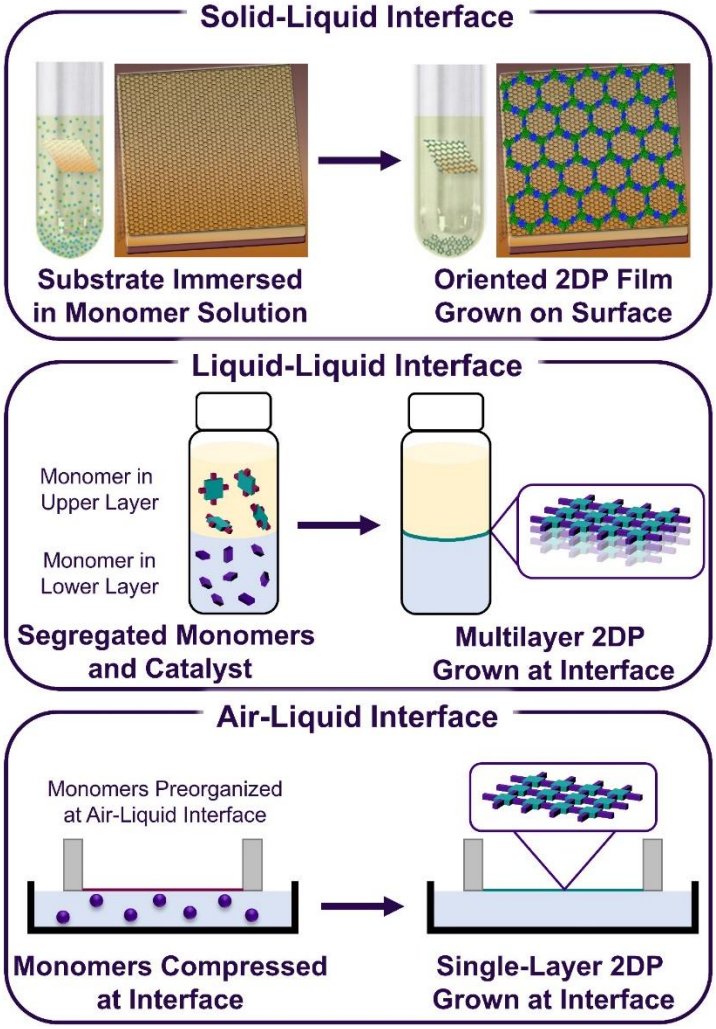

Figure 1.14. Different approaches used for interfacial 2D polymerization.

2.3.5 Solution-Based Interfacial Polymerization

Confining 2D polymerization to an interface limits the entropic penalty paid by transforming monomers to macromolecular sheets. For this reason, researchers have explored the preparation of

2DPs at many surfaces (**Figure 1.14**), including air-liquid,[179, 180] liquid-liquid,[147, 148, 181-183] and liquid-solid interfaces[158, 184-196]. In most cases, these syntheses not only take advantage of polymerization performed on a flat surface but also benefit from features such as dynamic bond formation or monomer preorganization. Below, we will explore these syntheses from a mechanistic perspective.

The first 2DP films were prepared by direct growth at solid-liquid interfaces. For example, immersing a graphene-supported substrate into a solution of monomer species showed that 2DPs readily form cofacially with the graphene surface.[184-186] The first report of this strategy speculated that the large van der Waals contact area and atomically flat surface both acted to template the formation of 2DPs polymerized from solution. Since the inception of this strategy, many other substrates and monomer systems have been shown to be amenable to this solid-liquid interfacial polymerization approach. Recently, mechanistic investigations into these solid-liquid 2D polymerizations revealed that the formation mechanisms on a surface are not wholly different from those observed in solution. For example, Liu and coworkers recently found that during the course of imine-linked 2D polymerization, an initially amorphous phase is observed before crystallization of the polymer film.[158] However, as discussed above, this 2DP system is particularly sensitive to workup, which may complicate mechanistic conclusions. Additionally, Dichtel and coworkers have recently found that the boronate ester-linked films prepared at solid-liquid interfaces under colloidal conditions likely proceed through a nucleation-elongation mechanism. Most importantly, they showed that monomers polymerize directly on a graphene surface, rather than first polymerizing in solution and then subsequently depositing. However, it was not possible to discern if small oligomers formed in solution prior to this on-surface polymerization. This direct growth

strategy produces some of the most crystalline and oriented 2DP films, which are ideal for many applications, including organic electronics. We suspect that as a mechanistic understanding of this strategy continues to develop, these approaches will continue to dominate the preparation of 2DP thin-film devices.

Strategies to prepare 2DPs at liquid-liquid and liquid-air interfaces have also been extensively developed. For instance, Zhang and coworkers deposited a tritopic amine and difunctional aldehyde onto a water surface and used Langmuir-Blodgett techniques to control their preorganization and polymerization.[180] In this case, precise structural characterization was not possible; however, characterization via Raman spectroscopy revealed the formation of the desired imine bonds. Soon after, Dichtel and coworkers prepared 2DPs at a liquid-liquid interface by segregating monomeric components and acid catalysts into separate phases.[147, 148, 197] Thick films polymerized by this method were characterized as 2DPs by grazing-incidence X-ray diffraction; however, thinner films produced by the same method did not provide an adequate diffraction signal to definitively establish their crystallinity. Banerjee and coworkers have also performed interfacial polymerization by segregating monomeric species into separate.[181, 198-201] Similar to early findings by Dichtel,[147, 148] Schlüter,[180] and others, few-layer 2DP films prepared by this strategy were immensely challenging to unambiguously characterize. However, this characterization challenge was recently overcome by Schlüter and coworkers, who showed that few- or single-layer 2DPs could be prepared by photoinduced [4+4]-cycloaddition at an air-water interface in a Langmuir-Blodgett trough.[202] These monolayer films were characterized by non-contact atomic force microscopy and scanning tunneling microscopy, which both showed the expected hexagonal

crystal structure. This was a major advance for 2D polymerization because it definitively demonstrated that monolayer 2DPs can be prepared through solution-based methods.

In addition to the use of dynamic bonds, other complementary strategies have been explored at a variety of interfaces. For example, Park and coworkers recently polymerized high-quality imine-linked 2DPs by slow introduction of monomers to a liquid-liquid interface.[203] Through this approach, they presumably controlled the nucleation and subsequent growth of 2DPs at this interface, which permitted the synthesis of monolayer 2DPs that were unambiguously characterized via scanning tunneling microscopy. Moreover, the approach of slow monomer introduction allowed for the creation of 2D heterostructures that may exhibit interesting physical phenomena.[203] As another example of a complementary interfacial polymerization strategy, Cuniberti, Dong, Feng, and coworkers prepared boronate-ester-linked porphyrinic 2DP films *via* a surfactant-monolayer-assisted method.[204] In this case, sodium oleyl sulfate guided the arrangement of a C_4 symmetric porphyrin monomer through supramolecular interactions, reducing its mobility at the interface and leading to the realization of highly crystalline 2DP films, as characterized by direct imaging via transmission electron microscopy. The surfactant-directed preorganization operative in this case likely contributed to the high-quality 2DPs prepared this way. Taken together, these reports demonstrate that combining approaches to control interfacial 2D polymerization is a promising method to prepare high-quality 2DP films down to the monolayer limit. For more extensive reading on this topic, we direct readers to several recent reviews of this topic.[83-85, 104, 205, 206]

Solution-based 2D polymerization is the most synthetically general method for the preparation of macromolecular sheets. The vast synthetic toolkit available to tune solution-phase reactivity and

polymerization processes undoubtedly contributes to this reality. However, challenges associated with irreversible precipitation and aggregation continue to limit the size of 2DPs prepared through solution-phase chemistries. While preliminary efforts have been made to address these limitations, the majority of 2DPs prepared with solution-based chemistry are still obtained as microcrystalline powders or polycrystalline films. However, recent efforts to combine dynamic bond-forming reactions with monomer preorganization and controlled polymerization processes are promising for the preparation of high-quality 2DPs. We suspect that as these complementary approaches mature, substantial progress will be made toward the reliable preparation of many 2DPs as large-area sheets.

1.10 Solvothermal Polymerizations

Solvothermal 2D polymerization is conducted by reacting solubilized topologically regular monomers at elevated temperatures to produce macromolecular sheets.[84] Typically, this produces insoluble polycrystalline 2DP powders or films that can be characterized by powder X-ray diffraction or grazing-incidence X-ray diffraction. Early iterations of this strategy assumed that dynamic bond-forming events were required to effectively produce macromolecular sheets. However, as solution-based strategies have matured, several irreversible polymerization chemistries have been demonstrated to produce 2DPs.[86, 207-210] Successful solution-based 2D polymerization likely relies on a confluence of factors including the efficiency of bond-forming reactions, topological regularity of monomers, and the energetic landscape of particular polymer systems. Regardless of these ambiguities, solution-based 2D polymerizations can be fine-tuned to optimize the successful synthesis of macromolecular sheets. For this reason, solution-based approaches are the most synthetically general 2D polymerization method, with more than 500 distinct structures produced through over 20 different polymerization chemistries, including linkages that rely on B-O, B-N, N-N, C-N, and C-C bond formation (**Figure 1.15**).[83-85, 110, 211] Many of these functionalities are a direct result of the reaction between monomers, though others are more easily accessed through post-synthetic modification of pre-polymerized 2DPs.[212] Moving forward, we anticipate that this rapid expansion of solution-based polymerization chemistries will continue, greatly increasing the scope of available 2DP structures and properties accessible through these methods. Here, we will describe the chemical structures of 2DPs produced through solution-based strategies.

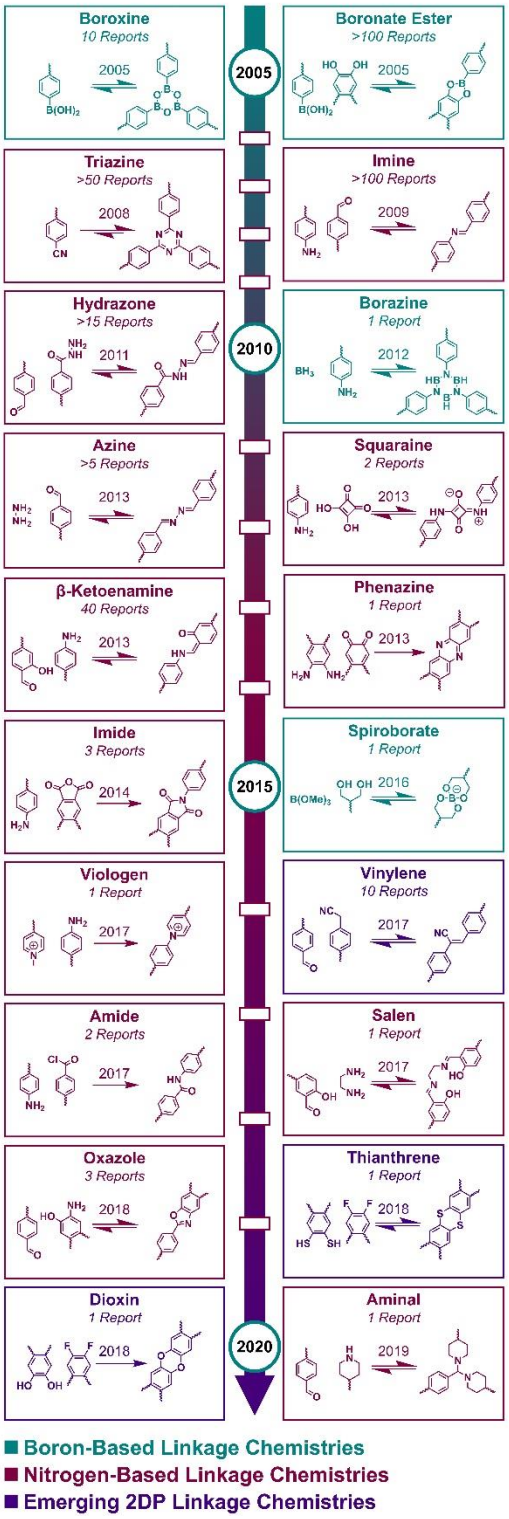

Figure 1.15. A timeline of solution-based chemistries used to prepare 2DPs.

1.11 Boron-Based Polymerization Chemistries

Yaghi and coworkers reported the first solution-based 2D polymerization that used the dehydrative trimerization of 1,4-phenylenebis(boronic) acid to produce a hexagonal boroxine-linked 2DP (reported as COF-1).[41] As a testament to the synthetic versatility of dynamic polymerization, this reversible condensation-hydrolysis reaction pair was quickly generalized for several 2D boroxine-linked networks using different polyfunctional aryl boronic acids (**Figure 1.16**).[213-218] Similar to linear polymerizations, various reaction conditions (e.g., solvents, temperatures, workup conditions) are suitable for the polymerization of boroxine-linked networks. Presumably, the ability to tune 2D polymerization conditions, such as adjusting the solvent to promote dynamic chemistry and monomer solubility, has contributed to the large number of structures accessed by dynamic 2D polymerization.[88, 219-229]

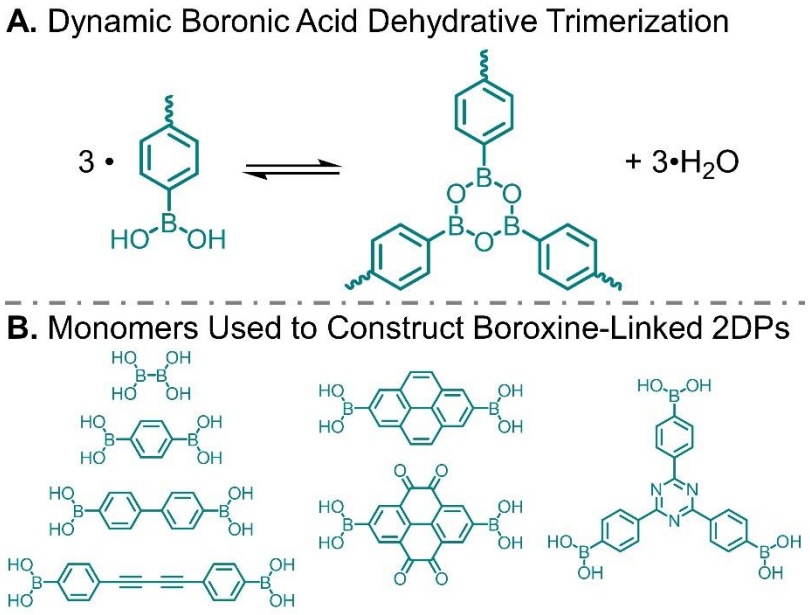

Figure 1.16. (A) Boronic acid dehydrative trimerization to produce boroxine-linked 2DPs. **(B)** Monomers used to prepare boroxine-linked 2DPs.

Boroxine-linked networks are, as a consequence of their reversible condensation chemistry, prone to depolymerization in the presence of water.[228] This hydrolytic instability is intrinsically linked to the highly reversible nature of these networks, which likely contributed to their early discovery. Despite this hydrolytic instability, boroxine-linked 2DPs are useful model systems since they are polymerized from a single monomer, which simplifies the stoichiometric balancing and rationalization of their emergent properties. For example, Jiang, [62] Dichtel,[63] and their coworkers have used boroxine-linked 2DPs to study intersheet electronic communication, which is more straightforward in single-chromophore networks than their multicomponent counterparts. As such,

boroxine-linked networks will continue to be valuable for studies that benefit from single-component 2D polymer systems. However, the hydrolytic instability of boroxine-linked 2DPs will likely limit an expansive investigation of boroxine-linked 2DPs, as they can be challenging to isolate and investigate.

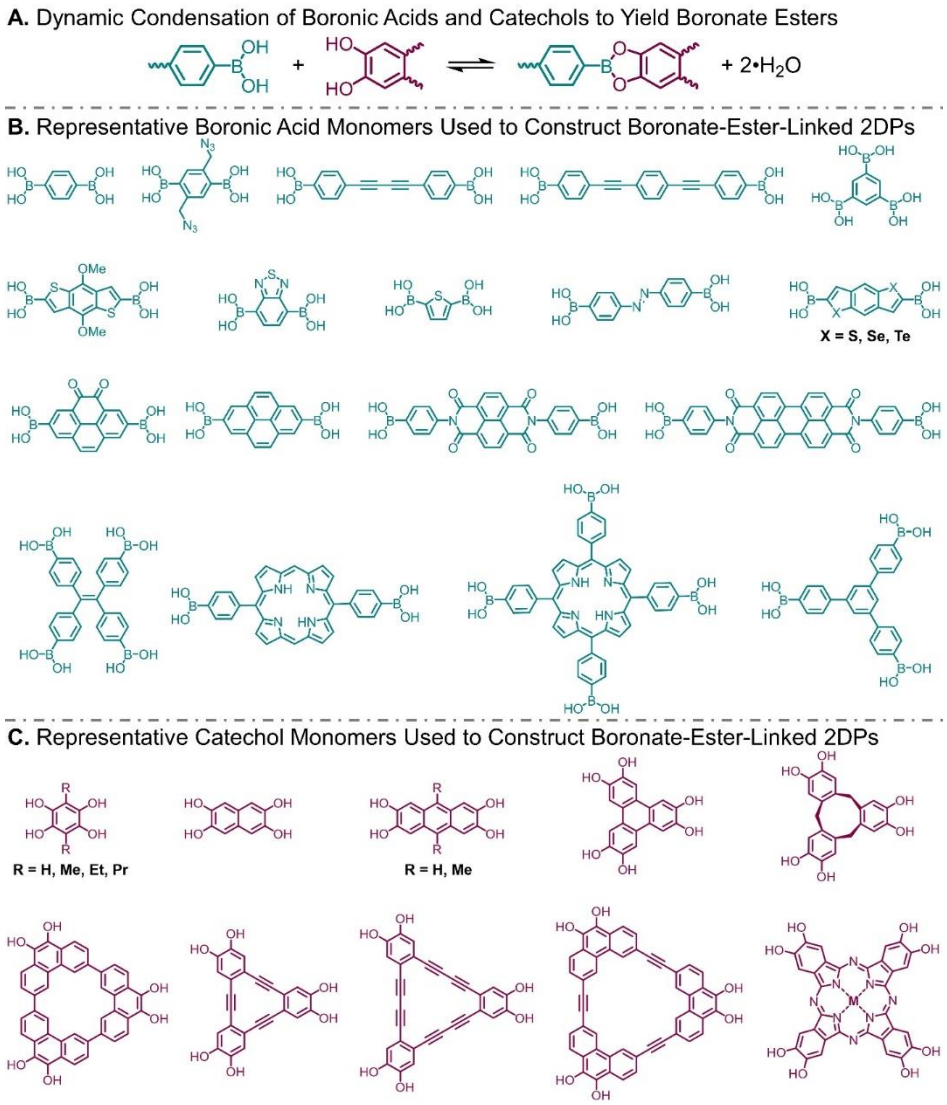

Figure 1.17. (A) Boronate-ester condensation reaction. **(B)** Representative boronic acid monomers used to prepare boronate-ester 2DPs. **(C)** Representative catechol monomers used to prepare boronate-ester 2DPs.

Bifunctional boronic acids condense with polyfunctional catechols to form boronate-ester-linked 2DPs (**Figure 1.17**).[41] To date, dozens of boronate-ester-linked 2DPs have been reported. In nearly

all cases, boronate-ester-linked 2DPs are prepared as polycrystalline powders by the direct condensation of polyfunctional aryl boronic acids and catechols, though notable exceptions will be described below. Importantly, boronate-ester-linked 2DPs are known to be more hydrolytically stable than their boroxine-linked counterparts.[156, 230-232] Enhanced hydrolytic stability combined with the vast number of easily accessible monomer species has made boronate-ester-linked 2DPs one of the most explored 2DP classes.

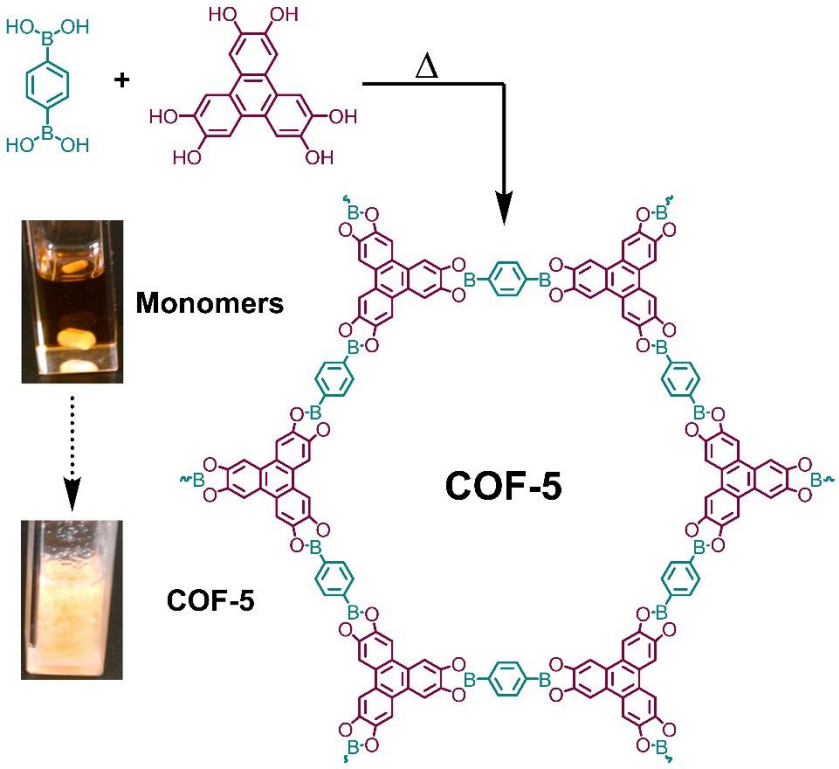

Figure 1.18. Conventional synthesis of the 2DP COF-5, and optical images of its starting appearance and final powder morphology.[121]

The first boronate-ester-linked 2DP (COF-5) was synthesized by heating 1,4-phenylenebis(boronic) acid and hexa(hydroxy)triphenylene until the network precipitated from solution (

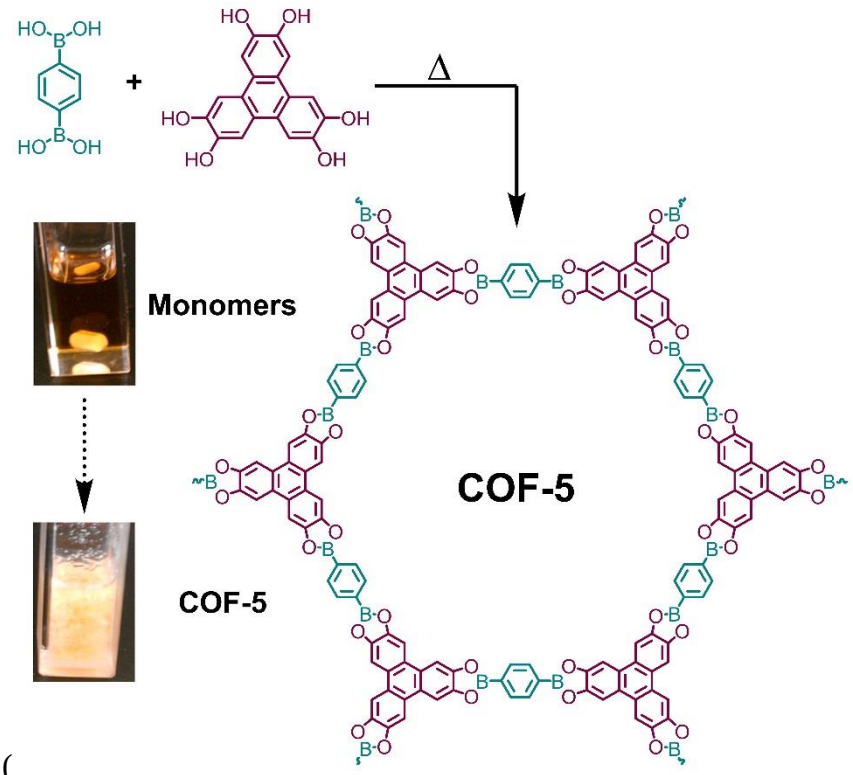

Figure 1.18).[41, 120, 121] Following this demonstration, various researchers expanded the number of suitable monomers to include other molecular motifs such as benzenes,[41, 59, 120, 121, 125, 191, 233-235] thiophenes,[236-238] anthracenes,[239] biphenylacetylenes,[174] triphenylenes,[41, 118, 125-127, 144, 234] truxenes,[240] tetraphenylethylenes,[241] porphyrins,[242, 243] phthalocyanines,[185, 242, 244-249] and their functionalized derivatives (**Figure 1.17B and 6C**). Boronate-ester condensation can occur under many conditions (*e.g.* solvents, temperatures, reaction times), which has facilitated the incorporation of many monomer classes into these networks. This tunability, combined with the reversible nature of the condensation, the planarity of catechol boronate-esters, and the large

availability of monomer species has driven the rapid generalization and investigation of boronate-ester-linked 2DPs.

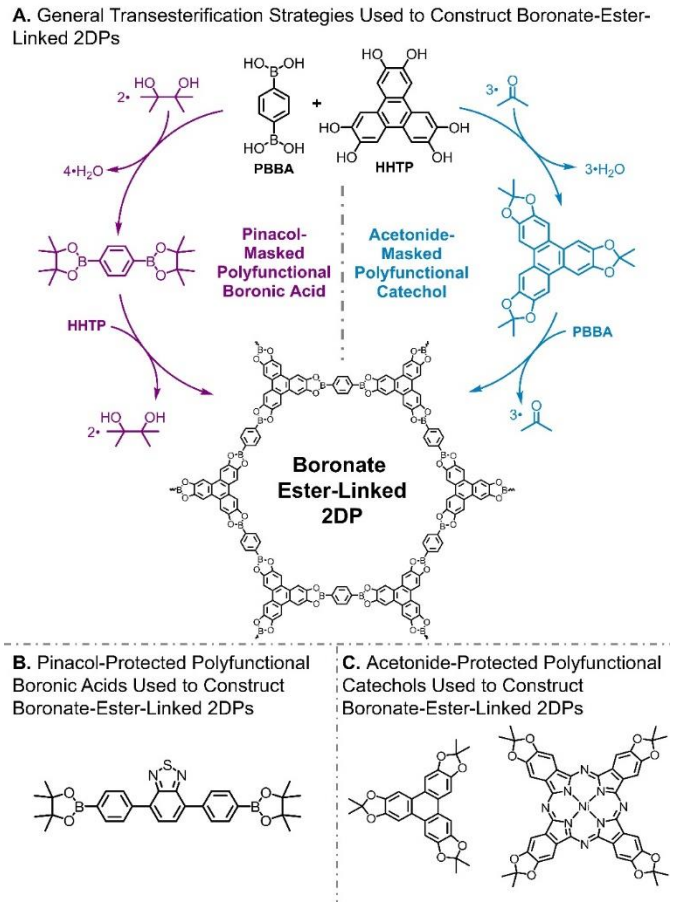

Figure 1.19. (A) Protected monomer strategies for the synthesis of boronate-ester-linked 2DPs. **(B)** Pinacol-protected boronic acids and **(C)** acetonide-protected catechols that have been used to prepare boronate-ester linked 2DPs.

In addition to the direct condensation of monomeric species, unreactive protected monomers can be used as 2DP precursors2 (**Figure 1.19**). For example, Bein and coworkers synthesized a

mesoporous boronate-ester-linked 2DP by the acid-catalyzed transesterification of pinacol-ester-protected boronic acids (**Figure 1.19B**).[122] This indirect approach allowed for the synthesis of high-quality 2DPs that were challenging to polymerize directly from catechols and boronic acids. The use of pinacol-ester-protected boronic acids affords two primary benefits to the 2D polymerization. First, it slows 2D polymerization, which limits nucleation and enhances annealing of molecular defects. Second, it increases the solubility of boronic acid monomers and their oligomers, which presumably leads to larger and more-crystalline 2D networks prior to precipitation. In a similar fashion, boronate-ester-linked 2DP formation has been achieved by deprotecting tris(acetonide)-protected polyols *in situ* that then react with free boronic acids (**Figure 1.19C**).[247, 249] This strategy has several advantages including that tris(acetonide)-protected polyols have increased solubility and are more oxidatively stable than their free polyol counterparts. These features allow for the synthesis of higher quality 2DPs than were obtained *via* direct condensation between unprotected monomers. As such, these protection-and-deprotection strategies remain a viable option for obtaining 2DPs that are challenging to produce by direct condensation of free catechols and boronic acids. However, as precipitation introduces an irreversible kinetic trap to these polymerizations, it can be challenging to determine the effects of these additional synthetic components.[119, 145] Taken together, the extensive number of monomers successfully polymerized through boronate-ester chemistry establishes this as one of the most synthetically versatile classes of 2DPs to date.

While other boron-linked 2DPs have been reported, an understanding of their syntheses, chemical variability, and intrinsic properties has been elusive. For example, El-Kaderi and coworkers synthesized a borazine-linked 2DP upon the thermal decomposition of an aminoborane under inert

atmosphere.[250] This crystalline network was shown to have high thermal stability and high surface area. It stored 1.5 wt% hydrogen gas at 1.0 bar and 77 K, which increases to 2.48 wt% at 15 bar. However, continued exploration of borazine-linked 2DPs has been limited by their substantial hydrolytic instability, which requires that their synthesis, isolation, purification, and characterization be conducted in a rigorously dry atmosphere. As another example of the diversity in boron-based 2D polymerization chemistries, aliphatic diols have been condensed with boronic acids to yield permanently ionic spiroborate-linked 2DPs that are of interest as solid electrolytes.[251, 252] Boronic acids have also been condensed with silanols to produce borosilicate-linked 3D frameworks, but this reaction has not yet been generalized to 2D polymerization.[253] While these 3D materials are beyond the scope of this review, these polymers show that enhanced hydrolytic stability can be imparted to crystalline polymers when boron linkages are four, rather than three, coordinate.

1.12 Schiff-Base Two-Dimensional Polymerizations

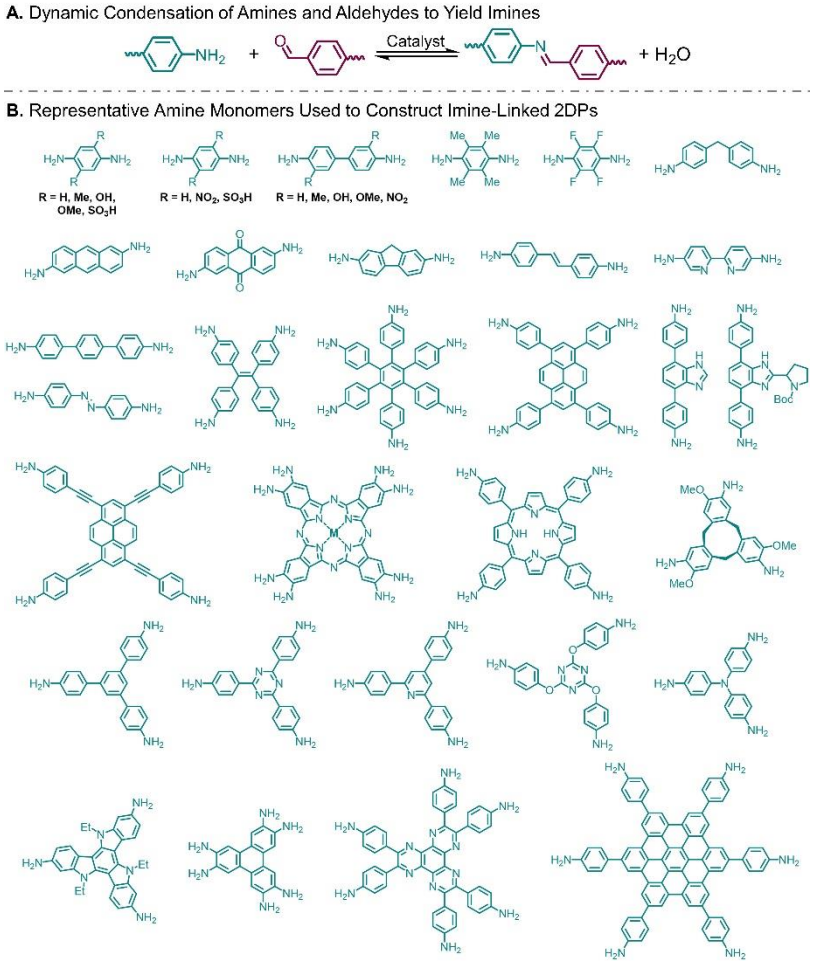

Figure 1.20. (A) Catalyzed reversible condensation of amines and aldehydes to produce imines. **(B)** Representative amine-functionalized monomers used to produce imine-linked 2DPs.

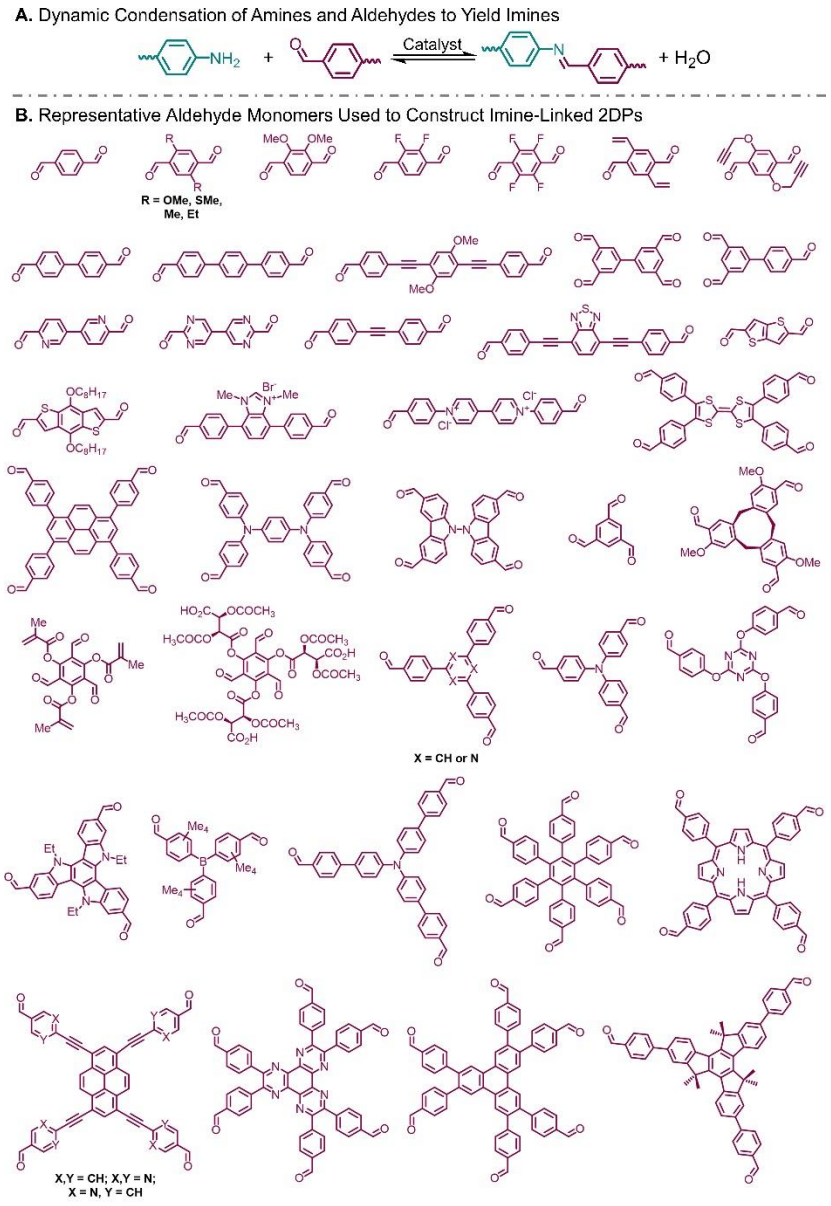

Figure 1.21. (A) Catalyzed reversible condensation of amines and aldehydes to produce imines. **(B)** Representative aldehyde-functionalized monomers used to produce imine-linked 2DPs.

Since the earliest reports of dynamic, boron-linked 2DPs, it was speculated that the reversible nature of boroxine and boronate-ester polymerization chemistries would lead to their spontaneous

depolymerization in the presence of water. Motivated to address the limited hydrolytic stability of boron-linked 2DPs, researchers began exploring dynamic Schiff-base 2D polymerization chemistries.[254] The enhanced hydrolytic stability, extensive monomer scope, and generalizable reaction conditions of Schiff-base-linked 2DPs has led to their expansion into the most explored and structurally diverse 2DPs (**Figure 1.20** and **Figure 1.21**).

Imine formation occurs by the condensation of an aldehyde and an amine (**Figure 1.20A**) and is the first and most well-studied Schiff-base 2D polymerization. Imine-linked systems have several advantages that have led to their expansion into the largest and most actively investigated 2DP classes. First, imine linkages are highly stable in neutral water and most organic solvents, unlike their boron-linked counterparts.[45] Second, a vast array of polyfunctional amines and aldehydes are available from commercial sources or short synthetic routes, providing efficient access to numerous structures (**Figure 1.20** and **Figure 1.21**). As a result, more than 200 imine-linked 2DPs have been reported.[255] For a comprehensive listing of monomers used to synthesize imine-linked frameworks, we direct readers to several recent reviews that explore the topic of imine-linked 2DPs more deeply.[83-85, 102, 205, 254, 256]

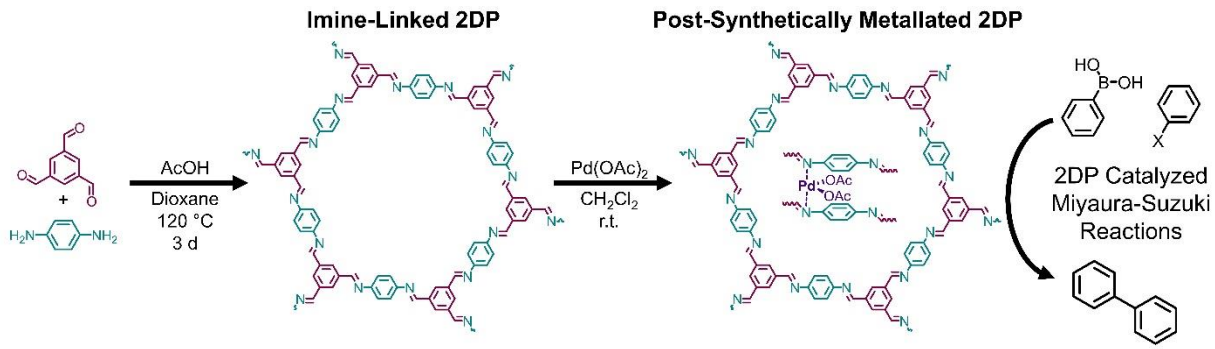

Figure 1.22. Synthesis of the first imine-linked 2DP, its proposed association with $Pd(OAc)_2$, and its subsequent use as a catalytic support.[257] Recent findings by Platero-Prats, Zamora, and coworkers found that Pd nanoparticles may also be operative in this cross-coupling reaction.[258]

The first use of dynamic imine formation to prepare topologically regular polymers was the synthesis of a 3D framework, COF-300, through the condensation of tetra-(4-anilyl)methane and terephthaldehyde.[259] Soon after this study demonstrated that dynamic imine chemistry could yield periodic 3D networks, Wang and coworkers condensed 1,3,5-triformylbenzene and 1,4-diaminobenzene into a crystalline 2DP.[257] This network's high hydrolytic stability allowed for its post-synthetic metallation with palladium acetate, which was used as a solid-state Suzuki-Miyaura catalytic support (**Figure 1.22**). This preliminary report demonstrated that imine-linked 2DPs form under catalyzed dynamic polymerization reaction conditions and are stable under a wide range of post-polymerization conditions, including exposure to water. This reasonable hydrolytic stability has driven the rapid expansion and investigation of imine-linked 2DPs.

The strategy used to prepare imine-linked 2DPs was quickly found to be general for the polymerization of other aromatic monomers including benzene,[130, 146-148, 151, 257, 260-267] anthracene,[268] thiadiazoline, pyrene,[188, 268] triazine,[269] tetrathiafulvalene,[270] hexaphenylbenzene,[271]

hexabenzocoronene,[271] pyridine,[272-277] hexaazatriphenylene,[278] tetraphenylethylene,[279] thiophene,[188, 280-282] porphyrin,[187, 283-289] and many functionalized derivatives (**Figure 1.20** and **Figure 1.21**).

Recently, Dichtel and coworkers developed a solvothermal transimination strategy to prepare highly crystalline imine-linked 2DPs (**Figure 1.23**).[124] Similar to the protection of polyols described above, amines protected by *N*-aryl benzophenones are generally more soluble and oxidatively stable than their free-amine counterparts. Additionally, because *N*-aryl benzophenone imines are sometimes produced as synthetic precursors of aryl amines, using them directly as monomers is also desirable. Similarly, the protection of aldehyde-functionalized monomers as acetals has also been explored to increase their solubility.[290] Taken together, the nearly limitless number of amine- and formyl-functionalized molecules, the diverse synthetic conditions suitable for their polymerization, and the enhanced hydrolytic stability of the resultant networks have enabled the broad investigation of imine-linked 2DPs. We expect that as mechanistic understanding of 2D imine polymerizations improves to the point where large-domain 2DPs can be generated as single crystals, these materials will be examined for their fundamental properties and will find applied use.

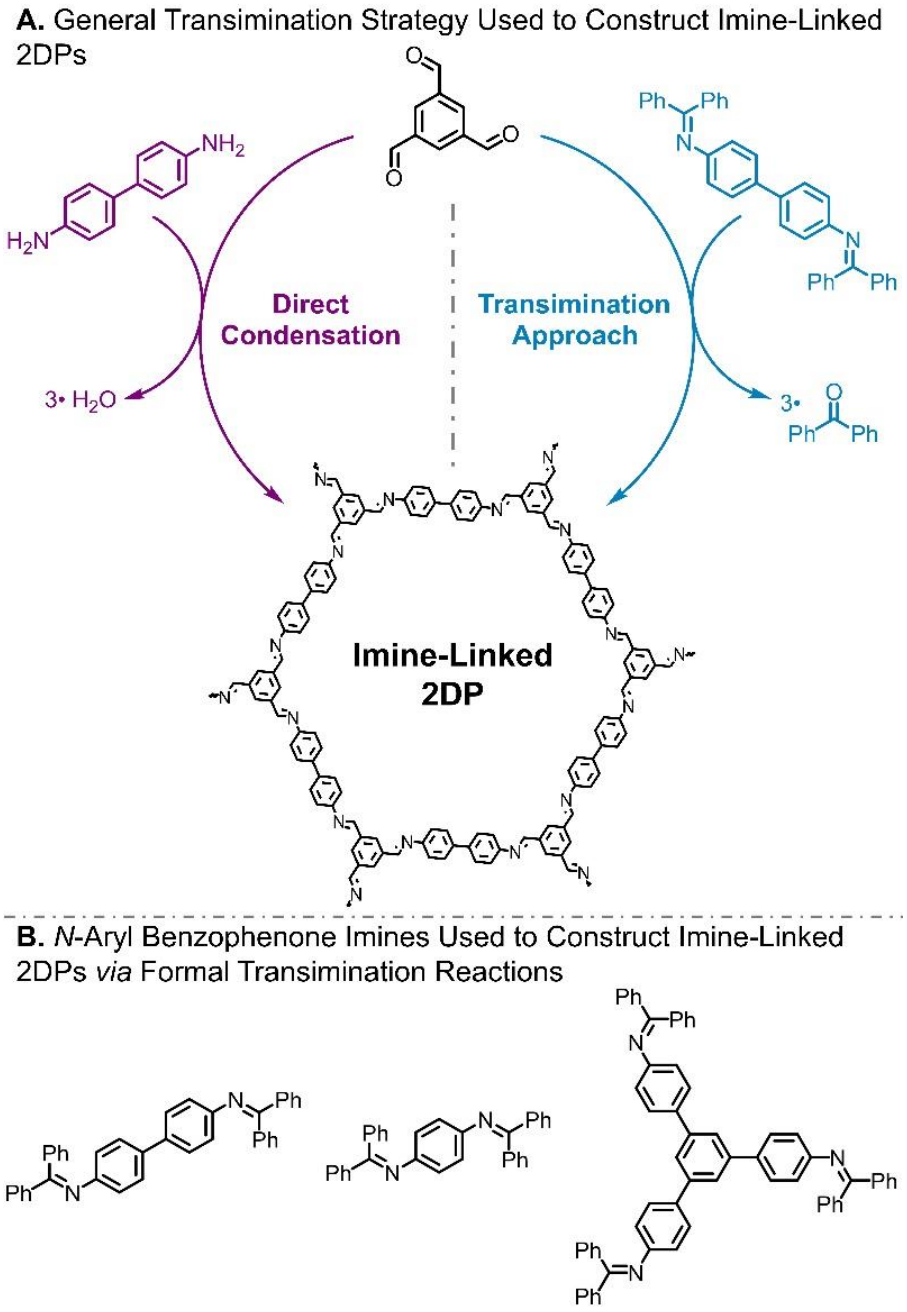

Figure 1.23. (A) Formal transimination strategy used to polymerize imine-linked 2DPs. **(B)** *N*-aryl benzophenone-protected amine monomers demonstrated as amenable to this approach.[124]

Expanding the scope of Schiff-base condensations for 2DP synthesis, Yaghi and coworkers reported hydrazone-linked 2D COFs from the condensation of aldehydes and acyl hydrazides, which effectively function as amines.[291] Soon after, Dichtel and coworkers noted that the weaker interlayer interactions of hydrazone-linked 2DPs, which arise as a consequence of their reduced planarity, lead to exfoliation of 2D sheets upon exposure to common organic solvents.[292] Similarly, Lotsch and coworkers designed a hydrazone-based 2DP capable of photocatalytic hydrogen production, which is enhanced upon exfoliation.[293] Other hydrazone-linked 2DPs have also been prepared *via* the direct condensation of aldehydes and acyl hydrazides. However, the structural flexibility of hydrazone-linked 2DPs makes their full characterization more challenging than that of more structurally rigid boronate-ester- and imine-linked 2DPs.[294-298] Additionally, the cumbersome synthetic routes and limited stability of acyl hydrazide monomers and the resulting 2DPs have constrained a more thorough exploration of this 2DP class.

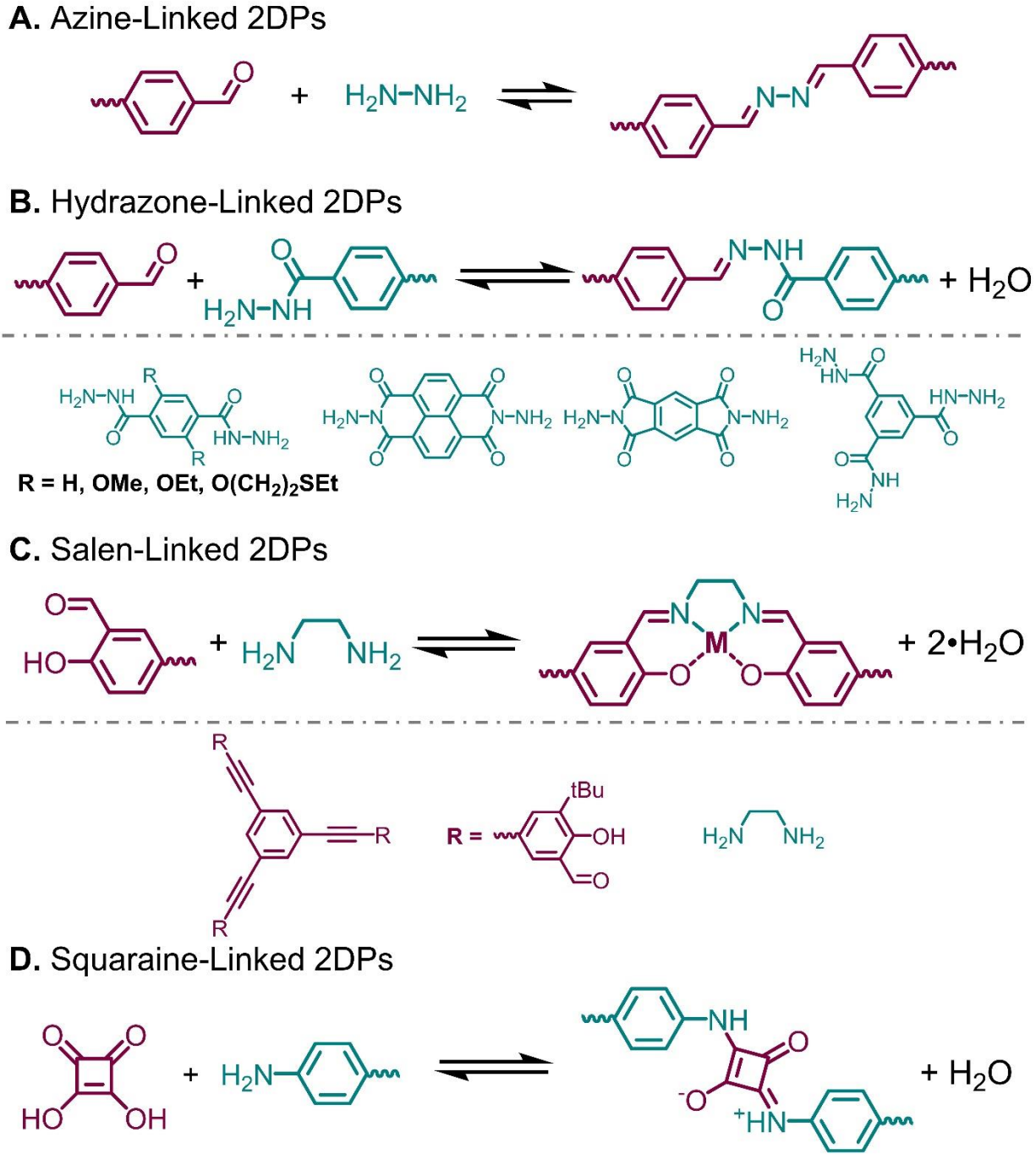

Figure 1.24. Other Schiff-base 2D polymerization linkage chemistries including **(A)** azines, **(B)** hydrazones, **(C)** salens, and **(D)** squaraines.

Similar to the use of acyl hydrazides as amine building blocks for Schiff-base 2D polymerization, alternative monomer sources that function effectively as either aldehydes and amines have also been explored (**Figure 1.24**). For example, hydrazine was used in place of a difunctional aryl amine to generate azine-linked frameworks (**Figure 1.24A**), and squaric acid was used as a carbonyl source to access squaraine-linked 2DPs (**Figure 1.24D**).[299-304] Nonaromatic alkyldiamines have been used to prepare salen-linked 2DPs (**Figure 1.24C**).[305, 306] Although the properties of these 2DPs have not been fully explored, differences in these linkage chemistries will likely lead to properties not available in other 2DP systems. For example, the photo-switchable character of azines can lead to dynamic switching behavior driven by light. Similarly, the ionic character of squaraines is of interest for applications that require structurally embedded ionic sites, such as porous solid-state electrolytes.[302, 303, 307, 308] Additionally, salen moieties have been used to reliably coordinate transition metals, which then function as single-site heterogeneous catalysts.[305, 306] The vast monomeric diversity in imine-linked 2DPs indicates that a similar degree of chemical versatility is synthetically feasible in other Schiff-based systems.[254] By tuning the monomer design while taking advantages of the stability and unique properties associated with different Schiff-based chemistries, an array of new functional materials are likely to emerge. As such, substantial opportunity remains for synthetic chemists to design and prepare monomers amenable to the polymerization of these other 2DP systems.

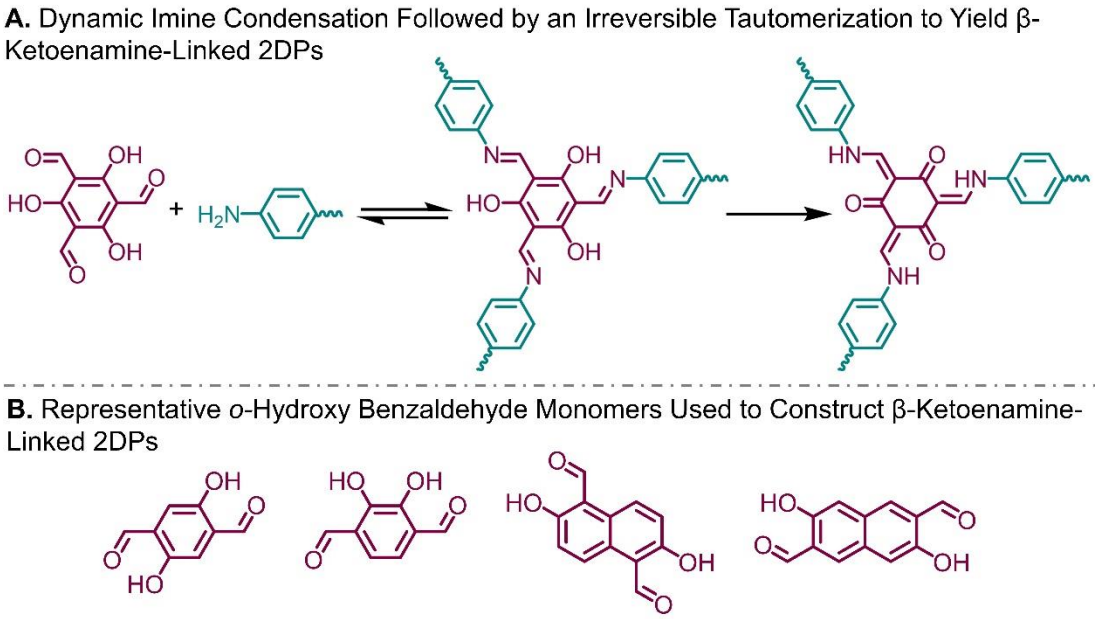

Figure 1.25. (A) Combined reversible-irreversible route to produce β-ketoenamine-linked 2DPs by imine condensation followed by tautomerization. **(B)** The *o*-hydroxybenzaldehyde monomers used to prepare β-ketoenamine-linked 2DPs.

While the reversibility of conventional Schiff-base condensation has resulted in a library of synthetically diverse 2DPs, the long-term stability of imine-linked 2DPs may still be limited in acidic or basic environments. To access 2DPs that are stable under more demanding conditions, Banerjee and coworkers developed a strategy to synthesize β-ketoenamine-linked 2DPs , which combined reversible and irreversible condensations.[309] Reacting polyfunctional *o*-hydroxybenzaldehyde monomers with polyfunctional aromatic amines under acidic conditions first establishes a dynamic equilibrium between the monomeric form and the corresponding imines. A less reversible keto-enol tautomerization occurs upon formation of the third imine, leading to the formation of chemically robust β-ketoenamine linkages. This realization has led to

the development of β-ketoenamine-linked 2DPs for applications that require stability in demanding chemical environments, such as sulfuric acid supporting electrolytes in some energy storage devices.[130, 166, 260, 276, 309-325] While β-ketoenamine-linked 2DPs are desirable for their chemical stability, historically they have been challenging to synthesize and are obtained primarily as polycrystalline powders with domain sizes smaller than those of their imine-linked counterparts. This low materials quality may be due to poor control over the rate of irreversible tautomerization, which limits error correction. Recently, Dichtel and coworkers synthesized higher-quality β-ketoenamine-linked 2DPs *via* a monomer exchange strategy from imine-linked 2DP analogues.[130] Starting from an imine-linked 2DP obtained from the condensation of polyfunctional amines and 1,3,5-triformylbenzene, the authors demonstrated that the 1,3,5-triformylbenzene units can be quantitatively exchanged with triformylphloroglucinol. This strategy produced highly crystalline β-ketoenamine-linked 2DPs, including examples that had been challenging to obtain by direct condensation. Taken together, β-ketoenamine-linked 2DPs are promising candidates for applications where chemically robust materials are needed. However, one major limitation for β-ketoenamine-linked 2DPs is that polyfunctional *o*-hydroxybenzaldehyde monomers are not readily available, and their preparation at large scales is not synthetically trivial. We anticipate that if synthetically efficient routes for these monomers can be developed, then the full potential of β-ketoenamine-linked 2DPs will be explored more thoroughly.

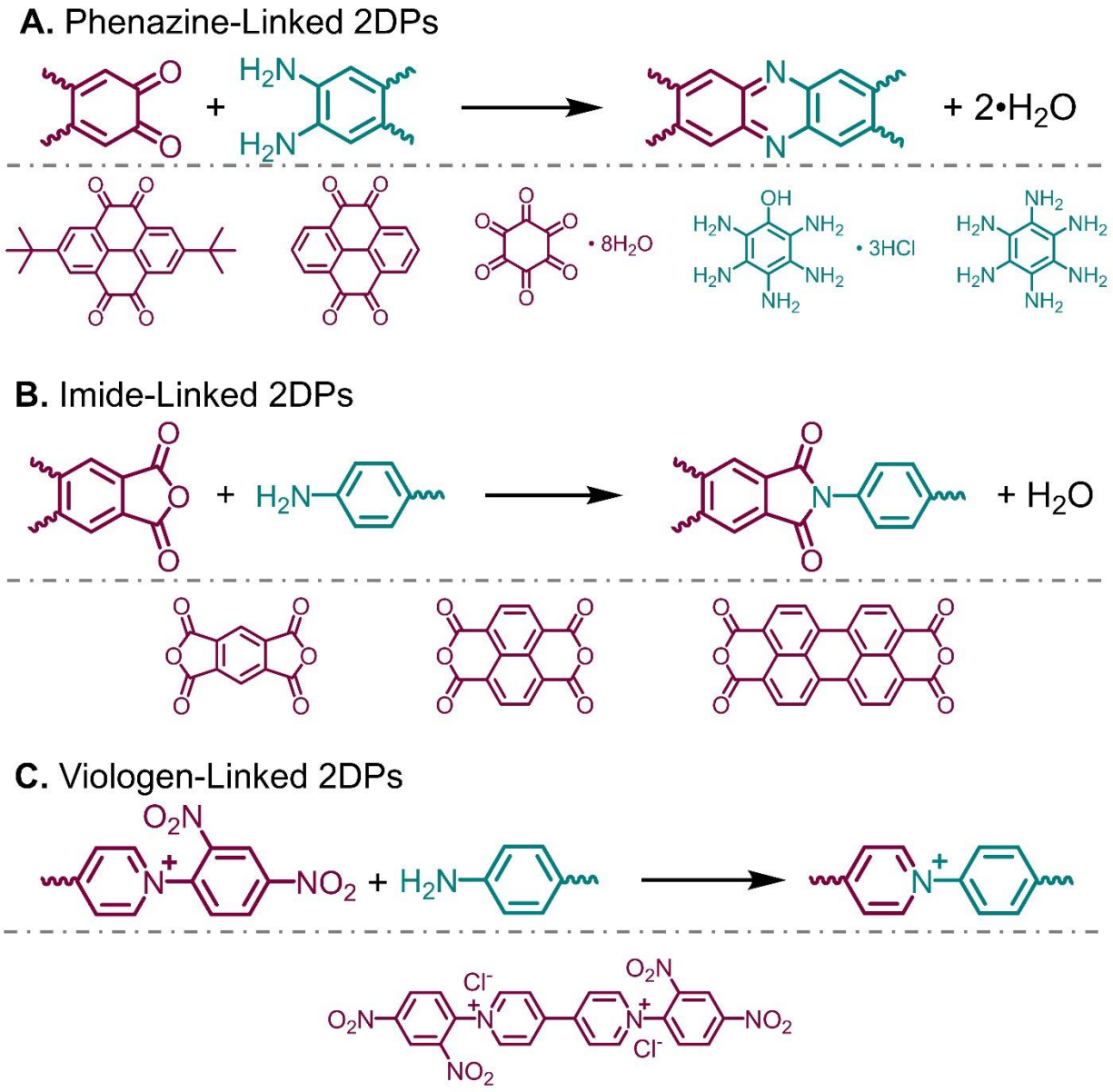

Figure 1.26. Aniline-based 2D polymerizations including **(A)** phenazine, **(B)** imide, and **(C)** viologen formation. These reactions are presumably irreversible once the final product is formed, although intermediate steps in their formation might be reversible.

Recently, imidization of a bifunctional pyromellitic dianhydride with aromatic triamines was used to synthesize imide-linked 2DPs (**Figure 1.26B**).[326] Soon after this demonstration, this synthetic approach was quickly generalized for the preparation of several other imide-linked 2DPs.[140, 142, 143, 327-329] Imide polymerization chemistry is significantly different from the Schiff-base chemistries discussed to this point because imidization is almost certainly irreversible under the polymerization conditions studied. Likewise, several other irreversible nitrogen-based chemistries have also been found to be amenable to the polymerization of 2DPs, as judged by their powder X-ray diffraction patterns. For example, crystalline viologen-linked frameworks were synthesized using the Zincke reaction by Trabolsi and coworkers (**Figure 1.26C**).[330] and 1,2-aromatic diamines were successfully condensed with polyones to generate phenazine-linked frameworks by Jiang and coworkers (**Figure 1.26A**).[331] Like the β-ketoenamine-linked 2DPs discussed above, these irreversible condensations might feature dynamic elementary reaction steps that allow for substantial error correction, which are locked into place through irreversible bond formation. Alternatively, the formation of these ordered networks, as characterized by powder X-ray diffraction, porosimetry, and electron microscopy, may be attributed to the ability of rigid monomers to form sufficiently large periodic domains without the benefits of dynamic error correction. Further mechanistic study of these 2D polymerizations is needed to differentiate these possibilities. In any case, these chemistries have led to the successful synthesis of far fewer 2DPs than more-dynamic polymerization chemistries such as imine or boronate-ester condensation. Additionally, it is currently unclear if these chemistries will be amenable to the synthesis of large-area single crystals. Notably, as a consequence of this reduced dynamicity, these networks are substantially more chemically stable than 2DPs formed using more reversible chemistries.

Presumably, combinations of dynamicity, structural regularity, and polymerization fidelity enable 2D polymerizations in all cases.

1.13 Triazine-Based Two-Dimensional Polymerizations

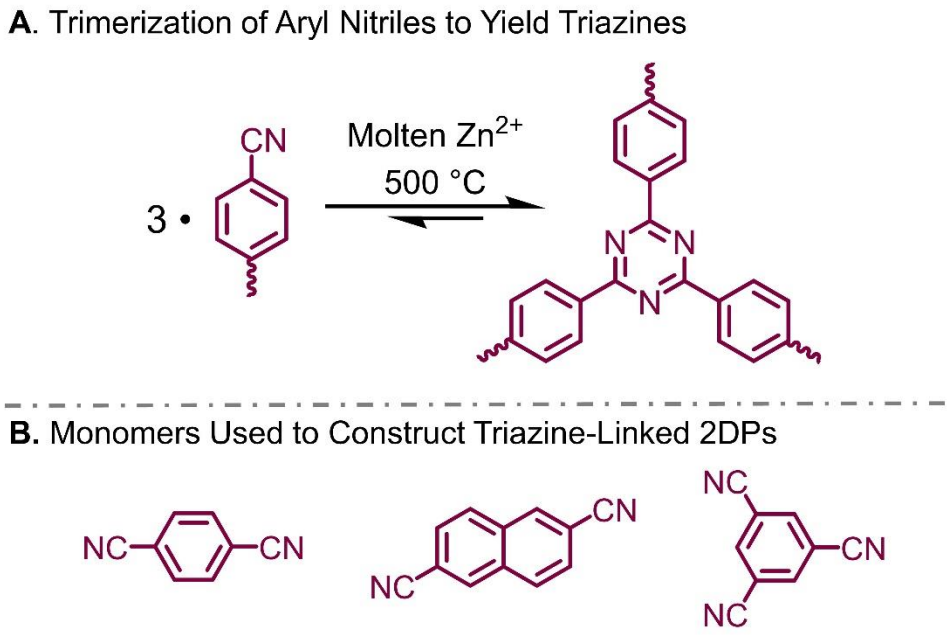

Figure 1.27. (A) Triazine formation by nitrile trimerization under ionothermal conditions. Other routes have also been explored. **(B)** Monomers used for the polymerization of triazine-linked 2DPs.

Another set of early 2DPs prepared from less dynamic chemistries are triazine-linked 2DPs, sometimes described as covalent triazine frameworks (CTFs; **Figure 1.27**).[332] These materials are among the most chemically robust frameworks known, with nitrile trimerization conducted under extreme conditions, such as molten $ZnCl_2$ ionothermal conditions to conduct the nitrile trimerization.[155, 269, 274, 332-372] The crystallinity of these systems is typically weaker than that of 2DPs prepared through conventional solvothermal processes. Additionally, the harsh ionothermal synthesis of these materials limit monomers to those that can survive these temperatures. For this

reason, only a limited number of monomers have been successfully polymerized as triazine-linked frameworks to date (**Figure 1.27B**). While recent advances have enabled the synthesis of these materials under milder conditions, such as at room temperature or under solvothermal acid-catalyzed conditions, further optimization of these conditions must be performed to expand their applicability to broader sets of monomers.[373-377] For a more comprehensive review of this topic, we direct readers to a recent review by Tan and coworkers.[332]

1.14. Emerging Two-Dimensional Polymerization Chemistries

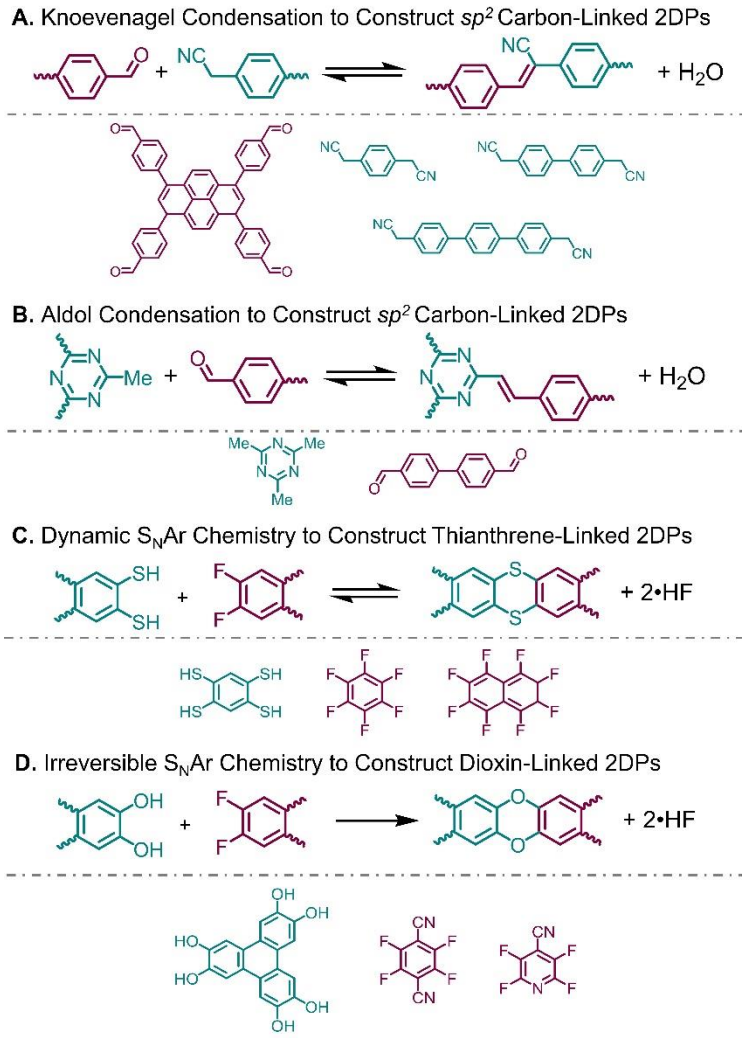

Figure 1.28. Emerging solution-based 2D polymerization chemistries including **(A)** Knoevenagle condensations, **(B)** aldol condensations, **(C)** thianthrene S_NAr reactions, and **(D)** dioxin formation.

In 2017, Jiang and coworkers overcame a long-standing challenge in 2DP synthesis by preparing structurally regular nets linked exclusively through sp^2-vinylene carbon-carbon bonds (**Figure 1.28A**).[378] Their approach takes advantage of a topologically directed Knoevenagel condensation,

which resulted in a remarkably stable, electroactive 2DP. Upon exposure to I_2 vapor, these materials are reported to become paramagnetic and conductive, associated with a single-electron oxidation of the pyrene subunits. These materials are therefore promising for ambitious applications such as organo-magnetics that rely on spin-correlated electron systems. While the reversibility of this chemistry is presumably limited, Jiang and coworkers have successfully expanded the number of monomers suitable for this approach.[208, 379] For example, a recently reported pyrene-containing structure was found to be highly luminescent when exfoliated into 2D sheets.[379] Additionally, Jiang and coworkers have reported that an all-sp^2 carbon-carbon-linked 2DP doped with platinum is an efficient photoreductant. The authors have described these properties more extensively in a recent review.[208, 380] We expect that a fundamental and applied interest in fully conjugated networks will inspire continued research efforts in this class of 2DPs.

Yaghi and coworkers incorporated vinylene groups by performing an aldol condensation between 2,4,6-trimethyl-1,3,5-triazine and 4,4'-biphenyldicarbaldeyde that ultimately yielded a 2DP polymerized through unfunctionalized olefins (**Figure 1.28B**).[210] These carbon-carbon linkages conferred high chemical stability, which enabled their use as catalytic supports for strong Lewis acids. While the general synthesis of 2DPs linked through entirely conjugated carbon-carbon bonds is of great interest, this strategy may be limited in its versatility because it requires a highly electron-withdrawing aromatic heterocycle to activate the benzyl protons for the polymerization. Nonetheless, the materials generated by this approach will likely enable fundamental studies of olefin-linked 2DPs, which are of substantial interest.[381]

Swager and coworkers recently demonstrated how controlled, dynamic nucleophilic aromatic substitution (S_NAr) chemistry could be used to generate 2DPs containing thianthrene linkages.

They found that thianthrene-based dynamic chemistry could be tracked *via* the exchange of model compounds and the formation of macrocyclic compounds.[382] This underappreciated dynamicity of thianthrene-forming S_NAr reactions was then used to synthesize high-quality 2DPs in near-quantitative yields (**Figure 1.28C**). Because thianthrene moieties are redox active and planarize upon a reversible oxidation, further exploration of this chemistry may enable the design of intrinsically redox-active 2DPs. Yaghi and coworkers developed a method to synthesize dioxin-linked 2DPs from catechols and perfluoroarenes (**Figure 1.28D**).[207] Unlike thianthrene-formation, the formation of dioxins is considerably less reversible, thereby limiting the error-correcting processes in this polymerization. The authors speculate that high-quality 2DPs are enabled by the limited conformations available to these fused systems, which could lead to fewer molecular defects. These nets are stable to both highly acidic and basic conditions, as demonstrated in part by the post-synthetic modification of the pore walls under demanding conditions. All of the materials generated using these unconventional polymerization chemistries are valuable to better understand the properties of 2DPs arising from their unique structures. However, due to the limited reversibility of these polymerization chemistries, these systems might prove challenging to directly synthesize as large-area single-crystalline 2DPs, which is a clear trend for boron- and Schiff-base-linked 2DPs. However, it is conceivable that polymerizations that take advantage of templation or preorganization effects may overcome these limitations.

1.15. Post-synthetic Transformations

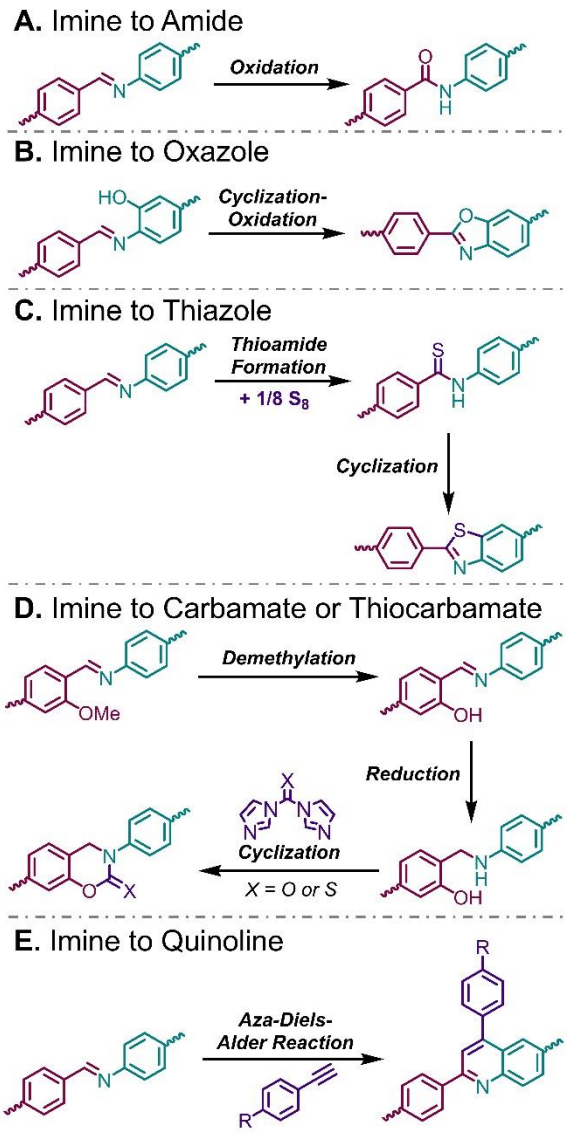

Figure 1.29. Post-synthetic modifications of imine-linked 2DPs to generate **(A)** amide-, **(B)** oxazole-, **(C)** thiazole-, **(D)** carbamate- or thiocarbamate-, or **(E)** quinoline-linked 2DPs.

Post-synthetic modification represents a versatile approach to diversify the chemical structures of 2DPs.[383] Many studies have established that the linkages themselves play a large role in determining the chemical and physical properties of the 2DP, primarily by determining the system's planarity, stability, and, in some cases, conjugation. While dynamic polymerization chemistries are beneficial for obtaining high-quality 2DPs, they do not necessarily provide the desired combination of properties. Recently, Yaghi and coworkers showed that dynamic imine linkages could be converted into more-stable amide linkages through a post-synthetic oxidation performed on a prepolymerized 2DP (**Figure 1.29**).[212] These 2DPs were highly crystalline, derived from their reversible imine-forming polymerizations, and chemically stable, due to their amide linkages. This approach has since been expanded to realize benzoxazole-,[384-388] quinoline-,[389] imidazole-,[390] amine-,[391] cyclic-carbamate-,[392] and cyclic-thiocarbamate-linked 2DPs[387, 393] by way of their imine-linked structural analogues (**Figure 1.29**). These synthetic strategies result in chemically robust, functionalized structures with emergent properties and functions challenging to access by direct polymerization. Furthermore, Lotsch and coworkers demonstrated the topochemical conversion of an imine-linked 2DP into a structurally similar thiazole-linked 2DP through thermal treatment with elemental sulfur.[393] The higher conjugation and larger electron density contrast of this 2DP allowed for its structural characterization by electron diffraction and TEM, which was challenging with the parent imine-linked 2DP. These representative examples demonstrate that post-synthetic modification enables the preparation of 2DPs with unique properties that would be challenging to install through direct polymerization. Going forward, post-synthetic modification will be leveraged to develop novel linkage chemistries, properties, and applications, not immediately accessible by direct 2D polymerization. For a more extensive

reading on post-synthetic transformations in dynamically polymerized 2DPs, we direct readers to a recent review on this topic.[383]

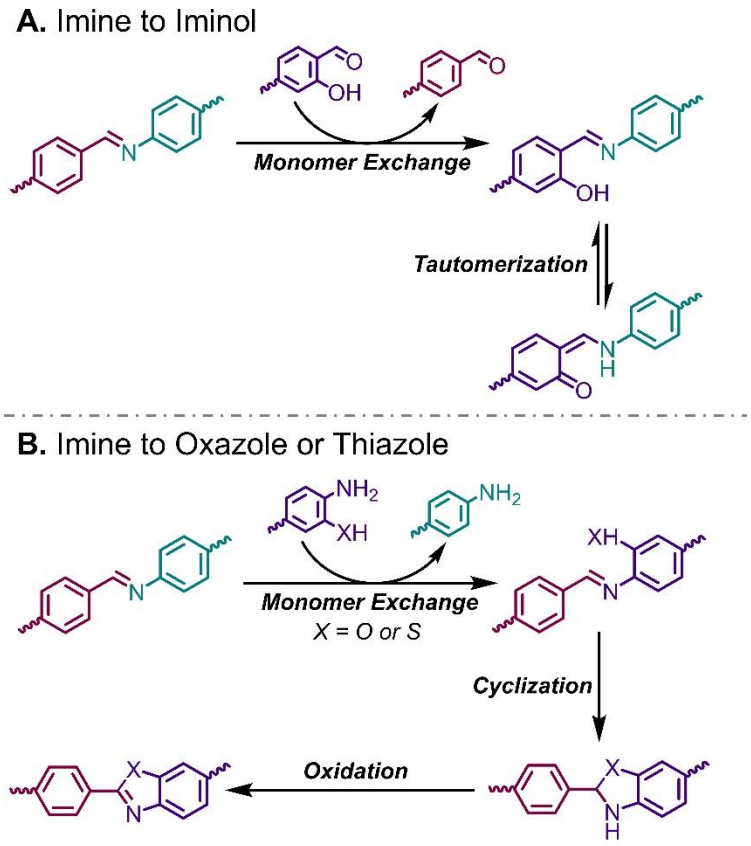

Figure 1.30. Monomer exchange reactions to produce **(A)** β-ketoenamine-linked and **(B)** oxazole- or thiazole-linked 2DPs.

In addition to the approaches that do not rely on breaking the imine C=N bond, other post-synthetic linkage transformations based on monomer exchange reactions have been realized. As discussed previously, Dichtel and coworkers recently transformed imine-linked 2DPs to their corresponding β-ketoenamine analogues by substituting their aldehyde component with structurally similar *o*-

hydroxybenzaldehydes **(Figure 1.30A**).[130] Upon this exchange, irreversible tautomerization occurs, thus generating higher-quality β-ketoenamine-linked 2DPs than are accessible by direct condensation. Building off of this approach, other linkage chemistries have also been accessed that are challenging *via* direct synthetic methods. For instance, Yaghi and coworkers demonstrated that monomer species flanked by phenolic or thiophenolic moieties could be quantitatively exchanged into the network.[212, 387, 392] Subsequent cyclization and oxidative reactions manifested in 2DPs containing thiazole or oxazole linkages (**Figure 1.30B**).[212, 387, 392] These results demonstrate that the imine linkages of 2DPs can serve as a traceless templating agent in the preparation of 2DPs with linkages that are challenging to attain as high-quality networks *via* direct synthetic methods.

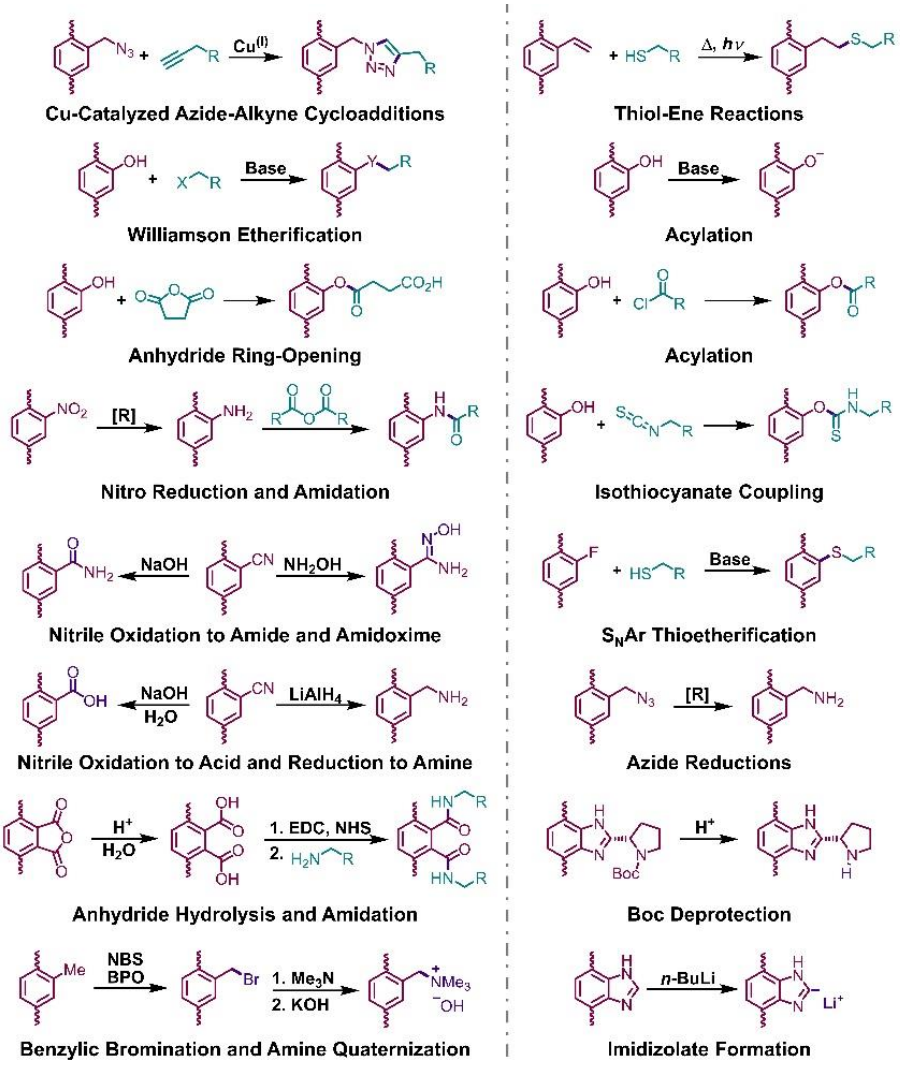

Figure 1.31. Representative post-synthetic modifications carried out on solution-synthesized 2DPs.

In addition to modifying the backbone of the 2DP through linkage transformations, pendant moieties can be installed on monomers to enable orthogonal post-synthetic 2DP pore. These reactions include Cu-catalyzed azide-alkyne cycloadditions (CuAAC), thiol-ene reactions, Michael additions, Williamson etherifications, and Staudinger reductions (**Figure 1.31**). For a

comprehensive review on post-synthetic transformations in 2DPs, we direct readers to a recent review by Segura and coworkers.[383] One of the major advantages of these approaches is that the degree of pore functionalization can be tuned by varying monomer feed ratios or by only partially reacting the pendant moieties. For instance, Helbling, Dichtel and coworkers installed pendant azide moieties on a functionalized terephthalaldehyde derivative, which was subsequently incorporated into an imine-linked 2DP in a variety of ratios. The pendant azide moieties were then reduced to the corresponding amines by a Staudinger reduction, and this material was used to remove anionic fluorinated alkyl substances from water.[394] This report established that pendant moieties thought to interfere with polymerization can be masked, and subsequently revealed in a post-synthetic fashion. Azide groups are also commonly used as coupling partners in CuAAC reactions. For instance, Jiang and coworkers prepared a 1,4-benzene bis(boronic acid) derivative with pendant azide moieties, which was incorporated into a phthalocyanine-based electron-donating 2DP. These 2DPs were then reacted with an ethynyl-functionalized fullerene to generate a photoelectric 2DP with segregated donor-acceptor segments.[395] Similarly, ethynyl-functionalized monomers have been incorporated into 2DPs and subsequently transformed into functionalized triazines suitable for organo-catalysis. Significant opportunities remain to develop highly functionalized structures from a small number of strategically designed monomers. As 2DPs increase in chemical complexity, the reactions used to functionalize their surfaces are likely to evolve as well. The continued diversification of 2DPs prepared by dynamic polymerization will undoubtedly drive the continued exploration of emergent properties and device potential in 2DPs accessed through *de novo* and post-synthetic modification approaches.

1.16. Concluding Thoughts

The long-standing goal of polymerizing macromolecular sheets has recently been realized. The emergence of this new branch of polymer chemistry has been enabled by scientific contributions from many fields including supramolecular chemistry, framework chemistry, and crystal engineering. To date, three 2D polymerization strategies have emerged as dominant approaches to the synthesis of macromolecular sheets, which can be broadly classified as solution-based, solvent-free on-surface, and topochemical approaches. These strategies can be divided into topochemical approaches, on-surface solvent-free approaches, and solution-based approaches each of which depends on some combination of monomer preorganization, templation, or dynamic bond-forming reactions. The ingenuity of polymer chemists has expanded these strategies immensely, which has resulted in the polymerization of more than 500 discrete 2DP structures.

Despite major advances in 2D polymerization over the last two decades, methods to prepare large-area, defect-free macromolecular sheets of arbitrary composition are by no means mature. Many challenges in 2D polymerization can be traced to a lack of foundational mechanistic understanding. Therefore, the continued investigation of 2D polymerization mechanisms is paramount for the continued development of this field. More fundamental than mechanistic understanding, polymer chemists have not yet developed the vernacular to discuss 2DPs at the same depth as other polymer architectures. For example, terms such as dispersity and molecular weight are not currently well defined for 2DPs, nor are they routinely measured or reported. This makes discussion and characterization of 2DPs and their emergent properties challenging. We suspect that as the synthesis and characterization toolkits become more refined for 2DPs, the language used to describe them will evolve as well. Ultimately, as the scientific understanding and descriptive

vocabulary surrounding 2D polymerization coevolve, so too will the quality and complexity of 2DPs.

The synthesis of chemically diverse, high-quality 2DPs will likely produce materials with unique combinations of properties not available in other materials. However, due to the synthetic challenges outlined in this Review, many of these properties have yet to be studied or rationally manipulated. This challenge predominantly arises as a consequence of the relatively uncontrolled polymerization strategies used to prepare many 2DPs. As these synthetic obstacles are overcome, it will become commonplace to unambiguously characterize the 2DP structure, leading to meaningful structure-property relationships in these materials. For instance, as large-area macromolecular sheets are reliably produced it will become possible to examine the intrinsic thermomechanical and optoelectronic properties of these materials, with confidence that measurements are not confounded by limited domain size or defects. Additionally, many properties of 2DPs are likely determined by their thickness. Therefore, as methods to prepare micron-size mono- and few-layer 2DPs using bottom-up and top-down approaches are developed, we expect that explorations of layer-dependent phenomena in 2DPs will be a fruitful area of study. These findings will certainly guide the development of 2DPs for real-world applications.

Toward this end, we have provided examples of proof-of-principle 2DP applications, many of which show promise as functional devices. Though care is certainly needed when characterizing 2DPs integrated into device-relevant platforms, since many of these 2DPs have been prepared using less-than-ideal polymerization strategies that certainly incorporate molecular defects and significant edge and surface sites into these structures. It is also frequently unclear whether the 2DP structure and properties are maintained within a device environment. Though just as linear

polymers were improved through decades of study and are now incorporated into our everyday lives, we anticipate that 2DPs will do so as well.

We foresee a promising future in 2D polymerization. In the near term, the constantly accelerating rate of research into 2DPs and their properties is certain to continue. This will undoubtedly drive innovations regarding their synthesis, properties, and eventual applications. Ultimately, particular applications are likely to emerge as promising for real-world deployment. This will mark the beginning of the next generation of 2DP science. We hope that this Review has laid a foundational outline for current challenges in 2D polymerization and will inspire the continued exploration of 2DPs, including their preparation and eventual application relevance.

In 1993, Roald Hoffman described synthetic 2D chemistry as an uncharted wasteland.[38] In this Dissertation, we hope to have convinced the reader that the grounds of 2D organic chemistry have now been cultivated, are beginning to blossom, and will soon be ripe for harvesting.

Chapter 2 : Seeded Growth of Single-Crystal Two-Dimensional Covalent Organic Frameworks

2.1 Abstract

Polymerizing monomers into periodic two-dimensional (2D) networks provides structurally precise, layered macromolecular sheets that exhibit desirable mechanical, optoelectrotronic, and molecular transport properties. 2D covalent organic frameworks (COFs) offer broad monomer scope but are generally isolated as powders comprised of aggregated

nanometer-scale crystallites. Here we control 2D COF formation using a two-step procedure, in which monomers are added slowly to pre-formed nanoparticle seeds. The resulting 2D COFs are isolated as single-crystalline, micron-sized particles. Transient absorption spectroscopy of the dispersed COF nanoparticles provides two to three orders of magnitude improvement in signal quality relative to polycrystalline powder samples and suggests exciton diffusion over longer length scales than those obtained through previous approaches. These findings will enable a broad exploration of synthetic 2D polymer structures and properties.

2.2. Introduction to 2D polymerization

Polymerizing monomers into periodic two-dimensional (2D) networks provides precise, macromolecular sheets linked by robust, covalent bonds.[396-399] 2D polymers differ from established linear, branched, or crosslinked polymer architectures and promise distinct combinations of properties that emerge from their designed structures and uniform, nanometer-scale pores.[399, 400] The limited scope or materials quality provided by current 2D polymerization methods bottleneck this promise.[400, 401] 2D polymers with large crystalline domains have been obtained by crystallizing tritopic monomers into layered crystals capable of topochemical photopolymerizations, some of which have been characterized as single-crystal to single-crystal transformations.[401-403] But the strict geometric requirements of topochemical polymerizations and difficulty of designing molecules that crystallize appropriately have limited the generality of this approach to just nine monomers across three design motifs. In contrast, the simultaneous polymerization and crystallization of monomers into 2D polymers known as covalent organic frameworks (COFs) is more general, with more than 200 reported examples.[404-425] However, 2D COFs typically form as insoluble, polycrystalline powders or films with small crystalline domains (typically smaller than 50 nm), which we attribute to poorly controlled nucleation and growth processes.[416, 417, 420] Wuest and coworkers reported three 3D COFs isolated as large single-crystals,[426] but these are linked by weak azodioxy bonds, are unstable to elevated temperatures and solvent removal, and have not been generalized to 2D COF single crystals. Here we report 2D COFs as discrete particles comprised of single crystalline domains with sizes ranging from 500 nm to 1.5 μm. They were prepared through a two-step approach that separates the nucleation and growth processes. These 2D COF samples have superior properties and can be studied more

rigorously than polycrystalline samples, as demonstrated by a transient absorption study that provides 1000-fold improved signal quality and evidence for exciton delocalization at length scales larger than the crystalline domains of the powders. These findings represent a major advance in 2D COF materials quality that will greatly broaden the monomer scope available for accessing well-defined 2D polymers.

2.3. Existing Mechanistic Understanding

2D COF formation is poorly understood because effective reaction conditions are identified by empirically screening for the formation of the desired materials as polycrystalline powders. The appropriate rates of polymerization and exchange processes needed for defect correction are unknown, and we postulate that identifying reactions that produce polycrystalline powders is inherently predisposed to identify conditions with uncontrolled nucleation. Our recent mechanistic studies of boronate ester-linked 2D COF formation revealed a nucleation-elongation process that was interrupted by the aggregation and precipitation of microcrystalline COF powders.[420] We later found that nitrile-containing cosolvents prevented aggregation and precipitation, resulting in stable colloidal suspensions of 30 nm crystalline 2D COF nanoparticles that could be solution processed into films.[413] Here we enlarge the COF colloids into faceted, single crystals with lateral dimensions greater than 1.5 μm through a second growth step in which additional monomers are introduced slowly to suppress further nucleation. This approach is shown to be general for three boronate ester-linked COFs, including a pyrene-containing structure previously shown to be photoconductive.[409] These seeded 2D COF polymerizations provide the first 2D COFs as non-

aggregated single crystals and demonstrate a means to obtain high-quality 2D polymers using modular and versatile directional bonding approaches.

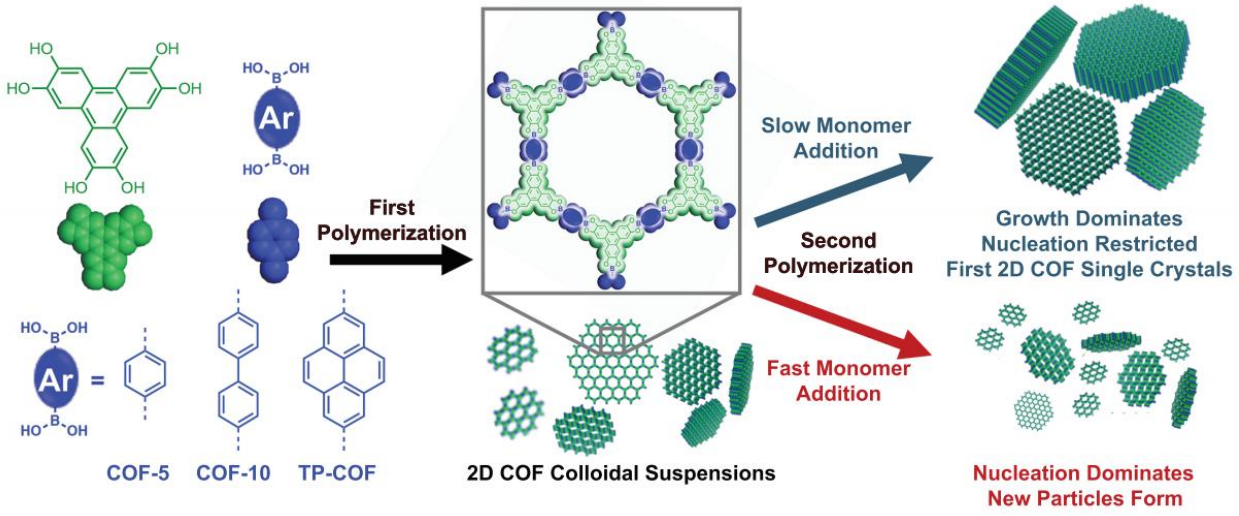

Figure 2.1. Schematic of controlled 2D polymerization. A two-step seeded growth approach provides 2D COF single crystals. When HHTP and a linear bis(boronic acid) monomer are condensed in a solvent mixture containing CH_3CN, crystalline 2D COF nanoparticles are formed as stable colloidal suspensions. These nanoparticles are enlarged in a second polymerization step in which the monomers are added to the solution slowly. If the monomers are added more quickly, their concentration increases above a critical nucleation threshold, which leads to uncontrolled nucleation and smaller average particle size.

2.4. Slow growth methods

The solvothermal condensation of 1,4-phenylenebis(boronic acid) (PBBA) and 2,3,6,7,10,11–hexahydroxytriphenylene (HHTP) in a mixture of 1,4-dioxane and mesitylene (4:1

v/*v*) affords a boronate ester-linked 2D COF (COF-5), which precipitates within minutes.[420] However, when 80 vol% of CH_3CN is included as a cosolvent, a stable colloidal suspension of COF-5 nanoparticles is obtained instead.[413] Having identified 2D COF polymerization conditions that prevent aggregation and precipitation, we hypothesized that newly introduced monomers would add to the existing nanoparticles rather than nucleating new particles under appropriate conditions. Indeed, adding monomers gradually to the reaction mixture limits the steady-state monomer concentration, and the colloids grow without forming new particles. In contrast, if the monomers are introduced quickly, their concentration increases above a critical nucleation concentration, and the reaction is dominated by the formation of new particles (Error! Reference source not found.) We prepared an initial COF-5 colloidal suspension by heating HHTP and PBBA to 90 °C in CH_3CN:1,4-dioxane:mesitylene (80:16:4 vol%) for 18 h. The formation of crystalline COF-5 colloids with an average diameter of 30 nm was confirmed by dynamic light scattering (DLS) and synchrotron small-angle and wide-angle X-ray scattering (SAXS/WAXS) experiments. At first, we screened conditions that provide seeded growth by adding monomers at various concentrations and rates and monitoring colloid size by DLS. These exploratory experiments were successful and provided COF-5 nanoparticles that had grown from 30 nm to 400 nm (see Supporting Information for experimental details, **Figure 2.6**). The 400 nm particles were employed in more careful growth studies depicted in Figure 2.2 because they are sufficiently large to easily differentiate newly formed colloids from the preexisting seeds using DLS and other tools.

2.5. Nucleation and Growth Processes

We observed both seeded growth and new particle formation regimes by adding monomers at different rates to dispersions of the 400 nm colloids. A COF-5 colloidal suspension was heated to 85 °C and separate solutions of PBBA (6 mM) and HHTP (4 mM) were simultaneously added using a syringe pump. The size distributions of the COF-5 nanoparticles were monitored by DLS and are plotted as a function of molar equivalents of the monomers added relative to those present in the initial colloids (equiv HHTP added / equiv HHTP in the COF-5 seed solution, **Figure 2.2**). When monomers are added slowly (0.10 equiv h^{-1}), the average particle size steadily increases (Figure 2.2A) and the size distribution remains monomodal as it shifts to larger sizes (**Figure 2.2C**). The added monomers are incorporated into the existing colloids, which grow from 400 to 1000 nm after 4.0 equiv HHTP are added, and no evidence for new nanoparticle formation was observed by DLS (**Figure 2.2C**), X-ray diffraction, or microscopy (see below). In contrast, when the monomers were added ten times faster (1.0 equiv h^{-1}), the average particle size began to decrease after 0.5 equiv of monomers were added (**Figure 2.2A**). The particle size distribution is bimodal with a new population at 50 nm after 0.8 equiv HHTP was added, and this population of smaller particles develops into the dominant signal in the DLS measurements as more monomers are added (**Figure 2.2C**). Control experiments in which the reaction solvent lacking HHTP and PBBA was added to the colloids resulted in no change of the size distribution of the colloids (**Figure 2.7**), indicating that the increased particle size observed during slow monomer addition is not attributable to Ostwald ripening or other particle fusion processes. These experiments indicate that the faster addition rate causes the monomer concentration to exceed that needed to nucleate new nanoparticles. Based on where the DLS curves for the fast and slow addition experiments

diverge, HHTP and PBBA concentrations of ca. 1 mM represent an upper bound needed for nucleation of new COF-5 particles under these conditions. However, this estimate of the critical nucleation concentration is likely to be influenced by several reaction parameters. These experiments demonstrate that COF-5 colloidal suspensions remain stable and available for continued 2D polymerization when the monomer concentrations are sufficiently low.

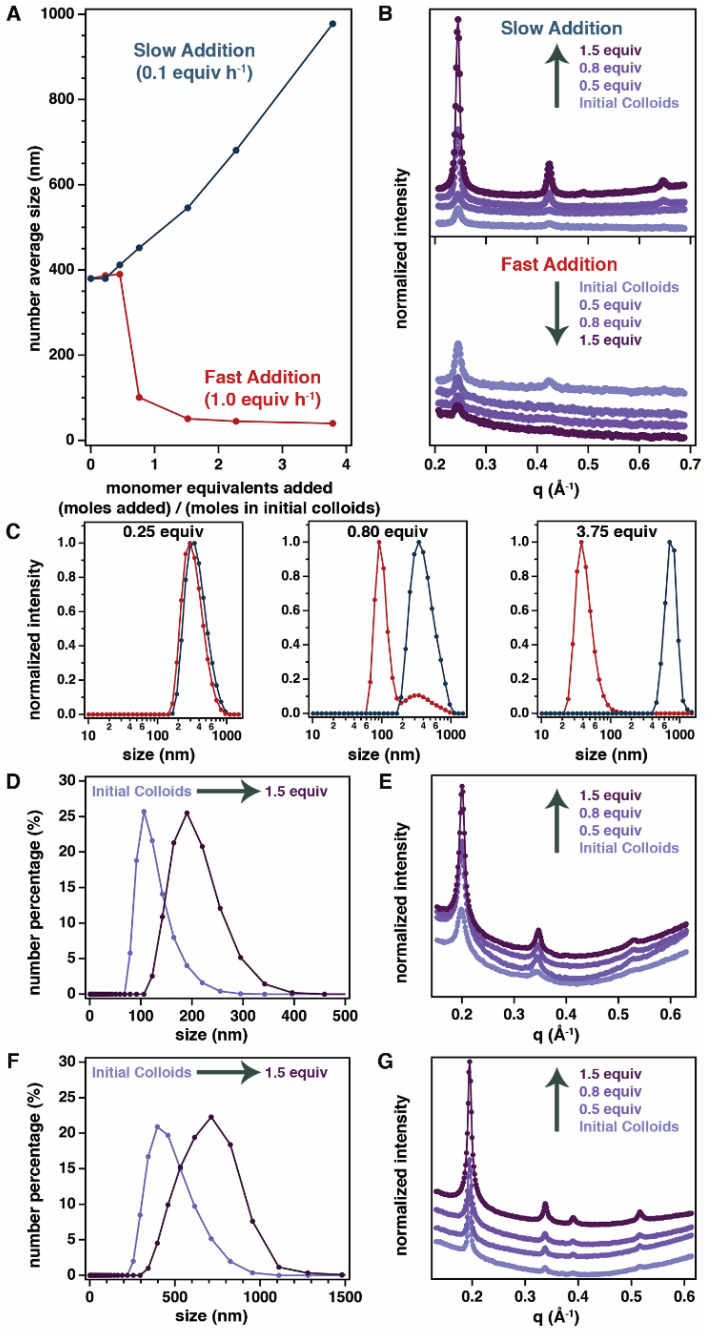

Figure 2.2. The monomer addition rate defines seeded growth and nucleation regimes. (A) The DLS number average size of COF-5 particles as a function of added monomer equivalents. **(B)** Wide-angle X-ray scattering of COF-5 particles as a function of the amount of added monomers at the two monomer addition rates. **(C)** DLS number average size distributions obtained

at three points shown in panel (A). **(D)** DLS number average size distributions for the initial and final particle sizes of COF-10 during slow monomer addition. **(E)** WAXS traces of COF-10 particles as a function of the amount of added monomers. **(F)** DLS number average size distributions for the initial and final particle sizes of TP-COF during slow monomer addition. **(G)** WAXS traces of TP-COF particles as a function of the amount of added monomers.

Simultaneous WAXS, which characterizes the crystallinity of the colloids, and SAXS, which tracks the average particle size, also differentiate the seeded growth and new particle formation regimes. In the seeded growth regime, the average crystallite size and particle size increase as monomers are added slowly. In contrast, the average crystallite size and particle size decrease when monomers are added quickly. The WAXS data indicate that the initial COF seeds diffract at q = 0.24 and 0.42 $Å^{-1}$, corresponding to the 100 and 010 Bragg directions of a hexagonal lattice with in-plane lattice parameters a = b = 29.9 Å (**Figure 2.10**). These parameters match well with calculated (30.0 Å) and measured (29.7 Å) values previously reported for COF-5 powders.[417] When monomers are added slowly, the 100 peak intensifies and sharpens, and the 200 and 210 Bragg peaks become visible at q = 0.48 and 0.64 $Å^{-1}$ after 0.8 equiv HHTP are added. These observations indicate that the size of the COF-5 crystalline domains and the crystallinity within the domain are increasing as the monomers are added to the solution. However, when monomers are added at 1.0 equiv h^{-1}, the WAXS peaks broaden and decrease in intensity, which is consistent with the nucleation of new particles with smaller crystalline domains. The SAXS results are fully consistent with the DLS studies described above, validating that the WAXS experiments were done under conditions relevant to each growth regime. The SAXS traces (**Figure 2.17**) trend

towards higher intensities at low scattering angles at the slow monomer addition rate (0.10 equiv h^{-1}), which indicates an increased average particle size. SAXS of solutions with rapid monomer addition (1.0 equiv h^{-1}) trend to lower intensities at low scattering angles, consistent with decreased average particle size. Together these experiments demonstrate that the average crystalline domain size of the COF-5 colloids increases along with the particle size as monomers are added sufficiently slowly to suppress nucleation.

2.6. A Chemically General Growth Strategy

We demonstrate the generality of the seeded growth approach for two other boronate ester-linked 2D COFs, COF-10 and TP-COF, which are synthesized by the condensation of HHTP with 4,4'-biphenylbis(boronic acid) and 2,7-pyrenebis(boronic acid), respectively. Both systems exhibited similar growth behavior as COF-5. For each network, an initial colloidal suspension was generated by heating HHTP and the corresponding boronic acid in a mixture of CH_3CN:1,4-dioxane:mesitylene (80:16:4 vol%) for 18 h at 90 °C. Once the colloids were formed, separate solutions of HHTP and the diboronic acid were added at 0.10 equiv h^{-1} to the 2D COF nanoparticle suspensions. DLS of the reaction solutions showed monomodal particle size distributions that shifted to larger average sizes as monomers were added. The DLS particle size of the COF-10 colloids shifted from 80 nm to 190 nm after 1.5 equiv HHTP and 2.25 equiv 4,4'-biphenylbisboronic acid were added (**Figure 2.2D**). The TP-COF's particle size (**Figure 2.2F**) increased from 400 nm to 750 nm after 1.50 equiv HHTP and 2.25 equiv 2,7-pyrenebis(boronic) acid were added at 0.10 equiv HHTP h^{-1}. These experiments suggest that nucleation is suppressed under these conditions and that the existing COF domains are enlarged through addition of the

added monomers. Furthermore, nucleation predominates when the monomer solutions are added quickly (1.0 equiv h^{-1}), resulting in smaller COF particle sizes of approximately 50 nm (**Figure 2.8** and **Figure 2.9**). We also used in-solution X-ray diffraction techniques to interrogate the crystallinity of these colloidal suspensions. For the TP-COF, WAXS peaks were observed at q = 0.19, 0.34, 0.39, and 0.52 $Å^{-1}$ (**Figure 2.2G**) corresponding to the Bragg directions 100, 110, 200, and 210 that were reported in its powder pattern (**Figure 2.12**).[408, 409] Likewise, COF-10 colloids diffraction peaks were observed at q = 0.20, 0.34, 0.52 $Å^{-1}$ **(Figure 2.2E**), which correspond to the 100, 110, and 210 Bragg diffractions (**Figure 2.11**).[409] These observations are consistent with those of the seeded growth of COF-5, in which the intensity of the diffraction peaks increases and the width (as judged by their full width at half of the maximum intensity) decreases. Here again, the 200 and 210 diffraction peaks become visible after 0.8 equiv HHTP are added to each initial sample. These observations indicate that as monomers are introduced to COF nanoparticles sufficiently slowly, they add to and enlarge existing crystalline domains.

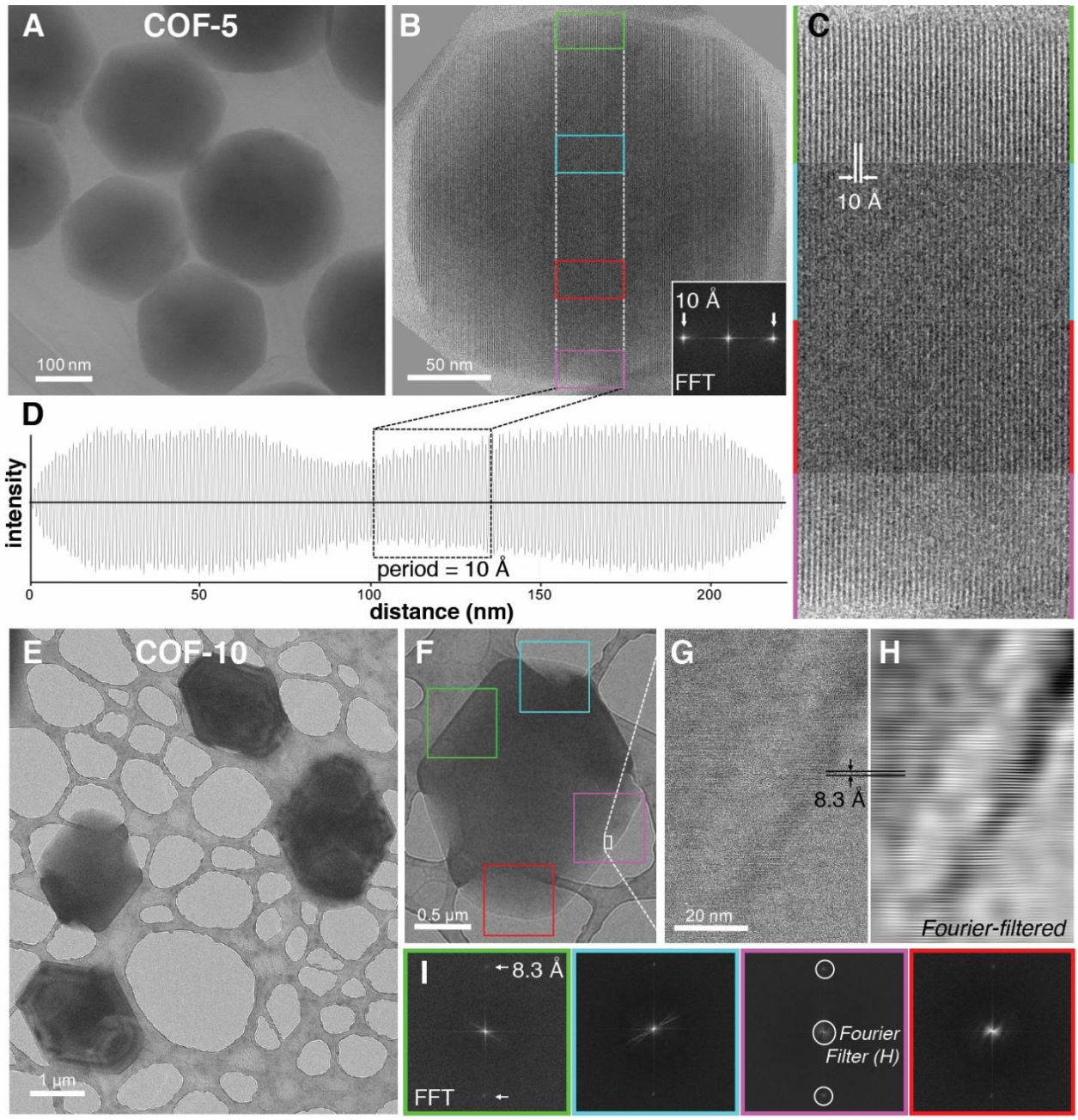

Figure 2.3. Low-dose HRTEM characterization of COF single-crystalline particles. (A-D) COF-5 and **(E-I)** COF-10 particles (cumulative dose per image: ~25 $e^-/Å^2s$). **(A, E)** Low-magnification images of the COF particles. **(B)** Lattice-resolution HRTEM image of a COF-5 particle with consistent lattice fringes extending across the entire particle. Inset: FFT of the image,

cropped at the predominant fringe spacing (~10 Å). **(C)** Four regions of interest at higher magnification (green, teal, red, and magenta) of the particle in **(B)**, which are aligned vertically and parallel with the 10 Å fringes. **(D)** Intensity profile plot (left-to-right across the particle) of the image in **(B)** after applying a bandpass filter. The periodicity of the intensity profile is constant and continuous with a period of ~10 Å. **(F)** Overview image of one COF-10 particle, from which higher magnifications images were acquired at four regions of interest (green, teal, magenta, and red). **(G)** Lattice-resolution HRTEM image at the lower-right edge of the particle where 8.3 Å lattice fringes are resolved, corresponding to d_{400}. **(H)** The HRTEM image in **(G)** after applying a Fourier-filter to select the central spot and the two 8.3 Å spots in the FFT. **(I)** The FFTs of the four high-magnification images from the four color-marked regions of interest in **(F)**.

2.7. Direct Imaging of Two-Dimensional Polymers

The enlarged COF nanoparticles were analyzed by low-dose, high-resolution transmission electron microscopy (TEM) to visualize their morphology, size, aspect ratio, and crystallinity (**Figure 2.3**). TEM imaging of discrete particles was possible for COF-5 and COF-10, with TP-COF appearing aggregated when prepared on TEM substrates, precluding detailed analysis of its lattice structure by microscopy (**Figure 2.13**). TEM imaging at low magnification revealed that the COF-5 particles (**Figure 2.3A**) have uniform six-fold symmetry and hexagonal faceting in projection. Most individual particles are 300-500 nm in diameter, with some reaching over 1 μm. The COF-5 particles are observed at random orientations by TEM (no preferential orientation when drop-cast on TEM substrates), and all orientations appear dimensionally isotropic. Lattice resolution images of individual COF-5 particles show that they are single-crystalline (**Figure 2.3B-**

D), as consistent and continuous lattice fringes extend throughout the particles. For the particle selected in **Figure 2.3B-D**, which is tilted just off a zone axis, the fringe spacing is ~10 Å (fitting d_{210} for COF-5), as measured by the fast Fourier transform (FFT, Figure 2.3B inset) and the left-to-right intensity profile (**Figure 2.3D**) of the particle. The magnified lattice images of vertically aligned regions in this particle show the continuous single-crystalline structure that extends vertically (parallel with the fringes) from edge-to-edge, as shown in several regions of a particle juxtaposed in Figure 2.3C. The intensity profile (**Figure 2.3D**) similarly shows that the single-crystalline structure is continuous horizontally (perpendicular to the fringes) from edge-to-edge.

The COF-10 particles (**Figure 2.3E-I**) are also highly uniform in size and morphology. They are hexagonally-faceted in projection yet lack the six-fold symmetry of the COF-5 particles; their sizes are predominantly 4-5 μm across their major length and *ca.* 3 μm across their minor length (Figure 2.3E). When prepared on TEM substrates, the particles preferentially orient with their inter-sheet stacking dimension normal to the substrate, which is likely caused by their z-dimension (particle thickness) being smaller than their lateral dimension (**Figure 2.14**). The large size of these particles (thickness ~0.5-1 μm), means that analysis was limited to their edges; many particles are too large for high-resolution TEM characterization. Therefore, we acquired high-magnification images at various regions of interest around the perimeter of a single particle that was sufficiently thin (**Figure 2.3F-H**). Lattice fringes (**Figure 2.3G-H**) cannot be visually resolved in the images for all regions, but the FFTs all contain more subtle periodic information, which reveal that all regions are consistently crystalline throughout the particle **(Figure 2.3H-I**). The FFTs of all four regions contain ~8.3 Å fringe spots (fitting d_{400} for COF-10) at the same radial location (**Figure 2.3I**), indicating that the crystal structure and crystal orientation is consistent at

each of the four regions of interest (**Figure 2.13**). These observations strongly suggest that the particle is a single continuous crystalline domain. We note that low-magnification images of the COF-10 particles contain very prominent diffraction contrast with no detectable grain boundaries, which is consistent with the particles being single crystals (**Figure 2.3E**). Collectively, the TEM characterization of the individual, single-crystalline COF-5 and COF-10 particles further indicate that the well-controlled, seeded growth procedure represents a major advance in COF materials quality and the modular synthesis of 2D polymers.

2.8. Size-dependent excitonic behavior in 2D polymers

The well-dispersed, single-crystalline COF colloids enable characterization of emergent electronic properties of these 2D layered assemblies that were not previously possible in polycrystalline aggregates. The optical signatures and exciton dynamics of the COF-5 colloids were characterized using optical transient absorption (TA) spectroscopy measurements. Delocalized excitons and charge carriers in 2D COFs have been of interest since the earliest reports of these materials, but their small crystalline domain sizes and aggregated powder forms have severely limited their characterization to qualitative photoconductivity measurements.[408, 422] Previous TA experiments on 2D COFs were performed on either polycrystalline samples dispersed in solvent or polycrystalline thin films.[406-410, 421] Although the first reported TA measurements showed a reasonable data quality, they were inconsistent with more recent results from the same group on the same systems, which were noisy and dominated by scattering. Similar noise sources were also observed in our TA measurements on COF-5 powder samples obtained by solvothermal growth (**Figure 2.16**). In comparison, the TA data from our dispersed COF-5 colloids show

approximately three orders of magnitude signal to noise enhancement compared to the powder sample measured under the same experimental conditions (**Figure 2.4B**). The well-defined structures of these colloids now make it possible to correlate their optical TA spectra to exciton dynamics and decay pathways inherent to the nature of the COF itself.

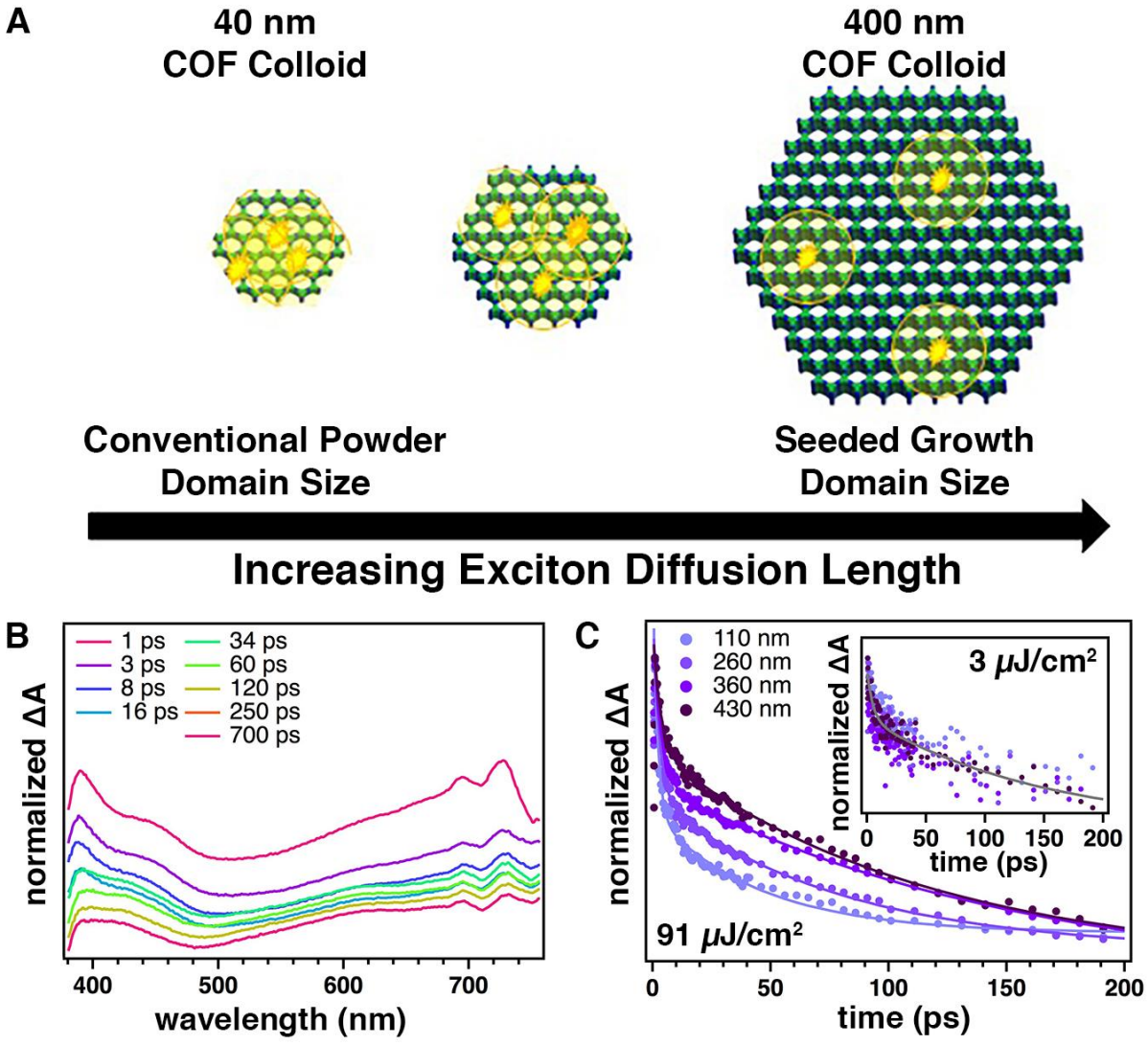

Figure 2.4. Exciton Diffusion Studies of COF-5 (A) Depiction of exciton distribution in COF-5 single crystals with different sizes highlighting exciton interactions at boundaries. **(B)** Transient absorption spectra (excitation wavelength 360 nm) as a function of indicated probe delay time for

110 nm sized COF-5 colloids. **(C)** exciton decay kinetics (dots) and fits (lines) of COF-5 colloids of different sizes at high photon fluence (91 μJ $pulse^{-1}$) observed at 410 nm. Inset: exciton decay kinetics (dots) and fit (line) at low photon fluence (3 μJ $pulse^{-1}$) observed at 410 nm.

TA spectroscopy was performed on COF-5 colloids of varying particle size and as a function of pump fluence. These spectra are dominated by a broad excited state absorption that decays on the timescale of hundreds of picoseconds while remaining spectrally consistent as well as a stimulated emission feature which was longer than the timescale of the experiment and subtracted to ensure consistent baselines for the timescale of observation. The identity of this feature is likely related to the singlet excitons of the triphenylene cores. However, dynamics clearly differ according to the particle size for high photon fluence with the emergence of faster decays not observed at the low photon fluences (**Figure 2.4C**, inset). They differentiate clearly according to the particle size at a high photon fluence with the emergence of faster decays than those at the low photon fluences (**Figure 2.4C**). We attribute this high fluence, fast exciton decay kinetics and particle size dependence at the high excitation photon fluences to exciton-exciton annihilation, which occurs when multiple excitons within a diffusion length of each other are excited within the same particle sufficiently close to each other so as to diffuse and interact. At a given number density, excitons in smaller COF crystallites more readily undergo exciton-exciton annihilation because they are confined to a smaller effective volume (**Figure 2.4A**). These combined observations demonstrate that COF colloid nanoparticles with unprecedented optical quality enable high quality spectroscopic measurements that were previously inaccessible. The fluence-sensitive exciton decay dynamics convey size-dependent photophysical properties and will enable an improved understanding and leveraging of emergent electronic processes in these materials.

2.9. Chapter 1 Supplementary Information

Materials and Methods

Materials

Reagents were purchased in reagent grade from commercial suppliers and used without further purification, unless otherwise described. Solvents were obtained from commercial sources and used without further purification.

Nuclear Magnetic Resonance

^{1}H and ^{13}C NMR spectra were acquired on 400 MHz Agilent DD MR-400 system and recorded at 25 °C. The spectra were calibrated using residual solvent as internal reference (DMSO: 2.5 ppm for ^{1}H NMR, 39.52 for ^{13}C NMR).

Dynamic Light Scattering

Dynamic Light Scattering (DLS) data were collected using a Malvern Zetasizer equipped with a 633nm He-Ne 5mW laser at room temperature in a quartz cuvette with a 10mm pathlength. Data was analyzed using the proprietary Zetasizer software.

Sonication

Sonication was performed using a Branson 3510 ultrasonic cleaner with a power output of 100W and a frequency of 42 kHz.

X-ray Diffraction

Small- and wide-angle X-ray scattering (SAXS/WAXS) patterns were collected at Argonne National Lab's Advanced Photon Source at both sectors 5-ID-D (DND-CAT) using a custom flow cell in a transmission geometry and 12-ID-D with a capillary transmission geometry. Experiments conducted at 12-ID-D were collected at a beam energy of 12 keV and experiments conducted at 5-ID-D were collected at a beam energy of 13.3 keV. 10 frames were collected for 1 second apiece on a set of Pilatus detectors, which were then summed and radially integrated to produce a linear XRD pattern using proprietary software available at the APS. Scattering intensity is reported as a function of the modulus of the scattering vector q, related to the scattering angle 2θ by the equation $q = (4\pi/\lambda) \sin \theta$, where λ is the X-ray wavelength. The sample-to-detector distance was adjusted to measure across relevant detection ranges. Capillary experiments were conducted using 2.0 mm OD borosilicate capillaries with 0.2 mm wall thicknesses purchased from Hilgenberg GmbH.

Syringe Pump

KD Scientific Model 100 syringe pumps were used to add monomers at controlled rates.

COF Modeling and Structural Refinement

Initial COF structures were constructed in Materials Studio ver 4.2 (Accelrys Inc.) with a primitive hexagonal unit cell with a P6/mmm space group. The *a* cell parameter was estimated according to the distance between the center of the vertices for each COF and c parameter was estimated as a typical π-stacking distance. Geometry optimized structures with optimized unit cell parameters were obtained using the Forcite software package with a Universal Force Field. The final molecular structure in a hexagonal unit cell was prepared by using geometrical parameters from

the optimized structure. Diffraction simulation and Pawley refinement were carried out using the Reflex software package. COF models and their simulated patterns were Pawley refined to experimental patterns iteratively until the RWP value converges. The refinement indicates a hexagonal crystal system with a unit cell described below. The pseudo-Voigt profile function was used for whole profile fitting. The final RWP and RP values were calculated to be less than 5% in all cases. Simulated XRD patterns were calculated from the refined unit cell and compared with the experimentally observed patterns.

TEM Sample Preparation

All COF samples (COF-5, COF-10, and TP-COF) were prepared by drop-casting ~3-4 µL (using a micropipette) of the COF sample solution (CH_3CN:1,4-dioxane:mesitylene, 80:16:4 by volume) after synthesis was complete onto lacey-carbon substrate (Cu mesh) TEM grids (Electron Microscopy Sciences, Hatfield, PA). The droplets of COF sample were allowed to sit on the grids in ambient conditions for ~20-30s, and were then wicked dry with filter paper. The prepared TEM grids were then stored in a desiccator until they were used for TEM characterization.

TEM Characterization

TEM was performed using a FEI (FEI Company, Hillsboro, OR) Polara cryoTEM operating at 200 keV equipped with a Gatan (Roper Technologies, Sarasota, FL) K2 “direct electron” detector (FEG extraction: 4350 V, FEG emission: 110 µA, spot size 5, 70 µm OL aperture, 70 µm CL aperture). The Polara cryoTEM is a cartridge-loaded microscope, where the column is continually maintained at *L*-N_2 temperature (< -180˚ C). The grids that were prepared previously and dried,

were loaded into the microscope's cartridge after being submerged in *L*-N_2, and the cartridge with grids was inserted into the microscope (maintained at *L*-N_2 temperature). The Polara was aligned for low-dose imaging, measuring the dose rate on the K2 detector through vacuum (no grid inserted). The dose rate used was 5.3 e^- $Å^{-2}$s for high-magnification (115 kx) images (1.78 Å pixel size, 3708 x 3838 pixels), with an image exposure of time of 5 s (~26.5 e^- $Å^{-2}$ cumulative dose per image). The dose rate was not directly measured for the low magnification images, but the dose rate was orders magnitude lower for those images than for the high magnification images (1ow magnification images: 1 s exposure time, 10.1034 nm pixel size, 1852 x 1918 pixels, binning 2). All image acquisition was done using SerialEM software (http://bio3d.colorado.edu/SerialEM/), which applies auto focusing on adjacent regions of the grid to minimize dose on the sample.

Transient Absorption Spectroscopy

Samples were suspended in mixture of 20:4:1 acetonitrile: dioxane: mesitylene for optical measurements, placed in 2 mm quartz cuvette, diluted with solvent mixture until absorbance was at .3 at 360 nm. Sample was translated during measurement. Transient absorption measurements were performed using a 2 kHz, 35 fs Ti:Sapphire amplifier. The 800 nm output was beamsplit to pump an optical parametric amplifier that produced tunable pump pulses which were frequency doubled using BBO to achieve 360 nm UV light pump light at the sample. The remaining split 800 nm light was time-delayed and focused into sapphire to produce a white light probe beam. Pump pulses were blocked using a 1 kHz chopper to compare probe intensity though the sample with and without photoexcitation. Pump spot sizes were measured via transmission through a pinhole. Probe light was monitored using CCD camera.

Supplementary Text

Synthesis of 2,7-Pyrenebis(boronic acid)

To a 250 mL RBF, bis(pinacolato)diboronic ester (1.00 g, 2.20 mmol, 1.00 equiv), sodium periodate (2.84 g, 13.4 mmol, 6.00 equiv), and THF:water (4:1 *v*/*v*, 60 mL) were added and the contents were stirred under N_2 for 30 min. HCl (1M, 3.1 mL) was added via syringe, and the reaction was stirred overnight. The reaction mixture was diluted with H_2O (60 mL), filtered through a Buchner funnel, and washed further with water (30 mL). The filtrate was extracted with EtOAc (3 x 50 mL) and the organic fractions were collected and washed with brine. The organic fraction was collected, dried with anhydrous $MgSO_4$, filtered, and the solvent was evaporated to provide a light brown solid. The solid residue was rinsed with hexanes (30 mL) and dried under air to give the product as a brown solid (470 mg, 74%). Analysis of the product matched a published report (*26*).

Synthesis of Colloidal COF Seeds

2,3,6,7,10,11-Hexahydroxytriphenylene (HHTP, 0.02 mmol) and the appropriate corresponding boronic acid (BA, 0.03 mmol) were dissolved in a mixture of CH_3CN:1,4-dioxane:mesitylene (80:16:4 by volume;10 mL) and sonicated for 10 min. The solution was passed through a 0.45 micron PTFE syringe filter to remove insoluble particulates. This solution was put into a 20 mL scintillation vial and sealed. This reaction mixture was heated without stirring to 90 °C for 18 h. which resulted in an indefinitely stable, translucent colloidal suspension.

Monomer Addition to Seeded COF Colloids

HHTP (4 mM) and a diboronic acid (6 mM) were dissolved in separate solutions of CH_3CN:1,4-dioxane:mesitylene (80:16:4 by volume) and sonicated for 10 min. These solutions were passed through a 0.45 micron PTFE syringe filter to remove insoluble particulates. These two solutions were then loaded into 50 mL syringes on a calibrated syringe pump. A COF colloidal suspension was heated to 85 °C, then the diboronic acid and HHTP solutions were added at the noted rate. Throughout monomer addition, 1 mL aliquots were taken to be analyzed by DLS and solution X-ray scattering experiments.

Throughout this manuscript, the amount of monomer added is described by the ratio of monomer added to the amount of monomer used to synthesize the colloidal seeds. For example, 5.0 mL of a 4.0 mM (0.020 mmol) HHTP solution and 5.0 mL of a 6.0 mM PBBA (0.030 mmol) solution added over 1 h to COF-5 seeds prepared using 0.02 mmol HHTP and 0.03 mmol PBBA, would correspond to an addition rate of 1.0 equiv h^{-1}. For simplicity, we define the addition rate in the context of moles of HHTP added, but the diboronic acid concentration is always maintained at 1.5-times the concentration of HHTP.

Growth of COF Colloidal Nanoparticles for Careful Growth Investigation

Initial experiments were performed to interrogate the influence of monomer addition rate on growth of COF particles using COF-5 as a model system. Through these experiments, it was found that faster addition rates resulted in no observed growth. We postulated that this observation was due to the continuous nucleation of COF particles of approximately 30 nm in size. However, it was difficult to differentiate starting colloidal seeds from newly nucleated species because of their

similar sizes. Therefore, we prepared a colloidal suspension of COF particles with an average size of approximately 400 nm to study the seeded growth and nucleation regimes shown in Figure 2. The 400 nm particles were prepared by adding 3.0 equiv of each monomer solution at 0.10 equiv h^{-1} to a solution of as-prepared COF-5 nanoparticles (see above for detailed procedures). The resulting COF particles were used as seeds for the growth experiments described above and in Figure 2.

Addition of Blank Solvent to COF Nanoparticles

Solvent (CH_3CN:1,4-dioxane:mesitylene 80:16:4 vol%) lacking the HHTP and PBBA monomers was added slowly to a solution of COF-5 colloids under the seeded growth conditions to determine if any annealing or ripening processes were operative. After 500 mL of the solvent mixture was added, only minor differences in size distribution were observed by DLS. These results are consistent with observations of COF nanoparticle dilutions reported by Smith *et al. (25)*

Fast Addition to COF-10 and TP-COF

Growth of COF-10 and TP-COF were performed at faster addition rates than those shown in Figure 3. The faster addition rate for these experiments was 0.50 equiv h^{-1} as compared to the slow addition rate of 0.10 equiv h^{-1}. 1.5 equiv HHTP were added at each of these rates. The average particle size decreases when the monomers are added quickly, and the average particle size increases when the monomers are added slowly. These results are consistent with the growth characteristics of COF-5 shown in Figure 2.

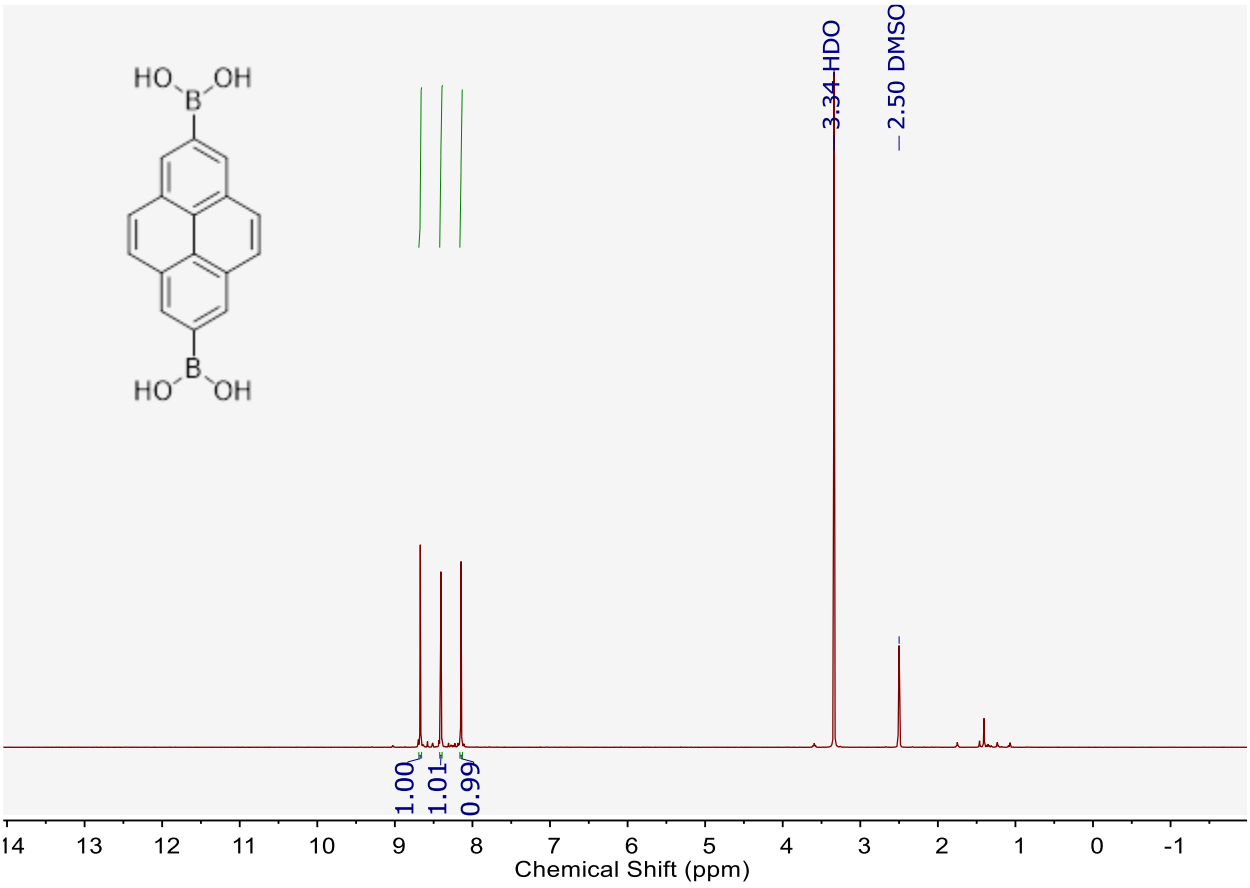

Figure 2.5. ^{1}H-NMR spectrum of 1,7-pyrenediboronic acid (25 °C, 500 MHz, DMSO-d_6).

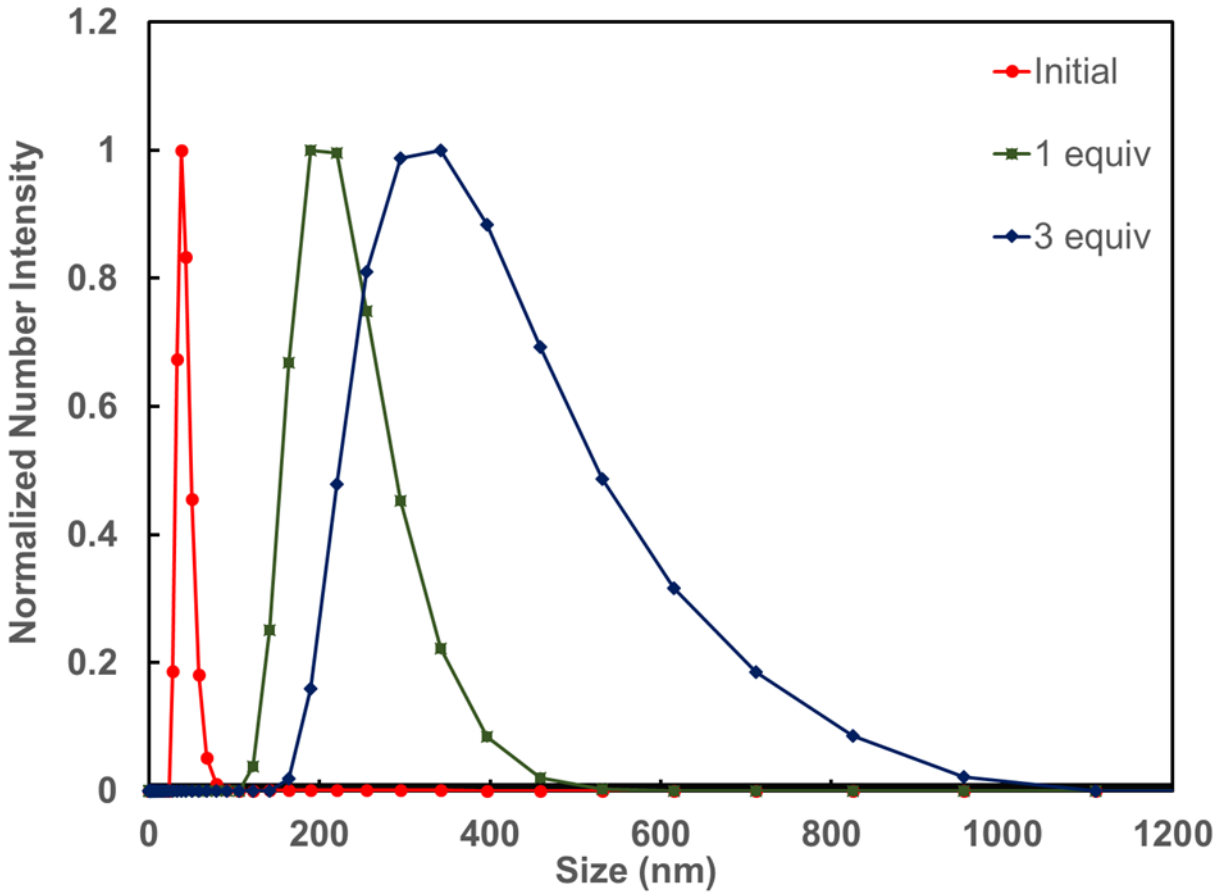

Figure 2.6. Growth of Initial COF Particles. DLS traces of COF particle solutions over the course of monomer addition at a rate of 0.1 equiv h^{-1}. as synthesized (red trace), after a 1 equiv addition (green trace) the size is seen to increase with a monomodal distribution, after 3 equiv addition (blue trace) the size increases further.

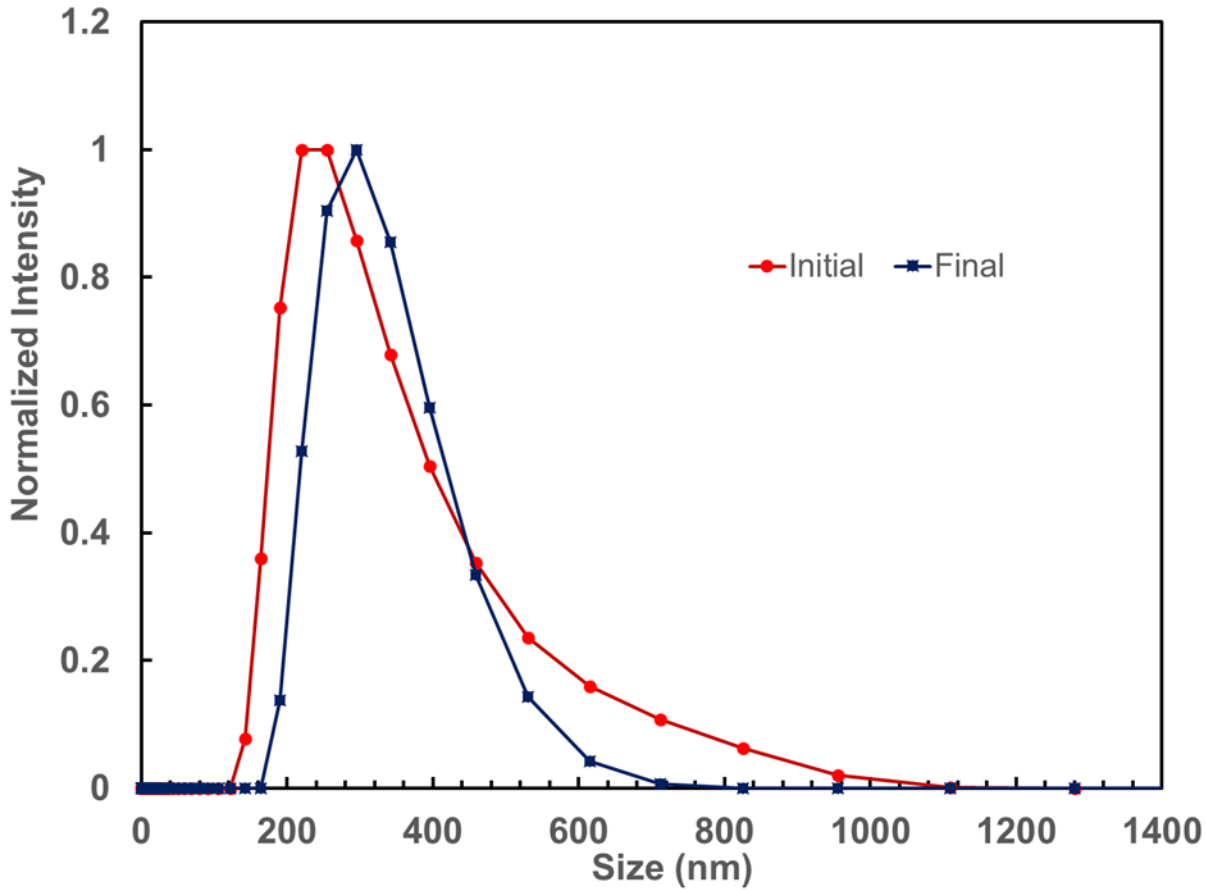

Figure 2.7. DLS of COF-5 nanoparticles before (red trace) and after (blue trace) dilution under the polymerization conditions.

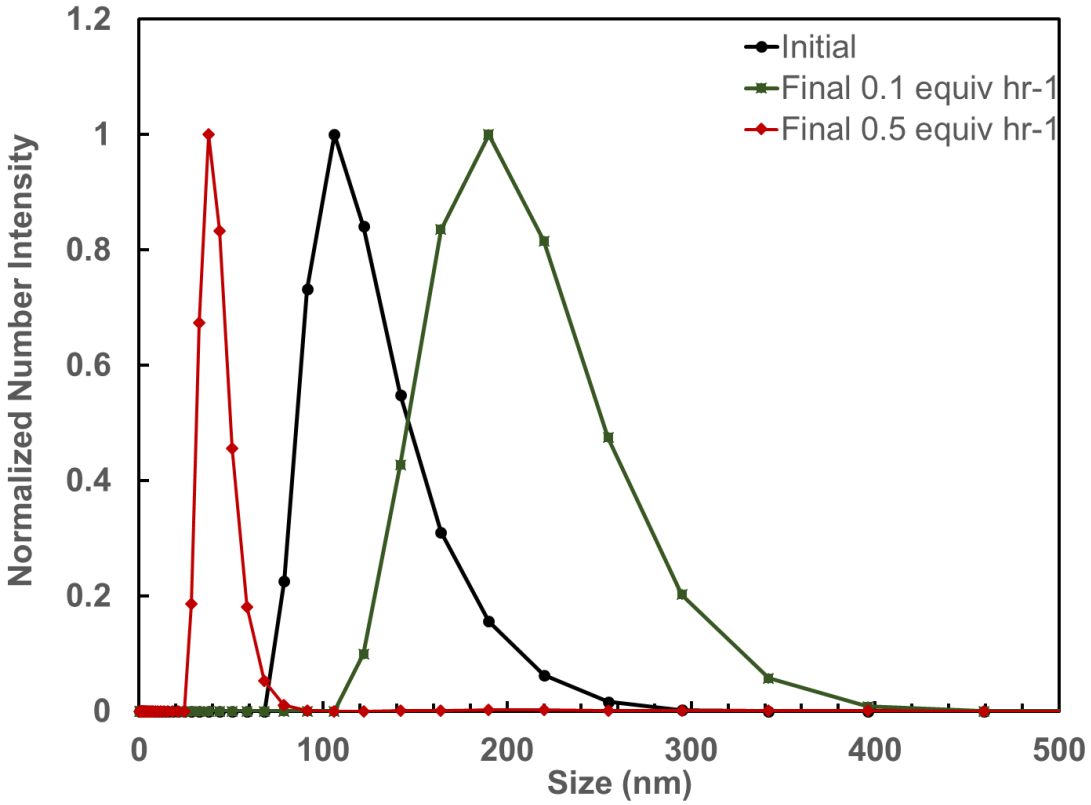

Figure 2.8. DLS of COF-10 particles as a function of monomer addition rate.

A solution of COF-10 particles (black trace) shifts to larger average particle size (green trace) upon slow addition of additional monomers. The average particle size decreases (red trace) when new monomers are added at the faster rate.

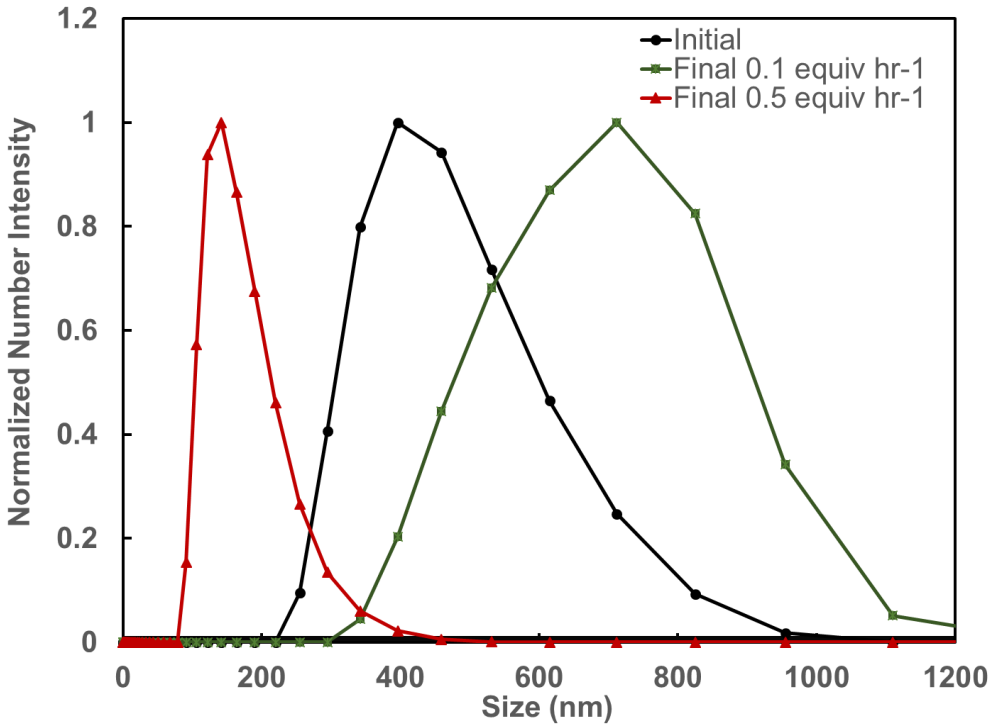

Figure 2.9. DLS of TP-COF particles as a function of monomer addition rate.

A solution of TP-COF particles (black trace) shifts to larger average particle size (green trace) upon slow addition of additional monomers. The average particle size decreases (red trace) when new monomers are added at the faster rate.

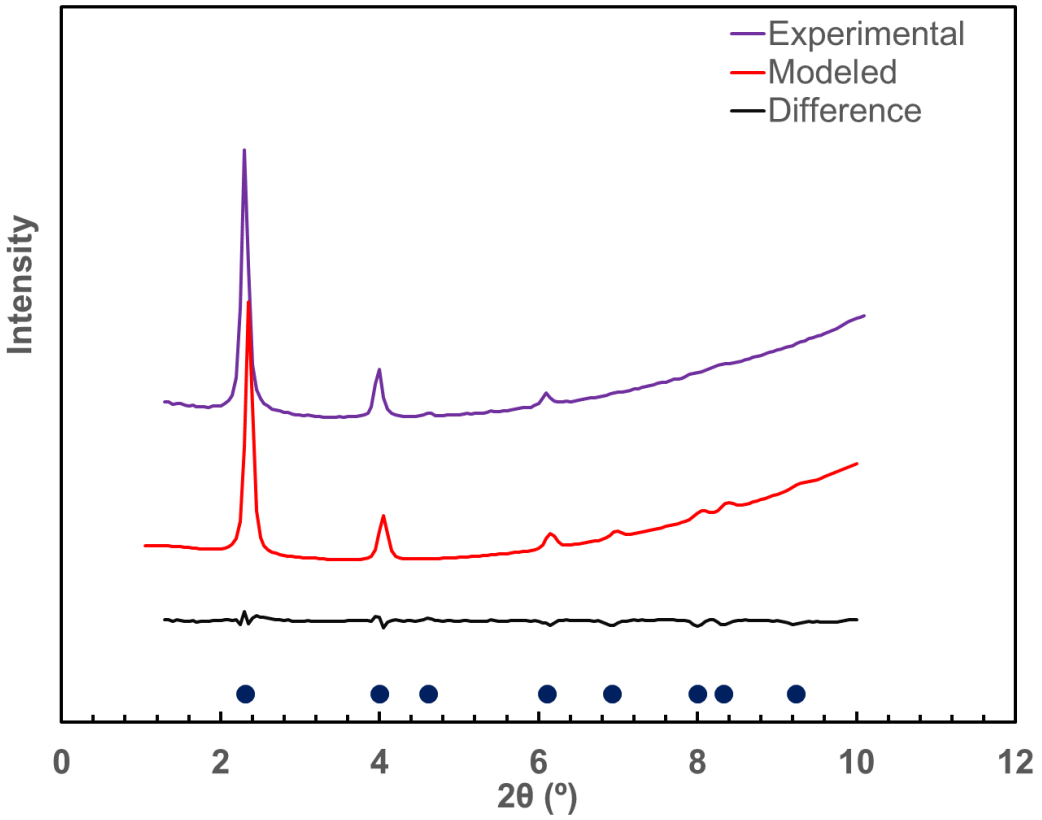

Figure 2.10. Pawley Refined versus Experimental Data of COF-5.

Comparison of experimentally obtained solution X-ray scattering (purple trace) and predicted X-ray scattering (red trace). The difference between the two traces is shown in black with the predicted peak locations noted with blue circles.

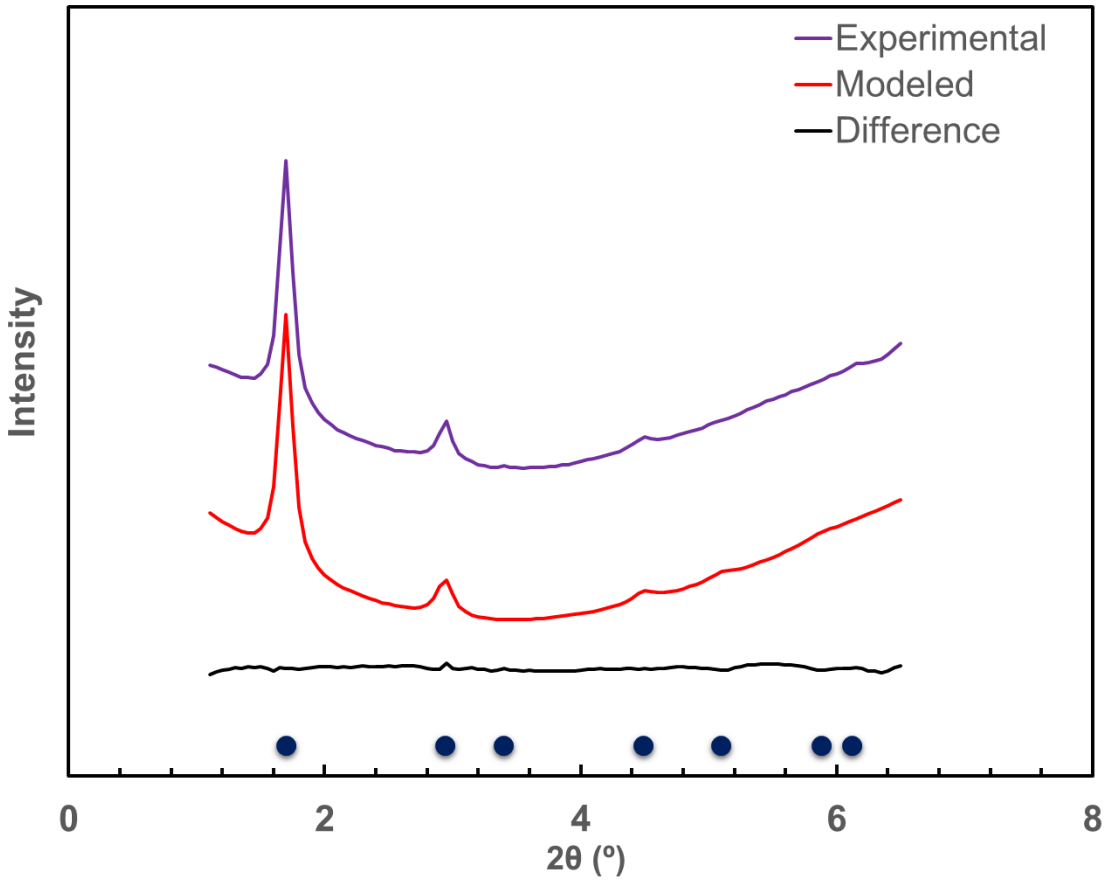

Figure 2.11. Pawley Refined versus Experimental Data of COF-10.

Comparison of experimentally obtained solution X-ray scattering (purple trace) and predicted X-ray scattering (red trace). The difference between the two traces is shown in black with the predicted peak locations noted with blue circles.

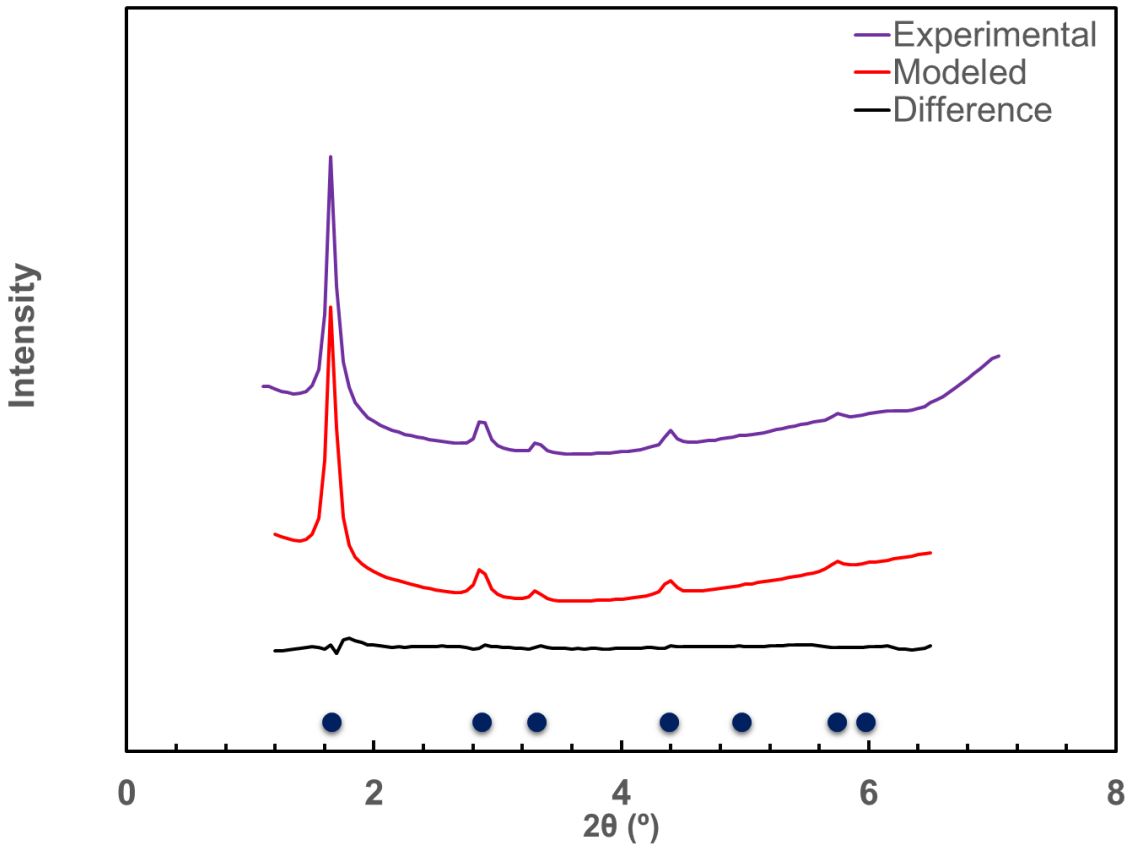

Figure 2.12. Pawley Refined versus Experimental Data TP-COF.

Comparison of experimentally obtained solution X-ray scattering (purple trace) and predicted X-ray scattering (red trace). The difference between the two traces is shown in black with the predicted peak locations noted with blue circles.

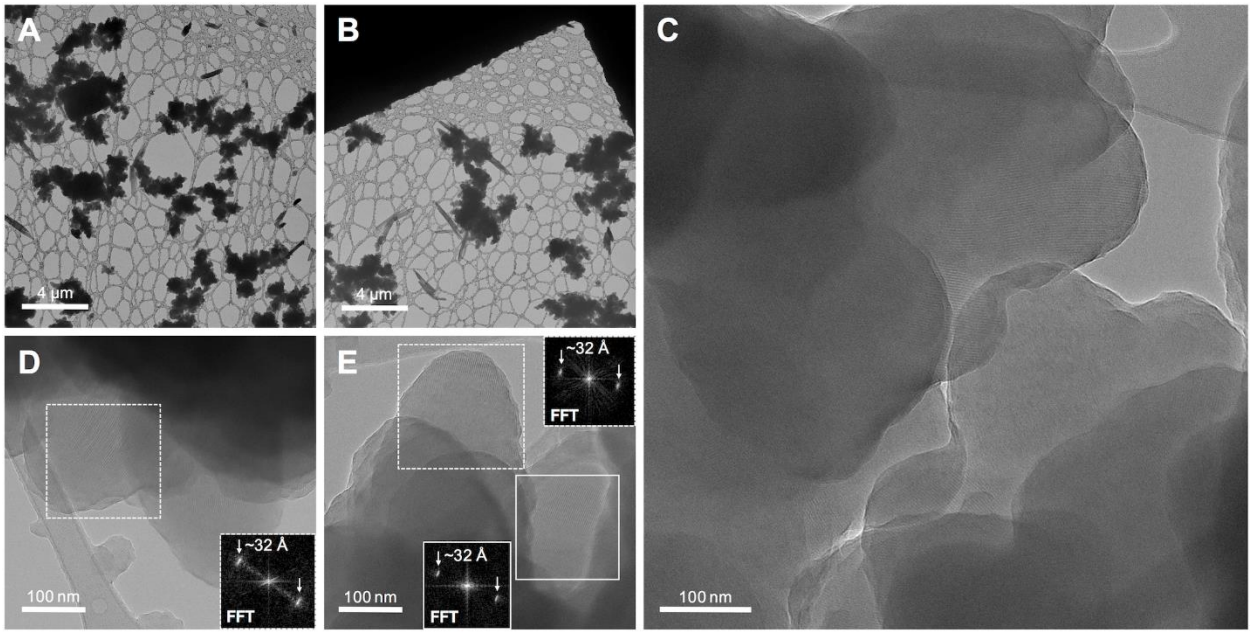

Figure 2.13. TEM characterization of TP-COF particles.

(A-B) Low magnification TEM image of the TP-COF particles that formed into large aggregates when prepared on lacey-carbon TEM substrates (unlike the COF-5 and COF-10 particles (Figure 4), which remained as discrete particles when prepared by the same methods on TEM substrates). (C-E) High magnification TEM images of the TP-COF particle aggregates where large particles that appear to be single crystals are captured (~25 e^- $Å^{-2}$ cumulative dose per image). These particles appear several hundred nanometers in diameter, but the aggregation of the particles into agglomerates prevents more detailed analysis. Insets in (D,E) are fast Fourier transforms (FFTs) of the regions of interest indicated by white boxes in each respective image. Each FFT contains periodic spots corresponding to ~32 Å (matching d_{100} for TP-COF), which represents the lattice fringe spacing for the image in the indicated region of interest.

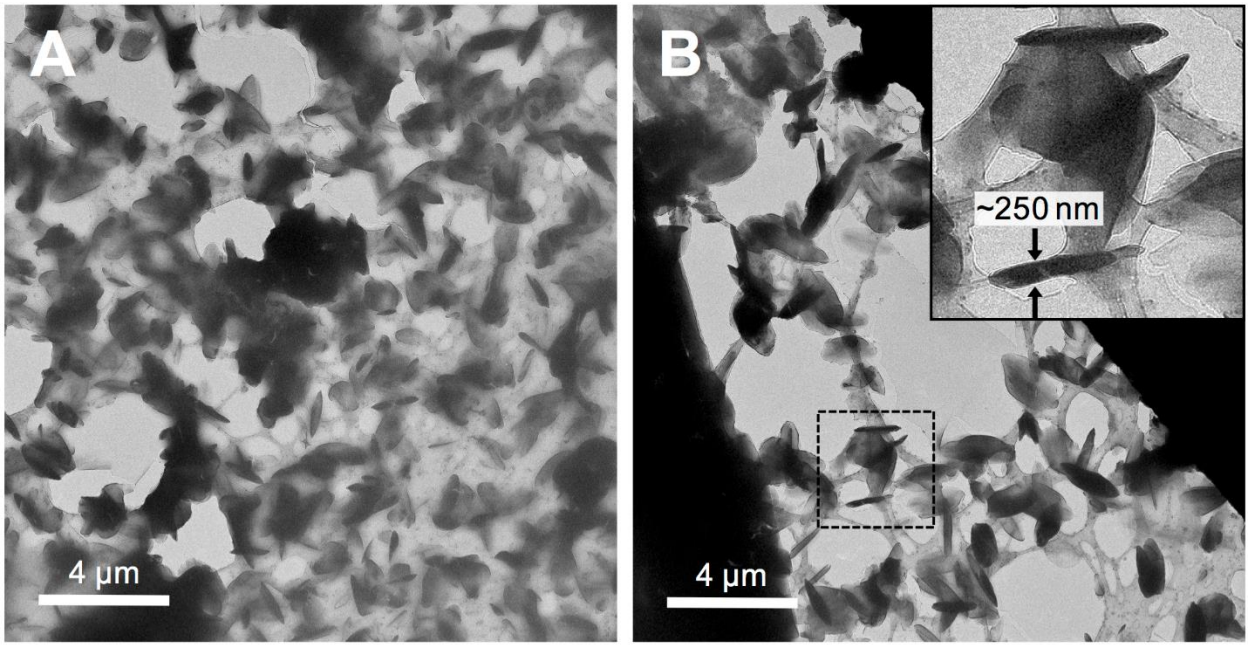

Figure 2.14. Cryo-TEM images of COF-10 particles that are randomly oriented on substrate. (A,B) Low magnification TEM images of COF-10 particles that are not lying flat with the inter-layer stacking direction normal to the TEM substrate. The particles are embedded in a thick layer of solvent, which is cryo-vitrified. Some particles are oriented with their z-thickness parallel to the TEM beam (inset in (B)). The z-thickness of the COF-10 particles is ~250-700 nm (platelet morphology). The black dashed box in (B) indicates the region of interest that is magnified in the inset.

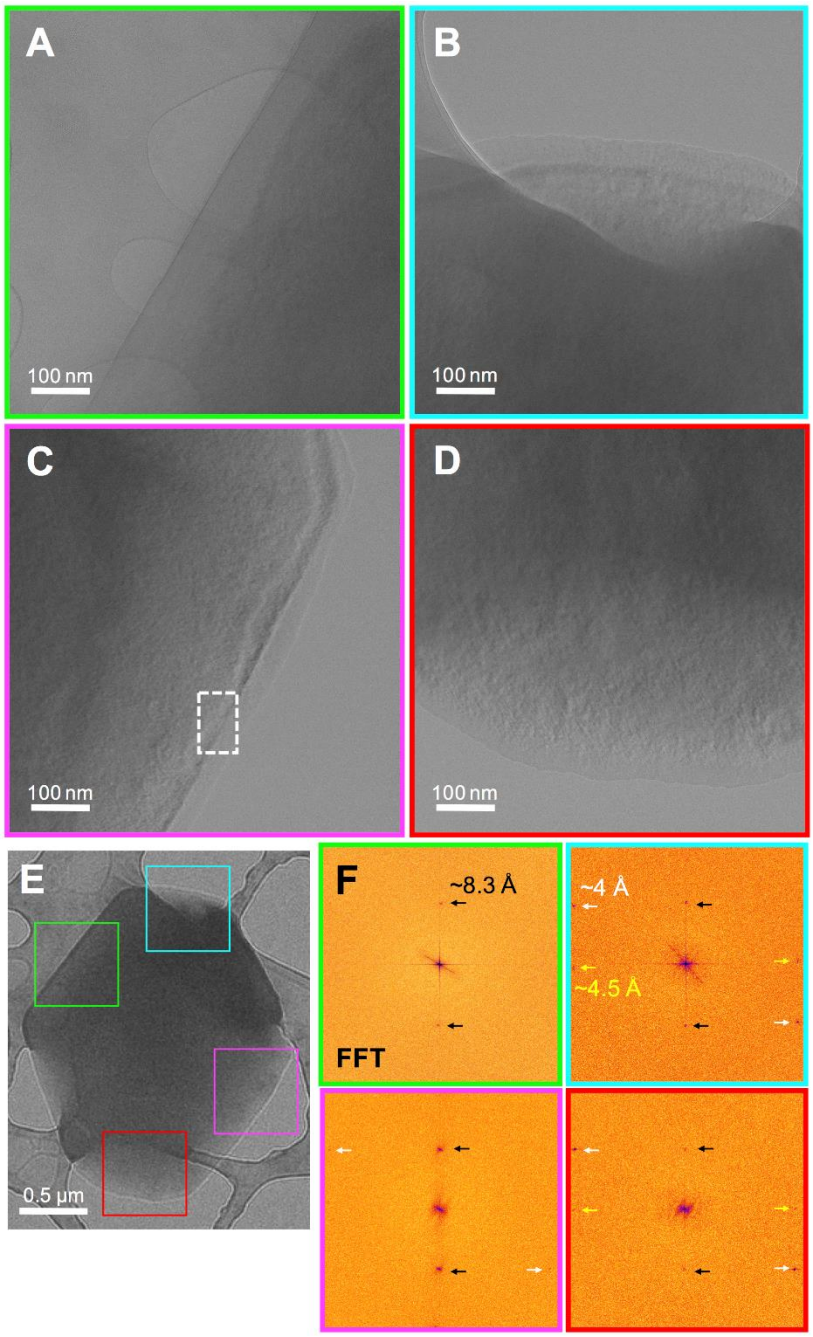

Figure 2.15. TEM Imaging Analysis around the perimeter of one COF-10 Particle.

(A-D) High magnification TEM images (~25 e- $Å^{-2}$ cumulative dose per image) taken at the 4 regions of interest that are marked by matching-color boxes (green, teal, magenta, and red, respectively) in (E). The white dashed box in (C) indicates the region of interest where 8.3 Å lattice

fringes could be visually detected in the raw TEM image; the enlarged image of this region is shown in Figure 4G,H. (E) Low magnification TEM image of the large COF-10 nanoparticle that the high-mag images in (A-D) were taken of (colored boxed indicate regions of the images in (A-D)). (F) Fast Fourier transforms (FFTs) of the four images in (A-D), where the outline colors of each FFT match those of the respective image in (A-D) and the corresponding regions in (E). The FFTs have had the "Fire (inverted)" Look Up Table applied. The black arrows indicate the 8.3 Å periodic spots that are at the same radial location in each of the four FFTs (the white arrows indicate 4 Å spots and the yellow arrows indicate 4.5 Å spots, which are not resolved in all 4 images/FFTs). The FFTs in (F) are the same as those shown in Figure 4I, but showing a larger range in Fourier space (and colored).

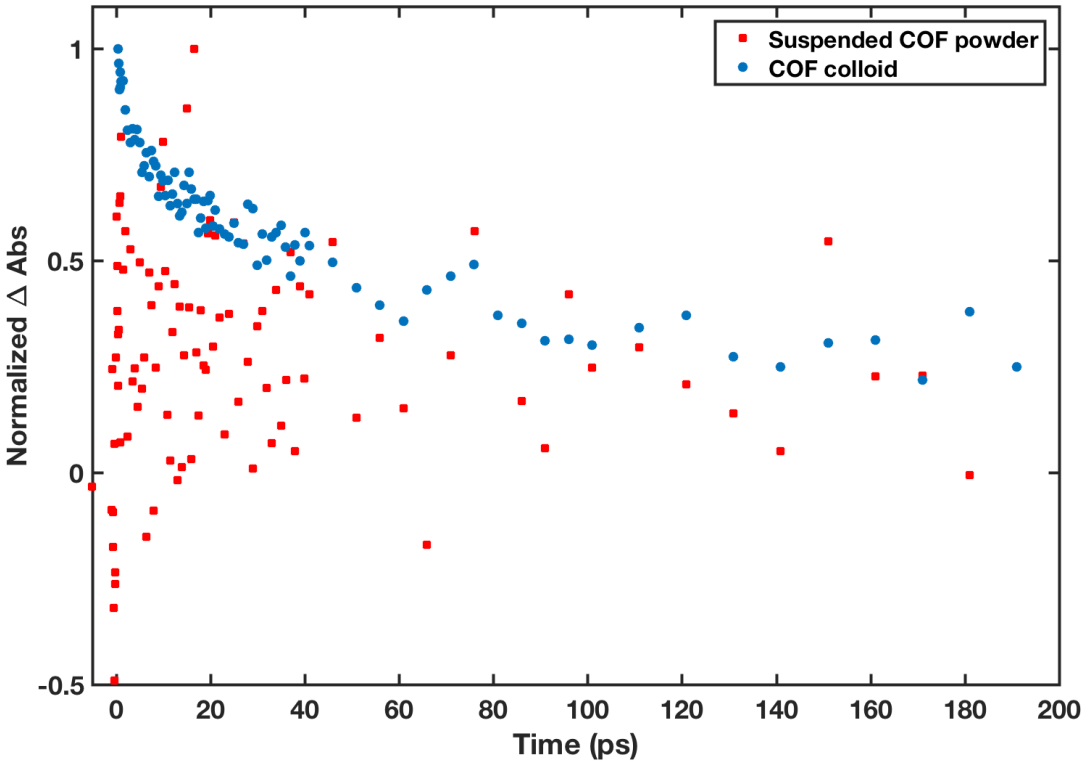

Figure 2.16. Transient Absorption (TA) spectroscopy of COF-5 colloids and powders.

Low data quality is observed with suspended COF-5 powders whereas COF-5 colloids give clean traces under identical conditions.

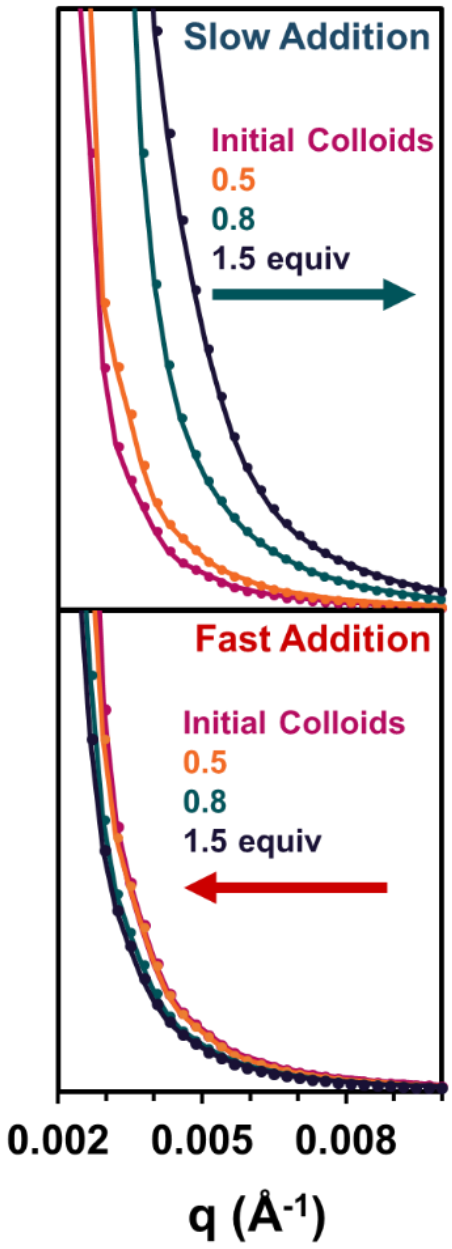

Figure 2.17. Small-Angle x-ray scattering (SAXS) of COF-5 particles as a function of the amount of added monomers at two monomer addition rates.

Table 2.1. Refined parameters determined from crystallographic refinement.

Hexagonal

P6/mmm

$\alpha = \beta = 90°$

$\gamma = 120°$

	a = b (Å)	c (Å)*
COF-5	29.6	3.5
COF-10	36.3	3.4
TP-COF	37.3	3.4

*Insufficient data was available to adequately refine the c parameter and these values are indicative of typical π-stacking distances.

Chapter 3 : Emissive Single-Crystalline Boroxine-Linked Colloidal Covalent Organic Frameworks

3.1 Abstract

The synthesis of periodic two-dimensional (2D) polymers and characterization of their optoelectronic behaviors are challenges at the forefront of polymer chemistry and materials science. Recently, we showed that layered 2D polymers known as 2D covalent organic frameworks (COFs) can be synthesized as single crystals by preparing COF particles as colloidal suspensions. Here we expand this approach from the condensation of boronic acids and catechols to the dehydrative trimerization of polyboronic acids. The resulting boroxine-linked colloids are the next class of 2D COFs to be obtained as single crystalline particles, as demonstrated here for four 2D COFs and one 3D COF. Colloidal stabilization enables detailed structural analysis by synchrotron X-ray diffraction and high-resolution transmission electron microscopy. Solution fluorescence spectroscopy revealed that the COF crystallites are highly emissive compared to their respective monomer solutions. Excitation emission matrix fluorescence spectroscopy indicated that the origin of this enhanced emission can be attributed to through-space communication of chromophores between COF sheets. These observations will motivate the development of colloidal COF systems as a platform to organize functional aromatic systems into precise and predictable assemblies with emergent properties.

3.2 Synthetic Design in 2D Polymers

The structural and functional diversity of layered, two-dimensional (2D) materials provides them with a collection of technologically useful properties.[427, 428] However, synthetically engineering 2D organic materials through polymerization with a desired combination of chemical functionality, porosity, topology, and electronic structure remains a challenge at the frontier of materials chemistry.[93, 398, 429] 2D covalent organic frameworks (COFs) are a class of stable,[430] layered, permanently porous polymers formed from the simultaneous polymerization and crystallization of directional subunits. 2D COFs are synthetically versatile materials, with several hundred reported structures to date,[205, 431] which have inspired interest in applications such as gas separations, catalysis, environmental remediation, energy storage, and optoelectronic devices.[206, 431-436] A limitation of 2D COFs is that they are typically isolated as polycrystalline powders, which complicates their structural, electronic, and optical characterization.[151, 437-439] Recently, we overcame this limitation by stabilizing boronate ester-linked COFs as colloidal suspensions by including nitrile-containing cosolvents in the reaction mixture (**Figure 3.1A**).[440, 441] We attributed this stabilization to the interaction of nitriles with boron-containing functional groups in the framework.[441] This hypothesis led us to postulate that other classes of boron-linked COFs might be stabilized in a similar way.

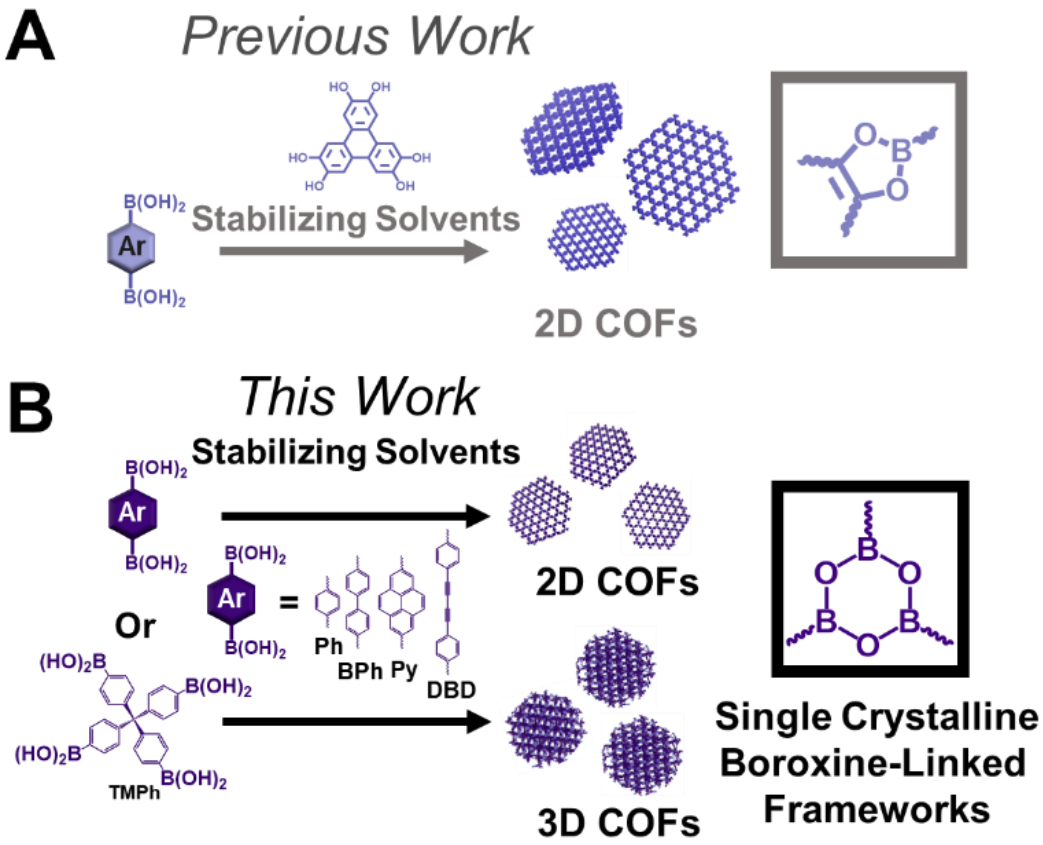

Figure 3.1. (A) Previous work demonstrating stabilization of 2D boronate-ester COFs as colloidal suspensions. **(B)** This work reports the colloidal stabilization of 2D and 3D boroxine-linked COFs, expanding the topological and chemical versatility of this strategy The self-condensation of polyboronic acids in the presence of electron-donating solvents produces colloidal boroxine-linked COFs. This approach is also amenable to the synthesis

The well-dispersed and isolable nature of these COF particles enables their structural analysis using low-dose high-resolution transmission electron microscopy (HR-TEM) and synchrotron X-ray diffraction (XRD). By combining these techniques, we can gain insight into the

interlayer arrangement of 2D polymer sheets, which is challenging to assign in powder COF systems but strongly affects their electronic structure.[442, 443] While performing these investigations, we noted that COF colloids were highly fluorescent compared to their respective monomers. Although the fluorescence of COF powders has been reported,[408, 409, 444-446] these experiments are typically complicated by the highly scattering nature of powder samples and the inherent ambiguities associated with possible emission from species at grain boundaries or impurities trapped in the solid-state. Here, dispersed, well-defined COF colloids enable sophisticated and informative spectroscopic characterization, including excitation-emission matrix fluorescence spectroscopy (EEMS). EEMS revealed that the enhanced emission of the COFs originates from the organization of fluorophores into 2D layered structures. We anticipate that these results will greatly impact approaches to COF synthesis and inform the understanding of through-space electronic communication in 2D polymers and other framework materials.

3.3. Controlled Polymerization of Boroxine-Linked 2DPs

We synthesized **Ph-COF** (previously reported[41] as COF-1) in mixtures of CH_3CN and 4:1 1,4-dioxane:mesitylene. The 1,4-phenylenebis(boronic acid) (PBBA) monomer was first dissolved in the specified solvent mixture at a concentration of 10 mM and then the container was sealed, sonicated, and heated to 90 °C for an additional 3 days (**Figure 3.2A**). When 0–30 vol% CH_3CN was included in the reaction mixture, a white precipitate formed over the course of 3 days. These precipitates were isolated and characterized via Fourier-transform infrared spectroscopy (FT-IR) and XRD, the results of which were consistent with previous reports of **Ph-COF** (**Figure 3.17** and **Figure 3.18**).[41] In contrast, no precipitation was observed when 30–80 vol% of CH_3CN was

included in the reaction mixture while over the course of 3 days these solutions changed from transparent to opaque-white suspensions (**Figure 3.2B**) that were stable for at least 6 months. When >80 vol% of CH_3CN was included in the reaction mixture, the heated monomer solution never became transparent, which we attribute to the insufficient solubility of PBBA under these conditions. These observations indicate that boroxine polymerization is not inhibited by the presence of CH_3CN and that a specific range of solvent mixtures is necessary for the successful solubilization of PBBA and stabilization of the **Ph-COF** particles.

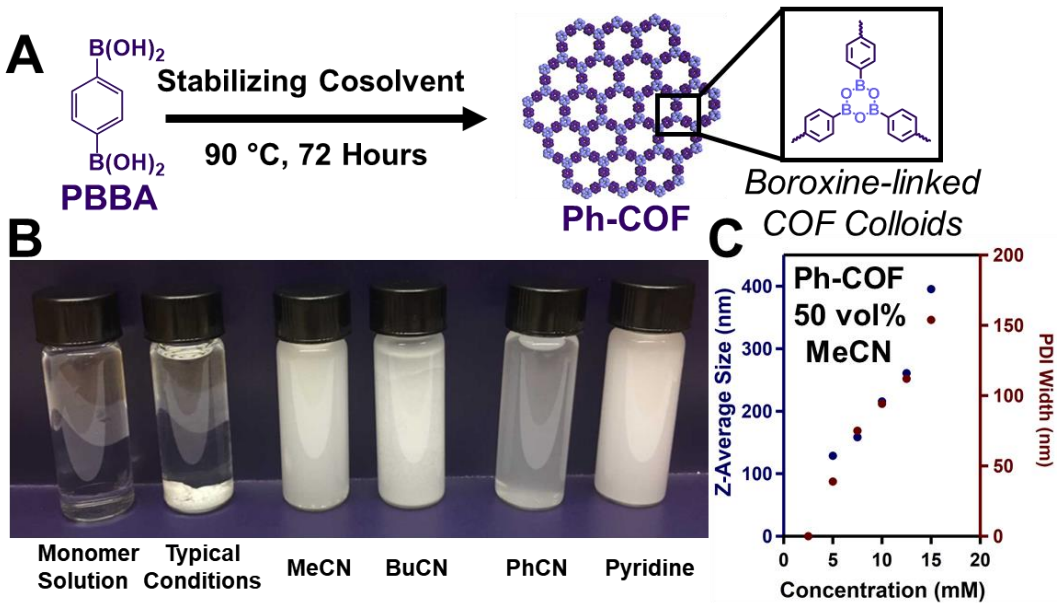

Figure 3.2. (A) Synthesis of boroxine-linked Ph-COF particles through solvothermal condensation of PBBA (10 mM). **(B)** Photograph comparing the transparent monomer solution to typically isolated Ph-COF powders[41] and dispersed Ph-COF crystallites synthesized in the presence of electron-donating solvents. **(C)** Dynamic light scattering (DLS) Z-average size and polydispersity index (PDI) of Ph-COF synthesized with variable initial PBBA concentrations.

3.4. Lewis-basic solvent stabilization

Inclusion of other nitrile cosolvents (butyronitrile [BuCN], propionitrile [PrCN], and benzonitrile [PhCN]) at 50 vol% of the solvent mixture stabilized **Ph-COF** particles in a similar fashion to CH_3CN, in which transparent solutions became cloudy during heating over 3 days (**Figure 3.2B**). The inclusion of pyridine in the reaction mixture also resulted in a colloidal suspension of **Ph-COF** particles. However, the transition to a cloudy suspension occurred within approximately 1 minute, which may be due to its stronger interaction with boroxines because of its increased basicity.[447] These results show that the inclusion of Lewis-basic cosolvents in boroxine-linked COF syntheses results in stable colloidal suspensions. These observations are consistent with previous reports that described Lewis-basic cosolvents coordinated to the Lewis-acidic sites of boron-linked COFs.[224, 448, 449] Taken together, stabilization by electron-donating solvents suggests a direct interaction between the cosolvent and COF surface, which we speculate is responsible for the observed colloidal stability, as has been found for other classes of nanoparticles.[450]

A central advantage of stable nanocrystal suspensions is that their size can be controlled by varying the synthesis and growth conditions.[440] **Ph-COF** particle sizes were controlled by varying the initial PBBA concentration. We found that concentrations lower than 5 mM did not produce colloidal particles, presumably because this is below the critical nucleation concentration for these conditions.[451] In contrast, concentrations above 15 mM were not initially soluble and produced a mixture of **Ph-COF** nanoparticles and powder precipitate. However, within the regime where **Ph-COF** nanoparticles were formed exclusively (5–15 mM PBBA), dynamic light scattering (DLS) measurements indicate that initial monomer concentration is positively correlated

with the Z-average size, with particle sizes ranging between 100 and 400 nm, and a polydispersity index (PDI) width between 50 and 200 nm (**Figure 3.2C**).[452] This behavior is consistent with linear condensation polymerizations in which the starting monomer concentration leads to larger average chain length and dispersity.[453] This observation highlights the potential of using colloidal nanocrystals as a platform to explore mechanisms of COF nucleation and elongation.[151, 440, 451]

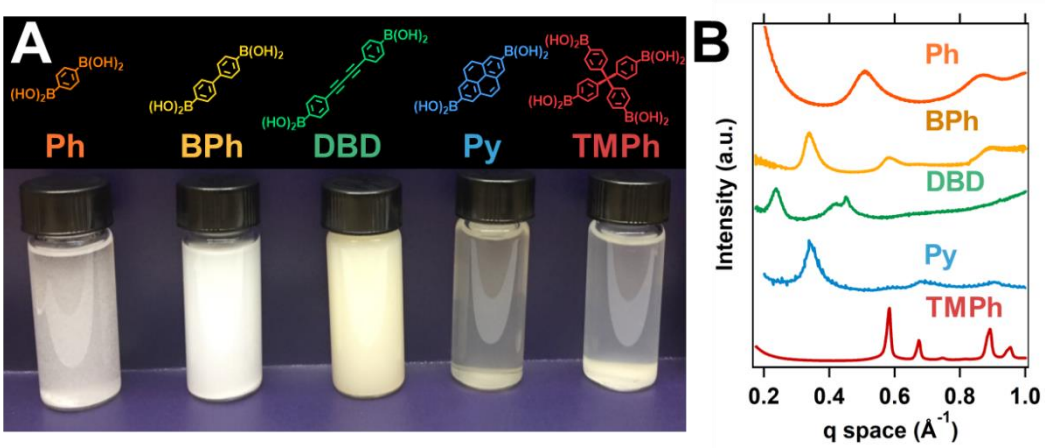

Figure 3.3. (A) Monomer structures and optical images of structurally diverse COF nanoparticle suspensions. **(B)** X-ray diffraction (grazing-incidence of drop-cast crystallites: **TMPh-COF** or *in solvo* wide-angle X-ray scattering: **Ph-COF**, **BPh-COF, DBD-COF, Py-COF**) of boroxine-linked COF nanocrystals.

3.5. A modular approach to boroxine-linked single-crystals

A defining feature of COF chemistry is the modular approach used to synthesize isoreticular crystalline, porous, organic polymers. Interested in understanding the synthetic versatility of boroxine-linked COF colloid stabilization, we self-condensed several polyfunctional boronic acids to form their corresponding boroxine-linked COFs, including 2,7-pyrenebisboronic

acid (**Py-COF**), tetraphenylmethylboronic acid (**TMPh-COF**), and two previously unreported COF structures condensed from, 4,4′-biphenylbisboronic acid (**BPh-COF**) and diphenylbutadiynebisboronic acid (**DBD-COF**). All self-condensations were performed in a solvent mixture of CH_3CN:1,4-dioxane:mesitylene (50:40:10 vol%) by heating the respective monomers of each COF at 90 °C for 3 days. The solutions became cloudy for all reactions investigated, indicating the formation of solution-stabilized nanoparticles (**Figure 3.3A**).[454]

Synchrotron X-ray diffraction of the colloidal boroxine-linked COF suspensions confirmed their crystallinity and identity (**Figure 3.3B**). Diffraction features were observed for **Ph-COF** at 0.55 $Å^{-1}$ and 0.85 $Å^{-1}$, corresponding to the (100) and (110) Bragg features, respectively. The location of these features is consistent with those reported by Côte *et al.*, which were assigned to an AB offset structure of **Ph-COF** in which adjacent layers are offset by half a unit cell (**Figure 3.12**).[41] However, the relative intensities of these features were inconsistent with this report. Due to the solvated nature of these crystallites, it was challenging for us to definitively assign their interlayer arrangement based on the few, weak diffraction signals observed here. The (100) diffraction feature for both the known **Py-COF** and previously unexplored **BPh-COF** occur at 0.39 $Å^{-1}$, consistent with the nearly equivalent lattice dimensions of these two COFs (**Figure 3.13** and **Figure 3.15**). This feature, along with higher order diffractions, allowed us to assign these materials as having AA eclipsed structures. The location of the primary diffraction feature ((200) at 0.21 $Å^{-1}$) for the newly synthesized **DBD-COF** was consistent with the hexagonal unit cell size expected for a linker of this length. However, its relative intensity pattern was unusual when compared to those of other hexagonally symmetric COFs.[455] Ultimately, we attributed this diffraction pattern to a partially offset structure. We hypothesize that this stacking is governed by

the interaction of stacked boroxines given the relatively weak van der Waals forces associated with the COF diphenylbutadiyne moieties.[174] Finally, the 3D boroxine-linked COF, **TMPh-COF**, produced diffraction features at 0.59, 0.62, 0.91, and 0.96 $Å^{-1}$, which correspond to the (211), (220), (310), and (321) features, respectively. This diffraction pattern is consistent with the previously reported (then called COF-102) non-interpenetrated *ctn* net for this material.[456] Together, these results show that colloidally stable particles exhibit the defining structural regularity of COF materials. Additionally, these diffraction results demonstrate that chemically and topologically diverse framework materials are amenable to colloidal stabilization. The limited number and strength of the diffraction features for 2D COFs, including those reported here, impedes definitive assignments of stacking arrangements.[433] Secondary structural characterization of agglomerated polycrystalline COF powders is also challenging and has limited the number of reports aimed at in-depth structural characterization using direct imaging techniques, such as electron microscopy.[457] In contrast, dispersed crystallites are an ideal morphology for microscopic structural characterization. With this in mind, we set out to explore COF nanocrystals via high-resolution transmission electron microscopy (HR-TEM).

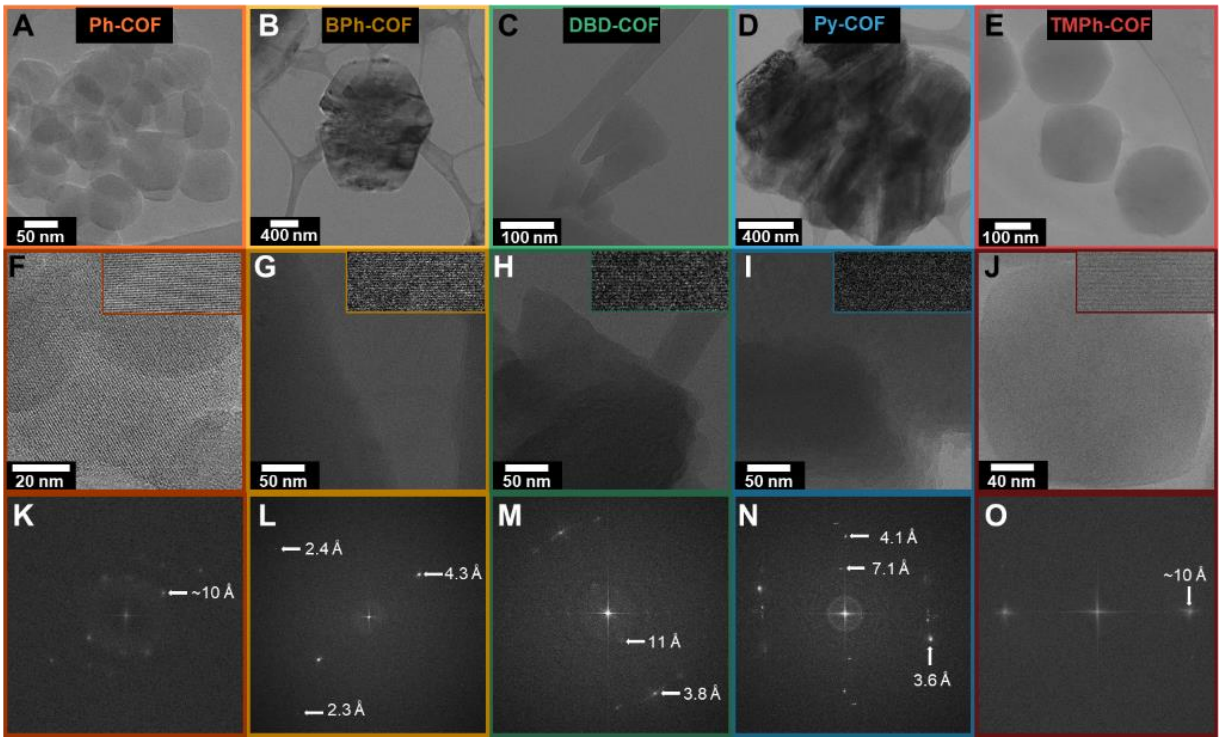

Figure 3.4. Orange: Ph-COF; Yellow: BPh-COF; Green: DBD-COF; Blue: Py-COF; Red: TMPh-COF. **(A-E)** Low-resolution TEM images of COF particles. **(F-J)** High-resolution TEM images of COF particles. Inset; lattice fringes of COF particles. **(K-O)** FFTs of COF particles.

3.6. Direct imaging of boroxine-linked 2D polymers

By TEM, 2D COFs are visible in micrographs as layered single-crystallites with sizes in agreement with DLS measurements (**Figure 3.4A-E)**. When the images of COF crystallites (**Figure 3.4F-J**) were subjected to a fast Fourier transform (FFT) (**Figure 3.4K-4O**), we found that all COF particles produced crystalline spot patterns rather than ring patterns, indicative of

single-grain crystallinity. This supports the existence of COF crystallites as single-crystalline particles when suspended, as was observed previously for colloidal boronate ester-linked 2D COFs.[440] For **Ph-COF**, discrete particles agglomerated upon drop-casting, but they maintained their hexagonal morphology with clearly visible lattice fringes extending from one end of the particles to the other, confirming the single-crystalline nature of the **Ph-COF** dispersed crystallites **(Figure 3.4A)**. For **Ph-COF**, FFT images exhibited a preeminent lattice spacing of 10 Å (d_{110}). This spacing is consistent with structural models of **Ph-COF** sheets stacked as alternating offset layers.[41] **Py-COF** appeared as agglomerated hexagonally faceted particles with lattice fringes observed at 7.1 Å (d_{200}), consistent with the *in solvo* XRD patterns of these materials. In addition to the d_{200} feature, the FFT pattern of **Py-COF** also exhibited d_{310} features at 4.1 Å. Similarly, the well-dispersed hexagonal **BPh-COF** particles have visible higher-order lattice fringes (d_{400}), consistent with their XRD pattern. For these three materials, a set of spots at 90° to the in-plane diffraction features is observed which is in accordance with the expected interlayer distance of 3–4 Å for van der Waals heterostructures. These d_{001} spacings suggests the interlayer distance associated with **BPh-COF** is smaller than that associated with **Py-COF**. We attribute this difference to a synchronized offset stacking of alternating phenyl rings that has been reported in other COF systems.[458] In contrast, such stacking is not possible in **Py-COF** because of its forced planarity. **DBD-COF** particles were present as predominantly trigonal particles. Furthermore, the observed preeminent lattice spacing of 11 Å is consistent with the model of these crystallites (d_{110}) generated through Pawley refinement of the experimentally collected X-ray diffraction patterns (**Figure 3.35 - Figure 3.38**). We expect that the prominence of the d_{210} lattice spacing in these crystallites is related to the offset structure assigned from the *in solvo* XRD patterns. The interlayer

arrangement of 2D COF sheets seen here adds to a growing body of evidence that interlayer arrangements of polymer sheets are governed by an array of intermolecular forces.[171, 458-461] Finally, the 3D **TMPh-COF** crystals were observed to be regularly faceted crystals with a preeminent lattice spacing of 10 Å. This observation is consistent with their previously reported non-interpenetrated *ctn* net.[456] Taken together, TEM imaging demonstrates that a second class of 2D COFs and 3D COFs can be synthesized as single-crystalline particles using a colloidal stabilization approach. Furthermore, these results indicate that emerging TEM technologies, such as direct electron detectors facilitating low-dose imaging, are promising tools in the exploration of interlayer arrangements of 2D polymer sheets and electron beam sensitive materials more generally. This interlayer arrangement remains challenging to observe using other characterization methods but is vastly important for a suite of emergent material properties.

3.7. Electronic Interactions in Layered 2D polymers

Another limitation of precipitated polycrystalline 2D COF powders is the difficulty associated with characterizing their intrinsic optical or electronic properties because of their propensity to scatter light.[462] However, because 2D materials are of interest for many electronic applications, it is of paramount importance to explore the optoelectronic nature of these materials. During the course of our investigation, we observed that all of the colloidal 2D COF suspensions were noticeably more fluorescent than their boronic acid monomers at the same fluorophore concentrations (**Figure 3.5**). Motivated by the results of our previous investigations into enhanced optical characterization of 2D COF colloids,[440, 463] we set out to explore the origin of enhanced

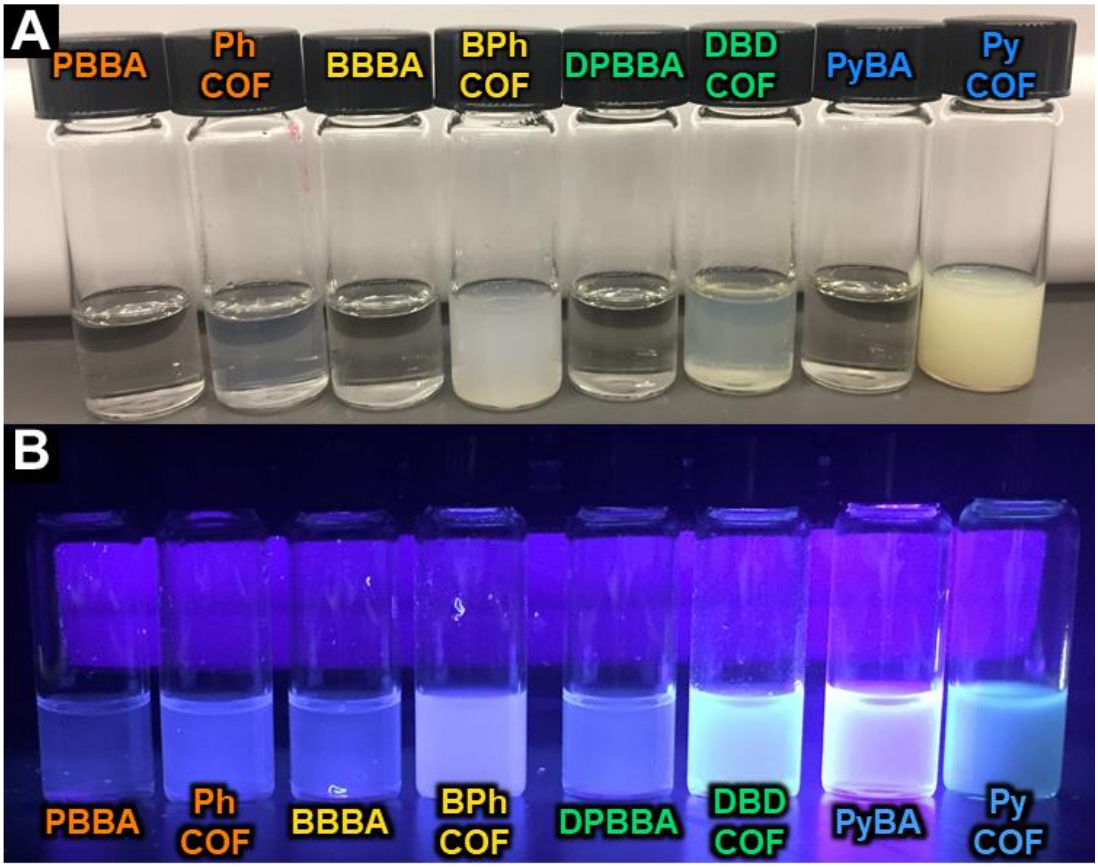

nanocrystal fluorescence using EEMS. While EEMS showed that all 2D COF colloids were more emissive than their respective monomers, we chose to focus our investigation on the highly fluorescent **Py-COF** and **DBD-COF** materials.

Figure 3.5. Orange: Ph-COF; Yellow: BPh-COF; Green: DBD-COF; Blue: Py-COF. Photographs of COF monomer solutions and their resultant COF nanocrystals **(A)** under natural light and **(B)** under UV irradiation.

EEMS shows that both **DBD-COF** (**Figure 3.6A**) and its respective DPBBA monomer have absorbance maxima at 365 nm (**Figure 3.6C**). However, the emission of **DBD-COF** at this wavelength is an order of magnitude more intense than the DPBBA monomer (**Figure 3.6C**). This

electronic communication was surprising because boroxines are not conjugated and therefore not thought to allow electronic coupling in the plane of covalent bonding.[228] However, the difference in monomer and COF fluorescence seen here indicates there is some electronic coupling between chromophores in the COF structure. We probed this effect further by quantifying the quantum yields of several of the COF colloids and their respective monomers. Absorption/emission measurements of the **DBD-COF** showed nearly an order of magnitude more intense emission than the DBD monomer, but no changes in the location of the optical features (**Figure 3.43**). We attribute this increased fluorescence to aggregation-induced emission, which has been noted for molecular aromatic systems in previous reports,[464, 465] here induced by restricted rotation of the chromophores in the layered 2D architecture. **Ph-COF** and **BPh-COF** show similarly enhanced emission intensity and no spectral shifts, albeit with lower quantum yields. These combined observations indicate that several boroxine-linked 2D COFs exhibit increased emission quantum yields associated with their layered structure, which restricts molecular motion.

Py-COF also exhibits more intense photoemission than its corresponding monomer (PyBA), but the COF's emission is blue-shifted (**Figure 3.5B**). Similar to the **DBD-COF**, the local excited-state emission of **Py-COF** broadened (**Figure 3.6D**), which we attribute to perturbed electronic states of the pyrene chromophores. EEMS of **Py-COF** shows that the emission blue-shifts 50 nm relative to the monomer at an excitation of 325 nm. This blue-shifted emission is accompanied by red-shifted absorption (**Figure 3.6D**). The quantum yield of the PyBA monomer is 15%, which increases slightly to 18% for the PyCOF. The shifts in absorption, emission, and quantum yield are all consistent with the organization of the pyrene chromophores into J-aggregates.[466, 467] Furthermore, **Py-COF** has an additional emission feature at 435 nm when

excited at 350 nm, which is consistent with the formation of an exciplex structure and has been observed in previous reports of organized molecular pyrenes (**Figure 3.6E**).[468] This observation is consistent with the assignment of **Py-COF** as an eclipsed structure having inter-sheet pyrenes in physical contact. Taken together, these results show how electronic communication in framework materials can occur in stacked systems even when not conjugated through covalent bonds. We expect that using nonconjugated COFs to exploit through-space electronic communication will feature prominently in future COF systems.

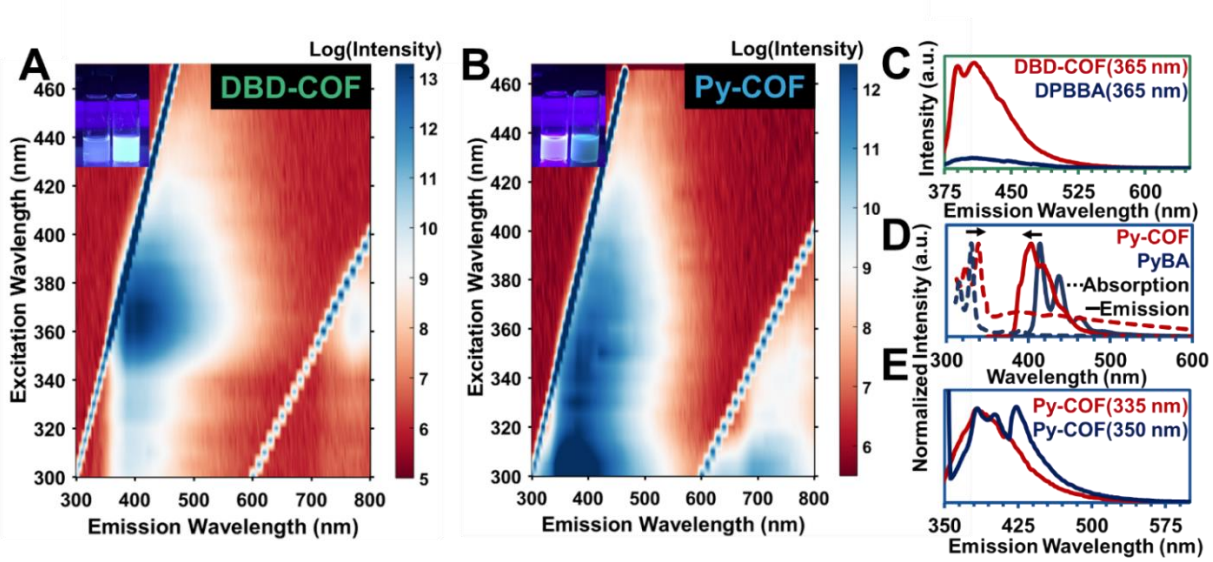

Figure 3.6. (A) EEMS of DBD-COF. Inset; optical image of DPBBA monomer (left) and DBD-COF (Right) under UV irradiation **(B)** EEMS of Py-COF. Inset; optical image of PyBA monomer (left) and Py-COF (Right) under UV irradiation. **(C)** Emission of DBD-COF compared to the DPBBA monomer at the same concentration. **(D)** Normalized absorption and emission intensity of Py-COF compared to the PyBA monomer showing a red-shift of the absorption spectra and blue shift and broadening of the emission spectra. **(E)** Normalized emission of Py-COF under two excitation wavelengths showing the emergence of an excimer emission (430 nm).

3.8. Conclusions

2D COFs are promising candidates for many applications, but their investigation and utility has been greatly hampered by the isolation of these materials as weakly polycrystalline aggregates. In the interest of adding 2D COFs to the ever-expanding suite of functional 2D materials, it is imperative to improve their quality and level of characterization, including an understanding of how stacking influences their optical properties. These findings demonstrate that colloidal stabilization of boroxine-linked frameworks occurs in the presence of electron-donating solvents. This strategy is amenable to the synthesis of four single-crystalline 2D COF materials, including two newly synthesized systems. Further, we show how this strategy can be topologically expanded to include a 3D COF. Synchrotron XRD and HR-TEM provided insight into the interlayer arrangement of these materials and confirmed their single-crystalline nature. Furthermore, stabilizing COFs as colloidal suspensions allowed us to probe the intrinsic optical properties of these materials with EEMS. The high-quality of the spectroscopy of these materials allowed us to assign the origin of the optical features to the formation of π-exciplexes, which is indicative of through-space electronic communication of chromophores brought into close proximity in the COF structure. We expect that future colloidal COFs will prove to be a versatile platform to investigate emergent optoelectronic phenomena in 2D polymer systems, such as triplet up-conversion, singlet-singlet annihilation, or photoredox processes.[469-471] Understanding these processes, enabled by access to highly crystalline materials obtained from controlled COF polymerizations, will ultimately facilitate the incorporation of 2D polymers into relevant optoelectronic devices.

3.9. Chapter 2 Supplementary Information

I. Materials and Methods.

Materials. All monomers, solvents, and catalysts were either purchased from commercial sources or prepared following literature reported protocols. All materials were used as received without further purification. Anhydrous THF was obtained from a solvent purification system (JC Myer System).

Solution Nuclear Magnetic Resonance. ^{1}H NMR spectra were acquired on a 400 MHz Agilent DD MR-400 system or Bruker Avance III 500 MHz spectrometer and recorded at 25 °C. All chemical shifts were calibrated using residual solvent as internal reference ($CDCl_3$: 7.26 ppm for ^{1}H NMR. DMSO: 2.5 ppm for ^{1}H NMR).

Dynamic Light Scattering. Dynamic light scattering (DLS) data were collected using a Malvern Zetasizer equipped with a 633nm He-Ne 5mW laser in a quartz cuvette with a 10mm pathlength at room temperature. Data was analyzed using the proprietary Zetasizer software.

Fourier-Transform Infrared Spectroscopy. Infrared spectra were collected on a Nicolet iS10 FT-IR spectrometer equipped with a ZnSe crystal in attenuated total reflection mode. Spectra were background subtracted to remove contribution from atmospheric species. Spectra as shown were not corrected or calibrated to any IR feature.

***In solvo* X-ray Diffraction.** Small- and wide-angle X-ray scattering (SAXS/WAXS) patterns were collected at Argonne National Lab's (ANL) Advanced Photon Source (APS) at both sectors 5-ID-D (DND-CAT) and 12-ID-D with a capillary transmission geometry. Experiments conducted at 12-ID-D were collected at a beam energy of 12 keV and experiments conducted at 5-ID-D were collected at a beam energy of 13.3 keV. Individual frames were collected on a set of Pilatus detectors, which were then summed and radially integrated to produce a linear XRD pattern using proprietary software available at the APS. Scattering intensity is reported as a function of the modulus of the scattering vector q, related to the scattering angle 2θ by the equation $q = (4\pi/\lambda) \sin \theta$, where λ is the X-ray wavelength. The sample-to-detector distance was adjusted to measure across relevant detection ranges. Capillary experiments were conducted using 2.0 mm OD borosilicate capillaries with 0.2 mm wall thicknesses purchased from Hilgenberg GmbH.

Grazing-Incidence X-ray Diffraction. As noted in the text, several reported X-ray scattering patterns were collected by drop casting undiluted samples of COF nanocrystals onto silicon wafers and allowing the solvent to evaporate. GIWAXS measurements were then performed at Advanced Photon Source at Argonne National Laboratory using the 8-ID-E Beamline under vacuum. The crystallites were irradiated until the detector was 80 % of saturated an incidence angle of 0.14° in vacuum using 10.92 keV (1.135 Å) X-rays. The scattering was recorded on a Pilatus 1 M detector located 228 mm from the sample. In all cases, significant silicon substrate scatter was observed. The raw images were merged, pixel coordinates were transformed to q-space, line cuts generated using GIXSGUI for Matlab.[472]

COF Modeling and Structural Refinement. Crystal modeling of the COF structures was carried out using the Materials Studio (ver.5.0) suite of programs by Accelrys.[473] The initial structures were constructed piecewise starting with a primitive hexagonal unit cell of a P6 space group. The cell parameter was estimated according to the distance between the center of the vertices for each COF, and c parameter was chosen as 3.35 Å, which has been observed for similar materials.[462] Initially, these structures were estimated to be eclipsed. The structures were optimized using a Geometry Optimization routine including energy minimization with cell parameters optimization, using the parameters from the Universal Force Field. Calculation of the simulated powder diffraction patterns and Pawley refinements were performed in the Materials Studio Reflex Plus Module using a Bragg-Brentano geometry. When the first ~2 features were seen to align but relative intensities were seen to be inconsistent, we assigned this to a noneclipsed structure. If this was the case, supercells of the crystallites were generated and different stackings (AB, ABC, partial AB, etc. were attempted). The intensity profile which matched most closely was used to refine. The observed diffraction patterns were subjected to a polynomial background subtraction and then to Pawley refinement wherein peak profile were refined using the Pseudo-Voigt peak shape function and asymmetry was corrected using the Berar-Baldinozzi function. Crystallite size was then estimated by the LeBail method which was Pawley refined to the experimental data.

Transmission Electron Microscopy Sample Preparation for Ph-COF and TMPh-COF. All COF samples (Ph-COF and TMPh-COF) were prepared by drop-casting ~3-4 µL (using a micropipette) of the COF sample solution (CH_3CN:1,4-dioxane:mesitylene, 50:40:10 by volume)

after synthesis was complete onto lacey-carbon substrate (Cu mesh) TEM grids (Electron Microscopy Sciences, Hatfield, PA). The droplets of COF sample were allowed to sit on the grids in ambient conditions for ~20-30s and were then wicked dry with filter paper. The prepared TEM grids were then stored in a desiccator until they were used for TEM characterization.

Transmission Electron Microscopy for Ph-COF and TMPh-COF. TEM was performed using a FEI (FEI Company, Hillsboro, OR) Polara cryoTEM operating at 200 keV equipped with a Gatan (Roper Technologies, Sarasota, FL) K2 "direct electron" detector (FEG extraction: 4350 V, FEG emission: 108 µA, spot size 5, 70 µm OL aperture, 70 µm CL aperture). The Polara cryoTEM is a cartridge-loaded microscope, where the column is continually maintained at L-N_2 temperature (<-180˚ C). The grids that were prepared previously and dried, were loaded into the microscope's cartridge after being submerged in L-N_2, and the cartridge with grids was inserted into the microscope (maintained at L-N_2 temperature). The Polara was aligned for low-dose imaging, measuring the dose rate on the K2 detector through vacuum (no grid inserted). The dose rate used was 5.12 e- $Å^{-2}$ s for high-magnification (115 kx) images (1.78 Å pixel size, 3708 x 3838 pixels), with an image exposure of time of 5 s (~25.6 e- $Å^{-2}$ cumulative dose per image). The dose rate was not directly measured for the low magnification images, but the dose rate was orders magnitude lower for those images than for the high magnification images (1ow magnification images: 1 s exposure time, 10.1034 nm pixel size, 1852 x 1918 pixels, binning 2). All image acquisition was performed using SerialEM software which applies auto focusing on adjacent regions of the grid to minimize dose on the sample.[474]

Transmission Electron Microscopy Sample Preparation for BPh-COF, DBD-COF, and Py-COF. All COF samples were prepared by drop-casting ~4 µL (using a micropipette) of the COF sample solution (CH_3CN:1,4-dioxane:mesitylene, 50:40:10 by volume) onto lacey-carbon substrate (Cu, 400 mesh) TEM grids (Ted Pella, Redding, CA). The droplets of COF sample were allowed to sit on the grids in ambient conditions for ~10 s and were then wicked dry with filter paper.

Transmission Electron Microscopy for BPh-COF, DBD-COF, and Py-COF. Low magnification TEM was performed using a JEOL (JEOL USA, Inc., Peabody, MA) ARM300 GrandARM TEM operating at 300 keV equipped with a Gatan (Gatan, Inc., Pleasanton, CA) OneView-IS camera (FEG Emission: 15 µA, spot size 4, 100 µm CL aperture, 40 µm objective aperture). All image acquisition was done using the Gatan Microscopy Suite (GMS), Digital Micrograph (Gatan, Inc., Pleasanton, CA).

High resolution TEM was performed using a JEOL (JEOL USA, Inc., Peabody, MA) 3200FS TEM operating at 300 keV equipped with a Gatan (Gatan, Inc., Pleasanton, CA) K2 summit direct electron detector (~5 e- $Å^{-2}$ s^{-1} dose per image) using Leginon where all alignment was done at 4k or lower.[475]

Fluorescence Spectroscopy Sample Preparation. Monomer solutions were prepared at a concentration of 15 mM in a 4 mL mixture of CH_3CN:1,4-dioxane:mesitylene (50:40:10 *v/v/v*).

This monomer solution was then sonicated for five minutes and briefly heated to aid in solvation of the monomers. This 4 mL sample was split into two fractions of 2 mL apiece and each sealed. One of these solutions was heated at 70 °C for 72 hours while the other was left at room temperature. Emission-Excitation Matrix Fluorescence Spectroscopy (EEMS) was performed on all samples.

Emission-Excitation Matrix Spectroscopy. Emission and excitation spectra were recorded on a Horiba Jobin Yvon Fluorolog-3 fluorescence spectrophotometer equipped with a 450 W Xe lamp, double excitation and double emission monochromators, a digital photon-counting photomultiplier and a secondary InGaAs detector for the NIR range. Correction for variations in lamp intensity over time and wavelength was achieved with a solid-state silicon photodiode as the reference. The spectra were further corrected for variations in photomultiplier response over wavelength and for the path difference between the sample and the reference by multiplication with emission correction curves generated on the instrument. Emission-Excitation Matrix Spectroscopy was conducted on these samples by scanning the emission profile of different excitation wavelengths.

Quantum Yield Measurements. Quantum yield measurements were conducted using a demountable cuvette with CaF_2 windows. Samples were loaded by first compressing the windows around a Teflon liner. Solution of either COF or COF monomer was then added to the cell by syringe addition through ports available in the cell. Absorbance spectra were then collected to identify the optical density and wavelength of maximum absorbance. This wavelength was then used to excite samples in the same CaF_2 cell and the emission was integrated. We compared the

emission of our species to a measured reference, diphenylanthracence in benzene, to identify the reported quantum yields.

Centrifugation. Centrifugation was conducted using an Eppendorf Centrifuge 5430 V 4.4. Samples were collected in falcon tubes, balanced, and spun for 5 minutes at 7830 rpm. This was repeated twice to attempt to remove any small species not firmly collected.

II. Synthetic Procedures for Covalent Organic Framework Monomers

Scheme 3.1. Synthesis of 2,7-Pyrenebisboronic acid

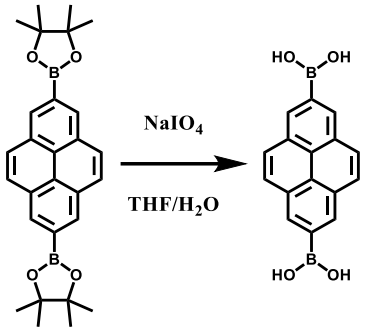

2,7-Pyrenebisboronic acid. This compound was synthesized according to published procedure[440] but with minor modification. In a 250 mL round bottom flask, bis(pinacoloto)diboronic ester (1.00 g, 2.20 mmol, 1.00 equiv) and sodium periodate (2.84 g, 13.4 mmol, 6.00 equiv) were dissolved in a THF:H_2O mixture (4:1 *v/v*, 60 mL). This mixture was stirred at room temperature with nitrogen actively bubbling through it for 30 minutes. (NOTE: HCl was **not** added to this reaction mixture as was done in previous reports thereby reducing orange/brown impurities in the final compound.) The reaction vessel was subsequently sealed and allowed to stir for an additional 24 hours. At this point, 60 mL of H_2O was added to the reaction mixture, which was then filtered through a Büchener funnel, and the product was washed with an additional 100 mL of H_2O. This product was then flushed with 100 mL of diethyl ether. This powder was dried under vacuum for 2 hours to afford a fine white powder (520 mg, 82%). NMR analysis of this product was consistent with a previous report.[440]

Scheme 3.2. Synthesis of Synthesis of 4,4'-Diphenylbutadiyne boronic acid

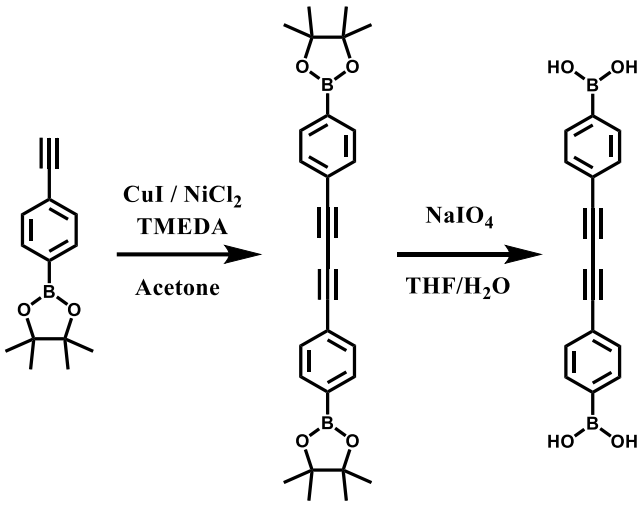

4,4'-Diphenylbutadiyne pinacole borane. The synthesis of this product was adapted from a previous report.[476] A 100 mL round bottom flask was charged with CuI (0.752 g, 3.94 mmol), $NiCl_2 \bullet 6H_2O$ (0.936 g, 3.94 mmol), and tetramethylethylenediamine (TMEDA) (1.836 g, 15.784 mmol). Acetone (50 mL) was added, and as the solids dissolved the mixture became dark green. 4-ethynylbenzeneboronic acid pinacole ester (18 g, 78.8 mmol) was added to this mixture, which was then stirred for 16 hours. The solvent was removed by rotary evaporation to yield a green residue that was washed with H_2O (300 mL). The resultant solid was isolated, subsequently recrystallized from CH_3CN as a white solid, collected via filtration, and dried under vacuum (5.25 g, 30 %). NMR analysis of this product was consistent with a previous report.[476]

4,4'-Diphenylbutadiyne boronic acid. The synthesis of this compound was adapted from a previous report.[477] In a 20 mL scintillation vial, 4,4'-diphenylbutadiyne pinacole borane (1.00 g, 2.20 mmol, 1.00 equiv) and sodium periodate (1.0 g, 5.00 mmol, 2.27 equiv) were dissolved in THF:H_2O (4:1 *v/v*, 12 mL). This mixture was stirred at room temperature with nitrogen actively bubbling through it for 30 minutes, after which 1M HCl (5 mL) was added via syringe. The

reaction vessel was subsequently sealed and allowed to stir for an additional 24 hours. At this point, the reaction mixture was poured into 50 mL of H_2O, filtered through a Büchener funnel, and washed with an additional 100 mL of H_2O. This product was then flushed with 100 mL of diethyl ether. This powder was dried under vacuum for 10 minutes to afford a fine white powder (444 mg, 69%). NMR analysis of this product was consistent with a previous report.[476]

Scheme 3.3. Synthesis of Synthesis of Tetra(4-dihydroxyborylphenyl)methane

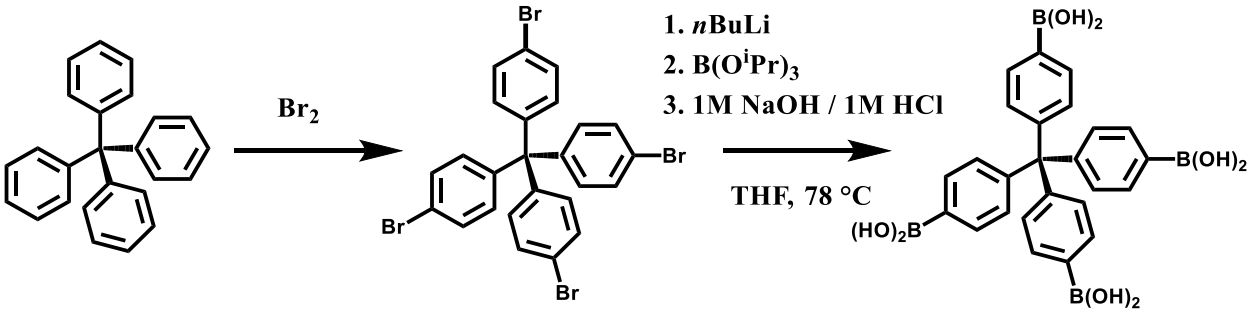

Tetra(4-bromophenyl)methane. The synthesis of this compound was adapted from a previous report.[478] A 100 ml three-necked flask was equipped with a magnetic stir bar and charged with tetraphenylmethane (9 g, 25 mmol). Two of the flask necks were covered with septa and a condenser with a hose at the top was inserted into the third neck, which was attached to a concentrated $Na_2S_2O_3$ solution. (Note: This was included so as to neutralize any escaped Br_2 gas in the following step.) Neat Br_2 (10 mL, 0.175 mmol) was added slowly via syringe to the stirring mixture through one of the septa, yielding a dark orange slurry that was stirred for an additional 20 minutes. This mixture was poured into cold ethanol (200 mL, -78 °C). The precipitated solid from this reaction was combined with saturated aqueous $NaHSO_3$ (80 mL) and filtered and washed with an additional 80 mL of $NaHSO_3$ two times. At this point, the filtered liquid was transparent.

The crude solid was recrystallized from a 1:1 chloroform/ethanol mixture and isolates as a pale yellow solid (5.85 g, 37 %). NMR analysis of this product was consistent with a previous report.[478]

Tetra(4-dihydroxyborylphenyl)methane. The synthesis of this compound was adapted from a previous report.[479] A solution of tetra(4-bromophenyl)methane (1.27 g, 2.00 mmol) in anhydrous THF (125 mL) was stirred at -78 °C under a N_2 atmosphere. To this, *n*-butyllithium (6.4 mL, 2.5 M THF, 16 mmol) was added dropwise via cannula through a pre-marked secondary container, after which the solution became cloudy. The resulting mixture continued to stir for 30 minutes at 78 °C, whereupon $B(O\text{-}^{i}Pr)_3$ (5.5 mL, 23.8 mmol) was added dropwise via cannula through a pre-marked secondary container. The mixture was stirred at -78 °C for an additional 20 minutes and then slowly warmed to room temperature, where it was stirred for an additional 12 hours. After acidification with 1 M HCl (25 mL), the mixture was concentrated by partial evaporation of volatiles under reduced pressure, which yielded a white solid. This concentrate was treated with 1M NaOH (25mL) and then filtered. The filtrate was acidified with 1M HCl until a white precipitate was observed. The precipitate was collected by filtration, washed with Et_2O, and dried under vacuum to afford tetra(4-dihydroxyborylphenyl)methane as a white solid (0.301 g, 30.4%). NMR Analysis of this product was consistent with a previous report.[479]

III. Nuclear Magnetic Resonance of Covalent Organic Framework Monomers

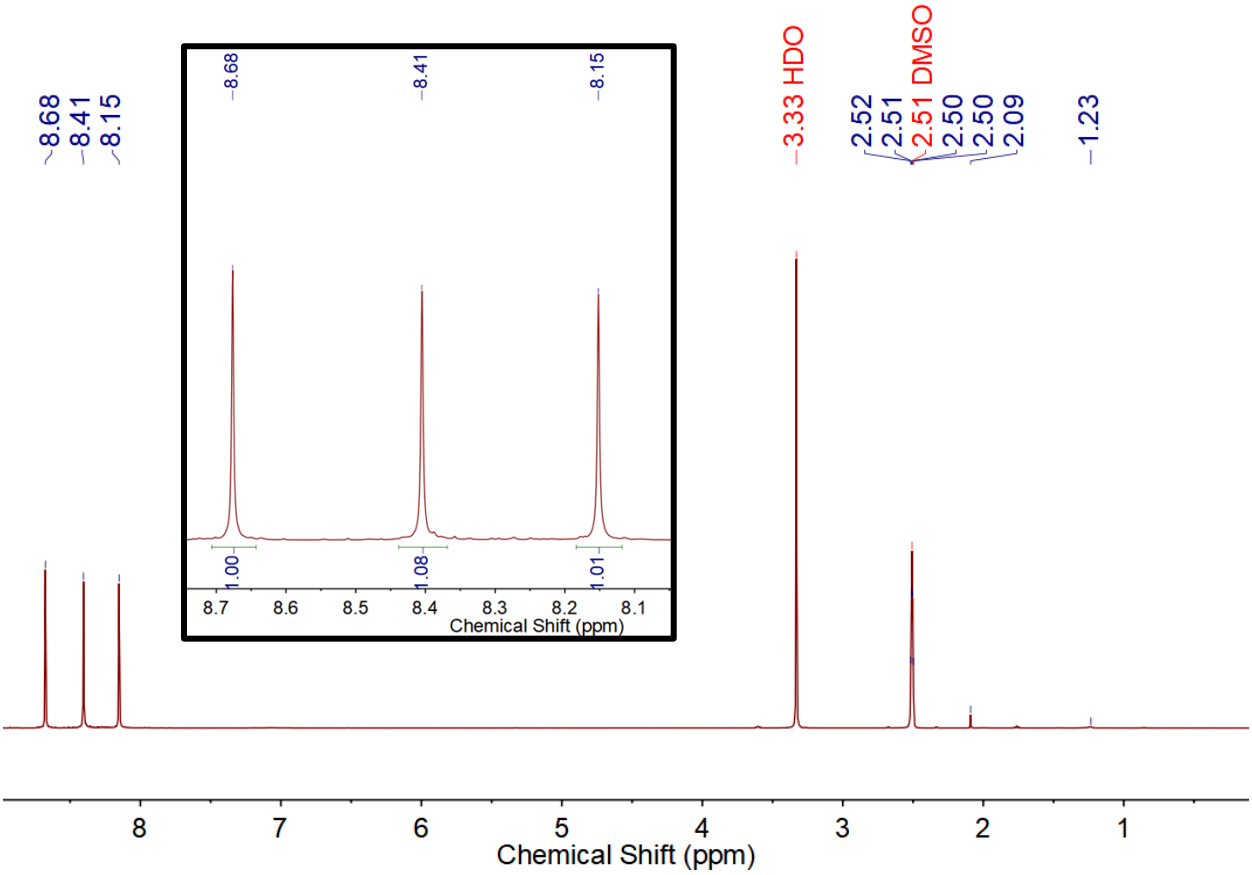

Figure 3.7. ^{1}H NMR of 2,7-Pyrenebisboronic acid DMSO-d_6

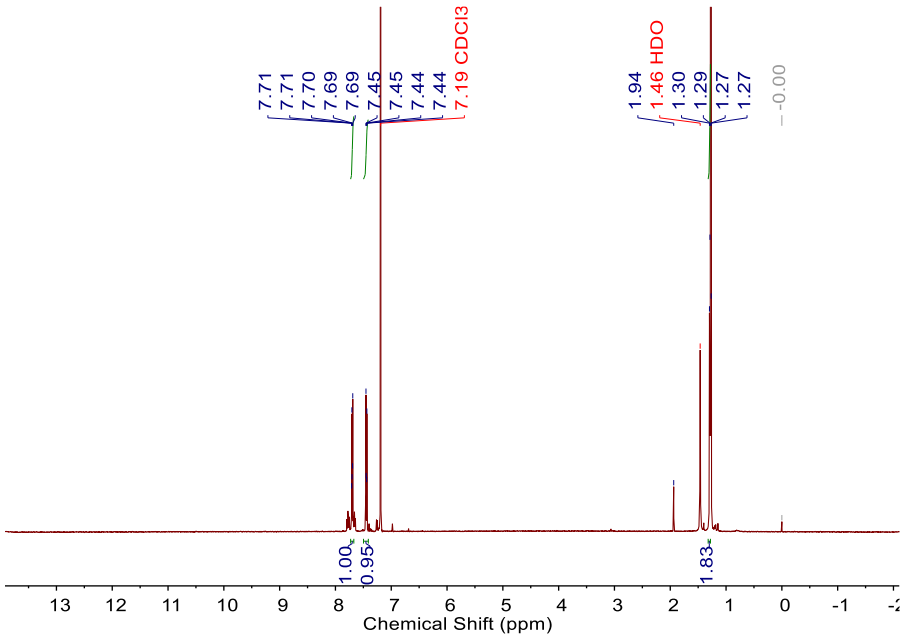

Figure 3.8. ^{1}H NMR of 4,4'-Diphenylbutadiyne pinacoleborane in $CDCl_3$

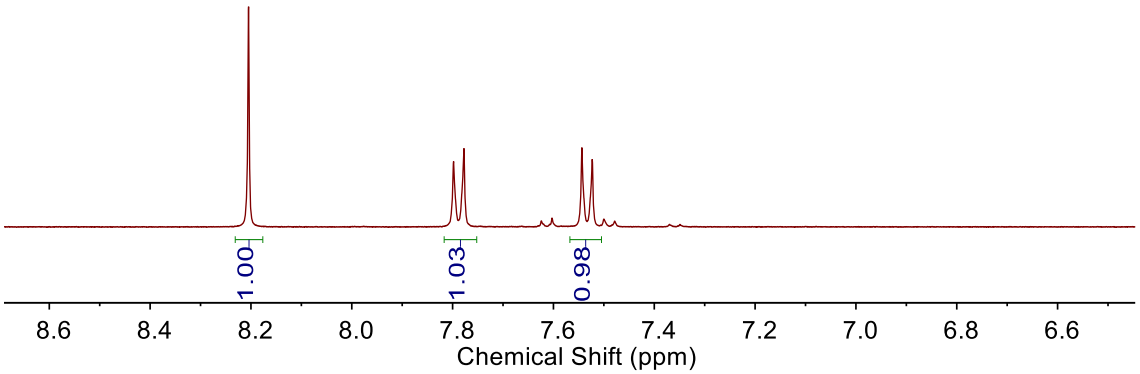

Figure 3.9. ^{1}H NMR of 4,4'-Diphenylbutadiyne boronic acid in DMSO-d_6

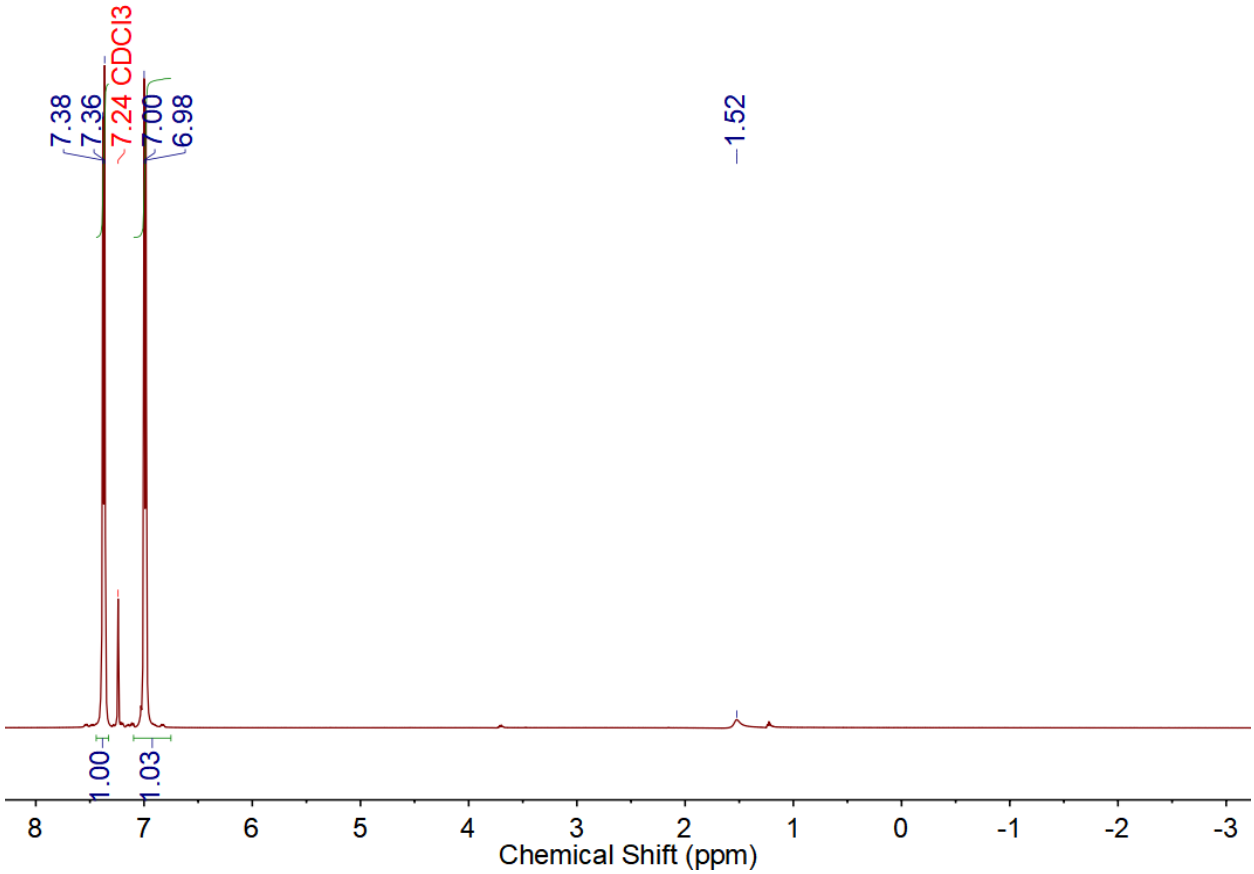

Figure 3.10. ^{1}H NMR of Tetra(4-bromophenyl)methane in $CDCl_3$

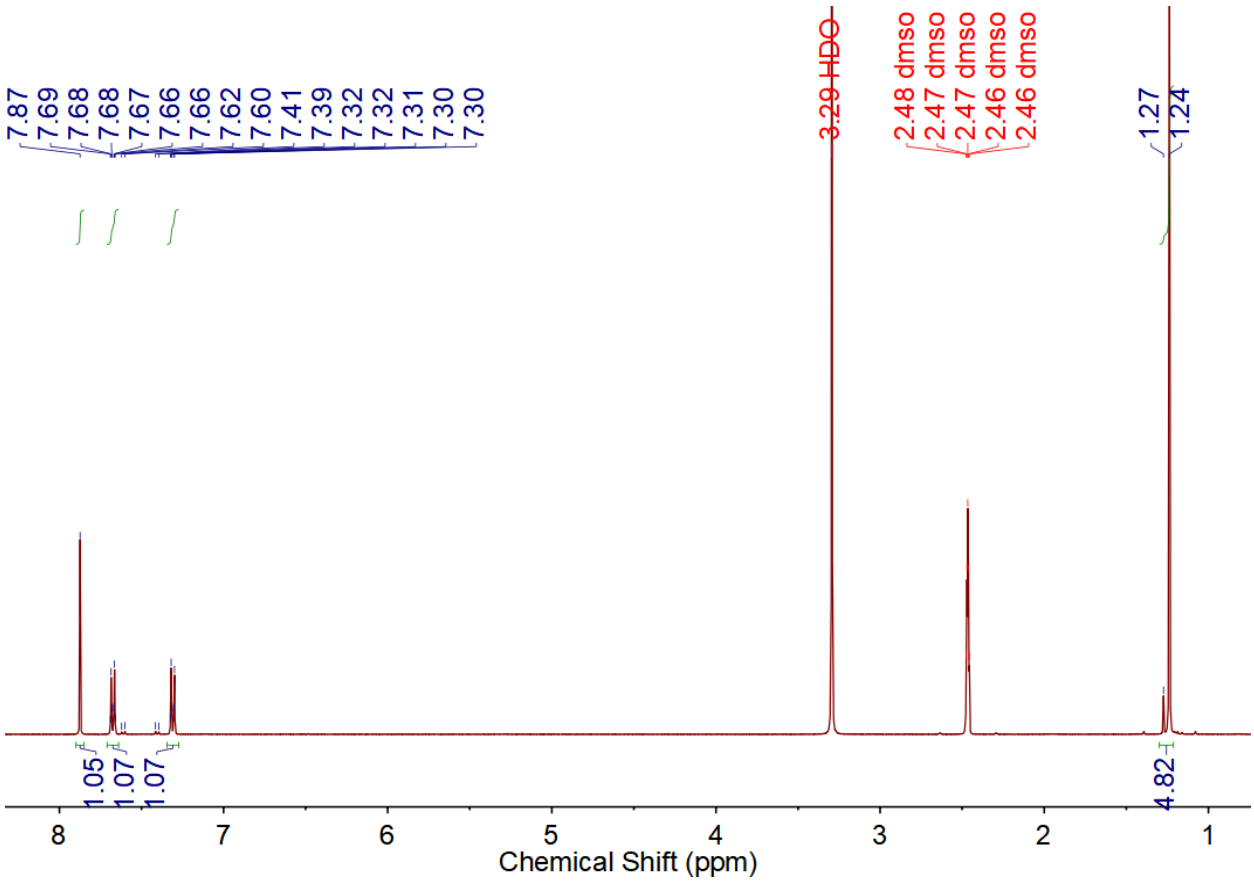

Figure 3.11. ^{1}H NMR of Tetra(4-dihydroxyborylphenyl)methane in DMSO-d_6

IV. Covalent Organic Framework Structures

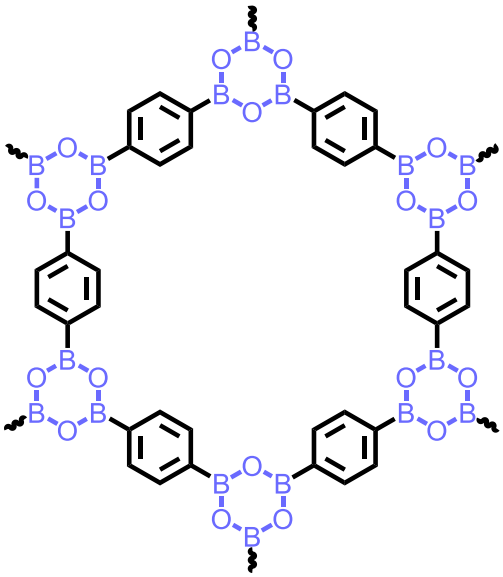

Figure 3.12. Structure of Ph-COF

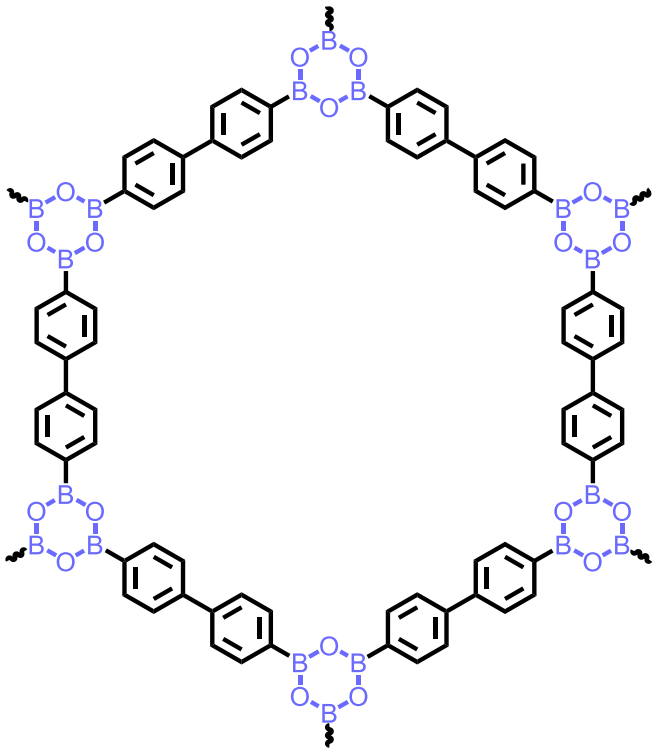

Figure 3.13. Structure of BPh-COF

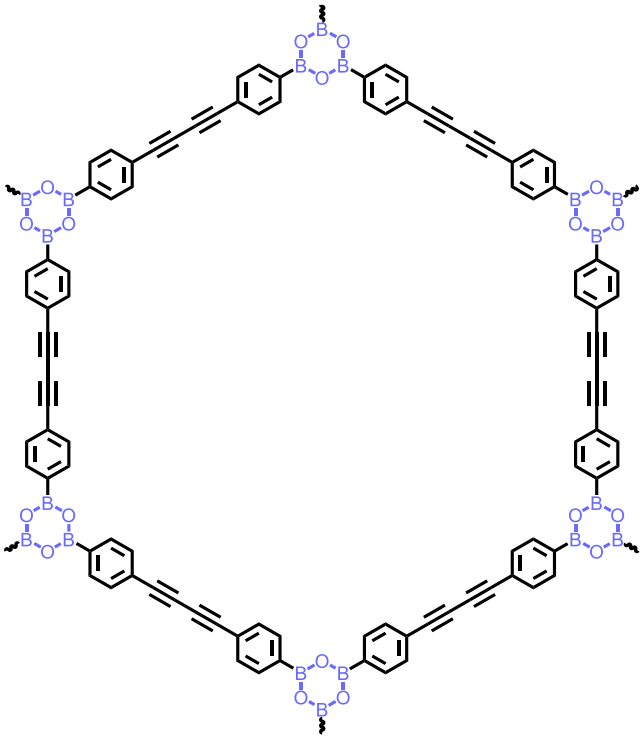

Figure 3.14. Structure of DBD-COF

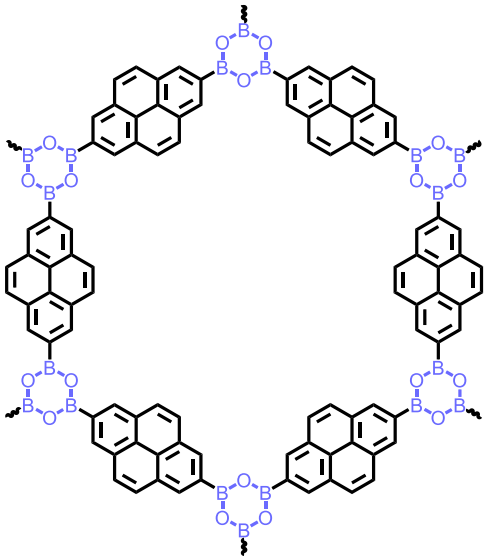

Figure 3.15. Structure of Py-COF

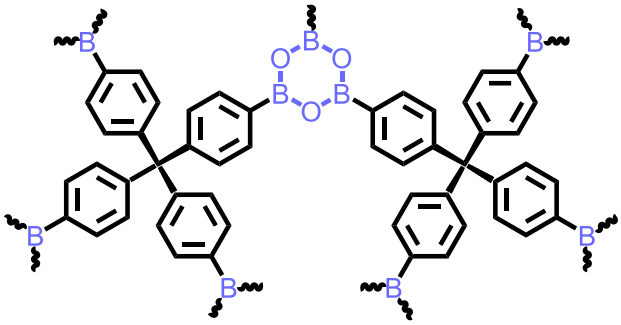

Figure 3.16. Structure of the three-dimensiaonl TMPh-COF

V. Synthesis of Covalent Organic Frameworks

Scheme 3.4. Synthesis of Ph-COF

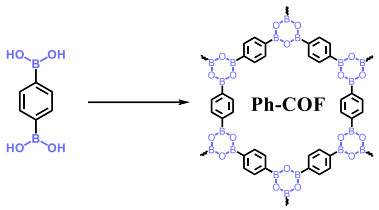

Ph-COF. Phenylenebisboronic acid (PBBA) (10 mM, 33.2 mg)* was dissolved in either a mixture of 4:1 1,4-dioxane:mesitylene (20 mL) when attempting powder synthesis of **Ph-COF** or a mixture of CH_3CN**:1,4-dioxane:mesitylene (20 mL) (50:40:10, *v*/*v*/*v*) *** when attempting colloidal syntheses. The PBBA solution was then heated to 70 °C for 72 hours. During this time, the clear solutions became white and opaque.

*For experiments where PBBA concentrations were varied, all other factors were kept the same.

**For experiments where other cosolvents were tested, those solvents were substituted for the acetonitrile.

***For experiments where the total ratio of solvents were varied, the mixtures varied between 90-0 CH_3CN vol % with the rest of the solvent being constructed from 1:4 mesitylene:1,4-dioxane.

Scheme 3.5. Synthesis of BPh-COF

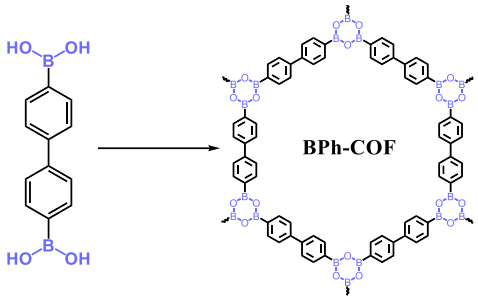

BPh-COF. Biphenylenebisboronic acid (BBBA) (10 mM, 12 mg) was dissolved in a mixture of CH_3CN:1,4-dioxane:mesitylene (5 mL) (50:40:10, *v*/*v*/*v*) when attempting colloidal syntheses. The BBBA solution was then heated to 70 °C for 72 hours. During this time, the clear solutions became white and opaque.

Scheme 3.6. Synthesis of DBD-COF

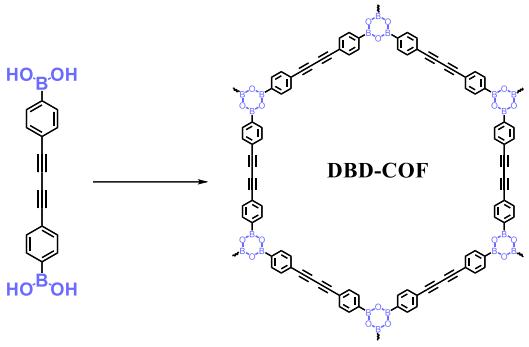

DBD-COF. Diphenylbutadiynbisboronic acid (DBD-BA) (10 mM, 14.5 mg) was dissolved in a mixture of CH_3CN:1,4-dioxane:mesitylene (5 mL) (50:40:10, *v*/*v*/*v*) when attempting colloidal syntheses. The DBD-BA solution was then heated to 70 °C for 72 hours. During this time, the clear solutions became white and opaque.

Scheme S3.7. Synthesis of Py-COF

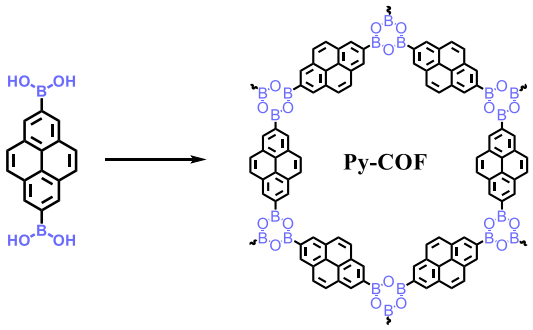

Py-COF. Pyrenebisboronic acid (PyBA) (10 mM, 14.5 mg) was dissolved in a mixture of CH_3CN:1,4-dioxane:mesitylene (5 mL) (50:40:10, *v*/*v*/*v*) when attempting colloidal syntheses. The Py-BA solution was then heated to 70 °C for 72 hours. During this time, the clear solutions became white and opaque.

Scheme S3.8. Synthesis of TMPh-COF

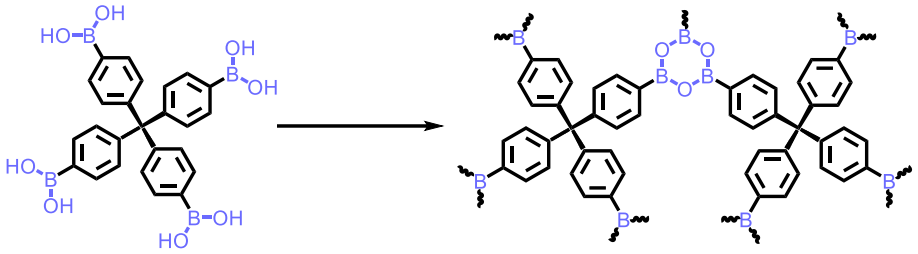

TMPh-COF. Tetrakis(phenlboronic acid)methane (TMPh-BA) (10 mM, 24.5 mg) was dissolved in a mixture of CH_3CN:1,4-dioxane:mesitylene (5 mL) (50:40:10, *v*/*v*/*v*) when attempting colloidal syntheses. The TMPh-BA solution was then heated to 70 °C for 72 hours. During this time, the clear solutions became white and opaque.

VI. Fourier-Transform Infrared Spectroscopy of Covalent Organic Frameworks

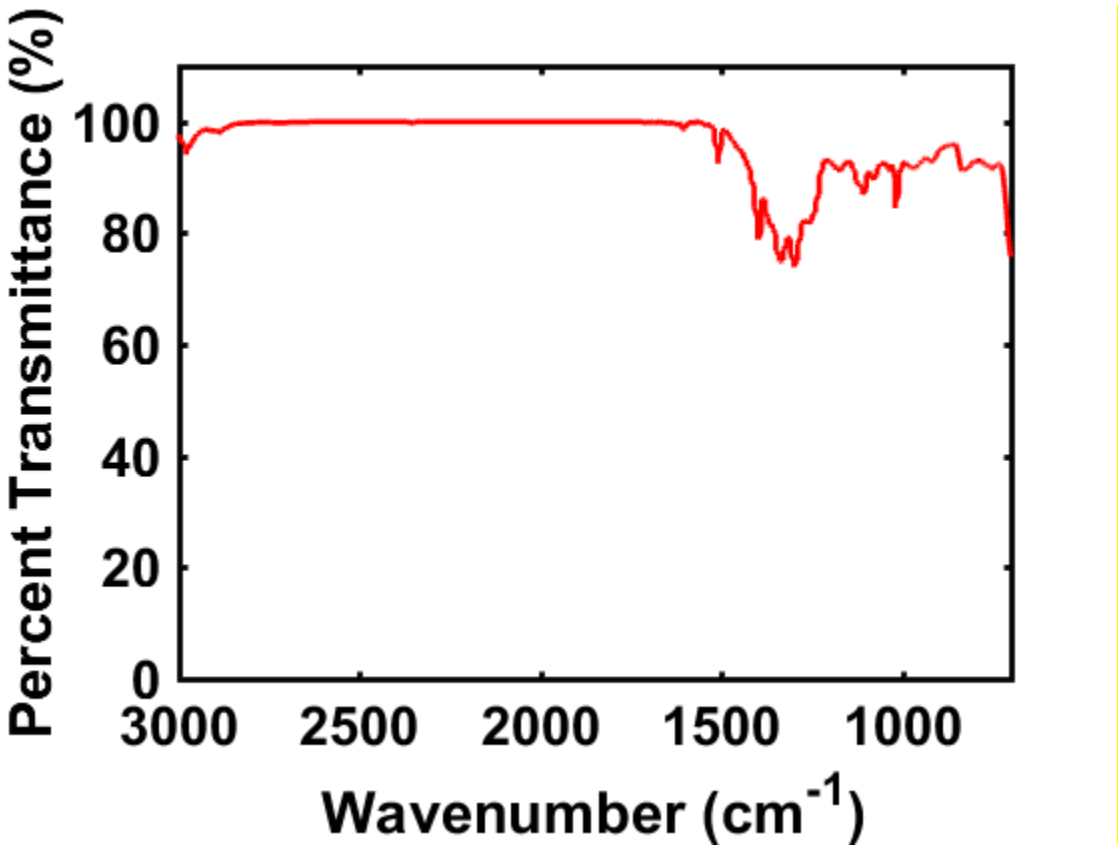

Figure 3.17. FT-IR of Ph-COF Powder

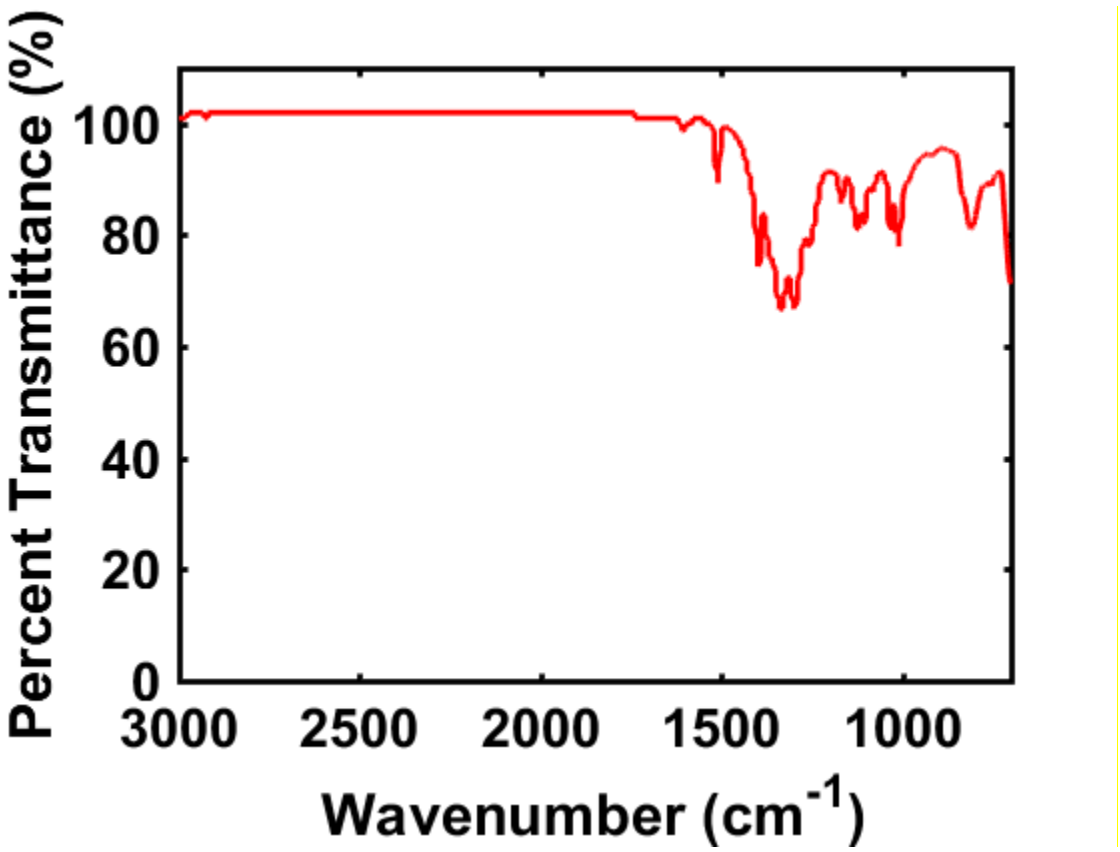

Figure 3.18. FT-IR of Ph-COF Colloids

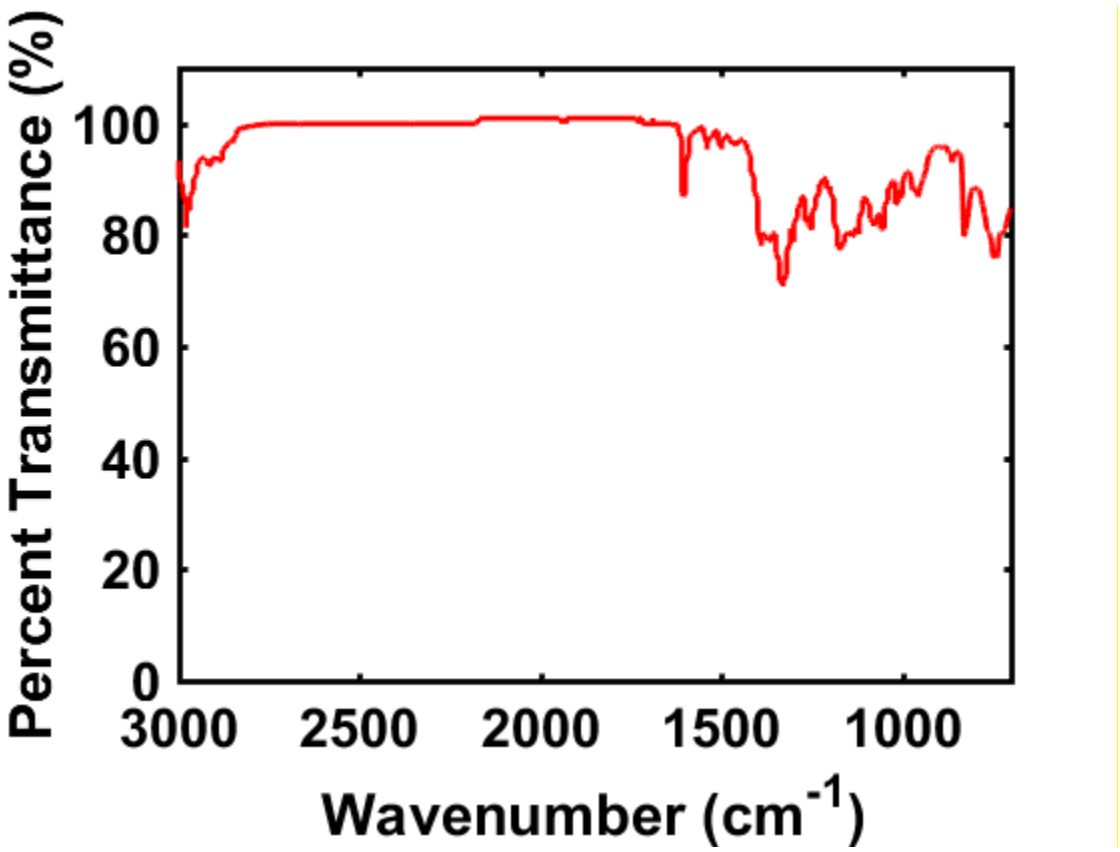

Figure 3.19. FT-IR of BPh-COF Colloids

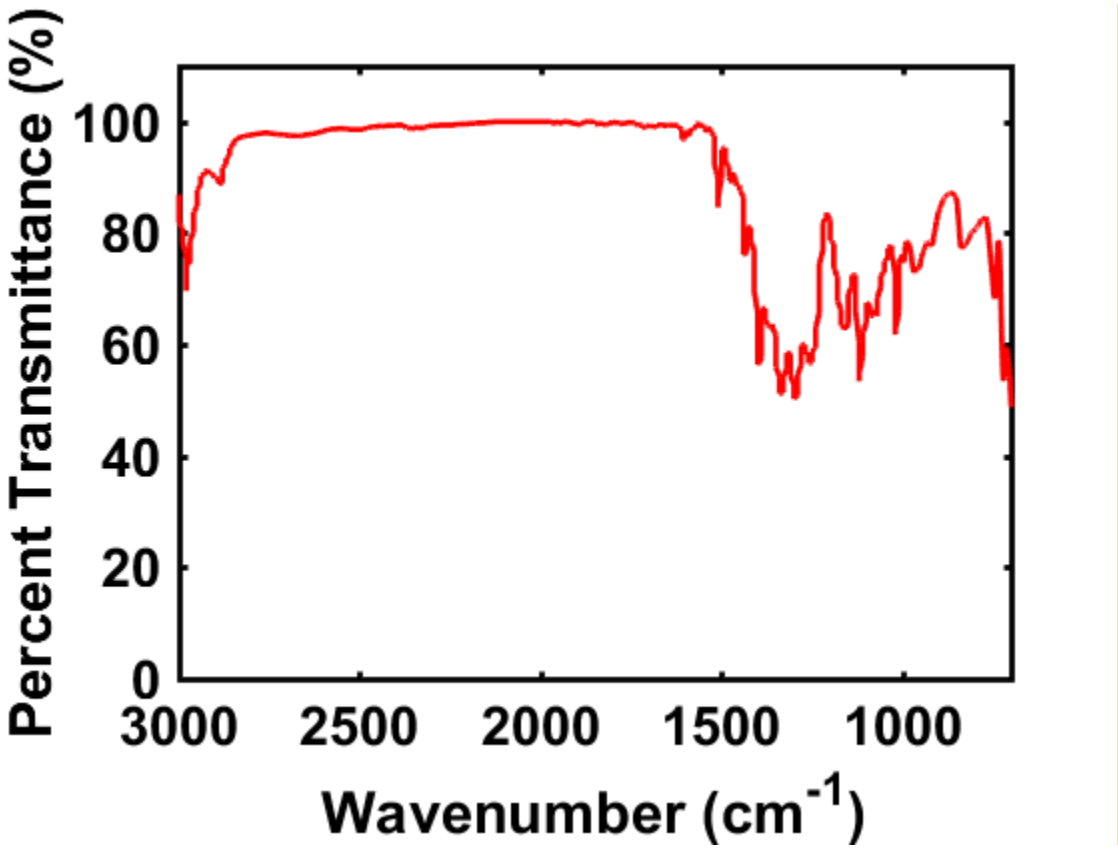

Figure 3.20. FT-IR of DBD-COF Colloids

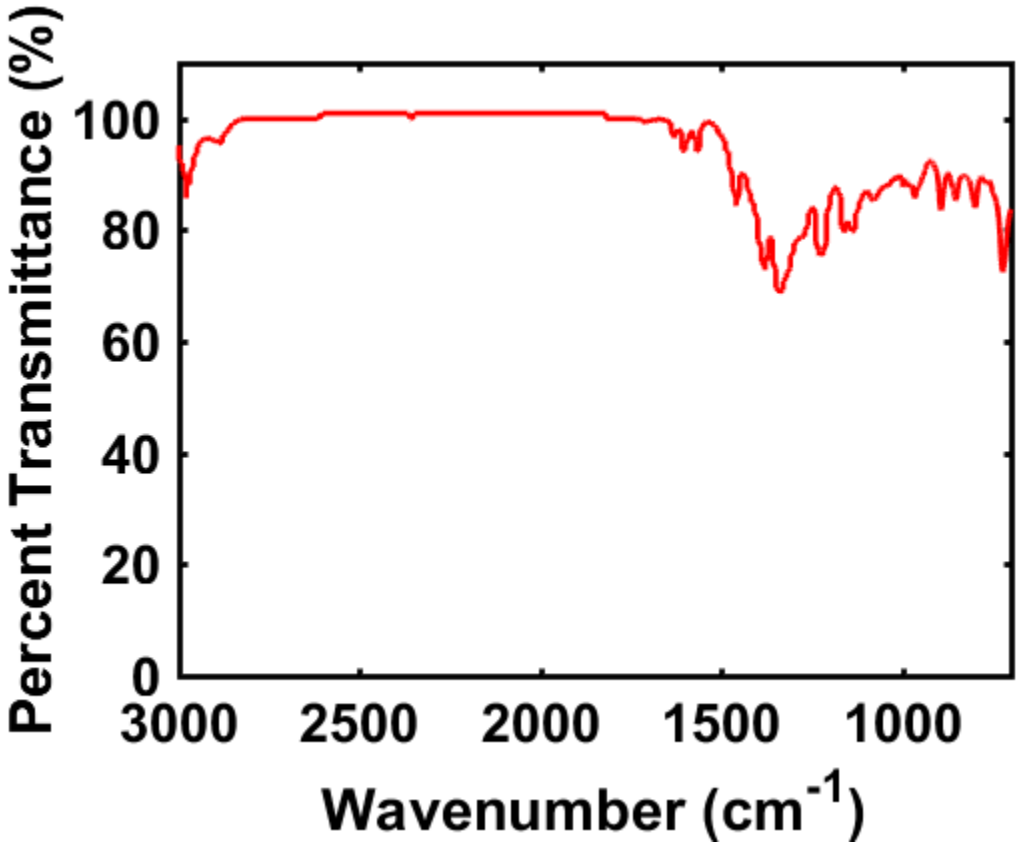

Figure 3.21. FT-IR of Py-COF Colloids

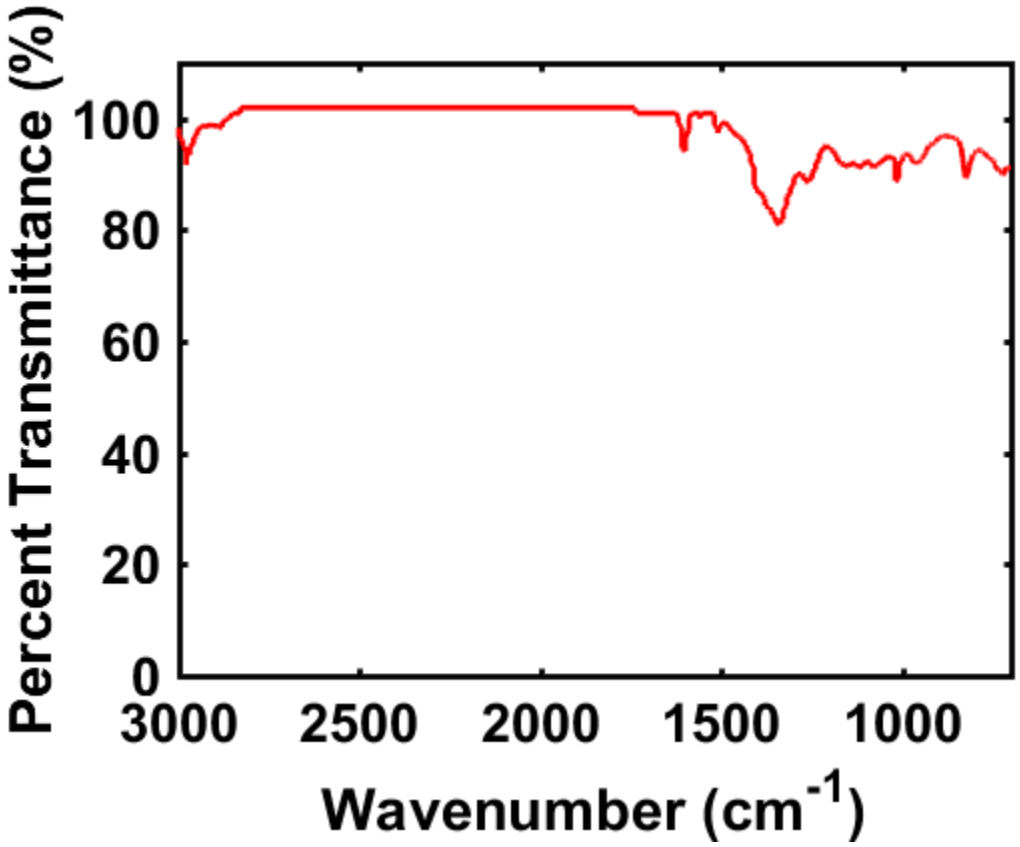

Figure 3.22. FT-IR of TMPh-COF Colloids

IV. Dynamic Light Scattering

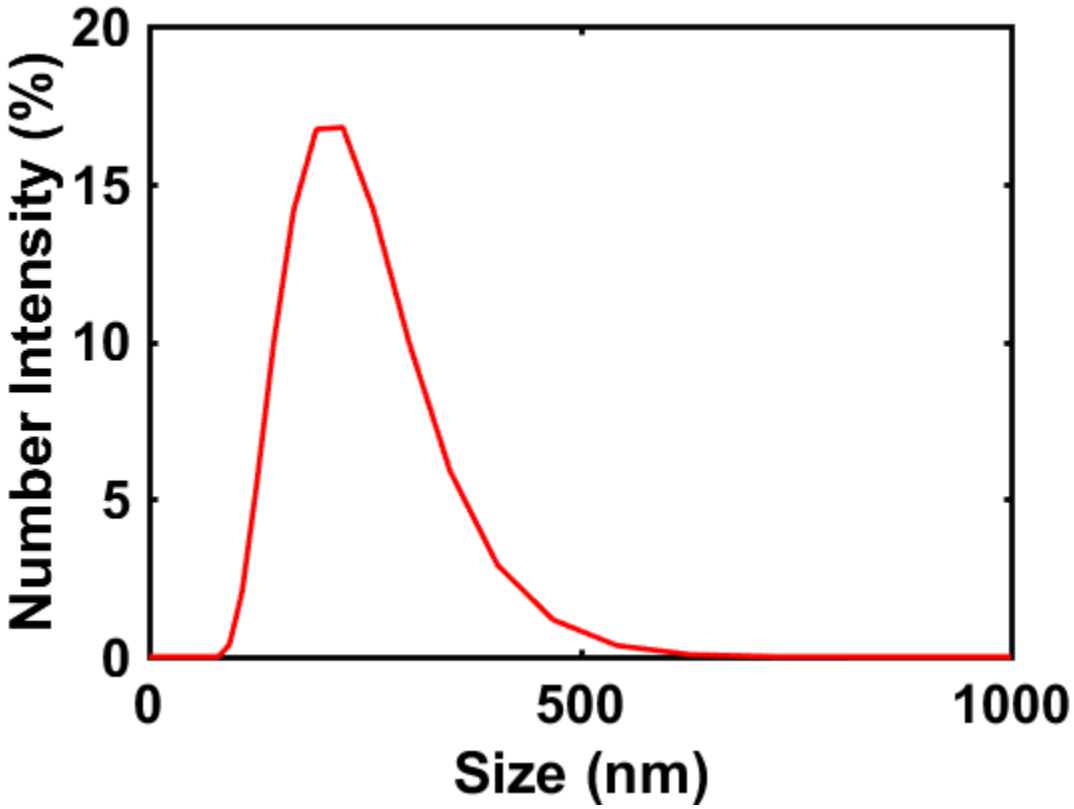

Figure 3.23. Dynamic light scattering number distribution of Ph-COF

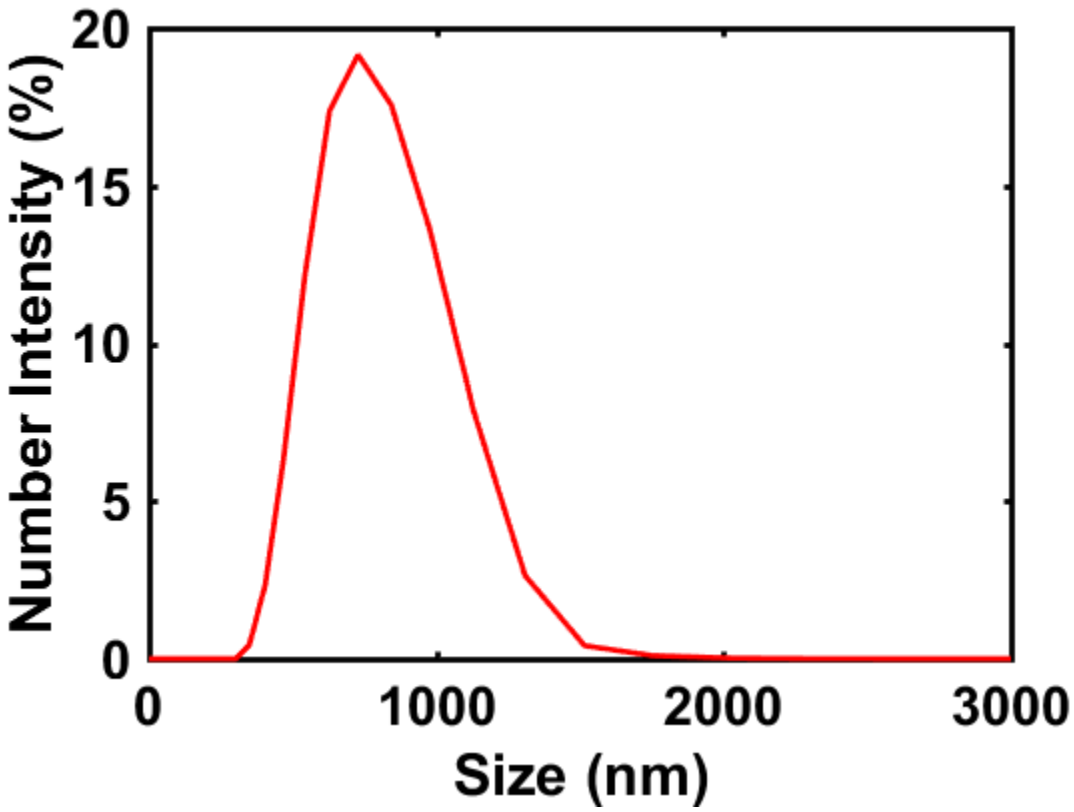

Figure 3.24. Dynamic light scattering number distribution of BPh-COF

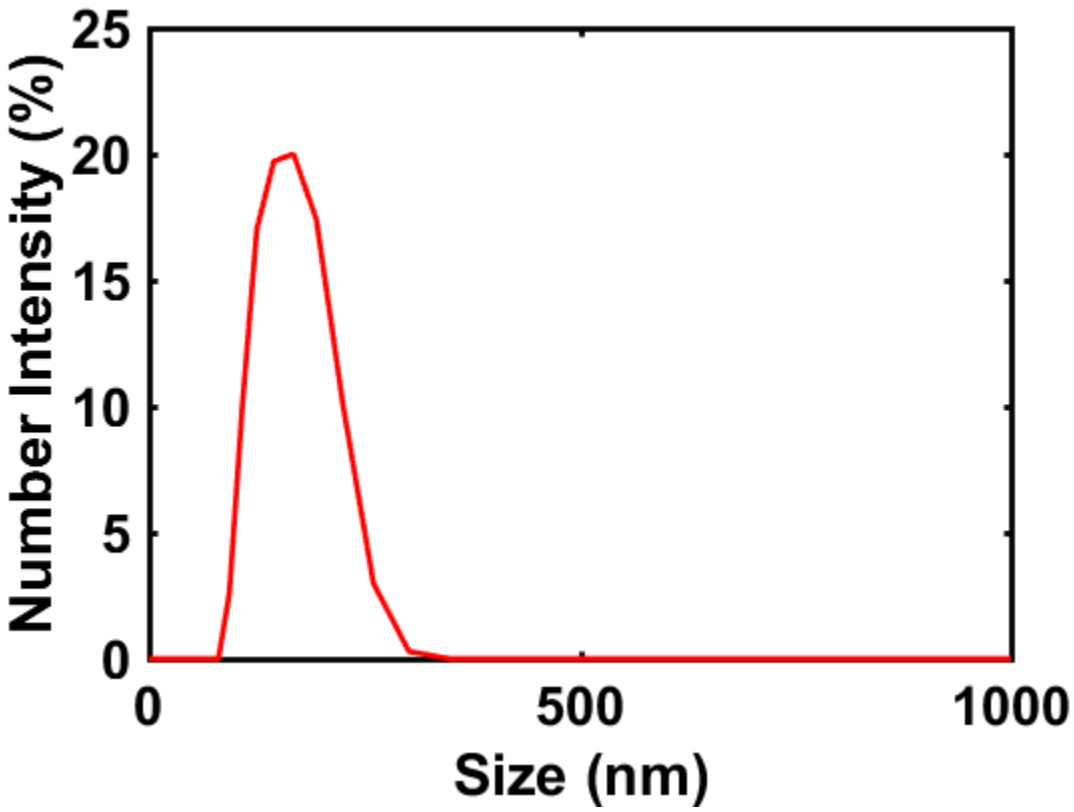

Figure 3.25. Dynamic light scattering number distribution of DBD-COF

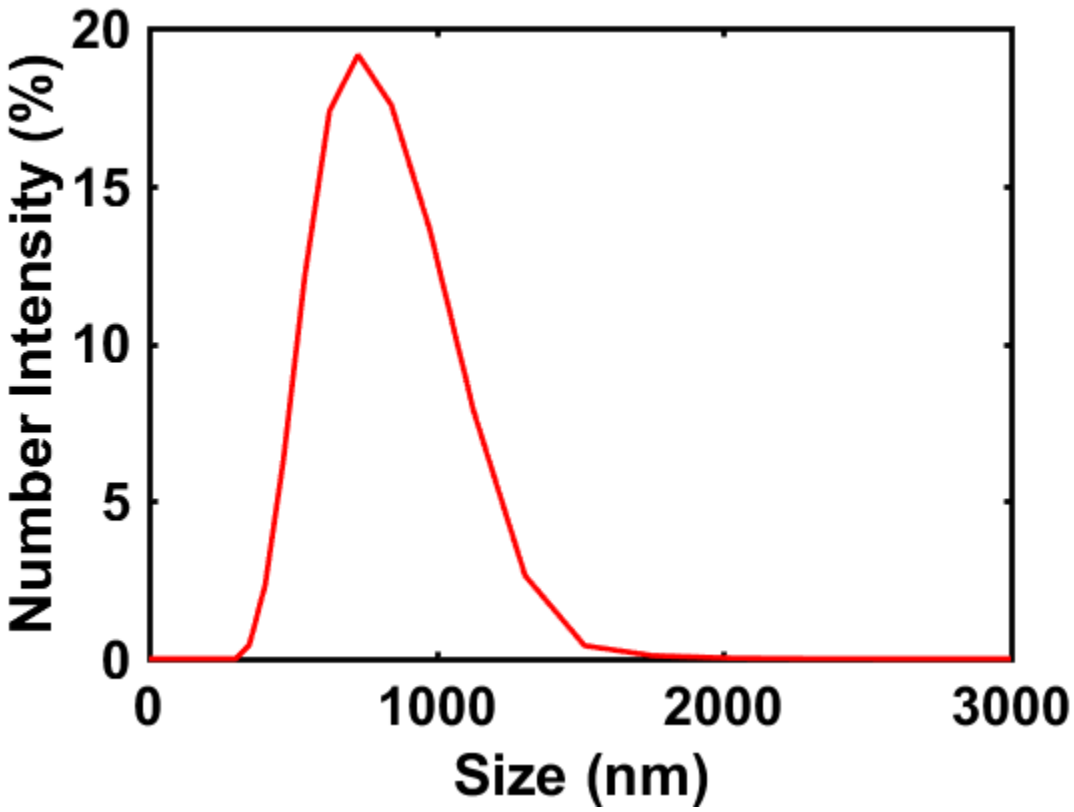

Figure 3.26. Dynamic light scattering number distribution of Py-COF

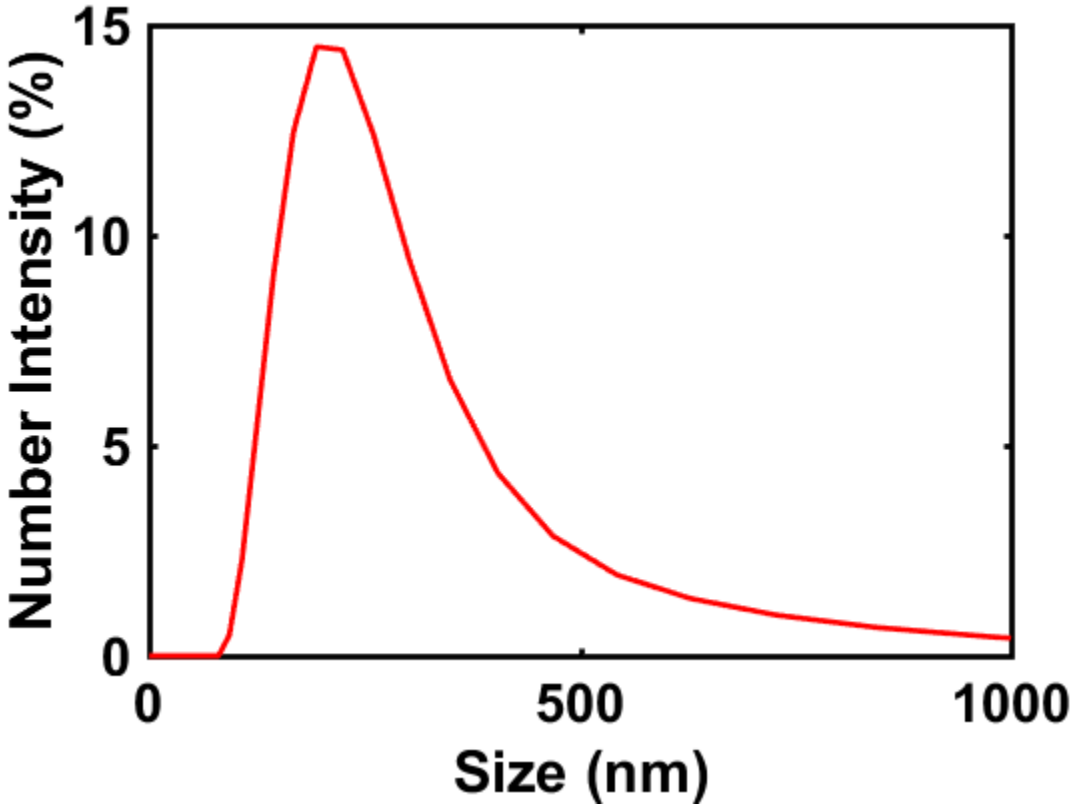

Figure 3.27. Dynamic light scattering number distribution of TMPh-COF

VIII. Powder X-ray Diffraction of Isolated COF Solids

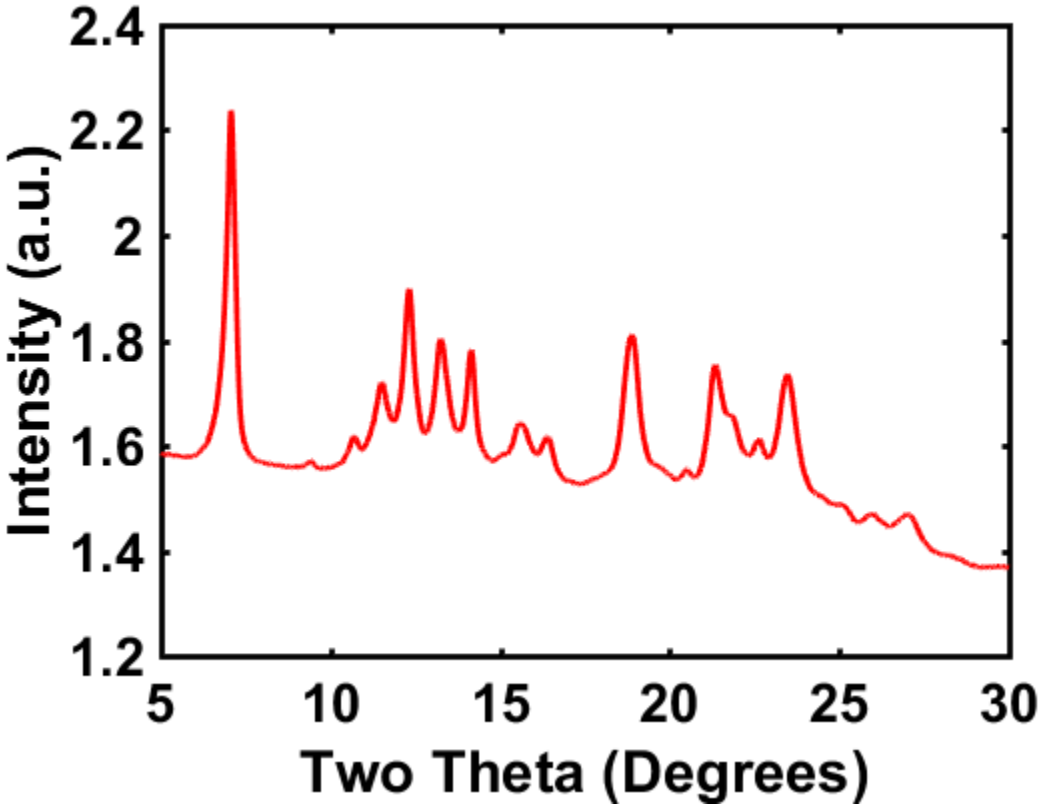

Figure 3.28. X-ray diffraction of wet Ph-COF

XIV. Covalent Organic Framework Structural Images

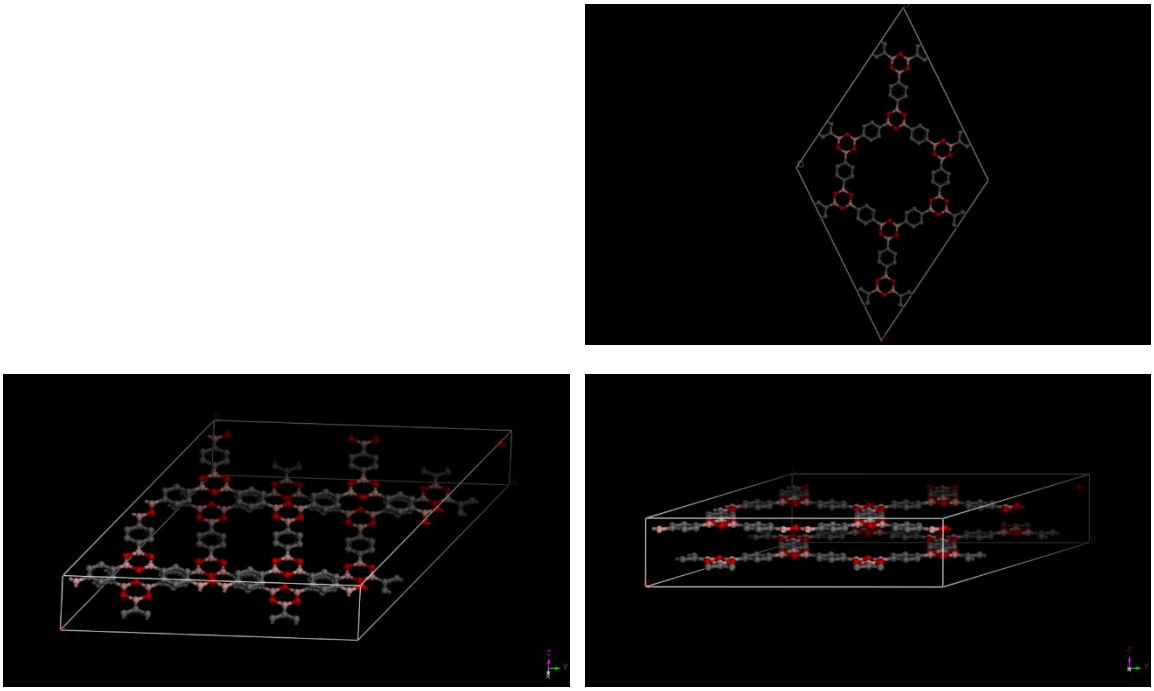

Figure 3.29. Structure of Ph-COF (0.5 *a/b* unit cell offset of layers)

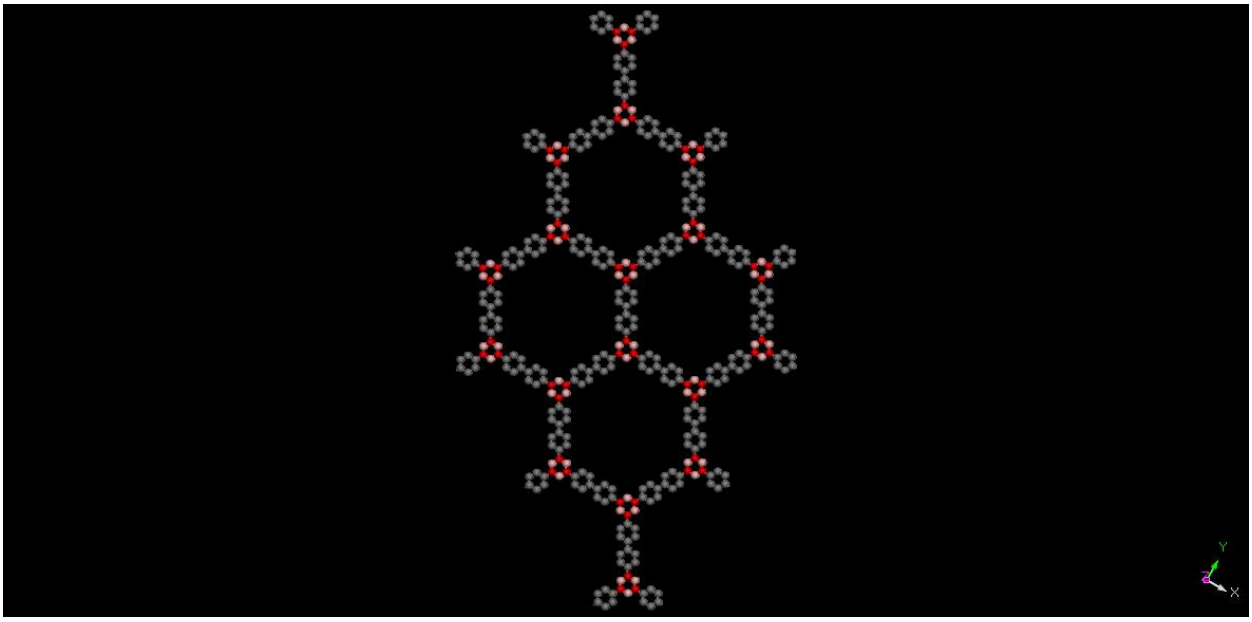

Figure 3.30. Structure of BPh-COF

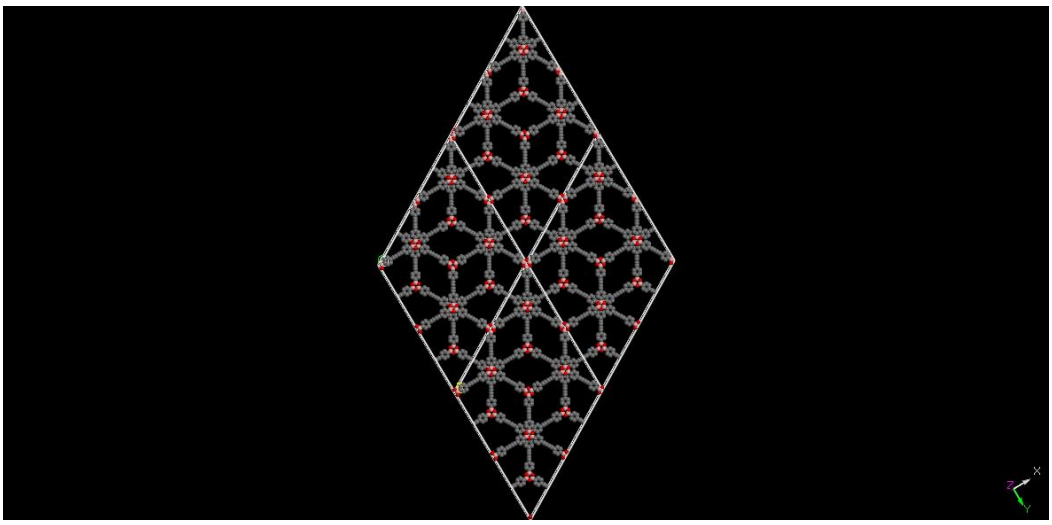

Figure 3.31. Structure of DBD-COF

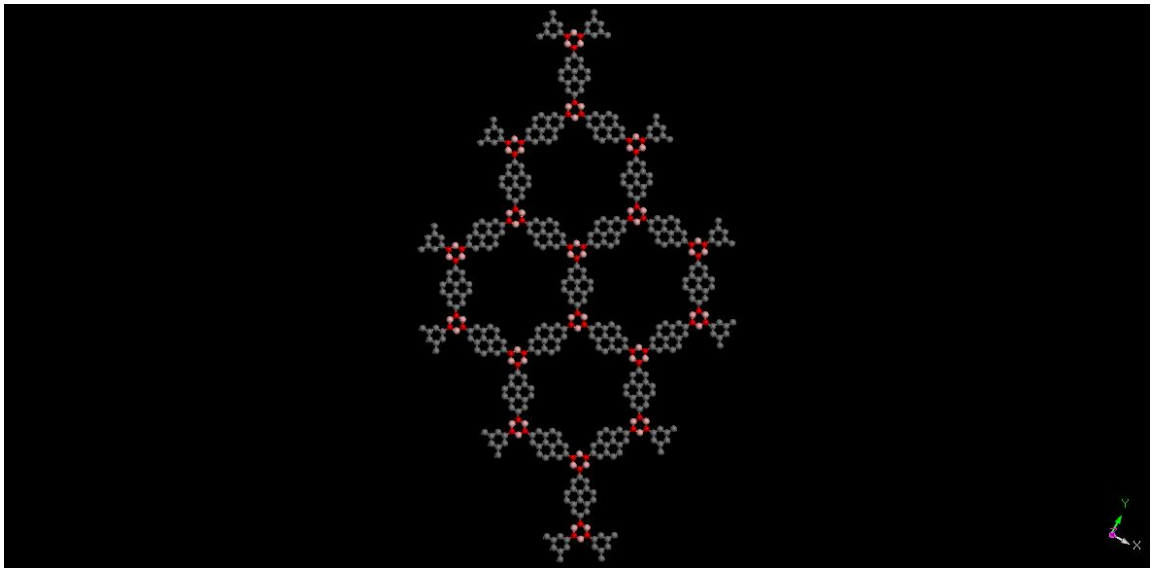

Figure 3.32. Structure of Py-COF

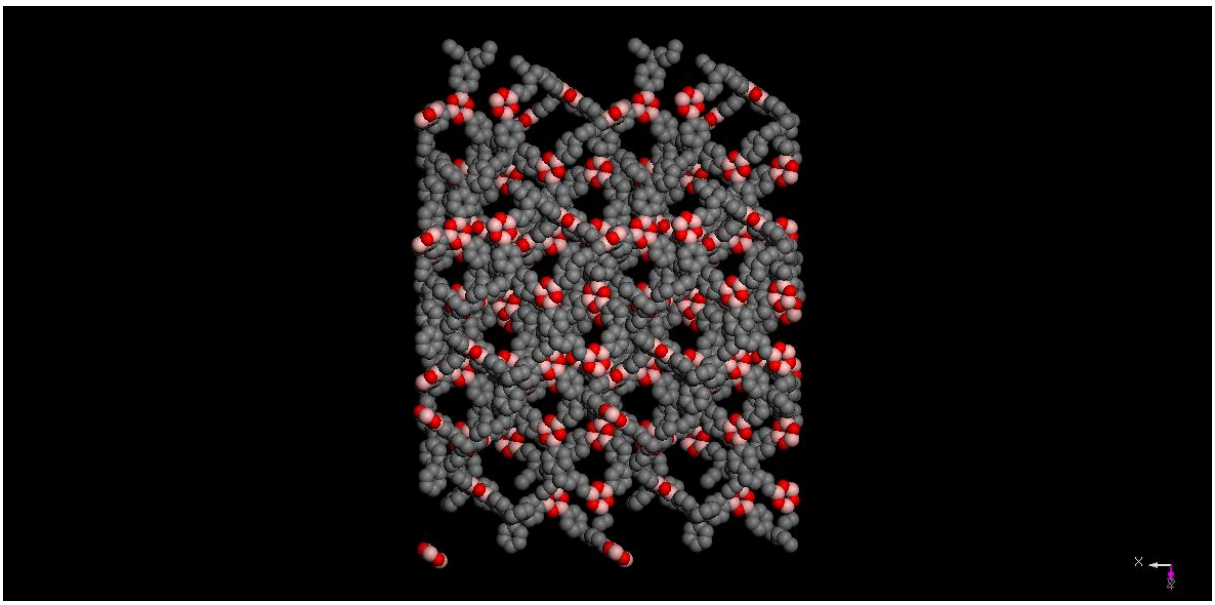

Figure 3.33. Structure of TMPh-COF

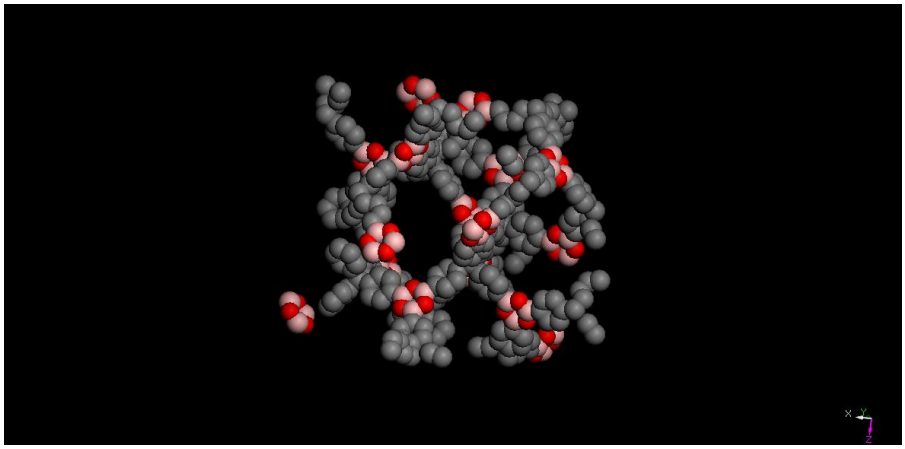

Figure 3.34. Structure of TMPh-COF – Zoomed in

X. Simulated COF Diffraction Patterns

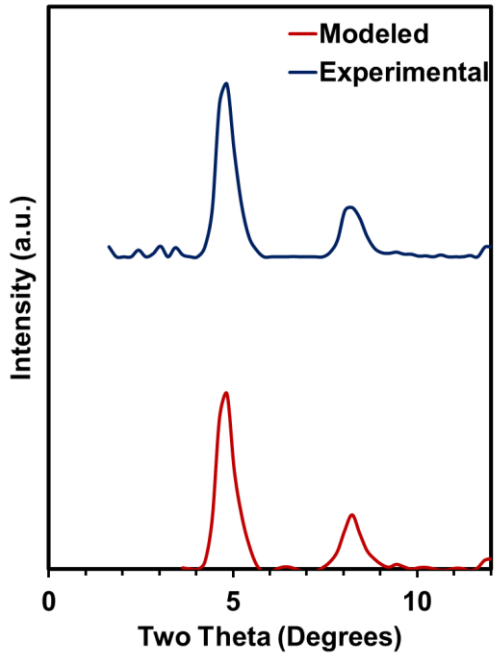

Figure 3.35. BPh-COF Diffraction Patterns

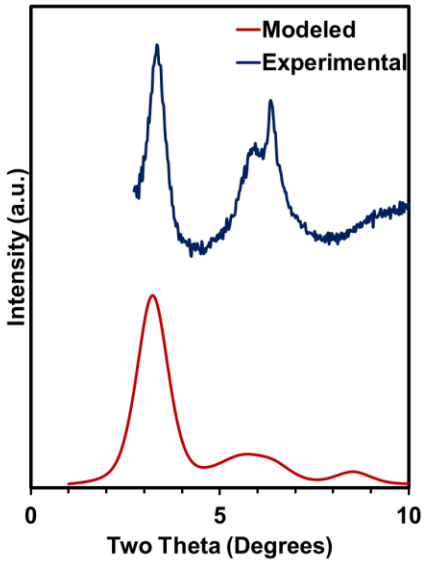

Figure 3.36. DBD-COF Diffraction Patterns

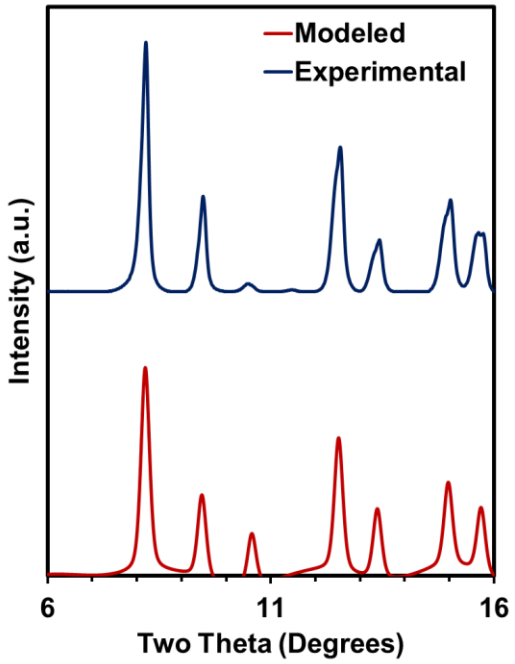

Figure 3.37. TMPh-COF Diffraction Patterns

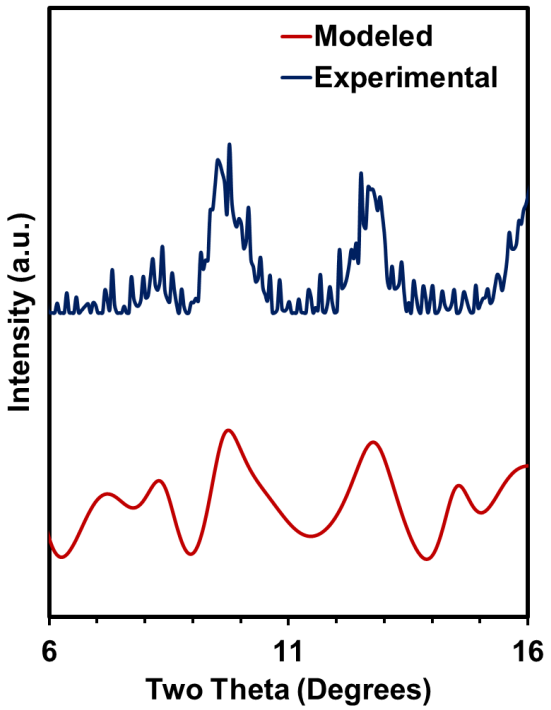

Figure 3.38. Py-COF Diffraction Patterns

XI. Photoluminescence Spectroscopy

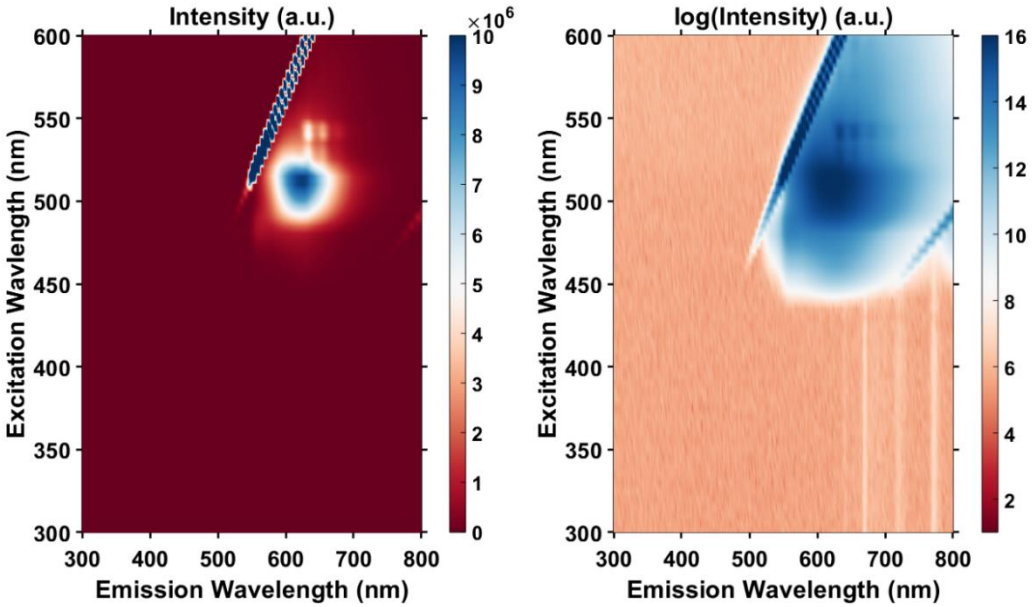

Figure 3.39. Excitation-Emission Matrix Spectroscopy of Ph-COF

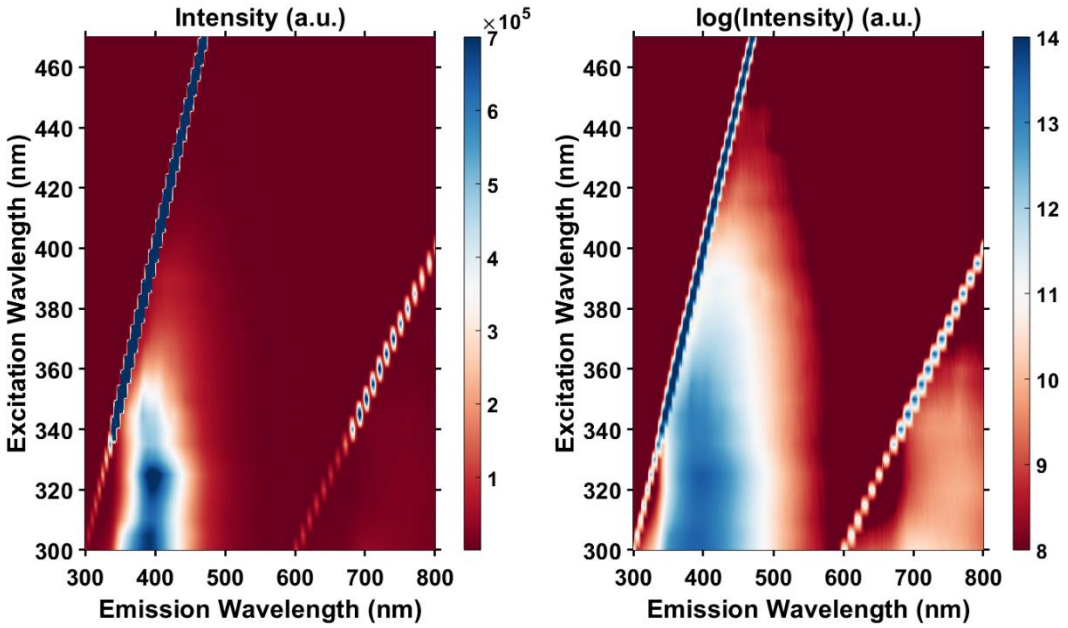

Figure 3.40. Excitation-Emission Matrix Spectroscopy of BPh-COF

XII. Transmission Electron Microscopy

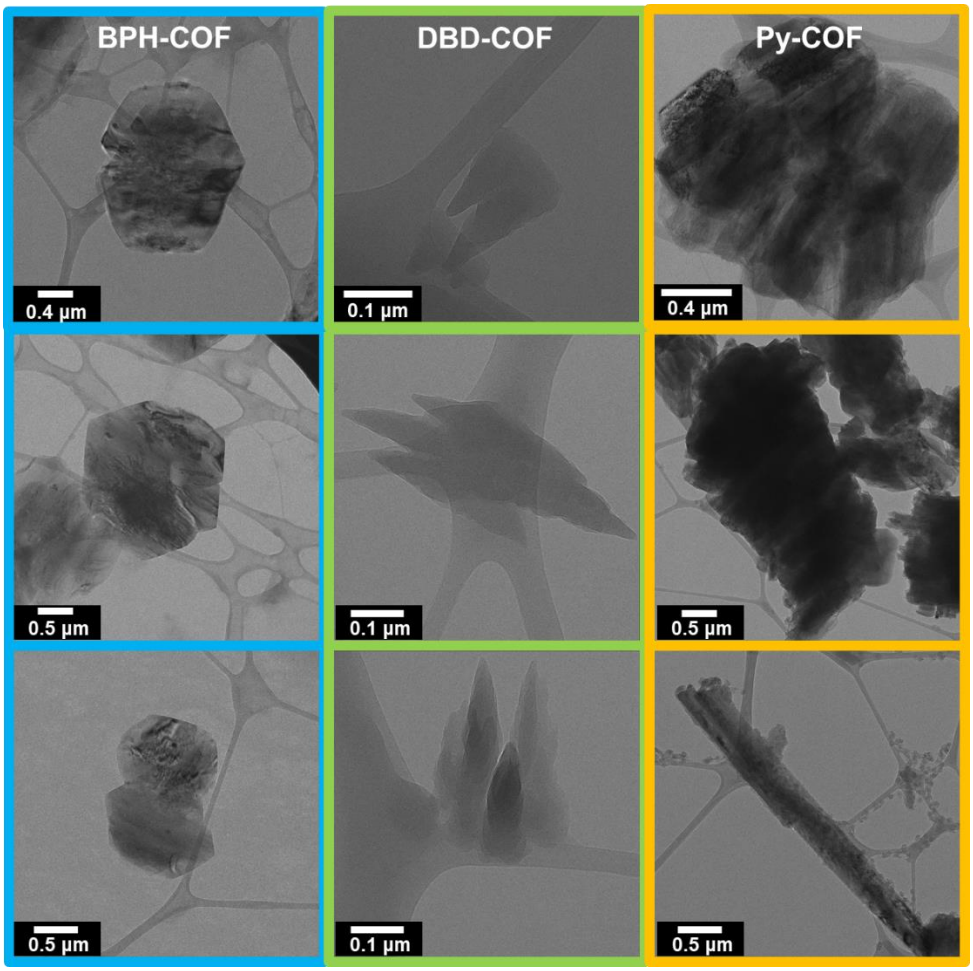

Figure 3.41. Additional TEM images of BPH-COF (Blue), DBD-COF (Green), and Py-COF (Yellow)

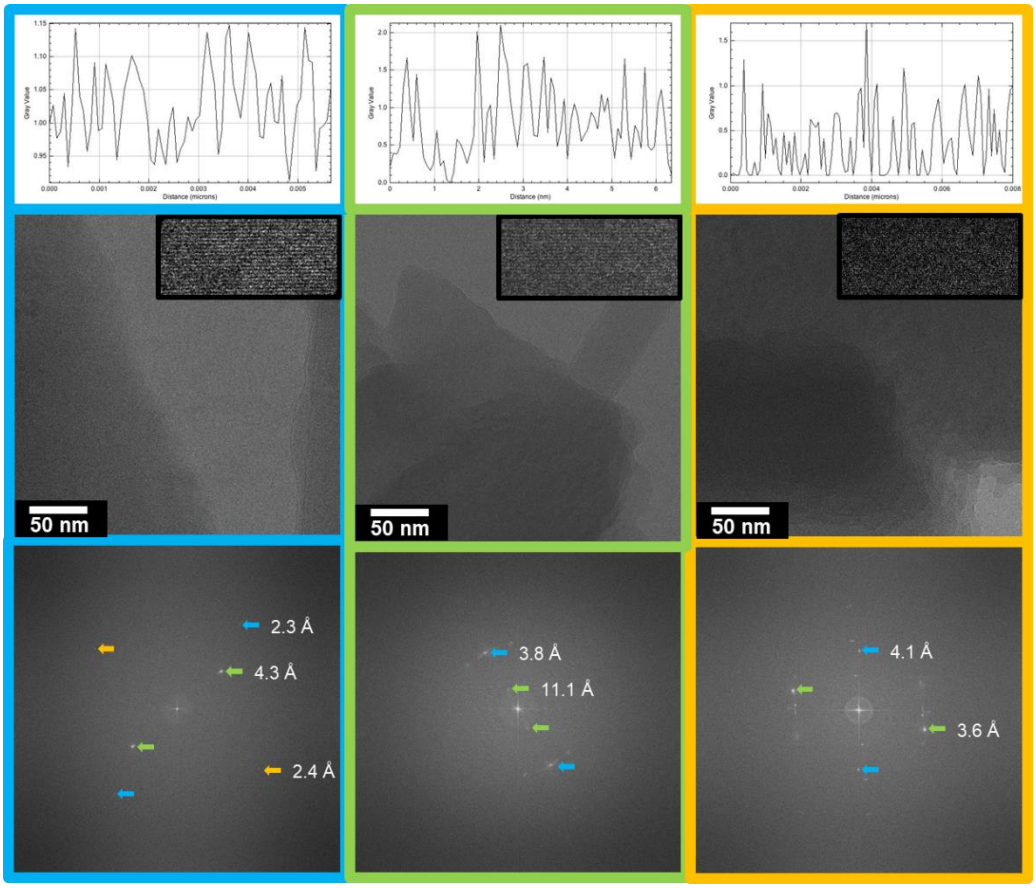

Figure 3.42. Additional High Resolution TEM images, BPH-COF (Blue), DBD-COF (Green), and Py-COF (Yellow)

XIII. Fluorescence of Powders

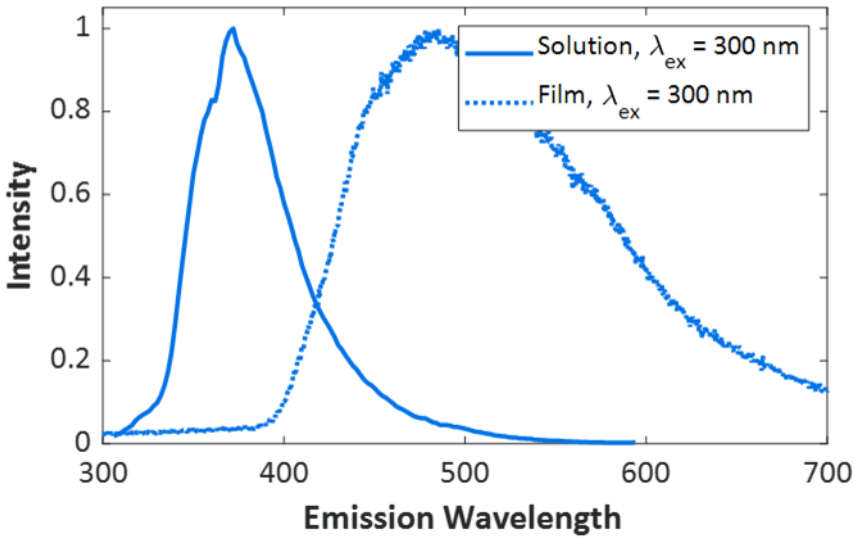

Figure 3.43. Fluorescence Spectroscopy of Py-COF

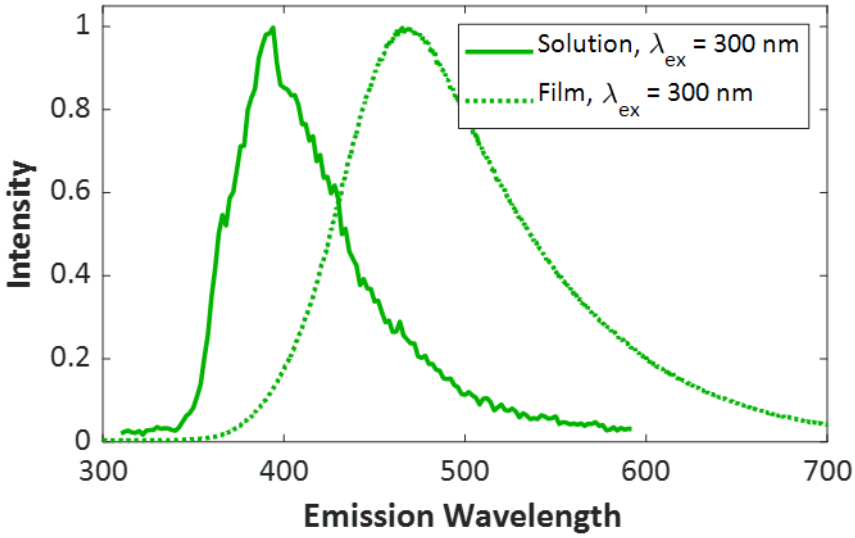

Figure 3.44. Fluorescence Spectroscopy of DBD-COF

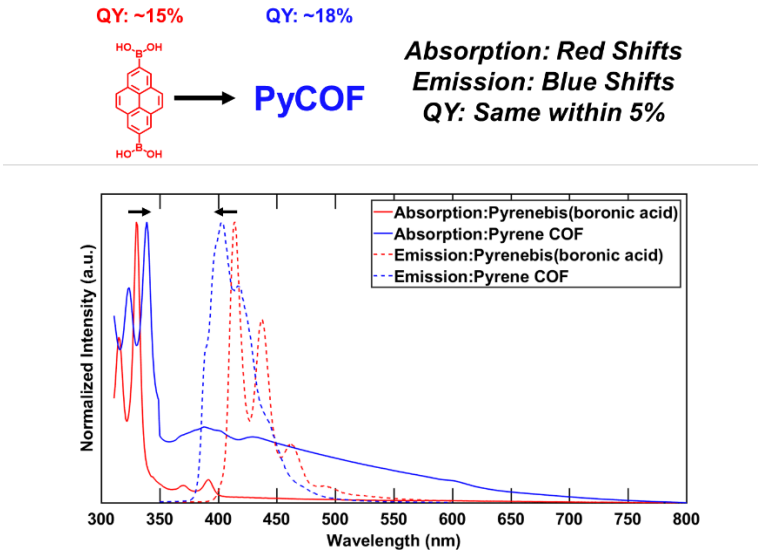

Figure 3.45. Absorption/Emission Spectroscopy of Py-COF

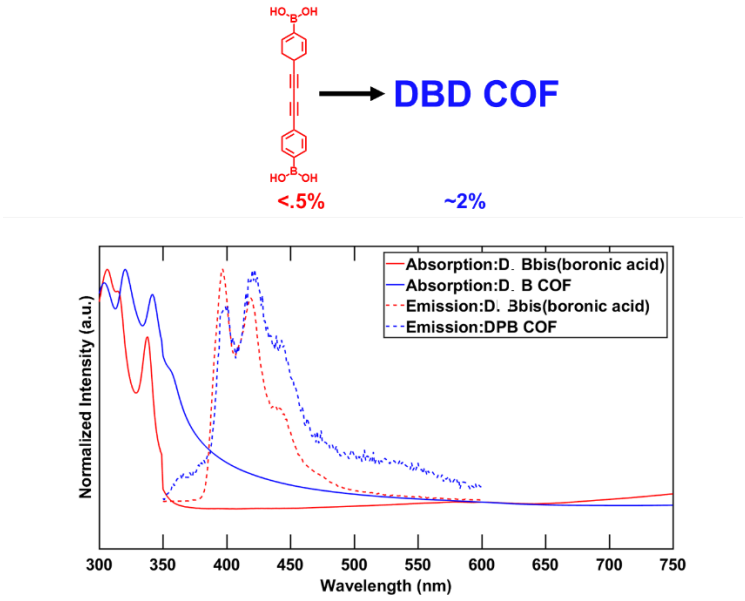

Figure 3.46. Absorption/Emission Spectroscopy of DBD-COF

Chapter 4 : Nucleation-Elongation Dynamics of Two-Dimensional Covalent Organic Frameworks

4.1 Abstract

Homogeneous two-dimensional (2D) polymerization is a poorly understood process in which topologically planar monomers react to form planar macromolecules, often termed 2D covalent organic frameworks (COFs). While these COFs have traditionally been limited to weakly crystalline aggregated powders, they were recently grown as micron-sized single crystals by temporally resolving the growth and nucleation processes. Here, we present a quantitative analysis of the nucleation and growth rates of 2D COFs via kinetic Monte Carlo (KMC) simulations using COF-5 as an example, which show that nucleation and growth have second-order and first-order dependences on monomer concentration, respectively. The computational results were confirmed experimentally by systematic measurements of COF nucleation and growth rates performed via *in situ* X-ray scattering, which validated the respective monomer concentration dependences of the nucleation and elongation processes. A major consequence is that there exists a threshold monomer concentration below which growth dominates over nucleation. Our computational and experimental findings rationalize recent empirical observations that, in the formation of 2D COF single crystals, growth dominates over nucleation when monomers are added slowly, so as to limit their steady-state concentration. This mechanistic understanding of the nucleation and growth processes will inform the rational control of polymerization in two dimensions and ultimately enable access to high-quality samples of designed two-dimensional polymers.

4.2. Introduction to Mechanistic Analysis

Two-dimensional (2D) polymerization is an emerging frontier in polymer science, which promises the development of rationally designed 2D materials.[480] 2D covalent organic frameworks (COFs) are a class of 2D polymers that are permanently porous, atomically regular, synthetically modular, and structurally versatile.[41, 398, 399, 481-490] These properties have inspired explorations of COFs for applications such as catalysis, molecular separations, energy storage, and optoelectronic devices.[491-510] However, their small crystalline domain sizes (< 100 nm) and empirical polymerization processes have impeded the study of their intrinsic properties. It has been suggested that the insufficient materials quality of the 2D COFs obtained to-date is likely due to uncontrolled nucleation-elongation processes in the reaction mixture.[416, 417, 420, 511] Unfortunately, the mechanisms established for other types of 2D materials[512-516] are not likely to apply due to the specific anisotropic features (*i.e.*, in-plane covalent linkages and out-of-plane van der Waals interactions) and regular porosity of 2D COFs. At present, characterizing the small, polydisperse, constantly evolving particles present in the early stages of COF polymerization remains a demanding experimental task. From a theoretical perspective, using an analytical approach to describe the nucleation and growth rates is also daunting because of the presence of many simultaneous growth processes and pathways.[517] Furthermore, the application of computational methods such as molecular dynamics (MD) simulations provides only limited information because of the short time scales that are accessible.[518]

Recently, Smith *et al.* developed a synthetic strategy that prevents agglomeration of COF particles by including CH_3CN in the solvent mixture. These conditions provide 2D COFs as stable colloidal

suspensions, which allows us to study the fundamental processes of COF formation and elongation in the absence of aggregation and precipitation of the COF products.[519] This approach enabled the temporal resolution of the growth and nucleation processes and the synthesis of several single-crystalline 2D COF colloids.[440] However, the underlying mechanism of COF formation remains poorly understood, which stands as a barrier to the general application of this approach. We also note that the COF formation process may vary among different chemistries, which, however, still requires further investigation. For example, imine COF formation has been suggested to proceed via an initial amorphous state,[520] although the formation of a crystalline network occurs more rapidly than noted in this early study.[521, 522] Here, we chose to focus on boronate ester-linked COFs, which represent model systems in mechanistic investigations for which both experimental and theoretical data are accessible.[420, 511] We use kinetic Monte Carlo (KMC) simulations to study their nucleation and elongation rates as a function of initial monomer concentration. Based on the simulation results, we are able to reach a *quantitative* understanding of the nucleation and growth rates, which we further validate via *in situ* X-ray scattering measurements. Overall our results allow us to rationalize why reducing the steady-state monomer concentration suppresses nucleation and favors crystallite growth, the strategy that has been successfully used in the fabrication of micron-sized 2D COF crystals.[440] This kinetic model will inspire other strategies to temporally resolve nucleation and growth. Similar control of initiation and propagation in linear polymerization has revolutionized precision polymer synthesis, and its further development in two-dimensional systems is key to fully realizing the potential of this longstanding missing topology in macromolecular science.

4.3. Growth Models

To probe the general dynamics of 2D COF polymerization, we focus on the boronate ester-linked COF-5, which is a frequently used model system in the study of 2D COFs.[420, 440, 511, 519, 523-525] COF-5 is formed from the condensation of 2,3,6,7,10,11-hexahydroxytriphenylene (HHTP) and 1,4-phenylenebis(boronic acid) (PBBA), as shown in **Scheme 4.1**. We have previously developed a kinetic Monte Carlo (KMC) model for 2D COF formation in solution, which makes use of a combination of experimentally and computationally derived parameters.[511] The KMC model describes nucleation and growth on the same basis and reproduces the experimental production curves of COF-5 very well by simulating four microscopic processes: bond formation (among monomers, oligomeric species, and crystallites), bond breakage (in oligomers and crystallites), out-of-plane stacking (among oligomeric species and crystallites) and destacking (in crystallites). We note that crystal boundaries coming from lattice mismatch (as indicated by quantum-chemistry calculations at 0 K[476, 526, 527]) were not included in the KMC model; lattice mismatch has indeed a dynamic nature at room temperature and is thus unlikely to lead to boundaries that prevent growth (see **Supporting Information**, **SI** for details). Here, in order to fully quantify the nucleation and growth rates, we carried out two sets of KMC simulations, based on modifications from our original KMC model.

Scheme 4.1. The two-step growth process of micron-sized crystals obtained by slowly adding monomers to COF nanoparticle seeds.[440]

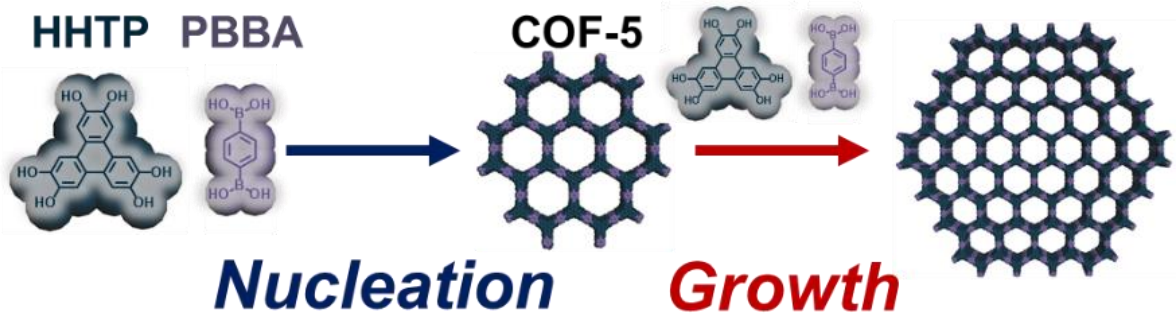

4.4. Simulated two-dimensional polymerization

The first set of simulations is designed to evaluate the nucleation rates. Nucleation in this context is defined as the occurrence of stable monodisperse nanoparticle suspensions, which we believe is involved with the stacking of metastable oligomeric species. Our earlier KMC simulations suggest that as particles (made of oligomers and their stacks) become larger, they have higher probabilities of eventually growing into crystals. Therefore, the size of the particle can serve as a criterion to identify nuclei in the simulations. Here, a threshold size of 50 monomers is used (the critical nucleus size is ~25 monomer units[511]). The identified nuclei are immediately removed from the system to suppress the impact of growth. The initial system contains 48,200 HHTP molecules and 72,300 PBBA molecules; the volume is varied in order to model different initial monomer concentrations. These amounts were chosen to minimize any finite-size effects (see **Figure 4.6** in the **SI**) while still allowing for practical simulation times. The simulations are stopped when the

nuclei that are generated correspond to 10% conversion of all monomers; in this way, the monomer concentrations do not vary significantly from their initial conditions. The nucleation rates are calculated through a linear fitting of nucleus production with time (additional computational details can be found in the **SI**). For each of the initial conditions, 20 simulations were run in order to reduce the statistical errors.

The second set of simulations focuses on the evaluation of growth rates by preventing additional nucleation after the appearance of the first nuclei, which is accomplished by eliminating stacking among oligomers, an essential step in the nucleation process.[511]. Growth in this context is defined as the subsequent expansion of the generated nuclei in the either in-plane or out-of-plane crystallographic directions. To model reliably large crystals, the system size is increased by a factor of ten so as to hold 482,000 HHTP molecules and 723,000 PBBA molecules. The simulations are completed when the crystal has grown to a size of 100,000 monomer units (which corresponds to less than 10% of the total number of monomers). The in-plane expansion/stacking rates are calculated by considering the evolution of the particle diameter/height *vs.* time. Similar to the first set of simulations, in order to obtain different initial monomer concentrations, the volume is varied while keeping the same number of monomers. We note that aggregation of nuclei and precipitation are not considered in the modeling, in order to be consistent with the experimental conditions used in this work (since nuclei form a colloidal suspension and do not aggregate or precipitate on the time scales studied).[519]

4.5. Nucleation and Expansion Rates

We focus on three properties: the nucleation rate (J_{nuc}, in mol L^{-1} s^{-1}), which is defined as the number of nuclei generated per volume unit per time interval; the in-plane (lateral) expansion rate ($v_{in\text{-}plane}$, in nm s^{-1}), which is the increment of the diameter (in-plane direction) of a crystallite per time interval; and the stacking (vertical expansion) rate ($v_{stacking}$, in nm s^{-1}), which is the increment in height (out-of-plane direction) of a crystallite per time interval. The results of the KMC simulations are shown in **Figure 4.1**. We found the following relationships among J_{nuc}, $v_{in\text{-}plane}$, and $v_{stacking}$, with respect to the monomer concentration ($C_{Monomer} = C_{HHTP} = 2/3\ C_{PBBA}$) –note that, for the sake of simplicity, we neglect the change in monomer concentration with respect to its initial value:

$$J_{nuc} = k_{nucleation} C_{monomer}^{2} \quad (1)$$

$$v_{in-plane} = k_{growth,in-plane} C_{monomer} \quad (2)$$

$$v_{stacking} = k_{growth,stacking} C_{monomer} \quad (3)$$

By considering a series of simulated monomer concentrations, we obtain that the $k_{nucleation}$, $k_{growth,in\text{-}plane}$, and $k_{growth,stacking}$ rate coefficients have values of 0.024 $L.mol^{-1}.s^{-1}$, 1,418 $nm.L.mol^{-1}.s^{-1}$ and 599 $nm.L.mol^{-1}.s^{-1}$, respectively. We note that these parameters correspond to COF-5. For the other 2D COFs, the linkage chemistry and the inter-layer interactions can vary; as a result, the absolute values of these constants are expected to be different. However, we anticipate the qualitative dynamics to be preserved.

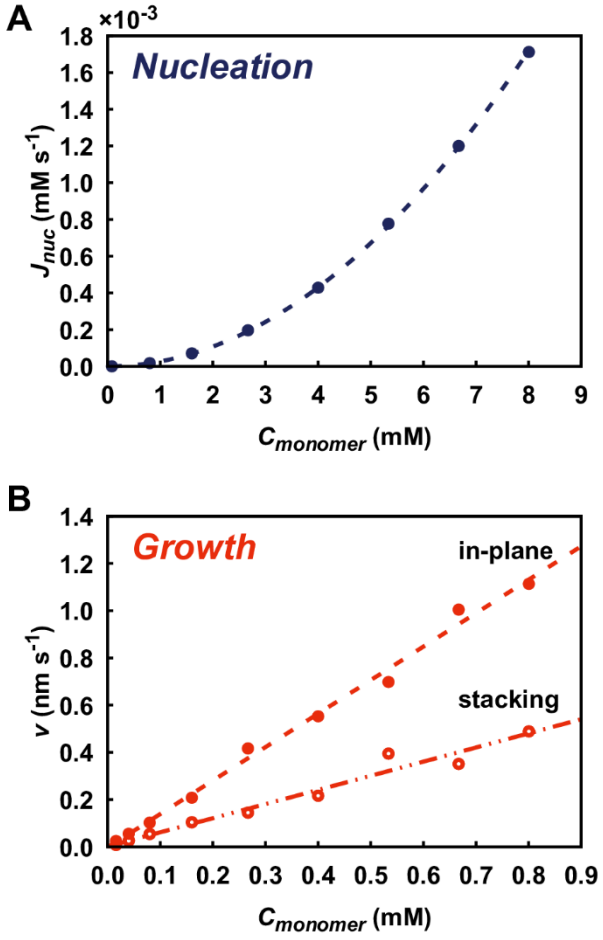

Figure 4.1. (A) KMC-simulated nucleation rate as a function of monomer concentration. **(B)** KMC-simulated in-plane and stacking growth rates as a function of monomer concentration.

Our earlier KMC simulations have revealed nonclassical features of the nucleation of 2D COFs.[511] Accordingly, the second-order dependence on monomer concentration discovered here differs from that described by classical nucleation theory.[528, 529] This second-order dependence can be understood as follows: Nucleation involves bond formation and stacking between oligomers, which are both second-order in the reactants;[511] it is possible that the nucleation speed is governed

by one of these two steps, leading to an overall second-order dependence, as shown by **Eq. (1)**. The first-order dependence of growth on monomer concentration can be rationalized by considering that, while any growth is formally a second-order process, given that one reactant is fixed in the crystal, the overall dynamics become pseudo first-order.

4.6. *in situ* X-ray scattering analysis

In order to characterize in depth the mechanism of 2D COF growth, we have measured the growth of the nanocrystalline colloidal suspensions. These COF-5 nanoparticle solutions[519] are much more suitable for mechanistic investigations than conventional agglomerated particles, since the heterogeneous processes of precipitation and aggregation are suppressed.

To probe the rate dependence of COF-5 nucleation or growth, we turned to *in situ* Small/Medium/Wide-Angle X-ray Synchrotron Scattering (SAXS/MAXS/WAXS) measurements. The simultaneous collection of these data sets allowed us to monitor the size and crystallinity of the particles in tandem, as the reaction proceeded. To probe the nucleation and growth processes independently, it was necessary to choose conditions under which the processes were temporally resolved. This was achieved by selecting monomer concentrations under which one process dominated, as was seen for COF-5 in a recent report by Evans *et al*.[440] To probe the nucleation behavior of COF-5, we prepared solutions of HHTP and PBBA at concentrations of over 1 mM, which were recently demonstrated to favor nucleation. After heating these solutions to 70 °C, we continuously monitored the MAXS pattern during COF-5 nucleation (**Figure 4.2A**). The integrated intensity of the <100> Bragg feature (~0.24 $Å^{-1}$) as a function of time was extracted

from these data (**Figure 4.2B**, inset). Finally, linear fits of signal intensity versus time were extracted, with intensity under these conditions considered to be proportional to nucleation rate. We observe a second-order relationship between the initial monomer concentration and the growth rate of the <100> signal intensity (**Figure 4.2B**). This observation is thus consistent with the results of the KMC simulations described above and supports a second-order dependence of COF nucleation on monomer concentration.

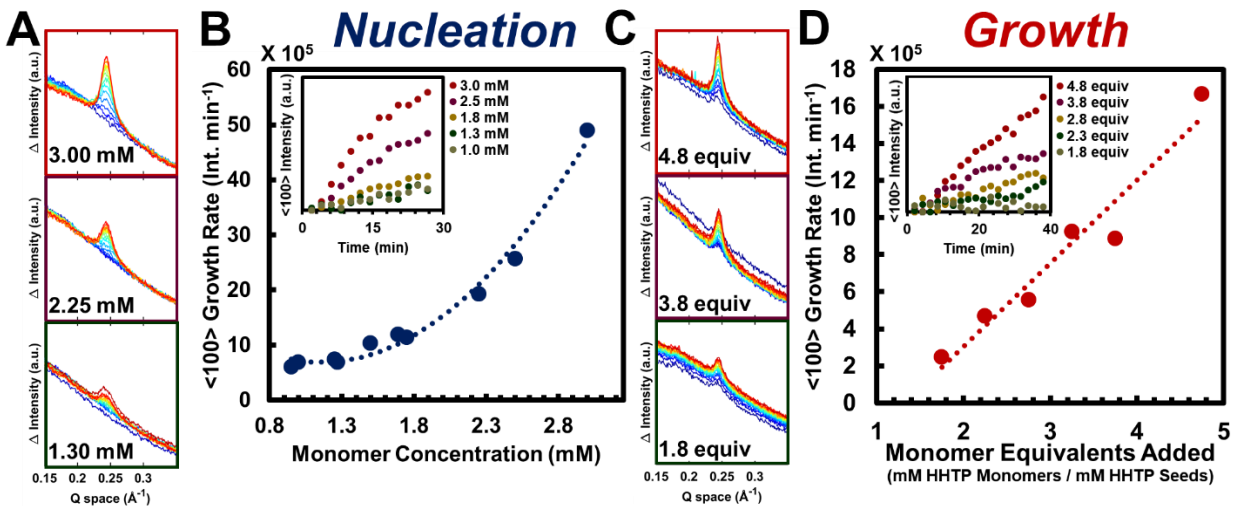

Figure 4.2. (A) MAXS traces as a function of time for selected data of **B**. **(B)** Rate of intensity of the <100> Bragg feature as a function of initial monomer concentration (inset: <100> intensity as a function of time for selected monomer concentrations). **(C)** MAXS traces as a function of time for selected data of **D**. **(D)** Rate of increase of intensity of the <100> Bragg feature as a function of monomer equivalents added (inset: <100> intensity as a function of time for selected equivalents added).

In order to probe the monomer dependence of growth, we sought to identify conditions under which nucleation would be suppressed, yet growth would occur at measurable rates. We first determined an upper concentration limit for growth experiments (0.7 mM) by allowing HHTP and PBBA to react in the absence of preexisting seed particles. No change in signal was observed, indicating that nucleation is suppressed at these time scales (**Figure 4.12**). It was also critical to identify concentrations of COF seeds that were observable while sufficiently dilute to allow for observable growth, which was ultimately optimized to an initial seed concentration. Mixtures of COF-5 seed particles at a constant particle density but variable free monomer equivalents (moles HHTP free monomer / moles of HHTP present in COF seeds) below this nucleation threshold were then prepared and heated to 70 °C (see **SI** for more details). Additionally, a sample was prepared by diluting the COF-5 seeds in the absence of additional monomers. Once again, the MAXS pattern was monitored as a function of time (**Figure 4.2C**), with extracted <100> intensities (**Figure 4.2D** inset) and rate of this intensity growth (**Figure 4.2D**) being determined as described for the nucleation experiment. Assuming that the initial nuclei have a monodisperse size, the change in peak intensity is proportional to crystal growth at small expansion. In this case, the <100> intensity growth rate is clearly linear with respect to the monomer equivalents (and therefore the initial monomer concentration) being added. As expected, under conditions where no additional monomers were added to the diluted COF seeds, the initial seed particles remained unchanged (**Figure 4.14**), which confirms that any enhancement in signal is not related to processes such as Ostwald ripening. Taken together, these results indicate that growth is a first-order process with respect to monomer concentration when the particle density of COF-5 seeds is held constant.

4.7. Broad Implications of Controlled Two-dimensional Polymerization

We stress that precise control of nucleation and growth rates is critical to fabricating high-quality 2D COF crystals. Based on the above results, it can be concluded that for COF-5 particles nucleation is an inherently higher-order process than growth. As we elaborate on in the following discussion, this difference in dynamics is the origin of the observation that nucleation and growth can be temporally resolved by controlling the monomer concentration, with nucleation being suppressed at lower monomer concentrations.

We now turn to a discussion of the relative strengths of nucleation and growth rates. One way to compare these rates is through monomer consumption. The monomer consumption rates for nucleation ($\omega_{monomer,nuc}$, in mol L^{-1} s^{-1}) and growth ($\omega_{monomer,growth}$, in mol L^{-1} s^{-1}) of a crystal has the following dependences on monomer concentration and crystal diameter (d) when assuming a cylindrical shape and a constant diameter-to-height ratio of the crystals:

$$\omega_{monomer,nuc} \propto C_{monomer}^{2} \tag{4}$$

$$\omega_{monomer,growth} \propto d^{2} C_{monomer} \tag{5}$$

If we assume a colloidal solution of uniform microcrystals, the initial monomer consumption rates from nucleation and growth as a function of the added monomers are sketched in **Figure 4.3A**. Therefore, the second- and first-order dependences of nucleation and growth rates on monomer concentration mean that there always exists a threshold concentration below which nucleation is

slower than growth (**Figure 4.3A**). This analysis thus rationalizes the recent findings that nucleation is suppressed when adding monomers slowly to the colloidal solution.[440, 530]

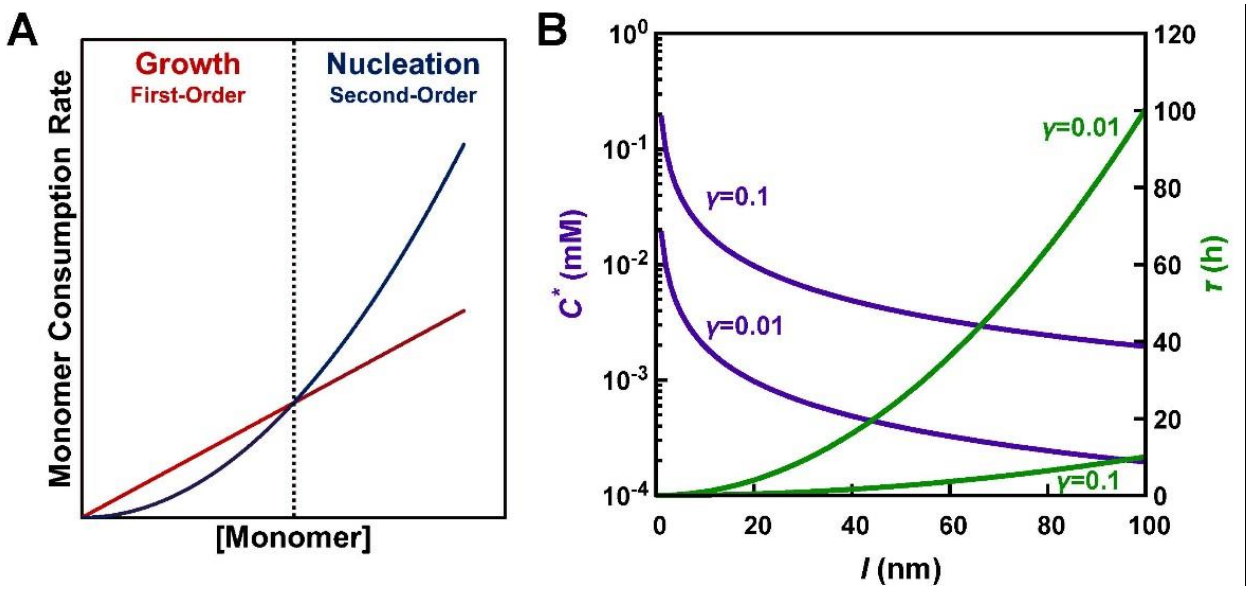

Figure 4.3. (A) Comparison of the initial monomer consumption dynamics of nucleation and growth when adding monomers to the nuclei solution for seeded growth. **(B)** Illustration of the critical monomer concentration and reaction time at different desired crystallite expansion (*l*). The value of $C_{nuc,0}$ is assumed to be 3.3×10^{-5} mM.

Understanding the relative rates of competing processes allows for guided experimental design of COF crystal growth by selecting a specific, steady-state monomer concentration. Higher monomer concentrations will speed the growth of existing colloids, yet complicates the suppression of the nucleation of new particles. Considering the interplay between nucleation and growth processes are always at play, it is challenging to completely eliminate nucleation. However, with the

objective of suppressing nucleation, we define γ as the number of newly nucleated species divided by the initial seed crystals (it can be understood as a proportionality factor between the occurrence of new crystals with respect to the existing ones) during a growth process in which the diameter of the existing crystals is extended by l. There exists a critical monomer concentration (C^*) that represents the upper theoretical limit for a specific combination of γ and l. By this definition, the monomer concentration in the reaction needs to be lower than C^* to achieve the desired crystal expansion while suppressing nucleation. Monomer concentrations above C^* lead to more frequent nucleation (increased γ) and smaller average crystal sizes. We find that C^* depends on the initial nuclei concentration ($C_{nuc,0}$) and can be expressed as:

$$C^* = \frac{\gamma C_{nuc,0} k_{growth,in-plane}}{l k_{nucleation}} \tag{6}$$

The monomer consumption rate $\omega_{consump}$ (from both nucleation and growth) gives information about the monomer amount that should be added to maintain a constant monomer concentration at $C_{monomer}$. When assuming the crystals to be cylindrical and under the condition that $\gamma \ll 1$, we find that $\omega_{consump}$ is expressed as:

$$\omega_{consump} = \frac{3\pi k_{growth,in-plane} \beta C_{nuc,0} C_{monomer}}{4\alpha} \left(k_{growth,in-plane} C_{monomer} t + d_0 \right)^2 + \mathrm{N_{nuc}} k_{nucleation} C_{monomer}^2 \tag{7}$$

where α is the diameter-to-height ratio of the crystal and d_0, the initial diameter of the crystals. It emerges from **Eq. (7)** that $\omega_{consump}$ is not constant but instead increases quadratically with time.

For practical 2D COF growth, the reaction time is also an important factor to be considered. The use of too low a monomer concentration should be avoided as it results in undesirably slow growth.

The shortest time for crystal growth is achieved when using $C_{monomer} = C^*$. In this case, the time required for the desired crystal expansion l is calculated to be:

$$\tau = \frac{l}{k_{growth,in-plane} C^*} = \frac{k_{nucleation} l^2}{k^2_{growth,in-plane} \gamma C_{nuc,0}} \quad (8)$$

A graphical illustration of **Eqs. (6)** and **(8)** is shown in **Figure 4.3B**. The quadratic dependence of time on desired growth coupled with the inverse dependence on γ means that growing ever larger crystals by slow monomer addition is likely to face practical challenges. Nevertheless, this analysis provides a theoretical reference for the monomer concentration to use during 2D COF fabrication, the amount of monomers to add, and the estimated time of crystal growth.

It is also possible to model the situation where the monomer solution is added at certain time intervals, which can be easier to achieve in practice than maintaining a constant monomer concentration. In this case, the monomer concentration decreases with time until new monomers are added to the reaction solution. The evolution of the particle sizes can be solved numerically. We consider an initial 10-mL seed solution with a crystallite size of 200 nm. A monomer solution (2 mM HHTP, 3 mM PBBA) is added to this solution every 10 min to allow the crystallites to grow. If 5-mL monomer solution is added each time, the average diameter of the crystals decreases, as shown in **Figure 4.4A**. However, if the amount of the added monomer solution is reduced to 0.05 mL, the average diameter of the crystals increases at the expense of longer reaction times (**Figure 4.4B**). **Figure 4.4C** and **D** show the crystal size distributions when the largest crystal has reached 250 nm. As can be seen, there are much less newly generated nuclei if the monomers are

added slowly (0.05 mL every 10 min). These features are consistent with recent experimental data.[440, 530]

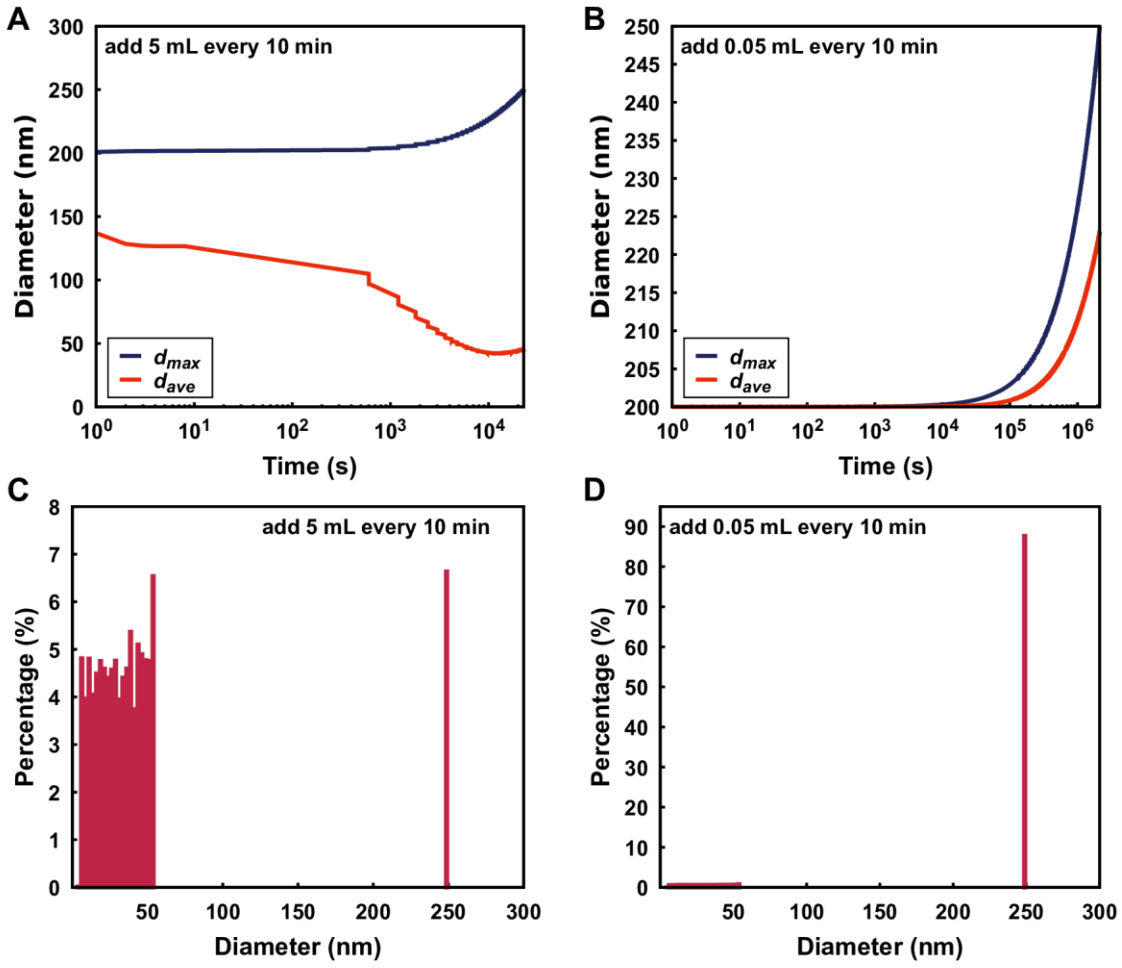

Figure 4.4. Evolution of the average and maximum crystal diameter in a seeded-growth approach from an initial colloidal solution (10 mL, d=200 nm, $C_{nuc,0}$=3.3×10^{-5} mM) at monomer (2 mM HHTP, 3 mM PBBA) addition intervals of 20 min with **(A)** 5 mL or **(B)** 0.05 mL at each loading. **(C)** and **(D)** show the crystal diameter distribution when the largest crystal has reached 250 nm.

The above theoretical analyses are critical to the rational control over 2D COF synthetic conditions, and therefore temporal resolution of different microscale processes relevant to COF growth. Furthermore, the model we have developed for COF growth suggests that mechanisms orthogonal to direct condensation (*e.g.*, formal transimination[531] and monomer exchange reactions[532]) should be explored further to determine how synthetic versatility can be introduced while taking advantage of controlled nucleation and elongation. We anticipate that combinations of strategies will likely be more effective than individual approaches.

The combination of kinetic Monte Carlo simulations and *in situ* X-ray scattering measurements has allowed us to develop a *quantitative* analysis of the nucleation and growth rates of 2D COFs, as represented by COF-5. The nucleation and growth processes have second-order and first-order dependences on monomer concentration, respectively. These different reaction orders explain why growth can be suppressed by controlling the speed of monomer addition. Based on this experimentally validated model, we were able to define a critical monomer concentration C^*, which provides insight into the optimal monomer concentration to use for 2D COF growth via slow addition of monomers to 2D COF colloidal seeds.

This understanding allows us to express several rules for the optimization of 2D COF synthesis. First, we find that C^* is proportional to the occurrence of new crystals with respect to the existing ones, while inversely proportional to the desired amount of expansion of the seed. Therefore, lower monomer concentrations should be selected when targeting fewer and larger crystallite domains. Secondly, C^* is linearly dependent on the number of nuclei in solution. This means that higher monomer concentrations may be used in solutions where the number of nuclei is also larger. Therefore, in solutions with more COF nanoparticles, the critical monomer concentration is

increased as well as the rate of monomer consumption directed toward crystal growth. However, this growth will be shared among the larger number of crystallite seeds, making this strategy ineffective for increasing the average crystallite domain size more quickly.

4.8. Concluding thoughts

The fundamental connection between C^* and the competition between nucleation and growth means that the reaction time has a quadratic dependence on the desired crystal expansion. While no theoretical upper limit exists in terms of a maximum COF size, the nonlinear dependence on time suggests that growing large crystals can rapidly become impractical. For example, as illustrated by **Eq. (8),** growing 1-mm long crystals for a value of γ (the proportionality factor between the occurrence of new crystals with respect to the existing ones) equal to 0.01, can take over 1,000,000 years. Thus, growing millimeter-sized 2D COF crystals from solution using a direct-condensation, seeded-growth approach remains challenging. However, this limitation is associated with the specific strategy of limiting nucleation only by maintaining a low monomer concentration. Other methods to limit nucleation, such as chemically increasing the transesterification rate associated with COF formation, might provide access to high-quality COFs under different kinetic regimes. New synthetic strategies are called for to achieve these goals.

Finally, we note that 2D COF formation and growth can rely on different mechanisms. Here, we have used COF-5 as a representative example and the conclusions thus likely apply to the series of boronate ester-linked COFs. It will be of interest to determine whether the set of empirical equations developed here can be extended to other types of 2D COFs for which different growth

mechanisms have been proposed. Such mechanistic investigations of chemically distinct systems are part of our ongoing collaborative efforts.

4.9. Chapter 4, Supplementary Information

Simulation Results

The parameters used in the KMC simulations have been documented in our previous work.[511] In the present KMC simulations, nuclei have been identified by setting a size threshold of 50 monomer units, which we choose to be slightly larger than the value of 40 monomer units used in our previous study [511] in order to ensure better identification. **Figure 4.5** shows a typical nucleus production curve. For each simulation, a linear fitting is performed. The nucleation rate corresponds to the fitted slope.

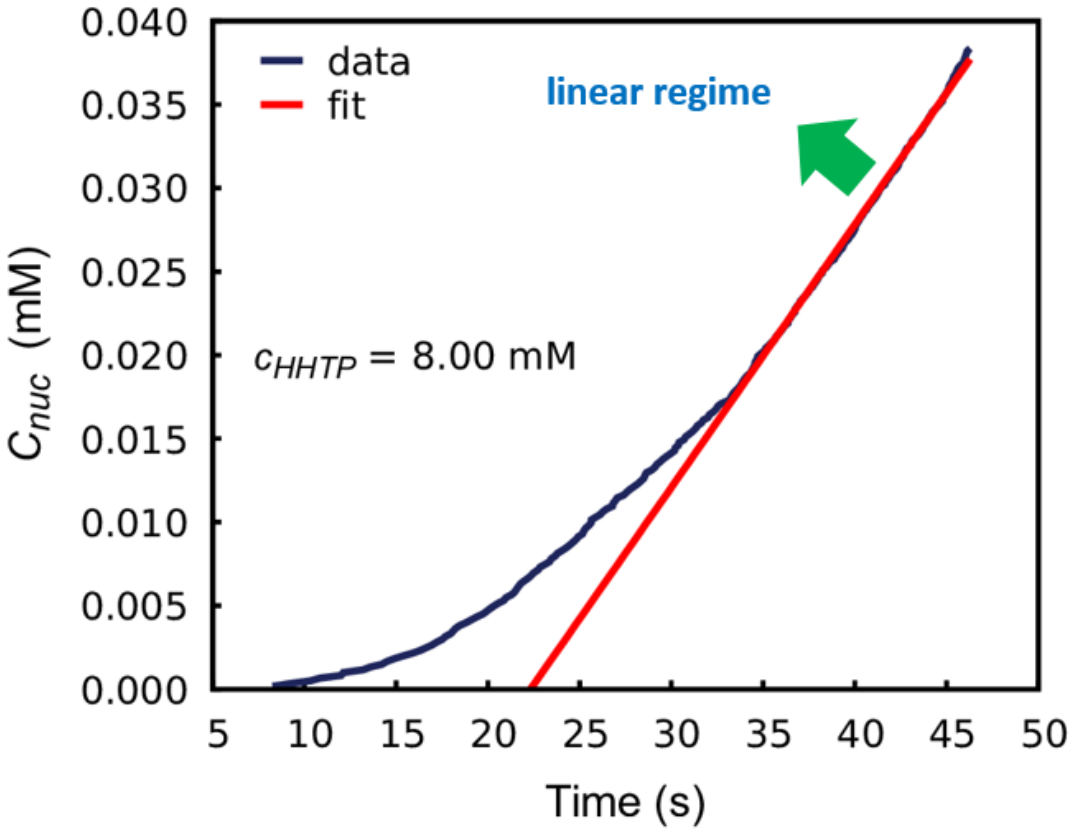

Figure 4.5. **Representative Linear Fitting Used in the KMC Simulations:** Illustration of the calculation of the nucleation rates.

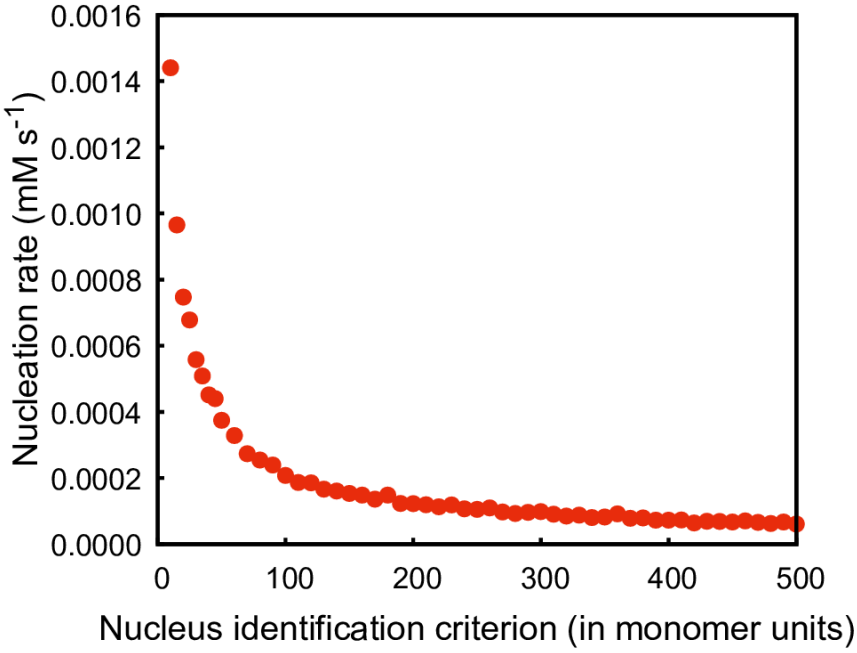

Figure 4.6. Impact of the size criterion in the identification of nuclei on the calculated nucleation rate.

For nucleation simulations, the total number of monomers is 120,500. We have checked that the error coming from the finite sizes of the simulation system is not significant, as shown **Figure 4.6**.

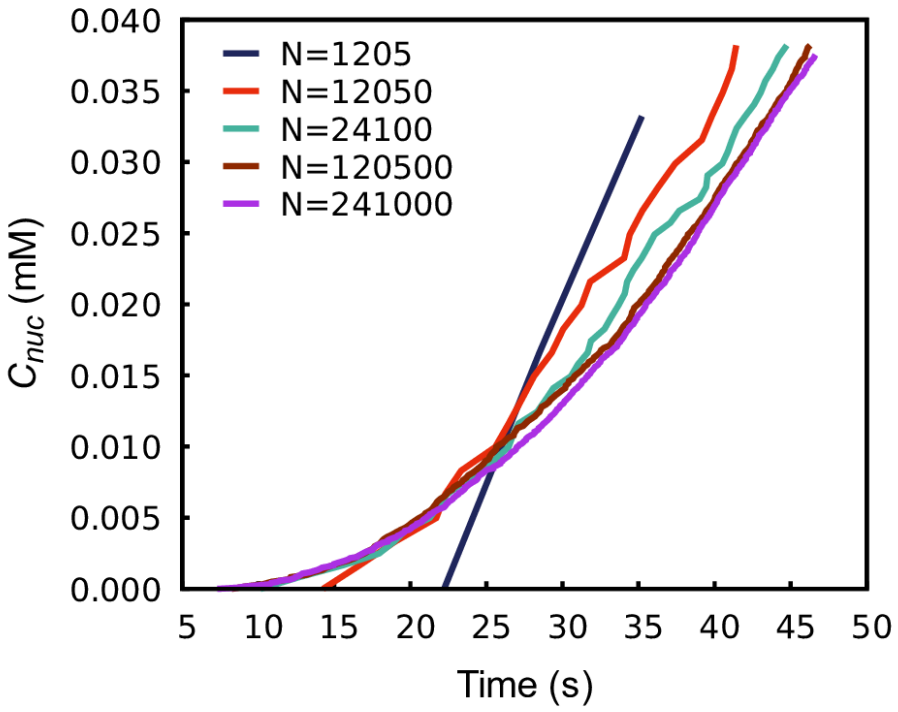

Figure 4.7. **Simulation Results for Different System Sizes in the KMC Simulations.** N is the total number of monomers. The concentrations of monomers are the same across all simulations.

The lateral expansion is found to be approximately linear with time. **Figure 4.6 and Figure 4.7** show a typical COF expansion in the course of the simulated growth and the top view of the final crystal, respectively. Linear fittings are performed on the crystal expansion results, see **Figure 4.5**. The lateral expansion rate thus corresponds to the fitted slope.

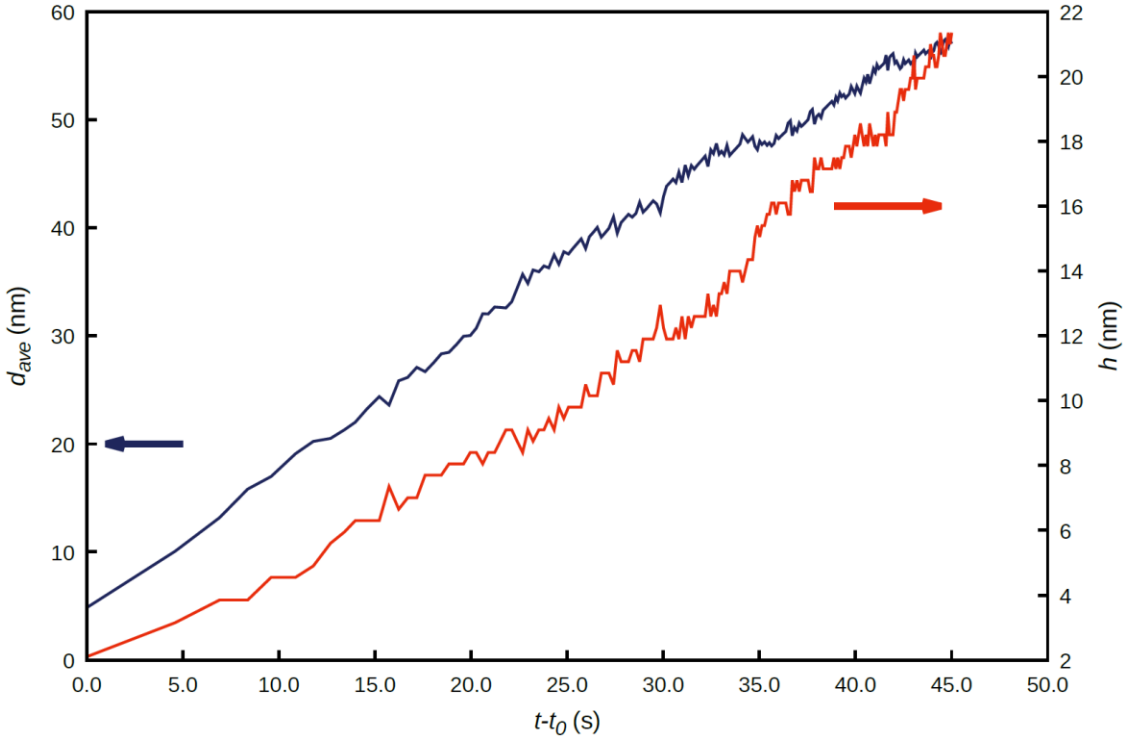

Figure 4.8. **Example of KMC Growth Result.** Illustration of the evolution of average diameter and height as a function of time.

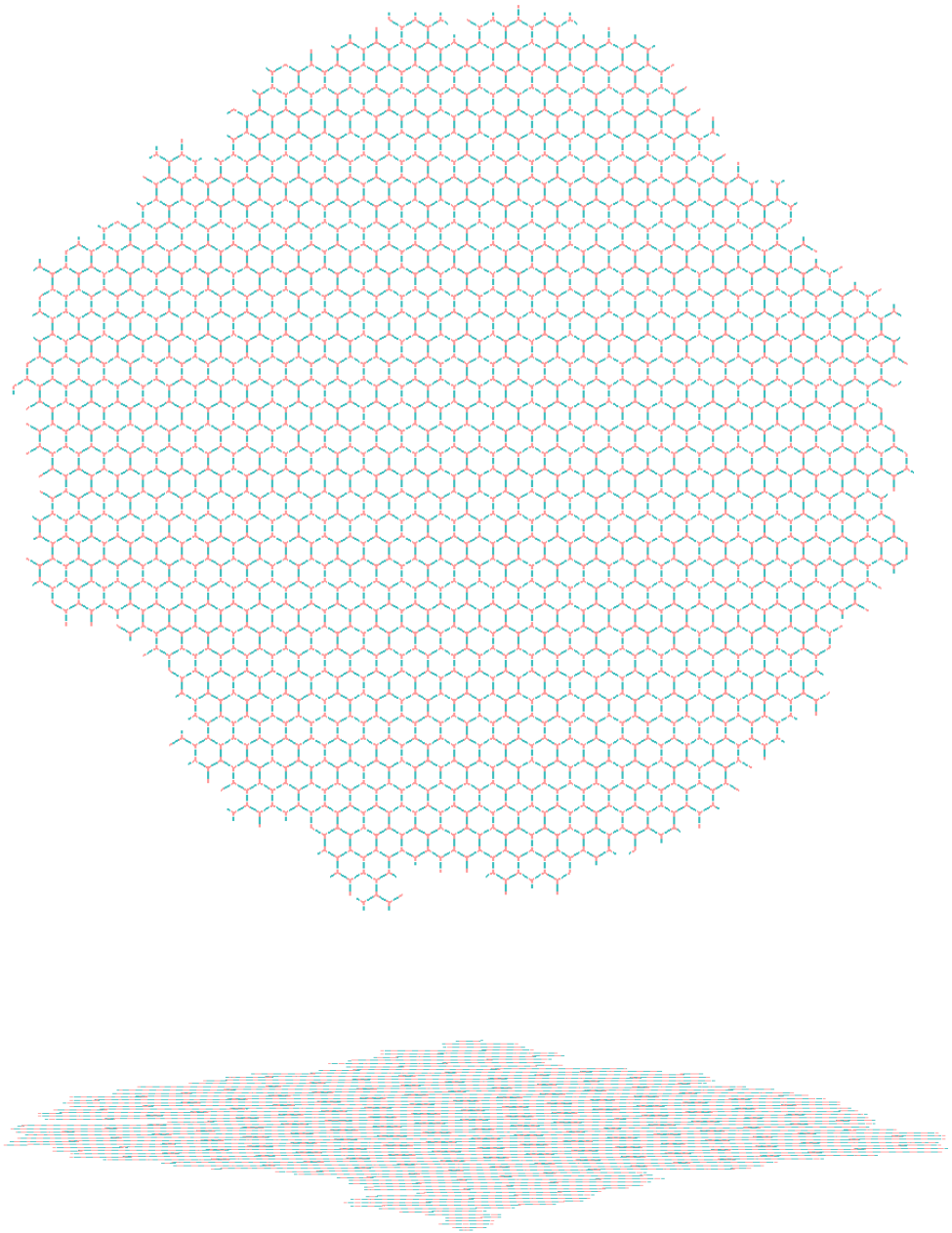

Figure 4.9. **COF-5 particle simulation.** Illustration of the final structure of the COF-5 crystal (top view and side view) from the KMC simulation.

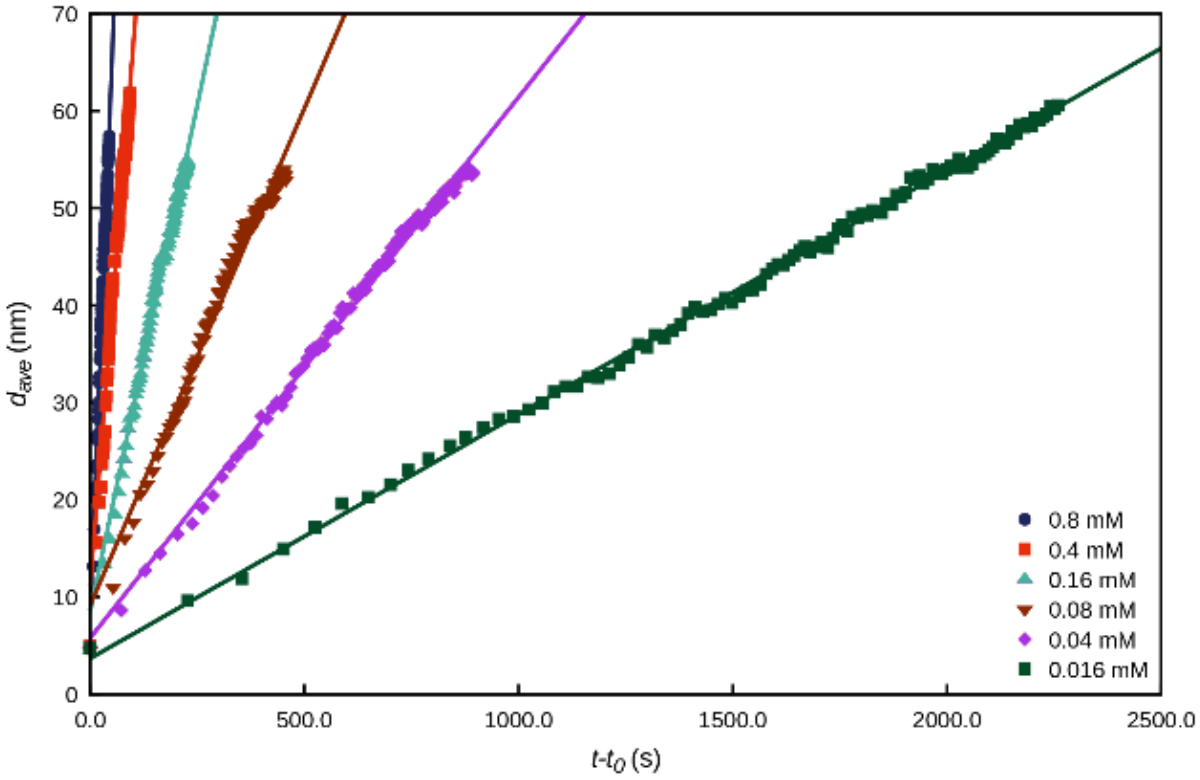

Figure 4.10. **Fitting of the Lateral Expansion Data.** Lateral expansion as a function of time and linear fittings.

Materials and Instrumentation

Materials

Acetonitrile, 1-4 Dioxane, and Mesitylene were purchased from Fisher Scientific. Phenylbisboronic acid (PBBA) was purchased from Sigma-Aldrich and hexahydroxytriphenylene (HHTP) was purchased from TCI America. All chemicals were used without further purification.

Instrumentation

Sonication. Sonication was performed with a Branson 3510 ultrasonic cleaner with a power output of 100W and a frequency of 42 kHz.

***In Situ* X-ray Scattering:** Small/Medium/Wide-Angle X-ray Scattering (SAXS/MAXS/WAXS) data were collected simultaneously at sector 5-ID-D of the Advanced Photon Source at Argonne National Laboratory. A beam energy of 17.0 KeV was used for these experiments. Patterns were collected with single 10 s frames on a series of 3 Pilatus 2D detectors which were then radially integrated. All samples were conducted in 1.5 mm borosilicate capillaries with a wall thickness of 0.01 mm available from Charles Supper Scientific. Patterns were assigned to be time = 0 seconds when the heater reached its steady state temperature of 70 °C (approximately 45 seconds). Patterns were baselined and then background subtracted from the starting time pattern to produce corrected patterns. The <100> Bragg feature of COF-5 (~0.24 $Å^{-1}$) was then integrated and plotted against the time of each pattern. Finally, the rate of increase in <100> signal intensity was determined by fitting the slope of the respective <100> intensity versus time for each experiment.

Synthesis of COF-5 Seeds

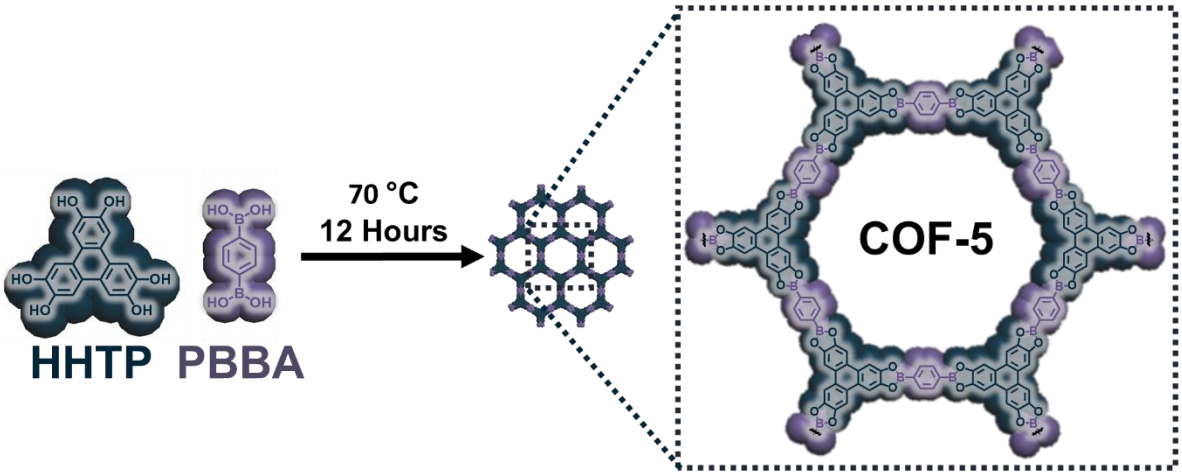

Figure 4.11. Synthesis Procedure of COF-5 Colloidal Seeds.

Hexahydroxytriphenylene (HHTP) and phenylbisboronicacid (PBBA) were added to a 20 mL mixture of CH_3CN:dioxane:mesitylene (80:16:4 vol%) at a concentration of 2 mM HHTP and 3 mM PBBA. This solution was sonicated until full dissolution of the monomers was observed. This solution was then heated in a scintillation vial overnight at 70 °C after which time the solution became opaque indicating the successful synthesis of COF-5 seed particles. These seeds were then used as prepared for COF growth experiments detailed below. This method is explained in further detail in Ref. [440]

Experimental *in situ* Scattering Details

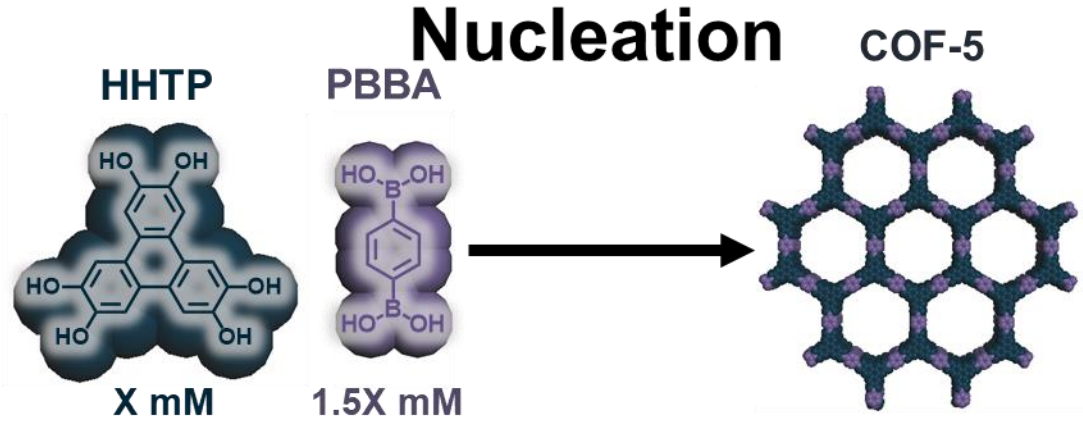

Figure 4.12. Nucleation Experiment. Schematic of how the nucleation experiments were conducted.

Nucleation Experiment: Hexahydroxytriphenylene (HHTP) and phenylbisboronicacid (PBBA) were added to a 20 mL mixture of CH_3CN:dioxane:mesitylene (80:16:4 vol%) in a 1:1.5 molar ratio at a concentration of double that specified in the experiment. For example, if the nucleation experiment was conducted at 2 mM, an HHTP solution of 4 mM and a PBBA solution of 6 mM would have been made independently. This is to prevent reaction before the mixing of the two monomers. These solutions were sonicated until full solvation of the monomers. The two monomer solutions were then mixed in a dram vial in a 1:1 volume ratio (final volume 1 mL) and were then diluted as specified to produce the specified monomer concentration. These solutions were then quickly shaken to ensure mixing. Approximately 100 µL of these solutions were then added to a borosilicate capillary and sealed using capillary sealing putty. These capillaries were immediately installed onto a multicapillary heating stage available at Sector 5-ID-D of the Advanced Photon

Source (APS) Argonne National Lab (ANL). This stage was then heated to 70 °C (< 1 min heating time) and allowed to react while continuous SAXS/MAXS/WAXS patterns were taken.

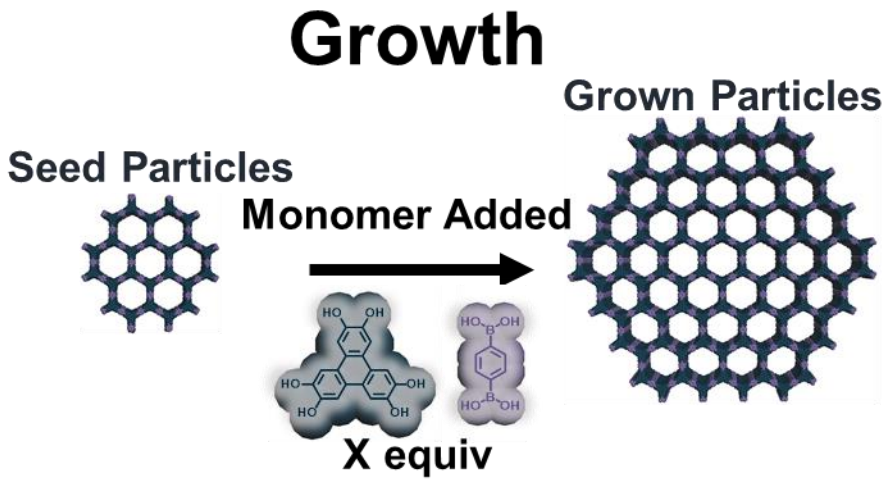

Figure 4.13. Growth Experiment. Schematic of how the growth experiments were conducted.

Growth Experiment: Hexahydroxytriphenylene (HHTP) and phenylbisboronicacid (PBBA) were added to a separate 20 mL mixture of CH_3CN:dioxane:mesitylene (80:16:4 vol%) at a concentration of 1 mM HHTP and 1.5 mM PBBA. These solutions were sonicated until full solvation of the monomers. The two monomer solutions were then mixed in a dram vial in a 1:1 volume ratio (final volume 2 mL) and quickly shaken. Dilutions were then performed in dram vials to produce different concentrations of monomer solutions with the same volume. The highest monomer concentration (0.48 mM) was chosen to temporally resolve nucleation and growth. The same amount of COF-5 seeds (COF-5 seeds diluted by a factor of 20, resulting in particle solution containing 0.1 mM HHTP and 0.15 mM PBBA) were then added to all reactions to keep the density

of seed particles identical. To ensure that Ostwald ripening or depolymerization were not relevant processes under these conditions, we also diluted our COF-5 seed particles and performed the experiment without the presence of additional monomers. Precise amounts of the dilution experiment are recorded below.

Table 4.1. Dilution Calculations. Calculations of how dilutions were conducted for COF-5 growth experiments.

Seed Stock (mL)	Blank Solvent (mL)	Monomer Amount (mL)	Resultant Monomer Concentration (mM)
0.1	0	1.9	0.48
0.1	0.4	1.5	0.38
0.1	0.6	1.3	0.33
0.1	0.8	1.1	0.28
0.1	1	0.9	0.23
0.1	1.2	0.7	0.18
0.1	1.9	0	0

Approximately 100 µL of these solutions were then added to a borosilicate capillary and sealed using capillary sealing putty. These capillaries were immediately installed onto a multicapillary heating stage available at Sector 5-ID-D of the Advanced Photon Source (APS) Argonne National Lab (ANL). This stage was then heated to 70 °C and allowed to react while continuous SAXS/MAXS/WAXS patterns were taken.

X-ray Scattering Control Experiments

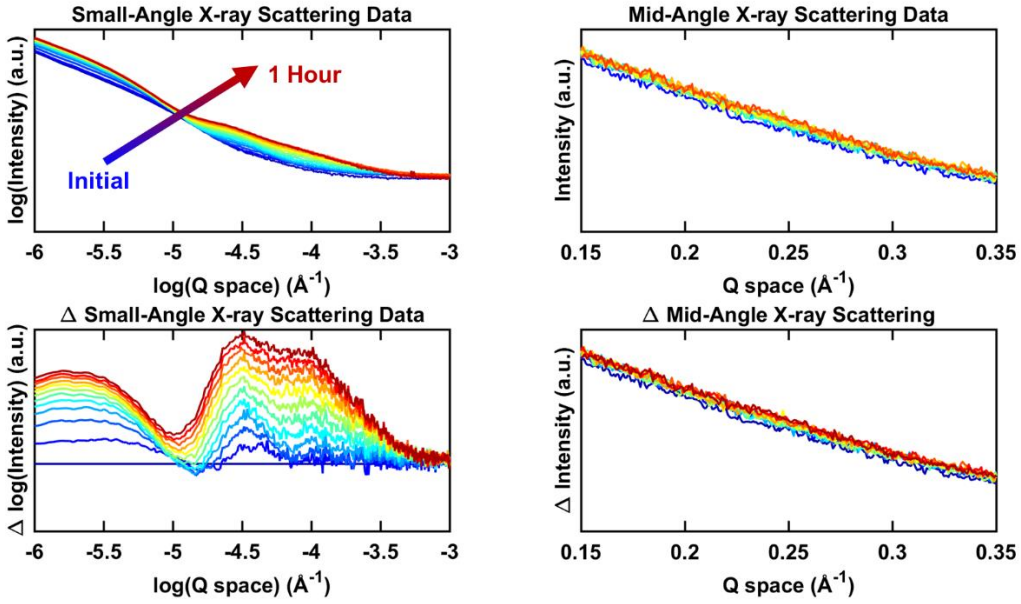

Figure 4.14. Nucleation Control. In situ X-ray scattering of 0.7 mM HHTP 1.1 mM PBBA solution over the course of 1 hour.

The background subtracted MAXS data shown in the bottom right corner demonstrates that under conditions where monomer concentration is sufficiently small results in no <100> diffraction feature and thus no substantial COF nucleation on the time-scales studied here. The background subtracted SAXS data shown in the bottom left corner shows that species of small sizes are formed over the course of this reaction. This validates previous understanding of COF nucleation where small oligomers are formed but never “nucleate” unless they reach a critical concentration.

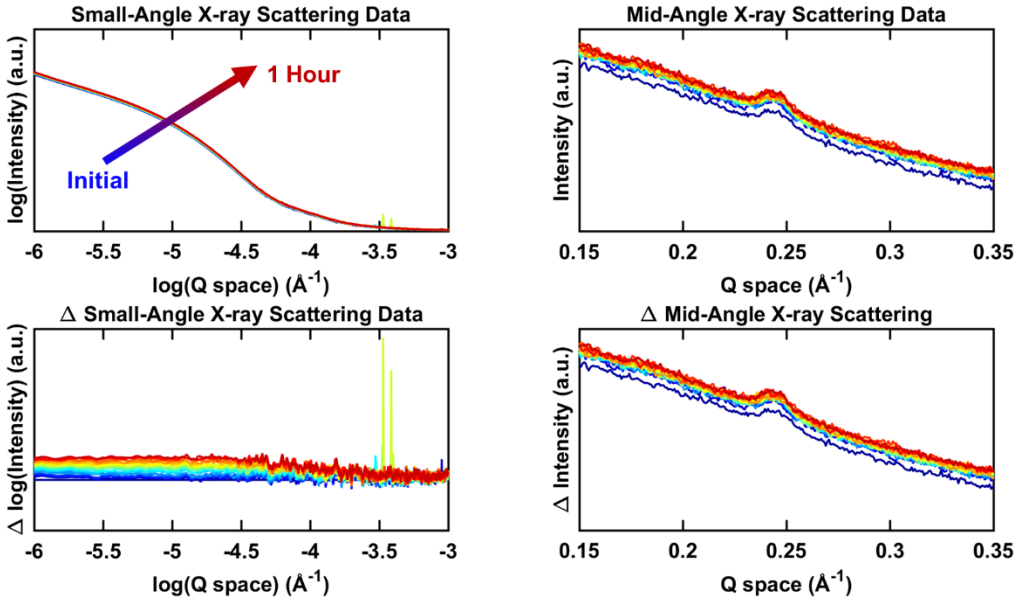

Figure 4.15. Growth Control. In situ X-ray scattering of COF-5 seeds heated in the presence of no additional monomer.

The MAXS data shown in the top right corner demonstrates that under conditions where no additional monomer is added no discernable difference in the <100> diffraction feature is noted. The background subtracted SAXS data shown in the bottom left corner shows that there is no discernable size change of the existing nucleation after the course of one hour. These experiments suggest that the increase in intensity seen under monomer addition conditions are due to growth and not processes such as Ostwald ripening. This is consistent with observations made previously.[440]

In Situ X-Ray Scattering Nucleation Results

All experiments were conducted over the course of approximately one hour. Conditions of each experiment are given in their respective figure headings. In these figures [Monomer] = [HHTP] = 2/3*[PBBA] is the concentration of monomers present at the beginning of the experiment.

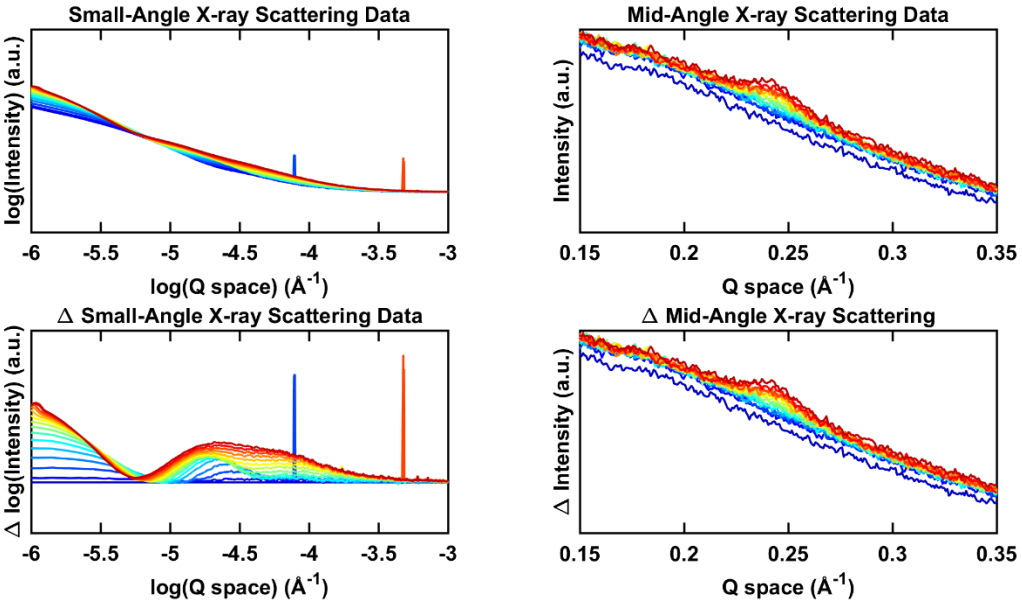

Figure 4.16. Nucleation Experiment [Monomer] = 0.9 mM (measurement 1).

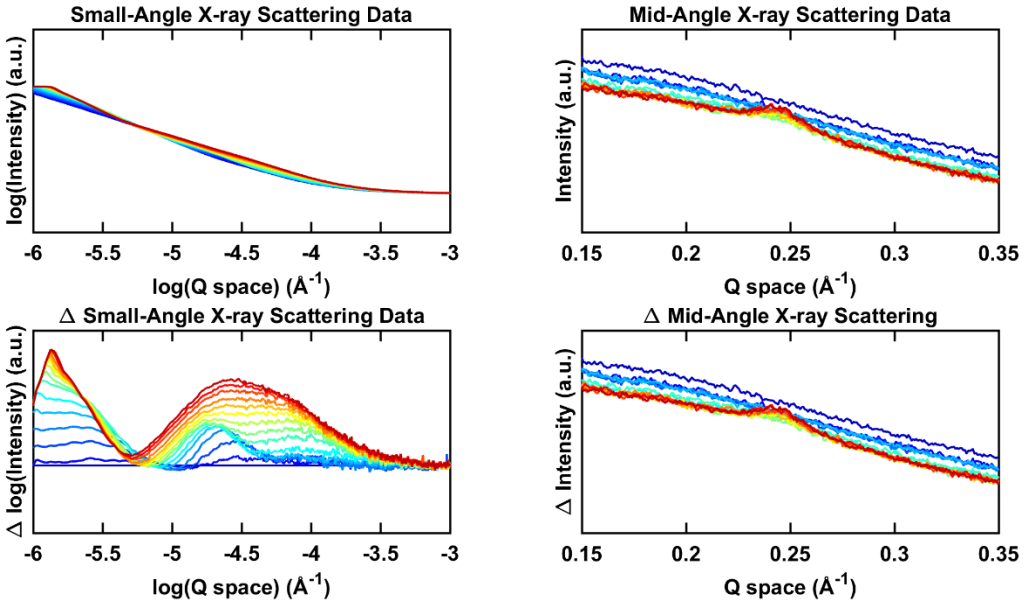

Figure 4.17. Nucleation Experiment [Monomer] = 0.9 mM (measurement 2).

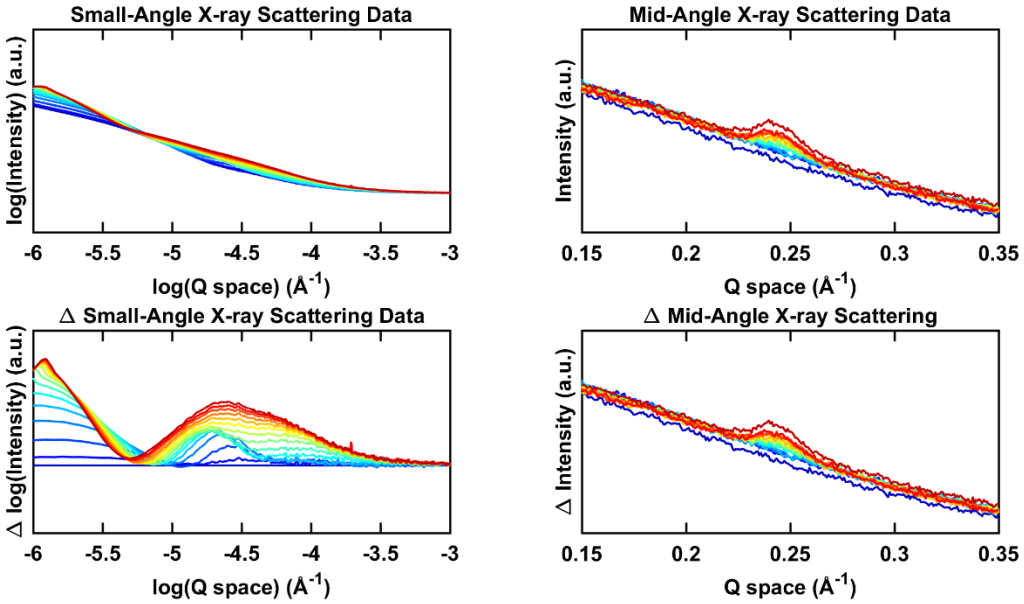

Figure 4.18. Nucleation Experiment [Monomer] = 1.1 mM (measurement 1).

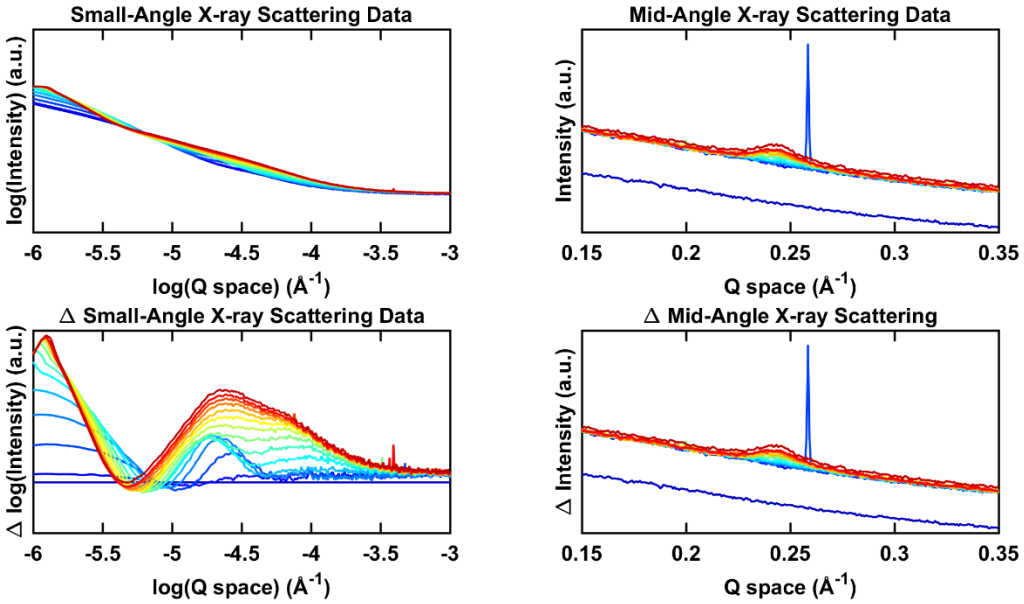

Figure 4.19. Nucleation Experiment [Monomer] = 1.1 mM (measurement 2).

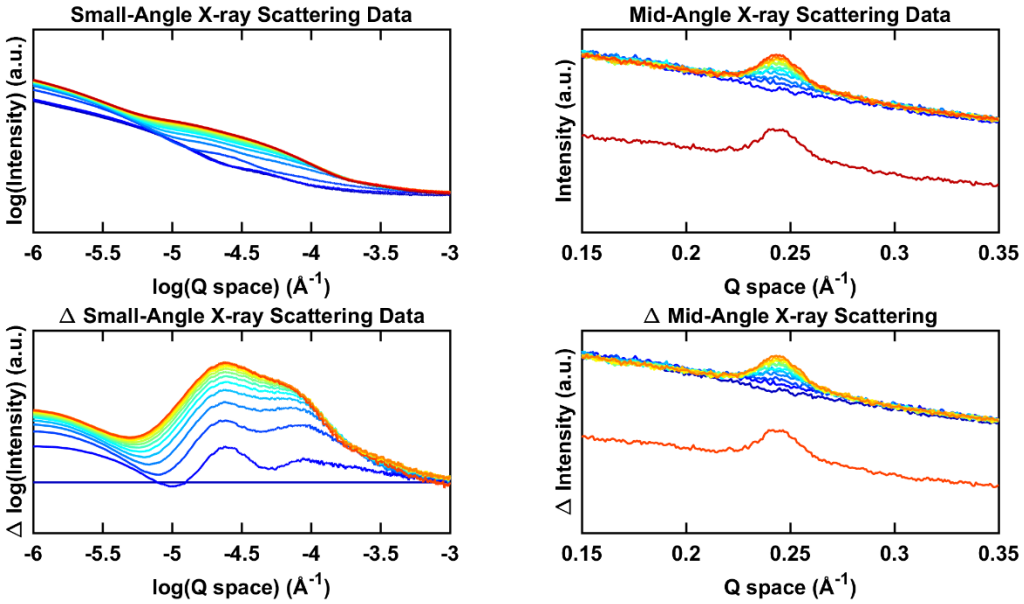

Figure 4.20. Nucleation Experiment [Monomer] = 1.3 mM (measurement 1).

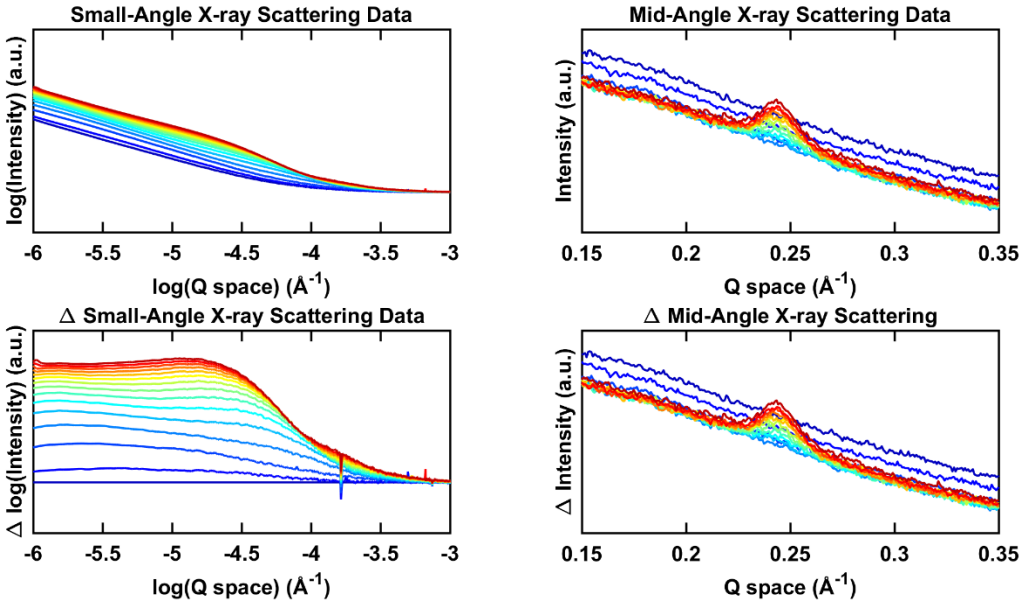

Figure 4.21. Nucleation Experiment [Monomer] = 1.3 mM (measurement 2).

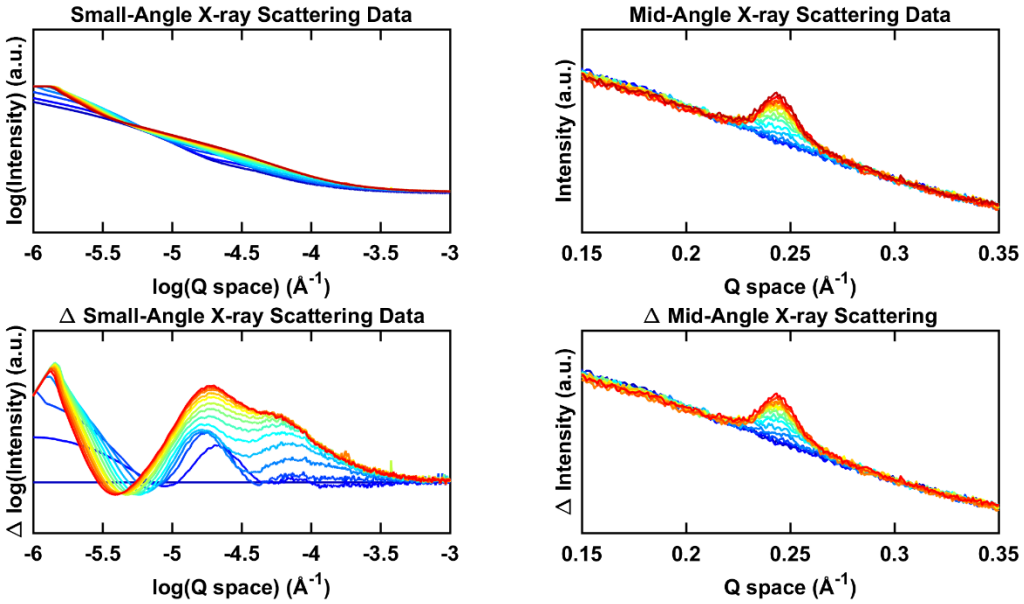

Figure 4.22. Nucleation Experiment [Monomer] = 1.5 mM.

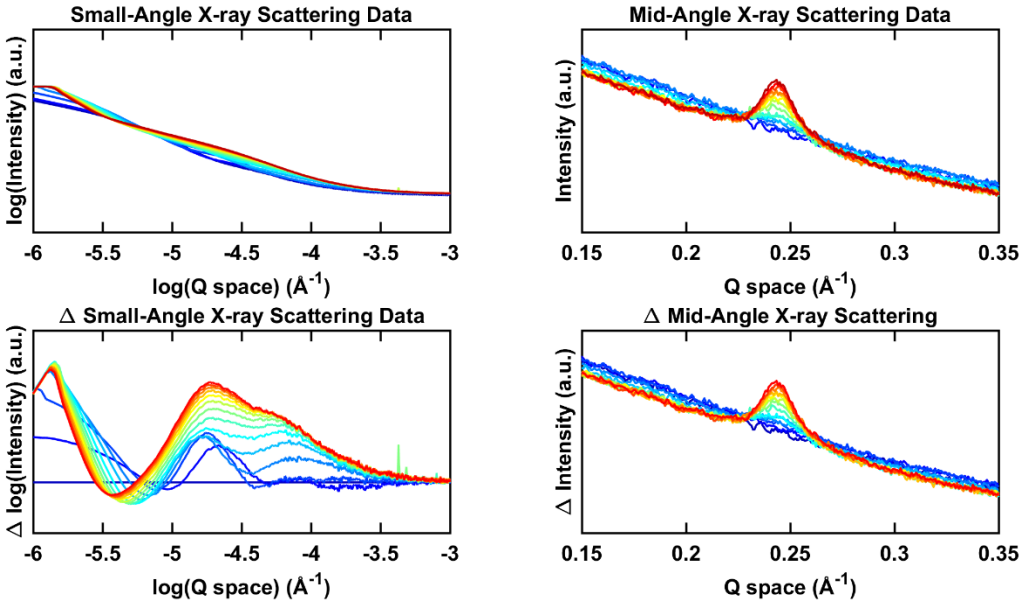

Figure 4.23. Nucleation Experiment [Monomer] = 1.8 mM.

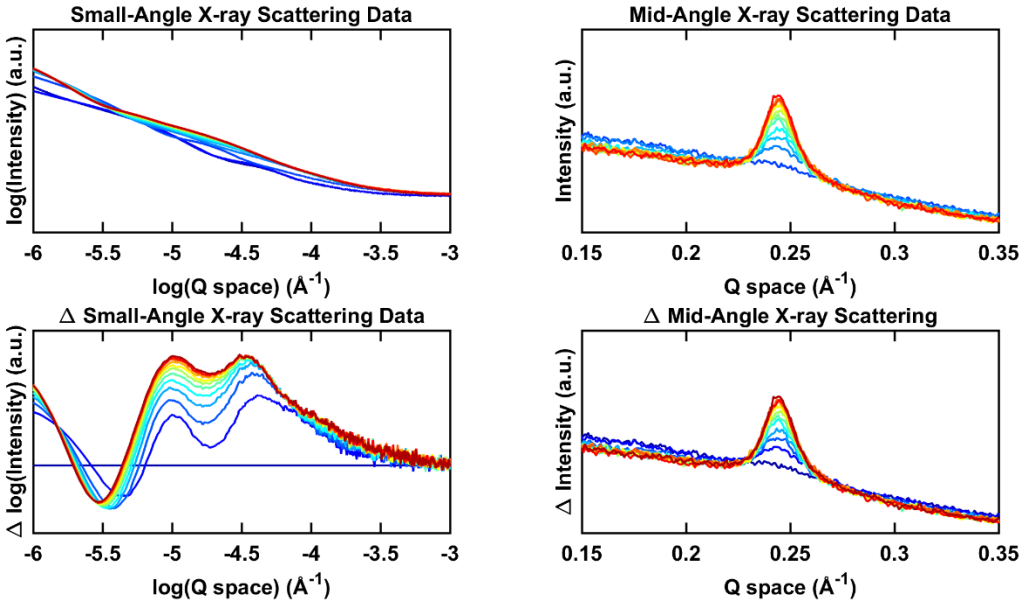

Figure 4.24. Nucleation Experiment [Monomer] = 2.3 mM.

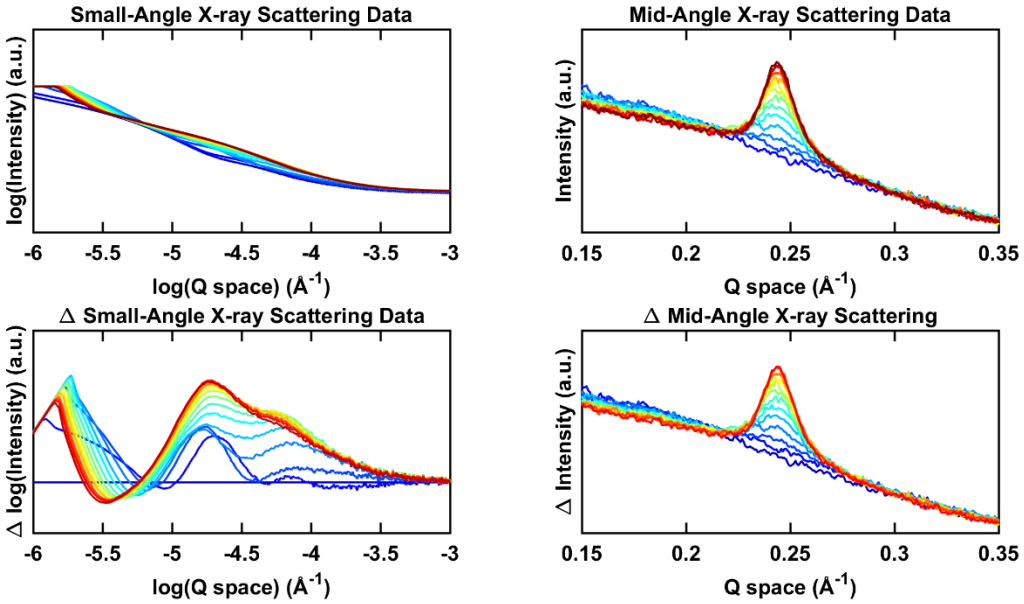

Figure 4.25. Nucleation Experiment [Monomer] = 3.0 mM.

In Situ X-Ray Scattering Growth Results

All experiments were conducted over the course of approximately one hour. Conditions of each experiment are given in their respective figure headings. In these figures [Monomer] = [HHTP] = 2/3*[PBBA] is related to the amount of monomer added to a consistent amount and concentration of preexisting COF-5 seeds.

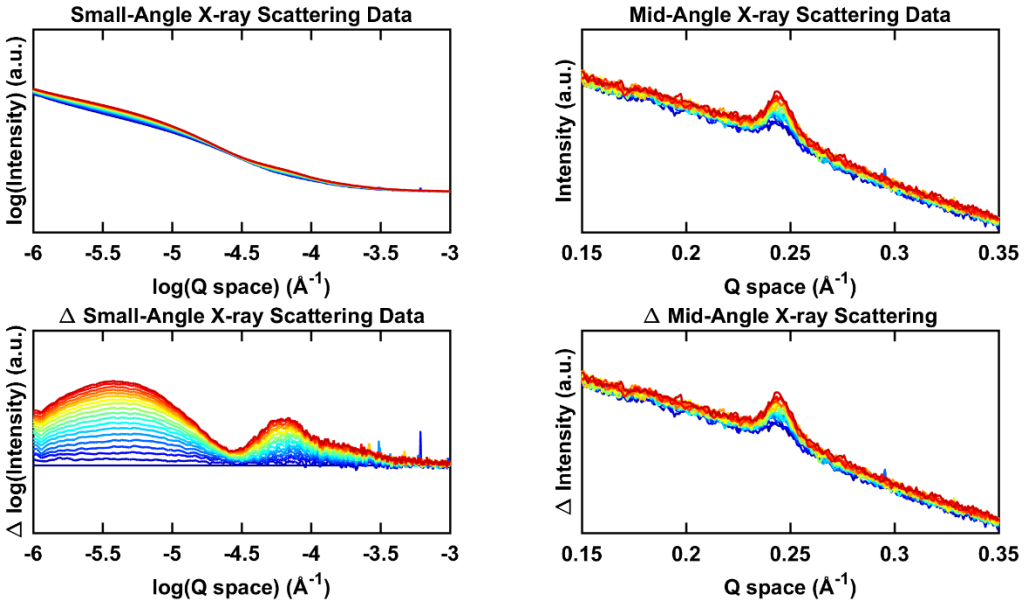

Figure 4.26. Growth Experiment [Monomer] = 0.18 mM.

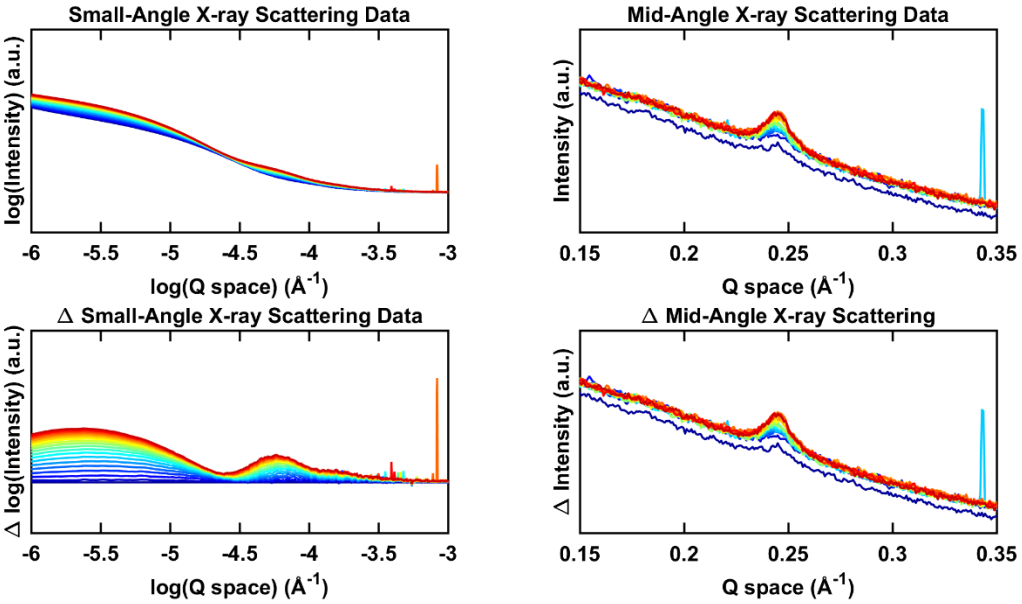

Figure 4.27. Growth Experiment [Monomer] = 0.23 mM.

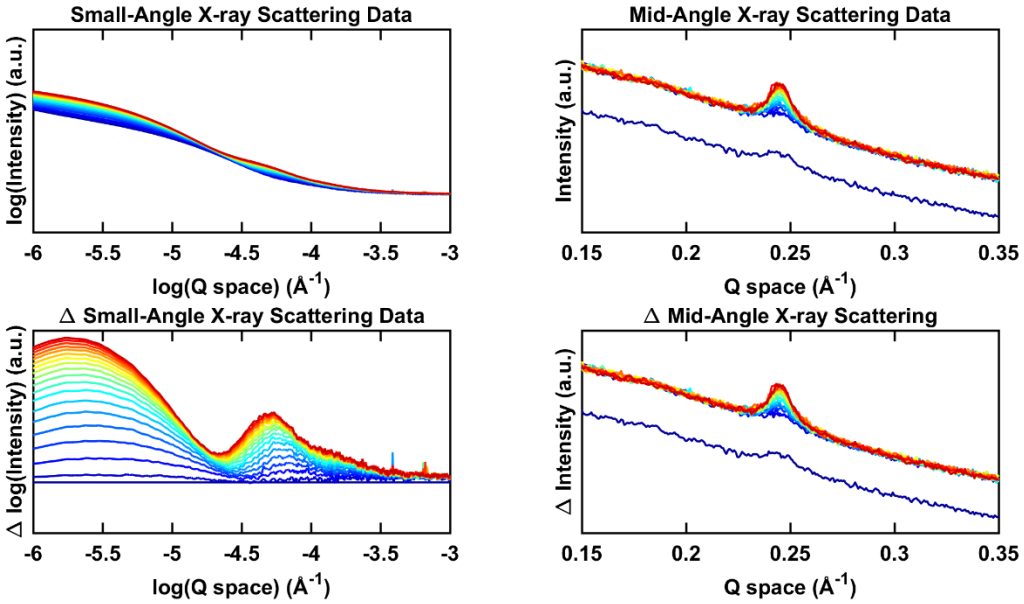

Figure 4.28. Growth Experiment [Monomer] = 0.28 mM.

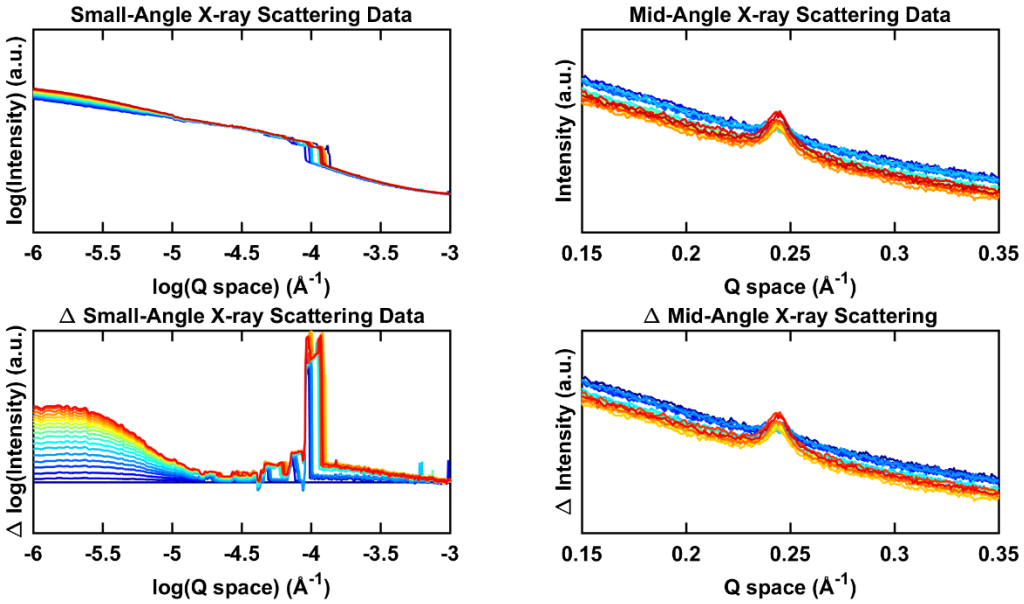

Figure 4.29. Growth Experiment [Monomer] = 0.33 mM.

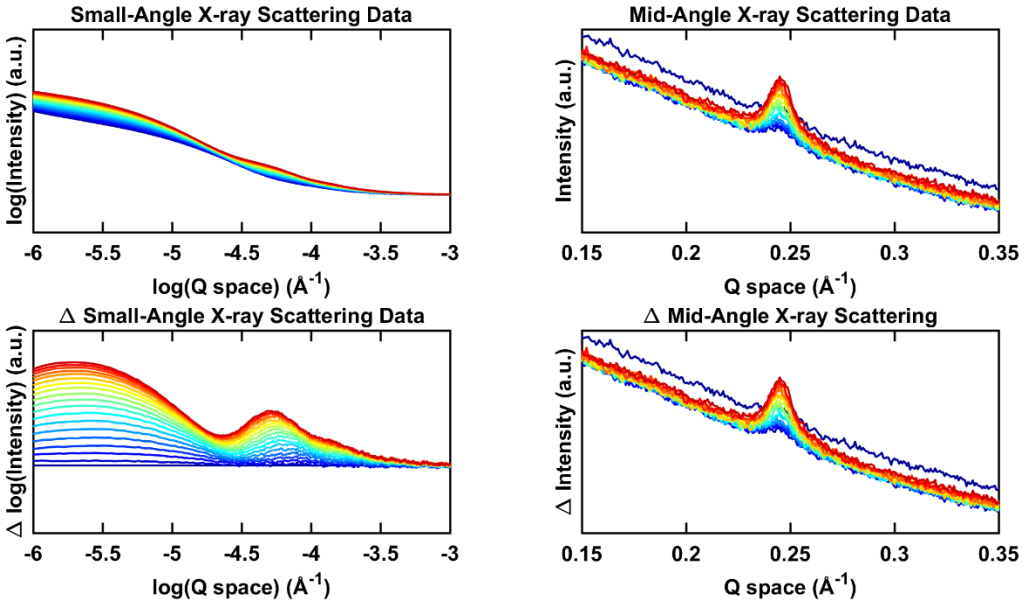

Figure 4.30. Growth Experiment [Monomer] = 0.38 mM.

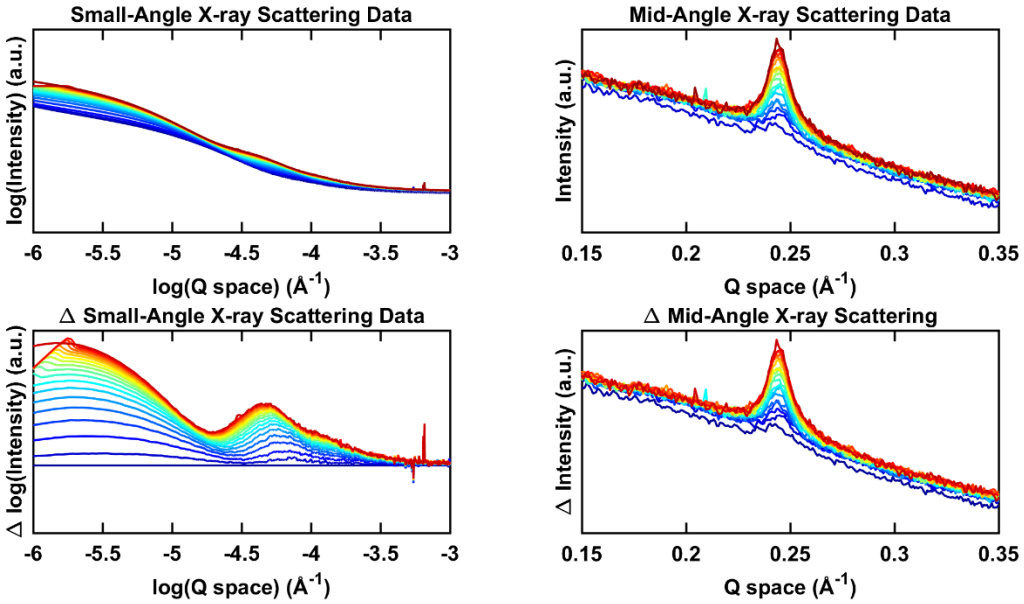

Figure 4.31. Growth Experiment [Monomer] = 0.48 mM.

***In Situ* X-Ray Scattering on Other Systems**

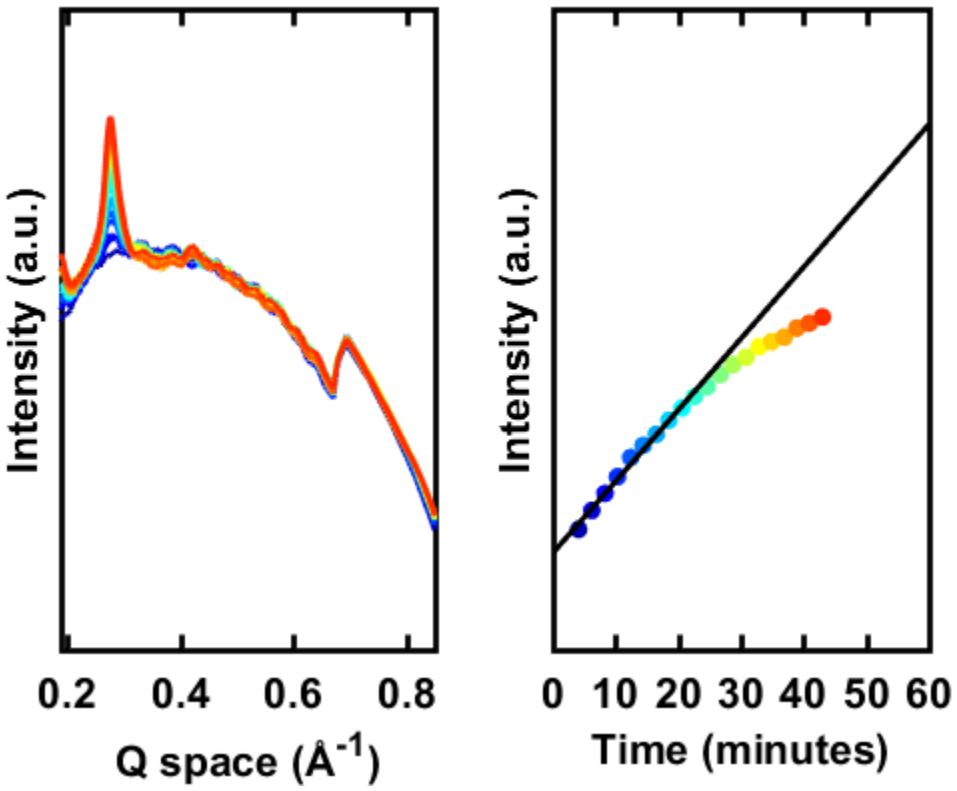

Figure 4.32. Nucleation Experiment on DPB-COF [4mM]. DPB-COF is Formed from the Condensation of 4,4'-Diphenylbutadiynebis(boronic acid) and 2,3,6,7,10,11-Hexahydroxytriphenylene.

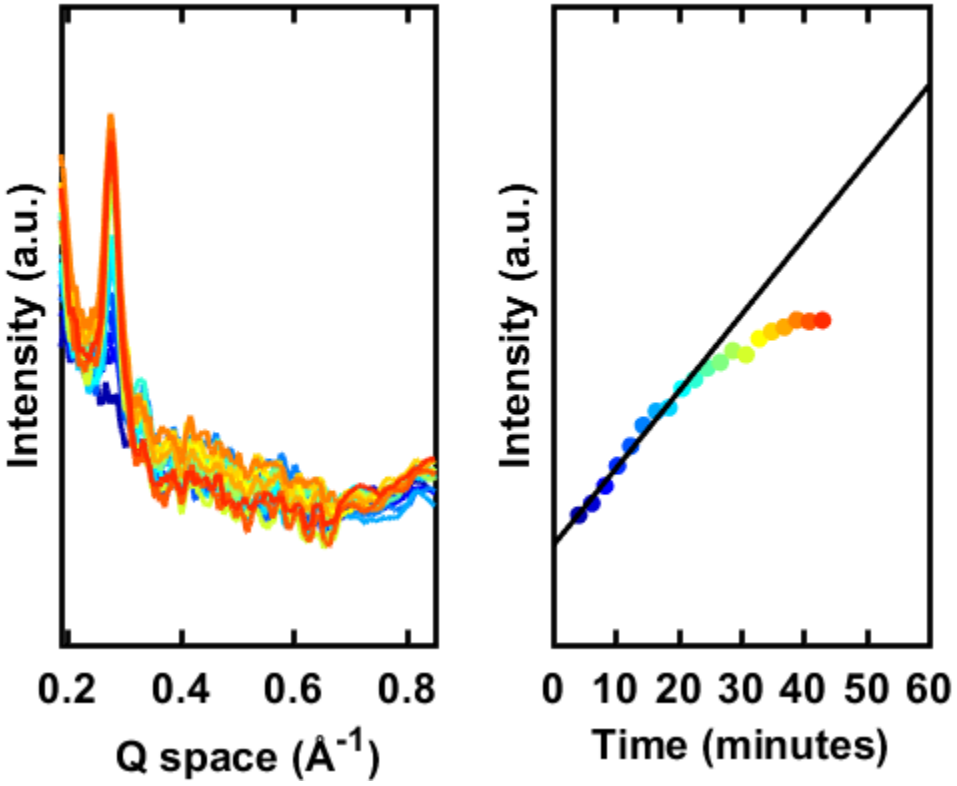

Figure 4.33. Nucleation Experiment on DPB-COF [2mM].

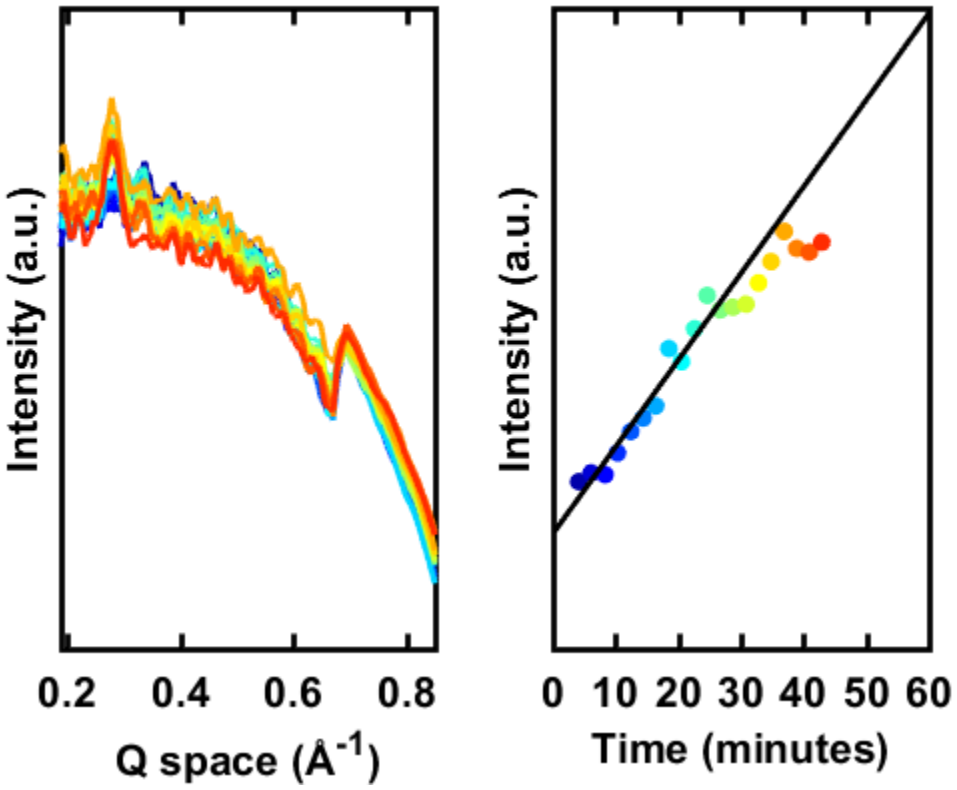

Figure 4.34. Nucleation Experiment on DPB-COF [1mM].

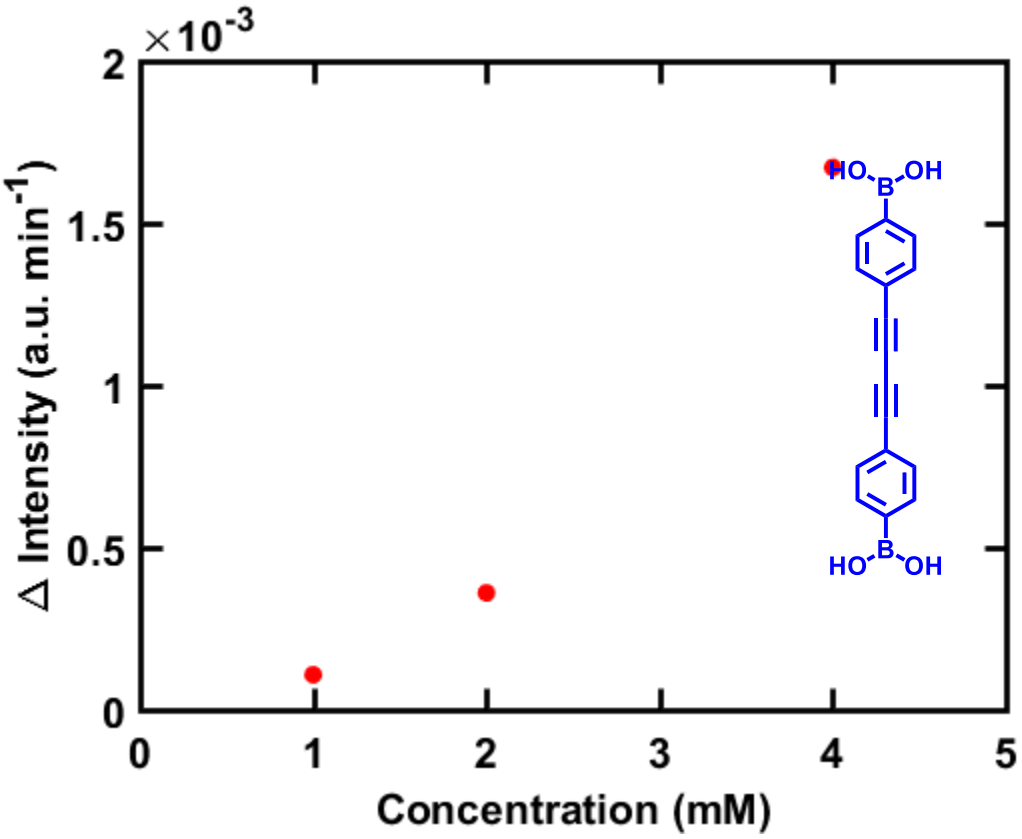

Figure 4.35. Rate of Intensity of the <100> Bragg Feature as a Function of Initial Monomer Concentration for DPB-COF. DPB-COF is Formed from the Condensation of 4,4'-Diphenylbutadiynebis(boronic acid) (inset) and 2,3,6,7,10,11-Hexahydroxytriphenylene.

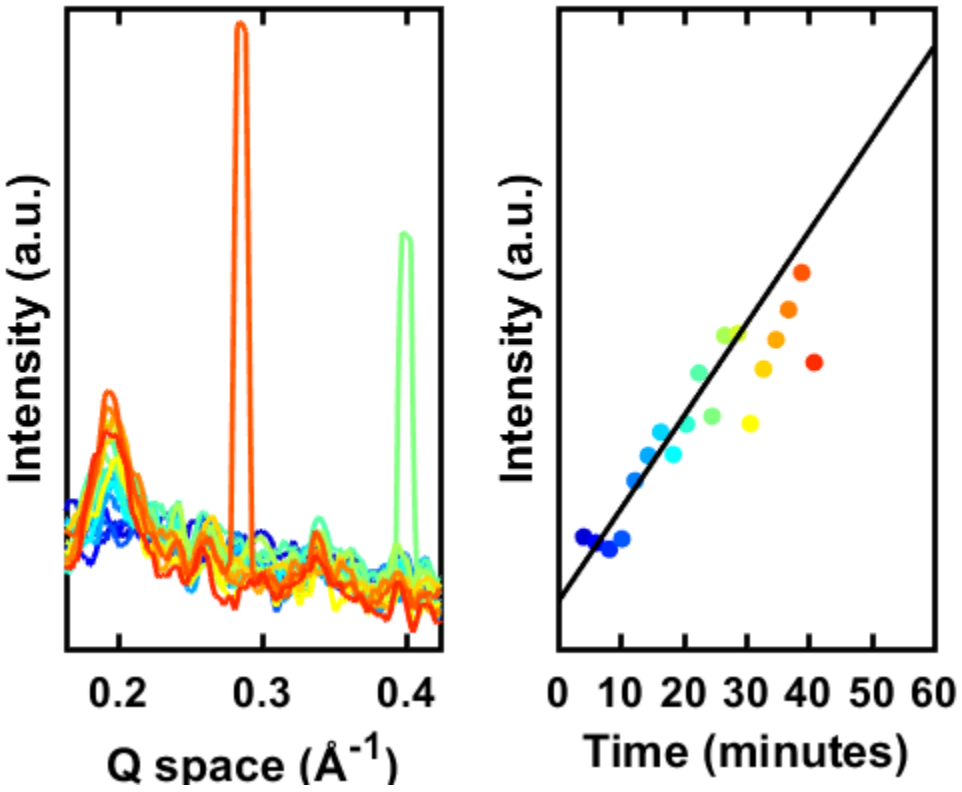

Figure 4.36. Nucleation Experiment on TP-COF [4mM]. TP-COF is Formed from the Condensation of 2,7-Pyrenebis(boronic acid) and 2,3,6,7,10,11-Hexahydroxytriphenylene.

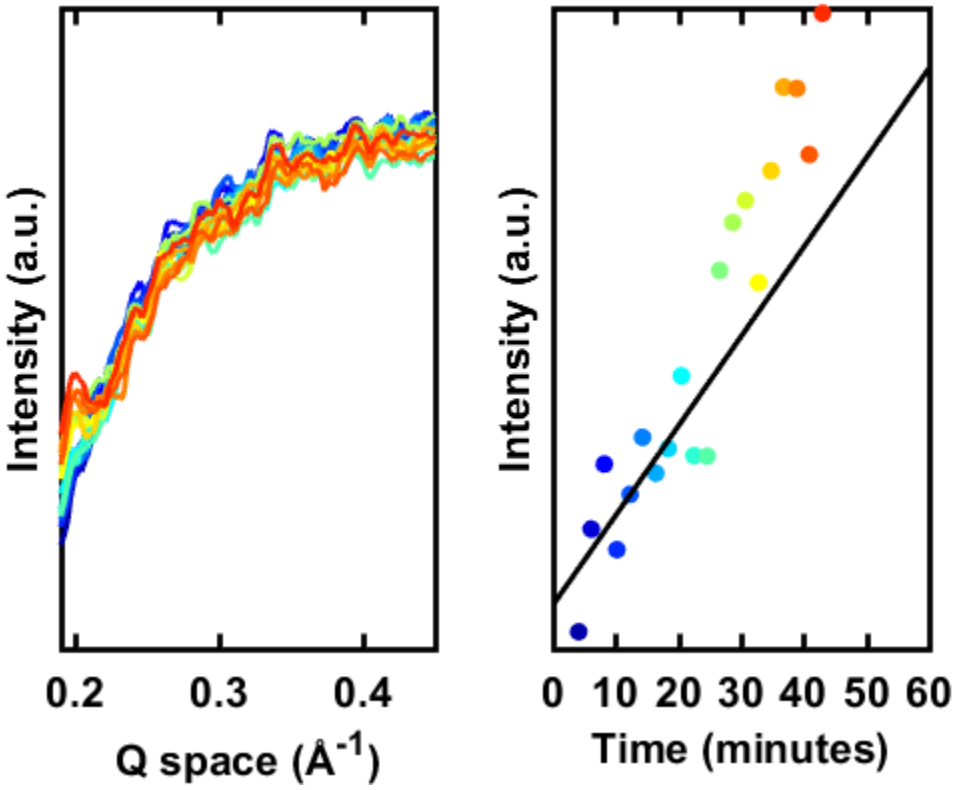

Figure 4.37. Nucleation Experiment on TP-COF [2mM].

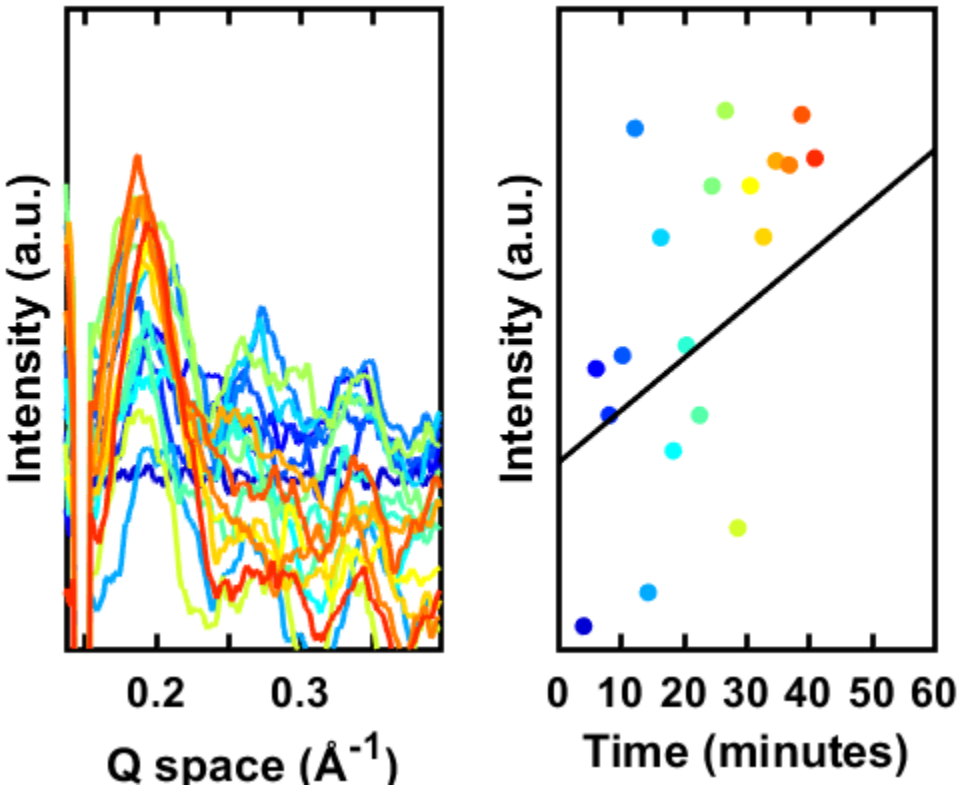

Figure 4.38. Nucleation Experiment on TP-COF [1mM].

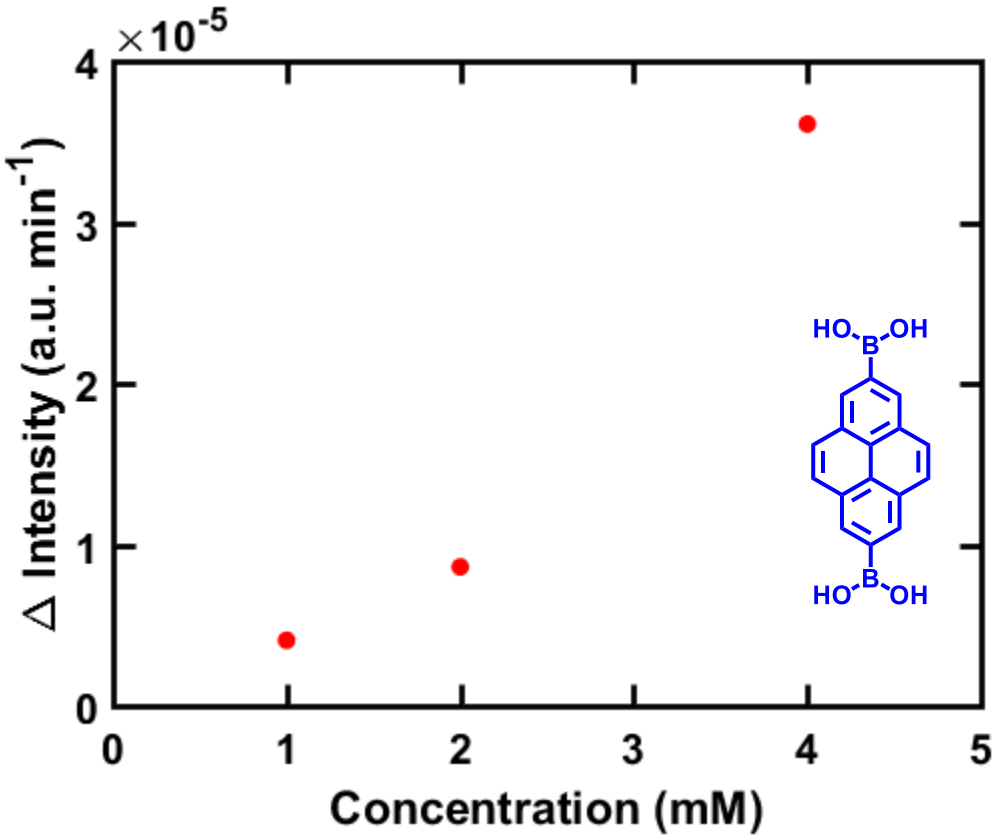

Figure 4.39. Rate of Intensity of the <100> Bragg Feature as a Function of Initial Monomer Concentration for TP-COF. TP-COF is Formed from the Condensation of 2,7-Pyrenebis(boronic acid) (inset) and 2,3,6,7,10,11-Hexahydroxytriphenylene.

Simulated X-ray Diffraction Models

COF powders were collected by centrifugation of colloidal suspensions and were rinsed with blank solvent mixture to remove unreacted starting materials. Powder X-ray diffraction (PXRD) patterns were obtained at room temperature on a STOE-STADI P powder diffractometer equipped with an asymmetric curved Germanium monochromator. (Cu-Kα radiation, λ = 1.54056 Å) and one-dimensional silicon strip detector (MYTHEN2 1K from DECTRIS). The line-focused Cu X-ray tube was operated at 40 kV and 40 mA. The as-obtained powder samples were sandwiched between two acetate foils (polymer sample with neither Bragg reflections nor broad peaks above 10° 2θ) mounted in flat plates with a disc opening diameter of 8 mm and measured in transmission geometry in a rotating holder. The patterns were recorded in the 2θ range of 0-36° for an overall exposure time of 25 min. The instrument was calibrated against a NIST Silicon standard (640d) prior to the measurement.

Crystal modeling of the COF structures was carried out using the Materials Studio (ver. 5.0) suite of programs by Accelrys. The initial structures were constructed piecewise starting with a primitive hexagonal unit cell with space group P6. The *a* cell parameter was estimated according to the distance between the center of the vertices for each COF, and the *c* parameter was arbitrarily chosen as 3.35 Å. The structures were optimized using the Geometry Optimization routine including energy minimization with cell parameters optimization, using the parameters from the Universal Force Field. Calculation of the simulated powder diffraction patterns and Pawley refinements were performed with the Materials Studio Reflex Plus Module using a Bragg-Brentano geometry. The observed diffraction patterns were subjected to a polynomial background subtraction and then to Pawley refinement wherein peak profiles were refined using the Pseudo-

Voigt peak shape function and asymmetry was corrected using the Berar-Baldinozzi function. Crystallite size was then estimated by the LeBail method which was Pawley refined to the experimental data.

The Pawley refined structure was then partially offset and a simulated pattern of this structure was also generated. These simulated patterns strongly suggest that the COF-5 synthesized structure is entirely eclipsed.

CIF Files of the Pawley refined structure are included as supplemental attachments.

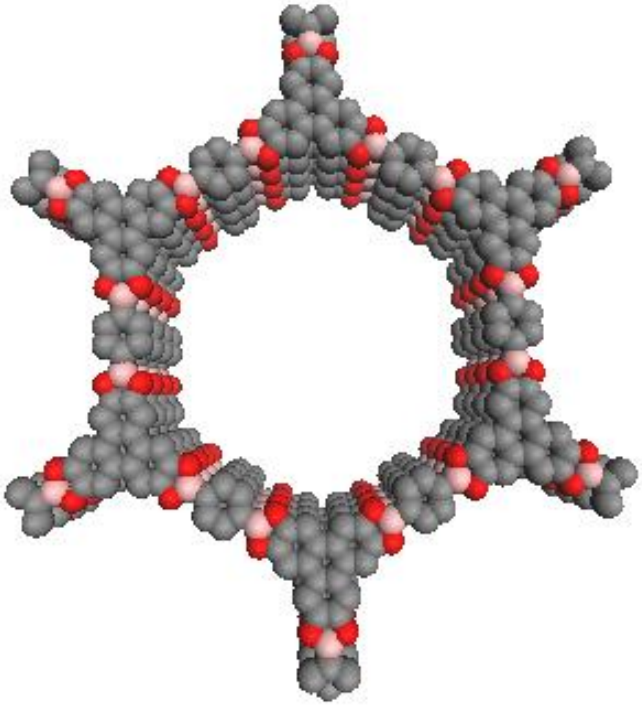

Figure 4.40. Eclipsed COF-5 Structure.

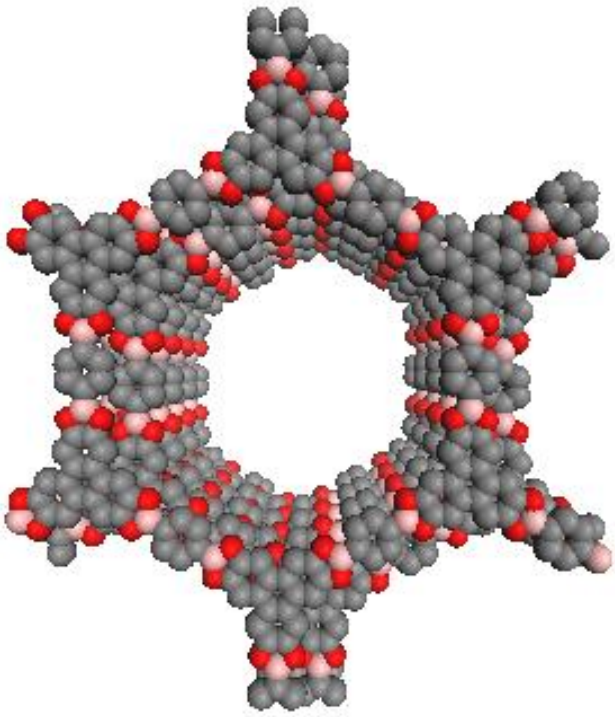

Figure 4.41. Offset COF-5 Structure.

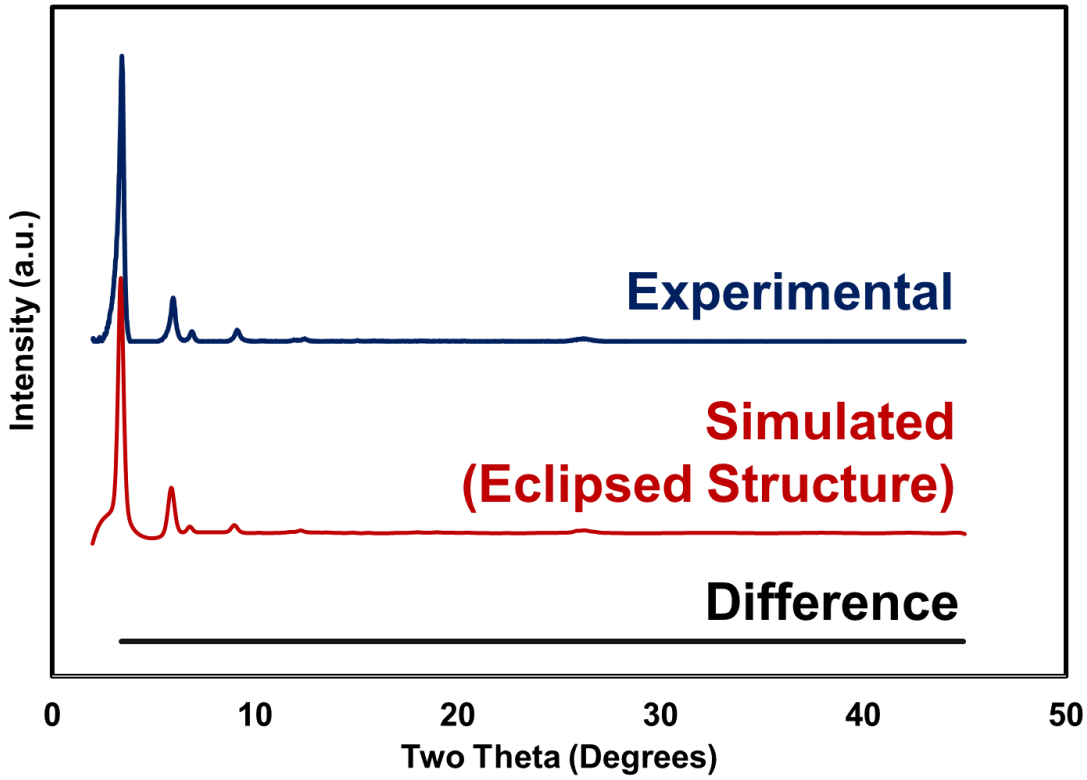

Figure 4.42. Comparison of the Experimental X-Ray Diffraction Patterns of COF-5 and Their Simulation Based on an Entirely Eclipsed Structure. The Simulated Data Include a LeBail Parameterization in the Pawley Refinement for Finite Grain Size Effects, Leading to Broadening of the Diffraction Features.

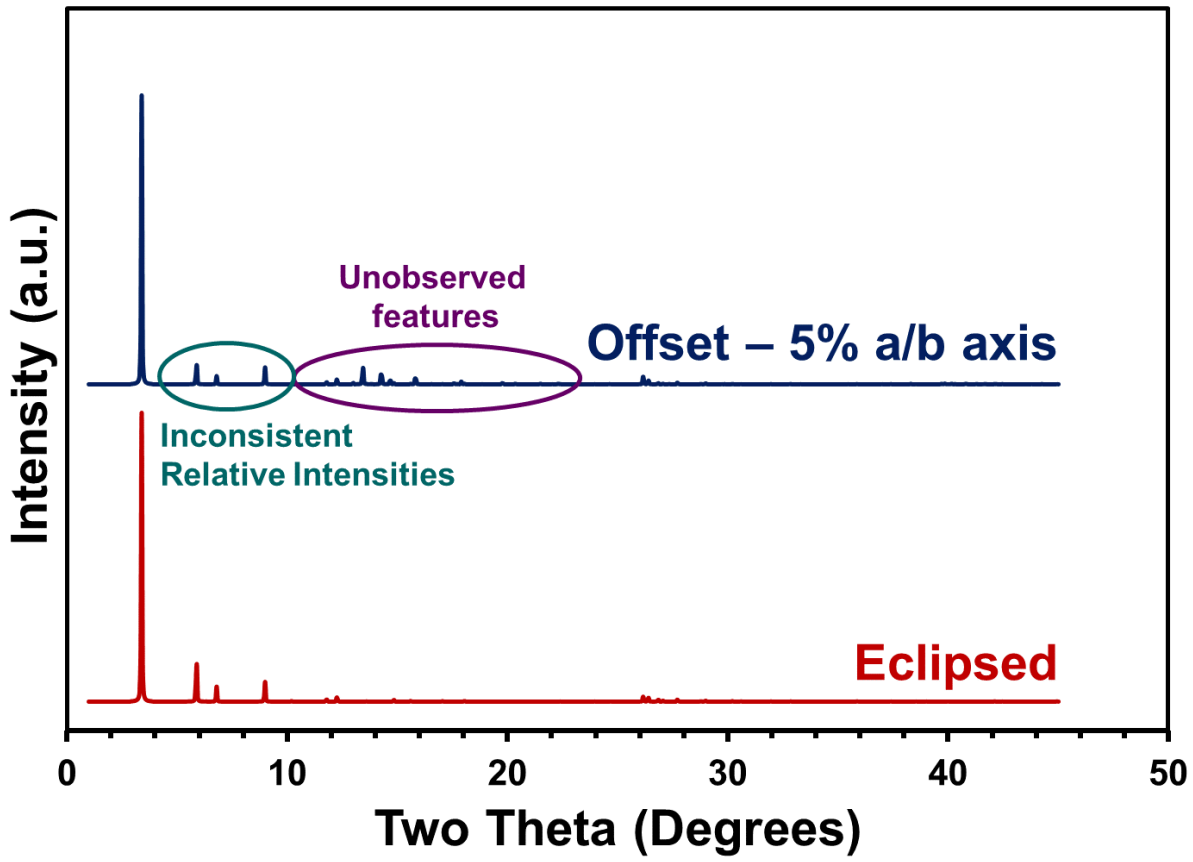

Figure 4.43. Comparison of the Simulated COF-5 X-Ray Diffraction Patterns Based on Eclipsed and Partially Offset Structures. Here, Infinite Grain Sizes Are Assumed. Green and Purple Circles Highlight the Peaks in the Partially Offset Structures That Are Inconsistent with the Experimental Data in Figure S37.

Derivation of Eqs. (4)-(8)

The monomer consumption rate from nucleation is the product of the nucleation rate and the nucleus size:

$$\omega_{monomer,nuc} = \mathrm{N_{nuc}} J_{nuc} \tag{S1}$$

where $\mathrm{N_{nuc}}$ is the nucleus size (in number of HHTP units).

We substitute Eq. (1) in the main text into Eq. (S1):

$$\omega_{monomer,nuc} = \mathrm{N_{nuc}} k_{nucleation} C_{monomer}^2 \tag{S2}$$

Therefore, we have:

$$\omega_{monomer,nuc} \propto C_{monomer}^2 \tag{S3}$$

Eq. (S3) is Eq. (4) in the main text.

For simplicity, we assume that 2D COFs have a cylindrical shape with a fixed diameter to height ratio α (=d/h) during growth. The volume of a crystal (V) is expressed as:

$$V = \frac{\pi d^2 h}{4} = \frac{\pi d^3}{4\alpha} \tag{S4}$$

The volume change of a crystal is:

$$\frac{dV}{dt} = \frac{dV}{dd}\frac{dd}{dt} \tag{S5}$$

Since dd/dt is in-plane growth rate, we have:

$$\frac{dV}{dt} = \frac{3\pi d^2 k_{growth,in-plane} C_{monomer}}{4\alpha} \tag{S6}$$

The total volume change of all crystals equals:

$$\frac{dV_{tot}}{dt} = \frac{3\pi d^2 k_{growth,in-plane} C_{monomer}}{4\alpha} C_{nuc,0} Vol \mathrm{N_A} \tag{S7}$$

where *Vol* is the volume of the solution and N_A is the Avogadro number. The total monomer number consumption is approximated to be proportional to the total volume change:

$$\omega_{monomer,growth} = \frac{dV_{tot}}{dt}\beta / \mathrm{N_A} / Vol \tag{S8}$$

where β (in nm^{-3}) is the number of monomer (HHTP) units per unit volume in the crystal.

Substituting Eq. (S7) into (S8), we have:

$$\omega_{monomer,growth} = \frac{3\pi d^2 k_{growth,in-plane} C_{nuc,0} \beta C_{monomer}}{4\alpha} \tag{S9}$$

Therefore, we have:

$$\omega_{monomer,growth} \propto d^2 C_{monomer} \tag{S10}$$

Eq. (S10) is Eq. (5) in the main text.

The total monomer consumption from nucleation and growth can be obtained by summing Eqs. (S2) and (S9)

$$\omega_{consump} = \frac{3\pi d^2 k_{growth,in-plane} C_{monomer}}{4\alpha} C_{nuc,0}\beta + \mathrm{N_{nuc}} k_{nucleation} C_{monomer}^2 \tag{S11}$$

Since:

$$d = k_{growth,in-plane} C_{monomer} t + d_0 \tag{S12}$$

We have:

$$\omega_{consump} = \frac{3\pi k_{growth,in-plane} \beta C_{nuc,0} C_{monomer}}{4\alpha} \left(k_{growth,in-plane} C_{monomer} t + d_0\right)^2 + \mathrm{N_{nuc}} k_{nucleation} C_{monomer}^2 \tag{S13}$$

Eq. (S13) is Eq. (7) in the main text.

At a constant monomer concentration, the time for in-plane growth by *l* is:

$$t_{growth} = \frac{l}{v_{in-plane}} = \frac{l}{k_{growth,in-plane} C_{monomer}} \tag{S14}$$

The time for the production of new nuclei of concentration of $\gamma C_{nuc,0}$ is:

$$t_{nuc=} \frac{\gamma C_{nuc,0}}{J_{nuc}} = \frac{\gamma C_{nuc,0}}{k_{nucleation} C_{monomer}^2} \tag{S15}$$

Let t_{growth}=t_{nuc}, we have:

$$C_{monomer} = \frac{\gamma C_{nuc,0} k_{growth,in-plane}}{l k_{nucleation}} \tag{S16}$$

By definition, C^*=$C_{monomer}$. Therefore, we have:

$$C^* = \frac{\gamma C_{nuc,0} k_{growth,in-plane}}{l k_{nucleation}} \tag{S17}$$

Eq. (S17) is Eq. (6) in the main text.

Substituing Eq. (S17) into Eq. (S14), we have:

$$t_{growth} = \frac{l}{k_{growth,in-plane} \frac{\gamma C_{nuc,0} k_{growth,in-plane}}{l k_{nucleation}}} = \frac{k_{nucleation} l^2}{k_{growth,in-plane} \gamma C_{nuc,0} k_{growth,in-plane}} \tag{S18}$$

Since τ=t_{growth}, we have:

$$\tau = \frac{k_{nucleation} l^2}{k_{growth,in-plane\,growth}^2 \gamma C_{nuc,0}} \tag{S19}$$

Eq. (S19) is Eq. (8) in the main text.

Chapter 5 : Thermal Buckling of Two-Dimensional Covalent Organic Frameworks

5.1 Abstract

Two-dimensional covalent organic frameworks (2D COFs) are periodic, permanently porous, and lightweight solids that are polymerized from topologically designed monomers. The predictable design and structural modularity of these materials make them promising candidates for applications including catalysis, environmental remediation, chemical separations, and organic electronics, many of which will require stability to mechanical and thermal stress. Based on their reinforced structures and high degradation temperatures as determined by thermal gravimetric analysis (TGA), many reports have claimed that COFs have excellent thermal stability. However, their stability to heat and pressure has not been probed using methods that report on structural changes rather than the loss of volatile compounds. Here we explore two structurally analogous 2D COFs with different polymerization chemistries using in operando X-ray diffraction, which demonstrates the loss of crystallinity at lower temperatures than the degradation temperatures measured by TGA. Density functional theory calculations suggest that an asymmetric buckling of the COF lattice is responsible for the observed loss of crystallinity. In addition to their thermal stability, x-ray diffraction of the 2D COFs under gas pressures up to 100 bar showed no loss in crystallinity or structural changes, indicating that these materials are robust to mechanical stress by applied pressure. We expect that these results will encourage further exploration of COF

stability as a function of framework design and isolated form, which will guide the design of frameworks that withstand demanding application-relevant conditions.

5.2 Thermal Stability of Two-dimensional Polymers

New classes of structurally regular, porous materials are approaching a level of maturity where they are being considered for industrial use.[533] Covalent organic frameworks (COFs) are an emerging class of highly stable, crystalline, permanently porous macromolecules.[534, 535] These properties make them attractive candidates for applications such as electrochemical energy storage,[536, 537] catalysis,[424, 538, 539] gas storage and separations,[540, 541] optoelectronics,[542, 543] and chemical sensing.[444] The realization of these applications will often require stability of the nanoscale COF structure to thermal and mechanical stresses. The high thermal stability of COFs has been inferred from thermogravimetric analysis (TGA), which indicates no loss of volatile products to temperatures as high as 800 °C.[41] Therefore, TGA indicating high thermal stability has fueled the hypothesis that COFs might be ideal candidates for applications such as chemical separations and catalysis, which require demanding thermal and mechanical stability.[544, 545] However, the thermal and pressure-induced degradation of the COF crystalline structure has not been studied. Because many emergent properties of COFs arise from their atomically precise structures; it is essential to investigate how thermal and mechanical stress affects their crystallinity and porosity. Here we perform the first structural deformation study of structurally similar but chemically distinct two-dimensional (2D) COFs by *in operando* synchrotron x-ray diffraction (XRD). During this study, we found that a crystalline-to-amorphous transition occurs at temperatures lower than degradation temperatures determined by TGA. Furthermore, a lattice contraction was observed for the COF systems as they were heated. The magnitudes of these in-

plane contractions were among the highest values observed for porous, crystalline systems.[546] Density functional theory (DFT) calculations support that the lattice contraction could be attributed to buckling of the 2D COF lattice. In addition to the thermal stability, we also explored the stability of these COFs to high-pressure gasses using *in operando* XRD. We found that the COF structure s unaffected by gas pressures up to 100 bar, which supports their promise as useful materials for gas storage and separations. [540, 541, 547]

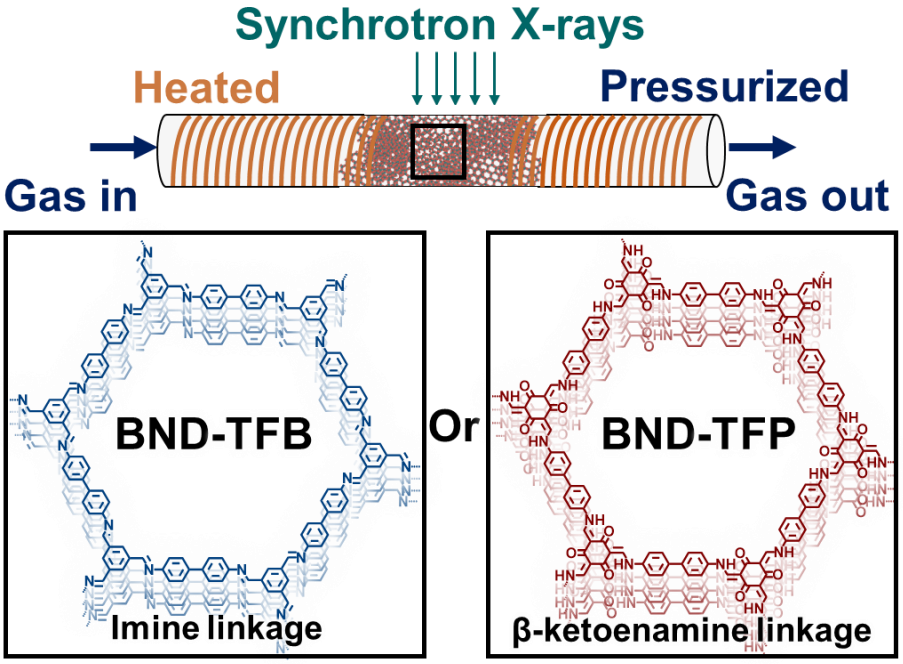

Figure 5.1 Schematic figure of measurement and COF structures studies. The two COFs measured by *in operando* x-ray diffraction are isostructural. BND-TFB is an imine-linked framework and BND-TFP is a β-ketoenamine-linked framework.

5.3. Results and Discussions

An imine-linked 2D COF (BND-TFB COF) was prepared through the transimination of 1,3,5-triformylbenzene and *N*-benzidine benzophenone imine, an approach that was recently shown to provide high-quality COF materials.[411] A chemically distinct but structurally similar 2D COF (BND-TFP), featuring the same benzidine groups linked by β-ketoenamines, was prepared through a monomer exchange reaction between BND-TFB and 2,4,6-triformylphloroglucinol (TFP). This monomer exchange process provides β-ketoenamine-linked COFs with superior crystallinity and BET surface areas than those prepared from the direct condensation of diamines and TFP.[548] Brunauer-Emmett-Teller (BET) surface area analysis, Fourier-transform infrared spectroscopy (FTIR), XRD, and solid-state ^{13}C NMR confirmed the formation of each COF (see Supplementary Information). Based on their BET surface areas (>2000 $m^2 g^{-1}$) and broadening of the XRD features due to finite grain size effects (see Supplementary Information), we were able to assign that the BND-TFB and BND-TFP COFs were of similar high quality.[548, 549]

5.4. Variable-temperature X-ray Diffraction

The thermal stability of each 2D COF was probed using variable-temperature XRD measurements performed at Sector 17 of the Advanced Photon Source (APS) at Argonne National Laboratory (ANL) (**Figure 5.1**). Under a constant flow of helium, powder samples of the BND-TFB and BND-TFP COFs were heated at a rate of 5 °C min^{-1}. XRD patterns of the microcrystalline powders were recorded continuously on a 2D Pilatus detector and were radially integrated to produce 1D patterns. It was noted that at a threshold temperature the <100> Bragg feature of the COF materials dropped

in intensity. We define a degradation temperature (T_{XRD}) at which the integrated 100 Bragg feature decreased below 80% of its original intensity. This temperature was then compared to the TGA degradation temperature (T_{TGA}) which was assigned at the local minimum of the first derivative of the mass with respect to temperature. [550]

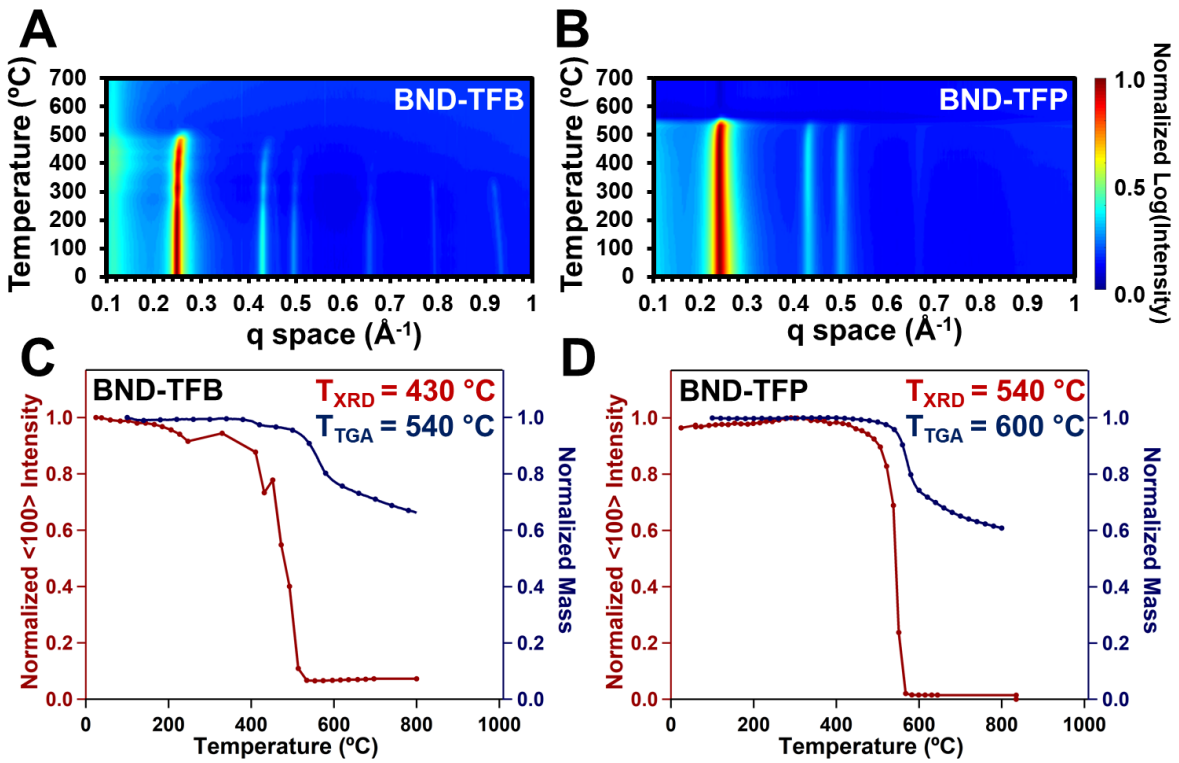

Figure 5.2. Thermal behavior of COF materials. XRD intensity heat maps over the course of a thermal ramp for **A)** BND-TFB and **B)** BND-TFP. Plots of the integrated 100 Bragg intensity compared to the TGA mass loss over the course of a thermal ramp for **C)** BND-TFB and **D)** BND-TFP.

5.5. Two-stage Thermal Degradation

The imine-linked COF, BND-TFB, underwent a gradual degradation with a T_{XRD} of approximately 430 °C (**Figure 5.2C**), after which the residual diffraction signal quickly and irreversibly dissipated (**Figure 5.2A**). The attenuation of the diffraction signal indicates the layered hexagonal structure of the COF degrades at this temperature. However, TGA showed that the primary mass loss event occurred at approximately 540 °C (**Figure 5.2C**), 110 °C higher than T_{XRD}. For the structurally analogous β-ketoenamine-linked COF, BND-TFP, the <100> intensity increased, and the peak shape sharpened until approximately 300 °C. We attribute this phenomenon to the liberation of volatile species, likely trace residual solvent molecules, intercalated into the COF network, whose removal decreased the overall network disorder and increased the electron density contrast of the vacant COF pores and the COF structure. After this minor initial increase in intensity, the COF structure underwent a sharp degradation at a T_{XRD} of 540 °C (**Figure 5.2C**). In contrast, the BND-TFP COF underwent a significant mass loss event at a T_{TGA} of 600 °C. The observation of two degradation temperatures, one related to the loss of crystallinity and the other related to the loss of mass, indicates that the COF forms an amorphous phase that subsequently degrades to volatile small molecules at higher temperatures. In this study, the temperature differential between T_{XRD} and T_{TGA} was found to be greater than 50 °C for both COFs. However, it is possible that other COFs may exhibit either larger or smaller differences between T_{TGA} and T_{XRD} as a function of other linkage chemistries, topologies, or monomer structures.

The β-ketoenamine-linked BND-TFP COF is considerably more stable than the structurally analogous imine-linked BND-TFB COF as judged by the 100 °C increase in both its T_{TGA} and T_{XRD}. Because BND-TFP and BND-TFB share the same structural morphology (*P6* tiled

hexagons), pore size (29 Å pore diameter), and approximate crystallite size (100 nm), this stability difference can be largely attributed to their different linkage chemistries. β-ketoenamine-linked COFs are also notably more hydrolytically stable than their imine-linked counterparts, although it is unclear if their increased thermal stability arises from the same phenomenon.[551, 552]

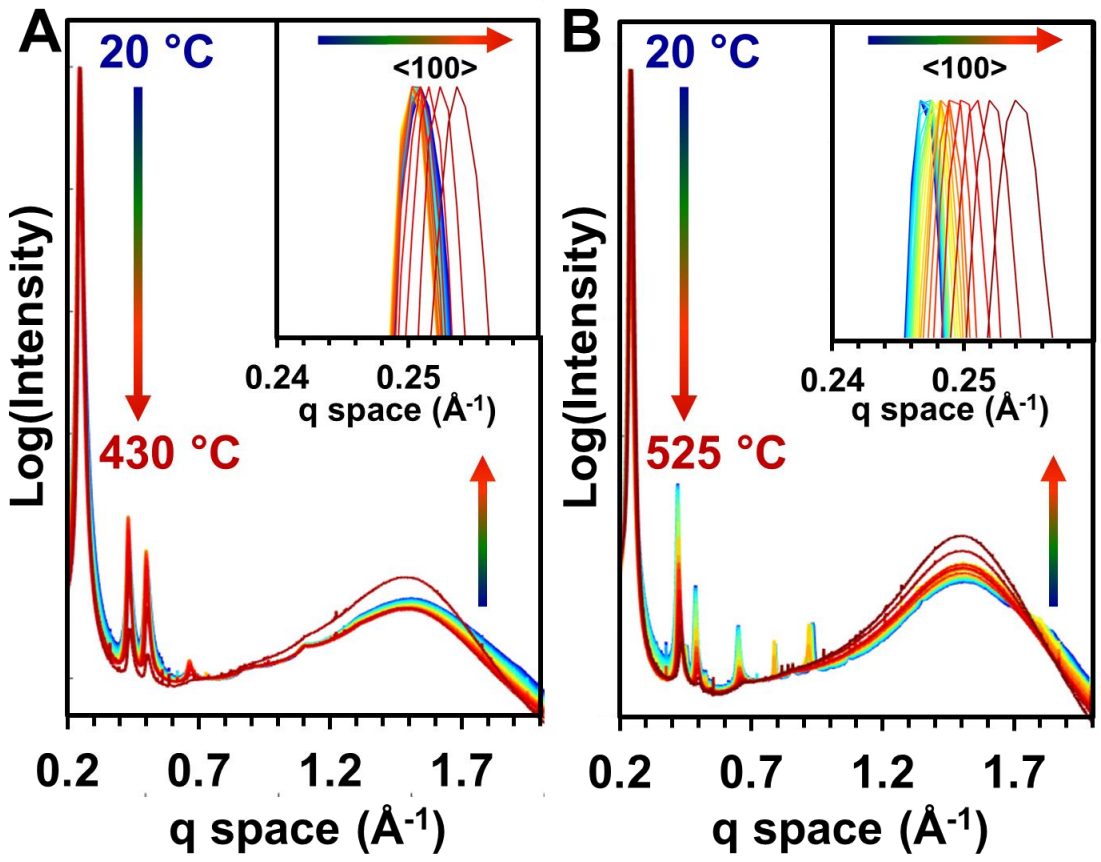

Figure 5.3 X-ray line plots over the course of thermal profile. Normalized x-ray intensities over the course of thermal heating demonstrating the change in relative peak intensities over the course of the heated experiment for **A)** BND-TFB and **B)** BND-TFP. Insets show the position of the 100 Bragg reflection (normalized intensities) over the course of the same thermal profile.

In examining the response of the crystalline network over the thermal ramp, we noted that the relative intensities and peak locations of the COF diffraction features were not constant, which provides insight into the mechanism of the crystalline-to-amorphous transition. In **Figure 5.3A**, the in-plane diffraction features (<100>, <110>, <200>, <210>) decrease in intensity when compared to the interlayer features (<001>, <111>). This decrease indicates a loss of in-plane crystallinity, even as the layered structure of the material is retained. During heating, the BND-TFB <100> Bragg diffraction feature trended to shorter real space distance, which is indicative of a lattice contraction. Analysis of the BND-TFP COF revealed a similar behavior, in which the in-plane features decreased relative to the out-of-plane features and the lattice contracted upon heating. Lattice contractions for metal-organic frameworks (MOFs) and zeolites have been attributed to the unusual physiochemical process of negative thermal expansion (NTE).[546, 553] However, the degree of in-plane lattice contractions of these 2D COFs, 5% and 9% for BND-TFB and BND-TFP, respectively, were among the highest lattice contraction values reported for porous materials.

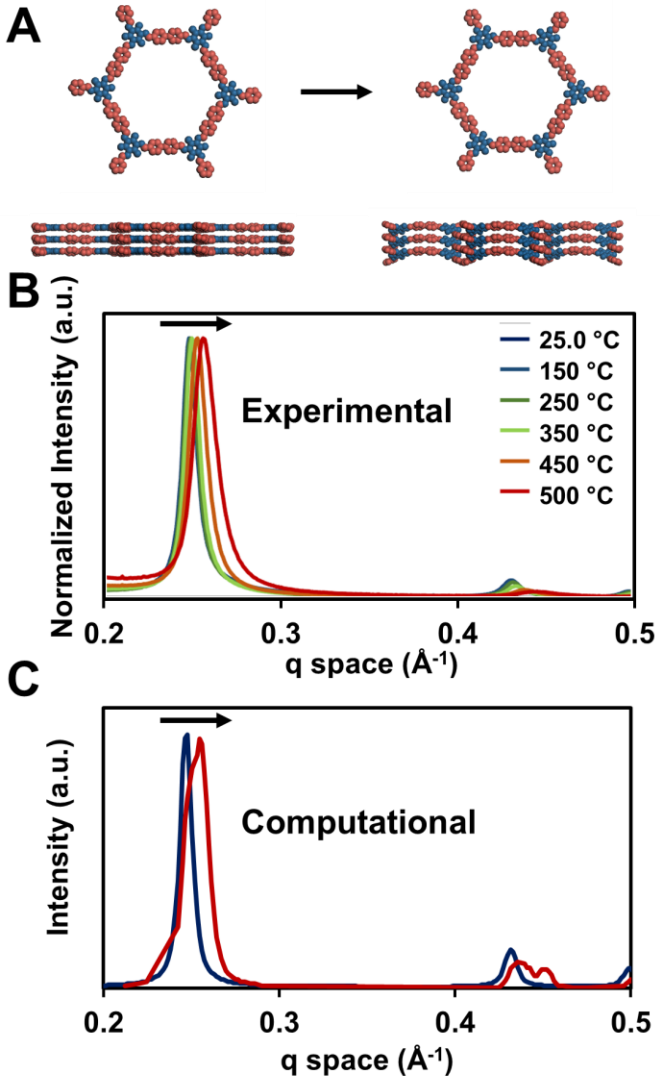

Figure 5.4. Proposed Buckling of BND-TFP. A) Initial BND-TFP structure transforming to the buckled phase under compressive strain. **B)** Experimental change in diffraction peak location over the course of a thermal ramp. **C)** Computational changes in diffraction peak.

5.6. Computational evidence for thermally induced buckling

DFT calculations, using the PBE-D3 functional, provide insight into the thermal contraction of these materials by examining the framework structure upon compression. The computational results confirmed the framework stiffens upon compression with the bulk modulus increasing as a function of pressure (**Figure 5.20**). This effect is commonly associated with materials that have positive thermal expansion and soften and expand as a function of temperature. The results also showed phonon softening upon lattice compression, possibly due to a soft mode linked to a change in the phase of the 2D layers. The geometry of the structure was relaxed to a volumetrically contracted phase, which agreed with the dynamic position of the <100> diffraction corresponding to buckling of the 2D planar layers. The buckled phase of BND-TFP is shown in Figure 4, along with the expected shift in the XRD pattern (**Figure 5.4C**). The asymmetry of the peaks in the buckled phase arises from the reduction in the symmetry of the COF as the *a* and *b* lattice parameters are no longer equivalent. This analysis is consistent with the structure undergoing a thermally-induced phase transition to a volumetrically contracted geometry and not, softening as a function of compression like materials described as possessing NTE.

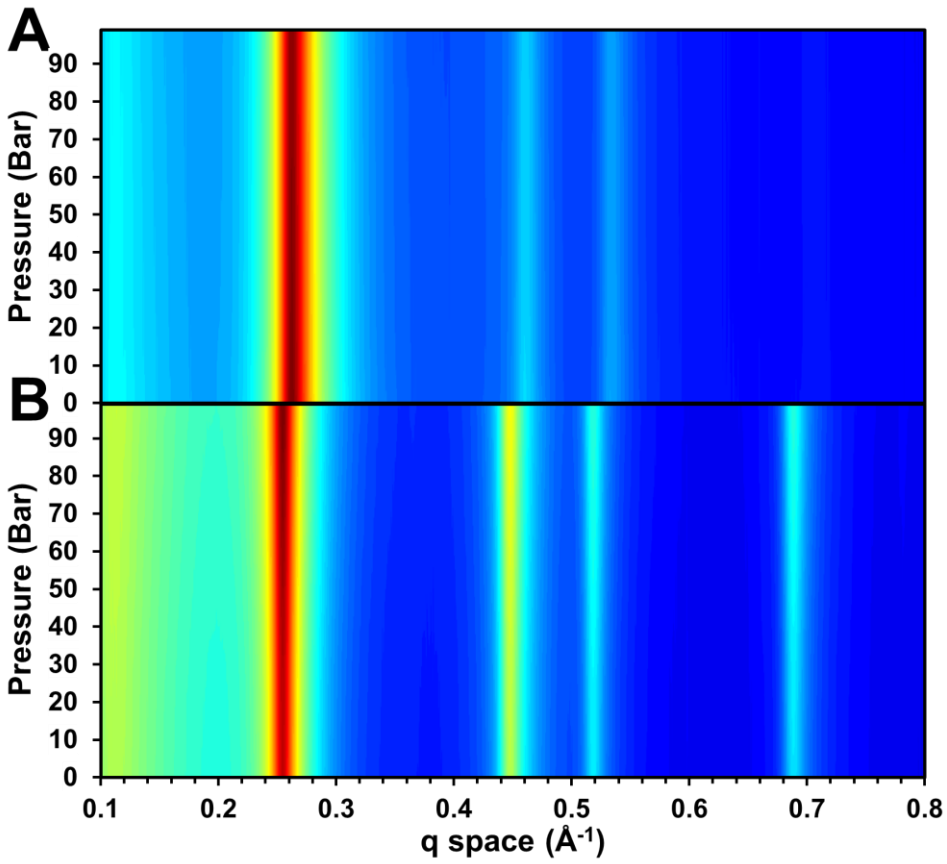

Figure 5.5. Pressure behavior of BND-TFB and BND-TFP. XRD intensity heat maps over the course of a pressure ramp under a He atmosphere for **A)** BND-TFB and **B)** BND-TFP.

In contrast to the structural changes observed at elevated temperatures, both COFs showed exceptional stability to mechanical stress introduced from high-pressure gasses. *In operando* mechanical stresses are frequently applied to porous materials either under the weight of the supports packed into a column or by the high pressures of gasses used in industrial processes.[554, 555] Capillaries filled with BND-TFB and BND-TFP COF powder were pressurized to 100 bar under a He atmosphere. No structural changes were observed in the XRD patterns of either COF up to 100 bar, at which point the capillary failed (**Figure 5.5**). These results demonstrate the robust

mechanical stability of COFs under high gas pressures, and so augments previous studies of COF powders under mechanical pressures.[9-10] Moreover, this indicates the stability of these 2D COFs is seemingly congruent with the pressure regimes required by the chemical industry.

5.7. Conclusions

COFs are an emerging class of permanently porous, synthetically modular, crystalline materials that have potential applications ranging from catalytic supports to energy storage materials. Much of the promise of these materials hinges on their ability to maintain their crystalline structure under operating conditions, which includes thermal and mechanical stresses. In this study, we have shown that COFs maintain their crystalline morphology under *in operando* conditions including temperatures of up to 500 °C and pressures of up to 100 bar. However, the thermal stability is lower than originally assumed by TGA measurements, which we have shown may be attributed to buckling of the 2D COF layers. We anticipate that these studies will inform and guide COF design for future applications, such as chemical separations and catalysis, that require highly stable, porous materials.

5.8. Chapter 5 Supplementary Information

Materials and Methods

Materials

Dry dichloromethane (DCM) was obtained by passing previously degassed solvents through activated alumina columns. All other reagents were purchased from commercial sources and used without further purification or prepared from them. Reactions were monitored by thin layer chromatography (TLC) carried out on EMD 250μm silica gel 60-F254 plates. Visualization was performed by UV light irradiation and potassium permanganate stain and heat.

Instrumentation

Nuclear Magnetic Resonance. ^{1}H and ^{13}C NMR spectra were acquired on Bruker AvanceIII-500 MHz equipped with a DHC CryoProbe and recorded at 25 °C. The spectra were calibrated using residual solvent as internal reference ($CDCl_3$: 7.26 ppm for ^{1}H NMR, 77.00 for ^{13}C NMR). Solid state ^{13}C CP/MAS NMR spectra of covalent organic frameworks were recorded on a Varian 400 MHz at a spin rate of 10,000 Hz and calibrated using adamantane as an external standard.

Infrared Spectroscopy. Infrared spectra were recorded on a Nicolet iS10 FT-IR spectrometer equipped with a diamond ATR attachment and are uncorrected.

High-Resolution Mass Spectrometry. High-resolution mass spectra were acquired on Agilent 6210A LC-TOF Mass Spectrometer, with Atmospheric Pressure Photoionization (APPI) as an ionization source. The instrument is equipped with an Agilent Series 1200 HPLC binary pump, and Autosampler, using Mass Hunter software. The samples were run using direct injection.

Microwave Reactor. Microwave reactions were performed on a CEM Discover SP unit, operating at 110 V, with microwave irradiation of 2.45 GHz, and a maximum microwave output of 300 W in 10 mL capacity Teflon-capped tubes. All reactions were performed using the "standard" method, where only the temperature point and run times were controlled.

Gas Adsorption. Gas adsorption isotherms were conducted on a Micromeritics ASAP 2420 Accelerated Surface Area and Porosity Analyzer. Typically, 20-50 mg samples were transferred to dried and tared analysis tubes equipped with filler rods and capped with a Transeal. The samples were heated to 40 °C at a rate of 1 °C/min and evacuated at 40 °C for 20 min, then heated to 100 °C at a rate of 1 °C/min heat, and evacuated at 100 °C until the outgas rate was ≤0.3 μmHg/min (holding the samples at 100 °C for 5 hours was sufficient), at which point the tube was weighed again to determine the mass of the activated sample. The tube was then transferred to the analysis port of the instrument. UHP-grade (99.999% purity) N_2 was used for all adsorption measurements. N_2 isotherms were generated by incremental exposure to nitrogen up to 760 mmHg (1 atm) in a liquid nitrogen (77 K) bath. Oil-free vacuum pumps and oil-free pressure regulators were used for

all measurements. Brunauer-Emmett-Teller (BET) surface areas were calculated from the linear region of the N_2 isotherm at 77 K within the pressure range P/P_0 of 0.05–0.10.

***In Operando* X-ray Diffraction Studies.** *In operando* x-ray diffraction was performed at sector 17 of the Advanced Photon Source Argonne National Laboratory. Samples were prepared by packing ~25 mg of COF sample into a thick-walled Kapton capillary and mounted into a sample holder available at the Sector 17. A thermocouple was then mounted in the center of the powder sample, inside of the Kapton capillary. The sample was then placed under a constant stream of helium and heated at a rate of 10 ˚C min^{-1} under a helium atmosphere. X-ray patterns were collected over the course of this heating on a 2D Pilatus detector approximately every minute by collecting ten frames per minute and averaging the counts of these ten frames. These frames were then radially integrated to produce a 1D diffraction patterns which were then analyzed.

Thermogravimetric Analysis. Thermogravimetric analysis (TGA) was performed on a Netzch Simultaneous Thermal Analysis (STA) system using approximately 5 mg of sample. The samples were heated to a designated temperature at a rate of 10 ˚C min^{-1} under a helium atmosphere.

Sonication. Sonication was performed with a Branson 3510 ultrasonic cleaner with a power output of 100W and a frequency of 42 kHz.

Experimental Procedures and Characterization of COF Monomers

Synthesis of Benzophenoneimine of benzidine (BND-Benzophenone).[411] To a 500mL flame-dried round-bottom flask, benzidine (5.10 g, 27.75 mmol, 1.0 equiv), benzophenone (10.11 g, 55.50 mmol, 2.0 equiv), 1,4-diazobicyclo[2.2.2]octane (DABCO) (18.69 g, 166.50 mmol, 6.0 equiv), and chlorobenzene (300 mL) were added and the contents were stirred at room temperature under a nitrogen atmosphere. Titanium (IV) chloride (4.56 mL, 41.64 mmol, 1.5 equiv) was syringed in portions over 15 min (1/4 of the portion at times 0min, 5min, 10min, and 15min). After the addition was complete, the reaction mixture was stirred for another 20 min at room temperature, then the flask was equipped with a reflux condenser, and the reaction stirred at 125 °C overnight (12 h). The reaction mixture was then cooled to about 40 °C and filtered while warm through a Buchner funnel equipped with a filter paper. The filtrate was then concentrated in vacuo. The crude product was purified by stirring in hot absolute ethanol/chloroform mixture (~3:1, ~1200 mL), performing a hot filtration through a cotton-plugged plastic funnel, and allowing the filtrate to slowly cool to room temperature, at which point the product crystallized. The flask was then further cooled in a refrigerator overnight. The solid was then collected and dried to give the product as a yellow/orange solid (8.22 g, 58% yield).

^{1}H NMR (500 MHz, $CDCl_3$) δ 7.76 – 7.70 (m, 4H), 7.47 – 7.41 (m, 2H), 7.38 (dd, *J* = 8.3, 6.7 Hz, 4H), 7.33 – 7.29 (m, 4H), 7.28 – 7.20 (m, 6H), 7.15 – 7.08 (m, 4H), 6.78 – 6.68 (m, 4H).

^{13}C NMR (126 MHz, $CDCl_3$) δ 168.11, 150.02, 139.71, 136.25, 135.39, 130.66, 129.50, 129.30, 128.58, 128.16, 128.02, 127.97, 126.55, 121.45.

Triformylphloroglucinol was prepared according to a reported procedure, and its NMR spectra was consistent with those previously reported.[556]

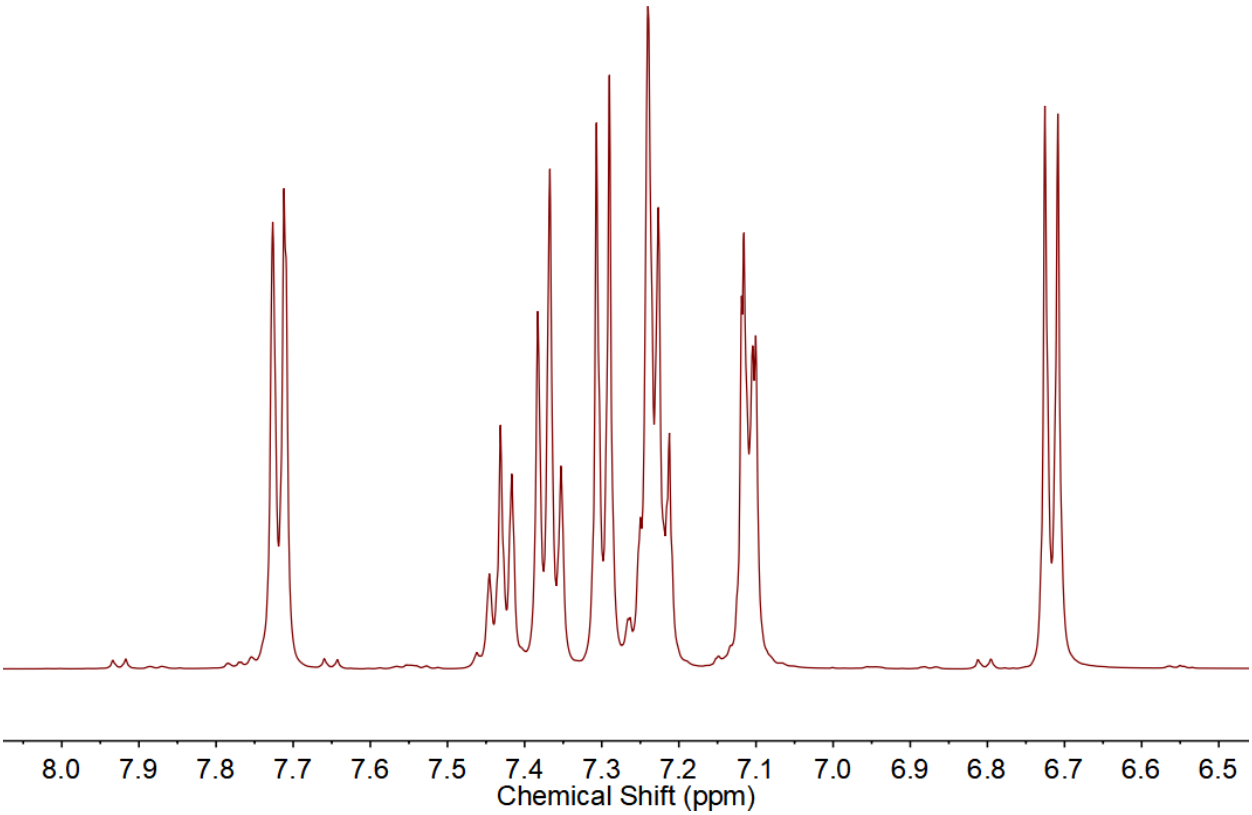

Figure 5.6. ^{1}H NMR spectrum (500 MHz, $CDCl_3$, 298 K) of BND-Benzophenone.

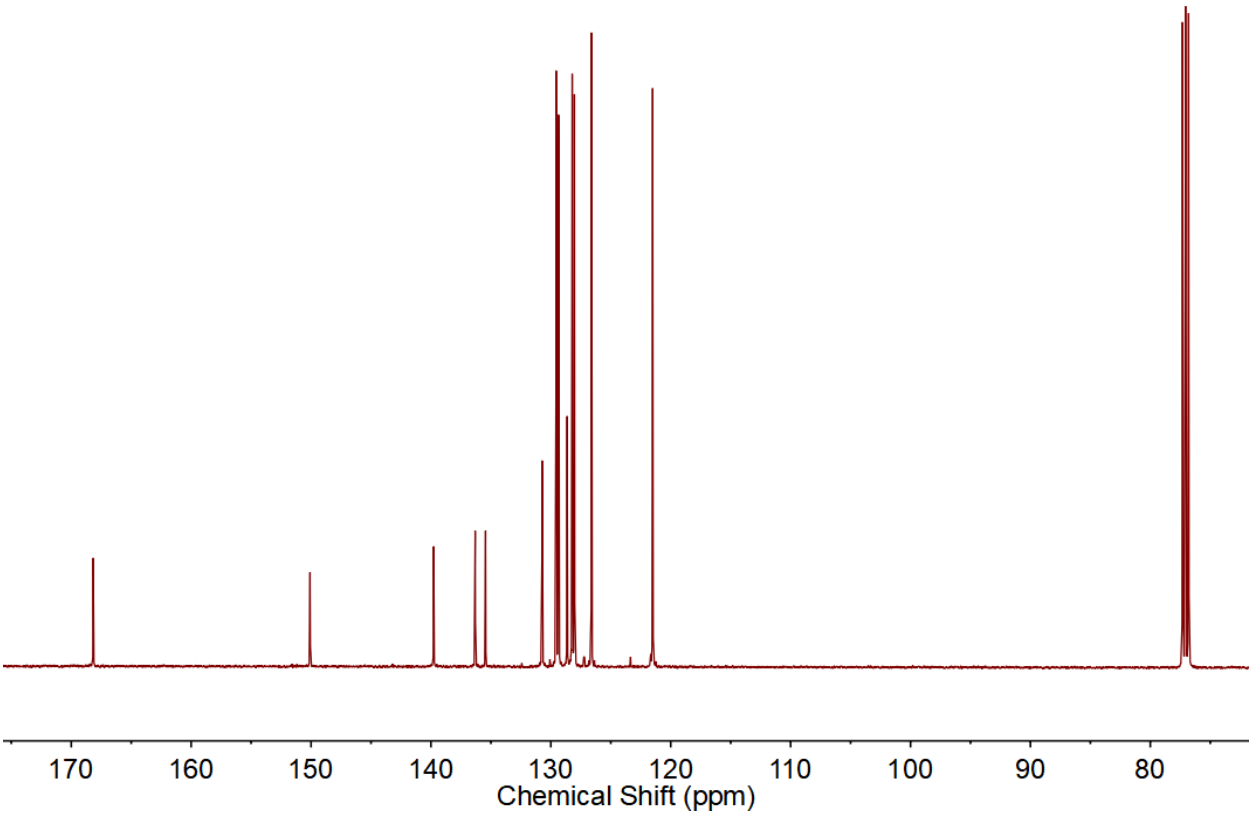

Figure 5.7.^{13}C NMR spectrum (126 MHz, $CDCl_3$, 298K) of BND-Benzophenone.

Experimental Procedures for COF Syntheses

Synthesis of BND-TFB COF: To a flame-dried 250 mL high-pressure flask with vacuum valve, 1,3,5-triformylbenzene (0.97 g, 6.0 mmol, 1.5 equiv) and benzidine-benzophenone (4.61 g, 9.0 mmol, 1.5 equiv) were added, followed by mesitylene:dioxane (1:1, 60.0 mL) along the walls of the flask (to push down any remaining solids remaining atop of the flask). The flask was sealed and sonicated at room temperature for 10 min, and then 6M acetic acid (10 mL) was added, and the flask was sealed again. The reaction mixture was then degassed through three freeze-pump-thaw cycles (vacuum <50 mTorr), after which the vacuum valve was switched to N_2, and the flask was charged with N_2 and sealed under positive N_2 pressure. The flask was then placed (no stirring) in a 120 °C pre-heated oil bath for three days. The flask was removed from the oil bath, allowed to cool, and filtered through a Buchner funnel equipped with a filter paper. Acetone was used to ensure all of the material is filtered from the flask to the Buchner funnel. The solid was collected and stirred in an Erlenmeyer flask in hot DMF (600 mL at 90 °C for 30min), and filtered while hot. This procedure was repeated two more times in DMF (600 mL at 90 °C for 30min), once in absolute ethanol (600 mL at 80 °C for 30min), and lastly once in acetone (600 mL at 60 °C). The material was then filtered, collected, placed in a vacuum chamber and dried at 120 °C for 24 h under vacuum to give an orange solid (1.98 g, 86%).

Synthesis of BND-TFP COF: To a flame-dried 150 mL high-pressure flask with vacuum valve, triformylphloroglucinol (0.63 g, 3.0 mmol, 1.0 equiv) and BND-TFB COF (1.15 g, 3.0 mmol, 1.0 equiv) were added, followed by mesitylene:dioxane (1:1, 30.0 mL) along the walls of the flask (to push down any remaining solids remaining atop of the flask). The flask was sealed and sonicated at room temperature for 10 min, and then 6M acetic acid (5 mL) was added, and the flask was sealed again. The reaction mixture was then degassed through three freeze-pump-thaw cycles (vacuum <50 mTorr), after which the vacuum valve was switched to N_2, and the flask was charged with N_2 and sealed under positive N_2 pressure. The flask was then placed (no stirring) in a 120 °C pre-heated oil bath for three days. The flask was removed from the oil bath, allowed to cool, and filtered through a Buchner funnel equipped with a filter paper. Acetone was used to ensure all of the material is filtered from the flask to the Buchner funnel. The solid was collected and stirred in an Erlenmeyer flask in hot DMF (600 mL at 90 °C for 30min) and filtered while hot. This procedure was repeated two more times in DMF (600 mL at 90 °C for 30min), once in absolute ethanol (600 mL at 80 °C for 30min), and lastly once in acetone (600 mL at 60 °C). The material was then filtered, collected, placed in a vacuum chamber and dried at 120 °C for 24 h under vacuum to give a red solid (1.25 g, 97%).

FT-IR Spectra of Covalent Organic Frameworks

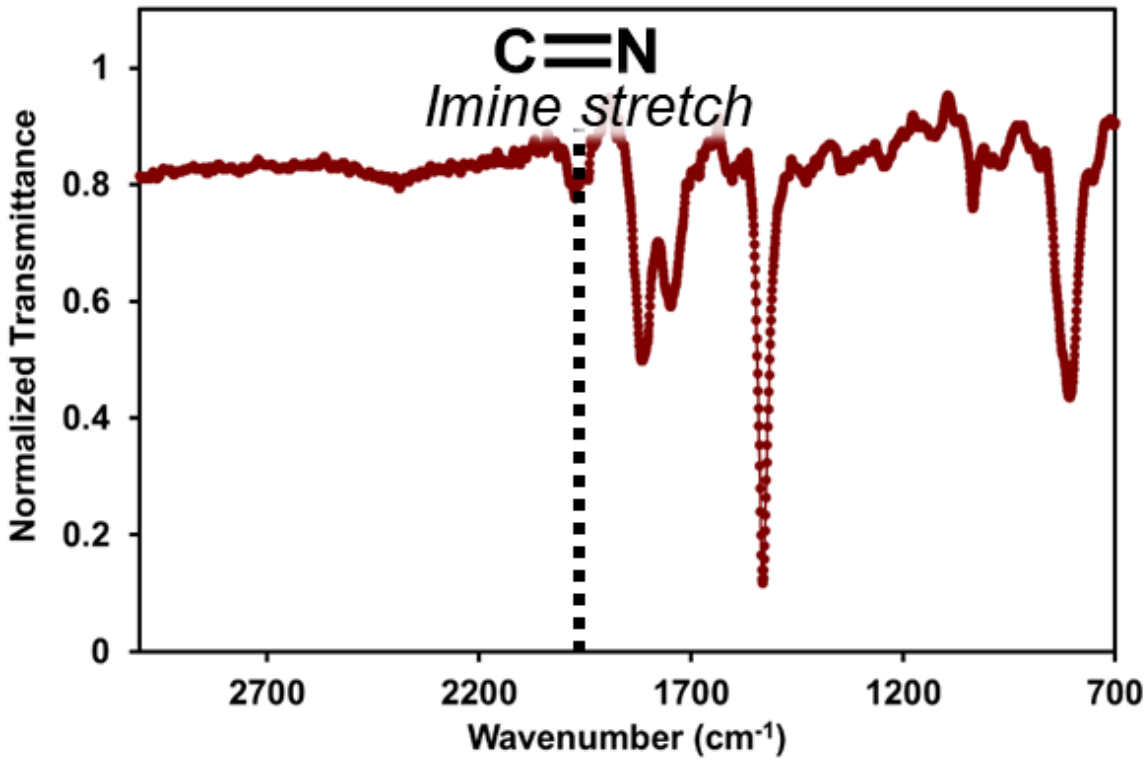

Figure 5.8. FT-IR spectrum of BND-TFB COF

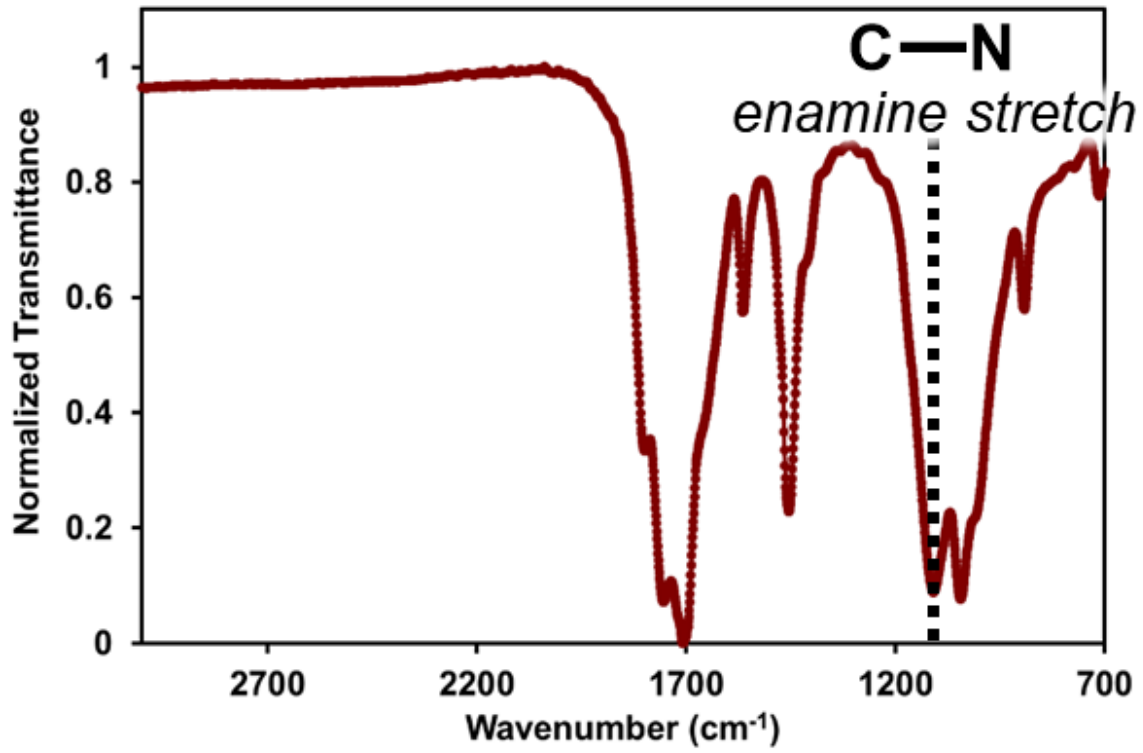

Figure 5.9.FT-IR spectrum of BND-TFP COF

CP-MAS ^{13}C NMR Spectra of COFs

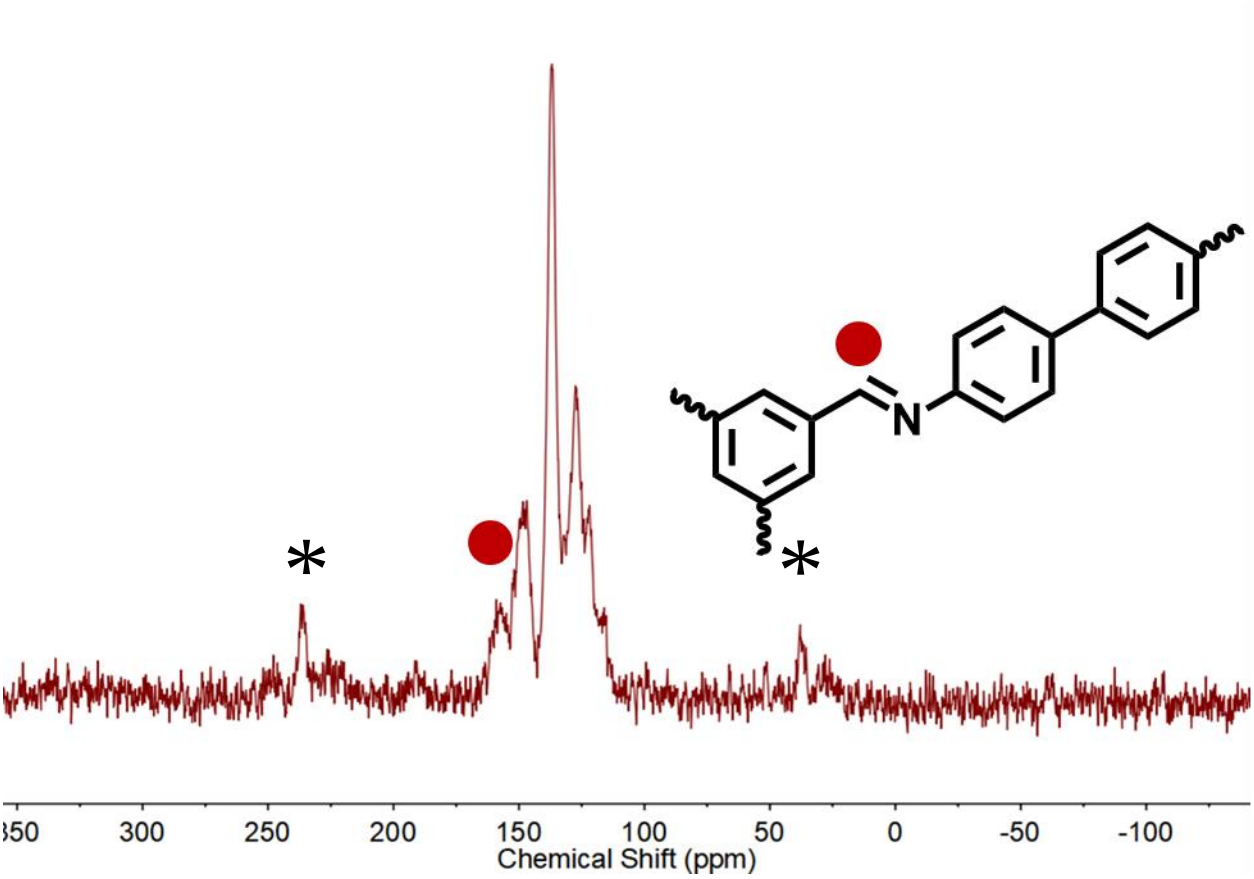

Figure 5.10. CP-MAS ^{13}C NMR spectrum of BND-TFB COF.

Spinning side bands are denoted by "*".

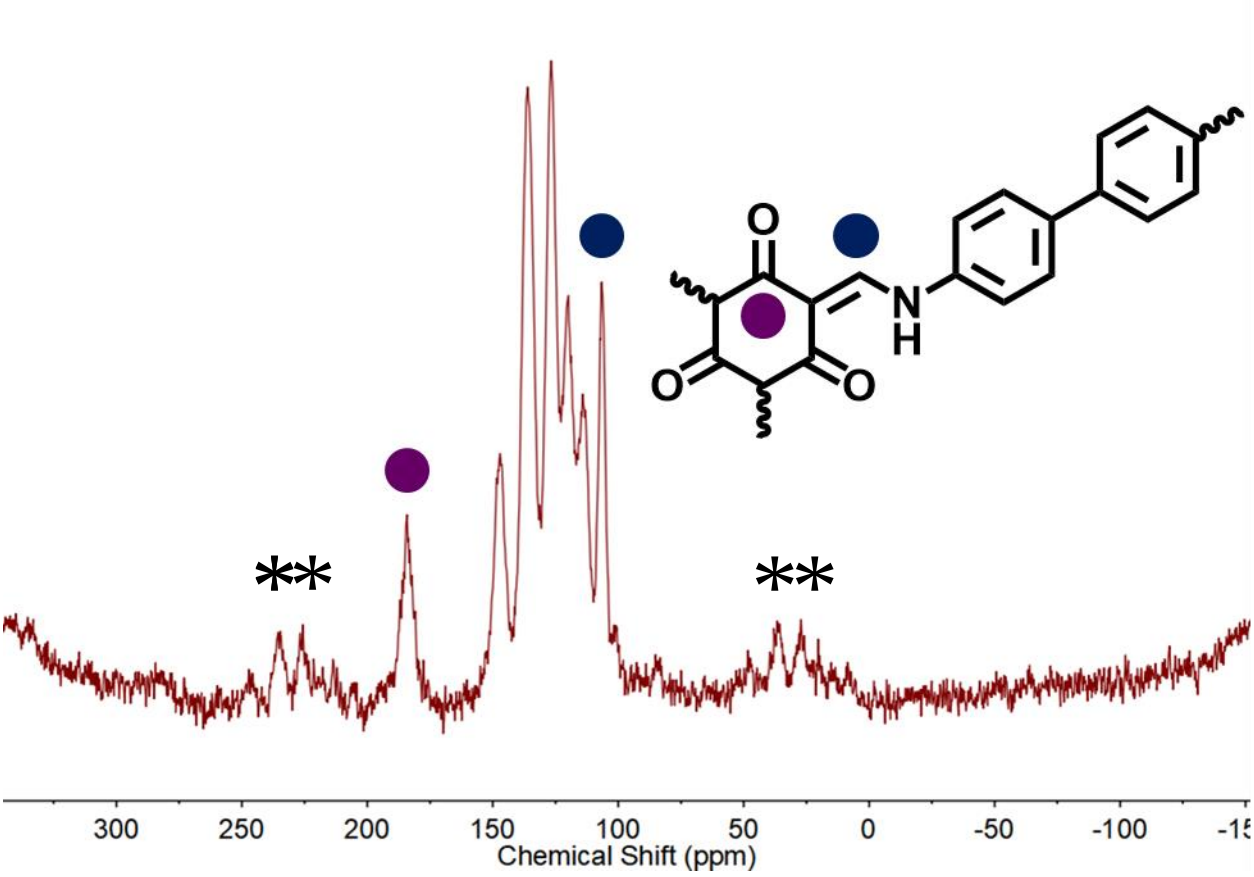

Figure 5.11. CP-MAS ^{13}C NMR spectrum of BND-TFP COF.

Spinning side bands are denoted by "*"

X-ray Diffraction of Covalent Organic Frameworks

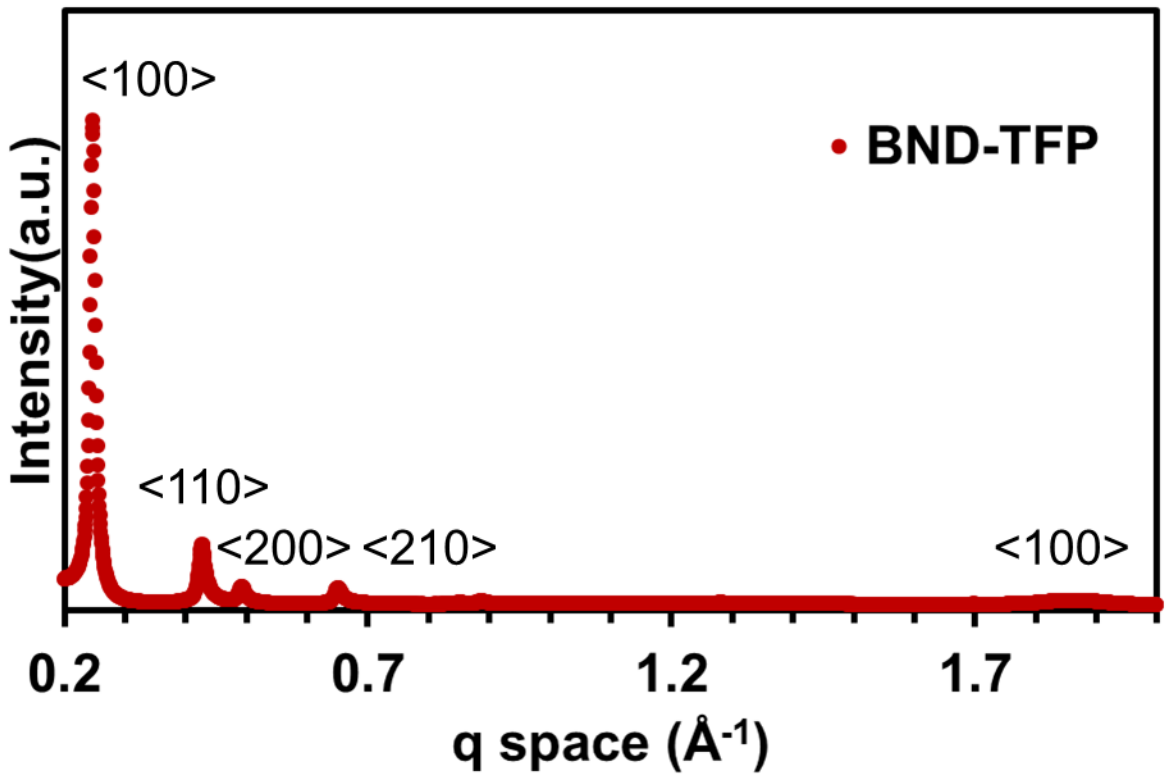

Figure 5.12. Room temperature x-ray diffraction pattern of BND-TFP COF

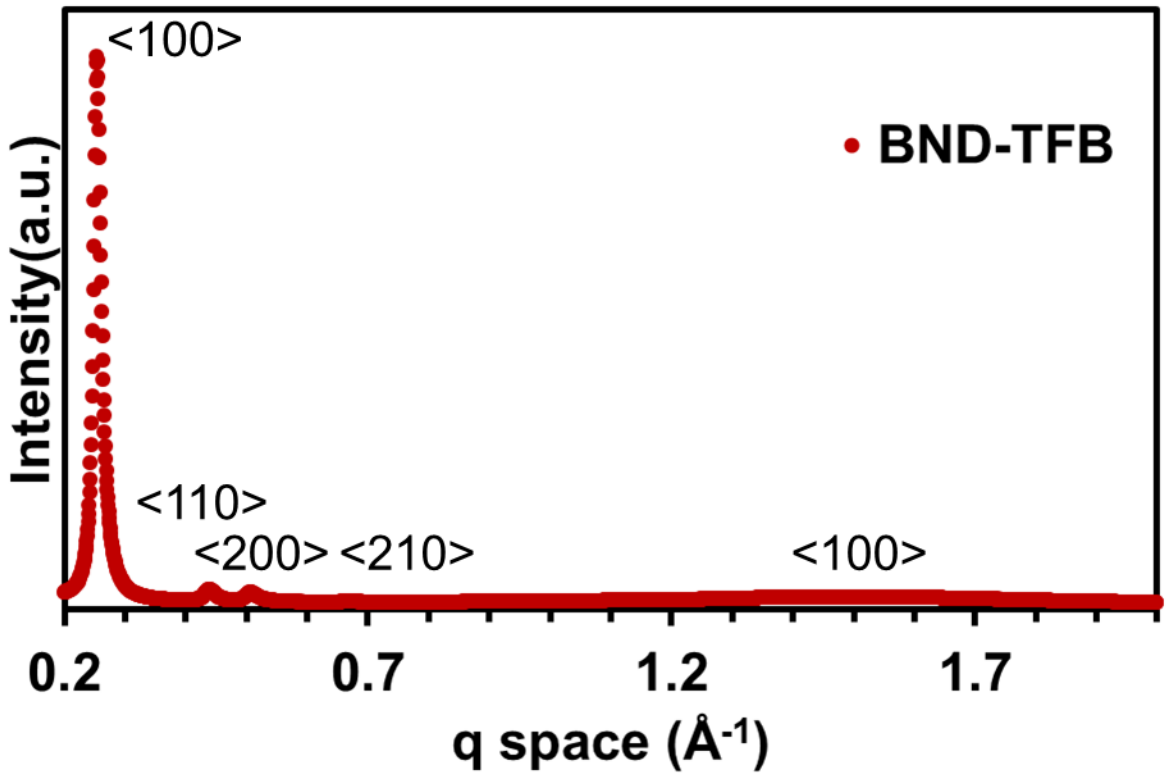

Figure 5.13. Room temperature x-ray diffraction pattern of BND-TFB COF

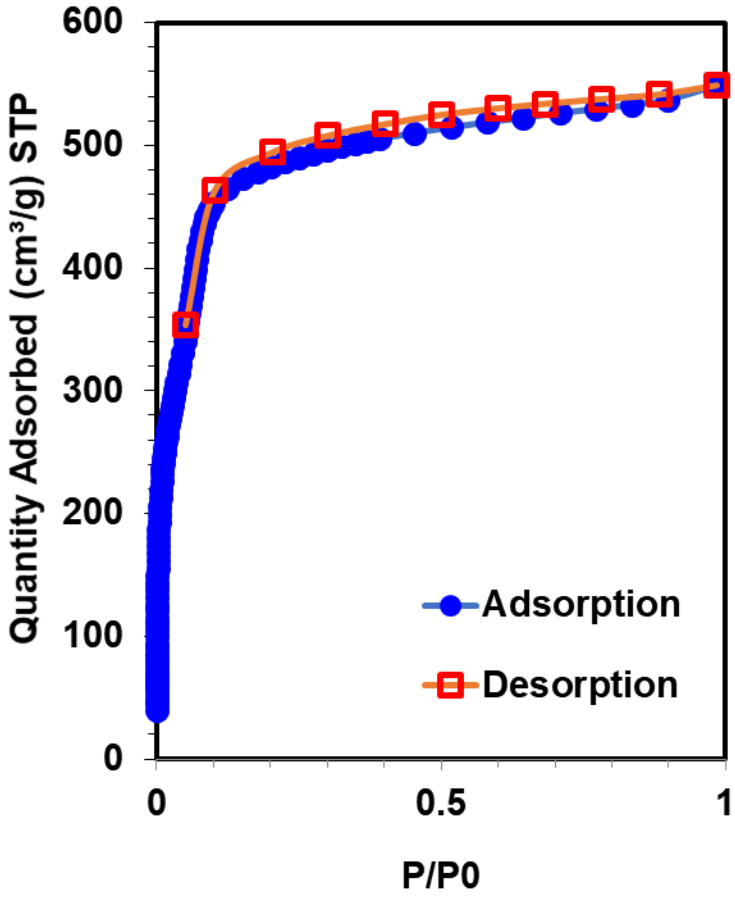

Figure 5.14. Nitrogen isotherm of BND-TFP COF

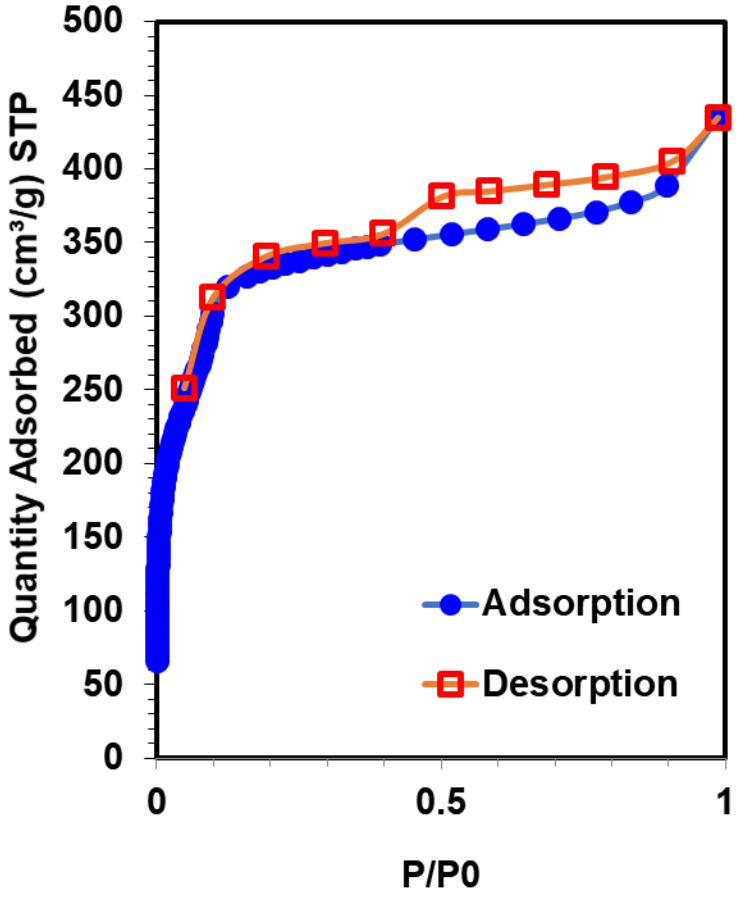

Figure 5.15. Nitrogen isotherm of BND-TFB COF

Pore Size Distributions of Covalent Organic Frameworks

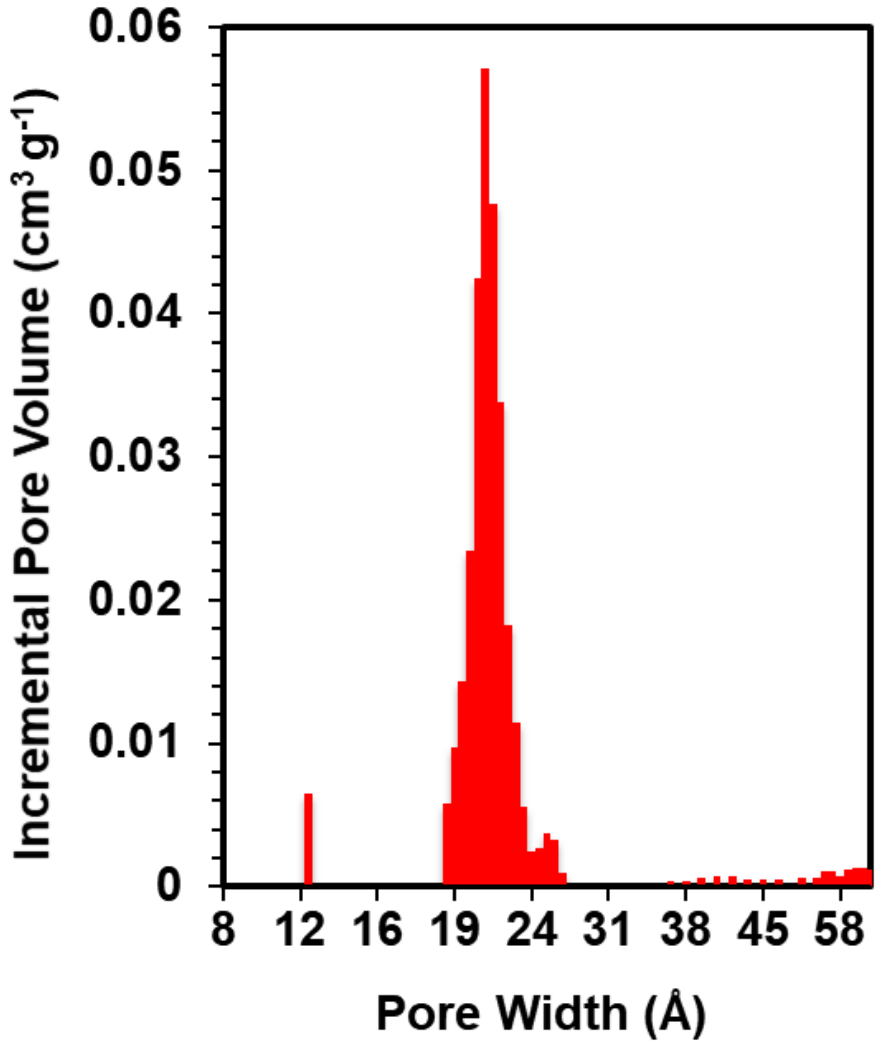

Figure 5.16. Pore size distribution of BND-TFP COF

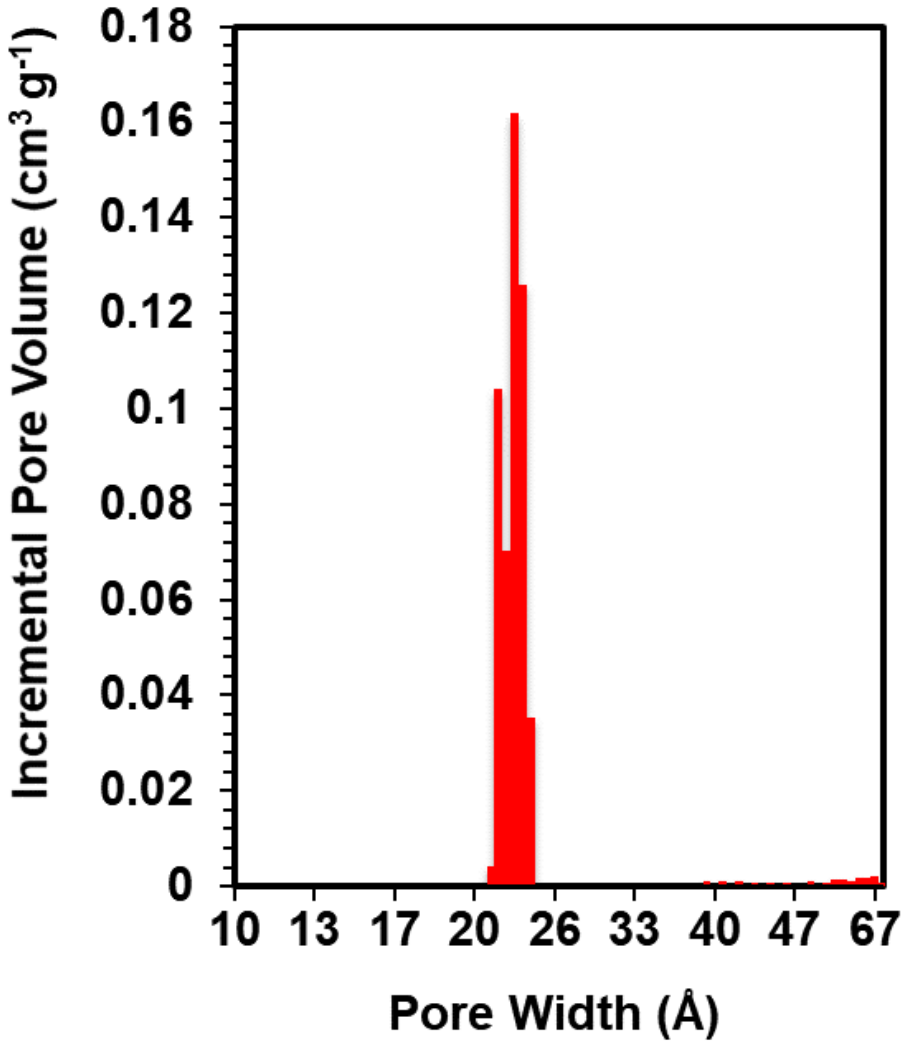

Figure 5.17. Pore size distribution of BND-TFB COF

Density Functional Theory (DFT) Calculations

Density functional theory (DFT) calculations were performed using the periodic *ab initio* code CRYSTAL17.[557, 558] The PBE exchange-correlation functional[559] was used with a semi-classical dispersion correction (PBE-D3)[560] to better account for the noncovalent interactions present in the 2D COF structures. The dispersion correction includes a BJ damped pairwise and three-body term to the DFT energies.[560] Each of the DFT calculations was performed with all-electron atom-centered Gaussian-type basis sets of double-zeta quality, similar to previous work on the electronic properties and dielectric response of other porous materials.[561]

The all-electron basis sets contained a total of 1,128 basis functions, corresponding to 450 electrons spread over 378 shells per unit cell for BND-TFP. The lattice parameters and atomic coordinates were optimized while maintaining the space group symmetry (*P6*) via a quasi-Newtonian algorithm.[562-566] The optimization was considered to have converged when the maximum and root-mean-square (RMS) gradient, and the maximum and RMS atomic displacements were simultaneously below 1.5×10^{-5}, 1.0×10^{-5}, 3.0×10^{-5} and 2.0×10^{-5} a.u., respectively.

Table 5.1. Summary of the calculated lattice parameters for BND-TFP.

BND-TFP				
Phase	*Lattice parameters* (Å)			
	a	*b*	*c*	*β*
Planar	30.03	30.03	3.61	120.0
Buckled	29.97	29.54	3.60	122.2
• The planar and buckled geometries have hexagonal and monoclinic symmetry respectively.				

The structural stability of BND-TFP upon compression was investigated using a similar procedure to that recently reported for MOF-5[567] by computing the energy at various optimized volumetrically constrained geometries and fitting the curve to an equation of state (EOS).[568] The bulk modulus values reported in the main text (Figure S13) were obtained from fitting the curve to a third-order isothermal Birch-Murnaghan EOS.[569] A series of volumetrically contracted and expanded geometries were investigated ranging from -10% to +4% and the resultant energy curve is shown in Figure S14. Within the experimental symmetry confinements of the initial structure (*P6*), the optimized equilibrium geometry was the most energetically favorable (minimum energy).

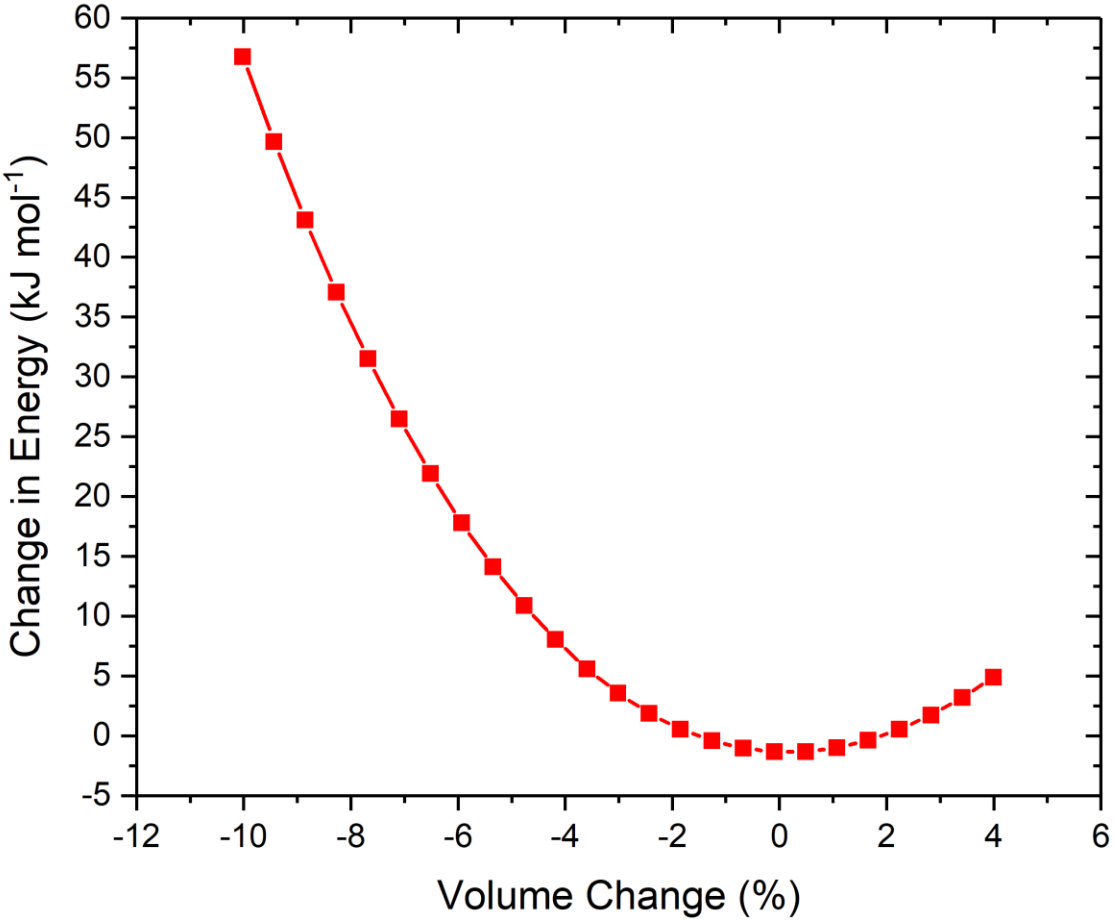

Figure 5.18. Change in energy upon compression an expansion with constant symmetry (*P6*).

However, upon further analysis of the volumetrically constrained geometries, the low-energy phonon modes were seen to soften as a function of compression, both with and without the correction for dispersion interactions (PBE and PBE-D3), and were imaginary for the PBE-D3 results indicating the possibility of a symmetry-reduced phase transition. The PBE-D3 results more accurately capture the inter-layer interactions and hence identify the phase instability at lower levels of compression compared to PBE. However, to calculate the specific level of compression required to induce the phase transition upon pressure, further investigation is needed. The size of the basis sets and number of radial and angular points defined for the integration grid were observed to affect the imaginary nature of the soft mode, and an in-depth analysis is out with the scope of the current work. To obtain structural insight into the new phase of BND-TFP, we analyzed the geometrical changes along the trajectory of the imaginary phonon mode and allowing for the associated symmetry reduction relaxed the resultant structure to optimize to the 'buckled' phase. The infrared (IR) absorption spectra of the optimized planar and buckled phases of BND-TFP are reported in Figure S15. The IR intensities were computed through the Berry Phase approach,[570] by evaluating the Born atomic tensors as polarization differences between the original and the distorted geometries.[571, 572] In the range of 650-3500 cm^{-1}, the spectral features did not change significantly in either position or intensity, in good agreement with experiment (Figure S15). Therefore, the slight shift in the experimental signal around 1600 cm^{-1} is likely due to thermal expansion of the lattice which is omitted from the computed spectra. Therefore, the vibrational modes involved do not appear to be significantly affected by the change from the planar to the buckled phase. The presence of multiple phases made analyzing the linear thermal response of the

crystalline lattice over a broad range challenging and will be investigated further in a more in-depth computational study.

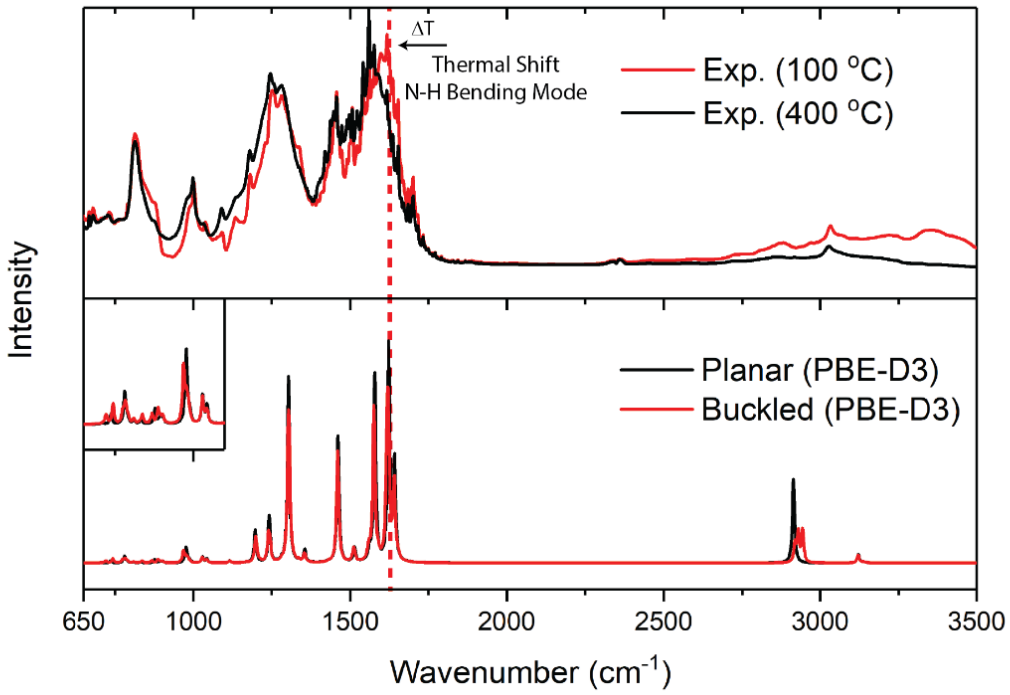

Figure 5.19. IR spectra of the planar and buckled phase of BND-TFP.

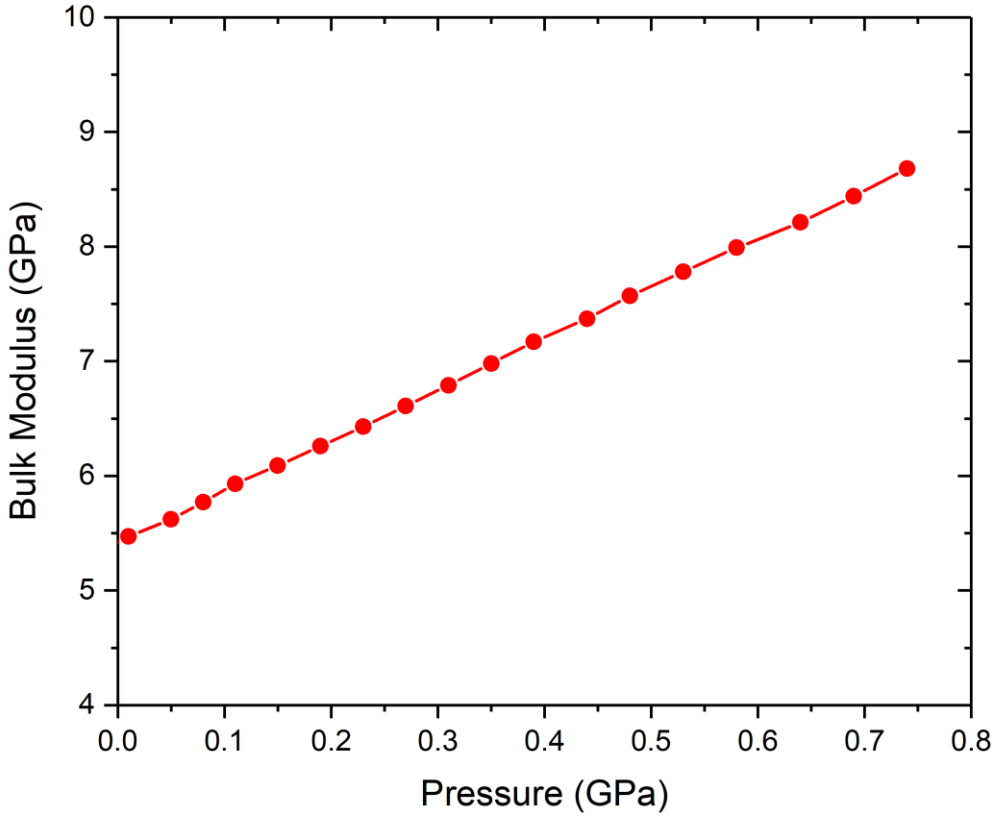

Figure 5.20. Bulk modulus as a function of pressure. Structural stiffening of BND-TFP occurs upon compression.

Chapter 6 : Trends in the Thermal Stability of Two-Dimensional Covalent Organic Frameworks

6.1 Abstract

Two-dimensional covalent organic frameworks (2D COFs) are synthetically diverse, layered macromolecules. Their covalent lattices are thought to confer high thermal stability, which is typically evaluated with thermogravimetric analysis (TGA). However, TGA measures the temperature at which volatile degradation products are formed and is insensitive to changes of the periodic structure of the COF. Here, we study the thermal stability of ten 2D COFs using a combination of variable-temperature X-ray diffraction, TGA, diffuse reflectance infrared spectroscopy, and density-functional theory calculations. We find that 2D COFs undergo a general two-step thermal degradation process. At a first degradation temperture, 2D COFs lose their crystallinity without chemical degradation. Then, at higher temperatures, they chemically degrade into volatile byproducts. Several trends emerge from this exploration of 2D COF stability. Boronate ester-linked COFs are generally more thermally stable than comparable imine-linked COFs. Smaller crystalline lattices are more robust to thermal degradation than chemically similar, larger lattices. Finally, pore-functionalized COFs degrade at significantly lower temperatures than their unfunctionalized analogues. These trends offer design criteria for thermally resilient 2D COF materials. These findings will inform and encourage a broader exploration of mechanical deformation in 2D networks, providing a necessary step towards their practical use.

6.2 An Introduction to Two-stage Degradation

Two-dimensional covalent organic frameworks (2D COFs) are a maturing class of modular, structurally regular, permanently porous, layered polymers. This unique combination of properties has inspired interest in several applications, many of which will require highly stable materials.[573, 574] Since the earliest reports of 2D COF synthesis, researchers have speculated that their strong and structurally regular covalent bonds would make them robust to chemical, thermal, and mechanical stress.[41, 456] Thermogravimetric analysis (TGA) performed in many 2D COF reports supported this view, in that temperatures as high as 800 °C are required to release volatile degradation byproducts.[41] Their desirable thermal stability has been noted as an important design criterion as COFs have been explored for applications such as sensing,[575-578] catalysis,[579, 580] optoelectronics,[576, 581-583] energy storage,[581, 584] and chemical separations,[147, 577, 585, 586] which sometimes operate under demanding thermomechanical stresses.

We recently compared the thermal stability of a pair of structurally similar but chemically distinct 2D COFs[587] using TGA and variable-temperature X-ray diffraction (VT-XRD, **Figure 6.1A**). Both COFs exhibited two degradation temperatures: a lower temperature at which the materials lose their periodicity (T_{XRD}) but retain their chemical structure, and a higher temperature (T_{TGA}) at which chemical degradation generates volatile byproducts (**Figure 6.1B**). VT-XRD and density functional theory (DFT) revealed evidence for buckling of these two COF lattices as they approach T_{XRD}, further suggesting that the COFs lose crystallographic registry through structural distortions prior to covalent depolymerization. These observations indicate that the structural regularity of COFs, which distinguishes them from conventional cross-linked polymer networks, is less thermally robust than is captured by TGA.

6.3. Interlayer interactions in 2D polymers

Recent indirect experimental evidence also supports the hypothesis that 2D COF layers are susceptible to structural deformation during isolation or characterization. For example, Bunck *et al.* found that hydrazone-linked networks spontaneously exfoliate when immersed in common organic solvents, which was attributed to the weak interlayer interactions of hydrazone-linked 2D COFs.[588] More recently, studies conducted by Sick *et al.* and Feriante *et al.* observed that many imine-linked 2D COFs became amorphous and lose porosity when exposed to vacuum.[159, 160] Gole *et al.* and Li *et al.* found that even with the nanoscale COF net preserved, mesoscale mechanical deformation of 2D layers is energetically feasible.[577, 589] These findings are consistent with earlier theoretical work on the mechanics of 2D polymers, which found their deformation is driven by entropic forces, similar to disorder in linear polymer networks.[590-593] These observations motivate a thorough investigation into the mechanics of covalent 2D networks, which have yet to be systematically explored. A deeper investigation into the thermomechanical deformations of layered crystalline polymers will be invaluable in developing the most promising applications of 2D COFs.

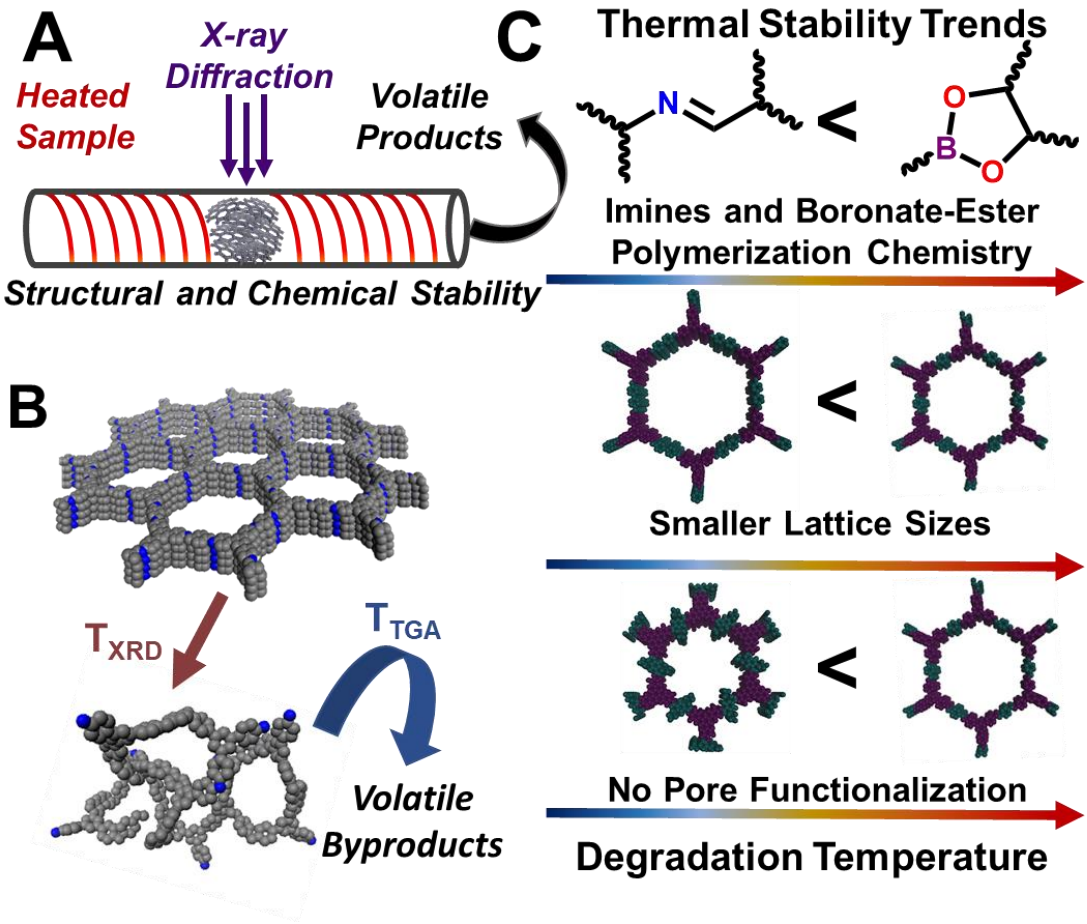

Figure 6.1. (A) Schematic illustration of variable-temperature measurements. **(B)** Schematic illustration of two different degradation processes studied in this work. **(C)** 2D COF Thermal stability trends observed in this work.

Herein, we characterize the thermal stability of ten 2D COFs and find that in all cases, the periodic COF structure deforms at lower temperatures than the degradation temperature assessed by TGA. Based on VT-XRD, TGA, diffuse reflectance infrared spectroscopy (DRIFTS), and DFT calculations, we conclude that all COFs become disordered without significant chemical

degradation at a temperature (T_{XRD}) lower than their T_{TGA} (**Figure 6.1A-B**). Several trends emerge from studying this process across many 2D COFs (**Figure 6.1C**). Boronate ester-linked materials are more stable than structurally similar imine-linked frameworks. Smaller lattices are more thermally stable than their larger analogues. Finally, the T_{XRD} of 2D COFs decreases in networks with functional groups in their pores, despite these groups not significantly impacting T_{TGA}. To more accurately assess the thermal stability of 2D polymers, structural analysis, including N_2 sorption measurements, XRD, or direct imaging should be used in conjunction with TGA. Furthermore, these results show that the fabrication or measurement of devices based on 2D COFs should be carefully considered, as processing techniques and temperatures, in some cases, are not benign. Overall, the structural trends for retaining crystallinity to relatively high temperatures suggest various strategies to control thermal stability through judicious design.

6.4 Synthesis and characterization of two-dimensional COF powders

To study their thermal stability, we prepared high-quality 2D COF powders via previously reported methods (**Scheme 6.1 – 6.21**).[41, 147, 394, 455, 594, 595] In all cases, room temperature XRD showed narrow 100 Bragg peaks and several higher-order diffraction features. By considering finite crystallite size broadening of the XRD patterns with full pattern Le Bail fitting, we ascertained that the crystallite domain sizes are on the order of 50–100 nm, consistent with reports of high-quality COFs in the literature (**Figure 6.18-Figure 6.87**).[455] Similarly, Brunauer-Emmett-Teller (BET) N_2 surface areas revealed experimental surfaces areas close to each COF's respective theoretical Connolly surface area and narrow pore width distributions consistent with Pawley refined

structures (**Figure 6.28-Figure 6.57**). Fourier-transform infrared (FT-IR) spectroscopy revealed near-complete polymerization conversion by the disappearance of monomer IR features and the emergence of the expected polymer IR features in their respective IR spectra (**Figure 6.78 - Figure 6.87**). Taken together, these experiments indicate that the materials used in this study are of similar or higher quality than those evaluated in leading literature reports.

6.5 Amorphization and Volatilization: Two Degradation Temperatures

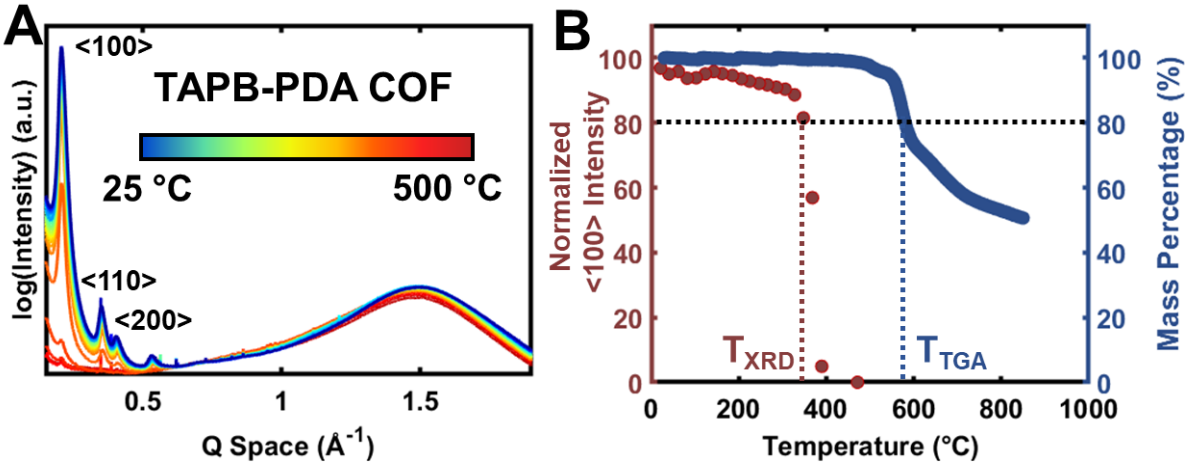

Figure 6.2. (A) Variable-temperature X-ray diffraction of TAPB-PDA COF. **(B)** Comparison of the 100 diffraction intensity and sample mass as a function of temperature.

VT-XRD reveals that T_{XRD} is lower than T_{TGA} for all 2D COFs investigated. As an example, we studied the thermal stability of the prototypical imine-linked 2D COF, TAPB-PDA, which is formed by condensing 1,3,5-tris(aminophenyl)benzene (TAPB) and 1,4-phenylenedialdehyde (PDA). The COF powder was heated at 10 °C min^{-1} under an inert atmosphere while continuously monitoring either the mass or synchrotron diffraction pattern (**Figure 6.2A**). We define the structural deformation temperature as either when the integrated 100 Bragg diffraction feature

(T_{XRD}) or the mass of the sample (T_{TGA}) dropped below 80% of their room-temperature values (**Figure 6.2B**).[582] TAPB-PDA thermally decomposes at 550 °C (T_{TGA}) (**Figure 6.2B**), which agrees with T_{TGA} reported for TAPB-PDA and other imine-linked frameworks in previous reports.[596-598] However, TAPB-PDA loses crystallinity at 320 °C (**Figure 6.2B**). This large difference (230 °C) highlights that the thermal degradation temperature assessed by TGA is not representative of COF structural stability. Additionally, the observation of two degradation temperatures, one related to the loss of crystallinity and another related to volatilization of the network, demonstrates that 2D COFs form an intermediate disordered phase that subsequently degrades to volatile species at higher temperatures.

6.6 Comparisons of COF Stability and Structural Trends

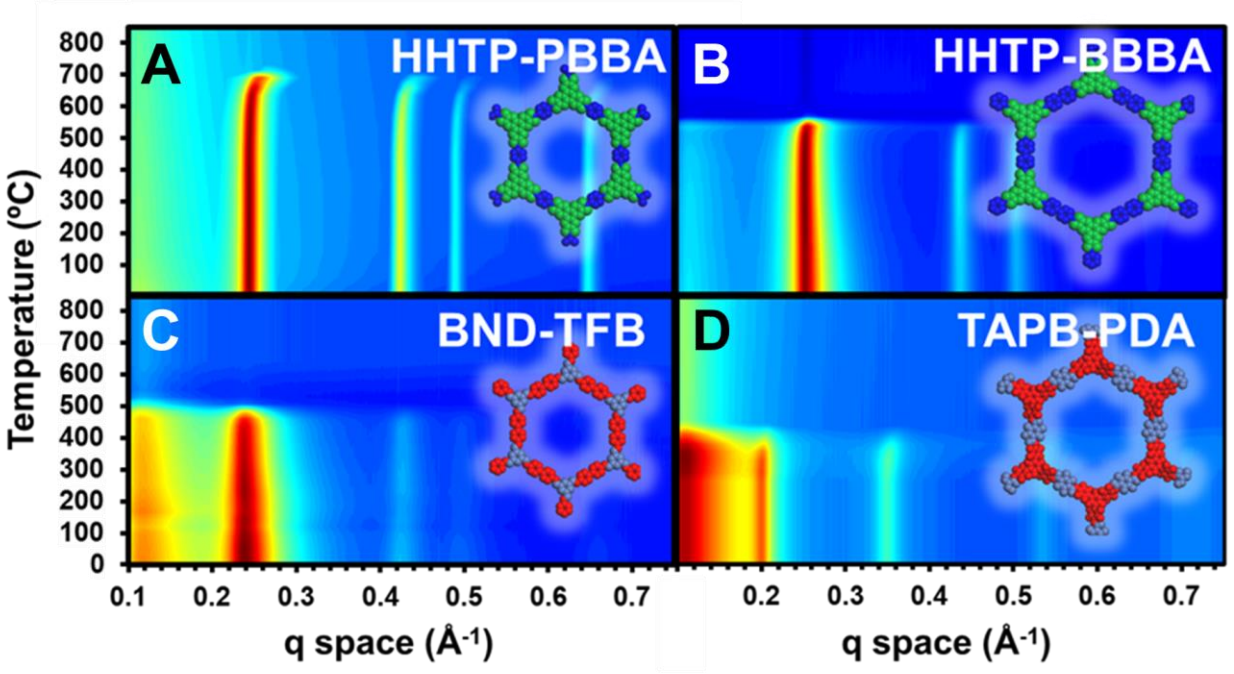

Figure 6.3. Variable-temperature X-ray scattering profiles of four commonly studied COFs: the boronate ester-linked **A)** HHTP-PBBA COF and **B)** HHTP-BBBA COF, and the imine-linked **C)** BND-TFB COF and **D)** TAPB-PDA COF.

The presence of two distinct degradation temperatures is general for all COFs that were studied, with boronate ester-linked networks with smaller lattices found to be more thermally stable than their larger analogues. This trend is evident by comparing the thermal stability of two hexagonal boronate ester-linked 2D COF frameworks, HHTP-PBBA (previously reported as COF-5)[41] and HHTP-BBBA (previously reported as COF-10),[594] which are synthesized by the condensation of 2,3,6,7,10,11-hexahydroxytriphenylene (HHTP) and 1,4-phenylenebis(-boronic acid) (PBBA) or

4,4′-biphenylbis(boronic acid) (BBBA), respectively. These hexagonal networks are chemically similar but differ primarily in their lattice sizes: HHTP-PBBA has an in-plane lattice size of 28 Å, and HHTP-BBBA has an in-plane lattice size of 34 Å. TGA revealed a primary mass loss event at T_{TGA} = 750 ℃ for HHTP-PBBA (**Figure 6.96**) and T_{TGA}= 500 ℃ for HHTP-BBBA (**Figure 6.97**), which are consistent with previous reports.[41, 456] However, HHTP-PBBA and HHTP-BBBA lose their crystallographic registry at T_{XRD} = 600 ℃ and T_{XRD} = 400 ℃, respectively (**Figure 6.3A and Figure 6.3B**). While boronate ester-linked COF's structures are stable to high temperatures, much like their imine-linked counterparts, they form a disordered phase prior to degrading to volatile by-products. Furthermore, because both T_{TGA} and T_{XRD} decrease in COFs with larger lattice sizes suggests that both the chemical and structural degradation mechanisms are related to the size of the crystalline COF lattice. This trend is also observed for imine-linked 2D COFs. We investigated two imine-linked- 2D COFs, TAPB-PDA and BND-TFB, which are synthesized by the condensation of tris(4-aminophenyl)benzene (TAPB) and 1,4-phenyldialdehyde (PDA) and *N*-benzidine benzophenone imine (BND) and 1,3,5-triformylbenzene (TFB), respectively. Both COFs exhibit a T_{TGA} of 550℃ (**Figure 6.98**).[596-598] Both imine-linked networks have lower T_{XRD}, with T_{XRD} = 365 ℃ for BND-TFB (**Figure 6.3C**) and T_{XRD} = 320 ℃ for TAPB-PDA (**Figure 6.3D**). In this case, the smaller BND-TFB (28 Å) is 45 ℃ more stable than TAPB-PDA (32 Å). Ostensibly, the lower stability of larger 2D networks is due to their larger free volumes, a higher number of deformation points (rotatable bonds) per unit cell, and additional accessible phonon modes. We suspect that a complex interplay of factors could lead to this observed trend in degradation temperature. These factors are all compatible with the understanding that structural

distortions in 2D layers are entropically driven. As a consequence of this trend, it is likely is a trade-off between increased pore size and decreased thermal stability.

By comparing chemically distinct COFs with similar lattice sizes and symmetries, COFs polymerized through boronate esters are observed to be more thermally stable than their imine-linked counterparts. Pawley refined crystal structures reveal that the imine-linked BND-TFB (28 Å) and boronate ester-linked HHTP-PBBA (29 Å) and the imine-linked TAPB-PDA (32 Å) and boronate ester-linked HHTP-BBBA (34 Å) are of similar unit cell sizes. In both cases, the boronate ester-linked frameworks are >100 ℃ more stable than imine-linked frameworks as judged by T_{XRD}. The increased thermal stability of boronate ester-linked frameworks may be related to the larger van der Waals surfaces of these HHTP-containing structures or may be more generally related to the increased structural rigidity of boronate-esters compared to those of imines.[599] These comparisons highlight an important consideration when selecting polymerization chemistries to be tailored for intended use of the COF. For example, boronate ester-linked frameworks are less hydrolytically stable than imine-linked frameworks, yet they may be preferable in anhydrous environments and applications wherein high thermal stabilities are desired.

6.7 Thermally Driven Buckling of Boronate Ester-Linked 2D COFs

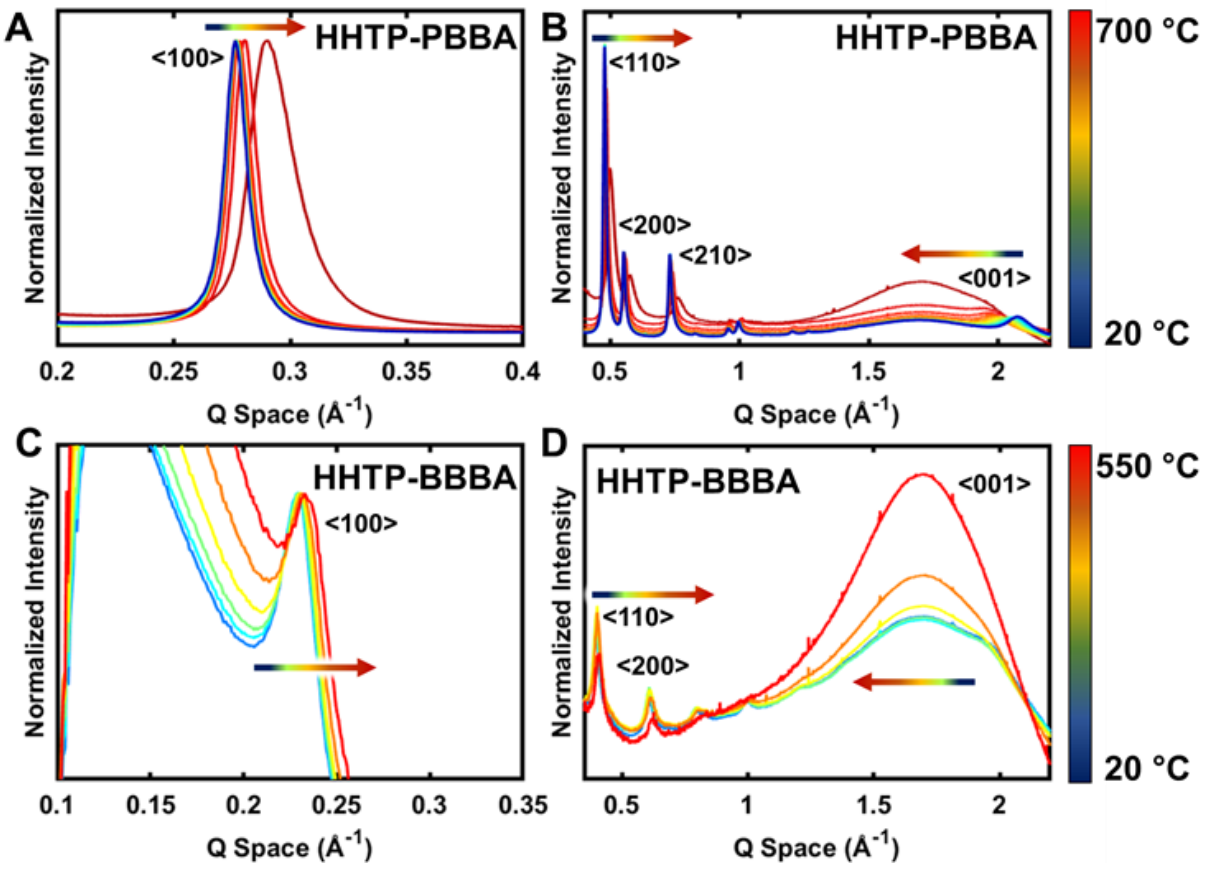

Figure 6.4. Normalized temperature-dependent X-ray diffraction profiles of **(A)** HHTP-PBBA small-angle scattering **(B**) HHTP-PBBA wide angle scattering **(C)** HHTP-BBBA small-angle scattering and **(D)** HHTP-BBBA wide angle scattering.

As boronate ester-linked frameworks approach T_{XRD}, their in-plane lattices contract, which provides insight into the mechanism of their transient amorphization. As both PBBA-HHTP and BBBA-HHTP were heated to their T_{XRD}, their in-plane Bragg diffraction features (100 (**Figure**

6.4A), 110, 200, 210 (**Figure 6.4C**) trended towards higher values in reciprocal space. The maximum diffraction feature trending towards higher values in reciprocal space corresponds to the in-plane crystallographic direction undergoing the unusual process of thermal contraction. In contrast, heating both COFs led to the maximum cross-plane diffraction features (001) shifting to lower reciprocal space (**Figure 6.4B and Figure 6.4D**), indicating thermal expansion. Recently, we proposed that these changes represented a phase change wherein 2D layers buckle with respect to each other, thereby shrinking the in-plane crystallographic direction.[600] The structural changes observed here for boronate ester-linked COFs support this hypothesis. Therefore, we suspect that amorphization is unlikely to correspond to chemical degradation of the network and is instead structural in nature, consistent with similar findings related to metal-organic frameworks.[601] Likely, a large amount of softening and expansion as a function of temperature for boronate ester-linked COFs is related to the high temperatures accessible by their thermally stable structures, large pore volumes, and a large number of accessible phonon modes in all-organic frameworks. These observations of dynamic COF structures may inspire their use when responsive, highly stable crystalline lattices are desirable.

In contrast to the behavior of the boronate ester-linked COFs, the imine-linked TAPB-PDA COF does not undergo the same degree of thermal contraction as it approaches its T_{XRD}. In TAPB-PDA and its structural analogues (**Figure 6.5A**), the diffraction features do not shift appreciably during heating (**Figure 6.2A** and **Figure 6.5B**). We suspect that the origin of this difference is the inherent distortions associated with TAPB-PDA. In boronate ester-linked frameworks, COF layers exhibit minimal out-of-plane distortions as a result of their highly planar monomers and the rigidity of boronate-ester bonds. In contrast, TAPB-PDA layers are considerably rotated (**Figure 6.35**),

which primarily from the steric strain of the tris(phenyl)benzene moiety. DFT calculations suggest that this rotational freedom allows for the relaxation of thermally induced stress without significant buckling of the 2D COF layer. This observation demonstrates that there are opportunities to prevent thermal contraction in 2D COFs. Taken together, these pairwise comparisons will guide the future design of 2D COFs with high stabilities and/or dynamic mechanical properties.

6.8 Thermal Stability of 2D COFs with Functionalized Pores

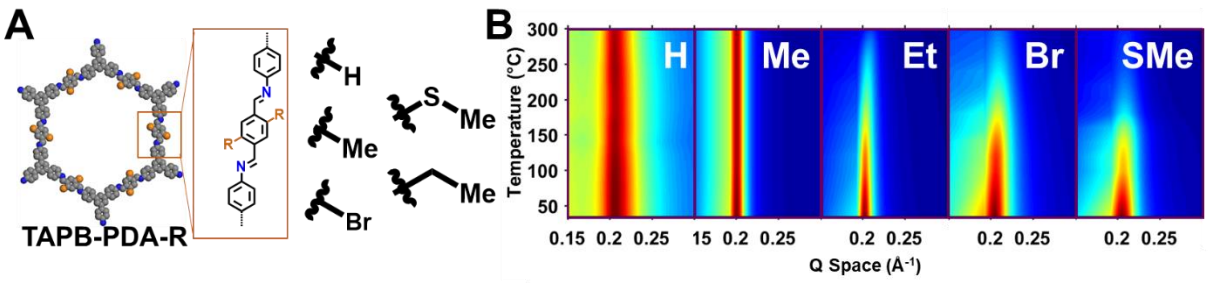

Figure 6.5. (A) Structures of pore-functionalized TAPB-PDA-R COFs. **(B)** VT-XRD of TAPB-PDA-R.

Chemically modifying the pores of a COF containing reactive pendant groups, sometimes known as pore-surface functionalization, is a powerful strategy to generate a diverse set of 2D COFs from a single precursor framework. This approach has been used to tailor COFs of interest for organic electronic devices, adsorbents, and membranes.[147, 394, 602] However, it is not known how side chains impact the thermal stability of the 2D COFs. We synthesized microcrystalline powders of functionalized TAPB-PDA-R COFs, where R = H, Me, Et, Br, SMe, by the condensation of TAPB and the corresponding 2,5-disubstituted terephthaldehyde (PDA-R)

(**Figure 6.2A**). In all cases, the T_{TGA} of these networks was similar to the parent TAPB-PDA (all approximately 500 ℃, **Figure 6.96 - Figure 6.105**). This finding suggests that bond breaking and subsequent volatilization likely originates along the parent framework backbone, not the side chains.

Despite their similar T_{TGA} values, the T_{XRD} of these networks varied greatly. The T_{XRD}s of the R= H, Me, Et, Br, SMe networks were >300℃, >300℃, 250℃, 150℃, and 125℃, respectively (**Figure 6.5B**). Taken together, this trend shows that as larger substituents are added to the pore surface, the temperature at which crystallinity is lost decreases. The reduced thermal stability of pore-functionalized networks may be related to the larger number of entropic states available to these networks, similar to entropic structural distortions in linear polymer systems,[603] or steric repulsion of the added functionalization in the pore. Both may cause significant disruption of interlayer interactions in 2D COF sheets, where larger, more mobile side chains act to force the layers apart as thermal energy is added to the system.

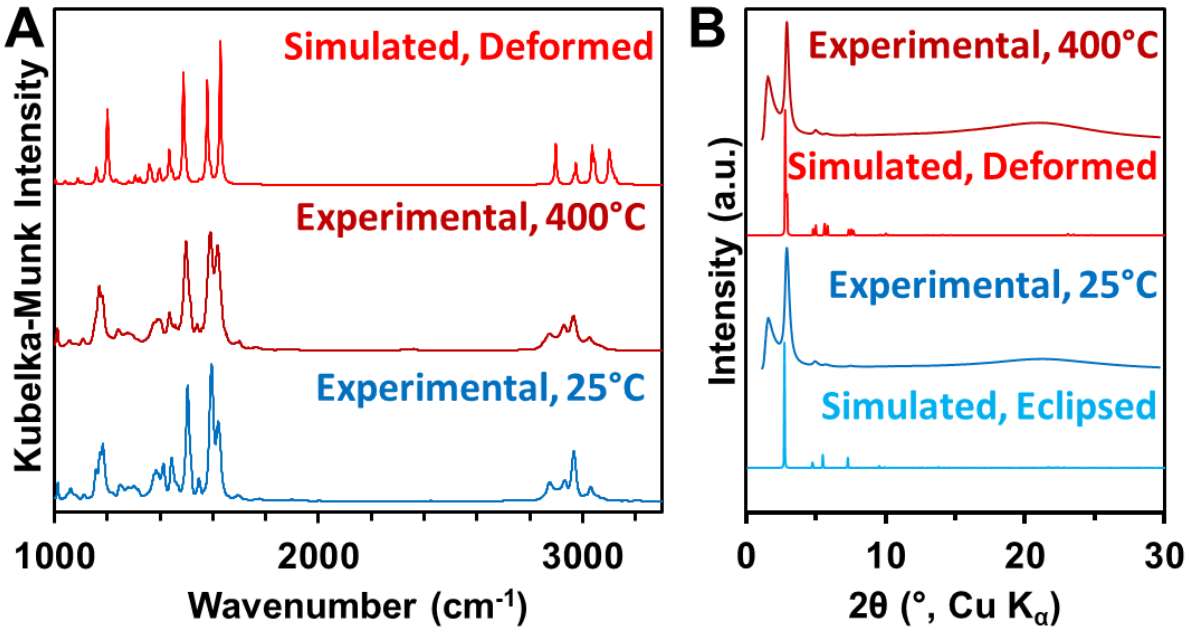

Figure 6.6. (A) Comparison of variable-temperature diffuse reflectance infrared spectra and calculated infrared spectra of TAPB-PDA-Et COF **(B)** Comparison of experimental variable-temperature X-ray diffraction patterns and simulated X-ray diffraction from DFT optimized eclipsed and deformed phases of TAPB-PDA-Et COF.

DRIFTS and DFT calculations suggest that the origin of the thermally induced disorder is the disrupted registry of COF layers. Consistent with the TGA, we find that most FT-IR features in TAPB-PDA-Me and TAPB-PDA-Et remain unchanged as the sample was heated to 500 ℃ (**Figure 6.6**). Specifically, we find that the imine-feature remains intact across the entirety of the thermal ramp in both materials, indicating that substantial hydrolysis or transimination does not occur as a function of temperature. The high wavenumber FT-IR features (2500 – 3300 cm^{-1}) shifted slightly in location and relative intensity as the sample was heated, which could be due to the increased flexibility of their methyl and ethyl groups, respectively (**Figure 6.6A**). This

observation is consistent with the hypothesis that the side chains cause structural distortions rather than chemical degradation. These experimental observations are consistent with computational results that show that the structures are unlikely to buckle or deform as significantly to previous studies on 2D COFs.[600] The DFT calculated IR spectrum from a relaxed structure is in strong agreement with experiment (**Figure 6.6A**). Similarly, simulated diffraction patterns from a DFT calculated deformed structure and perfectly eclipsed structure show that only minor structural differences arise as the TAPB-PDA-Et COF deforms, consistent with our experimental observations (**Figure 6.6B**). Taken together, the effects of pore functionalization are reminiscent of plasticization of 1D polymers and intercalation-driven exfoliation of 2D materials. As such, we suspect that pore functionalization may be a versatile platform to control thermomechanical processes in 2D polymers.

6.9 Chemically Reactive Pore Functionalization

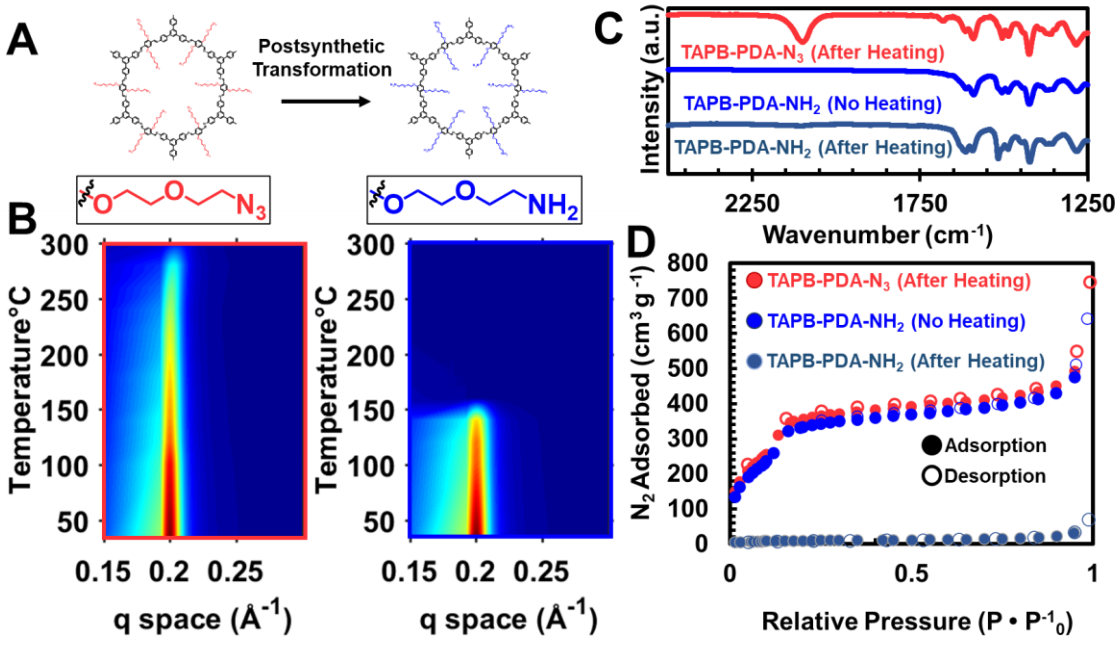

Figure 6.7. (A) Chemical structures of the TAPB-PDA-N_3 and TAPB-PDA-NH_2 COFs **(B)** VT-XRD of TAPB-PDA-N_3 and TAPB-PDA-NH_2 COF. (**C)** IR spectra of TAPB-PDA-N_3 and TAPB-PDA-NH_2 COF after heating and TAPB-PDA-NH_2 COF without heating. (**D)** N_2 isotherms of TAPB-PDA-N_3 and TAPB-PDA-NH_2 COF after heating and TAPB-PDA-NH_2 COF without heating.

In addition to structural distortions induced by smaller side chains, chemically active side chains also degrade the COF structure during thermal activation. To investigate the role of such side chains, we first synthesized TAPB-PDA-N_3, by condensing TAPB and a PDA with an azide-functionalized glycol chain (**Figure 6.7A**). The azides were reduced to amines to produce TAPB-PDA-NH_2 in quantitative yield. Despite being nearly identical in size, the amine-functionalized network (T_{XRD} = 120 ℃) degrades 50 ℃ lower than its azide-functionalized counterpart (T_{XRD} =

170 ℃) (**Figure 6.7B**). The amine-functionalized framework had unique transient diffraction features that appeared before its amorphization (**Figure 6.7B**), which led us to speculate that the amines were reacting in the solid-state by nucleophilic addition to the imine linkages of the COF. This process is feasible in the monomer; upon reduction of PDA-N_3 to PDA-NH_2, an intramolecular condensation with its aldehydes occurs in high yields (>70%), which prevented its direct polymerization into a COF (**Figure 6.113**). The low temperature of amorphization for TAPB-PDA-NH_2 allowed us to study the degradation of this network using N_2 porosimetry. Before N_2 sorption isotherm measurements, samples are frequently heated to remove volatile solvents. However, when TAPB-PDA- NH_2 was degassed at 100 ℃ for 15 hours, it became amorphous and nonporous (**Figure 6.7D**). In contrast, TAPB-PDA-N_3 survived degassing at 100 ℃ for 15 hours with retention of its high surface area. However, when degassed at room temperature TAPB-PDA-NH_2 retained its high surface area suggesting that even mild heating drove amorphization in this network. FT-IR measurements performed before and after degassing of TAPB-PDA-NH_2 COF shows limited changes, both of which are similar to the parent TAPB-PDA COF and TAPB-PDA-N_3 COF, which does not preclude that substantial transimination has occurred (**Figure 6.7C**). Taken together, these results suggest that solid-state reactions can occur under thermal stresses when incompatible chemistries are present in the same framework. However, it also points to a more exciting possibility that COFs with designed, thermally switchable depolymerization processes might be realized by controlled functional group manipulations.

6.10. Conclusions

COFs are an emerging class of crystalline, permanently porous, polymers with proposed applications ranging from catalyst supports to energy storage materials. Due to their covalently bonded network structures, these materials are thought to be highly stable. TGA experiments have historically supported this view. Variable-temperature X-ray diffraction experiments demonstrate that the thermal degradation processes of 2D COFs are more complex. In the ten COFs studied here, amorphization occurs well before degradation is detected by TGA. These experiments suggest several trends between chemical structure and stability. First, boronate ester-linked 2D COFs are more stable than their imine-linked counterparts. Second, smaller networks were more thermally stable than their larger analogues. Finally, pore functionalization reduces the thermal stability of the periodic COF structure, in some cases by hundreds of degrees Celsius. A combination of experimental X-ray diffraction experiments and DFT calculations suggest that this amorphization process arises from structural deformation of COF layers, not substantial bond breakage. These findings suggest that the thermal stability of 2D COFs can be designed rationally by considering these fundamental trends and developing new strategies to tune the mechanics of 2D networks, such as reinforcing layers with secondary non-covalent interactions.[604]

Furthermore, these results should encourage a broader re-evaluation of 2D COF stability. Several instances of COFs being damaged by benign conditions, such as vacuum and mild heating, have now been reported. We suspect that in many cases, COF syntheses may be deemed unsuccessful due to their thermomechanical instability rather than polymerization failure. Moreover, seemingly innocuous isolation, property measurements, or device integration processes may damage the COF structure more is commonly appreciated. Therefore, it is essential that COFs with emergent

properties be structurally characterized in their application-relevant forms (i.e., films, membranes, colloids), ideally both before and after the property of interest is measured. This guideline is even more important when measuring phenomena likely to be sensitive to the regular structure of 2D COFs, including electronic, optical, or magnetic properties. We also hope that this understanding will encourage further investigations into the origin of the amorphization, the intermediate disordered phase, and methods to control thermal stability. These insights will enable future 2D COFs to exhibit useful emergent properties that leverage their precise and designable molecular architectures, while achieving sufficient stability for applications.

6.11. Chapter 6, Supplementary Information

Materials and Instrumentation

Materials

Reagents were purchased from commercial grade suppliers and used without further purification, unless otherwise described. Anhydrous solvents were obtained from a solvent purification system (JC Meyer System).

Instrumentation

Nuclear Magnetic Resonance (NMR) Spectroscopy. ^{1}H and ^{13}C NMR spectra were acquired on a Bruker AvanceIII-500 MHz spectrometer with a CryoProbe 5mm DCH w/ Z-Gradient, or on a 400 MHz Agilent DD MR-400 spectrometer using an AutoX 5mm probe w/ Z-Gradient. All spectra were recorded at 25°C unless specified otherwise. All spectra were calibrated using residual solvent as an internal reference ($CDCl_3$: 7.26 ppm for ^{1}H NMR, 77.00 for ^{13}C NMR; THF-d_8: 3.58, 1.73 ppm for ^{1}H NMR, 67.57, 25.37 ppm for ^{13}C NMR). Data are reported as follows: chemical shift, multiplicity (s = singlet, d = doublet, t = triplet, q = quartet, sep = septet, m = multiplet, *br* = broad, dd = doublet of doublets), coupling constants (Hz), and integration.

High-Resolution Mass Spectrometry (HRMS). High-resolution mass spectra were acquired on an Agilent 6210A LC-TOF Mass Spectrometer, with Atmospheric Pressure Photoionization

(APPI) as an ion source. The instrument is equipped with an Agilent Series 1200 HPLC binary pump and autosampler. All samples were run using direct injection.

Sonication. Sonication was performed with a Branson 3510 ultrasonic cleaner with a power output of 100 W and a frequency of 42 kHz.

Critical Point Dryer. The supercritical drying procedure was performed in Tousimis Samdri795 critical point dryer. Prior to the supercritical drying process, all samples were placed in tea bags (ETS Drawstring Tea Filters, sold by English Tea Store, Amazon.com) and then soaked in absolute ethanol to keep the samples wet (typically 5–15 min). The drying chamber is first cooled ('cool' valve meter set to 0.40), and the tea bags containing the samples were then placed in it, and the chamber is filled with absolute ethanol and then sealed. The chamber was then filled with liquid CO_2 ('fill' valve meter set to 0.40), and after 2 min, the samples were purged for 30 min ('purge-vent' valve meter set to 0.15, and 'purge timer' valve meter set to 6). The temperature was then raised to 40°C resulting in a chamber pressure of around 1300 psi, which is well above the critical point of CO_2. The chamber was held above the critical point for 30 min, after which the CO_2 source was turned off, and the pressure was released over a period of 30 min ('bleed' valve meter set at 0.07). The samples were then transferred to vials and their final mass were weighed.

X-Ray Diffraction. Small- and wide-angle X-ray scattering (SAXS/WAXS) patterns were collected at Argonne National Lab's (ANL) Advanced Photon Source (APS) at sector 5-IDD

(DND-CAT) in a capillary transmission geometry. Experiments conducted at 5-ID-D were collected at a beam energy of 13.3 keV. Experiments were conducted by placing COF powders into capilarries filled with quartz wool. These capillaries then had their sealed ends removed and were connected to a constant flow of argon and placed into a heating block. Individual frames were collected on a set of Pilatus detectors, which were then summed and radially integrated to produce a linear XRD pattern using proprietary software available at the APS. Scattering intensity is reported as a function of the modulus of the scattering vector q, related to the scattering angle 2θ by the equation $q = (4\pi/\lambda) \sin \theta$, where λ is the X-ray wavelength. The sample-to-detector distance was adjusted to measure across relevant detection ranges. Capillary experiments were conducted using 2.0 mm OD borosilicate capillaries with 0.2 mm wall thicknesses purchased from Hilgenberg GmbH.

Variable Temperature X-Ray Diffraction Studies. *In operando* X-ray diffraction was performed at sector 17 of the Advanced Photon Source, Argonne National Laboratory. Samples were prepared by packing ~25 mg of COF sample into a thick-walled Kapton capillary and mounted into a sample holder available at the Sector 17. A thermocouple was then mounted in the center of the powder sample, inside of the Kapton capillary. The sample was then placed under a constant stream of helium and heated at a rate of $10°C•min^{-1}$ under a helium atmosphere. Diffraction patterns were collected over the course of this heating on a 2D Pilatus detector approximately every minute by collecting ten frames per minute and averaging the counts of these ten frames. These frames were then radially integrated to produce 1D diffraction patterns, which were then analyzed.

COF Modeling and Structural Refinement. Crystal modeling of the COF structures was carried out using the Materials Studio (ver. 5.0) suite of programs by Accelrys. The initial structures were S5 constructed piecewise starting with a primitive hexagonal unit cell of a P6 space group. The cell parameter was estimated according to the distance between the center of the vertices for each COF, and c parameter was chosen as 3.35 Å, which has been observed for similar materials. [3] Initially, these structures were estimated to be eclipsed. The structures were optimized using a Geometry Optimization routine including energy minimization with cell parameters optimization, using the parameters from the Universal Force Field. Calculation of the simulated powder diffraction patterns and Pawley refinements were performed in the Materials Studio Reflex Plus Module using a Bragg-Brentano geometry. When the first ~2 features were seen to align but relative intensities were seen to be inconsistent, we assigned this to a non-eclipsed structure. If this was the case, supercells of the crystallites were generated and different stackings (AB, ABC, partial AB, etc. were attempted). The intensity profile which matched most closely was used to refine. In the COFs reported here, eclipsed structures were found to be most consistent with the diffraction patterns obtained here. Prior to refinement of functionalized TAPB-PDA-R COFs, the functionalized R component was assigned to have occupancy at both the 2,5 and 2′,5′ position of the phenyl ring it is attached to, so as to account for its prochirality. The observed diffraction patterns were subjected to a polynomial background subtraction and then to Pawley refinement wherein peak profile were refined using the Pseudo-Voigt peak shape function and asymmetry was corrected using the Berar-Baldinozzi function. Crystallite size was then estimated by the LeBail method which was Pawley refined to the experimental data.

Fourier-Transfer Infrared Spectroscopy (FT-IR). Infrared spectra were collected on a Nicolet iS10 FT-IR spectrometer equipped with a ZnSe crystal in attenuated total reflection mode. Spectra were background subtracted to remove contribution from atmospheric species. Spectra as shown were not corrected or calibrated to any IR feature.

Diffuse Reflectance for Infrared Fourier Transform Spectroscopy (DRIFTS). DRIFTS experiments were conducted on a Thermo-fisher 6700 infrared spectrometer with a Harrick Praying Mantis attachment. Powder samples were loaded into the attachment with a KBr carrier to reduce the optical density of the COF powders. These samples were then heated at 5˚C•min^{-1} under a constant argon flow with constant monitoring of their infrared spectra.

Thermal Gravimetric Analysis (TGA). Thermogravimetric analysis (TGA) was performed on a Netzch Simultaneous Thermal Analysis (STA) system using approximately 5 mg of sample. The samples were heated to a designated temperature at a rate of 10°C•min^{-1} under a helium atmosphere.

Nitrogen Sorption Measurements. Gas sorption isotherms were conducted on a Micromeritics ASAP 2420 Accelerated Surface Area and Porosity Analyzer. Typically, 20-40 mg samples were transferred to dried and tared analysis tubes and capped with a Transeal. The samples were heated to 40°C at a rate of 1°C•min^{-1} and evacuated at 40°C for 20 min, then heated to 100°C at a rate of

1°C•min^{-1} heat, and evacuated at 100°C until the outgas rate was ≤0.4 μmHg•min^{-1}, at which point the tube was weighed again to determine the mass of the activated sample. The tube was then transferred to the analysis port of the instrument. UHP-grade (99.999% purity) N_2 was used for all adsorption measurements. N_2 isotherms were generated by incremental exposure to nitrogen up to 760 mmHg (1 atm) in a liquid nitrogen (77 K) bath. Oil-free vacuum pumps and oil-free pressure regulators were used for all measurements. Brunauer-Emmett-Teller (BET) surface areas were calculated from the linear region of the N_2 isotherm at 77 K within the pressure range P/P_0 of 0.05-0.10.

Density Functional Theory (DFT) Calculations. First-principles density functional theory (DFT) calculations were performed using the periodic *ab initio* code CRYSTAL17.[558] The PBE exchange-correlation functional was used with a semi-classical dispersion correction (PBE-D3) to better account for the noncovalent interactions present in the 2D COF structures.[559, 560] The dispersion correction included a pairwise and three-body Becke-Johnson (BJ) damping-function.[560] Each of the DFT calculations was performed with all-electron atom-centered Gaussian-type basis sets of triple-zeta quality, similar to our previous work.[605-607]

The all-electron basis sets contained a total of 1,848 and 2,232 basis functions, corresponding to 522 and 618 electrons spread over 972 and 1,188 shells per unit cell for TAPB-PDA and TAPB-PDA-Et respectively. The lattice parameters and atomic coordinates were optimized using a quasi-Newtonian algorithm[562-566] while initially maintaining the space group symmetry (*P6*) and then reducing the symmetry (*P1*) after scanning the resultant vibrational modes. The presence of imaginary modes when performing the DFT vibrational frequency calculations with *P6* symmetry

would indicate that the crystallographic space group symmetry for TAPB-PDA and TAPB-PDA-Et may be reduced from the idealized *P6* space group, primarily when negating thermal effects. However, the size of the basis sets and number of radial and angular points defined for the integration grid have been reported to have an impact on the imaginary nature of the soft modes, and an in-depth analysis is out with the scope of the current work. Therefore, to obtain structural insight into the deformed structures, we analyzed the geometrical changes along the trajectory of the phonon modes, and allowing for the associated symmetry reduction relaxed the resultant geometries.

The infrared (IR) absorption spectra of TAPB-PDA and TAPB PDA-Et are reported in Figure S105. The IR intensities were computed through the Berry Phase approach, by evaluating the Born atomic tensors as polarization differences between the original and the distorted geometries.[570] In the range of 650–3500 cm^{-1}, the spectral features did not change significantly in either position or intensity and are in excellent agreement with experiment data. Therefore, the vibrational modes involved do not appear to be substantially affected by the change from the high symmetry planar phase to the deformed low symmetry phase.

Synthetic Procedures

Scheme 6.1. Synthesis of 2-(2-azido-ethoxy)-ethanol (S1).

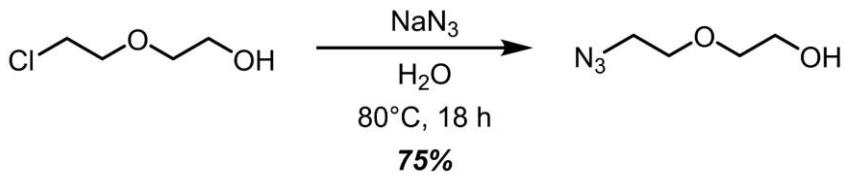

Synthesis of 2-(2-azido-ethoxy)-ethanol.

2-(2-azido-ethoxy)-ethanol was synthesized *via* slight modifications of literature procedures. All spectroscopic data is consistent with what has previously been reported.[608, 609]

To a 500 mL flame-dried round bottom flask, a solution of 2-(2-chloro-ethoxy)-ethanol (35.4 g, 284 mmol) in deionized H_2O (180 mL) and NaN_3 (46.2 g, 710 mmol, 2.5 equiv) were added. The reaction mixture was stirred at 80°C under a nitrogen atmosphere for 18 h then poured into a NaOH solution (5% (*w/v*), 300 mL) and extracted with diethyl ether (5 × 300 mL). The organic layer was dried over $MgSO_4$ and evaporated to dryness to afford **S1** (27.7 g, 75%) as a colorless oil. All spectroscopic data is consistent with what has previously been reported.

Scheme 6.2. Synthesis of 2-(2-azido-ethoxy)-ethyl-4-methylbenzenesulfonate (**S2**).

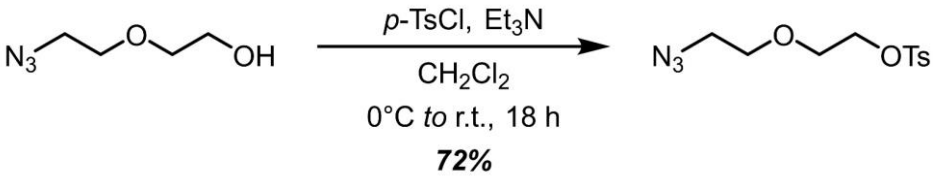

Synthesis of 2-(2-azido-ethoxy)-ethyl-4-methylbenzenesulfonate.

Synthesis of 2-(2-azido-ethoxy)-ethyl-4-methylbenzenesulfonate was prepared *via* slight modifications of literature procedures. All spectroscopic data is consistent with what has previously been reported. [608, 609]

To a 1000 mL flame-dried round bottom flask, a solution of 2-(2-azido-ethoxy)-ethanol (**S1**, 20.0 g, 153 mmol) in dry CH_2Cl_2 (600 mL) and Et_3N (27 mL, 184 mmol, 1.5 equiv) were added. The reaction mixture was cooled to 0 ˚C and *p*-TsCl (34.8 g, 184 mmol, 1.2 equiv) was added. The solution was stirred at 0°C for 1 h, allowed to warm to room temperature and stirred for another 17 h under a nitrogen atmosphere. The solution was washed with $NaHCO_3$ (3 × 800 mL), H_2O (3 x 800 mL), and brine (3 × 800 mL), dried over $MgSO_4$, and evaporated to dryness to afford **S2** (31.3 g, 72%) as a colorless oil. All spectroscopic data is consistent with what has previously been reported.

Scheme 6.3. Synthesis of 2,5-hydroxy-1,4-dibenzaldehyde **(S3)**.

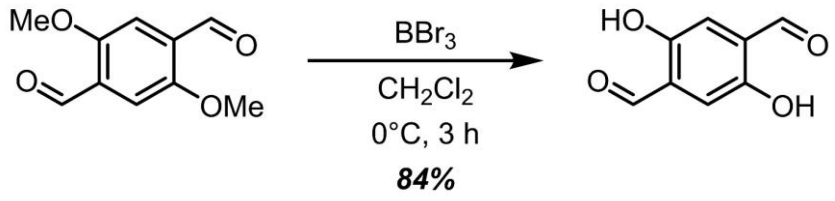

Synthesis of 2,5-hydroxy-1,4-dibenzaldehyde.

Synthesis of 2,5-hydroxy-1,4-dibenzaldehyde was prepared *via* slight modifications of literature procedures. All spectroscopic data is consistent with what has previously been reported.[609, 610]

To a flame-dried 250 mL round bottom flask, a solution of 2,5-dimethoxy-1,4-dibenzaldehyde (3.0 g, 15 mmol) in dry CH_2Cl_2 (100 mL) was added. The reaction mixture was cooled to 0°C and BBr_3 (1.0 M in CH_2Cl_2, 42 mL) was added dropwise. The solution was stirred at 0°C for 3 h and diluted with H_2O (150 mL), and the organic layer was separated. The aqueous layer was extracted with hot EtOAc (3 × 120 mL) and the combined organic layer was dried over $MgSO_4$, filtered, and evaporated to dryness. Recrystallization from boiling EtOAc afforded **S3** (2.2 g, 84%) as orange crystals. All spectroscopic data is consistent with what has previously been reported.

Scheme 6.4. Synthesis of Azide Modified Terephthalaldehyde (**S4**).

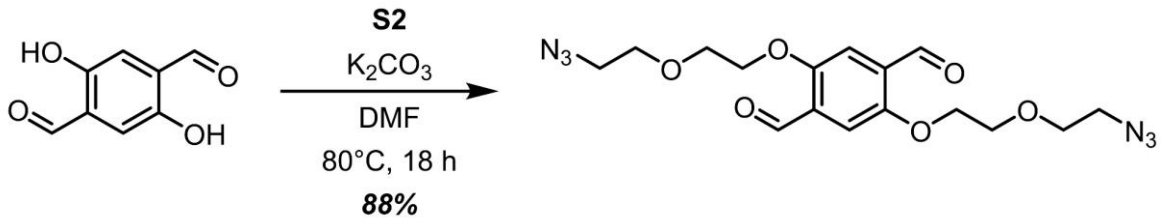

Synthesis of Azide Modified Terephthalaldehyde.

The azide modified terephthalaldehyde was prepared *via* a reported procedure.[609]

To a flame-dried 1000 mL round bottom flask, a solution of 2,5-hydroxy-1,4-dibenzaldehyde (S3, 4.0 g, 24 mmol) and 2-(2-azido-ethoxy)-ethyl-4-methylbenzenesulfonate (S2, 16.4 g, 57 mmol, 2.4 equiv) in dry DMF (400 mL) was added, followed by K_2CO_3 (26.0 g, 193 mmol). The reaction mixture was stirred at 80°C for 18 h, diluted with water (1000 mL), and extracted with hot EtOAc (5 × 600 mL). The combined organic layer was dried over MgSO4, filtered, and evaporated to dryness. Silica gel column chromatography (SiO_2, Hex/EtOAc = 3/2) afforded **S4** (8.2 g, 88%) as yellow crystals.

^{1}H NMR (500 MHz, $CDCl_3$) δ 10.51 (s, 2H), 7.46 (s, 2H), 4.28-4.26 (m, 4H), 3.90-3.88 (m, 4H), 3.73-3.71 (t, *J* = 4.9 Hz, 4H), 3.40-3.38 (t, *J* = 5.0Hz, 4H) ppm.

^{13}C NMR (126 MHz, $CHCl_3$) δ 189.11, 155.10, 129.48, 112.17, 70.34, 69.45, 68.76, 50.65 ppm.

HRMS calculated for $[C_{16}H_{20}NaN_6O_6Na]^+$ 415.1337, found: 415.1348.

Scheme 6.5. Synthesis of 2,5-dibromoterephthalaldehyde (**S5**).

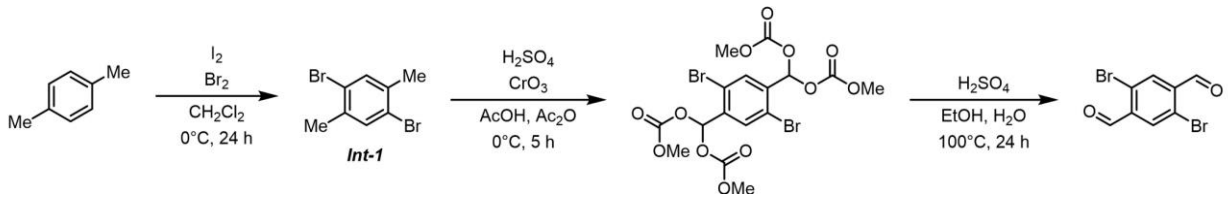

Synthesis of 2,5-dibromoterephthalaldehyde.

2,5-dibromoterephthalaldehyde was prepared *via* the reported synthesis described below. All spectroscopic data is consistent with what has previously been reported.[611]

Bromine (2.05 equiv) was added dropwise over the course of 30 min to an ice-cold solution of *p*-xylene (1.00 equiv) and iodine (0.008 equiv). Caution was taken to exclude light from the reaction mixture during this process. After stirring for 24 h at room temperature, 20% KOH was added to the solution and the reaction was allowed to equilibrate back to room temperature. The aqueous solution was decanted, and the remaining residue was recrystallized from EtOH (3×) to yield ***Int-1***.

To a suspension of ***Int-1*** (8.0 g) in AcOH (40 mL) and Ac_2O (80 mL) was added H_2SO_4 (28 mL) at 0°C. CrO_3 (12 g) was then added to the reaction mixture in portions. After complete addition of CrO_3 the resulting mixture was vigorously stirred at 0°C for 5 h. The green slurry was then poured into ice water and filtered. The collected white solid (diacetate) was washed with water and cold MeOH.

The diacetate was then hydrolyzed by refluxing with a mixture of water (40 mL), EtOH (40 mL), and sulfuric acid (4 mL) for 5 h. After the mixture had cooled, the pale-yellow solid was isolated *via* filtration. This crude product was purified *via* recrystallization from chloroform to yield pure **S5**.

Scheme 6.6. Synthesis of 2,5-dimethylterephthalaldehyde (**S6**).

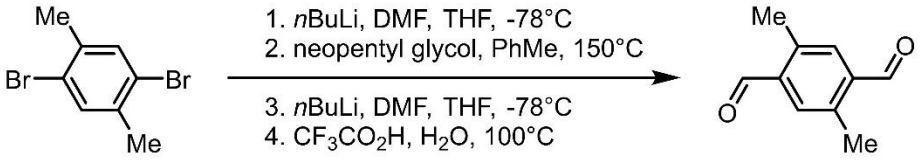

Synthesis of 2,5-dimethylterephthalaldehyde.

2,5-dimethylterephthalaldehyde was prepared *via* a reported literature procedure.[612] All spectroscopic data is consistent with what has previously been reported.[612, 613]

In a Schlenk flask, 1,4-dibromo-2,5-dimethylbenzene (A, 18.00 g, 68.19 mmol) was dissolved in dry THF (200 mL) under N_2 and cooled to -78°C. *n*BuLi (2.5 M in hexanes, 30 mL, 75.0 mmol) was added dropwise via cannula. The mixture was allowed to stir at -78°C for 15 min before dry DMF (11 mL) was added. The reaction was allowed to warm to rt while stirring for 2 h, after which it was charged with concentrated HCl. The mixture was extracted with Et_2O two times, and the combined organic layers were washed with brine, dried over MgSO4, and concentrated under reduced pressure. The residue was used without further purification and was refluxed overnight in a Dean-Stark apparatus with toluene (130 mL), neopentyl glycol (14.2 g), and *p*-TsOH (2.42 g). The mixture was washed with a saturated $NaHCO_3$ solution, water, brine, and dried over $MgSO_4$ before concentration under reduced pressure. The residue was treated a second time as described above with the same amounts of *n*BuLi and DMF under the same conditions (the protection using neopentyl glycol was not repeated). After isolation, the product was refluxed in water (16 mL) and

TFA (120 mL) for 15 min. The mixture was concentrated under reduced pressure and charged with CH_2Cl_2. It was then washed with saturated $NaHCO_3$ solution, brined, dried over $MgSO_4$, and concentrated under reduced pressure. The resulting liquid (which was a saturated solution of PDA-Me in residual DMF) was placed in a freezer overnight. The resulting **S6** precipitate was isolated *via* filtration and washed with hexanes. Isolated yield of **S6**: 3.34 g (30.2%).

^{1}H NMR (500 MHz, $CDCl_3$) δ 10.33 (s, 2H), 7.69 (s, 2H), 2.69 (s, 6H) ppm.

^{13}C NMR (125 MHz, $CDCl_3$) δ 192.34, 138.30, 137.06, 134.84, 18.95 ppm.

Scheme 6.7. Synthesis of 2,5-ethylterephthalaldehyde (**S7**).

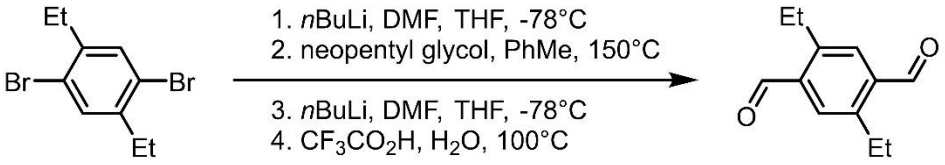

Synthesis of 2,5-ethylterephthalaldehyde.

2,5-diethylterephthalaldehyde was prepared *via* a reported literature procedure.[612]All spectroscopic data is consistent with what has previously been reported.[612]

In a Schlenk flask, 1,4-dibromo-2,5-diethylbenzene (10.00 g, 34.2 mmol) was dissolved in dry THF (100 mL) under N_2 and cooled to -78°C. *n*BuLi (2.5 M in hexanes, 15 mL, 37.5 mmol) was added dropwise via cannula. The mixture was allowed to stir at -78°C for 15 min before dry DMF (6 mL) was added. The reaction was allowed to warm to rt while stirring for 2 h, after which it was charged with concentrated HCl. The mixture was extracted with Et_2O two times, and the combined organic layers were washed with brine, dried over MgSO4, and concentrated under reduced pressure. The residue was used without further purification and was refluxed overnight in a Dean-Stark apparatus with toluene (65 mL), neopentyl glycol (7.13 g), and *p*-TsOH (1.21 g). The mixture was washed with a saturated $NaHCO_3$ solution, water, brine, and dried over $MgSO_4$ before concentration under reduced pressure. The residue was treated a second time as described above with the same amounts of *n*BuLi and DMF under the same conditions (the protection using neopentyl glycol was not repeated). After isolation, the product was refluxed in water (8 mL) and

TFA (65 mL) for 15 min. The mixture was concentrated under reduced pressure and charged with CH_2Cl_2. It was then washed with saturated $NaHCO_3$ solution, brined, dried over $MgSO_4$, and concentrated under reduced pressure. The resulting liquid (which was a saturated solution of PDA-Et in residual DMF) was placed in a freezer overnight. The resulting **S7** precipitate was isolated *via* filtration and washed with hexanes. Isolated yield of **S7**: 1.98 g (30.4%).

^{1}H NMR (500 MHz, $CDCl_3$) δ 10.36 (s, 2H), 7.75 (s, 2H), 3.10 (q, 4H), 1.30 (t, 6H) ppm.

^{13}C NMR (125 MHz, $CDCl_3$) δ 191.12, 144.73, 136.87, 132.93, 25.19, 16.35 ppm.

Scheme 6.8. Synthesis of 2,5-bis(methylthio)terephthaldehyde (**S8**).

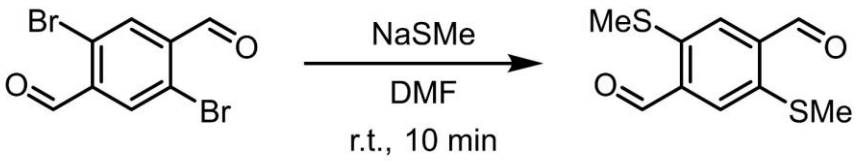

Synthesis of 2,5-bis(methylthio)terephthaldehyde.

2,5-bis(methylthio)terephthaldehyde was prepared *via* a reported procedure. All spectroscopic data is consistent with what has previously been reported.[614]

To a solution of 2,5-dibromoterephthalaldehyde (synthesis previously described) (1.00 equiv) in DMF was added sodium methanethiolate (2.35 equiv), and the resulting mixture was stirred at room temperature for 10 min. The mixture was poured into diluted HCl (*c.a.* 1 M), and extracted into $CHCl_3$ (3×). The combined organic layers were washed with water and brine, dried over $MgSO_4$, and concentrated *in vacuo*. The crude solid was then purified *via* column chromatography (SiO_2, CH_2Cl_2) to yield **S8** as a pale orange solid. All spectroscopic data is consistent with what has previously been reported.

Scheme 6.9. Synthesis of benzophenoneimine of benzidine (BND) (**S9**).

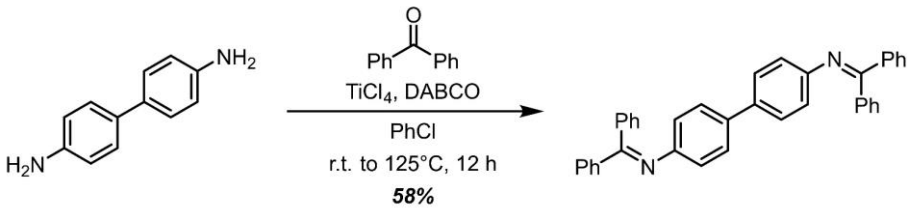

Synthesis of the benzophenoneimine of benzidine.

The benzophenoneimine of benzidine was prepared *via* a reported procedure. All spectroscopic data is consistent with what has previously been reported.[411]

To a 500mL flame-dried round-bottom flask, benzidine (1.70 g, 9.25 mmol), benzophenone (3.37 g, 18.50 mmol, 1.0 equiv per NH2 funcionality), 1,4- diazobicyclo[2.2.2]octane (DABCO) (6.23 g, 55.50 mmol, 6.0 equiv), and PhCl (100 mL) were added and the contents were stirred at room temperature under a nitrogen atmosphere. Titanium(IV) chloride (1.52 mL, 13.88 mmol, 1.5 equiv) was syringed in portions over 15 min (1/4 of the portion at times 0 min, 5 min, 10 min, and 15 min). After the addition was complete, the reaction mixture was stirred for another 20 min at room temperature, then the flask was equipped with a reflux condenser, and the reaction stirred at 125°C overnight (12 h). The reaction mixture was then cooled to about 40°C, and filtered while warm through a Buchner funnel equipped with a filter paper. The filtrate was then concentrated in vacuo, and the crude product (3.89 g) was purified by stirring in a mixture of hot EtOH and $CHCl_3$ (3:1, 400 mL), preforming a hot filtration through a cotton-plugged plastic funnel, and allowing the filtrate to slowly cool to room temperature, at which point the product started to crystallize. The

flask was then put in the fridge overnight to induce further crystallization. The solid was then collected via filtration to yield **S9** (2.74 g, 58%) as a yellow/orange solid.

^{1}H NMR (500 MHz, $CDCl_3$) δ 7.76 – 7.70 (m, 4H), 7.47 – 7.41 (m, 2H), 7.38 (dd, J = 8.3, 6.7 Hz, 4H), 7.33 – 7.29 (m, 4H), 7.28 – 7.20 (m, 6H), 7.15 – 7.08 (m, 4H), 6.78 – 6.68 (m, 4H) ppm.

^{13}C NMR (126 MHz, $CDCl_3$) δ 168.11, 150.02, 139.71, 136.25, 135.39, 130.66, 129.50, 129.30, 128.58, 128.16, 128.02, 127.97, 126.55, 121.45 ppm.

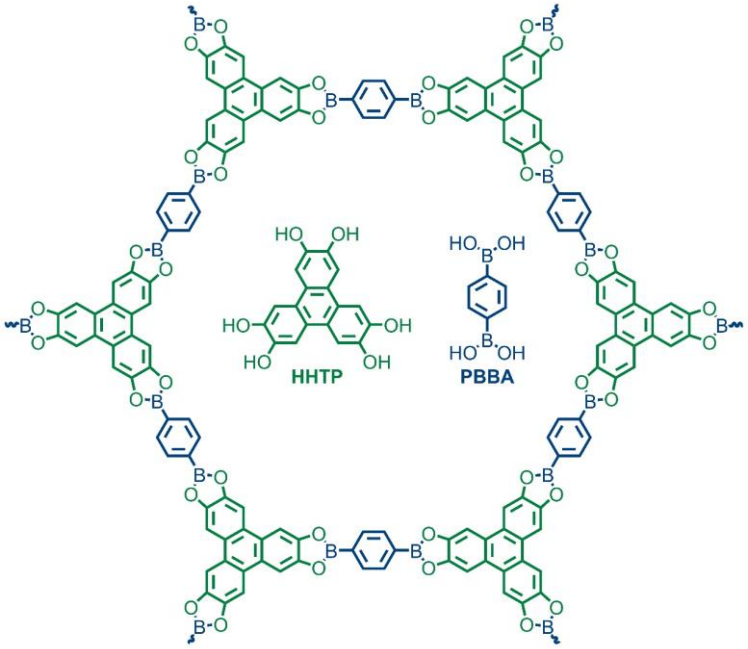

Figure 6.8. Structure of HHTP-PBBA COF and the monomers from which it is constructed.

Scheme 6.10. Synthesis of HHTP-PBBA COF (COF-5).

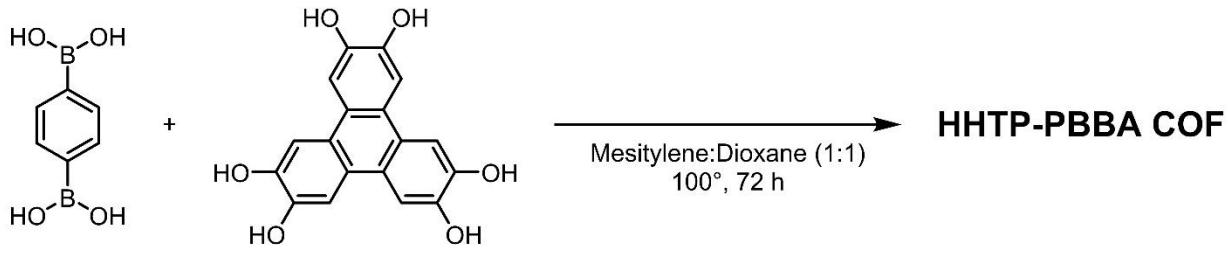

Synthesis of the HHTP-PBBA COF.

HHTP-PBBA COF was prepared *via* a slight modification of a reported literature procedure.[615]

A 20 mL scintillation vial was charged with 1,4-benzene-bisboronic acid (PBBA) (1.5 equiv), 2,3,6,7,10,11-hexahydroxytriphenylene (HHTP) (1.0 equiv), and a mesitylene:dioxane solution (1:1 *v*/*v*). The reaction mixture was heated at 100°C for 72 h to yield a free-flowing gray-purple powder. After 72 h, the reaction was cooled to room temperature and the resulting powder was isolated *via* filtration. The crude material was washed with copious amounts of anhydrous acetone before being dried again under high vacuum.

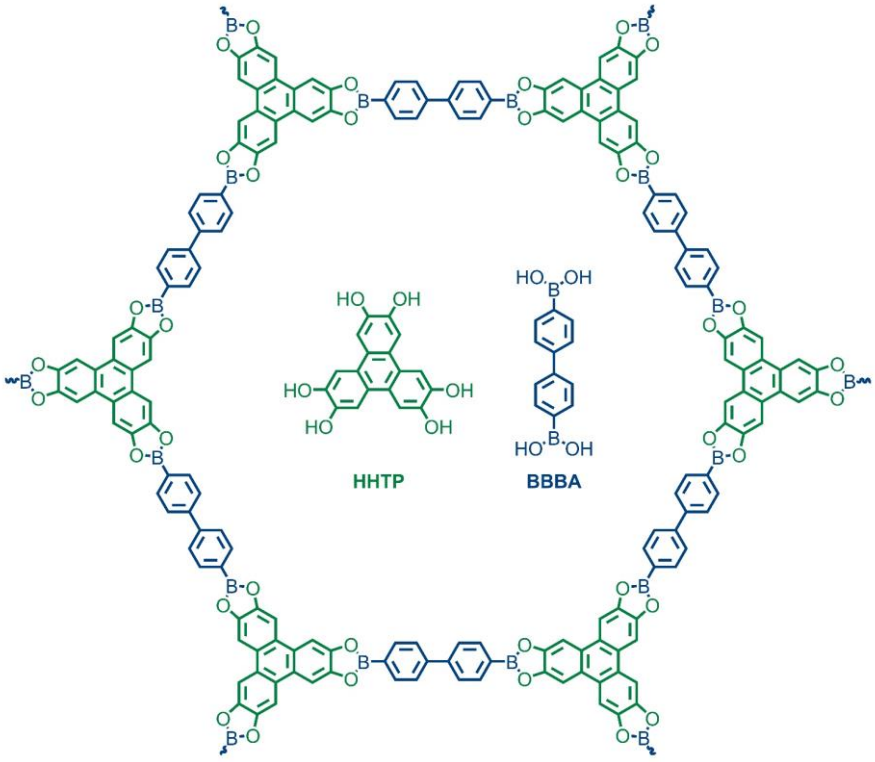

Figure 6.9. Structure of HHTP-BBBA COF and the monomers from which it is constructed.

Scheme 6.11. Synthesis of HHTP-BBBA COF (COF-10).

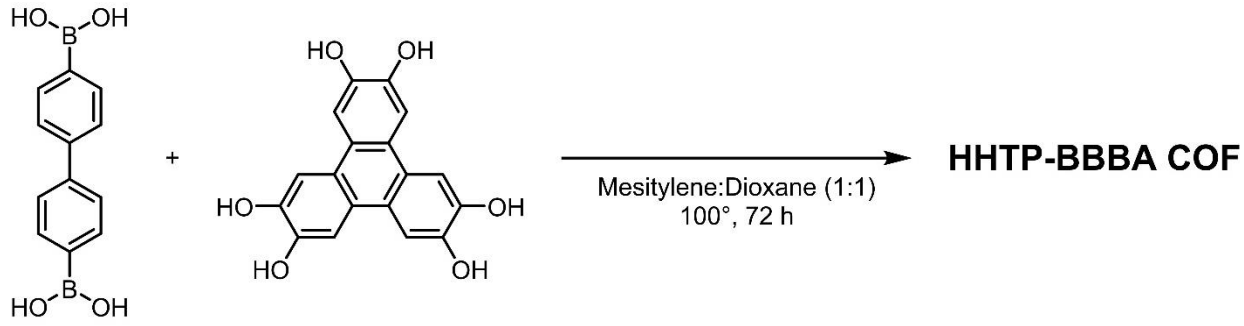

Synthesis of the HHTP-BBBA COF.

HHTP-BBBA COF was prepared *via* a slight modification of a reported literature procedure.[615]

A 20 mL scintillation vial was charged with 1,4-biphenyl-bisboronic acid (BBBA) (1.5 equiv), 2,3,6,7,10,11-hexahydroxytriphenylene (HHTP) (1.0 equiv), and a mesitylene:dioxane solution (1:1 *v*/*v*). The reaction mixture was heated at 100°C for 72 h to yield a free-flowing gray-purple powder. After 72 h, the reaction was cooled to room temperature and the resulting powder was isolated *via* filtration. The crude material was washed with copious amounts of anhydrous acetone before being dried again under high vacuum.

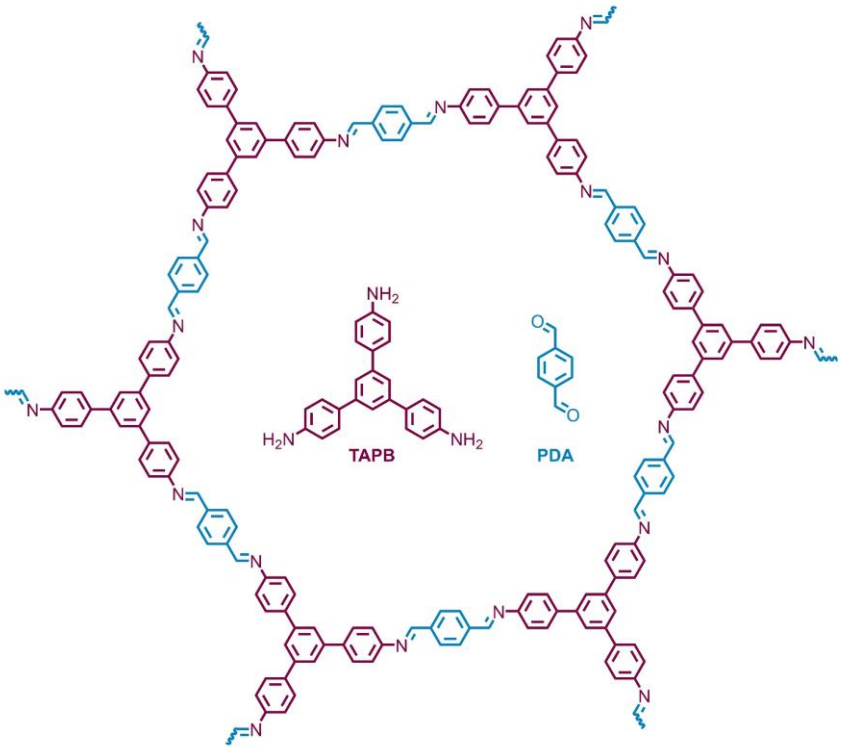

Figure 6.10. Structure of TAPB-PDA- COF and the monomers from which it is constructed.

Scheme 6.12. Synthesis of TAPB-PDA- COF.

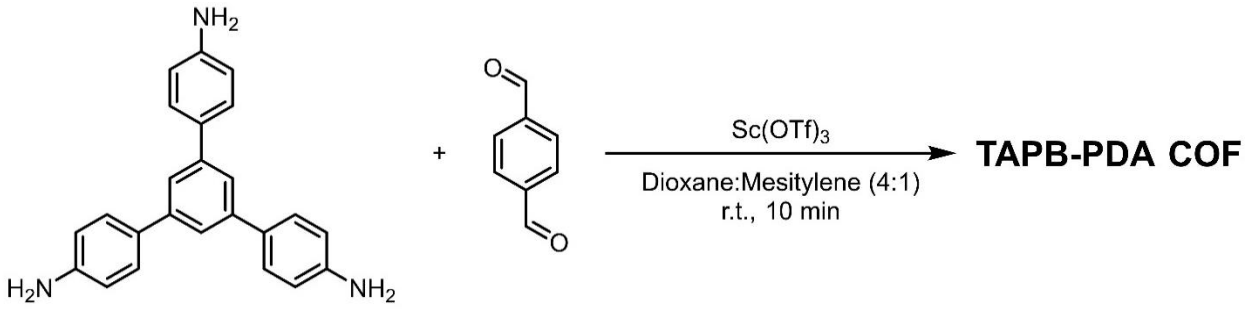

Synthesis of TAPB-PDA COF.

TAPB-PDA COF was prepared *via* a reported literature procedure.[612, 616, 617]

A 20 mL scintillation vial was charged with 1,3,5-tris(4-aminophenyl)benzene (1.0 equiv), terephthalaldehyde (1.5 equiv). A 1,4-dioxane/mesitylene solution (4:1 v/v) was added, and the resulting suspension was sonicated at room temperature until the monomers were fully dissolved. Scandium(III) trifluoromethanesulfonate (0.018 equiv) was added, and the resulting suspension was sonicated briefly. The vial was closed with a plastic cap for 10 min. The reaction mixture was transferred to a container and while wet, precipitates were activated by Soxhlet extraction using CH_3OH for 12 h, followed by supercritical CO_2 drying.

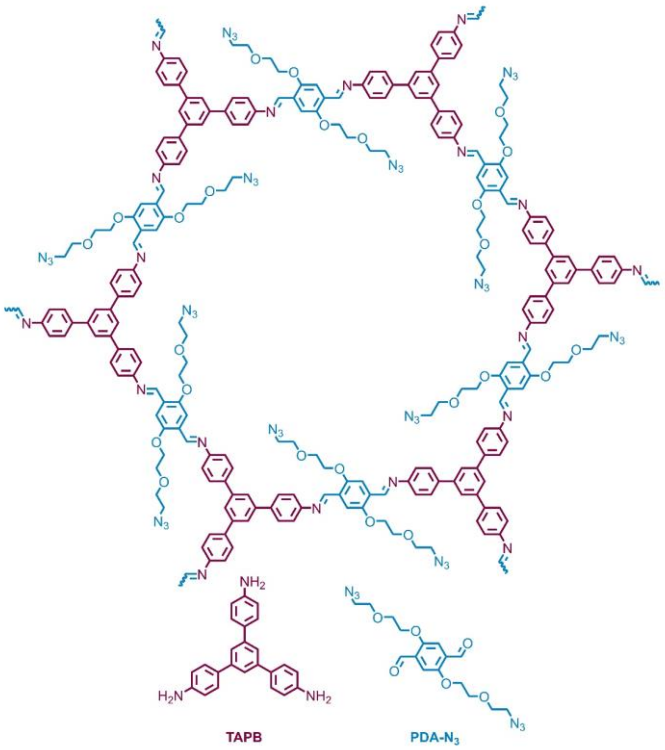

Figure 6.11. Structure of TAPB-PDA-N_3 COF and the monomers from which it is constructed.

Scheme 6.13. Synthesis of TAPB-PDA-N_3 COF.

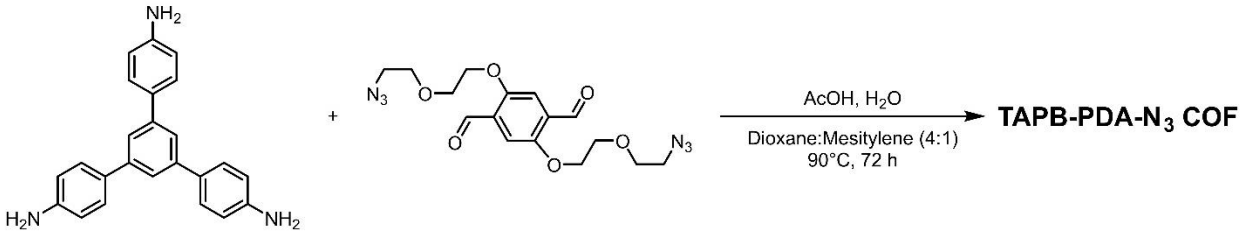

Synthesis of TAPB-PDA-N_3 COF.

TAPB-PDA-N_3 COF was prepared *via* a reported literature procedure.[609]

A 20 mL scintillation vial was charged with 1,3,5-tris(4-aminophenyl)benzene (105 mg, 0.3 mmol) and PDA-N_3 (0.45 mmol). A 1,4-dioxane/mesitylene solution (4:1 *v/v*) was added, and the

resulting suspension was sonicated at room temperature until the monomers were fully dissolved. Glacial AcOH (3.6 mL) and H_2O (2.4 mL) were added, and the resulting solution was heated at 90°C for 72 h. The reaction mixture was transferred to a tea bag and washed with methanol in a Soxhlet extractor for 18 h. The material was then activated by supercritical CO_2 followed by drying under vacuum at room temperature for 5 h that afforded the TAPB-PDA-N_3 COF (200 mg, 75%) as a yellow solid.

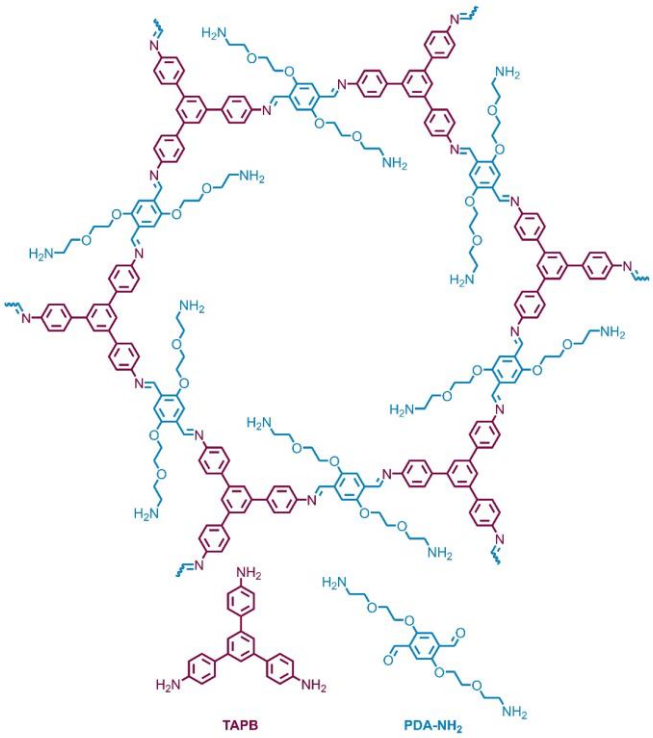

Figure 6.12. Structure of TAPB-PDA-NH_2 COF and the monomers from which it is constructed.

Scheme 6.14. Synthesis of TAPB-PDA-NH_2 COF.

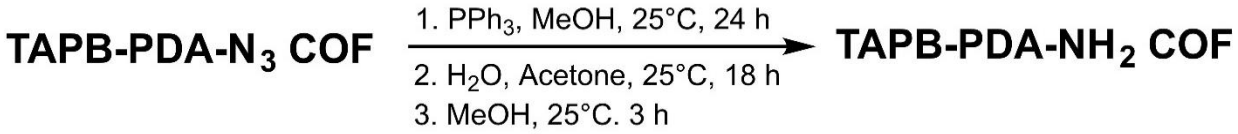

Synthesis of TAPB-PDA-NH_2 COF.

TAPB-PDA-NH_2 COF was prepared *via* a reported literature procedure.[609]

To a flame-dried 25 mL round bottom flask, a suspension of TAPB-PDA-N_3 COF (100 mg, 0.34 mmol by imine) in dry CH_3OH (10 mL) was added, followed by PPh_3 (1.3 g, 5.1 mmol, 15 equiv).

After 24 h at 25°C, the suspension was filtered in a tea bag and immersed in 4% (*v/v*) H_2O in acetone for 18 h and in methanol for 3 h. The material was subjected to the supercritical CO_2 drying followed by the vacuum drying at room temperature for 5 h that afforded TAPB-PDA-NH_2 COF (89 mg, 97%) as a yellow solid.

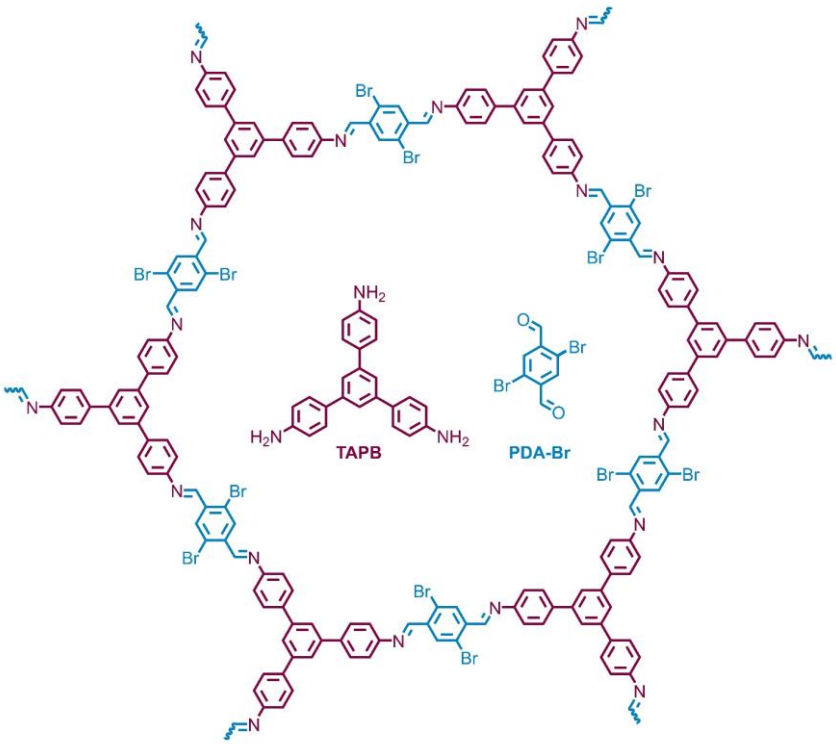

Figure 6.13. Structure of TAPB-PDA-Br COF and the monomers from which it is constructed.

Scheme 6.15. Synthesis of TAPB-PDA-Br COF.

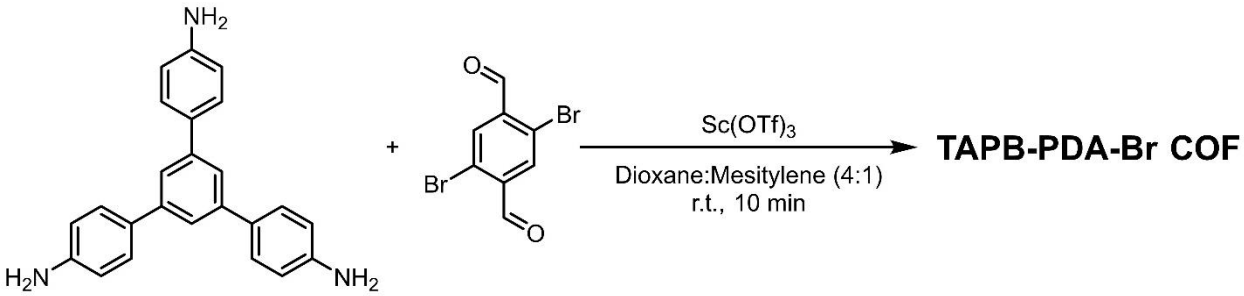

Synthesis of TAPB-PDA-Br COF.

TAPB-PDA-Br COF was prepared *via* a slight modification of a reported literature procedure.[616]

A 20 mL scintillation vial was charged with 1,3,5-tris(4-aminophenyl)benzene (1.0 equiv), 2,5-dibromoterephthalaldehyde (1.5 equiv). A 1,4-dioxane/mesitylene solution (4:1 v/v) was added, and the resulting suspension was sonicated at room temperature until the monomers were fully dissolved. Scandium(III) trifluoromethanesulfonate (0.018 equiv) was added, and the resulting suspension was sonicated briefly. The vial was closed with a plastic cap for 10 min. The reaction mixture was transferred to a container and while wet, precipitates were activated by Soxhlet extraction using CH_3OH for 12 h, followed by supercritical CO_2 drying.

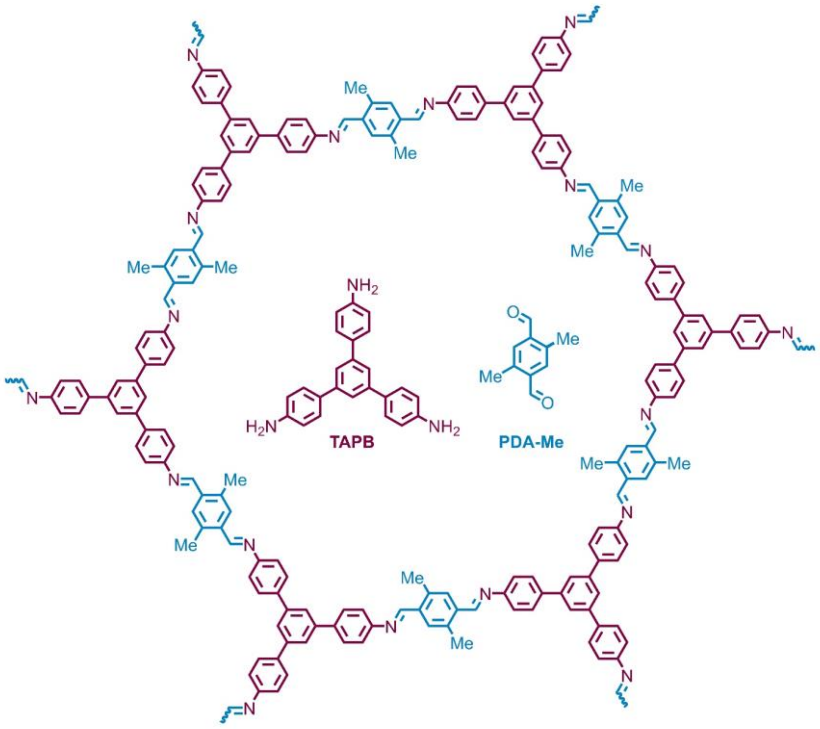

Figure 6.14. Structure of TAPB-PDA-Me COF and the monomers from which it is constructed.

Scheme 6.16. Synthesis of TAPB-PDA-Me COF.

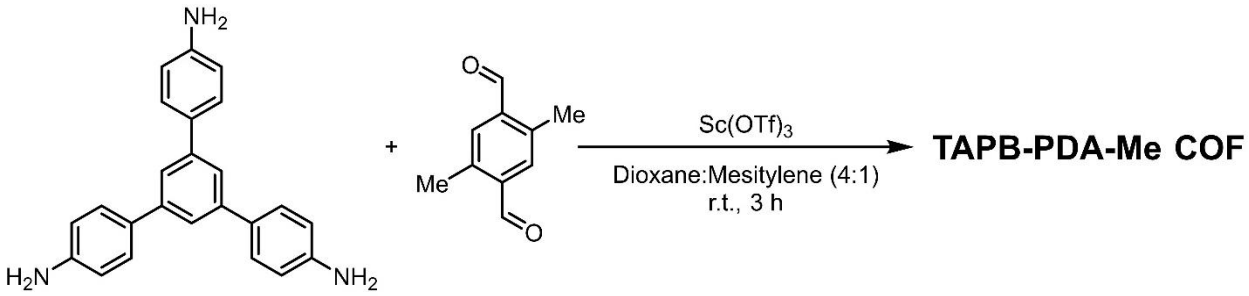

Synthesis of TAPB-PDA-Me COF.

TAPB-PDA-Me COF was prepared *via* a reported literature procedure.[612, 616]

A 20 mL scintillation vial was charged with 1,3,5-tris(4-aminophenyl)benzene (1.0 equiv), 2,5-bis(methylthio)terephthalaldehyde (1.5 equiv). A 1,4-dioxane/mesitylene solution (4:1 v/v) was added, and the resulting suspension was sonicated at room temperature until the monomers were fully dissolved. Scandium(III) trifluoromethanesulfonate (0.018 equiv) was added, and the resulting suspension was sonicated briefly. The vial was closed with a plastic cap for 3 h. The reaction mixture was transferred to a container and while wet, precipitates were activated by Soxhlet extraction using CH_3OH for 12 h, followed by supercritical CO_2 drying.

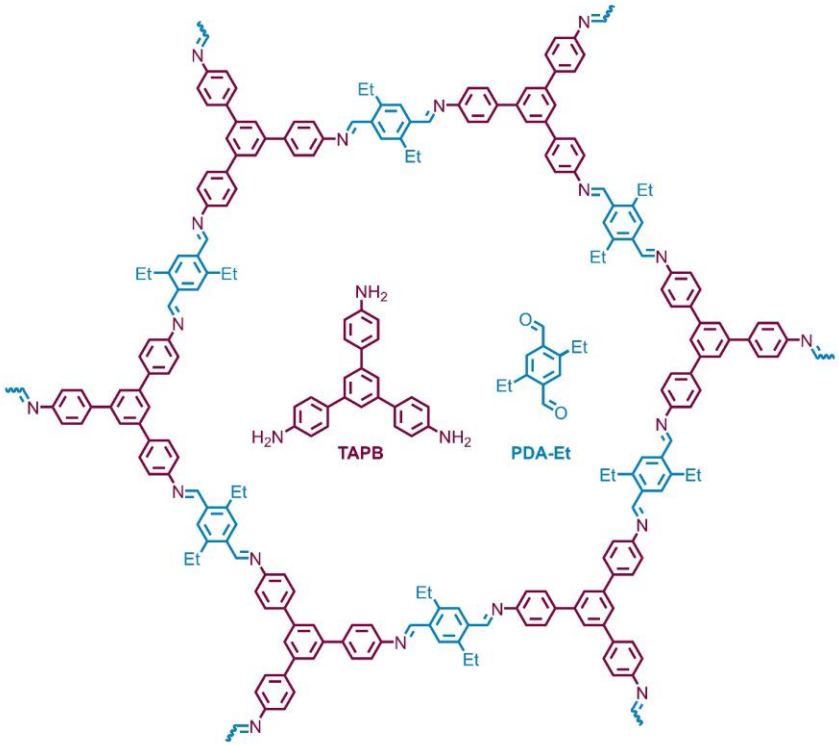

Figure 6.15. Structure of TAPB-PDA-Et COF and the monomers from which it is constructed.

Scheme 6.17. Synthesis of TAPB-PDA-Et COF.

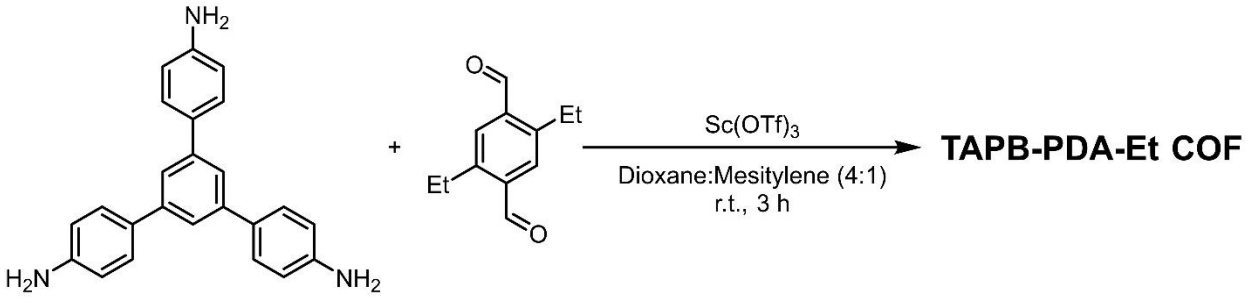

Synthesis of TAPB-PDA-Et COF.

TAPB-PDA-Et COF was prepared *via* a reported literature procedure.[612, 616]

A 20 mL scintillation vial was charged with 1,3,5-tris(4-aminophenyl)benzene (1.0 equiv), 2,5-bis(methylthio)terephthalaldehyde (1.5 equiv). A 1,4-dioxane/mesitylene solution (4:1 v/v) was added, and the resulting suspension was sonicated at room temperature until the monomers were fully dissolved. Scandium(III) trifluoromethanesulfonate (0.018 equiv) was added, and the resulting suspension was sonicated briefly. The vial was closed with a plastic cap for 3 h. The reaction mixture was transferred to a container and while wet, precipitates were activated by Soxhlet extraction using CH_3OH for 12 h, followed by supercritical CO_2 drying.

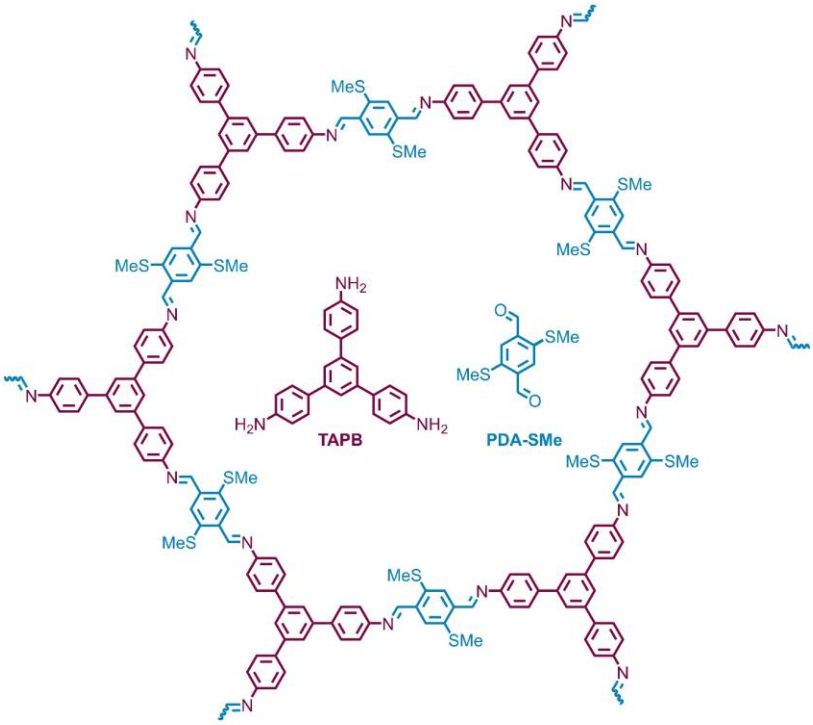

Figure 6.16. Structure of TAPB-PDA-SMe COF and the monomers from which it is constructed.

Scheme 6.18. Synthesis of TAPB-PDA-SMe COF.

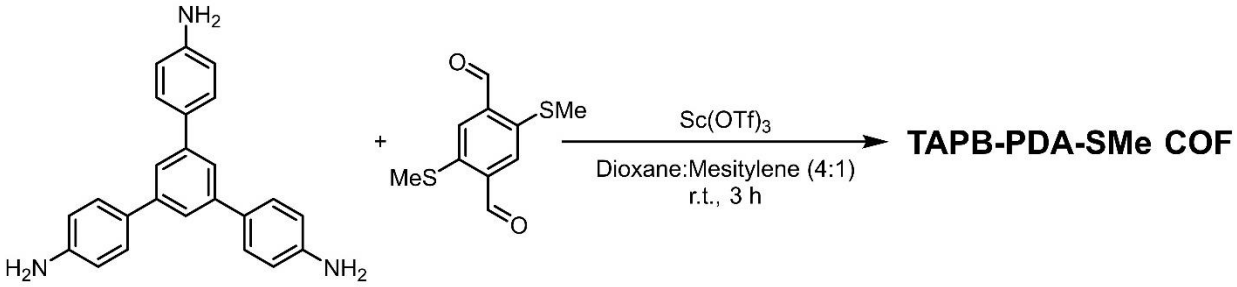

Synthesis of TAPB-PDA-SMe COF.

TAPB-PDA-SMe COF was prepared *via* a slight modification of a reported literature procedure.[612, 616]

A 20 mL scintillation vial was charged with 1,3,5-tris(4-aminophenyl)benzene (1.0 equiv), 2,5-bis(methylthio)terephthalaldehyde (1.5 equiv). A 1,4-dioxane/mesitylene solution (4:1 v/v) was added, and the resulting suspension was sonicated at room temperature until the monomers were fully dissolved. Scandium(III) trifluoromethanesulfonate (0.018 equiv) was added, and the resulting suspension was sonicated briefly. The vial was closed with a plastic cap for 3 h. The reaction mixture was transferred to a container and while wet, precipitates were activated by Soxhlet extraction using CH_3OH for 12 h, followed by supercritical CO_2 drying.

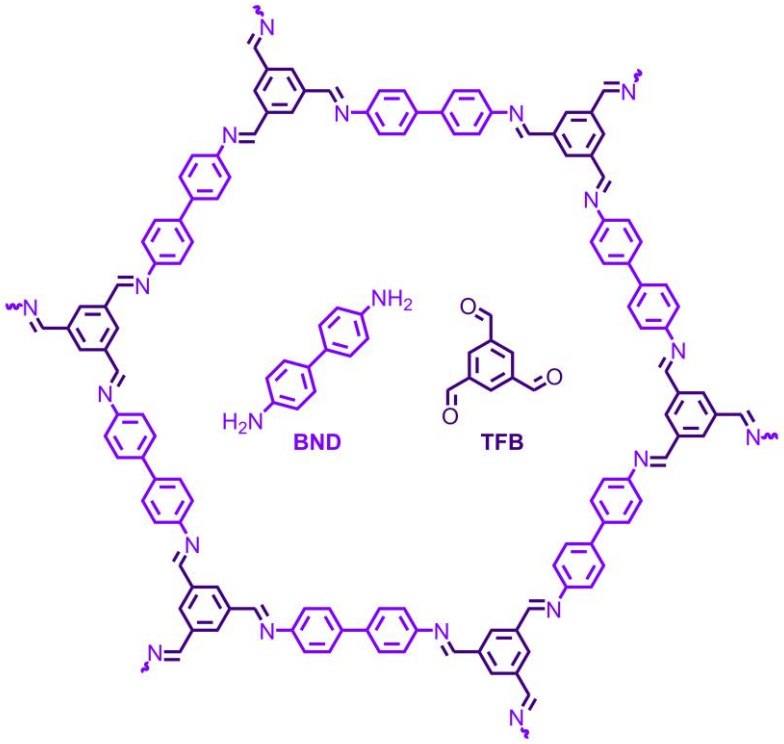

Figure 6.17. Structure of BND-TFB COF and the monomers from which it is constructed.

Scheme 6.19. Synthesis of BND-TFB COF.

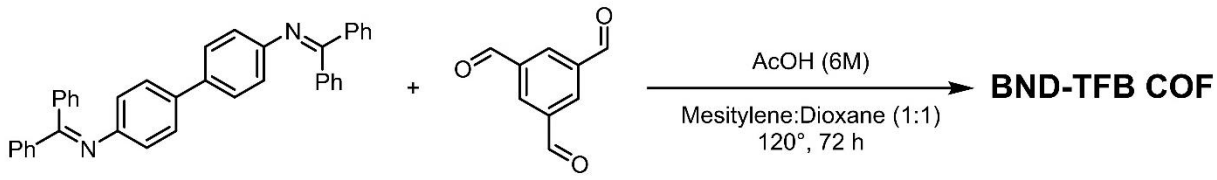

Synthesis of BND-TFB COF.

BND-TFB COF was prepared *via* a reported literature procedure.[411]

To a flame-dried 250 mL high-pressure flask with vacuum valve, 1,3,5-triformylbenzene (0.97 g, 6.0 mmol, 1.5 equiv) and benzidine-benzophenone (4.61 g, 9.0 mmol, 1.5 equiv) were added, followed by mesitylene:dioxane (1:1, 60.0 mL) along the walls of the flask (to push down any remaining solids remaining atop of the flask). The flask was sealed and sonicated at room temperature for 10 min, and then 6M acetic acid (10 mL) was added, and the flask was sealed again. The reaction mixture was then degassed through three freeze-pump-thaw cycles (vacuum <50 mTorr), after which the vacuum valve was switched to N_2, and the flask was charged with N_2 and sealed under positive N_2 pressure. The flask was then placed (no stirring) in a 120 °C pre-heated oil bath for three days. The flask was removed from the oil bath, allowed to cool, and filtered through a Buchner funnel equipped with a filter paper. Acetone was used to ensure all of the material is filtered from the flask to the Buchner funnel. The solid was collected and stirred in an Erlenmeyer flask in hot DMF (600 mL at 90°C for 30min), and filtered while hot. This procedure was repeated two more times in DMF (600 mL at 90°C for 30min), once in absolute ethanol (600 mL at 80°C for 30min), and lastly once in acetone (600 mL at 60°C). The material was then filtered, collected, placed in a vacuum chamber, and dried at 120°C for 24 h under vacuum to give an orange solid (1.98 g, 86%).

Ambient X-ray Diffraction

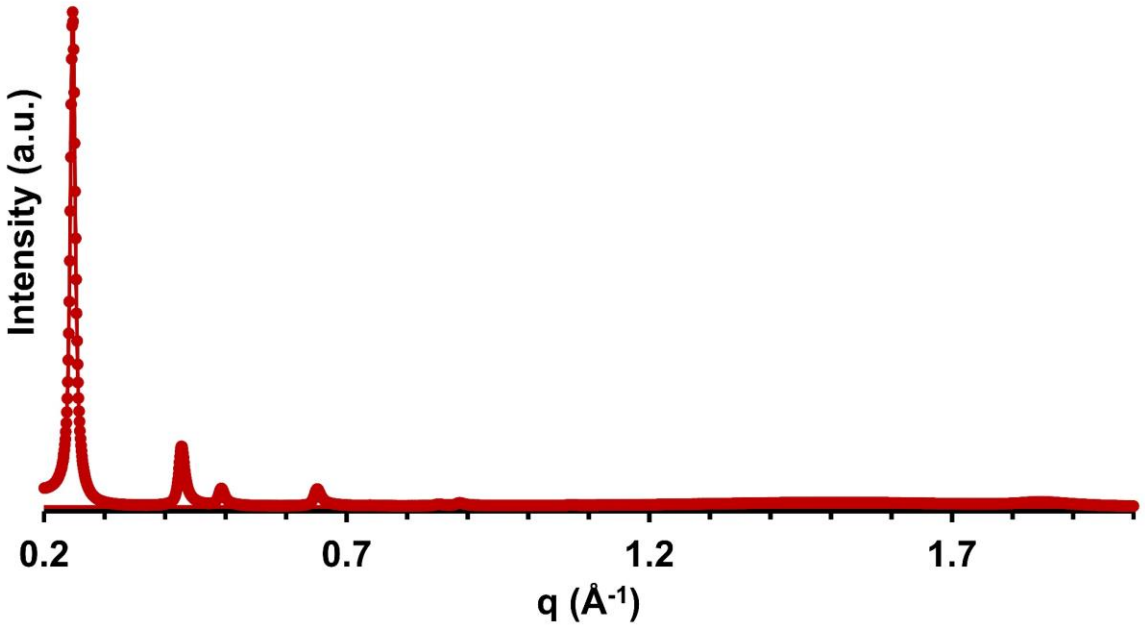

Figure 6.18. Ambient X-ray diffraction pattern of HHTP-PBBA COF.

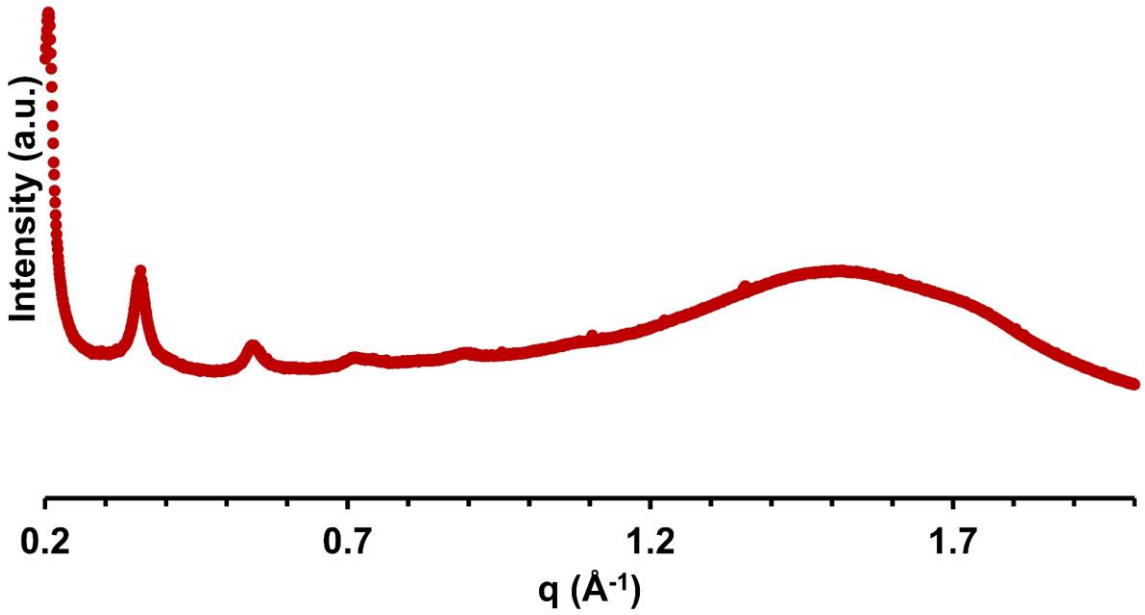

Figure 6.19. Ambient X-ray diffraction pattern of HHTP-BBBA COF.

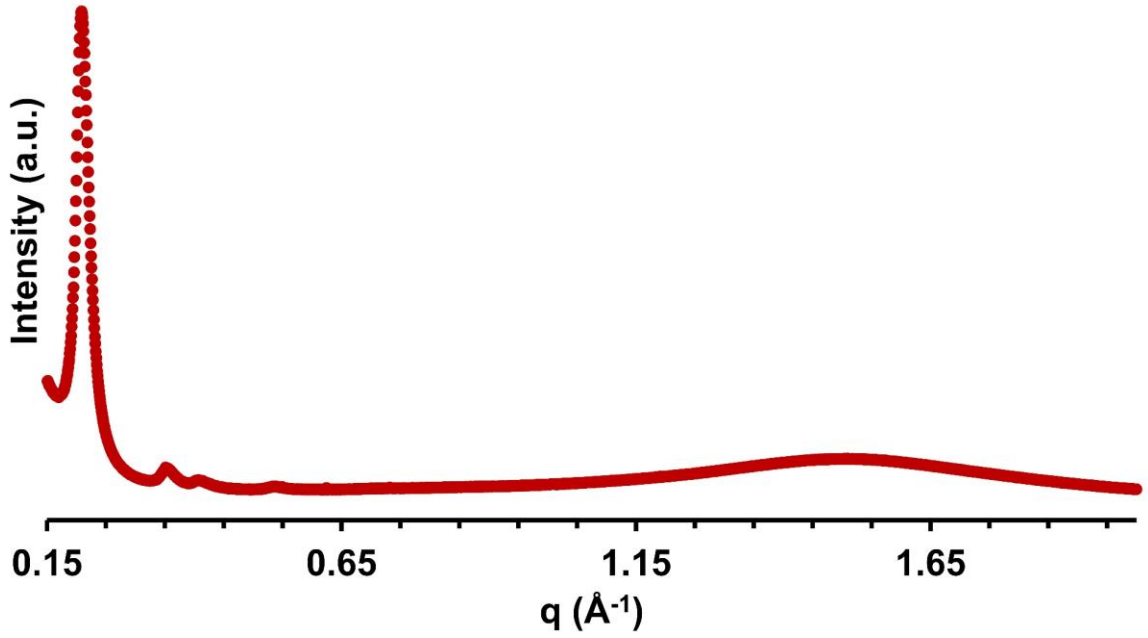

Figure 6.20. Ambient X-ray diffraction pattern of TAPB-PDA COF.

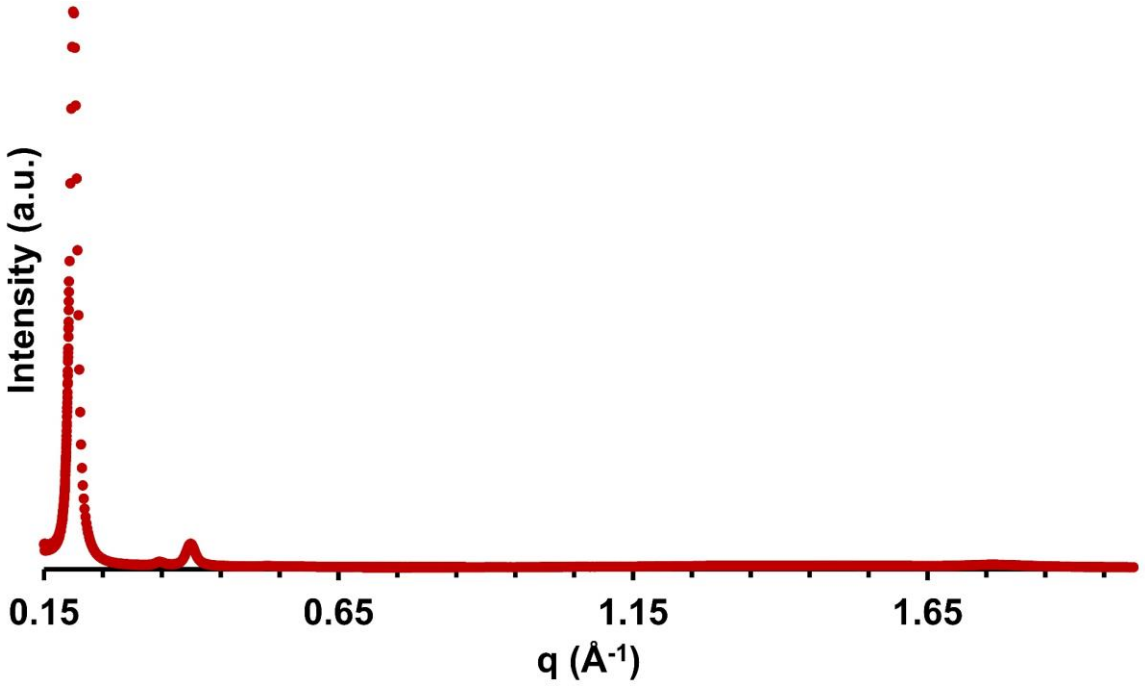

Figure 6.21. Ambient X-ray diffraction pattern of TAPB-PDA-N_3 COF.

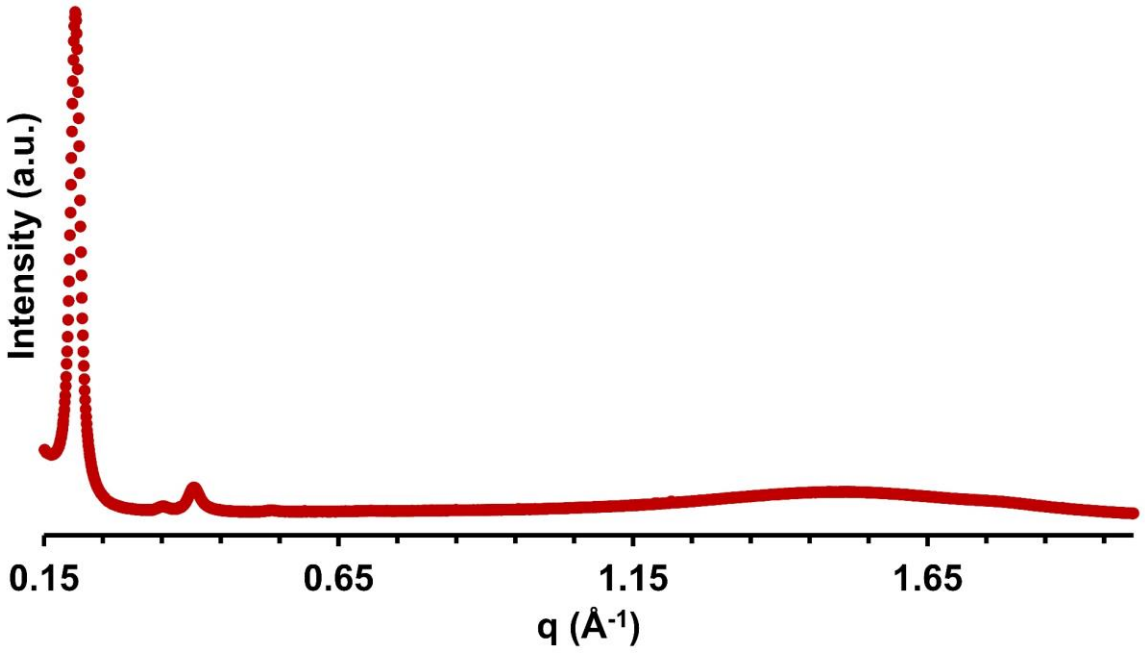

Figure 6.22. Ambient X-ray diffraction pattern of TAPB-PDA-NH_2 COF.

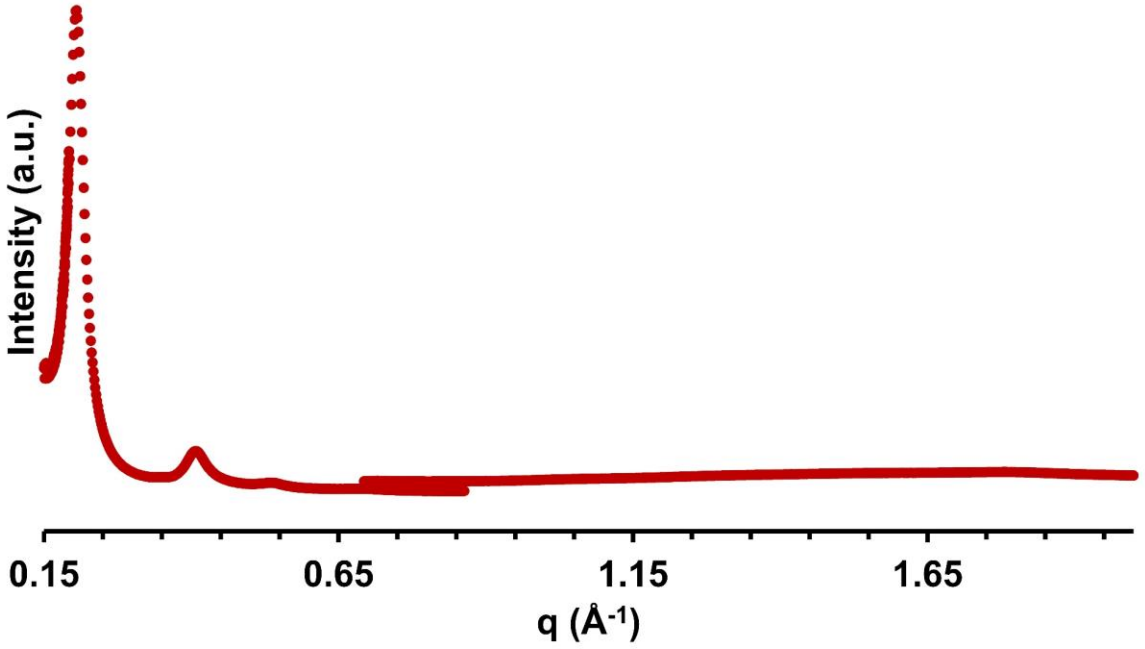

Figure 6.23. Ambient X-ray diffraction pattern of TAPB-PDA-Br COF.

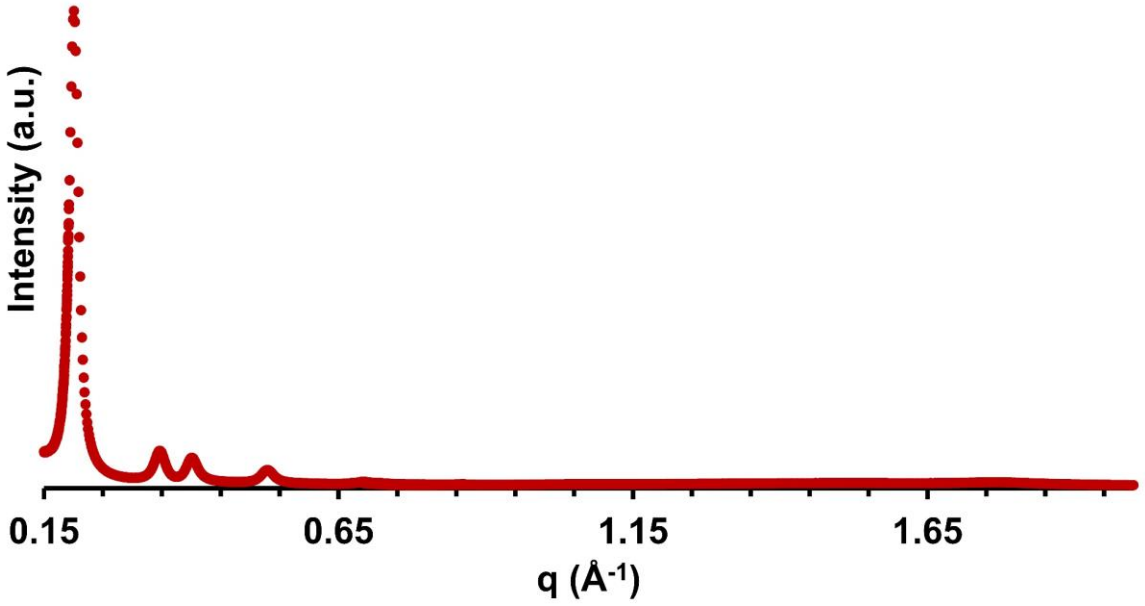

Figure 6.24. Ambient X-ray diffraction pattern of TAPB-PDA-Me COF.

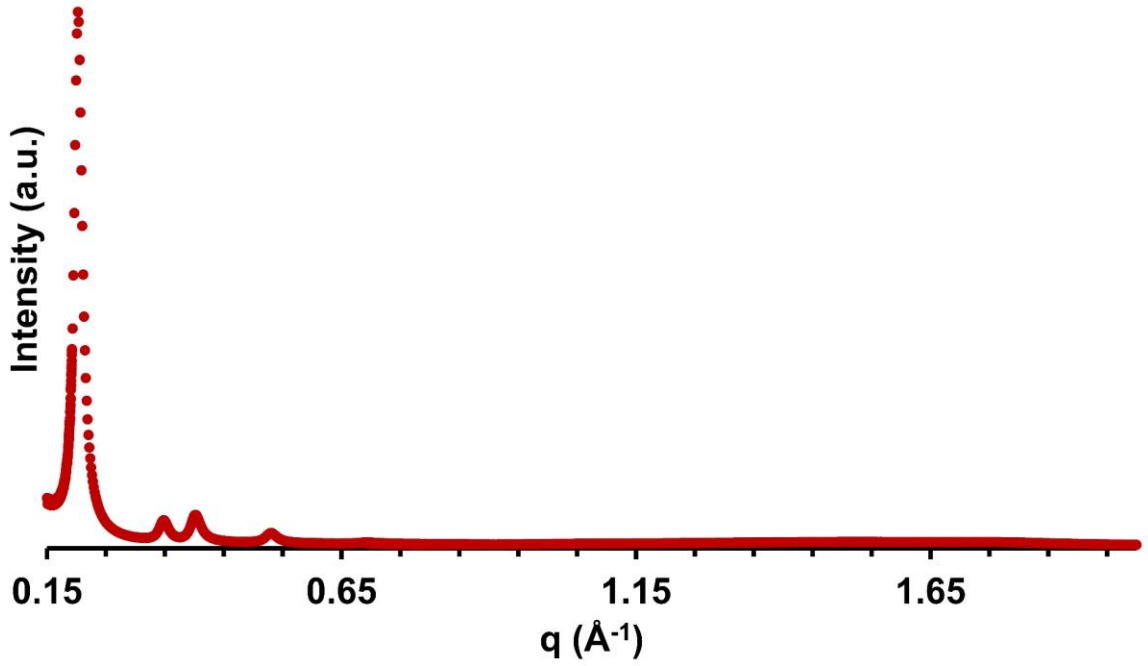

Figure 6.25. Ambient X-ray diffraction pattern of TAPB-PDA-Et COF.

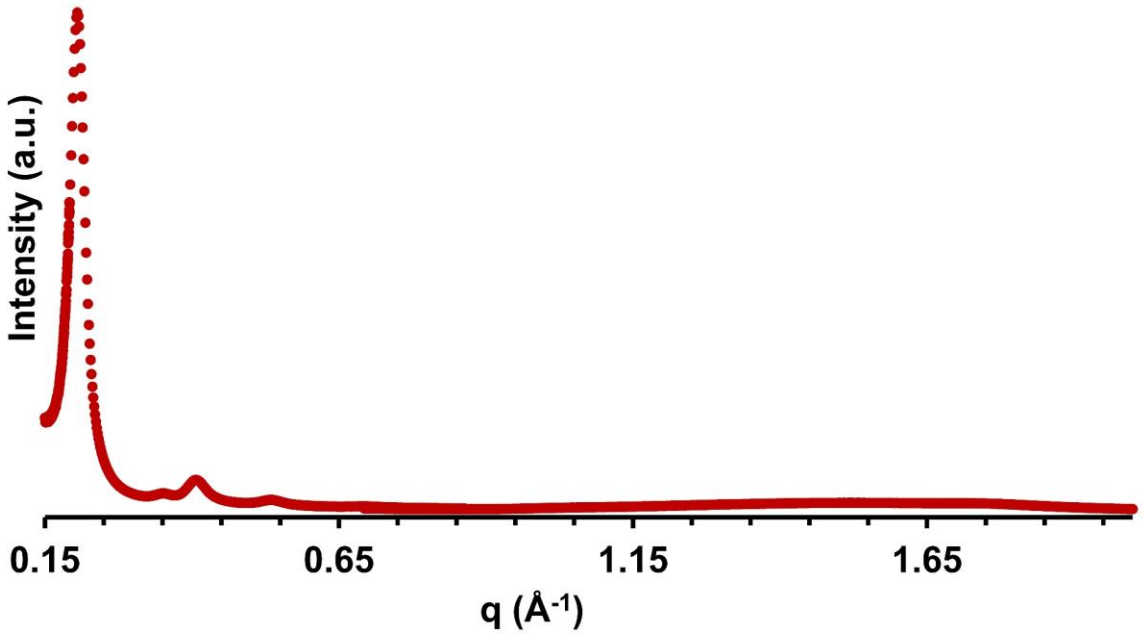

Figure 6.26. Ambient X-ray diffraction pattern of TAPB-PDA-SMe COF.

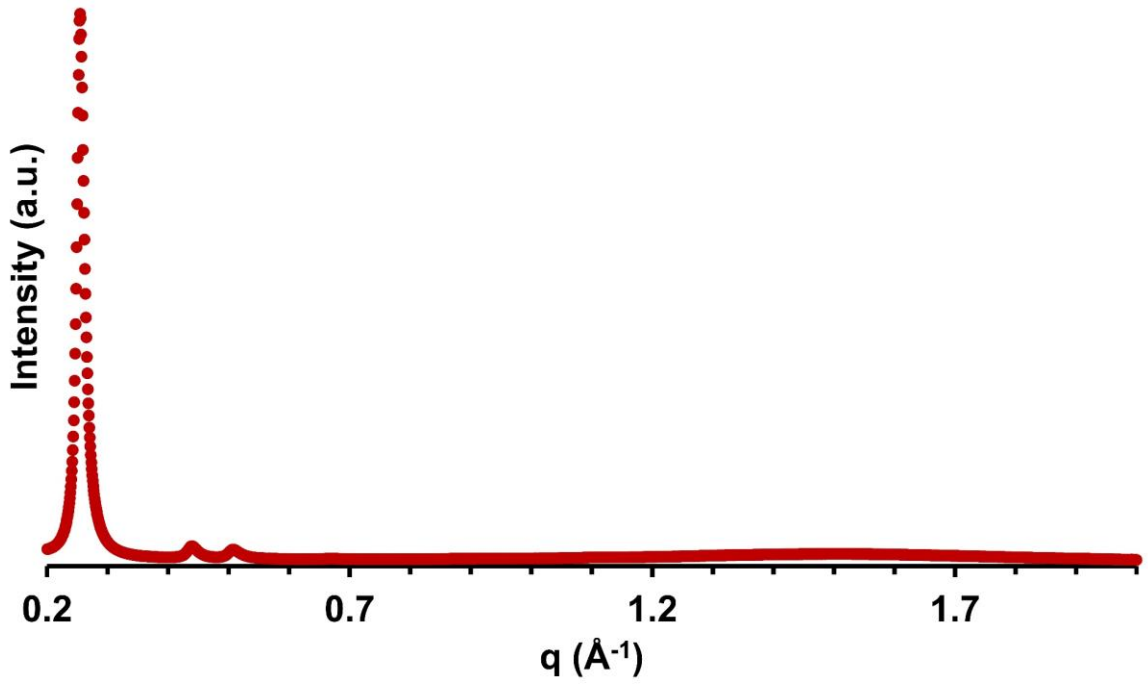

Figure 6.27. Ambient X-ray diffraction pattern of BND-TFB COF.

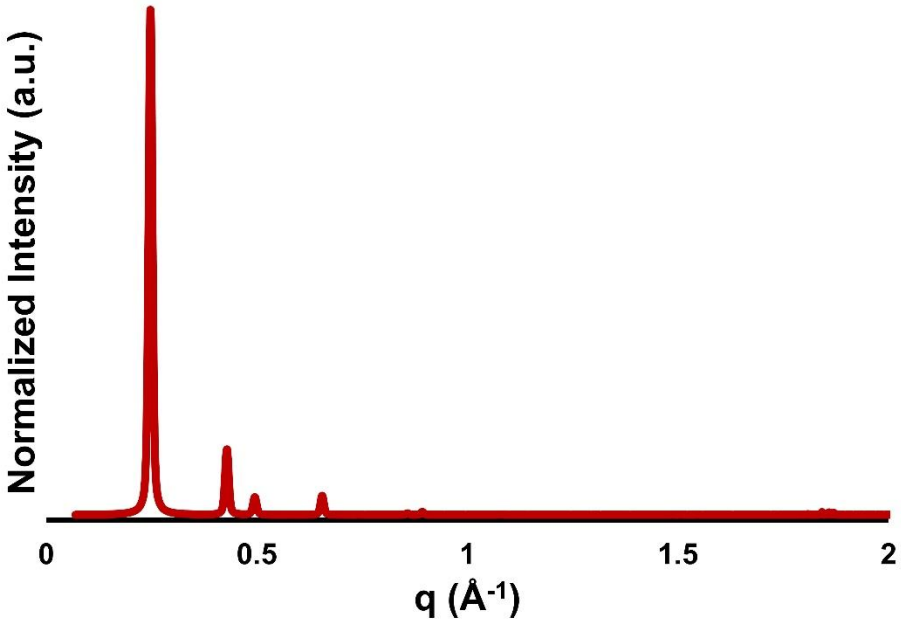

Figure 6.28. Refined diffraction pattern of HHTP-PBBA COF.

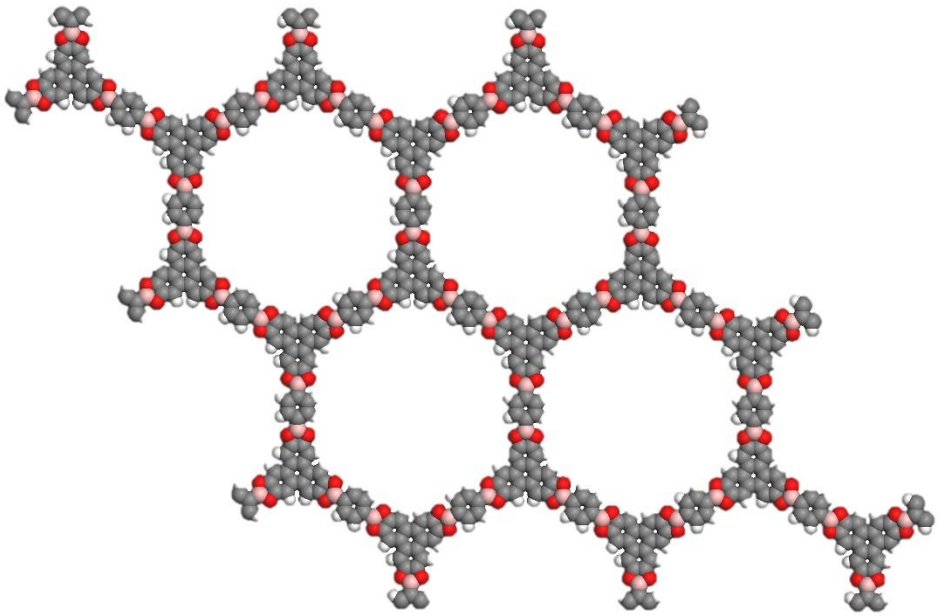

Figure 6.29. Refined structure of HHTP-PBBA COF.

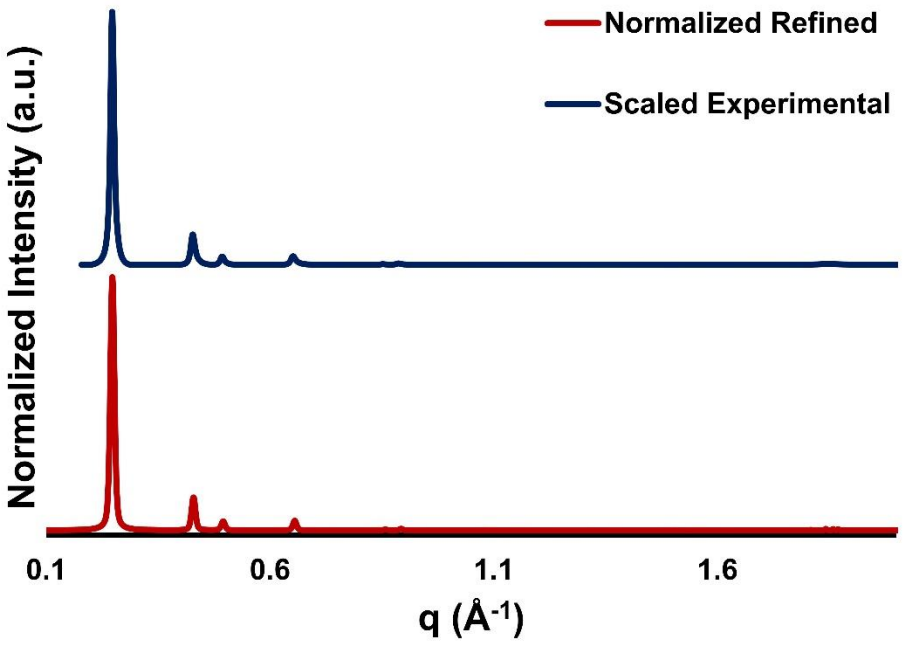

Figure 6.30. Comparison of refined diffraction pattern of HHTP-PBBA COF.

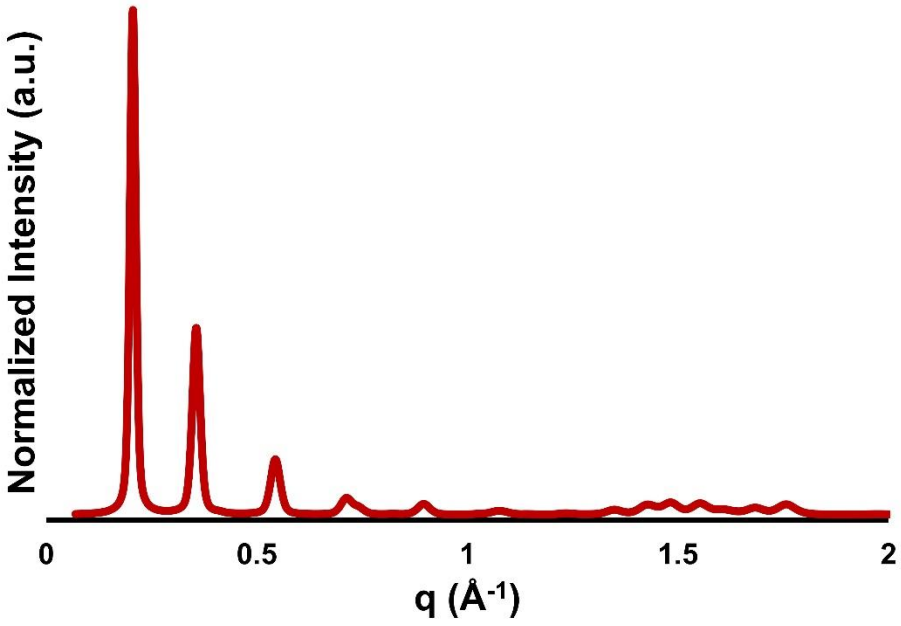

Figure 6.31. Refined diffraction pattern of HHTP-BBBA COF.

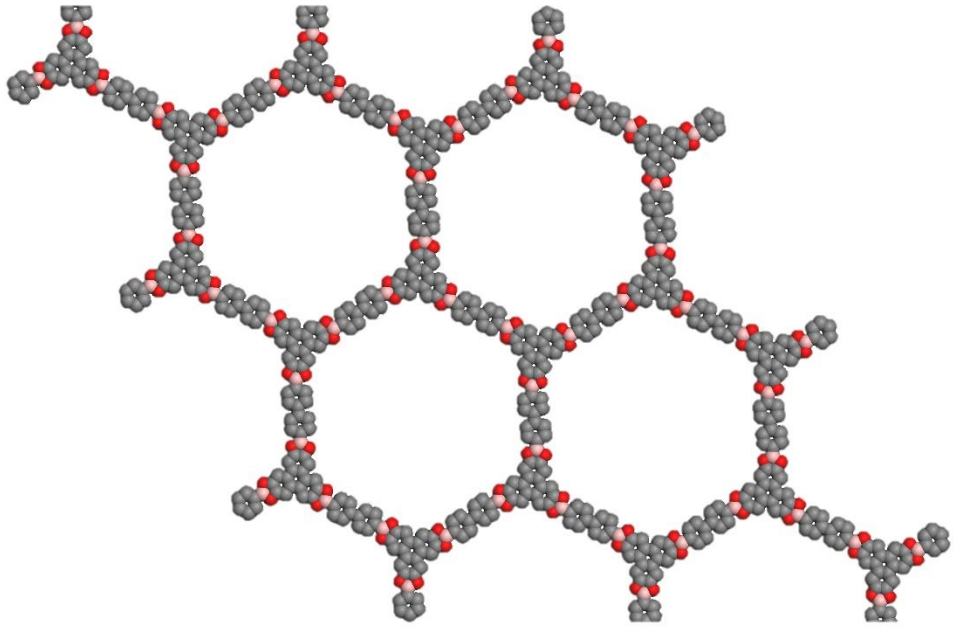

Figure 6.32. Refined structure of HHTP-BBBA COF

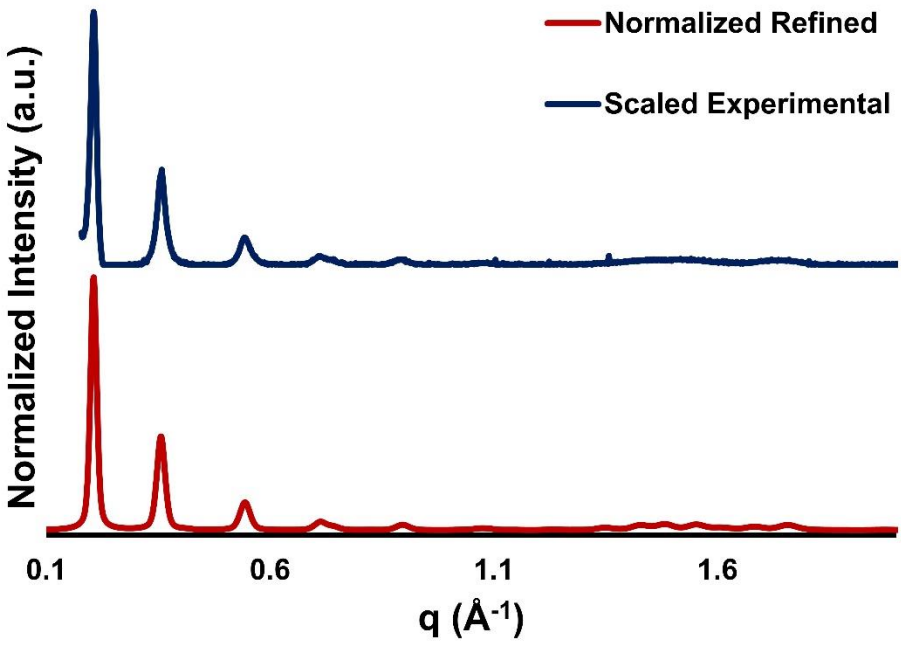

Figure 6.33. Comparison of refined diffraction pattern of HHTP-BBBA COF.

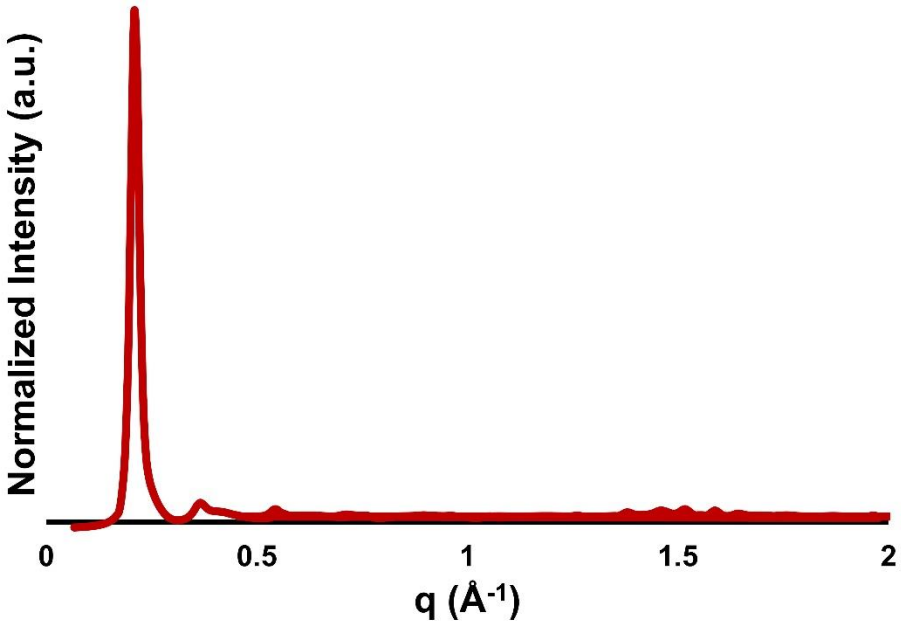

Figure 6.34. Refined diffraction pattern of TAPB-PDA COF.

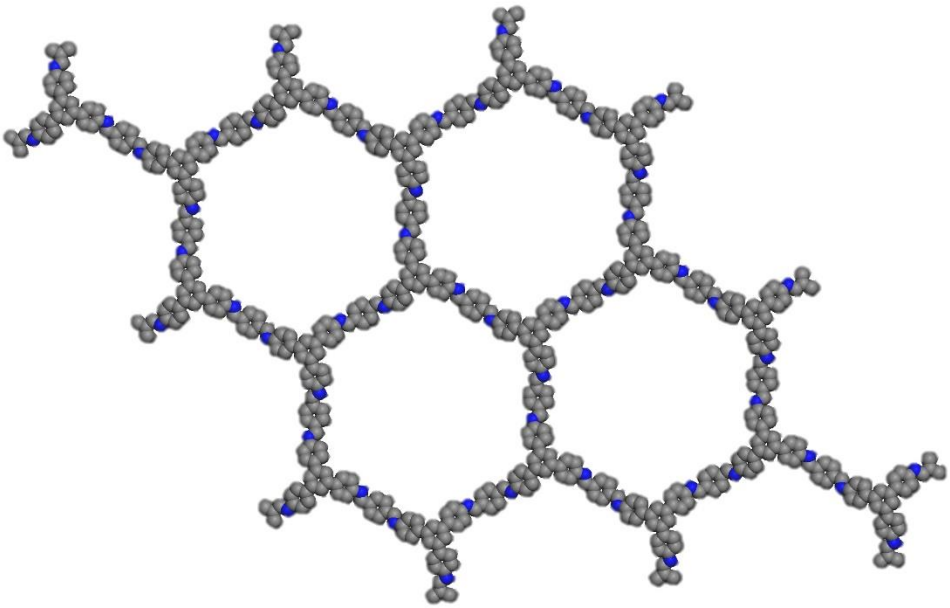

Figure 6.35. Refined structure of TAPB-PDA COF.

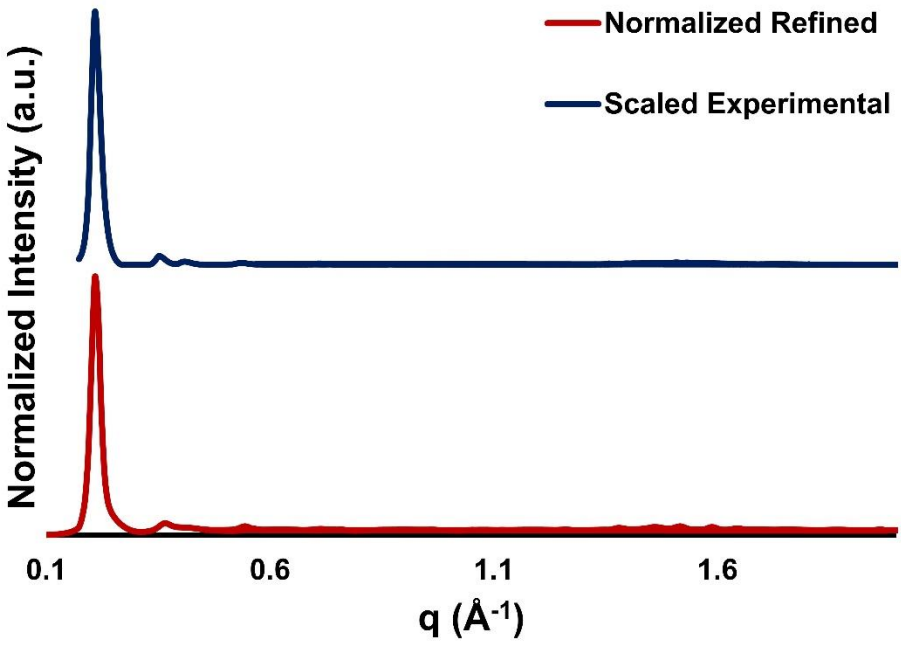

Figure 6.36. Comparison of refined diffraction pattern of TAPB-PDA COF.

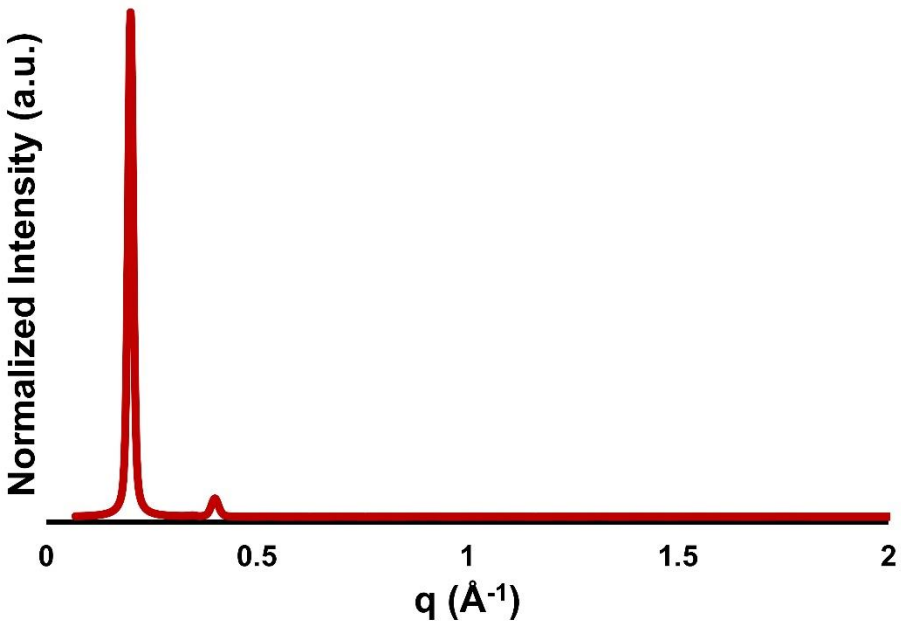

Figure 6.37. Refined diffraction pattern of TAPB-PDA-N_3 COF.

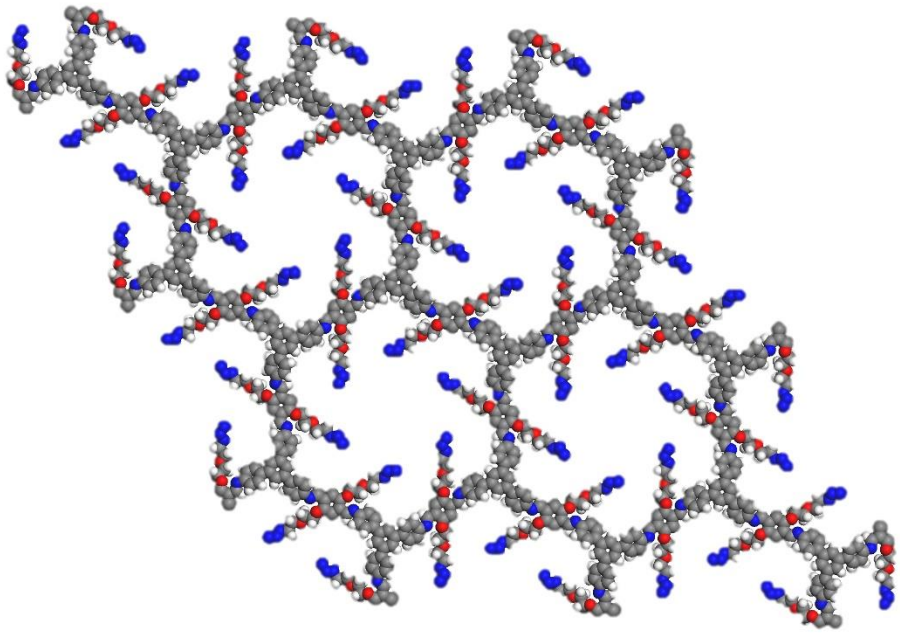

Figure 6.38. Refined structure of TAPB-PDA-N_3 COF.

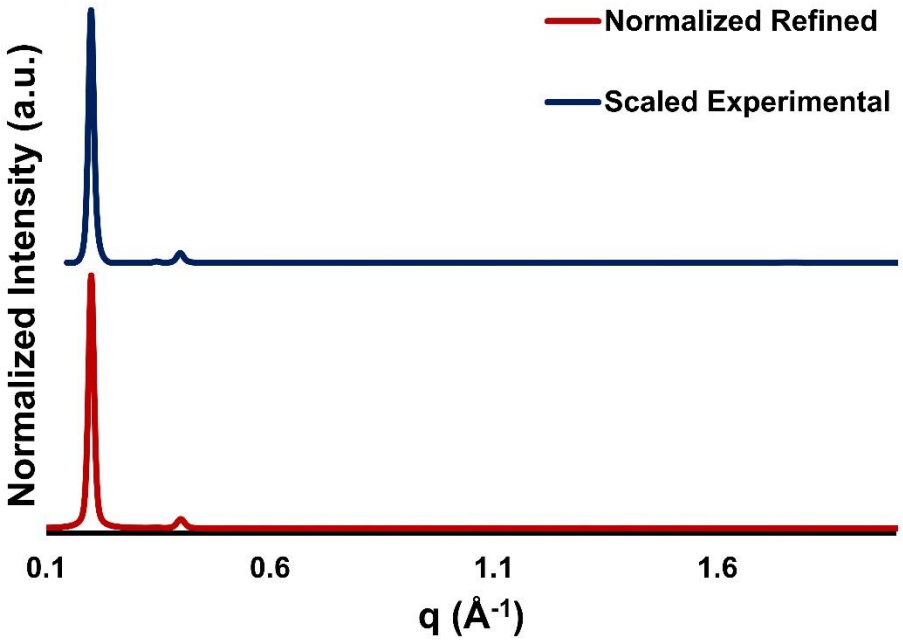

Figure 6.39. Comparison of refined diffraction pattern of TAPB-PDA-N_3 COF.

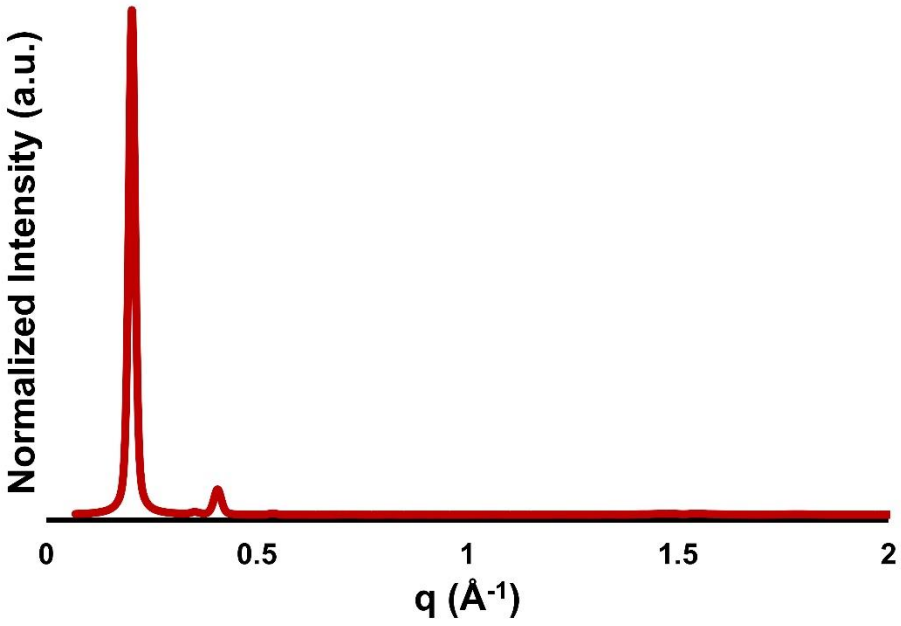

Figure 6.40. Refined diffraction pattern of TAPB-PDA-NH_2 COF.

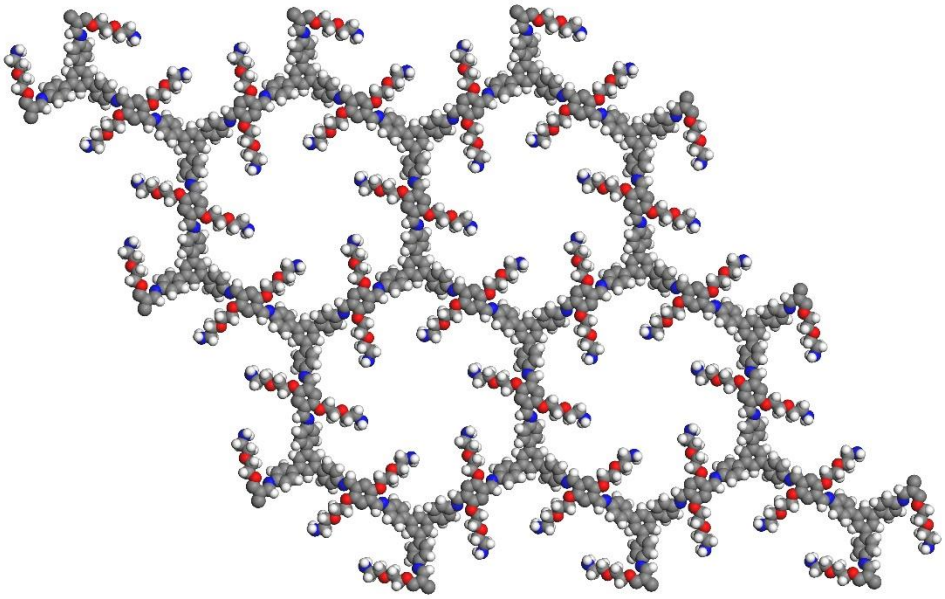

Figure 6.41. Refined structure of TAPB-PDA-NH_2 COF.

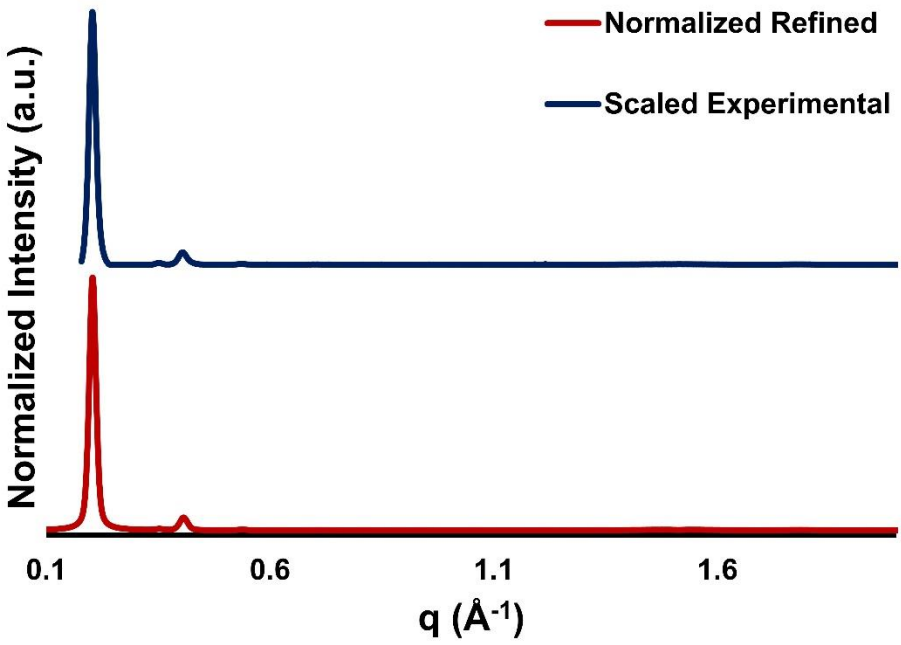

Figure 6.42. Comparison of refined diffraction pattern of TAPB-PDA-NH_2 COF.

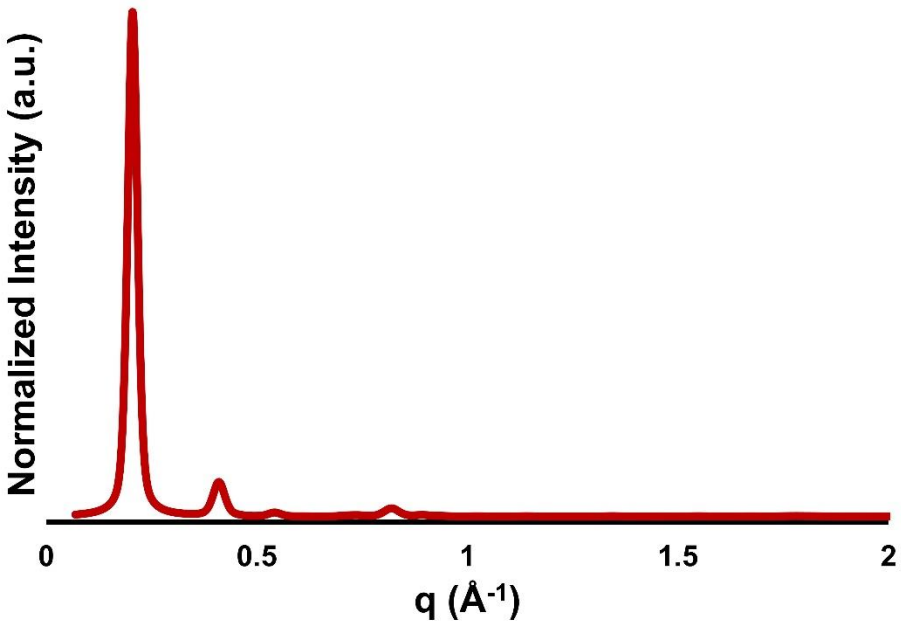

Figure 6.43. Refined diffraction pattern of TAPB-PDA-Br COF.

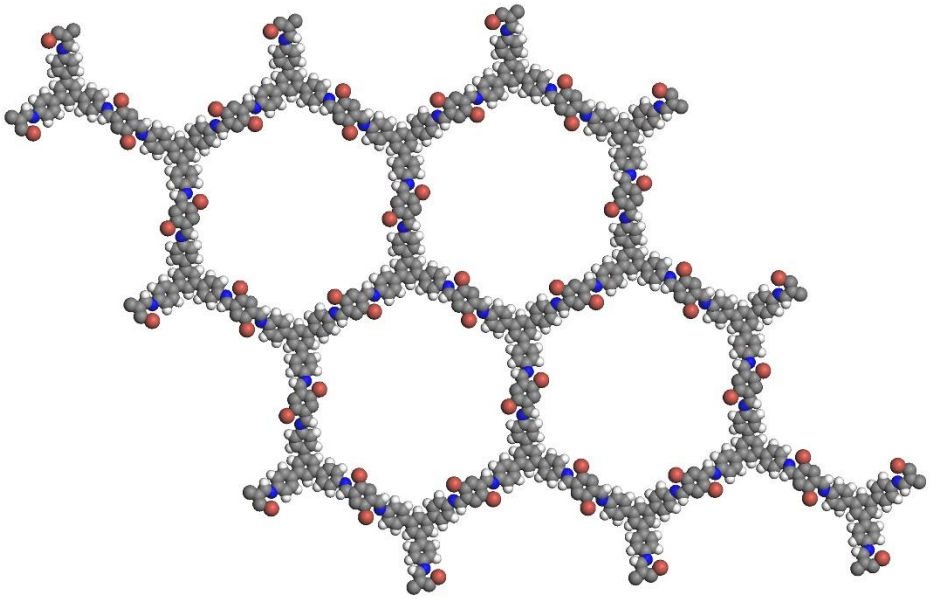

Figure 6.44. Refined structure of TAPB-PDA-Br COF.

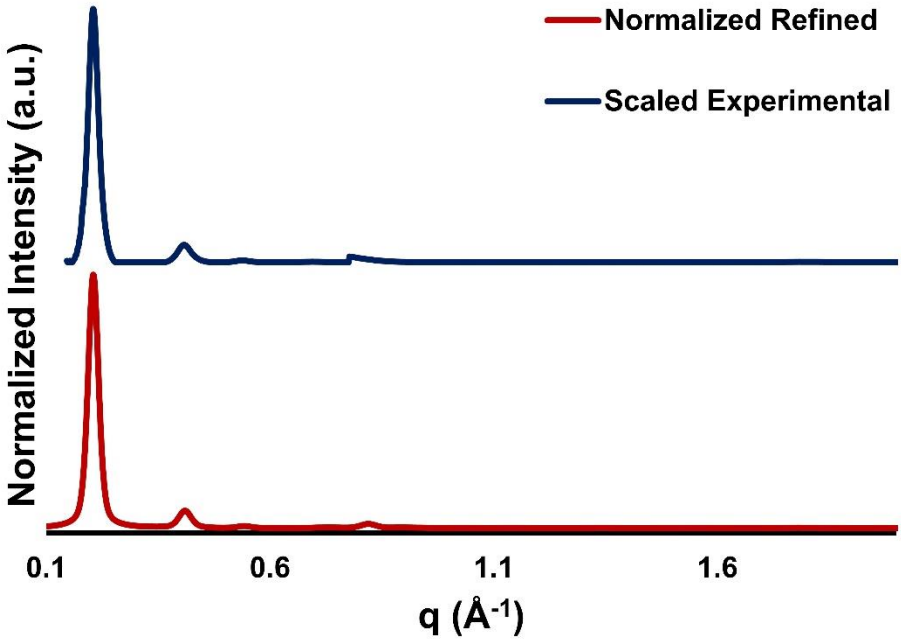

Figure 6.45. Comparison of refined diffraction pattern of TAPB-PDA-Br COF.

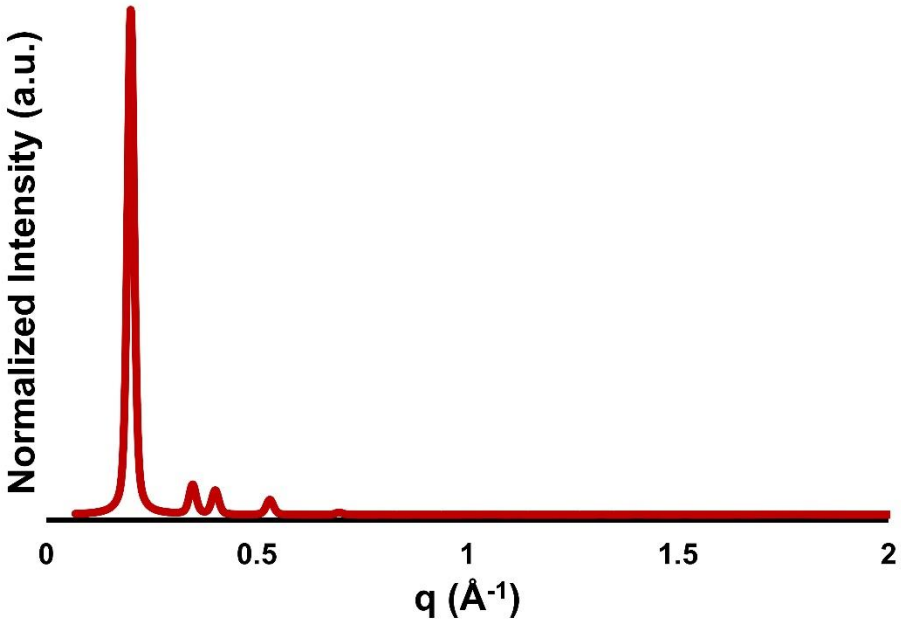

Figure 6.46. Refined diffraction pattern of TAPB-PDA-Me COF.

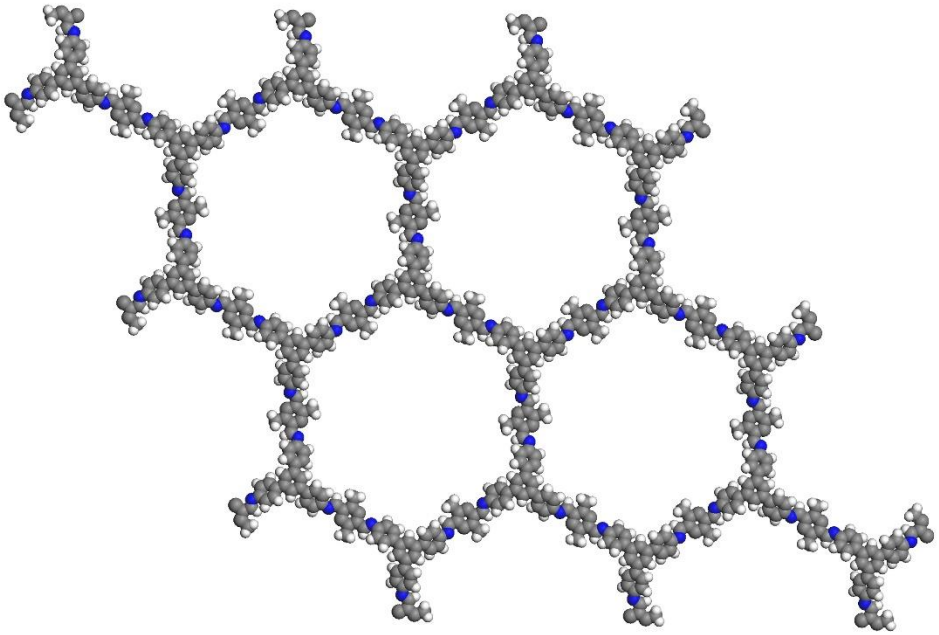

Figure 6.47. Refined structure of TAPB-PDA-Me COF.

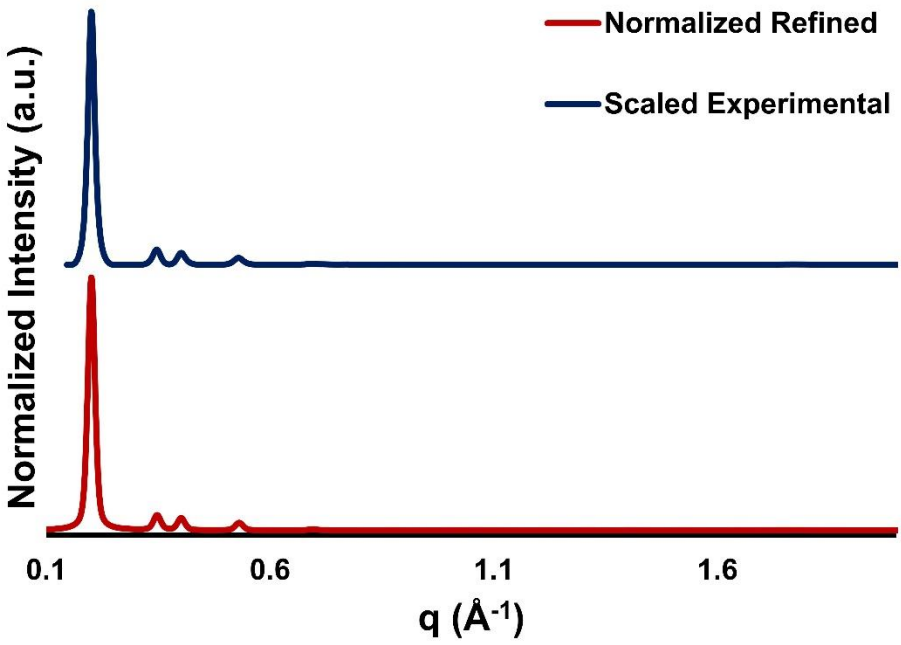

Figure 6.48. Comparison of refined diffraction pattern of TAPB-PDA-Me COF.

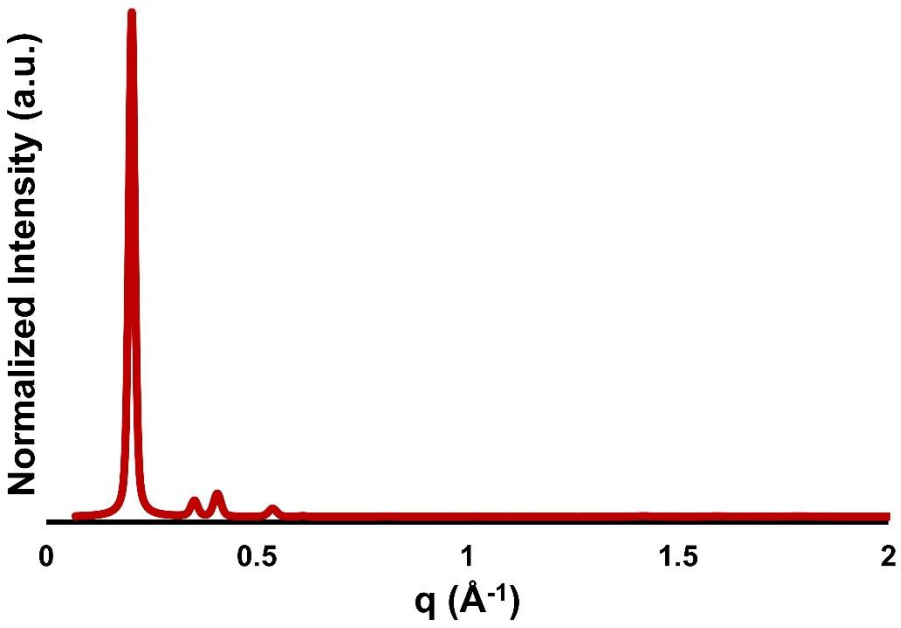

Figure 6.49. Refined diffraction pattern of TAPB-PDA-Et COF.

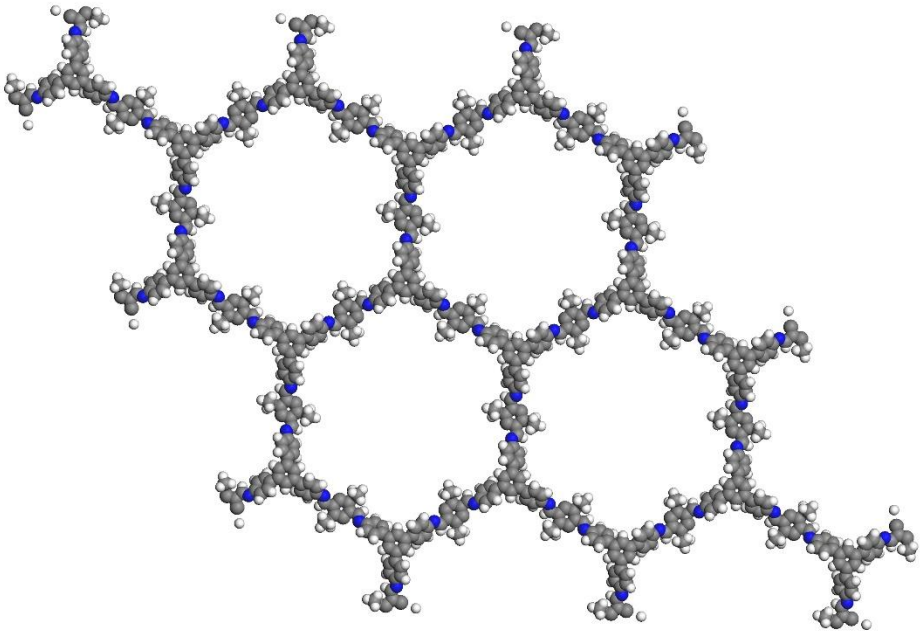

Figure 6.50. Refined structure of TAPB-PDA-Et COF.

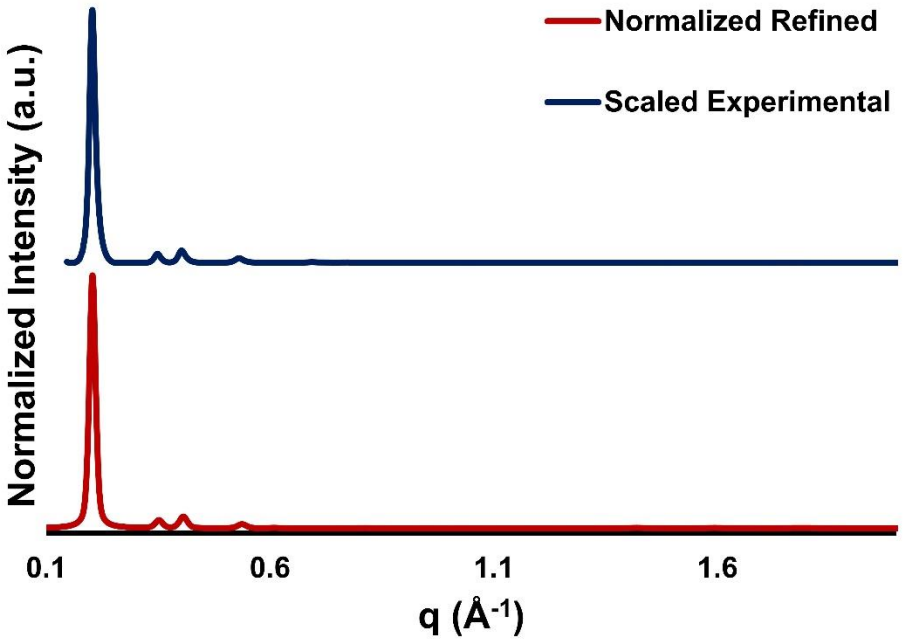

Figure 6.51. Comparison of refined diffraction pattern of TAPB-PDA-Et COF.

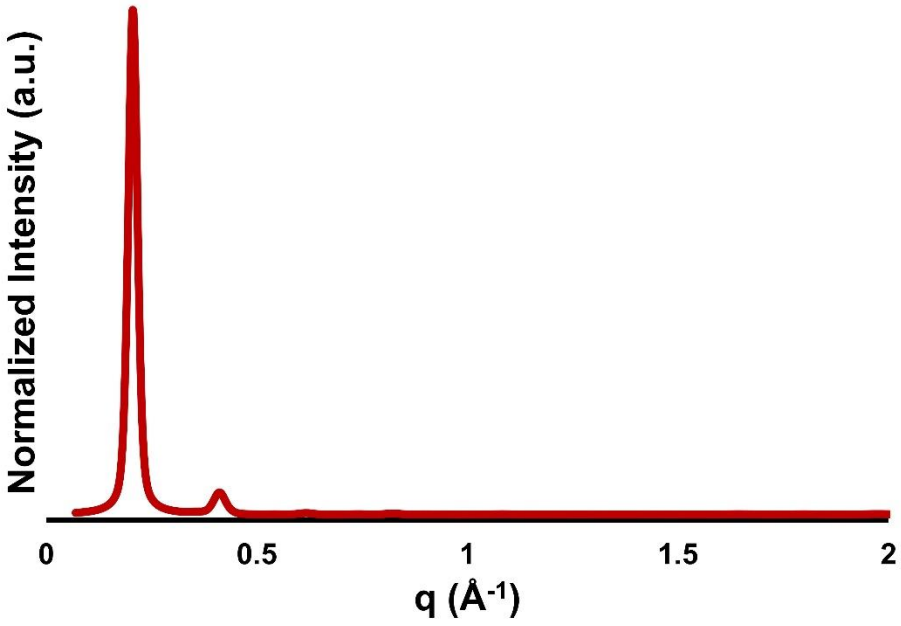

Figure 6.52. Refined diffraction pattern of TAPB-PDA-SMe COF.

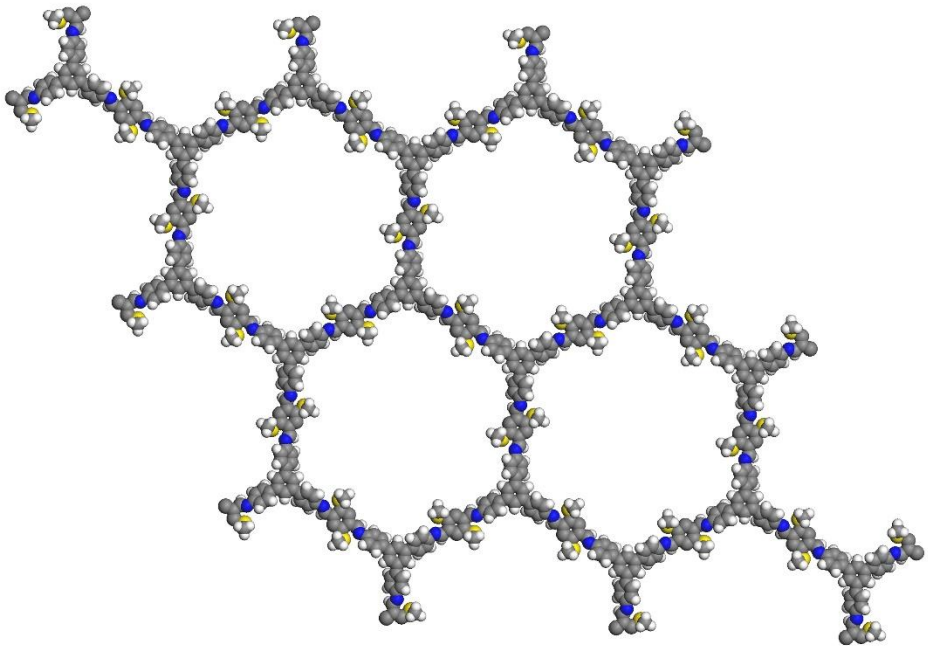

Figure 6.53. Refined structure of TAPB-PDA-SMe COF.

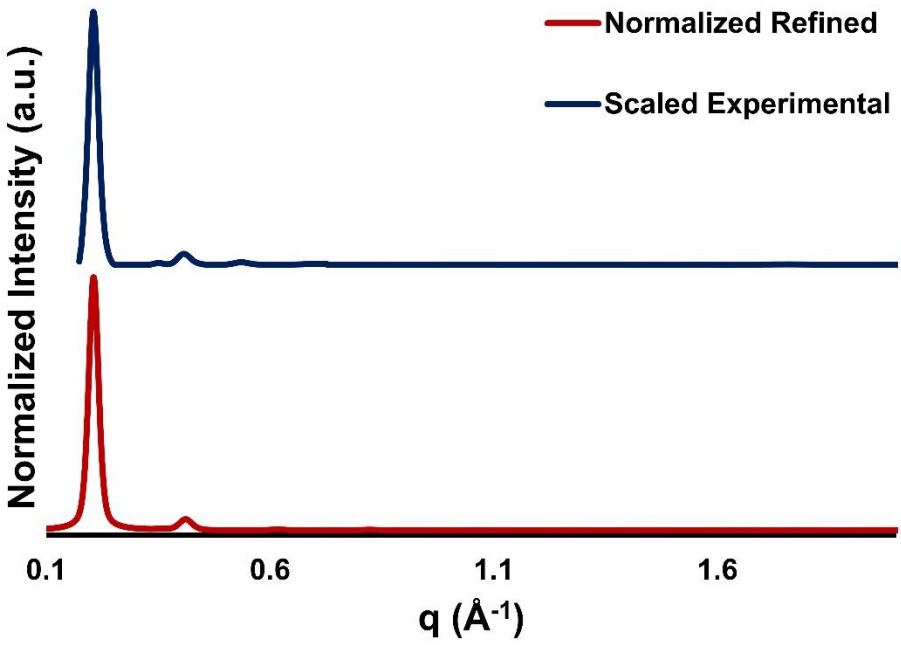

Figure 6.54. Comparison of refined diffraction pattern of TAPB-PDA-SMe COF.

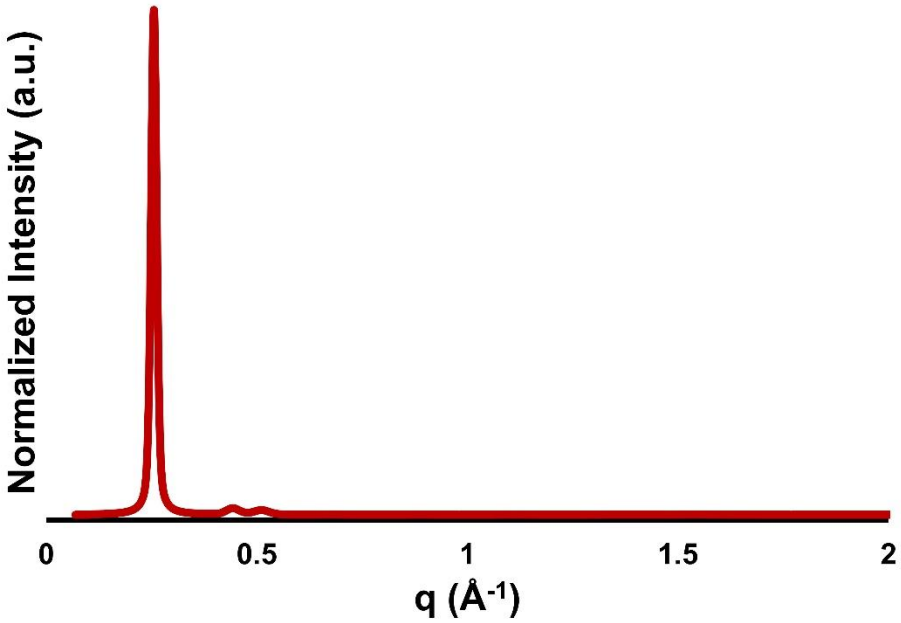

Figure 6.55. Refined diffraction pattern of BND-TFB COF.

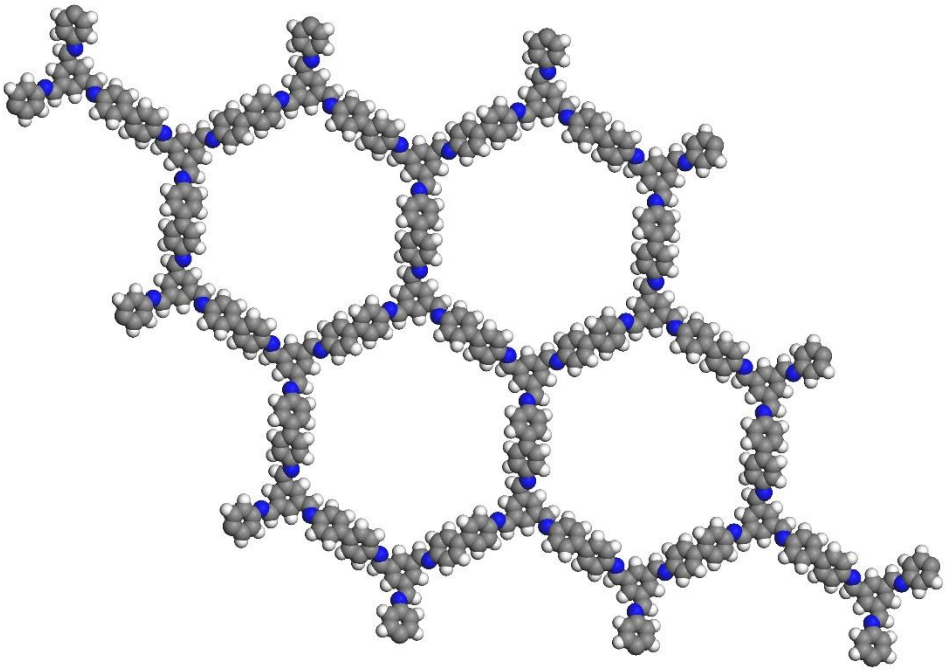

Figure 6.56. Refined structure of BND-TFB COF.

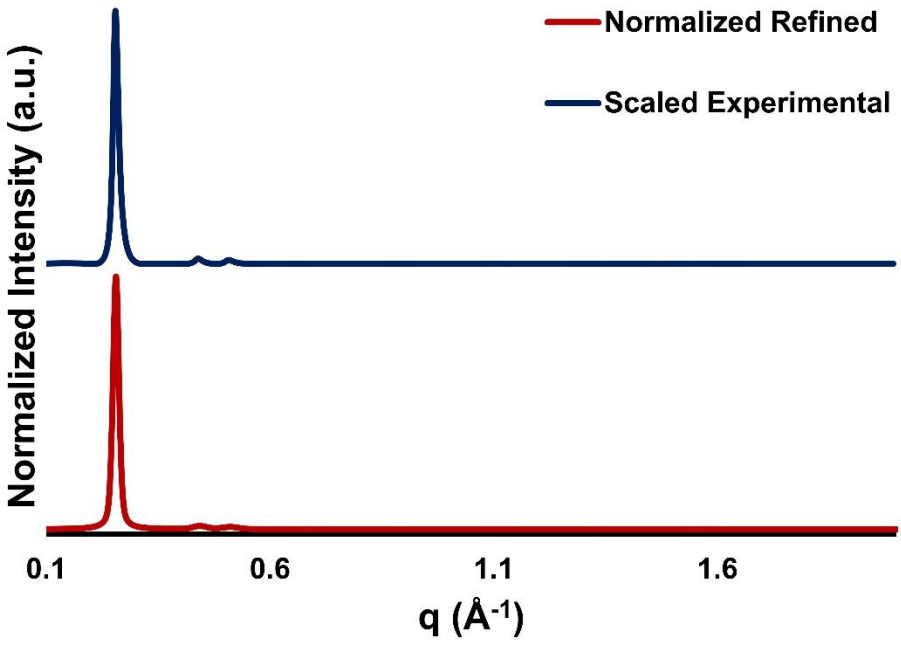

Figure 6.57. Comparison of refined diffraction pattern of BND-TFB COF.

Nitrogen Sorption Measurements

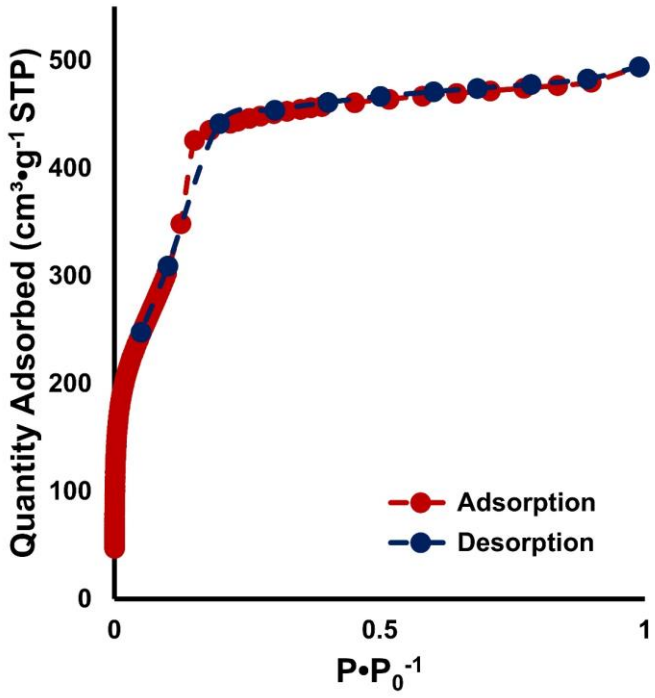

Figure 6.58. Nitrogen isotherm recorded at 77 K for HHTP-PBBA COF.

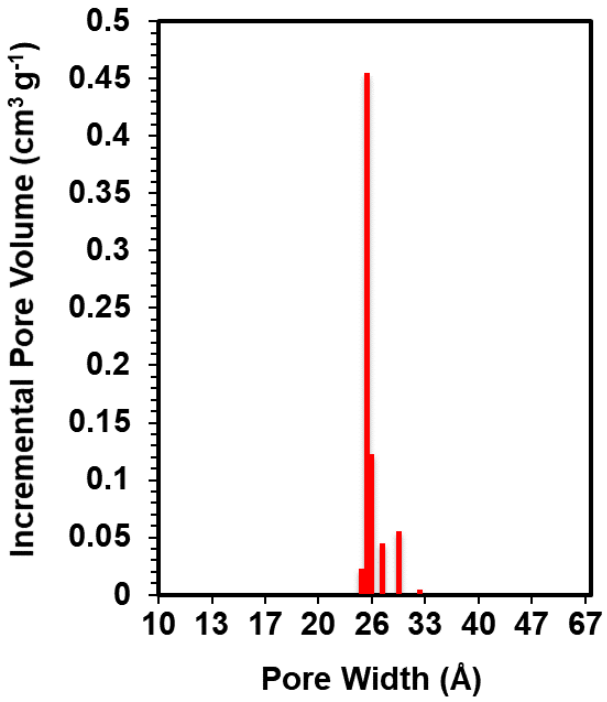

Figure 6.59. Pore size distribution of HHTP-PBBA COF.

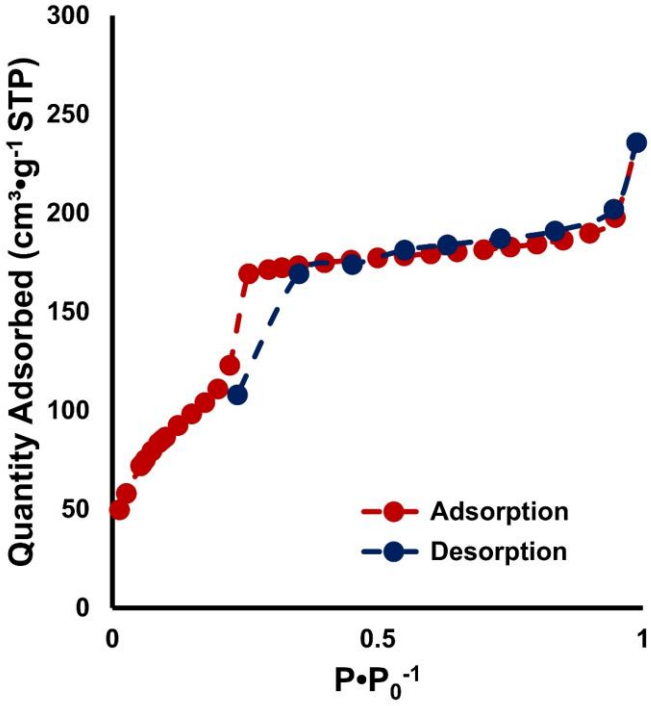

Figure 6.60. Nitrogen isotherm recorded at 77 K for HHTP-BBBA COF.

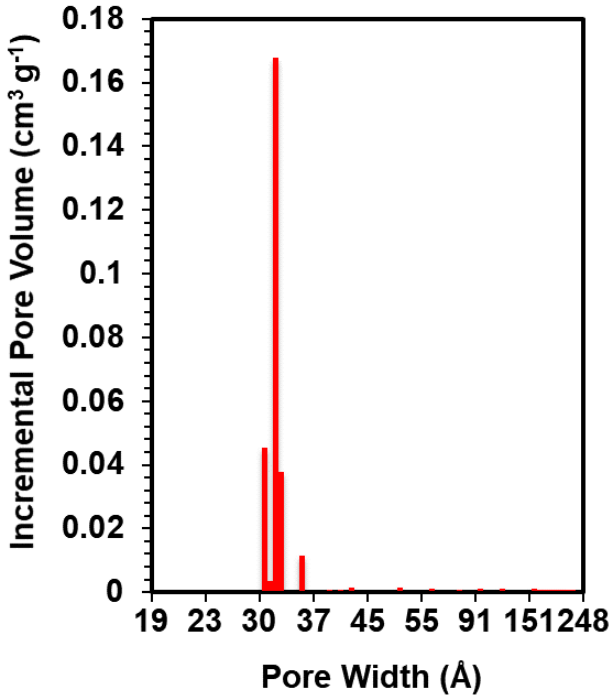

Figure 6.61. Pore size distribution of HHTP-BBBA COF.

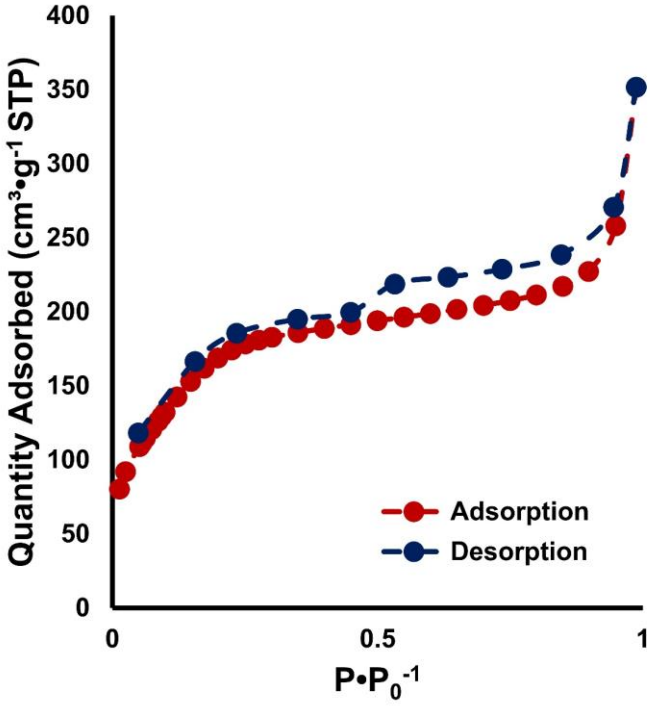

Figure 6.62. Nitrogen isotherm recorded at 77 K for TAPB-PDA COF.

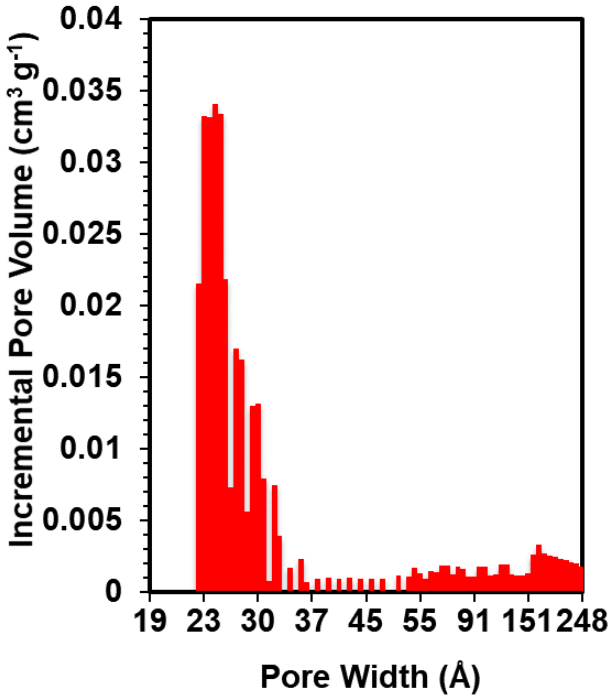

Figure 6.63. Pore size distribution of TAPB-PDA COF.

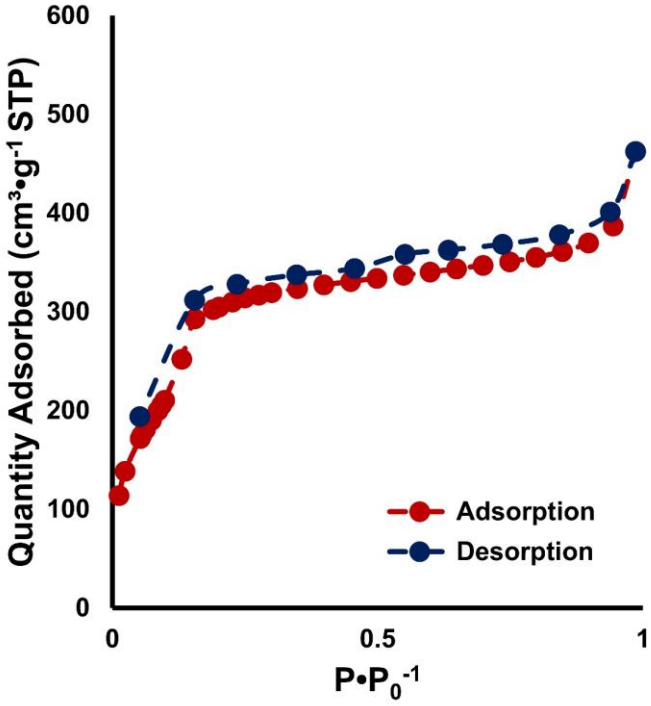

Figure 6.64. Nitrogen isotherm recorded at 77 K for TAPB-PDA-N_3 COF.

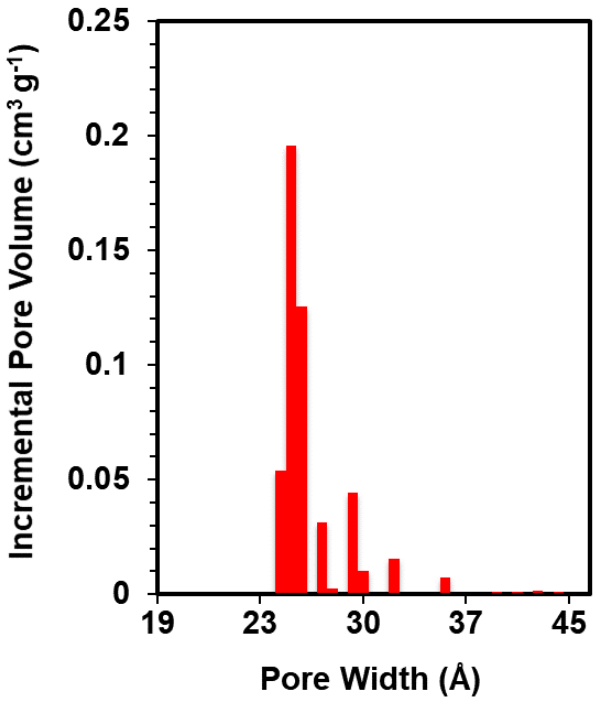

Figure 6.65. Pore size distribution of TAPB-PDA-N_3 COF.

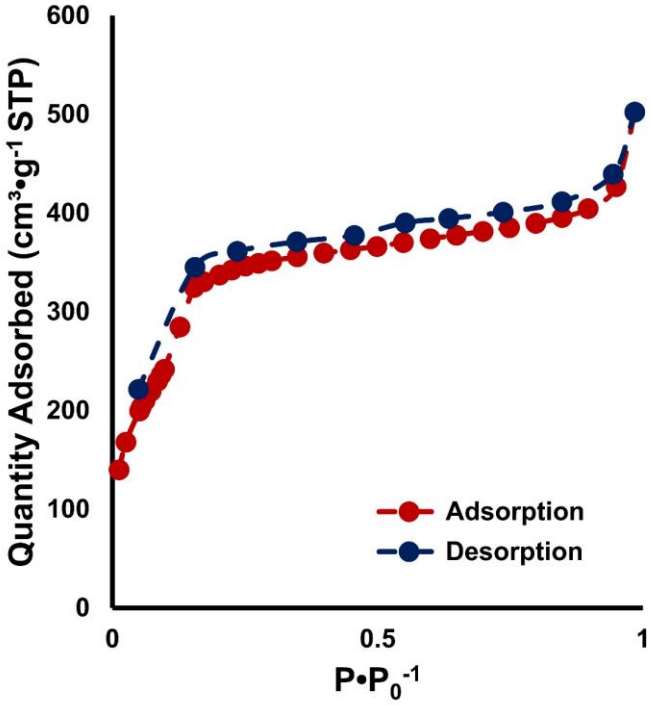

Figure 6.66. Nitrogen isotherm recorded at 77 K for TAPB-PDA-NH_2 COF.

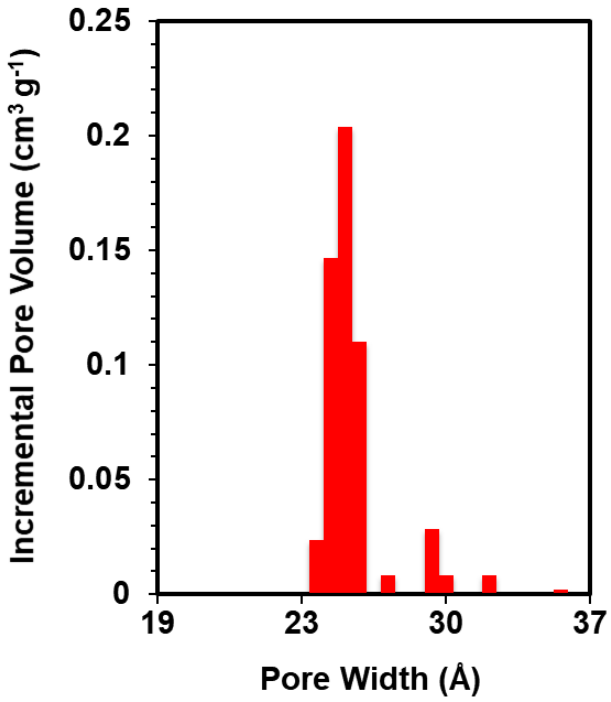

Figure 6.67. Pore size distribution of TAPB-PDA-NH_2 COF.

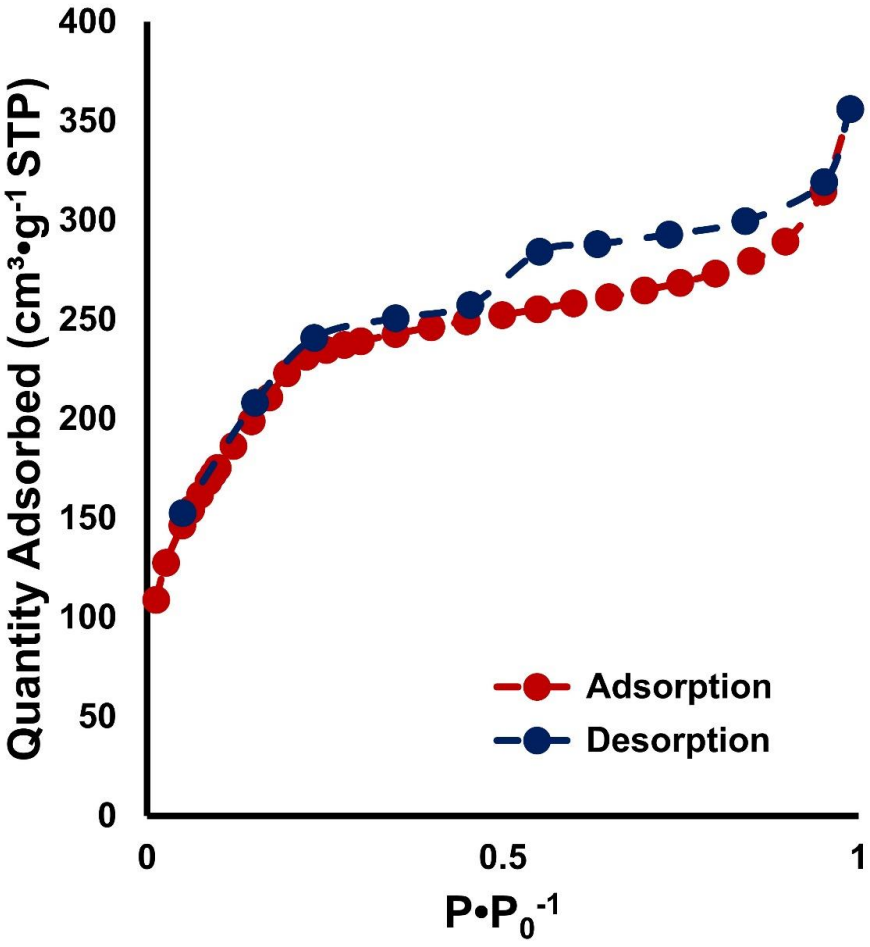

Figure 6.68. Nitrogen isotherm recorded at 77 K for TAPB-PDA-Br COF.

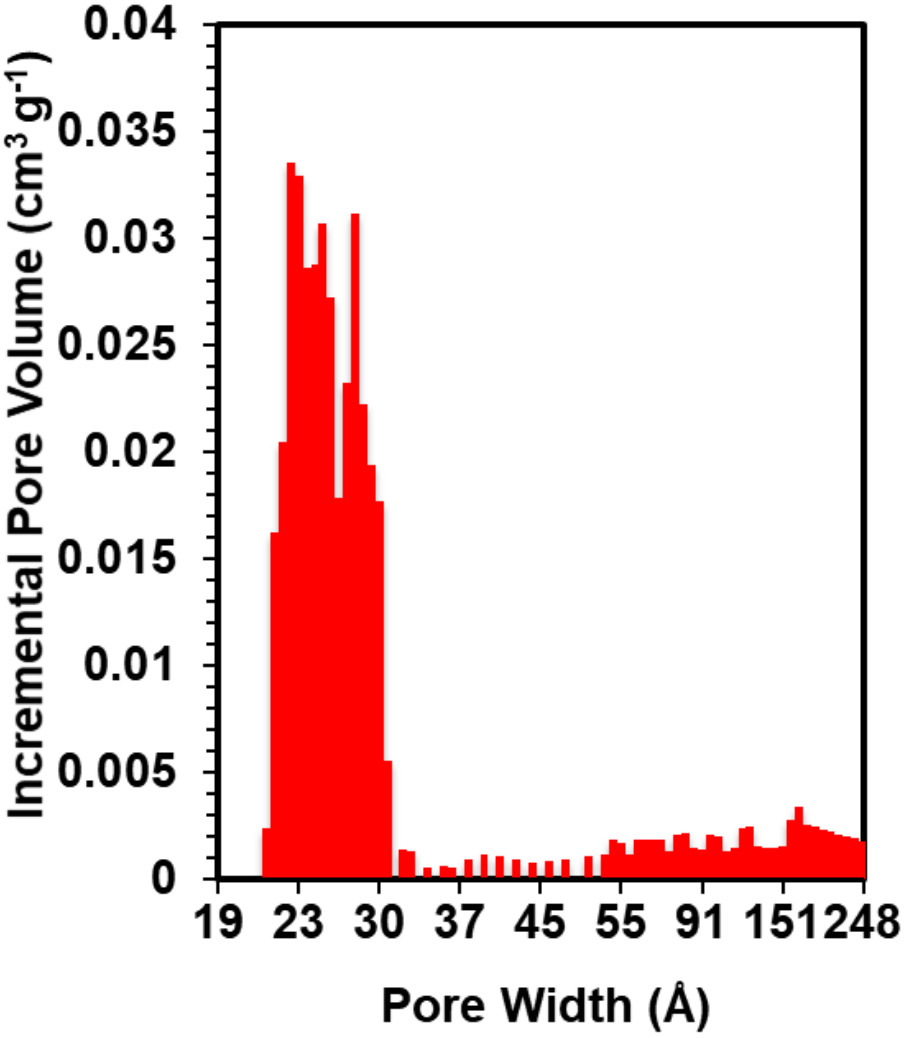

Figure 6.69. Pore size distribution of TAPB-PDA-Br COF.

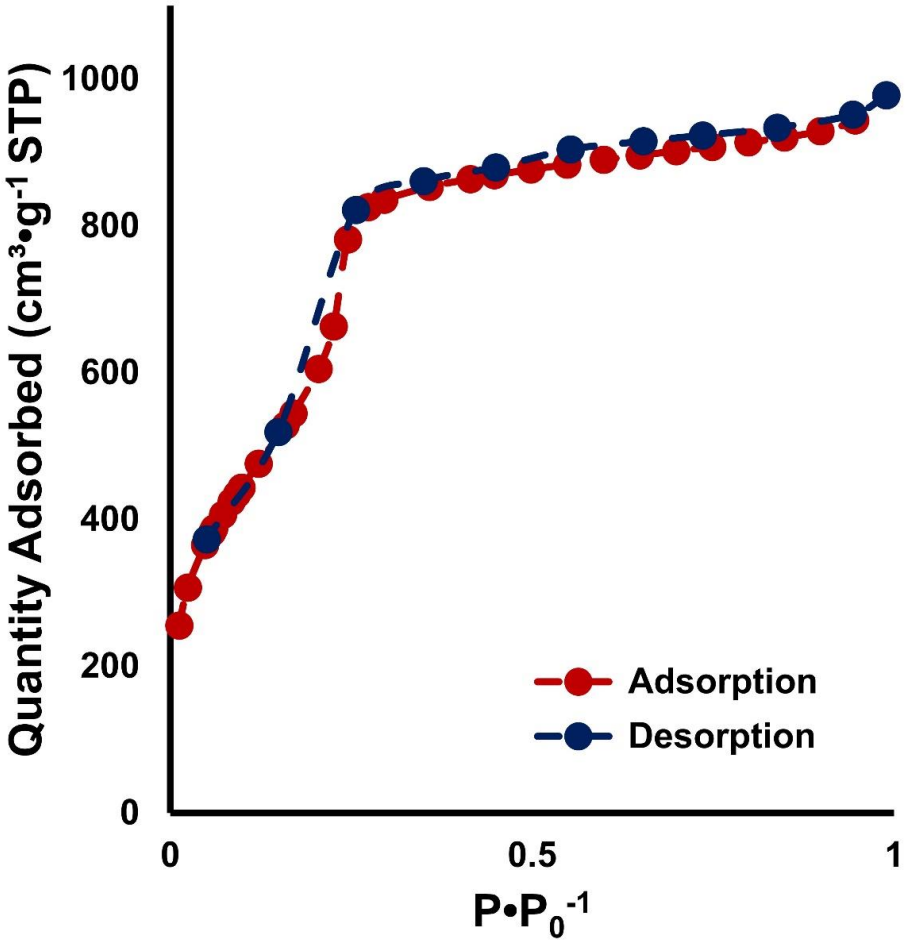

Figure 6.70. Nitrogen isotherm recorded at 77 K for TAPB-PDA-Me COF.

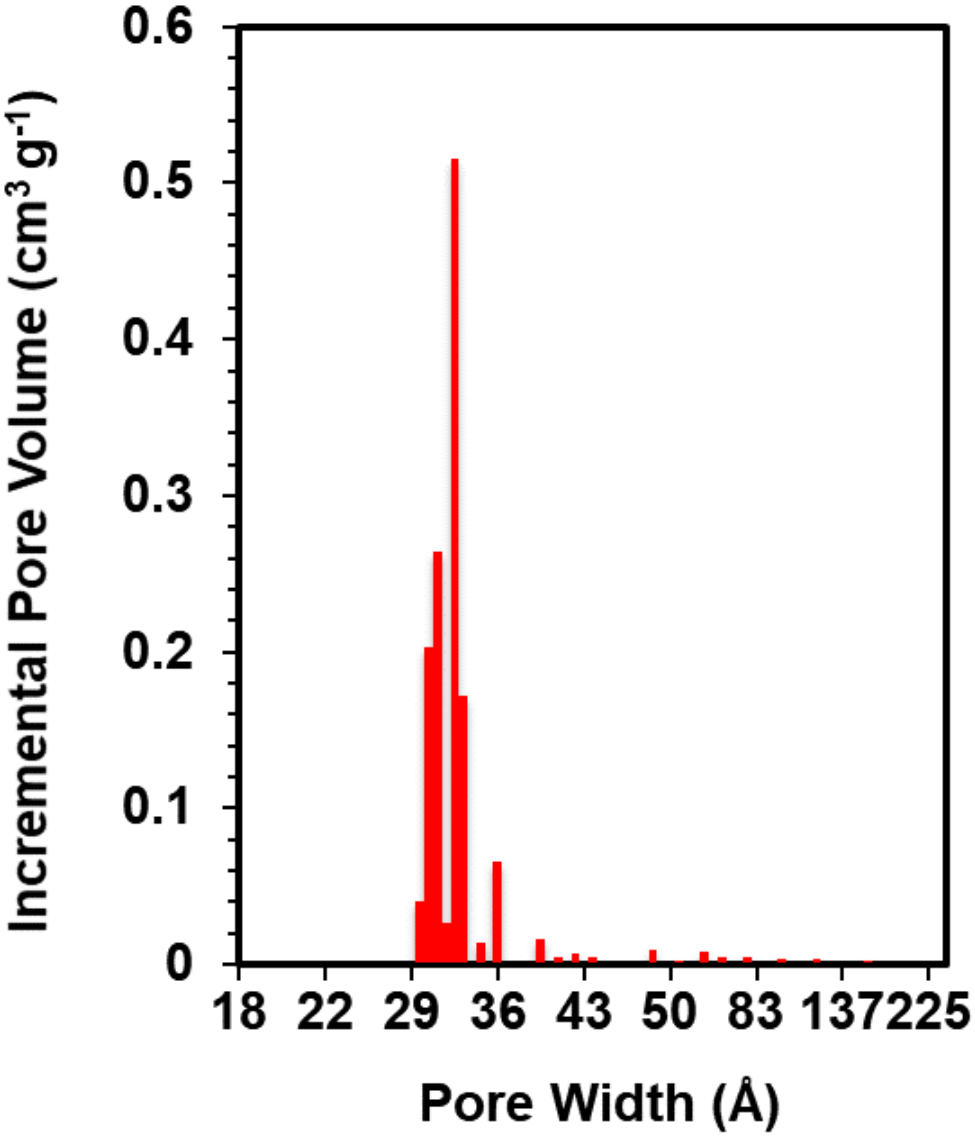

Figure 6.71. Pore size distribution of TAPB-PDA-Me COF.

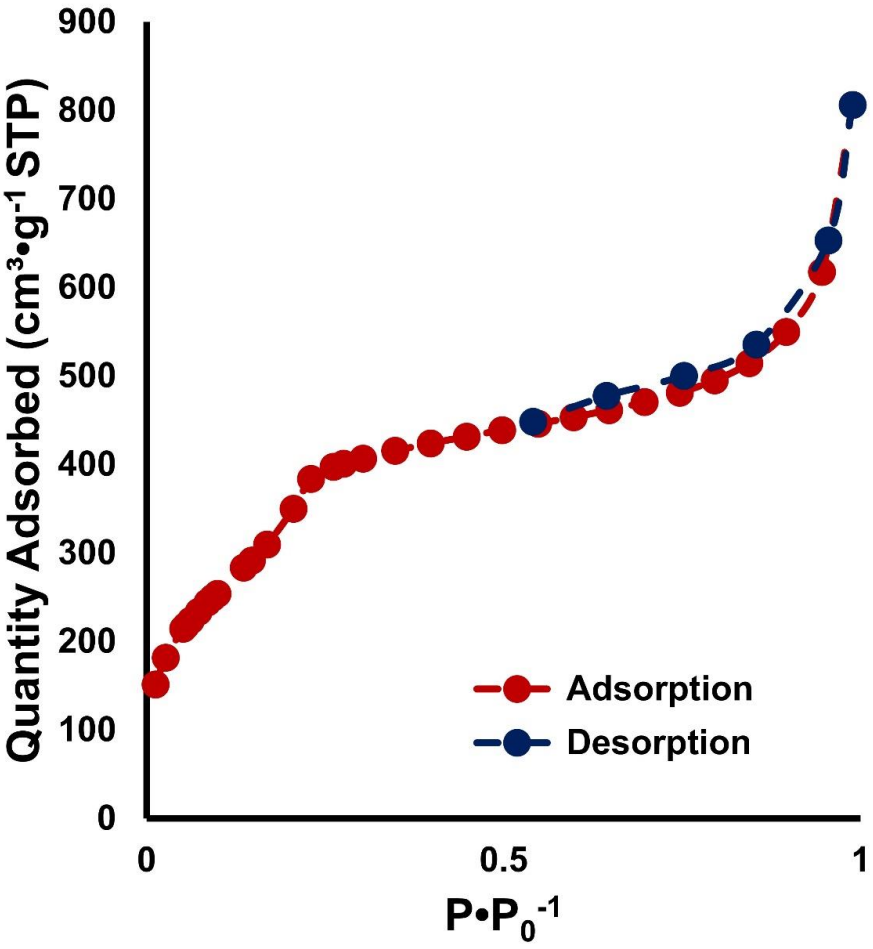

Figure 6.72. Nitrogen isotherm recorded at 77 K for TAPB-PDA-Et COF.

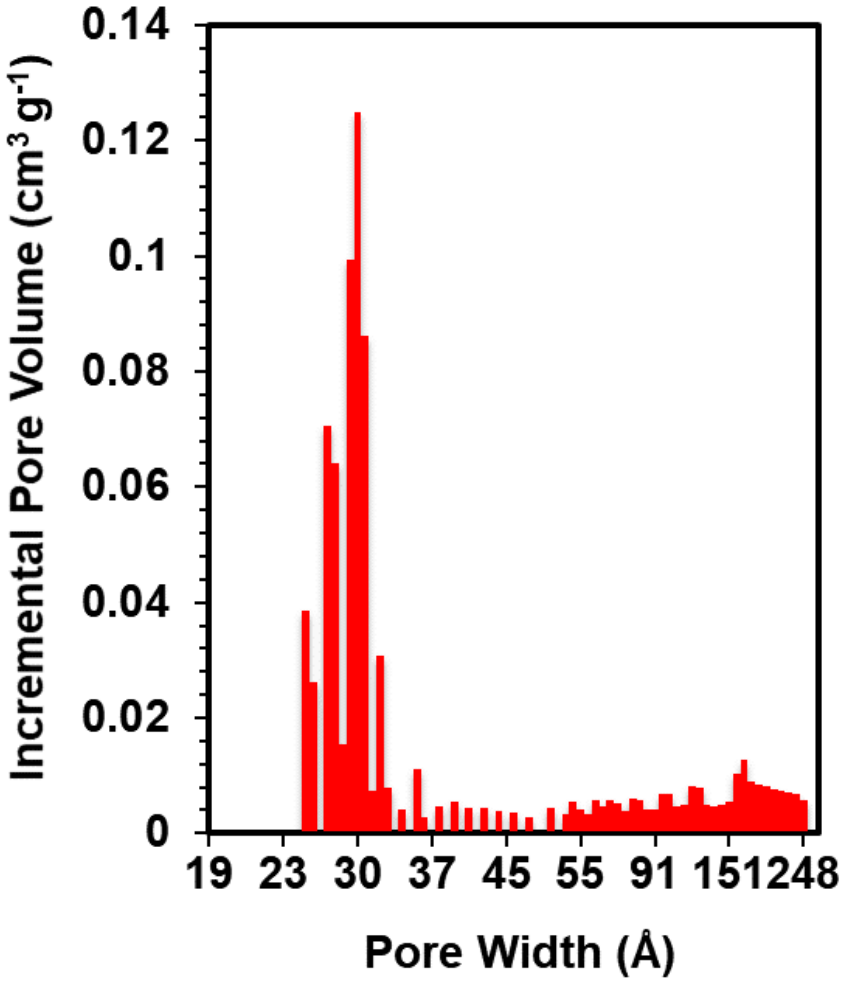

Figure 6.73. Pore size distribution of TAPB-PDA-Et COF.

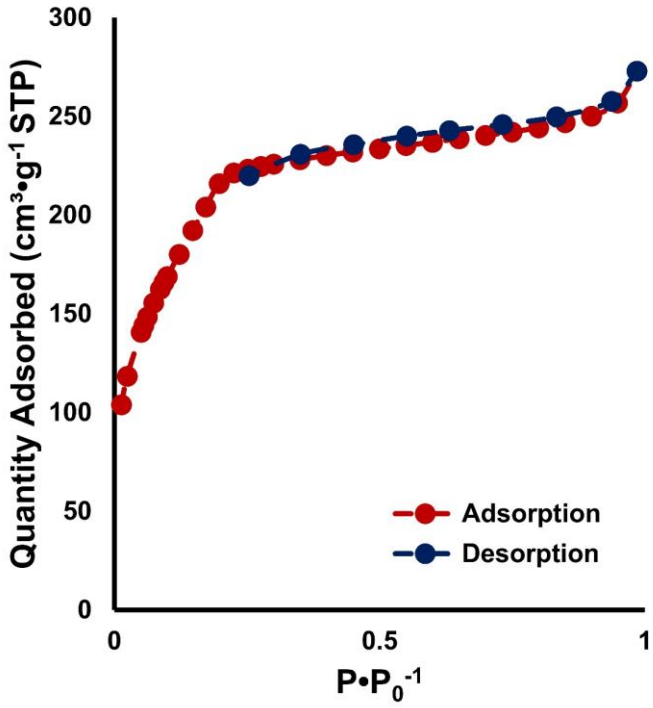

Figure 6.74. Nitrogen isotherm recorded at 77 K for TAPB-PDA-SMe COF.

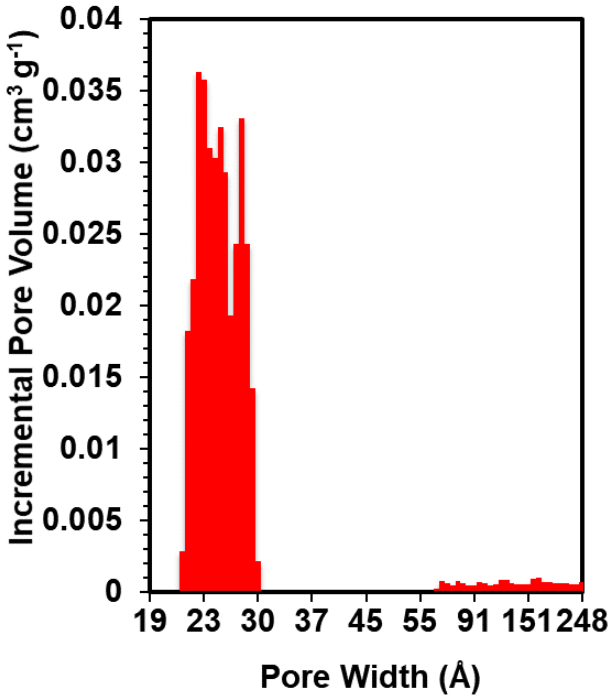

Figure 6.75. Pore size distribution of TAPB-PDA-SMe COF.

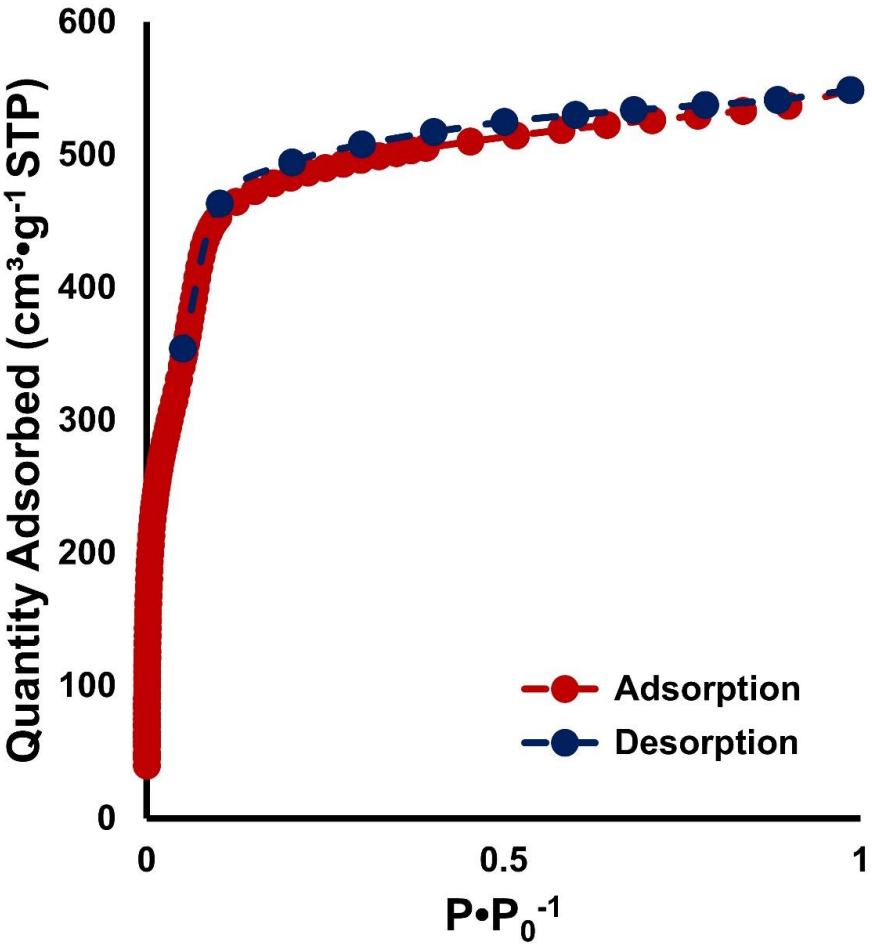

Figure 6.76. Nitrogen isotherm recorded at 77 K for BND-TFB COF.

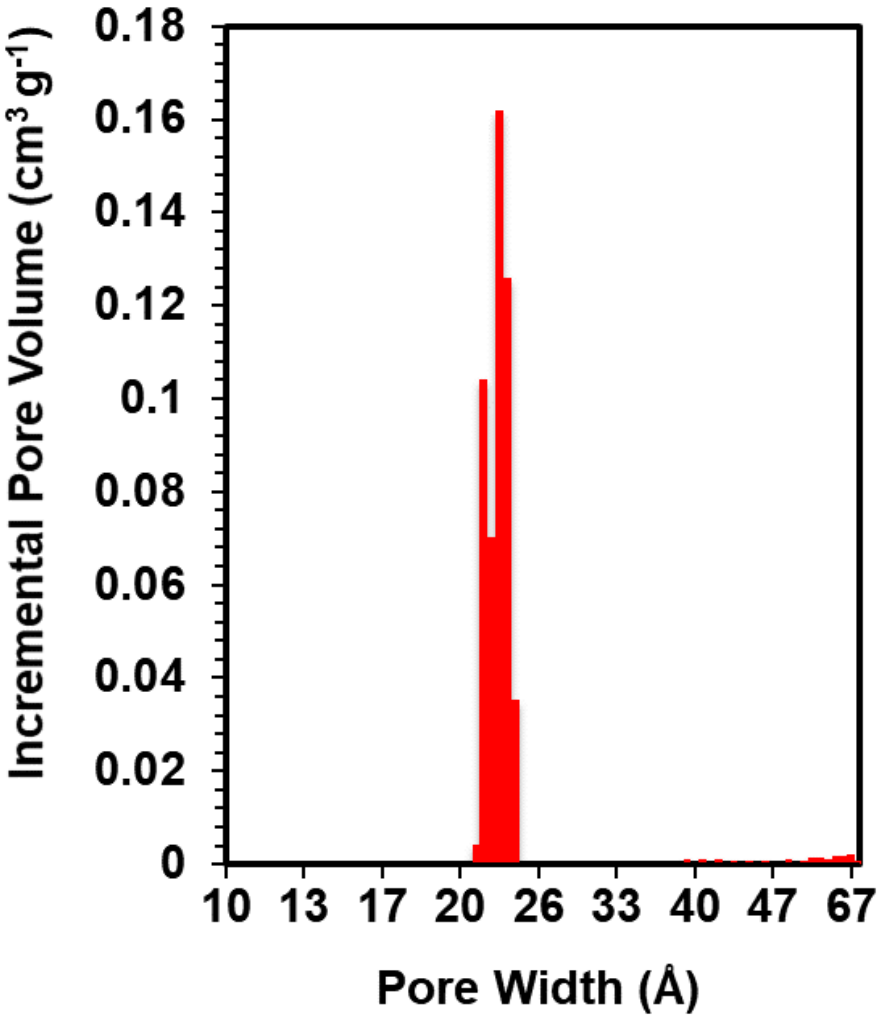

Figure 6.77. Pore size distribution of BND-TFB COF.

Fourier-Transform Infrared Spectroscopy

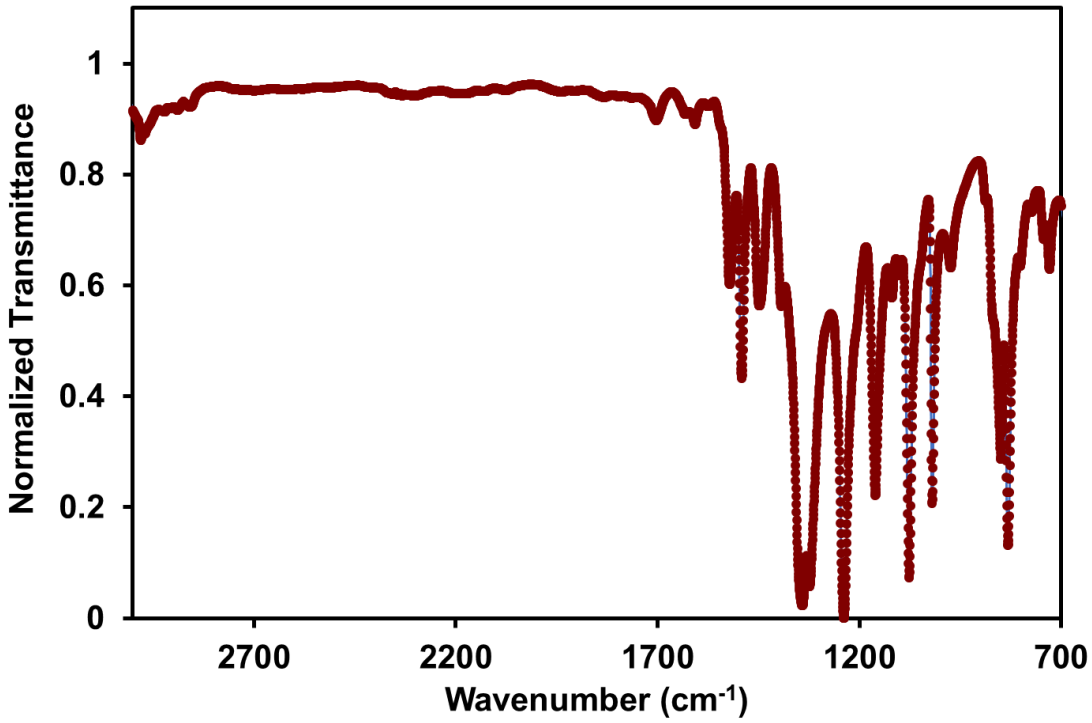

Figure 6.78. FT-IR Spectra of HHTP-PBBA COF.

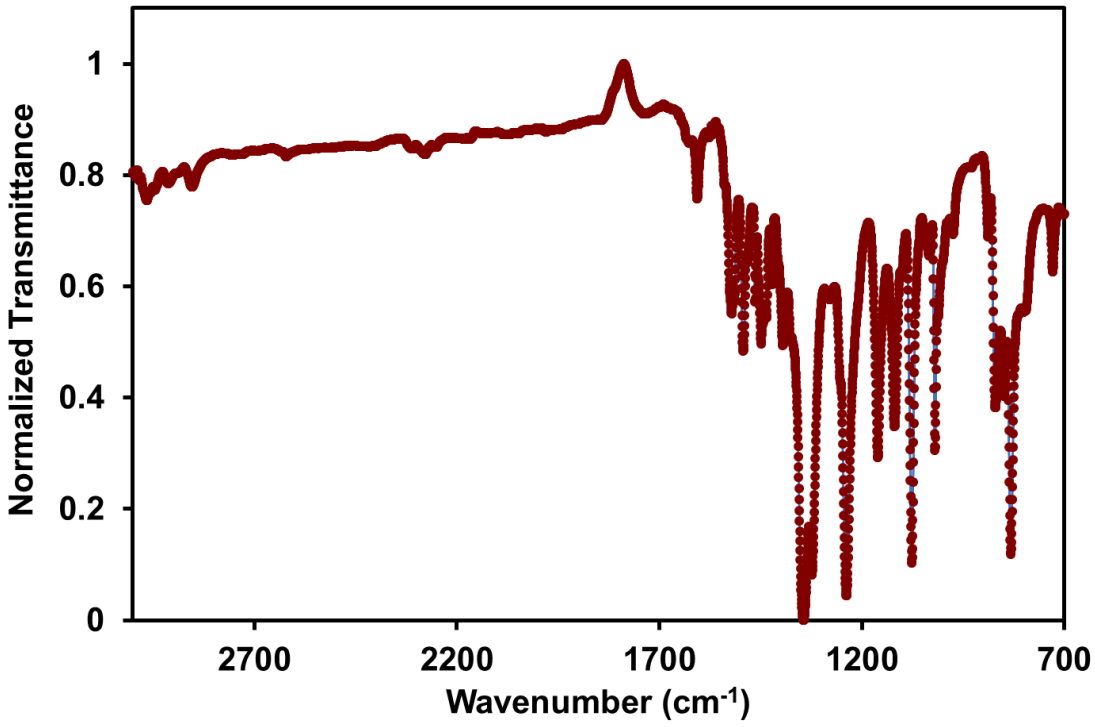

Figure 6.79. FT-IR Spectra of HHTP-BBBA COF.

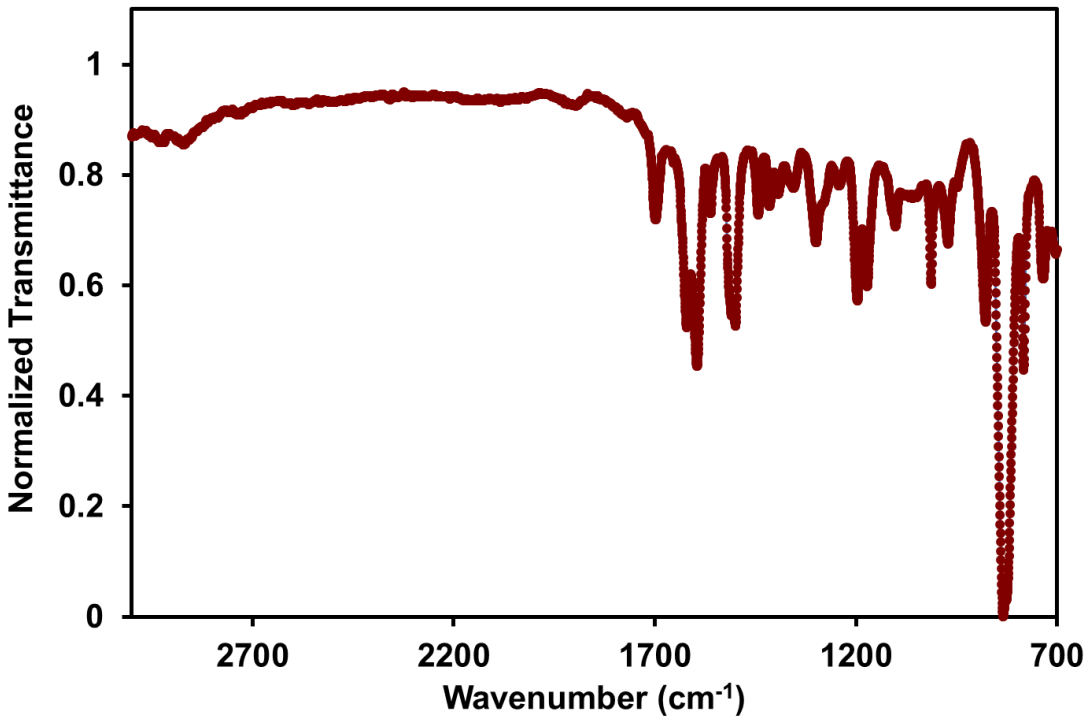

Figure 6.80. FT-IR Spectra of TAPB-PDA COF.

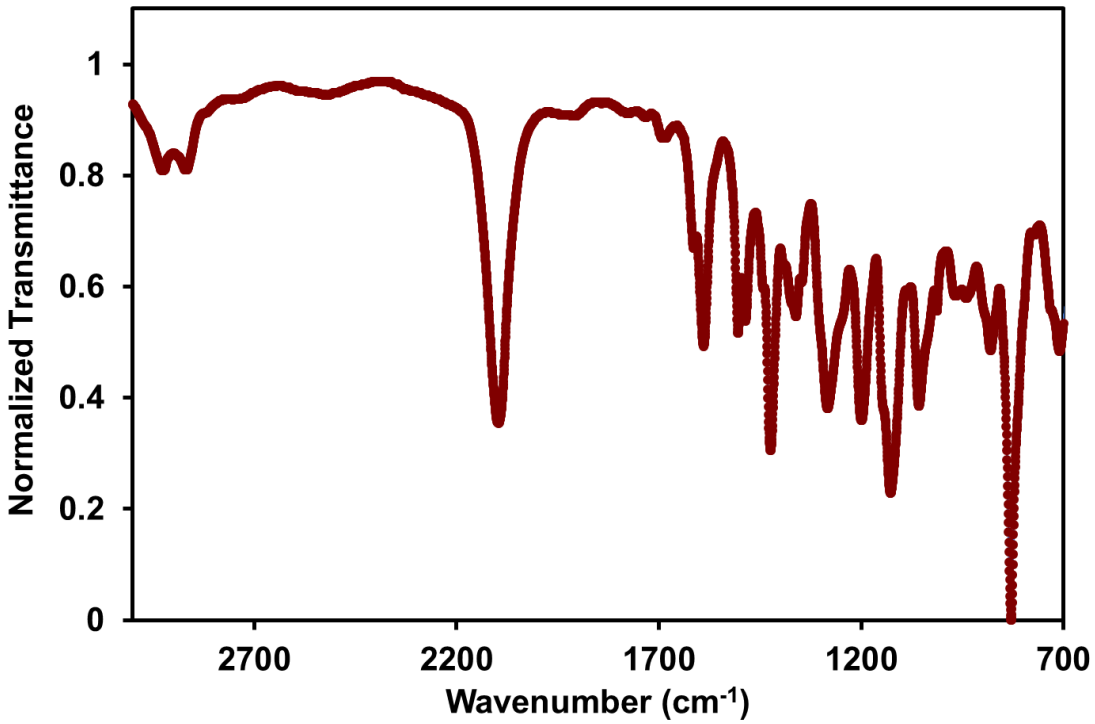

Figure 6.81. FT-IR Spectra of TAPB-PDA-N_3 COF.

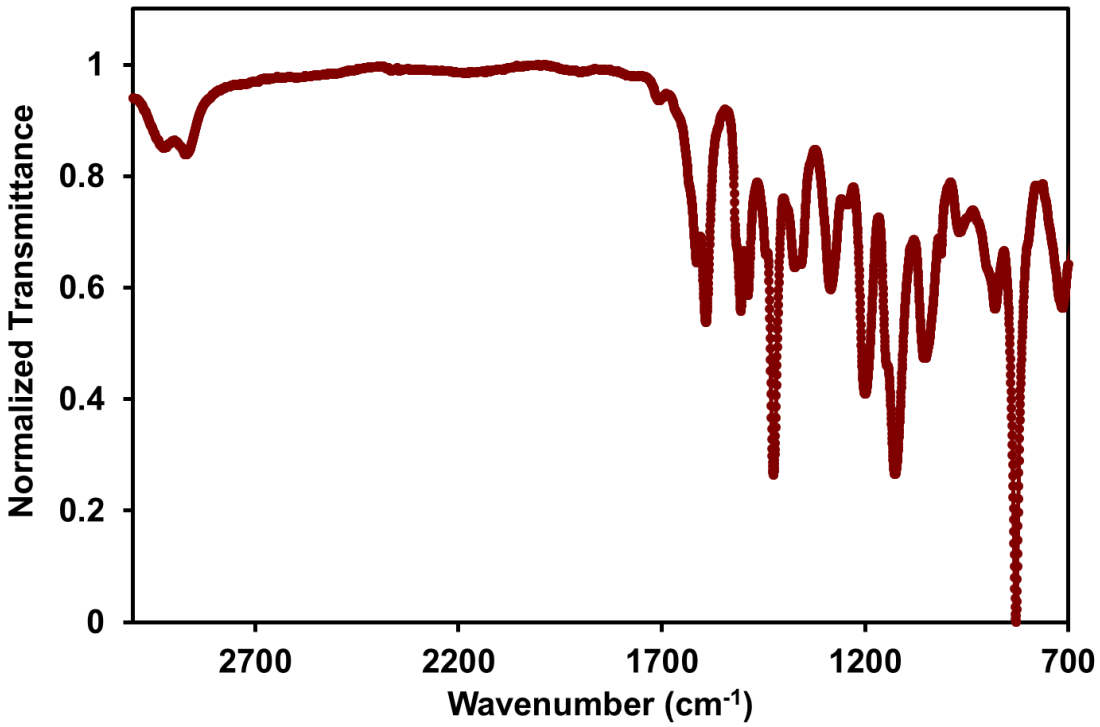

Figure 6.82. FT-IR Spectra of TAPB-PDA-NH_2 COF.

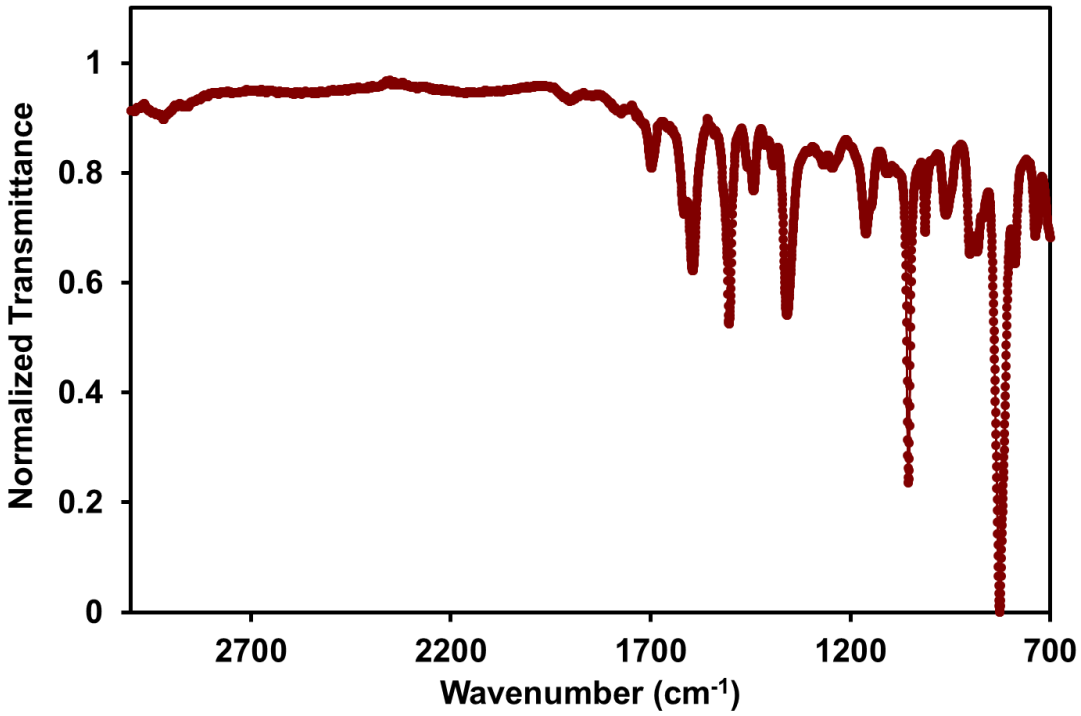

Figure 6.83. FT-IR Spectra of TAPB-PDA-Br COF.

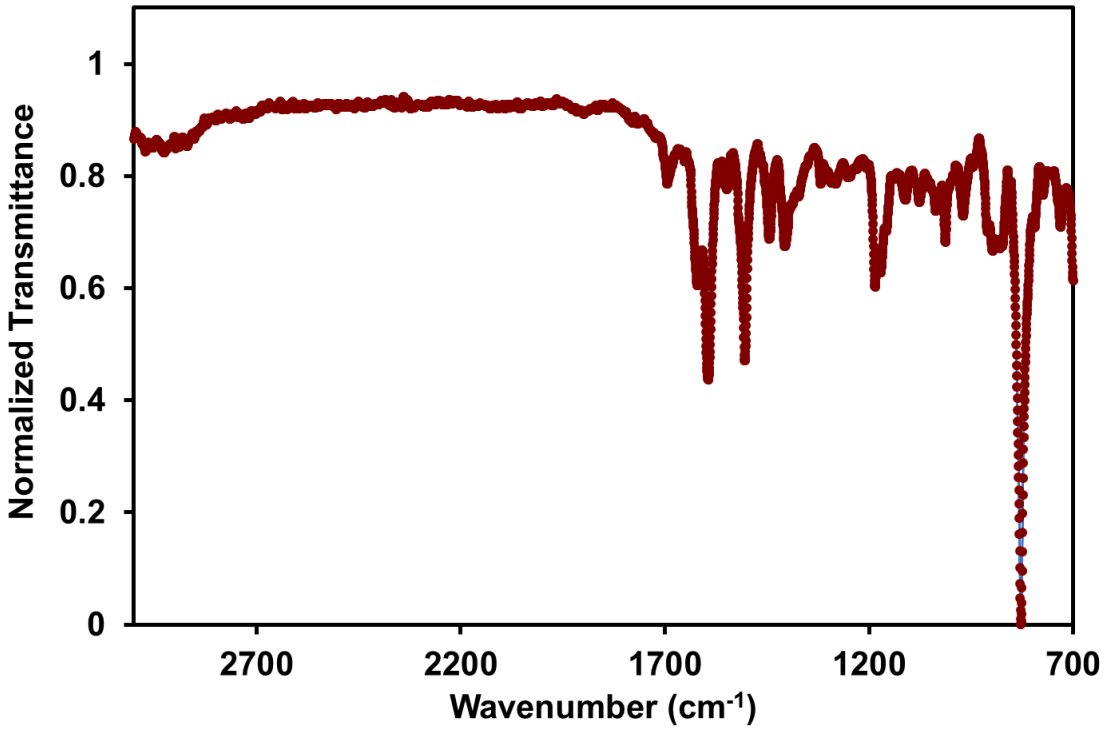

Figure 6.84. FT-IR Spectra of TAPB-PDA-Me COF.

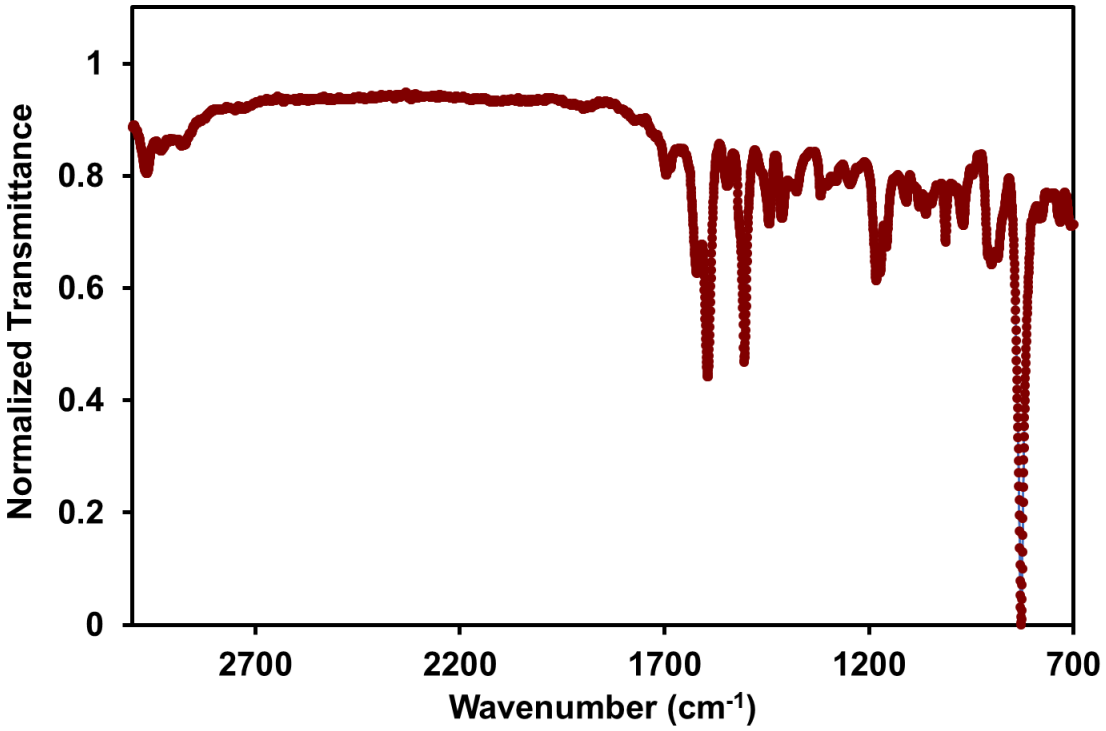

Figure 6.85. FT-IR Spectra of TAPB-PDA-Et COF.

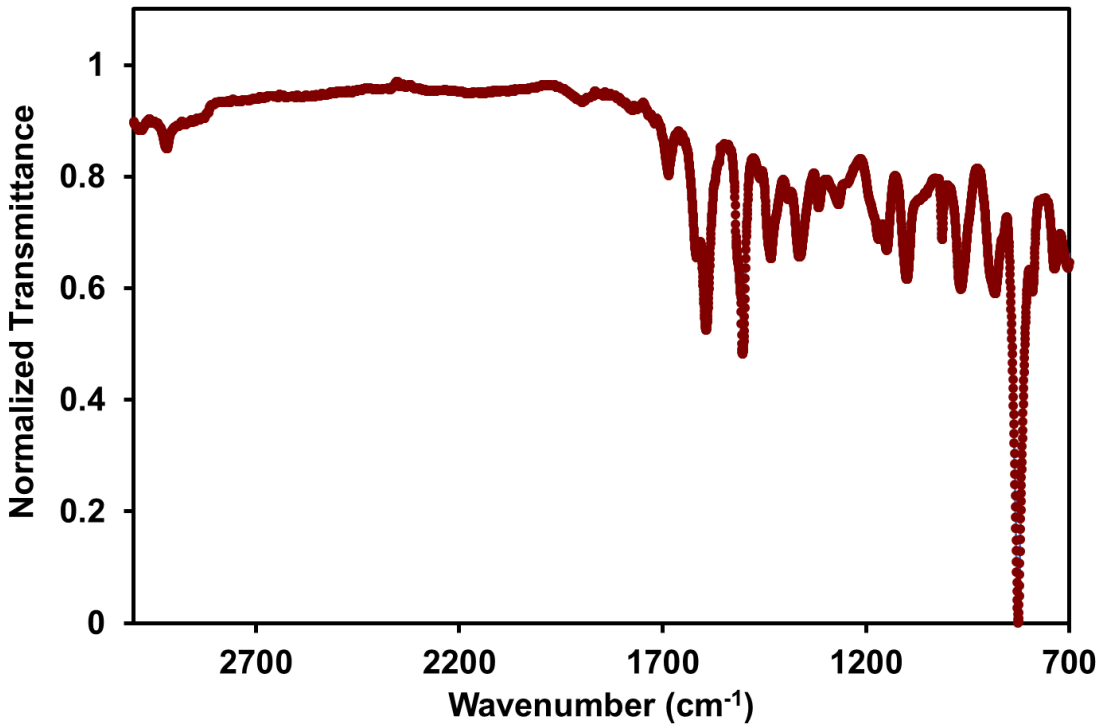

Figure 6.86. FT-IR Spectra of TAPB-PDA-SMe COF.

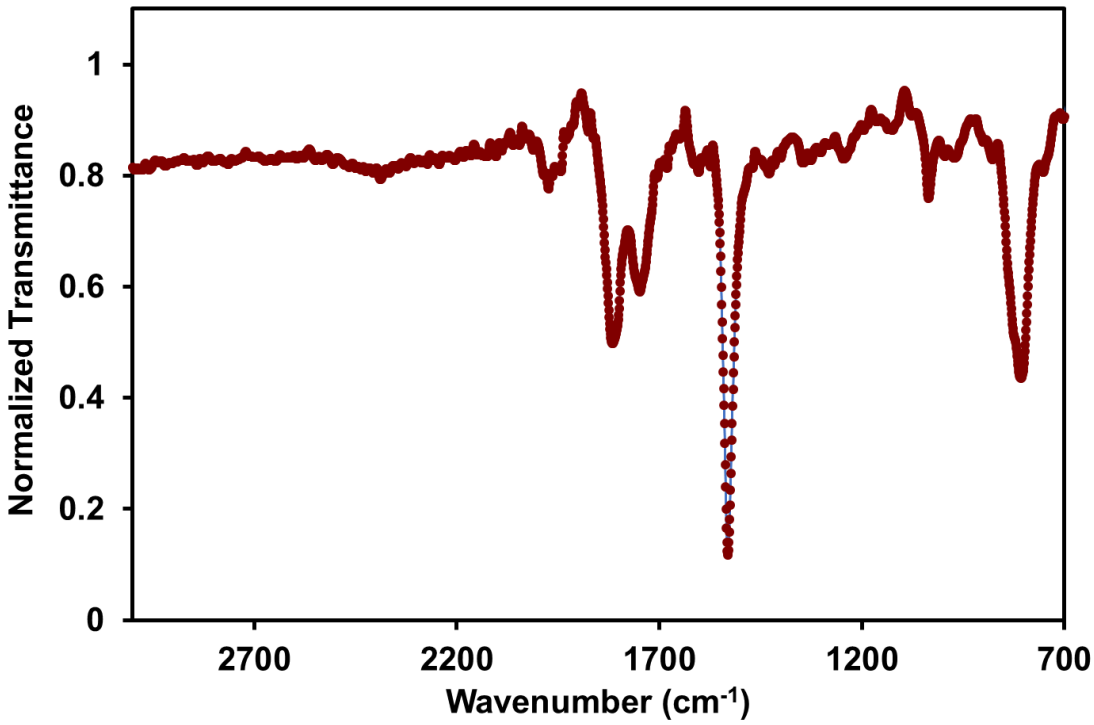

Figure 6.87. FT-IR Spectra of BND-TFB COF.

Diffuse Reflectance Infrared Fourier Transform Spectroscopy

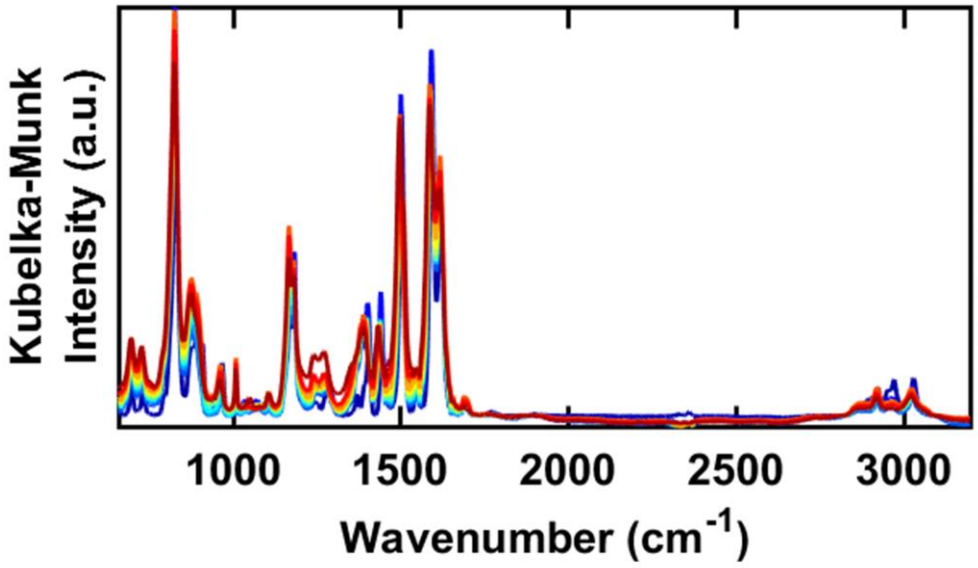

Figure 6.88. Full DRIFTS spectra of TAPB-PDA-Me COF.

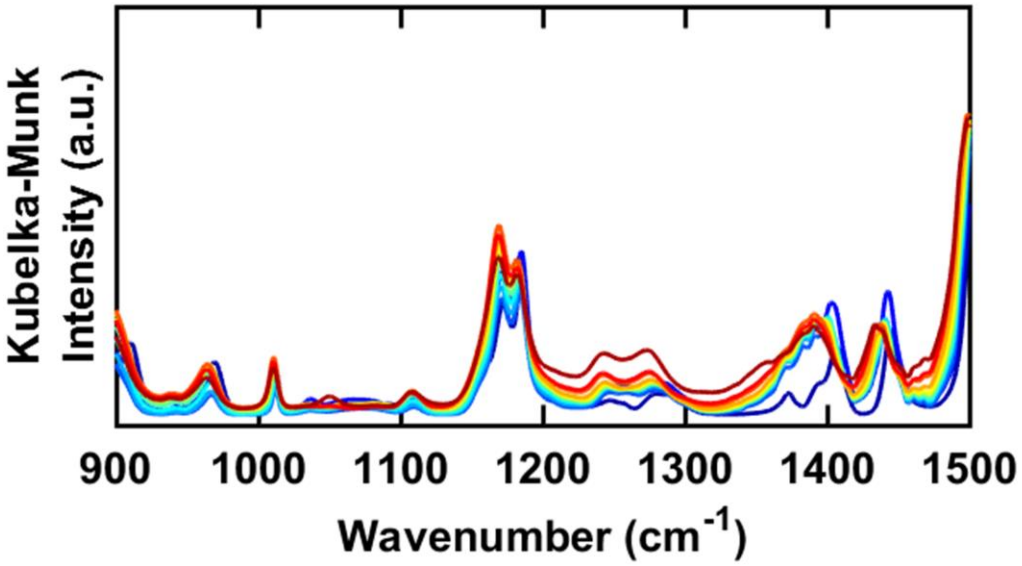

Figure 6.89. DRIFTS spectra of TAPB-PDA-Me COF from 900–1500 cm^{-1}.

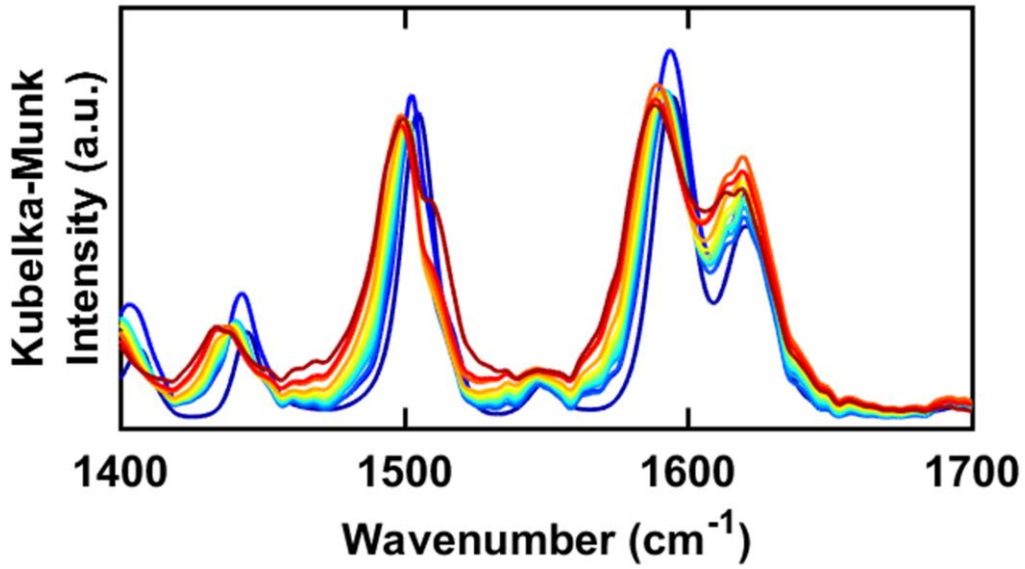

Figure 6.90. DRIFTS spectra of TAPB-PDA-Me COF from 1400–1700 cm^{-1}.

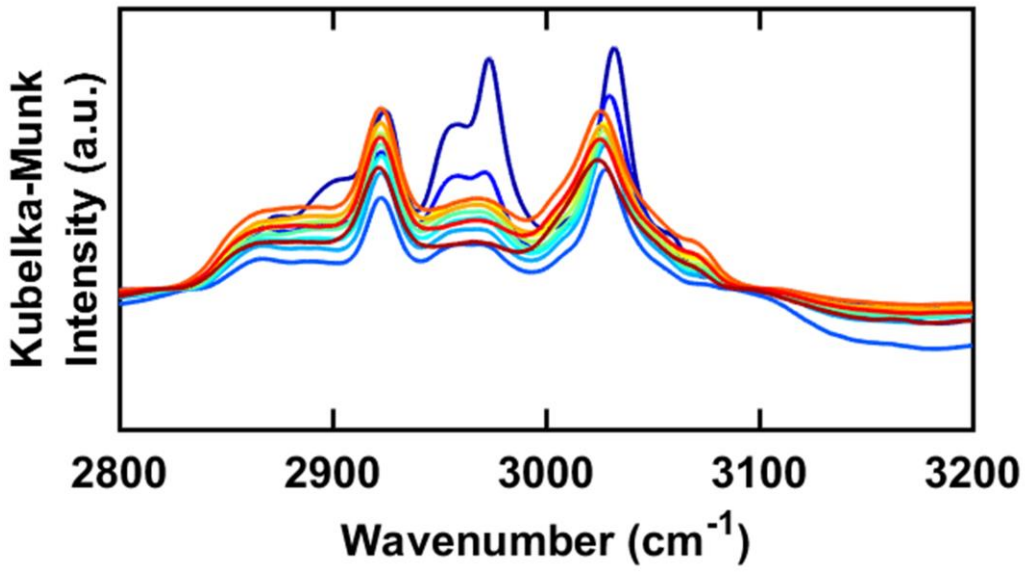

Figure 6.91. DRIFTS spectra of TAPB-PDA-Me COF from 2800–3200 cm^{-1}.

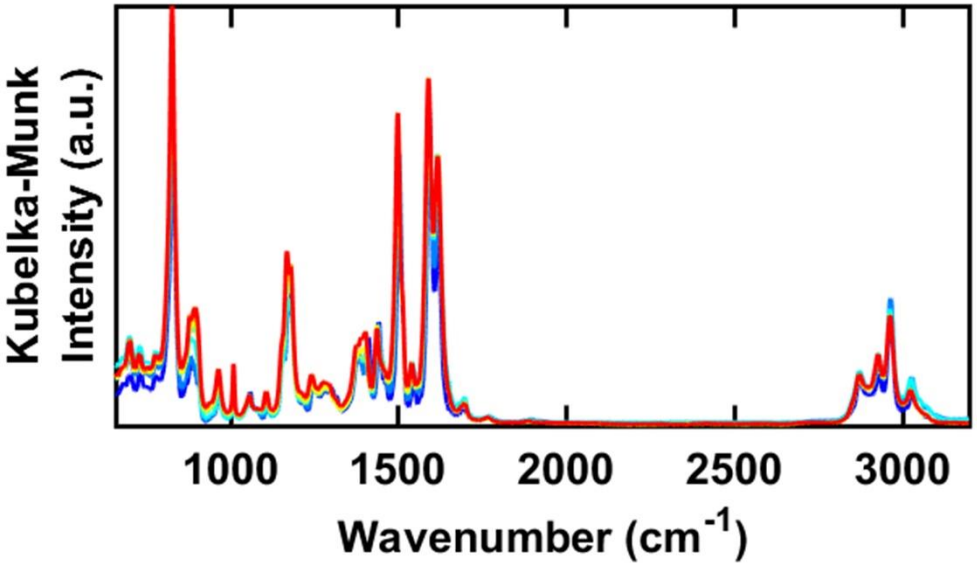

Figure 6.92. Full DRIFTS spectra of TAPB-PDA-Et COF.

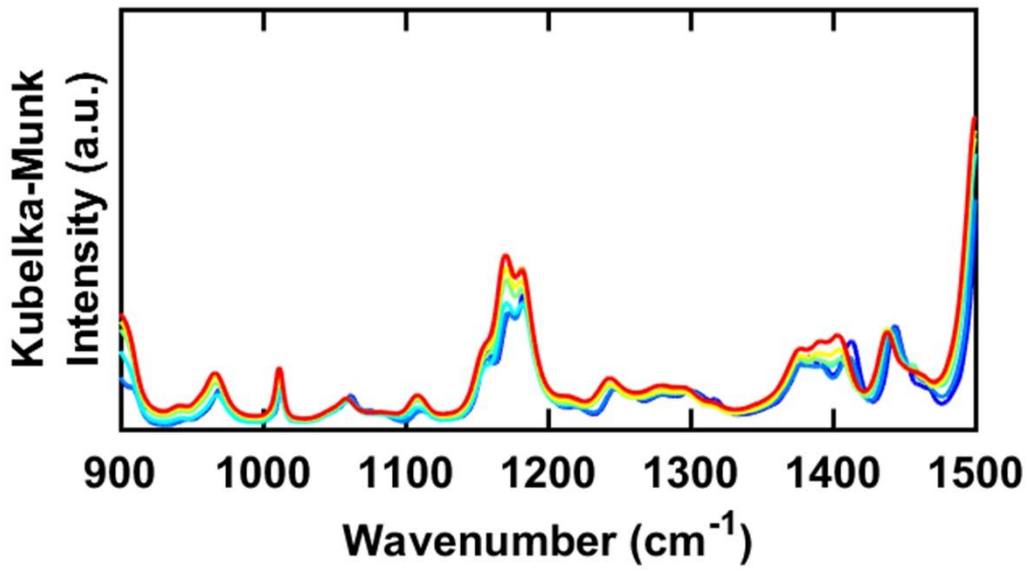

Figure 6.93. DRIFTS spectra of TAPB-PDA-Et COF from 900–1500 cm^{-1}.

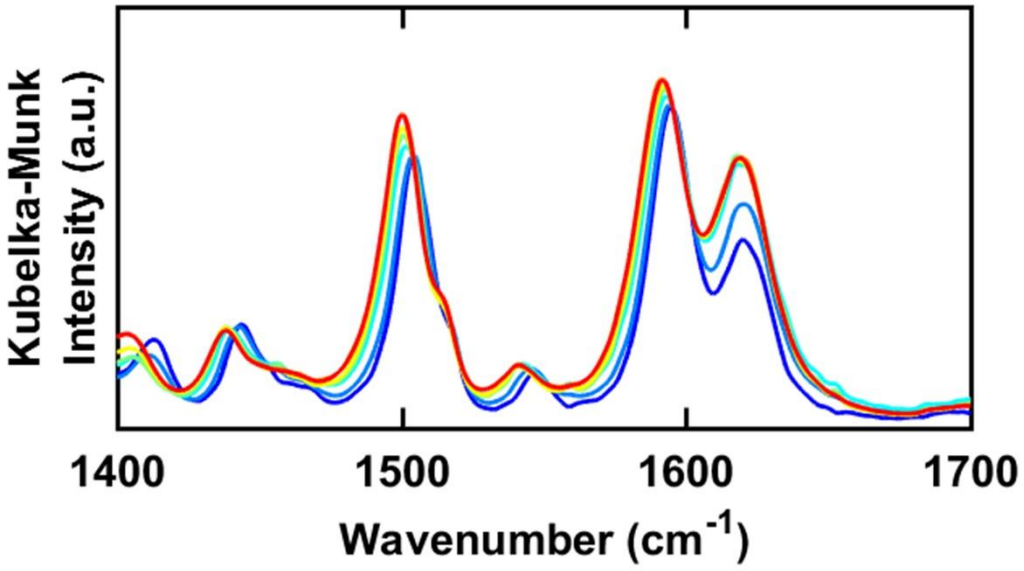

Figure 6.94. DRIFTS spectra of TAPB-PDA-Et COF from 1400–1700 cm^{-1}.

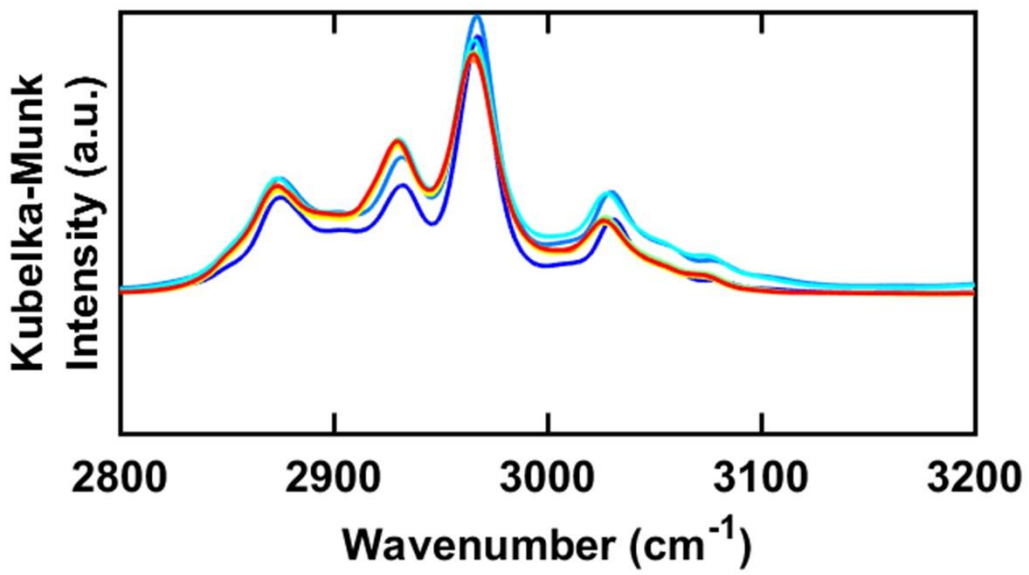

Figure 6.95. DRIFTS spectra of TAPB-PDA-Et COF from 2800–3200 cm^{-1}.

Thermogravimetric Analysis

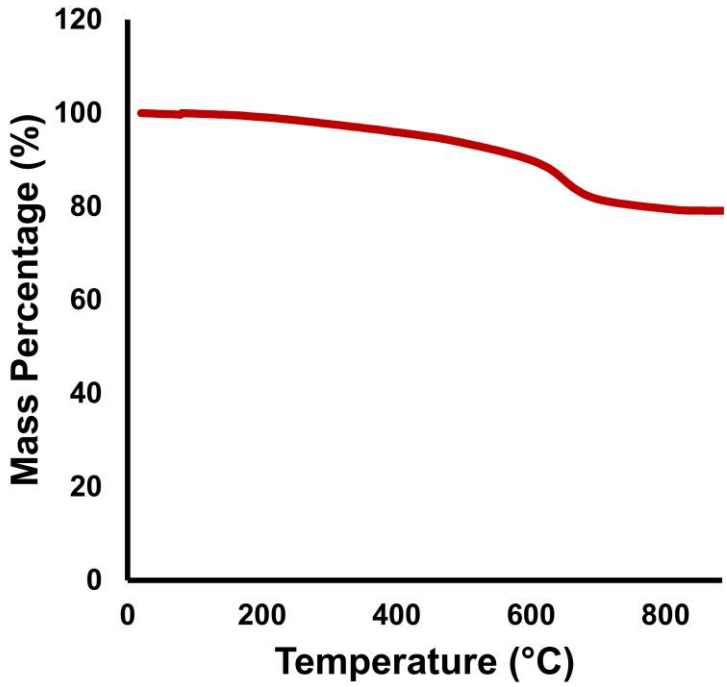

Figure 6.96. TGA of HHTP-PBBA COF.

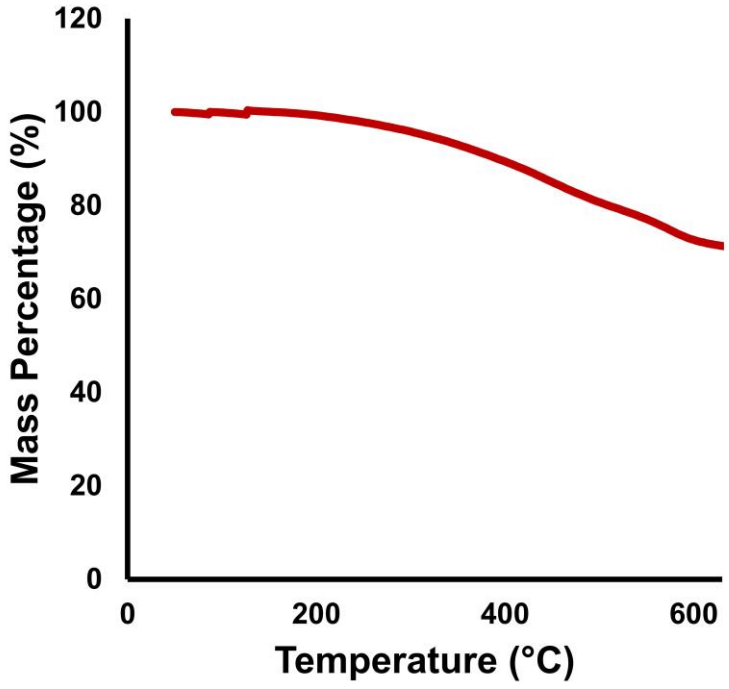

Figure 6.97. TGA of HHTP-BBBA COF.

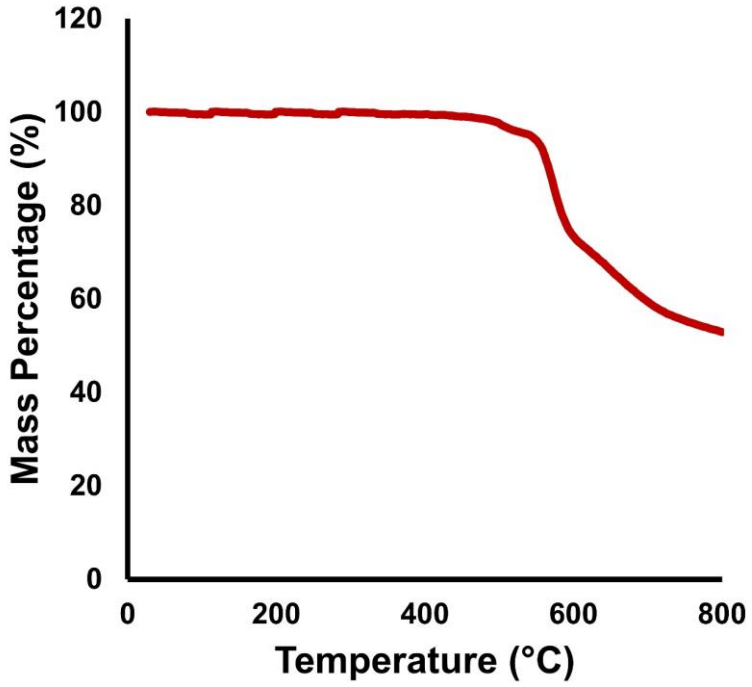

Figure 6.98. TGA of TAPB-PDA COF.

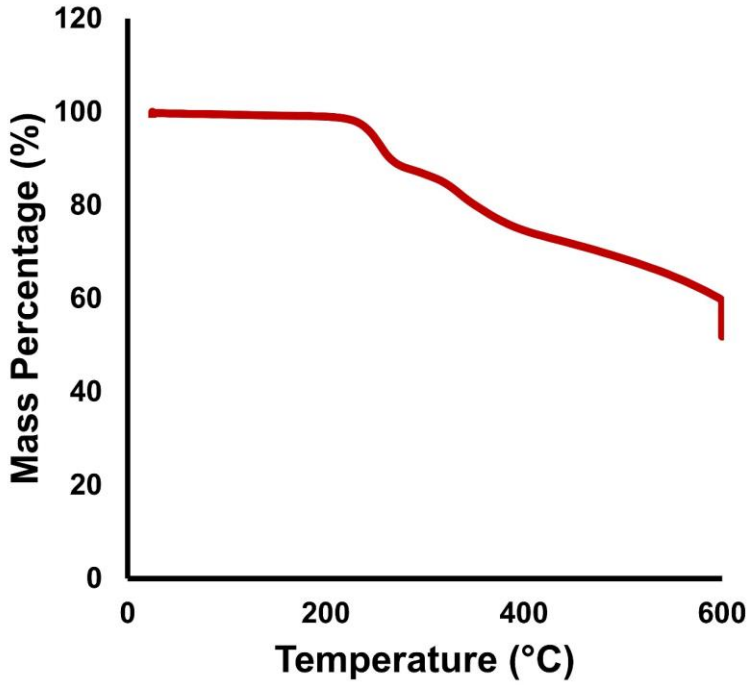

Figure 6.99. TGA of TAPB-PDA-N_3 COF.

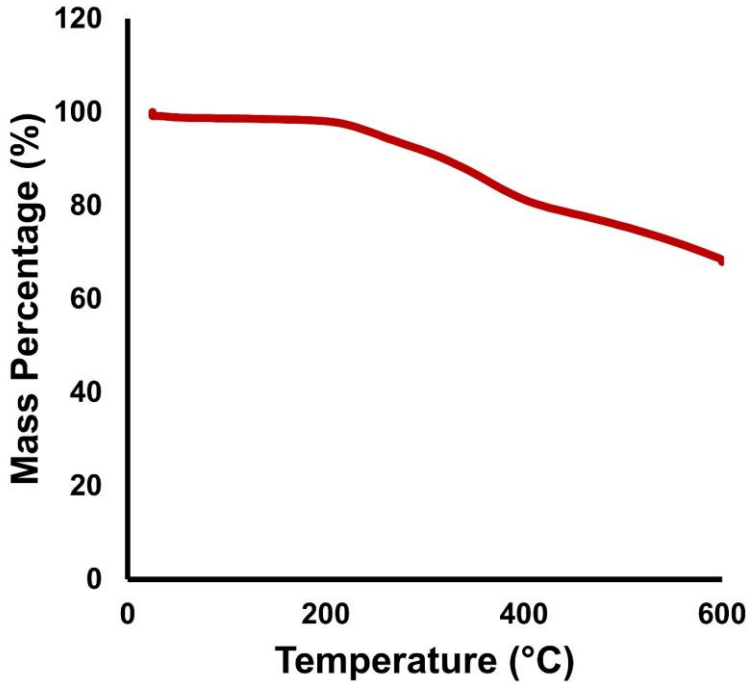

Figure 6.100. TGA of TAPB-PDA-NH_2 COF.

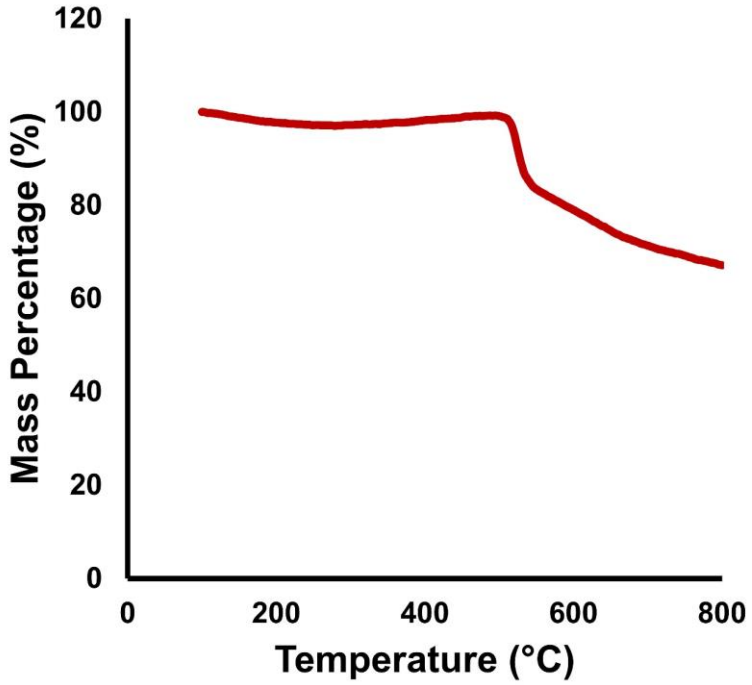

Figure 6.101. TGA of TAPB-PDA-Br COF.

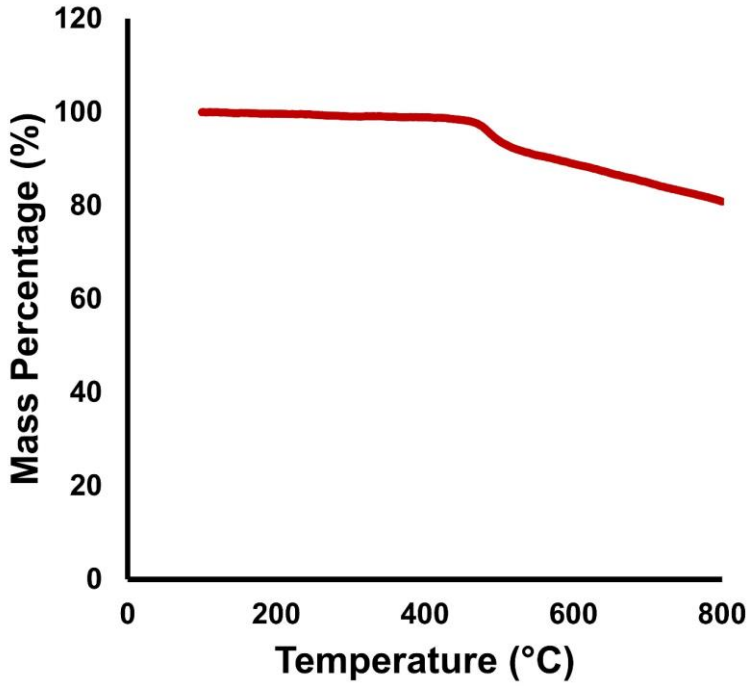

Figure 6.102. TGA of TAPB-PDA-Me COF.

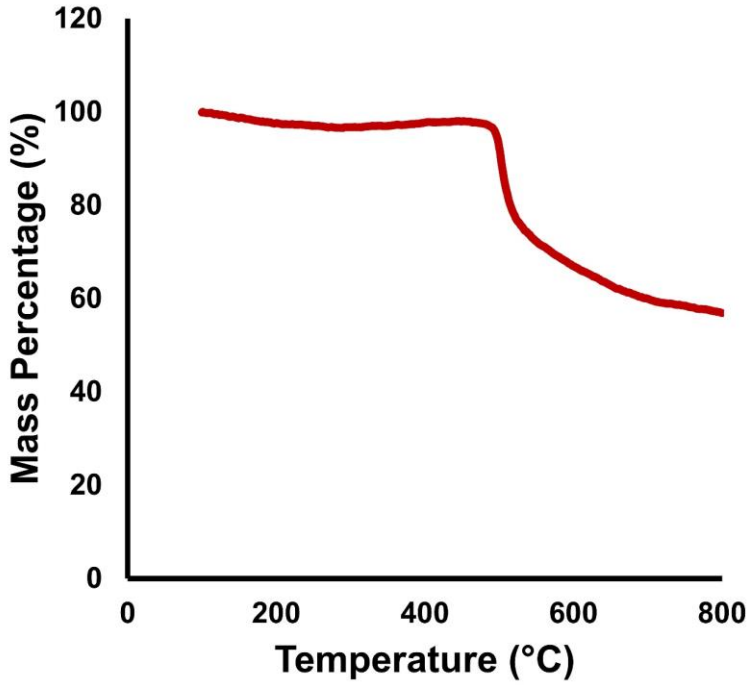

Figure 6.103. TGA of TAPB-PDA-Et COF.

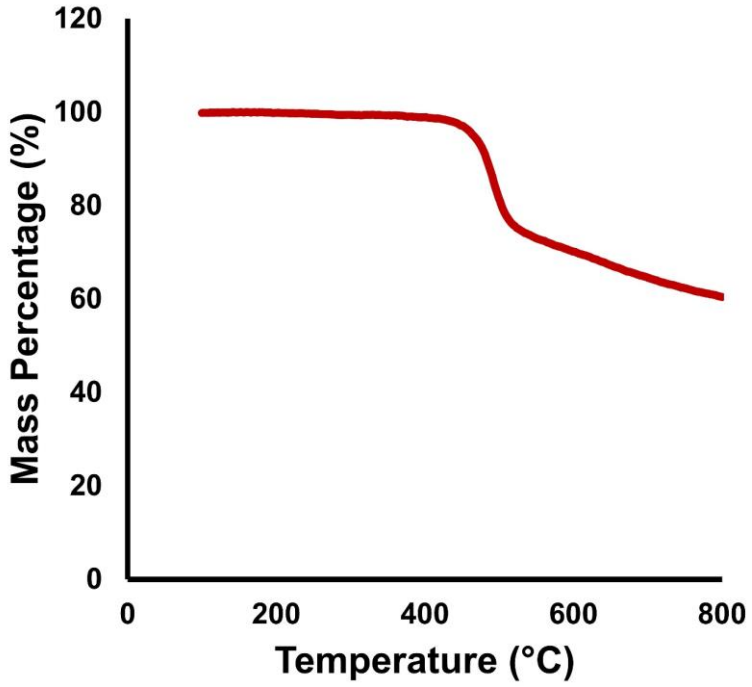

Figure 6.104. TGA of TAPB-PDA-SMe COF.

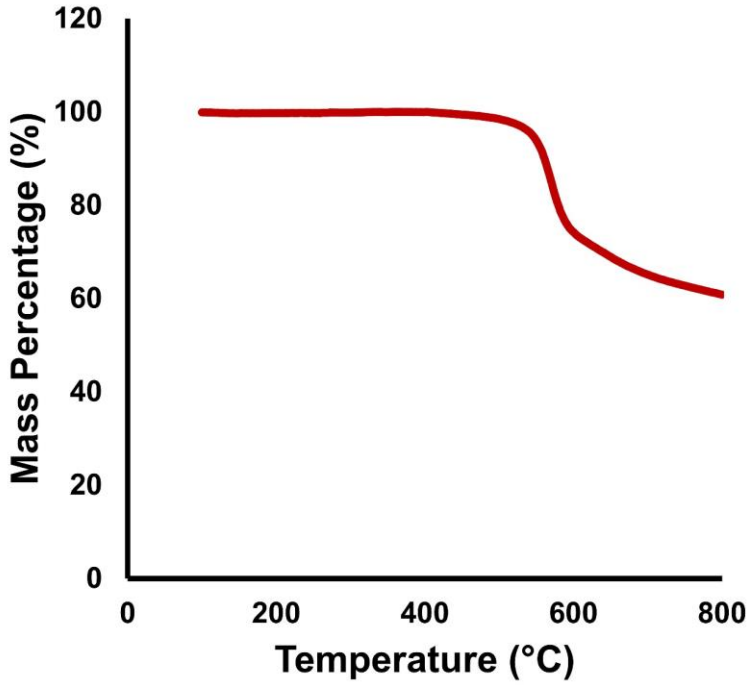

Figure 6.105. TGA of BND-TFB COF.

Density Functional Theory Calculations

Table 6.1. Summary of the calculated lattice parameters for TPB-PDA COF.

TAPB-PDA							
Phase	*Lattice parameters* (Å)						
	a	*b*	*c*	*α*	*β*	*γ*	Volume ($Å^3$)
Planar	37.20	37.20	4.04	90.0	90.0	120.0	4837
Deformed	37.03	37.25	4.05	97.8	85.3	120.0	4795
• The planar and deformed geometries have hexagonal and triclinic symmetry, respectively.							

Table 6.2. Summary of the calculated lattice parameters for TPB-PDA-Et COF.

TAPB-PDA-Et							
Phase	*Lattice parameters* (Å)						
	a	*b*	*c*	*α*	*β*	*γ*	Volume ($Å^3$)
Planar	37.04	37.04	4.10	90.0	90.0	120.0	4877
Deformed	37.48	37.34	4.08	70.7	109.0	121.1	4795
• The planar and deformed geometries have hexagonal and triclinic symmetry, respectively.							

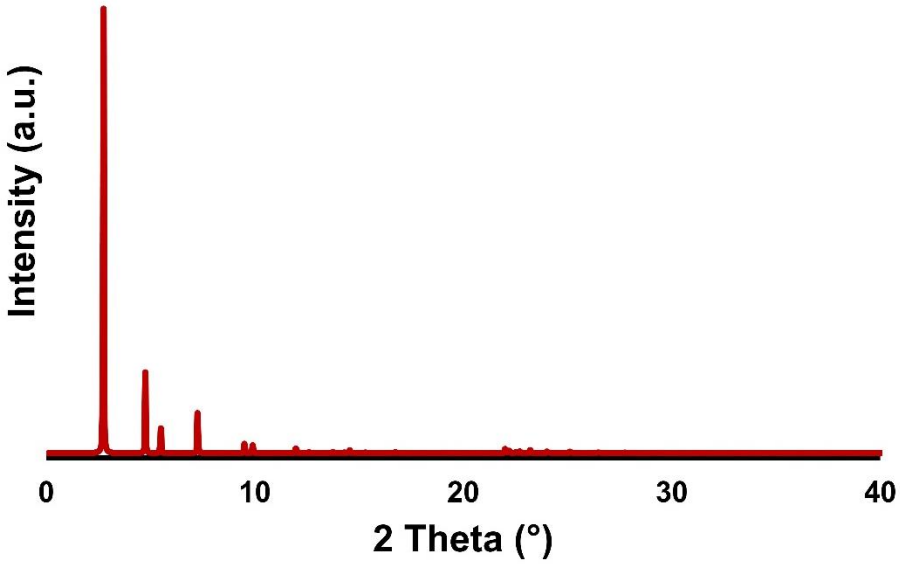

Figure 6.106. Simulated eclipsed XRD pattern of TAPB-PDA COF.

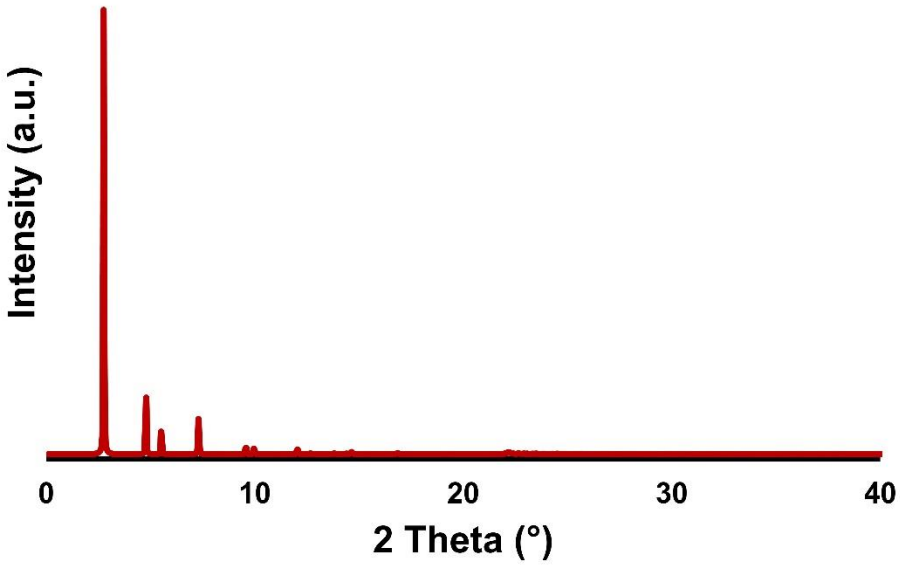

Figure 6.107. Simulated relaxed XRD pattern of TAPB-PDA COF.

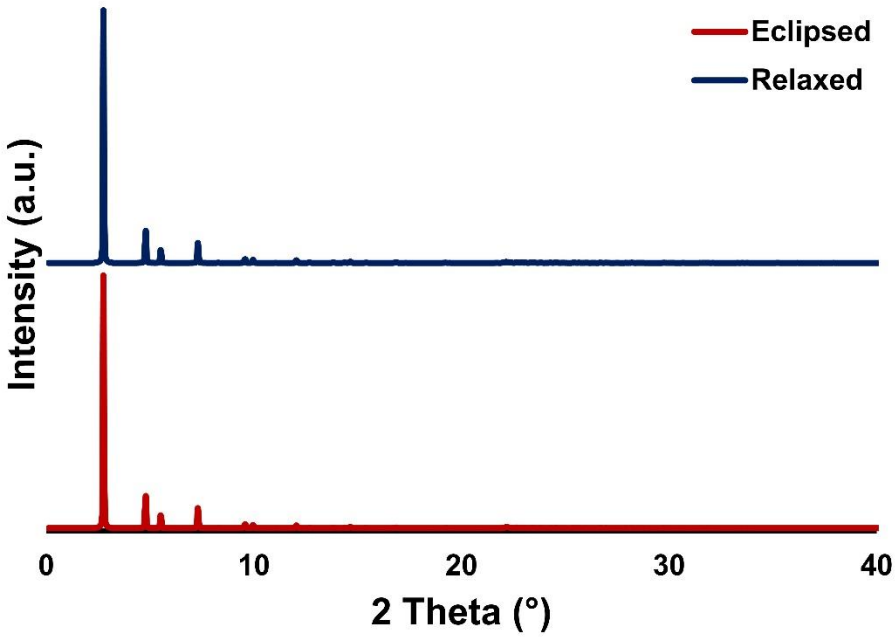

Figure 6.108. Comparison of simulated relaxed and eclipsed XRD patterns of TAPB-PDA COF.

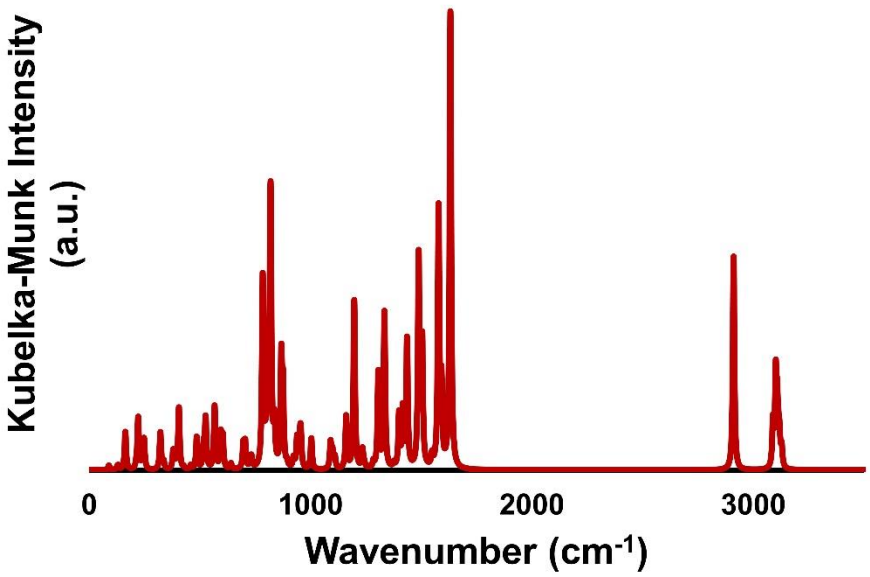

Figure 6.109. Full simulated IR spectra of TAPB-PDA COF.

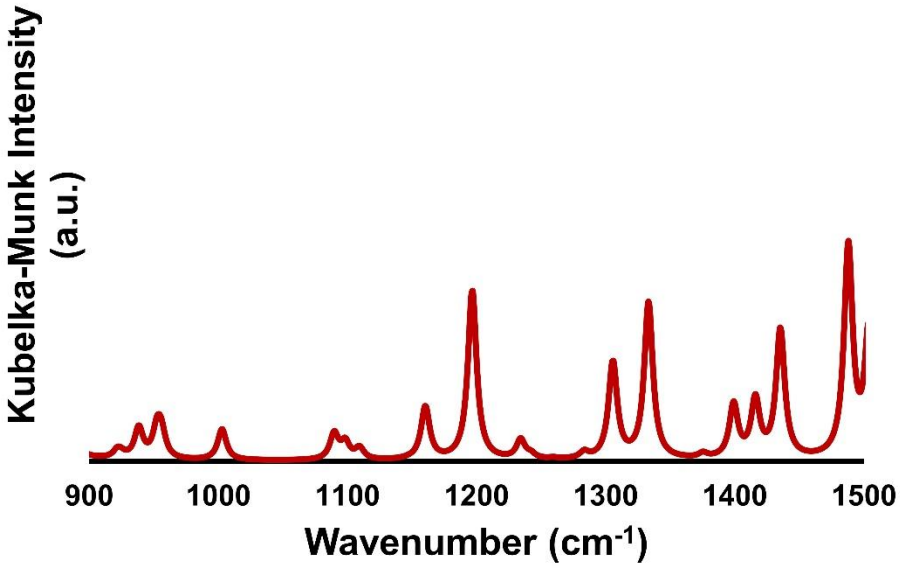

Figure 6.110. Simulated IR spectra of TAPB-PDA COF from 900–1500 cm^{-1}.

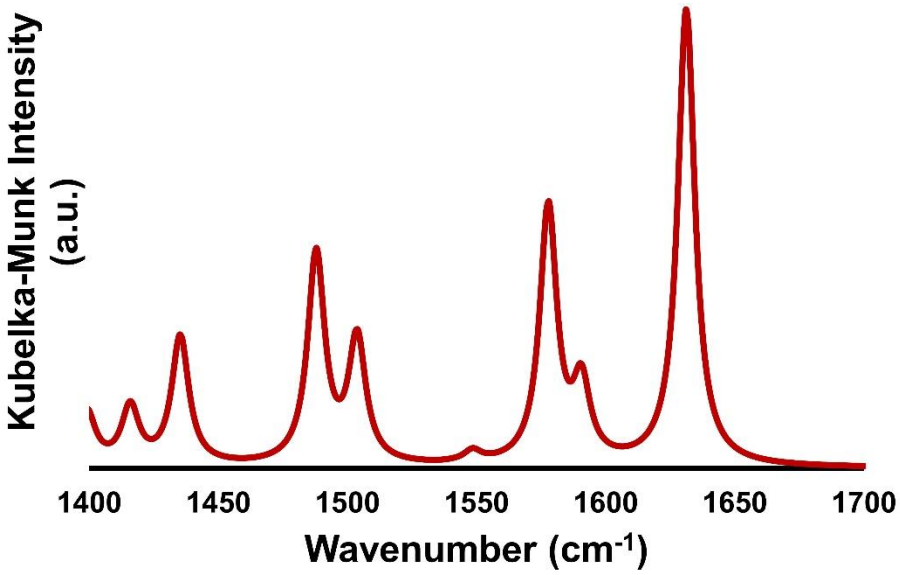

Figure 6.111. Simulated IR spectra of TAPB-PDA COF from 1400–1700 cm^{-1}.

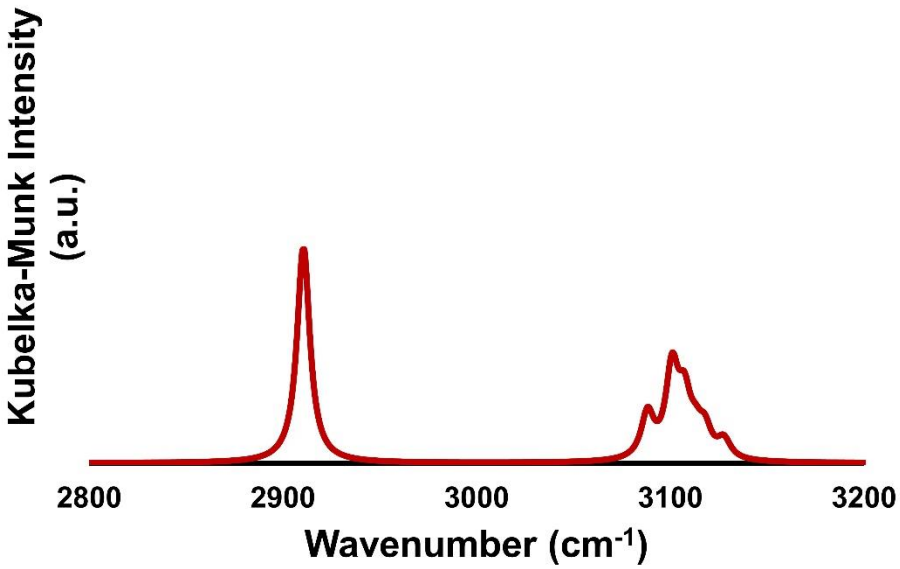

Figure 6.112. Simulated IR spectra of TAPB-PDA COF from 2800–3200 cm^{-1}.

PDA-NH_2 Self-Condensation Control Reaction

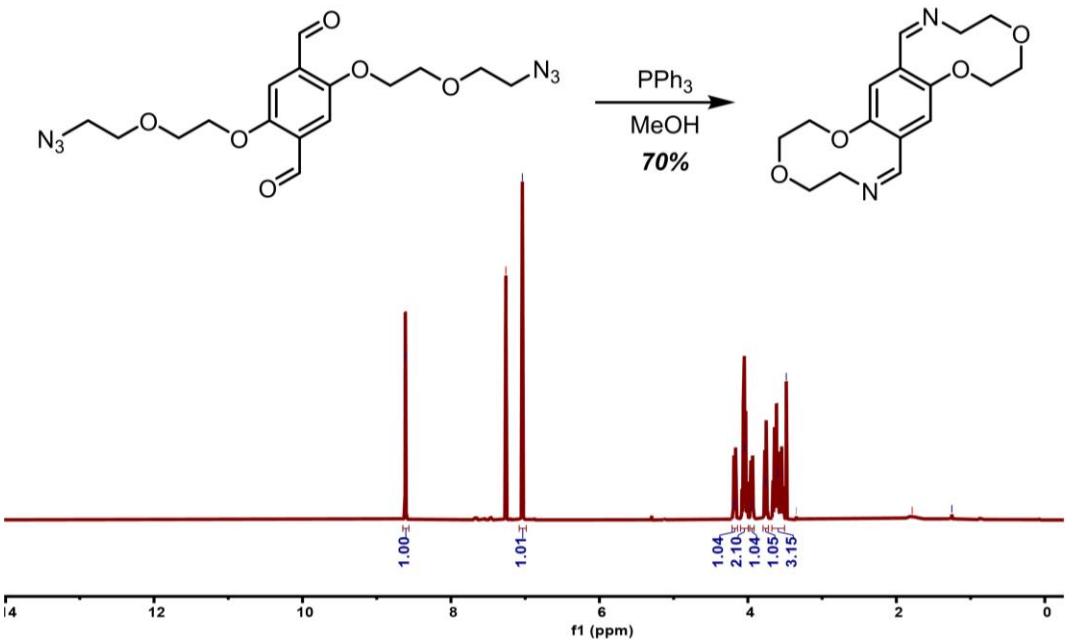

Figure 6.113. ^1H NMR ($CDCl_3$, 500 MHz, 298 K) of the self-condensation of PDA-NH_2 upon reduction of the azide starting material.

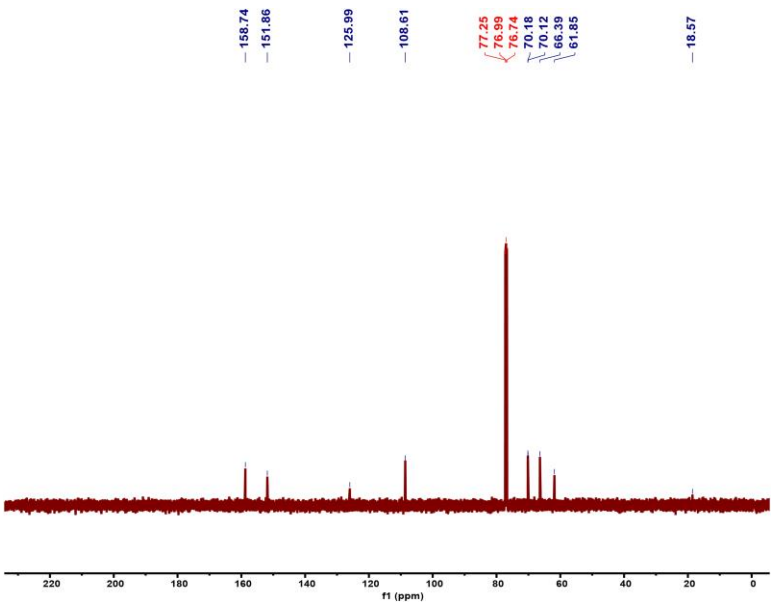

Figure 6.114. ^{13}C NMR ($CDCl_3$, 126 MHz, 298 K) of the self-condensation of PDA-NH_2 upon reduction of the azide starting material.

Chapter 7 : Humidity Sensing Through Reversible Isomerization of a Covalent Organic Framework

7.1 Abstract

Here we report that a covalent organic framework (COF), which contains 2,5-di(imine)-substituted 1,4-dihydroxybenzene (diiminol) moieties, undergoes color changes in the presence of solvents or solvent vapor that are rapid, passive, reversible, and easily detectable by the naked eye. A new visible absorption band appears in the presence of polar solvents, especially water, suggesting reversible conversion to another species. This reversibility is attributed to the ability of the diiminol to rapidly tautomerize to an iminol/*cis*-ketoenamine, and its inability to doubly tautomerize to a diketoenamine. Density functional theory (DFT) calculations suggest similar energies for the two tautomers in the presence of water, but that the diiminol is much more stable in its absence. Time-dependent DFT calculations confirm that the iminol/*cis*-ketoenamine absorbs at longer wavelength than the diiminol, and indicate this absorption has significant charge-transfer character. A colorimetric humidity sensing device constructed from an oriented thin film of the COF responded quickly to water vapor and was stable for months. These results suggest that tautomerization-induced electronic-structure changes can be exploited in COF platforms to give rapid, reversible, sensing in systems that exhibit long-term stability.

7.2 An Introduction to Solid-state Tautomerization

Tautomers are constitutional isomers that are interconverted by migration of an atom or group of atoms – most commonly a proton – from one site to another (see, for example, Figure 1A). This chemical change is often rapid, and the relative stability of the tautomers can depend strongly on the surrounding environment, including the presence or absence of volatile species. Because tautomers often display rapid interconversion, sensitivity to different chemical stimuli, and switchable optical behavior, they have found extensive use as molecular probes.[618] However, solid-state systems in which tautomers have distinct properties and sensitivity to relevant atmospheric changes are much less common. Moreover, the extent of this property change is correlated to the accessibility of tautomeric sites to volatile analytes, which presents a challenge that, to date, has limited solid-state sensing based upon tautomerization. Due to these challenges, porous polymer systems might be better suited for tautomeric sensing than other materials into which diffusion of an analyte is more difficult.

Covalent organic frameworks (COFs) are permanently porous and structurally precise polymer networks,[106, 619-622] the chemical versatility and porosity of which make them an attractive platform for the detection of volatile analytes. For example, Auras and coworkers recently explored solvatochromism in COF films as a mechanism for rapid humidity sensing.[623] Although this COF system exhibited impressive response times (~200 ms), the optical response was limited to the polarity-induced stabilization of an excited state with charge-transfer character, and as such, the change in the spectrum was relatively small (a 20-30 nm shift in absorption edge). In contrast to solvatochromism, which relies on stabilization of a single chromophore, analyte-induced tautomerism forms a new chromophore, potentially offering a larger spectral change.

Iminol-to-ketoenamine tautomerism (Figure 1A) is well known in COF materials. In particular, iminol groups are formed when COFs are made from 2,4,6-triformylphloroglucinol (TFP) and amines, but they irreversibly tautomerize during the polymerization to yield β-ketoenamine-linked COFs (**Figure 7.1B**).[455, 624-626] The stability of the β-ketoenamine tautomer precludes using TFP for tautomeric sensing but suggests that components with fewer hydroxyl groups might be suitable candidates for solid-state vapor sensing.[627] Tautomerization-induced color changes in a COF on exposure to water have been reported; however, in that report, formation of the stable trans-ketoenamine form[13] was irreversible at room temperature, meaning that sensors based on this recognition element would require thermal regeneration (**Figure 7.13**). We hypothesized that COFs based on 2,5-dihydroxyterephthaldehyde (PDA-OH) might exhibit dynamic tautomerization because the bis-ketoenamine species, for which a closed-shell non-zwitterionic resonance structure cannot be drawn, is likely to be energetically disfavored after the first ketoenamine formation (**Figure 7.1C**). Importantly, to investigate this approach, the complementary amine monomer used to form a PDA-OH-containing COF should be weakly absorbing in the visible region in order not to mask the tautomerically induced change of color upon exposure of the COF to water vapor. This consideration led us to choose the UV-absorbing 1,3,5-tris(4-aminophenyl)benzene (TAPB) as a suitable condensation partner. Although the corresponding COF, here named **TAPB-PDA-OH**, has previously been reported,[628] dramatic color changes in the presence of polar solvents or humid air were not described.[629] Comparison to structural analogues of this material using 2,5-dibutoxyterephthaldehyde (PDA-OBu) and terepthaldehyde (PDA),[151] which cannot undergo iminol-to-ketoenamine tautomerism (**Figure 7.1D**), along with theoretical modeling of the optical behavior of model tautomers, supports our

hypothesis of a water-induced diiminol-to-ketoenamine tautomerization. A proof-of-principle **TAPB-PDA-OH** COF sensor rapidly responds to changes in relative humidity and showed no attenuation in performance over a period of at least two months.

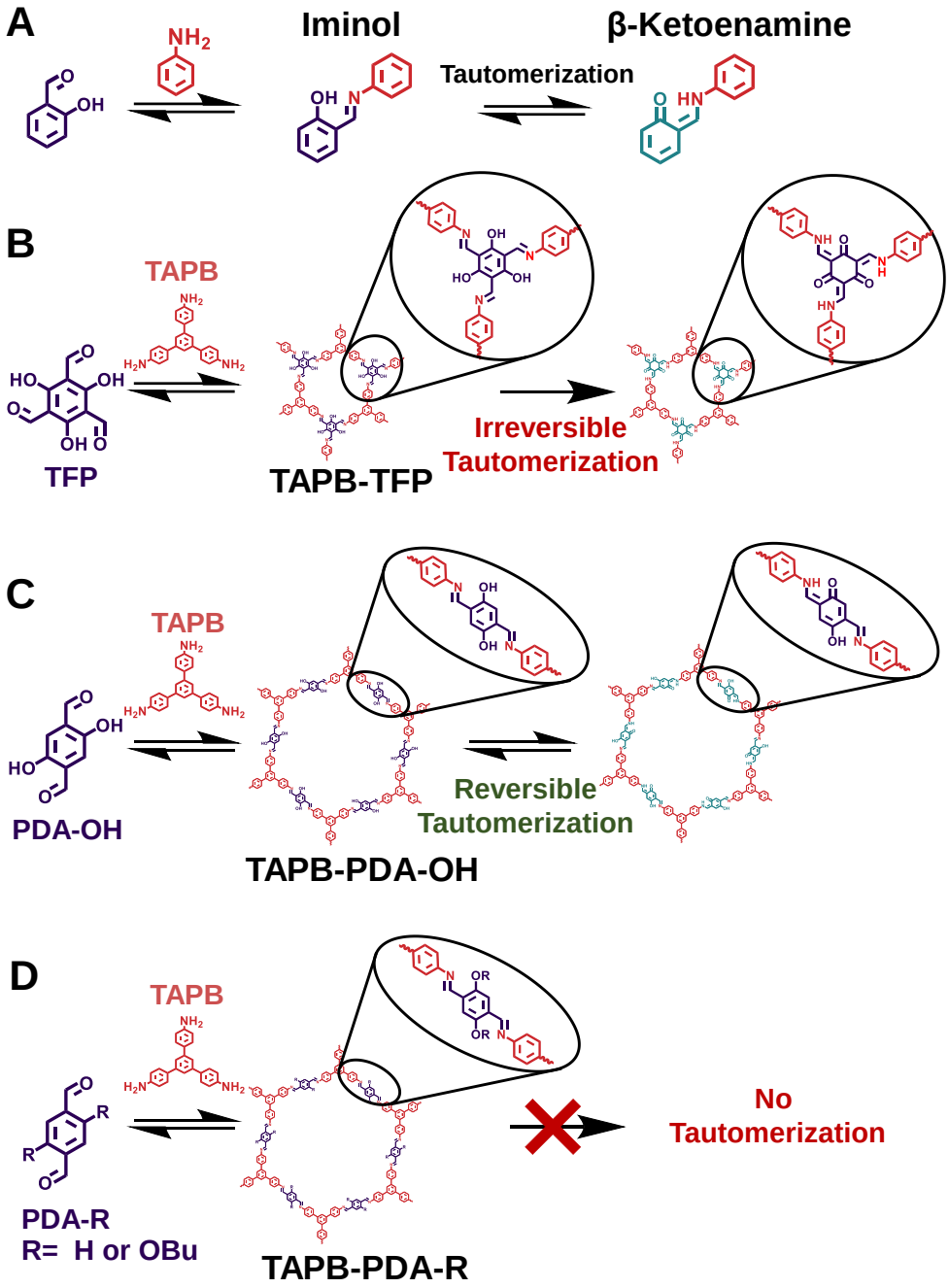

Figure 7.1. A) Imine condensation between aniline and *o*-hydroxybenzaldehyde leads to an iminol that can tautomerize via single proton transfer to generate a *cis*-ketoenamine. **B)** Imine condensation between TAPB and TFP leads to an iminol product that rapidly and irreversibly

converts to its *β*-ketoenamine tautomer. **C)** Imine condensation between TAPB and 2,5-dihydroxyterephthaldehyde leads to an iminol product (**TAPB-PDA-OH** COF) that can only tautomerize to a 'single *cis*-ketoenamine' and leads to a dynamic equilibrium of the diiminol and iminol/*cis*-ketoenamine forms. **D)** Imine condensation between TAPB and terephthaldehyde or 2,5-dibutoxyterephthaldehyde leads to formation of **TAPB-PDA** or **TAPB-PDA-OBu**[630] COF, respectively, where the tautomerization is not possible.

7.3. Synthesis and Characterization of Covalent Organic Frameworks

COFs were synthesized as powders by conventional solvothermal methods,[631] (see Supporting Information for more details). Fourier-transform infrared (FT-IR) spectroscopy confirmed the imine condensation by the disappearance of the aldehyde (1660–1680 cm^{-1}) and amine (3300–3450 cm^{-1}) stretching modes and a concomitant increase in the intensity of the C=N stretching modes at 1610–1620 cm^{-1} (**Figure 7.7 - Figure 7.9**), consistent with the presence of predominantly iminol linkages. Powder X-ray diffraction (PXRD) confirmed the structural regularity and high quality of the COFs, indicating the appearance of several diffraction features that can be indexed as the (100), (110), (200), and (210) Bragg reflections of a hexagonal lattice (**Figure 7.2B, D, F**), while a weak peak at higher angle can be assigned to a (00l) reflection. By comparison to simulated powder diffraction patterns we infer that all COFs are hexagonally tessellated sheets that eclipse one another with ca. 3 Å interlayer separations. Furthermore, Le Bail fitting of the PXRD pattern indicated that all COFs have an approximate in-plane domain size of ca. 100 nm.[632] Nitrogen sorption isotherms were collected for these materials, all of which displayed hysteresis-free type

IV isotherms indicative of well-ordered mesopores that are filled as monolayers initially, but are subject to capillary condensation as they form multilayers.[633] Brunauer-Emmett–Teller (BET) analysis revealed that the **TAPB-PDA**, **TAPB-PDA-OH** and **TAPB-PDA-OBu** COFs had surface areas of 2100, 2250 and 2000 $m^2 g^{-1}$, respectively (**Figure 7.2C, E, G**), near their respective Connolly surface areas of 2300, 2350 and 2200 $m^2 g^{-1}$.[634] The pore-size distribution derived from nonlocal density functional theory (DFT) show a narrow distribution of pore sizes for all materials with average pore size (30 Å) consistent with the modeled eclipsed structures (**Figure 7.11**).[635] Using a Monte-Carlo algorithm with water as a probe molecule, we calculated that ca. 10 water molecules per iminol moiety can fit within the **TAPB-PDA-OH** COF pores, suggesting that this material will be amenable to accepting solvent vapor into its pores. Furthermore, the experimentally determined pore sizes and high surface areas of these materials indicate that analytes can rapidly access the tautomerically active sites.

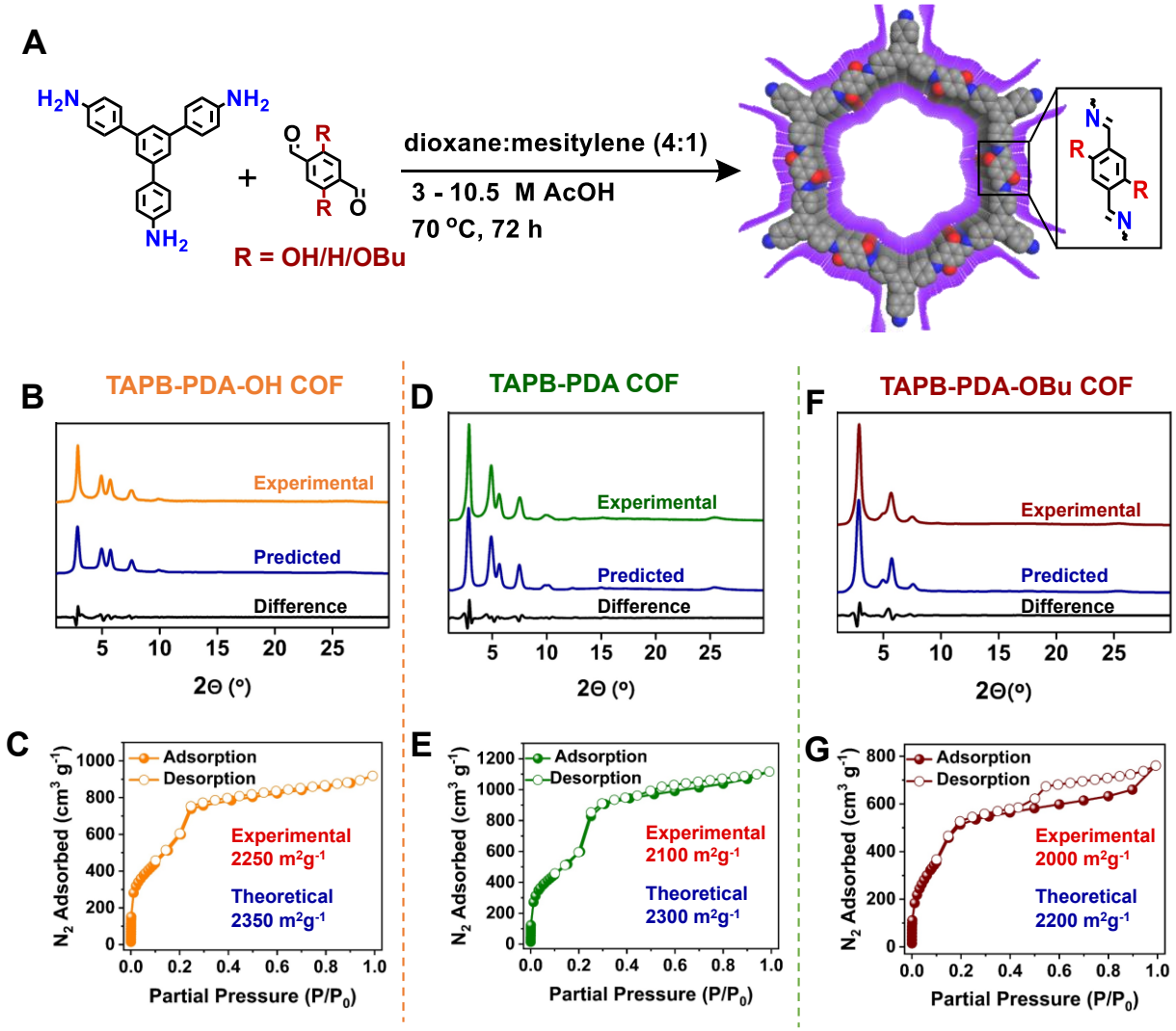

Figure 7.2. A Synthesis and chemical structures of the **TAPB-PDA-OH**,[13] **TAPB-PDA,** and **TAPB-PDA-OBu** COFs. The purple surface shows the high surface area and accessibility of tautomeric sites for the **TAPB-PDA-OH** COF. **B, D, F** Experimental and predicted (Pawley-refined, eclipsed stacking PXRDs) of the three COFs. **C, E, G** N_2 adsorption-desorption isotherms of the three COFs.

7.4 Solvent-dependent Optical Behavior

The **TAPB-PDA-OH** COF changes color when its dry form is solvated (**Figure 7.3A**). Diffuse reflectance spectroscopy (DRS) showed that the orange COF has an absorption onset of 572 nm (2.2 eV). A new band with an onset at approximately 690 nm (1.8 eV) emerges when the COF is soaked in solvents of increasing polarity. This difference is particularly pronounced when **TAPB-PDA-OH** COF is exposed to water, which results in a dark coloration and absorption spanning the entire visible region (**Figure 7.3A**).

In the previous report[636] of humidity sensing in a COF, which had more pronounced donor-acceptor character than the present COFs, a red-shift of the long-wavelength absorption edge is seen as the solvent polarity is increased; this was attributed to solvatochromism, i.e., preferential stabilization of the excited state in more polar solvents. The behavior of **TAPB-PDA-OH** (**Figure 7.3A**) is qualitatively different. Figures 3B and 3C show the dependence of the absorption at 600 nm – as measured by the increase in the Kubelka-Munk function at that wavelength relative to that of the dry COF, $\Delta K\text{-}M_{600}$ – on the solvent H-bonding and polarity parameter, $E_T N$,[637] and, for the case of H-bond-donor solvents, the solvent acidity, respectively; both plots show fairly similar trends. For solvents of low to moderate polarity – tetrahydrofuran (THF), dichloromethane (DCM), acetone, acetonitrile, 2-propanol, 1-butanol, and ethanol – $\Delta K\text{-}M_{600}$ is approximately linearly dependent on $E_T N$ (**Figure 7.3B**).[637] However, this increase in absorption is not accompanied by a significant shift of the main absorption edge (**Figure 7.3A**), as one would expect for simple solvatochromism, suggesting growth of a new feature distinct from that responsible for the main absorption edge. In higher polarity solvents ($E_T N > 0.7$), there is a marked deviation from linearity in the plot of $\Delta K\text{-}M_{600}$ vs. $E_T N$ (or pK_a) and the absorption at 600 nm is more clearly attributable

to the formation of increasing quantities of a new chromophore. The retention of the feature at ca. 540 nm in the most polar environment examined, indicates that only a fraction of the initial chromophores are converted to the new chromophore. To examine the plausibility of assigning the new chromophore as the *cis*-iminol/ketoenamine tautomer, we turned to the small-molecule model compound, **BPH**, obtained from condensing aniline with 2,5-dihydroxyterephthaldehyde. This and several related compounds were previously shown to exhibit solvent-dependent equilibria between diiminol and iminol/ketoenamine forms, which absorb at λ_{max} = ca. 435 and ca. 540 nm, respectively.[638] We also resynthesized **BPH** and observed similar behavior (**Figure 7.14**); in particular, both dichloromethane and ethanol solutions exhibit similar short wavelength absorptions attributed to the diiminol, with negligible solvatochromism of this band, while the long-wavelength band, attributed to the iminol/ketoenamine, is seen only in ethanol. Furthermore, time-dependent (TD) DFT calculations on the diiminol form of **BPH** (see SI for details) also suggest that its spectrum is only weakly dependent on the presence of water (**Figure 7.3D**),[639] whereas that of its iminol/*cis*-ketoenamine tautomer has a much longer absorption wavelength (**Figure 7.3D**). The natural transition orbitals indicate that this transition is associated with charge transfer from the enamine and imine arms to the central aromatic ring (**Figure 7.3D**). We also compared the absorbance of **TAPB-PDA** and **TAPB-PDA-OBu** COFs, neither of which are capable of tautomerization, under wet and dry conditions (**Figure 7.19**). Although both exhibited limited solvatochromism, i.e., a solvent-dependent shift of the main absorption edge, consistent with their weak donor-acceptor nature, neither exhibited the pronounced optical changes seen in the **TAPB-PDA-OH** COF.

To investigate the effect of structural regularity on the observed optical behavior, a largely amorphous cross-linked polymer was synthesized from TAPB and PDA-OH (see Supporting Information Section VII for synthesis and characterization). While FT-IR confirmed imine polymerization, nitrogen sorption measurements showed that this material was of far lower surface area (ca. 40 m^2 g^{-1}). When exposed to water, the cross-linked polymer exhibited a substantially diminished optical response (**Figure 7.13**), which we attribute to the restricted accessibility of the tautomeric sites in an amorphous cross-linked network. This contrasting behavior between a crystalline 2D COF and an amorphous polymer of similar chemical composition expands the growing body of literature that demonstrates the promise of structurally regular and porous materials for sensing applications.[640]

7.5 Chemically General Solid-state Tautomerization

To test the generality of this tautomerization phenomenon, a **TAPPy-PDA-OH** COF (TAPPy = 1,3,6,8-tetrakis(4-aminophenyl)pyrene) was also synthesized (see Supporting Information for more details). This COF exhibits only moderate crystallinity as judged from its PXRD diffraction pattern (**Figure 7.29**) and BET surface area analysis (320 m^2 g^{-1}, **Figure 7.30**). This COF similarly exhibited qualitatively similar behavior to **TAPB-PDA-OH** COF, acquiring a dark coloration in wet media (**Figure 7.31**) and a new absorption feature at ca. 600 nm. Compared to **TAPB-PDA-OH** COF, the new feature seen for **TAPPy-PDA-OH** under wet conditions is less prominent, suggesting the position of equilibrium lies further towards the diiminol in the pyrene COF. This may be partially due to the lower surface area of the pyrene material, leading to fewer

tautomeric sites being accessible to solvent, but may also reflect subtle effects of the different chemical structures on the energetics associated with the equilibria.

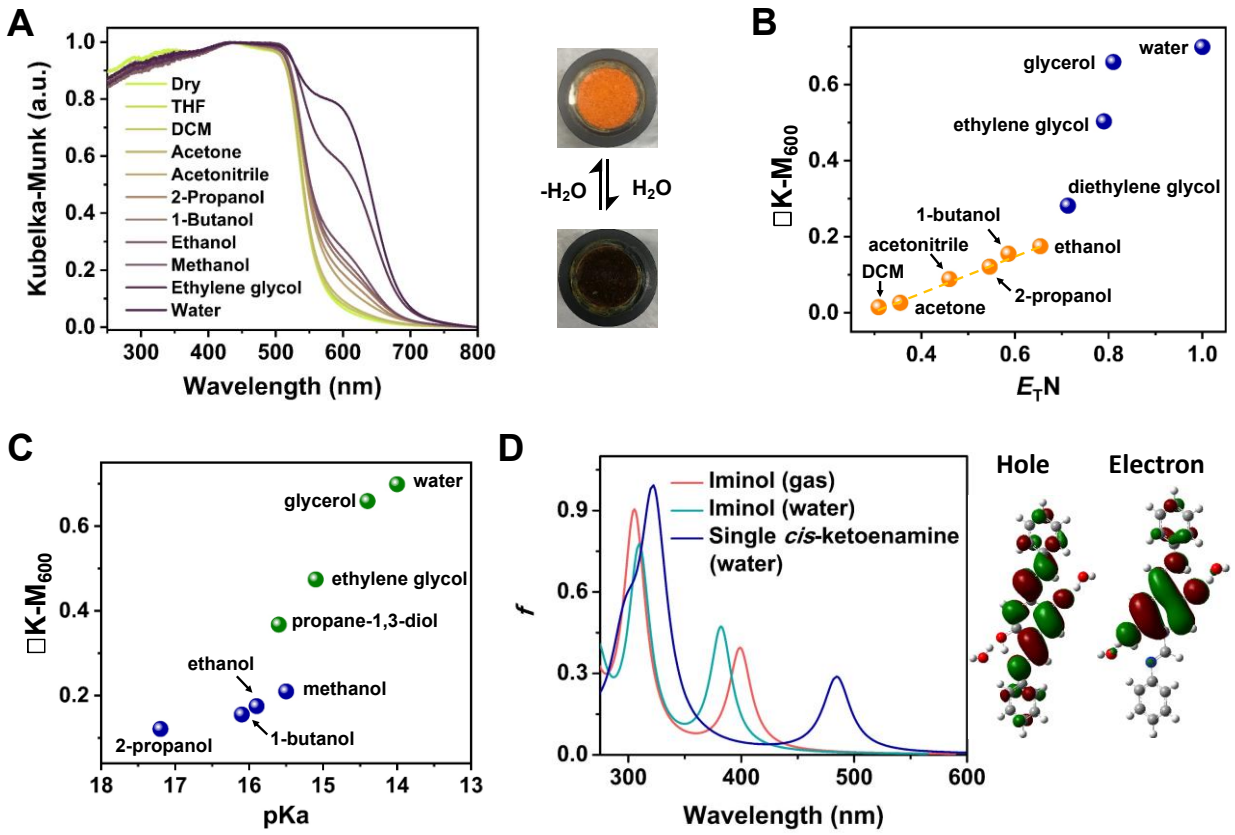

Figure 7.3. A Diffuse reflectance spectroscopy (DRS) plots for **TAPB-PDA-OH** COF powder in different solvents; photographs of the dry and wet COFs are shown to the right. **B** Plot of change of absorption strength (measured by the Kubelka-Munk function) at 600 nm versus E_TN parameter: the near-linear trend is broken for strongly H-bonding solvents. **C** Plot of change of absorbance at 600 nm versus pK_a for H-bonding solvents. **D** Calculated UV-Vis spectra of the tautomers of model compound **BPH** in the gas phase and in the presence of water. The hole and electron natural transition orbitals for the low-energy transition of the single *cis*-ketoenamine form (with two molecules of water present) are shown to the right.

7.6 Reversible Structural and Chemical Responses

Having established the optical response of the **TAPB-PDA-OH** COF to solvent, particularly strong H-bond donors, we investigated the nature and reversibility of other associated structural and spectroscopic changes. FT-IR spectra of the dry and fully wet samples of **TAPB-PDA-OH** COF show a subtle change in the pattern of stretching modes in the range 1570–1660 cm^{-1}, while other portions largely remain unaffected (**Figure 7.27**). The similarity of FT-IRs is partly attributable to the incomplete conversion to the new chromophore noted above. In addition, DFT-simulated IR spectra (**Figure 7.27**) indicate that, in any case, bis-iminol and the *cis*-iminol/ketoenamine forms of model compound **BPH** exhibit only minor differences. However, these differences are consistent with the experimental observations. Firstly, the C—O stretch associated with the "keto" moiety is predicted to be very weak and at lower frequency than a typical isolated C=O bond (**Figure 7.27**), explaining the absence of a typical C=O-like feature. Secondly, the increased strength of the imine C=N stretch predicted for the *cis*-iminol/ketoenamine tautomer is consistent with our observation of a broad peak for the COF exposed to water at 1650 cm^{-1} (**Figure 7.17A**).[626, 627] However, a contribution from excess water complicates the observed FT-IR spectrum of the fully wet COF (**Figure 7.17A**). FT-IR of a partially wet sample allowed observation of changes within the framework more clearly (**Figure 7.17B**). Changes in the FT-IR peaks at approximately 1040, 1190, 1231, 1288, 1519, 1577, 1600 and 1643 cm^{-1} indicate that new vibrational modes are being accessed in the COF structure upon exposure to water vapor, which is consistent with the framework's tautomerization (**Figure 7.17B**). Raman spectroscopy, which is less sensitive to signals from free water, showed similar evidences for reversible tautomerization (**Figure 7.17C**). While both IR and Raman spectroscopy show new features upon exposure to

water, a definitive assignment of the frequencies is challenging due to the unique mixed enol-ketoenamine structure, potential partial conversion, and intense evolving backgrounds from the evaporating water. Solid-state ^{13}C cross-polarization magic angle spinning (CP-MAS) nuclear magnetic resonance (NMR) spectra of both the dry and wet **TAPB-PDA-OH** COF were acquired (**Figure 7.4A**). Again, the changes are subtle, but the intensity of the resonance centered at 153 ppm, assigned to the imine carbon using DFT simulations for model compound BPH (**Figure 7.26**), diminishes significantly on exposure of the dry COF to water. A new peak is observed as a shoulder at ca. 105 ppm, and, by comparison to the DFT calculations, can be assigned to the carbon atom of the phenyl ring *ortho* to the enamine nitrogen atom.[625,641] Absence of a typical 'carbonyl' peak above 160 ppm is presumably due to the unconventional nature of the carbonyl from its resonance contributions, which appears more upfield shifted and mixed with other aromatic signals. Overall, both ^{13}C CP-MAS and FT-IR data are consistent with the DFT-optimized structure of BPH, which indicates a C—O bond length of 1.26 Å in the single *cis*-ketoenamine form (**Figure 7.23**), between those of a typical C—O (1.4 Å) and C=O (1.2 Å) bonds, and explains why the "C=O" NMR chemical shift and stretching frequency are low when compared to typical ketone features (**Figure 7.26**). In previous literature, the TAPPy-TT (TT = thieno[3,2-*b*]thiophene-2,5-dicarboxaldehyde) COF, in which isomerization is not possible and the solvent-dependence of spectra is presumably entirely due to conventional solvatochromism, exhibited nearly identical ^{13}C NMR spectra in its dry and wet forms.[636] Thus, the differences between the ^{13}C NMR spectra of the dry and wet **TAPB-PDA-OH** COF further supports our hypothesis of a chemical change in general, and tautomerization in particular, in this COF.

7.7 *in situ* X-ray diffraction

We measured the diffraction patterns of the **TAPB-PDA-OH** COF in the presence of a variety of solvents using synchrotron X-ray radiation. Across a range of solvents, the COF crystallinity was unaffected, with the same number and approximate shape of diffraction features being observed in each case. However, the position of the in-plane diffraction features shifted when immersed in water. In particular, the (100) diffraction feature shifted to a real-space d-spacing of 32 Å, which, as the COF dried, relaxed to its original position of 28 Å (**Figure 7.4B**). This expanded unit cell may originate from the combination of bond-length differences and out-of-plane distortions of the ketoenamine and iminol tautomers and hints that responsive breathing behavior could be engineered in framework materials through the incorporation of tautomerically active states.[642-644]

Taken together, the various spectroscopic and structural changes observed are all consistent with substantial solvent-mediated tautomerism in the **TAPB-PDA-OH** COF. DFT calculations on the model compound **BPH** (Figure 4C) indicate that the diiminol tautomer is strongly preferred in the gas phase, consistent with the properties of the dry COF. However, in the presence of two water molecules, the diiminol and *cis*-iminol/ketoenamine are nearly isoenergetic, with the latter being only 0.09 eV (ca. 2 kcal mol^{-1}, ca. 3.6 k_BT at room temperature) less stable (**Figure 7.4C**), consistent with the presence of significant quantities of both tautomers in the presence of water. As expected, the double *cis*-ketoenamine tautomer is significantly less stable (by 0.40 eV/9.2 kcal mol^{-1}/ca. 16 k_BT) than the single *cis*-iminol/ketoenamine, consistent with the cross-conjugation present in the single *cis*-ketoenamine and the absence of a non-zwitterionic closed-shell resonance structure for the double ketoenamine, suggesting that the double *cis*-ketoenamine is unlikely to be

present in more than trace amounts (**Figure 7.24**). Formation of *trans*-iminol/ketoenamine was also found to significantly less favorable (by 0.47 eV/10.8 kcal mol^{-1}/19 k_BT) than that of the *cis*-iminol/ketoenamine formation, strongly suggesting that the observed optical changes are not attributable to defect sites in the COF with *trans* geometries (**Figure 7.23**)

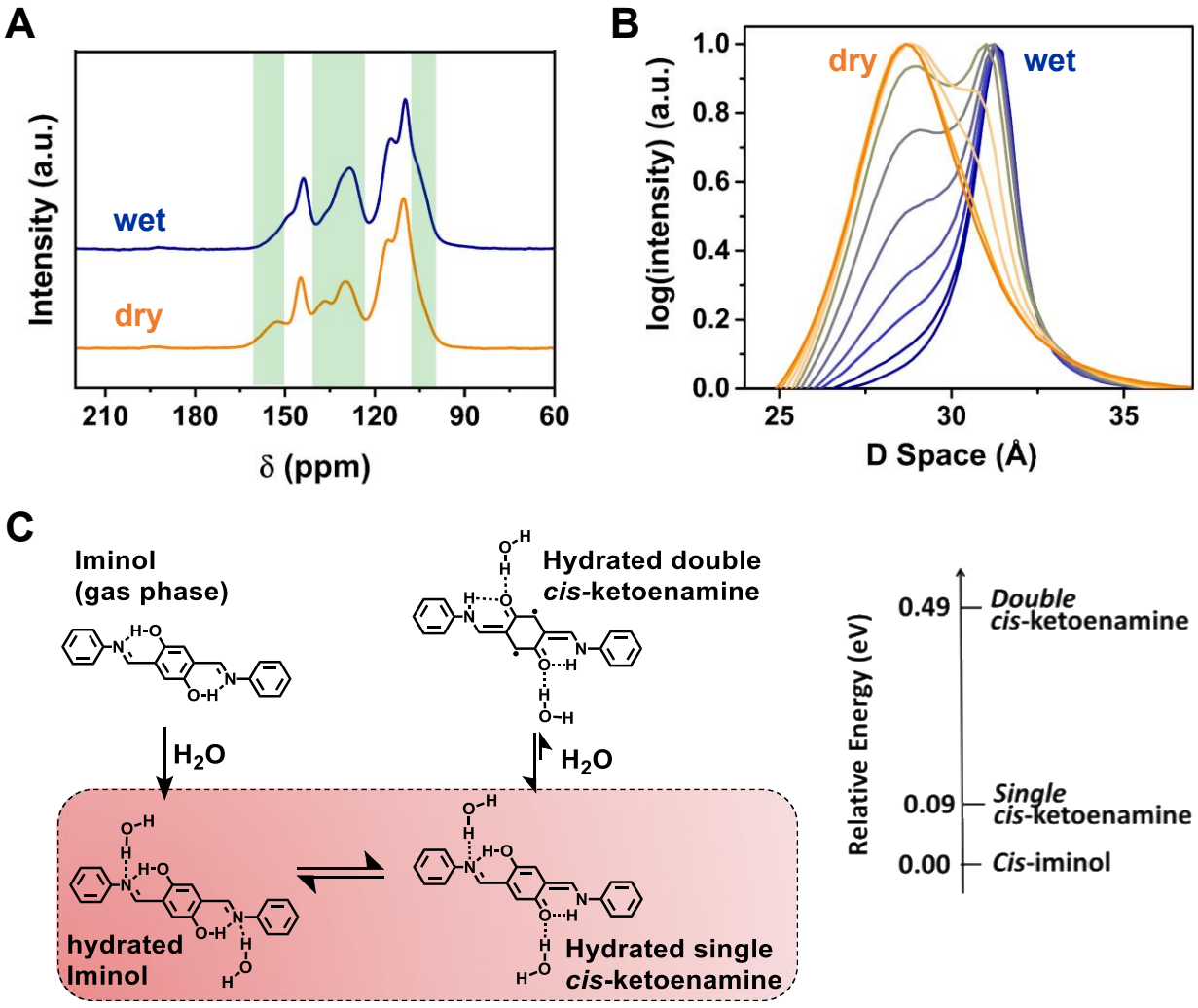

Figure 7.4. A CP-MAS ^{13}C NMR spectra of dry and wet **TAPB-PDA-OH** COF shows diminution of the imine peak at ca. 160 ppm and appearance of a new feature at ca. 105 ppm. **B** Synchrotron X-ray scattering pattern of the wet **TAPB-PDA-OH** COF as it dries. **C** Chemical structures of the

different tautomers of small-molecule model compound **BPH** with DFT relative energies in the presence of water are shown on the right.

7.8 Reversible tautomeric switching

As the wet **TAPB-PDA-OH** COF dries, it reverts to a state that is indistinguishable from the original sample. For example, the FT-IR spectra of the two dry materials – before and after exposure to water – are nearly identical (**Figure 7.5A**), indicating the reversibility of the process, as expected for a tautomerization. Importantly, the BET surface area and X-ray diffraction pattern of the dried COF are almost unchanged from the as-synthesized material (**Figure 7.5B and Figure 7.5C**). This lack of hysteresis demonstrates that the structural changes are reversible when water is removed from the framework. These experiments suggest that tautomerism is an appealing sensing mechanism for applications that require long-term stability.

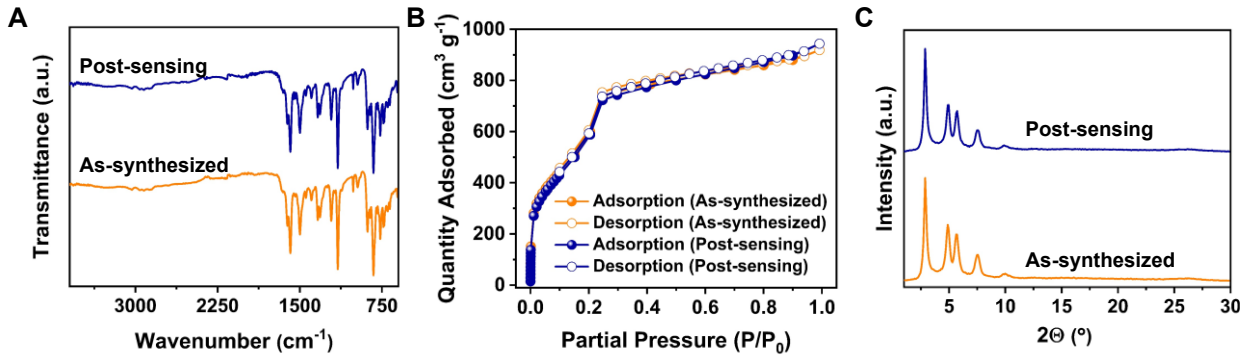

Figure 7.5. Orange and blue traces correspond to as-synthesized and post-sensing (as-synthesized COF was soaked in water and then dried by critical point drying) **TAPB-PDA-OH** COFs, respectively. **A** FT-IR showing no damage to chemical linkages during the wetting process.

B Sorption isotherms are similar showing no deleterious effects in the pore structures due to wetting with water. **C** PXRDs showing wetting the COF does not affect the crystalline diffraction.

7.9 Humidity-sensing

To exploit the dynamic and reversible nature of the solvent response of the **TAPB-PDA-OH** COF, we fabricated a humidity detector in which the absorbance of a thin film of the COF is monitored by transmission UV-vis spectroscopy (see supporting information for details, Section XIII). We synthesized films with thicknesses of ca. 200 nm, which we anticipated would allow for substantial diffusion and thus rapid access of the volatile analytes, but also sufficient optical density to allow for sensing (**Figure 7.6A**). To further enhance diffusive access to COF pores, the COFs were synthesized as highly oriented films with the pores perpendicular to the substrate. This orientation is confirmed by grazing-incidence wide-angle X-ray scattering (GI-WAXS) where the in-plane diffraction ((100) Bragg feature) is predominantly seen in the q_{xy} plane and the out-of-plane diffraction ((001) Bragg feature) is located along the q_z plane (**Figure 7.6B**). Upon exposure to humidity, the optical responses of the COF films were found to be similar to those of the COF powders (**Figure 7.32**).

A humidity sensing experiment (see Supporting Information Section XIV for the experimental details) was performed in which dry and water-saturated air were alternately passed over the film and changes in the absorbance of the COF at 600 nm, ΔA_{600}, were monitored (**Figure 7.6C**). The **TAPB-PDA-OH** COF displayed a fast response of 9 s as the environment changes

from dry to humid and less than 1 s when the humid air was changed to dry air. Slower responses to humidity (23 s), and lower values of ΔA_{600} (60% relative to that obtained using water-saturated air), were obtained in a film using unsaturated, but moist, air (**Figure 7.35**), and the value of $\Delta K\text{-}M_{600}$ for powders (**Figure 7.35**) increases with exposure to air of increasing relative humidity, together indicating that both films and powders can potentially be used as sensors of relative humidity. On the other hand, the amorphous film of **TAPB-PDA-OH** cross-linked polymer exhibited much slower response (ca. 130 s, **Figure 7.34**) than the corresponding COF, likely due to restricted accessibility and slow diffusion of the vapor and emphasizing the importance of the regular and open COF structure for rapid sensing. **TAPB-PDA** COF films did not exhibit any humidity-sensing changes in optical behavior, consistent with the observation in the powder, while the **TAPB-PDA-OBu** COF film displayed only small increases in absorbance (attributable to the weak solvatochromism seen in powders) and an overall slower mediachromic response (ca. 15 s, **Figure 7.37**). We hypothesize that the slower response is in part due to its more hydrophobic pores; regardless, the slow kinetics of the already weakly responsive butoxy-functionalized COF suggest that side chains can be used to tune sensor performance in future COF designs.

The sensors were passively regenerated when the humid environment was replaced with dry atmosphere. For example, we exposed the films to human breath and observed the same rapid and reversible optical switching. The **TAPB-PDA-OH** COF response is highly reversible over multiple cycles of exposure to dry and wet air; even after more than a month of ambient storage, we found that the performance of the last sensing experiment was indistinguishable from the first sensing, indicating the high-fidelity nature of this sensor (**Figure 7.6D**). The stable, reversible,

passive, nature of this sensing behavior suggests that specific, highly responsive, rapid tautomeric sensing in a more engineered COF platform is worth further exploration.

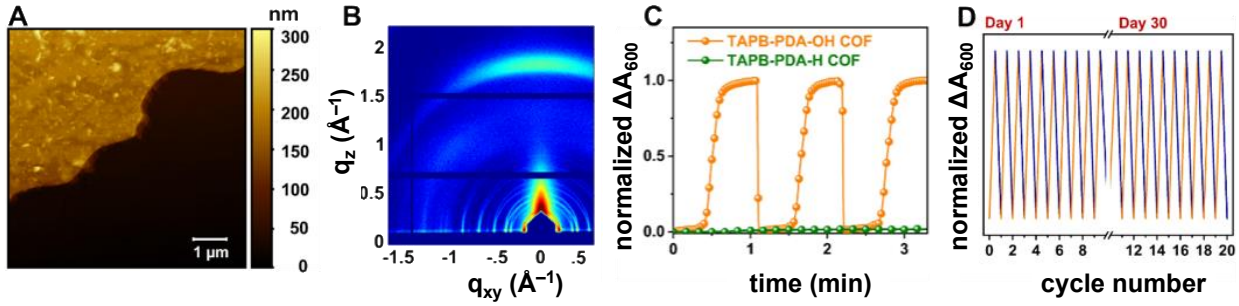

Figure 7.6. A AFM images of the **TAPB-PDA-OH** COF film. **B** GIWAXS of the as-synthesized **TAPB-PDA-OH** COF films. **C** Humidity sensing using **TAPB-PDA-OH** COF films using the change in absorbance at 600 nm; **TAPB-PDA** COF films shows no response to humidity. **D** Humidity sensing using **TAPB-PDA-OH** films over multiple cycles. The break shows a gap of more than one month of usage. The similar response observed after one month attests to its stability.

7.10 Conclusions

A COF containing 2,5-di(imine)-substituted 1,4-dihydroxybenzene moieties undergoes a dramatic change in color, clearly visible to the naked eye, on exposure to strong hydrogen-bond-donor solvents, especially water, and moist air. UV-vis spectroscopy, NMR spectroscopy, and density functional theory calculations clearly distinguished between the solvatochromism associated with other MOFs and COFs and the more complex and dramatic solvent-induced color change found in the **TAPB-PDA-OH** COF. In particular, a strong new absorption feature is seen

in humid environments is, by comparison of spectroscopic data with experimental and computational data for model compounds, assigned to tautomerization of some of the diiminol moieties to iminol/*cis*-ketoenamine chromophores. We attribute this dynamic tautomerization to similar energies of these two tautomers, while preventing tautomerization to a 'double *cis*-ketoenamine' due to cross-conjugation effects. The new absorption feature is attributed to a charge-transfer-type excited state, resulting from a stronger acceptor nature of the central ring of the iminol/ketoenamine tautomer relative to that of the diiminol. COFs incorporating similar diiminol motifs with the same connectivity have previously been reported, but have also incorporated chromophores, such as porphyrins or phthalocyanines, whose strong visible absorption may have obscured the optical changes associated with tautomerization.[645] A prototype humidity sensor was found to be rapidly and passively regenerated and was active for at least two months. We anticipate that our demonstration of the viability of practical tautomeric sensing will inspire engineered devices capable of complex sensing responses for volatile analytes in these materials. Furthermore, we hope that these materials will find substantial interest as components in Internet of Things systems where passive and long-term stable sensors are a necessity.[646]

7.11 Chapter 7, Supplementary Information

Materials, Methods and Instrumentation

Materials. All monomers, solvents, and catalysts were either purchased from commercial sources or prepared following literature reported protocols. In particular, 1,3,5-tris(4-aminophenyl)benzene (TAPB) and mesitylene were procured from Alfa-Aesar. Terephthaldehyde and dioxane were purchased from Sigma-Aldrich. All materials were used as received without further purification. Glacial acetic acid was purchased from Fischer Scientific and used without additional purification. Deionized water was used throughout all experiments.

Solution Nuclear Magnetic Resonance Spectroscopy. ^{1}H Nuclear Magnetic Resonance (NMR) spectra were acquired using a Bruker Avance III 400 MHz spectrometer using $CDCl_3$ as the solvent at 25 °C. The chemical shifts were calibrated using the residual proton signal or the ^{13}C signal of the solvent as an internal reference ($CDCl_3$: 7.26 ppm for ^{1}H NMR, 77.00 ppm for ^{13}C NMR).

Solid-State ^{13}C CP/MAS NMR Spectroscopy. ^{13}C Cross Polarization (CP) Magic Angle Spinning (MAS) spectra were recorded using a Bruker AV3-HD 300 NMR spectrometer operating at a ^{1}H frequency of 300 MHz. Samples were investigated using a HX MAS probe operating with 4mm MAS rotors at a selected spinning speed of 8 kHz. The contact time was 3 ms during a ramp-shaped 1H pulse. The chemical shifts were calibrated using adamantane as an external reference.

^{2}H MAS NMR Spectroscopy. TAPB-PDA-OH COF samples were immersed in D_2O for 1 min at room temperature. Excess D_2O was removed by blotting with a filter paper and the samples were subsequently rigorously dried under vacuum. These samples were then subjected to ^{2}H MAS NMR investigation. ^{2}H MAS NMR spectra were recorded using a HXY triple resonance MAS

probe on a Bruker AV3-400 NMR spectrometer (^{2}H frequency of 62 MHz) using a rotor synchronized solid-echo sequence where the spacing between pulse was set to be exactly one rotor period and the repetition delay was set to 4 s. It was necessary to accumulate 8192 scans to obtain data with a sufficiently high signal:noise ratio. The excitation profile of the NMR probe was non-uniform. Hence experimental data were quite distorted with respect to the expected symmetry with respect to a mirror axis perpendicular to the excitation frequency as expected for a spin with I=1. As a compromise, the spectrum was symmetrized at the cost of destroying any chemical shift information associated with the center-peak and each spinning side band.

Fourier-Transform Infrared Spectroscopy. Infrared spectra were recorded on Shimadzu Prestige 21 FT-IR in attenuated total reflection mode using solid COF powder with an atmospheric background subtracted from all recorded spectra.

Diffuse Reflectance Spectroscopy (DRS). The DRS spectra were recorded at room temperature on a Cary 5000 UV-vis spectrometer equipped with an integrating sphere in the wavelength range 200–800 nm. The samples either in the dry or wet form were gently ground before all measurements. The scan rate was 400 nm/min with a resolution of 0.66 nm. Finely ground $BaSO_4$ was used as a reference. The absorption spectra were then obtained by using the Kulbeka-Munk function: $K\text{-}M = (1\text{-}R)^2/2R$, where R is the reflectance.

UV-Vis Spectroscopy of COF Films. UV-Vis absorbance spectra were recorded on a Cary 5000 UV-Vis-NIR spectrophotometer equipped with a mercury lamp. Substrates were mounted in a Cary film holder such that the film was perpendicular to the beam. Spectra were taken over a wavelength range of 200-850 nm with a 5 min collection time and 1 nm resolution.

Powder X-ray Diffraction. Powder x-ray diffraction (PXRD) patterns were recorded on a Malvern Panalytical Empyrean diffractometer in 2θ Bragg-Brentano geometry employing Cu Kα (λ = 1.5406 Å) line focused radiation at 40 kV, 45 mA power and equipped with a PIXcel Medipix3 3D detector by Malvern PANalytical. Samples were placed on a silicon zero-background sample holder and then the sample surface was leveled with a clean microscope slide. No sample grinding was used prior to analysis unless otherwise stated. Data were mesured using a continuous 2θ scan from 1.0–40º θ, while rotating. For all samples, no features are observed at θ > 30°, and diffractograms are presented from 0–30° θ for visual clarity.

***In Situ* X-ray Diffraction.** Small- and wide-angle X-ray scattering (SAXS/WAXS) patterns were collected at Argonne National Lab's Advanced Photon Source sectors 5-ID-D (DND-CAT) using a capillary transmission geometry. Experiments were conducted at a beam energy of 13.3 keV. 1 frame was collected for 1 second on a set of Pilatus detectors, which were then summed and radially integrated to produce a linear PXRD pattern using proprietary software available at the APS. Scattering intensity is reported as a function of the modulus of the scattering vector q, related to the scattering angle 2θ by the equation $q = (4\pi/\lambda) \sin \theta$, where λ is the x-ray wavelength. The sample-to-detector distance was adjusted to measure across relevant detection ranges of q. Capillary experiments were conducted using 2.0 mm OD borosilicate capillaries with 0.2 mm wall thicknesses purchased from Hilgenberg GmbH.

Grazing-Incidence X-ray Diffraction. GIWAXS measurements were performed at Advanced Photon Source at Argonne National Laboratory using the 8-ID-E Beamline. The films were irradiated to yield ca. 80% saturation of the detector at an incidence angle of 0.14° in vacuum using 10.92 keV (1.135 Å) x-rays. The scattering was recorded on a Pilatus 1 M detector located 228

mm from the sample. The raw images were merged, pixel coordinates were transformed to q-space, and line cuts generated using GIXSGUI for Matlab. For all patterns, we compared their transformed 1D patterns to the transmission polycrystallite diffraction patterns, all of which were found to be consistent.[647, 648-2]

Critical Point Drying. The supercritical drying procedure was performed in a Tousimis Samdri795 critical point dryer. Prior to the supercritical drying process, all samples were placed in tea bags (ETS Drawstring Tea Filters, sold by English Tea Store, Amazon.com) and then soaked in absolute ethanol to keep the samples wet (typically 5-15 min). The drying chamber is first cooled ('cool' valve meter set to 0.40), and the tea bags containing the samples were then placed in it, and the chamber is filled with absolute ethanol and then sealed. The chamber was then filled with liquid CO_2 ('fill' valve meter set to 0.40), and after 2 min, the samples were purged for 30 min ('purge-vent' valve meter set to 0.15, and 'purge timer' valve meter set to 6). The temperature was then raised to 40 °C, resulting in a chamber pressure of around 1300 psi, which is well above the critical point of CO_2. The chamber was held above the critical point for 30 min, after which the CO_2 source was turned off, and the pressure was released over a period of 30 min ('bleed' valve meter set at 0.07). The samples were then transferred to vials and their final mass were weighed.

Nitrogen Sorption Isotherms. Nitrogen sorption isotherms were collected on a Micromeritics 3Flex Physisorption Surface Area and Porosimetry Analyzer using between 10 and 50 mg. Samples were transferred to dried and tared analysis tubes equipped rubber cap. Samples were heated from room temperature to 150 °C at a rate of 10 °C/min and held at that temperature for 3 h under nitrogen flow to degas the COF samples. Nitrogen isotherms were collected by incremental exposure of N_2 up to 760 mmHg (1 atm) using UHP-grade (99.999% purity) N_2 at 77 K in a liquid

nitrogen bath. N_2 adsorption/desorption isotherms, BET surface areas, pore size distributions and other derived measurements were generated using the instruments native software (3Flex Share Version 5.0k). Oil-free vacuum pumps and oil-free pressure regulators were used for all measurements. Brunauer-Emmett-Teller (BET) surface areas were calculated from the linear region of the N_2 isotherm at 77 K within the pressure range P/P_0 of 0.05–0.10 so that the linear model fit had an R^2 of greater than 0.999.

Structural Modeling. Crystal modeling of the COF structures was carried out using the Materials Studio (ver.5.0) suite of programs by Accelrys. The initial structures were constructed piecewise starting with a primitive hexagonal unit cell with space group P6. The *a/b* cell parameter was estimated according to the distance between the center of the vertices for each COF, and *c* parameter was chosen as 3.35 Å, which has been observed for similar materials. The structures were optimized using a Geometry Optimization routine including energy minimization with cell-parameter optimization, using the parameters from the Universal Force Field. Calculation of the simulated powder diffraction patterns and Pawley refinements were performed in the Materials Studio Reflex Plus Module using a Bragg-Brentano geometry. The observed diffraction patterns were subjected to a polynomial background subtraction and then to Pawley refinement wherein peak profile were refined using the Pseudo-Voigt peak shape function and asymmetry was corrected using the Berar-Baldinozzi function. Crystallite size was then estimated by the LeBail method which was Pawley refined to the experimental data.

Connolly Surface Area Calculation. After a refined structure was simulated via diffraction modeling as described above, we went on to calculate the theoretical surface area for our structures. This was done using a Connolly method (sometimes known as a solvent-excluded surface method

or molecular surface method). This method can be described as rolling a ball along a molecular surface to assess its accessible surface. More precise descriptions and details of this method can be found in the initial report of this approach.[3,4] We performed this calculation using the Crystal Surfaces and Volumes module of MaterialsStudio using the parameters for molecular nitrogen as the adsorbate. This yielded a surface area per unit cell, which could then be converted to the surface area per gram value which is reported in the manuscript.

Solvent Accessibility Calculations. Theoretical water loading on the COF structure was calculated using the sorption module of Materials Studio by applying a Monte Carlo algorithm where water molecules were added to the unit cell until no additional molecules could be added based on their Van der Waals radii.

Atomic Force Microscopy. Atomic force microscopy (AFM) images were taken using a SPID Bruker FastScan AFM using a tapping mode. Films were scored using Teflon tipped forceps before imaging to create a level substrate surface to which we could compare the height of the film.

Density Functional Theory Calculations. Ground-state geometry optimizations and single-point calculations on the iminol and ketoenamine model compounds were performed using density functional theory (DFT) method with the tuned long-range corrected ωB97X-D functional and 6-31G (d) basis set, which has been demonstrated to describe molecular geometric and electronic properties reliably.[5-6] The time-dependent density functional theory (TD-DFT) approach was then employed to study the electronic excited states and simulate the optical absorption spectra. Natural transition orbitals (NTOs)[7] were used to visualize the hole and electron wavefunctions in the excited states. All quantum-chemical calculations were performed with the Gaussian 09 Rev D01 program.5

Humidity Sensing Experiments. Dry films were loaded in glass scintillation vials, which were subsequently capped with septa. The set up was placed on the UV-vis sample holder such that the film is facing the detector. Through the septum, three needles were introduced, which were used as a dry nitrogen inlet, a humid nitrogen inlet, and an outlet. To obtain the humid nitrogen, nitrogen gas was bubbled through three closed water reservoirs before entering into the detection chamber. The switching between humid and dry nitrogen gases was performed manually using a three-way valve. Changes in absorbance were recorded as the environment was changed from dry to wet and vice versa in a Cary 5000 UV-Vis spectrometer. Response times were calculated by a linear onset method by calculating the time taken for the sample to increase its response amount from 10-80% of the maximum response.

II. Synthetic Procedures for Covalent Organic Framework Monomers

Scheme 7.1. Synthesis of 2,5-dibutoxyterepthaldehyde and 2,5-dihydroxyterephthaldehyde.

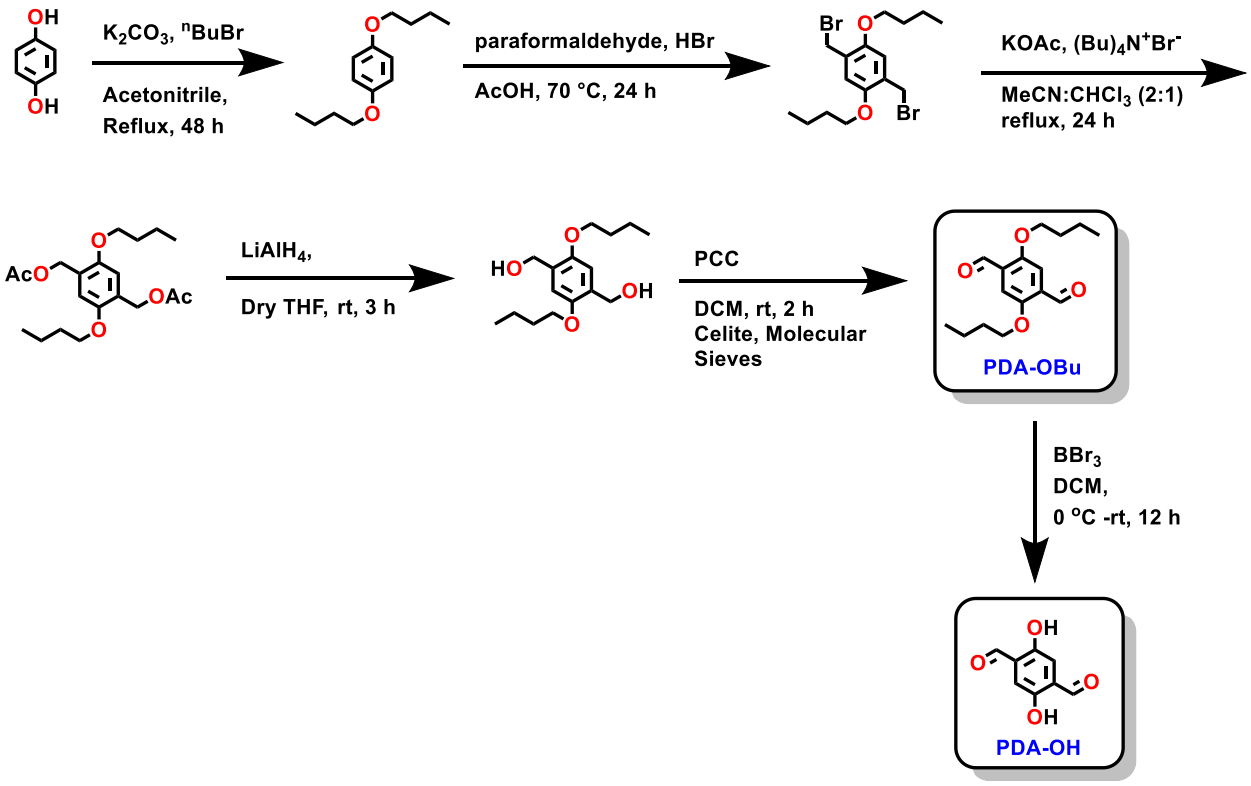

Synthesis of 1,4-bis(butyloxy)benzene. A suspension of hydroquinone (10.00 g, 90.81 mmol), bromobutane (38.20 g, 272.5 mmol), and potassium carbonate (37.65 g, 272.45 mmol) in 180 mL of acetonitrile was refluxed for 48 h under nitrogen atmosphere. After 48 h, the reaction mixture was cooled, and then the solvent was removed using rotary evaporation. The obtained brown solid was melted, then poured into water, producing a precipitate which was filtered and dried under high vacuum overnight to obtain an off-white solid (yield 16.24 g, 80%). The ^{1}H NMR

spectrumwas consistent with literature.[9] ^{1}H NMR ($CDCl_3$, 400 MHz): δ (ppm) = 6.82 (s, 2H), 3.91 (t, *J* = 8.0 Hz, 4H), 1.71-1.78 (m, 4H), 1.44-1.53 (m, 4H), 0.97 (t, *J* = 8.0 Hz, 6H).

Synthesis of 1,4-dibromomethyl-2,5-dibutyloxybenzene. 1,4-Dibutyloxybenzene (16.24 g, 73.05 mmol) and paraformaldehyde (4.61 g, 153.4 mmol) were weighed into a clean and dry 500 mL three-neck round bottom flask. The flask was evacuated, flushed with nitrogen, and 200 mL of acetic acid was added and stirred to form a suspension. To this 31 mL of hydrobromic acid in acetic acid (33% wt/wt) was added slowly. The reaction was heated to 70 °C, stirred overnight, and its progress was monitored via thin-layer chromatography. The reaction mixture was poured into 500 mL of ice-cold water, producing an unfilterable fine white precipitate. The water/precipitate mixture was extracted three times with a total of 300 mL of dichloromethane. The combined organic layers were washed with deionized water, then dried over anhydrous sodium sulfate. The dichloromethane was removed using rotary evaporation, yielding a black solid, which was purified using a short silica-gel column and 500 mL of 1:5 dichloromethane:hexanes as the eluent. The solvent was removed via rotary evaporator, yielding 5.35 g (18% if pure) of a brown solid which was carried forward without further purification. ^{1}H NMR ($CDCl_3$, 400 MHz): δ (ppm) = 6.85 (s, 2H), 4.53 (s, 4H), 3.99 (t, *J* = 6.0 Hz, 4H), 1.76-1.83 (m, 4H), 1.49-1.57 (m, 4H), 0.99 (t, *J* = 8.0 Hz, 6H).

Synthesis of (2,5-dibutoxy-1,4-phenylene)bis(methylene) diacetate. 1,4-Bis(bromomethyl)-2,5-dibutoxybenzene (4.49 g, 11.00 mmol) and potassium acetate (3.24 g, 33.00 mmol) were weighed into a three-neck round bottom flask. The flask was evacuated and then flushed with nitrogen. 100 mL of acetonitrile and 50 mL of chloroform were added to the flask. The reaction mixture was refluxed overnight. After cooling to room temperature, the reaction mixture was

poured into 300 mL of water and extracted chloroform (3 × 100 mL). The combined organic extracts were washed three times with 300 mL water, then dried over anhydrous sodium sulfate. The solution was evaporated using rotary evaporation and subsequently dried under high vacuum for 24 hours at room temperature to yield 3.69 g (77%, assuming pure 1,4-dibromomethyl-2,5-dibutyloxybenzene starting material) of the desired compound, which was directly used in the next step. ^{1}H NMR ($CDCl_3$, 400 MHz): δ (ppm) = 6.88 (s, 2H), 5.13 (s, 4H), 3.95 (t, *J* = 6.0 Hz, 4H), 2.10 (s, 6H), 1.71-1.78 (m, 4H), 1.44-1.53 (m, 4H), 0.97 (t, *J* = 6.0 Hz, 6H).

Synthesis of (2,5-dibutoxy-1,4-phenylene)dimethanol. Lithium aluminum hydride (1.91 g, 50.3 mmol) was suspended in 150 mL of dry THF under an inert atmosphere. A solution of (2,5-bis(butoxy)-1,4-phenylene)dimethanol, (3.69 g, 10.1 mmol) in 50 mL THF was added dropwise to the $LiAlH_4$ suspension. The reaction was stirred at room temperature 3 h. The reaction was quenched using 50 mL of ice-cold ethyl acetate. The reaction mixture was then poured into 400 mL water and extracted with ethyl acetate (3 × 200 mL). The combined extracts were washed with water, dried over anhydrous sodium sulfate, and dried using rotary evaporation. Drying under high vacuum yielded the desired product as a colorless solid (2.07 g, 73%).[10] ^{1}H NMR ($CDCl_3$, 400 MHz): δ (ppm) = 6.85 (s, 2H), 4.66 (d, *J* = 4.0 Hz, 4H), 3.99 (t, *J* = 8.0 Hz, 4H), 2.39 (t, *J* = 8.0 Hz, 2H), 1.76-1.80 (m, 4H), 1.44-1.53 (m, 4H), 0.98 (t, *J* = 8.0 Hz, 6H).

Synthesis of 2,5-dibutoxyterephthalaldehyde. 1.643 g (5.818 mmol) of (2,5-dibutoxy-1,4-phenylene)dimethanol was dissolved in 100 mL dry dicholoromethane and added to 5.016 grams of PCC (23.27 mmol), with 20 grams of celite and 20 grams of molecular sieves in a nitrogen flushed round bottom flask. The resulting mixture was stirred for 2 h under nitrogen at room temperature, then was filtered through a pad of silica gel. The solvent was removed via rotary

evaporation to yield a solid product, which was purified using a short silica gel column eluted with dicholoromethane until no more yellow coloration was observed in the eluent flow. Removal of the solvent afforded the final compound as a bright fluorescent yellow compound (1.01 g, 57%). The ^{1}H NMR spectrum was consistent with previous reports.[9] ^{1}H NMR ($CDCl_3$, 400 MHz): δ (ppm) = 10.52 (s, 2H), 7.43 (s, 2H), 4.10 t, *J* = 8.0 Hz, 4H), 1.79-1.86 (m, 4H), 1.47-1.56 (m, 4H), 0.99 (t, *J* = 8.0 Hz, 6H).

Synthesis of 2,5-dihydroxyterepthaldehyde. This compound was synthesized by dealkylation of the 2,5-dibutoxyterephthaldehyde. A 250 mL round-bottom flask was charged with 2.5-dibutoxy terephthaldehyde (2 g, 7.2 mmol, 1 equivalent) and 50 mL dicholoromethane. The solution was cooled to 0 °C and then BBr_3 (1 M in dicholoromethane) solution (21.6 mL, 21.6 mmol, 3 equivalents) was added dropwise. Subsequently the reaction was warmed to room temperature and stirred 12 h. At the end of this period, the mixture was then cooled to 0 °C and quenched by very careful dropwise addition of water. The mixture was extracted with dicholoromethane, dried over anhydrous Na_2SO_4, and solvent was removed using rotary evaporation to obtain a yellow solid (1.16 g, yield: 98%). Collected NMR spectra were consistent with previous reports[11] of this material. ^{1}H NMR ($CDCl_3$, 400 MHz): δ (ppm) = 10.24 (s, 2H), 9.98 (s, 2H), 7.28 (s, 2H).

III. Covalent Organic Frameworks Synthetic Procedures

General procedure of the synthesis of the COFs. 1,3,5-tris(aminophenyl)benzene (TAPB) and aromatic dialdehyde (PDA-X) are weighed into a screw-capped scintillation vial in a 2:3 molar ratio. A solvent mixture of 4:1 p-dioxane:mesitylene are added and the mixture is pre-heated to dissolve the monomers. To this transparent solution, aqueous acetic acid is added. The mixture is then heated at 70 °C for 72 h. After this period, the mixture is cooled to room temperature, filtered, and washed with approximately 100 mL of methanol and activated using supercritical carbon dioxide ($scCO_2$) critical point drying prior to characterization.

TAPB-PDA COF. TAPB (55 mg, 0.16 mmol, 2 equivalents), terephthaldehyde (31 mg, 0.23 mmol, 3 equivalents), dioxane (5 mL) and mesitylene (1.25 mL) were charged in a 20 mL scintillation vial. The mixture was sealed and heated to 70 °C until dissolution of the monomers was observed, after which an AcOH solution (3 mL, 10.5 M) was added. The solution gelled within minutes and the mixture was maintained at 70 °C for 72 h without stirring. The work up procedure as described above afforded the **TAPB-PDA** COF as a yellow solid (70 mg, 89% yield).

TAPB-PDA-OH COF. TAPB (20 mg, 0.06 mmol, 2 equivalents), 2,5-dihydroxyterephthaldehyde (14 mg, 0.09 mmol, 3 equivalents), dioxane (1.6 mL) and mesitylene (0.4 mL) were charged in a 20 mL scintillation vial. The mixture was sealed and heated to 70 °C until dissolution of the monomers was observed. At this point, AcOH solution (0.2 mL, 3 M) was added. The solution gelled within minutes and the mixture was maintained at 70 °C for 72 h without stirring. The work up procedure as described above afforded the **TAPB-PDA-OH** COF as an orange solid (32 mg, 93% yield).

TAPB-PDA-OBu COF. TAPB (33 mg, 0.09 mmol, 2 equivalents), 2,5-dibutoxyterephthaldehyde (27 mg, 0.14 mmol, 3 equivalents), dioxane (1.6 mL) and mesitylene (0.4 mL) were charged in a 20 mL scintillation vial. The mixture was sealed and heated to 70 °C until dissolution of the monomers was observed. At this point, AcOH solution (1 mL, 10.5 M) was added. The solution gelled within minutes and the mixture was maintained at 70 °C for 72 h without stirring. The work up procedure as described above afforded the **TAPB-PDA-OBu** COF as a yellow solid (51 mg, 88% yield).

TAPPy-PDA-OH COF. 1,3,6,8-Tetrakis(4-aminophenyl)pyrene[12] (TAPPy) (30 mg, 0.05 mmol, 1 equivalent), 2,5-dihydroxyterephthaldehyde (18 mg, 0.11 mmol, 2 equivalents), dioxane (1.6 mL) and mesitylene (0.4 mL) were charged in a 20 mL scintillation vial. The mixture was sealed and heated to 70 °C until dissolution of the monomers was observed. The mixture was sealed and heated to 70 °C until dissolution of the monomers was observed. At this point, AcOH solution (0.2 mL, 3 M) was added. The solution gelled within minutes and the mixture was maintained at 70 °C for 72 h without stirring. The work up procedure as described above afforded the **TAPPy-PDA-OH** COF as an orange solid (42 mg, 90% yield).

IV. Covalent Organic Frameworks Fourier-Transform Infrared Spectroscopy

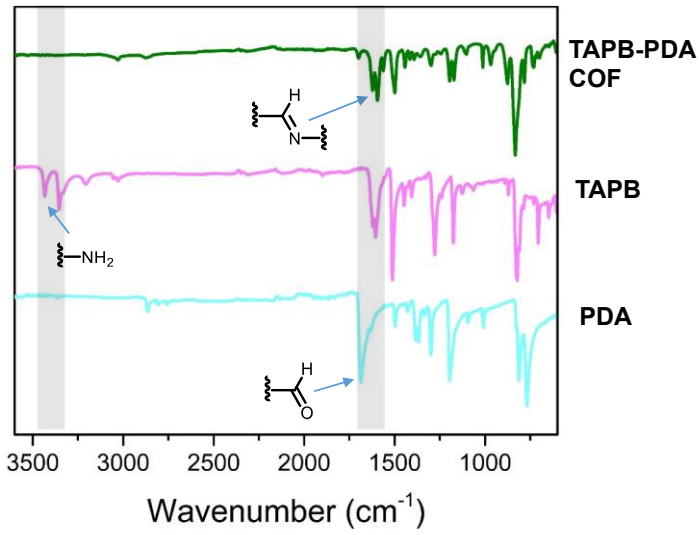

Figure 7.7. FT-IR spectra of **TAPB-PDA** COF, TAPB and PDA. The disappearances of aldehyde peak of PDA-H and amine peak of TAPB and appearances of imine peak in **TAPB-PDA** COF indicates successful imine condensation.

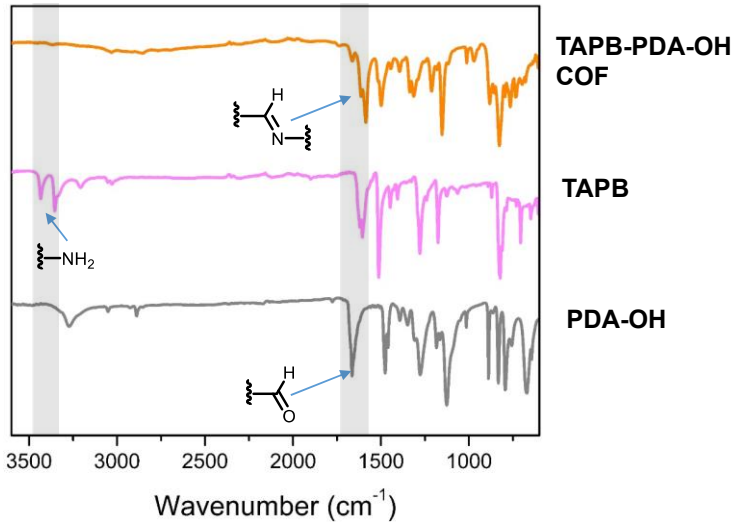

Figure 7.8. FT-IR spectra of **TAPB-PDA-OH** COF, TAPB and PDA-OH. The disappearances of aldehyde peak of PDA-OH and amine peak of TAPB and appearances of imine peak in **TAPB-PDA-OH** COF suggests successful imine condensation.

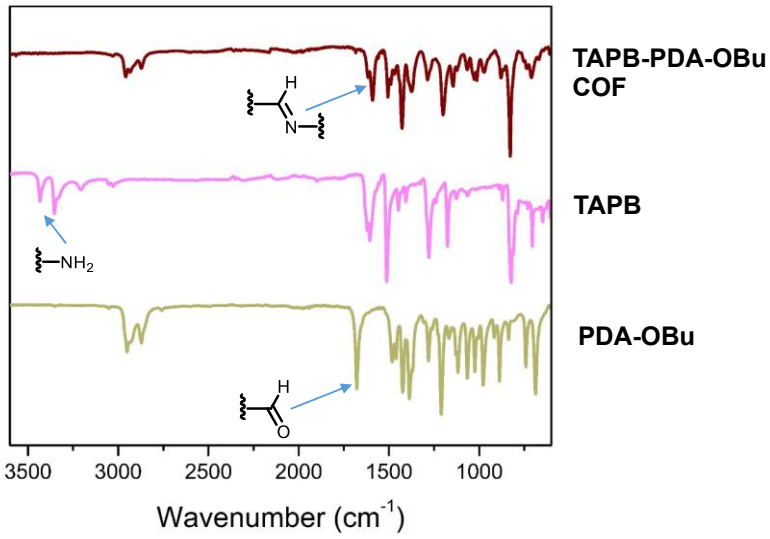

Figure 7.9. FT-IR spectra of **TAPB-PDA-OBu** COF, TAPB and PDA-OBu. The disappearances of aldehyde peak of PDA-OBu and amine peak of TAPB and appearances of imine peak in **TAPB-PDA-OBu** COF suggests successful imine condensation reaction.

V. Covalent Organic Frameworks Nitrogen Sorption Studies

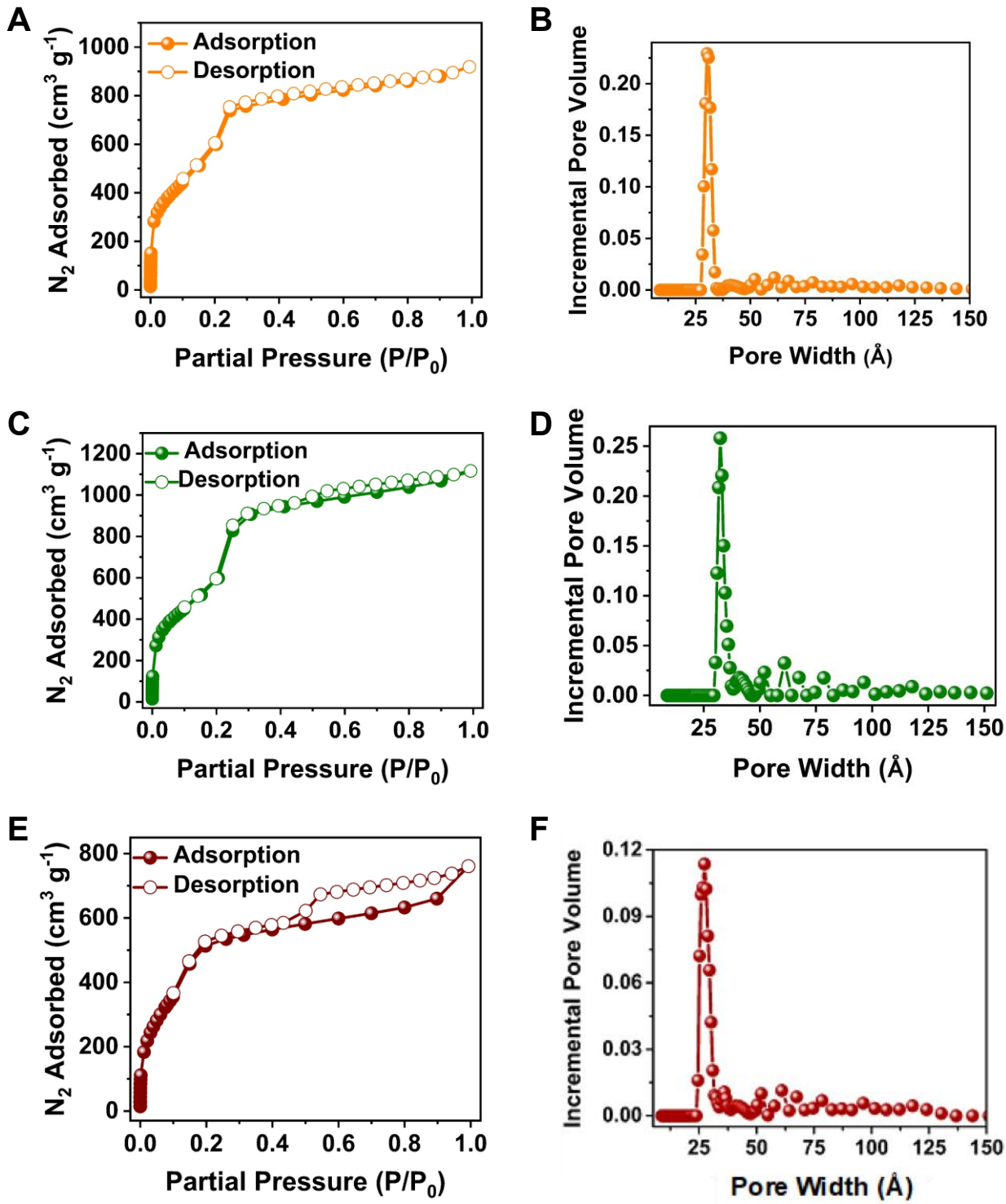

Figure 7.10. N_2 adsorption-desorption isotherms (left) and pore size distributions (right) for the **TAPB-PDA-OH** COF (**A** and **B**), **TAPB-PDA** COF (**C** and **D**) and **TAPB-PDA-OBu** COF (**E** and **F**).

VI. Optical Data for the TAPB-PDA/OBu COFs and a Model Compound

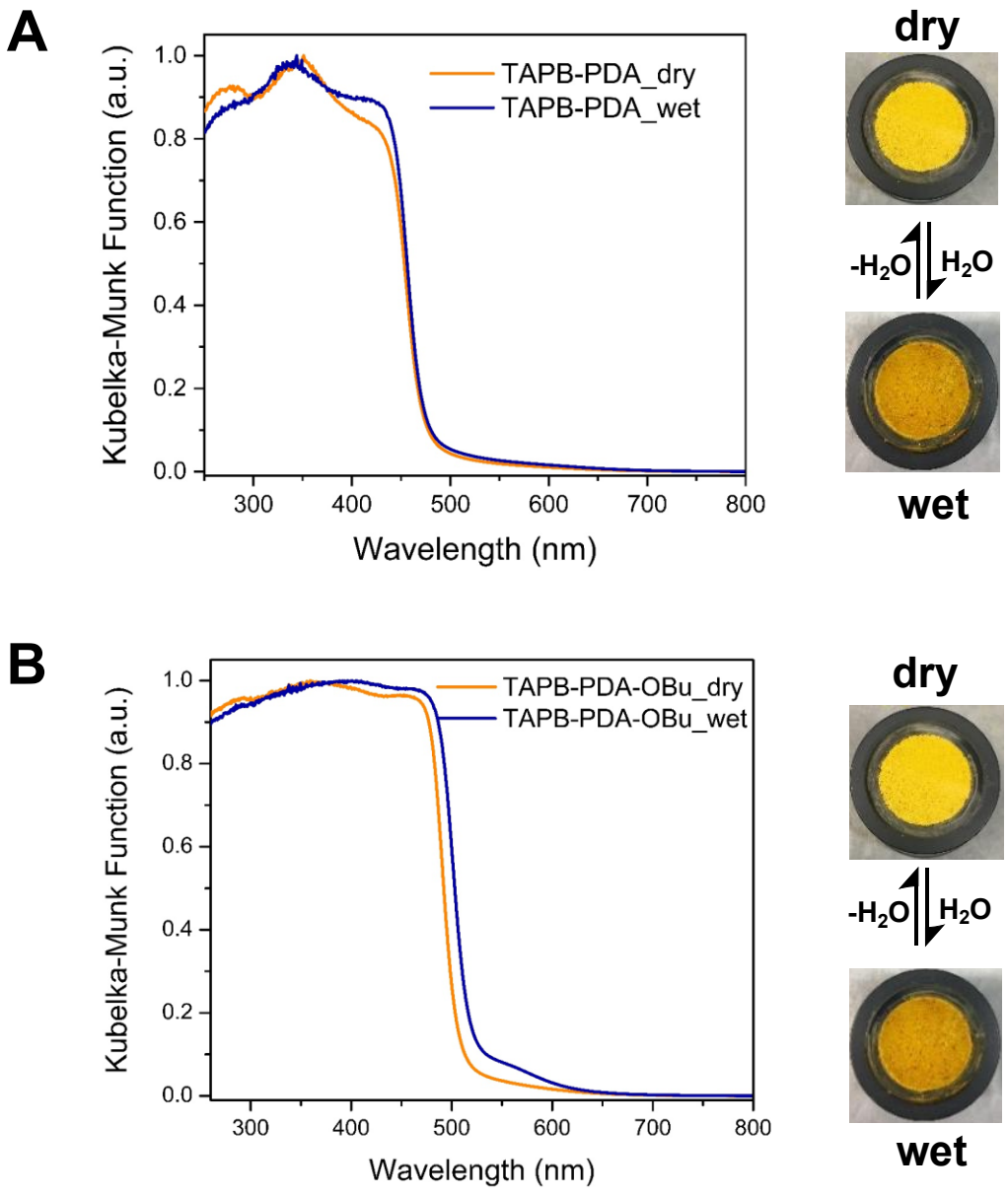

Figure 7.11. A) Diffuse reflectance spectra (DRS) of **TAPB-PDA** COF when dry and wetted. **B)** DRS spectra of **TAPB-PDA-OBu** COF when dry and wetted.

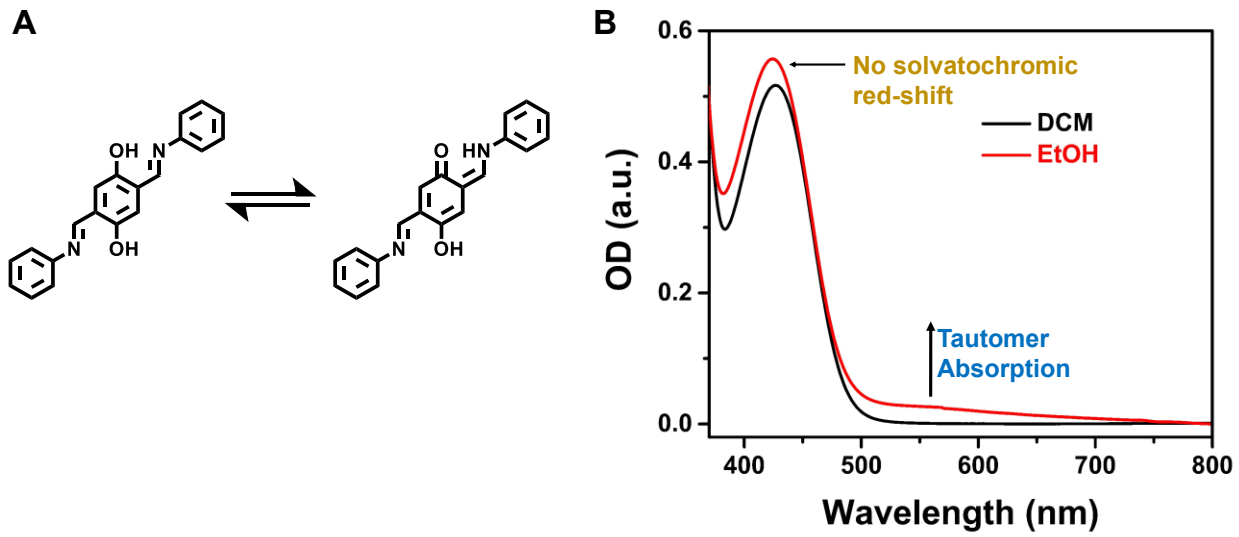

Figure 7.12. A) Model iminol compound (**BPH**)[13] and its tautomer. **B)** UV-vis absorption spectra of the model iminol compound in DCM and ethanol. It is clear that the model compound does not exhibit any solvatochromic red shift but a new broad peak grows due presumably to the formation of the tautomer. This is consistent with literature[14] and our DFT calculations.

VII. Synthesis and Characterization of Amorphous, Nonporous, TAPB-PDA-OH Polymer

Synthesis. TAPB (20 mg, 0.06 mmol, 2 equivalents), 2,5-dihydroxyterephthaldehyde (14 mg, 0.09 mmol, 3 equivalents), dioxane (1.6 mL) and mesitylene (0.4 mL) were charged in a 20 mL scintillation vial. The mixture was sealed and heated to 70 °C until dissolution of the monomers was observed. At this point, AcOH solution (0.2 mL, 3 M) was added. The solution gelled within minutes and the mixture was heated at 70 °C for 10 min without stirring. The work up procedure as described above for other COFs afforded the **TAPB-PDA-OH** polymer as a yellow solid (32 mg, 93% yield).

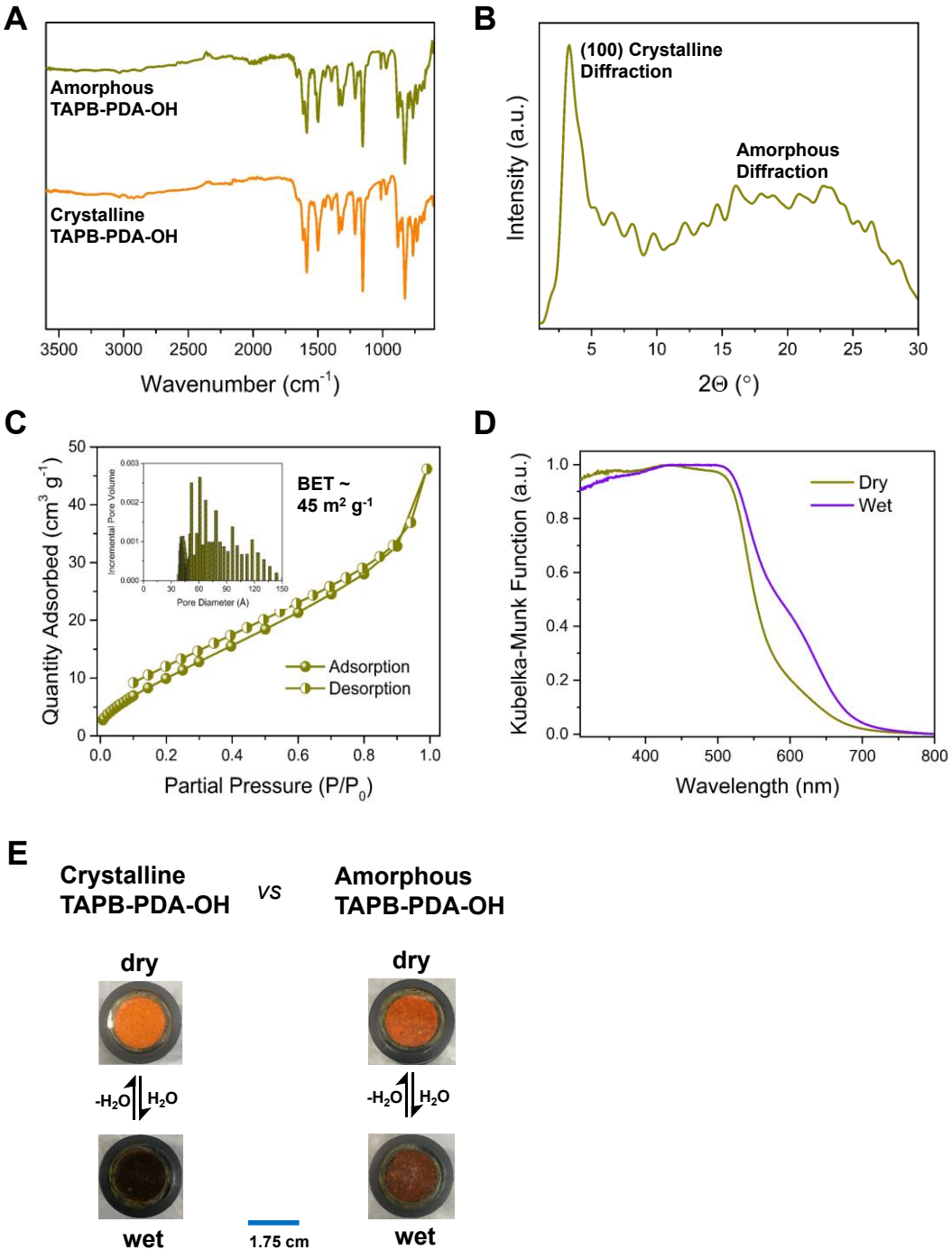

Figure 7.13. Structure, characterization and optical data of the amorphous TAPB-PDA-OH solid. **A)** FT-IR spectra of the amorphous and crystalline structures. **B)** PXRD pattern showing little

crystalline diffraction with a large amorphous hump at 10–30°. **C)** Sorption isotherm showing little adsorption in the microporous region, and the corresponding BET surface area is ca. 45 $m^2 g^{-1}$. In the inset is shown pore size distribution that is very broad. **D)** DRS of the dry and wet solid. **E** Photograph of the dry and wet samples of the amorphous and crystalline materials, showing the more pronounced response of the crystalline material.

VIII. Tautomerization Schemes

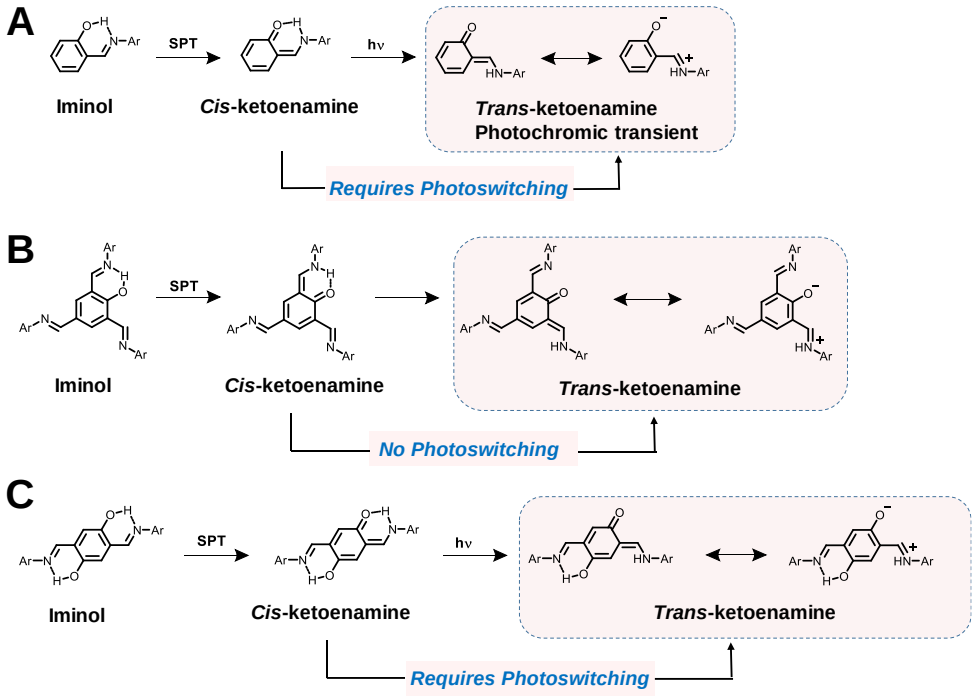

Figure 7.14. A) Tautomeric shift in an *o*-iminophenol via single proton transfer (SPT) to generate *cis*-ketoenamine. The cis-ketoenamine can convert to a *trans*-ketoenamine under UV irradiation. **B)** *m*-disubstituted iminophenol can undergo a similar SPT to generate the *cis*-ketoenamine, which even in the absence of UV irradiation can convert to *trans*-ketoenamine (colored species) by another SPT. TAPB-TFP COF contains this active moiety and therefore displays water-mediated chromism via formation of both *cis*- and *trans*-ketoenamines. **C)** 2,5-Diiminosubstituted-1,4-bisphenol can only form *cis*-ketoenamine in the absence of UV irradiation.[13]

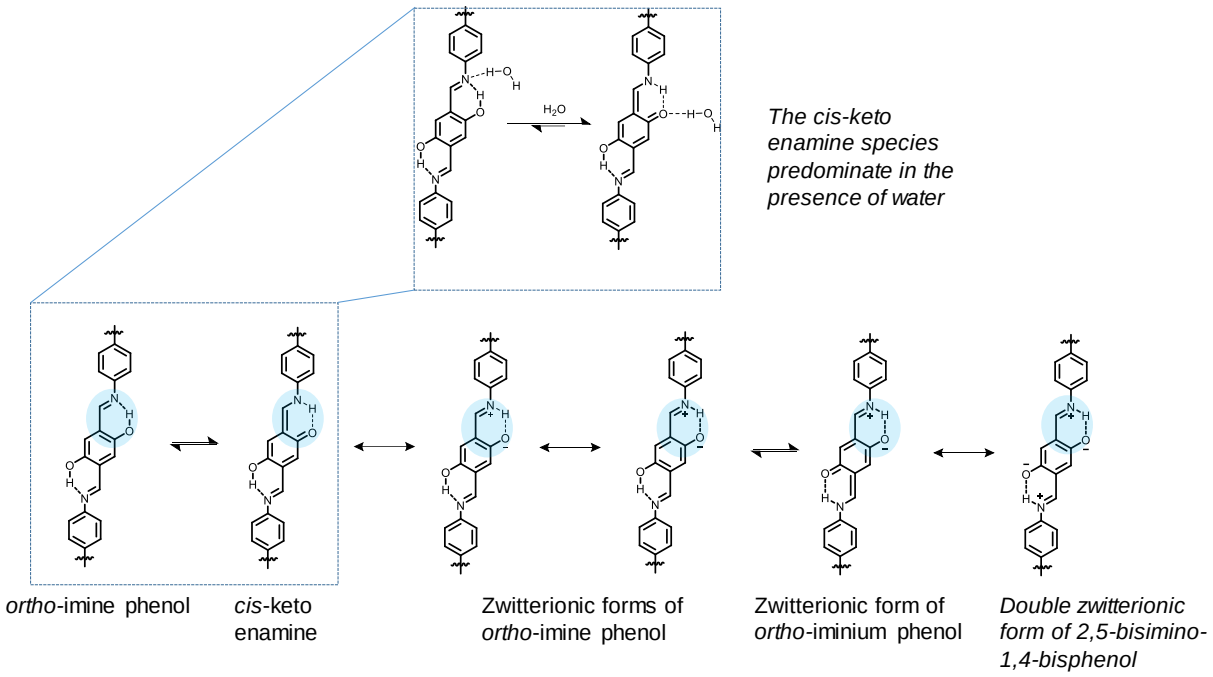

Figure 7.15. Possible species that may, in principle, be present. These species can exist in equilibrium and their relative amount as well as their extinction coefficients will determine the mediachromic effects.

IX. Wet/Dry Fourier-Transform Infrared and Raman Spectroscopies of TAPB-PDA-OH COF

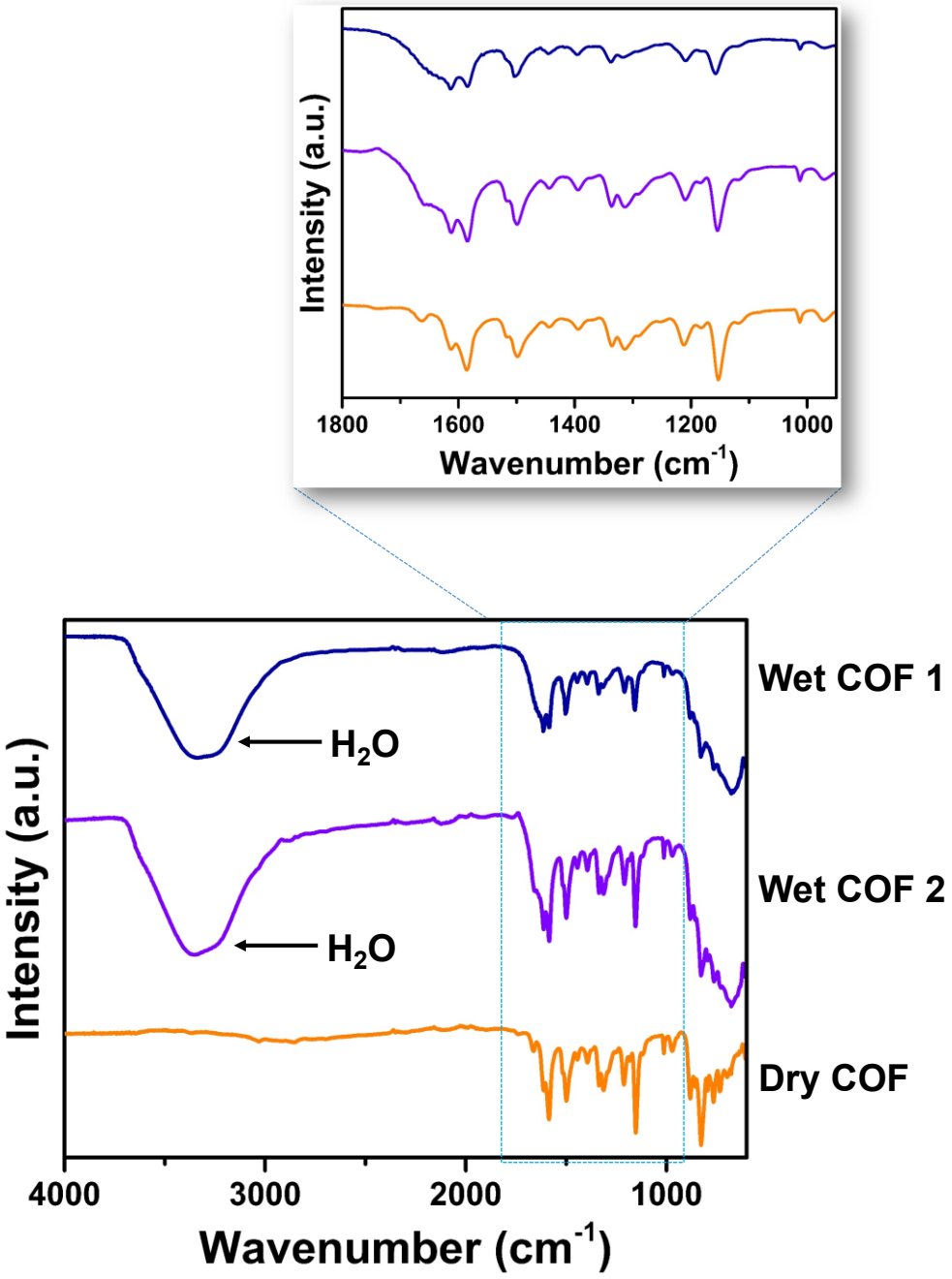

Figure 7.16. FT-IR of the dry and wet **TAPB-PDA-OH** COF. Note that there are not large changes in the IR spectra between the dry and wet COFs. The most noticeable changes are around 1650 cm^{-1} and may be due to increased strength of the imine stretching mode, as predicted by DFT. Interestingly, depending on the sample, small variations in the relative peak intensities were noted in the wet COF samples, which indicate that this equilibrium is sensitive to perturbation; it likely depends on both the sample quality (site accessibility) and the amount of water.

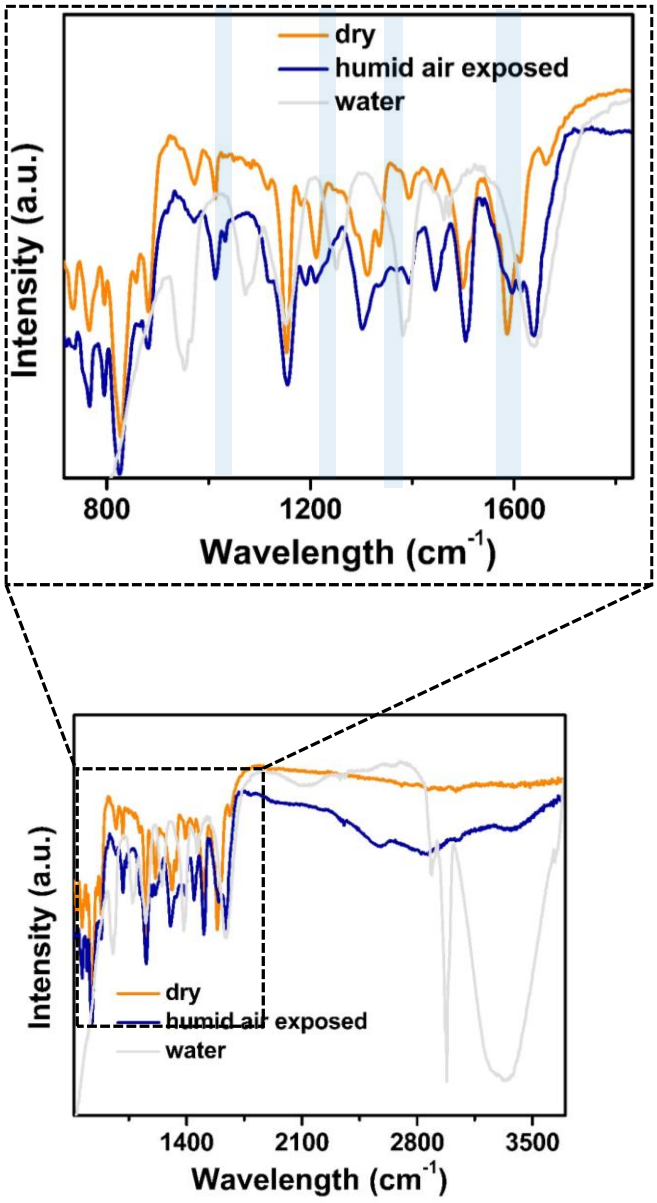

Figure 7.17. FT-IR of the dry and humid air exposed **TAPB-PDA-OH** COF. Note again that changes are subtle but more obvious as we largely eliminated water contribution in the data, The changes are highlighted and appears at approximately 1040, 1190, 1231, 1288, 1519, 1577, 1600 and 1643 cm^{-1}. The feature at 1643 overlaps with the water peak. However, note that the typical stretching frequencies of water are significantly subdued above 3000 cm-1. This indicates that this

peak may either be due to trapped water inside the framework that do not behave like free water molecules and is H-bonded. There are several other peaks which appear at same positions as that of the dry sample, but the intensities are greatly altered suggesting changes in the framework. As noted above and in the main text, this equilibrium is sensitive to perturbation; it likely depends on both the sample quality (site accessibility) and the amount of water. It is also noteworthy that pressing of COF powder on ATR crsytals also led to visual changes, which may affect the data.

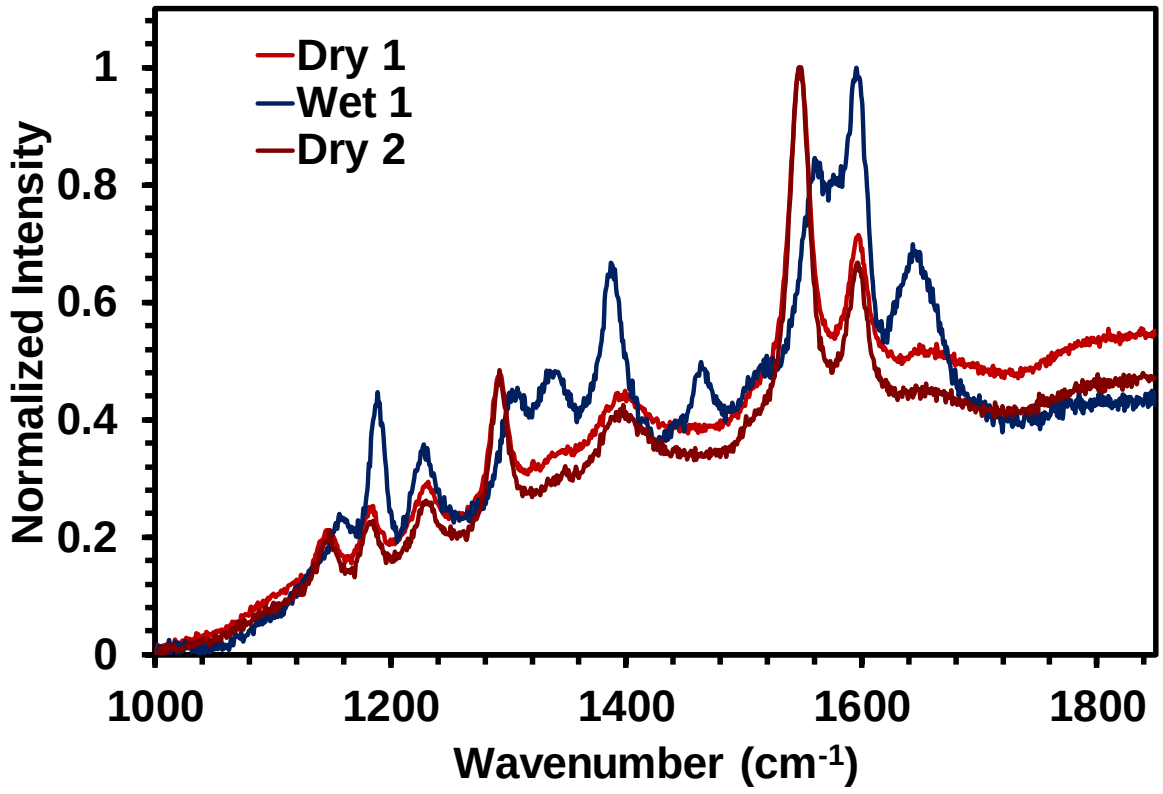

Figure 7.18. Raman spectra of the dry and wet **TAPB-PDA-OH** COF. Since Raman, scattering due to water are weak, the changes in the framework are more obvious. Definitive assignments of the Raman bands are difficult, but changes are reversible upon water addition and removal.

X. Acid-Base Optical Spectroscopy for TAPB-PDA-X COFs

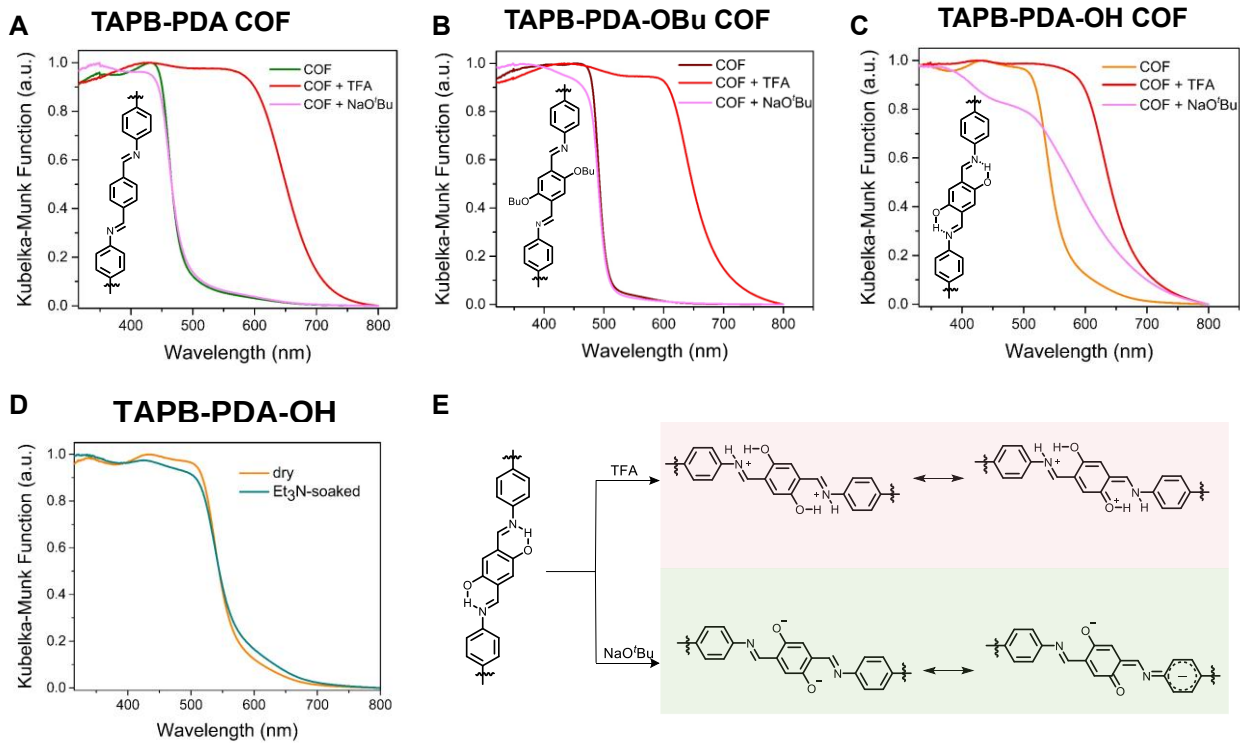

Figure 7.19. A, B, C) DRS of the dry, acid- and base-treated **TAPB-PDA/-OBu/-OH** COFs. All COFs exhibited red-shifted response in acid due to protonation of the imine moiety. Only **TAPB-PDA-OH** COF exhibited slight base-mediated response due to partial deprotonation of the phenolic moieties. **D)** DRS of dry and Et_3N-soaked **TAPB-PDA-OH** COF. Et_3N has marginal effect in the DRS of **TAPB-PDA-OH** COF. **E)** The structures of the chromophores expected in the extreme situation of protonation and deprotonation.

Discussion: The donor and acceptor strengths of ketoenamine-iminol tautomers are known to be influenced by protonation/deprotonation. The acceptor strength of the imine moiety can be enhanced by an acidic proton, by either the formation of a hydrogen bond between a H-donor and the imine, inducing a partial positive charge on the imine acceptor, or by protonation to form the positively charged iminium functional group. Similarly, a base can either act as a hydrogen bond acceptor with the phenolic moiety as the donor or fully deprotonated phenolate. In the presence of an amphiprotic species, each of these mechanisms may be relevant and both mechanisms are expected to cause a red-shift in the CT band, which may manifest in the water-triggered **TAPB-PDA-OH** COF chromism. Two limiting cases – protonation of the imine by trifluoroacetic acid (TFA) and deprotonation of phenol by sodium *tert*-butoxide – were examined to give insight into the results obtained in aqueous media. All three COFs contain the imine acceptor group, and upon treatment with TFA exhibited a new CT band at longer wavelength (Figures S11A, B, C). This is consistent with the protonation mechanism laid out above; however, the fact that water alone does not cause any red-shift in **TAPB-PDA** COF is in direct contrast with a protonation mechanism when in the presence of water alone. When treated with NaO^tBu the TAPB-PDA and **TAPB-PDA-OBu** COFs, which each lack a phenolic proton that can be abstracted by the alkoxide base, did not show any change in the DRS, whereas the NaO^tBu-treated **TAPB-PDA-OH** COF exhibited a broad red-shifted CT band at a longer wavelength (> 550 nm, Figure S11C). Presumably deprotonation of the phenolic OH groups to afford phenoxide groups is responsible for this optical difference. For these reasons, we infer that a set of mechanisms which are difficult to deconvolute participate in the primarily tautomeric mediachromism.

XI. Wet/Dry ^{2}H NMR Spectroscopy of TAPB-PDA-OH COF soaked with D_2O

The as-synthesized COF did not exhibit any detectable signal due to D under standard experimental conditions, as expected from the low natural abundance of D. The D_2O-exchanged COF sample exhibited a weak but detectable ^{2}H NMR signal under conditions of magic angle spinning (MAS) at 10 kHz. Notably many peaks were observed, which indicated that this signal is not due to "free" D_2O. A series of peaks separated by the spinning MAS speed was observed. These peaks outline an envelope consistent with a typical Pake spectrum characterized by a quadrupolar splitting of ca. 120 kHz. This observation is a clear indication that the D nuclei are not experiencing any large-angle molecular motions (for example, rotation about a two-fold axis would lead to ca. half of this splitting), and, therefore, must be incorporated in a rigid position in the COF.

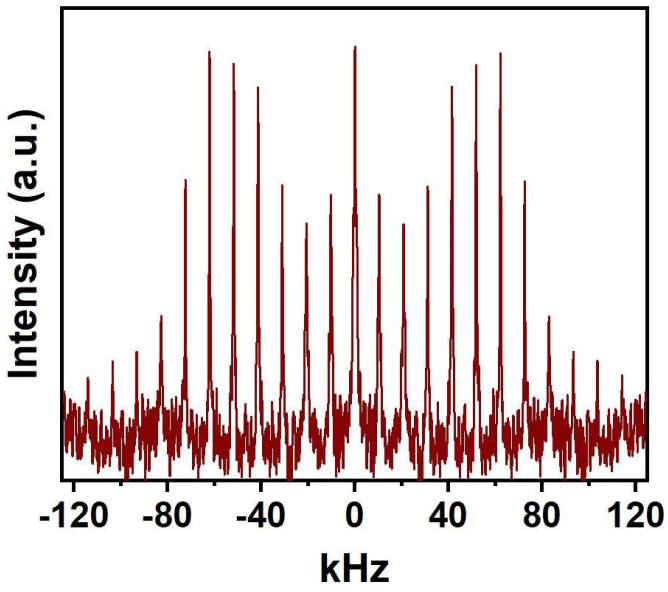

Figure 7.20. ^{2}H NMR spectrum of the D_2O exchanged COF.

XII. Density-Functional Theory Calculations

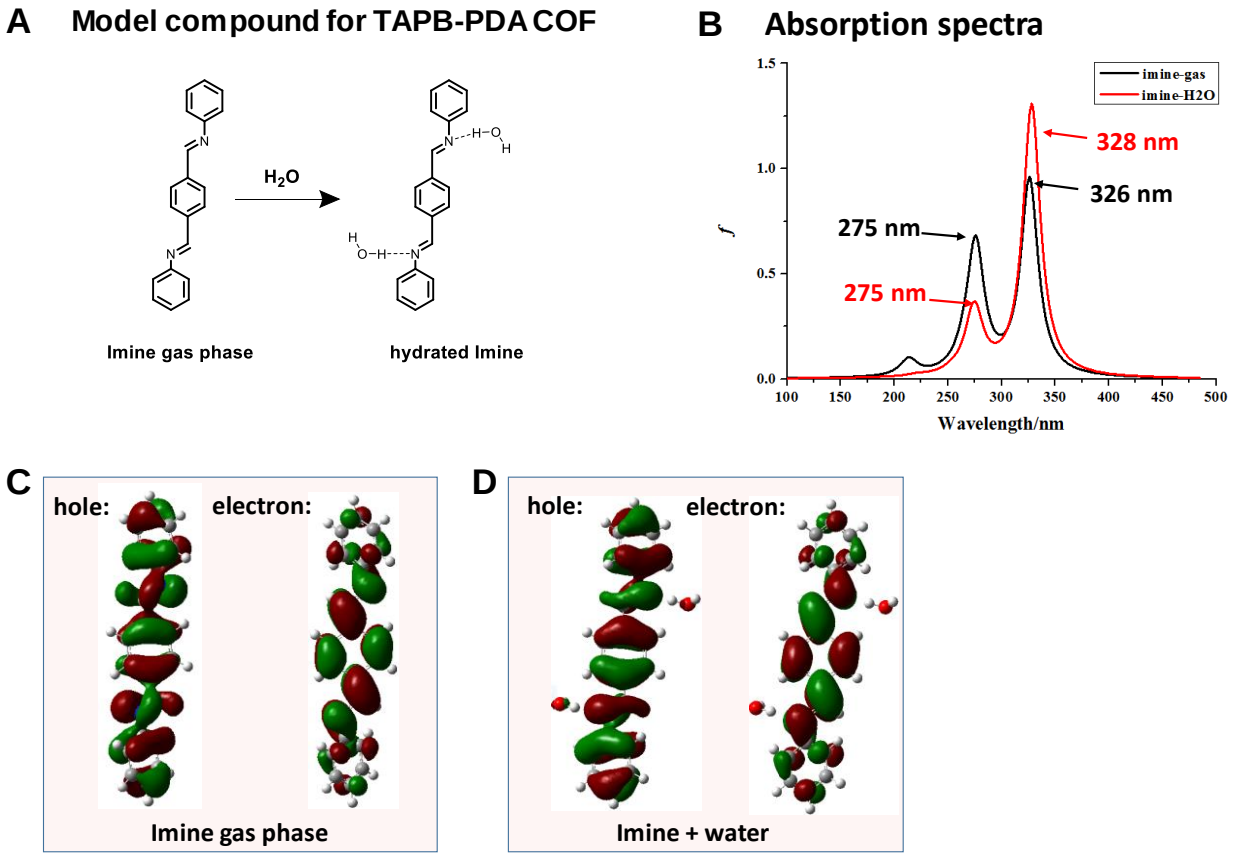

Figure 7.21. A) BPH as the model imine compound for the **TAPB-PDA** COF in the gas phase and in hydrated conditions. **B)** Calculated absorption spectra in the gas phase and in the presence of water, showing that solvatochromic changes are negligible. **C)** Hole and electron natural transition orbitals for the imine compound in the gas phase. **D)** Hole and electron natural transition orbitals for the imine compound in the presence of water; note that the charge-transfer character is negligible in **BPH**.

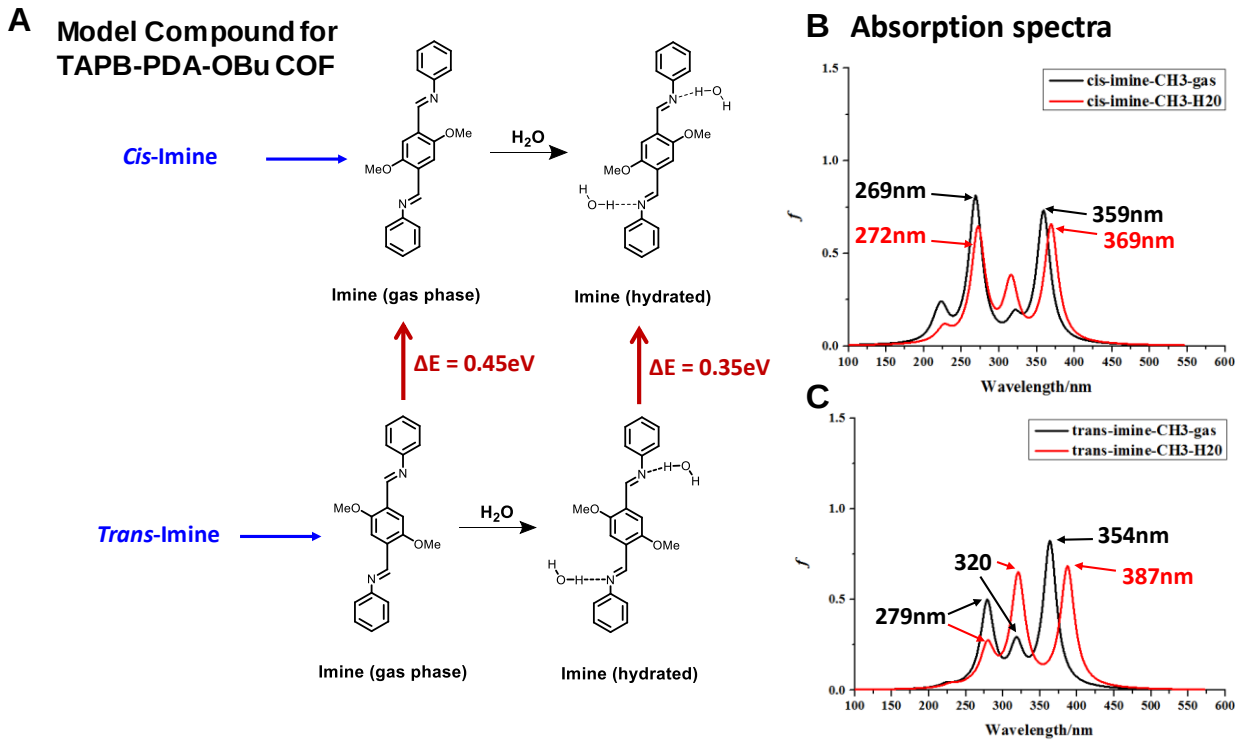

Figure 7.22. A A methoxy-substituted imine compound as the model for the **TAPB-PDA-OBu** COF. Note that the *trans*-imine is more stable than the cis-imine in both the gas phase and hydrated conditions, indicating a likely trans-geometry of the butoxy groups in the **TAPB-PDA-OBu** COF. **B** Calculated UV-vis spectra of the *cis*-imine compound in the gas phase and in the presence of water; the two calculated spectra are very similar. **C** Calculated UV-vis spectra of the *trans*-imine compound in the gas phase and in the presence of water; the spectrum in the presence of water is slightly red-shifted due to solvatochromism, which is consistent with the experimental observation for the **TAPB-PDA-OBu** COF.

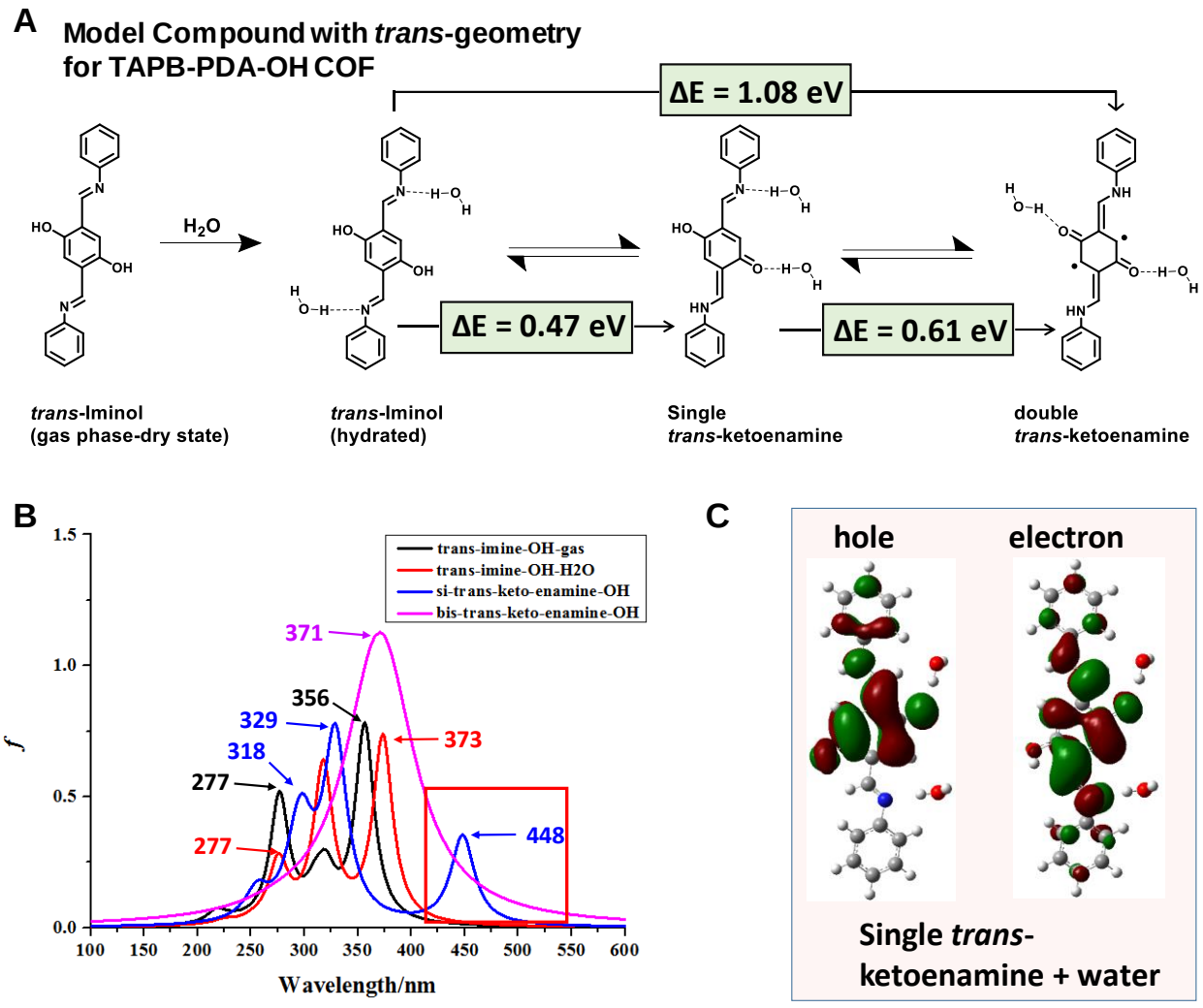

Figure 7.23. A) *Trans* **BPH** as the model for the **TAPB-PDA-OH** COF with *trans*-geometry. This compound can undergo tautomerism to a single *trans*-ketoenamine and further to a double *trans*-ketoenamine. The calculated energy costs associated with these tautomerisms are much higher than for the *cis*-geometry. **B)** Calculated UV-vis spectra of the *trans*-imine compounds in the gas phase and in the presence of water. Note that there is a slight solvatochromic shift in the presence of water, which was also noted for the *trans*-methoxy substituted model compound above. Notably, single *trans*-ketoenamine also has a longer-wavelength peak similar to that in the *cis*

compound. **C)** Hole and electron natural transition orbitals for the single *trans*-ketoenamine compound in the presence of water.

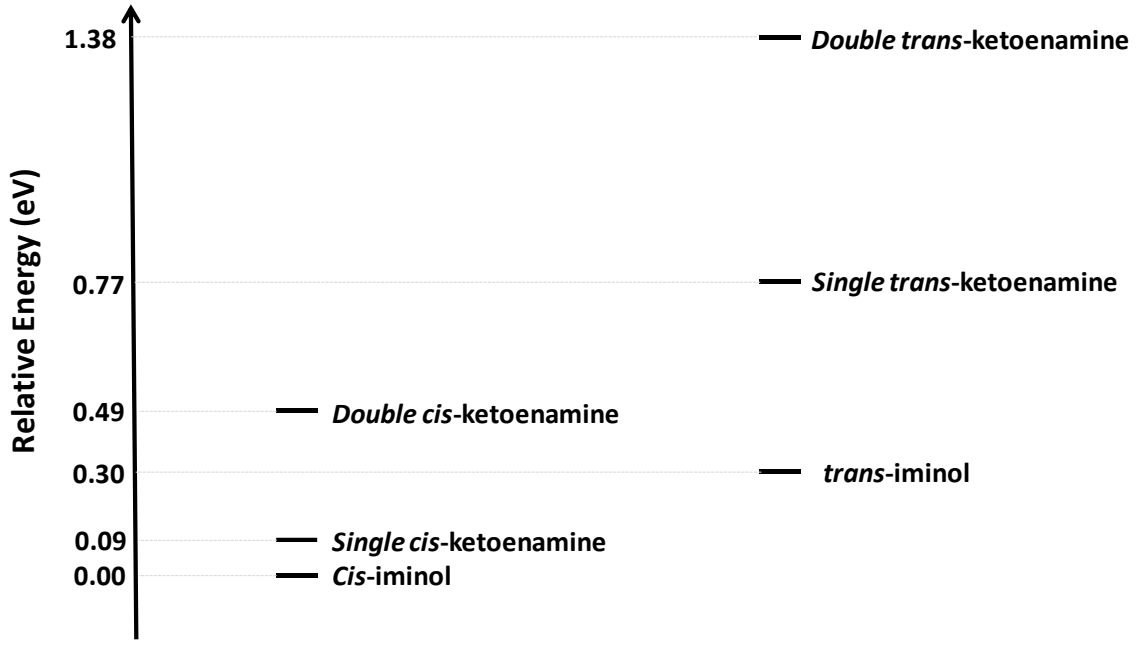

Figure 7.24. Relative energies of the different species calculated for the di-iminol and ketoenamine tautomers of model compound **BPH** in the presence of water.

Optimized geometries

***Cis*-iminol** ***Single Cis*-ketoenamine**

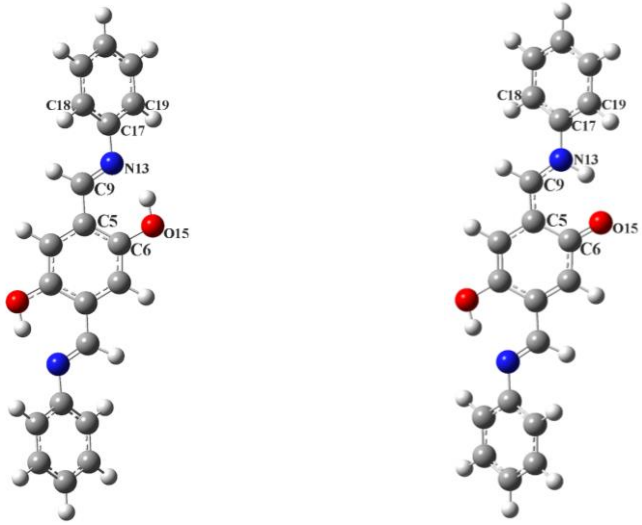

Table for associated bond lengths and angles

compound	Phase	O15-C6 (Å)	C6-C5 (Å)	C5-C9 (Å)	C9-N13 (Å)	N13-C17 (Å)	C9-N13-C17-C18 (º)
***Cis*-iminol**	gas	1.34	1.42	1.46	1.28	1.41	39.6
***Cis*-iminol**	H_2O	1.35	1.42	1.46	1.28	1.41	38.3
Single ***Cis*-ketoenamine**	H_2O	1.27	1.45	1.40	1.32	1.41	27.1

Figure 7.25. Optimized geometries of the **BPH** and its tautomer single *cis*-ketoenamine, with selected bond lengths and angles.

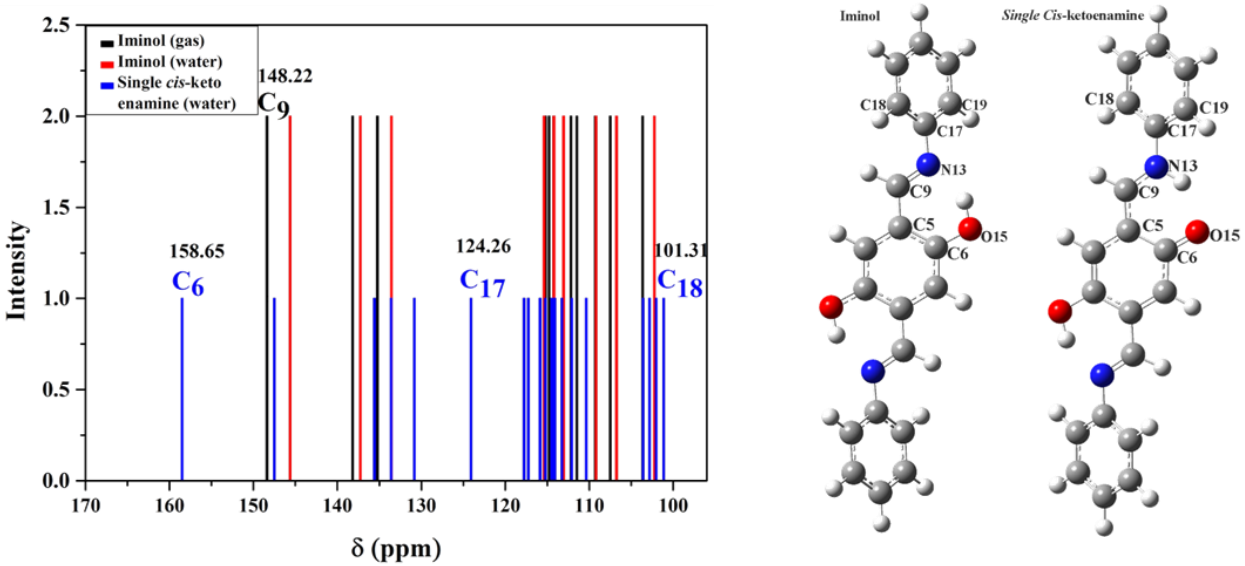

Figure 7.26. Predicted NMR chemical shifts of the *cis*-iminol (**BPH**) (gas: black; wet: red) and single *cis*-ketoenamine (wet: blue). For the numbering of the carbon, refer to the figure in the right. Note that "keto" carbon of the single *cis*-ketoenamine appears at 158 ppm, which reflects contributions of a zwitterionic iminium/phenolate resonance structure. Also, note that the theory predicts somewhat downfield shift for the residual imine peaks in single *cis*-ketoenamine with respect to the imine carbon peaks for the *cis*-iminol.

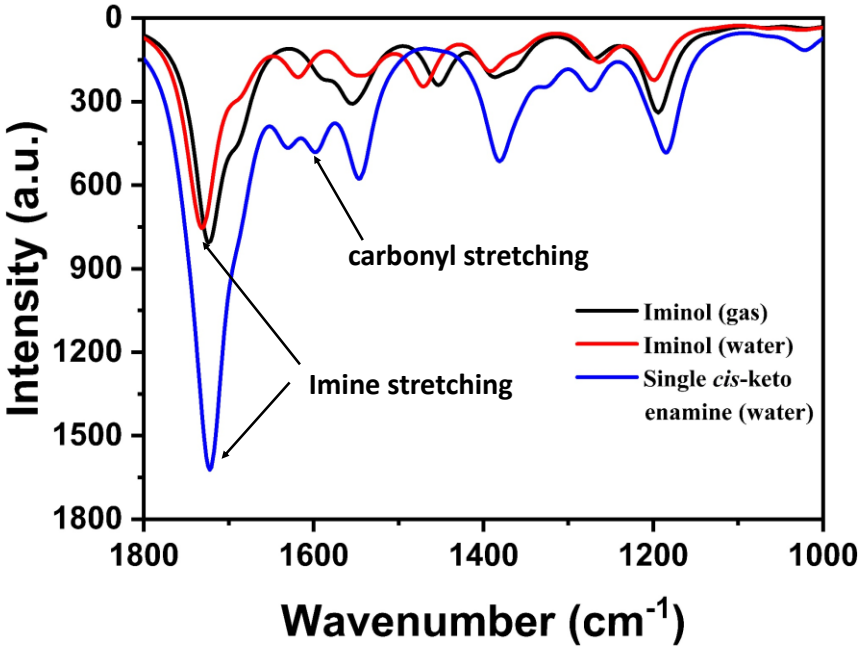

Figure 7.27. Predicted IR frequencies of **BPH**: *cis*-iminol (gas: black; wet: red) and single *cis*-ketoenamine (wet: blue)

XIII. Comparison of Experimental and Predicted XRD Patterns for COFs

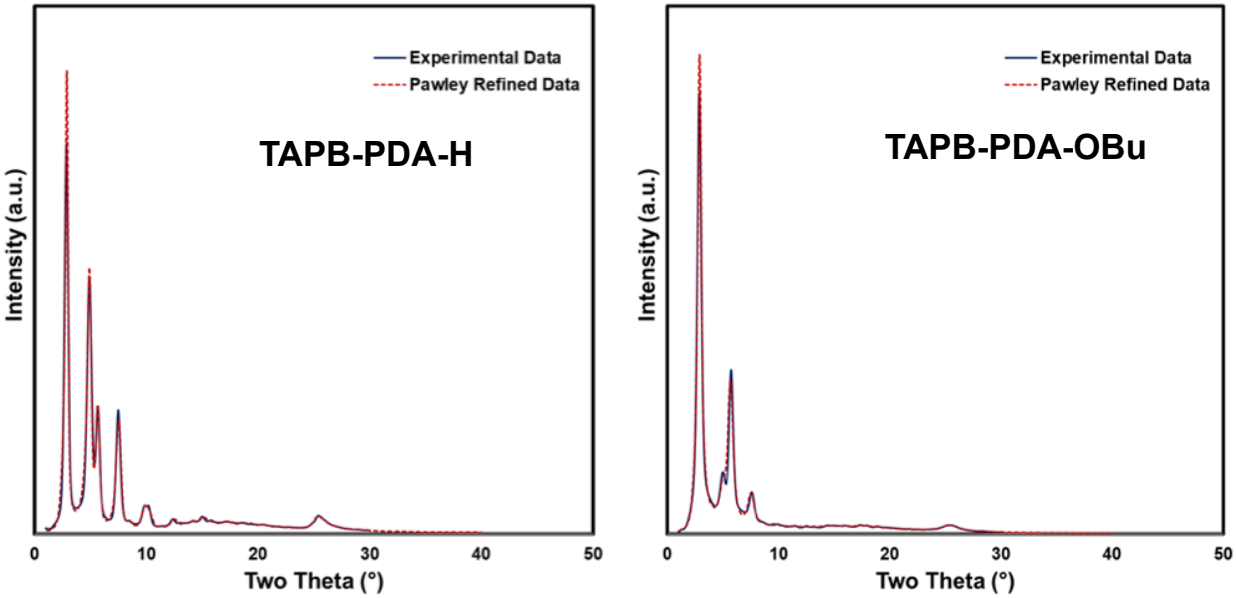

Figure 7.28. Experimental and predicted (Pawley refined, eclipsed) PXRD patterns of the COFs.

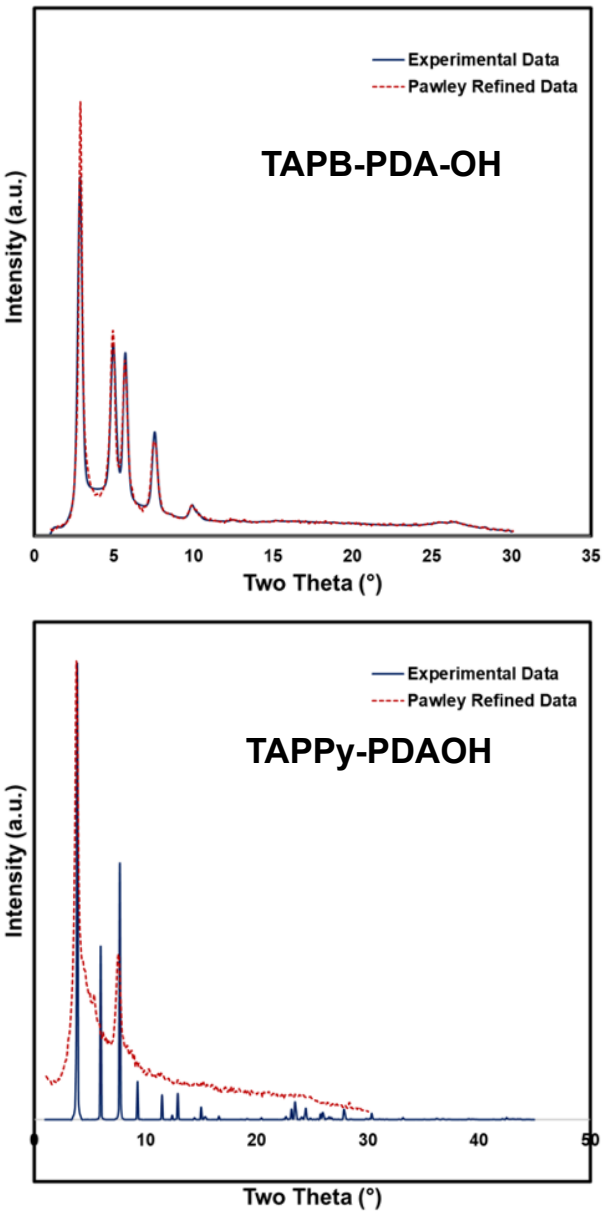

Figure 7.29. Experimental and predicted (Pawley refined, eclipsed) PXRD patterns of the COFs.

XIV. Characterization of the TAPPy-PDA-OH COF.

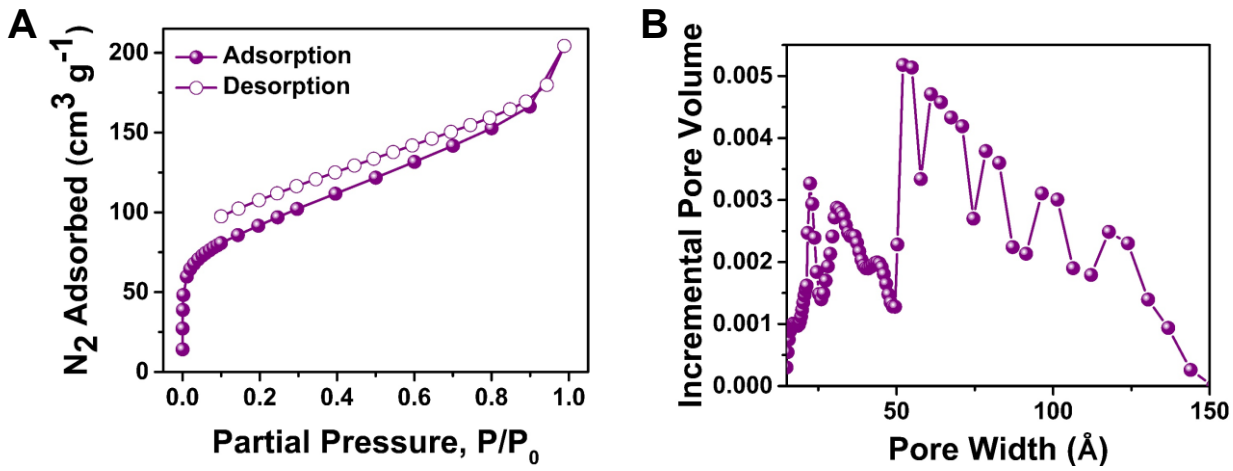

Figure 7.30. Nitrogen sorption isotherm (**A**) and pore size distribution (**B**) of the **TAPPy-PDA-OH** COF.

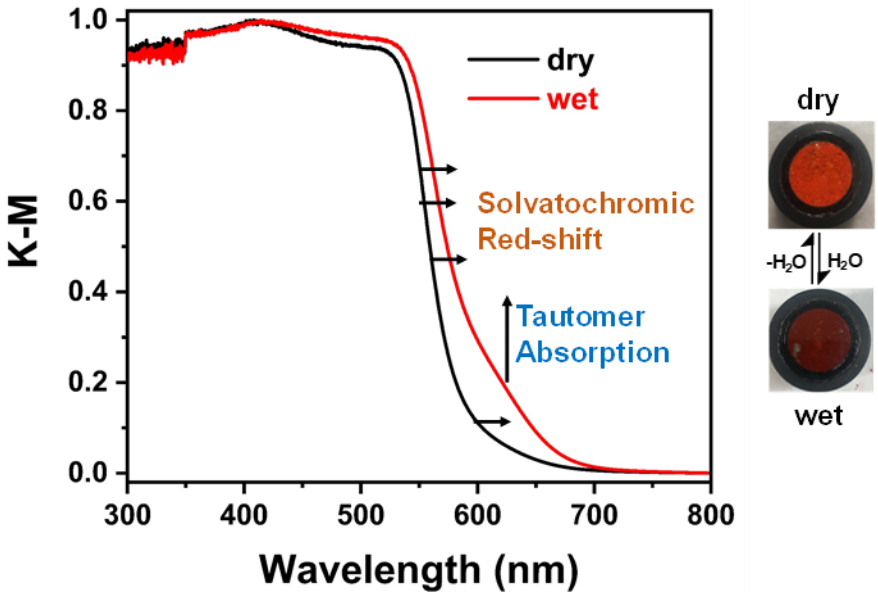

Figure 7.31. DRS spectra of the dry and wet samples of **TAPPy-PDA-OH** COF. The extent of tautomerism is limited in this system (due at least partly to its quality and accessibility of tautomeric sites) but one can clearly observe the growth of a new peak at approximately 600 nm.

XV. Synthesis of COF Thin Films

COF Films were synthesized by immersing a fused silica substrate into a solvothermal reaction mixture. First, a 10 mL solution (4:1 *p*-dioxane:mesitylene) of 5 mM TAPB (1 equiv, 17.5 mg) and 7.5 mM aromatic dialdehyde (1.5 equiv: PDA: 10.0 mg, PDA-OH: 12.4 mg, PDA-OBu: 20.9 mg) was created by bath sonicating the COF monomers to dissolve them in the specified solvent mixture. To this solution, a fused silica substrate was added such that it was fully immersed in the reaction solvent. Then, 5 vol% (500 µL) of 9M aqueous acetic acid was added as a catalyst. These samples were sealed and heated to 70 °C for 3 days at which point a film deposited onto the surface of this substrate was observed as well as the precipitation of bulk COF powder.

Finally, these samples were cooled to room temperature and the substrates were removed from the reaction mixture. At this point, samples were placed in a clean solution of methanol and bath sonicated for one minute. This process was repeated ten times to attempt the removal of all non-COF film materials. Finally, the substrates were allowed to dry in air. At this point, the COF film substrates were found to be yellow but optically transparent with very minor scattering.

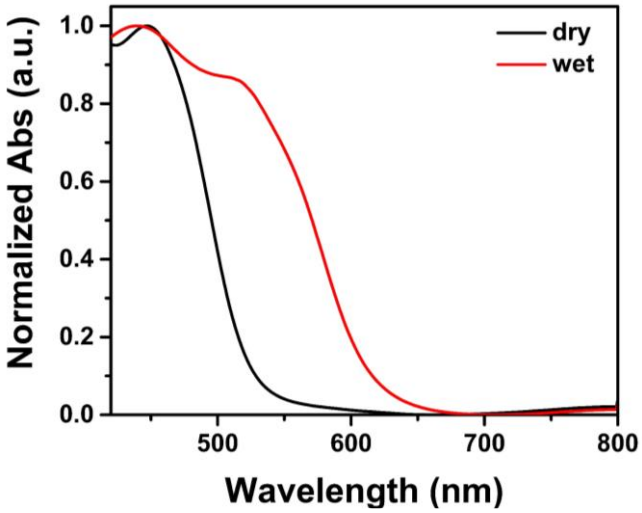

Figure 7.32. Absorbance spectra of the dry and wet films of the **TAPB-PDA-OH** COF.

XVI. COF Thin Film Humidity Sensing Experiments

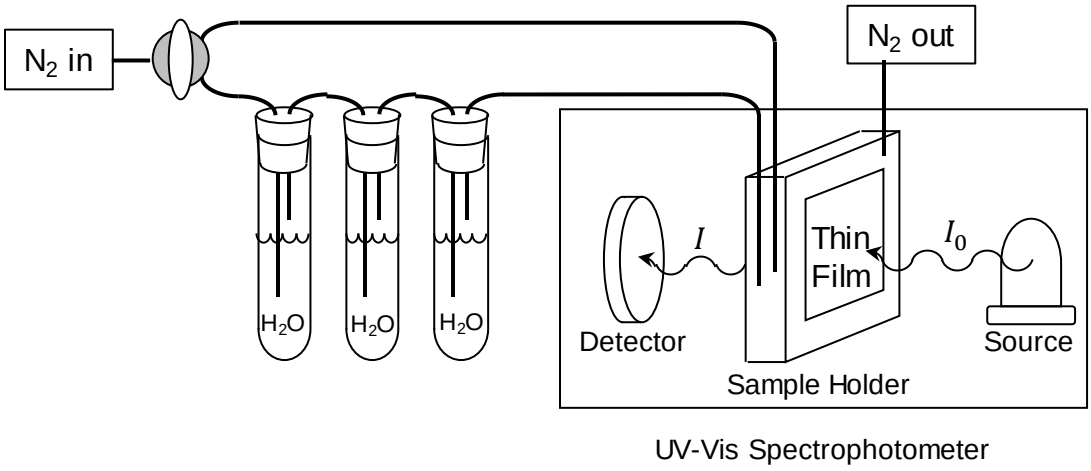

Figure 7.33. Humidity sensing schematics.

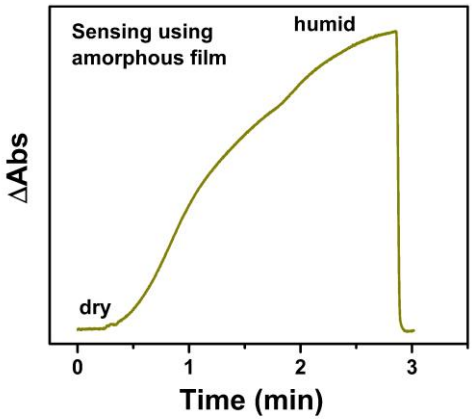

Figure 7.34. Humidity sensing using amorphous film of **TAPB-PDA-OH** cross-linked polymer. The response time was 129 seconds for the dry to humid environment.

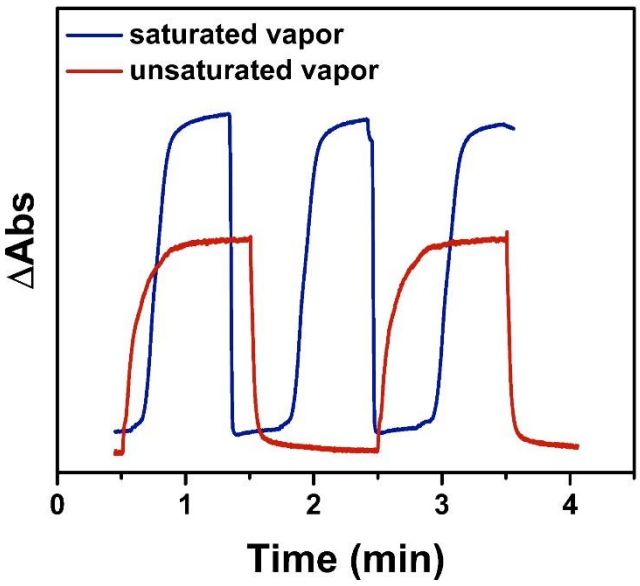

Figure 7.35. Humidity sensing of a saturated and unsaturated air. Faster and larger response were observed for a saturated air, whereas an unsaturated vapor (obtained by a secondary nitrogen flow) indicated slower and smaller response. This qualitatively indicated that relative humidity can be distinguished using this COF film.

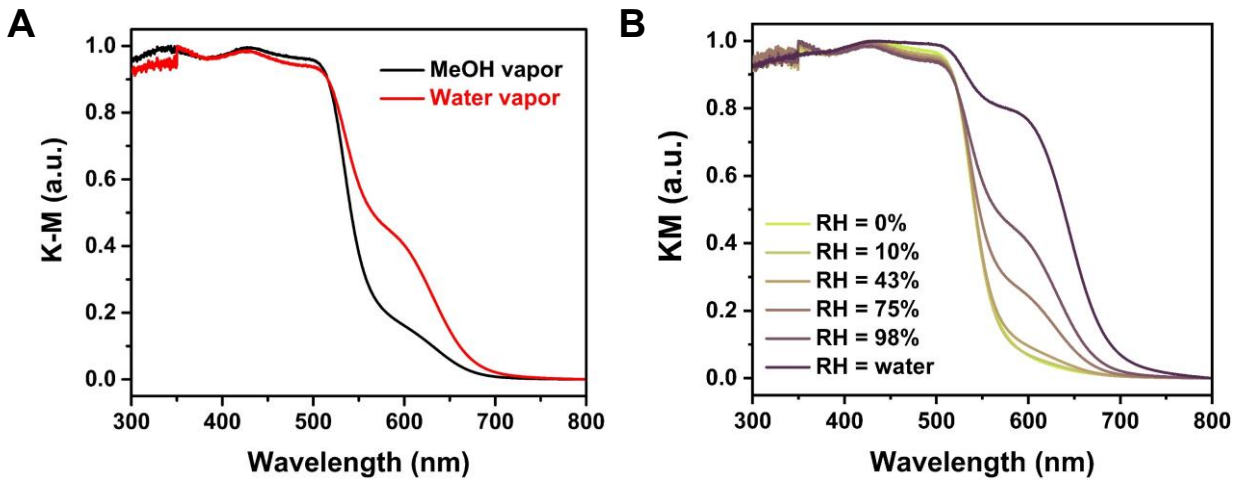

Figure 7.36. **A** DRS of methanol and water vapor exposed samples of the **TAPB-PDA-OH** COFs. Note that the absorbance at 600 nm is significantly pronounced for the water vapor. **B** DRS spectra of the COFs exposed to different levels of humidity. The corresponding humidity environments were created by a closed environment of saturated salts of NaOH (RH ~ 10%), K_2CO_3 (RH ~ 43%), NaCl (RH = 75%) and K_2SO_4 (RH = 98%).[649]

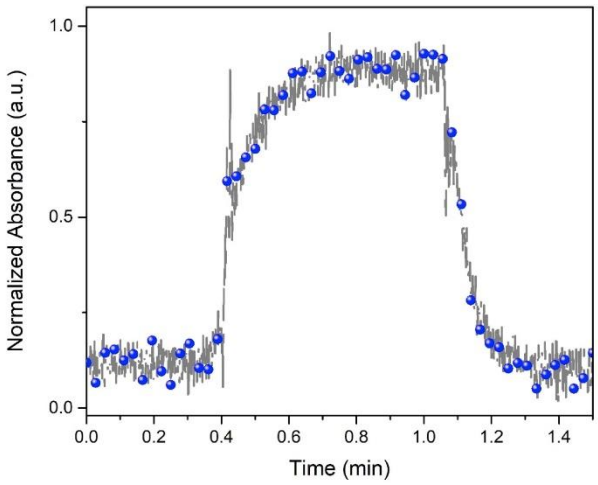

Figure 7.37. Humidity sensing using thin films of **TAPB-PDA-OBu** COF thin films at 560 nm. A slow response is observed, which may be due to hydrophobic moieties present inside the pores.

Chapter 8 : High-Sensitivity Acoustic Molecular Sensors Based on Large-Area, Spray-Coated Two-Dimensional Covalent Organic Frameworks

8.1 Abstract

Two-dimensional covalent organic frameworks (2D COFs) are a unique materials platform that combines covalent connectivity, structural regularity, and molecularly precise porosity. However, 2D COFs typically form aggregates that cannot be dispersed in solution, thus limiting their reliable integration into devices via additive manufacturing. In this work, we build off recent efforts that produced stable colloidal suspensions of boronate ester-linked 2D COFs by spray-coating large-area 2D COF thin films without the need for additional post-synthetic processing. This scalable additive manufacturing approach is synthetically general, with five different 2D COFs prepared as colloidal inks and subsequently spray-coated onto a diverse range of substrates. Moreover, this method enables the deposition of multiple 2D COF materials simultaneously, which is not possible by polymerizing COFs on substrates directly. When combined with stencil masks, spray-coated 2D COFs are deposited in minutes as thin films larger than 200 cm^2 with line resolutions below 50 μm. To demonstrate that this deposition scheme preserves the desirable attributes of 2D COFs and enables functional devices, spray-coated 2D COF thin films were incorporated as the active material in acoustic sensors. These 2D COF-based sensors have a 10 ppb limit-of-quantification for trimethylamine, which places them among the most sensitive sensors for meat and seafood spoilage. Overall, this work establishes a scalable additive manufacturing technique that enables the integration of 2D COFs into thin-film device architectures.

8.2 Introduction to Processing 2D Polymers

Two-dimensional covalent organic frameworks (2D COFs) are structurally regular and synthetically versatile (>400 reported structures) layered 2D polymers with high surface areas (>2000 m^2 g^{-1}) and robust covalent bonds.[106, 650] This combination of properties makes 2D COFs promising for a variety of applications, including nanofiltration membranes,[147, 651, 652] charge-storage devices,[581, 584, 653] and chemical sensors.[576, 587, 653-658] Despite this promise, conventionally isolated polycrystalline 2D COF powders are insoluble and effectively unprocessable, which has limited their integration into thin-film device architectures.[206, 659, 660] This limitation has inspired the exploration of numerous thin-film fabrication approaches, including direct polymerization on substrates,[583, 661] continuous flow methods,[191, 662, 663] interfacial polymerization,[147, 179, 182] and electrophoretic deposition.[664] However, none of these methods are general across many substrate materials, amenable to scale-up, patternable, and operationally straightforward. For example, Bein and coworkers recently demonstrated how COF powders could be electrophoretically deposited onto a substrate, which was well suited for the fabrication of photocatalytic supports.[664] However, this approach requires that the substrate be conductive, is not easily patternable, and involves multiple processing steps. Although these emerging fabrication approaches have suggested the potential of 2D COF thin films in preliminary devices, their full technological promise remains restricted by the absence of a scalable additive manufacturing pathway.

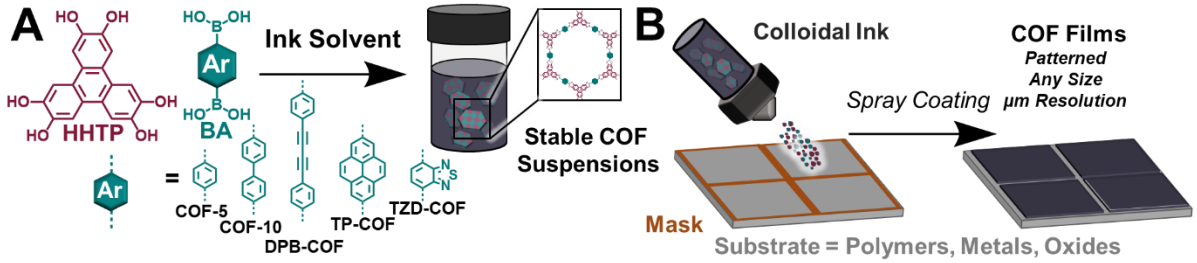

Figure 8.1 A) Synthesis of boronate-ester linked COF colloidal inks. **B)** Patterned spray-coating of COFs through a stencil mask.

8.3 Patterned Spray Coating

Recently, we prepared several 2D COFs as stable colloidal suspensions, which is a form amenable to solution-processing methods (**Figure 8.1A**).[125, 127, 151, 582, 665, 666] Using these colloidal suspensions as a starting point, here we demonstrate spray coating of 2D COF thin-films in a manner that retains their crystallinity, as assessed by X-ray diffraction (XRD) (**Figure 8.1B**). This additive manufacturing approach is demonstrated to be generalizable to five different 2D COF films on metal, polymer, and oxide substrates. Furthermore, spray coating is shown to be rapid, patternable, and highly scalable in addition to enabling mixtures of different COF colloids to be co-deposited in controlled ratios, which is not possible by other methods. In particular, we spray-coated exceptionally large-area 2D COF thin-films in excess of 200 cm^2 while maintaining sub-50 μm line resolution via stencil masking. As a demonstration that spray coating preserves the desirable attributes of 2D COFs, we fabricated acoustic sensors based on 2D COF thin-film active layers.[667] The sensors were fabricated in under two minutes, at scale, with less than 100 μg of active material, allowing the detection of several volatile analytes with exceptionally high responsivities for polar compounds, including volatile amines, which are target analytes of meat and seafood decay.[668-670] Ultimately, these 2D COF-based sensors showed a 10 ppb limit-of-

quantification for volatile trimethylamine (TMA), which is among the highest sensitivity reported to-date and well within the target range for meat spoilage detection.[668-670] These results thus establish a scalable additive manufacturing approach for 2D COF thin films that is likely to expedite the implementation of these materials in high-performance technologies. Boronate ester-linked 2D COFs were prepared as colloidal nanoparticle solutions to be used as inks for spray coating (**Figure 8.1A and Figure 8.2A**).[127, 582, 665] Dynamic light scattering (DLS, **Figure 8.2B**) and *in solvo* XRD (**Figure 8.2C**) indicate that the solutions contain 2D COFs as crystalline nanoparticles with a typical diameter of 50 nm. Diffraction patterns of evaporated COF-5 inks that were dropcast onto a SiO_2 wafer and heated to 100 °C show that the resulting thin films retain the COF-5 crystallinity (**Figure 8.2C**) and exhibit N_2 isotherms, surface areas (S_{BET} = 1900 m^2 g^{-1}), and pore size distributions consistent with similar experiments performed on COF-5 colloidal nanocrystals(**Figure 8.2D-E**).[127] DLS, XRD, and N_2 sorption measurements are additionally consistent with transmission electron micrographs, which indicate that COF-5 particles are single-crystalline and approximately 50 nm in diameter (**Figure 8.2F-H**). Taken together, these experiments confirm that COF-5 inks are of high-quality and can survive deposition into thin films without substantial loss of their desirable properties.

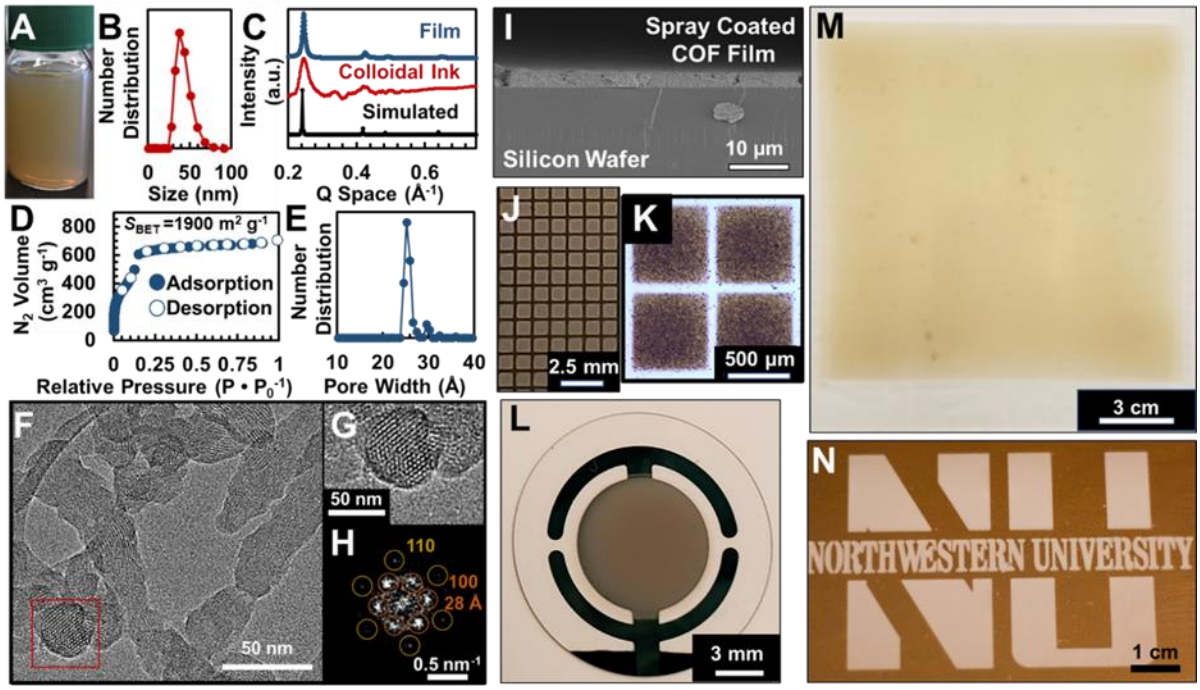

Figure 8.2 A) Optical image of COF-5 ink. **B)** DLS number distribution of COF-5 inks. **C)** XRD patterns of COF-5 inks and films. **D)** N_2 isotherm of a COF-5 film and **E)** its extracted pore size distribution. **F)** TEM image of a population of COF-5 particles and **G)** enlarged face-on particle with its **H)** fast Fourier transform. **I)** SEM image of a spray-coated COF film. **J)** Fine-resolution print of COF-5 squares and **K)** its magnified optical microscopy image on SiO_2. **L) S**pray-coated COF-5 on a Ti QCM wafer. **M)** Large-area COF-5 print on SiO_2. **N)** Patterned COF-5 print on Kapton.

Spray coating COF-5 colloidal inks through stencil masks provides homogeneously patterned COF thin-films. First, we heated our target substrate to 100 °C to expedite evaporation of the carrier solvent, which produced more uniform films than ambient temperature spray coating. Then, by fixing a commercial Iwata airbrush 8 cm from a heated substrate we consistently and reproducibly deposited as-prepared COF colloidal suspensions as optically uniform films in less than five

minutes (**Figure 8.25 - Figure 8.59**). Furthermore, spray-coating is amenable to depositing COF-5 films on oxides, metals, and polymers (**Figure 8.2I-N**). Isotropic XRD patterns of these films are consistent with simulated patterns of randomly oriented COF-5 crystallites and are found to remain crystalline even after 18 months of ambient storage, consistent with the high stability of boronate ester-linked 2D COFs.[671] To evaluate scalability and compatibility with large-area deposition, we successfully prepared a 225 cm^2 COF-5 thin-film by spray coating (**Figure 8.2M**).[664] In addition, an optically homogeneous macroscopic array of finely printed COF-5 squares achieved line resolutions smaller than 50 μm (**Figure 8.2J-K**). Finally, we spray-coated COF-5 using a patterned mask with centimeter dimensions (**Figure 8.2N**), which resulted in prints with tight line edges and optically homogeneous print thickness, thus demonstrating that this method can be used to fabricate COF thin-films at-scale in a spatially controlled manner with high resolution.

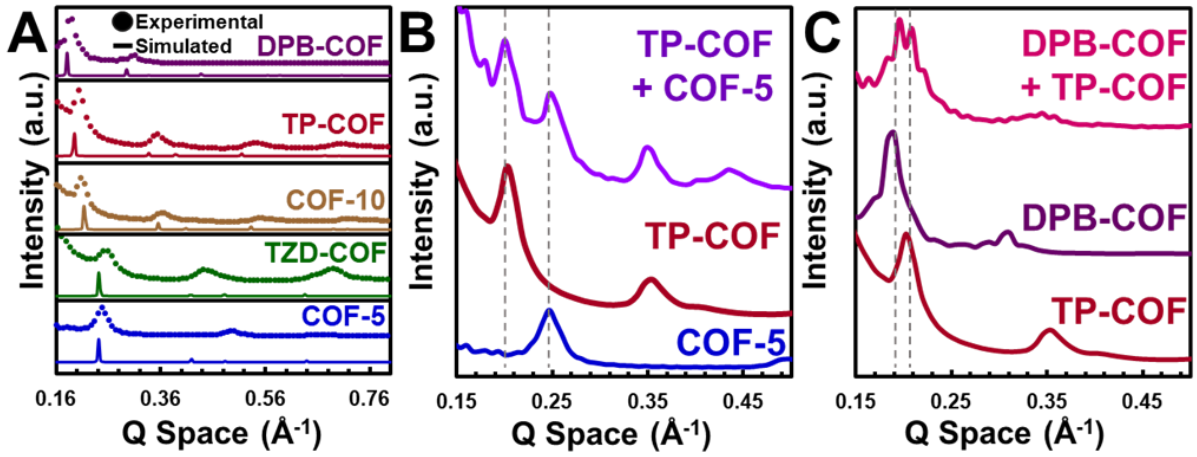

Figure 8.3. A) X-ray scattering patterns of printed COF materials (circles) and their simulated scattering patterns (lines). **B)** XRD pattern of COF-5, TP-COF, and their mixed print. **C)** XRD pattern of TP-COF, DPB-COF, and their mixed print.

8.4 A Chemically General Processing Approach

After characterizing films comprised of COF-5, the generality of this method was evaluated for four other 2D COFs thin films. To fabricate these films, we first synthesized COF colloidal suspensions, all of which were found to be 50-150 nm in diameter by DLS and highly crystalline by *in situ* XRD (**Figure 8.15** - **Figure 8.21**). The resulting spray-coated 2D COF films were highly crystalline with XRD patterns matching simulated patterns, showing that all of the COFs survived the deposition procedure (**Figure 8.3A**). Given access to multiple 2D COF inks, spray coating enables facile deposition of sequential layers or larger amounts of material. For example, three volumes of TP-COF inks were deposited (500, 1000, and 1500 µL), which exhibited indistinguishable XRD patterns (**Figure 8.18 - Figure 8.21**). Another noteworthy feature of spray-

coating is that two or more COFs inks can be mixed, allowing materials to be co-deposited to form bulk heterojunctions, which is not possible by directly growing COF films on a substrate. Two mixed COF inks were formulated containing TP-COF:COF-5 and TP-COF:DPB-COF in 1:1 vol ratios. In both cases, XRD patterns of these printed films had diffraction features of both materials, indicating that two populations of COF nanoparticles were deposited (**Figure 8.3B and 3C**).

To verify that the spray-coated films preserve the properties of 2D COFs, acoustic sensing devices were prepared by spray-coating 500 µL of COF-5 ink onto Ti-coated quartz crystal microbalance (QCM) acoustic resonators. The spray-coated films appeared uniform by optical microscopy (**Figure 8.25 - Figure 8.26**), but SEM of similarly prepared films revealed microscale porosity likely caused by the rapid drying of low-boiling solvents during deposition (**Figure 8.36 - Figure 8.49**). Although high-boiling solvents would likely reduce this microscale inhomogeneity, this change would require higher temperature processing conditions that are not compatible with QCM wafers.[672] Furthermore, the presence of microscale porosity is helpful in a sensing context since it provides pathways for efficient analyte transport and adsorption throughout the thickness of the film.

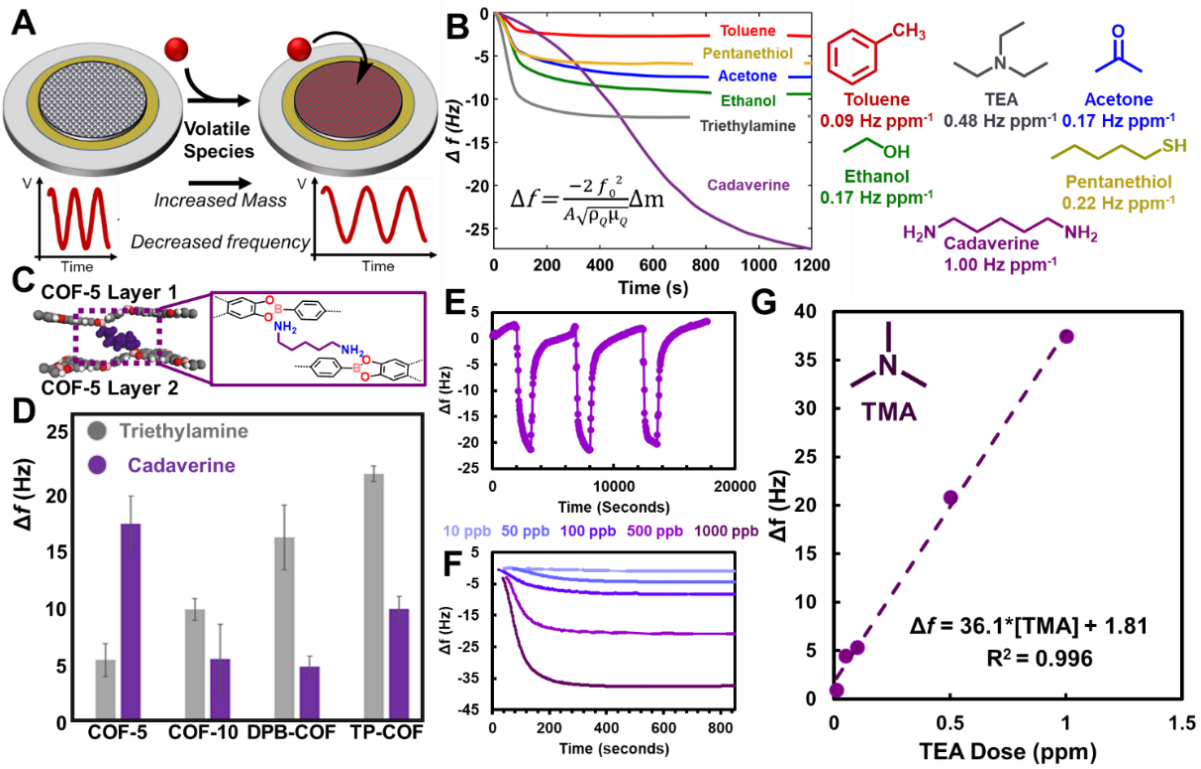

Figure 8.4. A) Acoustic vapor sensor schematic. **B)** Frequency response of a COF-5 sensor to several volatile analytes with structures and dose-normalized responsivities shown on the right. Inset: Sauerbrey equation. **C)** Computationally optimized structure of cadaverine binding between two COF-5 layers. **D)** Amine responsivity of the four COFs studied. **E)** Recyclability of TP-COF dosed with 500 ppb TMA, with N_2 purging between doses. **F)** Dose-dependent frequency response of a TP-COF sensor to TMA. **G)** TP-COF sensor calibration curve for TMA dose-response with the extracted concentration-frequency relationship.

8.5 Volatile Amine Sensing

Following COF-5 film deposition, the acoustic resonators were placed inside a sealed sensing environment, which was dosed with volatile analytes. In acoustic sensing, analytes are adsorbed to the active material, which increases its effective total mass. This increase is detected as a QCM frequency shift (Δf) and quantified using the Sauerbrey equation (**Figure 8.4**). In our testing, all species adsorbed to 95% of their equilibrium values within 75 sec, which we attribute to efficient mass transport that is facilitated by the high surface areas and textured morphology of the COF films. Polar analytes, such as ethanol and triethylamine (Δf > 8 Hz shift, TEA), interact more strongly with the COF-5 active material than nonpolar materials such as toluene (Δf < 3 Hz shift) (**Figure 8.4B**). When dose-normalized, toluene, acetone, ethanol, pentanethiol, TEA, and cadaverine exhibit responsivities of 0.09, 0.17, 0.17, 0.22, 0.48, 1.00 Hz ppm^{-1}, respectively, which also shows that more polar, Lewis-basic analytes are adsorbed more strongly than nonpolar analytes. By comparing these dose-normalized responses. COF-5 is found to have a two-fold selectivity for volatile amines, which guided us to explore other COF materials as the active material for the sensing of these molecules.

Devices based on four different boronate-ester linked COFs detect TEA at concentrations of 22 ppm (**Figure 8.4D**), which is consistent with the Lewis-basic analyte interacting with Lewis-acidic boron atoms in the frameworks. Density functional theory (DFT) calculations support this proposed sensing mechanism by showing that the Lewis-basic nitrogen atoms of amines preferentially adsorb to Lewis-acidic sites in the COF-5 crystal (**Figure 8.4C**). We experimentally observe that COF-5 has a noticeably unconventional adsorption profile and high affinities for cadaverine, which is not observed in other COF sensors **(Figure 8.4B and Figure 8.4D).** The

computational results also support that multi-site absorption is responsible for this behavior, where cadaverine can intercalate between two COF-5 layers, effectively bridging two boron sites (**Figure 8.4C**). This result demonstrates that spray-coated COFs preserve their structural regularity to yield impressive selectivities and sensitivities in acoustic sensors.

To further evaluate trimethylamine (TMA) sensors, an important analyte for diagnosing meat spoilage, we focused on devices based on TP-COF, which showed the highest sensitivity for TEA. To examine the recyclability of TP-COF, we exposed the material to 500 ppb TMA until saturation was observed and then flushed the atmosphere with dry N_2 to remove the analyte (**Figure 8.4E**). For all exposures of 500 ppb TMA, a response of $|\Delta f|$ = 21 Hz was observed. Similarly, we found that the sensing profile shape, including an equilibration time of less than 5 min, remained nearly unchanged over three dosing cycles. This observation suggests that TP-COF is not irreversibly altered by amine adsorption/desorption cycles, thereby allowing TP-COF to be regenerated by exposure to fresh atmosphere. By examining the TMA dose-dependent response, we extract that TP-COF has a linear responsivity of 36.1 Hz ppm^{-1}_{TMA} (**Figure 8.4F and Figure 8.4G**), thus enabling TMA quantification to concentrations as low as 10 ppb, which is the lower limit of dosing for our atmospheric testing apparatus and below the freshness target detection limit for meat spoilage.[668-670]

In conclusion, we have demonstrated a patternable and scalable additive manufacturing method that results in 2D COF thin films on arbitrary substrates. This method enables the integration of 2D COFs, both as pure materials and as mixtures, into thin-film devices. Five 2D COF colloidal inks were spray-coated at high-speed, large-scale, and micron-scale resolution either in isolation or as mixtures onto several substrates. The functionality of the spray-coated 2D

COF thin films was confirmed by incorporating boronate ester-linked 2D COFs as the active layers in QCM-based volatile amine sensors, where their porosity and Lewis acidity provide superlative performance for detecting volatile amines such as TMA at concentrations as low as 10 ppb. Ultimately, this general additive manufacturing approach will enable the unique characteristics of 2D COFs to be explored and leveraged in a diverse range of thin-film devices.

Supplementary Information

A. Materials and Instrumentation

I. Materials

Reagents were purchased from commercial grade suppliers and used without further purification, unless otherwise described. Anhydrous solvents were obtained from a solvent purification system (JC Meyer System).

II. Instrumentation

Sonication. Sonication was performed with a Branson 3510 ultrasonic cleaner with a power output of 100 W and a frequency of 42 kHz.

***In Situ* Wide-Angle X-Ray Scattering (WAXS).** Small- and wide-angle X-ray scattering (SAXS/WAXS) patterns were collected at Argonne National Lab's (ANL) Advanced Photon Source (APS) at both sectors 5-IDD (DND-CAT) and 12-ID-D with a capillary transmission geometry. All liquid cell experiments were conducted on COF colloids as-prepared. Experiments conducted at 12-ID-D were collected at a beam energy of 12 keV and experiments conducted at 5-ID-D were collected at a beam energy of 13.3 keV. Individual frames were collected on a set of Pilatus detectors, which were then summed and radially integrated to produce a linear XRD pattern using proprietary software available at the APS. Scattering intensity is reported as a function of the modulus of the scattering vector q, related to the scattering angle 2θ by the equation $q = (4\pi/\lambda)$

sin θ, where λ is the X-ray wavelength. The sample-to-detector distance was adjusted to measure across relevant detection ranges. Capillary experiments were conducted using 2.0 mm OD borosilicate capillaries with 0.2 mm wall thicknesses purchased from Hilgenberg GmbH.

Grazing Incidence X-Ray Diffraction (GI-XRD). GI-XRD measurements were performed at the Advanced Photon Source (APS) at Argonne National Laboratory (ANL) using the 8-ID-E Beamline under vacuum. The crystallites were irradiated until the detector was 80% saturated at an incidence angle of 0.14° in vacuum using 10.92 keV (1.135 Å) X-rays. The scattering was recorded on a Pilatus 1 M detector located 228 mm from the sample. In all cases, significant silicon substrate scatter was observed. The raw images were merged, pixel coordinates were transformed to q-space, and line cuts were generated using GIXSGUI for Matlab.[1]

COF Modeling and Structural Refinement. Crystal modeling of the COF structures was carried out using the Materials Studio (ver.5.0) suite of programs by Accelrys.[2] The initial structures were S5 constructed piecewise starting with a primitive hexagonal unit cell of a P6 space group. The cell parameter was estimated according to the distance between the center of the vertices for each COF, and the c parameter was chosen as 3.35 Å, which has been observed for similar materials. [3] Initially, these structures were estimated to be eclipsed. The structures were optimized using a Geometry Optimization routine including energy minimization with cell parameters optimization, using the parameters from the Universal Force Field. Calculation of the simulated powder diffraction patterns and Pawley refinements were performed in the Materials Studio Reflex Plus Module using a Bragg-Brentano geometry. When the first ~2 features were seen to align but

relative intensities were seen to be inconsistent, we assigned this to a non-eclipsed structure. If this was the case, supercells of the crystallites were generated and different stackings (AB, ABC, partial AB, etc. were attempted). The intensity profile that matched most closely was used to refine. In the COFs reported here, eclipsed structures were found to be most consistent with the measured diffraction patterns. Prior to refinement of TZD-COF, the TZD component was assigned to have occupancy on each side of the phenyl ring it is attached to, so as to account for its prochirality. The observed diffraction patterns were subjected to a polynomial background subtraction and then to Pawley refinement wherein peak profiles were refined using the Pseudo-Voigt peak shape function and asymmetry was corrected using the Berar-Baldinozzi function. Crystallite size was then estimated by the LeBail method, which was Pawley refined to the experimental data.

Dynamic Light Scattering (DLS). Dynamic Light Scattering (DLS) data were collected using a Malvern Zetasizer equipped with a 633nm He-Ne 5mW laser at room temperature in a quartz cuvette with a 10mm pathlength. All DLS scattering vectors were interpreted with a spherical shape factor. Data was analyzed using the proprietary Zetasizer software.

Nanoparticle Tracking Analysis (NTA). Nanoparticle tracking analysis was conducted on COF colloids as prepared using a Malvern Nanosight300 using a 488 nm laser module. NTA was equipped with quartz windows and metal interlocks to prevent damage by the organic solvents used. 100 μL of COF colloids were loaded in between the quartz windows at which point the instrument was calibrated for a depth of view to maximize the photon efficiency. Videos were then taken.

Transmission Electron Microscopy. TEM was performed using a JEOL (JEOL USA, Inc., Peabody, MA) ARM300 GrandARM TEM operating at 300 keV equipped with a Gatan (Gatan, Inc., Pleasanton, CA) OneView-IS camera (FEG Emission: 15 μA, spot size 5). All image acquisition was done using the Gatan Microscopy Suite (GMS), Digital Micrograph (Gatan, Inc., Pleasanton, CA).

Nitrogen Sorption Measurements. Gas sorption isotherms were conducted on a Micromeritics ASAP 2420 Accelerated Surface Area and Porosity Analyzer. Typically, 20-40 mg samples were transferred to dried and tared analysis tubes and capped with a Transeal. The samples were heated to 40°C at a rate of 1°C•min^{-1} and evacuated at 40°C for 20 min, then heated to 100 °C at a rate of 1°C•min^{-1} heat, and evacuated at 100°C until the outgas rate was ≤0.4 μmHg•min^{-1}, at which point the tube was weighed again to determine the mass of the activated sample. The tube was then transferred to the analysis port of the instrument. UHP-grade (99.999% purity) N_2 was used for all adsorption measurements. N_2 isotherms were generated by incremental exposure to nitrogen up to 760 mmHg (1 atm) in a liquid nitrogen (77 K) bath. Oil-free vacuum pumps and oil-free pressure regulators were used for all measurements. Brunauer-Emmett-Teller (BET) surface areas were calculated from the linear region of the N_2 isotherm at 77 K within the pressure range P/P_0 of 0.05-0.10.

Scanning Electron Microscopy (SEM). Samples collected for SEM characterization had COF spray coated onto silica wafers or titanium coated silica wafers using a PDMS mask to limit the area of deposition. The samples were then cleaved and mounted with carbon tape or double-sided

copper taper on vertical SEM mounts. Each sample was coated with 7 nm of osmium to create a conformal conductive coating prior to imaging. Images were collected with a Hitachi SU 8030 scanning electron microscope.

Optical Microscopy. Optical images were collected with an Olympus BX51RF Microscope from samples with COF spray coated onto the surface of titanium-coated silica wafers. Both metal and PDMs stencils were used for patterning COFs. Images of large-area prints were taken with a Canon EOS Rebel T3i and Samsung S9 cell phone built-in camera.

Profilometry. Film height characterization was completed with a Veeco Dektak 150 Surface Profiler with a 5 μm stylus tip and 5 mN of downward force. Films were coated on QCM wafers with a PDMS mask with a 2.22 cm (7/8 in) diameter hole.

COF Printing. Spray coating of samples was completed with an Iwata HP-CH Airbursh connected to a Dewalt Pancake Air Compressor with a pressure reducer between the compressor and air brush. For mounted deposition of material, the airbrush was mounted on a lab stand with two three-armed clamps 8 cm above the hotplate surface. The hotplate was heated to 100 ˚C and the substrate was placed beneath the nozzle with a PDMS mask or a metal mask held with rare earth magnets. A pressure of 20 PSIG was applied to the air brush, and the atomizer nozzle on the Iwata airbrush was fully open. Prior to coating the first sample, 0.25 mL of ink was deposited onto aluminum foil to prime the airbrush and ensure the full amount of material was deposited on the substrate of

interest. For larger samples, the substrates were placed on a hotplate heated to 100 ˚C and COFs were deposited with a handheld airbrush moved above the substrate to coat the entire area.

Substrate Patterning. Patterning of COF on substrates was completed with metal and PDMS masks. For the PDMS mask, we used Dow Corning Sylgard 184 PDMS. The two-part liquid components were mixed per the manufacturer instructions and poured into a plastic petri dish. The dish was place under vacuum for two hours to remove any air bubbles and then cured at 100 ˚C for two hours to cure the material. A rubber mallet and punch were used to cut holes in the PDMS or the PDMS was cut with a razor blade to create masks. Stainless steel masks were ordered from stencil.com with square sizes of 250, 500, and 800 μm. A magnetic plate was placed on top of a hotplate prior to spray coating, and the substrate for coating was set between the metal plate and mask. The mask was held in place with rare earth magnets to ensure close contact between the mask and substrate when spray coating. The Northwestern University logo was etched from a sheet of aluminum and used in a similar manner to the stainless-steel masks.

Quartz Crystal Microbalance (QCM) COF Sensing. Volatile analyte sensing was performed in one of two dosing chambers. In all cases, acoustic sensing was accomplished using a QCM200 produced by Stanford Research Systems. All sensing experiments were performed using Ti-coated 1-inch quartz crystals with a native 5 MHz resonant frequency.

For high concentration dosing: QCM wafers with deposited COF active material were first inserted into the QCM paddle. This QCM paddle was then loaded into a two-neck glass flask equipped with a Teflon stir bar. The vessel was then purged with dry N_2 for several minutes to purify the sensing atmosphere. The vessel was then sealed and the QCM resonant frequency was allowed to equilibrate over five minutes. Then, 1 μL of liquid analyte was taken into a 2 μL syringe and injected directly onto the Teflon stir bar, which was spinning to homogenize the sensing environment. The injection time was then noted as time zero. The vessel was then closed for 20 min while monitoring of the QCM resonant frequency once every 10 s. Finally, the chamber was opened and flushed with dry N_2 until the QCM returned to its initial frequency.

For low concentration dosing: QCM wafers with deposited COF active material were first inserted into the QCM paddle. This paddle was then loaded into a metal sensing chamber. Dry N_2 was used to flush the sensing system at a rate of 500 $cm^3 \bullet min^{-1}$ for 30 min. After this flushing was finished, the desired analyte was introduced into the sensing environment at the concentration noted. The injection time was then noted as time zero. The sensing behavior was then monitored for 30 min while monitoring of the QCM resonant frequency once every 10 s. Finally, the sensing environment was flushed for one hour.

B. Synthetic Procedures

Scheme 8.1. Synthesis of 2,1,3-Benzothiadiazole-4,7-diboronic acid.

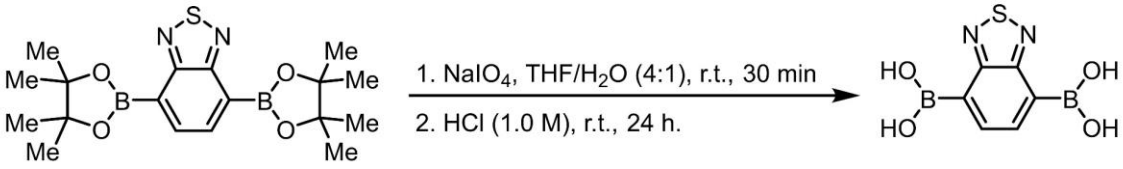

Synthesis of 2,1,3-Benzothiadiazole-4,7-diboronic acid.

2,1,3-Benzothiadiazole-4,7-diboronic acid was synthesized *via* slight modifications of literature procedures. All spectroscopic data is consistent with what has previously been reported.[4]

A mixture of 2,1,3-benzothiadiazole-4,7-bis(pinacolato)diboronic ester (5.0 g, 12.9 mmol) and sodium periodate (16.5 g, 77.3 mmol) in THF (165 mL) and water (41 mL) was stirred under N_2 at r.t. for 30 minutes. Hydrochloric acid (1.0 M, 21 mL) was slowly added to the stirring mixture over the course of 15 minutes. After complete addition, the resulting solution was stirred for 24 h. under a constant stream of N_2. After 24 h., the THF was removed *in vacuo* and the resulting precipitate was isolated by filtration. The precipitate was washed with water, hexanes, and diethyl ether to afford 2,1,3-Benzothiadiazole-4,7-diboronic acid as a light yellow, crystalline solid.

Scheme 8.2. Synthesis of pyrene-2,7-bis(boronic acid).

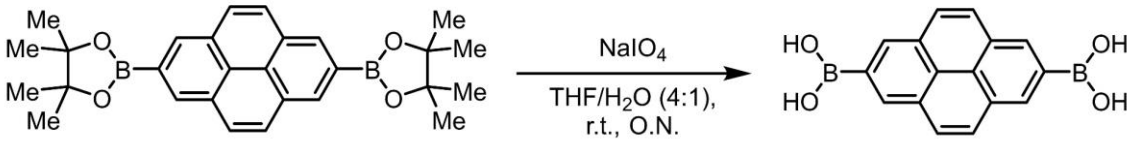

Synthesis of pyrene-2,7-bis(boronic acid):

Pyrene-2,7-bis(boronic acid) was prepared *via* slight modifications of literature procedures. All spectroscopic data is consistent with what has previously been reported. [5]

Pyrene-2,7-diboronic ester (1.0 g, 2.21 mmol) was dissolved in THF (48 mL) and water (12 mL). To the stirring solution was added sodium periodate (2.84 g, 13.25 mmol) and the resulting solution was stirred under N_2 at room temperature overnight. The reaction was then filtered and washed with water (350 mL) taking special care not to allow the solid to dry on the filter paper. The solid residue was then rinsed with hexanes and diethyl ether and dried under vacuum.

Scheme 8.3. Synthesis of 4,4'-diphenylbutadiynebis(boronic acid).

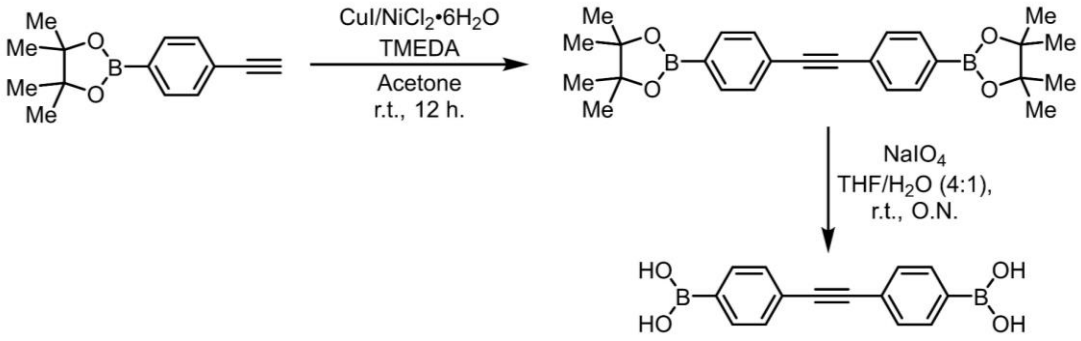

Synthesis of 4,4'-diphenylbutadiynebis(boronic acid):

4,4'-diphenylbutadiynebis(boronic acid) was prepared *via* slight modifications of literature procedures. All spectroscopic data is consistent with what has previously been reported.[6]

TMEDA (0.459 g, 3.946 mmol), CuI (0.188 g, 0.986 mmol), and $NiCl_2•6H_2O$ (0.234 g, 0.986 mmol) were suspended in acetone (13 mL) under an atmosphere of air. The mixture became dark green after 10 min. 4-ethynylbenzeneboronic acid pinacol ester (4.50 g, 19.7 mmol) was then added and the resulting solution was stirred for 12 h. Upon completion of the reaction, the solvent was removed *in vacuo* and the resulting residue was washed with water (50 mL) and recrystallized from MeCN to provide the intermediate structure as a white solid.

The intermediate diboronate ester (400 mg, 0.88 mmol) and $NaIO_4$ (400 mg, 2.0 mmol) were dissolved in THF (4.5 mL) and water (1.5 mL) and stirred at room temperature, under a N_2 atmosphere overnight. After the reaction was complete, the reaction was diluted with water (20 mL) and the resulting precipitates were recovered *via* filtration. The recovered solid was washed with additional water (20 mL) and hexanes (10 mL) to yield 4,4'-diphenylbutadiynebis(boronic acid) as a white solid.

Scheme 8.4. General synthesis of colloidal COFs.

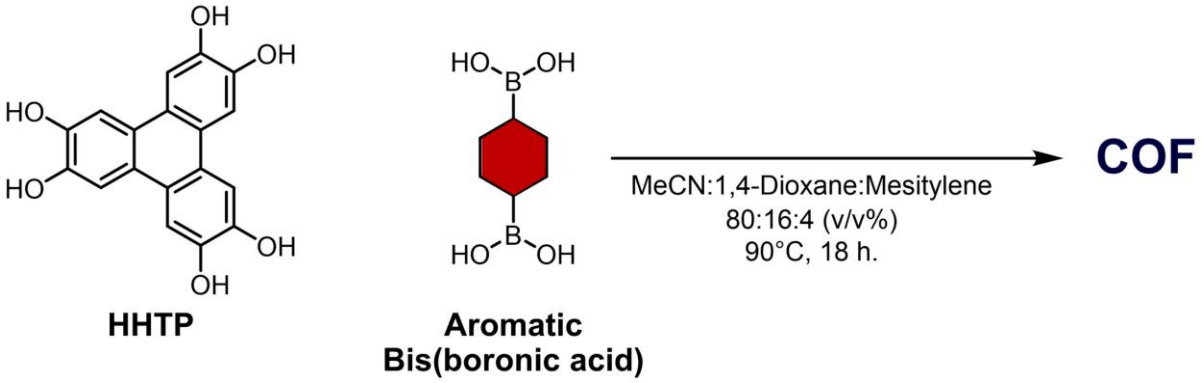

General Synthesis of colloidal COFs: All COFs were prepared *via* a reported procedure.[7]

2,3,6,7,10,11-Hexahydroxytriphenylene (HHTP, 2 mmol) and the appropriate corresponding boronic acid (BA, 3 mmol) were dissolved in a mixture of MeCN:1,4-dioxane:mesitylene (80:16:4 by volume; 20 mL) and sonicated for 10 min. The solution was passed through a 0.45-micron PTFE syringe filter to remove insoluble particulates. This solution was transferred into a 20 mL scintillation vial and sealed. This reaction mixture was heated without stirring to 80 °C overnight, which resulted in an indefinitely stable, translucent colloidal suspension.

C. *In Solvo* X-Ray Scattering

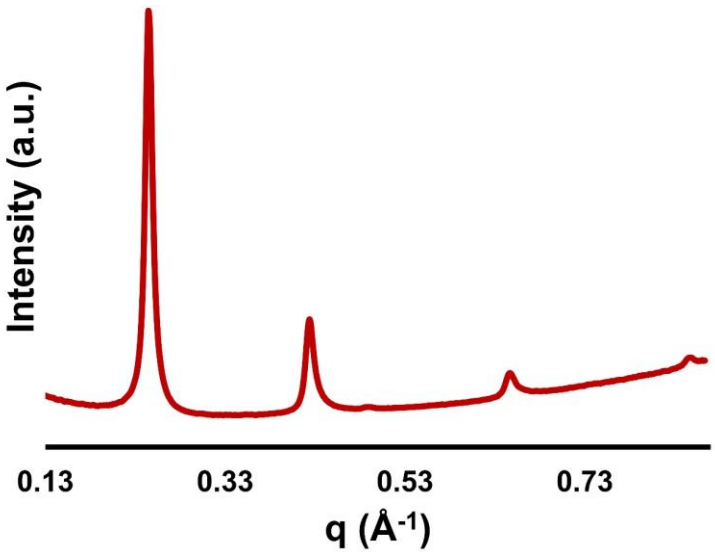

Figure 8.5. *In solvo* X-ray scattering pattern of COF-5.

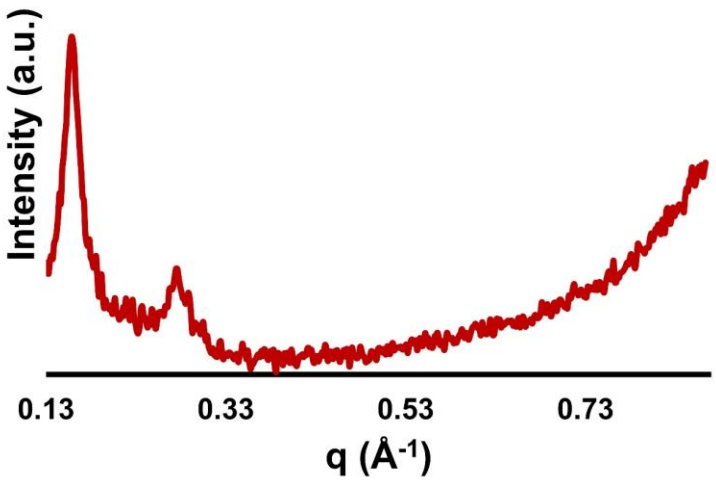

Figure 8.6. *In solvo* X-ray scattering pattern of DPB-COF.

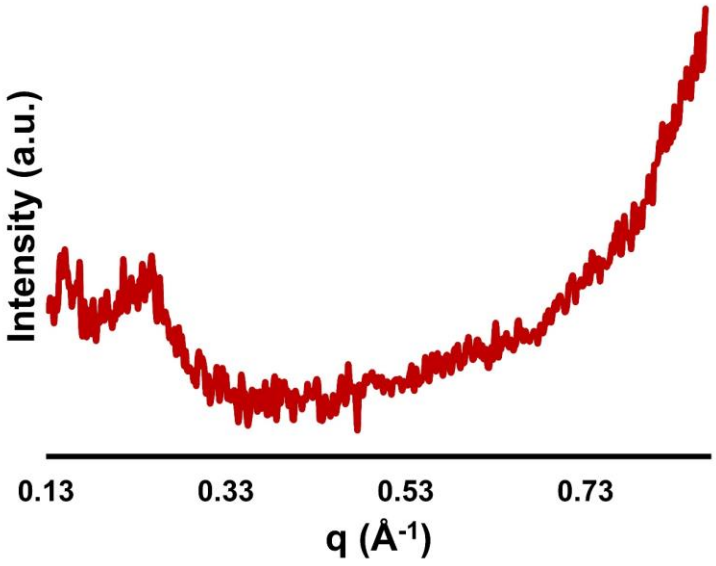

Figure 8.7. *In solvo* X-ray scattering pattern of TZD-COF.

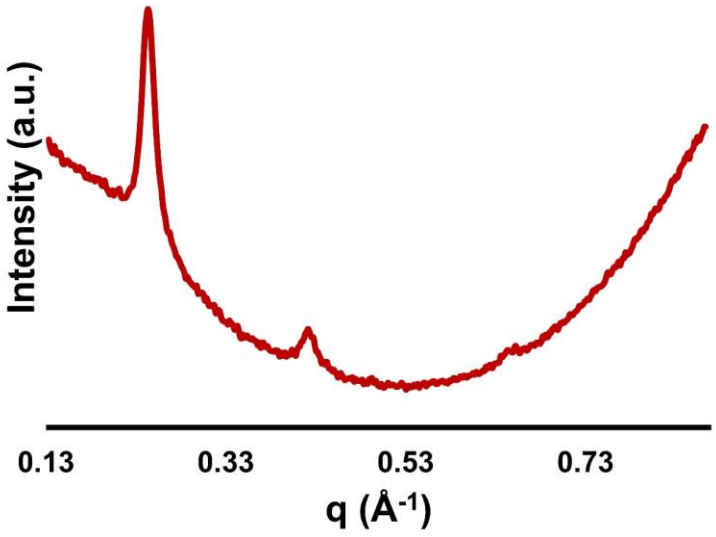

Figure 8.8. *In solvo* X-ray scattering pattern of TP-COF.

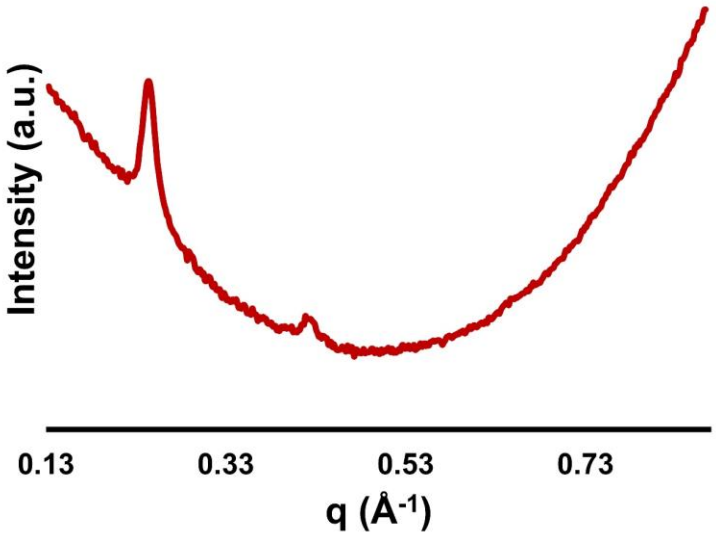

Figure 8.9. *In solvo* X-ray scattering pattern of COF-10.

D. Dynamic Light Scattering

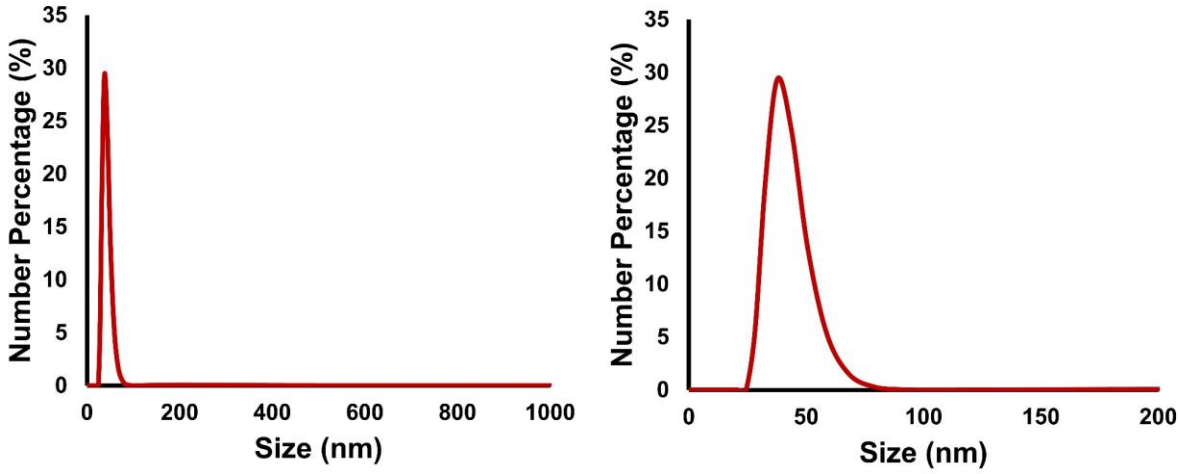

Figure 8.10. DLS trace of COF-5 colloids.

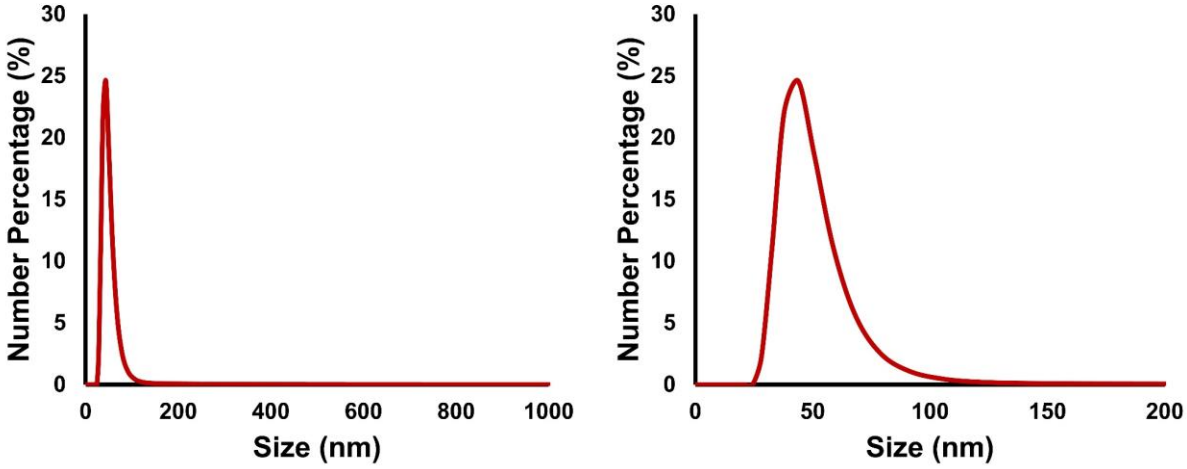

Figure 8.11. DLS trace of DPB-COF colloids.

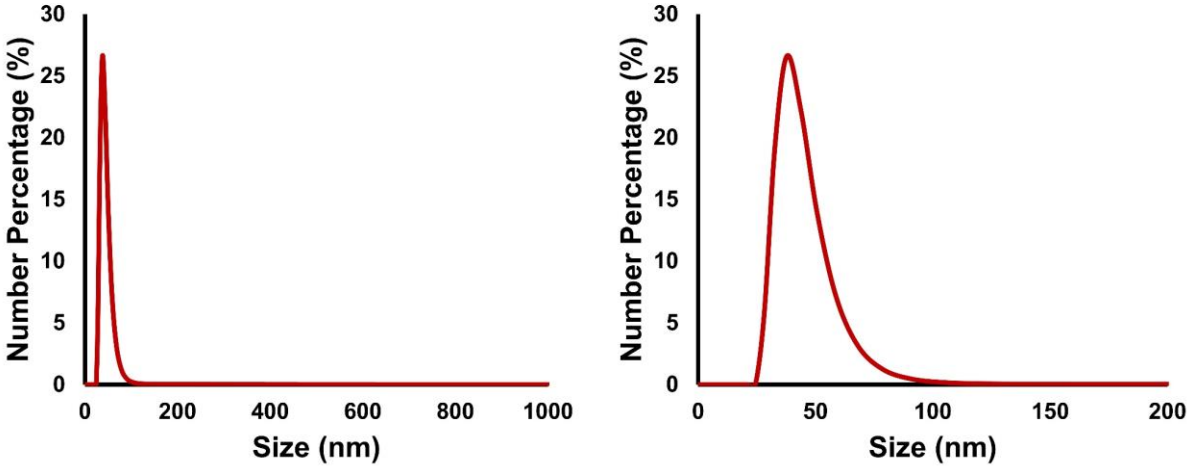

Figure 8.12. DLS trace of TZD-COF colloids.

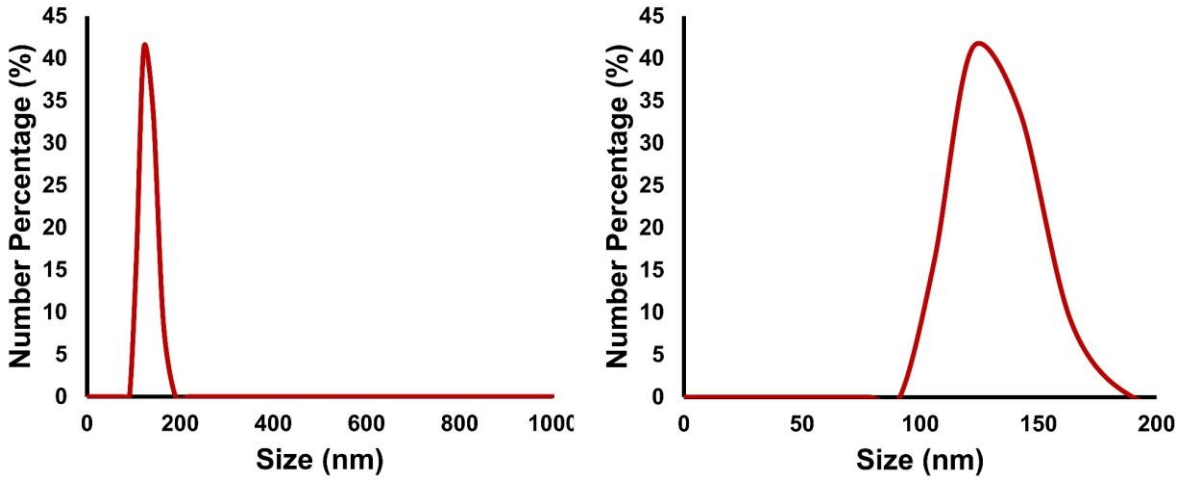

Figure 8.13. DLS trace of TP-COF colloids.

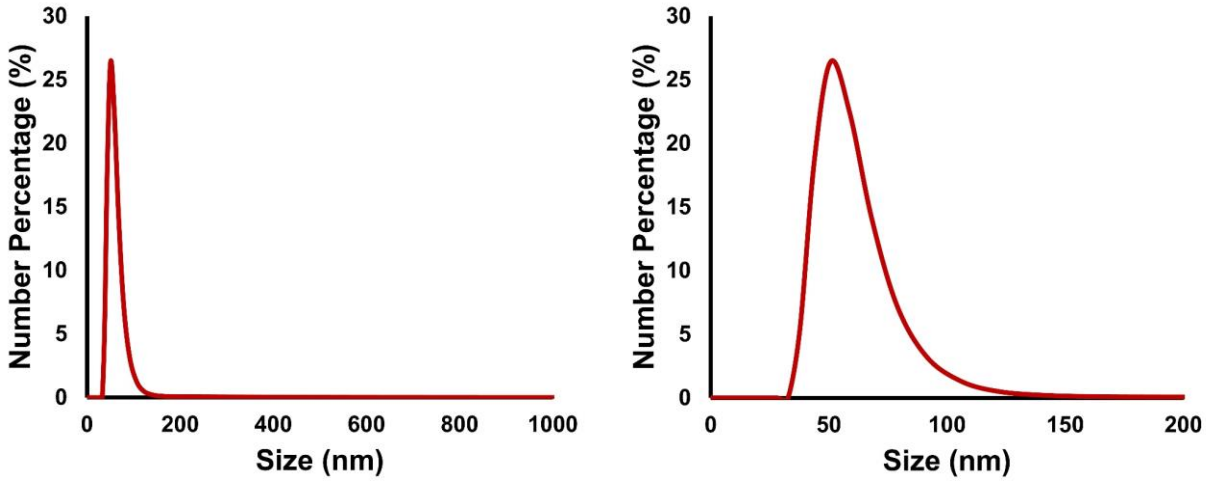

Figure 8.14. DLS trace of COF-10 colloids.

E. Grazing Incidence X-Ray Diffraction

In some instances, features corresponding to the substrate are observed at Q spaces greater than 1 $Å^{-1}$.

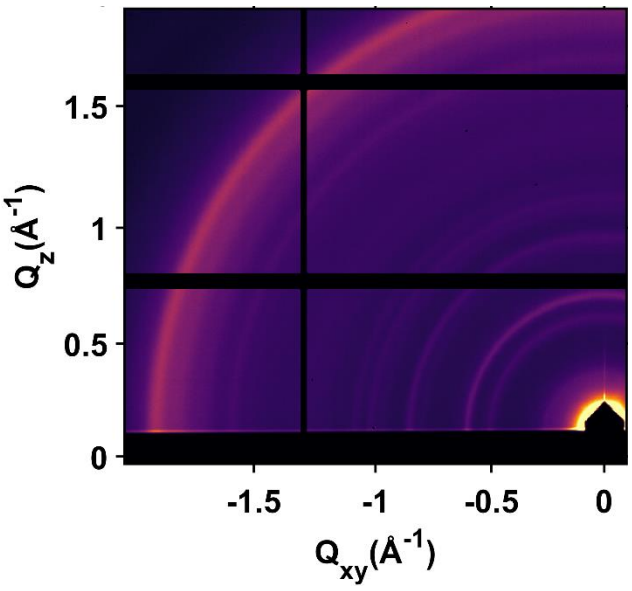

Figure 8.15. GI-XRD pattern of a spray-coated film of TZD-COF.

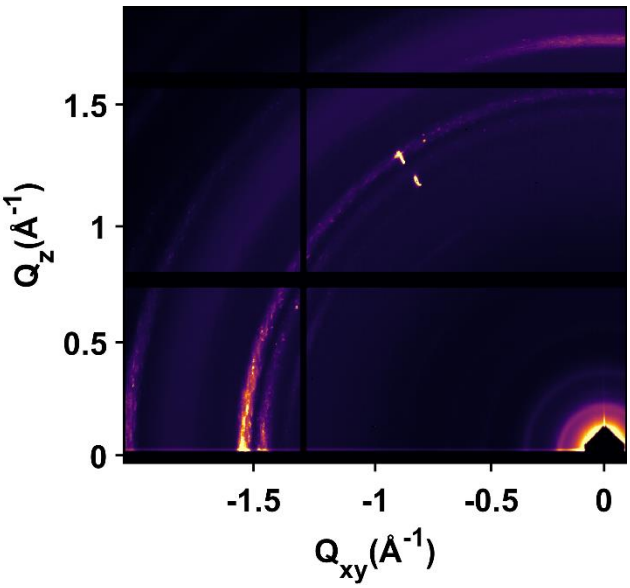

Figure 8.16. GI-XRD pattern of a spray-coated film of COF-10.

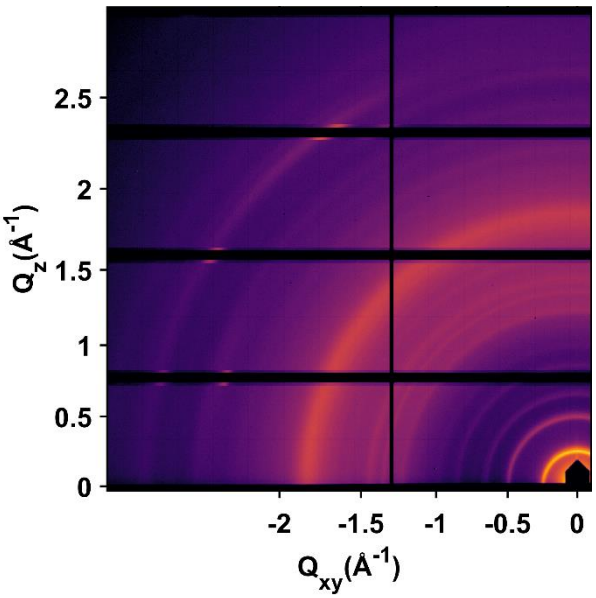

Figure 8.17. GI-XRD pattern of a spray-coated film of DPB-COF.

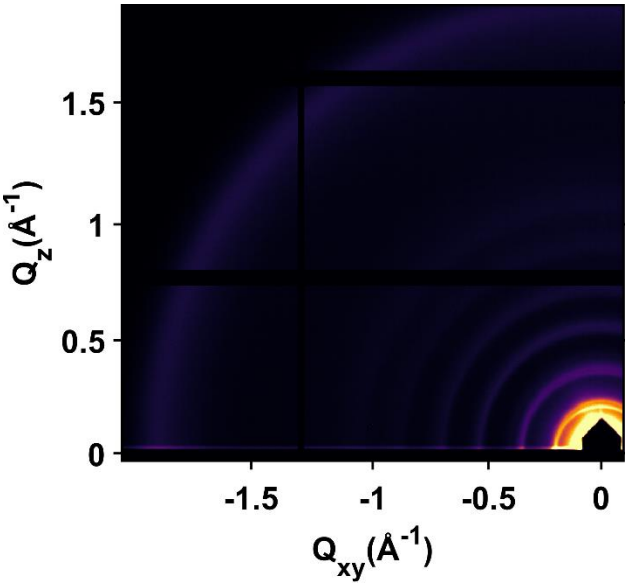

Figure 8.18. GI-XRD pattern of a spray-coated film of TP-COF with 500 μL of material.

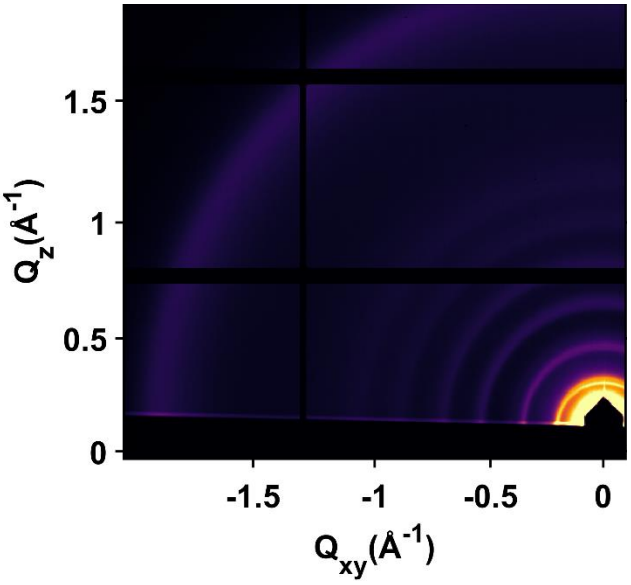

Figure 8.19. GI-XRD pattern of a spray-coated film of TP-COF with 1000 μL of material.

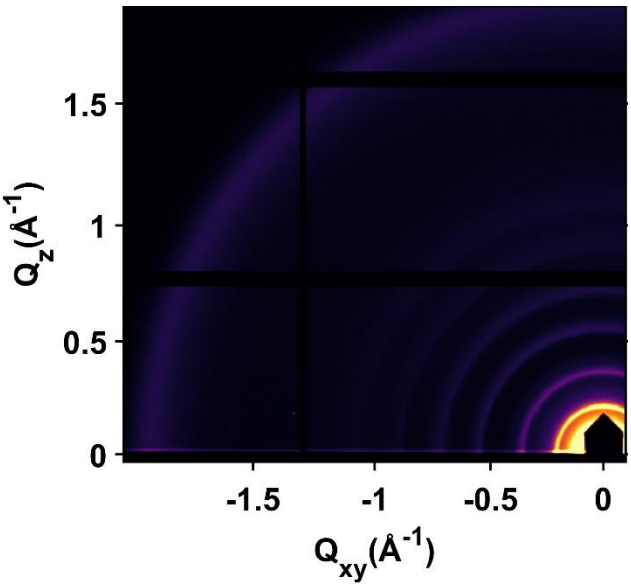

Figure 8.20. GI-XRD pattern of a spray-coated film of TP-COF with 1500 μL of material.

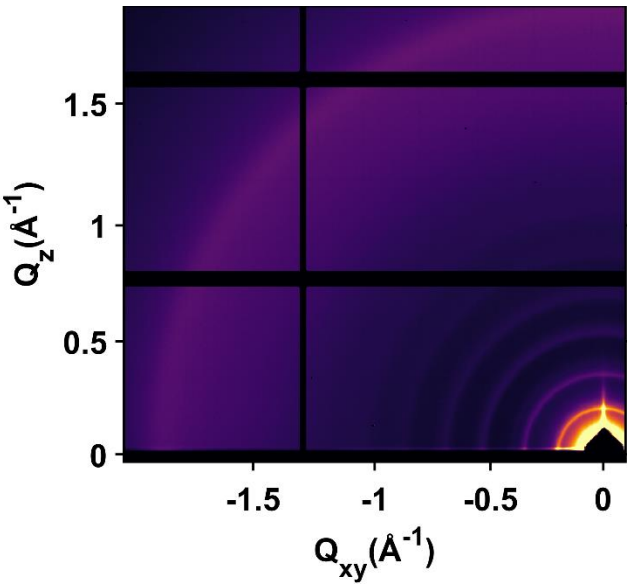

Figure 8.21. GI-XRD pattern of a spray-coated film of TP-COF with 2000 μL of material.

F. Surface Area Measurements

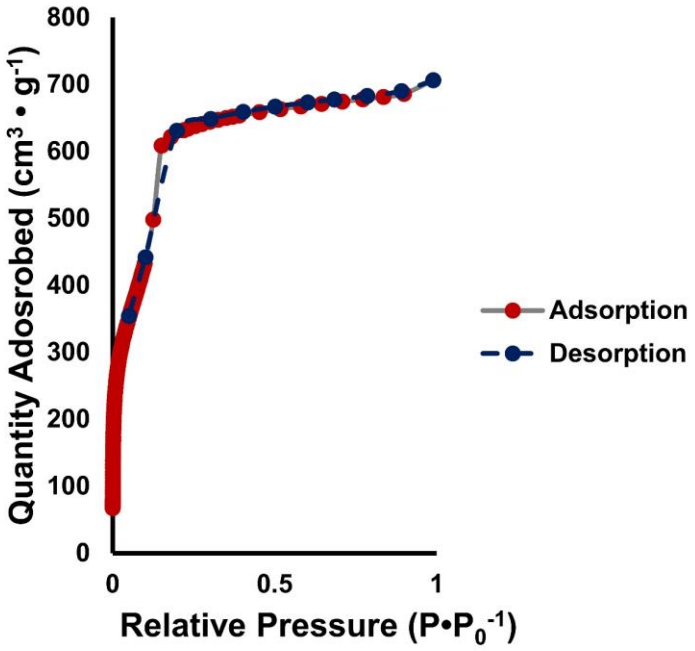

Figure 8.22. Nitrogen isotherm recorded at 77 K for COF-5.

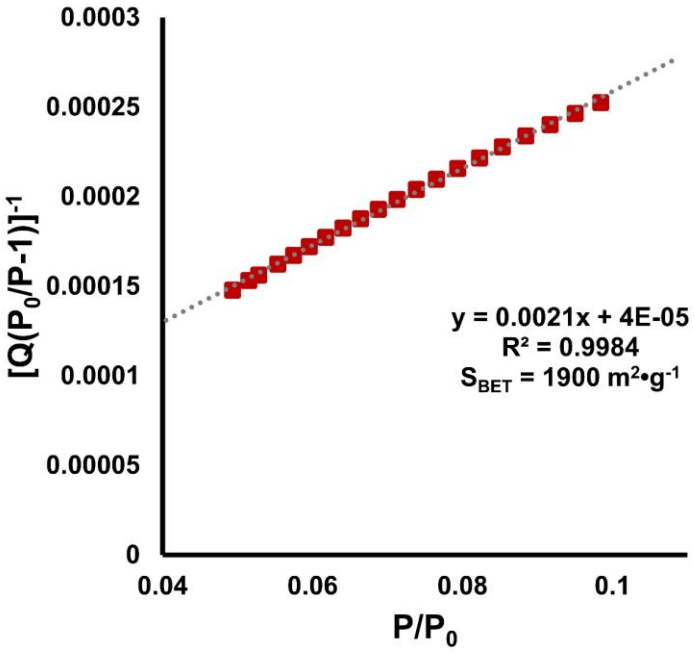

Figure 8.23. BET plot for COF-5.

G. Scanning Electron Microscopy and Optical Images

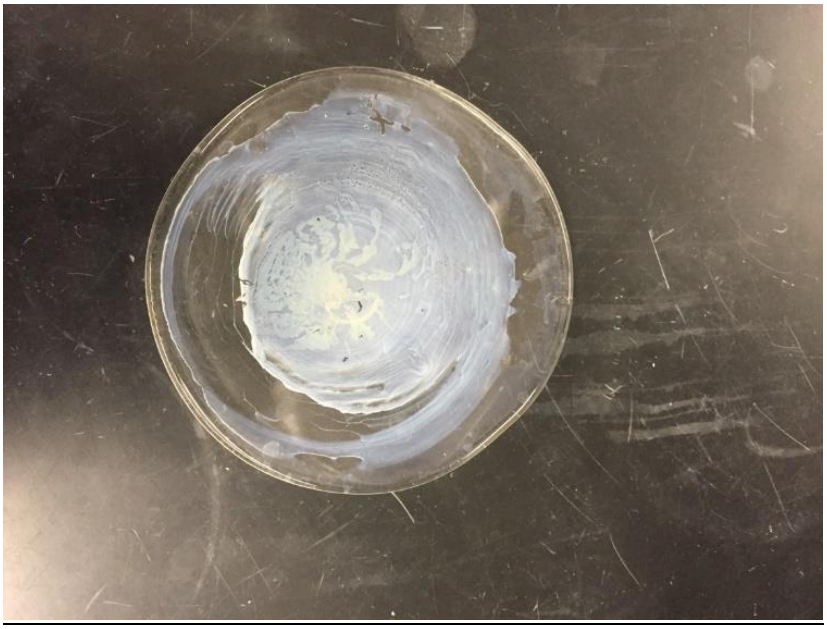

Figure 8.24. Optical image of a poor-quality film prepared by dropcasting.

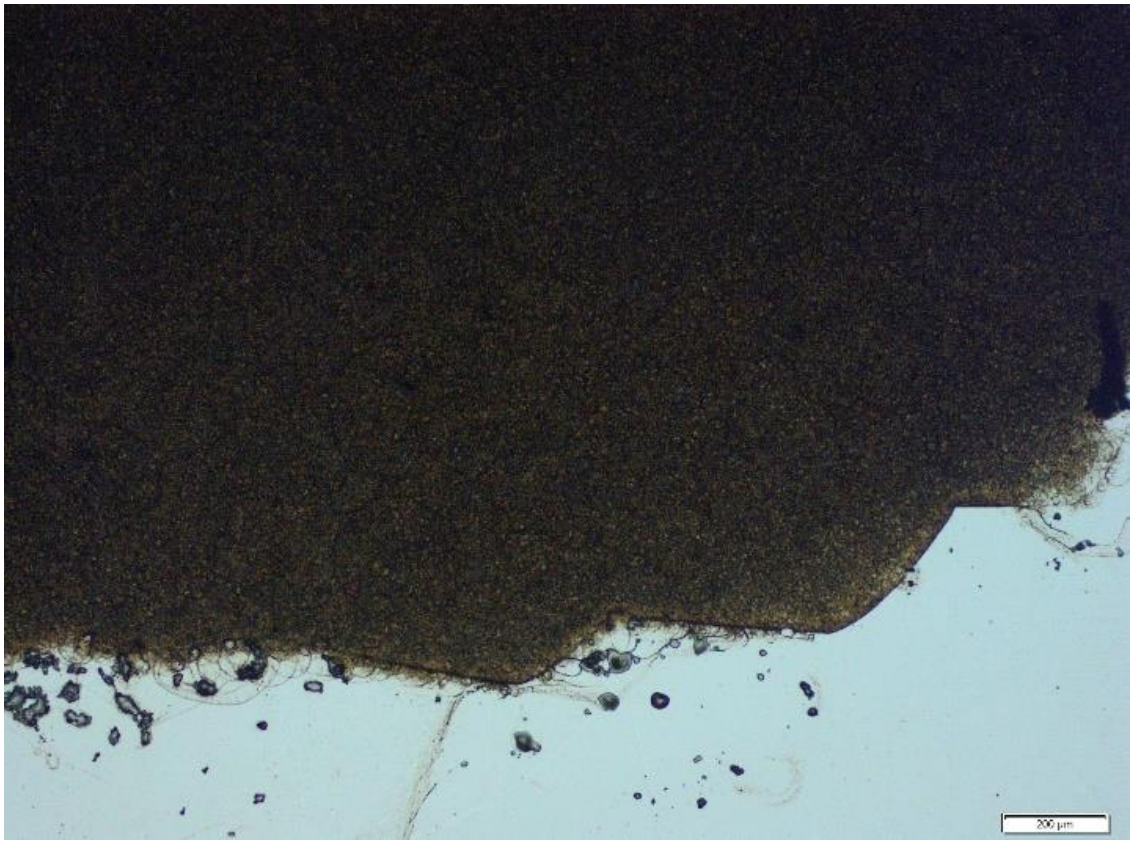

Figure 8.25. Low magnification optical image of COF-5 on Ti.

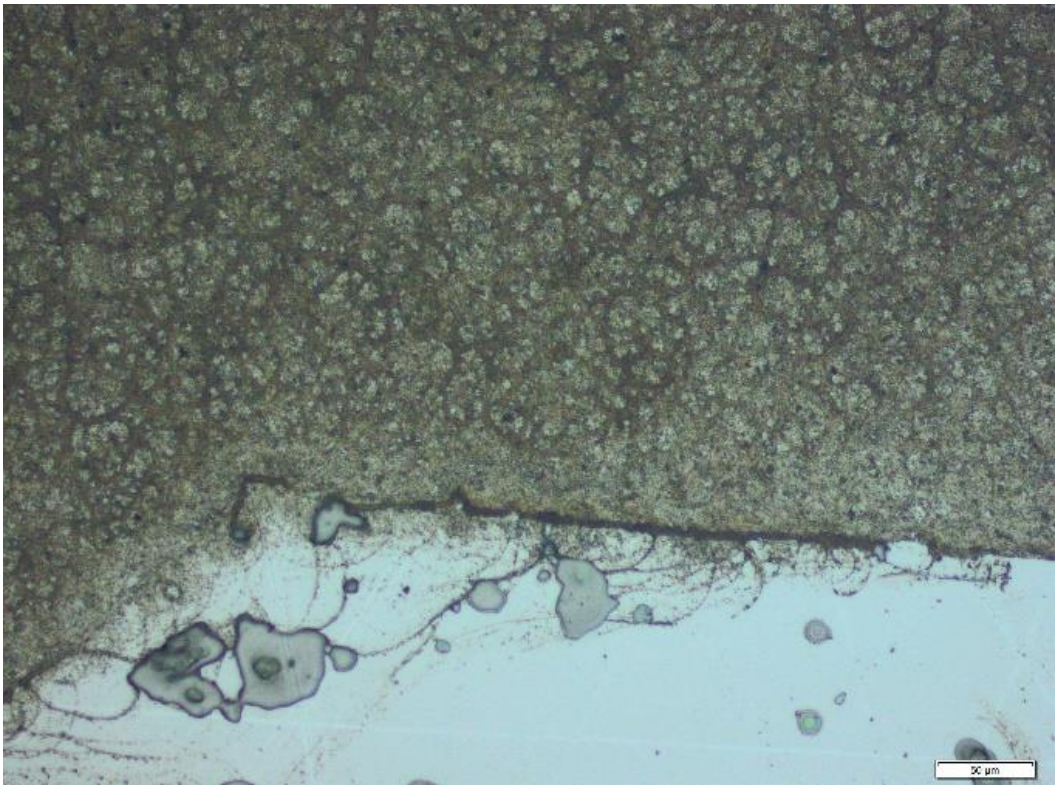

Figure 8.26. High magnification optical image of COF-5 on Ti.

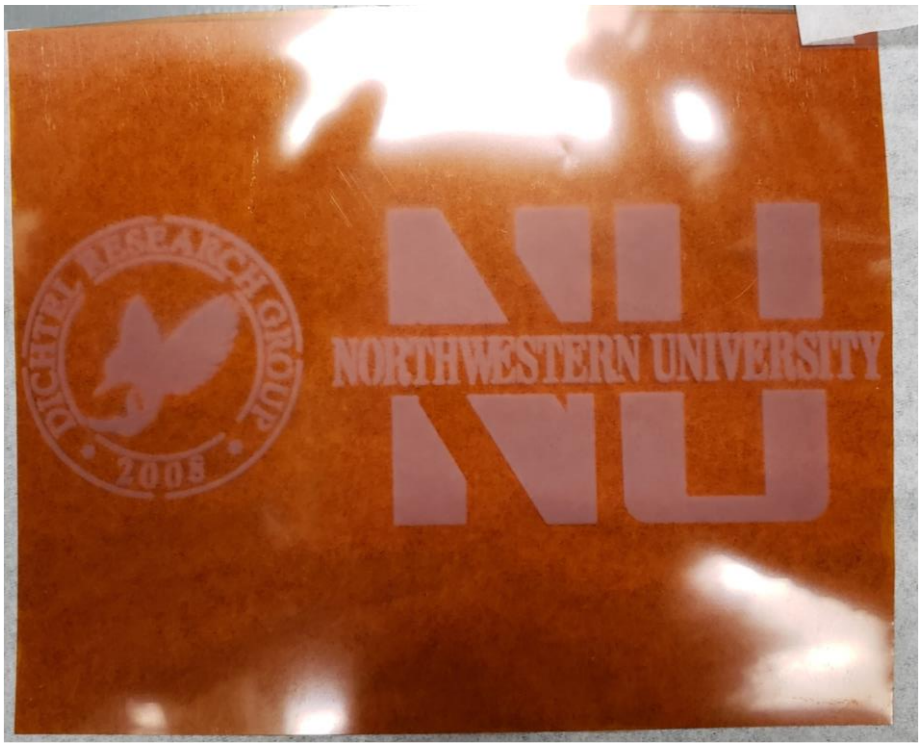

Figure 8.27. Optical image of printed logos on Kapton.

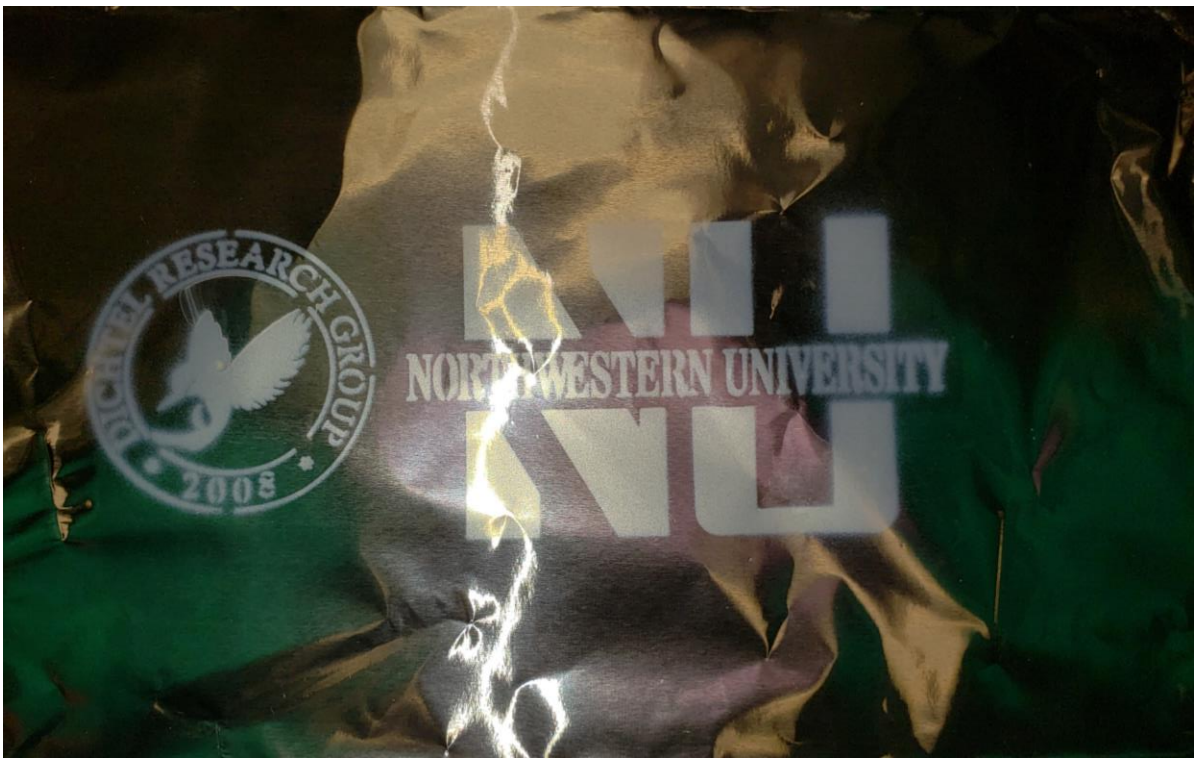

Figure 8.28. Optical image of printed logos on aluminum foil.

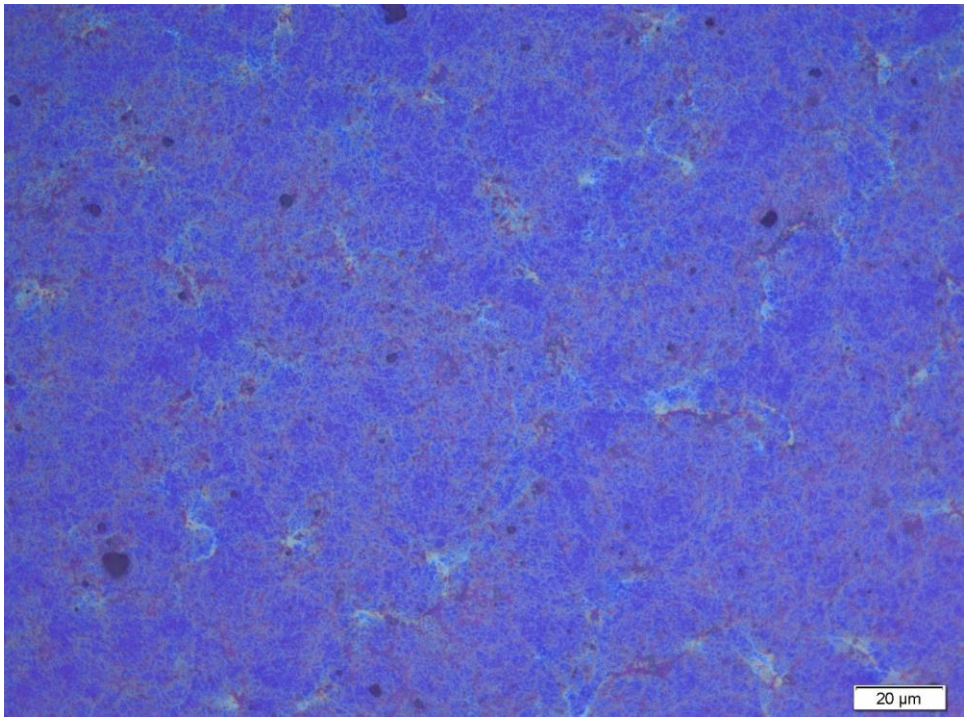

Figure 8.29. Optical microscopy image of 100 µL of printed COF-5 on SiO_2.

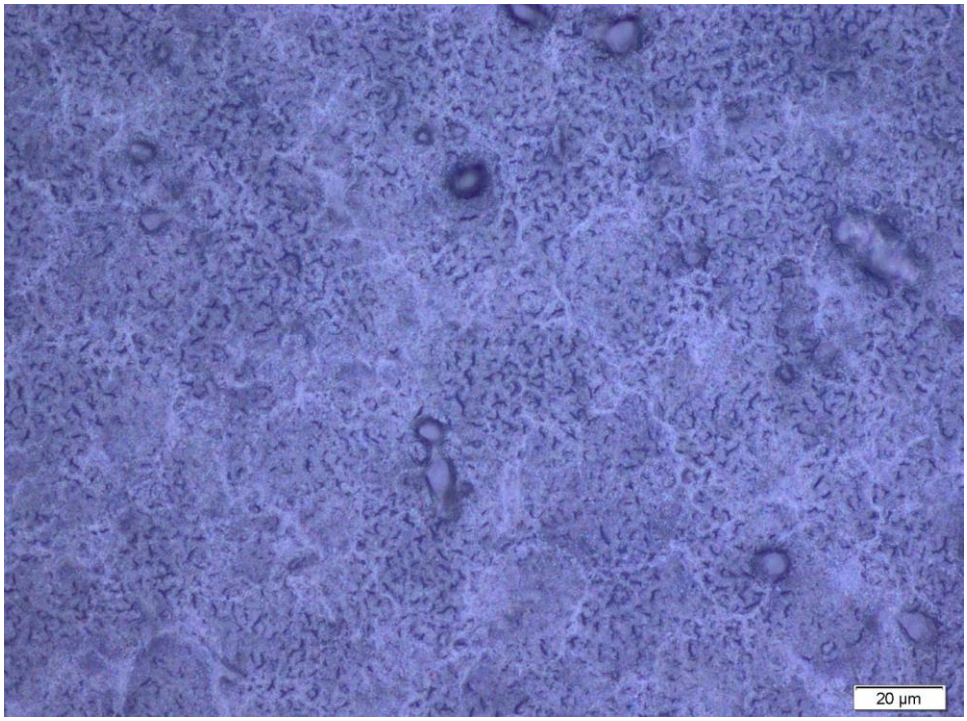

Figure 8.30. Optical microscopy image of 200 µL of printed COF-5 on SiO_2.

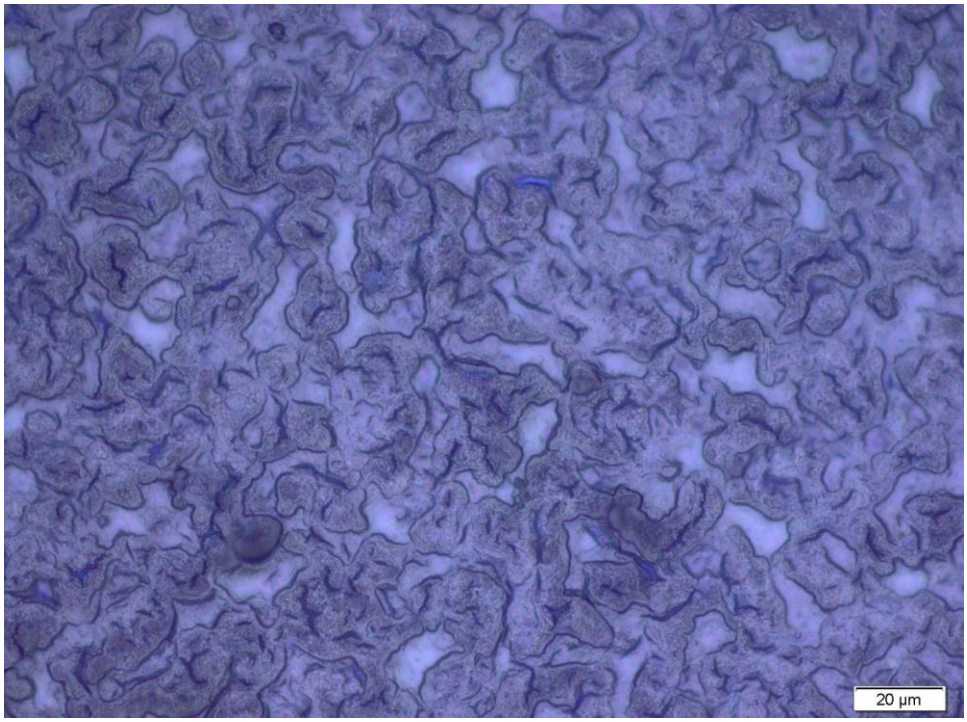

Figure 8.31. Optical microscopy image of 250 µL of printed COF-5 on SiO_2.

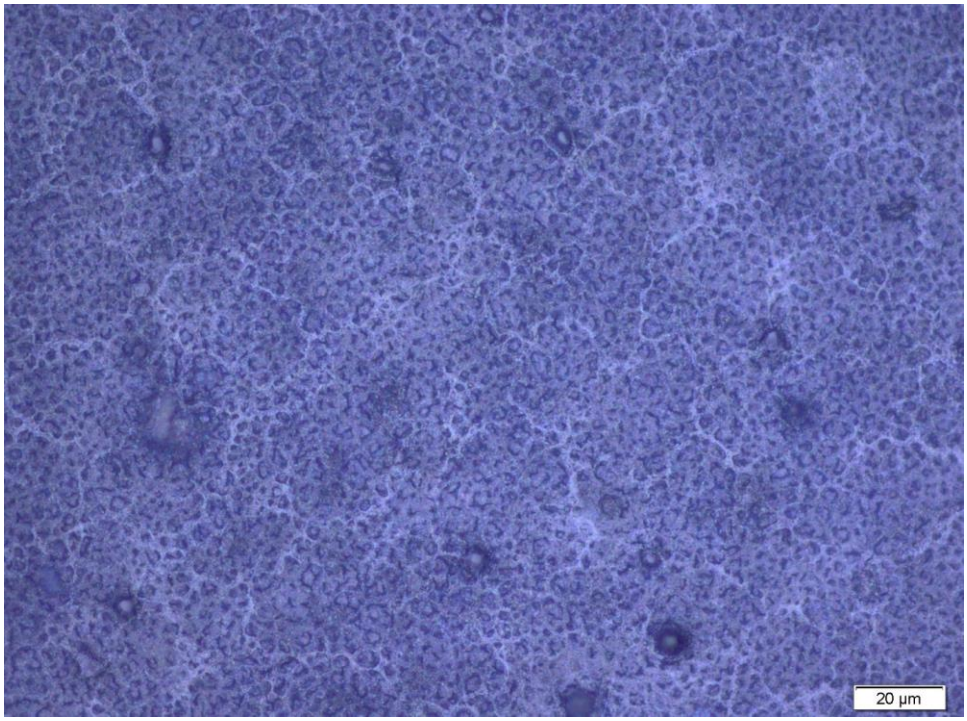

Figure 8.32. Optical microscopy image of 300 µL of printed COF-5 on SiO_2.

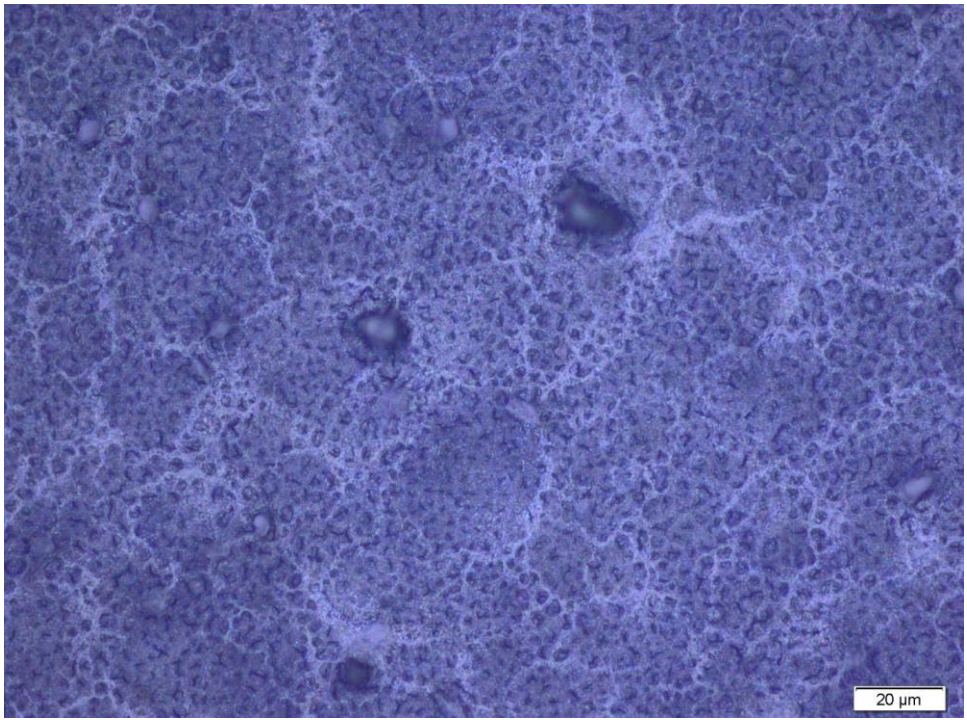

Figure 8.33. Optical microscopy image of 400 µL of printed COF-5 on SiO_2.

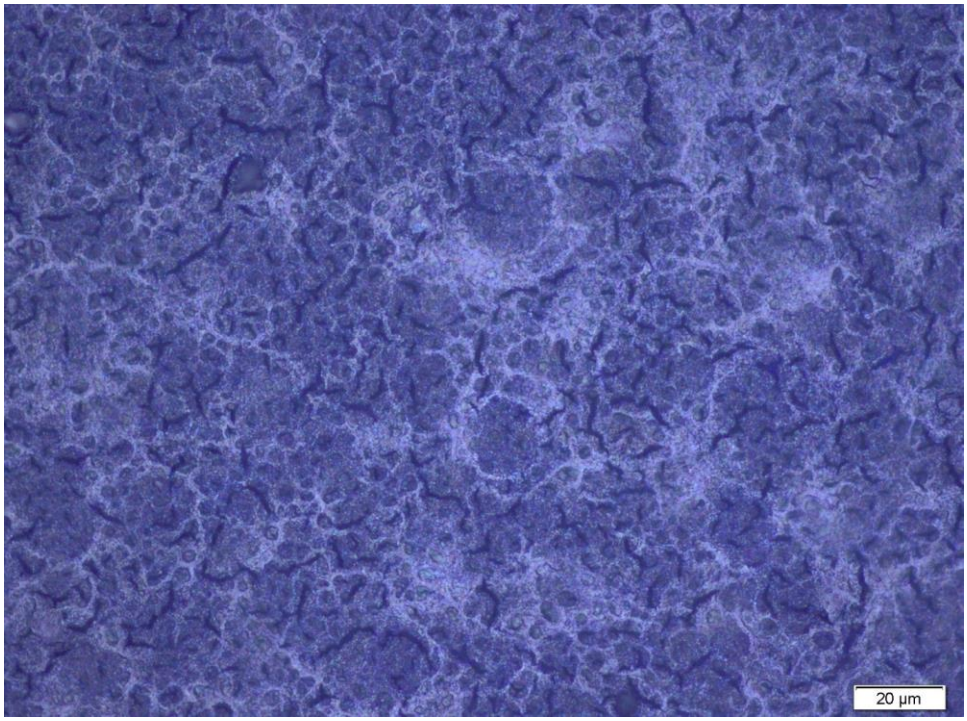

Figure 8.34. Optical microscopy image of 500 µL of printed COF-5 on SiO_2.

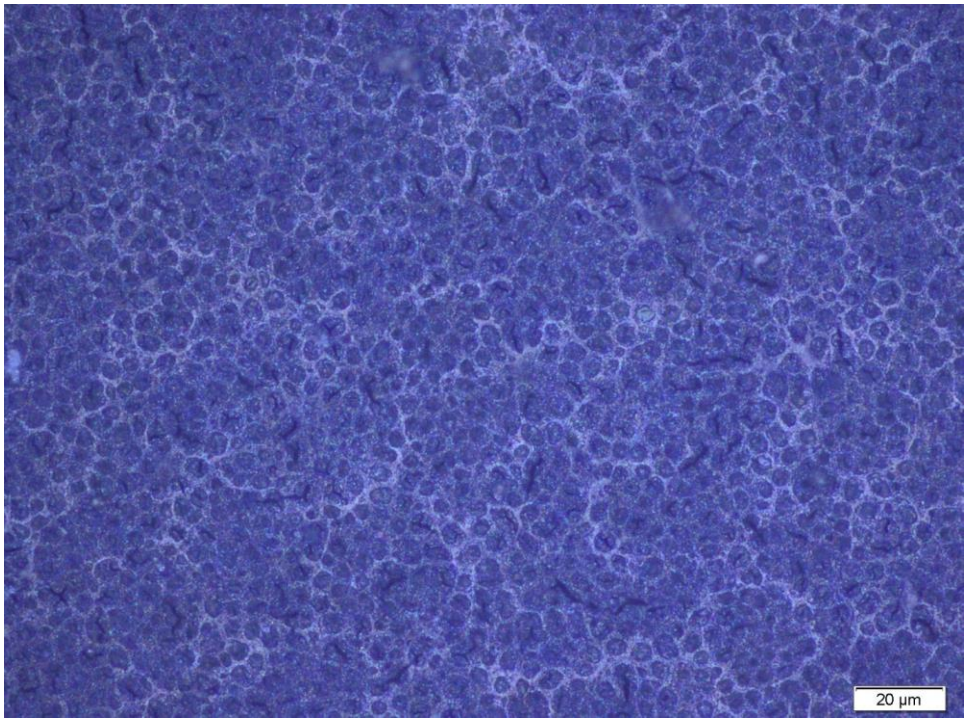

Figure 8.35. Optical microscopy image of 750 µL of printed COF-5 on SiO_2.

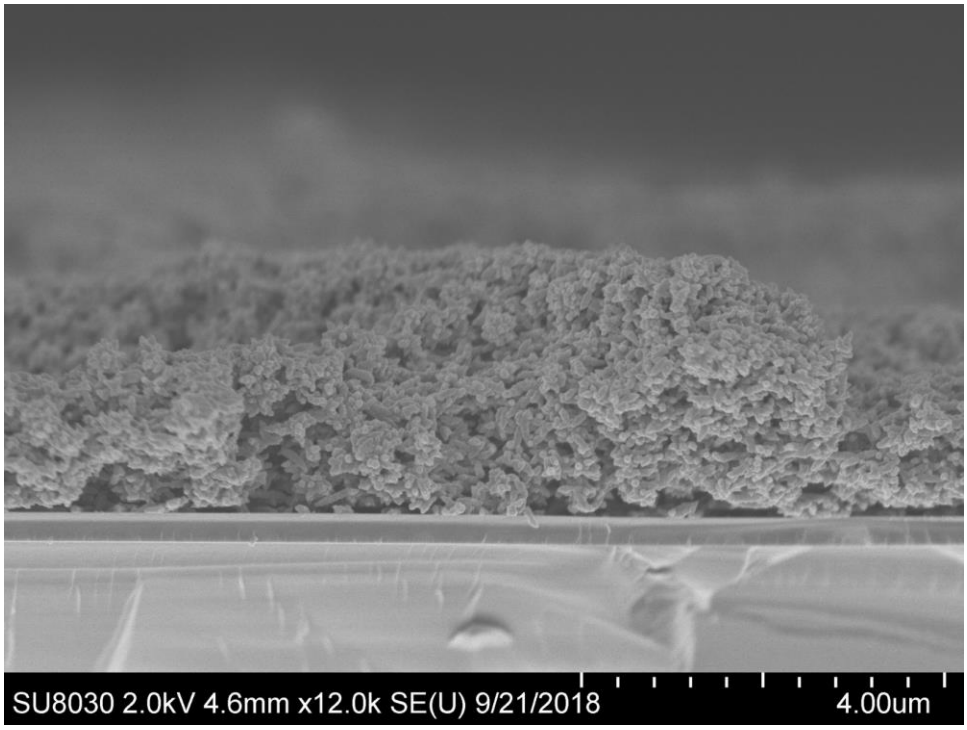

Figure 8.36. Scanning electron micrograph of 1 mL of printed COF-5 on SiO_2.

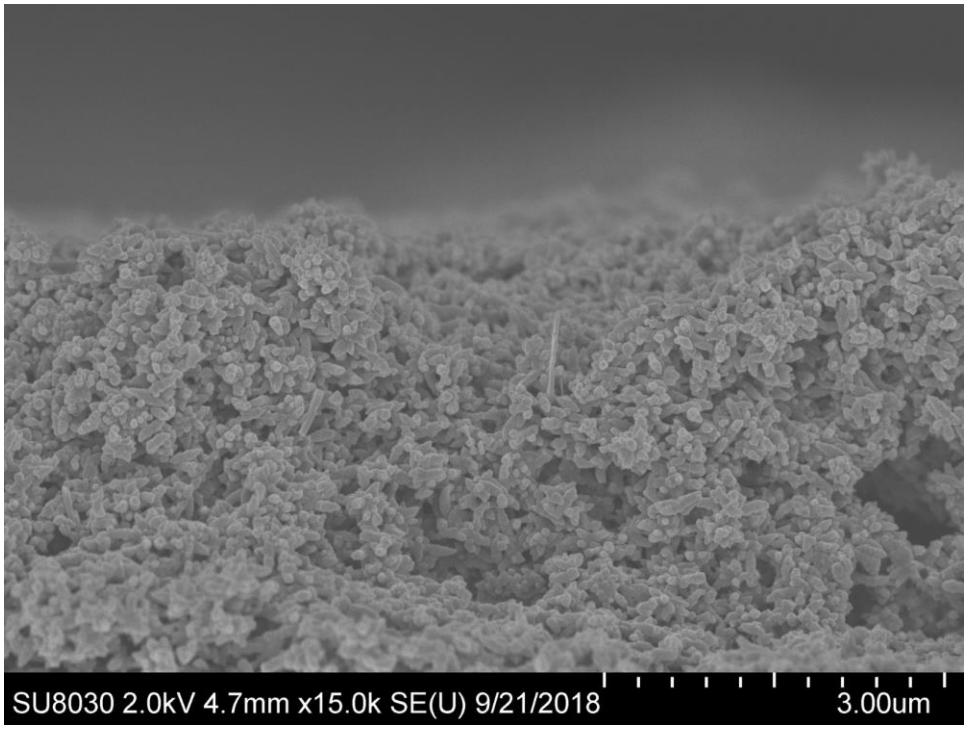

Figure 8.37. Scanning electron micrograph of 2 mL of printed COF-5 on SiO_2.

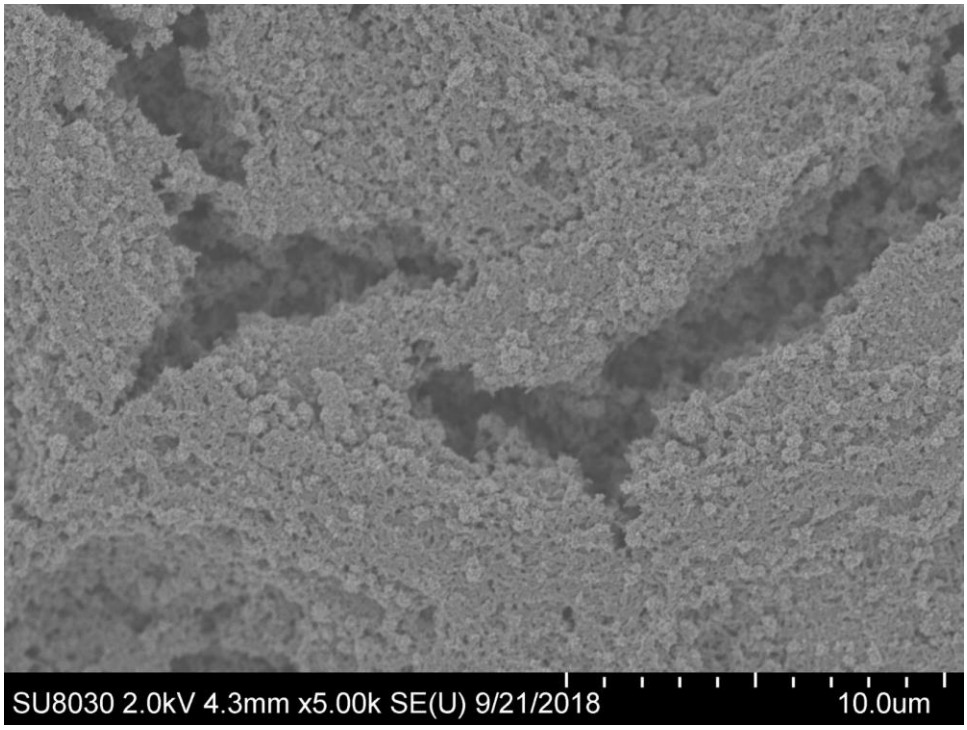

Figure 8.38. Top view scanning electron micrograph of 1 mL of printed COF-5 on SiO_2.

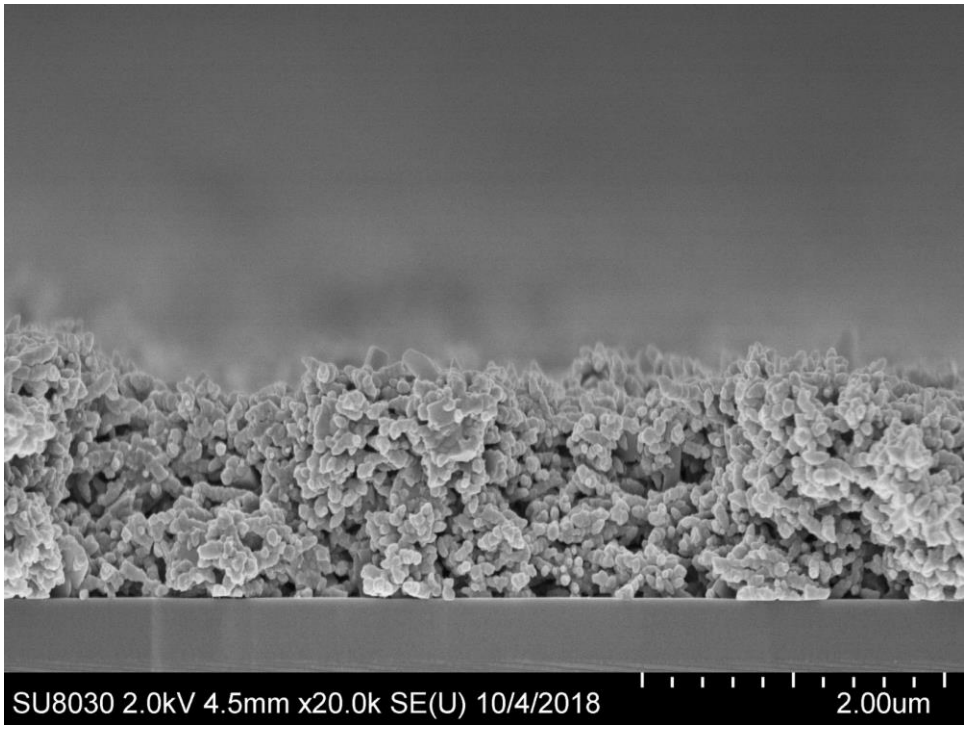

Figure 8.39. Scanning electron micrograph of 500 μL of printed COF-5 on SiO_2.

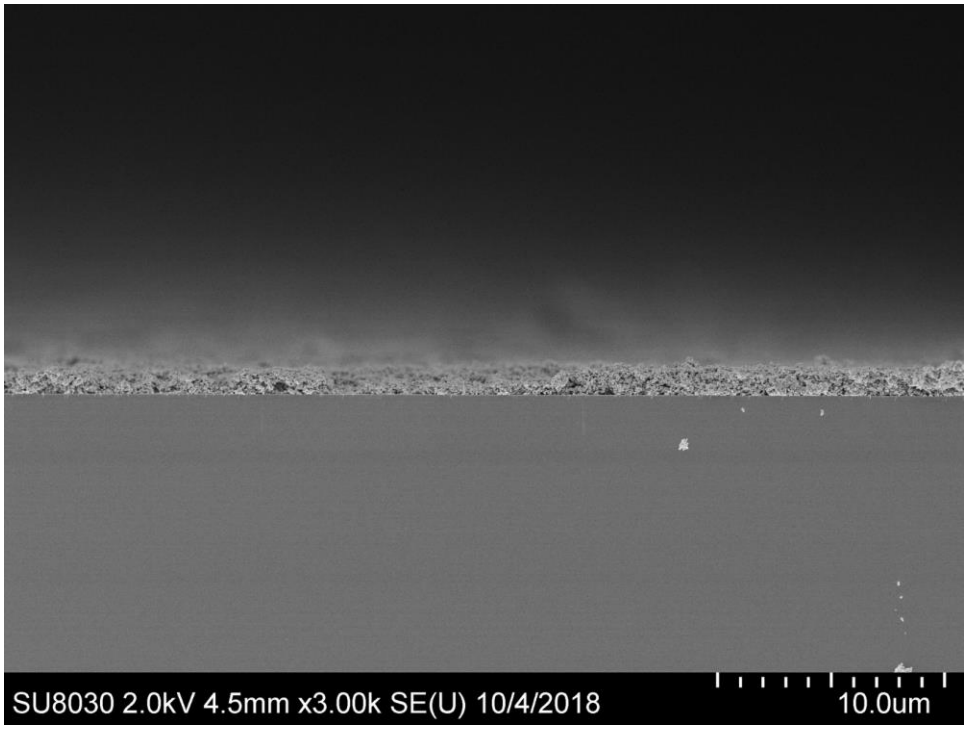

Figure 8.40. Wide view scanning electron micrograph of 500 μL of printed COF-5 on SiO_2.

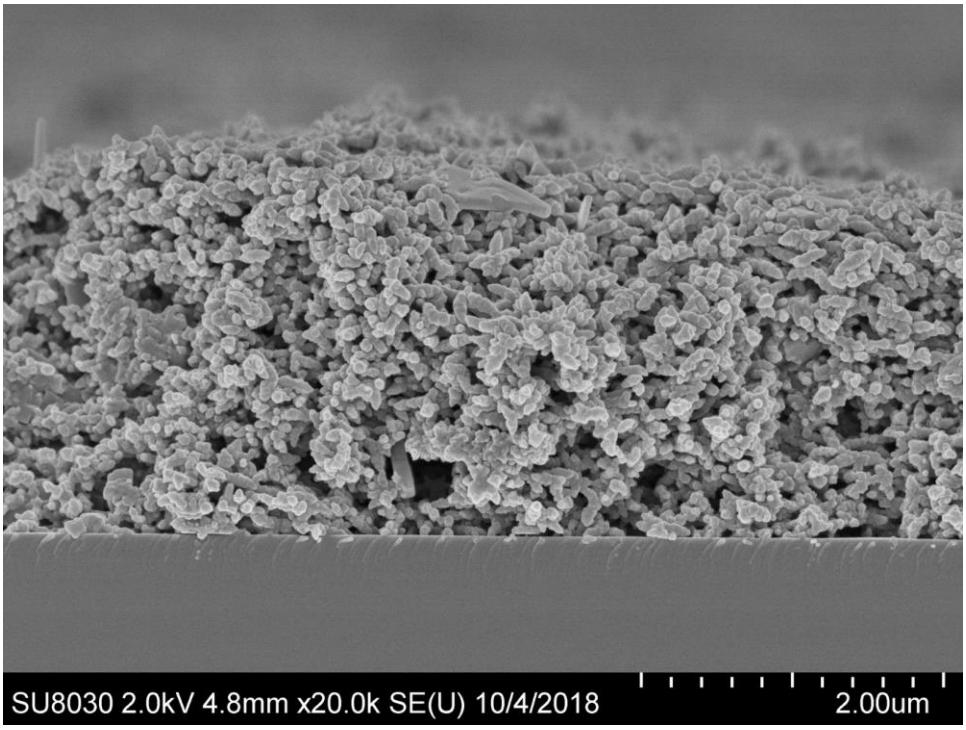

Figure 8.41. Scanning electron micrograph of 3 mL of printed COF-5 on SiO_2.

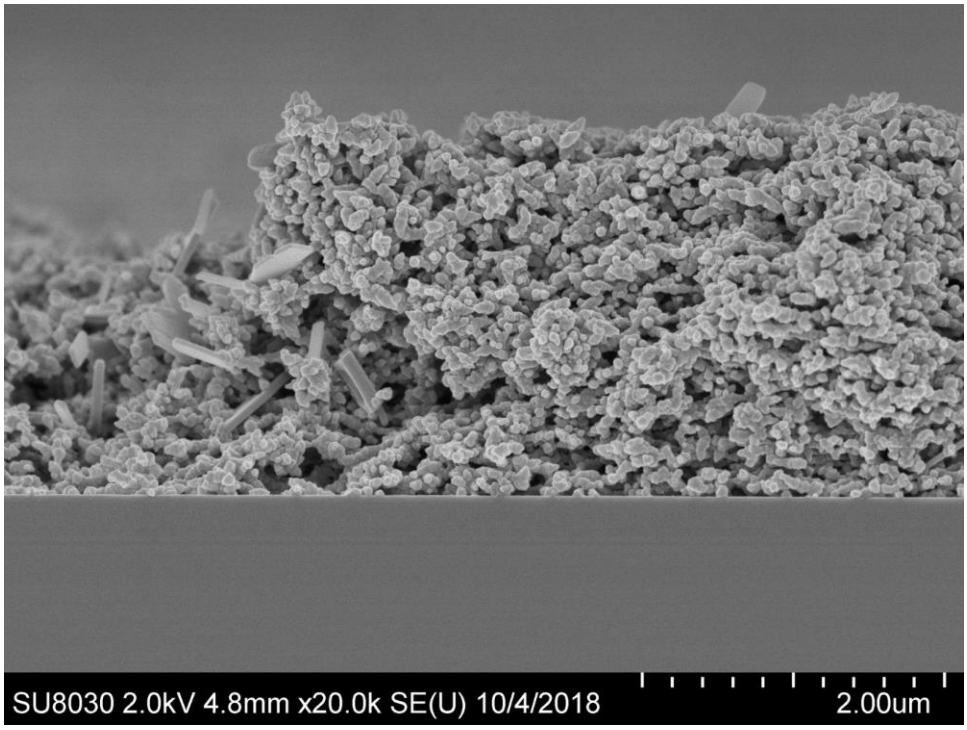

Figure 8.42. Scanning electron micrograph of 3 mL of printed COF-5 on SiO_2.

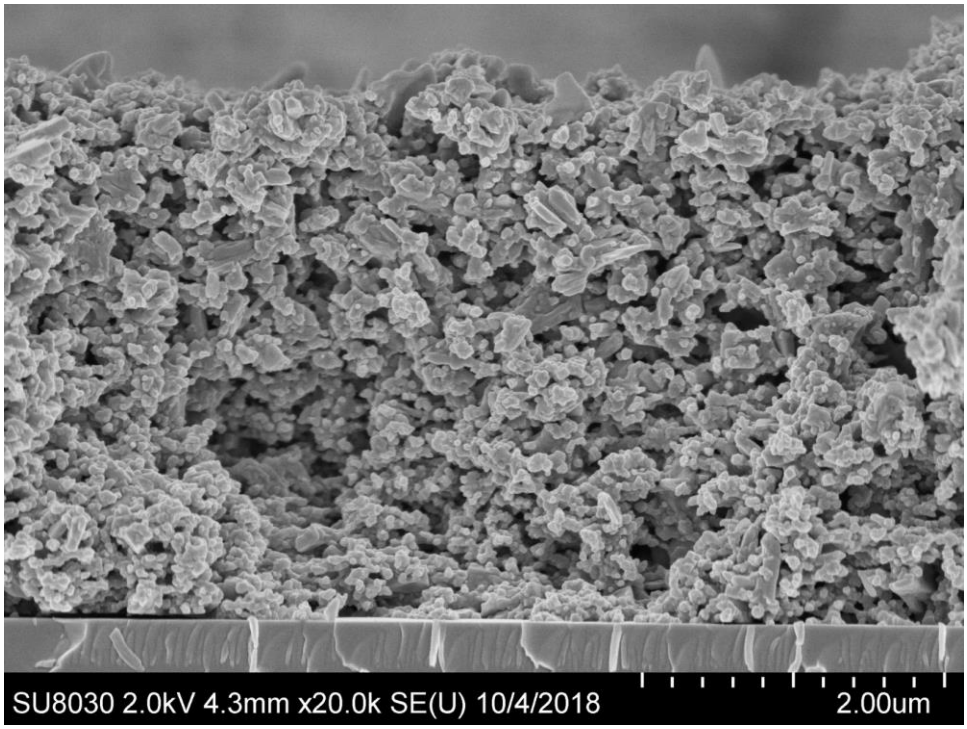

Figure 8.43. Scanning electron micrograph of 5 mL of printed COF-5 on SiO_2.

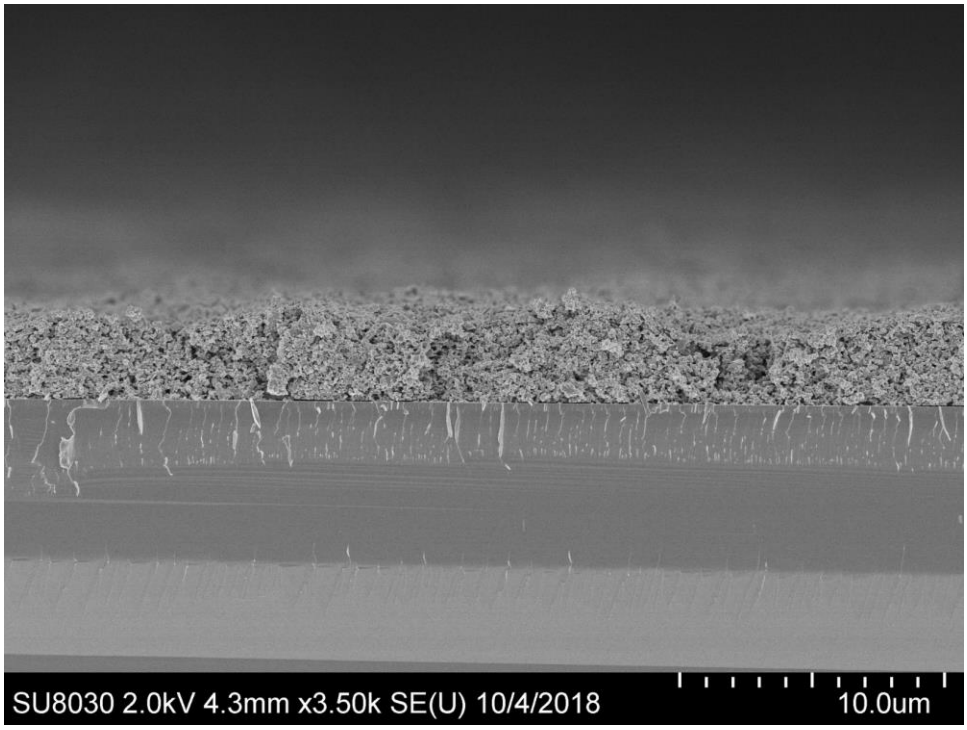

Figure 8.44. Scanning electron micrograph of 5 mL of printed COF-5 on SiO_2.

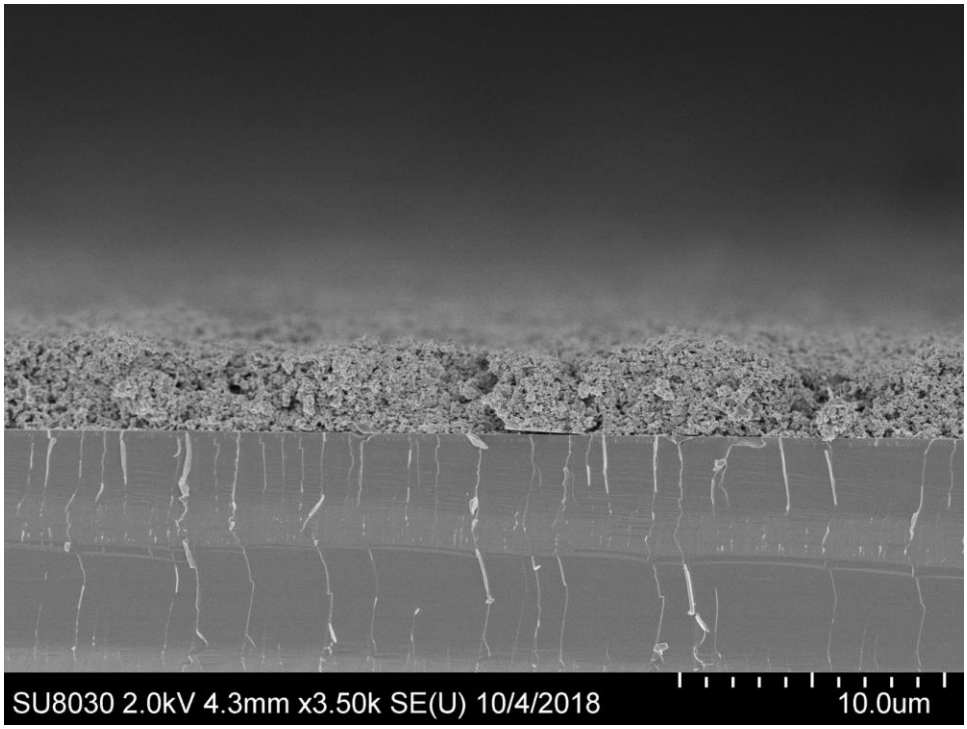

Figure 8.45. Scanning electron micrograph of 5 mL of printed COF-5 on SiO_2.

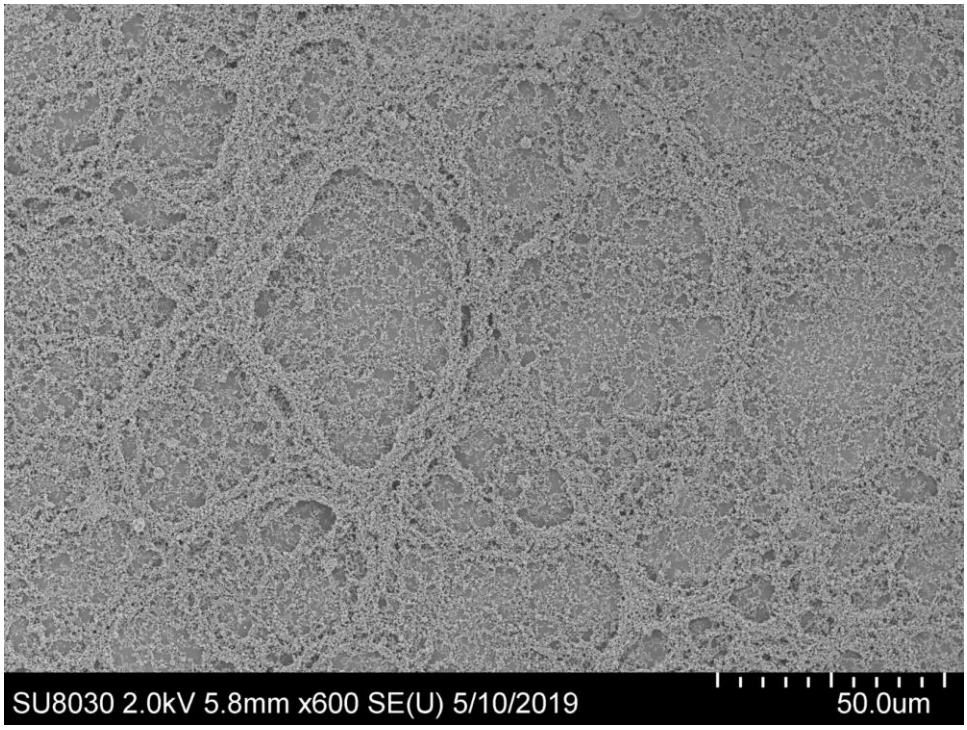

Figure 8.46. Scanning electron micrograph of 1.5 mL of printed COF-5 on SiO_2.

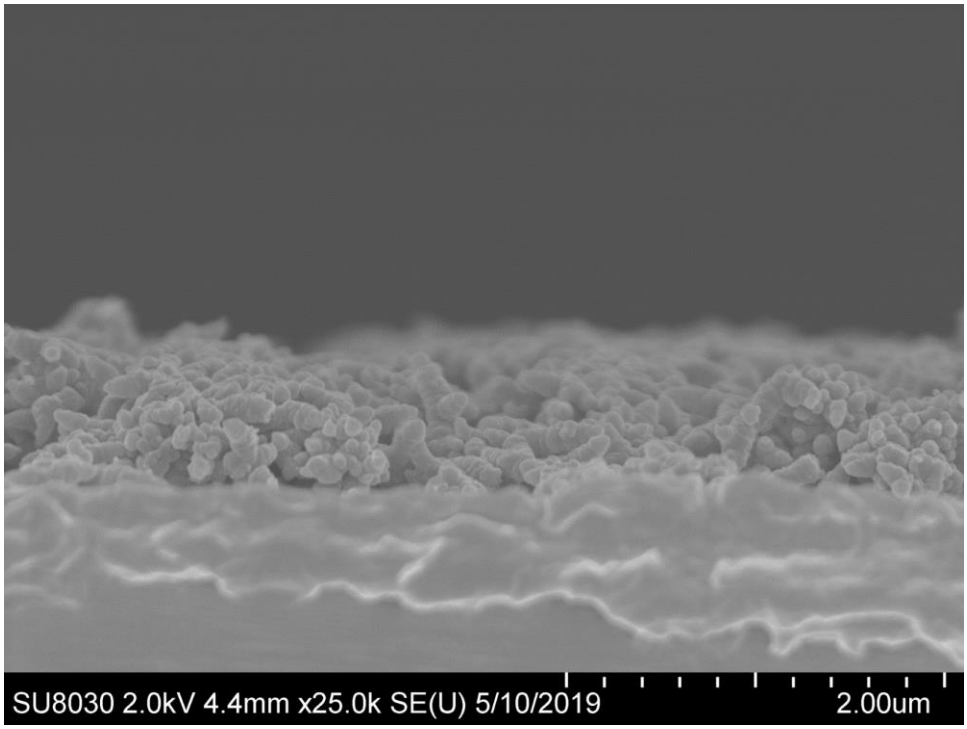

Figure 8.47. Wide view scanning electron micrograph of 500 μL of printed COF-5 on SiO_2.

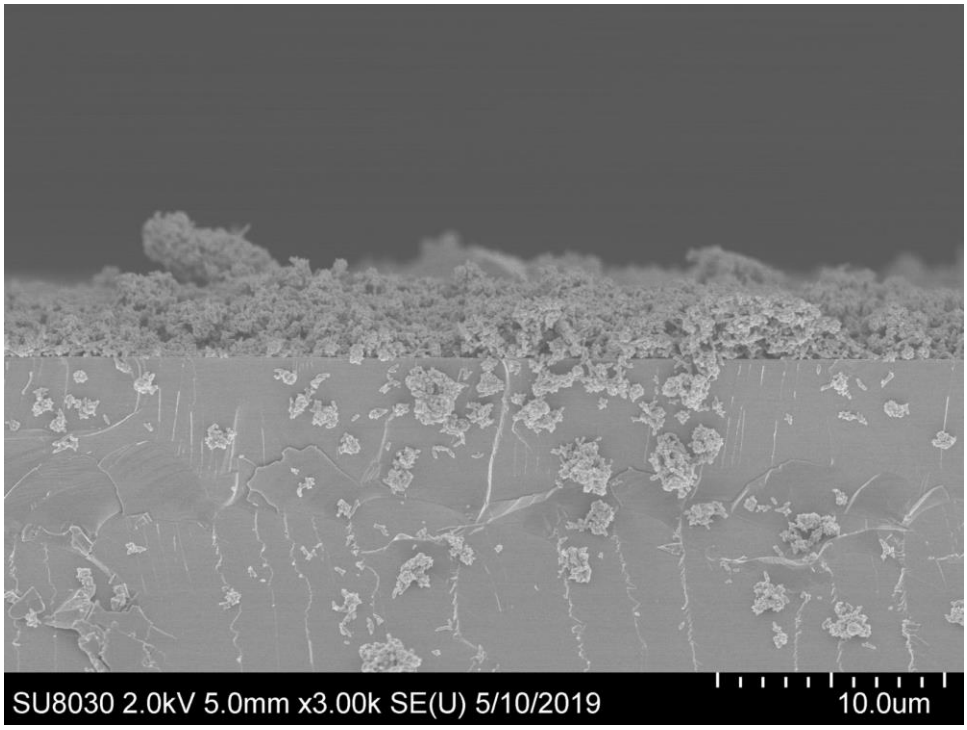

Figure 8.48. Scanning electron micrograph of 1.5 mL of printed COF-5 on SiO_2.

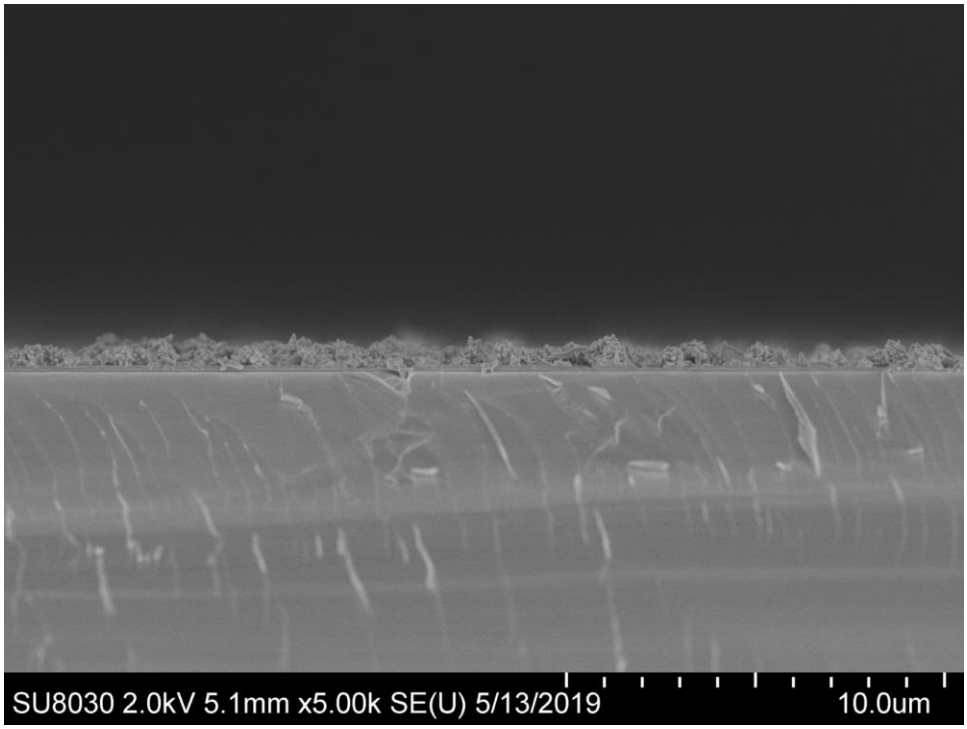

Figure 8.49. Wide view scanning electron micrograph of 750 μL of printed COF-5 on SiO_2.

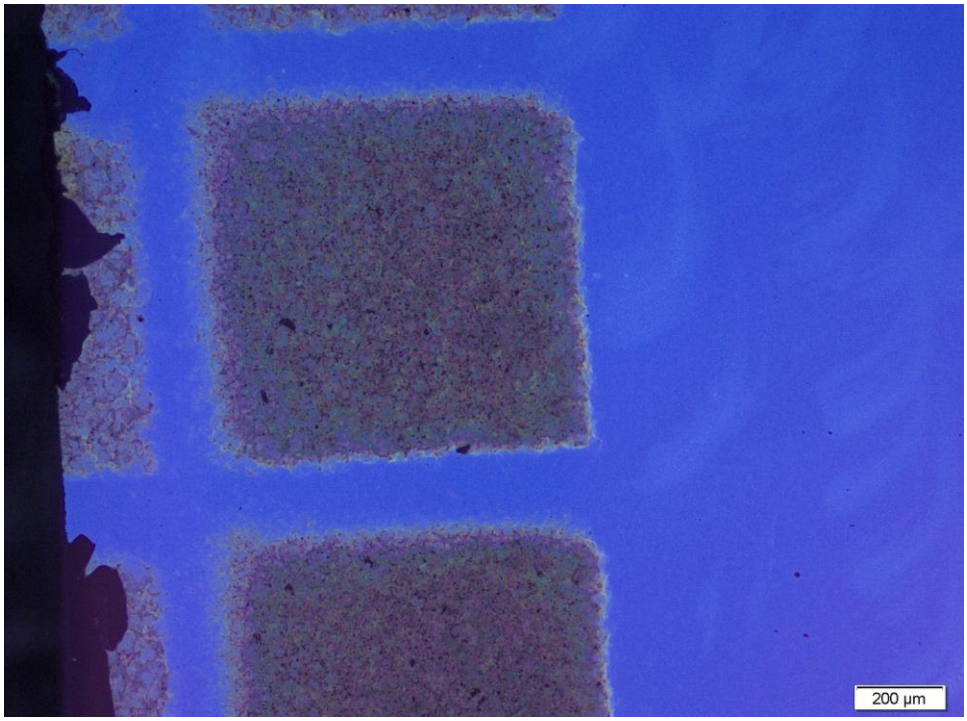

Figure 8.50. High-resolution optical images of patterned COF-5 on SiO_2.

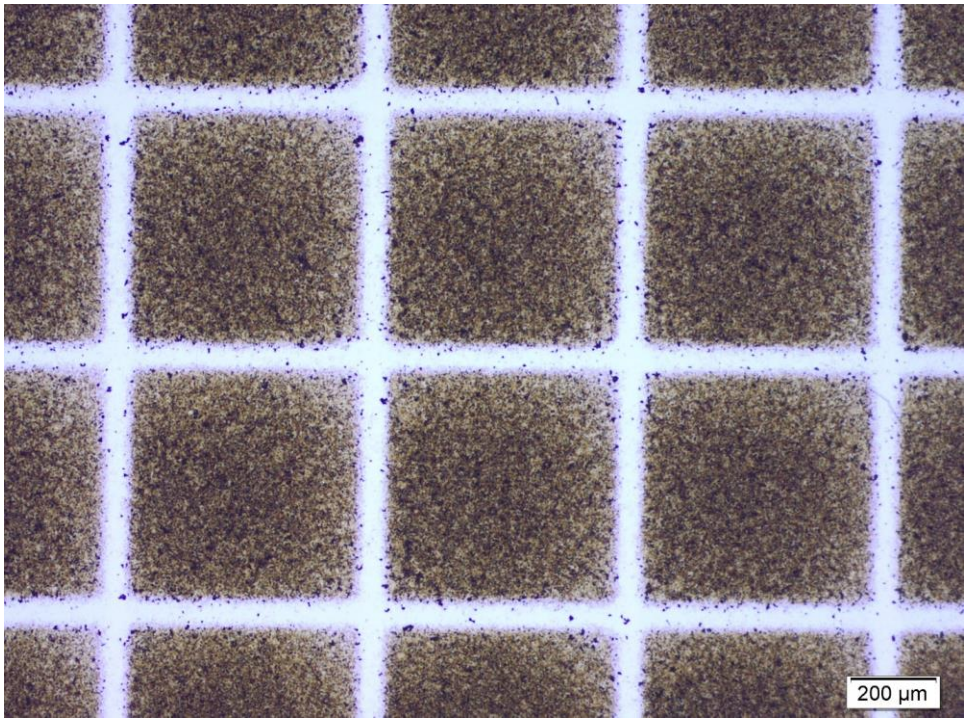

Figure 8.51. High-resolution optical images of patterned COF-5 on SiO_2.

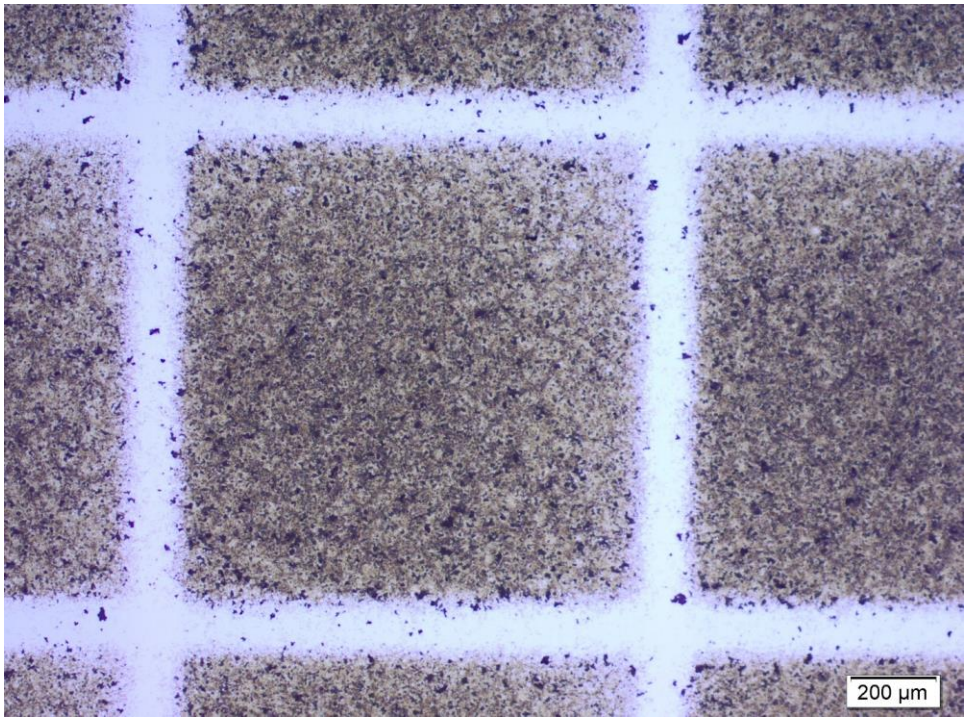

Figure 8.52. High-resolution optical images of patterned COF-5 on SiO_2.

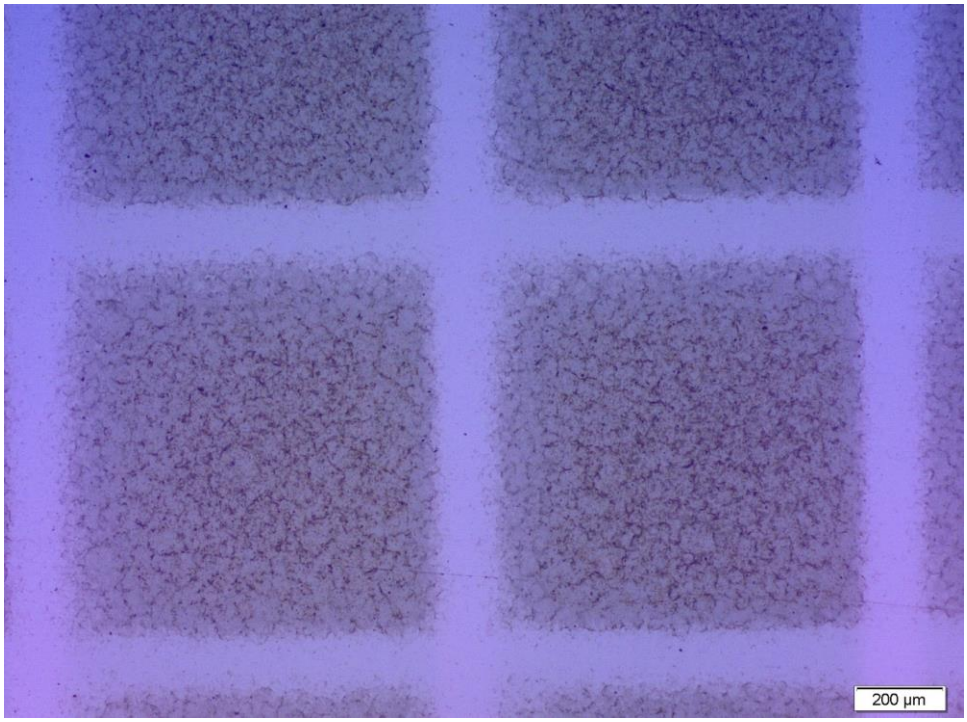

Figure 8.53. High-resolution optical images of patterned COF-5 on SiO_2.

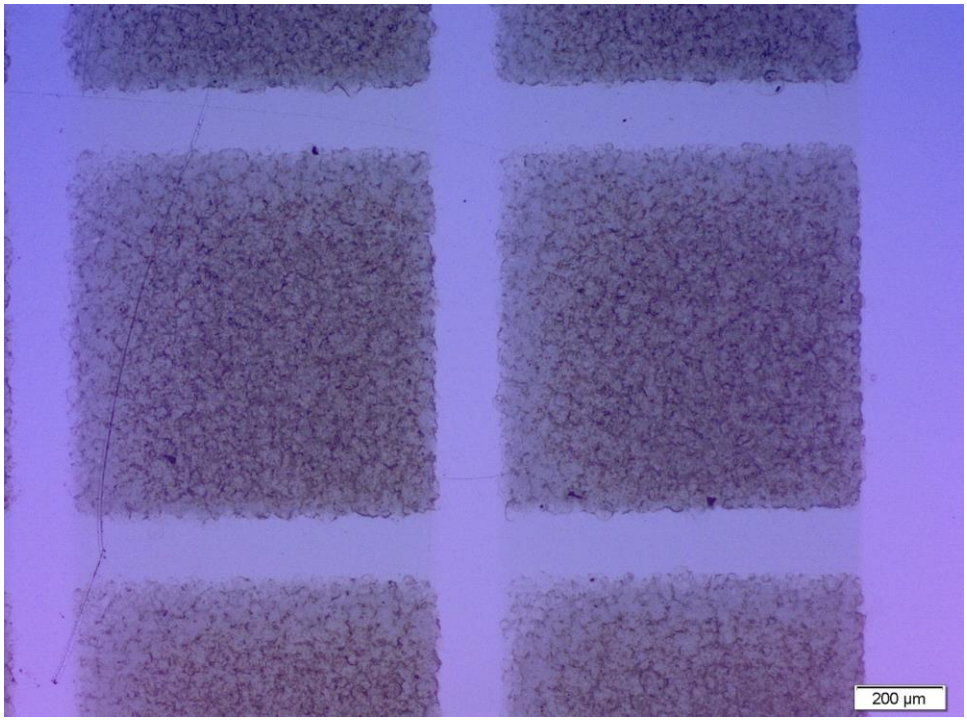

Figure 8.54. High-resolution optical images of patterned COF-5 on SiO_2.

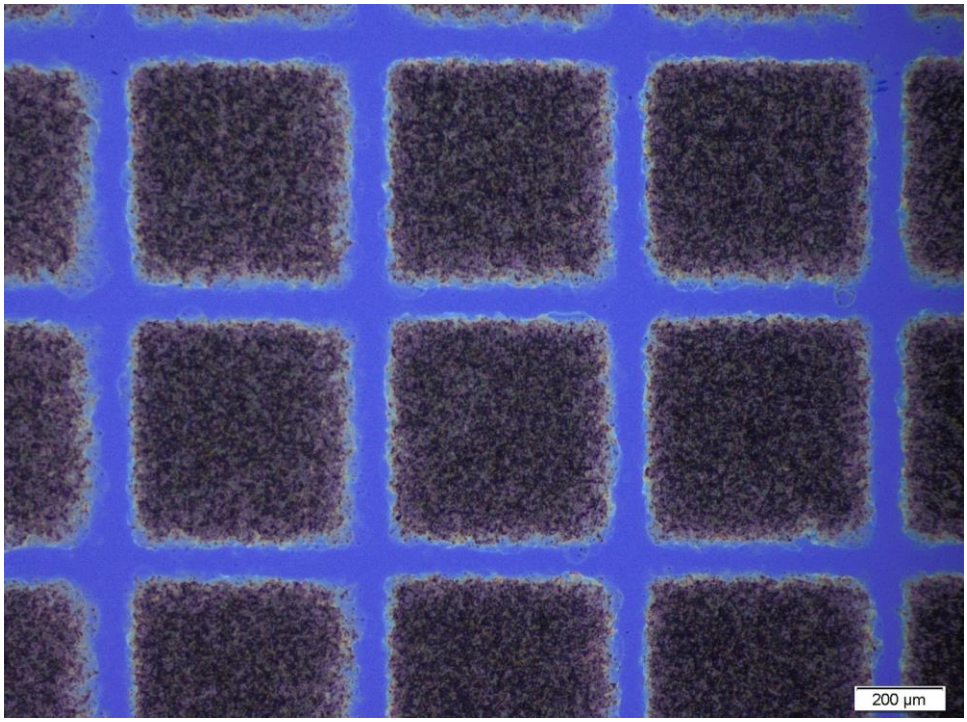

Figure 8.55. High-resolution optical images of patterned COF-5 on SiO_2.

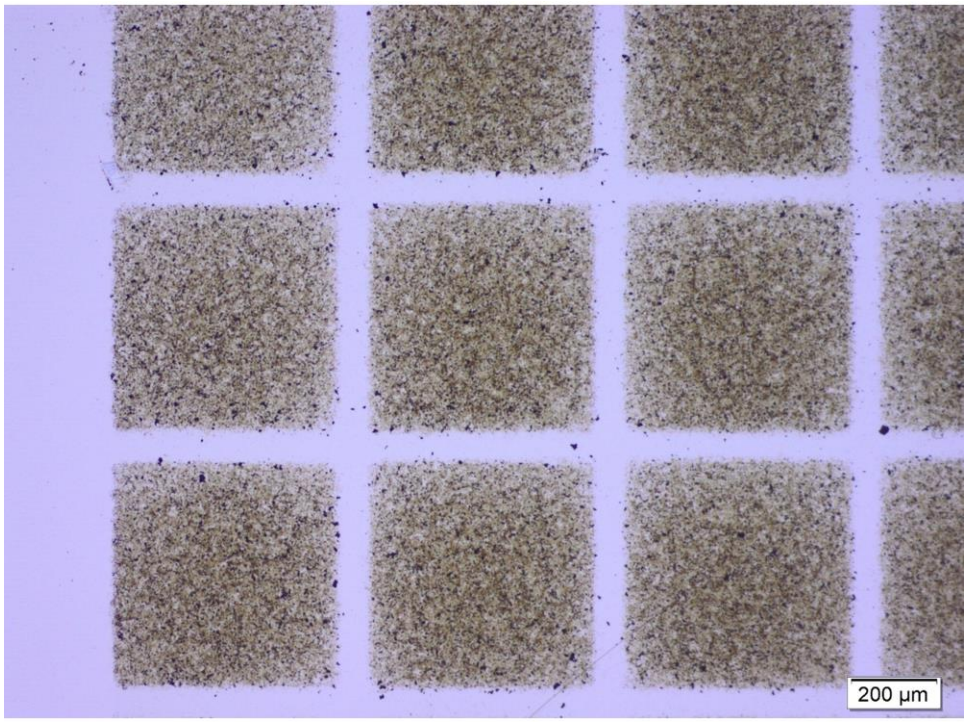

Figure 8.56. High-resolution optical images of patterned COF-5 on SiO_2.

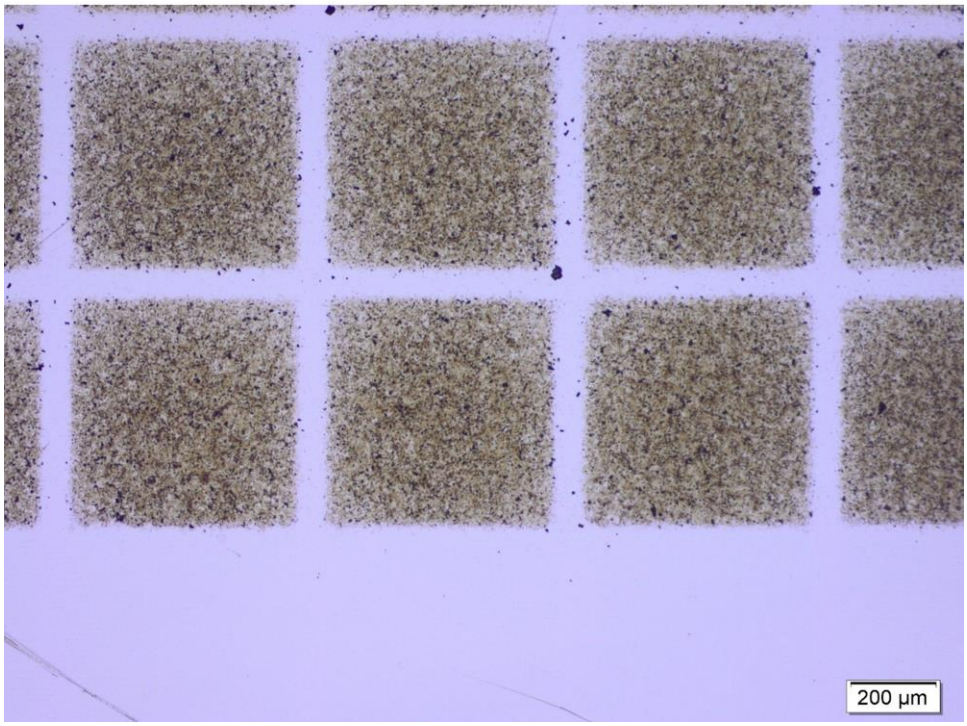

Figure 8.57. High-resolution optical images of patterned COF-5 on SiO_2.

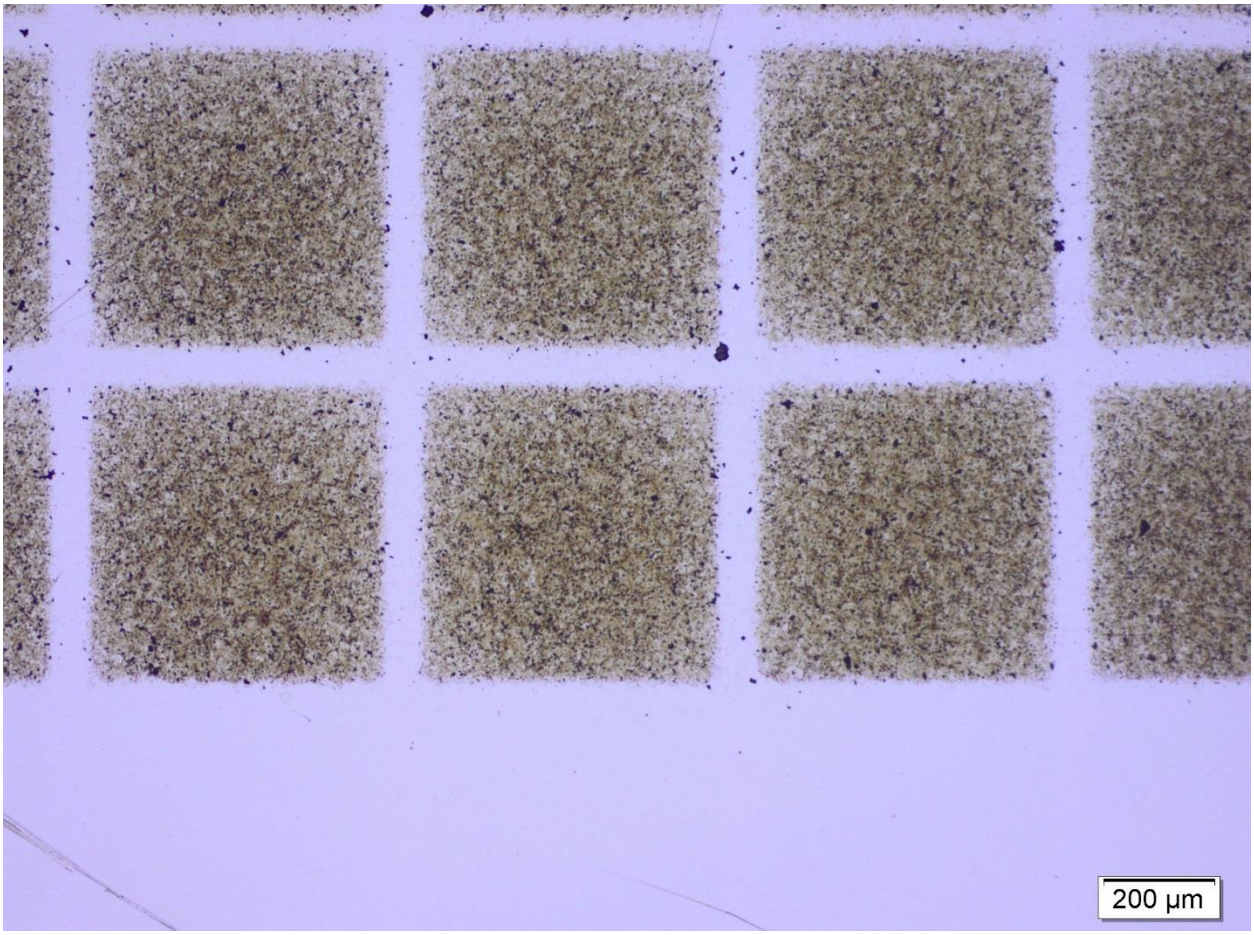

Figure 8.58. High-resolution optical images of patterned COF-5 on SiO_2.

Figure 8.59. Optical image of spray-coated COF-10 on a QCM wafer.

H. COF Printing Setup Details

Figure 8.60. Image of COF printing setup.

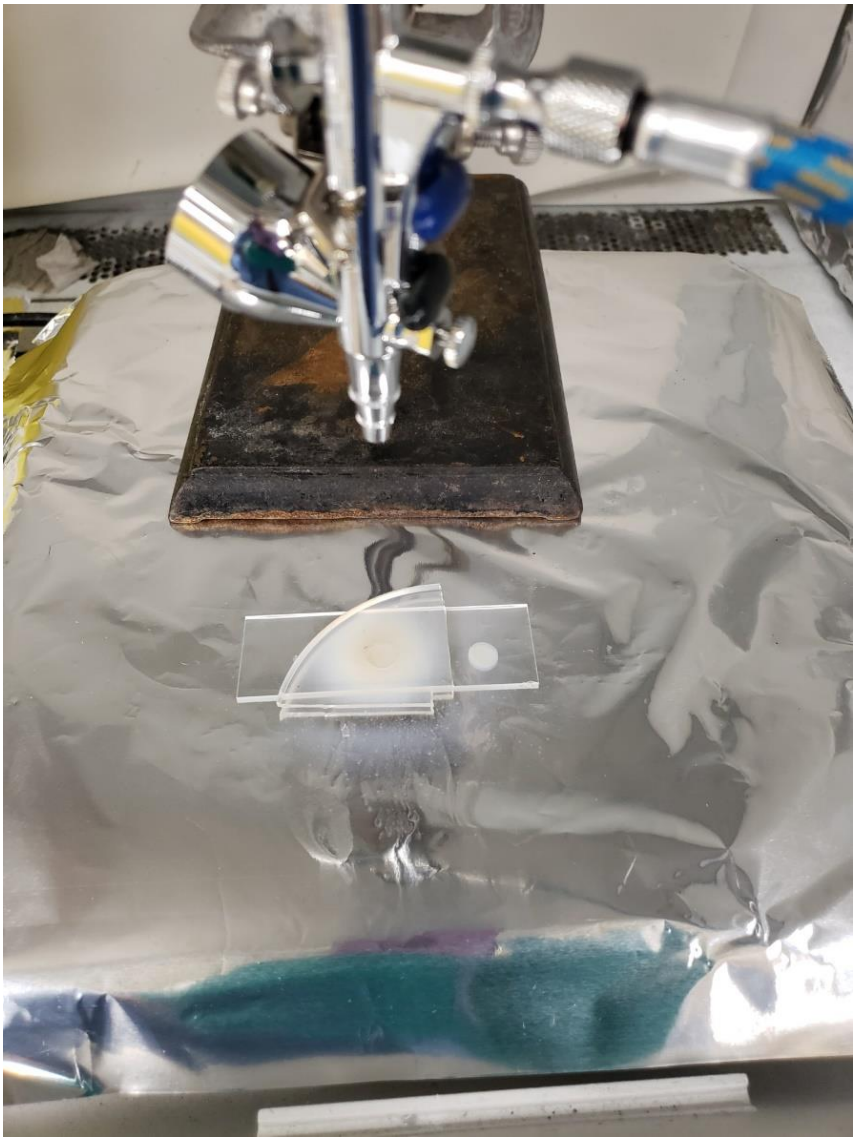

Figure 8.61. Image of COF printing setup.

I. COF Sensing Experimental Details

Figure 8.62. Image of QCM chamber used for COF sensing measurements.

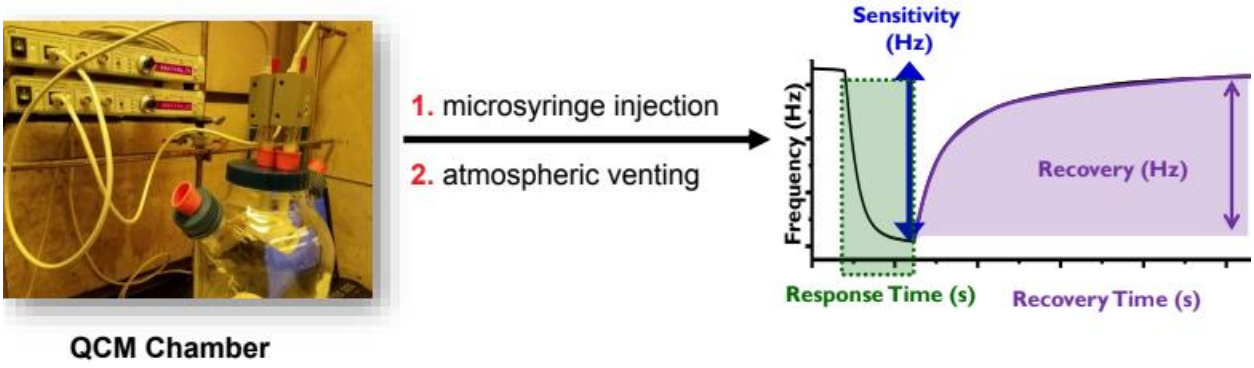

Figure 8.63. Schematic of workflow in QCM COF sensing measurements.

J. Computational Results

Electronic structure calculations were performed using the periodic *ab initio* code CRYSTAL17.[8] The HSE-3C density functional method was used as it has been shown to be numerically robust and more efficient than similar methods such as PBEh-3C.[9] The HSE-3C method has also been suggested to be more suited for narrow energy bandgap cases, such as framework materials. In the current study, the additional computational efficiency was beneficial, especially for the structures containing guest molecules (cadaverine and triethylamine) as the space-group symmetry is reduced to triclinic. A modified double-ζ basis set known as def2-mSVP was used as recommended for optimal performance with the composite density functional method.[10]

The lattice parameters and atomic coordinates were optimized using a quasi-Newtonian algorithm.[11-14] while initially maintaining the space group symmetry of COF-5 (*P6*) and then reducing the symmetry (*P1*) after adding the guest molecules. The host-guest structures were obtained from an optimized geometry of COF-5 modified by inserting the guest molecules of cadaverine and triethylamine manually at a concentration of one and two molecules per unit cell, respectively. The reasoning for adding two of the latter molecules was to match the number of B-N bonding interactions. It is worth noting that the specific changes to the geometry of the COF-5 structure and the lattice parameters are dependent on the concentration of the guest molecules. Therefore, the precise deformation of the 2D layers and expansion of the lattice would likely be more periodic and ordered than what would be observed experimentally.

K. Monomer Conversion Experiments

We investigated the monomer conversion by synthesizing COF inks in deuterated solvents (80:16:4 vol % CD_3CN:1,4-dioxane-*d*6:mesitylene-*d*12) with an internal standard (1,3,5-trichlorobenzene 2mM). Initially, NMR features related to both monomers are present in the expected concentrations and ratios. After heating the mixture at 80 °C, the solution became colloidal after which it was cooled to room temperature and centrifuged at 7800 rpm for 20 min. The NMR spectrum of the supernatant contained the internal standard with no discernable signals associated with residual monomers. However, when the collected precipitate was exposed to MeOH, which hydrolyzes the COF particles, we observed complete recovery of the monomer species and their methoxy adducts (**Figure S60**).

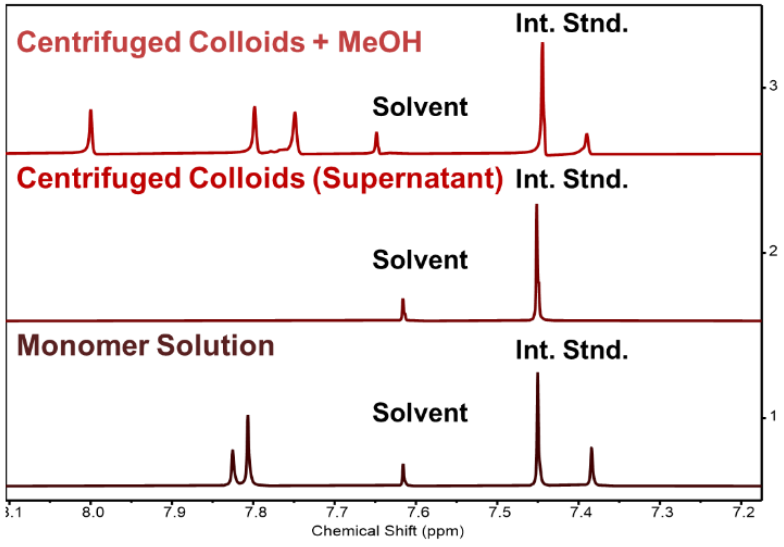

Figure 8.64. ^{1}H NMR of monomer solution, the supernatant from centrifuged COF inks, and the product of the collected COF inks when exposed to MeOH.

Separately, we immersed a spray coated COF-5 film in the same deuterated solvent mixture (80:16:4 vol % CD_3CN:1,4-dioxane-d6:mesitylene-d12) with an internal standard (1,3,5-trichlorobenzene 2 mM) for 10 min at room temperature (**Figure S61**). This solution remained transparent, and its NMR spectrum also did not contain signals for the monomer species. We were interested to know if this was related to the poor solubility of HHTP and PBBA. As such, we dropcast solutions of PBBA and HHTP monomer separately and performed the same experiment. In this case, we observed signals for both monomers, suggesting that limited solubility was not preventing their observation in the COF-5 colloid experiments.

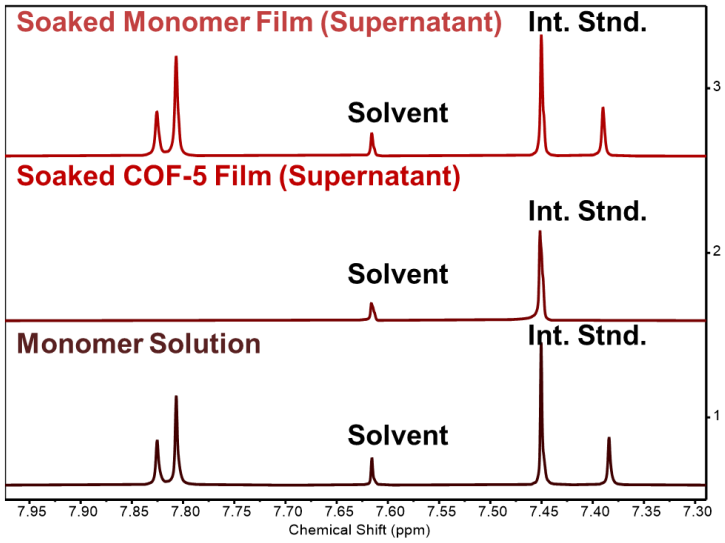

Figure 8.65. ^{1}H NMR of monomer solution and the product of COF and monomer films immersed in clean solvent mixtures.

Taken together, we find these results to demonstrate that conversion of monomer species to colloidal nanoparticles is near quantitative.

Chapter 9 : Thermally Conductive, Ultra-Low-k Dielectric Layers Based on Two-Dimensional Covalent Organic Frameworks

9.1 Abstract

As the features of microprocessors continue to be miniaturized, low dielectric constant (low-***k***) materials are necessary to limit electronic crosstalk, charge buildup, and signal propagation delay. However, all known low-*k* dielectrics exhibit low thermal conductivities, which complicate heat dissipation in high power-density chips. 2D covalent organic frameworks (2D COFs) combine immense permanent porosities, which may lead to low dielectric permittivities, and periodic layered structures, which may grant relatively high thermal conductivities. However, conventional synthetic routes produce 2D COFs that are unsuitable for the evaluation of these properties and integration into devices. Here we report the fabrication of high-quality COF thin films, which enable time- and frequency-domain thermoreflectance and impedance spectroscopy measurements. These measurements reveal that 2D COFs have high thermal conductivities (1 W m^{-1} K^{-1}) for porous solids with ultra-low dielectric permittivities (***k*** = 1.6). These results show that oriented, layered 2D polymers are promising next-generation dielectric layers and that these molecularly precise materials offer unique and tunable property combinations.

9.2 Introduction to Low-*k* Dielectrics

To take advantage of sub-10 nanometer integrated circuit components, interlayer low-dielectric constant (low-***k***) materials with high thermal conductivities must be developed[673-675]. As

dielectric layers have thinned, electronic crosstalk and capacitive signal delay significantly diminish device performance. The Semiconductor Industry Association has identified the development of mechanically robust, thermally stable, few-nanometer, low-***k*** (***k*** < 2.4) and ultra-low-***k*** (***k*** < 1.9) materials as needed to address this challenge[676, 677]. Ultimately, the realization of such materials will reduce parasitic capacitance, enabling faster gate operations and minimizing dynamic power dissipation[673, 678, 679]. Towards this end, two major classes of low-***k*** dielectric materials have been developed: 1) organic materials that are inherently low-***k*** because of the limited polarizability of covalent bonds and 2) porous oxides that are low-***k*** as a result of their large free volumes. However, all known low-***k*** materials have large thermal resistances that arise from their disordered morphologies and high porosities[680-683], which limit high power density chip performance due to inadequate heat management[674-677].

9.3 Thin-film Fabrication Techniques

Two-dimensional covalent organic frameworks (2D COFs) are a class of modular, molecularly precise, highly porous, layered polymer sheets[106, 684]. These attributes impart a unique combination of physical properties compared to conventional polymers, such as high thermomechanical stabilities and low densities[684]. Challenges associated with characterizing conventionally isolated polycrystalline COF powders have restricted the exploration of many 2D COF properties. To address this challenge, COFs have been fabricated as thin films via direct growth[425, 583], exfoliation[583, 685, 686], or interfacial polymerization[182, 425, 687]. However, none of these methods have proven general for wafer-scale synthesis of oriented and crystalline COF films without powder contamination. Synthetic limitations have hindered the evaluation of COFs'

fundamental properties related to their use as low-***k*** dielectric layers,[659] even as Wang and coworkers demonstrated preliminary promise for using 2D COFs for this purpose[688].

Here, we synthesize high-quality wafer-scale boronate ester-linked 2D COF films through a templated colloidal approach, which prevents powder contamination. Previously, we have found that supported graphene substrates template the formation of oriented 2D COF thin films[425]. However, films obtained by this method are often unsuitable for device measurements because of contamination by insoluble COF powders that form during the synthesis. Recently, we found that the use of nitrile cosolvents prevents the precipitation of insoluble products and instead provide COFs as solution-stable colloidal suspensions[125, 659, 665, 666]. Here, we use colloidal approaches to grow COF thin films of few-nm roughness with controllable thicknesses on device-relevant substrates without contamination by insoluble precipitates. This approach is demonstrated for five 2D COFs, including a previously unreported structure, which are synthesized on both graphene and monolayer MoS_2. Furthermore, these 2D COF films are amenable to sequential polymerization cycles, enabling nanometer precise thickness control not possible in traditional precipitant-contaminated solvothermal syntheses.

The unprecedented quality of these films enables the measurement of thermomechanical and optoelectronic properties of COF films. Optical absorption and emission spectroscopies showed that boronate ester-linked COF films are electronically insulating. These results are consistent with density functional theory (DFT) calculations that predict pristine COF-5 films have an indirect electronic bandgap of 3.6 eV and a direct bandgap of 3.9 eV. Impedance spectroscopy performed on COF-5 thin films reveals that they are electronically insulating, ultra-low-***k*** (***k*** < 1.7)

dielectric layers, which are consistent with DFT-calculated low electronic dielectric tensors ($\varepsilon_{xx,yy,zz} < 2$) for all COFs investigated.

Due to their regularly porous, covalently linked, layered structure, 2D COFs circumvent the low thermal conductivities that afflict leading low-***k*** dielectrics. Using time- and frequency-domain thermoreflectance (TDTR and FDTR, respectively) and molecular dynamics (MD) simulations, we find that 2D COFs have a unique combination of low densities ($\rho < 1$ g cm^{-3}) and relatively high thermal conductivities ($\kappa > 0.8$ W m^{-1} K^{-1} in the cross-plane direction with a predicted anisotropy ratio of >3 in the in-plane direction). These findings show that 2D COFs are promising as ultra-low-***k*** dielectrics with desirable heat management characteristics. More broadly, accessing high-quality 2D COF thin films provides a means to rationally design solid-state organic materials to unlock technologically useful combinations of properties.

9.4 Results and Discussion

2D COF films were polymerized directly by a templated colloidal approach. First, a SiO_2-supported graphene or an Al_2O_3-supported monolayer MoS_2 was submerged into a solution of 2,3,6,7,10,11-hexahydroxytriphenylene (HHTP) and a difunctional aryl boronic acid (**Figure 9.1A, Figure 9.14 - Figure 9.19**). The polymerization mixtures were then sealed and heated to 85 °C for 12 h. Finally, the substrate was removed from the reaction mixture, rinsed with clean solvent, and dried. Prior to robust structural characterization, we observed that an optically homogenous film had formed across the entirety of the substrate (**Figure 9.21**). To probe whether these films were being polymerized from solution or whether colloidal species were templating on the surface, we immersed a graphene-supported substrate in a prepolymerized colloidal 2D COF suspension and subjected it to the polymerization conditions. We find that no films form in the

presence of prepolymerized reaction mixtures. Taken together, these observations suggest that homogenous nucleation occurs in solution and templated-heterogeneous nucleation occurs on the substrate simultaneously, which then polymerize independently.

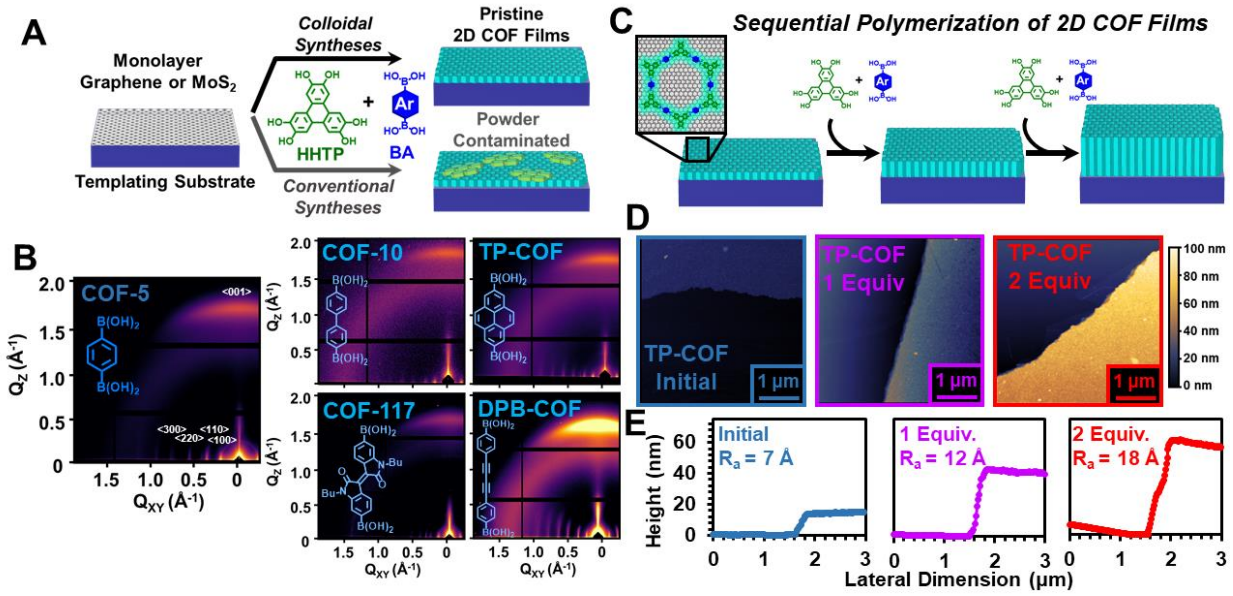

Figure 9.1 Templated colloidal polymerization of boronate-ester linked COF films. A) Synthesis and structure of boronate-ester linked COF films. B) Grazing-incidence wide-angle X-ray scattering patterns of COF films. C) Sequential polymerization of COF films by introduction of monomer. D) Atomic force micrographs of sequentially polymerized TP-COF films. E) Line-cuts of sequentially polymerized TP-COF films in D.

All 2D COF films are found to be crystalline, oriented, and smooth. Atomic force microscopy (AFM) reveals that the materials are obtained as thin films (< 75 nm) with <5 nm root-mean-square roughness in all cases (**Figure 9.26 - Figure 9.30)**. 2D grazing-incidence wide-angle X-ray scattering (GI-WAXS) patterns of all COFs showed prominent in-plane Bragg diffraction

features concentrated along the Q_{xy} axis and cross-plane Bragg features concentrated along the Q_z axis (**Figure 9.1B, Figure 9.31 - Figure 9.45**), which show that 2D COF layers are oriented parallel to the substrate surface. By assessing the azimuthal dispersity of the interlayer <001> Bragg feature (~2 $Å^{-1}$) intensity, we find that these films have a smaller full-width at half-maximum than those reported by other approaches. We attribute the weaker orientation of previously prepared films to the contamination by unoriented precipitates formed during their synthesis (**Figure 9.47**)[425, 583]. In all cases, radially integrated diffraction patterns were found to agree well with simulated COF diffraction patterns, confirming the successful synthesis of the expected COF networks (**Figure 9.41 - Figure 9.45**). The large number and sharp line shapes of diffraction features observed in these two patterns indicate that all COF films prepared by our colloidal method are highly crystalline. Thus, we find these films to be highly homogenous, crystalline, and oriented.

The high quality of these films allows for their repeated polymerization by the introduction of unreacted monomers (**Figure 9.1C**). Typically, COF film thickness is controlled by modifying the starting monomer concentration used for their polymerization. However, when we attempted to polymerize COF-5 films with higher monomer concentrations, we found that resultant COF films, while thicker, were substantially less oriented and smooth (**Figure 9.19**). This finding is consistent with our recent observations of uncontrolled nucleation and growth at higher monomer concentrations[665, 689]. However, by polymerizing COF films using this templated growth approach, removing the substrate, immersing this substrate in a fresh monomer solution, and resubjecting it to the polymerization conditions, we can continue the polymerization of our films without a reduction in film quality. As an example, we sequentially increase the thickness of the TP-COF

films from 20 nm, to 40 nm, to 60 nm over the course of three equivalent polymerizations (**Figure 9.1D** and **Figure 9.1E**). In each sequential polymerization, we find that the roughness, crystallinity, and film orientation as evaluated by AFM and GI-WAXS do not discernably change (**Figure 9.36 - Figure 9.40**). Collectively, these observations demonstrate that templated colloidal polymerization offers a level of synthetic control not available in previously reported 2D polymerization strategies.

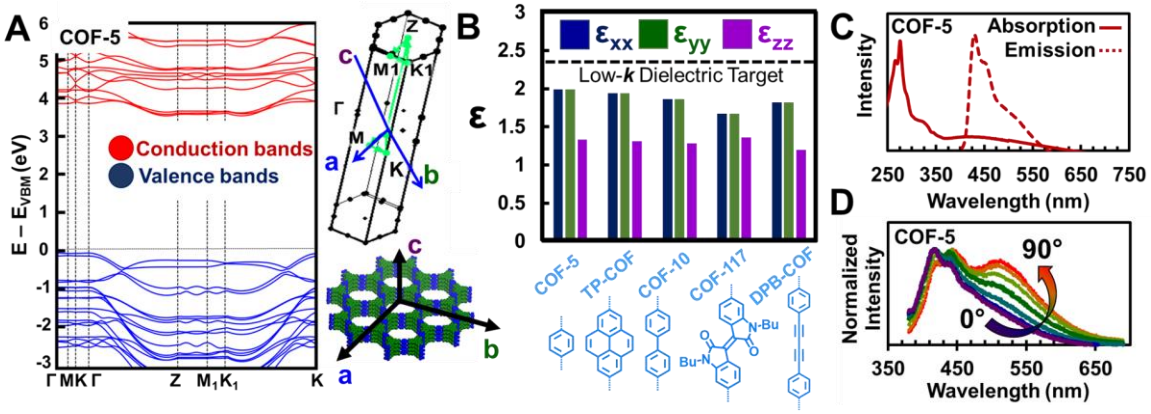

Figure 9.2. Optoelectronic properties of COF films. A) Electronic band structures calculated at the DFT/PBE0 level for COF-5 and the corresponding Brillouin zone. **B)** Electronic dielectric tensors calculated at the DFT/PBE level for all COFs studied **C)** Optical absorption and emission ($\lambda_{Excitation}$ = 325 nm) profiles for COF-5. **D)** Polarization dependent emission of COF-5 films, that resolves the in-plane (purple, 0°) component from the cross-plane (red, 90°) component.

Boronate ester-linked 2D COF films studied here are sufficiently electrically insulating to serve as dielectric layers. DFT calculations using the PBE0 functional predict that COF-5 has an indirect bandgap of 3.6 eV and a direct gap of 3.9 eV (**Figure 9.2A**). The DFT-calculated band

structures have minimal band dispersion along the in-plane direction (Γ-M-K-Γ and Z-M_1-K_1) in both their valence and conduction bands, indicating low in-plane charge-carrier mobility. However, band dispersions of 0.4 eV along the out-of-plane direction in both the valence and conduction bands can be observed, which suggests that anisotropic charge transport may occur in COF-5 crystallites, as has been observed previously[665]. The DFT-calculated diagonal components of the static electronic dielectric tensors (ε_{xx}, ε_{yy}, and ε_{zz}) are less than 2 for the five boronate ester-linked 2D COFs studied. As such, they are all candidate low-***k*** dielectrics (**Figure 9.2B**). We note that in COF-5 the ionic contribution to the total static dielectric tensor is calculated to be negligible (**Table 9.3**); thus, we only considered the electronic contribution to the dielectric tensor in the other four 2D COFs. Experimentally, we find that the first COF-5 optical absorption feature occurs at approximately 325 nm (3.8 eV), which is consistent with the predicted DFT bandgap (**Figure 9.2C**). When the COF-5 structure is excited at 325 nm, we find that its emission profile is similar to monomeric HHTP, consistent with the limited electronic conjugation across boronate-ester bonds[690]. Ultimately, these experimental and computational studies show that crystalline, 2D COF layers are electronically insulating and as pristine crystallites are promising as low-***k*** dielectrics.

9.5 Anisotropic Optical Emission

The pristine nature of the films prepared by colloidal syntheses permits the observation of their anisotropic optical emission. The polarization-dependent emission of a COF-5 film has a strong cross-plane emission feature at 530 nm, which has been previously assigned to the formation of triphenylene exciplexes (**Figure 9.2D**)[690]. The observation of these cross-plane features suggests that the COF-5 films are highly oriented across the entirety of the sample. In contrast, polarization-dependent emission anisotropy is found to be far weaker in COF-5 films

grown on the substrates under non-colloidal conditions (**Figure 9.47**)[425]. This finding agrees with our understanding that previously obtained materials were likely contaminated with unoriented aggregates, which complicated their reliable measurement and subsequent integration into devices. Taken together, these measurements show that the COF films studied here are high quality.

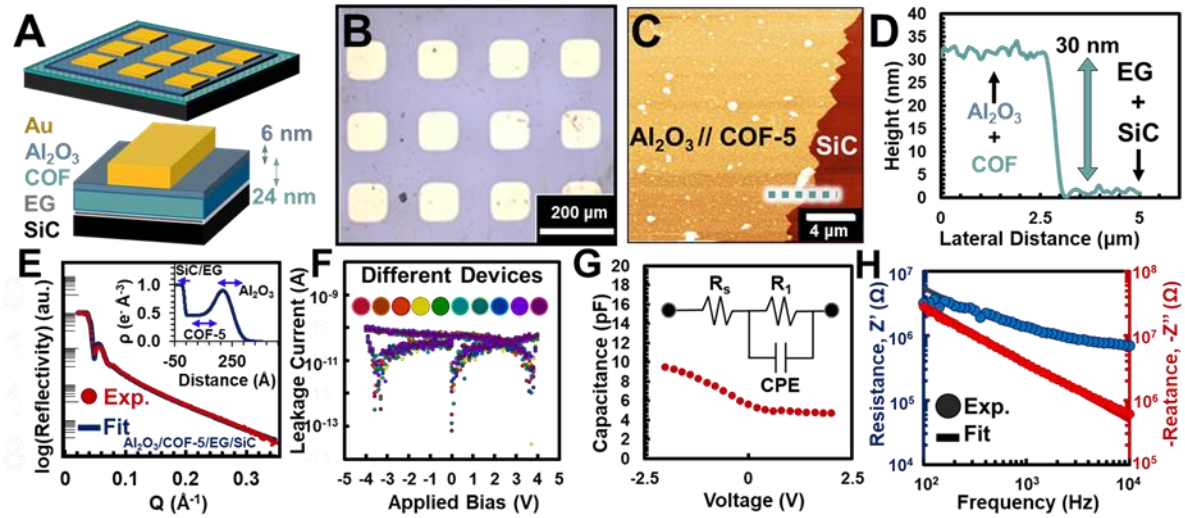

Figure 9.3. COF-5 dielectric layer impedance measurements. A) Schematic of Au contacted Al_2O_3/COF-5 dielectric bilayer capacitors grown on epitaxial graphene (EG)/SiC wafers. **B)** Optical microscopy image of a patterned array of Au pads on full coverage Al_2O_3/COF-5/EG/SiC. **C)** AFM micrograph of the Al_2O_3/COF bilayer revealing a step edge at a scratch. **D)** Height profile extracted from the AFM green linecut in Figure 3C. **E)** X-ray reflectivity (XRR) data and the model fit of the Al_2O_3/COF-5/EG/SiC layered structure. Inset: Extracted electron density profile from XRR fit. **F)** Leakage current versus the applied bias voltage across ten different COF devices shown in Figure 3E. **G)** Capacitance of the Al_2O_3/COF-5 bilayer as a function of applied voltage measured at 1 kHz with a 100 mV signal. Inset: Modeled equivalent circuit of impedance behavior fit in Figure 3H. **H)** Bode plots of the real (resistance, Z') and imaginary (reactance, Z") impedance components and respective model fits.

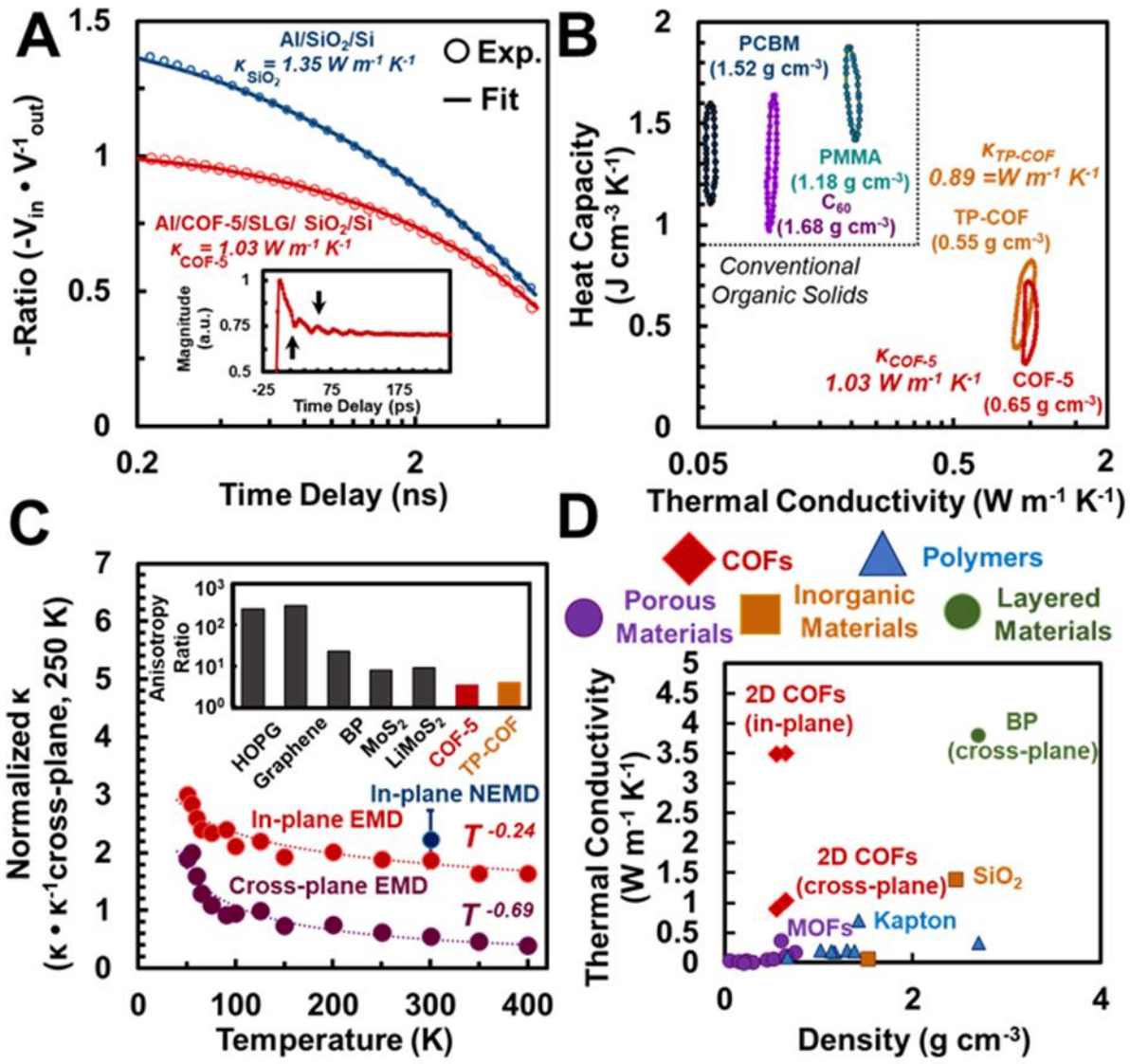

Figure 9.4. Thermal Properties of 2D COF Thin Films. A) Characteristic TDTR data as a function of pump-probe delay time and analytical model fits. Inset: picosecond acoustics. **B)** Contour plots of thermal conductivity and heat capacity at a 95% confidence interval. **C)** Molecular dynamics simulations of temperature-dependent thermal conductivities. Dashed lines

represent analytical fits generated from the temperature dependence shown. **D)** Density and thermal conductivity of common materials.

9.6 Thermally Conductive Layers

COF thin films are found to be substantially more thermally conductive than previously studied low-***k*** dielectrics. To measure the thermal properties of COF thin films with time-domain thermoreflectance we first deposited Al transducer layers (see supporting information for a more detailed description of measurement) onto several sub-100 nm thick COF films (**Figure 9.62**). From TDTR measurements, we extract the COFs' longitudinal sound speeds, heat capacities, and cross-plane thermal conductivities (

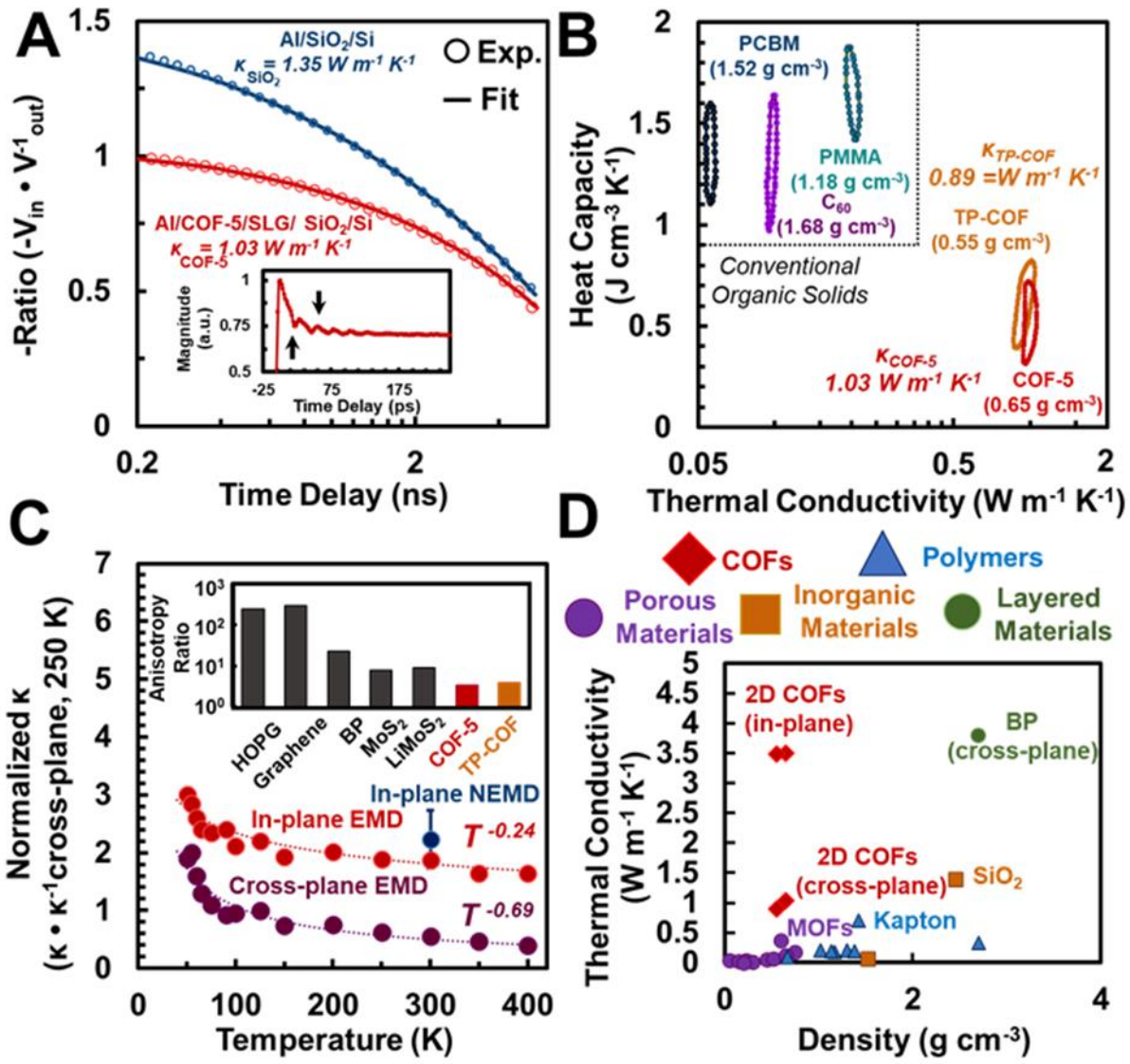

Figure 9.4). Fitted TDTR data revealed that COF-5 and TP-COF have volumetric heat capacities of $C_{v,\,COF\text{-}5} = 0.52 \pm 0.08$ J cm^{-3} K^{-1} and $C_{v,\,TP\text{-}COF} = 0.56 \pm 0.09$ J cm^{-3} K^{-1} and cross-plane thermal conductivities of $\kappa_{COF\text{-}5} = 1.03 \pm 0.15$ W m^{-1} K^{-1} and $\kappa_{TP\text{-}COF} = 0.89 \pm 0.14$ W m^{-1} K^{-1} within a 95% confidence interval, respectively (

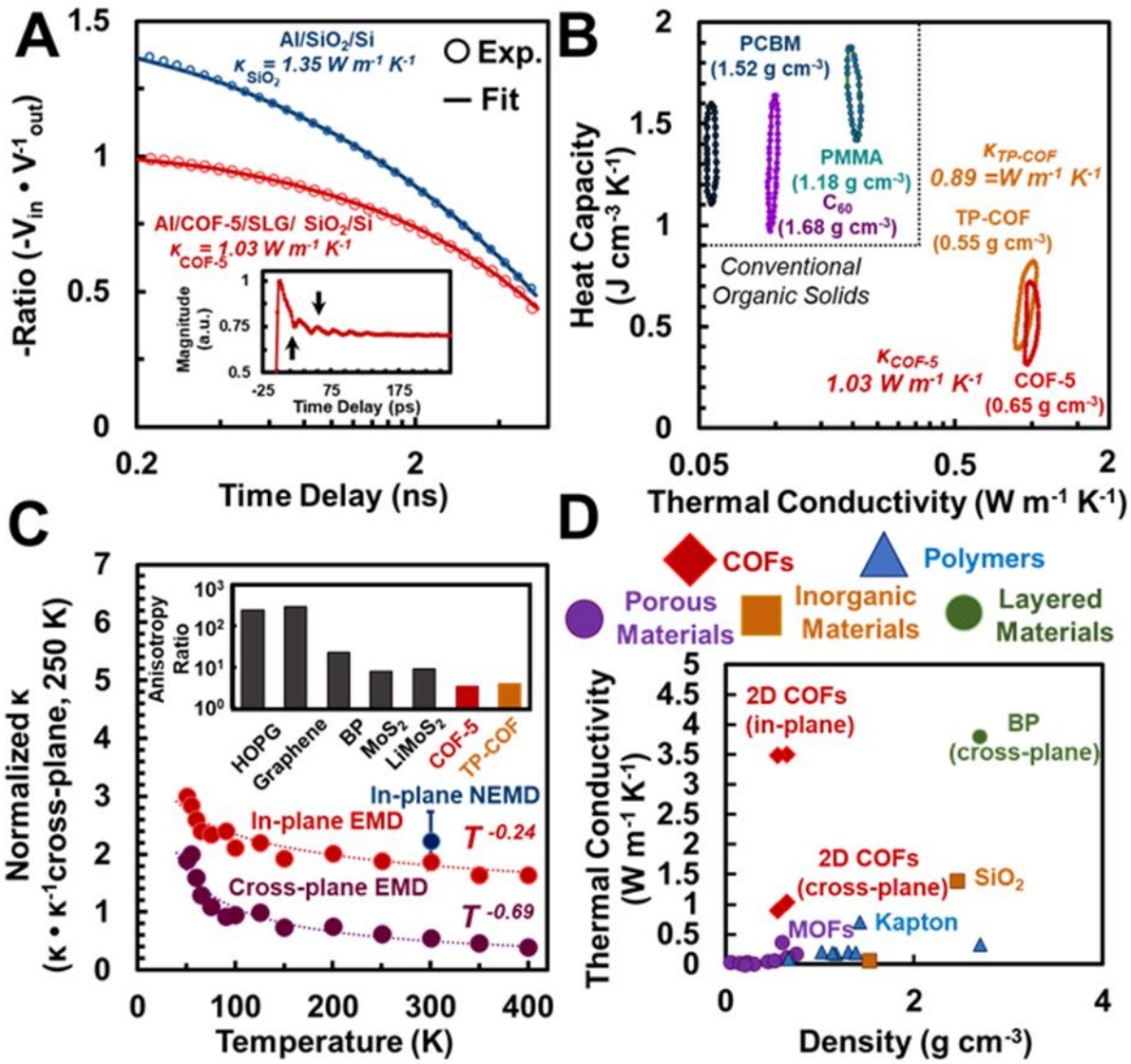

Figure 9.4B). These values are corroborated with FDTR measurements performed independently (**Figure 9.57 - Figure 9.62**). We also find that the interfacial thermal conductances across the COF/Al and COF/SLG interfaces are quite high (h_K > 100 MW m^{-2} K^{-1}; **Figure 9.60**), which highlights another advantage of COF films that are well-interfaced to their underlying substrate.

Compared to other organic or porous materials, 2D COFs have unusually high thermal conductivities. This finding is consistent with the structural regularity, large porosities, strong interlayer interactions, and low heat capacities unique to 2D COFs. From picosecond acoustics, we determine sound speeds for COF-5 (

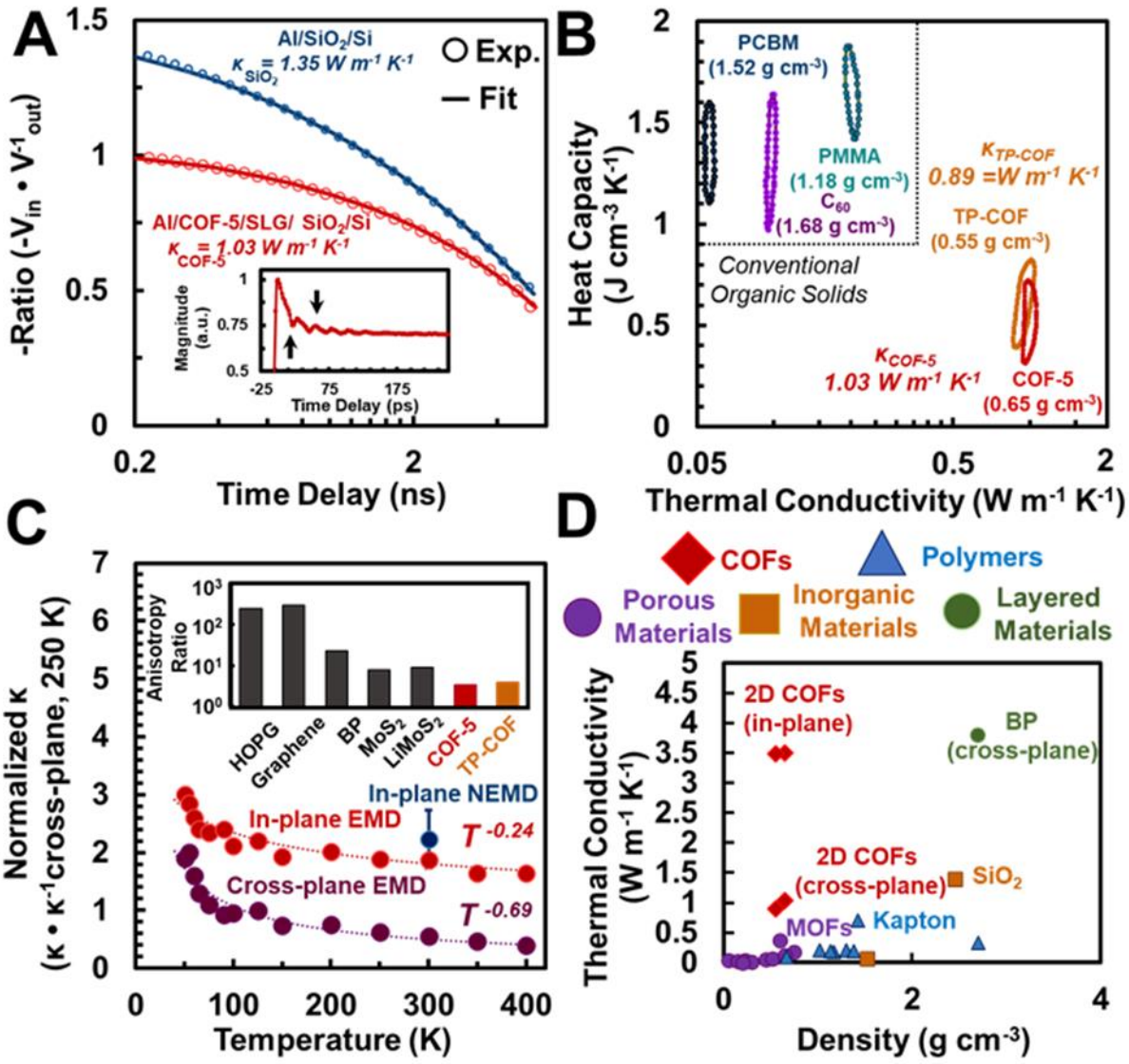

Figure 9.4A, inset) and TP-COF to be 2000 ± 300 m s^{-1} and 1900 ± 300 m s^{-1}, respectively. These sound speeds are higher than those recently observed in MOFs (e.g. MOF-5: 1184 m s^{-1}) despite similar porosity to the two COFs studied here.[691, 692] These relatively high thermal conductivities and longitudinal sound speeds (as compared to other porous materials) demonstrate how unique thermal properties arise from COF's covalently linked, layered, precisely porous structures.

Molecular dynamics (MD) simulations give additional insight into COF-5's high anisotropic thermal conductivities. The MD-predicted cross-plane thermal conductivities are slightly lower than the measured values (see supporting information for more discussion), which could be a consequence of the insufficiencies of the interatomic potential used to model our 2D COFs. However, these differences are equivalent in all crystallographic directions and so, through the same analysis, we extract an anisotropy ratio of 3.4 between in-plane and cross-plane COF-5 thermal conductivities (

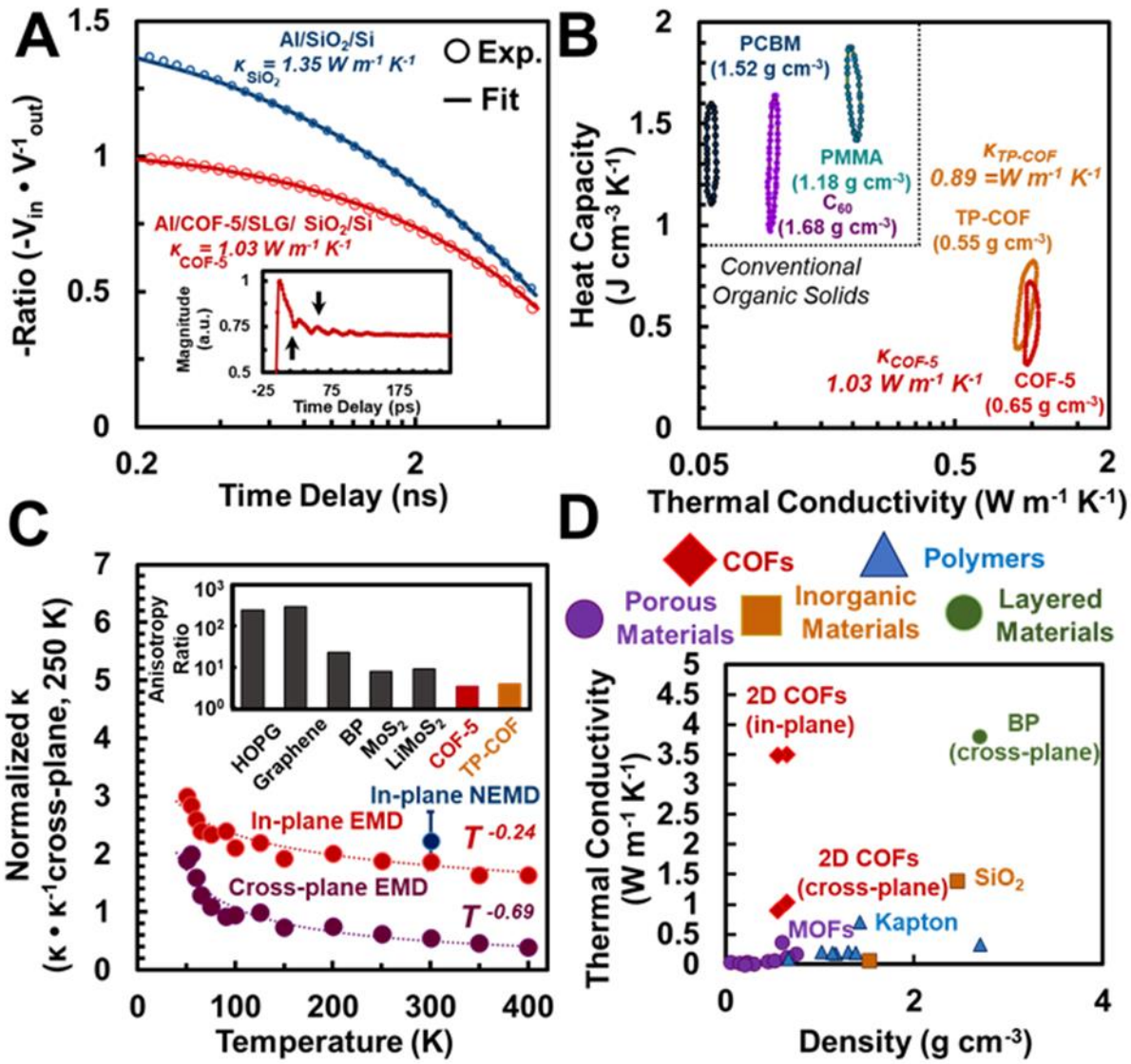

Figure 9.4C). By this approach, we predict that the in-plane $\kappa_{COF\text{-}5} = 3.5$ W m^{-1} K^{-1}. These absolute thermal conductivities and anisotropy ratios are lower for 2D COFs than other layered crystals (

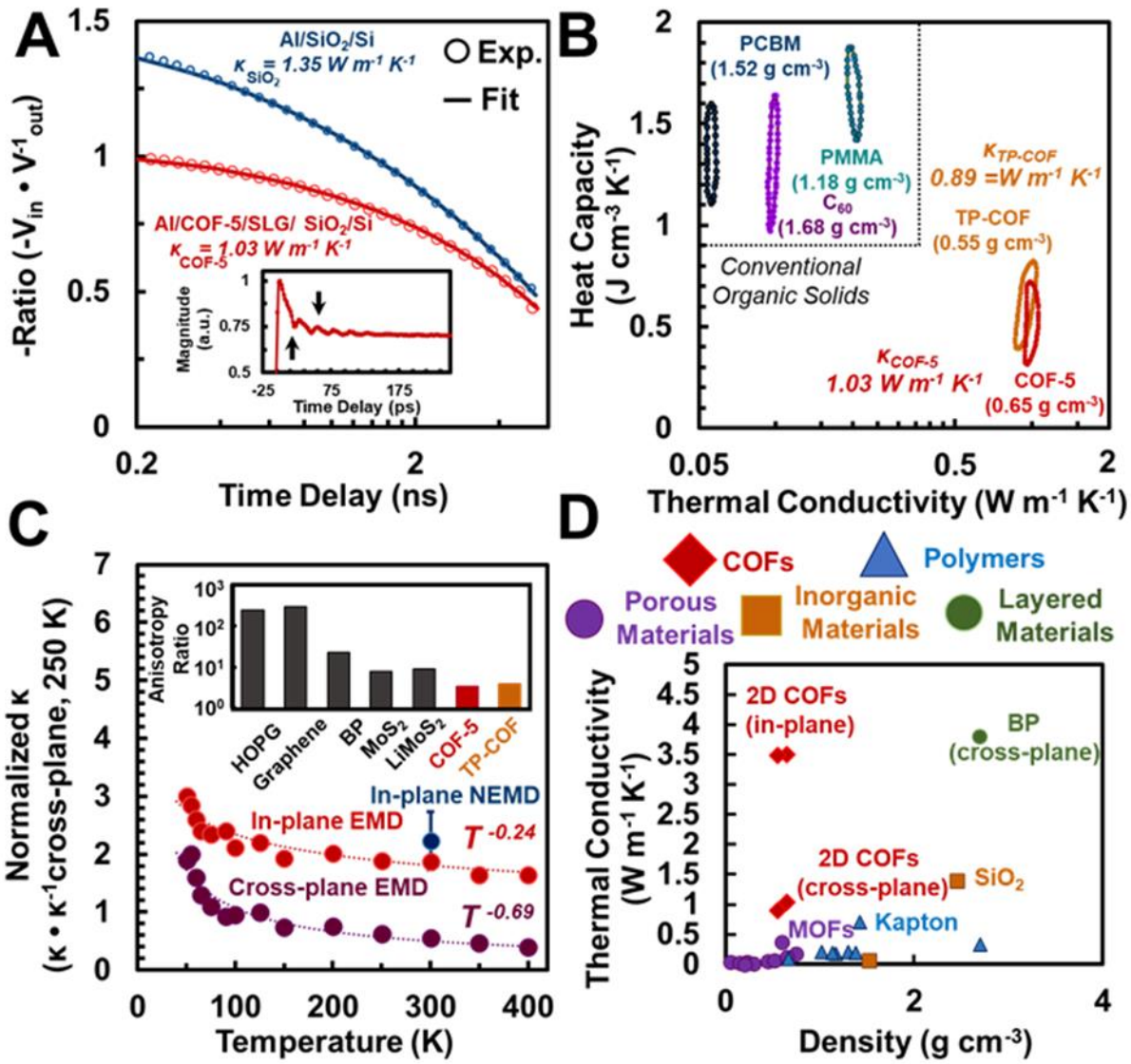

Figure 9.4C, inset), which likely arises as a function of periodic voids in their van der Waals surface. The temperature dependent thermal conductivities of COF-5 in the range of 50 K – 400 K are shown to exhibit a $T^{-0.24}$ and $T^{-0.69}$ dependence in the in-plane and cross-plane directions, respectively (

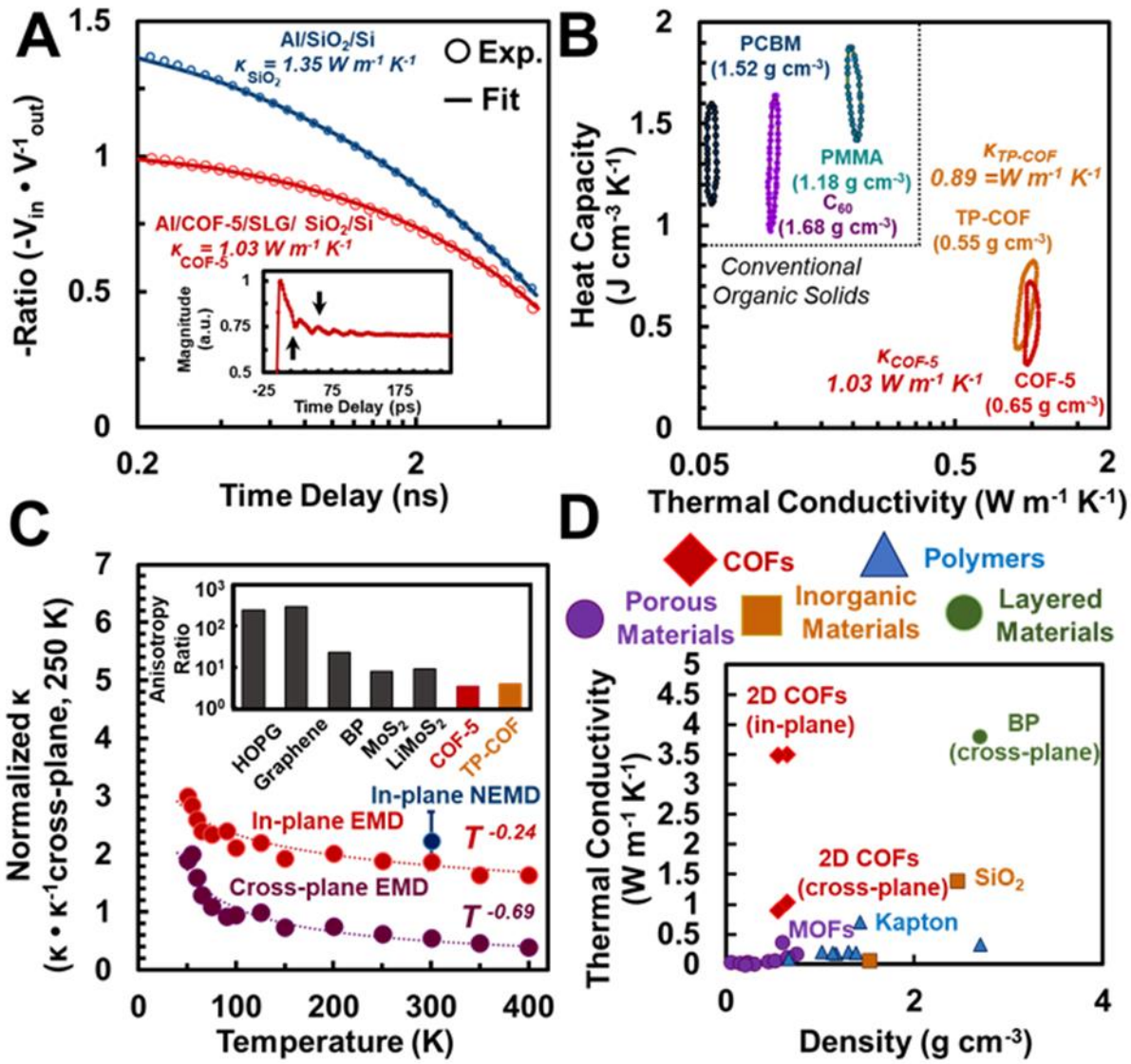

Figure 9.4C). These temperature dependencies suggest that anharmonic processes dictate the thermal transport in the cross-plane direction more heavily than the in-plane direction[693].

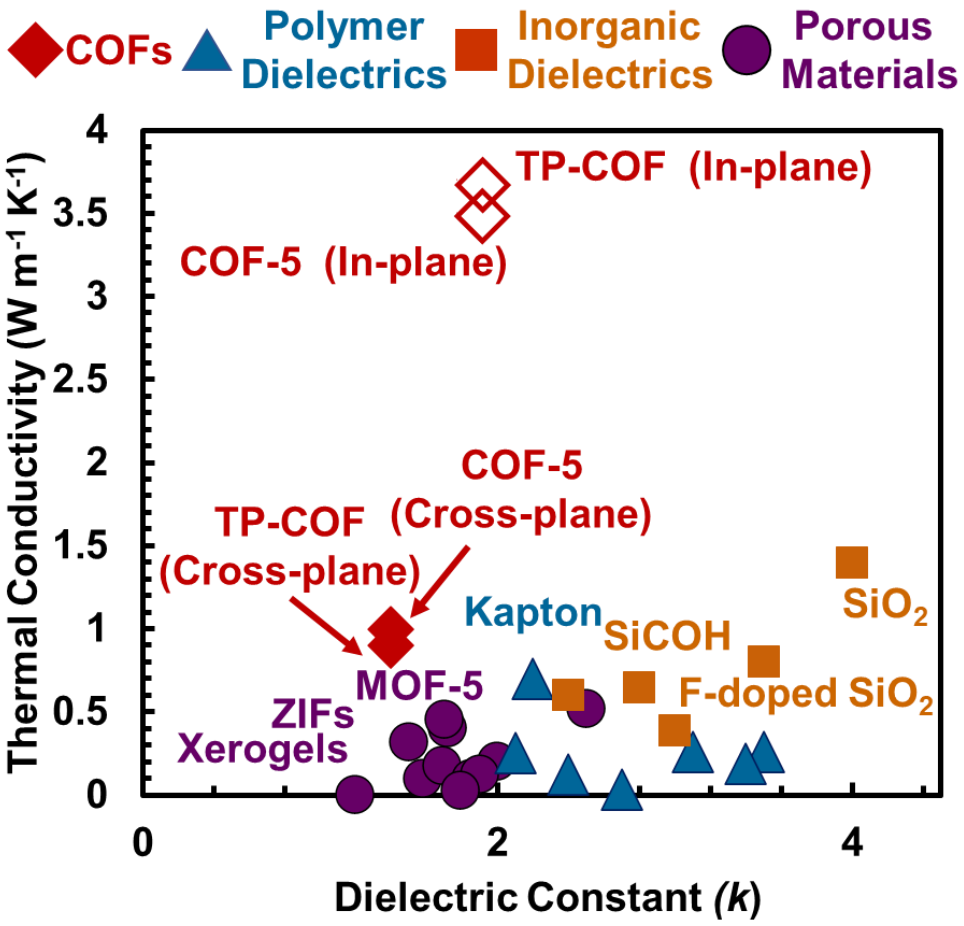

Figure 9.5. Meta-analysis of thermal conductivities in low-*k* dielectrics. Filled diamonds are experimentally measured thermal conductivities and open diamonds are evaluated using computational techniques. For initial reports of the values included in the plot we direct the reader to the supplementary information.

2D COFs overcome the traditional tradeoff between dielectric permittivity and thermal conductivity found in all known low-***k*** dielectric materials (**Figure 9.5**). For example, dense amorphous metal oxides such as Al_2O_3 or HfO_2 are relatively thermally conductive compared to

low-density aerogels, which are thermally insulating due to their porous structure and tortuous solid networks[680, 694, 695]. Although the densities of 2D COFs are comparable to those of aerogels, their thermal conductivities are comparable to those of materials that are an order of magnitude more dense, such as conventional amorphous metal oxide dielectrics[695]. This uniquely high thermal conductivity is most likely driven by the well-interfaced van der Waals contact of porous 2D polymers that are arranged as eclipsed stacks. Furthermore, we suspect that the thermomechanical properties of 2D COFs could be modulated by the introduction of molecular guests, as has been observed in other porous materials, which unlocks the possibility of responsive materials[696, 697]. Taken together, 2D COFs mark a new regime of materials design that combines low densities with high thermal conductivities.

In conclusion, we find that 2D COFs unique combination of structural, thermal, and electronic properties make them promising as low-***k*** dielectric layers. Through a templated colloidal synthetic approach, we access smooth COF thin-film dielectrics of tailorable thickness on technologically relevant substrates. Through our experimental and computational investigations, we find that 2D boronate ester-linked 2D COFs are electronically insulating, consistent with their lack of long-range conjugation, and are low-***k*** dielectrics, consistent with their permanent porosities. We also find that 2D COFs exhibit unusually high thermal conductivities for low density, low-***k*** dielectrics, a combination of properties that was recently identified by the *International Roadmap for Semiconductors* as a necessary materials development for next-generation integrated circuits. Taken together, these results demonstrate that exotic combinations of properties can be unlocked by using synthetic chemistry to generate precise

materials. We suspect that these findings will inspire a broad investigation of designer function in synthetically diverse 2D polymers.

9.7. Chapter 9, Supplementary Information

Materials and Methods

Materials

All monomers, solvents, and catalysts were either purchased from commercial sources or prepared following literature reported protocols. All materials were used as received without further purification. Anhydrous THF was obtained from a solvent purification system (JC Myer System).

Instrumentation

Nuclear Magnetic Resonance. ^{1}H NMR spectra were acquired on a 400 MHz Agilent DD MR-400 system or Bruker Avance III 500 MHz spectrometer and recorded at 25 °C. All chemical shifts were calibrated using residual solvent as internal reference ($CDCl_3$: 7.26 ppm for ^{1}H NMR. DMSO: 2.5 ppm for ^{1}H NMR).

Grazing-Incidence X-ray Diffractions. GIWAXS measurements were performed at either:

Advanced Photon Source at Argonne National Laboratory using the 8-ID-E Beamline under vacuum. All measurements were conducted with an incidence angle of 0.14° using 10.92 keV (λ = 1.135 Å) X-rays. The scattered photons were recorded on a Pilatus 1 M detector located 228 mm from the sample. Exposure times were varied such that the pixel with maximum counts was at

80% of saturation. In some cases, significant silicon substrate scatter was observed. The raw images were merged, pixel coordinates were transformed to q-space, and line cuts were generated using GIXSGUI for Matlab.[647]

or

Advanced Light Source-Lawrence Berkeley National Laboratory using Beamline Station 7.3.3 under a He atmosphere. A photon energy of 10 keV (λ = 1.24 Å). Data was collected by a Pilatus 2M detector with a pixel size of 0.172 × 0.172 mm and 1475 × 1679 pixels used to capture the 2D scattering patterns at a distance of 300 mm from the sample. A silver behenate standard was used as a calibrant. The grazing angle, α, was varied from 0.08° to 0.25°. Data were analyzed using the Nika macro for Igor Pro.[698]

All data is shown as a function of the scattering vector:

$$Q = \frac{4\pi}{\lambda}\sin(\theta) \qquad (1)$$

Simulated X-ray Diffraction. Simulations of 2D COF X-ray scattering profiles were carried out

in MaterialsStudio (ver.5.0). First, the unit cell was constructed piecewise in a primitive P6 unit cell with the *a=b* lattice parameter set to be approximately the distance between two COF vertices based on approximate molecular bond lengths. The *c* parameter was set to be 3.5 Å, which is the interlayer spacing of graphene. We then used a Forcite geometry optimization routine with a universal forcefield to optimize the unit cell size with convergence tolerances of Energy = 10^{-3} kcal mol^{-1} and Force = 0.5 kcal mol^{-1} $Å^{-1}$.

Diffraction simulation and Pawley refinement were carried out using the Reflex software package. COF models and their simulated patterns were Pawley refined to experimental patterns iteratively until the RWP value converges. The pseudo-Voigt profile function was used for whole profile fitting. The final RWP and RP values were calculated to be less than 5% in all cases. Simulated XRD patterns were calculated from the refined unit cell and compared with the experimentally observed patterns.

X-ray Reflectivity. XRR measurements were carried out using a Rigaku ATXG diffractometer equipped with an 18 kW Cu rotating anode (λ = 1.5418 Å) operating at a voltage of 50 kV and a current of 240 mA, with a collimated beam of 0.1 mm x 2 mm (0.2 mm^2). All measurements are plotted in terms of the scattering vector *Q* (Eq. 1), normalized to the measured incident beam intensity, and corrected for geometrical footprint and background signal. The XRR analysis was performed using Motofit software.[699] Three different systems were studied: COF-5/EG/SiC, COF-5/EG/SiO_2/Si and Al_2O_3/COF-5/EG/SiO_2/Si. The fittings show a well-resolved electron density

profile which confirms no intermixing or degradation of the COF-5 film. All the electron densities correspond to the expected bulk-like values. The electron density for the COF-5 film was a free parameter determined from the fit. The fitting parameters are included in the tables. The fit determined electron density profiles are shown as insets in each of the XRR figures.

Fluorescence Spectroscopy. Emission and excitation spectra were recorded on a Horiba Jobin Yvon Fluorolog-3 fluorescence spectrophotometer equipped with a 450 W Xe lamp, emission and excitation polarizer, double excitation and double emission monochromators, a digital photon-counting photomultiplier and a secondary InGaAs detector for the NIR range. Correction for variations in lamp intensity over time and wavelength was achieved using a solid-state silicon photodiode as the reference. The spectra were further corrected for variations in photomultiplier response over wavelength and for the path difference between the sample and the reference by multiplication with emission correction curves generated on the instrument. To collect emission spectra of the 2D COF films, films were mounted in a proprietary film holder. When emission polarization was noted as “normalized”, we divided the intensity of all emission intensities by the maximum emission intensity.

Atomic Force Microscopy. Atomic force microscopy (AFM) was conducted using the facilities at the Northwestern Atomic and Nanoscale Characterization Experiment Center (NUANCE) on a SPID Bruker FastScan AFM using a gold tip under the non-contact mode in air. To prepare films for imaging, they were scored with a pair of Teflon-coated forceps so as to not damage the

underlying Si. These films were then imaged across the score to evaluate their thickness and roughness.

Scanning Electron Microscopy. 2D COF films were cleaved and mounted with carbon tape or double-sided copper taper on vertical SEM mounts. Each sample was coated with 7 nm of Os (SPI Osmium Coater, with OsO_4 as a volatile source) to create a conformal conductive coating prior to imaging. Images were collected with a Hitachi SU 8030 scanning electron microscope with an acceleration voltage of 5 kV at a magnification of 80,000.

Preparation of epitaxial graphene on SiC. Epitaxial graphene was grown on 4H-SiC(0001) wafers (Cree, Inc.) by ultra-high vacuum (UHV) annealing. The SiC wafers were diced into 5x9 mm rectangles (American Precision Dicing, Inc.) and the resulting substrates were first degreased via sonication in acetone and isopropanol before being introduced into the UHV chamber with base pressure ~$5 \cdot 10^{-11}$ Torr. Substrates were degassed for 12 hours at 500 °C prior to graphitization at 1200 °C for 20 minutes while maintaining chamber pressure below $5 \cdot 10^{-8}$ Torr. During annealing, substrate temperature was monitored using an infrared pyrometer ($\varepsilon = 0.85$).

Capacitor Fabrication and Characterization. First, atomic layer deposition (ALD) was used to grow Al_2O_3 on COF-coated EG-SiC substrates using a Savannah S100 ALD reactor (Cambridge

Nanotech, Cambridge MA). The substrates were loaded into the chamber pre-heated to 100 ̊C. The base pressure of the chamber was maintained at 0.8 Torr with a constant N_2 flow rate of 20 sccm. The growth was done at 100 ̊C by exposing samples to sequential doses of the metal oxide precursor (trimethyl aluminum (TMA), Aldrich, 99%) and deionized water interspersed with dry N_2 purge steps between each precursor dose. For Al_2O_3 growth, a single ALD cycle consisted of a TMA pulse for 0.015 s and a 30 s purge, followed by a H_2O pulse for 0.015 s and a second 30 s purge. During growth, TMA precursor bottles were kept at room temperature. An approximately 6-nm-thick Al_2O_3 was grown on COF layer by using 75 pulses of TMA using 0.8 Å/cycle growth rate, as verified independently for atomic force microscopy and ellipsometry. The thickness of Al_2O_3/COF-5 dielectric bilayer was extracted from topography images (Figure 3c,d) using tapping mode in an Asylum Cypher AFM system.

Parallel plate capacitors were completed by growing 100-nm-thick Au films on Al_2O_3/COF-5 dielectric bilayer using a thermal evaporator (Nano38, Kurt J. Lesker Company). The evaporation was done through a shadow mask with rectangular holes of 100 μm x 100 μm using a growth rate of 1 Å/sec.

Impedance Measurements.

Impedance measurements were carried out by a Solartron 1260 impedance analyzer using an AC amplitude of 100 mV in a frequency range of 100 Hz to 10 kHz. This frequency range was chosen

because the signal was too noisy below 100 Hz and series resistance from the SiC wafer interfered with measurements above 10 kHz. Au pads were contacted by tungsten cat whisker soft-probes (Signatone, SE-SM) to avoid puncturing the COF dielectric. Capacitance-frequency (C-f) measurements were performed at zero dc bias, and capacitance-voltage (C-V) measurements were conducted at 1 kHz. Capacitance values were verified independently using the C-V module of a 4200 Semiconductor Characterization System (SCS), Keithley Instruments. Leakage measurements were also carried by the 4200 SCS system using a remote current preamplifier. Impedance data was analyzed by model fitting using ZPlot/ZView software from Scribner Associates, Inc.

General Synthesis of COF Films. First, a graphene-coated Si/SiO_2 substrate (1 cm^2 UniversityWafer, Inc.) was placed into a scintillation vial. Then, solutions of HHTP (2 mM) and bisboronic acid (3 mM) were prepared separately in a solvent blend of 80/16/4 vol CH_3CN:1,4-dioxane:1,3,5-trimethylbenzene. These solutions were then filtered to remove any insoluble particulates. These solutions were then added in a 1:1 vol ratio to the substate-containing scintillation vial, producing a 20 mL solution of 1 mM HHTP and 1.5 mM PBBA. This scintillation vial was then sealed and heated to 80 °C for 24 hrs. After 24 hrs, a milky suspension had formed in the scintillation vial. Approximately 90% of the solution was then decanted and diluted with fresh 80/16/4 vol CH_3CN:1,4-dioxane:1,3,5-trimethylbenzene. This procedure was repeated 3 times to sufficiently dilute any colloidal species present in solution. The wafer was then removed from solvent with forceps and allowed to dry in air producing a conformal coating on the graphene substrate.

Grazing-incidence X-ray Diffraction. All grazing-incidence X-ray wide-angle scattering shown in the manuscript was performed at the Advanced Photon Source at Argonne National Laboratory using the 8-ID-E Beamline under vacuum. The crystallites were irradiated until the detector was 80 % of saturated an incidence angle of 0.14° in using 10.92 keV (λ = 1.135 Å) X-rays. The scattering was recorded on a Pilatus 1 M detector located 228 mm from the sample. In some cases, significant silicon substrate scatter was observed. The raw images were merged, pixel coordinates were transformed to q-space, line cuts generated using GIXSGUI for Matlab.[647]

Density Functional Theory. The macroscopic static dielectric tensors considering the electronic contribution[700] are calculated with density functional theory (DFT) method at the PBE level using the Vienna Ab initio Simulation Package (VASP)[701] with D3 Vdw corrections. Γ-centered Monkhorst-Pack *k*-meshes are adopted in both geometry optimizations and (SCF (see Table SX). The convergence criterion for the total energy is 10^{-8} eV and 0.01 eV Å^{-1} for the forces. Gaussian smearing is 0.01 eV. The lattice parameters after geometry optimization of each COF are shown in Table S1. The off-diagonal components in the calculated macroscopic static dielectric tensors are negligibly small.

Fluorescence Spectroscopy. Emission and excitation spectra were recorded on a Horiba Jobin Yvon Fluorolog-3 fluorescence spectrophotometer equipped with a 450 W Xe lamp, emission and excitation polarizer, double excitation and double emission monochromators, and a digital photon-counting photomultiplier. Correction for variations in lamp intensity over time and wavelength was achieved using a solid-state silicon photodiode as the reference. The spectra were further corrected for variations in photomultiplier response over wavelength and for the path difference between the sample and the reference by multiplication with emission correction curves generated

on the instrument. To collect polarization-dependent emission spectra of the 2D COF films, films were mounted in a proprietary film holder and a polarizer was put into the emission path. When emission polarization was noted as “normalized”, we divided the intensity of all emission intensities by the maximum emission intensity.

Device Measurement. Impedance measurements were carried out by a Solartron 1260 impedance analyzer using an AC amplitude of 100 mV in a frequency range of 100 Hz to 10 kHz. This frequency range was chosen because the signal was too noisy below 100 Hz and series resistance from the SiC wafer interfered with measurements above 10 kHz. Au pads were contacted by tungsten cat whisker soft-probes (Signatone, SE-SM) to avoid puncturing the COF dielectric. Capacitance-frequency (C-f) measurements were performed at zero dc bias, and capacitance-voltage (C-V) measurements were conducted at 1 kHz. Capacitance values were verified independently using the C-V module of a 4200 Semiconductor Characterization System (SCS), Keithley Instruments. Leakage measurements were also carried by the 4200 SCS system using a remote current preamplifier.

Heat Capacity and Thermal Conductivity Measurements. In our TDTR setup, sub-picosecond laser pulses emanate from a Ti:Saphhire oscillator at 80MHz repetition rate. The pulses are separated into a pump path that heats up the sample and a time-delayed probe path that is reflected from the Al transducer. The reflected probe beam provides a measure of the change in the thermoreflectance due to the decay of the thermal energy deposited by the pump beam. A modulation of 8.8 MHz is applied by an electro-optic modulator on the pump beam and the ratio of the in-phase to out-of-phase signal of the reflected probe beam recorded at that frequency by a lock-in amplifier ($-V_{in}/V_{out}$) for up to 5.5 ns after the initial heating event. The pump and probe

beams are focused on to the Al transducer at $1/e^2$ radii values of 10 and 5 μm, respectively. To simultaneously measure the thermal conductivity and heat capacity of our COFs, we fit a three-layer thermal model to our experimental data. We also perform FDTR measurements on our COF-5 sample. Similar to TDTR, FDTR is also a laser-based metrology implemented to measure thermal properties of a sample. The Au-coated sample is periodically heated via a sinusoidally modulated (100 kHz - 5 MHz) pump laser at 488 nm wavelength. The sample's temperature will fluctuate with the same frequency as the pump laser, but with a time delay. This phase delay is characteristic of the thermal properties of the sample. The temperature is measured using a concentric probe laser (532 nm), which is sensitive to the thermoreflectance of Au. The frequency-dependent time delay measured as a phase delay of the reflected probe laser with respect to the pump laser modulation frequency is measured with a photodiode connected to a lock-in amplifier. For more information, see the Supporting Information.

MD Simulation. Our molecular dynamics (MD) simulations are performed with the LAMMPS code[702] and the interatomic interactions are described by the adaptive intermolecular reactive empirical bond order (AIREBO) potential.[703] We apply periodic boundary conditions in all directions. The computational domains are equilibrated under the Nose-Hoover thermostat and barostat,[704] (which is the NPT integration with the number of particles, pressure and temperature of the system held constant) for a total of 1ns at 0 bar pressure. Following the NPT integration, an NVT integration (with constant volume and number of particles) is prescribed to fully equilibrate the structures at the desired temperature for another 1 ns. Note, we prescribe a time step of 0.5 fs for all our simulations. After equilibration, the thermal conductivities of our COFs at different temperatures predicted via the Green-Kubo (GK) approach under the EMD framework. In this

formalism, the thermal conductivities of our COFs along the x-,y-(in-plane) and z-(cross-plane) directions are calculated as,

$$\kappa_{x,y,z} = \frac{1}{k_B V T^2} \int_0^\infty < S_{x,y,z}(t) \bullet S_{x,y,z}(0) > dt \qquad (1)$$

Here t is time, T and V are the temperature and volume of the systems, respectively, and $< S_{x,y,z}(t)\, S_{x,y,z}(0) >$ is the component of the heat current autocorrelation function (HCACF) in the prescribed directions.

Monomer Synthetic Procedures

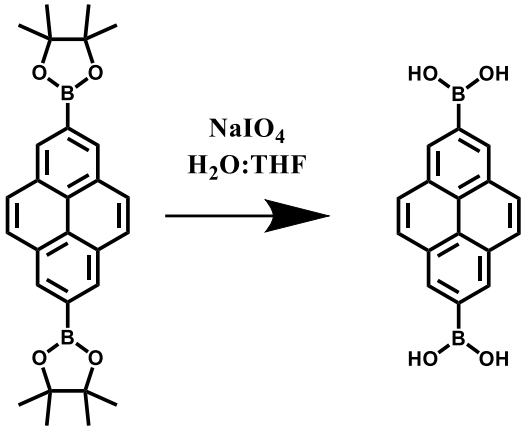

Scheme 9.1. Synthesis of 2,7-pyrenebisboronic acid (PyBA)

Synthesis of 2,7-pyrenebisboronic acid. PyBA was prepared by an adaptation of a previously reported synthesis.[705] A THF:H_2O mixture (300 mL, 4:1 vol) of pyrene-2,7-diboronicester (5g, 11 mmol, 1.0 equiv.) and $NaIO_4$ (3.5 g, 27.5 mmol, 2.5 equiv.) was prepared in a 500 mL RBF and stirred at room temperature for 16 hrs under N_2. During the course of this reaction, a white precipitate was formed. The reaction mixture was then diluted with H_2O (300 mL) and filtered. During filtration, the product was washed with an additional 300 mL of H_2O, taking care to not allow the product to dry completely on the filter paper. The product was then flushed with hexanes and dried, which produced a white powder (2.6 g, 81%). ^{1}H NMR analysis of this product was consistent with a previous report.[705]

^{1}H NMR (400 MHz, DMSO-d_6, 298 K): δ ppm 8.68 (4H, s, 1,3,6,7-H-pyrene), 8.44 (4H, s, 4,5,9,10-H-pyrene), 8.16 (4H, s, BO–H)

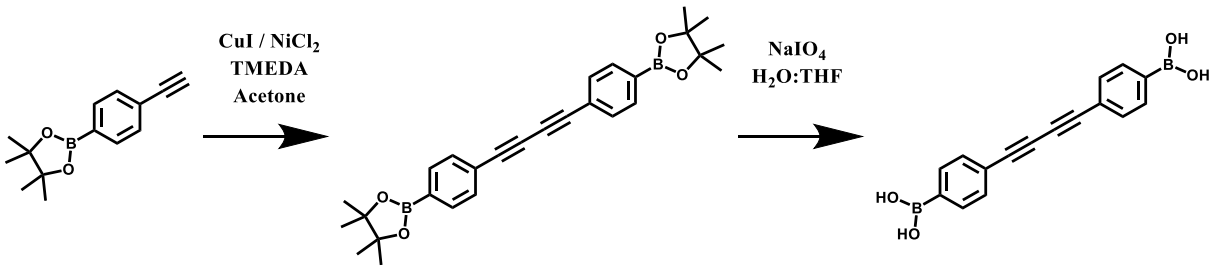

Scheme 9.2. Synthesis of 4,4′-diphenylbutadiynebis(boronic acid)

Synthesis of 4,4′-diphenylbutadiynebis(pinacolborane). The synthesis of this product was adapted from a previous report.[174] A 100 mL round bottom flask was charged with CuI (0.752 g, 3.94 mmol, .05 equiv.), NiCl2● $6H_2O$ (0.936 g, 3.94 mmol, .05 equiv.), and tetramethylethylenediamine (TMEDA) (1.836 g, 15.784 mmol, 0.25 equiv.). Acetone (50 mL) was added, and as the solids dissolved the mixture became dark green. 4-ethynylbenzeneboronic acid pinacole ester (18 g, 78.8 mmol, 1.0 equiv.) was added to this mixture, which was then stirred for 16 hours. The solvent was removed by rotary evaporation to yield a green residue that was washed with H_2O (300 mL). The resultant solid was isolated via filtration through a Büchener funnel. This solid was subsequently recrystallized from CH_3CN as a white solid, collected via filtration through a Büchener funnel, and dried under vacuum (5.25 g, 12 mmol, 30 %). ^{1}H NMR analysis of this product was consistent with a previous report.[174]

^{1}H-NMR ($CDCl_3$, 400 MHz, 298 K) δ 7.65 (d, J = 9.0 Hz, 4H); 7.52 (d, J = 9.0 Hz, 4H); 1.34 (s, 24H).

Synthesis of 4,4′-diphenylbutadiynebis(boronic acid). The synthesis of this compound was adapted from a previous report.[174] In a 20 mL scintillation vial, 4,4'-diphenylbutadiyne pinacole borane (1.00 g, 2.20 mmol, 1.00 equiv.) and sodium periodate (1.0 g, 5.00 mmol, 2.27 equiv.) were dissolved in THF:H2O (4:1 v/v, 30 mL). This mixture was stirred at room temperature with nitrogen actively bubbling through it for 30 minutes, after which 1M HCl (5 mL) was added via syringe. The reaction vessel was subsequently sealed and allowed to stir for an additional 24 hours. At this point, the reaction mixture was poured into 100 mL of H_2O, filtered through a Büchener funnel, and washed with an additional 100 mL of H_2O. This product was then flushed with 100 mL of diethyl ether. This powder was dried under vacuum for 10 minutes to afford a fine white powder (444 mg, 1.5 mmol, 69%). ^{1}H NMR analysis of this product was consistent with a previous report.[174]

^{1}H-NMR (DMSO-d_6, 400 MHz, 298 K) δ 8.26 (s, 4H); 7.82 (d, J = 7.5 Hz, 4H); 7.57 (d, J = 7.5 Hz, 4H).

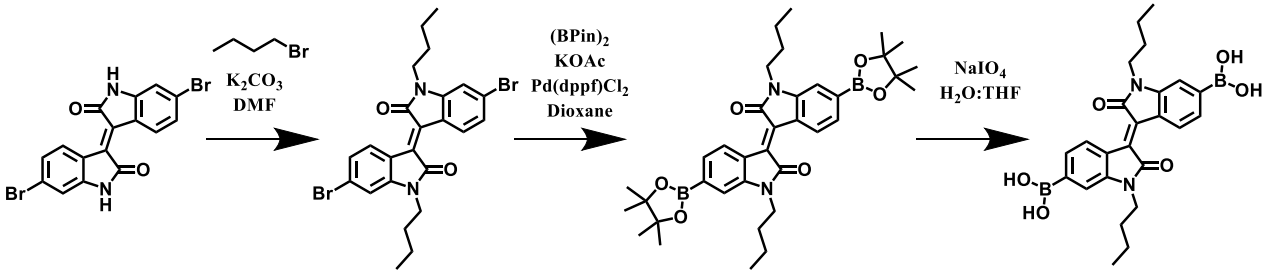

Scheme 9.3. Synthesis of N,N'-dihexyl-6,6'-isoindigobis(boronic acid)

Synthesis of *N,N*'-dibutyl-6,6'-bisbromoisoindigo. To a flame-dried 300 mL RBF, dibromoisoinidio (750 mg, 1.785 mmol, 1.0 equiv.), K_2CO_3 (1.65 g, 11.90 mmol, 6.67 equiv.), and DMF (32 mL) were added. Then, butylbromide (0.56 mL, 5.24 mmol, 2.93 equiv.) was added via syringe and heated to 110 °C. After 14 hours, the reaction mixture was cooled to room temperature and quenched with saturated NH_4Cl. The product was then extracted with EtOAc (2 X 100 mL). These fractions were then combined, washed with water (5 X 100 mL) and brine (2 X 100 mL). The organic fraction was then collected, dried with anhydrous $MgSO_4$, filtered, and concentrated *in vacuo* to give *N,N*'-dihexyl-6,6'-bisbromoisoindigo as a deep red product (590 mg, 1.1 mmol, 62%). ^{1}H NMR analysis of this product was consistent with a previous report.[706]

^{1}H NMR (400 MHz, cdcl$_3$) δ 9.07 (d, *J* = 8.6 Hz, 1H), 7.17 (dd, *J* = 8.6, 1.9 Hz, 1H), 6.93 (d, *J* = 1.9 Hz, 1H), 3.74 (t, *J* = 7.4 Hz, 2H), 1.66 (d, *J* = 7.4 Hz, 2H), 1.41 (d, *J* = 7.8 Hz, 2H), 0.97 (t, *J* = 7.4 Hz, 3H).

Synthesis of *N,N*'-dibutyl-6,6'-isoindigobis(pinacolborane). The following were added to a 50 mL Schlenk flask: N,N'-dihexyl-6,6'-bisbromoisoindigo (500 mg, 0.94 mmol, 1.0 equiv.), $(BPin)_2$ (596 mg, 2.35 mmol, 2.5 equiv), KOAc (332 mg, 3.38 mmol, 3.6 equiv.), $Pd(dppf)Cl_2 \bullet CH_2Cl_2$ (80 mg, 0.09 mmol, 0.10 equiv.), and 1,4-dioxane (8 mL). This flask was then closed with a septum and degassed under constant N_2 flow for 15 min. The reaction mixture was then heated at 80 °C for 40 hrs. Then, the reaction was cooled to room temperature and diluted with CH_2Cl_2. This mixture was then passed through a silica gel plug on a fritted funnel and washed with CH_2Cl_2. The filtrate was then concentrated *in vacuo* to yield a sticky red residue, which was mixed with MeOH (15 mL) and placed in a freezer. After 2 hrs, the precipitate was collected and dried to give *N*,*N*'-dihexyl-6,6'-isoindigobis(pinacolborane) as a deep red product (510 mg, .82 mmol, 87%). ^{1}H NMR analysis of this product was consistent with a previous report.[706]

^{1}H NMR (499 MHz, $cdcl_3$) δ 9.15 (d, *J* = 7.9 Hz, 1H), 7.49 (dd, *J* = 7.9, 1.1 Hz, 1H), 7.15 (s, 1H), 3.81 (t, *J* = 7.4 Hz, 2H), 1.73 – 1.68 (m, 2H), 1.46 – 1.41 (m, 2H), 1.37 (s, 12H), 0.97 (t, *J* = 7.4 Hz, 3H).

Synthesis of *N,N*'-dibutyl-6,6'-isoindigobis(boronic acid). To a 20 mL scintillation vial *N*,*N*'-dihexyl-6,6'-isoindigobis(pinacolborane) (100 mg, 0.16 mmol, 1.0 equiv.), $NaIO_4$ (85 mg, 0.4 mmol, 2.5 equiv.), a THF:H_2O 4:1 vol. (15 mL) were added. The vial was then placed under N_2. After 3 days, the reaction was diluted with H_2O (15 mL) and filtered while continuously adding

water (50 mL), taking care to not let the product dry to completion on the filter paper. Finally, the product was washed with hexanes and dried under vacuum. This yielded *N*,*N*'-dihexyl-6,6'-isoindigobis(boronic acid) as a bright red solid (52 mg, .112 mmol, 70% yield). Reliable NMR analysis was not possible due to insolubility of the product.

Monomer Nuclear Magnetic Resonance

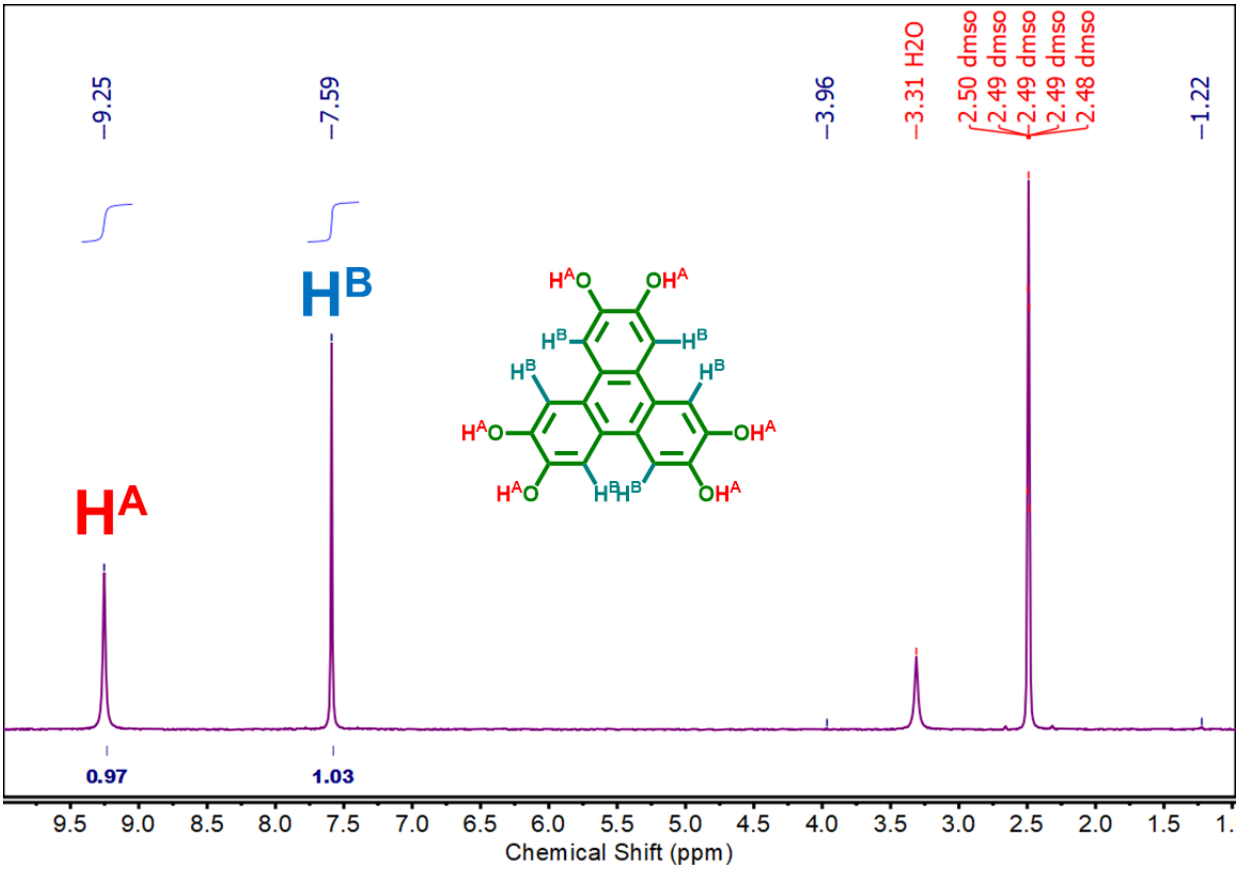

Figure 9.6. ^{1}H nuclear magnetic resonance spectra of 2,3,6,7,10,11-Hexahydroxytriphenylene Hydrate (HHTP), purchased from TCI America

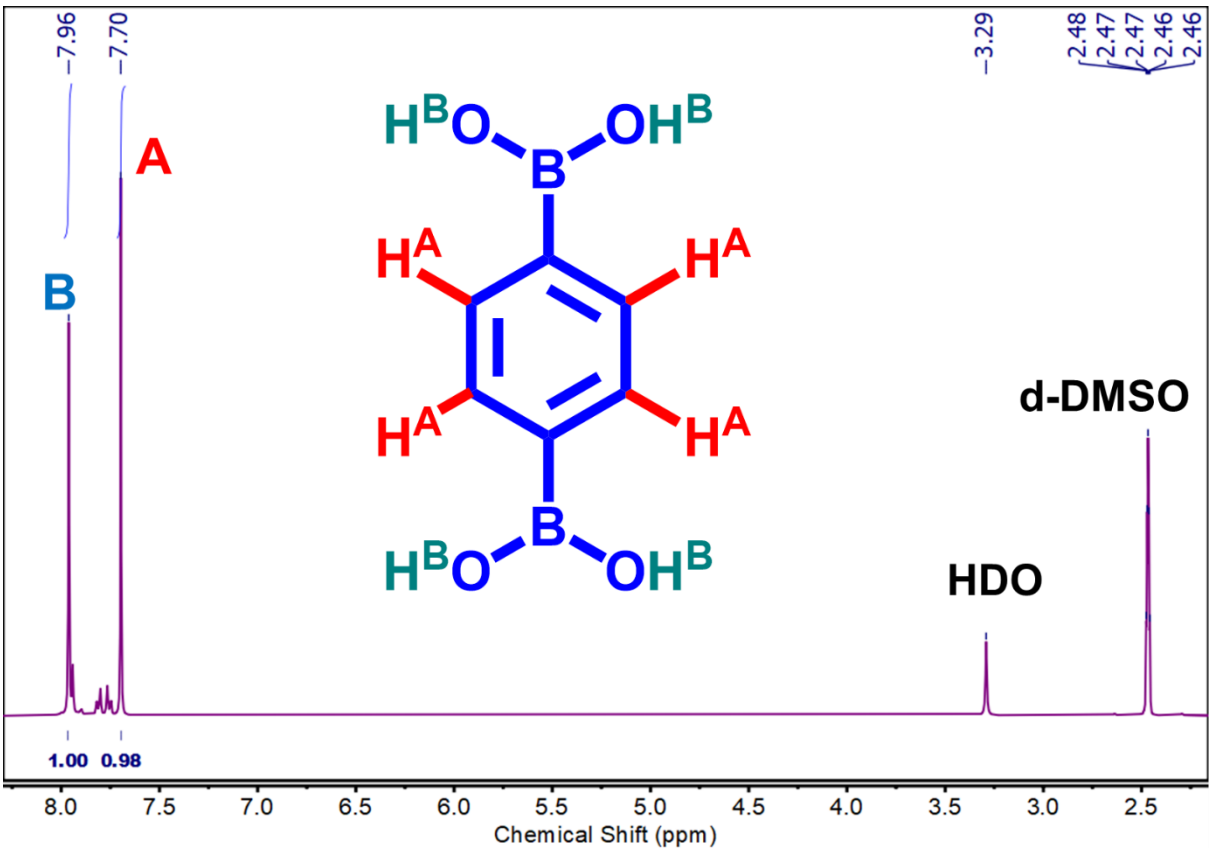

Figure 9.7. [1]H nuclear magnetic resonance spectra of 1,4-phenylenebisboronic acid (PBBA), purchased from Sigma Aldrich

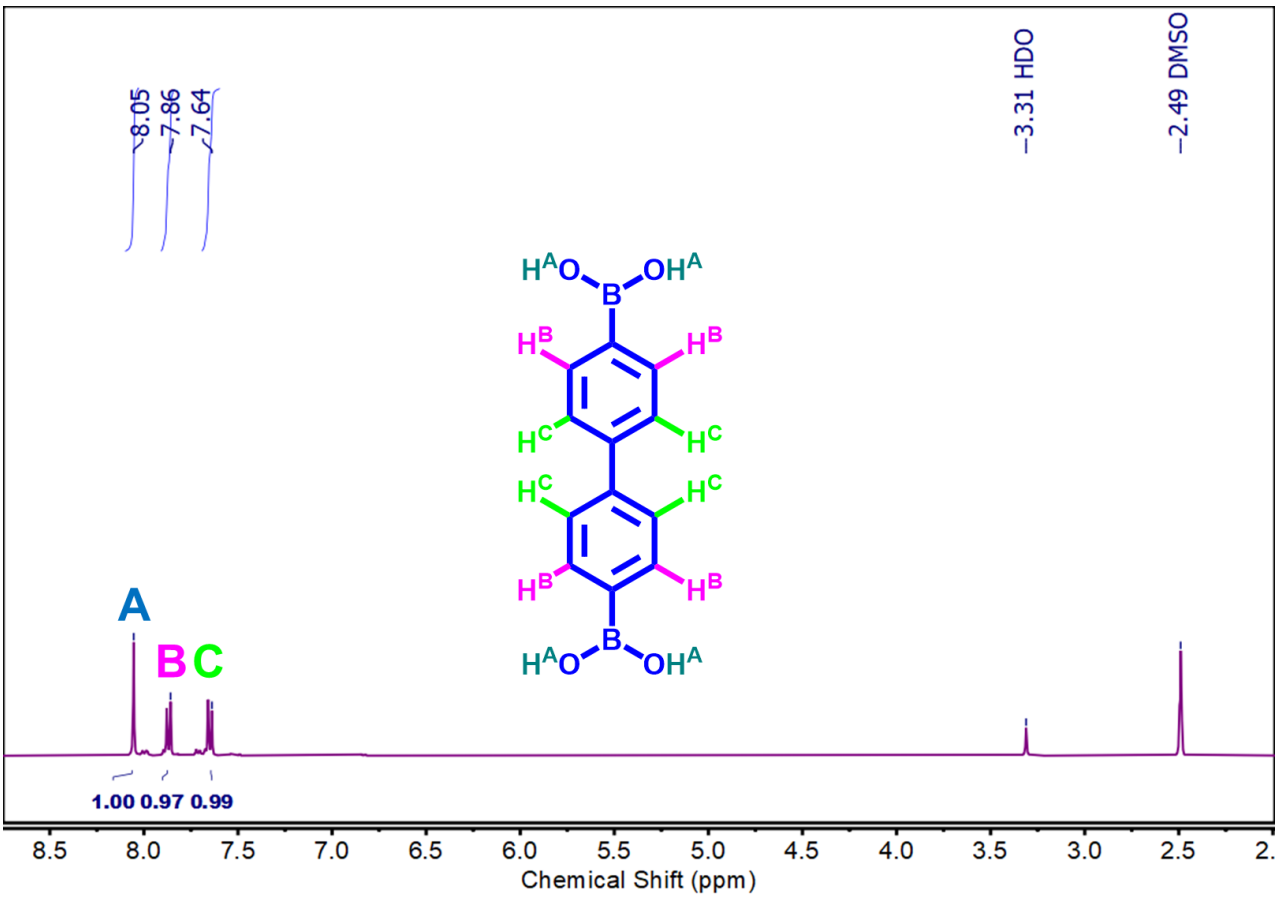

Figure 9.8. ^{1}H nuclear magnetic resonance spectra of 4,4'-biphenylbisboronic acid (BBBA), purchased from Sigma Aldrich

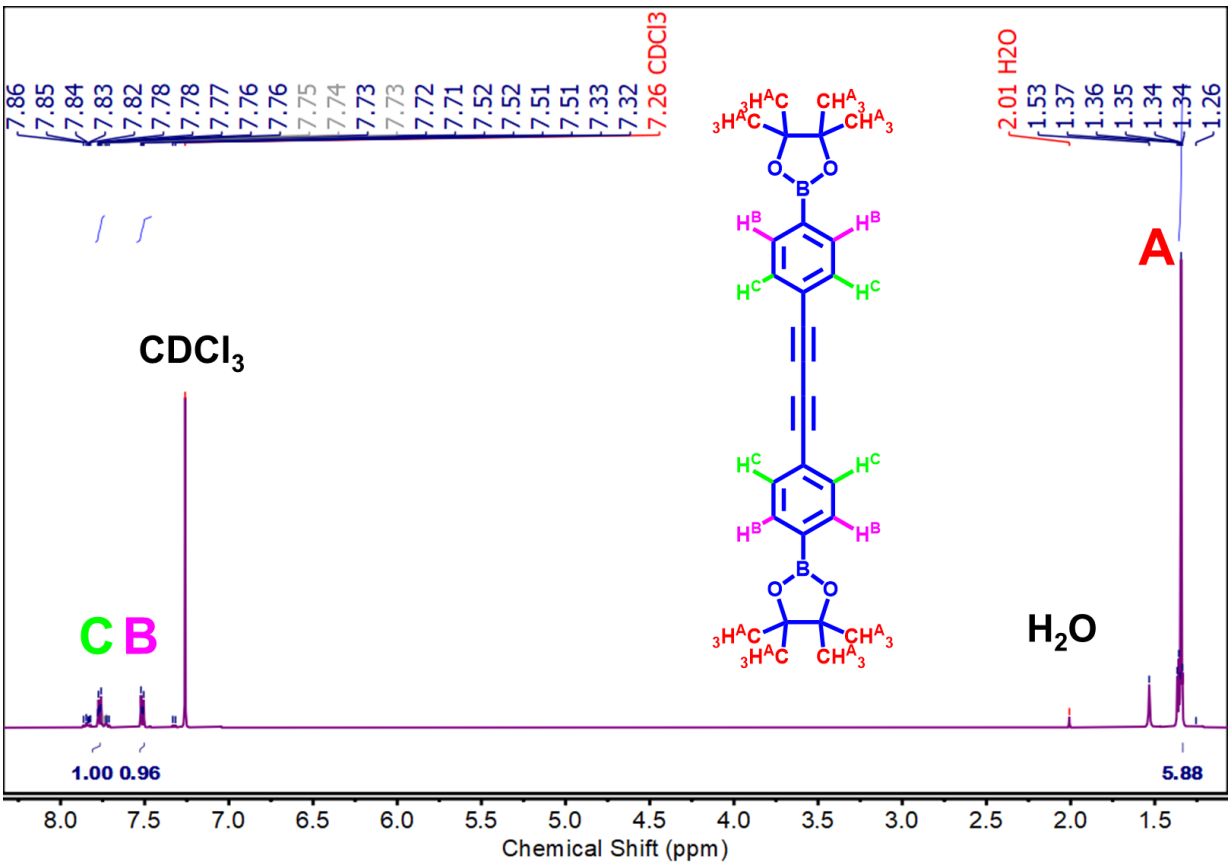

Figure 9.9. ^{1}H nuclear magnetic resonance spectra of

4,4′-diphenylbutadiynebis(pinacolborane)

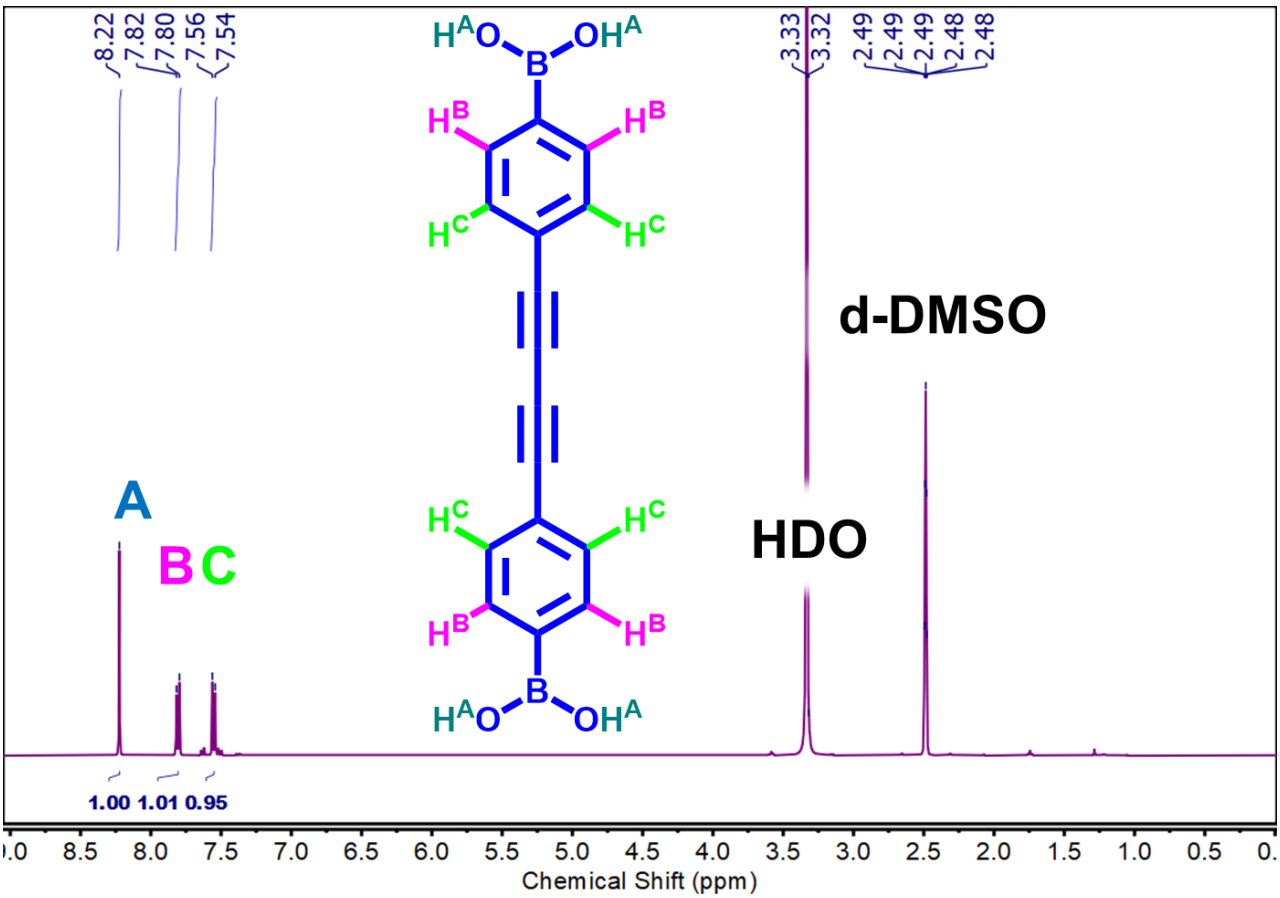

Figure 9.10. ^{1}H nuclear magnetic resonance spectra of

4,4′-diphenylbutadiynebis(boronic acid)

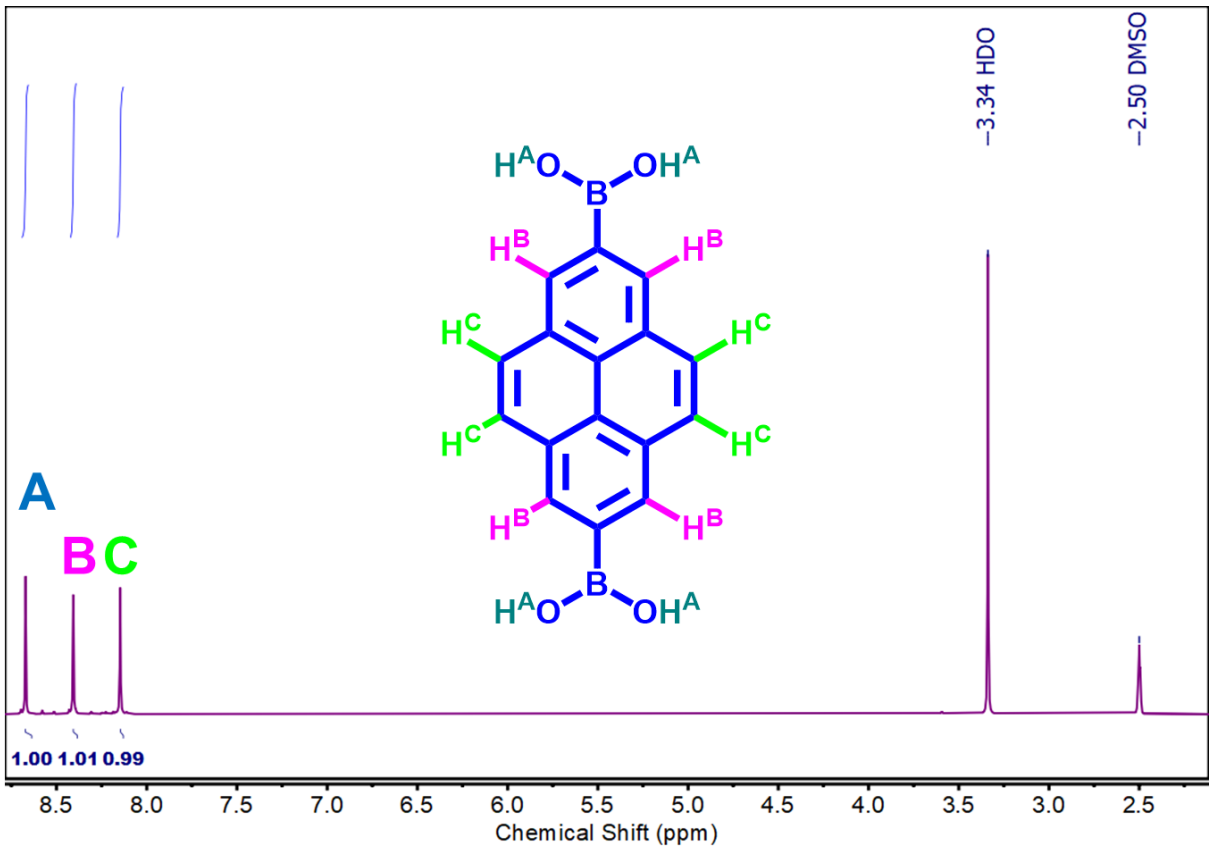

Figure 9.11. ^{1}H nuclear magnetic resonance spectra of

2,7-pyrenebis(boronic acid)

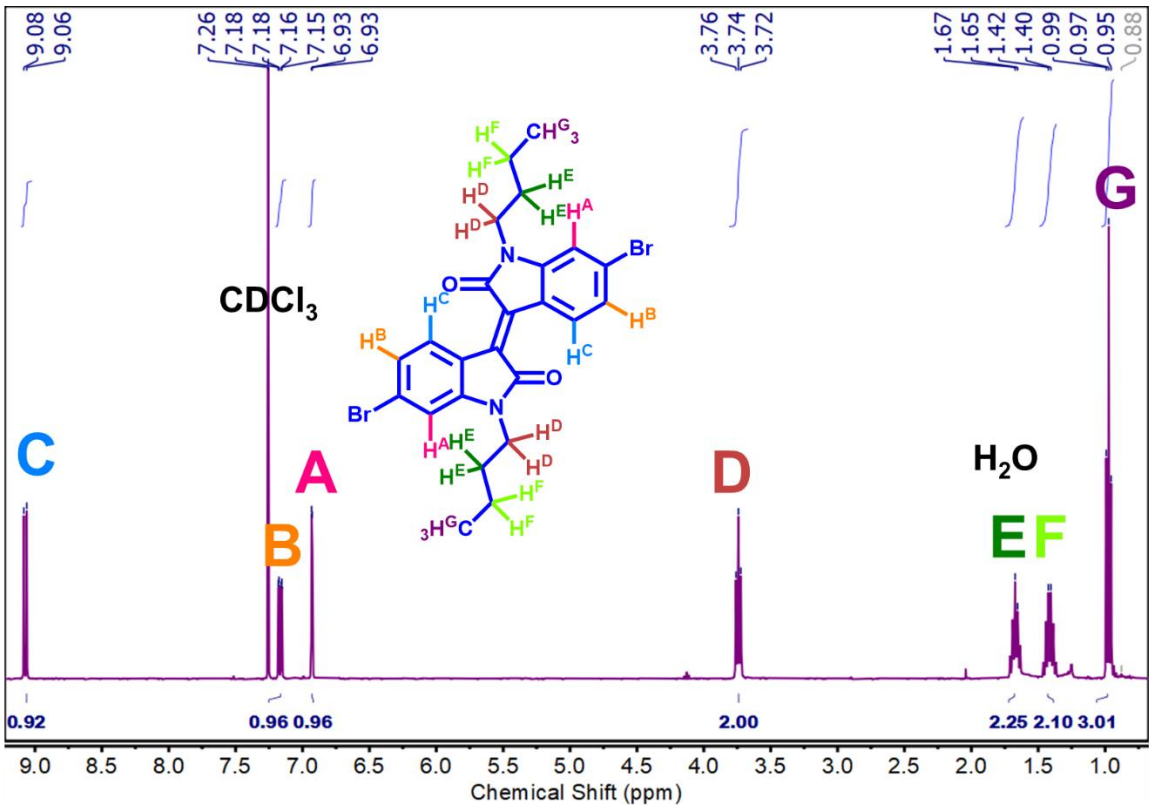

Figure 9.12. ^{1}H nuclear magnetic resonance spectra of *N*,*N*'-dibutyl-6,6'-bisbromoisoindigo

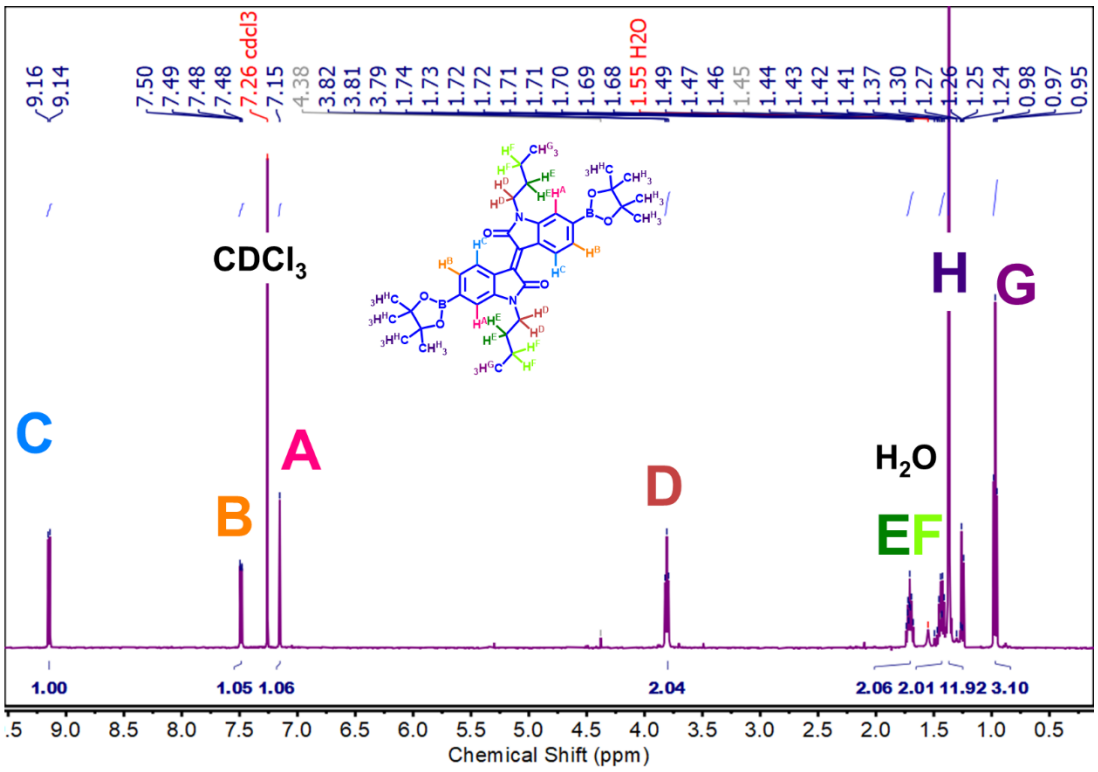

Figure 9.13. ^{1}H nuclear magnetic resonance spectra of *N*,*N*'-dibutyl-6,6'-bis(pinacolborane)isoindigo

2D COF Synthetic Procedures

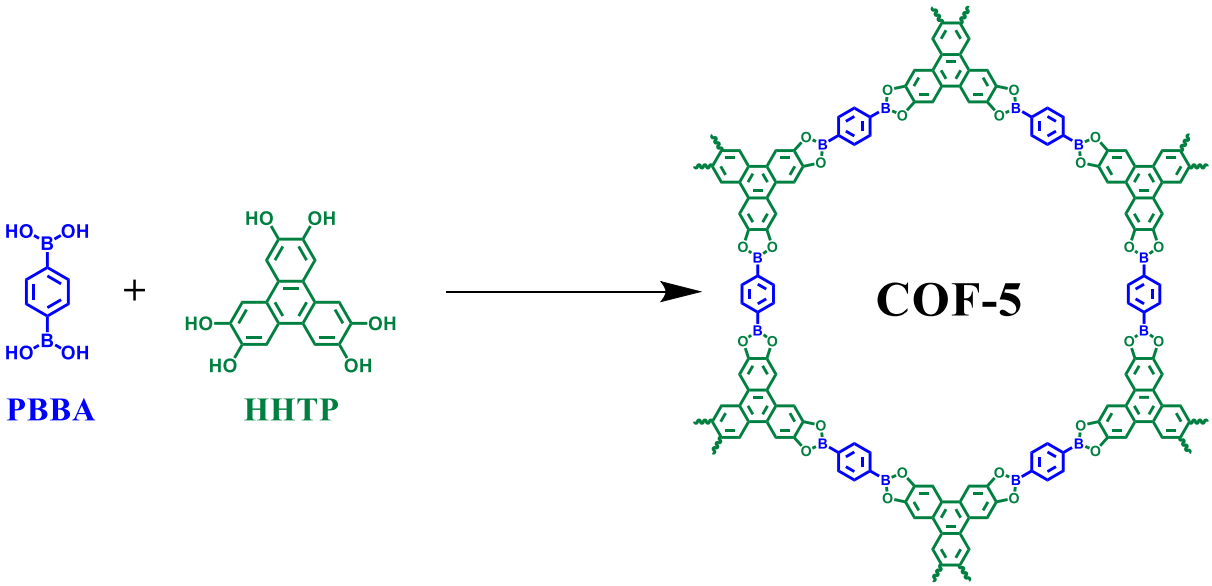

Figure 9.14. Synthesis of COF-5 Films

2D COF-5 Films. First, a graphene-coated Si/SiO_2 (1 cm X 1 cm, UniversityWafer, Inc.) was placed into a scintillation vial. Then, solutions of HHTP (2 mM) and PBBA (3 mM) were prepared separately in a solvent blend of 80/16/4 vol CH_3CN:1,4-dioxane:1,3,5-trimethylbenzene. These solutions were then filtered to remove any insoluble particulates. These solutions were then added in a 1:1 vol ratio to the substate-containing scintillation vial, producing a 20 mL solution of 1 mM HHTP and 1.5 mM PBBA. This scintillation vial was then sealed and heated to 80 °C for 24 hrs. After 24 hrs, a milky suspension had formed in the scintillation vial. Approximately 90% of the solution was then decanted and diluted with fresh 80/16/4 vol CH_3CN:1,4-dioxane:1,3,5-trimethylbenzene. This procedure was repeated 3 times to sufficiently dilute any colloidal species present in solution. The wafer was then removed from solvent with forceps and allowed to dry in air.

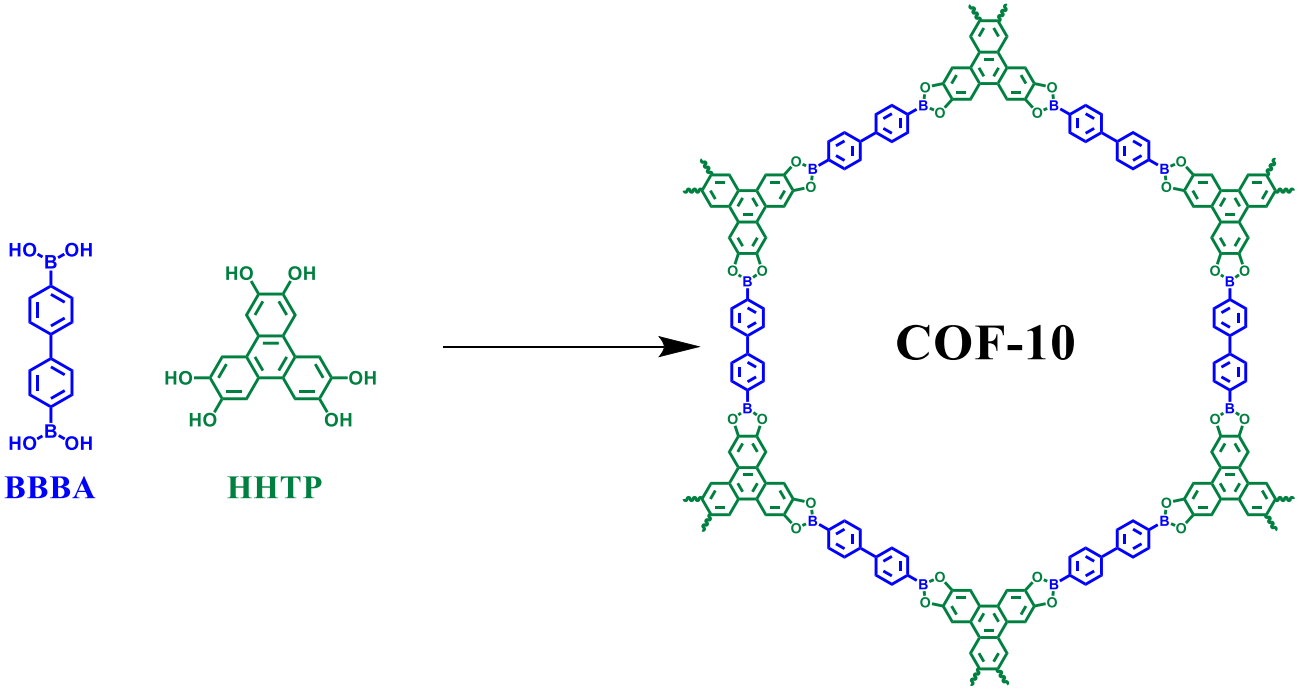

Figure 9.15. Synthesis of COF-10 Films

2D COF-10 Films. First, a graphene-coated Si/SiO_2 (1 cm X 1 cm, UniversityWafer, Inc.) was placed into a scintillation vial. Then, solutions of HHTP (2 mM) and BBBA (3 mM) were prepared separately in a solvent blend of 80/16/4 vol CH_3CN:1,4-dioxane:1,3,5-trimethylbenzene. These solutions were then filtered to remove any insoluble particulates. These solutions were then added in a 1:1 vol ratio to the substate-containing scintillation vial, producing a 20 mL solution of 1 mM HHTP and 1.5 mM BBBA. This scintillation vial was then sealed and heated to 80 °C for 24 hrs. After 24 hrs, a milky suspension had formed in the scintillation vial. Approximately 90% of the solution was then decanted and diluted with fresh 80/16/4 vol CH_3CN:1,4-dioxane:1,3,5-trimethylbenzene. This procedure was repeated 3 times to sufficiently dilute any colloidal species present in solution. The wafer was then removed from solvent with forceps and allowed to dry in air.

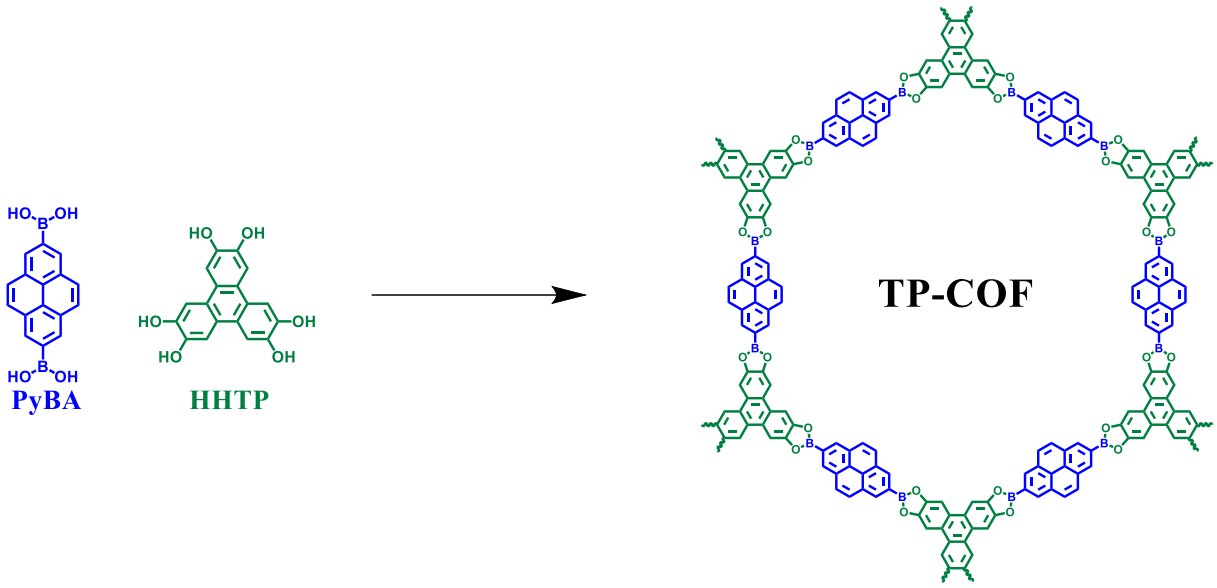

Figure 9.16. Synthesis of TP-COF Films

2D TP-COF Films. First, a graphene-coated Si/SiO_2 (1 cm X 1 cm, UniversityWafer, Inc.) was placed into a scintillation vial. Then, solutions of HHTP (2 mM) and PyBA (3 mM) were prepared separately in a solvent blend of 80/16/4 vol CH_3CN:1,4-dioxane:1,3,5-trimethylbenzene. These solutions were then filtered to remove any insoluble particulates. These solutions were then added in a 1:1 vol ratio to the substate-containing scintillation vial, producing a 20 mL solution of 1 mM HHTP and 1.5 mM PyBA. This scintillation vial was then sealed and heated to 80 °C for 24 hrs. After 24 hrs, a milky suspension had formed in the scintillation vial. Approximately 90% of the solution was then decanted and diluted with fresh 80/16/4 vol CH_3CN:1,4-dioxane:1,3,5-trimethylbenzene. This procedure was repeated 3 times to sufficiently dilute any colloidal species present in solution. The wafer was then removed from solvent with forceps and allowed to dry in air.

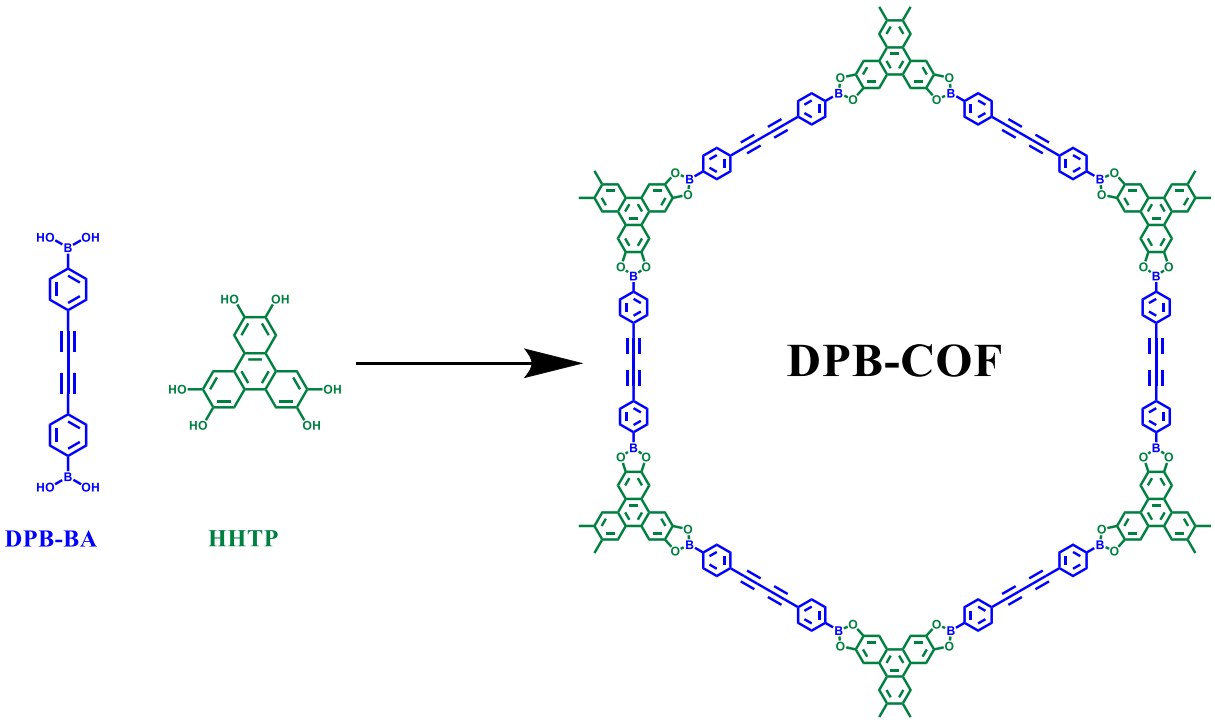

Figure 9.17. Synthesis of DPB-COF Films

2D DPB-COF Films. First, a graphene-coated Si/SiO_2 (1 cm X 1 cm, UniversityWafer, Inc.) was placed into a scintillation vial. Then, solutions of HHTP (2 mM) and DPB-BA (3 mM) were prepared separately in a solvent blend of 80/16/4 vol CH_3CN:1,4-dioxane:1,3,5-trimethylbenzene. These solutions were then filtered to remove any insoluble particulates. These solutions were then added in a 1:1 vol ratio to the substate-containing scintillation vial, producing a 20 mL solution of 1 mM HHTP and 1.5 mM DPB-BA. This scintillation vial was then sealed and heated to 80 °C for 24 hrs. After 24 hrs, a milky suspension had formed in the scintillation vial. Approximately 90% of the solution was then decanted and diluted with fresh 80/16/4 vol CH_3CN:1,4-dioxane:1,3,5-

trimethylbenzene. This procedure was repeated 3 times to sufficiently dilute any colloidal species present in solution. The wafer was then removed from solvent with forceps and allowed to dry in air.

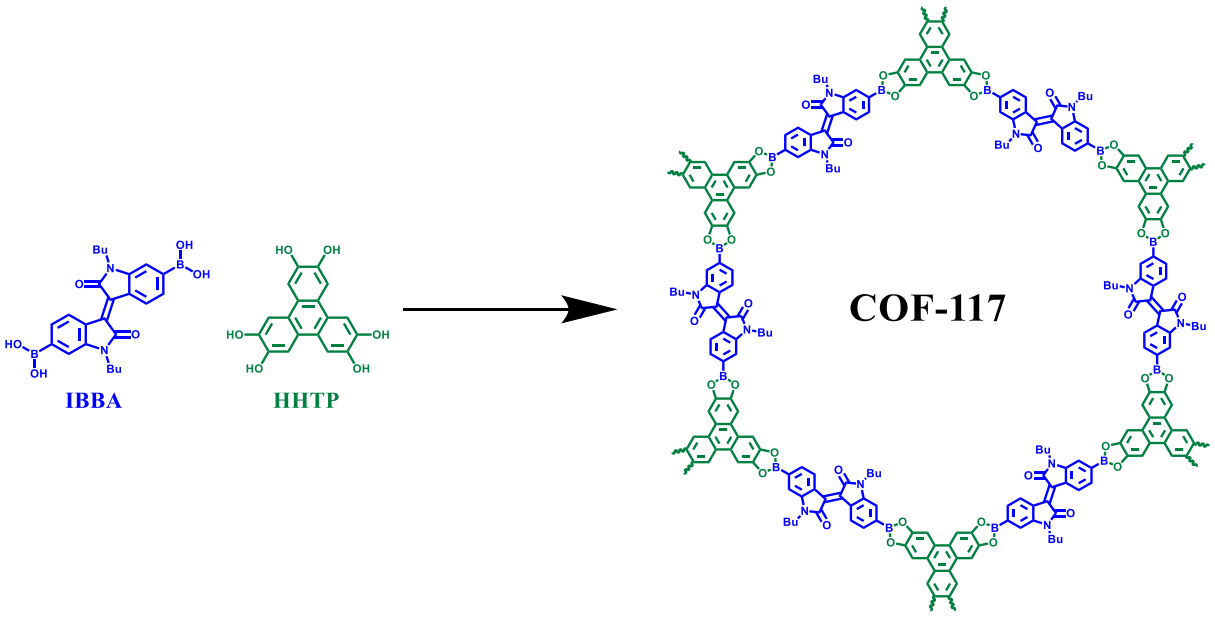

Figure 9.18. Synthesis of COF-117 Films

2D COF-117 Films. First, a graphene-coated Si/SiO_2 (1 cm X 1 cm, UniversityWafer, Inc.) was placed into a scintillation vial. Then, solutions of HHTP (2 mM) and IBBA (3 mM) were prepared separately in a solvent blend of 80/16/4 vol CH_3CN:1,4-dioxane:1,3,5-trimethylbenzene. These solutions were then filtered to remove any insoluble particulates. These solutions were then added in a 1:1 vol ratio to the substate-containing scintillation vial, producing a 20 mL solution of 1 mM HHTP and 1.5 mM IBBA. This scintillation vial was then sealed and heated to 80 °C for 24 hrs. After 24 hrs, a milky suspension had formed in the scintillation vial. Approximately 90% of the solution was then decanted and diluted with fresh 80/16/4 vol CH_3CN:1,4-dioxane:1,3,5-trimethylbenzene. This procedure was repeated 3 times to sufficiently dilute any colloidal species present in solution. The wafer was then removed from solvent with forceps and allowed to dry in air.

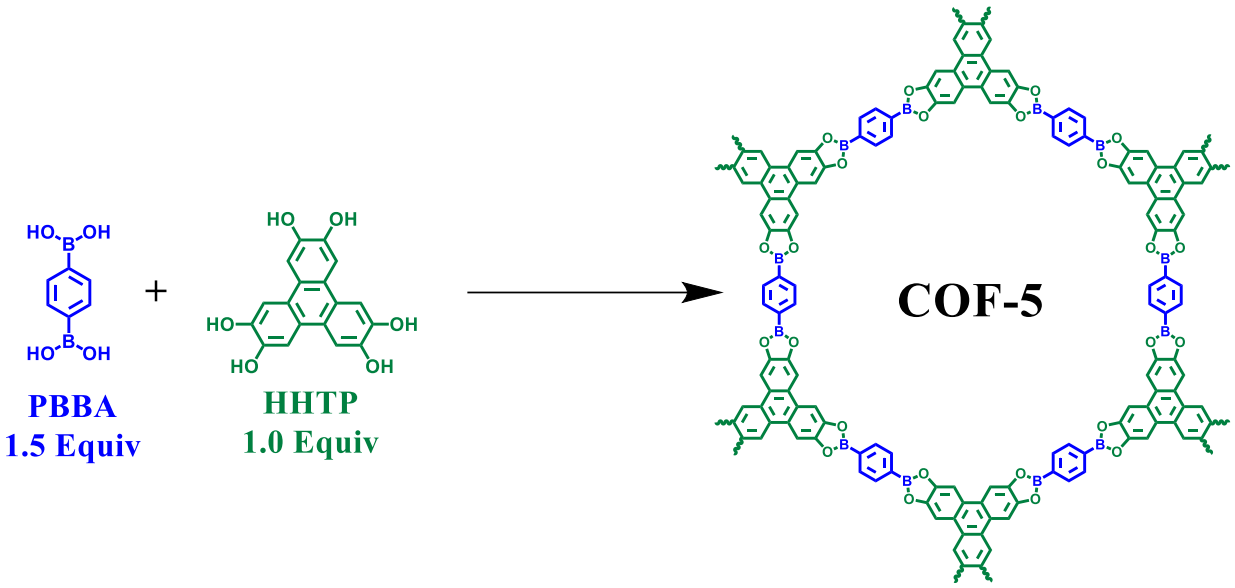

Figure 9.19. Synthesis of COF-5 Films at Higher Concentrations

2D COF-5 Films Prepared at Different Concentrations. First, a graphene-coated Si/SiO_2 (1 cm X 1 cm, UniversityWafer, Inc.) was placed into a scintillation vial. Then, solutions of HHTP (10 mM) and PBBA (15 mM) were prepared separately in a solvent blend of 80/16/4 vol CH_3CN:1,4-dioxane:1,3,5-trimethylbenzene. These solutions were then filtered to remove any insoluble particulates.

These solutions were then mixed in a 1:1 vol ratio, which was then diluted with additional 80/16/4 vol CH_3CN:1,4-dioxane:1,3,5-trimethylbenzene to yield solutions with HHTP concentrations of 5 mM (PBBA = 7.5 mM), 2 mM (PBBA = 3 mM), 1 mM (PBBA = 1.5 mM), and 0.5 mM (PBBA = 0.75 mM). These solutions were then added to the scintillation vial that contained the graphene-supported substrate. This scintillation vial was then sealed and heated to 80 °C for 24 hrs. After 24

hrs, a milky suspension had formed in the scintillation vial. Approximately 90% of the solution was then decanted and diluted with fresh 80/16/4 vol CH_3CN:1,4-dioxane:1,3,5-trimethylbenzene. This procedure was repeated 3 times to sufficiently dilute any colloidal species present in solution. The wafer was then removed from solvent with forceps and allowed to dry in air.

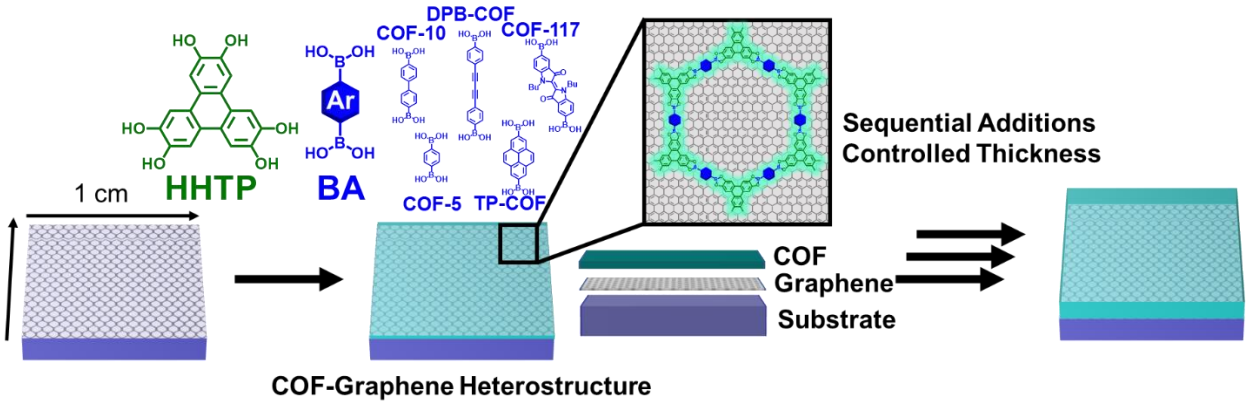

Figure 9.20. Multigrowth procedure of COF Films

Multigrowth COF Films. First, a graphene-coated Si/SiO_2 (1 cm X 1 cm, UniversityWafer, Inc.) was placed into a scintillation vial. Then, solutions of HHTP (2 mM) and corresponding boronic acid (3 mM) were prepared separately in a solvent blend of 80/16/4 vol CH_3CN:1,4-dioxane:1,3,5-trimethylbenzene. These solutions were then filtered to remove any insoluble particulates. These solutions were then mixed in a 1:1 vol ratio. This solution was then added to the scintillation vial that contained the graphene-supported substrate. This scintillation vial was then sealed and heated to 80 °C for 24 hrs. After 24 hrs, a milky suspension had formed in the scintillation vial. Approximately 90% of the solution was then decanted and diluted with fresh 80/16/4 vol CH_3CN:1,4-dioxane:1,3,5-trimethylbenzene. This procedure was repeated 3 times to sufficiently dilute any colloidal species present in solution.

Then, to instigate another round of growth, additional monomer species (prepared as described above) were added to the scintillation vial containing the wafer. This scintillation vial was then

sealed and heated to 80 °C for 24 hrs. After 24 hrs, a milky suspension had formed in the scintillation vial. Approximately 90% of the solution was then decanted and diluted with fresh 80/16/4 vol CH_3CN:1,4-dioxane:1,3,5-trimethylbenzene. This procedure was repeated 3 times to sufficiently dilute any colloidal species present in solution.

This procedure was repeated for as many times as described. Finally, the wafer was removed from solvent with forceps and allowed to dry in air.

Optical Microscopy Images

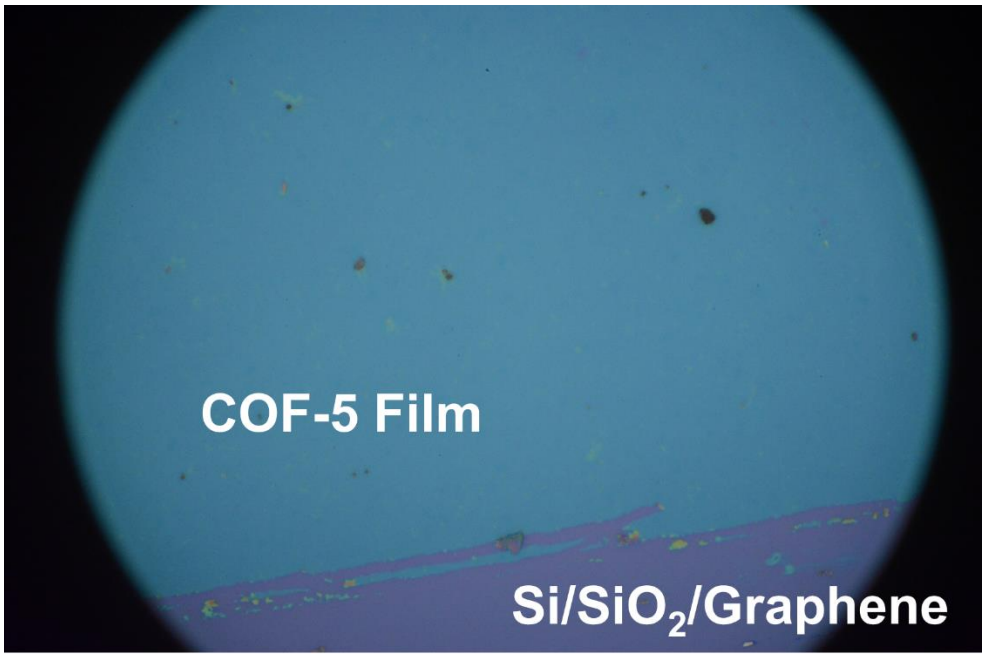

Figure 9.21. Optical Microscopy Image of COF-5/SiO_2/Si grown under colloidal conditions

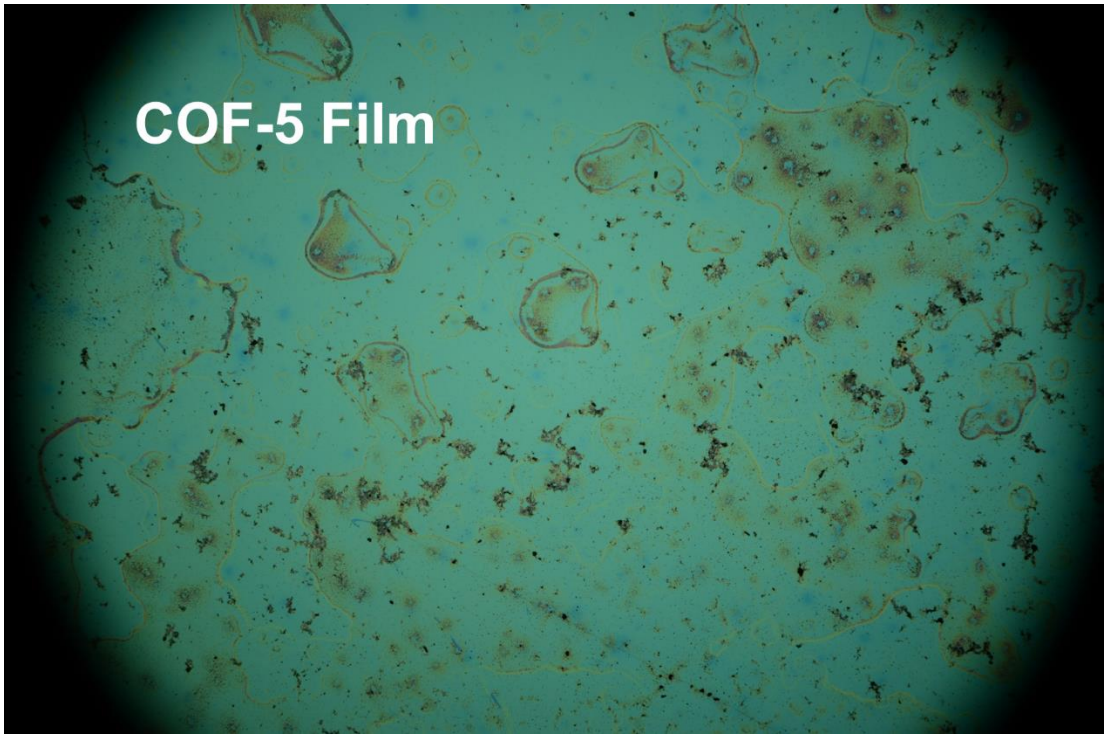

Figure 9.22. Optical Microscopy Image of COF-5/SiO_2/Si grown under previously reported solvothermal conditions.[425]

Atomic Force Microscopy

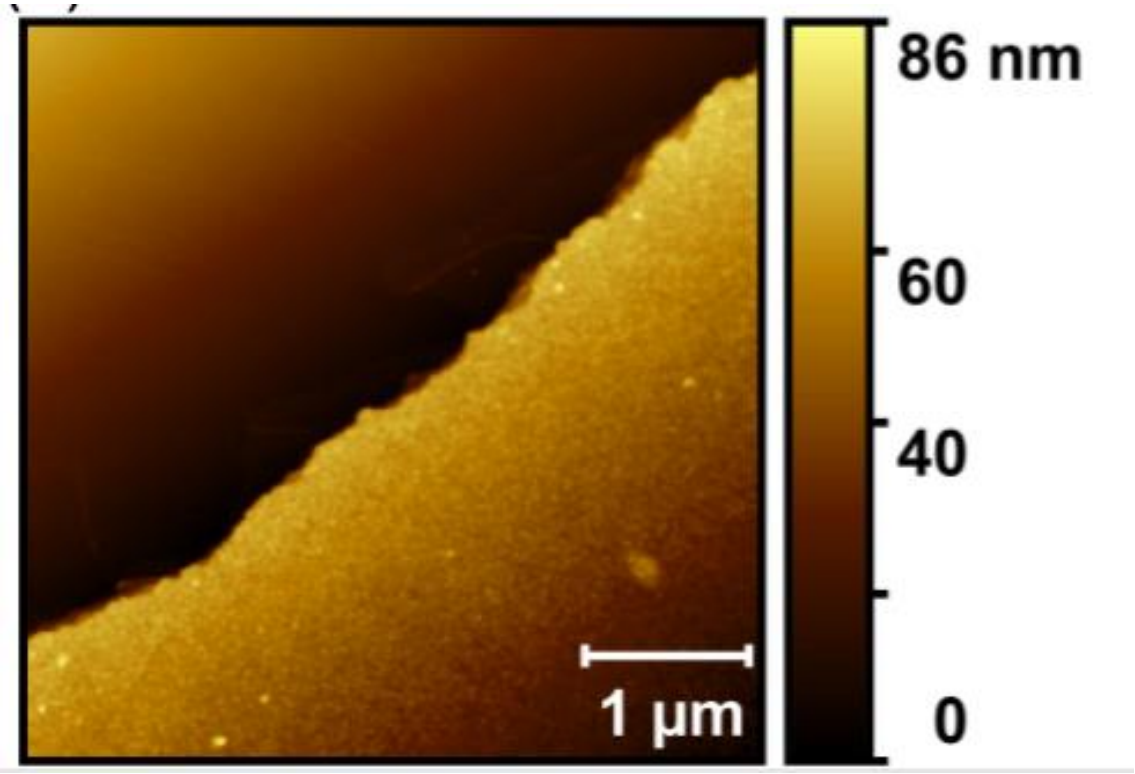

Figure 9.23. Atomic force micrograph of COF-5 film used for thermal property measurement

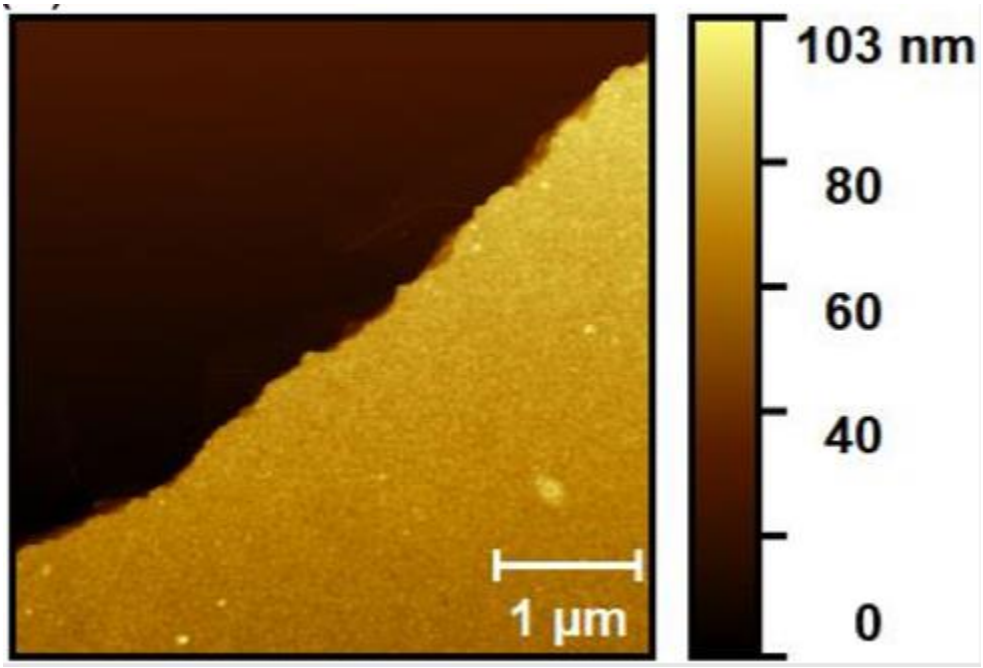

Figure 9.24. Atomic force micrograph of TP-COF film used for thermal property measurement

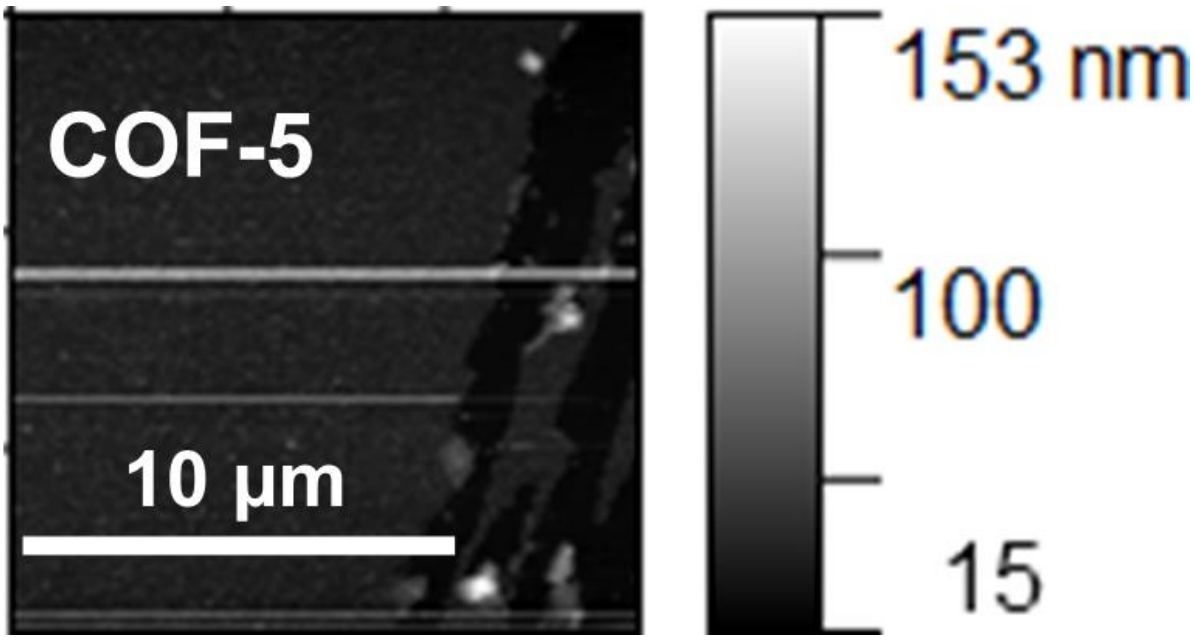

Figure 9.25. COF-5 film prepared using colloidal conditions

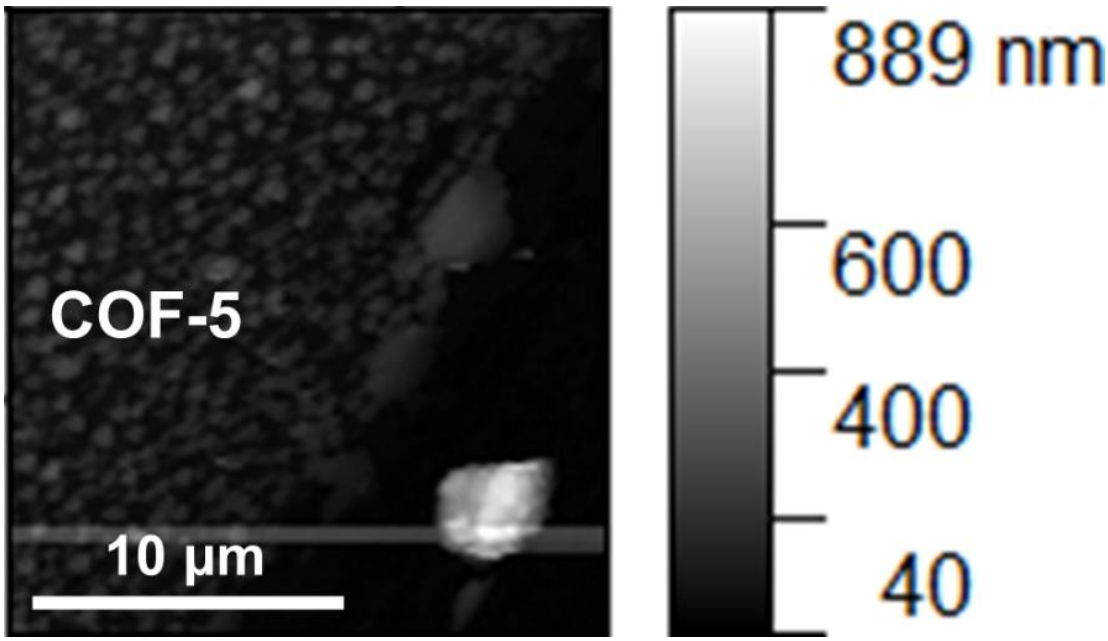

Figure 9.26. Atomic force micrograph of COF-5 film prepared using previously reported solvothermal conditions.[425]

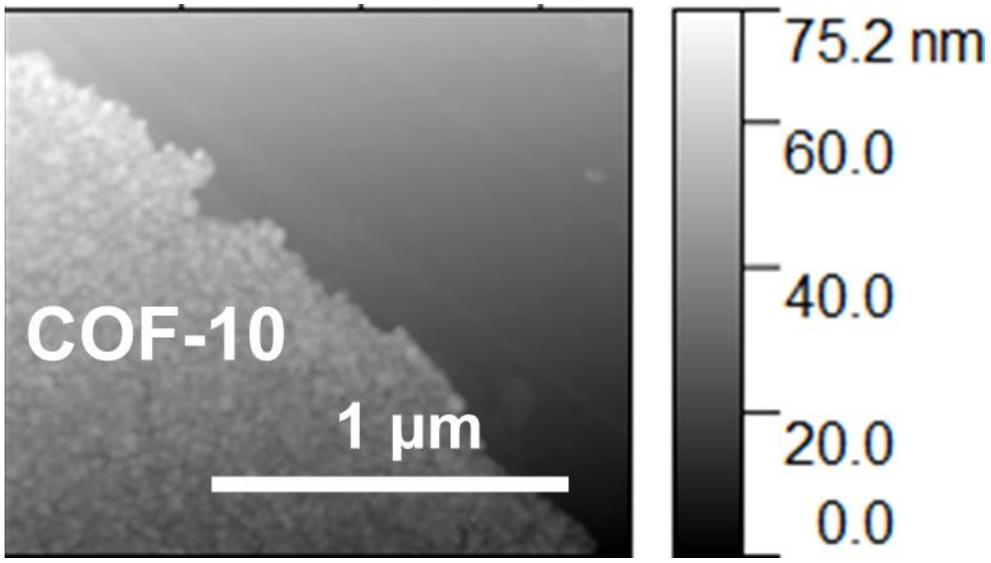

Figure 9.27. Atomic force micrograph of COF-10 produced using colloidal conditions

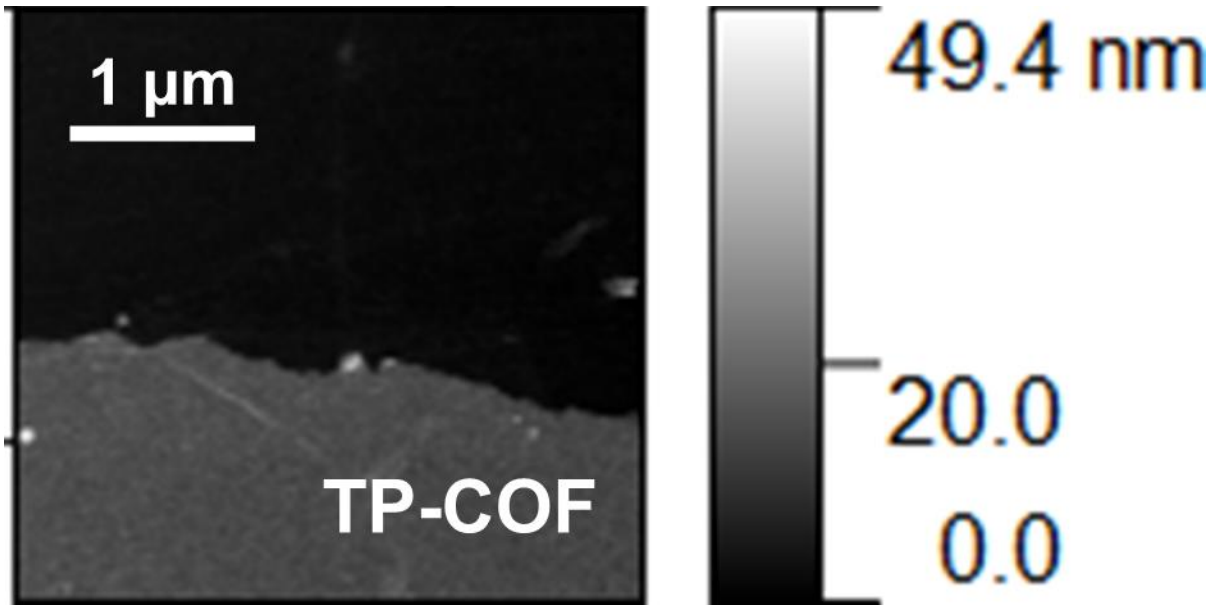

Figure 9.28. Atomic force micrograph of TP-COF produced using colloidal conditions

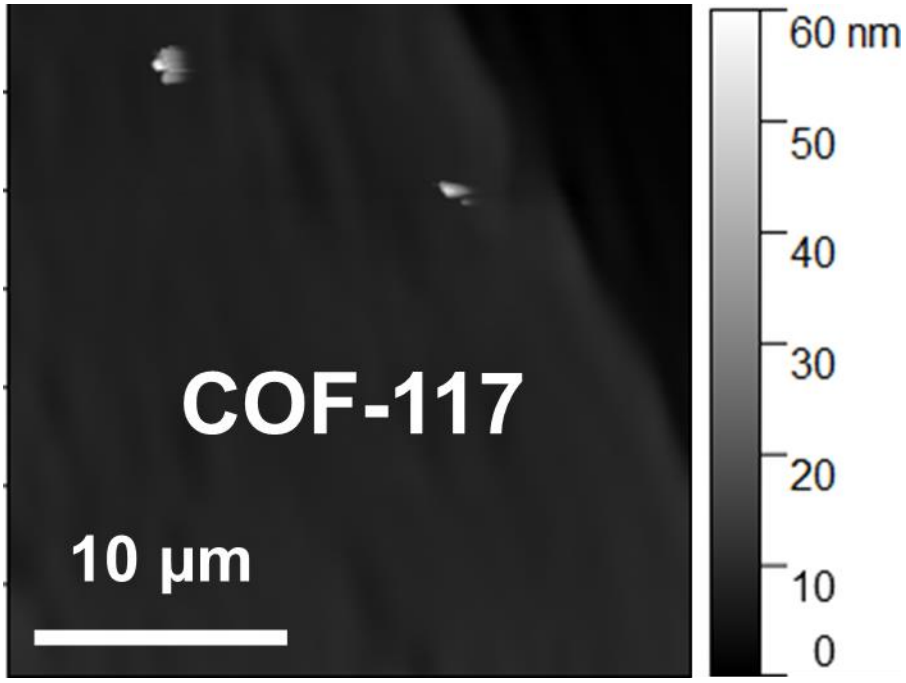

Figure 9.29. Atomic force micrograph of COF-117 produced using colloidal conditions

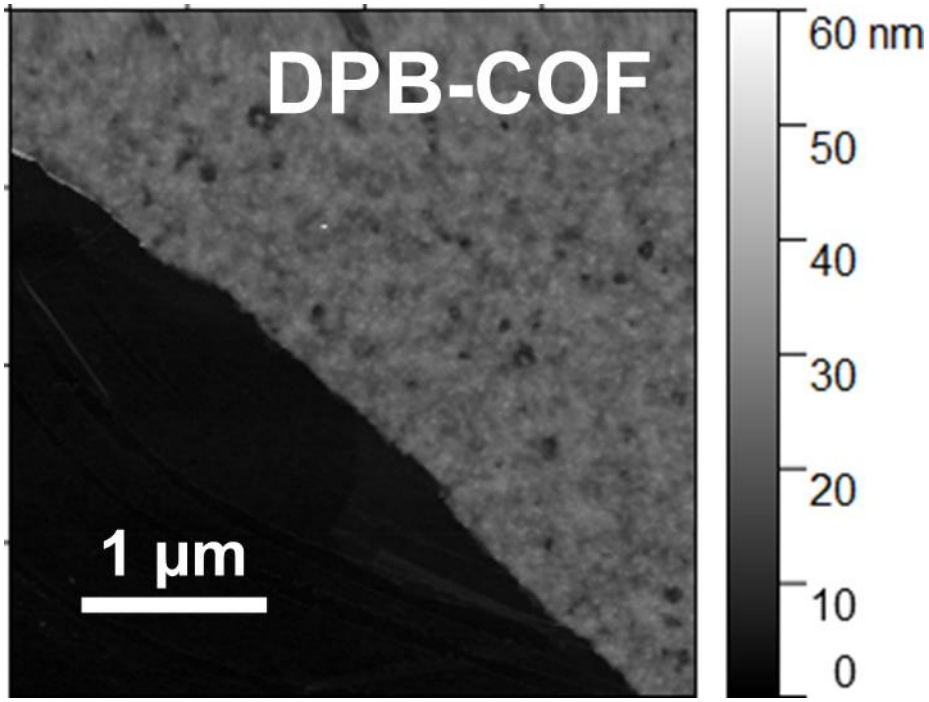

Figure 9.30. Atomic force micrograph of DPB-COF produced using colloidal conditions

Grazing Incidence X-ray Diffraction

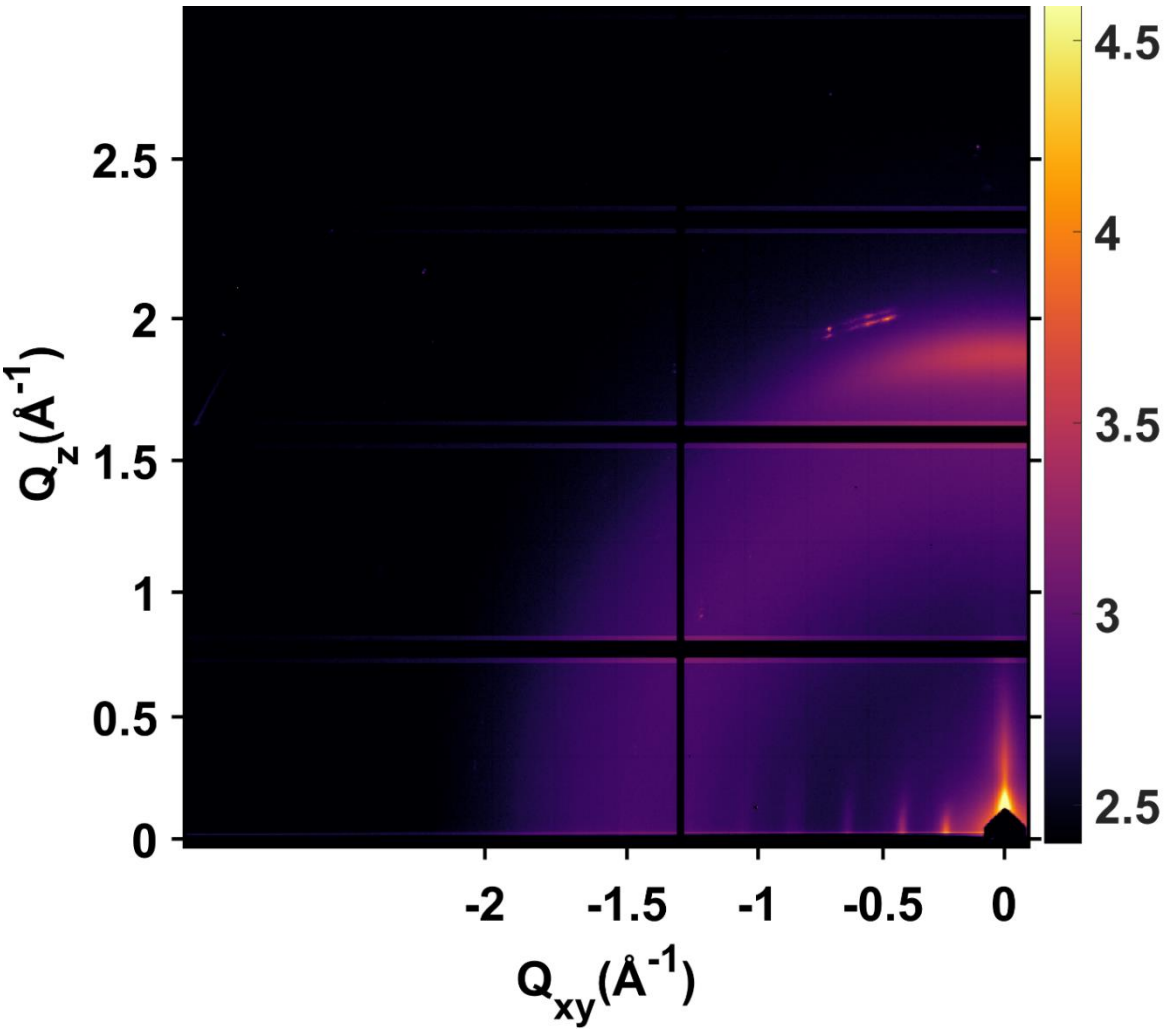

Figure 9.31. 2D Grazing-incidence X-ray diffraction Pattern of COF-5/SiO_2/Si grown by colloidal conditions

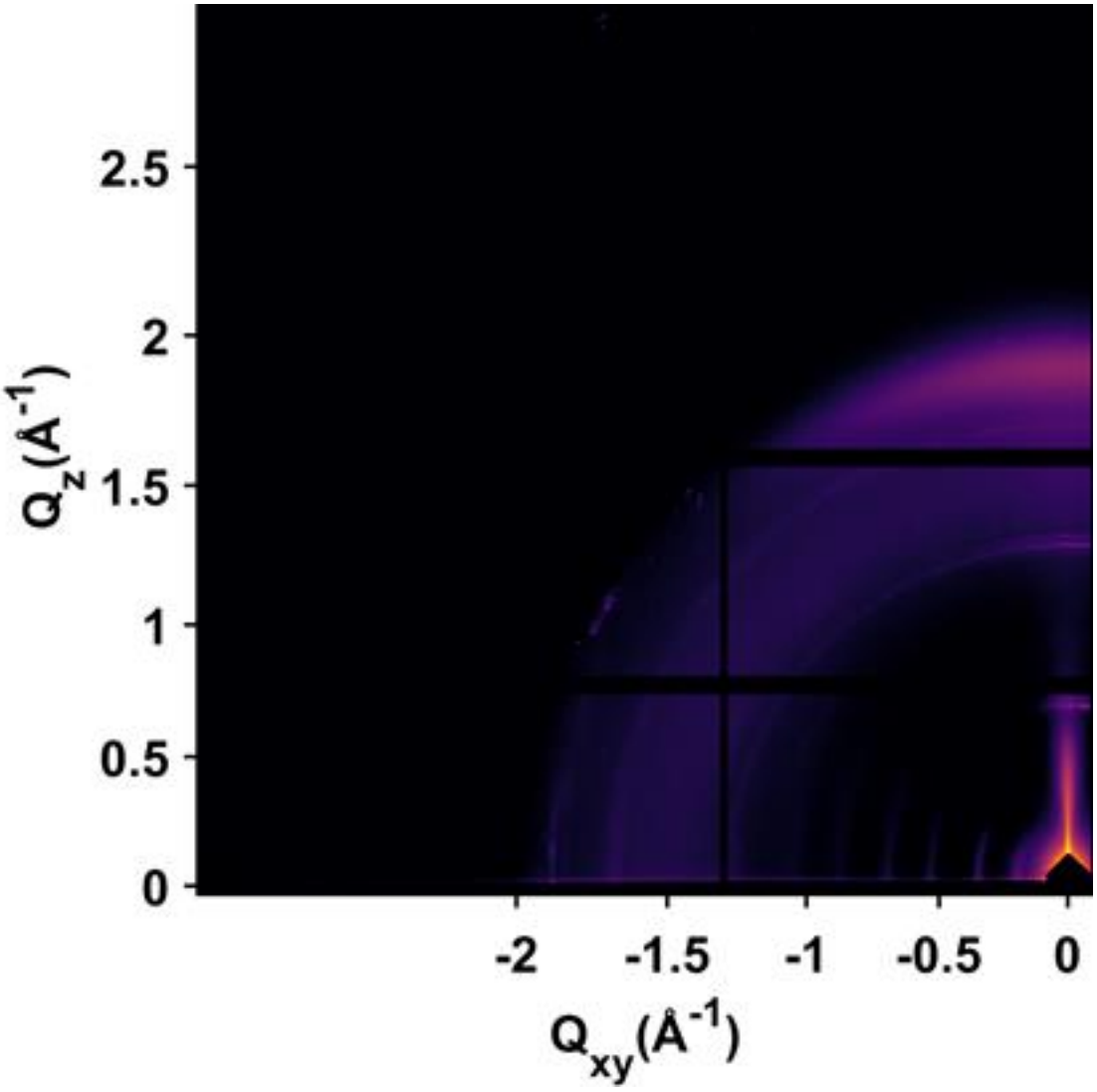

Figure 9.32. 2D Grazing-incidence X-ray diffraction Pattern of COF-10/SiO_2/Si grown by colloidal conditions

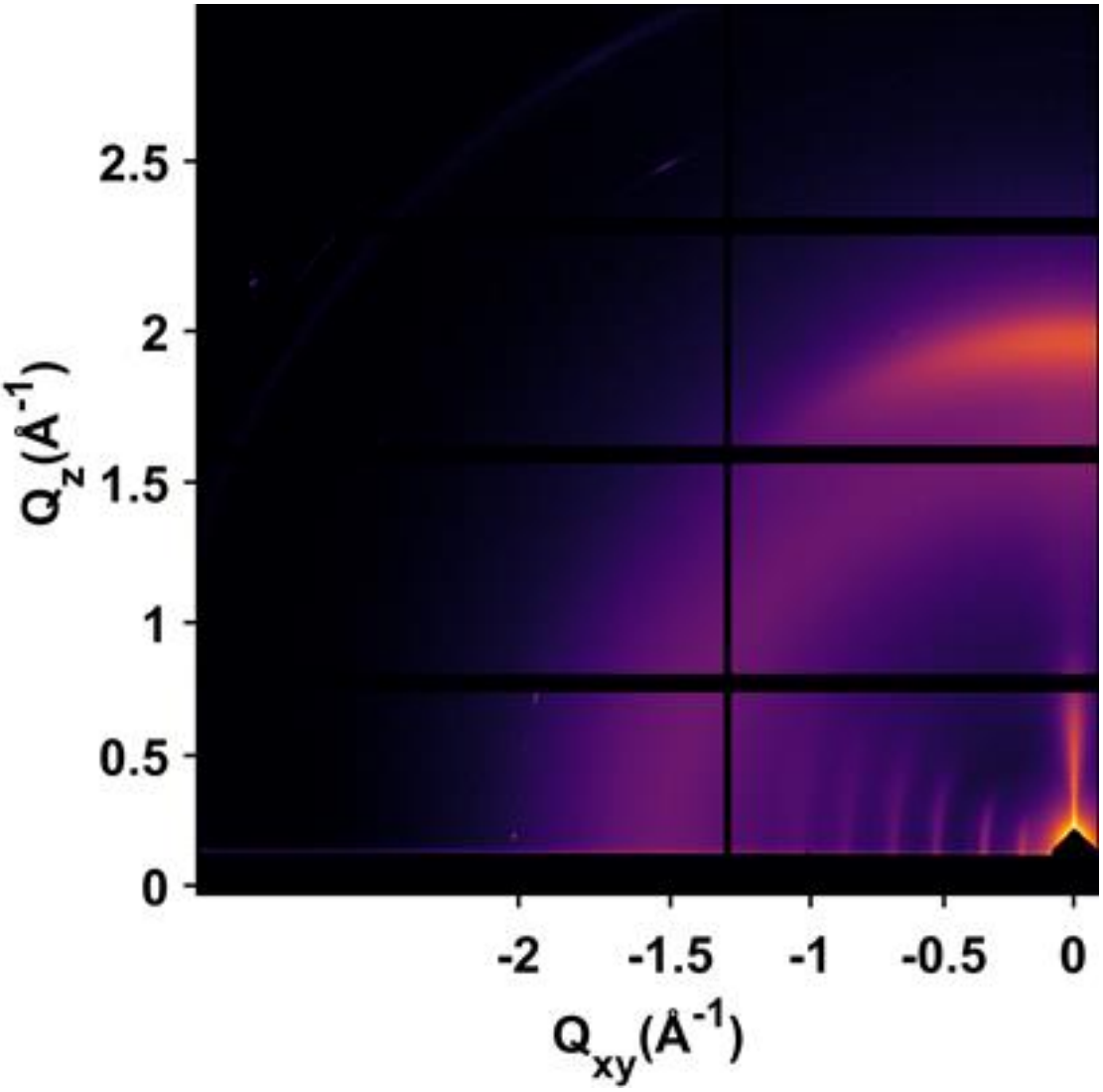

Figure 9.33. 2D Grazing-incidence X-ray diffraction Pattern of TP-COF/SiO_2/Si grown by colloidal conditions

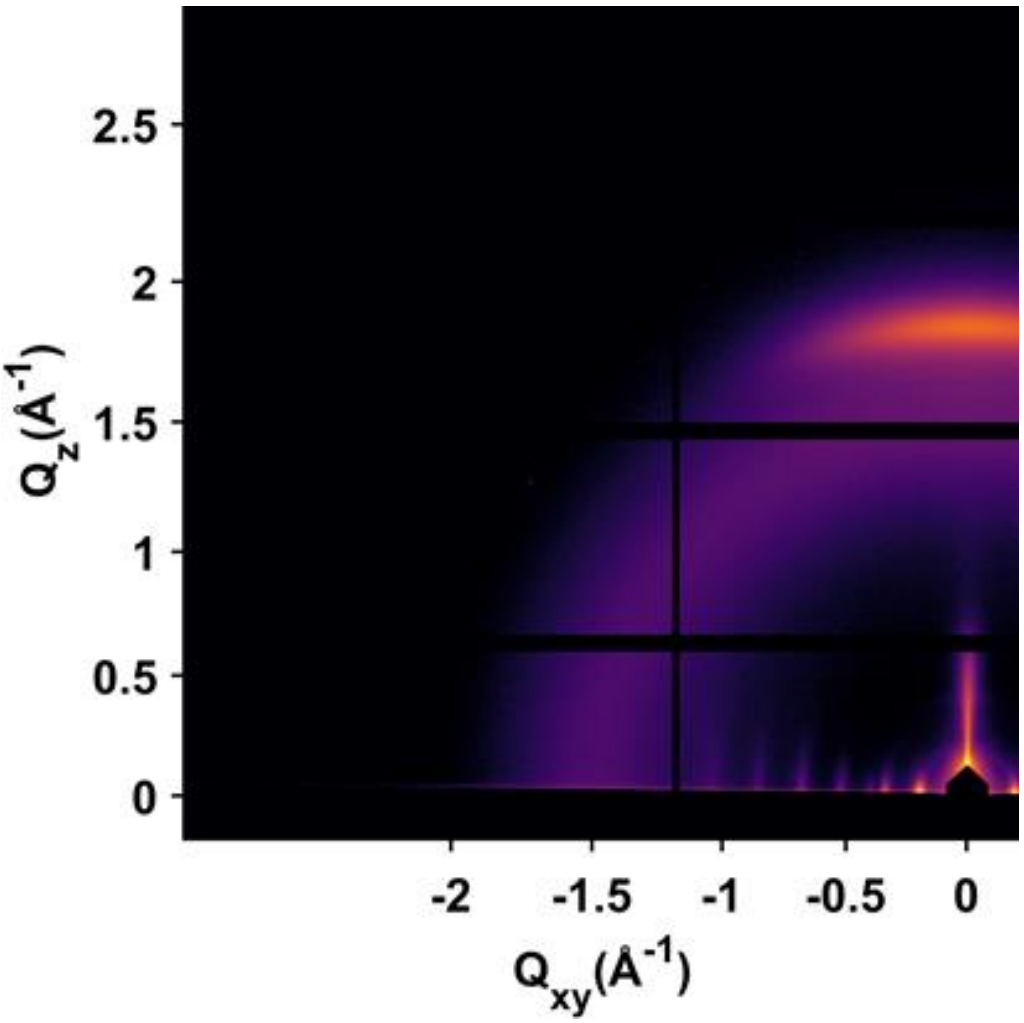

Figure 9.34. 2D Grazing-incidence X-ray diffraction Pattern of DPB-COF/SiO_2/Si grown by colloidal conditions

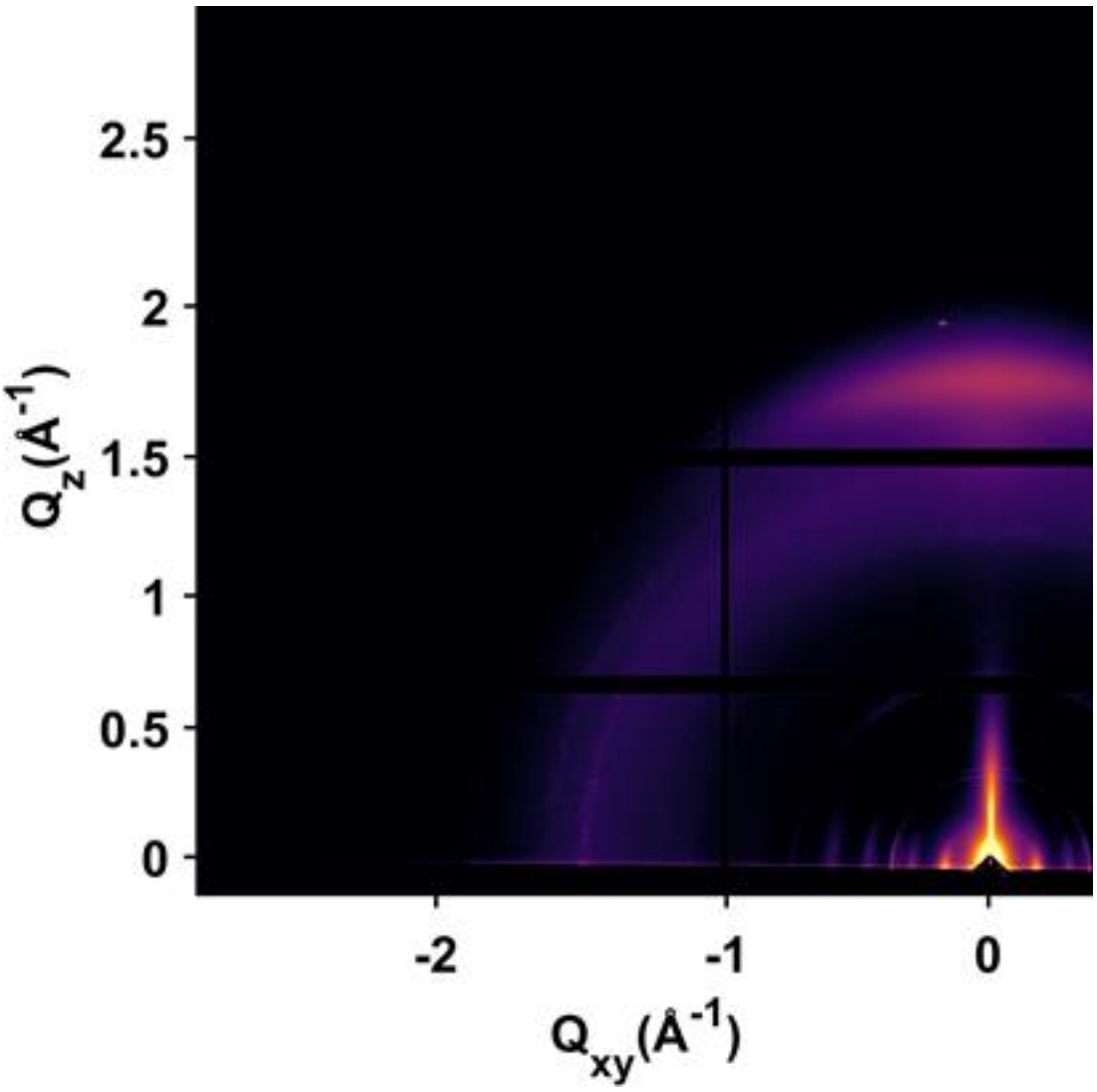

Figure 9.35. 2D Grazing-incidence X-ray diffraction Pattern of COF-117/SiO_2/Si grown by colloidal conditions

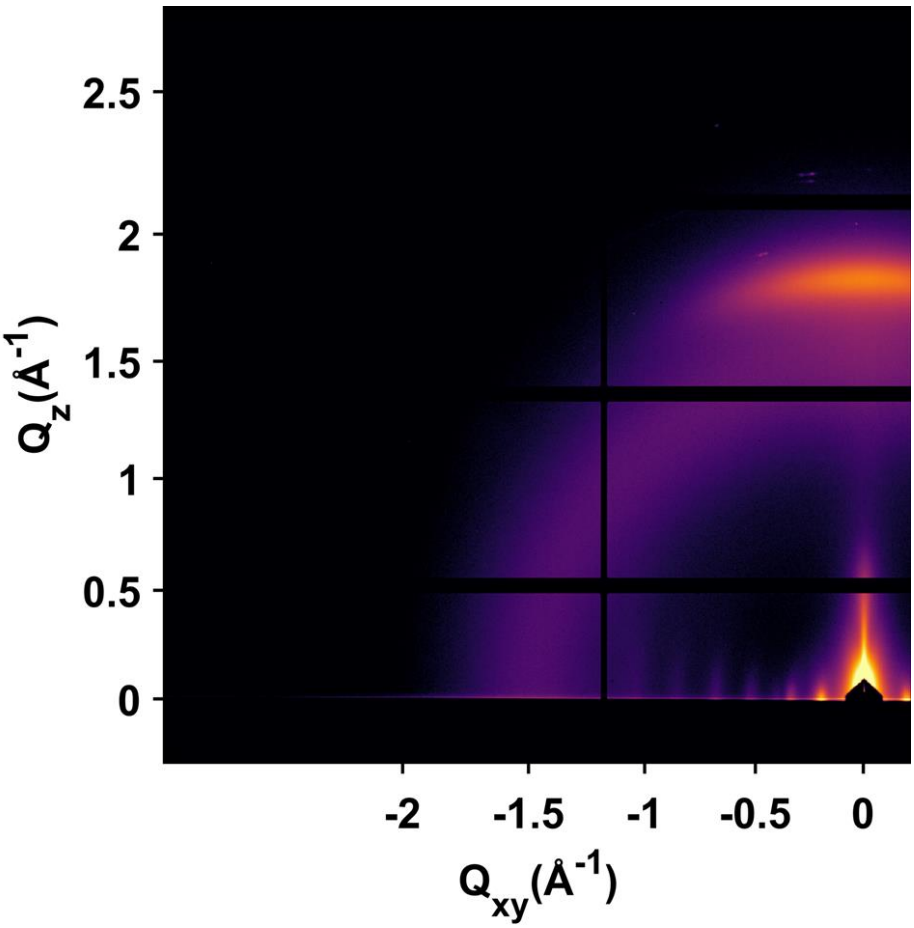

Figure 9.36. 2D Grazing-incidence X-ray diffraction Pattern of TP-COF/SiO_2/Si grown by colloidal conditions after one monomer polymerization cycle

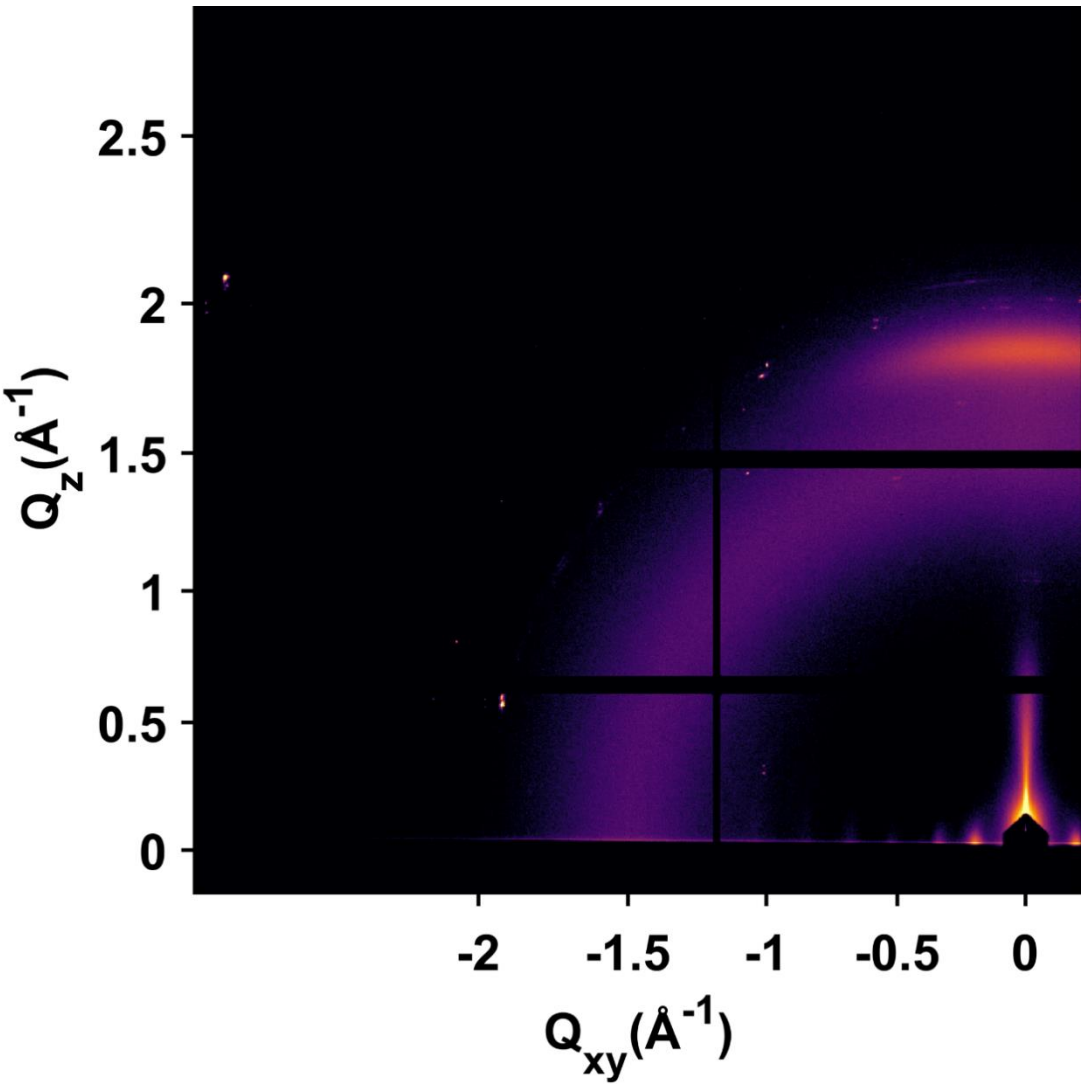

Figure S32. 2D Grazing-incidence X-ray diffraction Pattern of TP-COF/SiO_2/Si grown by colloidal conditions after two monomer polymerization cycles

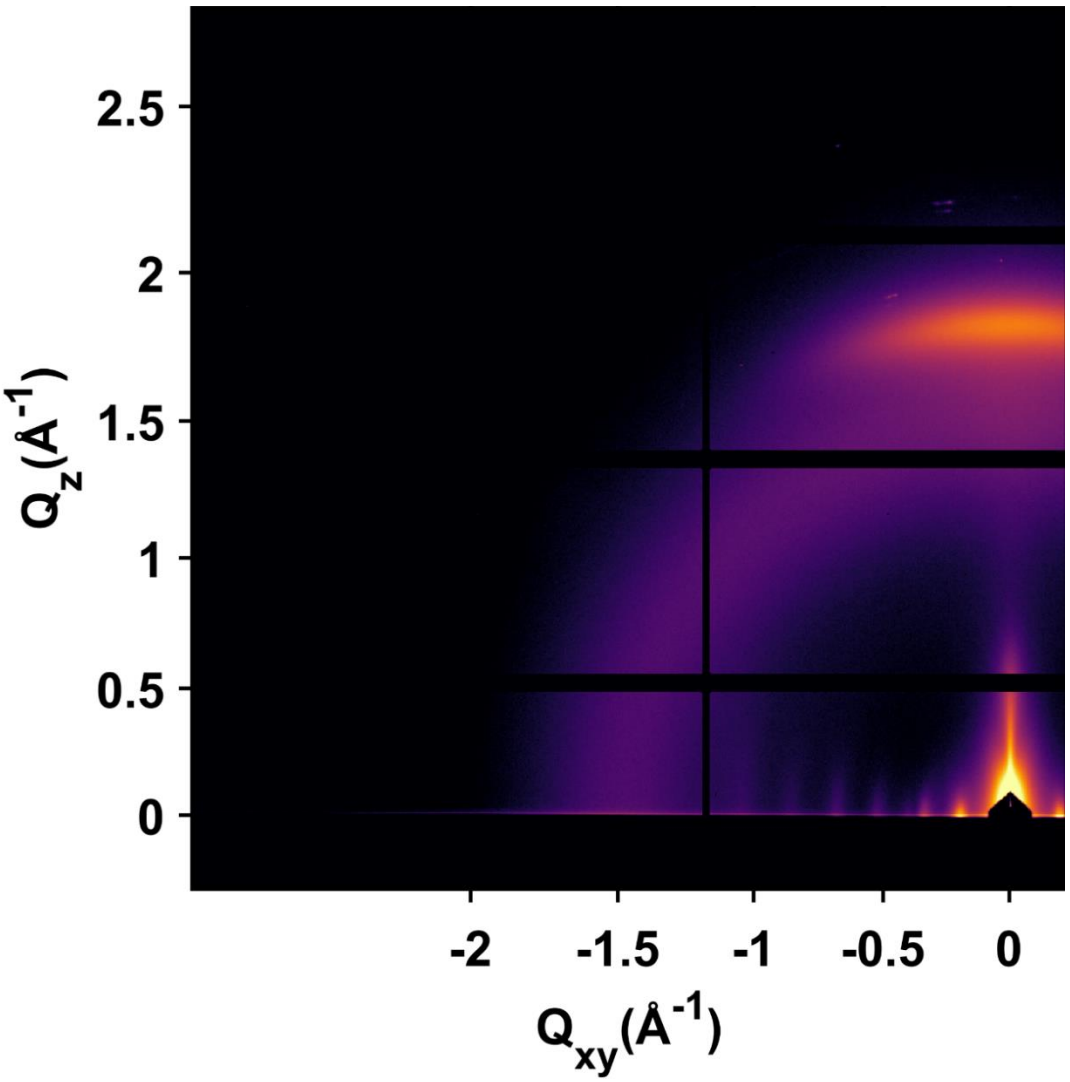

Figure 9.37. 2D Grazing-incidence X-ray diffraction Pattern of TP-COF/SiO_2/Si grown by colloidal conditions after three monomer polymerization cycles

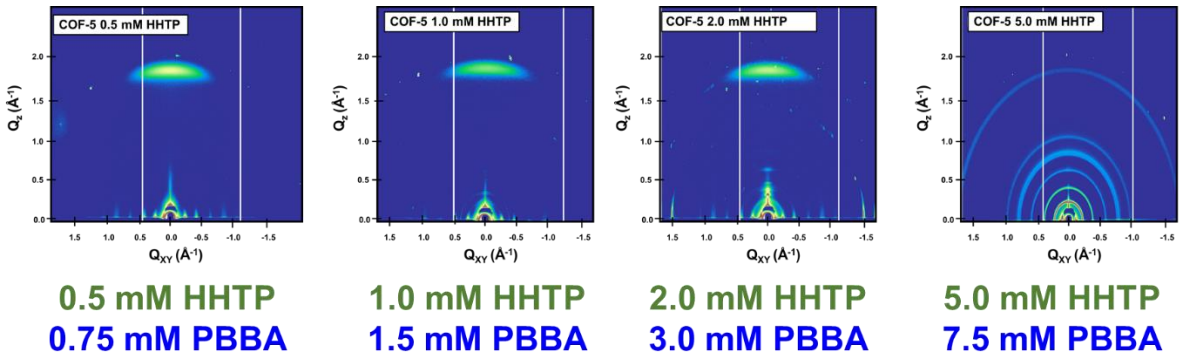

Figure 9.38. 2D Grazing-incidence X-ray diffraction Patterns of COF-5/SiO_2/Si polymerized from different initial monomer concentrations under colloidal conditions.

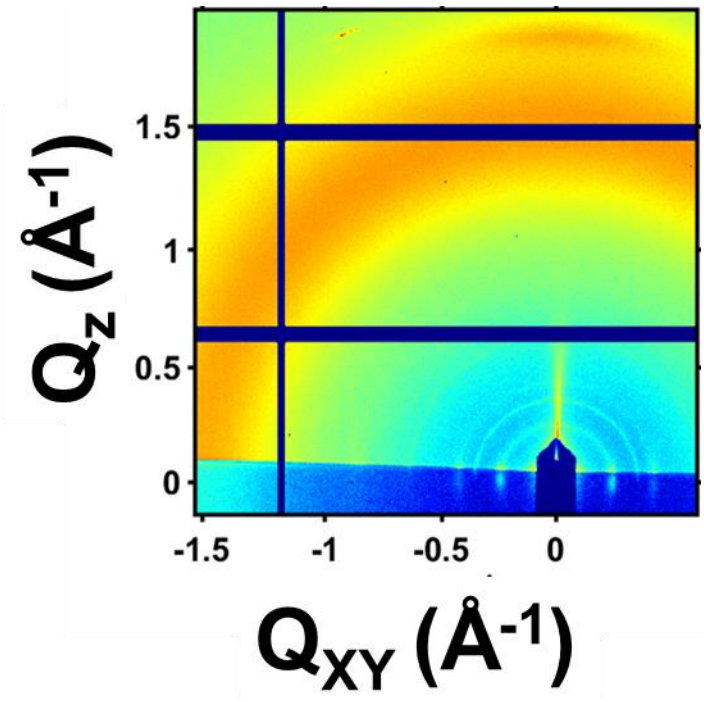

Figure 9.39. 2D Grazing-incidence X-ray diffraction Patterns of COF-5/SiO_2/Si polymerized from solvothermal noncolloidal conditions.[425]

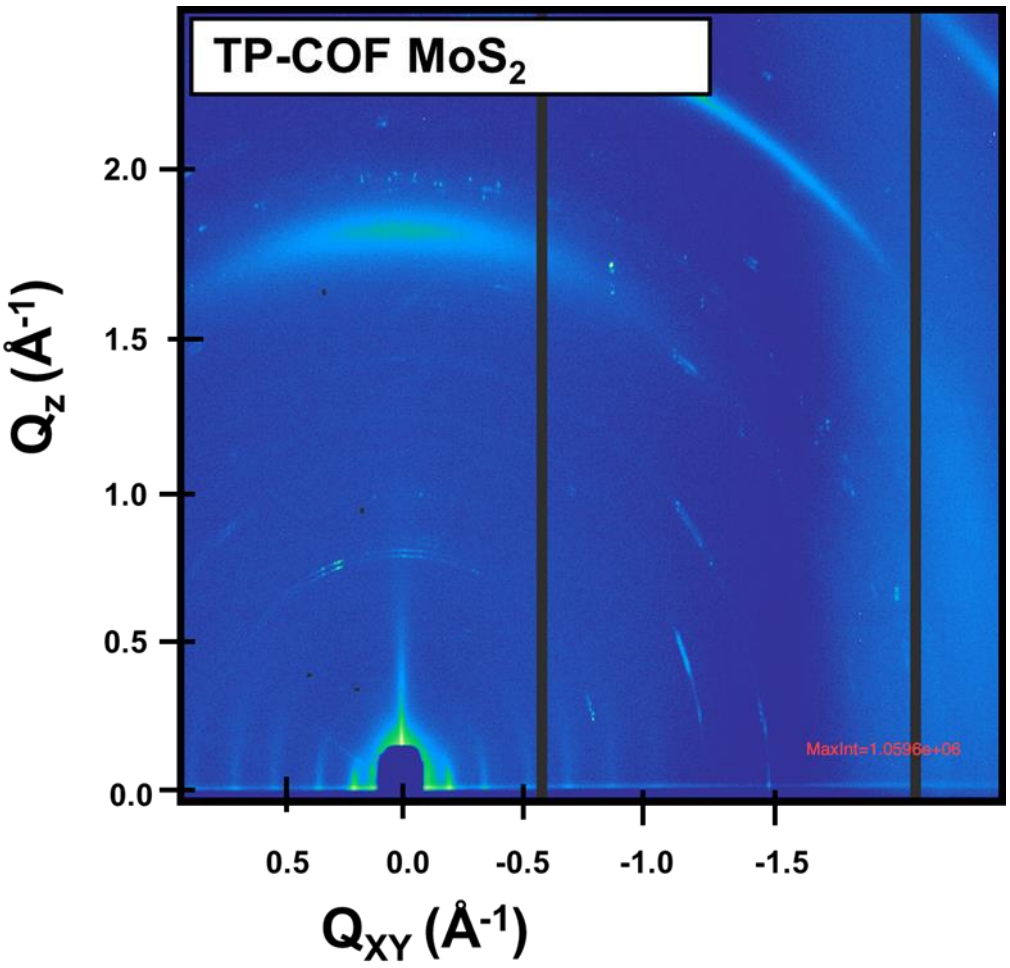

Figure 9.40. 2D Grazing-incidence X-ray diffraction Patterns of TP-COF/MoS_2/Al_2O_3 polymerized from solvothermal noncolloidal conditions

Simulated and Experimental X-ray Diffraction Patterns

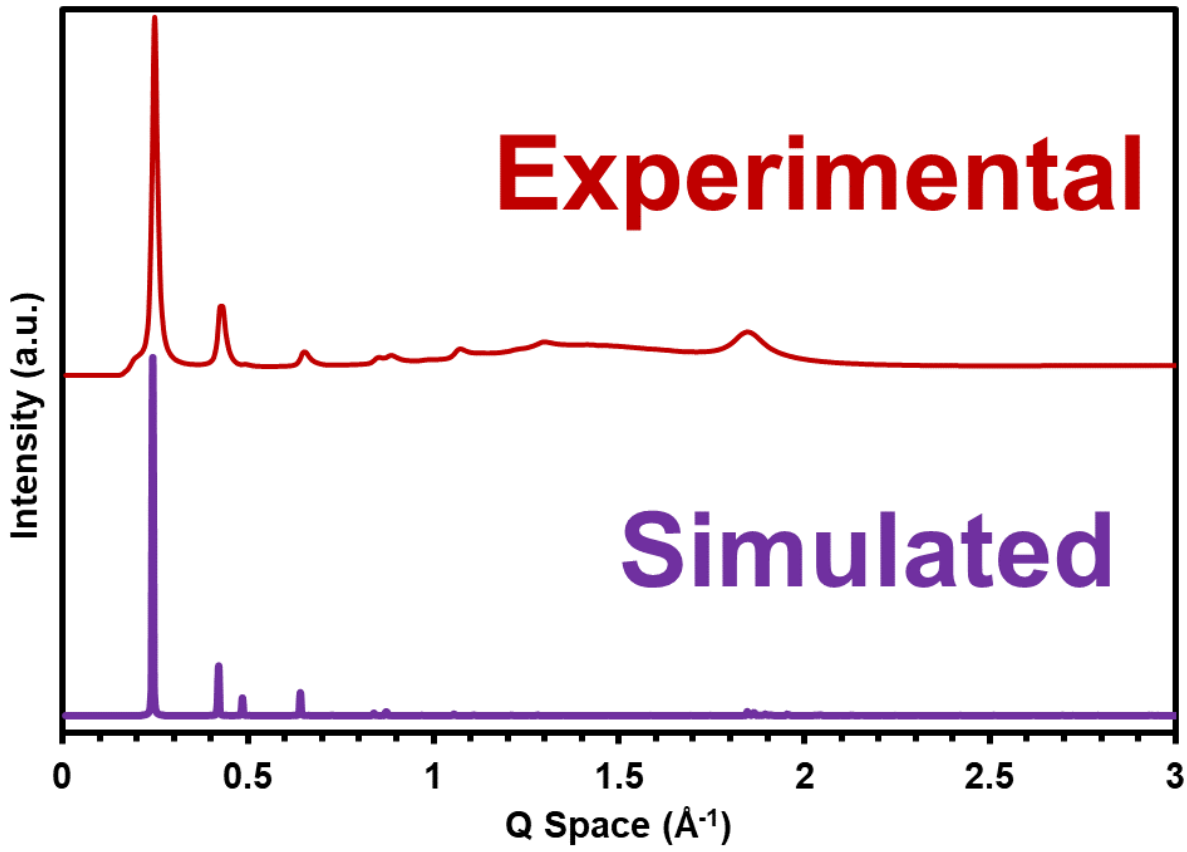

Figure 9.41. Linear experimental X-ray diffraction pattern extracted from 2D GI-WAXS pattern of COF-5 and simulated X-ray diffraction pattern from a geometry optimized COF-5 crystallite.

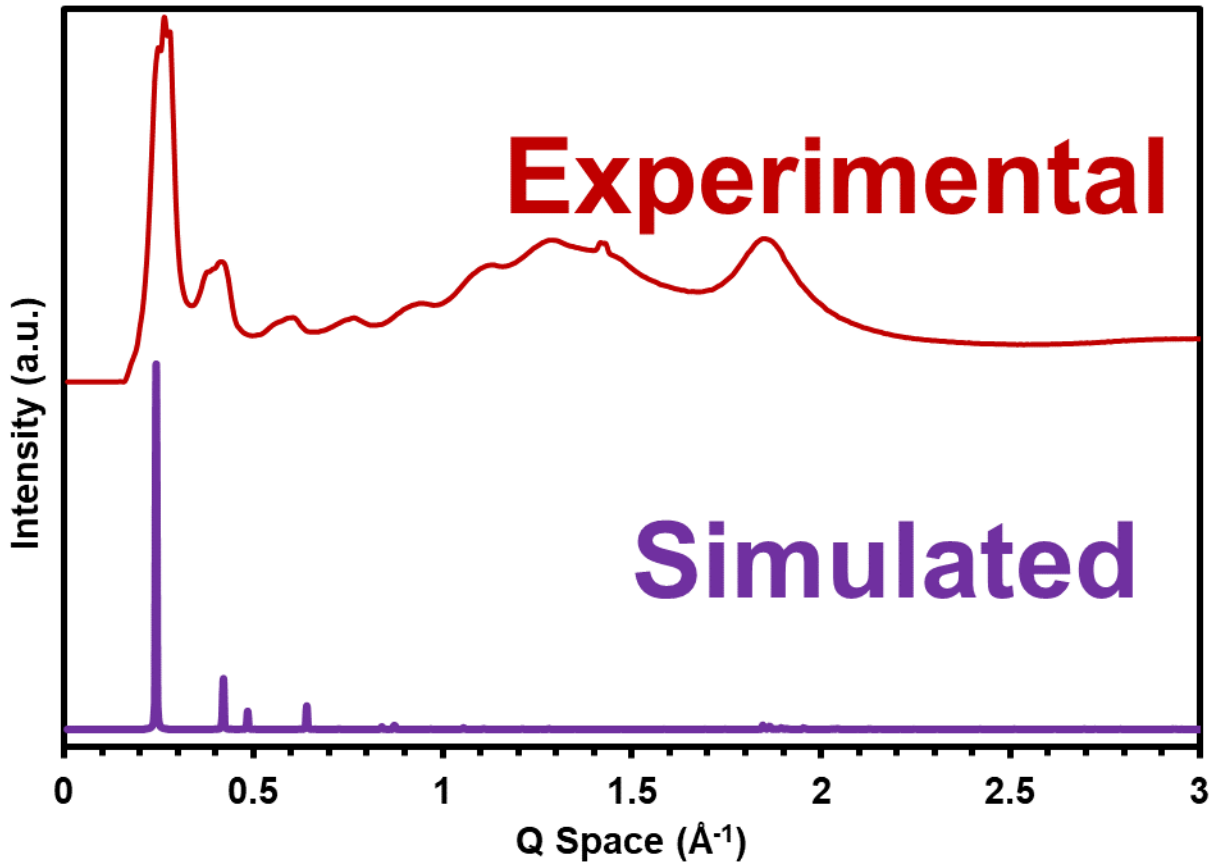

Figure 9.42. Linear experimental X-ray diffraction pattern extracted from 2D GI-WAXS pattern of COF-10 and simulated X-ray diffraction pattern from a geometry optimized COF-10 crystallite.

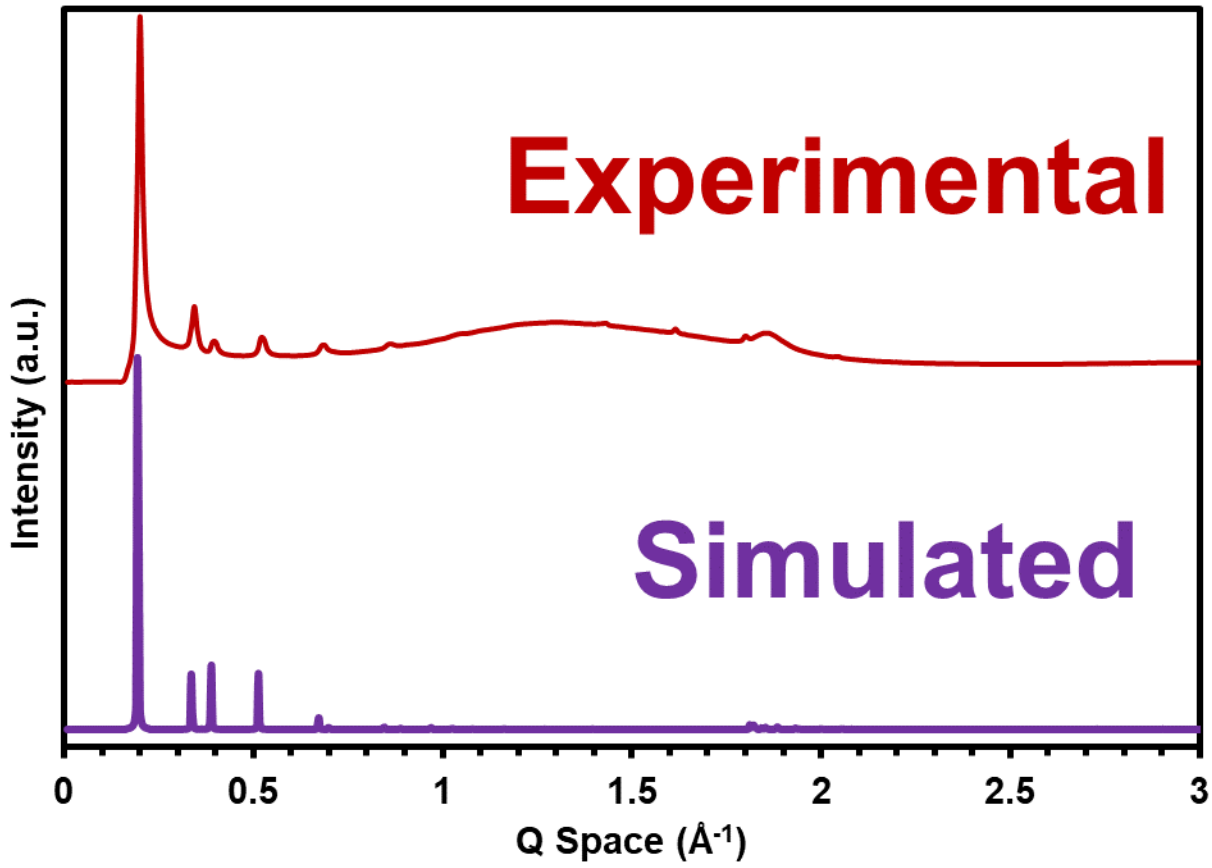

Figure 9.43. Linear experimental X-ray diffraction pattern extracted from 2D GI-WAXS pattern of TP-COF and simulated X-ray diffraction pattern from a geometry optimized TP-COF crystallite.

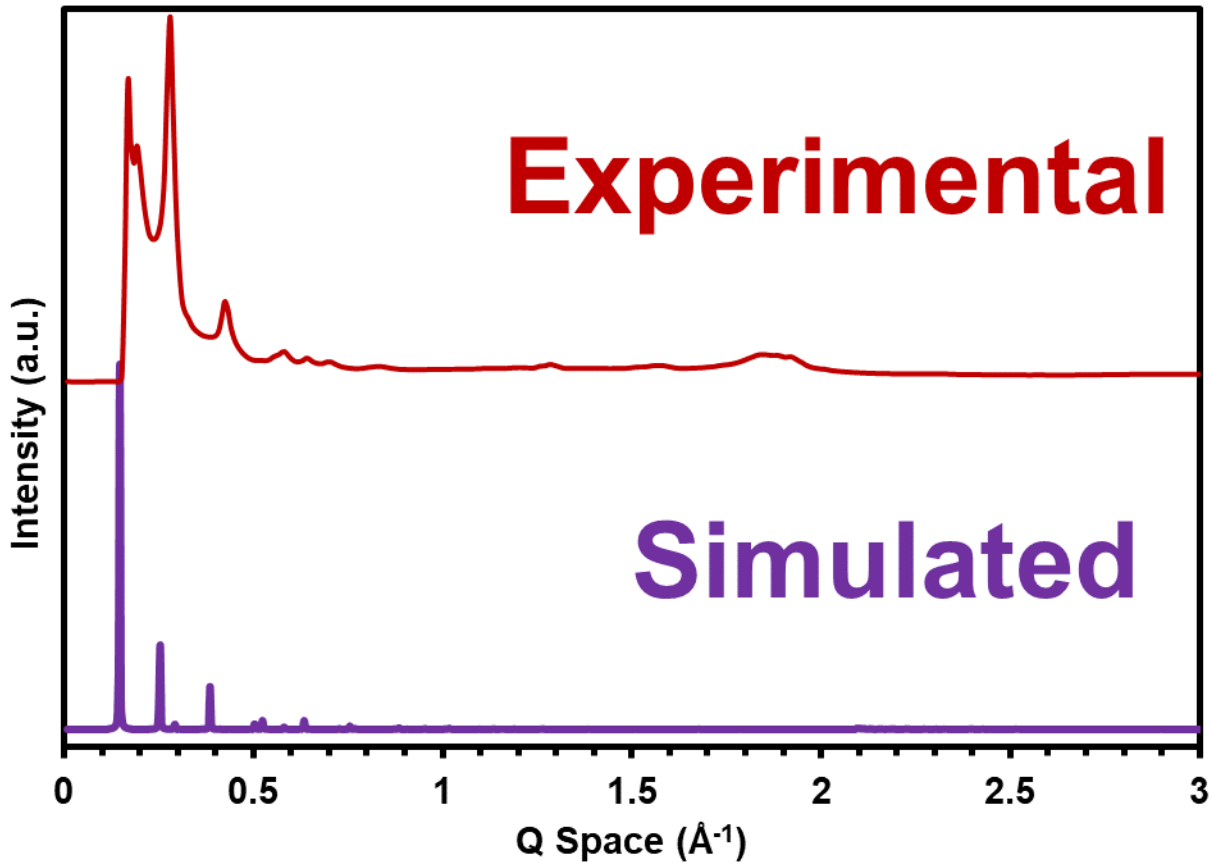

Figure 9.44. Linear experimental X-ray diffraction pattern extracted from 2D GI-WAXS pattern of DPB-COF and simulated X-ray diffraction pattern from a geometry optimized DPB-COF crystallite.

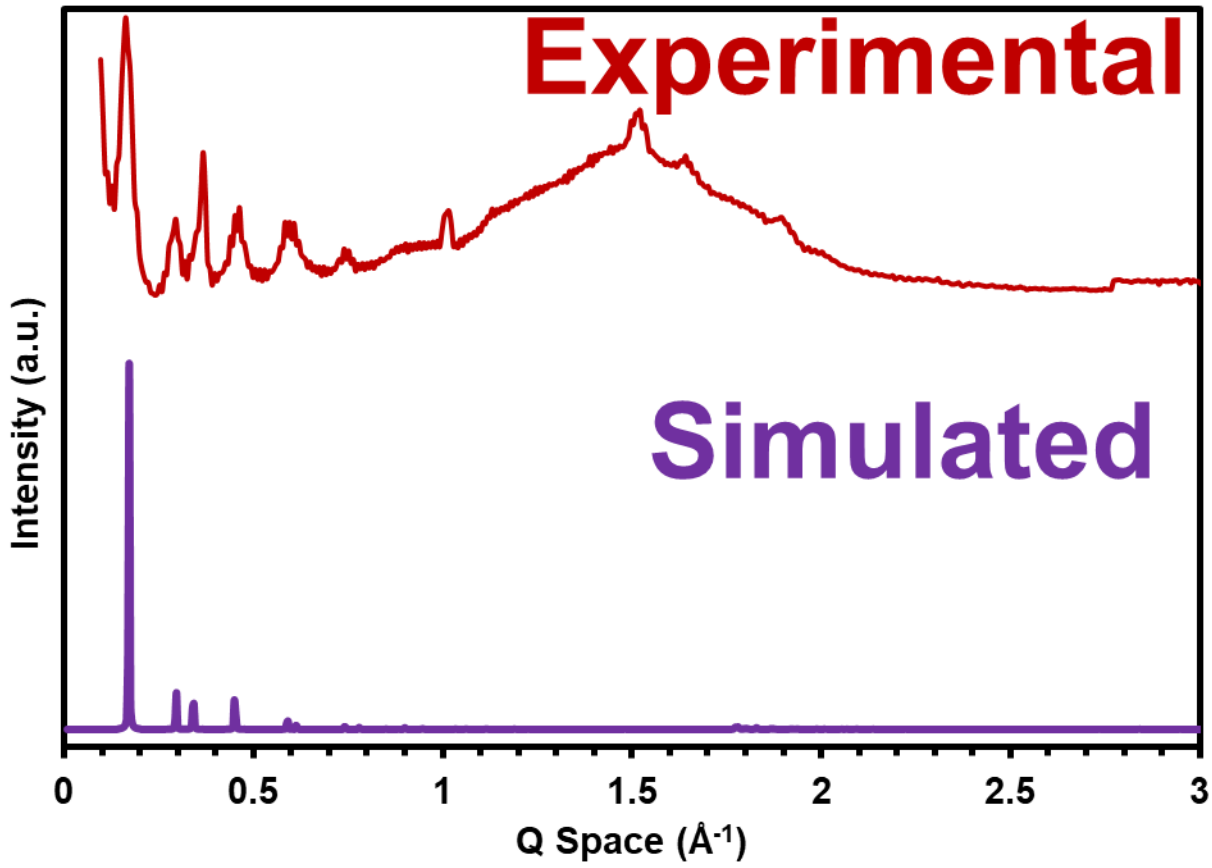

Figure 9.45. Linear experimental X-ray diffraction pattern extracted from 2D GI-WAXS pattern of COF-117 and simulated X-ray diffraction pattern from a geometry optimized COF-117 crystallite.

Density Functional Theory (DFT) Calculations

The electronic band structures of COF-5 were calculated with the CRYSTAL17 package[707, 708] at the DFT PBE0 level[709, 710] using the POB-TZVF basis set with D3 van der Waals (vdW) corrections[711]. 2 x 2 x 14 and 2 x 2 x 18 Γ-centered Monkhorst-Pack *k*-meshes were adopted in the geometry optimizations and self-consistent calculations (SCF), respectively.

The macroscopic static dielectric tensors taking account of the electronic contributions[700] were calculated at the DFT PBE level using the Vienna Ab initio Simulation Package (VASP) [701] and D3 vdW corrections. Γ-centered Monkhorst-Pack *k*-meshes were adopted in both geometry optimizations and SCF calculations (see **Table S1**). The convergence criterion for the total energy was set at 10^{-8} eV; the one for the forces was set at 0.01 eV $Å^{-1}$. We considered a Gaussian smearing of 0.01 eV. The lattice parameters after geometry optimization of each COF are shown in **Table S2**. The off-diagonal components in the calculated macroscopic static dielectric tensors are vanishingly small. The ionic contributions to the macroscopic static dielectric tensors of COF-5 were calculated via density functional perturbation theory (DFPT)[712] using VASP.

Table 9.1. Γ-centered Monkhorst-Pack *k*-meshes applied in the DFT/PBE calculations for the five COFs.Γ-centered Monkhorst-Pack *k*-meshes applied for each COF

	COF-5	TP-COF	COF-10	COF-117	DPB-COF
Optimization	1 × 1 × 8	1 × 1 × 10	1 × 1 × 10	1 × 1 × 11	1 × 1 × 12
SCF	2 × 2 × 16	2 × 2 × 20	2 × 2 × 20	2 × 2 × 22	2 × 2 × 24

Table 9.2. Optimized crystal structures at the DFT/PBE level for the five COFs.

	a(Å)	b(Å)	c(Å)	α(°)	β(°)	γ(°)
COF-5	30.17	30.17	3.73	90.00	90.00	120.00
TP-COF	37.53	37.53	3.72	90.00	90.00	120.00
COF-10	37.72	37.72	3.71	90.00	90.00	120.00
COF-117	41.98	41.98	4.08	90.00	90.00	120.02
DPB-COF	46.53	46.53	3.74	90.00	90.00	120.00

Table 9.3. Ionic and electronic contributions to the COF-5 dielectric tensors.

	ε_{xx}	ε_{yy}	ε_{zz}
Ionic contributions	0.3	0.1	0.0
Electronic contribution	2.0	2.0	1.3
Total	2.3	2.1	1.4

Polarization Dependent Emission of 2D COF Films

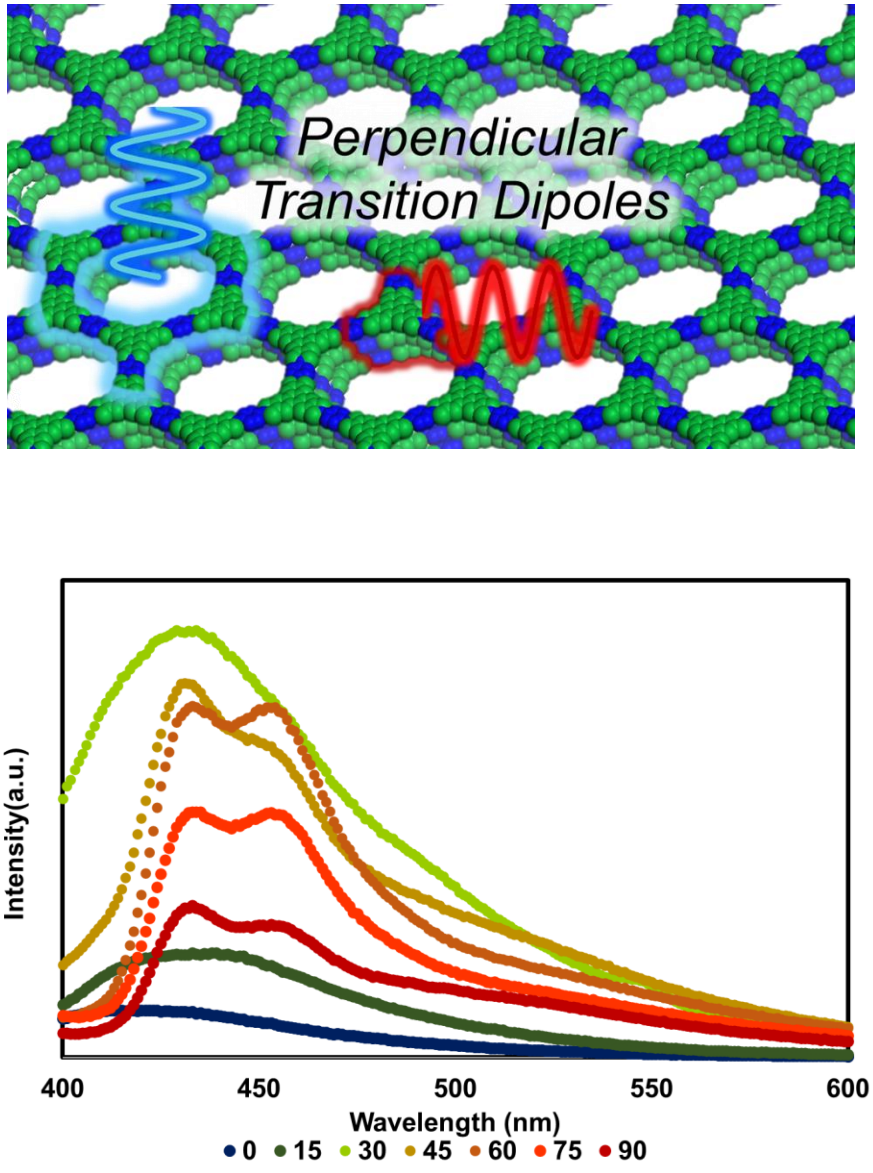

Figure 9.46. Polarization dependent emission of TP-COF films

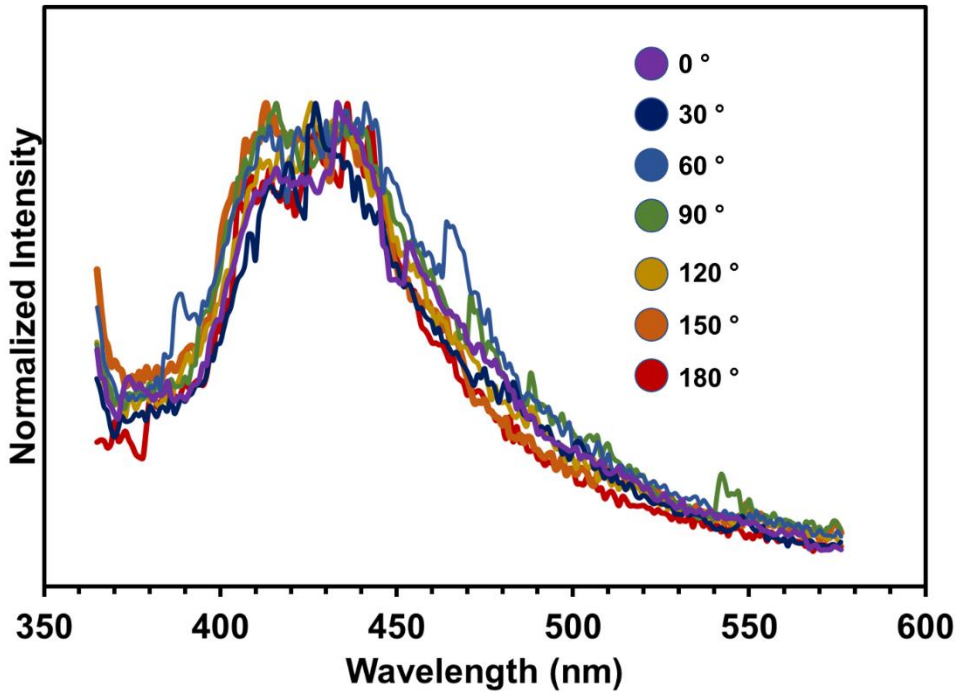

Figure 9.47. Polarization dependent emission of COF-5 films produced via solvothermal synthesis

Scanning Electron Microscopy

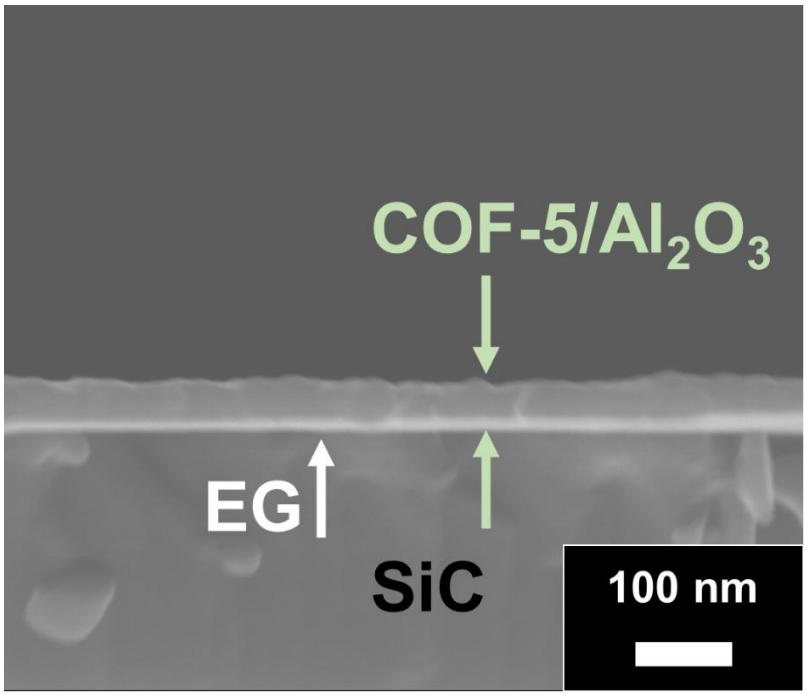

Figure 9.48. Cross-sectional scanning electron micrograph of COF-5/Al_2O_3/EG/SiC

X-ray Reflectivity of 2D COF Films and Devices

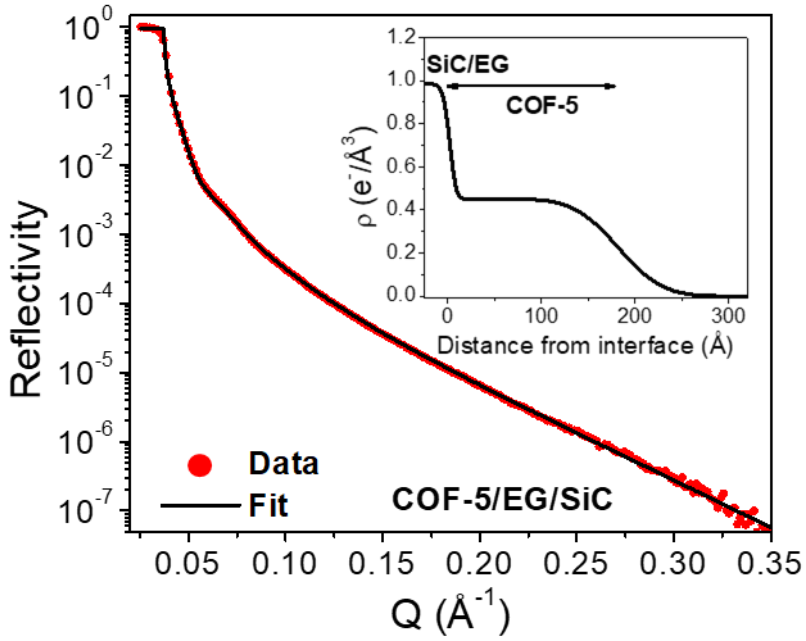

Figure 9.49. X-ray reflectivity profiles of COF-5/EG/SiC. Inset: Extracted Electron Density Profile.

Table 9.4. XRR fitting parameters from figure S45.

	Thickness (Å)	Roughness (Å)	e^- density ($e^- Å^{-3}$)
COF-5	**177.7**	**37.3**	**0.452**
EG	**4.0**	**4.6**	**0.678**
SiC	**-**	**5.6**	**0.983**

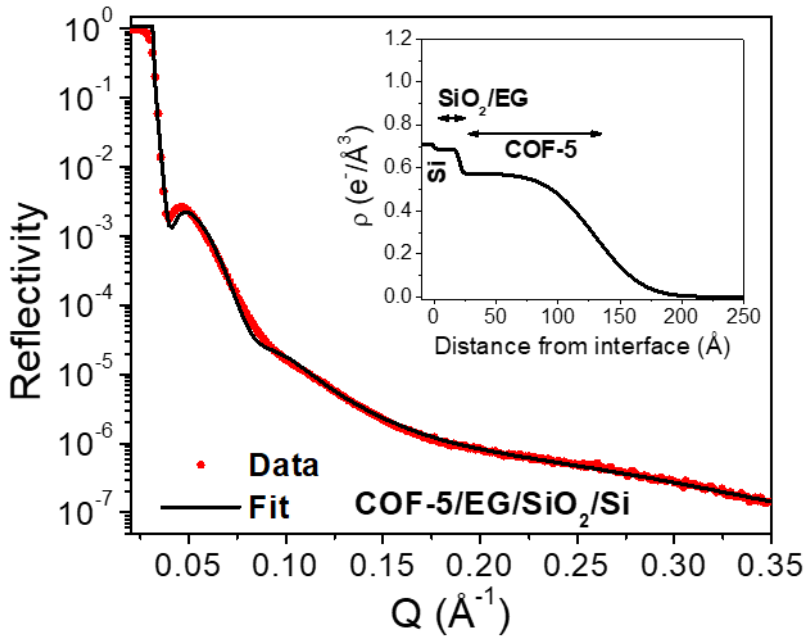

Figure 9.50. X-ray reflectivity data a fit of COF-5/EG/SiO2/Si. Inset: Electron density profile extracted from the XRR fit.

Table 9.5. XRR fitting parameters from figure S46

	Thickness (Å)	Roughness (Å)	e^- density ($e^- Å^{-3}$)
COF-5	**108.8**	**30.4**	**0.573**
SiO_2/EG	**20.5**	**2.1**	**0.688**
Si	**-**	**1.0**	**0.709**

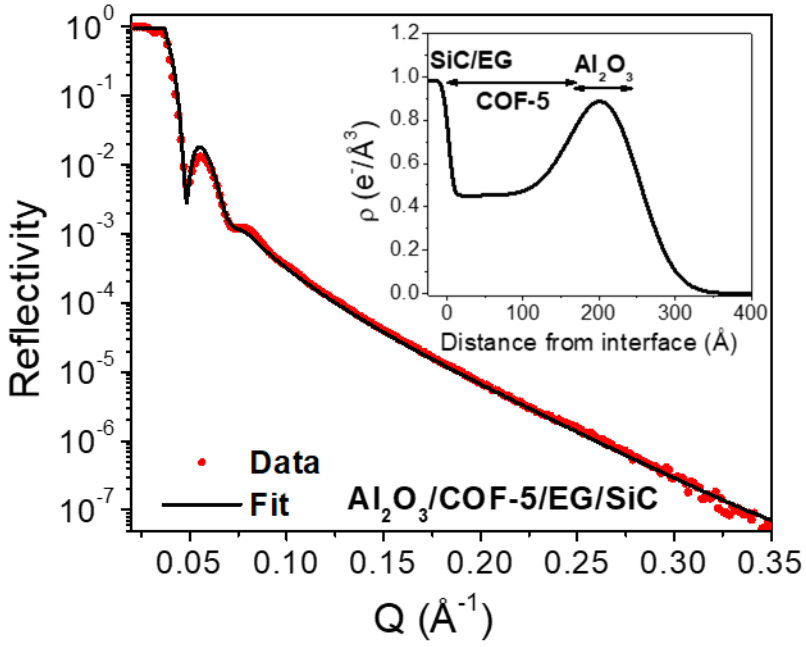

Figure 9.51. X-ray reflectivity profiles of Al_2O_3/COF-5/EG/SiO_2/Si Inset: Extracted Electron Density Profile.

Table 9.6. XRR fitting parameters from figure S47. .

	Thickness (Å)	Roughness (Å)	e^- density ($e^- Å^{-3}$)
Al_2O_3	**75.1**	**38.7**	**1.192**
COF-5	**168.9**	**38.5**	**0.452**
EG	**3.99**	**4.6**	**0.678**
SiC	**-**	**5.6**	**0.983**

2D COF Film Device Measurements

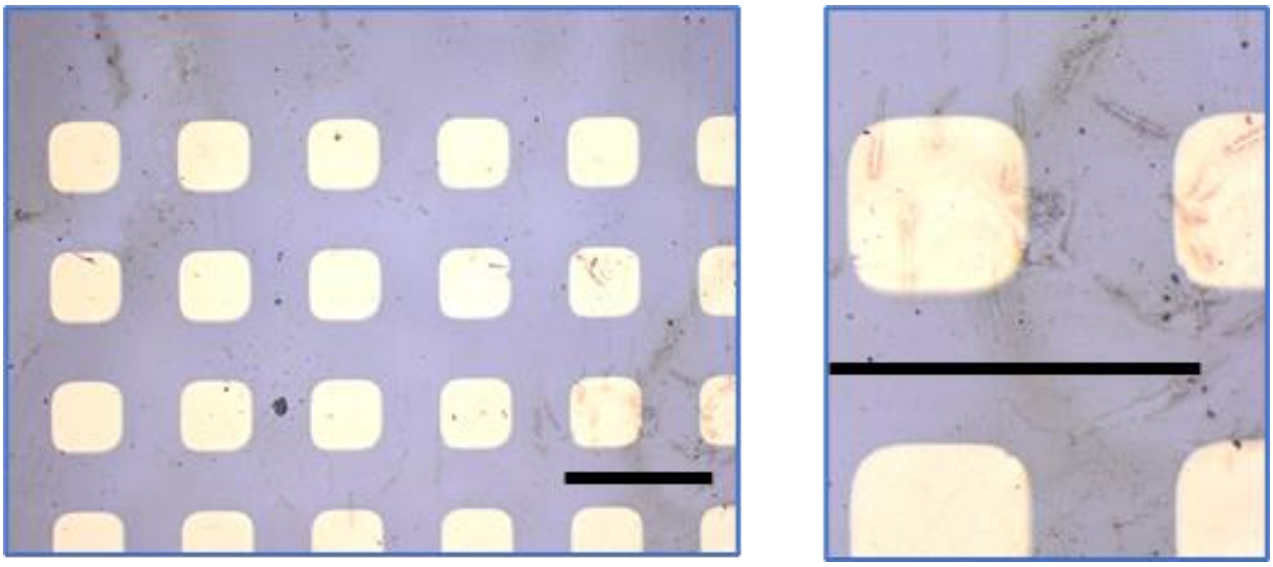

Figure 9.52. Optical microscope images of Al_2O_3/COF-5/EG/SiC (Scale Bar = 200 μm)

The area of each Au pad is roughly 100,000 μm^2 (10^{-8} m^2) as determined from the optical image on the right.

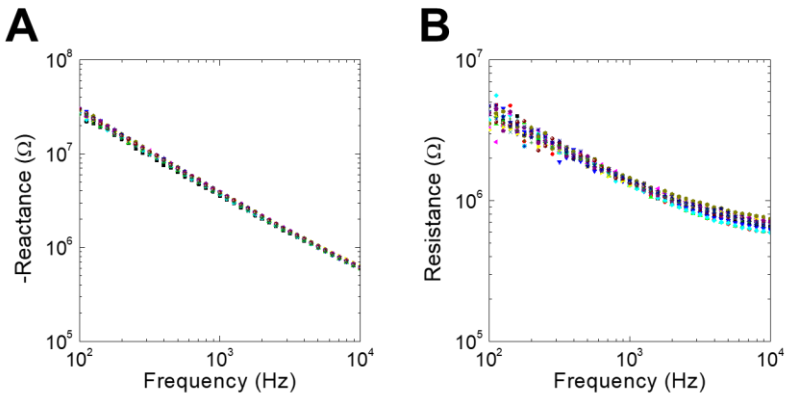

Figure 9.53. (A), (B) Bode plots showing tight distribution of real and imaginary parts of the impedance for 10 different COF-5 devices across the EG/SiC chip. The extracted capacitance is found vary by less than 10% over an area of 25 mm^2.

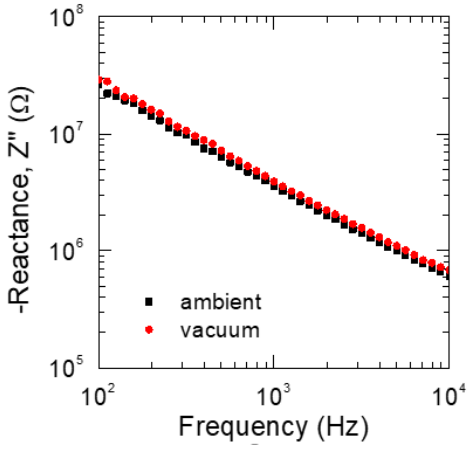

Figure 9.54. Plot of negative reactance (-Z”) versus frequency of a Al2O3/COF-5 dielectric bilayer capacitor in ambient (relative humidity ~62 %) and in vacuum (pressure = 2 x 10-5 torr).

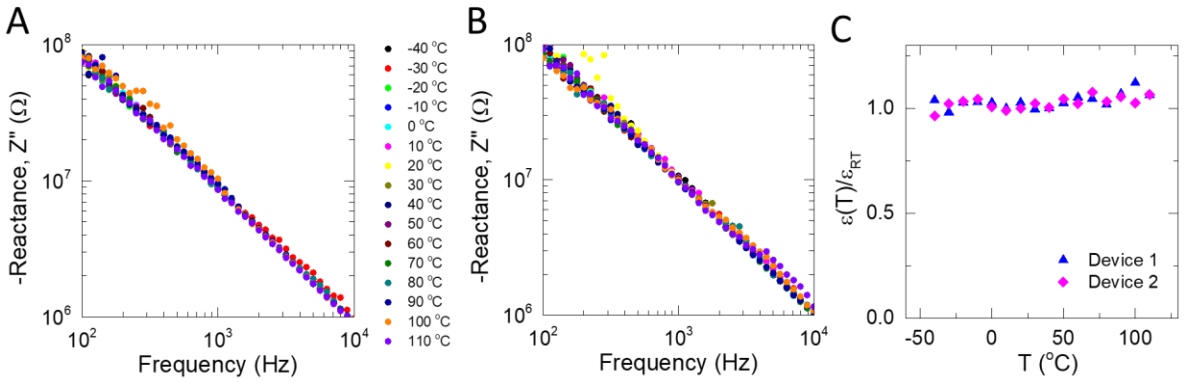

Figure 9.55. (A-B) Plot of negative reactance (-Z") of two different Al2O3 dielectric bilayer capacitor devices as a function of temperature (-40 °C - 110 °C). **(C)** Plot of the normalized dielectric constant across this temperature range for two devices, demonstrating that the dielectric constant is invariant across this temperature range.

Thermoreflectance Measurements

A. Sample Preparation. To prepare our samples for time-domain thermoreflectance (TDTR), we first deposit an 80 nm thick Al transducing layer via electron beam evaporation at $6 \cdot 10^{-6}$ Torr.

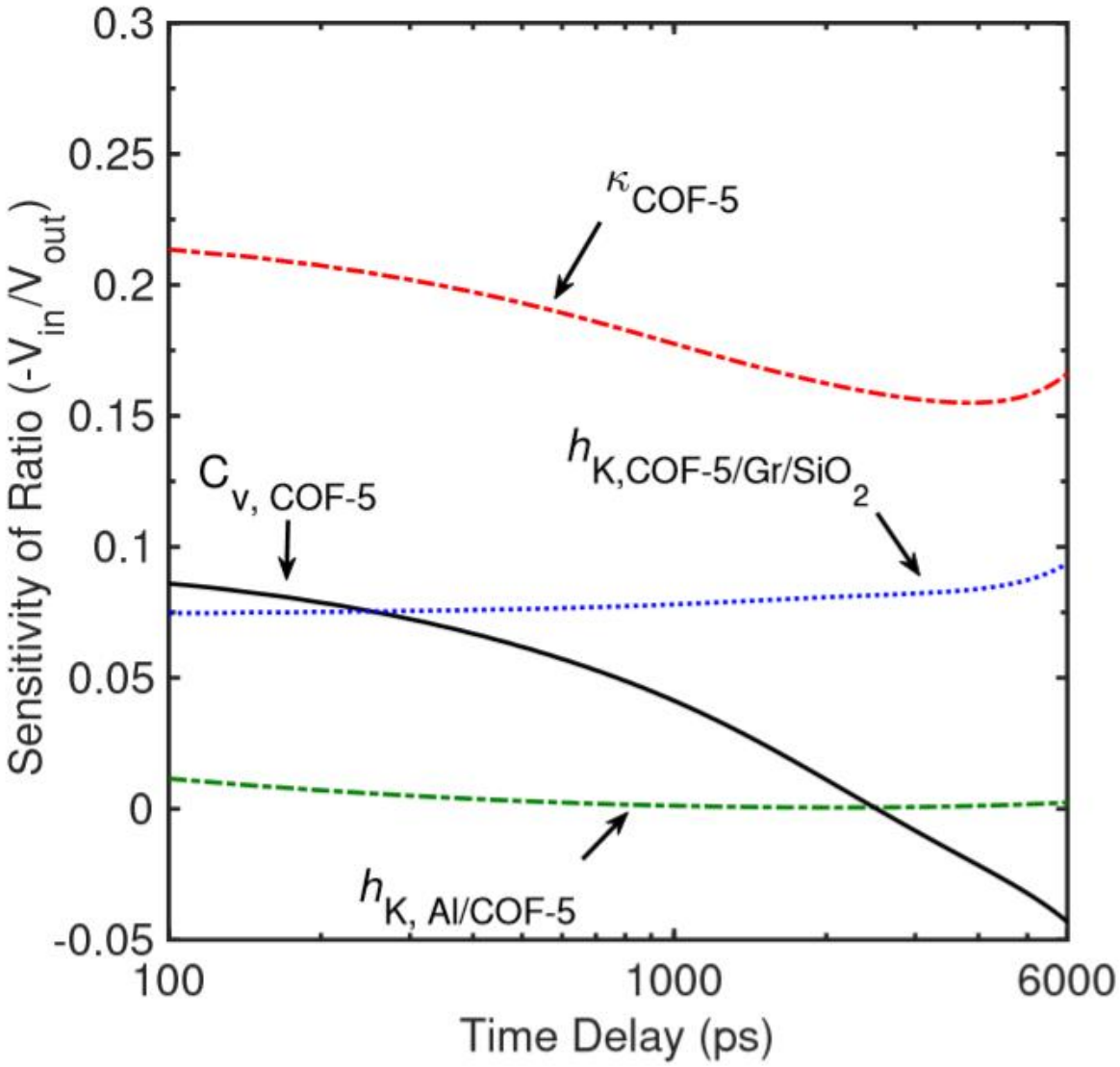

Figure 9.56. Sensitivity of the ratio of the in-phase (V_{in}) and out-of-phase (V_{out}) signals for COF-

5 at 8.8 MHz modulation frequency.

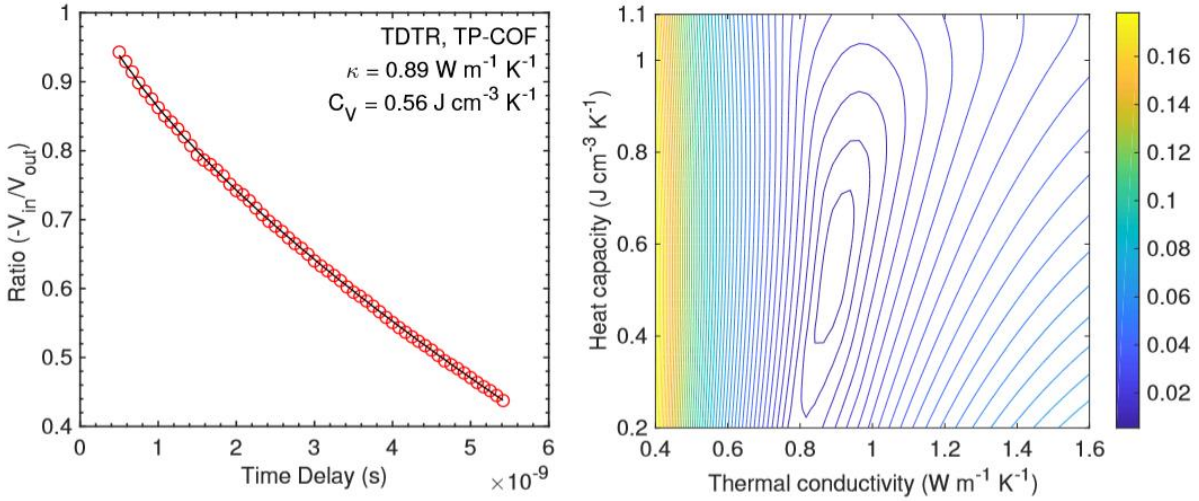

Figure 9.57. (Left) Characteristic TDTR data along with the best-fit curve for TP-COF. (Right) Sensitivity contour plot showing the interrelationship between the measured heat capacity and thermal conductivity of our 2D TP-COF

B. TDTR Measurements. In our TDTR setup, sub-picosecond laser pulses emanate from a Ti:Saphhire oscillator at 80MHz repetition rate. The pulses are separated into a pump path that heats up the sample and a time-delayed probe path that is reflected from the Al transducer. The reflected probe beam provides a measure of the change in the thermoreflectance due to the decay of the thermal energy deposited by the pump beam. A modulation of 8.8 MHz is applied by an electro-optic modulator on the pump beam and the ratio of the in-phase to out-of-phase signal of the reflected probe beam recorded at that frequency by a lock-in amplifier ($-V_{in}/V_{out}$) for up to 5.5 ns after the initial heating event. The pump and probe beams are focused on to the Al transducer at e^{-2} radii values of 10 and 5 μm for our pump and probe spots, respectively.

To simultaneously measure the thermal conductivity and heat capacity of our COFs, we fit a three-layer thermal model to our experimental data. However, we first consider the appropriate range of pump-probe delay times, in which the thermal model is extremely sensitive to changes in the thermophysical quantities. This is quantified by the sensitivity of the ratio (V_{in}/V_{out}) to the various thermal properties defined by,

$$S\alpha = \frac{\partial ln\left(\frac{Vin}{Vout}\right)}{\partial ln(\alpha)} \qquad (2)$$

where α is the thermophysical parameter of interest.[713] **Figure S50** shows the sensitivities of the ratio to thethermophysical parameters of the three-layer thermal model. The sensitivity to the

thermal conductivity of COF-5, $\kappa_{COF\text{-}5}$, is relatively large compared to the other parameters for the entire time delay. The large and dynamic sensitivity of the heat capacity of our COF film (C_v) also allows for the simultaneous measurement of these two physical properties with relatively good precision, therefore, we treat κ_{COF} and C_v as adjustable parameters in our analytical model to fit the TDTR data for the entire pump-probe delay time.

Characteristic TDTR data and the best-fit of the thermal model for TP-COF at 8.8MHz modulation frequency is shown in **Figure S51**. **Figure S51** shows the sensitivity contour plot describing the interrelationship between the measured heat capacity and thermal conductivity of TP-COF at 8.845 MHz modulation frequency. Note, the contour plot represents the mean square deviation of our thermal model to the TDTR data with the various combinations of heat capacity and thermal conductivity as input parameters.[714, 715] The standard deviation between our model and data is determined as,

$$\sigma = \frac{\sum_{j=0}^{n} (R_{m,j} - R_{d,j})^2}{n} \qquad (3)$$

where R_m and R*d* are the ratios from the model and data, respectively, and *n* is the total number of time delays considered.

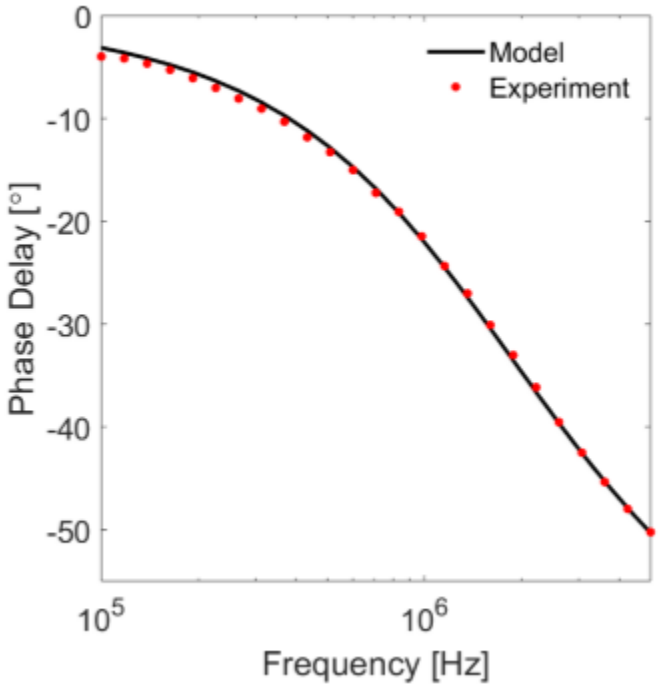

Figure 9.58. Phase delay data and fit as a function of modulation frequency for a representative FDTR experiment.

C. Thermal boundary conductance.

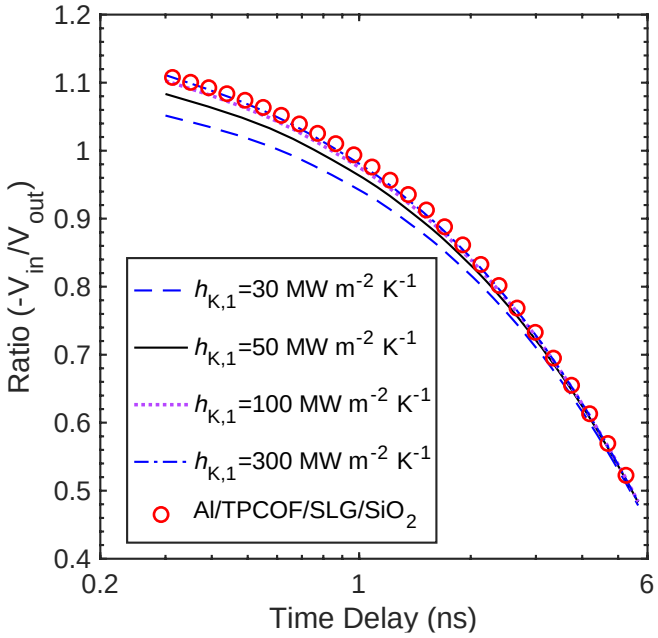

Figure 9.59. Analytical fits to the TDTR experimental data with different values of thermal boundary conductances across Al/COF interface $h_{K,1}$, while other parameters in the thermal model are unchanged.

From time-domain thermoreflectance measurements, we determine that the thermal resistivity of the Al/COF-5 boundary is minimal (**Fig. S55**). As observed from the analytical fits to our TDTR results with varying thermal boundary conductance (h_K) at the Al/COF interface, h_K < 70 MW m^{-2} K^{-1} results in poor fits to the experimental data as shown in Fig. R1 below. In contrast, higher h_K values optimize the fits for the early pump-probe time delays (especially at t < 1 ns). Moreover, increasing the value of h_K > 100 MW m^{-2} K^{-1} at the Al/COF interface has negligible influence on the best-fit to our experimental data. These results suggest that h_K at Al/COF is considerably higher than the conductance of our COF films.

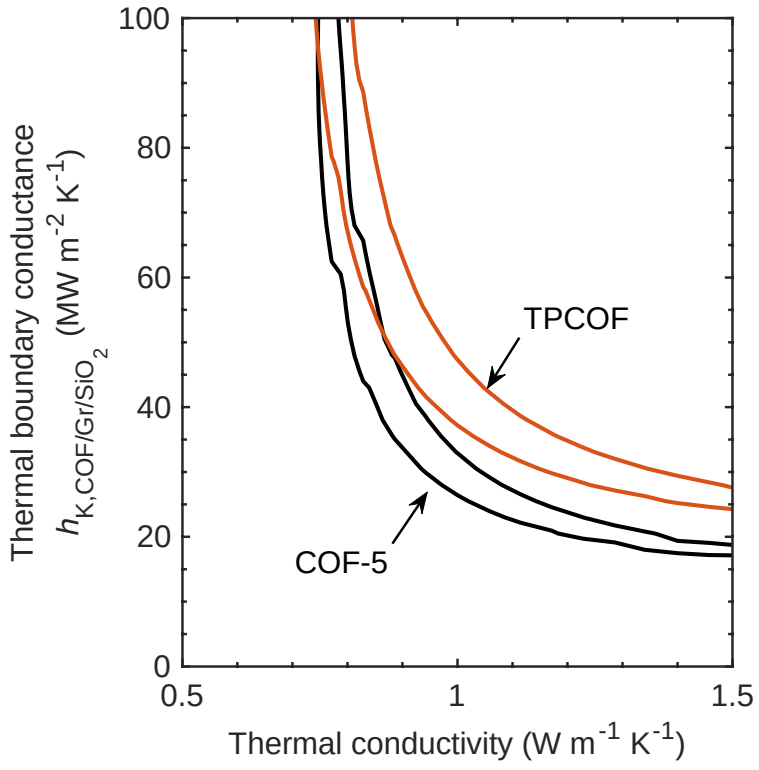

Figure 9.60. Sensitivity contour plot showing the interrelationship between thermal boundary conductance and thermal conductivity of our 2D COFs.

We plot sensitivity contour plots (**Fig. S56**) that represent the mean square deviation of the analytical model to our TDTR data with various combinations of thermal conductivity of COF (κ_{COF}) and $h_{K,2}$ at COF/SLG/SiO_2 interface as input parameters in our three-layer model. A combination of low $h_{K,2}$ (< 30 MW m^{-2} K^{-1}) and relatively high κ_{COF} (> 1.3 W m^{-1} K^{-1}) produce the best-fits suggesting that the resistance at the interface dominates heat transfer in the cross-plane direction. As such, we assign a lower bound of 30 MW m^{-2} K^{-1} to $h_{K,2}$ from our measurements.

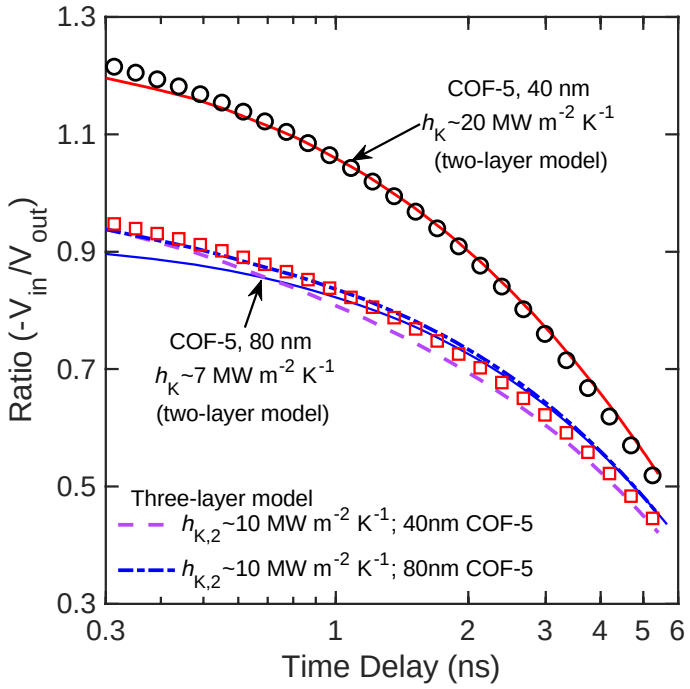

Figure 9.61. TDTR data for COF-5 films of 40 nm and 80 nm thickness along with the best-fit curves. The solid lines represent two-layer thermal model (for an Al/SiO_2 system) with thermal

boundary conductance (h_K) as fitting parameter. The dashed and dotted-dashed lines represent three-layer thermal model with high interfacial resistances (R_K) across the COF-5/graphene/SiO_2 interface ($R_{K,2}$~10^{-7} m^2 K W^{-1}; $h_{K,2}$~10 MW m^{-2} K^{-1}) for 40 nm and 80 nm COF-5 thicknesses. A high interfacial resistance would result in poor fits to the experimental data, which suggests that interfacial resistances are much lower than the bulk resistance posed by the 2D COF thin film. As such, we are predominantly sensitive to the intrinsic thermal resistance of the 2D COF in this measurement.

In the scenario where interfacial resistances dominate heat transfer, decreasing the film thickness will have a negligible effect on total thermal transport. However, if heat transfer is dominated by the intrinsic resistance of the film, a change in the thickness results in a noteable change in the total conductance across the sample. To differentiate between these different possibilities, we synthesized an additional COF-5 film with a different thickness of that measured previously. TDTR measurements (**Figure S57**, open points) and two-layer thermal model (interfacial resistances considered as a single component) best fits (**Figure S57,** solid lines) reveals a thermal conductivity thickness dependence. To show how the fits would change if interfacial resistance would be the dominant resistance in our model, we also plot predictions from a three-layer model where we prescribe a low conductance (high resistance) across the COF-5/SLG/SiO_2 ($h_{K,2}$~ 10 MW m^{-2} K^{-1}) for 40 nm and 80 nm COF-5 samples (dashed line and dotted-dashed lines, respectively). For the scenario where thermal transport is dominated by interfacial resistance, the model predicts similar behavior for the two thicknesses, which is inconsistent with our TDTR data.

D. Frequency-Domain Thermoreflectance. To cross-validate and gain confidence in our TDTR results, we perform Frequency domain thermoreflectance (FDTR) measurements on our COF-5 sample. Similar to TDTR, FDTR is also a laser-based metrology implemented to measure thermal properties of a sample.[716, 717] A thin (73.1 nm measured by KLA Tencor P-15 Profilometer) coating of Au is sputter deposited (PerkinElmer6J) on top of the sample. The Au-coated sample is periodically heated via a sinusoidally modulated (100 kHz - 5 MHz) pump laser at 488 nm wavelength. The sample's temperature will fluctuate with the same frequency as the pump laser, but with a time delay. The phase delay is characteristic of the thermal properties of the sample. The temperature is measured using a concentric probe laser (532nm), which is sensitive to the thermoreflectance of Au. The frequency-dependent time delay measured as a phase delay of the reflected probe laser with respect to the pump laser modulation frequency is measured with a photodiode connected to a lock-in amplifier. The phase delay, as shown in **Fig. S52**, is fit to an analytical solution to heat diffusion equation for a layered, semi-infinite solid to extract the thermal conductivity of the COF-5 sample. Our TDTR analysis also has sensitivity to the thermal boundary conductance across the COF-5/single layer graphene/SiO2 interface. By using the heat capacities determined via MD and FDTR (see below), we fit for a thermal boundary conductance of ~30 MW m^{-2} K^{-1}, in reasonable agreement with previous measurements across similar (single layer graphene/SiO2) interfaces.[718]

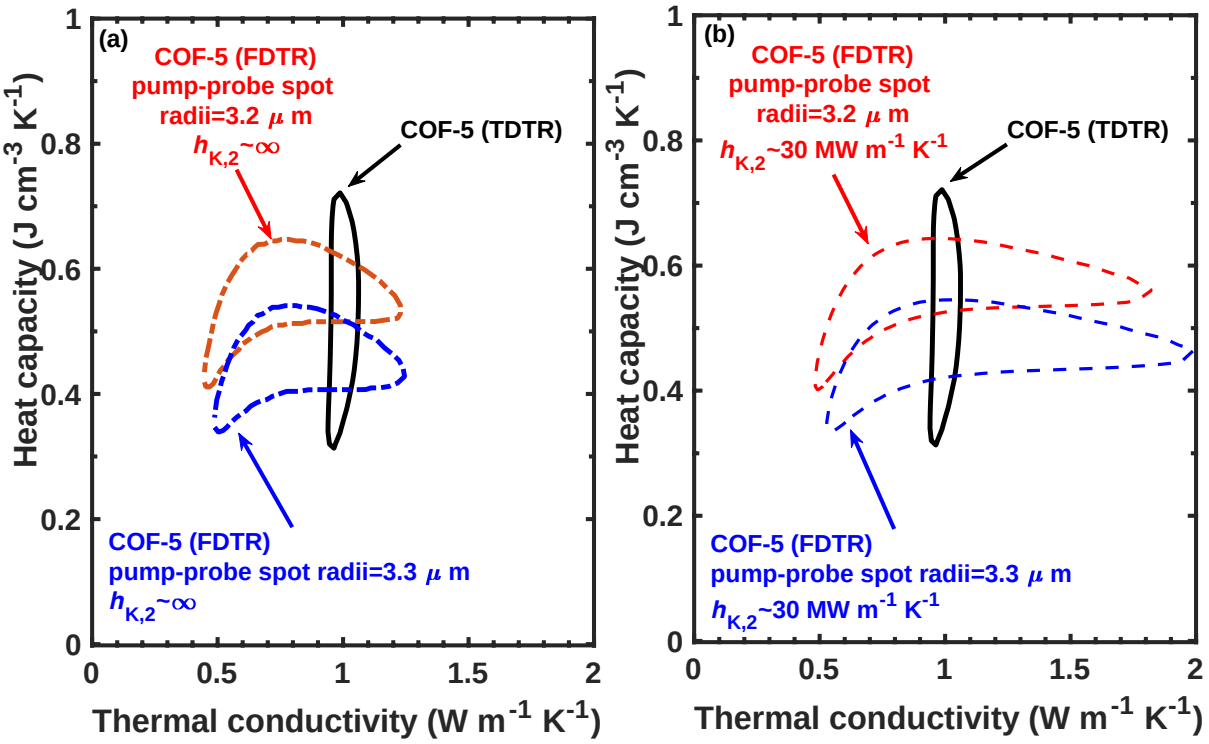

Figure 9.62. Contours at 1.2×Minimum MSE for FDTR data averaged over four experiments for COF-5, as a function of assumed heat capacity and thermal conductivity for 3.2 µm (red dashed line) and 3.3 µm (blue dashed line) pump-probe spot radii (a) without a resistance at the interface and (b) with a finite thermal boundary conductance at the COF-5/SLG/SiO_2 ($h_{K,2}$ ~ 30 MW m^{-2} K^{-1}). For comparison, we also include the contour from our TDTR measurement on the same sample

COF thermal conductivity is the targeted property, but its value depends on the heat capacity of the COF, which is also unknown. We evaluated the quality of the fit between the model and data based on the mean squared error (MSE). The MSE was calculated assuming a range of thermal conductivity and heat capacity combinations and averaged for four independent data sets. In Fig.S4 we plot the global minimum MSE and a contour at 1.2 times the global minimum MSE for two different spot radii (red for a radius of 3.2 μm and blue for a radius of 3.3μm). The predicted values of thermal conductivity (κ_{COF}) and heat capacity (C_V) are sensitive to the spot size. The contours indicate that a range of $0.5 < \kappa < 2$ W m^{-1} K^{-1} and $0.33 < C < 0.63$ J cm^{-3} K^{-1} could be reasonably interpreted from the FDTR experiments. Though FDTR is less sensitive to κ than TDTR, the range of values for C and κ overlap (as shown in **Fig. S53**) and FDTR serves to strengthen the conclusion reached by TDTR.

E. Uncertainty Analysis for Thermal Properties.

To determine the uncertainties in our measurements for C_v and κ_{COF}, we use a combination of sensitivity contour analysis along with the changes in the predicted values of C_v and κ_{COF} based on perturbing different parameters in our three-layer thermal model within their error bounds. For example, we measure the thermal conductivity of aluminum as 126 ± 4 W m^{-1} K^{-1} using the four-point probe method and determine its thickness as 80 ± 3 nm using picosecond acoustics. Therefore, the uncertainty in our measured C_v and κ_{COF} includes the error associated with our thickness measurement of the aluminum transducer and its thermal conductivity, κ_{Al}. Perturbing the thickness of aluminum by 3 nm changes κ_{COF} by ~11 % and C_v by ~6 %. Whereas the error in κ_{Al} leads to a relatively lower uncertainty (of < 2 %) associated with both κ_{COF} and C_v measurements. We note that the uncertainty in C_v is relatively higher than the uncertainty in κ_{COF} since perturbing the thermal conductivity by ~2 % changes the heat capacity by ~ 20 % as shown in the sensitivity contour plot in Fig. S53. We use FDTR technique discussed in detail in the following section to reduce the uncertainty associated with our C_v measurement. We note that the biggest uncertainty to our measurements is due to the unknown $h_{K,2}$ (at the COF/Single-layer-graphene/SiO_2 interface) for which we can only set a lower estimate of ~ 50 MW m^{-2} K^{-1} as we detail below.

Molecular Dynamics Simulations

Our molecular dynamics (MD) simulations are performed with the LAMMPS code[719] and the interatomic interactions are described by the adaptive intermolecular reactive empirical bond order (AIREBO) potential.[703] We apply periodic boundary conditions in all directions. The computational domains are equilibrated under the Nose-Hoover thermostat and barostat,[720] (which is the NPT83 integration with the number of particles, pressure and temperature of the system held constant) for a total of 1ns at 0 bar pressure. Following the NPT integration, an NVT integration (with constant volume and number of particles) is prescribed to fully equilibrate the structures at the desired temperature for another 1 ns. Note, we prescribe a time step of 0.5 fs for all our simulations. **Figure S45a** shows an example of our computational domain for the COF-5 and the unit cell of the COF-5 is shown in **Fig S45b**. For the simulations, we vary the total cross-plane thickness, d, and length of the computational domain, L, to check for size effects in our thermal conductivity predictions as detailed below.

After equilibration, the thermal conductivities of our COFs at different temperatures predicted via the Green-Kubo (GK) approach under the EMD framework. In this formalism, the thermal conductivities of our COFs along the x-,y-(in-plane) and z-(cross-plane) directions are calculated as,

$$\kappa_{x,y,z} = \frac{1}{k_B V T^2} \int_0^\infty < S_{x,y,z}(t) \bullet S_{x,y,z}(0) > dt \qquad (4)$$

Here t is time, T and V are the temperature and volume of the systems, respectively, and $< S_{x,y,z}(t)\, S_{x,y,z}(0) >$ is the component of the heat current autocorrelation function (HCACF) in the prescribed directions.

To ensure that the HCACF decays to zero, we set the total correlation time period for the integration of the HCACF to 50 ps as shown in the inset of **Fig. 55**. The heat current is computed every 10 time steps during the data collection period, after which, integration is carried out to calculate the converged thermal conductivity for our COF-5 structure. The converged thermal conductivity is determined by averaging from 10 ps to 50 ps as shown in **Fig. S56** (dashed line). We note that since the main goal of our simulations is to establish a comparative analysis of in-plane and cross-plane thermal conductivity, we refrain from comparing our experimentally determined cross-plane thermal conductivity with our MD predictions. Moreover, the choice of the interatomic potential has large implications on the thermal conductivity predictions for similar covalently bonded carbon structures.[721-723]

The GK approach has been extensively used to predict the lattice thermal conductivity of different crystalline and amorphous material systems.[724-731] However, there has been considerable ambiguity in efficiently calculating the thermal conductivity via Eq. 4 due to uncertainties associated with finite simulation times and domain sizes.[725-727, 729, 732-736] To ensure that the EMD-predicted thermal conductivities are not influenced by size effects, the dimensions of the simulation box are chosen to produce converged values of thermal conductivities. To this end, the thermal conductivities of structures with cross-sections of 15×13 nm^2 and 30×26 nm^2 are comparable within uncertainties. Similarly, the thermal conductivities of structures with computational domain sizes of 15.1×13.1×3.4 nm^3, and 15.1×13.1×10.2 nm^3 are also similar within uncertainties.

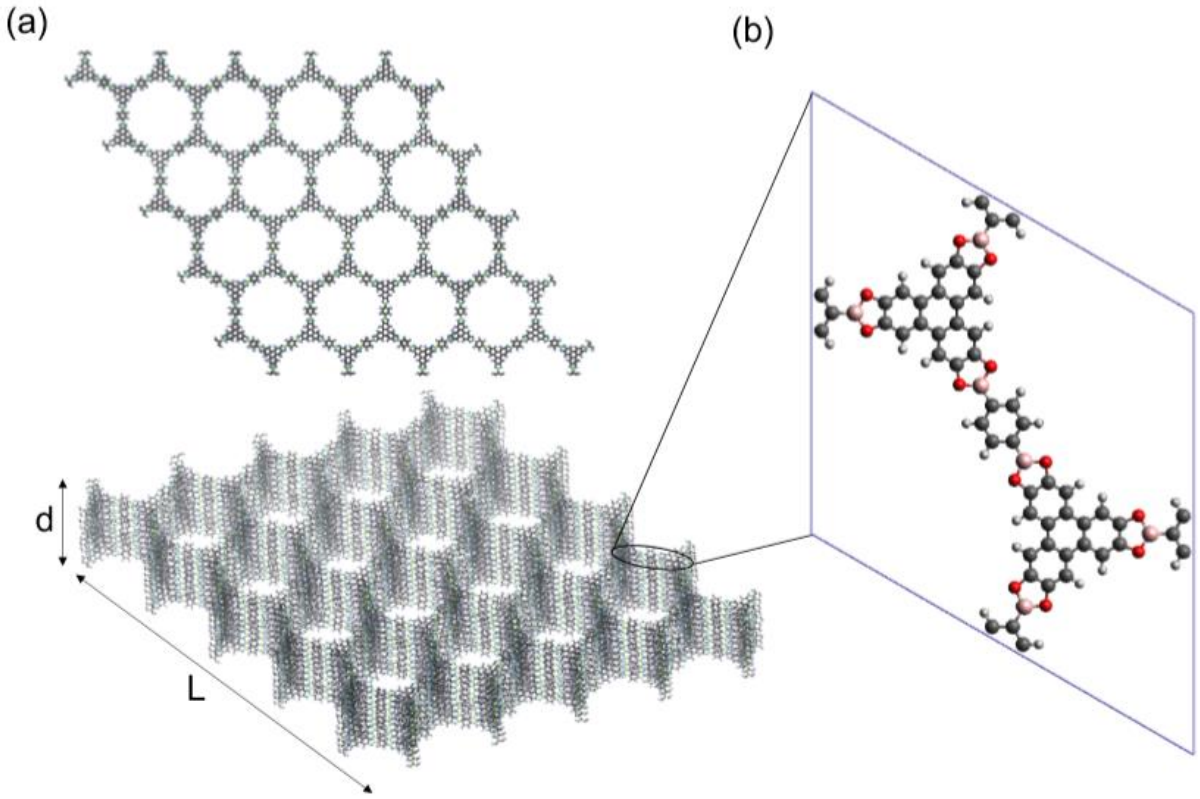

Figure 9.63. (a) Schematic of the computational domain of the COF-5 structure used for our molecular dynamics simulations. (b) Schematic of the unit cell of the COF-5 structure with different atomic species represented by the different colors.

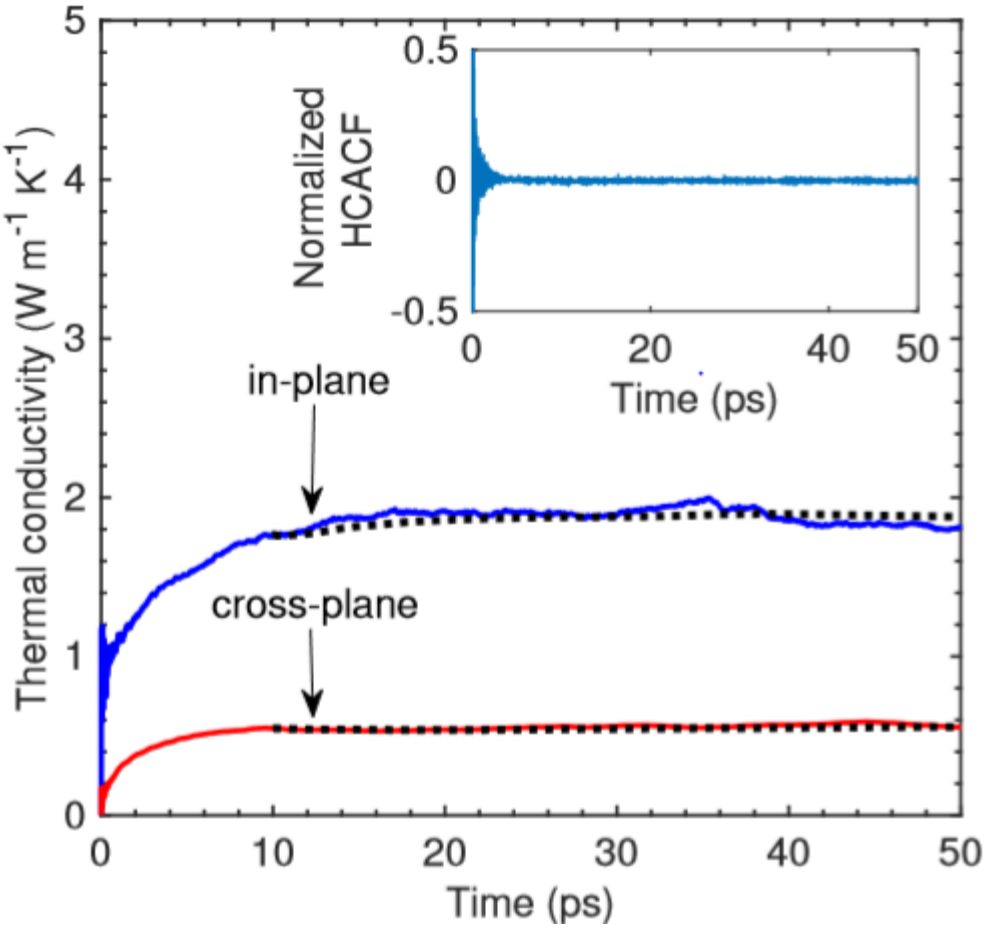

Figure 9.64. Converged values of in-plane and cross-plane thermal conductivities obtained for our COF-5 structure from the integral of the heat current autocorrelation function (HCACF). (inset) Normalized HCACF vs time for our COF-5 structure which shows that the HCACF decays to zero within the first 10 ps.

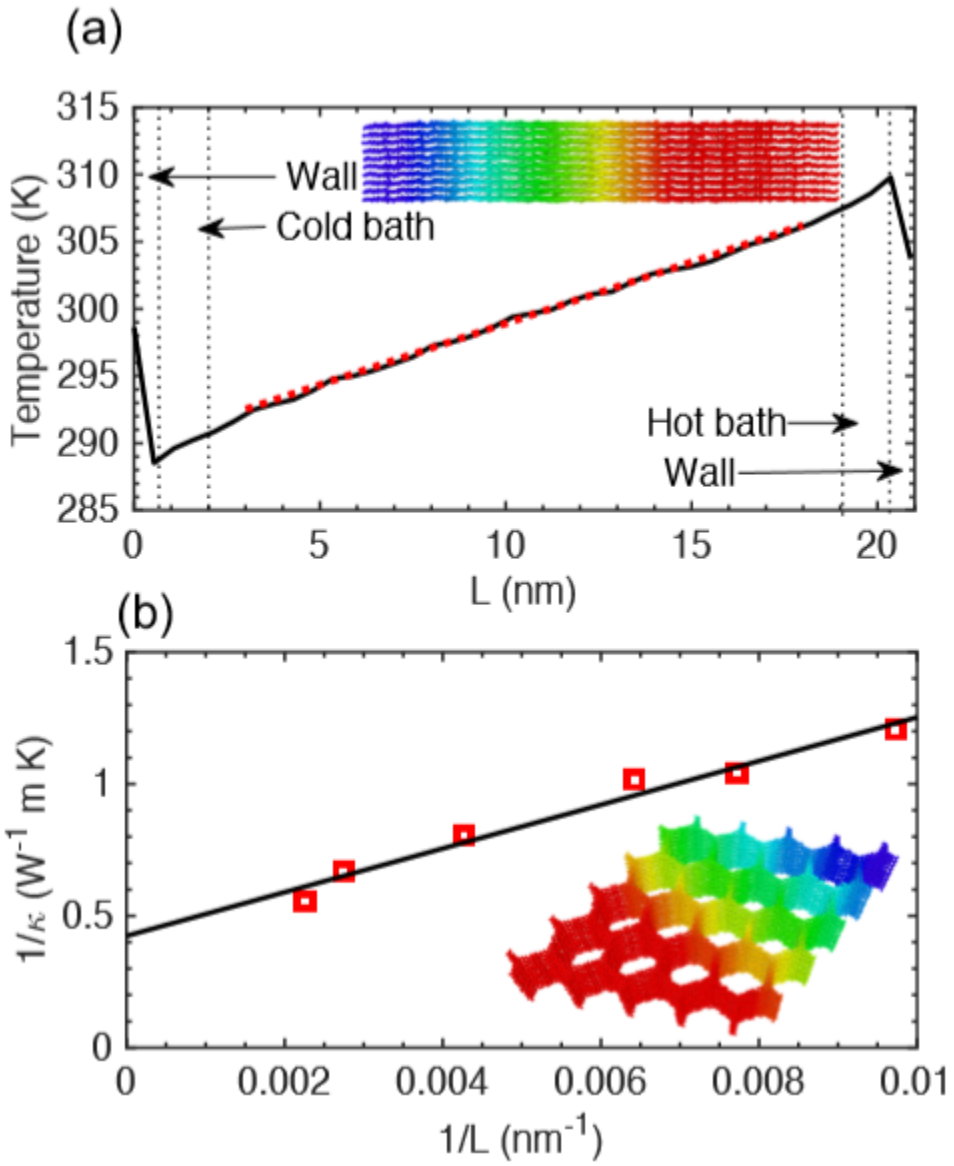

Figure 9.65. (a)Example of the time-averaged steady-state temperature profile in the in-plane direction of the COF-5 structure. (b) NEMD-predicted inverse of size-dependent thermal conductivities vs inverse of the computational domain length in the applied heat flux direction, which is the in-plane direction for our COF structure.

Since there has been contention on the use of the heat current calculations in LAMMPS to predict the thermal conductivity of structures with many-body interatomic potentials,[737, 738] we run nonequilibrium MD (NEMD) simulations to gain more confidence in our in-plane thermal conductivity predictions for our COF-5 structure. For the NEMD simulations, a steady-state temperature gradient is established by adding a fixed amount of energy per time step to a heat bath at one end of the computational domain, while removing an equal amount of heat from a cold bath at the other end of the domain; energy is added and removed at specified rate of 0.4 eV ps^{-1} under the microcanonical ensemble where the number of atoms (N), volume (V), and energy (E) of the system are held constant. A fixed wall at either side of the domain is enforced for our NEMD simulations. The temperature profile along the in-plane direction is obtained by averaging the temperature of the atoms along equally spaced bins in the applied heat flux direction for a total of 10 ns and the thermal conductivity is predicted via Fourier's law; the initial 3 ns of data are ignored to create time-averaged steady-state temperature profiles as shown in Fig. S8a. We calculate thermal conductivities for different domain lengths to accurately predict the bulk in-plane thermal conductivity of our COF-5 structure. For this, we plot the inverse of thermal conductivity, κ^{-1}, as a function of the inverse of the computational domain length, d^{-1}, which shows a linear trend as shown in **Fig. S56b**, and extrapolate to $d^{-1} = 0$ to predict the size-independent thermal conductivity.[739] The result of the NEMD simulations and EMD simulations are shown in **Fig 4c** of the manuscript. Our EMD simulations underpredict the cross-plane thermal conductivity of COF-5, which could potentially be due to the insufficiencies in the interatomic potential used to describe the COF structures. However, the fact that our experimental measurements are higher in comparison to the defect-free pristine structures simulated in our MD calculations, exemplifies the

high quality of our crystalline 2D COFs studied in this work. From our EMD and NEMD simulations, we predict an in-plane thermal conductivity of ~2 W m^{-1} K^{-1} and an anisotropy ratio of ~4 between the in-plane and cross-plane thermal conductivity predictions.

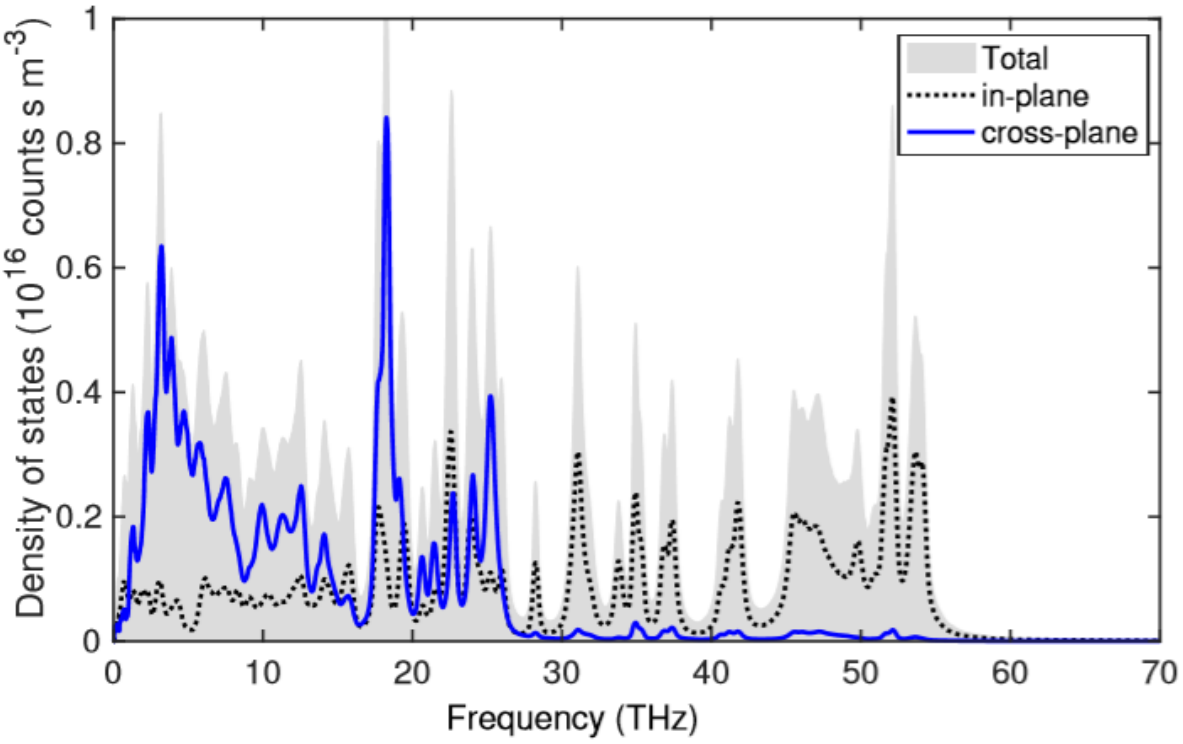

Figure 9.66. MD-predicted vibrational density of states for COF-5.

To get an estimate for the heat capacity of these COFs, we calculate the vibrational density of states (DOS) from our MD simulations. The velocities of the atoms in the COF-5 structure are output every 10 time steps for a total of 1ns. A velocity autocorrelation function algorithm is used to obtain the local phonon DOS in the cross-plane and in-plane directions as shown in **Fig. S57**. The density of states, D(ω), is obtained from the Fourier transform (F) of the velocity correlation function (VACF).[724] The Welch method of power spectral density estimation is applied to obtain the D(ω) and is normalized as follows,

$$D(\omega) = \frac{1}{2} m\mathcal{F}(VACF)\left(\frac{1}{k_B T}\rho\right) \qquad (5)$$

where m is the atomic mass, k_B is the Boltzmann constant, T is the local temperature, and ρ is the atomic density. We use the DOS to calculate the room temperature heat capacity as,

$$C_V = \int_0^{\omega_c} h\omega D(\omega) \frac{df}{dT} d\omega \qquad (6)$$

where ω_c is the cutoff frequency, and f is the Bose-Einstein distribution. We estimate a value of C_V~0.54 J cm^{-3} K^{-1} for our COF-5 at room temperature, which agrees well with our experimentally determined value (C_V~0.52±0.08 J cm^{-3} K^{-1}).

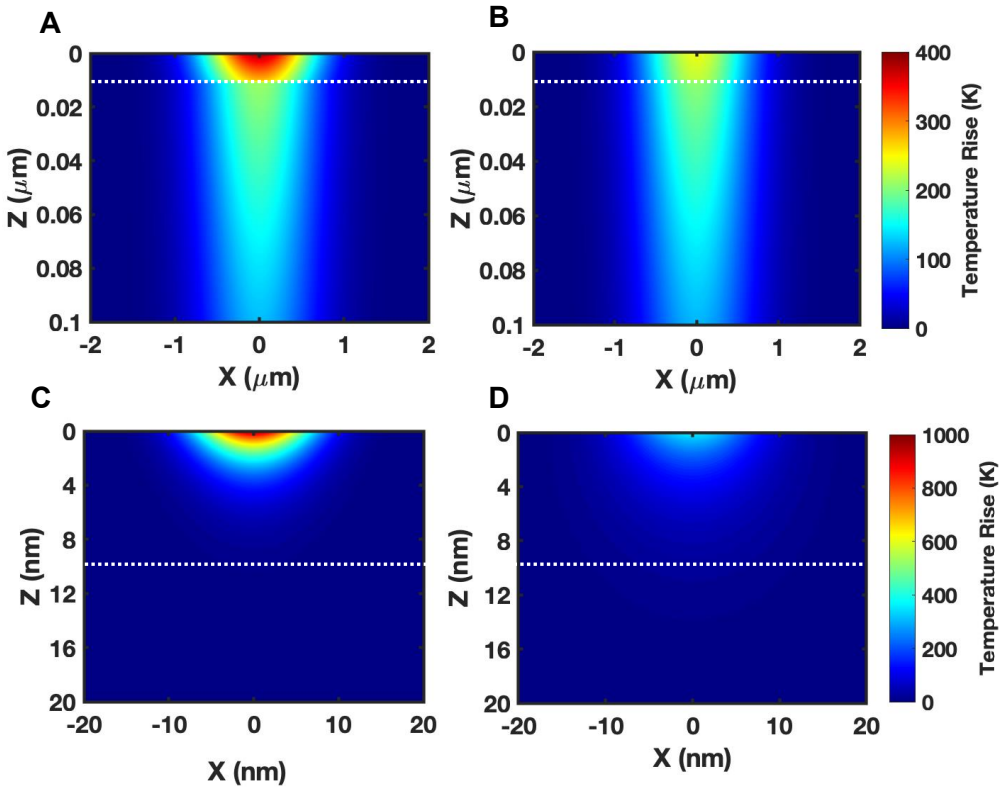

Figure 9.67 Temperature profiles as a function of radius and depth for a 10 nm conventional low-*k* dielectric thin film (with κ = 0.2 W m^{-1} K^{-1}) and for a 10 nm 2D COF/SLG/SiO_2 sample subjected to radially symmetric Gaussian surface heating event. Temperature profiles resulting from a heating event with 1/e^2 radius of 1 μm and an average absorbed power of ~4 mW in (A) a conventional 10 nm low-*k* dielectric thin film as compared that in a (B) 10 nm 2D COF/SLG/SiO_2 sample. Temperature profiles resulting from a heating event with 1/e^2 radius of 10 nm and an average absorbed power of ~4 mW in (C) a conventional 10 nm low-*k* dielectric thin film as compared to that in a (D) 10 nm 2D COF/SLG/SiO_2 sample.

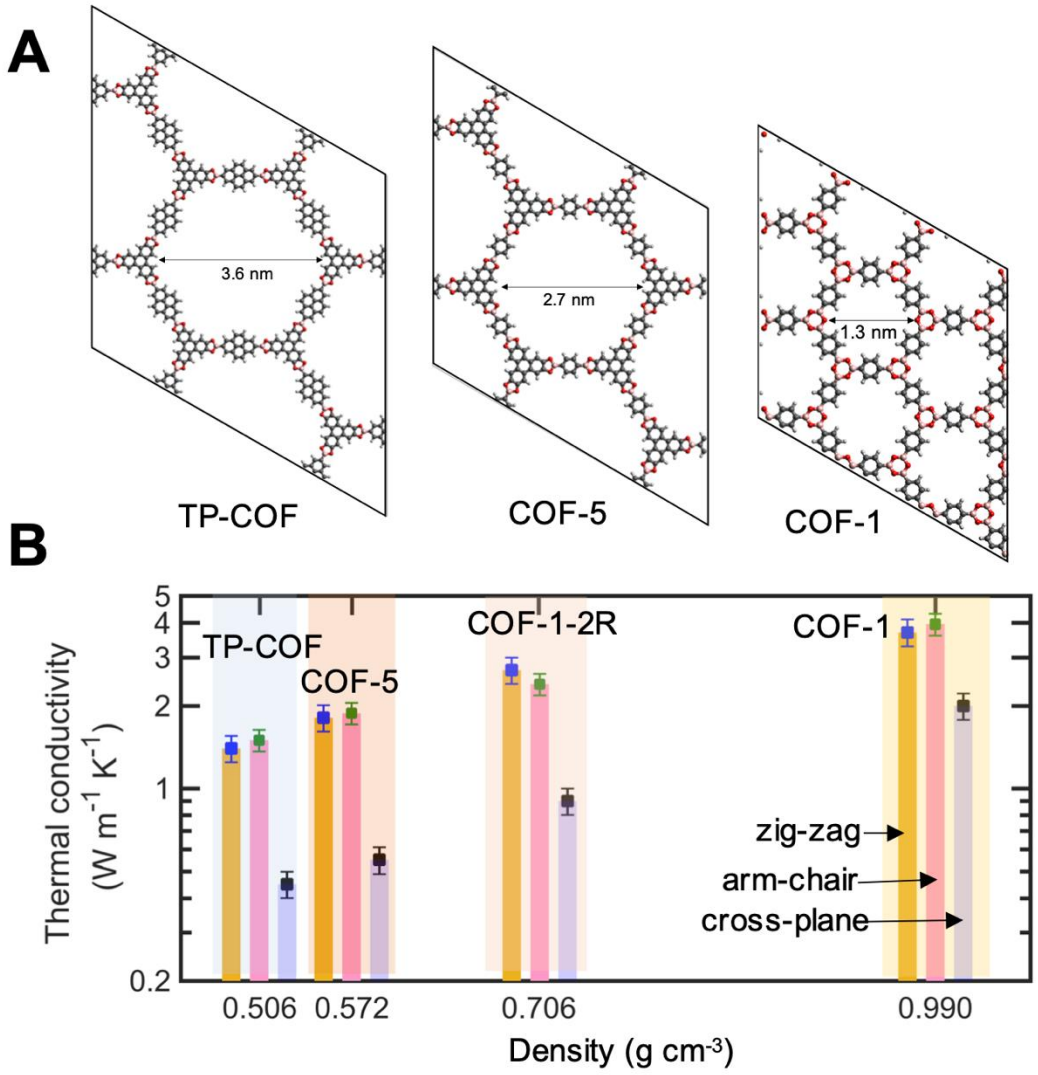

Figure 9.68 (A) Schematic illustration of the different molecular structures of COFs studied via MD simulations. To investigate the effect of varying porosities while maintaining similar internal microstructure, we modify the COF-1 structure by adding a phenyl ring to the linkers (COF-1-2R, where `R' stands for `rings'). (B) The thermal conductivity in the three principle directions for the COFs scales linearly as a function of their density suggesting that porosity can significantly control thermal transport in both in-plane and cross-plane directions in 2D COFs.

Meta-Data Analysis

Table 9.7. Meta-analysis of other low-*k* dielectrics that have reported thermal conductivities.

Material	Dielectric Constant	Thermal Conductivity ($W m^{-1} K^{-1}$)	Density ($g cm^{-3}$)	References
Porous Silicon Oxide Aerogel	2.1	0.14	0.8	A.Delan et al./Microelectronic Engineering 70 (2003) 280–284
Orion, Porous SiOCH	2.2	0.16	1.04	A.Delan et al./Microelectronic Engineering 70 (2003) 280–284
methyl silsesquioxane	2.2	0.19	0.95	A.Delan et al./Microelectronic Engineering 70 (2003) 280–284
Philk, Porous Oxide	1.9	0.15	0.9	A.Delan et al./Microelectronic Engineering 70 (2003) 280–284
SiLK, Porous Organic Polymer	2.1	0.11	1.2	A.Delan et al./Microelectronic Engineering 70 (2003) 280–284
Fluorinated Carbon Polymer	2.3	0.13	1.84	A.Delan et al./Microelectronic Engineering 70 (2003) 280–284
MOF-5	2.7	0.1	0.5	H. Guo et al. / Microporous and Mesoporous Materials 221 (2016) 40-47
ZIF-4	1.85	0.28	1.2	Tan et al. / Phys. Chem. Let 9 (2018) 2678-2684
ZIF-7	2	0.21	1.25	Tan et al. / Phys. Chem. Let 9 (2018) 2678-2684
ZIF-8	1.65	0.3	0.95	Tan et al. / Phys. Chem. Let 9 (2018) 2678-2684
SiO_2 Xerogels	1.65	0.08	0.5	Plawsky et al./J. Vac. Sci. Technol. B 17 (1999) 205-210
SiO2 Xerogels	1.8	0.1	0.6	Plawsky et al./J. Vac. Sci. Technol. B 17 (1999) 205-210
SiO2 Xerogels	2	0.14	0.7	Plawsky et al./J. Vac. Sci. Technol. B 17 (1999) 205-210
Polyvinylchloride	4	0.21	1.38	G. Maier / Prog. Polym. Sci. 26 (2001) 3-654
Polyamide, (Nylon 66)	3.8	0.23	1.14	G. Maier / Prog. Polym. Sci. 26 (2001) 3-654
Polysulfone	1.52	0.26	1.24	G. Maier / Prog. Polym. Sci. 26 (2001) 3-654
Polyimide (Kapton)	3.4	0.8	1.42	G. Maier / Prog. Polym. Sci. 26 (2001) 3-654
Polytetrafluoroethylene	2.02	0.25	2.2	G. Maier / Prog. Polym. Sci. 26 (2001) 3-654
Polystyrene	2.7	0.03	1	G. Maier / Prog. Polym. Sci. 26 (2001) 3-654
Amorphous SiO_2	3.8	0.8	2.65	G. Ozin et al./Materials Today 9 (2006) 22-31
Crystalline SiO_2	3.8	1.3	2.65	G. Ozin et al./Materials Today 9 (2006) 22-31
Fluorine-Doped SiO_2	3.55	0.8	2.21	G. Ozin et al./Materials Today 9 (2006) 22-31
Organosilicate Glass	3	0.39	1.4	G. Ozin et al./Materials Today 9 (2006) 22-31
Al_2O_3	7.8	12	3.95	G. Ozin et al./Materials Today 9 (2006) 22-31

Chapter 10 : Mapping Grains, Boundaries, and Defects in Polycrystalline Covalent Organic Framework Thin Films

10.1 Abstract

To improve their synthesis and ultimately realize the technical promise of two-dimensional covalent organic frameworks (2D COFs), it is imperative that a robust understanding of their structure be developed. However, high-resolution transmission electron microscopy (HR-TEM) imaging of such beam-sensitive materials is an outstanding characterization challenge. Here, we overcome this challenge by leveraging low electron flux imaging conditions and high-speed direct electron counting detectors to acquire high-resolution images of 2D COF films. We developed a Fourier mapping technique to rapidly extract nanoscale structural information from those TEM images. This post-processing script analyzes the evolution of 2D Fourier-transforms across a TEM image, which yields information about polycrystalline domain orientations and enables quantification of average domain sizes. Moreover, this approach provides information about several types of defects present in a film, such as overlapping grains and various types of grain boundaries. We also find that the preeminent origin of defects in COF-5 films, a prototypical boronate-ester linked COF, arises as a consequence of broken B-O bonds formed during polymerization. These results highlight that the nanoscale features observed are a direct consequence of chemical phenomena. Taken together, this mapping approach provides previously unavailable information about the fundamental microstructure and crystallographic underpinnings

of 2D COF films, which will guide the development of future 2D polymerization strategies and help realize the goal of using 2D COFs in a host of thin-film device architectures.

10.2. Introduction to Film Characterization

Two-dimensional (2D) covalent organic frameworks (COFs) are synthetically versatile 2D polymers that have a unique confluence of covalent connectivity, permanent porosity, and structural precision.[1–3] This combination of properties has inspired interest in 2D COFs as catalysts,[4–6] membranes,[7–10] and organic electronic devices.[11–13] However, to leverage their unique combination of properties, 2D COFs must be integrated into thin-film device architectures, rather than aggregated powders.[14,15] Many 2D COF film fabrication approaches have been investigated including interfacial polymerization,[9,16] exfoliation followed by solution casting,[17,18] and solvothermal growth.[19–21] Of these methods, solvothermal growth, where films are grown directly on a solid support, has proven to be an operationally simple method for growing highly crystalline and vertically oriented films.[20] However, these films are often contaminated by insoluble powder aggregates formed during synthesis which further complicates direct imaging.[20] Although conventionally prepared films have been studied extensively by bulk characterization methods, such as grazing incidence X-ray diffraction (GIWAXS), these ensemble measurements are insensitive to nanoscale inhomogeneities that arise as a consequence of defects or domain edges. These uncharacterized domain boundaries and defects are likely to impact the performance of 2D COF thin films in device or membrane applications. Here, we leverage newly developed synthetic conditions for synthesizing 2D boronate ester-linked COFs as stable colloidal suspensions,[22] which now also enable the preparation of 2D COF films that are not contaminated by precipitated bulk powders. These synthetic developments enable a new frontier in nanoscale characterization of 2D

polymers because high-quality samples are a prerequisite for direct imaging of grain boundaries and defects in thin films.

Nanoscale features are routinely studied in beam-stable 2D materials, such as transition metal dichalcogenides (TMDs) and graphene, and are known to produce exotic physical phenomena and impact macroscale device performance.[23,24] Imaging techniques such as electron backscatter diffraction (EBSD) in scanning electron microscopy (SEM) and dark-field transmission electron microscopy (DF-TEM) have enabled atomic-resolution imaging of these beam-stable nanoscale crystallites and their grain boundaries.[23–26] In addition, electron diffraction techniques are particularly useful for identifying crystallite orientations and generating spatially resolved maps of those orientations by tracking the evolution of the electron diffraction patterns.[23,24,27] However, despite the versatility of these techniques, they typically require a focused electron beam and long acquisition times for generating adequate signal to noise ratios, both of which result in high electron fluxes.[28,29] These constraints have impeded the application of these techniques for high-resolution imaging of soft materials, such as all-organic COFs, which are particularly sensitive to electron beam damage.[30–34] Despite the well-known beam sensitivity of COFs, few TEM studies mention the use of low-flux imaging conditions or report the cumulative electron flux used to acquire an image.[35,36] In most cases, TEM characterization of COFs has been limited to analysis of the morphology and arrangement of the COF mesopores or pore channels of small sample areas. [13,19,37–44] Beyond traditional real space imaging, there are some reports of using electron diffraction[45,46] or fast Fourier transform (FFT)[35,47] patterns to identify crystallite orientations. Furthermore, there is only a single example of using TEM to identify grain boundaries, grain orientations, and edge dislocations of a particularly robust triphenyl triazine

thiazole-linked COF.[48] Beyond these limited examples, nanoscale structural characterization of COFs remains extremely challenging and is limited to frameworks composed of highly beam-stable linkages.

Here, we develop an automated post-processing mapping technique for extracting nanoscale information directly from HR-TEM images of four beam-sensitive boronate ester-linked COF thin films. The script analyzes the change in 2D Fourier-transforms across an image to identify the locations, orientations, and shapes of the grains and grain boundaries of beam-sensitive materials without the need for large electron fluxes or long acquisition times. By combining recent TEM hardware developments, such as high-resolution direct electron counting detectors,[33,35,49–51] and our post-processing approach, this technique provides a high-throughput method for evaluating the synthesis of beam-sensitive polycrystalline materials at the nanoscale for the first time. This approach reveals that COF-5 films have small, irregularly shaped domains with domain edges that are most commonly offset by a 12º relative rotation, which we attribute to the formation of a hemi-boronate ester. By providing researchers with previously unavailable information about fundamental chemical and structural aspects of 2D polymerizations, this mapping approach will enable improved polymerization strategies for producing high-performance COFs in thin-film device architectures.

10.3. Film Polymerization Methods

To prepare COF thin films suitable for TEM analysis, we polymerized 2D boronate ester-linked COFs directly onto graphene-coated TEM grids. The four boronate ester-linked 2D COFs studied are COF-5, COF-10, DPB-COF, and TP-COF which are synthesized by the condensation of 2,3,6,7,10,11-hexahydroxytriphenylene (HHTP) with 1,4-phenylenebis(boronic acid),

4,4′-biphenylbis(boronic acid), 4,4′-diphenylbutadiynebis(boronic acid),[52] and 2,7-pyrenebis(boronic acid),[53] respectively. For all systems, monomer solutions of HHTP (1 mM) and the corresponding boronic acid (1.5 mM) in CH_3CN:1,4-dioxane:mesitylene (80/16/4 v/v/v) were prepared. This solution was then transferred to a vial containing both a graphene-coated silicon dioxide (SiO_2) substrate, which was used for bulk characterization techniques, and a graphene-coated TEM grid. There, the two substrates were grown under the same conditions to enable their direct comparison. The sealed vial was then heated to 70 ºC for 24 h to produce a colloidal solution and a templated COF thin film on the graphene surfaces (**Figure 10.1A**). Using colloidal synthetic conditions no precipitates were formed, which facilitated the direct imaging of these 2D COF thin films.

10.4. Bulk COF Characterization

Bulk characterization of the COF films indicated that the colloidal growth conditions produce highly crystalline, oriented thin films on graphene/SiO_2 substrates. GIWAXS revealed that the COF films were highly crystalline and oriented on the graphene-coated SiO_2 substrates. (**Figure 10.1F-1I**). In all cases the scattered intensities of the Bragg peaks are concentrated near $Q_z = 0$, which is indicative of an oriented 2D layered material. Extrapolated 1D diffraction patterns ($Q_z = 0$) display sharp diffraction peaks that are consistent with simulated patterns for each COF with (100) peaks at 0.24, 0.20, 0.16, and 0.19 $Å^{-1}$ for COF-5 (**Figure 10.1F**), COF-10 (**Figure 10.1G**), DPB-COF (**Figure 10.1H**), and TP-COF (**Figure 10.1I**), respectively. To provide an estimate of the orientational order, or mosaicity, of the film we analyzed the width (in Q_{xy}) of the (001) peaks, which appear as diffuse arcs centered around $Q_z = 1.85$ $Å^{-1}$. This analysis indicates that in the COF-5 film most grains are oriented within 11° of the surface normal (**Figure 10.31**),

which is improved compared to previous COF-5 films grown under other conditions.[20] We also subjected the other boronate ester-linked 2D COF films to this analysis and found they are also highly oriented with most grains oriented within 10° for COF-10, 14° for DPB-COF, and 11° for TP-COF (**Figure 10.31 - Figure 10.34**). Additionally, Scherrer analysis of the GIWAXS patterns suggested an average crystalline domain size of 50 nm for COF-5. However, this analysis only gives an average value rather than a distribution of sizes, is limited to nanoscale crystallites (<200 nm), and fails to take other factors for peak broadening into account such as dislocations, stacking faults, and grain boundaries. Therefore, while GIWAXS measurements suggest that these films are highly crystalline and oriented, this data fails to provide nanoscale information regarding how the COF crystalline domains are stitched together at the atomic level to form grains and grain boundaries.

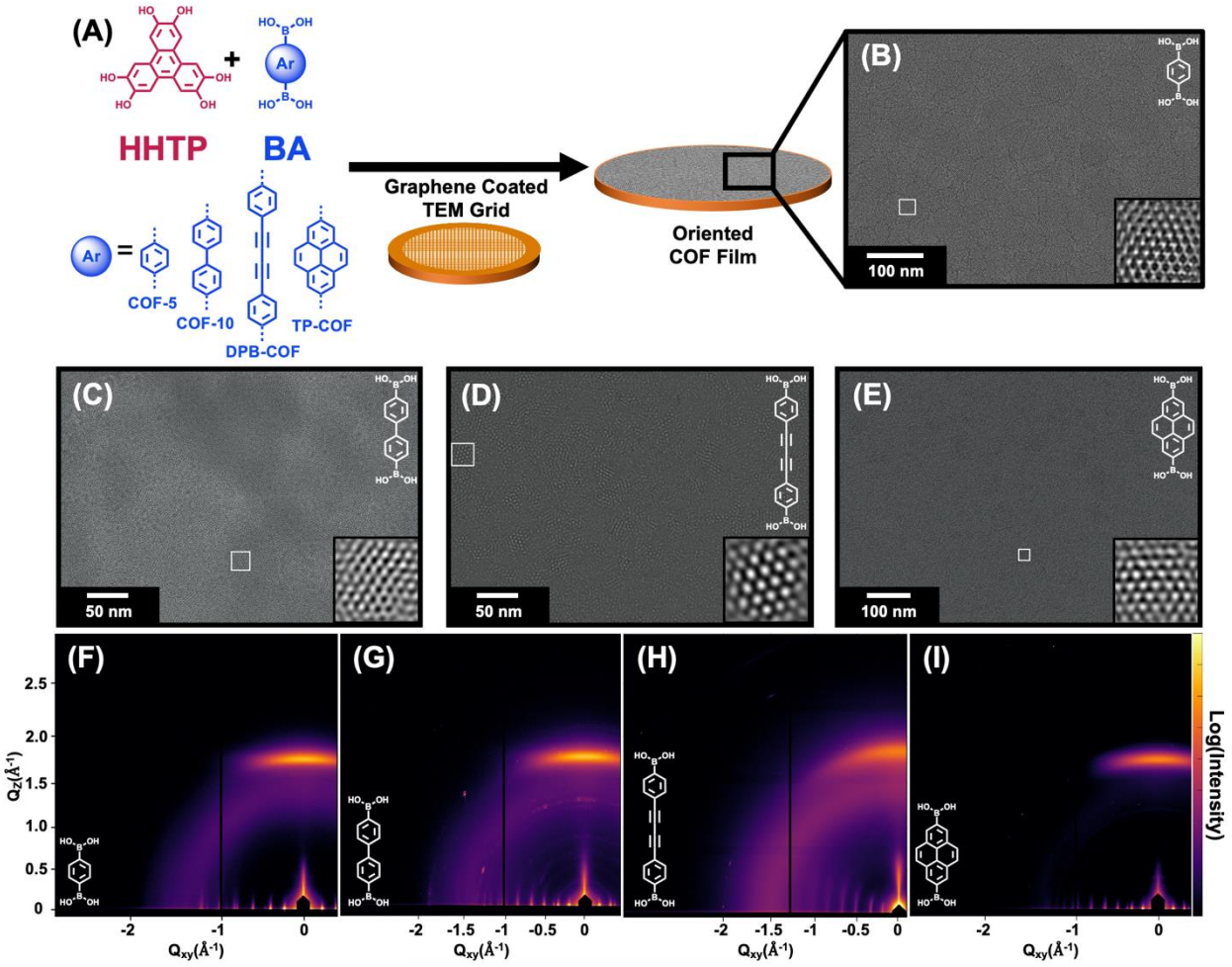

Figure 10.1 (A) Schematic of the synthesis of boronate ester-linked COF films on graphene-coated TEM grids. (**B-E**) TEM images of oriented COF films: (**B**, COF-5) dose rate of 13.81 e^{-} $Å^{-2}$ s^{-1} and cumulative dose of 13.75 e^{-} $Å^{-2}$; (**C**, COF-10) dose rate of 17.35 e^{-} $Å^{-2}$ s^{-1} and cumulative dose of 17.28 e^{-} $Å^{-2}$; (**D**, DPB-COF) dose rate of 16.45 e^{-} $Å^{-2}$ s^{-1} and cumulative dose of 6.40 e^{-} $Å^{-2}$; (**E**, TP-COF) dose rate of 2.12 e^{-} $Å^{-2}$ s^{-1} and cumulative dose of 0.41 e^{-} $Å^{-2}$. Insets: Magnified image of the small boxed region in each micrograph after bandpass filtering. (**F-I**) GIWAXS of COF films on graphene-coated SiO_2 grown concurrently with the TEM grids: (**F**) COF-5, (**G**) COF-10, (**H**) DPB-COF, and (**I**) TP-COF.

10.5. An automated Fourier-mapping approach

Next, we used TEM to elucidate the nanoscale structure of the four COF thin films. To accommodate the beam sensitivity of COF materials, we used low-flux imaging conditions on a TEM equipped with a direct electron counting detector, which enabled the acquisition of high-resolution images using short acquisition times and low electron fluxes. In all cases, the films spanned the holes of the TEM grid, as confirmed by low-resolution TEM, and were polycrystalline with domains of varying size, shape, and crystallite orientation (**Figure 10.1B - Figure 10.1E, Figure 10.8 - Figure 10.12**). In particular, the COF-5 film displayed excellent surface coverage and maintained its crystallinity over large portions (>10 μm) of the grid, as evidenced by TEM (**Figure 10.7 - Figure 10.8**). While COF films can be imaged with standard CCD-based cameras, these efforts are extremely challenging and largely limited to small areas of apparently stable network regions. For these reasons we find that using an ultrasensitive electron counting camera enables more reliable imaging of these thin, beam-sensitive materials. These qualitative observations led us to realize that the quality of these materials could enable the extraction of reliable quantitative information which would require the development of new image analysis tools.

10.6. An Automated Mapping Script

With this in mind, we developed a method to extract quantifiable nanoscale information such as domain size, shape, and grain boundary prevalence from TEM images using an automated

post-processing Fourier-mapping approach. First, we import a lattice resolution TEM image of a polycrystalline film (**Figure 10.2A**). Next, the TEM image is subjected to a 2D fast Fourier transform (FFT) that is radially integrated in Q_{xy} space to find the predominant repeat spacing in the image[54] (**Figure 10.2B**). The program then uses this full-image FFT and partial image FFT as training data to optimize radial sensitivity, mapping resolution, and signal to noise as a function of a region of interest (ROI) size, which determines the size of the box that will be scanned across the entire image to yield the most informative map (**Figure 10.13 - Figure 10.14**, see Supporting Information for a detailed description of selecting these parameters). After analysis, we determined that a ROI square with side lengths of about twenty crystallographic cells is optimal for mapping. For example, for COF-5 films we used a ROI of 500 pixels (55 nm), which is small enough to capture a single domain in a frame but large enough to provide adequate signal for mapping. Next, we determine how much the ROIs will overlap as they are rastered across the image, which effectively determines the resolution of the resultant maps. After testing several different resolutions we determined that a resolution size slightly greater than the expected (100) spacing of the COF provides a well resolved domain map without adding unnecessary computational burden (**Figure 10.15 - Figure 10.21**). For example, for COF-5 films, which have a (100) spacing of 2.8 nm, we selected a 3 nm resolution for the mapping algorithm.

FFT patterns obtained at appropriate spacing over large-area micrographs differentiate the orientations of adjacent crystalline domains. A Fourier transform mathematically decomposes a function into a continuous spectrum of its frequency components. Therefore, periodic structures, or lattice fringes, in a real-space TEM image can be transformed into an inverse space FFT pattern with sharp, symmetric spots where the direction of the spots reflects the orientation of the

crystallite. The FFT of a perfectly oriented boronate ester-linked COF film with hexagonal pores lying head-on would have six spots of equal intensity that are 60° apart (**Figure 10.2A - Figure 10.2B**). In practice, however, crystallites can lie on the substrate in random orientations. Therefore, a slightly tilted hexagonal net results in a FFT pattern with projected symmetries that depict the preferential grain tilt and rotation directions (e.g. two-spots, rather than six) (**Figure 10.2D, Figure 10.21).** The symmetry and intensity of these spots are highly sensitive to slight changes in the film, including thickness variations of the COF or minor height differences from the substrate. Given that FFT patterns are produced via a mathematical transformation of the image, they represent a convenient and powerful tool for studying the crystallinity of beam sensitive materials.

With these resultant FFT patterns from a variety of grain configurations and the appropriate selection of mapping parameters, we can then proceed to map the TEM images by rastering the ROI across the image, generating 2D FFTs at each location, and azimuthally integrating the FFT intensity to determine the phi (ϕ) position of the most intense spot (**Figure 10.2B**). Using the repeat spacing determined from the full image, each FFT is bandpass filtered to focus our analysis to the spacing associated with the predominant crystallographic axis (**Figure 10.2C**). For each ROI, the script locates the FFT spot with the maximum intensity and measures corresponding phi degree (**Figure 10.2D**) in order to identify the size, location, and orientation of each domain. If the phi degree of the maximum intensity spot in a given FFT differs by a value greater than the phi degree binning number compared to the surrounding FFTs, that corresponds to a new domain in the image (**Figure 10.20**). Different colors are then assigned to each crystalline domain orientation, as defined by the phi angle measured in each FFT, resulting in a color-coded crystal-orientation domain map (**Figure 10.2D - Figure 10.2E, Figure 10.21**). In this work we focus our attention on

four beam-sensitive boronate ester-linked COF films (**Figure 10.22 - Figure 10.29**), however this strategy can be used to map TEM images of any polycrystalline material (**Figure 10.30**).

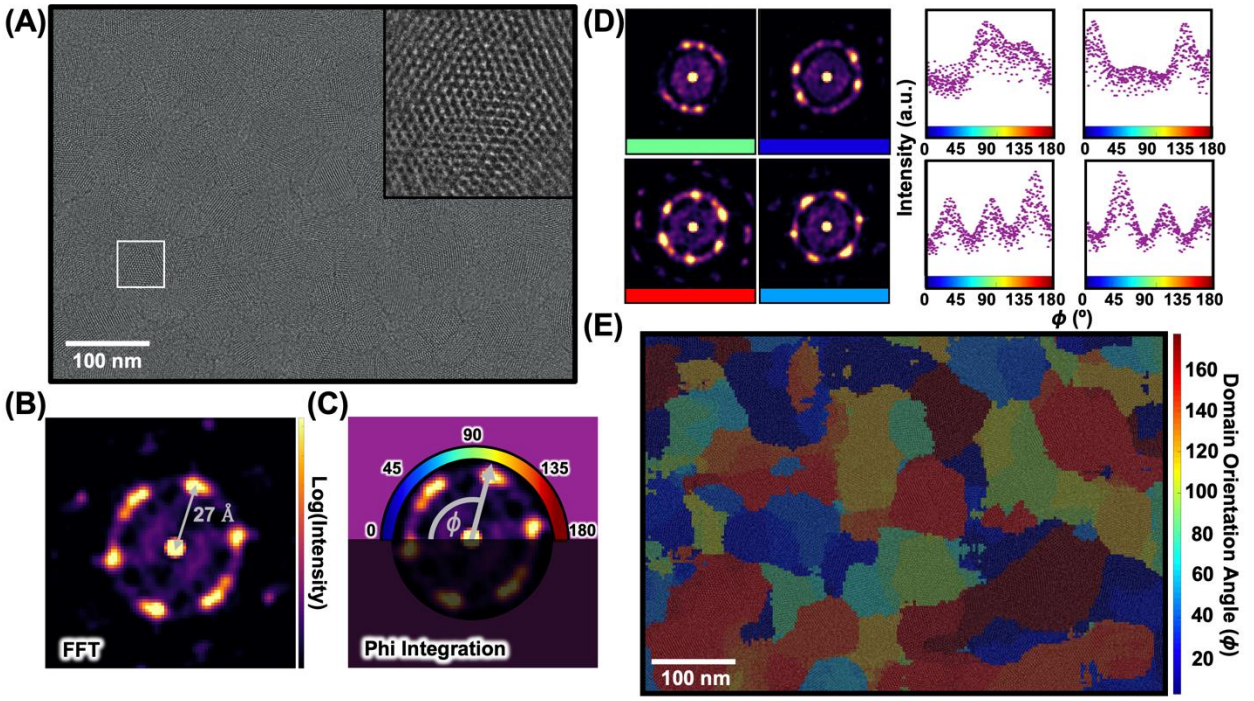

Figure 10.2. Schematic of automated domain mapping procedure. (**A**) COF-5 HR-TEM image taken with a cumulative dose of 14 e^{-} $Å^{-2}$. Inset: magnified image of boxed region in (**A**) displaying polycrystalline COF-5 lattice fringes. (**B**) FFTs are generated by sweeping a ROI across the image. (**C**) A bandpass filter is then applied to each FFT and a radial phi (ϕ) integration is applied to identify the locations of the highest intensity. (**D**) The FFT patterns are then analyzed to locate the maximum intensity spot and the corresponding phi angle, which corresponds to a different color. The colors corresponding to the phi angles measured for each FFT are shown in the colored bar below the FFT patterns. (**E**) The image is then mapped using the colors corresponding to the different phi angles and overlaid on the initial TEM image.

By analyzing the statistical distribution of grain sizes in a given COF-5 film across four TEM images, we observed irregularly shaped domains with small average crystallite sizes. First, we took lattice-resolution TEM images of several different regions in a single COF-5 film (**Figure 10.3A**). We then subjected those images to the automated domain orientation mapping script using the parameters previously described (**Figure 10.2**). Once the images were mapped, we used the script to extract the size of the individual domains (**Figure 10.3A**). The histogram in **Figure 10.3B** displays the grain sizes observed in the four COF-5 film images, showing that most domains are relatively small. This distribution is best evaluated by plotting the probability density, which represents the likelihood of finding a domain of a given size in a film (**Figure 10.3C**). The average domain area in a COF-5 film is 3350 nm^2, which corresponds to a square grain with sides that are approximately 58 nm in length. In addition to gathering statistical grain size information, this analysis also provides a method for generally evaluating the shapes of the crystalline domains. All of the COF-5 film images displayed irregularly shaped domains and relatively small crystallites lying on the graphene substrate in several different orientations (**Figure 10.3A**). This same observation was made when studying the mapped images of other boronate ester-linked films suggesting that whatever impedes the growth of domains in our model COF-5 system is also operative in other boronate ester-linked COFs (**Figure 10.27 - Figure 10.29**). We hypothesize that the irregular shapes observed are likely due to uncontrolled nucleation and growth mechanisms and therefore expect that higher quality materials can be generated if these parameters can be better controlled.

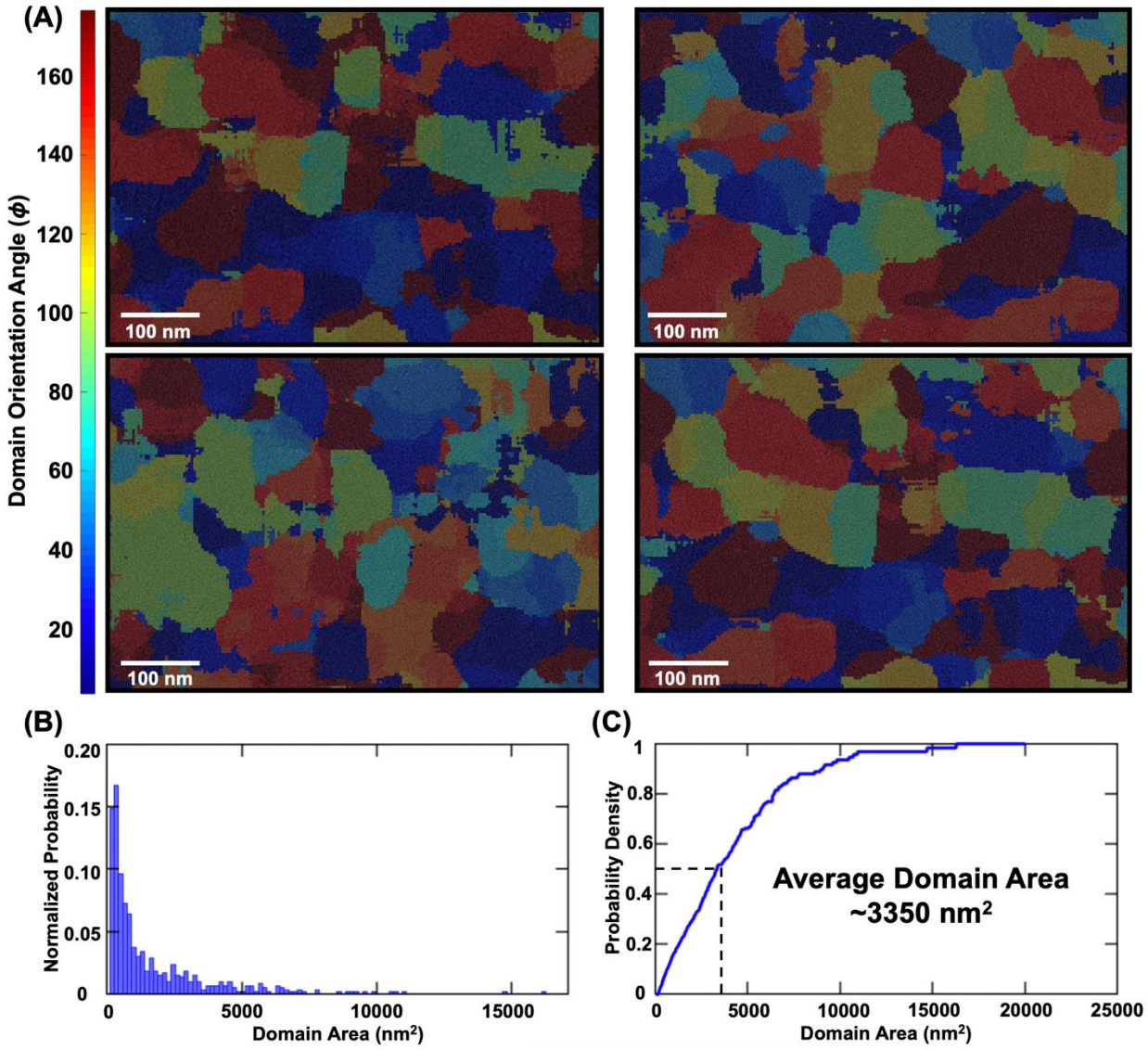

Figure 10.3. Statistical analysis of crystalline domain area. (A) Four COF-5 film TEM images taken from the same TEM grid with the same magnification and a cumulative dose per image of ~14 e^{-} $Å^{-2}$ for each image. (B) Histogram of domain areas compiled from the images in (A). (C) Probability density plot showing the likelihood of a film having a domain of a certain area with the dotted lines highlighting the average domain area expected.

10.7. Nanoscale Defects

In addition to identifying grain size and orientation, this automated mapping strategy also reveals nanoscale features of crystalline films such as overlapping sheets and tilt grain boundaries by analyzing the change in phi angle and intensity of the FFT spots across the mapped image. In the map shown in **Figure 10.4A**, each color represents a distinct domain orientation, meaning that at the interface of one color with another, a domain boundary is present. When analyzing the changes in FFTs across boundaries we observed two primary features: overlapping sheets and tilt grain boundaries (**Figure 10.4A**). We identified these features by selecting regions in the mapped image that showed a visible transition from one color, or domain orientation, to another (**Figure 10.4B - Figure 10.4C**). We then took those cropped regions and scanned a ROI box across the area, generating bandpass filtered FFTs as the ROI box moved from left to right (cyan to magenta) and radially integrating the intensities (**Figure 10.4D - Figure 10.4E**). To identify the type of transition, we looked at the intensity variation of the FFT spots as we moved across the cropped region, which has been previously used to analyze defects in other 2D materials (**Figure 10.4F - Figure 10.4G**). In **Figure 10.4F** we observe that the intensity of the FFT spots at 155º remains constant throughout the cropped region, as shown by the spots marked in red in the FFTs (**Figure 10.4D**). However, the FFT spots at 55º which are marked in blue (**Figure 10.4D**) consistently decrease in intensity as we move the ROI from left to right (cyan to magenta). This suggests that on the left side of the cropped region we have both domains present but as we move across the image only the 155º domain orientation remains. Since the integrated intensity is not constant over the transition this indicates that the transition observed is due to a local overlapping of two misoriented COF domains. This is in contrast to what we observe in **Figure 10.4G** where the

intensity sum remains constant as we move from the domain with a lattice orientation of 117º, marked in yellow in the FFTs, to a domain with a lattice orientation of 155º, marked in red in the FFTs (**Figure 10.4E**), which is indicative of a tilt grain boundary without any overlapping regions. In addition to the FFT spots at 117º and 155º in the cropped region, we also observe a third set of spots at 57º that has a constant intensity throughout the image, suggesting that there is a crystalline domain with a different orientation lying outside of the focal plane. In addition to observing overlapping sheets and tilt grain boundaries, we can also use this method to analyze domains that have folds or bends as well as defect-free regions (**Figure 10.22 - Figure 10.25**).

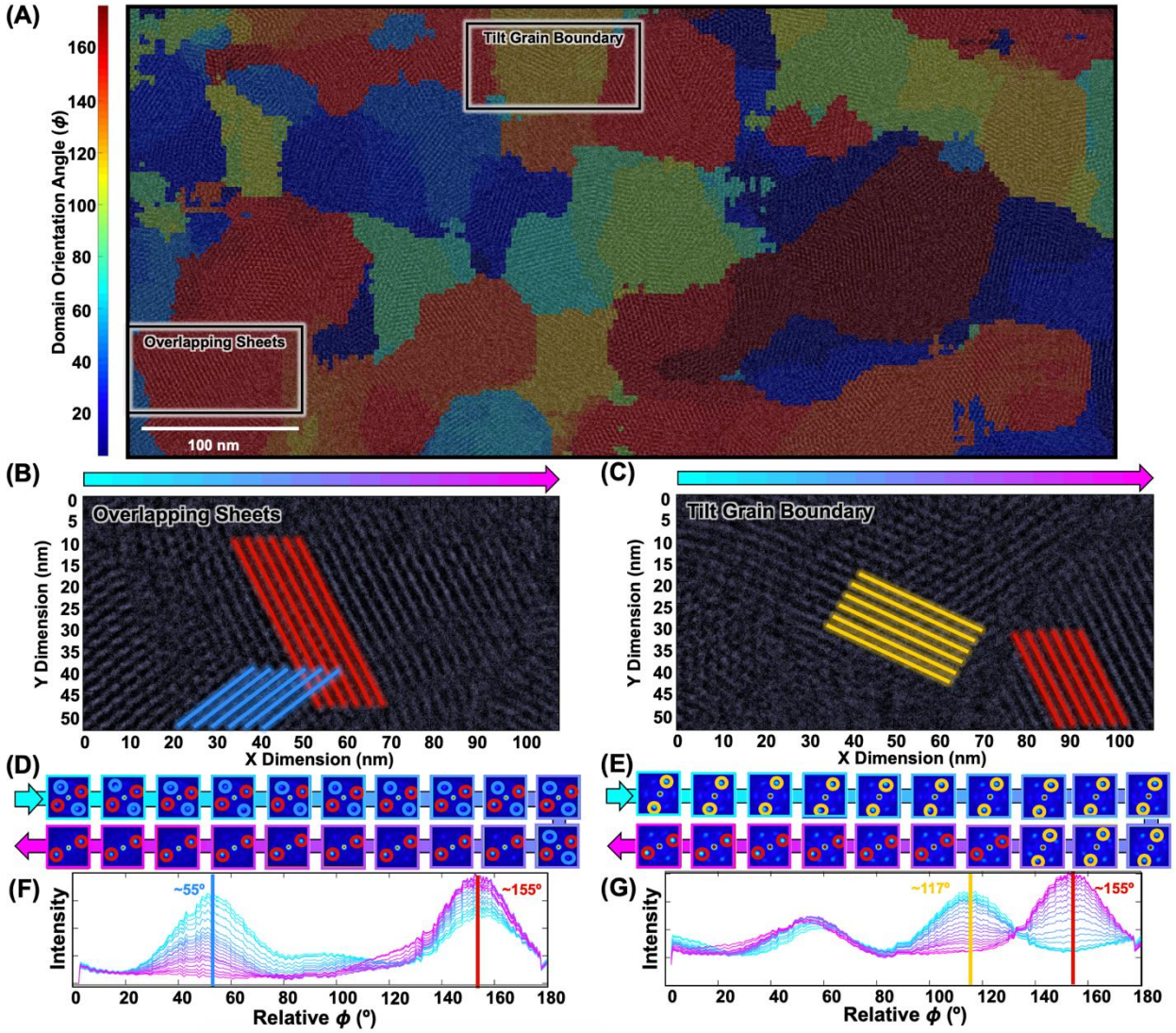

Figure 10.4. Analysis of COF-5 grain boundaries. (**A**) Domain mapped HR-TEM image of COF-5 film. Boxed regions display different kinds of domains and grain boundaries observed in the image. Two types of grain boundaries are observed: (**B, D, F**) overlapping sheets and (**C, E, G**) tilt grain boundary. (**B, C**) Zoomed in regions of COF-5 film HR-TEM image with colored lines overlaid corresponding to the phi angles of the crystalline domain orientations observed: (**B**) Blue and red lines correspond to domain orientations of 55º and 155º, respectively; (**C**) Yellow and red lines correspond to domain orientations of 117º and 155º, respectively. (**D, E**) FFT patterns

of regions moving from right to left (cyan to magenta) in the cropped images shown in B and C: (**D**) Overlapping sheets are apparent based on the coexistence of the two sets of FFT spots in the patterns; (**E**) A tilt grain boundary is observed based on the simultaneous disappearance of the 117º domain (yellow) and appearance of the 155º domain (red). (**F, G**) Plots displaying the relative phi intensities moving from right to left (cyan to magenta) in the cropped images which show the changes in the grain orientation the image.

Statistical analysis of the COF-5 grain boundaries and defects over several TEM images reveals that the most common change in grain orientation between two adjacent domains is approximately 12º. To study the grain boundaries of the films, we measure the change in domain orientation as the ROI moves from one domain, or color, on the map to the next (**Figure 10.5A**). Since each 2D FFT pattern is by definition bilaterally symmetric, we measure domain orientations from 0 to 180º. By the same logic, the absolute difference between two domain orientations is constrained from 0 to 90º (**Figure 10.26**). Through statistical analysis of COF-5 film HR-TEM images **Figure 10.3A**), we observe that the most common change in grain orientation between adjacent domains is 12º, which is shown as a deep purple color on the grain boundary maps (**Figure 10.5B**). Considering fundamental organic bonding angles, we suspected that this 12º offset between adjacent domains could be attributed to the difference between an sp^3 (109.5º) and sp^2 (120º) site. Chemically, we understood that this bonding difference could result as a consequence of a hemi-boronate-ester defect, where only half of the functionality of a catechol condenses with a boronic acid (**Figure 10.5E**), because this would result in adjacent sp^3 and sp^2 sites. To evaluate this hypothesis more quantitatively, we constructed a monolayer supercell of a COF-5 crystallite

with an embedded broken B-O bond point defect. We then performed a geometry optimization routine to reduce stresses that originate as a function of that defect. We find that a broken B-O bond results in a 12º rotational difference between the orientation of the two simulated crystalline domains (**Figure 10.5D - Figure 10.5E**), consistent with our experimental imaging analysis. Furthermore, we find that as the simulated structure relaxes, random non-faceted domain edges are produced. Experimentally, we also find that domain edges between COF crystallites are highly random. This is in contrast to materials such as graphene that are known to have distorted pentagons and heptagons at domain interfaces.[23,24] This observation suggests that as COF layers are polymerized on surface, molecular bonding defects are introduced into the layers that lead to mesoscale domain boundaries. Presumably, if these defects could be more efficiently annealed out of the final structure, larger crystalline domain sizes could be obtained.

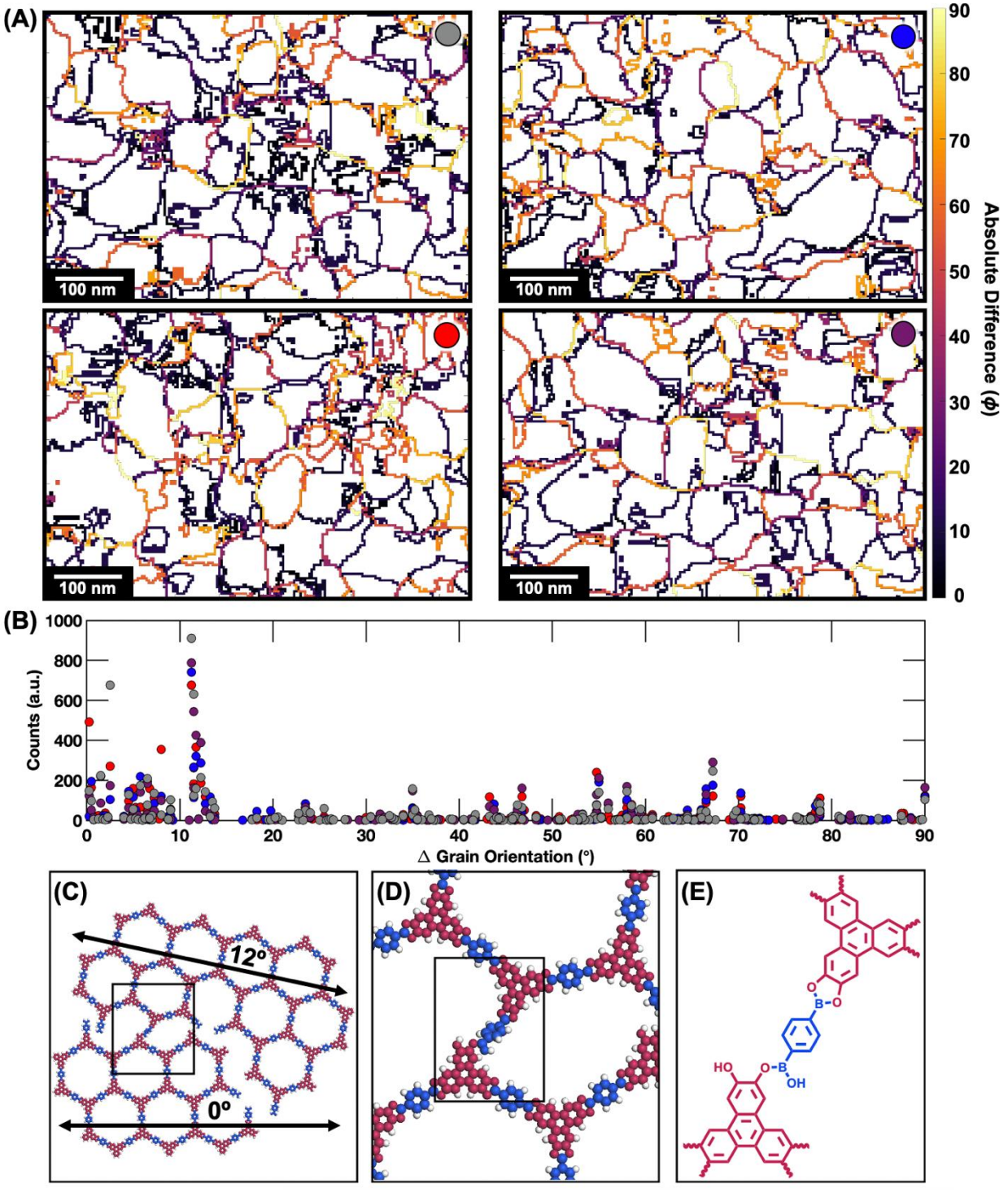

Figure 10.5. Statistical analysis of grain orientation. (**A**) Grain boundary maps of four COF-5 film TEM images taken from the same TEM grid with the same magnification and a cumulative

dose per image of ~14 e^{-} $Å^{-2}$ for each image. (**B**) Scatter plot showing the relative change in grain orientation angle measured for every grain boundary shown in (**A**) where the color of the dot corresponds to a particular image as shown in the top right corner of the images in (**A**). (**C**) Geometry optimized structured generated using a universal force field displaying ~12º change in grain orientation between two domains. (**D**) Magnified image of boxed region in (**C**). (**E**) Schematic of boxed region in (**D**) showing the broken B-O bond that causes the formation of a grain boundary.

10.8. Conclusions

The combination of an improved method for preparing uncontaminated 2D COF films and HR-TEM images taken using low electron flux conditions and high-speed direct electron counting detectors, revealed the overall polycrystalline structure of these emerging materials and provided insight into their grain boundaries and defects for the first time. An automated post-processing Fourier mapping technique applied to the TEM images rapidly extracted these nanoscale features, which are otherwise difficult to obtain for beam-sensitive 2D boronate ester-linked COF thin films. Using this method, we identified the locations, orientations, and shapes of crystalline domains by relying on the information provided by FFT patterns across a TEM image. We also extracted quantitative information such as distributions of domain size and studied nanoscale features such as point defects and grain boundaries. By applying this method to a COF-5 film, we observed irregularly shaped domains with small average crystallite sizes of approximately 3350 nm^2. Additionally, analysis of domain interfaces revealed regions with overlapping sheets and tilt grain boundaries where the most common difference in grain orientation between two adjacent domains

was 12º. We attribute this 12º difference to a hemi-boronate ester bonding defect that occurs during the polymerization and leads to mesoscale domain boundaries, highlighting that the observations enabled by this approach have real chemical consequences and provide previously unavailable information about fundamental aspects of 2D polymerizations. We anticipate that the nanoscale information provided by this method will guide the development of 2D COF thin film polymerization strategies to produce higher quality materials, which is a necessary step towards their use in a host of thin-film device architectures.

10.9. Chapter 10, Supplementary Information

Materials

2,7-pyrenebis(boronic acid)[1] and 4,4′-diphenylbutadiynebis(boronic acid)[2] were prepared according to literature conditions. NMR data is consistent with those previously reported. Reagents were purchased in reagent grade from commercial suppliers and used without further purification, unless otherwise described. Solvents were obtained from commercial sources and used without further purification.

PELCO® Single Layer Graphene TEM Support Films on Lacey Carbon, 300 Mesh Copper Grids (Ted Pella, Redding, CA) were used for all TEM experiments. The thickness for a single layer of graphene is approximately 0.35 nm with a transparency on the order of 96.4%.

Monolayer graphene SiO_2/Si (10mm x 10mm) substrates (University Wafer) were used for all GI-WAXS and AFM experiments.

Optical Images of Single Layer Graphene Coated TEM Grids and SiO_2 Substrates

Optical images of the TEM grids were obtained using a trinocular biological compound microscope (T490B-PL, AmScope) equipped with an 18 MP camera.

Grazing-Incidence Wide-Angle X-Ray Diffraction

Grazing-incidence x-ray scattering (GI-WAXS) measurements were performed at Sector 8-ID-E (beam energy = 10.92 keV) of the Advanced Photon Source at Argonne National Laboratory. Samples were placed under vacuum and aligned to provide an incident angle of ~0.14°. Frames were collected for an amount of time such that max pixel intensity did not exceed 80%. Diffraction patterns were collected using a Pilatus 2D detector. All radially integrated patterns were found to agree with previously reported diffraction patterns.

Atomic Force Microscopy

Atomic force microscopy (AFM) images were collected using a Bruker Dimension Fastscan AFM in tapping mode under an ambient environment. Samples were imaged as synthesized.

Transmission Electron Microscopy

TEM was performed using a JEOL (JEOL USA, Inc., Peabody, MA) ARM300F GrandARM TEM operating at 300 keV equipped with a Gatan (Gatan, Inc., Pleasanton, CA) K3-IS “direct electron” detector (FEG Emission: 15 µA, spot size 5, 150 µm CL aperture). The ARM300F was aligned for low-dose imaging, measuring the dose rate on the K3 detector through vacuum (no grid inserted). The dose rate was measured to be 2.1-19.6 e^{-} $Å^{-2}$ s^{-1} (5760 x 4092 pixels) with an image exposure times of 0.2-1 s (0.4-19.5 e^{-} $Å^{-2}$ cumulative dose per image).

For Figures S2-S3 TEM was performed using a JEOL (JEOL USA, Inc., Peabody, MA) ARM200CF Aberration-Corrected STEM/TEM operated at 200 keV equipped with a Gatan (Gatan, Inc., Pleasanton, CA) K2 “direct electron” detector (FEG Emission: 5 μA, spot size 3, 150 μm CL aperture). The ARM200CF was aligned for low-dose imaging, measuring the dose rate on the K2 detector through vacuum (no grid inserted). The dose rate was measured to be 3-3.7 e^{-} $Å^{-2}$ s^{-1} (3710 x 3838 pixels) with an image exposure times of 1 s (3-3.6 e^{-} $Å^{-2}$ cumulative dose per image).

All image acquisition was done using the Gatan Microscopy Suite (GMS), Digital Micrograph (Gatan, Inc., Pleasanton, CA).

Geometry Optimization

Simulations of molecular defects in 2D COF monolayers were carried out in MaterialsStudio (ver.5.0). First, the unit cell was constructed piecewise in a highly symmetric *P6/mmm* unit cell with the $a=b$ lattice parameter set to be approximately the distance between two COF vertices. The c parameter was set to be 3.5 Å, which is the interlayer spacing of graphene. We then used a Forcite geometry optimization routine with a universal forcefield to optimize the unit cell size with convergence tolerances of: Energy = 10^{-3} kcal mol^{-1} and Force = 0.5 kcal mol^{-1} $Å^{-1}$. This routine produced the COF-5 unit cell we have observed in previous reports. We then created a supercell monolayer of this structure (approximately 5a X 5b). Next, we removed all crystallographic

constraints to produce a large-area COF-5 sheet. Then, we selected an unreacted boronic acid at the edge of a COF crystal and installed a hemiboronate-ester at that position. From that position we constructed a second pristine COF sheet from that defect site of approximately the same size as the first. Once a crude version of the defective COF sheet was produced, we then conducted a geometry optimization routine using Forcite with the convergance tolerances of 10^{-5} kcal mol^{-1} and 10^{-3} kcal mol^{-1} $Å^{-1}$ and displacement of 10^{-5} Å. This produced the structure observed in Figure X.XX that showed a 12-degree offset between domains. Importantly, each individual COF domain, outside of the defective boundary, relaxed nicely to the expected COF structure.

I. Experimental Procedures

Synthesis of Colloidal COF Films and TEM Sample Preparation

2,3,6,7,10,11-Hexahydroxytriphenylene (HHTP, 1 mM) and the appropriate corresponding boronic acid (BA, 1.5 mM) were dissolved in a mixture of CH_3CN:1,4-dioxane:mesitylene (80/16/4 v/v/v; 200 mL) and sonicated for 5 min. The solution was passed through Fisherbrand qualitative grade plain filter paper (diameter: 5.5 cm, P4 grade) via vacuum filtration to remove insoluble particulates.

All COF films (COF-5, TP-COF, DPB-COF, and COF-10) were prepared via solvothermal growth. For each system, 20 mL of monomer solution was placed in a 20 mL scintillation vial. A PELCO© single layer graphene (lacey-carbon, Cu, 300 mesh) TEM grid (Ted Pella, Redding, CA) and a 10mm x 10mm monolayer graphene SiO_2/Si substrate (University Wafer) was placed in each vial. The vials were sealed and heated on a hotplate at 70 °C without stirring for 24 h, which resulted in stable, colloidal suspensions.

The colloidal solutions were then decanted from the vials and the TEM grid and substrate were retrieved using tweezers. The TEM grids were immediately rinsed with fresh CH_3CN:1,4-dioxane:mesitylene (80/16/4 v/v/v; 20 mL) solvent and allowed to dry open to air. The TEM grids were then stored in a standard grid box inside of a desiccator prior to imaging.

Mapping Script Information

Scripts were written using MATLAB version 2019b. Image and Metadata importing was done using a modified version of a file publicly available on MATLAB's Central File Exchange.[3]

The user first selects a region of interest (ROI) size in pixels, known as the pixel frame. This number is the side of a square in pixels. A smaller ROI has advantages in terms of resolution and amount of data while a larger ROI has improved signal to noise. For this work we selected an ROI size that houses at least three repeat units. Next, a spatial resolution is selected, corresponding to the size of the square in the final mapped image. The resolution determines how much the ROIs overlap as they raster across the image. The entire image is then subjected to a two-dimensional (2D) Fourier-transform, which is then integrated in Q_{xy} space to find the location of the primary repeat spacing in the image. This is then transformed to a real space number, which is used to determine appropriate bandpass filtering in later steps. Alternatively, the user can specify the repeat unit spacing in real space, if that spacing is known *a priori*. Next, the ROI is scanned across the entire image, generating FFTs at each ROI and radially integrating the intensities (phi integration). The location of the maximum intensity spot in each FFT and corresponding phi degree are then extracted. If the phi degree of the maximum intensity spot in the FFT differs by greater than the phi degree binning number (imposed by the user in the script) that corresponds to a new domain in the image. Each color in the domain orientation map corresponds to a specific lattice orientation as defined by the phi angle measured from the FFTs.

Unless otherwise noted, the resolution, pixel frame, and phi degree binning used to map the images in this manuscript were 3 nm, 500 pixel frames, and 5º, respectively.

All scripts are available on GitHub.

Optical Images of Graphene Coated TEM Grids and SiO_2/Si Substrates

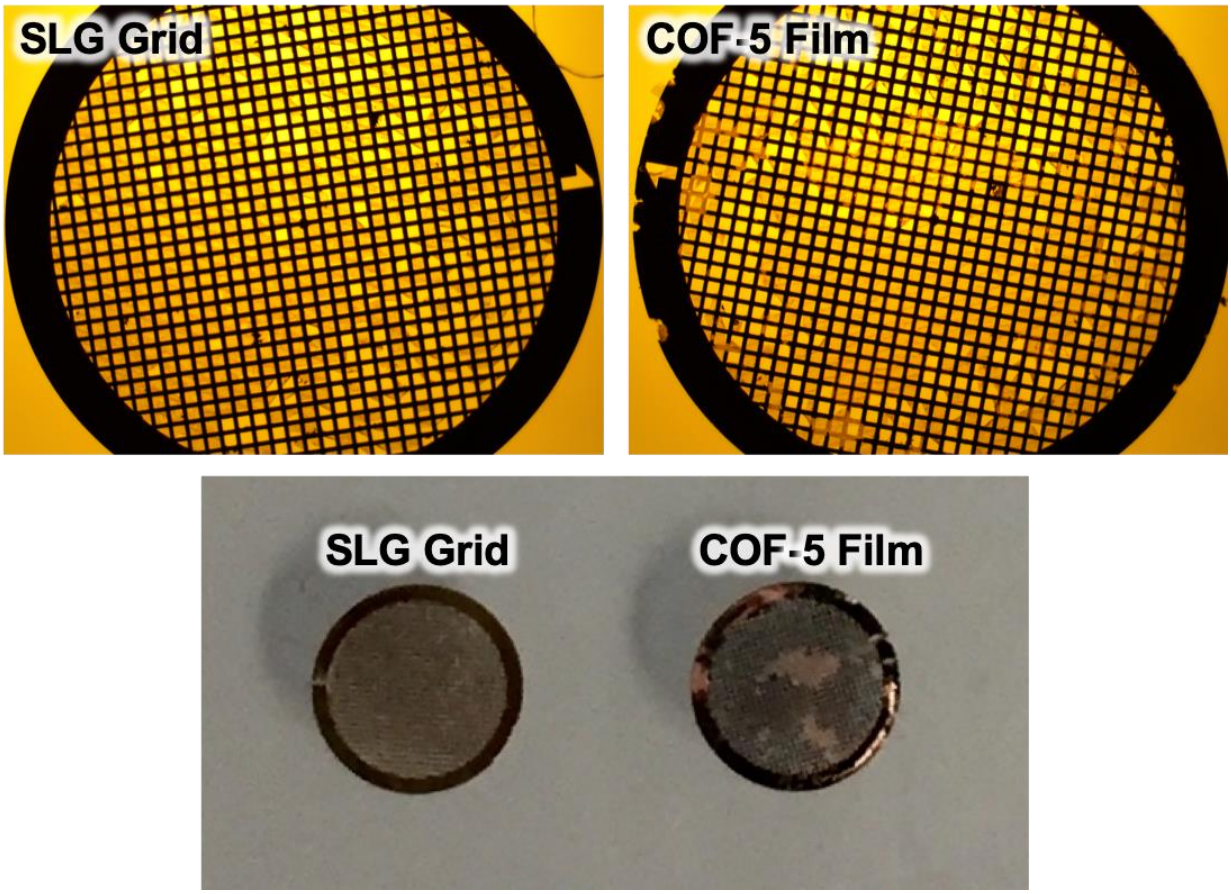

Figure 10.6. Optical images of the single layer graphene coated TEM grids before (right) and after (left) COF-5 film growth. Image of the grid were taken after extensive handling of the grid which caused several of the tears in the film.

Transmission Electron Microscopy Images

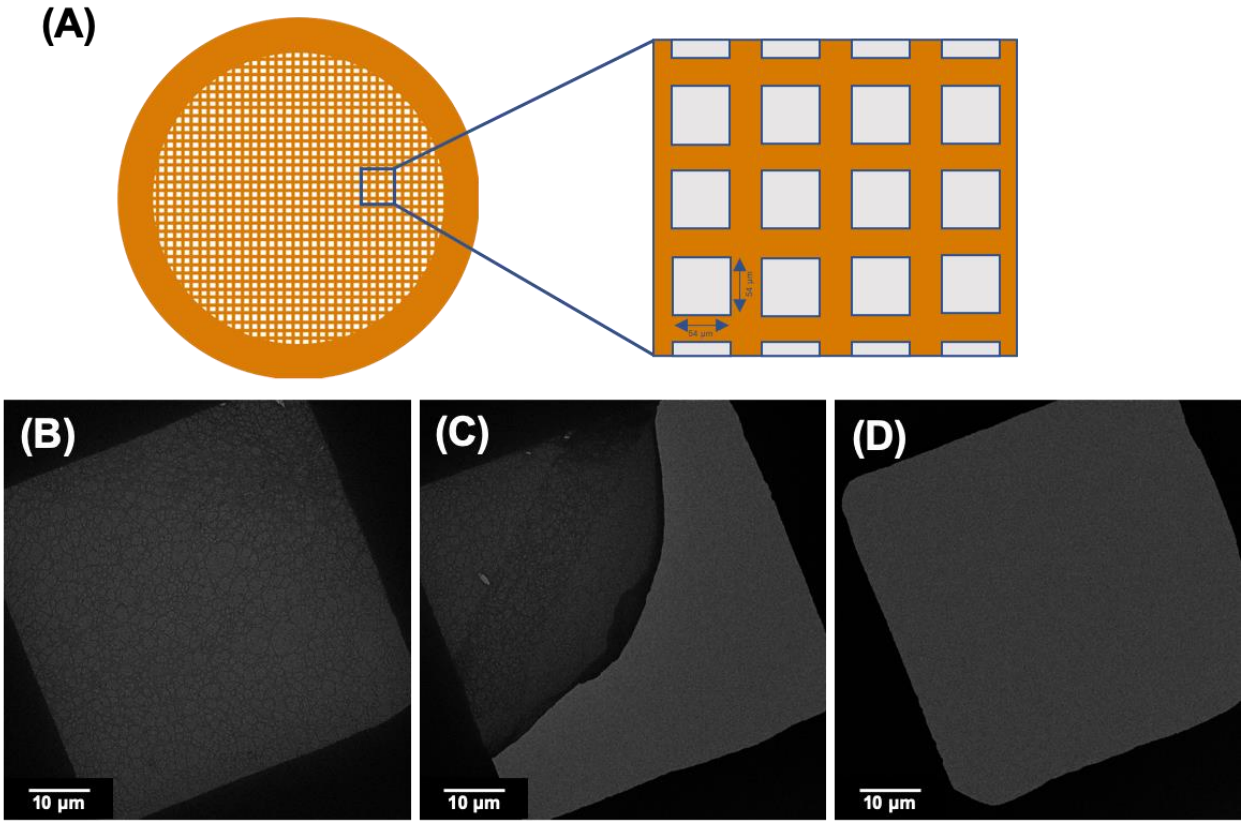

Figure 10.7. (A) Schematic showing a standard TEM grid with 54 µm x 54 µm square windows. Low magnification TEM images showing different possible conditions of the TEM grid bars after film synthesis: **(B)** fully coated with lacey carbon and COF film, **(C)** partially covered with the COF film rolled towards the upper right corner, and **(D)** completely empty.

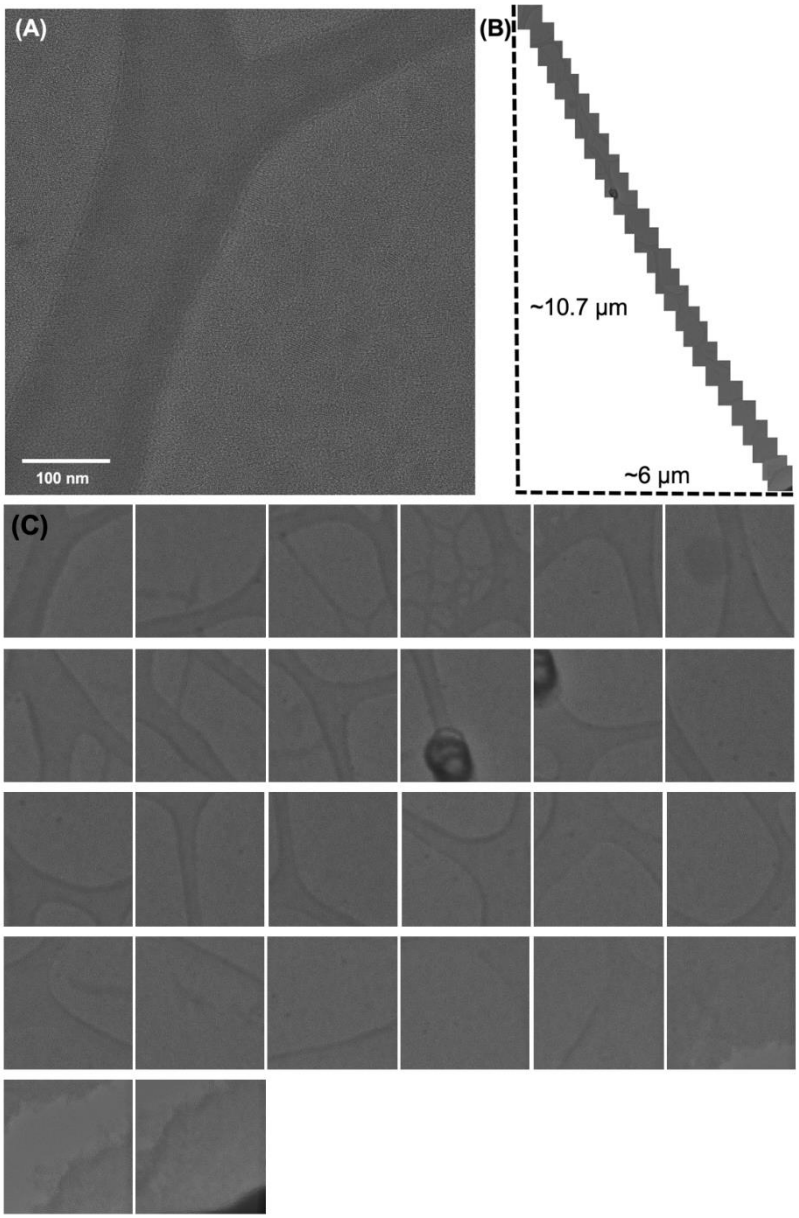

Figure 10.8. (A) Lattice resolution image of a COF-5 film. **(B)** 26 images taken at the same magnification moving by a set value within a single 54 µm x 54 µm grid bar showing the extent of crystalline COF-5 film coverage. **(C)** TEM images shown in (B) prior to stitching them together, where each image is approximately 530 nm x 550 nm.

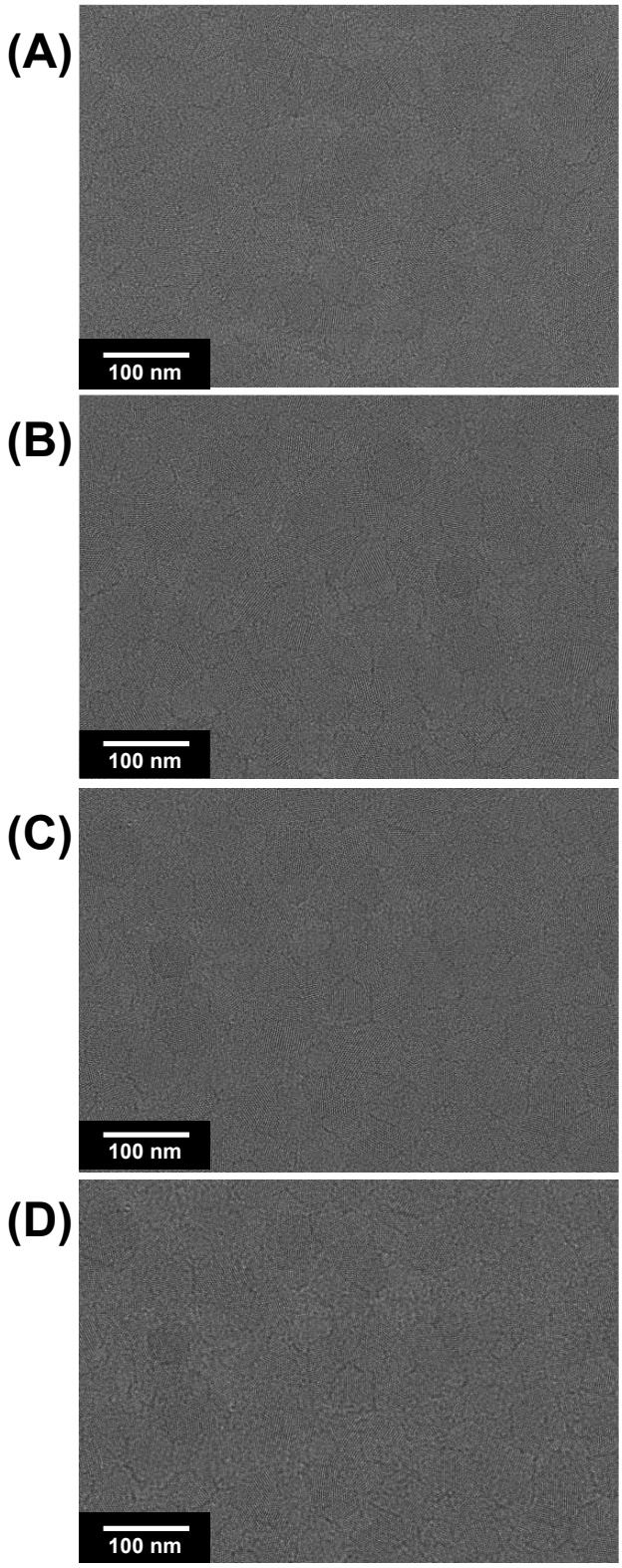
(A)
100 nm
(B)
100 nm
(C)
100 nm
(D)
100 nm

Figure 10.9. Additional TEM images of COF-5 film grown on single layer graphene TEM grids. Dose Rate / Cumulative Dose: **(A)** 13.90 e^{-} $Å^{-2}$ s^{-1} / 13.84 e^{-} $Å^{-2}$, **(B)** 13.81 e^{-} $Å^{-2}$ s^{-1} / 13.75 e^{-} $Å^{-2}$, **(C)** 13.81 e^{-} $Å^{-2}$ s^{-1} / 13.75 e^{-} $Å^{-2}$, and **(D)** 12.64 e^{-} $Å^{-2}$ s^{-1} / 12.59 e^{-} $Å^{-2}$.

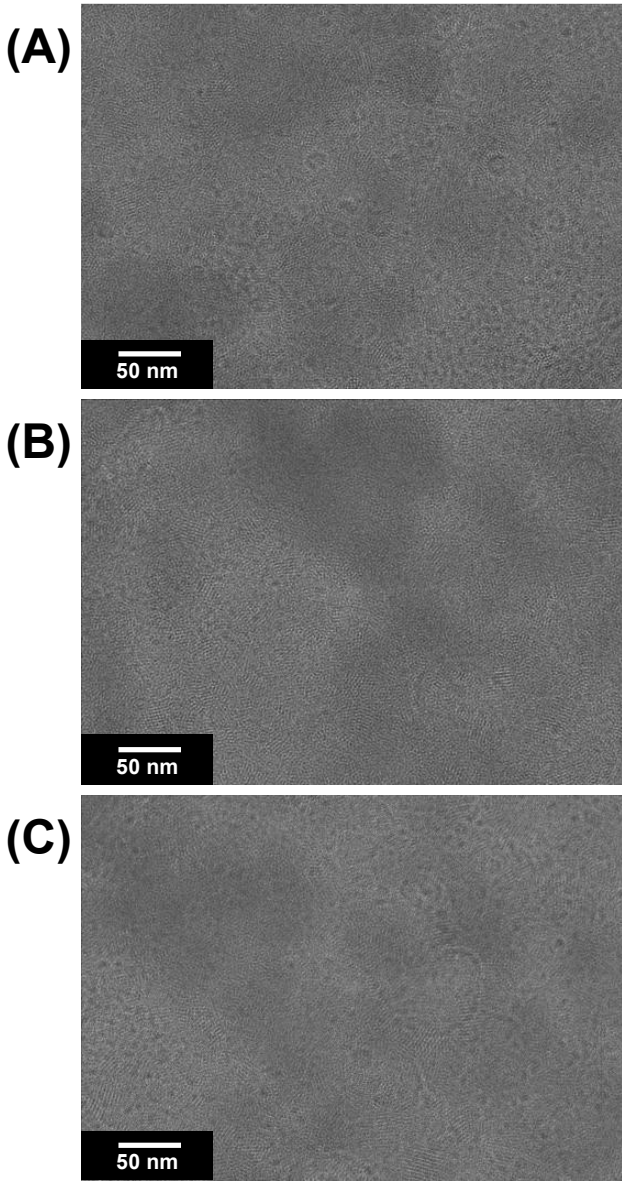

Figure 10.10. Additional TEM images of COF-10 film grown on single layer graphene TEM grids. Dose Rate / Cumulative Dose: **(A)** 17.41 e^{-} $Å^{-2}$ s^{-1} / 17.38 e^{-} $Å^{-2}$, **(B)** 17.31 e^{-} $Å^{-2}$ s^{-1} / 17.28 e^{-} $Å^{-2}$, and **(C)** 17.35 e^{-} $Å^{-2}$ s^{-1} / 17.32 e^{-} $Å^{-2}$.

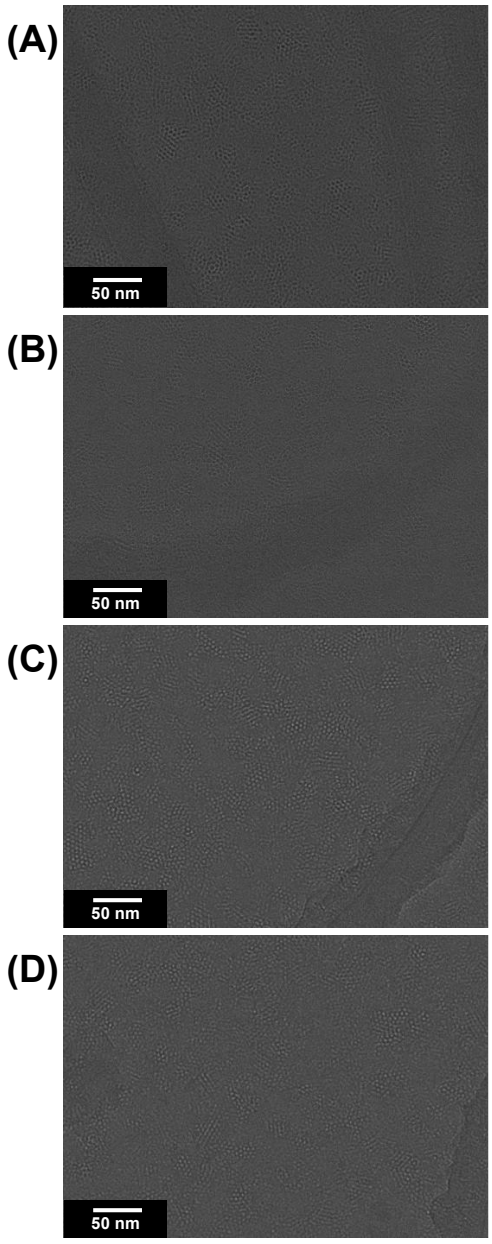

Figure 10.11. Additional TEM images of DPB-COF film grown on single layer graphene TEM grids. Dose Rate / Cumulative Dose: **(A)** 9.60 e^{-} $Å^{-2}$ s^{-1} / 3.73 e^{-} $Å^{-2}$, **(B)** 10.77 e^{-} $Å^{-2}$ s^{-1} / 4.19 e^{-} $Å^{-2}$, **(C)** 16.49 e^{-} $Å^{-2}$ s^{-1} / 6.41 e^{-} $Å^{-2}$, and **(D)** 16.43 e^{-} $Å^{-2}$ s^{-1} / 6.39 e^{-} $Å^{-2}$.

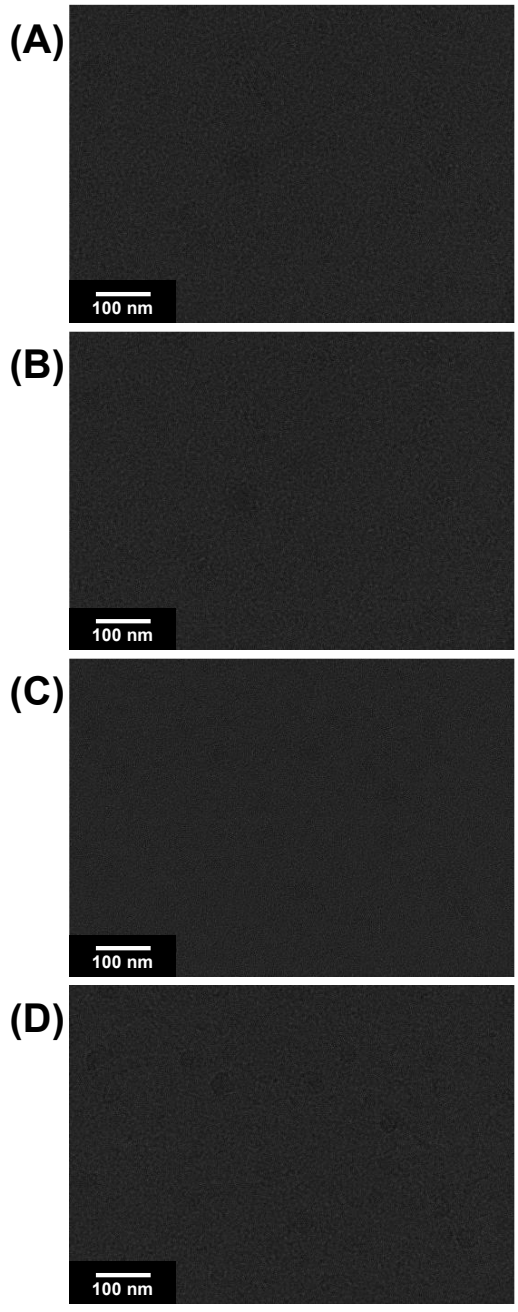

Figure 10.12. Additional TEM images of TP-COF film grown on single layer graphene TEM grids. Dose Rate / Cumulative Dose: **(A)** 2.11 e^{-} $Å^{-2}$ s^{-1} / 0.40 e^{-} $Å^{-2}$, **(B)** 2.11 e^{-} $Å^{-2}$ s^{-1} / 0.41 e^{-} $Å^{-2}$, **(C)** 2.12 e^{-} $Å^{-2}$ s^{-1} / 0.41 e^{-} $Å^{-2}$, and **(D)** 2.15 e^{-} $Å^{-2}$ s^{-1} / 0.41 e^{-} $Å^{-2}$.

MATLAB Script: Selecting a ROI/Pixel Frame

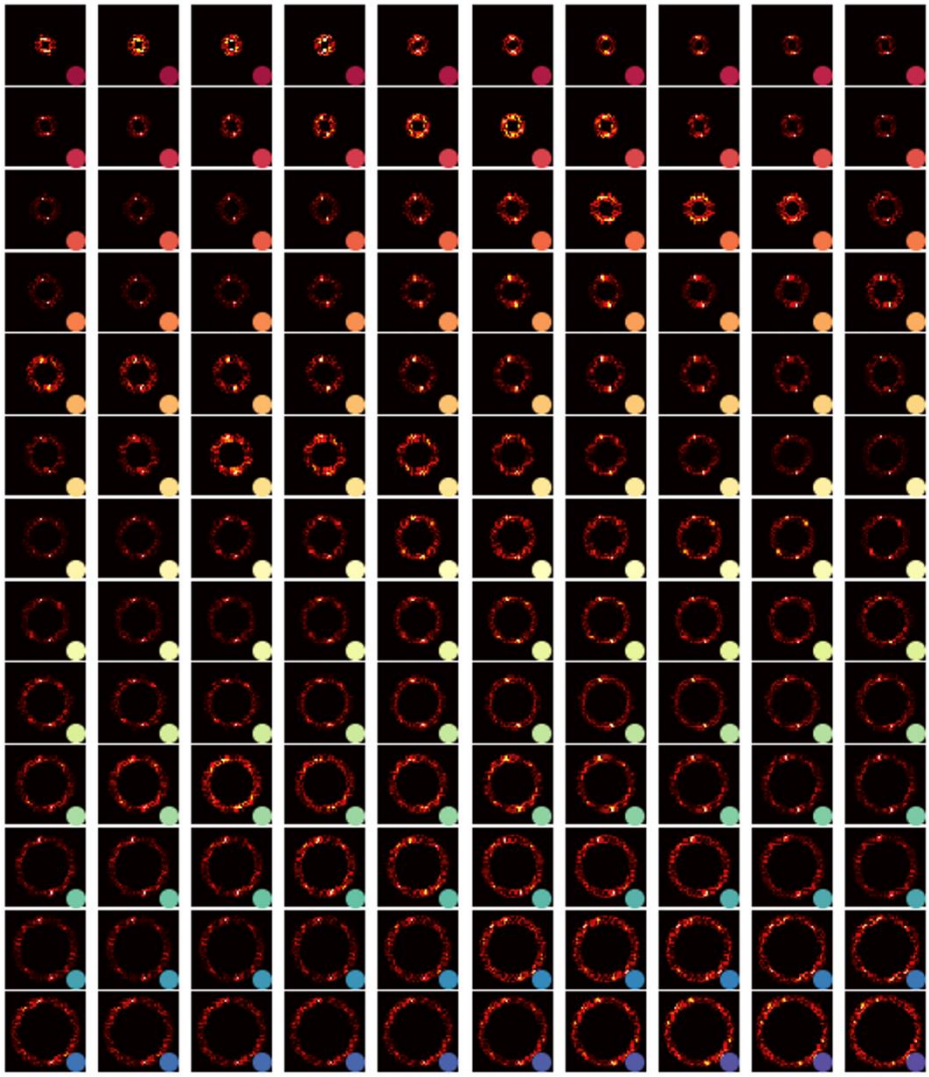

Figure 10.13. 2D Fourier transforms of the COF-5 film HR-TEM image shown in Figure 2A with ROI sizes between 300 (red) and 500 (purple) pixels. The images are bandpass filtered using the MATLAB mapping script previously described. Signal to noise ratios are then extracted to select the optimal ROI size for the image.

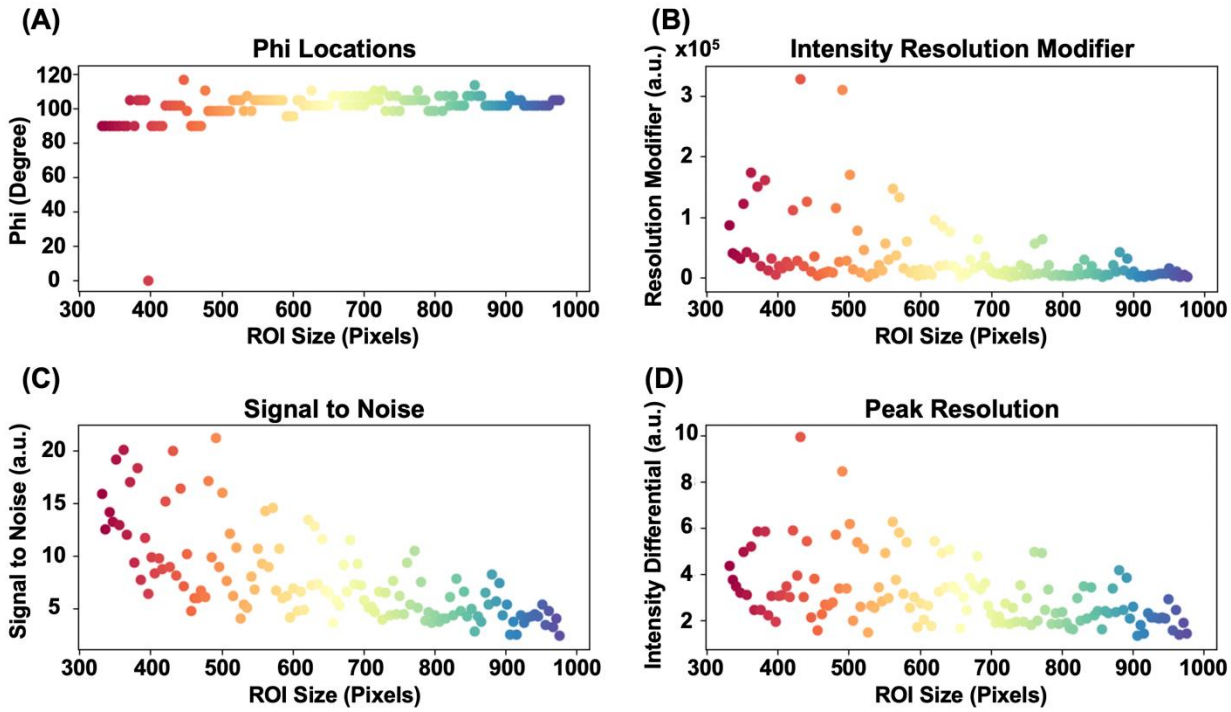

Figure 10.14. (A) Location of the most intense phi spot as a function of ROI size. At small ROIs, the script is unable to precisely assign the phi value which is needed to later used to construct a domain ma because of the limited number of pixels, and therefore limited phi resolution, of the 2D Fourier transform. **(B)** The product of (C) and (D) versus pixel size which, in conjunction with the phi resolution, is used to assign the optimal ROI size for a given image. **(C)** Signal to noise versus ROI size is computed by assessing the maximum intensity versus the variance in binned phi intensity. **(D)** Peak resolution versus ROI size is determined by the ratio of the local maximum intensities, which yields a higher value when a single set of FFT spots are observed.

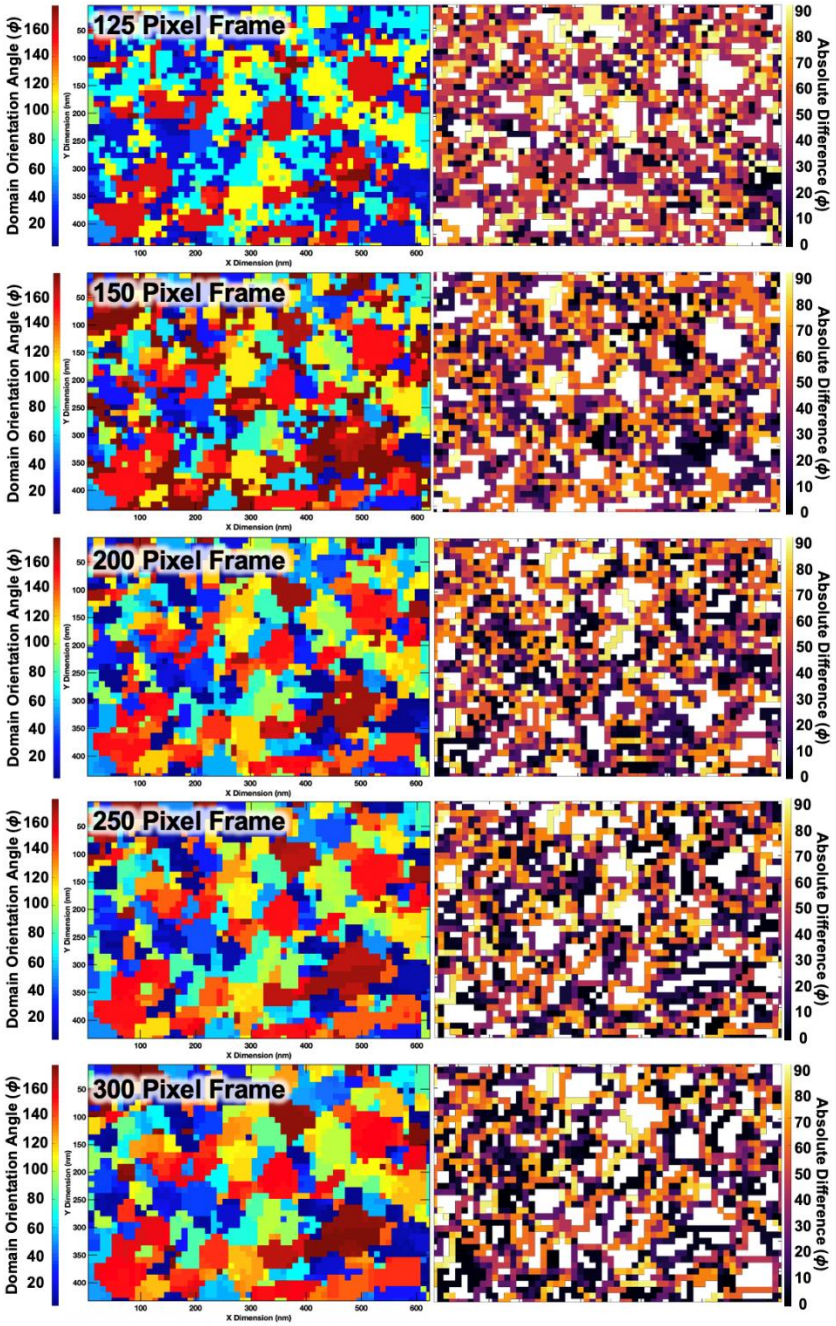

Figure 10.15. Selection of mapping pixel frame for the COF-5 film HR-TEM image shown in Figure 2A. Domain map (left) and corresponding grain boundary map (right) for pixel frames ranging from 125-300 (3º phi binning used).

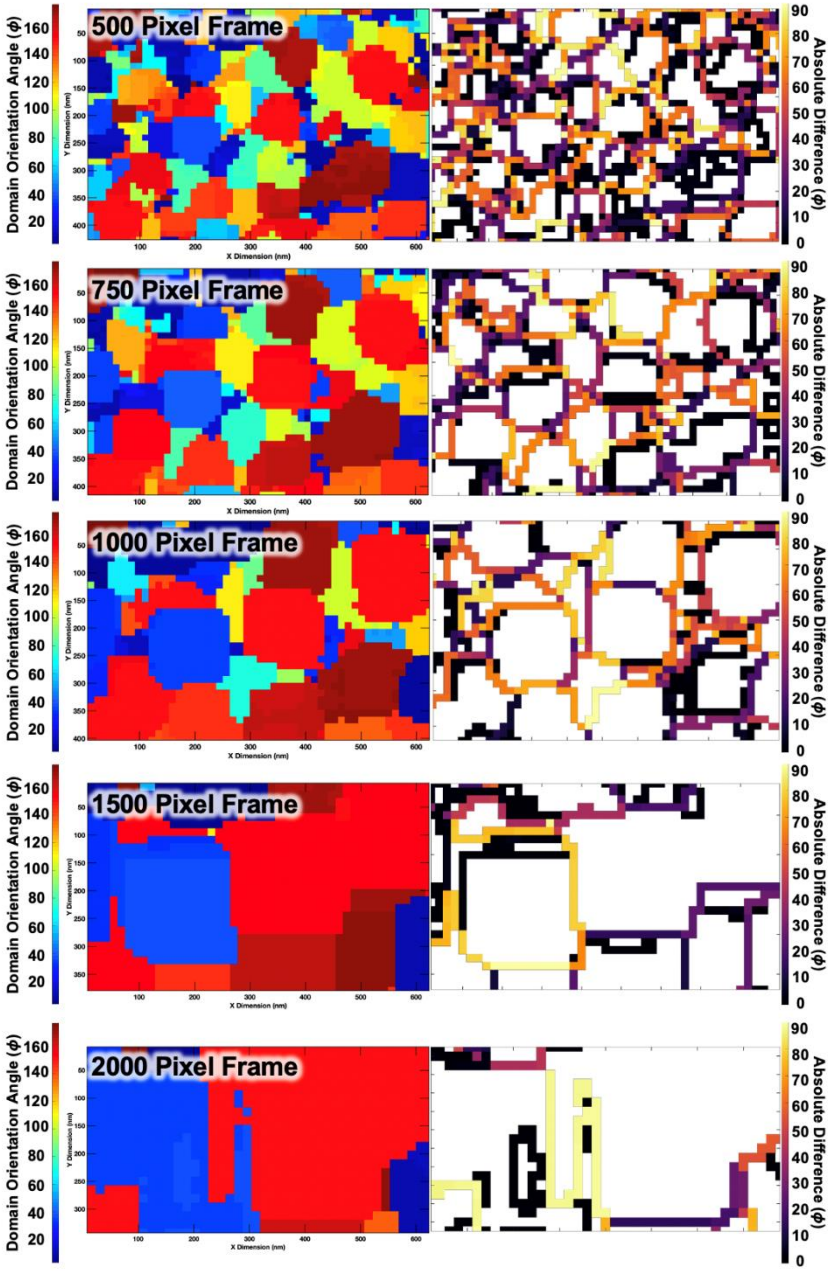

Figure 10.16. Selection of mapping pixel frame for the COF-5 film HR-TEM image shown in Figure 2A. Domain map (left) and corresponding grain boundary map (right) for pixel frames ranging from 500-2000 (3º phi binning used).

MATLAB Script: Selecting Mapping Resolution

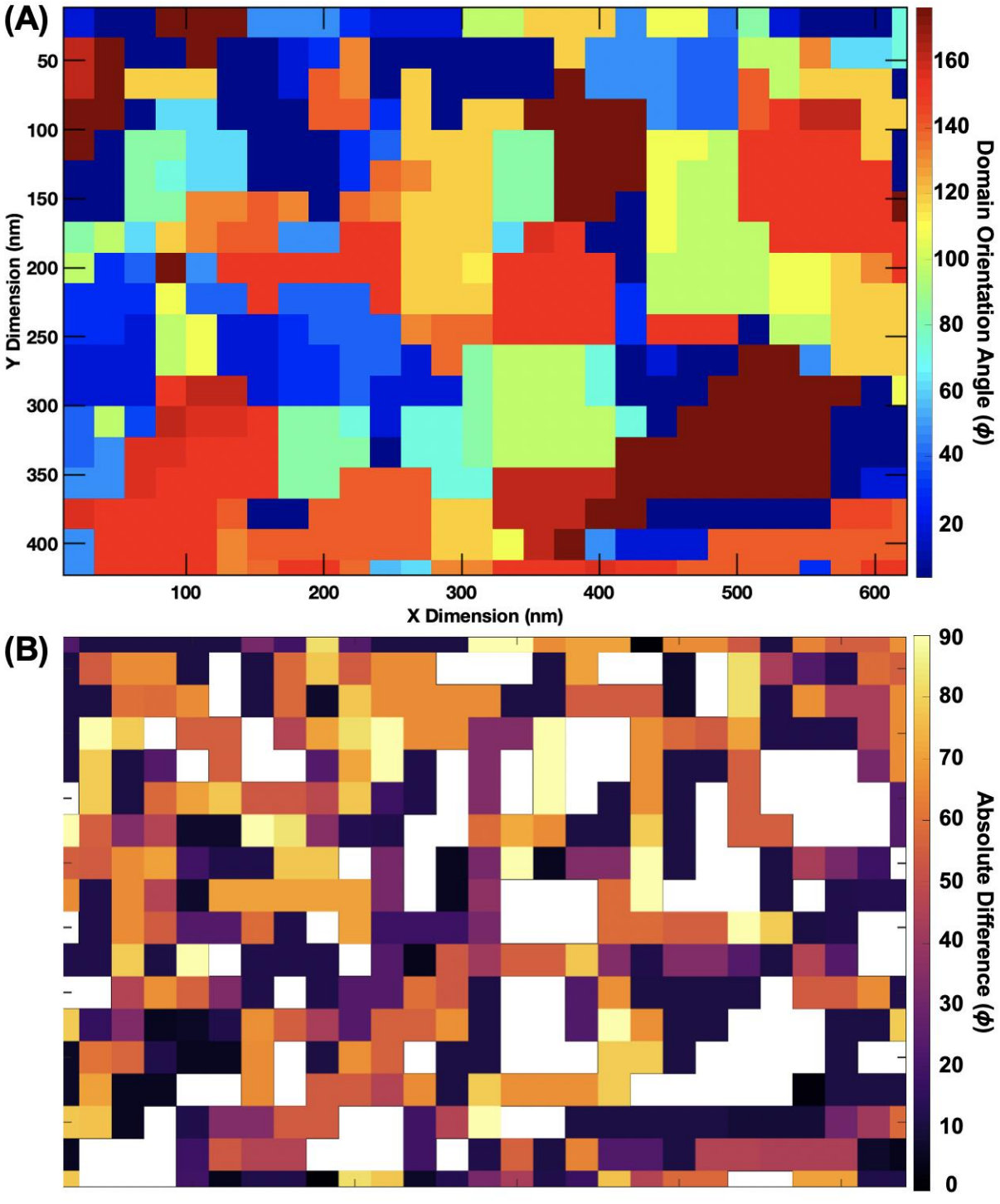

Figure 10.17. Selection of mapping spatial resolution for the COF-5 film HR-TEM image shown Figure 2A. **(A)** Domain map using a 20 nm resolution. **(B)** Grain boundary map using a 20 nm resolution.

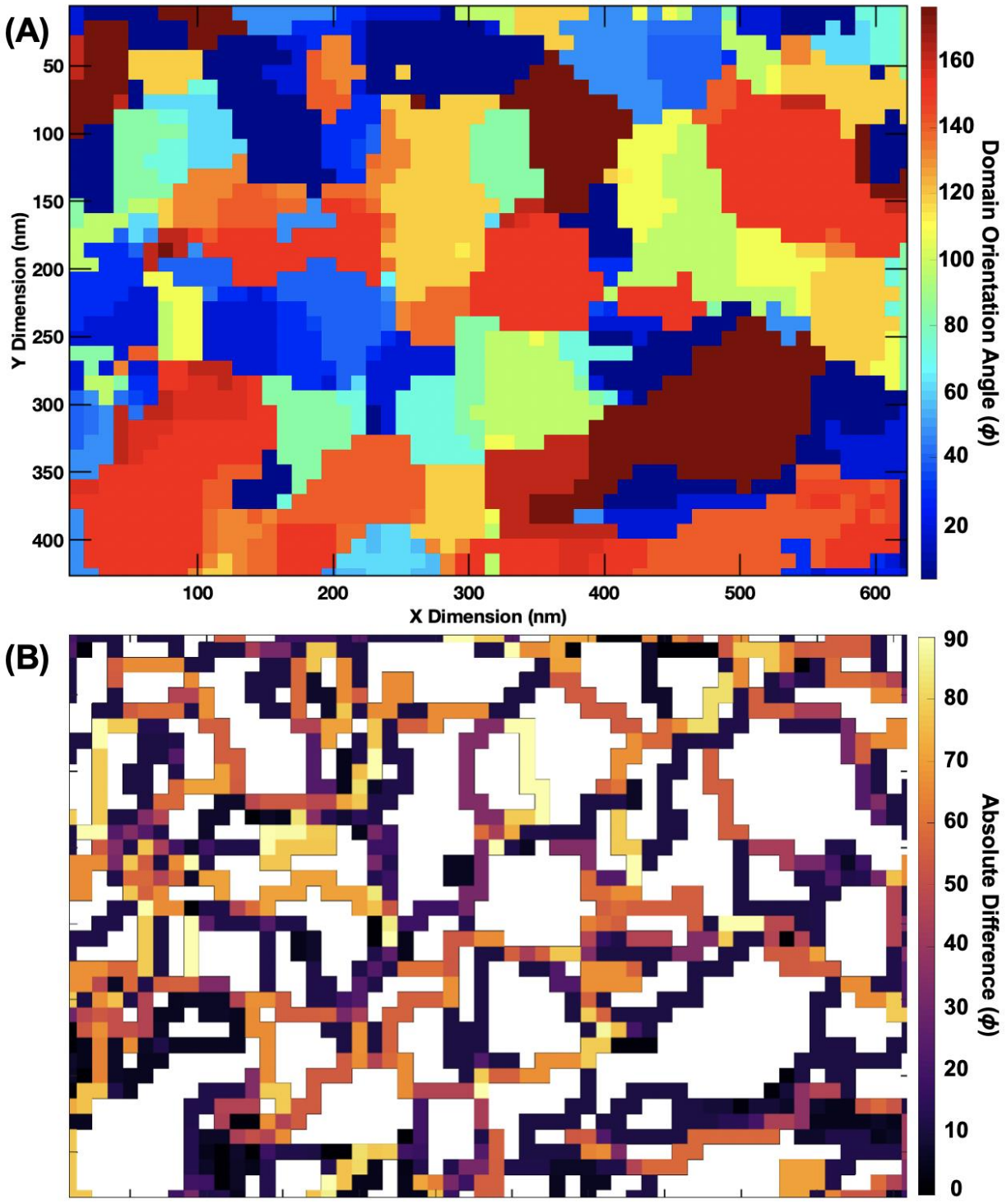
(A)
Y Dimension (nm)
50
100
150
200
250
300
350
400
100
200
300
400
500
600
X Dimension (nm)
160
140
120
100
80
60
40
20
Domain Orientation Angle (ϕ)
(B)
90
80
70
60
50
40
30
20
10
0
Absolute Difference (ϕ)

Figure 10.18. Selection of mapping spatial resolution for the COF-5 film HR-TEM image shown Figure 2A. **(A)** Domain map using a 10 nm resolution. **(B)** Grain boundary map using a 10 nm resolution.

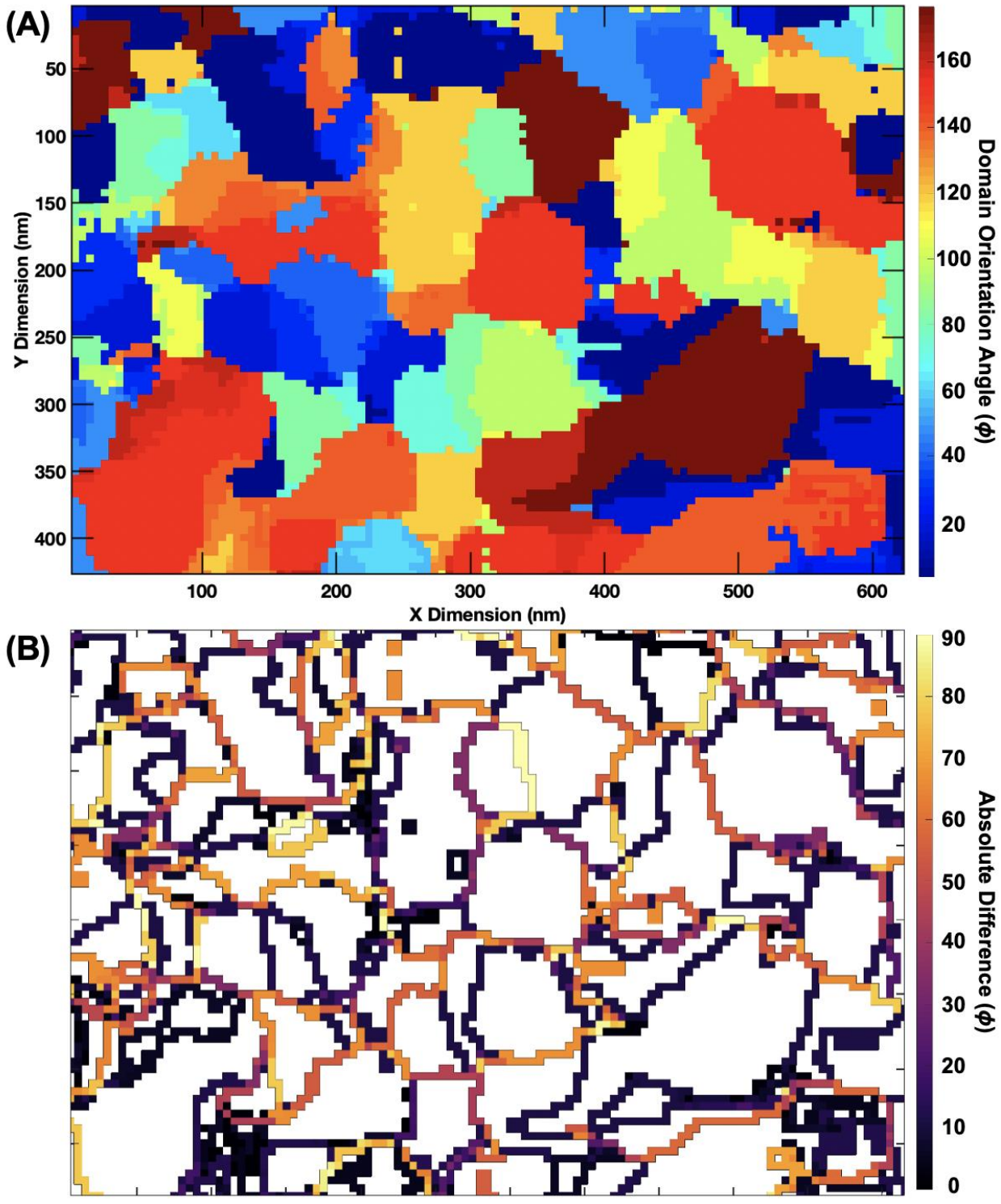
(A)
Y Dimension (nm)
50
100
150
200
250
300
350
400
100
200
300
400
500
600
X Dimension (nm)
160
140
120
100
80
60
40
20
Domain Orientation Angle (ϕ)
(B)
90
80
70
60
50
40
30
20
10
0
Absolute Difference (ϕ)

Figure 10.19. Selection of mapping spatial resolution for the COF-5 film HR-TEM image shown Figure 2A. **(A)** Domain map using a 5 nm resolution. **(B)** Grain boundary map using a 5 nm resolution.

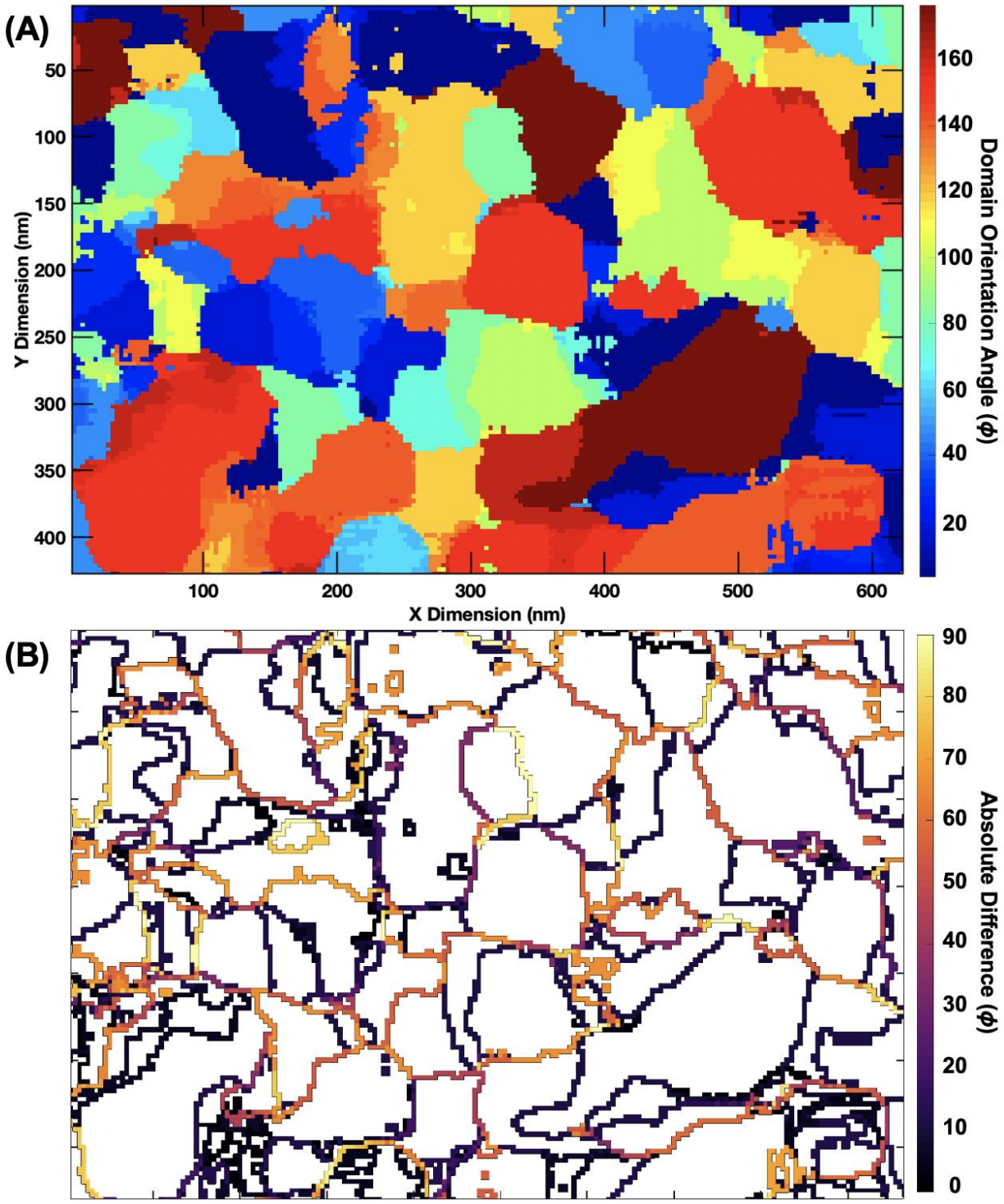
(A)
Y Dimension (nm)
50
100
150
200
250
300
350
400
100
200
300
400
500
600
X Dimension (nm)
160
140
120
100
80
60
40
20
Domain Orientation Angle (ϕ)
(B)
90
80
70
60
50
40
30
20
10
0
Absolute Difference (ϕ)

Figure 10.20. Selection of mapping spatial resolution for the COF-5 film HR-TEM image shown Figure 2A. **(A)** Domain map using a 3 nm resolution. **(B)** Grain boundary map using a 3 nm resolution.

MATLAB Script: Selecting Phi Degree Binning

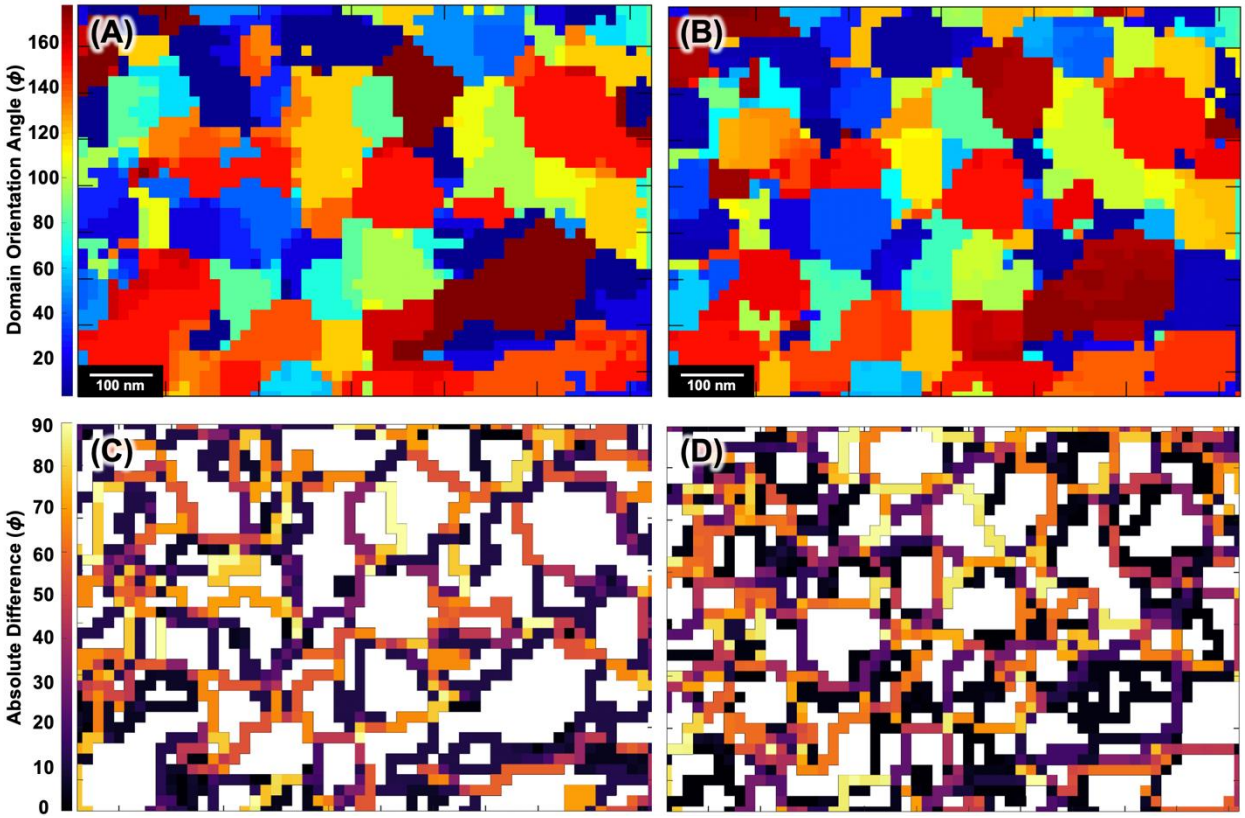

Figure 10.21. Selection of phi degree binning for the COF-5 film HR-TEM image shown in Figure 2A. **(A)** Domain orientation map using 10 nm resolution, 500 pixel size, and 5º phi binning. **(B)** Domain orientation map using 10 nm resolution, 500 pixel size, and 3º phi binning. **(C)** Corresponding grain boundary map using same parameters as (A). **(D)** Corresponding grain boundary map using same parameters as (B).

MATLAB Script: Domain Mapping

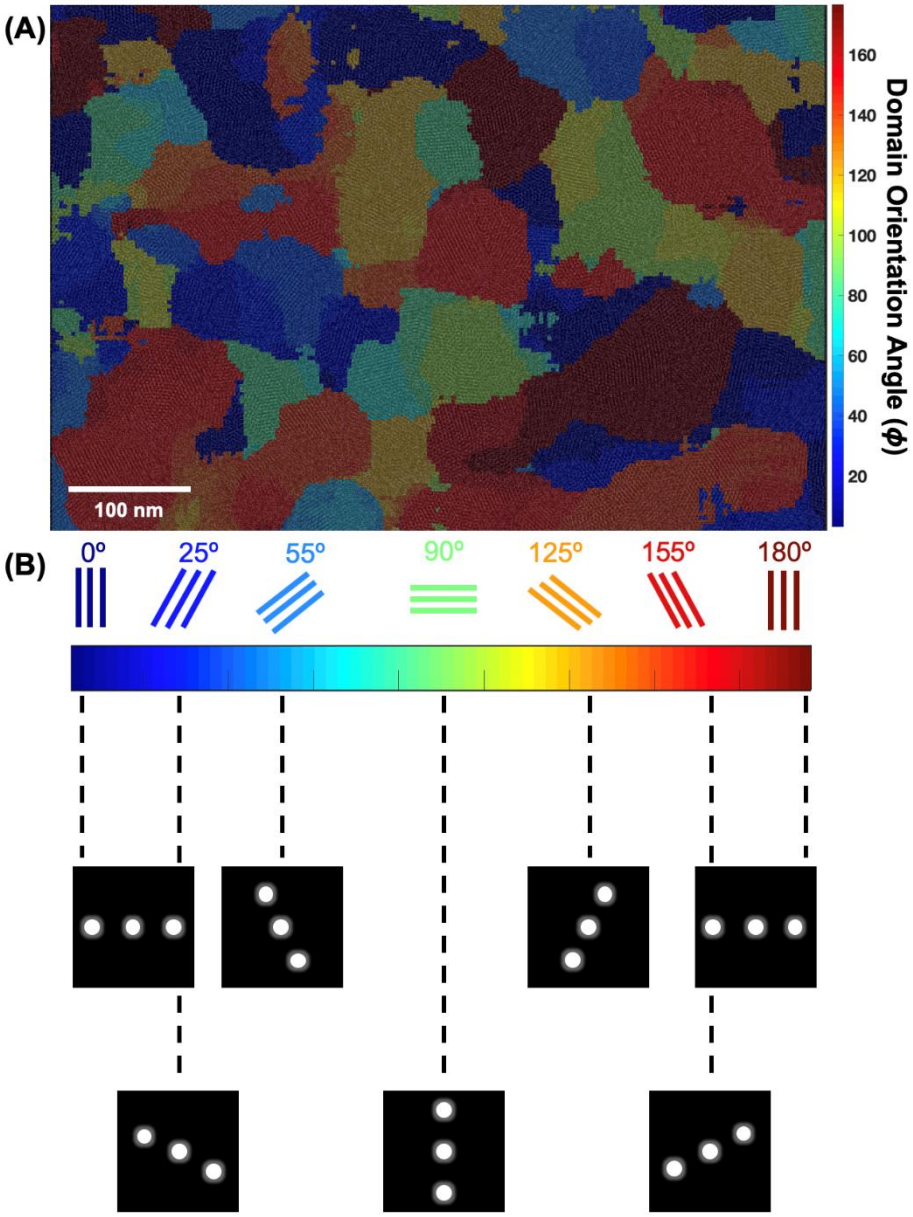

Figure 10.22. (A) Domain mapped COF-5 film TEM image. **(B)** Schematic showing the lattice angle and FFT that correspond to the different colors in the mapped image.

Analysis of COF-5 Grain Boundaries

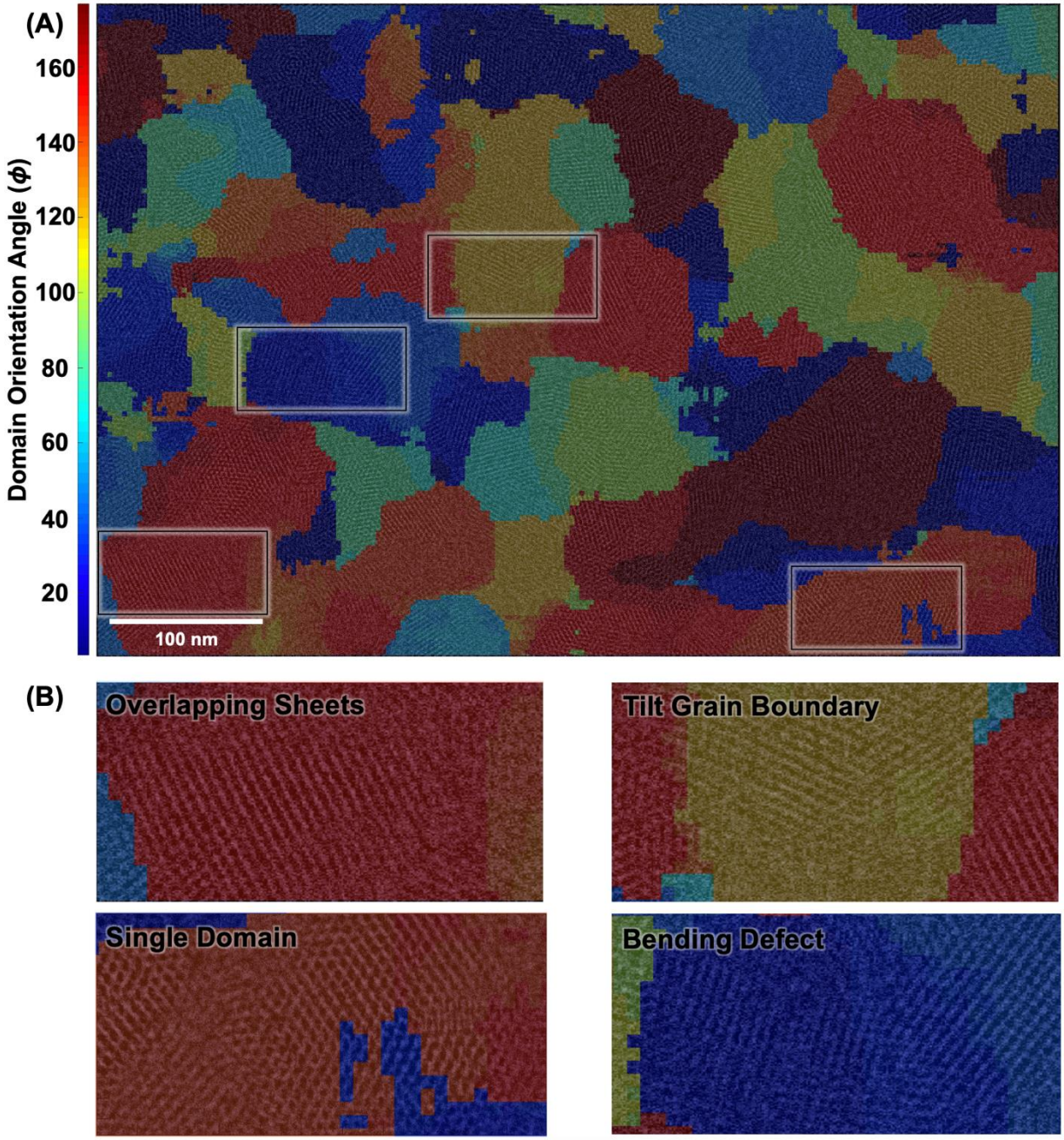

Figure 10.23. (A) Domain mapped COF-5 film TEM image with boxed regions corresponding to different types of grain boundaries or domains. **(B)** Magnified images of boxed regions in (A) showing the different types of regions.

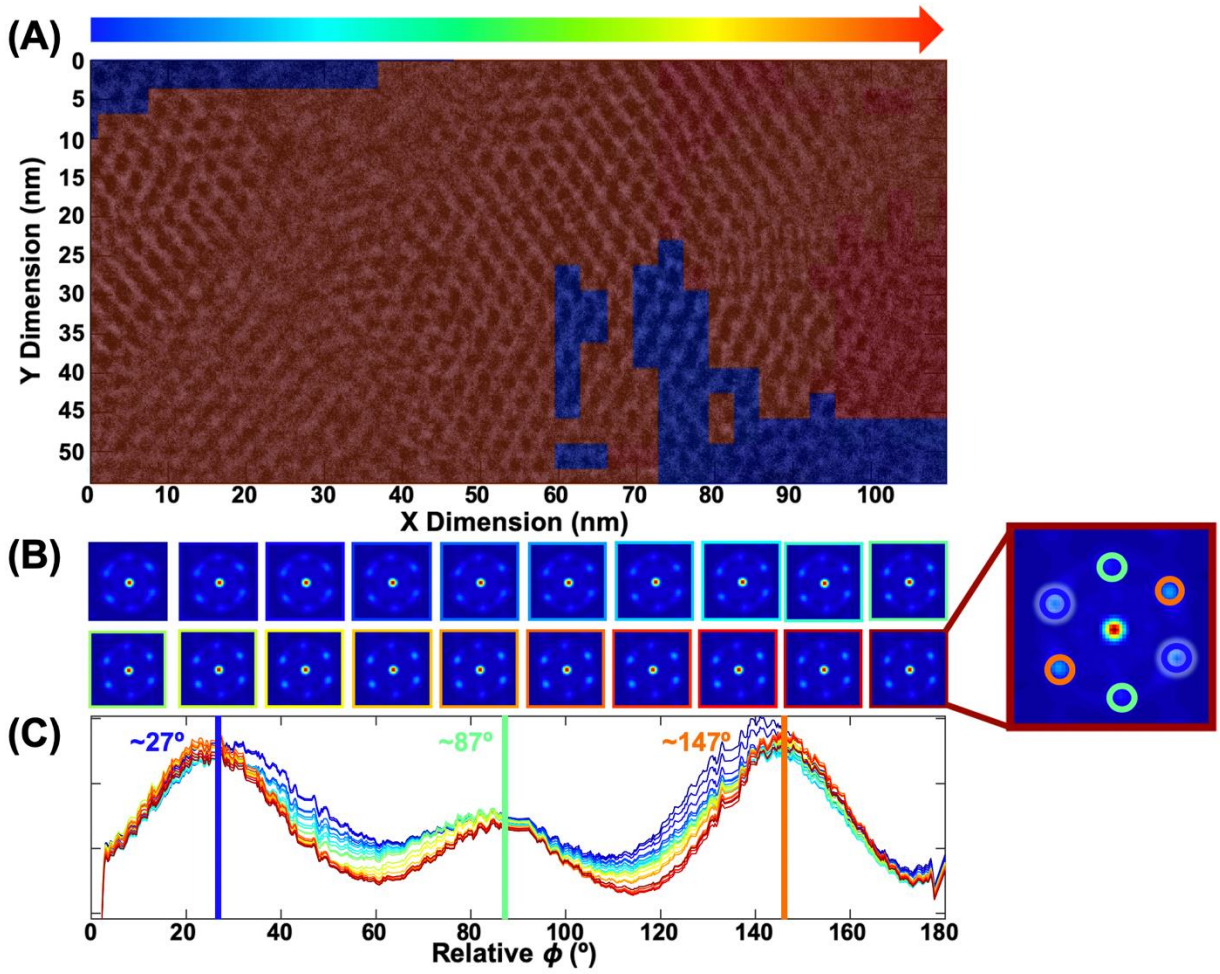

Figure 10.24. (A) Zoomed in region of COF-5 film HR-TEM image showing predominately a single crystalline domain. **(B)** FFT patterns of regions moving from right to left (blue to red) in the cropped image shown in (A). **(C)** Plot displaying the relative phi intensities which show the changes in grain orientation throughout the image.

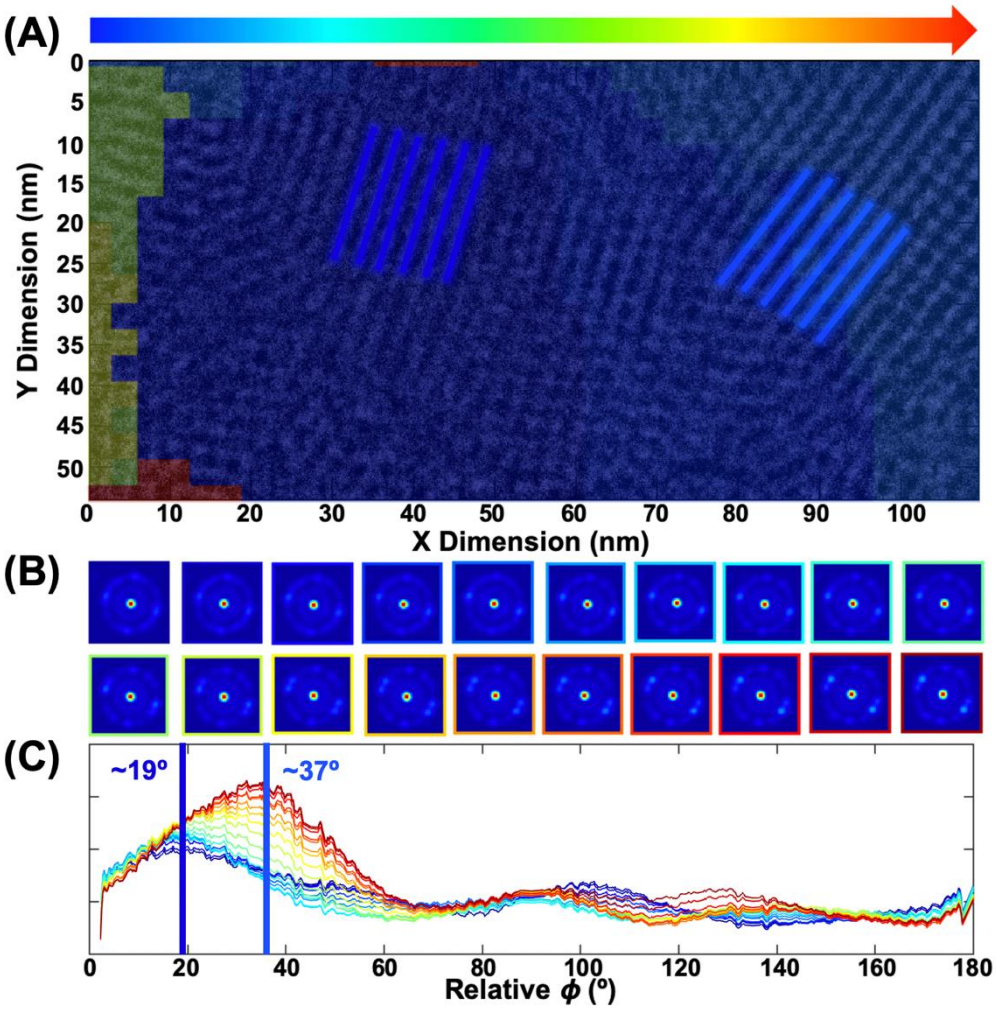

Figure 10.25. (A) Zoomed in region of COF-5 film HR-TEM image showing a bending defect. **(B)** FFT patterns of regions moving from right to left (blue to red) in the cropped image shown in (A). **(C)** Plot displaying the relative phi intensities which show the changes in grain orientation throughout the image.

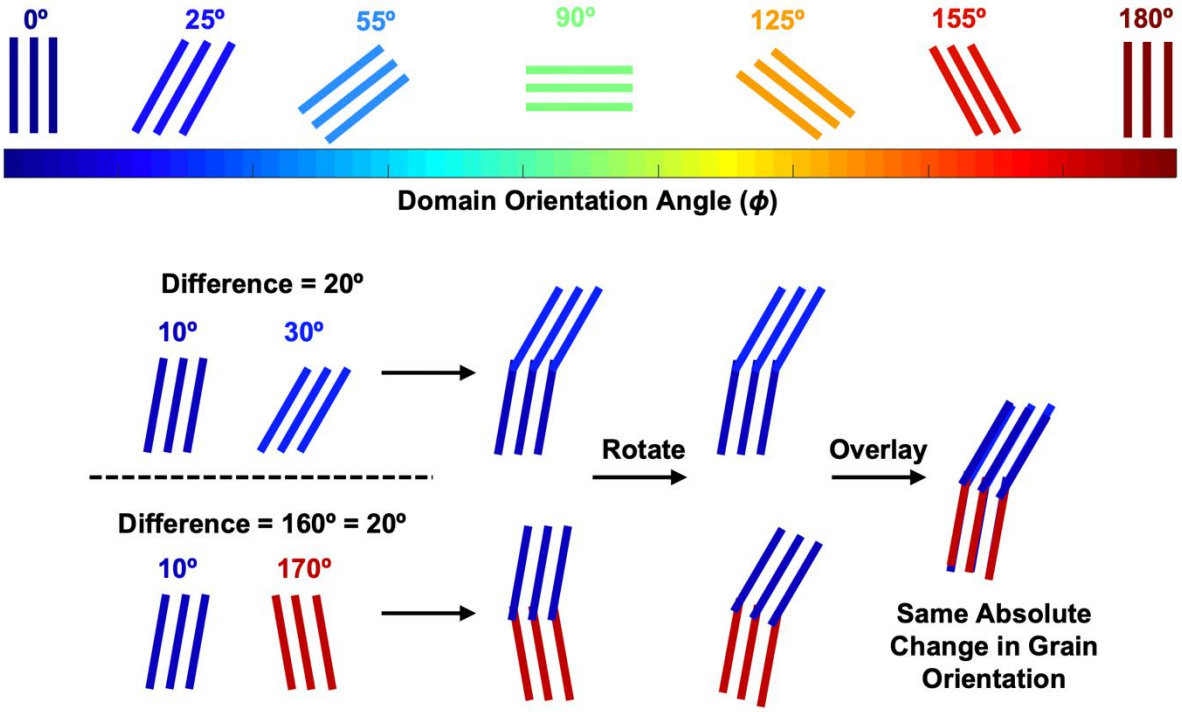

Figure 10.26. Schematic showing the absolute difference in grain orientation between adjacent crystalline domains. A domain with an orientation of 10° that is adjacent to a 30° domain has the same absolute change in grain orientation as a domain with an orientation of 10° that is adjacent to a 170° domain because in both cases the absolute difference is 20°.

Mapping other boronate-ester linked COFs

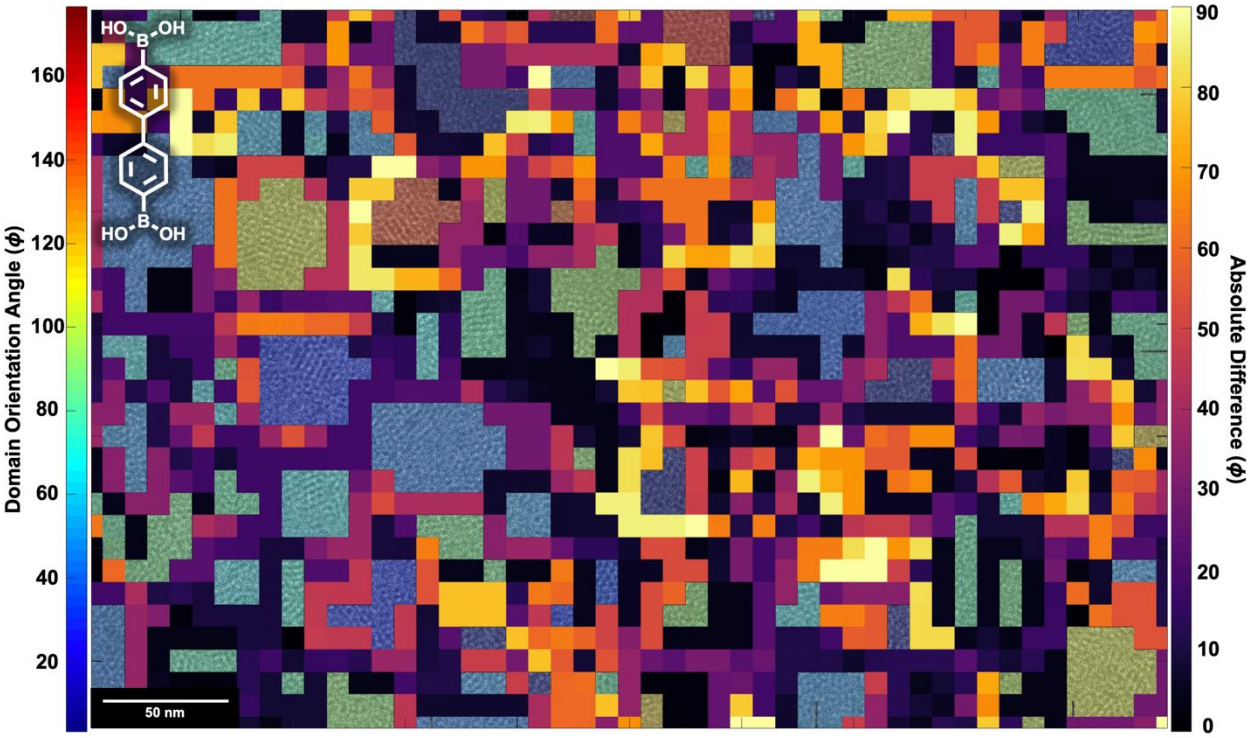

Figure 10.27. HR-TEM image of a COF-10 film grown on a graphene coated TEM (Figure 1C) with domain orientation map and grain boundary map overlaid. Dose Rate: 17.35 e^{-} $Å^{-2}$ s^{-1} Cumulative Dose: 17.28 e^{-} $Å^{-2}$. Mapping parameters: 8 nm resolution, 500 pixel frame, 5º phi binning.

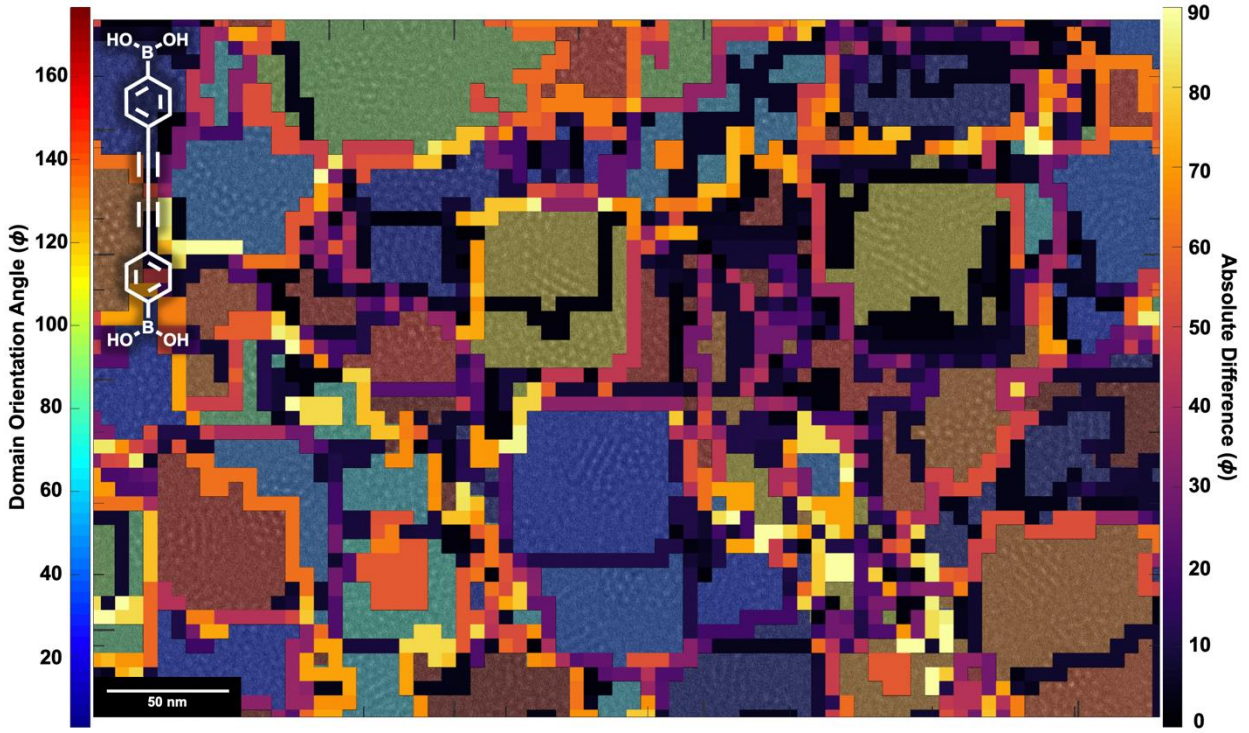

Figure 10.28. HR-TEM image of a DPB-COF film grown on a graphene coated TEM (Figure 1D) with domain orientation map and grain boundary map overlaid. Dose Rate: 16.45 e^{-} $Å^{-2}$ s^{-1} Cumulative Dose: 6.40 e^{-} $Å^{-2}$. Mapping parameters: 5 nm resolution, 750 pixel frame, 5º phi binning.

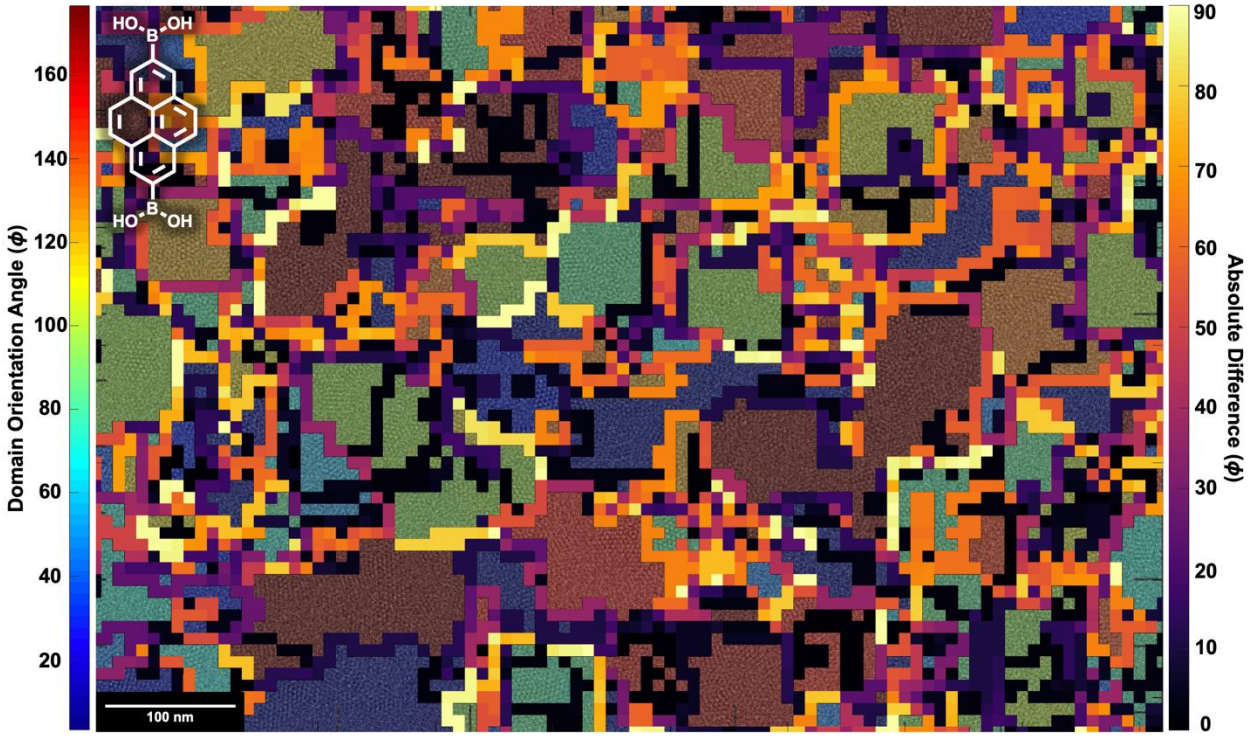

Figure 10.29. HR-TEM image of a TP-COF film grown on a graphene coated TEM (Figure 1D) with domain orientation map and grain boundary map overlaid. Dose Rate: 2.12 e^{-} $Å^{-2}$ s^{-1} Cumulative Dose: 0.41 e^{-} $Å^{-2}$. Mapping parameters: 8 nm resolution, 500 pixel frame, 5º phi binning.

Mapping Other Materials

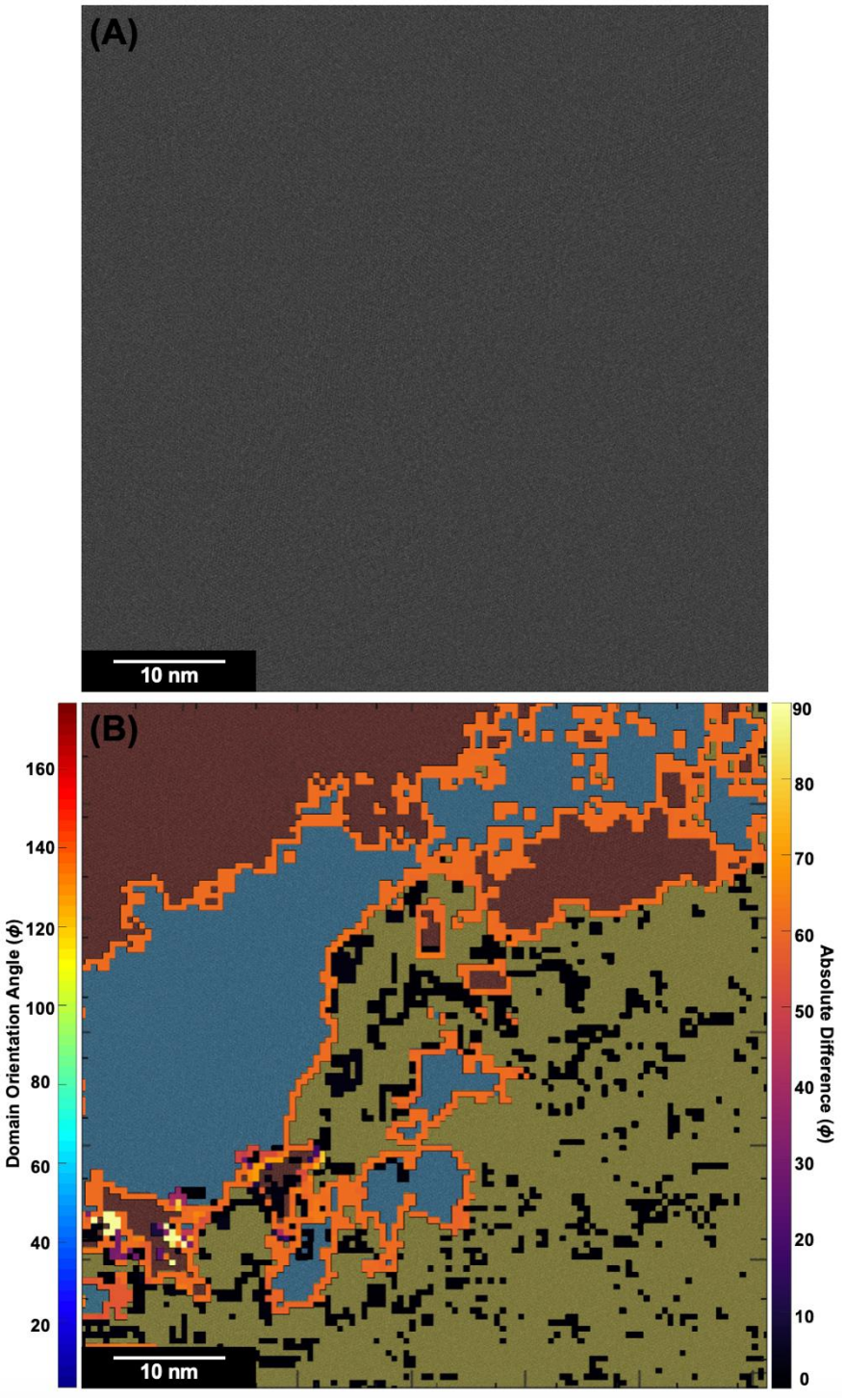

Figure 10.30. (A) HR-TEM image of a MoS_2 region collected using dose fractionation within 36 frames with a total acquisition time of 0.45 s and a dose rate of 17 e^{-} px^{-1} s^{-1}.[4] **(B)** Domain orientation map and grain boundary map overlaid on the HR-TEM image. Mapping parameters: 0.5 nm resolution, 250 pixel frame, 5º phi binning.

Grazing-Incidence Wide-Angle X-Ray Scattering

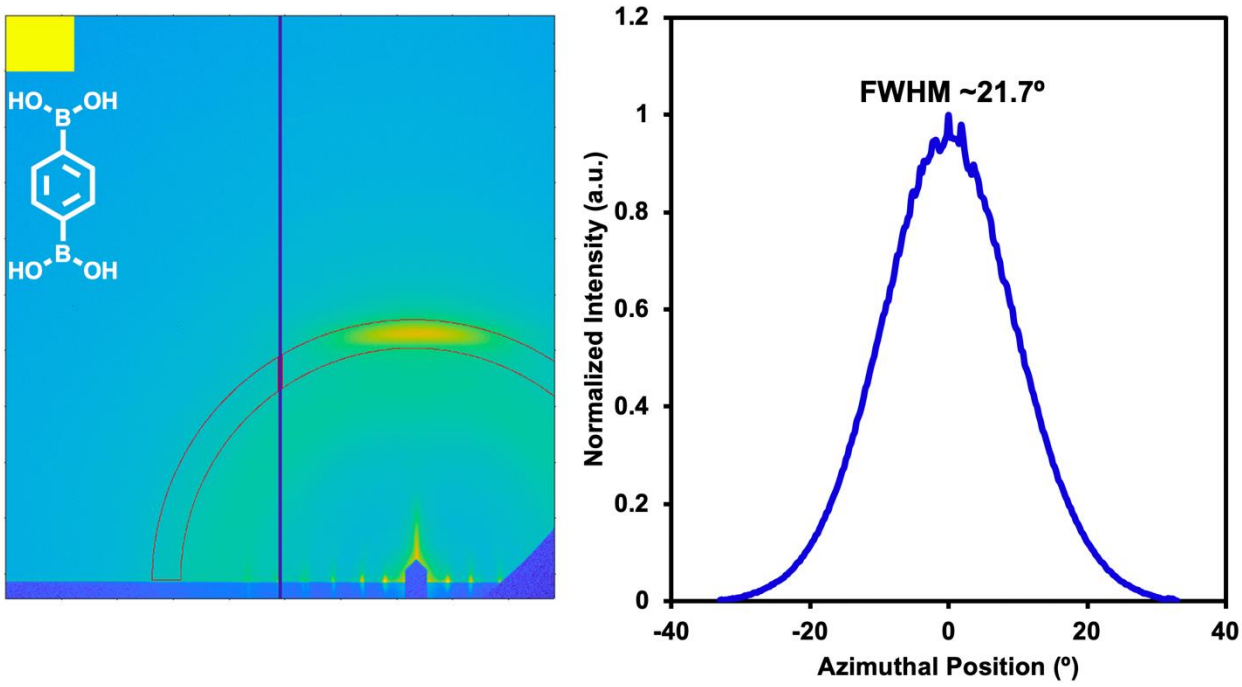

Figure 10.31. Estimate of the angular distribution using the azimuthal position of the (001) peak in the GIWAXS pattern. GIWAXS pattern for COF-5 with a mask (marked in red) selecting the (001) peak (left). Normalized, background subtracted line cut of the (001) peak with a measured FWHM of ~21.7° (right).

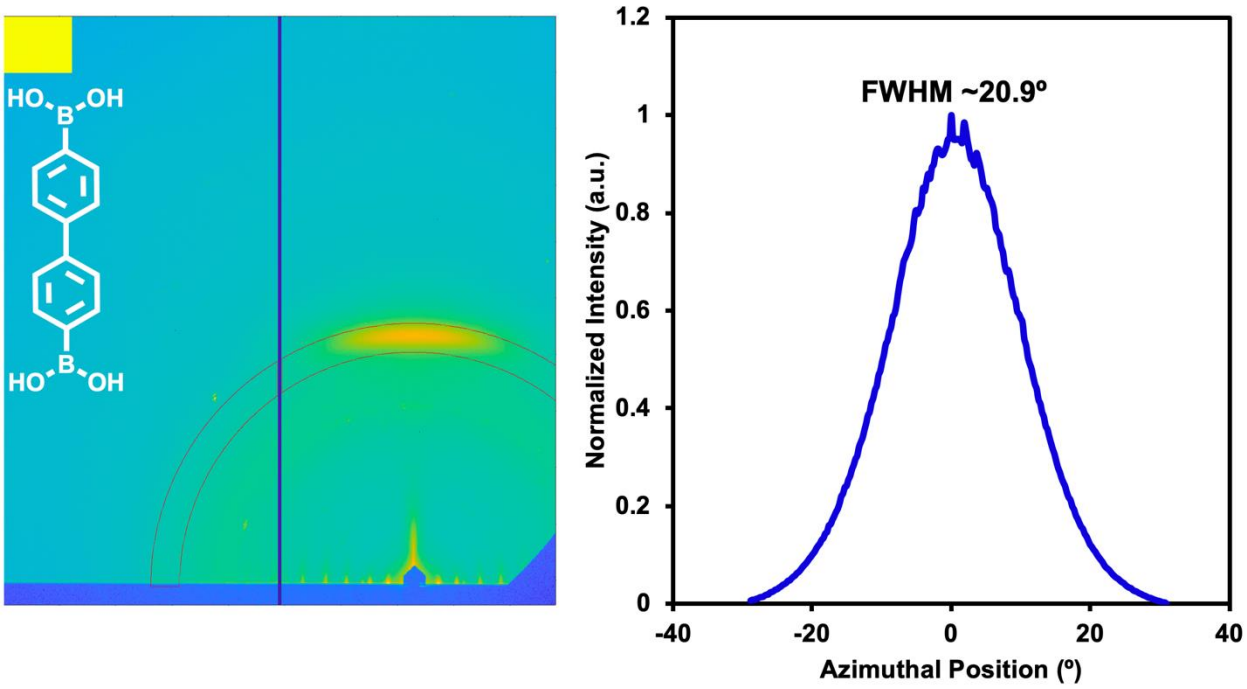

Figure 10.32. Estimate of the angular distribution using the azimuthal position of the (001) peak in the GIWAXS pattern. GIWAXS pattern for COF-10 with a mask (marked in red) selecting the (001) peak (left). Normalized, background subtracted line cut of the (001) peak with a measured FWHM of ~20.9° (right).

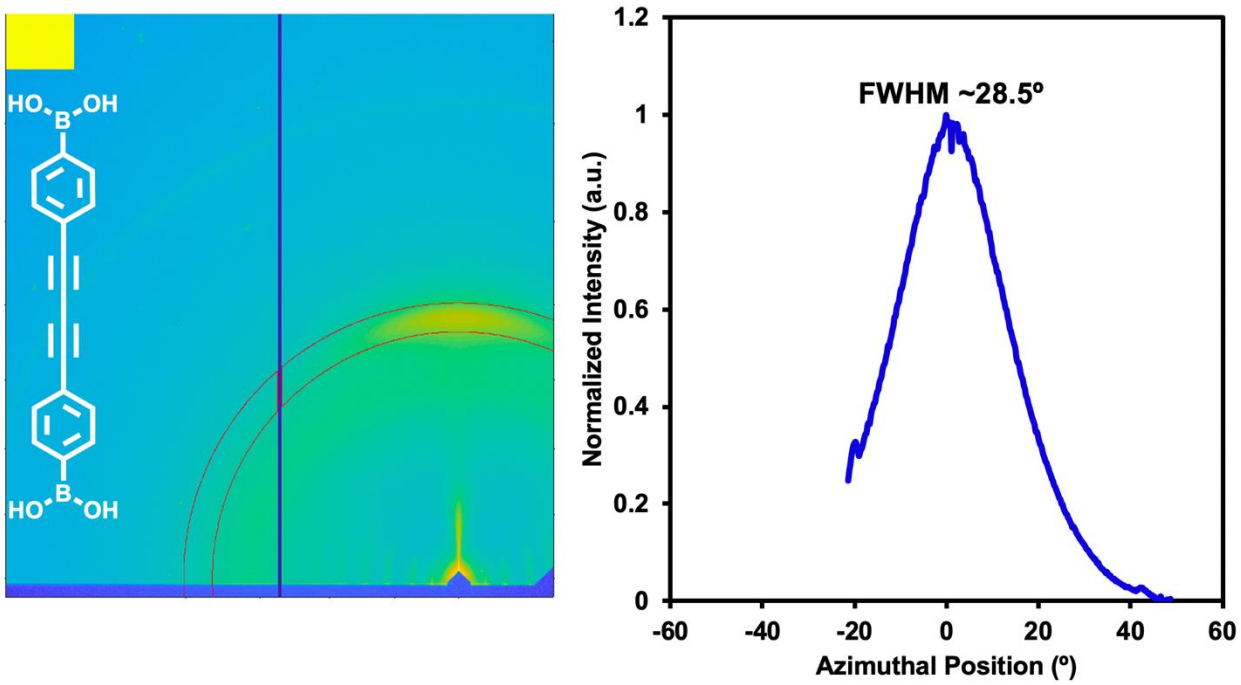

Figure 10.33. Estimate of the angular distribution using the azimuthal position of the (001) peak in the GIWAXS pattern. GIWAXS pattern for DPB-COF with a mask (marked in red) selecting the (001) peak (left). Normalized, background subtracted line cut of the (001) peak with a measured FWHM of ~28.5° (right).

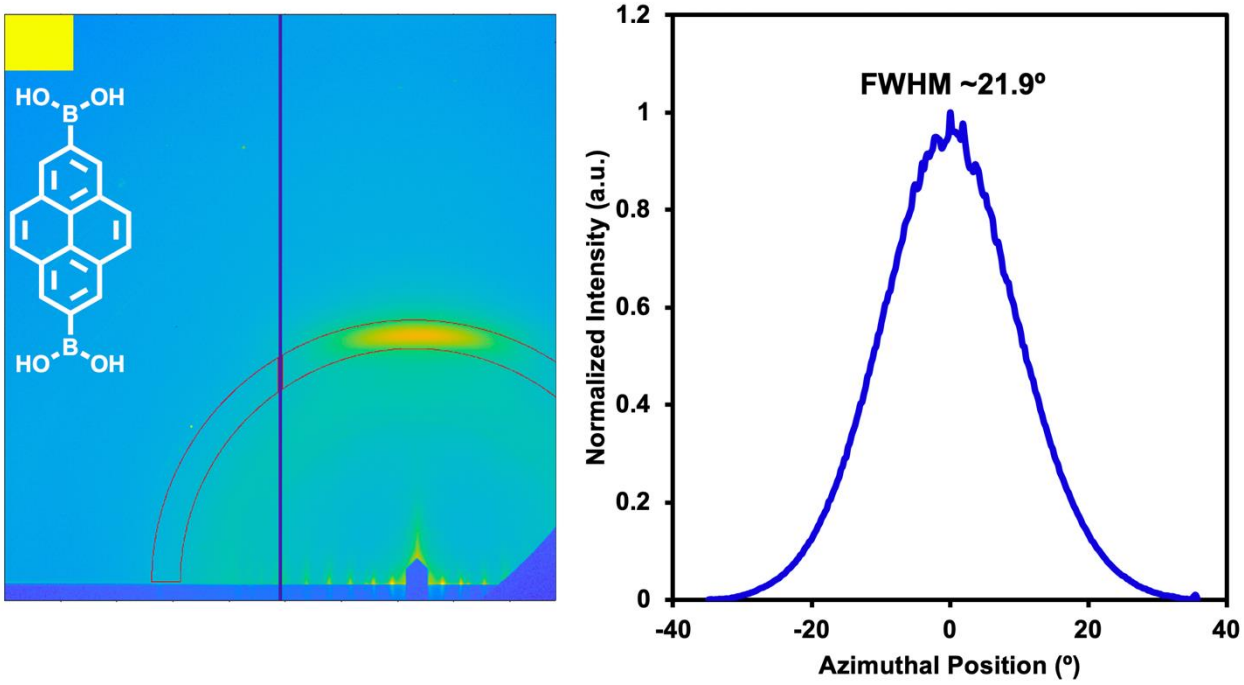

Figure 10.34. Estimate of the angular distribution using the azimuthal position of the (001) peak in the GIWAXS pattern. GIWAXS pattern for TP-COF with a mask (marked in red) selecting the (001) peak (left). Normalized, background subtracted line cut of the (001) peak with a measured FWHM of ~21.9° (right).

Chapter 11 : Controlled Molecular Doping Yields Semiconducting Paramagnetic Two-Dimensional Polymers

11.1 Abstract

Two-dimensional covalent organic frameworks (2D COFs) have attracted attention as structurally well-defined organic semiconductors. However, the bulk conductivities of intrinsic 2D COF semiconductors are low, which limits their application potential. Here we overcome this constraint by synthesizing two naphthalene diimide (NDI) containing 2D COFs, that upon exposure to molecular reductants exhibit a 108 enhancement of their electronic conductivities. Following molecular reduction with CoCp2, both 2D COFs retain their structural order and exhibit optical and electron-spin resonance spectroscopic features consistent with the presence of NDI-radical anions. Transient microwave spectroscopy shows that NDI-containing COFs are intrinsically semiconducting (2 eV > optical bandgaps) with long-lived charge-separated states. Density functional theory calculations reveal that the strongest electronic couplings exist in the out-of-plane (π-stacking) crystallographic directions, which suggests that electronic transport through NDI stacks is primarily responsible for bulk electronic conductivity. Maximum bulk electronic conductivities of both COFs are observed at substoichiometric doping with CoCp2. At this doping level, the conductivities of both COFs vary over two-orders-of-magnitude depending on the dopant identity. When doped with (RuCp*mes)2 the conductivities of both COFs approach 0.1 S cm-1, which approaches the highest values for n-type doped NDI-based 1D polymers. Overall, this study indicates that controlled molecular doping is a useful approach to access structurally well-defined, paramagnetic, organic semiconductors with high bulk electronic conductivities that may be of interest for many electronic or spintronic devices.

11.2 Introduction to Electrical Conductivity in 2D polymers

Two-dimensional covalent organic frameworks (2D COFs) are macromolecular sheets that combine permanent porosity with long-range order.[84] This periodicity enables the deterministic placement of chemical functionality in porous organic materials. This structural regularity, in principle, can lead to emergent electronic and magnetic phenomena that are of interest for electronic and spintronic devices.[41, 84, 740, 741] For example, computational and spectroscopic investigations have revealed that long-lived charge-separated states exist in some semiconducting 2D COFs.[84, 189, 190, 242, 281, 505, 741-749] However, the experimentally measured bulk conductivities of 2D COFs are low, which have historically limited fundamental investigations and the incorporation of 2D COFs into many devices. Low conductivities are likely attributable to poor conjugation across many COF linkages, large number of trap states in defect-prone materials, and the small number of intrinsic electronic carriers present in all 2D COFs explored thus far. Addressing the long-standing challenge of poor electronic conductivity in 2D polymers will yield porous, structurally precise, organic semiconductors, which are of interest for many devices including chemical sensors, optoelectronics,[750, 751] spin-valves,[752] and thermoelectrics.[753]

Electrical doping with molecular redox agents can be used to increase conductivity – at low doping levels by filling electronic trap states and at higher levels by contributing free charge carriers – via chemical oxidation (*p*-type doping) or reduction (*n*-type doping).[754-757] Despite the development of molecular doping techniques for organic molecules and linear polymers, doping of 2D COFs has not been extensively investigated.[755, 756, 758] Currently, all doping efforts in 2D COFs have relied on *p*-type doping using I_2 vapor,[505, 743, 748] which often results in poorly defined numbers of carriers injected into these materials.[759] Here, we explore controlled *n*-doping using molecular

reductants that are introduced in controlled stoichiometric amounts and undergo irreversible redox processes with semiconducting 2D COFs. Controlled *n*-doping enables a systematic investigation of the electronic and magnetic properties in 2D COFs at defined carrier densities for the first time.

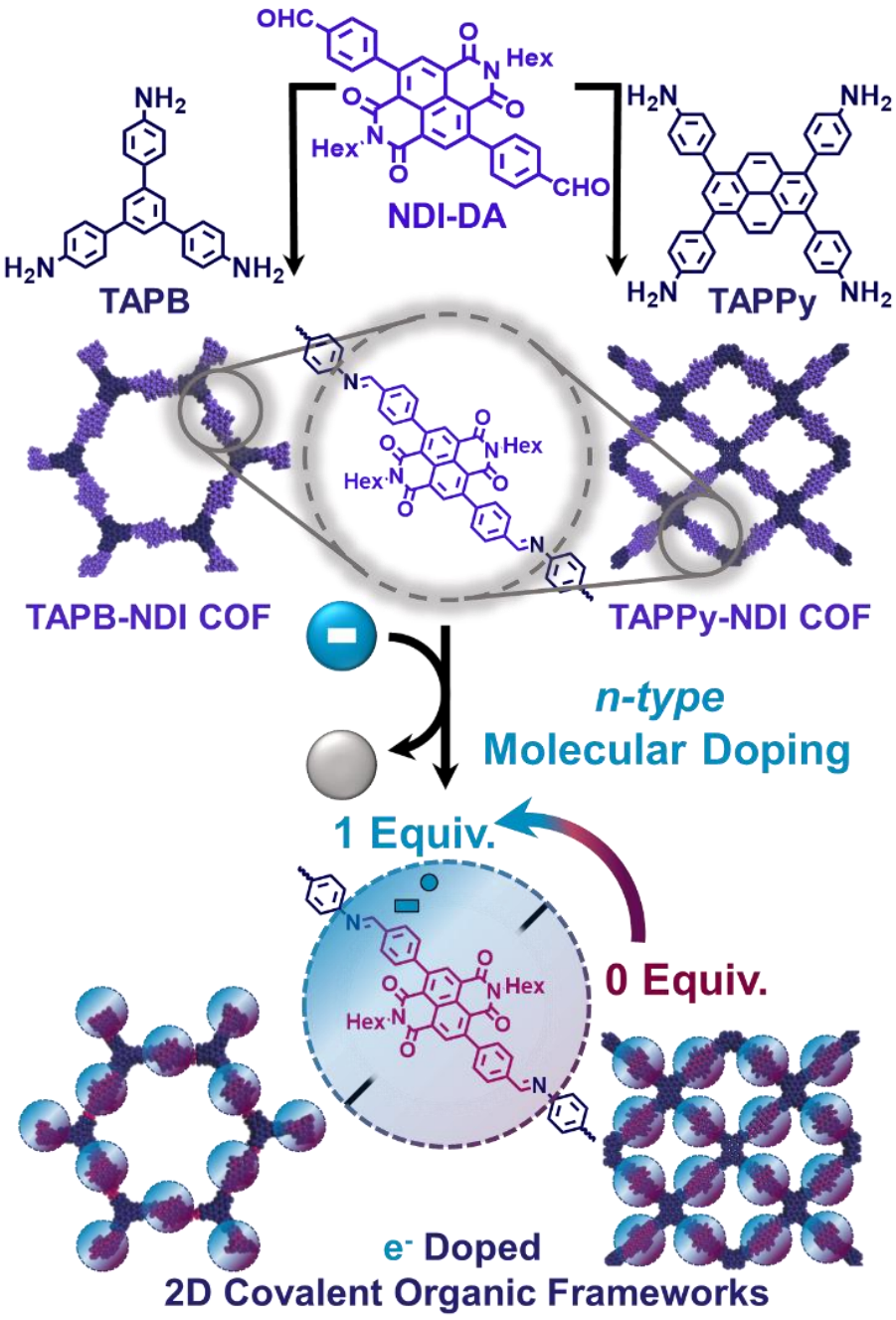

Figure 11.1 Synthesis of redox-active NDI-containing 2D COFs followed by controlled doping with defined stoichiometric amounts of molecular reductants (*n*-doping).

To accomplish our goal of exploring systematically doped COFs, we synthesize two semiconducting 2D COFs that contain naphthalene diimide (NDI) moieties and then *n*-dope them in defined stoichiometric amounts using various molecular reductants (**Figure 11.1**).[760] Both COFs retain their crystallinity after doping, thus yielding structurally defined, organic semiconductors with well-controlled numbers of charge carriers. Maximum electronic conductivities are observed at substoichiometric levels, consistent with populating each COF unit cell with one charge carrier. Computational and experimental studies suggest that this electronic conductivity is dominated by an inter-plane hopping mechanism.[761] These findings demonstrate that significant bulk conductivities can be observed in the absence of large in-plane conjugation, which has been the most prevalent design focus for electronically conductive COFs to-date. We also find that dopant identity has a significant impact on the measured electronic conductivities, which presents another design parameter to control the electronic properties of 2D COF semiconductors. Finally, the presence of singly reduced NDI-species, i.e. NDI radical anions ($NDI^{\bullet-}$), produces structurally regular 2D COF semiconductors with unpaired electronic spins. Taken together, controlled molecular doping is shown to be a powerful strategy to access paramagnetic 2D COF semiconductors, which are of interest for many organic electronic and spintronic devices.

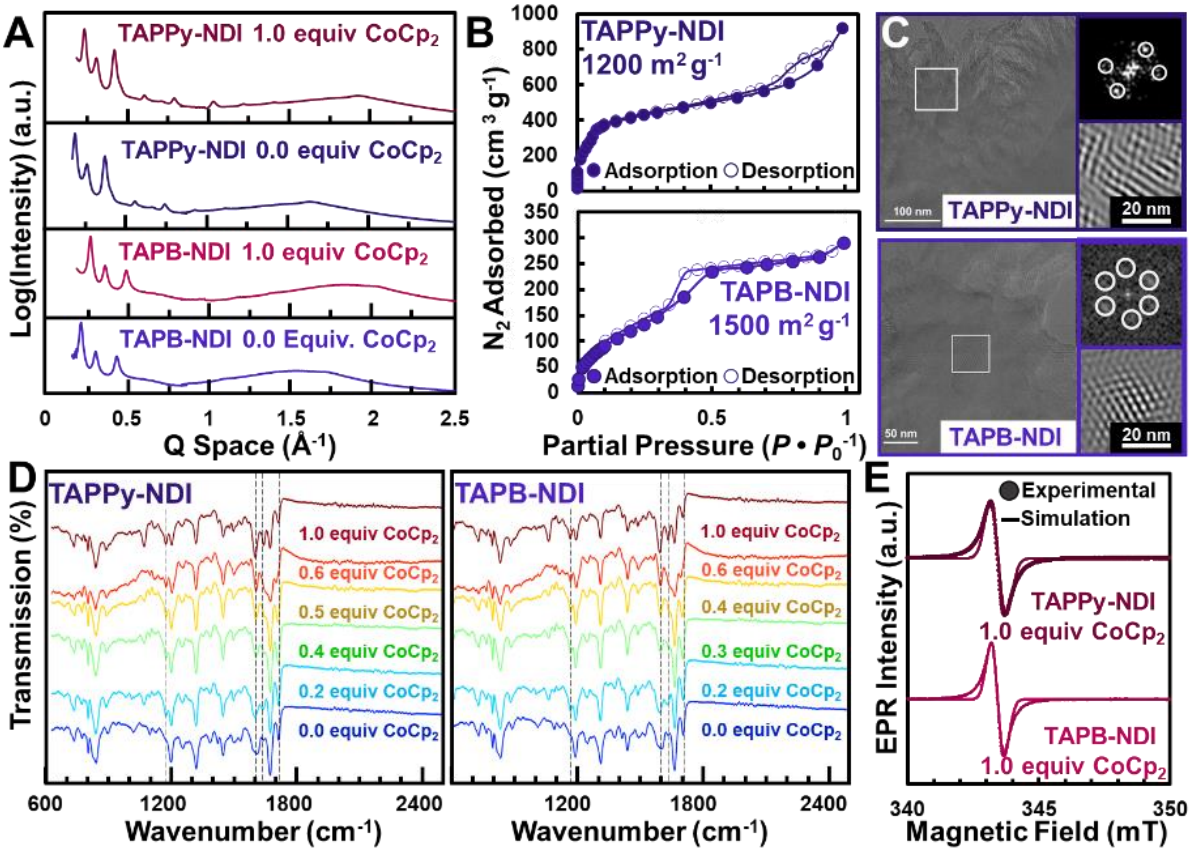

Figure 11.2 Chemical and structural characterization of doped and native COFs A. Synchrotron X-ray diffraction of both native and fully doped (1 equiv $CoCp_2$ per NDI) NDI-based COFs. **B.** N_2 sorption isotherms for TAPPy-NDI COF (top) and TAPB-NDI COF (bottom). **C.** High-resolution transmission electron micrograph of TAPPy-NDI COF (top) and TAPB-NDI COF (bottom) with a Fourier-transform of a particular region (white box, top right) and a band-pass filtered image of that region (bottom right). **D.** Fourier-transform infrared spectroscopy of COFs variably doped with $CoCp_2$. **E.** Continuous-wave electron paramagnetic resonance spectroscopy of doped NDI-based COFs.

11.3 Molecular Doping of 2D Polymers

Two NDI-based 2D COFs with different topologies were synthesized as high-quality polycrystalline powders (**Figure 11.1**).[762] NDI was chosen as an electron acceptor because its well-defined redox potentials are accessible by many molecular reductants and its extensive exploration in organic semiconductor devices.[760] The NDI was difunctionalized with formylbenzene units at its 3- and 7-positions (NDI-DA, **Figure 11.1**) to permit its integration into an imine-linked 2D COF. NDI-DA was then condensed with either 1,3,5-tris(4-aminophenyl)benzene (TAPB) or 1,3,6,8-tetrakis(4-aminophenyl)pyrene (TAPPy) under acetic acid-catalyzed conditions, which yielded polycrystalline powders of hexagonal TAPB-NDI COF and tetragonal TAPPy-NDI COF, respectively. Following polymerization and isolation, Fourier-transform infrared (FT-IR) spectroscopy revealed the emergence of the expected imine stretching frequency at 1670 cm^{-1} (**Figure 11.2D**). The amine (3000 cm^{-1}) and aldehyde (1710 cm^{-1}) FT-IR signals were reduced upon polymerization, which is consistent with the formation of imine bonds (**Figure 11.15 and Figure 11.16**).[763] Synchrotron X-ray diffraction (XRD) patterns of both TAPB-NDI and TAPPy-NDI COF powders have many sharp higher-order diffraction features (**Figure 11.2A**). The Pawley refined structures of the expected hexagonal TAPB-NDI COF lattice and tetragonal TAPPy-NDI COF lattice were found to match well with the respective experimental observations.[764] When finite grain size feature broadening was considered, the average in-plane crystallographic length of both COFs was determined to be approximately 100 nm, consistent with contemporary reports of high-quality 2D COF powders.[130] Both 2D polymers exhibited type IV N_2 isotherms with negligible hysteresis. Brunauer-Emmet-Teller surface area analysis performed on these isotherms revealed surface areas of 1500 $m^2\ g^{-1}$

and 1200 m^2 g^{-1} for TAPB-NDI COF and TAPPy-NDI COF, respectively (**Figure 11.2B**). From these N_2 isotherms, sharp pore size distributions centered at 2.9 nm and 3.4 nm were extracted for TAPB-NDI COF and TAPPy-NDI COF, both of which are consistent with their Pawley refined pore-structures. Transmission electron microscopy (TEM) images of both 2D COFs show that these powders are isolated as crystalline sheets with lateral dimensions of 100 nm (**Figure 11.2C**). Two-dimensional Fourier-transforms and band-pass filtered images of the TEM images reveal that hexagonally and tetragonally symmetric networks are isolated for TAPB-NDI COF and TAPPy-NDI COF, respectively (**Figure 11.2C insets**). These measurements unambiguously reveal that both TAPB-NDI COF and TAPPy-NDI COF are prepared as high-quality polycrystalline powders.

Cobaltocene ($CoCp_2$) was used to singly reduce the NDI units to introduce unpaired electrons into both networks. Both COFs were *n*-doped by immersing a known amount of polycrystalline powder into $CoCp_2$ THF solutions for at least 16 h under a N_2 atmosphere. The COFs were then recovered by filtration, rinsed with THF, and characterized, all under an inert atmosphere. Based on the redox potentials of NDI-DA, an equivalent imine-containing NDI compound, and the COF networks determined by cyclic voltammetry (CV), complete conversion of the NDI (-0.9 V vs. $FeCp_2$)[765] to its radical anion ($NDI^{\bullet-}$) by $CoCp_2$ (-1.3 V vs. $FeCp_2$)[766] is expected. After introducing controlled stoichiometric amounts of $CoCp_2$, we observe an immediate and pronounced darkening of both NDI-based COF powders. As both COF powders are doped with increasing amounts of $CoCp_2$, a feature at 1720 cm^{-1} is seen to disappear and a feature at 1620 cm^{-1} is seen to appear, both of which are consistent with reduction of NDI to $NDI^{\bullet-}$ (**Figure 11.2D**). Adding >1 equiv of $CoCp_2$ to either COF results in spectra indistinguishable from those of doped with 1.0 equiv of $CoCp_2$, which suggests that the reaction to generate $NDI^{\bullet-}$ occurs quantitatively and that $CoCp_2$ is an

insufficiently strong reductant to doubly reduce NDI to NDI^{2-} (-1.6 V vs. $FeCp_2$), which is consistent with CV measurements and the redox potentials of molecular NDIs.[760, 766] After doping both COFs with 1.0 equiv of $CoCp_2$, a pronounced continuous-wave electron paramagnetic resonance (CW-EPR) signal was observed. Simulation of the spectra with the Hamiltonian, $\hat{H} = g_{iso}\mu_B \boldsymbol{SH}$, yields values of 2.00 for g_{iso}, for both TAPPY-NDI and TAPB-NDI. The simulation matches well with the experimental data, and the g_{iso} tensors are consistent with NDI-centered radicals (**Figure 11.2E**). Taken together, these results reveal that NDIs within the COF framework can be singly reduced by exposure to controlled amounts of $CoCp_2$.

After complete reduction (1.0 equiv $CoCp_2$), the diffraction patterns of both 2D COFs change only slightly (**Figure 11.2A**), which indicates that the lattice is not substantially perturbed by the presence of embedded $NDI^{\bullet-}$ radical anions or the $CoCp_2^+$ counterions, which are presumably located in the channels and along the periphery of COF crystallites. However, minor shifts of the in-plane diffraction feature (0.1 $Å^{-1}$ < Q Space < 0.5 $Å^{-1}$) to lower scattering vector and the out-of-plane diffraction feature (1.5 $Å^{-1}$ < Q Space < 2.5 $Å^{-1}$) to higher scattering vector are observed. This suggests that to accommodate the charges, counterions, and changes in bond length produced upon doping, the COF lattice becomes slightly more planar with tighter interlayer packing. Taken together, these results reveal that NDI-based COFs with well-defined numbers of electronic carriers and paramagnetic centers can be produced through exposure to $CoCp_2$.

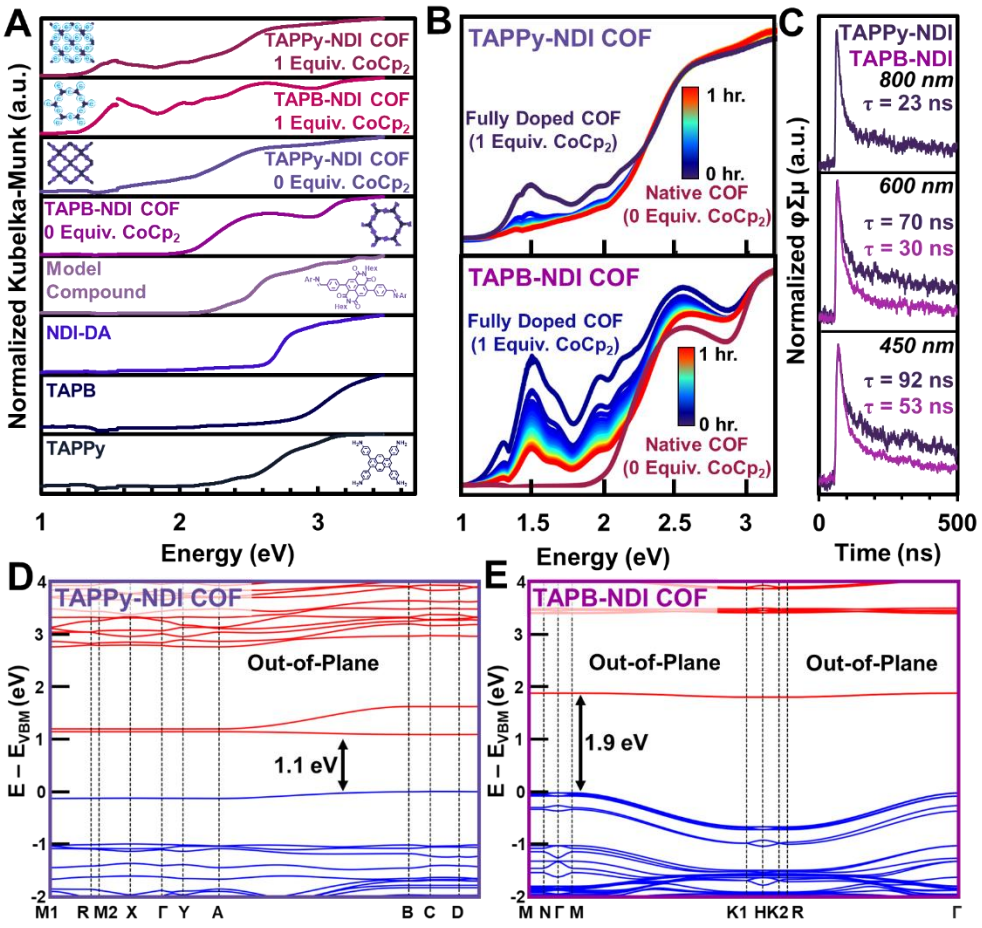

Figure 11.3 Optical characterization of monomers, model compounds, pristine COFs, and doped COFs. A. Diffuse-reflectance ultraviolet-visible-near-IR spectroscopy of monomers, model compounds, pristine NDI-containing COFs, and fully doped (1.0 equiv. $CoCp_2$ per NDI) NDI-containing COFs. **B.** Diffuse-reflectance ultraviolet-visible-near-IR spectroscopy during temporal evolution of fully doped NDI-containing COFs to entirely undoped on exposure to air. **C.** Time-resolved flash-photolysis microwave conductivity of both pristine NDI-containing COFs and their charge-carrier lifetimes, inset text shows the excitation wavelength and the amplitude-weighted lifetime, $\langle\tau\rangle$. **D.** Calculated density functional theory band structures for pristine multilayer TAPPy-NDI COF and **E.** TAPB-NDI COF.

11.4 Semiconducting 2D Polymers

Both NDI-based COFs were found to have low energy (< 2 eV) optical transitions in their native and doped state. Tauc analysis of diffuse-reflectance ultraviolet-visible (DR-UVVis) spectroscopy revealed that powders of the NDI-DA, TAPB, and TAPPy monomers all have optical transitions above 2.25 eV, which likely originate from isolated molecular transitions and not delocalized electronic bands (**Figure 11.3A**). By condensing NDI-DA with a 4-*tert*-butylaniline, we determined that imine formation subtly shifted the absorption edge of NDI-DA by 0.30 eV, consistent with both enhanced conjugation and charge-transfer behavior across an aromatic imine. However, COF polymerization produced pronounced electronic shifts (> 0.6 eV) to yield optical bandgaps of 1.8 eV and 1.3 eV for TAPB-NDI COF and TAPPy-NDI COF (**Figure 11.3A**). These transitions demonstrate that more electronically delocalized structures are produced during polymerization of NDIs into a layered 2D polymer. When fully doped (1.0 equiv. $CoCp_2$) the optical bandgap of TAPB-NDI COF and TAPPy-NDI COF are further red-shifted to 1.25 eV and 1.15 eV, respectively, both of which are consistent with the presence of $NDI^{\bullet-}$ subunits.[767,768] We also observe the emergence of higher order optical transitions between 1.5 eV and 2.5 eV, which further suggest the presence of $NDI^{\bullet-}$ subunits. When exposed to air, $NDI^{\bullet-}$ is known to oxidize back to its native state (NDI), which we observed over the course of one hour for $NDI^{\bullet-}$-containing frameworks using FT-IR spectroscopy. Therefore, continually collecting DR-UVVis spectra of a fully doped COF sample while the sample is exposed to air allows us to examine many intermediately doped states within a single experiment. As both COFs are exposed to air, we find that the optical absorption features associated with the $NDI^{\bullet-}$ state gradually decrease. Similarly,

we find that the FT-IR spectra and XRD patterns of doped NDI-COFs following oxidation are indistinguishable from those of the pristine material (**Figure 11.17**-**Figure 11.20**). These findings suggest that NDI-containing COFs have low energy optical transitions and can be chemically reduced and then re-oxidized without significant chemical or structural degradation.

Flash-photolysis time-resolved microwave conductivity (fp-TRMC) shows that both COFs exhibit semiconducting properties and long-lived free charge carriers. By exciting a sample with an optical laser (5 ns pulse) and then monitoring the transient microwave absorption at 9 GHz, the product of the mobility and number of free charge carriers, denoted as $\varphi\Sigma\mu$, and the lifetimes of these species can be extracted in a contactless manner. When excited at 2.76 eV (450 nm) and 2.07 eV (600 nm), TAPPy-NDI COF and TAPB-NDI COF both showed appreciable photoconductivity with $\varphi\Sigma\mu$ values of 5×10^{-5} $cm^2V^{-1}s^{-1}$. When excited at 1.55 eV (800 nm), only the TAPPy-NDI COF exhibited a measurable photoresponse ($\varphi\Sigma\mu$ of 5×10^{-5} $cm^2V^{-1}s^{-1}$) consistent with the optical bandgaps assessed by DR-UVVis. Analysis of the amplitude weighted average lifetimes of free charges, $<\tau>$, reveals that TAPPy-NDI COF has excited states with lifetimes double that of TAPB-NDI COF. In all fp-TRMC measurements, a short-time component reveals that a significant population of mobile charges are annihilated in less than 12 ns. This behavior is consistent with exciton-charge combination or trapping at crystalline defects. However, the difference of the long-time components (>280 ns) reveals that some population of free charges are significantly long-lived in both materials. Under all excitation wavelengths, the long-time component of TAPPy-NDI COF was approximately 100 ns longer than TAPB-NDI COF. This suggests that charge carriers are more mobile in the TAPPy-NDI COF than the TAPB-NDI COF.

11.5 Density Functional Theory Calculations

To gain insight into the electronic structure of the NDI-containing COFs, we performed band-structure calculations using density functional theory (DFT) calculations at the PBO3 level for the geometry optimized bulk crystals (**Table 11.4**). While we recognize that the materials themselves are likely to exhibit hopping-type transport between localized redox sites, rather than band-type transport, the calculation of such a band structure enables us to assess the extent of electronic coupling in different crystallographic directions. The calculations suggest bandgaps ($E_{CB} - E_{VB}$) of 1.1 eV and 1.9 eV for TAPPy-NDI COF and TAPB-NDI COF, respectively, both of which are qualitatively consistent with optical absorption and fp-TRMC measurements. In both cases the conduction band dispersions are modest (0.1 eV > for both COFs), indicating that there is weak electronic coupling between NDI units. We also note that direct transitions in both COF systems occur in the cross-plane direction, suggesting that the out-of-plane coupling is more relevant than in-plane coupling. To qualitatively investigate inter- vs. intra-layer effects on COF electronic structure, we also calculated the electronic band structure for monolayer TAPB-NDI COF and TAPPy-NDI COF. In the absence of multilayer stacking, flat conduction and valence bands with larger band gaps are observed, which indicates that the intra-layer coupling between NDI units is very weak. This finding suggests that obtaining regular interlayer stacking will be necessary to obtain the highest bulk electronic conductivity in these material. The combination of computational experiments and static- and transient-optical spectroscopies motivated us to interrogate the bulk electronic conductivity of *n*-doped COF semiconductors.

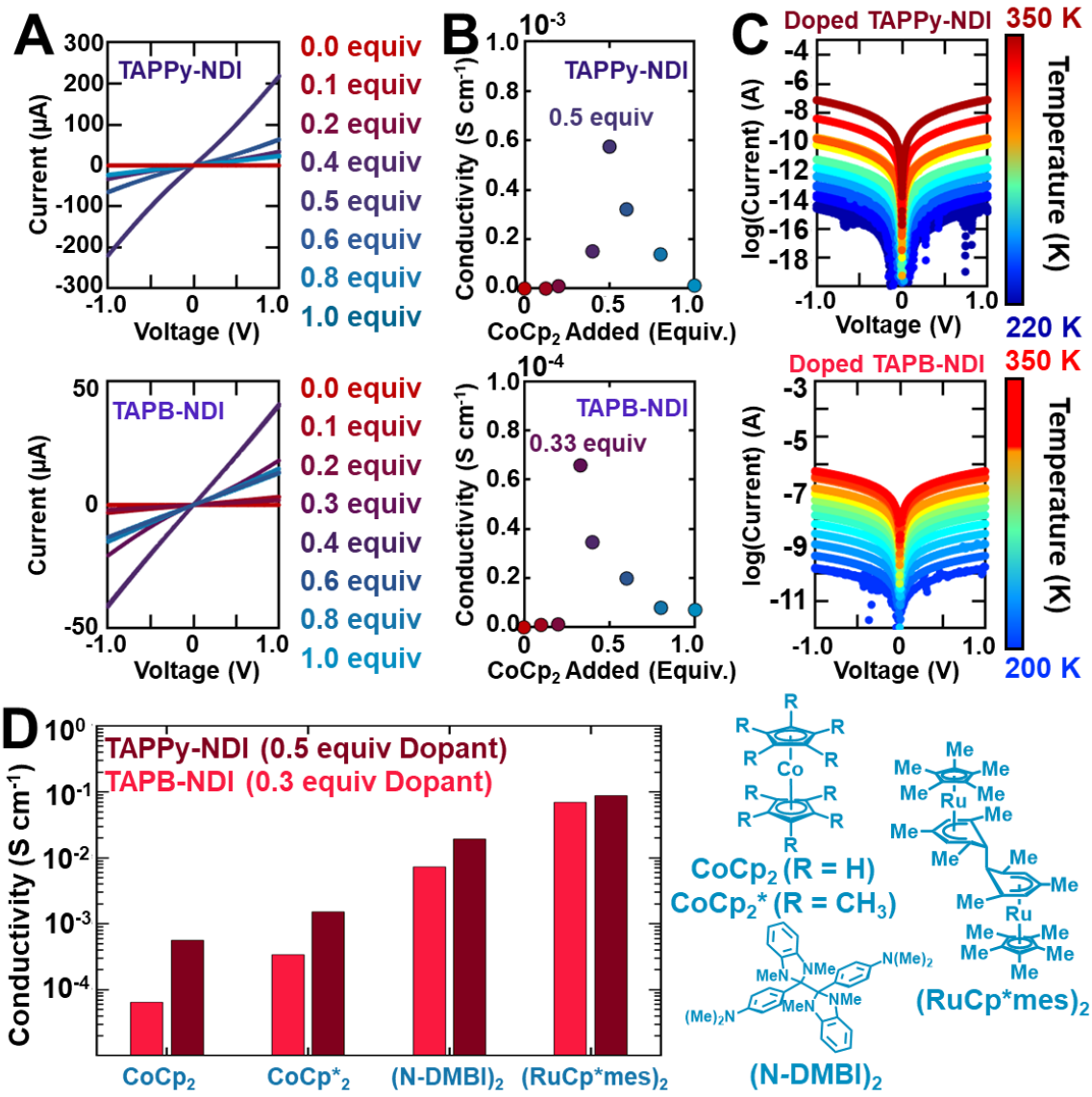

Figure 11.4 Conductivity measurements of variably doped NDI-containing 2D COFs A. Current-voltage measurements of variably doped TAPPy-NDI COF (top) and TAPB-NDI COF (bottom) and **B.** extracted conductivities from **A**. **C.** Temperature-dependent conductivity of TAPPy-NDI COF (0.5 equiv $CoCp_2$, top) and of TAPB-NDI COF (1.0 equiv $CoCp_2$, bottom). **D.** Extracted conductivities of NDI-based COFs doped with a variety of molecular *n*-dopants.

11.6 Bulk Conductivity of Doped Semiconducting 2D Polymers

Two-probe pressed pellet conductivity measurements reveal that both COFs become several orders of magnitude more conductive upon doping. To measure the bulk electronic conductivity of NDI-based COFs we gently press powders between two copper rods and measure the current responses as a function of applied bias, with several voltage sweeps in both polarization directions. In all cases, no hysteresis was observed, which led us to consider these pressed pellets as idealized Ohmic resistors. From this analysis, the conductivity of undoped TAPB-NDI COF and TAPPy-NDI COF are both less than 10^{-10} S cm^{-1}, which is expected of chemically pure intrinsic semiconductors with greater than 1 eV bandgaps at room temperature. The electronic conductivities gradually increased to a maximum of 6×10^{-4} *S* cm^{-1} for TAPPy-NDI COF and 7×10^{-5} *S* cm^{-1} for TAPB-NDI COF as electrons are injected into these materials. This order-of-magnitude difference in conductivity is consistent with fp-TRMC measurements that show charge-carriers are longer lived in TAPPy-NDI COF. In both cases maximum conductivity is observed at substoichiometric doping levels, with TAPB-NDI COF having an optimal doping of 0.33 equiv $CoCp_2$ and TAPPy-NDI COF having an optimal doping of 0.50 equiv $CoCp_2$. This highlights another advantage of controlled stoichiometric doping, for which optimal charge carrier concentrations can be reliably targeted.

Variable-temperature conductivity experiments reveal that electronic mobilities are positively correlated with thermal energy, suggestive of a hopping transport mechanism. As the temperature is decreased by 100 K, the electronic conductivity of both doped COFs decreases over 5 orders of magnitude with an Arrhenius relationship. These experiments indicate that charge-transport occurs primarily through a hopping mechanism, which is frequently observed when redox-active sites

within weakly dispersive bands are held in close proximity, such as the van der Waals contact in the macromolecular sheets studied here.[761] However, more mechanistic analysis is necessary to definitively determine the charge-transport pathways that lead to the enhanced electronic conductivities observed here. Together, these results demonstrate that electronically conductive *n*-type 2D COF semiconductors can be produced by controlled molecular doping.

Dopant identity substantially impacts the observed electronic conductivity of NDI-based COFs. In all cases, we examined other *n*-dopants at the optimal stoichiometric level identified using $CoCp_2$ (i.e. 0.5 equiv injected charge carrier for TAPPy-NDI and 0.33 equiv injected charge carrier for TAPB-NDI). The dopants examined were $CoCp^*_2$ (-1.9 V vs $FeCp_2$), $(N\text{-}DMBI)_2$ (-2.0 eV vs $FeCp_2$),[769] and $(RuCp^*mes)_2$ (-2.0 eV vs $FeCp_2$).[770] The latter two dopants contribute two electrons per dopant molecule, which was accounted for in the stoichiometry calculations. In all cases, the NDI-based COF powders changed colors dramatically after doping, which is consistent with our observations of $CoCp_2$ doped COFs and the redox potentials of the other dopants studied. After *n*-doping TAPPy-NDI COF is always more conductive than the TAPB-NDI. For both COFs, doping with $(RuCp^*mes)_2$ results in maximum conductivities of nearly 0.1 S cm^{-1}. Assuming that one electron per unit cell is contributed by the dopant, as discussed above and taking into account the lattice parameters from X-ray diffraction, these conductivities can also be used to estimate average charge-carrier mobilities of .01 $cm^2\ V^{-1}\ s^{-1}$ and 0.006 $cm^2\ V^{-1}\ s^{-1}$ for $(RuCp^*mes)_2$-doped TAPPy-NDI COF and TAPB-NDI, respectively (See supporting information). These values are higher than those reported for many NDI conjugated polymers and comparable to the best values reported for such materials.[771] However, they still fall short of the highest conductivity values reported for the most developed *p*- (> 200 S cm^{-1})[758, 772, 773] and *n*-doped organic materials (10 S cm^{-1}).[774]

Presumably, the bulk conductivities and mobilities reported here are also limited by the pressed pellet sample geometry, which contributes significant interfacial resistance. Therefore, it is conceivable that intrinsic intercrystallite transport may be significantly higher.

At this stage, it is challenging to precisely assign the origin of the maximal substoichiometric doping and the conductivity-dopant relationship that we have uncovered for the NDI-based 2D COFs studied here. Presumably a combination of structural rearrangements, counterion charge density, dielectric constant, and other subtle features all contribute to optimized doping conditions.[750] Despite these unknowns, the bulk conductivities reported here demonstrate that paramagnetic, semiconducting 2D COFs with appreciable electronic transport can be accessed by controlled molecular doping. More importantly, this approach enables the systematic investigation of paramagnetic and electronic behavior in crystalline organic systems at controlled carrier densities, which will be critical for the advancement of electronic 2D COF design. Controlled molecular doping is a promising advance, which will undoubtedly inspire future investigations of other chemically and topologically distinct redox-active 2D COFs and their associated electronic and spintronic devices.

11.7. Supplementary Information

A. Materials and Methods

Materials

All monomers, solvents, and catalysts were either purchased from commercial sources or prepared following literature reported protocols. All materials were used as received without further purification. Anhydrous THF was obtained from a solvent purification system (JC Myer System). Specifically, the following chemicals were obtained from the noted suppliers.

Napthalenedianhydride: Sigma-Aldrich, Item No. N818

1,3-Dibromo-5,5-dimethylhydantoin: Sigma-Aldrich, Item No. 157902

n-hexylamine: Sigma-Aldrich

Instrumentation

Nuclear Magnetic Resonance. ^{1}H NMR spectra were acquired on a 400 MHz Agilent DD MR-400 system or Bruker Avance III 500 MHz spectrometer and recorded at 25 °C. All chemical shifts were calibrated using residual solvent as internal reference ($CDCl_3$: 7.26 ppm for ^{1}H NMR. DMSO: 2.5 ppm for ^{1}H NMR).

Sonication. Sonication was performed with a Branson 3510 ultrasonic cleaner with a power output of 100W and a frequency of 42 kHz.

Supercritical CO_2 Drying. The supercritical drying procedure was performed in Tousimis Samdri795 critical point dryer. Prior to the supercritical drying process, all samples were placed in tea bags (ETS Drawstring Tea Filters, sold by English Tea Store, Amazon.com) and then soaked in absolute ethanol to keep the samples wet (typically 5-15 min). The drying chamber is first cooled ('cool' valve meter set to 0.40), and the tea bags containing the samples were then placed in it, and the chamber is filled with absolute ethanol and then sealed. The chamber was then filled with liquid CO2 ('fill' valve meter set to 0.40), and after 2 minutes, the samples were purged for 30 min ('purge-vent' valve meter set to 0.15, and 'purge timer' valve meter set to 6). The temperature was then raised to 40 °C resulting in a chamber pressure of around 1300 psi, which is well above the critical point of CO2. The chamber was held above the critical point for 30 min, after which the CO2 source was turned off, and the pressure was released over a period of 30 min ('bleed' valve meter set at 0.07). The samples were then transferred to vials and their final mass were weighed.

Nitrogen Porosimetry. N_2 sorption isotherms were collected on a Micromeritics ASAP 2420 Accelerated Surface Area and Porosity Analyzer. Typically, 20-50 mg samples were transferred to dried and tared analysis tubes equipped with filler rods and capped with a Transeal. The samples were heated to 40 °C at a rate of 1 °C min^{-1} and evacuated at 40 °C for 20 min, then heated to 100

°C at a rate of 1 °C min^{-1} heat, and evacuated at 100 °C until the outgas rate was ≤0.3 μmHg min^{-1} (holding the samples at 100 °C for 5 hr was found to be sufficient), at which point the tube was weighed again to determine the mass of the activated sample. The tube was then transferred to the analysis port of the instrument. UHP-grade (99.999% purity) N2 was used for all adsorption measurements. N_2 isotherms were generated by incremental exposure to nitrogen up to 760 mmHg (1 atm) in a liquid nitrogen (77 K) bath. Oil-free vacuum pumps and oil-free pressure regulators were used for all measurements. Brunauer-Emmett-Teller (BET) surface areas were calculated from the linear region of the N2 isotherm at 77 K within the pressure range P P_0^{-1} shown in BET plots below.

Ambient Atmosphere Fourier-transform Infrared Spectroscopy. Infrared spectra were recorded on a Nicolet iS10 FT-IR spectrometer equipped with a ZnSe ATR attachment. All spectra are recorded with a resolution of 4 cm^{-1}. All spectra are background subtracted and shown normalized to the same feature.

Inert Atmosphere Fourier-transform Infrared Spectroscopy. Infrared spectra were recorded on a Bruker Alpha FTIR spectrometer equipped with an attenuated total reflectance accessory and diamond anvil with a resolution of 4cm^{-1}. All spectra are background subtracted and shown normalized to the same feature.

Electron Paramagnetic Resonance Spectroscopy. Electron paramagnetic resonance samples were sealed within quartz tubes of appropriate size for an X-band resonator cavity under an atmosphere of nitrogen. Electron paramagnetic resonance spectra were then taken at 77 K at X-band frequencies (30 mm, 10 GHz). Data were fit using….

Diffuse Reflectance Ultraviolet-Visible Spectroscopy. Diffuse-reflectance ultraviolet-visible spectra were taken with a Varian Cary 5000 spectrophotometer using a Praying Mantis diffuse reflectance attachment. In all cases, samples were manually aligned to yield appropriate signal at low wavelengths. When samples were taken under inert atmosphere, a self-contained sample holder was loaded under inert atmosphere.

Flash-Photolysis Time-resolved Microwave Conductivity. Our fp-TRMC measurement system and methods has been described in detail elsewhere. Photoexcitation was performed using a Nd:YAG (Spectraphysics Quanta Ray SP Pro 230-30H) laser (355 nm) with a laser power of 9 W at 30 Hz to pump an optical parametric oscillator (Spectraphysics GWU PremiScan ULD/500) with variable output over the range of 410 – 2500 nm with 7 ns pulses. Samples were purged continuously with N_2 during these measurements. Blank quartz substrates were used to evaluate the lower limit of measurable yield-mobility products. For more information on sample preparation and measurement details, we direct readers to **Section J**.

Electrochemistry. Electrochemistry experiments were conducted on a Princeton Applied

Research VersaSTAT 3 potentiostat. All experiments were conducted using a standard three electrode cell configuration using a fritted three compartment cell with a modified glassy carbon as the working electrode, a 27 gauge Pt wire coiled as the counter electrode, and an Ag/AgCl reference electrode in CH_3CN.

Synchrotron X-ray Diffraction. Synchrotron powder X-ray diffraction was collected at either Sector 5 or 12 of the Advanced Photon Source, Argonne National Lab. Experiments were collected at either 17 keV or 13.3 keV. In all cases, the number of frames and exposure times was optimized for signal-to-noise. All frames were then summed and radially integrated to produce a linear PXRD pattern using proprietary software available at the APS. All experiments were conducted using a transmission geometry with samples placed in 2.0 mm OD borosilicate capillaries with 0.2 mm wall thicknesses purchased from Hilgenberg GmbH. When doped samples were measured, the samples were sealed within these capillaries under a nitrogen atmosphere. The sample-to-detector distance was adjusted to measure across relevant detection ranges of q. Scattering intensity is reported as a function of the modulus of the scattering vector Q, related to the scattering angle 2θ by the equation $Q = (4\pi/\lambda) \sin \theta$, where λ is the x-ray wavelength (**Equation 1**).

$$Q = \frac{4\pi}{\lambda}\sin(\theta) \qquad (1)$$

Simulated X-ray Diffraction. Simulations of 2D COF X-ray scattering profiles were carried out

in MaterialsStudio (ver.5.0). First, the unit cell was constructed piecewise in a primitive P6 unit cell with the *a=b* lattice parameter set to be approximately the distance between two COF vertices based on approximate molecular bond lengths. The *c* parameter was set to be 3.5 Å, which is the interlayer spacing of graphene. We then used a Forcite geometry optimization routine with a universal forcefield to optimize the unit cell size with convergence tolerances of Energy = 10^{-3} kcal mol^{-1} and Force = 0.5 kcal mol^{-1} $Å^{-1}$.

Diffraction simulation and Pawley refinement were carried out using the Reflex software package. COF models and their simulated patterns were Pawley refined to experimental patterns iteratively until the RWP value converges. The pseudo-Voigt profile function was used for whole profile fitting. The final RWP and RP values were calculated to be less than 5% in all cases. Simulated XRD patterns were calculated from the refined unit cell and compared with the experimentally observed patterns.

Connolly Surface Area Calculation. After a refined structure was simulated via diffraction modeling as described above, we went on to calculate the theoretical surface area for our structures. This was done using a Connolly method (sometimes known as a solvent-excluded surface method or molecular surface method). This method can be described as rolling a ball along a molecular surface to assess its accessible surface. More precise descriptions and details of this method can be found in the initial report of this approach. 3,4 We performed this calculation using the Crystal Surfaces and Volumes module of MaterialsStudio using the parameters for molecular nitrogen as

the adsorbate. This yielded a surface area per unit cell, which could then be converted to the surface area per gram value which is reported in the manuscript.

Transmission Electron Microscopy. TEM was performed using a JEOL (JEOL USA, Inc., Peabody, MA) ARM200CF Aberration-Corrected STEM/TEM operated at 200 keV equipped with a Gatan (Gatan, Inc., Pleasanton, CA) K2 "direct electron" detector (FEG Emission: 15 μA, spot size 5, 150 μm CL aperture). The ARM200CF was aligned for low-dose imaging, measuring the dose rate on the K2 detector through vacuum (no grid inserted). The dose rate was measured to be 6.8 e^{-} $Å^{-2}$ s^{-1} (3710 x 3838 pixels) for TAPPy-NDI and 10.9 e^{-} $Å^{-2}$ s^{-1} (3710 x 3838 pixels) for TAPB-NDI with image exposure times of 0.98 s (6.7 and 10.7 e^{-} $Å^{-2}$ cumulative dose per image, respectively). All image acquisition was done using the Gatan Microscopy Suite (GMS), Digital Micrograph (Gatan, Inc., Pleasanton, CA).

Variable-Doping Pressed Pellet Electronic Conductivity. Doping protocols are explained extensively in Section D. Briefly, polycrystalline COF powders were exposed to variable stoichiometric amounts of molecular reductant in a THF solution for a minimum of 16 hrs. These powders were then isolated by filtration. Then, we loaded these powders into a hollowed glass rod. The powders were finger tightened between the rods and the two copper bars were then equipped to a potentiostat. We ran several potential sweeps in both bias directions to check for hysteretic behavior. In all cases, we observed no hysteresis, which led us to consider these materials as idealized Ohmic resistors. At the end of the experiment, we measured the length of the pressed

pellet using dial calipers by measuring the difference of the full assembly with and without the powders. This distance, with the obtained IV curves, was used to evaluate the Ohmic resistance.

Variable-Temperature Pressed Pellet Electronic Conductivity. Variable-temperature conductivity measurements were obtained by loading powder samples pressed between two copper electrodes into a cryostat. Starting at high temperatures we monitored the I-V response of these pressed pellets. Then, we repeated this behavior as we iteratively dropped the sample temperature. In all cases, we waited for the temperature to stabilize.

B. Molecular Syntheses

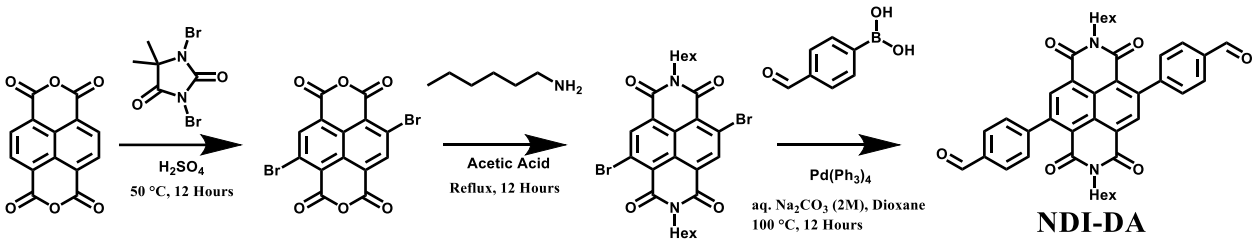

Figure 11.5. Total synthesis of NDI-DA.

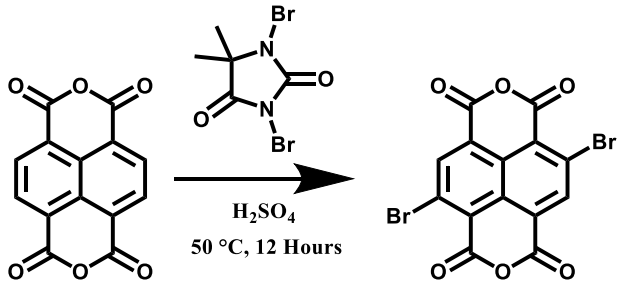

Figure 11.6. Synthesis of 3,7-dibromonapthalenedianhydride

This synthesis was adapted from a previous report.[762] In single-necked round bottom flask (500 mL), NDA (10 g, 37.3 mmol, 1.0 equiv.) was slurried in concentrated sulfuric acid (150 mL) at ambient temperature. This mixture was stirred at room temperature for 5 min to obtain a solution. 1,3-Dibromo-5,5-dimethylhydantoin (15 g, 52.6 mmol, 1.4 equiv.) was added in four portions over a period of 1 hr at room temperature. The resulting brown solution was then stirred at 50 °C for 10 hr. The mixture was then poured into crushed ice (250 g), which resulted in a precipitated solid. The precipitated solid was filtered, washed with water (200 mL) then with methanol (200 mL), and finally dried under vacuum to afford crude product, which was further purified by crystallization from DMF. During crystallization, the ring-opened carboxylic acid containing side

products preferentially crystallized, leaving the supernatant with pure 3,7-dibromonapthalenediimide, which was isolation through precipitation by addition of methanol. The product was then obtained as a yellow solid by filtration and dried under vacuum (11.05 g, 69% yield). Characterization of this molecule was consistent with a previous report.[762]

^{1}H NMR (400 MHz, DMSO-d_6): H=8.78 ppm (s, 2H)

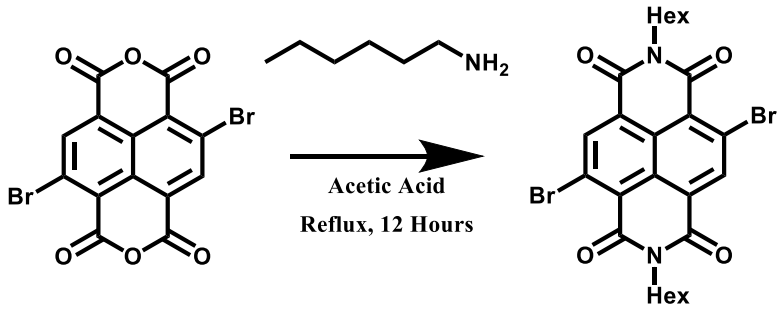

Figure 11.7. Synthesis of *N*-hexyl 3,7-di(bromo)napthalenediimide

This synthesis was adapted from a previous report.[762] 3,7-dibromonapthalenedianhydride (5 g, 11.7 mmol, 1.0 equiv.) was added to a flame-dried 500 mL round bottom flask filled with glacial acetic acid (350 mL) and *n*-hexylamine (5.9 g, 7.7 mL, 58.5 mmol, 5 equiv.). This reaction mixture was refluxed for 30 min under a constant stream of dry N_2, allowed to cool for 16 hr, and then was poured into methanol (500 mL). The precipitate of this reaction was collected by filtration, washed extensively with methanol, and dried under vacuum. The product was then isolated from this crude solid by dissolving the product in $CHCl_3$, stirring this mixture, and then adding methanol dropwise to this mixture until the desired product begins to precipitate. This yellow solid was then collected by filtration and identified as pure *N*-hexyl 3,7-di(bromo)napthalenediimide (9.6 g, 82% yield). Characterization of this molecule was consistent with a previous report.[762]

^{1}H NMR (400 MHz, DMSO-d_6): H=8.78 ppm (s, 2H)

*Note: We observed that small amounts of water led to partial ring opening of our anhydride under these reaction conditions. Removing this side-product was found to be challenging and required separation by column chromatography (silica, 3:2 dichloromethane/hexanes). Drying procedures

(flame drying glassware and operating under a dry N_2 stream) were found to limit the formation of this side-product substantially.

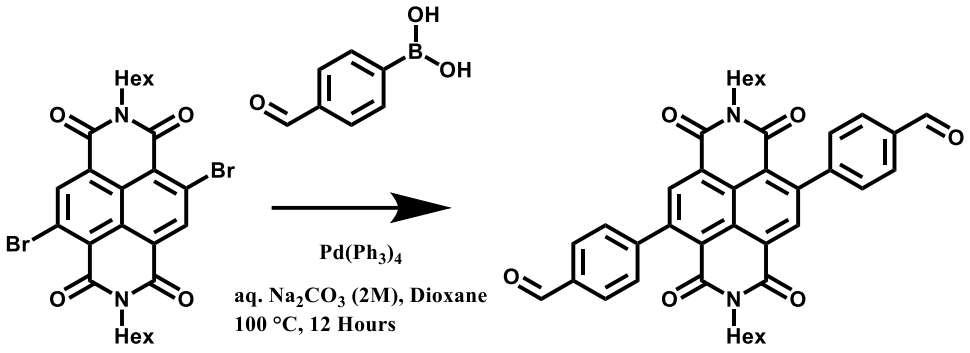

Figure 11.8. Synthesis of *N*-hexyl 3,7-di(formylbenzene)napthalenediimide

This synthesis was adapted from a previous report.[762] *N*-hexyl 3,7-di(bromo)napthalenediimide (4g, 7.75 mmol) was combined with 1-formyl, 4-boronic acid benzene (3g, 20.2 mmol) in 100 mL of dioxane and 33 mL of H_2O and 7g Na_2CO_3. This mixture was degassed for 30 min and 150 mg PdPh34 was then refluxed for three days. The solvent was removed, the solid collected, and was then subjected to a column (50%-0% Hexanes, 50%-100% DCM) and flushed with DCM until the second band came off the column (orange). The third band was collected by flushing with MeOH. Characterization of this molecule was consistent with a previous report.[762]

^{1}H NMR (400 MHz, DMSO-d_6): H=8.78 ppm (s, 2H)

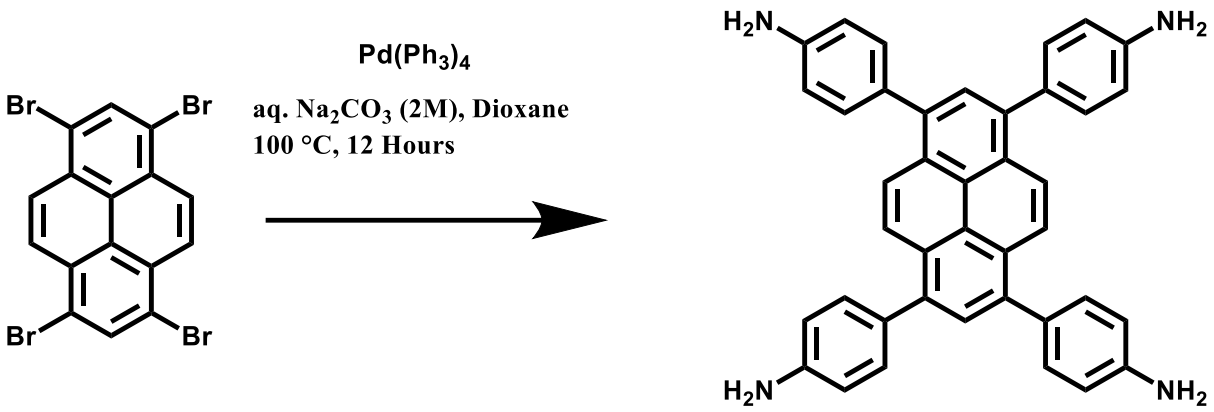

Figure 11.9. Synthesis of 1,3,6,8-tetra(aminophenyl)pyrene

This synthesis was adapted from a previous report.[775]

A reaction mixture containing 1,3,6,8-tetrabromopyrene (1482 mg, 2.86 mmol, 1.0 eq.), 4-aminophenylboronic acid pinacol ester (3010 mg, 13.7 mmol, 4.8 eq.), K_2CO_3 (2175 mg, 15.7 mmol, 5.5 eq.) and $Pd(PPh_3)_4$ (330 mg, 0.29 mmol, 10 mol%) in 32 mL 1,4-dioxane and 8 mL H2O was heated to reflux (115 °C) for 3 days. After cooling to room temperature, H2O was added. The resulting precipitate was collected via filtration and was washed with H2O and MeOH. Recrystallization from 1,4-dioxane, followed by drying under high vacuum furnished the title compound, co-crystallized with approximately 1.5 dioxane molecules per formula unit, as a bright yellow powder (1792 mg, 2.56 mmol, 90%). Characterization was consistent with a previous report.[775]

^{1}H NMR (400 MHz, DMSO-d6): 8.13 (s, 4 H), 7.79 (s, 2 H), 7.34 (d, J = 8.4 Hz, 8 H), 6.77 (d, J = 8.5 Hz, 8 H), 5.30 (s, 8 H), 3.56 (s, 12 H, dioxane).

^{13}C NMR (100 MHz, DMSO-d6): 148.2, 137.1, 131.0, 129.0, 127.6, 126.7, 126.1, 124.4, 113.9, 66.3 (dioxane).

C. Dopant Syntheses

Dopant Synthesis. $(N\text{-}DMBI)_2$ and $(RuCp^*mes)_2$ were synthesized as recently described.[769]

D. Framework Syntheses

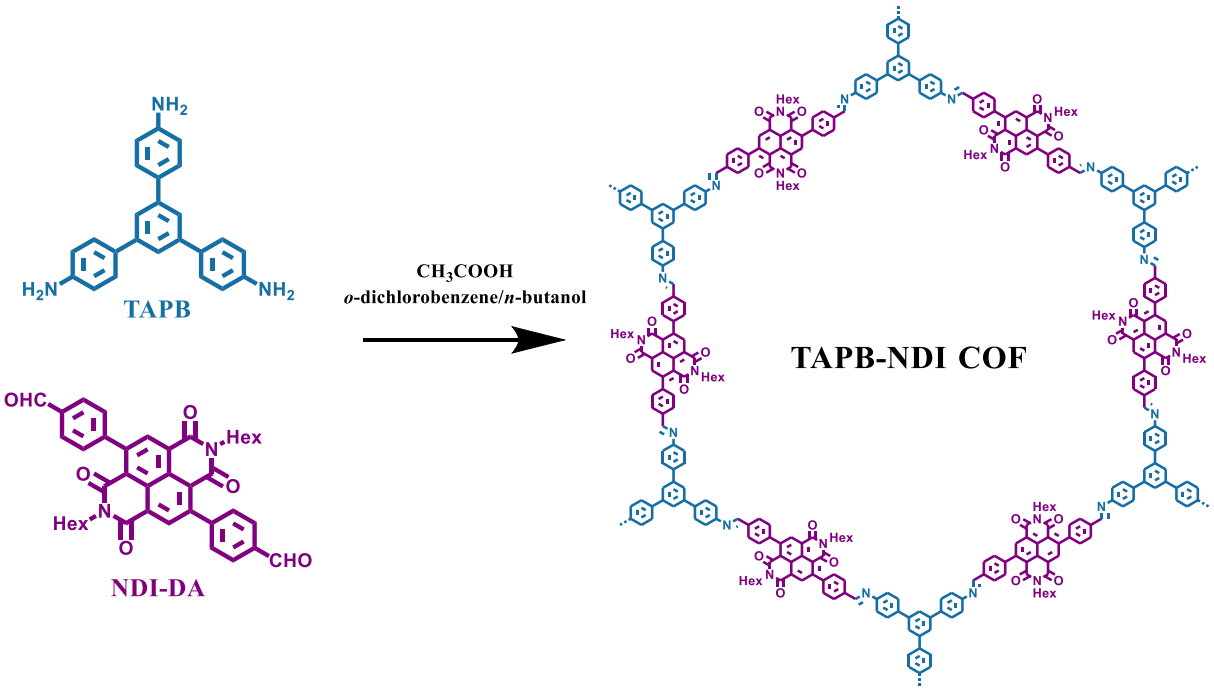

Figure 11.10. Synthesis of TAPB-NDI COF

TAPB-NDI COF powders were synthesized under solvothermal conditions. To produce these materials, (4-aminophenyl)benzene (TAPB, 5 mmol, 1 equiv.) and naphthalene diimide dialdehyde (NDI-DA,.5 mmol, 1.5 equiv.) were dissolved in a mixture of 1:1 *o*-dichlorobenzene:*n*-butanol by sonicating for ten min. Then, a 9M CH_3COOH (acetic acid, 10 vol%) was added to the mixture. At this point, the mixture was sealed and heated to 90°C in a scintillation vial on an aluminum pie block. These samples were allowed to heat for three days, at which point they were filtered and rinsed extensively with MeOH (100 mL). Finally, these samples were subjected to $scCO_2$ drying.

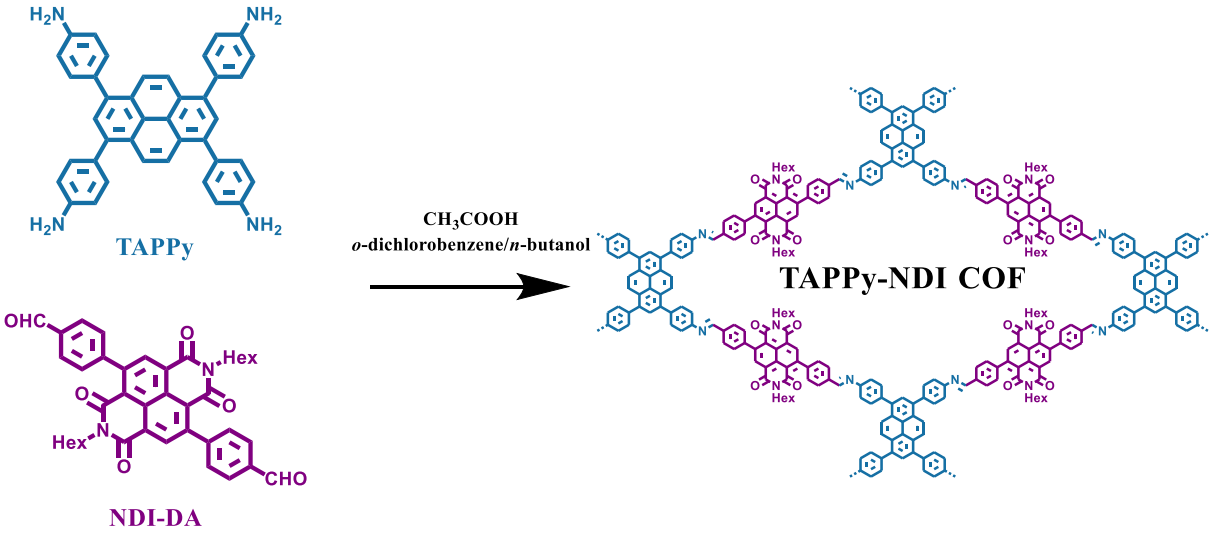

Figure 11.11. Synthesis of TAPPy-NDI COF

TAPPy-NDI COF powders were synthesized under solvothermal conditions. To produce these materials, tetra(4-aminophenyl)pyrene (TAPPy, 5 mmol, 1 equiv.) and naphthalene diimide dialdehyde (NDI-DA, 7.5 mmol, 1.5 equiv.) were dissolved in a mixture of 1:1 *o*-dichlorobenzene:*n*-butanol by sonicating for ten min. Then, a 9M CH_3COOH (acetic acid, 10 vol%) was added to the mixture. At this point, the mixture was sealed and heated to 90°C in a scintillation vial on an aluminum pie block. These samples were allowed to heat for three days, at which point they were filtered and rinsed extensively with MeOH (100 mL). Finally, these samples were subjected to $scCO_2$ drying.

E. Molecular Doping Protocols

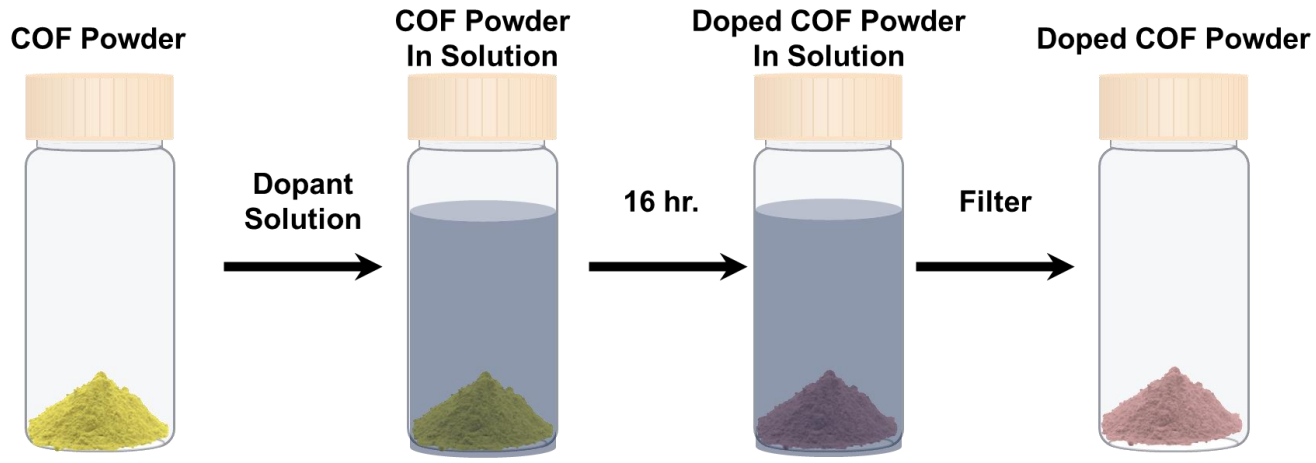

Figure 11.12. Illustration of the general doping protocol.

General Procedure: COF powders (typically 25-50 mg) were preweighed into prelabeled vials under a N_2 atmosphere. Then, separately, a molecular dopant solution was prepared at a known concentration in anhydrous solvent (See Table below for representative calculation details). Then, a volume of this molecular dopant solution was added to the COF powders in amounts to target the desired doping ratio. Nearly immediately the undoped COF powders were found to transform from a light yellow orange to a dark burgundy. COF powders then sat undisturbed within the dopant solution for at least 16 hr. These solutions were then filtered and rinsed extensively (50 mL) with clean solvent (the same as was used to dissolve molecular dopants). After doping, the COF powders were found to be a dark burgundy and were noticeably prone to static charging.

Table 11.1. Representative calculations for doping of NDI-Based COFs.

TAPB-NDI Mass/Redox Center	**868**	**g mol^{-1}**
TAPPy-NDI Mass/Redox Center	**917**	**g mol^{-1}**
Molecular Weight $CoCp_2$	**189**	**g mol^{-1}**
Stock Solution Volume	**100**	**mL**
Mass of $CoCp_2$	**50**	**mg**
TAPB-NDI COF Per Sample	50	mg
Moles Redox Cite Per Sample	0.0576	mmol

TAPB-NDI Doping	Equiv.	$CoCp_2$ (mmol)	$CoCp_2$ (mg)	$CoCp_2$ (mL)
0.0 Equiv	0	0.00	0.0	**0.0**
0.2 Equiv	0.2	0.01	2.2	**4.4**
0.33 Equiv	0.33	0.02	3.6	**7.2**
0.4 Equiv	0.4	0.02	4.4	**8.7**
0.6 Equiv	0.6	0.03	6.5	**13.1**
0.8 Equiv	0.8	0.05	8.7	**17.4**
1.0 Equiv	1	0.06	10.9	**21.8**

TAPPy-NDI COF Per Sample	50	mg
Moles Redox Cite Per Sample	0.0545	mmol

TAPPy-NDI Doping	Equiv.	$CoCp_2$ (mmol)	$CoCp_2$ (mg)	$CoCp_2$ (mL)
0.0 Equiv	0	0.00	0.0	**0.0**
0.2 Equiv	0.2	0.01	2.1	**4.1**
0.4 Equiv	0.4	0.02	4.1	**8.2**
0.5 Equiv	0.5	0.03	5.2	**10.3**
0.6 Equiv	0.6	0.03	6.2	**12.4**
0.8 Equiv	0.8	0.04	8.2	**16.5**
1.0 Equiv	1	0.05	10.3	**20.6**

F. Optical Images

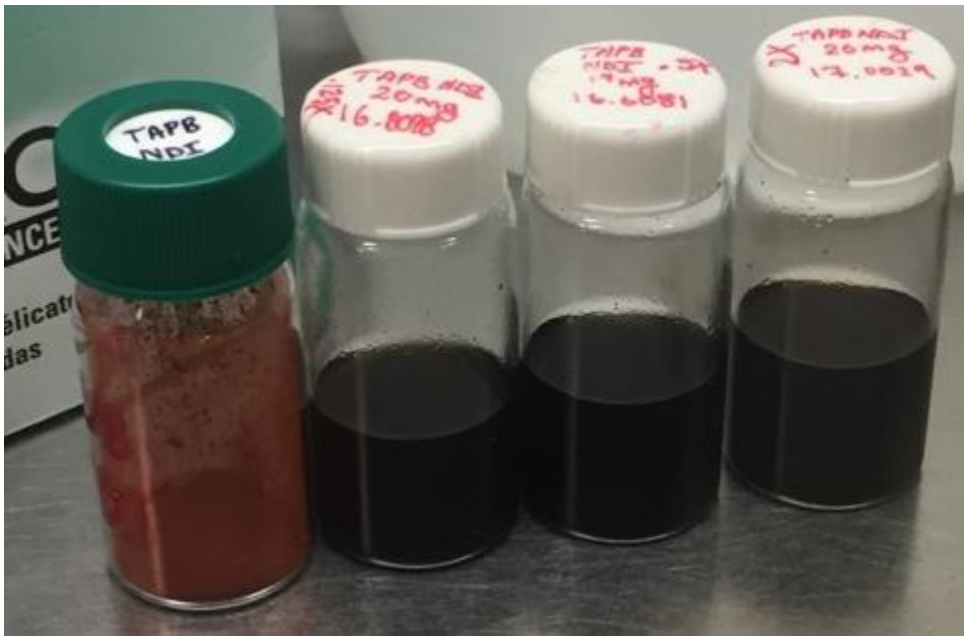

Figure 11.13. Representative photograph following molecular reduction of NDI-based COFs. COF powders start orange-red but immediately turn dark upon exposure to any amount of $CoCp_2$.

Figure 11.14. Representative photograph of molecular reduction of NDI-based COFs. Dark COF powders have settled to the bottom of the vial and the supernatant is now yellow, consistent with the oxidation of $CoCp_2$ to $CoCp_2^+$.

G. Fourier-Transform Infrared Spectroscopy

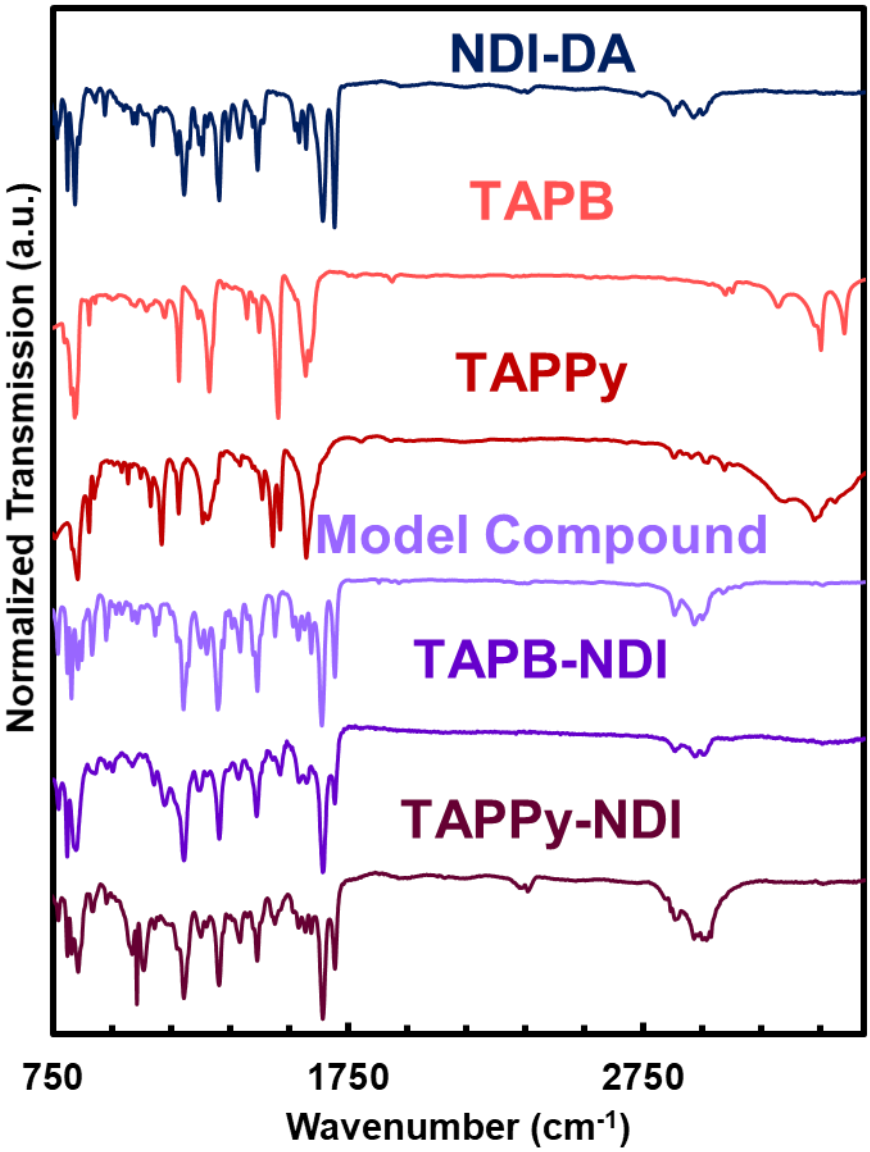

Figure 11.15. Comparison of FT-IR spectra of monomers, an imine model compound, and the two native COFs.

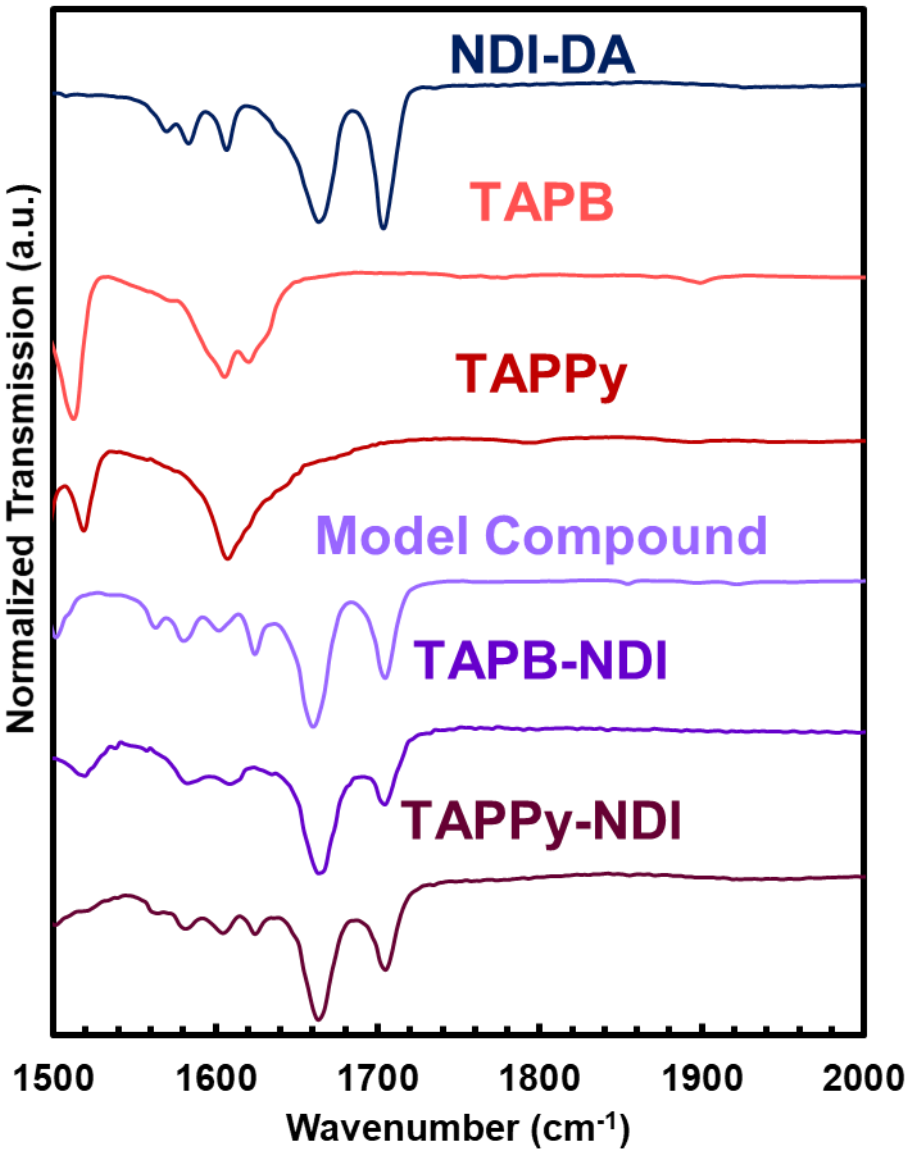

Figure 11.16. Comparison of FT-IR spectra of monomers, an imine model compound, and the two native COFs with a narrow field of view.

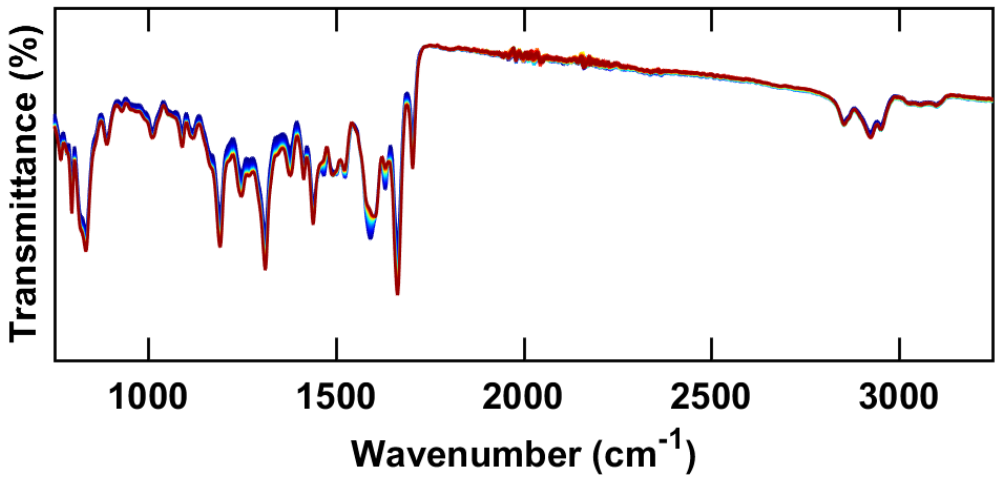

Figure 11.17. FT-IR spectroscopy during temporal evolution of fully doped TAPPy-NDI COF upon exposure to air over the course of one hour. Isobestic points are suggested of a complete transform from one species to another.

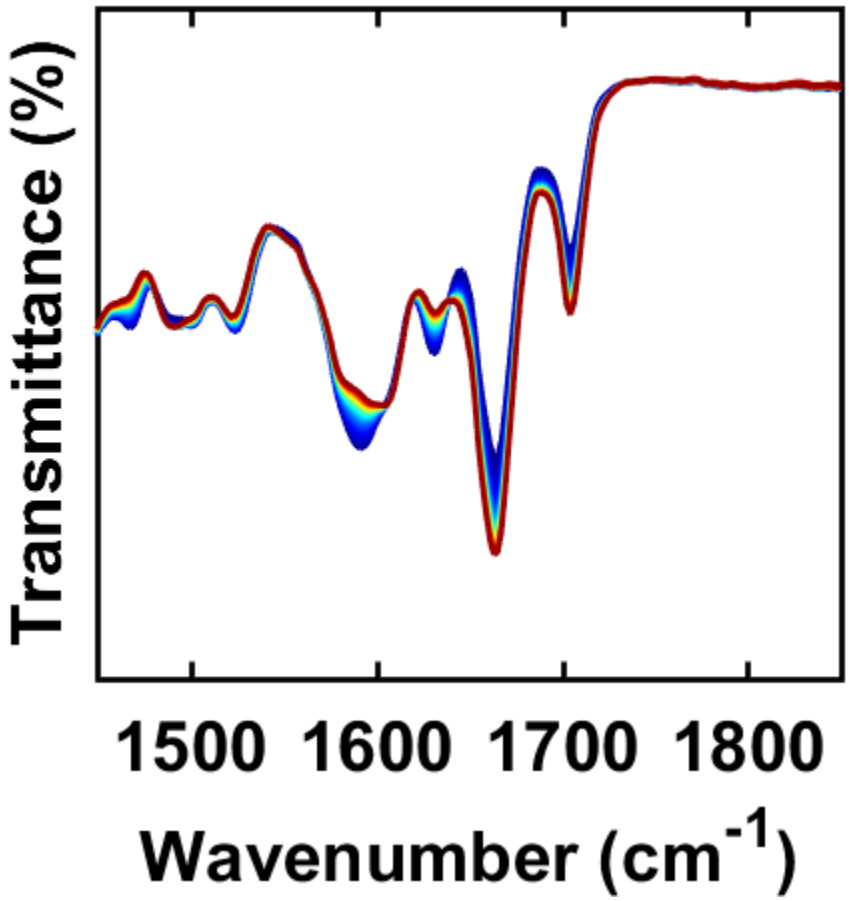

Figure 11.18. Narrrow field of view FT-IR spectroscopy during temporal evolution of fully doped TAPPy-NDI COF upon exposure to air over the course of one hour. Isobestic points are suggested of a complete transform from one species to another.

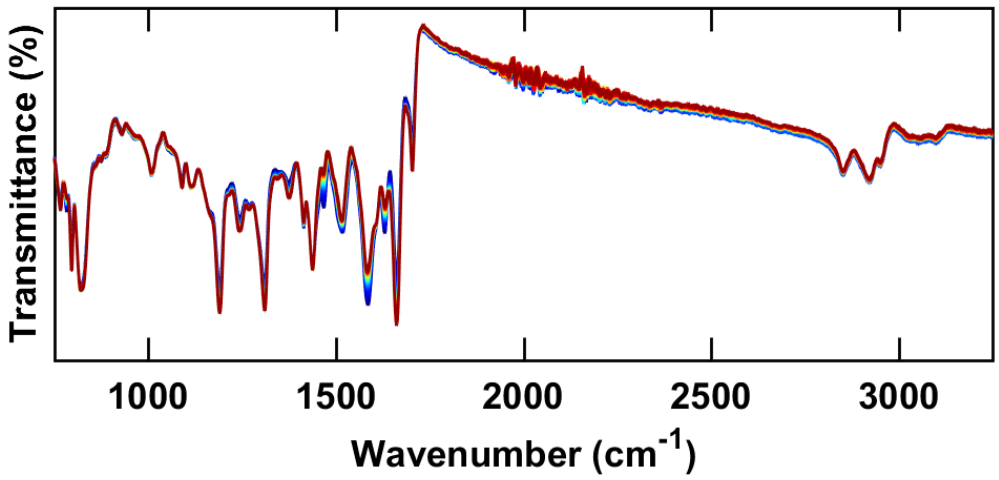

Figure 11.19. FT-IR spectroscopy during temporal evolution of fully doped TAPB-NDI COF upon exposure to air over the course of one hour. Isobestic points are suggested of a complete transform from one species to another.

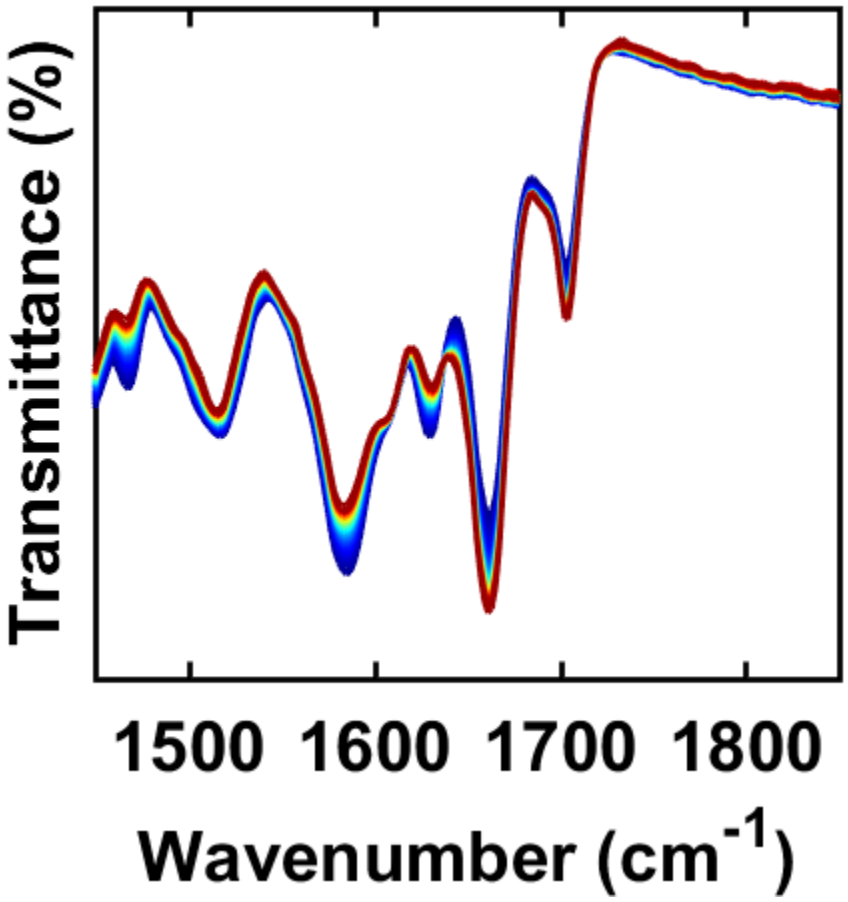

Figure 11.20. Narrow field of view FT-IR spectroscopy during temporal evolution of fully doped TAPB-NDI COF upon exposure to air over the course of one hour. Isobestic points are suggested of a complete transform from one species to another.

H. Transmission Electron Microscopy

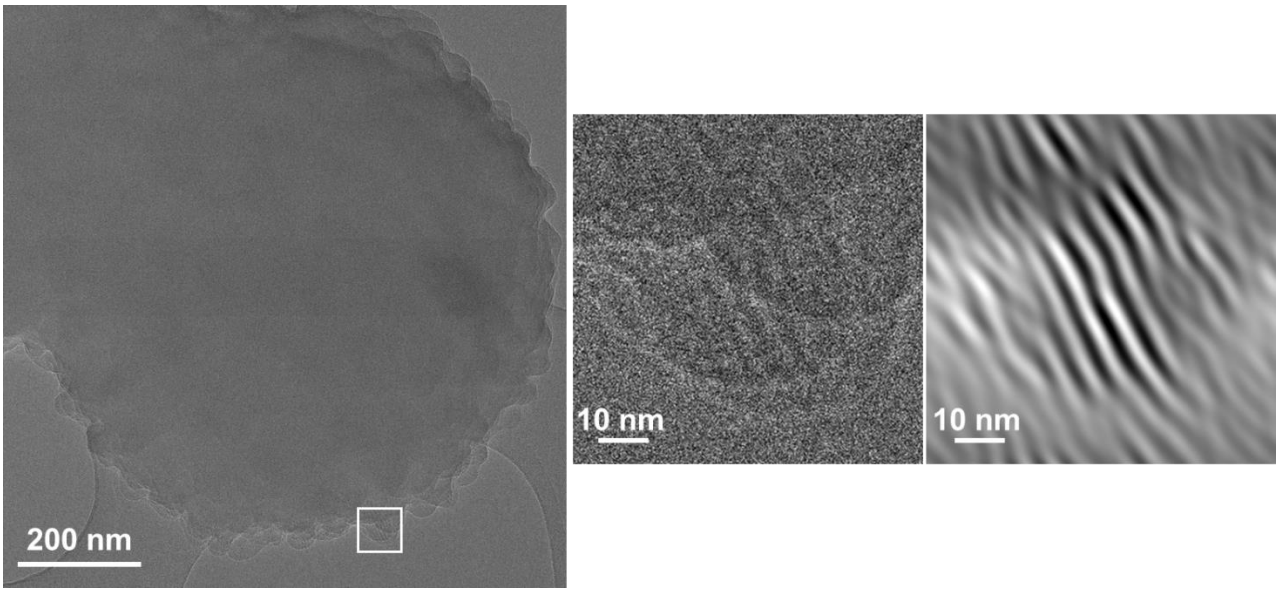

Figure 11.21. Transmission electron micrographs with a large-field-of-view (left), zoomed in (middle), and band-pass filtered (right) of TAPB-NDI COF.

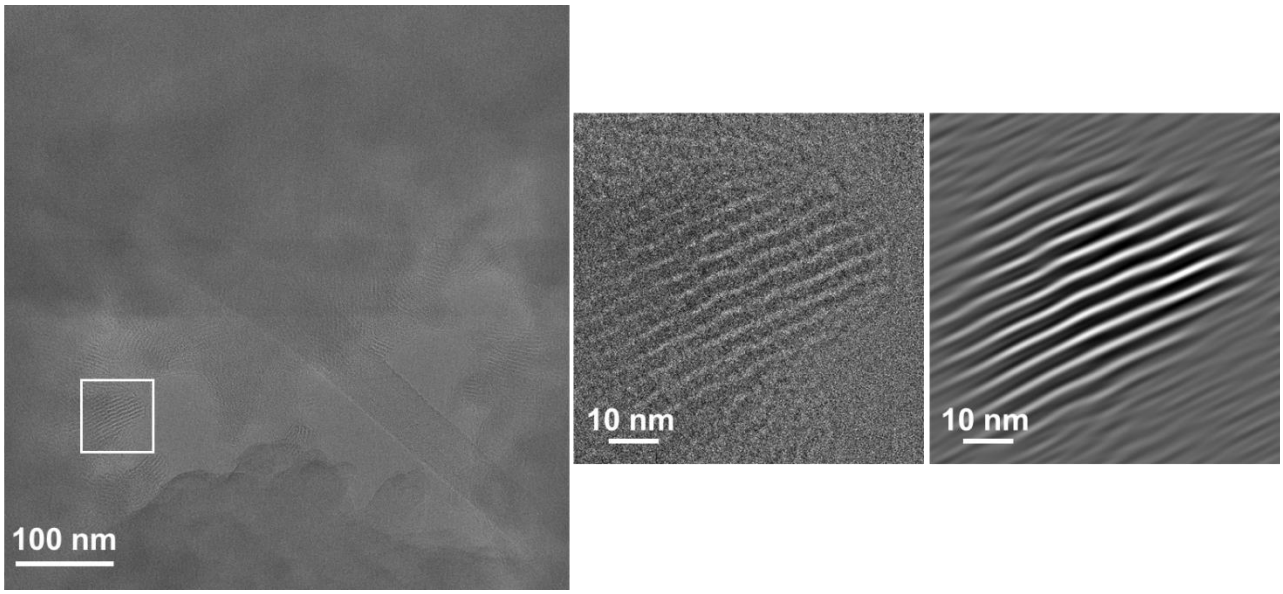

Figure 11.22. Transmission electron micrographs with a large-field-of-view (left), zoomed in (middle), and band-pass filtered (right) of TAPB-NDI COF.

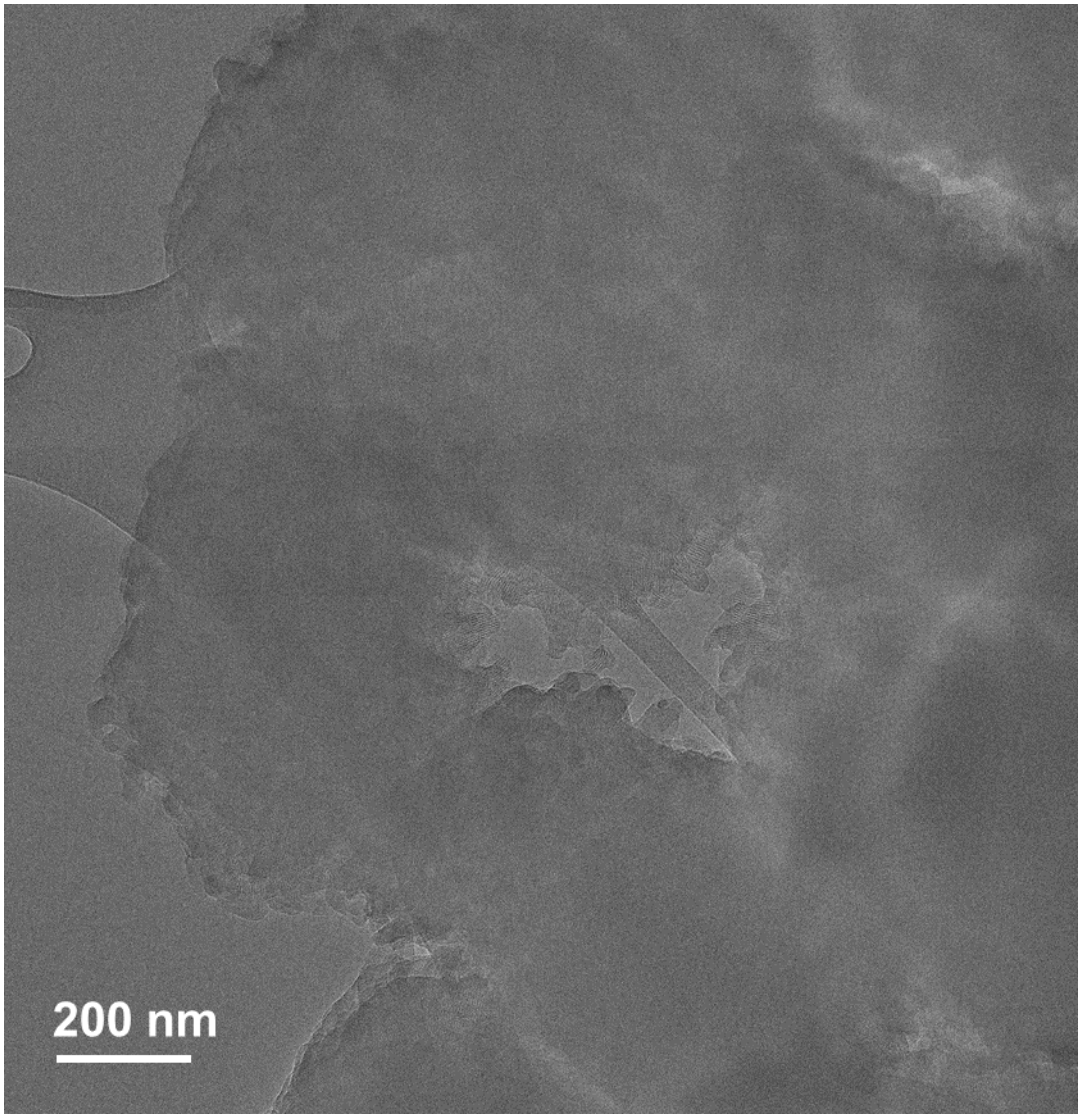

Figure 11.23. Transmission electron micrographs with a large-field-of-view of TAPB-NDI COF.

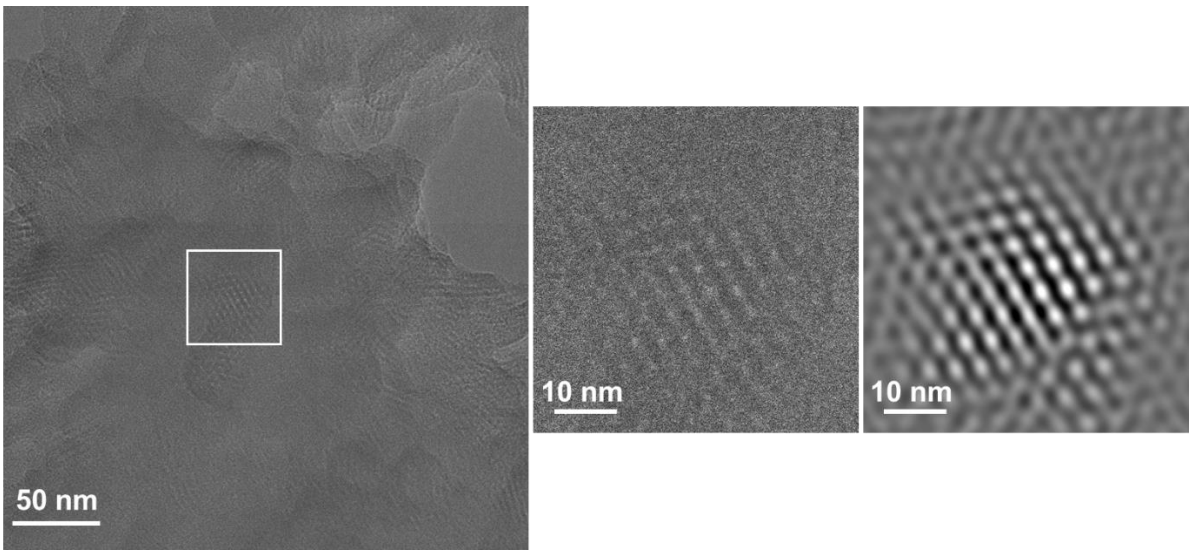

Figure 11.24. Transmission electron micrographs with a large-field-of-view (left), zoomed in (middle), and band-pass filtered (right) of TAPB-NDI COF.

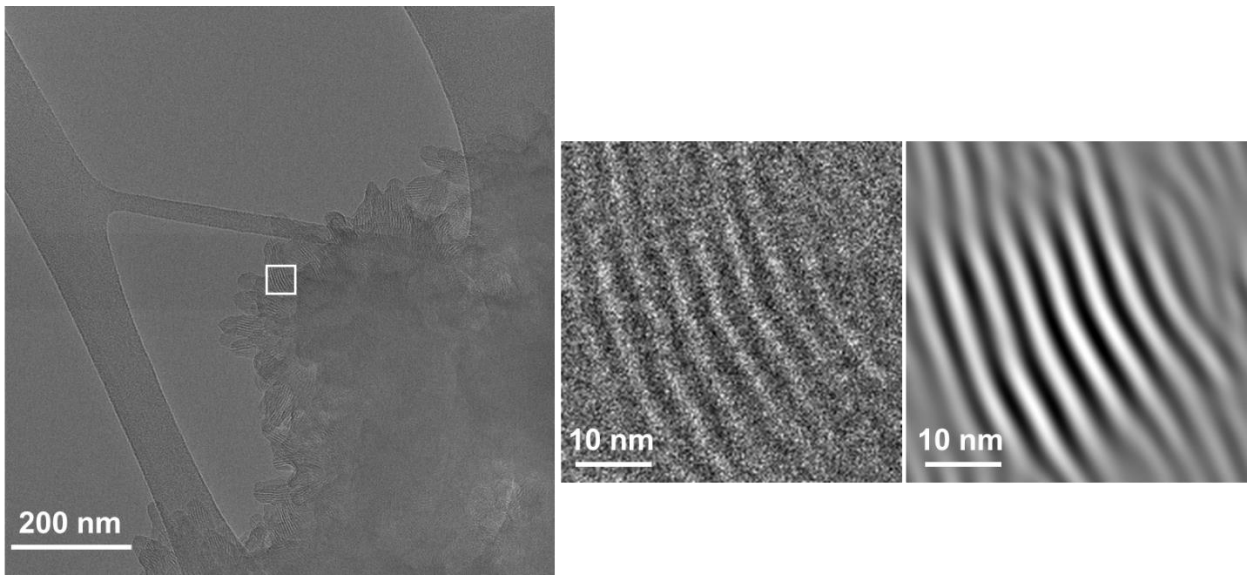

Figure 11.25. Transmission electron micrographs with a large-field-of-view (left), zoomed in (middle), and band-pass filtered (right) of TAPB-NDI COF.

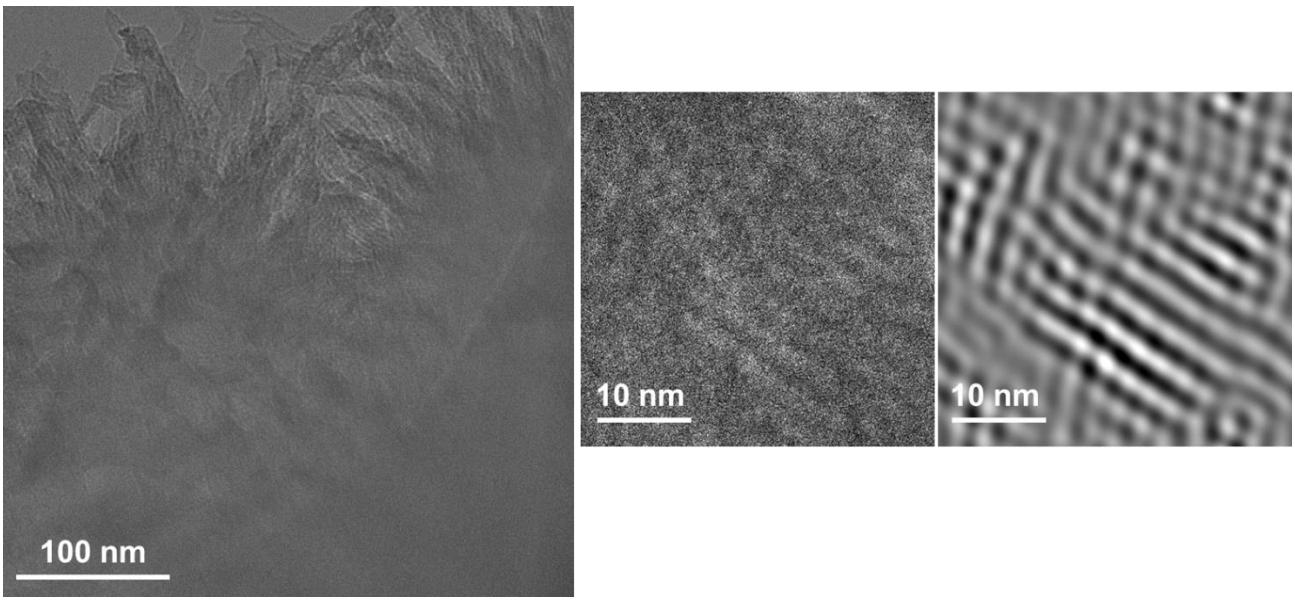

Figure 11.26. Transmission electron micrographs with a large-field-of-view (left), zoomed in (middle), and band-pass filtered (right) of TAPPy-NDI COF.

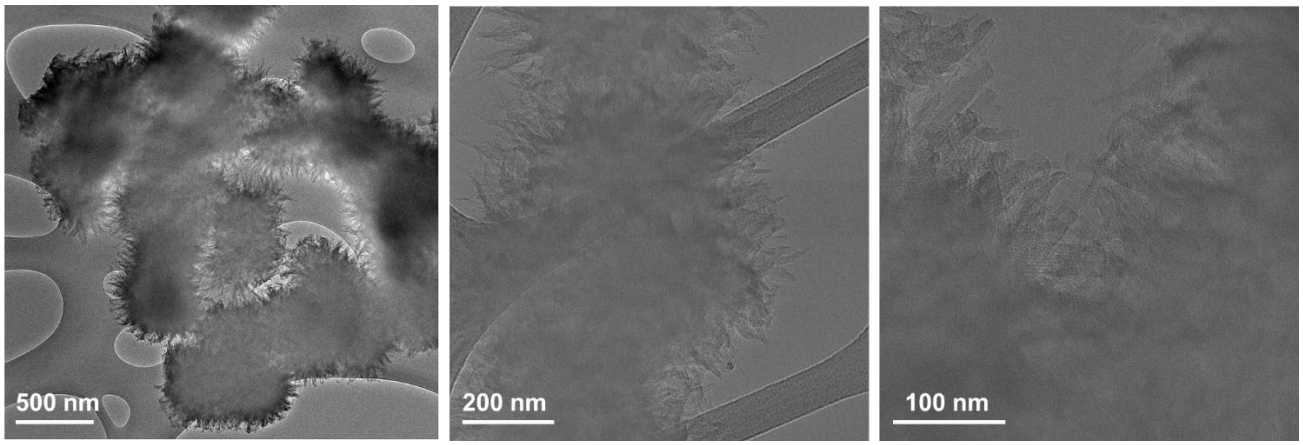

Figure 11.27. Transmission electron micrographs with a large-field-of-view (left), zoomed in (middle and right) of TAPPy-NDI COF.

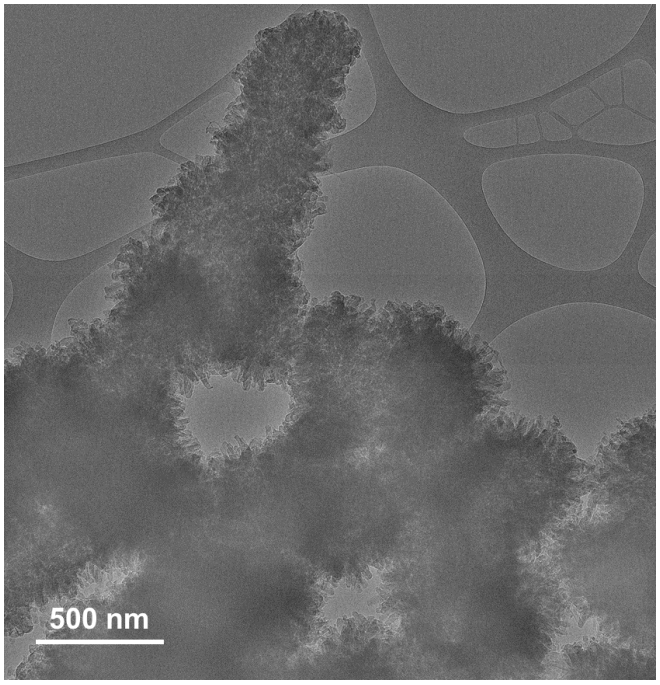

Figure 11.28. Transmission electron micrographs with a large-field-of-view TAPPy-NDI COF.

I. Diffuse-Reflectance Ultraviolet-Visible-Near-Infrared Spectroscopy

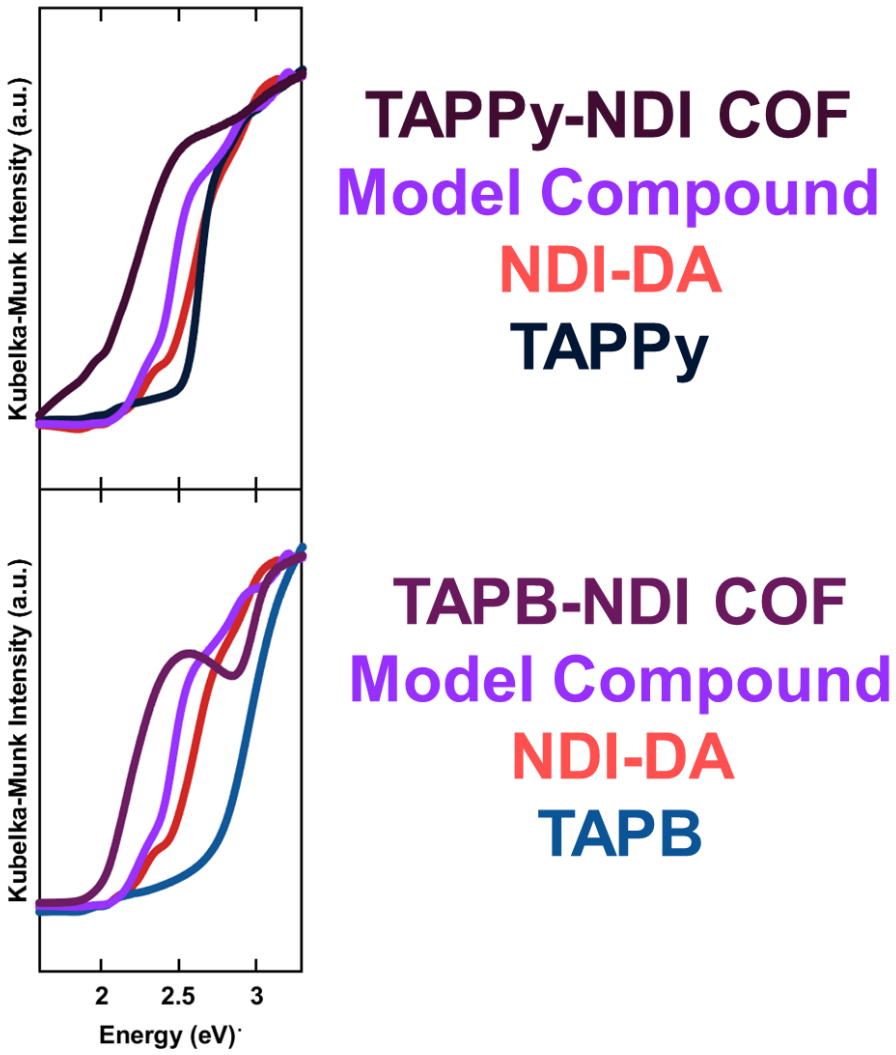

Figure 11.29. Overlayed diffusion-reflectance spectroscopy of monomers, model compounds, and covalent organic frameworks.

J. Flash Photolysis Time Resolved Microwave Conductivity

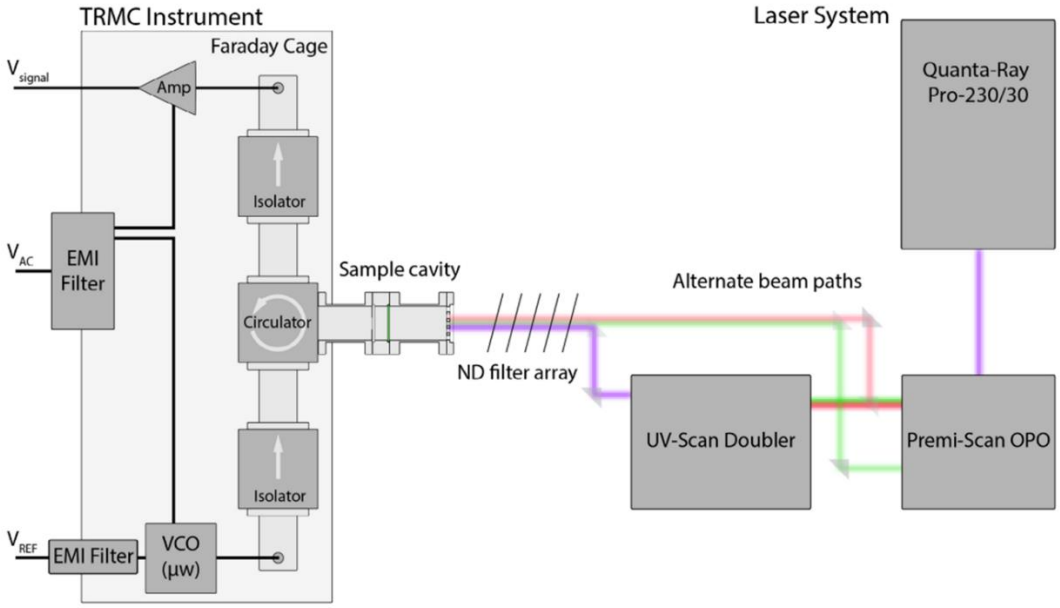

Figure 11.30. Schematic of the TRMC measurement.

Flash-photolysis time-resolved microwave conductivity (fp-TRMC) measurements were performed at three photon energies (1.55, 2.07, and 2.76 eV) on undoped TAPB-NDI COF, TAPPy-NDI COF, and NDI monomer films to 1) establish photoconductivity at photon energies greater than or equal to the optical band edges described in the previous section, and 2) identify differences in photoconductivity and free charge lifetimes between the NDI-COFs. Since our ~9 GHz microwave probe is only sensitive to free charges, this contactless measurement selectively detects free electrons and holes resulting from photoexcitation using a *ca.* 5 ns laser pulse at a single wavelength. Assuming negligible recombination within the instrument response, the maximum change in conductance (ΔG) due to photoinduced carriers is quantitatively related to the yield-mobility product ($\varphi\Sigma\mu$) shown in the left-hand side equation 2 (below),

$$\phi \sum_i \mu_i = \phi(\mu_e + \mu_h) = \frac{\Delta G}{\beta e I_o F_A} \qquad \text{(Equation 2)}$$

where φ is quantum yield of free electrons and holes, $\Sigma\mu$ is the sum of the GHz electron (μ_e) and hole (μ_h) mobilities, β is ratio of the microwave cavity dimensions, *e* is elementary charge, I_o is the laser intensity in units of photons/cm^2/pulse, and F_A is the fraction of photons absorbed at the excitation frequency.

Due to the insolubility of the NDI-COFs the deposition of uniform films was facilitated by dispersing polycrystalline COF powder in an electronically inert polystyrene matrix. Film making details are described in the SI. Results from fp-TRMC, including $\varphi\Sigma\mu$ values at different excitation

energies, amplitude-weighted average time constants (<t>), and biexponential transient fit parameters are shown in Table 1 in the SI. When excited at 2.76 and 2.07 eV, TAPB-NDI and TAPPy-NDI films showed appreciable photoconductivity and comparable φΣμ values (*ca.* 5 x 10^{-5} cm^2/Vs). In agreement with the DR-UVVis spectra from earlier, TAPB-NDI showed no measurable photoconductivity when excited with 1.55 eV photons (i.e. sub-optical gap) whereas TAPPy-NDI demonstrated φΣμ values similar to measurements using greater photon energies. An NDI monomer-polystyrene film was used as a control to establish that the photoconductivity response of the COFs differed from precursor compounds in a way that is consistent with our optical measurements. Indeed, the NDI monomer with an optical gap >2.5 eV only showed appreciable photoconductivity (φΣμ ~ 0.9 x 10^{-5} cm^2/Vs) at 2.76 eV, based on the lack of signal above the microwave cavity background at <2.07 eV photon energies. We suspect φΣμ values for the NDI monomer-polystyrene film approaching those for COFs (*ca.* 1 x 10^{-5} cm^2/Vs) at 2.76 eV is likely explained by the presence of sizable NDI aggregates or perhaps crystallites that form during the relatively slow film drying time typical of drop casting. Since NDI materials are well known n-type transport materials, the values measured here likely originate from a small number of photogenerated free electrons (i.e. low φ) with sizable mobilities.

φΣμ values for the COFs reported here are comparable to a zinc porphyrin COF from our previous work measured under similar conditions. In reference to the Kubo analysis performed in that study – although the average crystallite size (~100 nm) in TAPB-NDI and TAPPy-NDI COF powders in this work is greater than that (~30 nm) for Thomas et al., we argue that one should expect similar limitations to the maximum attainable AC mobility (*ca.* 10^{-2} cm^2/Vs). In addition to possible

crystalline imperfections and a low, but realistic charge yield (likely < 10%), we believe the a (electron + hole) GHz AC mobility within these COF crystallites of *ca.* 10^{-4} cm^2/Vs or greater is reasonable.

Analysis of the amplitude-weighted average lifetime of free charges (<t>, Table 1) revealed that charges in TAPPy-NDI:polystyrene films lived nominally twice as long as those in TAPB-NDI:polystyrene. The origin of this difference is clear when looking at the optimized global fit parameters of the double exponential used to fit the transients. Table 2 shows that the weighting of short- (T1) and long-time (T2) components for both COFs are comparable and that the longer-time component of TAPPy-NDI is *ca.* 100 ns longer than TAPB-NDI (at 2.07 and 2.76 eV). The similarity in A1 and T1 for both COFs indicates that the difference in the long-time component is the dominant contributor to the disparity in <t>. The short-time component suggests that a significant population of mobile charges are annihilated in <12 ns. Since the yield is expected to be low – corroborated by a relatively fluence-independent <t> and T1/T2 values – we suspect exciton-charge annihilation or trapping related to crystalline defects are the primary charge annihilation pathways. However, the difference in the population of long-lived charge species living *ca.* 300-400 ns is clearly seen in representative transients in Figure 3C. Interestingly, <t> for both COFs decreased concomitantly with photon energy. Although the origin of this is unclear, the photon energy-dependence on lifetime may be related to the proximity in which excitons/free charges are generated to traps or other defects in the crystallites that may coincide with more delocalized (i.e. low energy) transitions.

Table 11.2. fp-TRMC results: at three excitation energies, amplitude-weighted average time constants (<t>), and biexponential, global fit parameters.

	Exc. (eV)	NDI-DA:PS	TAPB-NDI:PS	TAPPy-NDI:PS
$\varphi\Sigma\mu$ (10^{-5} cm^2 V^{-1} s^{-1})	2.76	~0.9	6 ± 2	5 ± 1
	2.07		8 ± 2	5 ± 1
	1.55			3 ± 2
<t> (ns)	2.76	~300	56 ± 3	96 ± 5
	2.07		32 ± 15	66 ± 4
	1.55			28 ± 7

Table 11.3. Summary of biexponential fit parameters for a representative fluence

	TAPB-NDI:polystyrene film			
λ_{ex} (eV)	**A1**	**T1 (ns)**	**A2**	**T2 (ns)**
2.76	4.22E-05	12.1	1.01E-05	296
2.07	5.33E-05	9.8	8.88E-06	286
	TAPPy-NDI:polystyrene film			
	A1	**T1 (ns)**	**A2**	**T2 (ns)**
2.76	3.23E-05	7.3	5.40E-06	410
2.07	4.21E-05	5.7	7.14E-06	371
	2.07E-05	4.2	1.72E-06	363

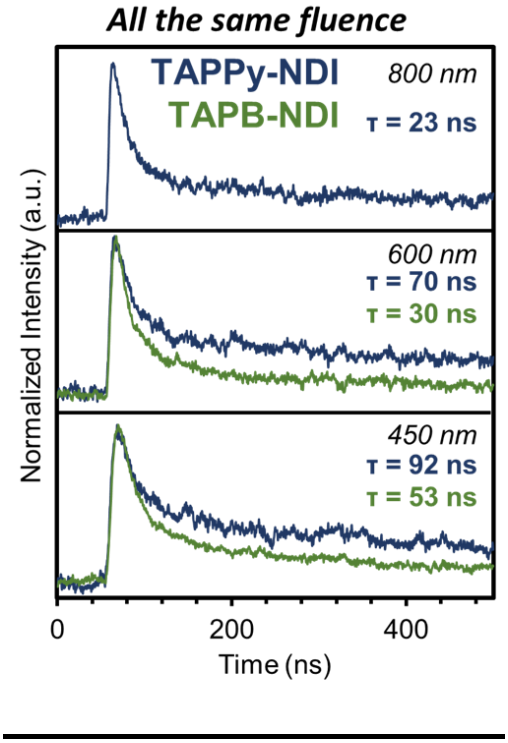

Figure 11.31 Normalized TRMC response with different excitation laser energies

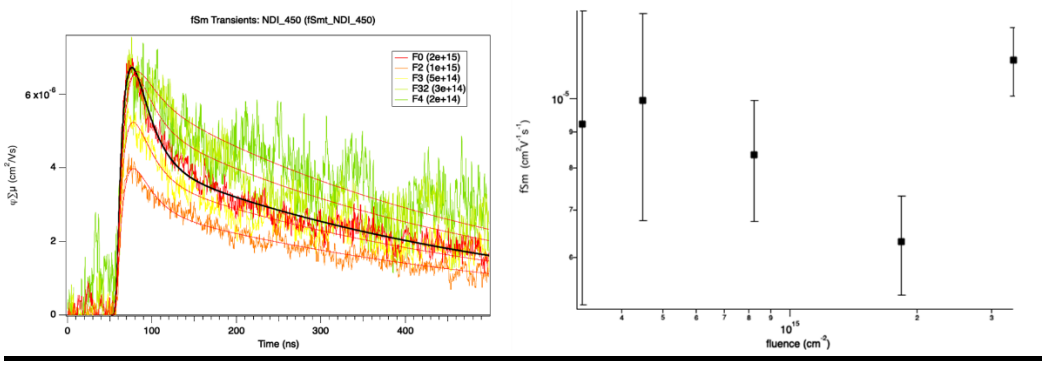

Figure 11.32 Fluence-dependent TRMC response

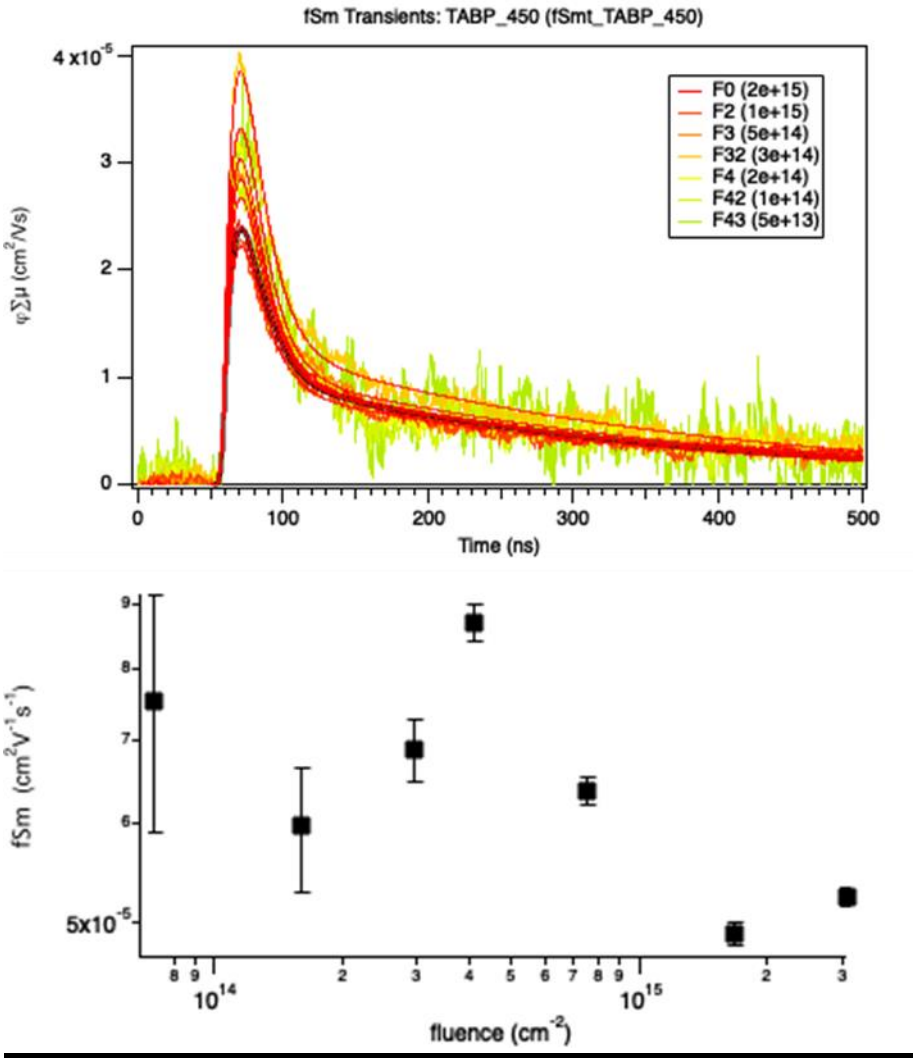

Figure 11.33 Fluence-dependent TRMC response

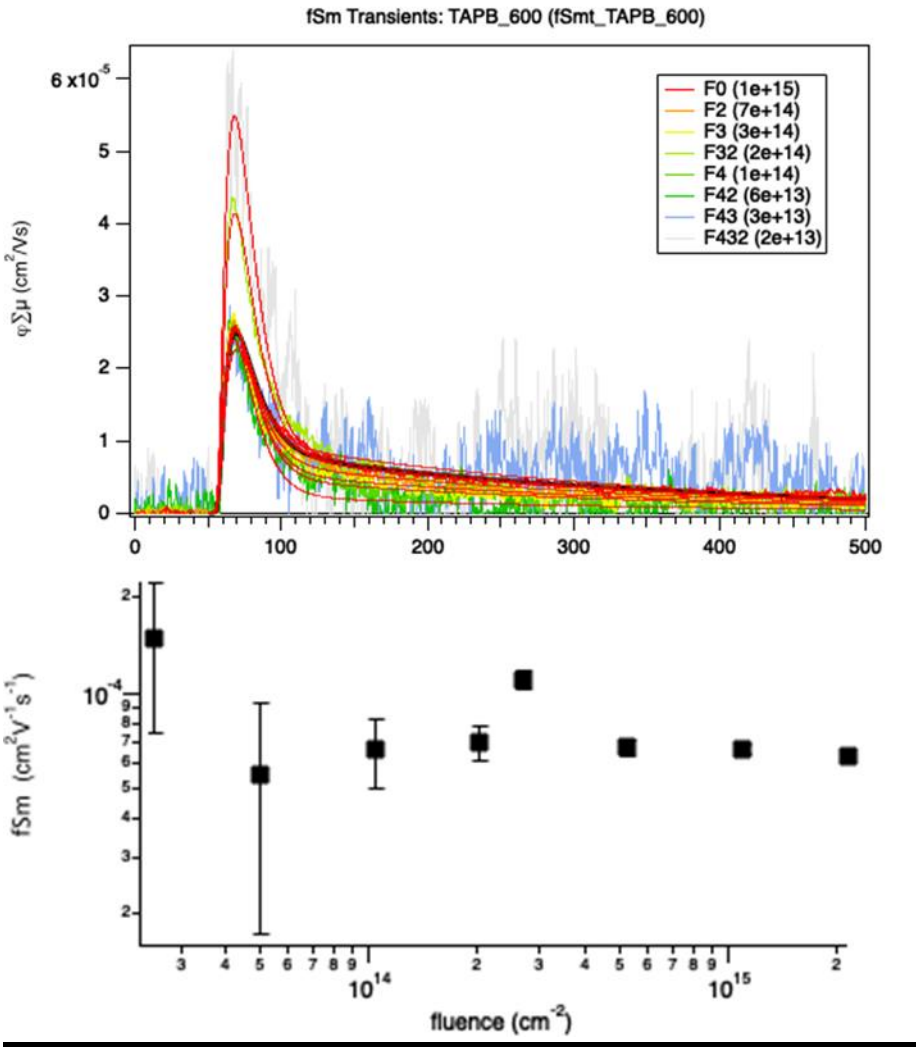

Figure 11.34 Fluence-dependent TRMC response

450 nm

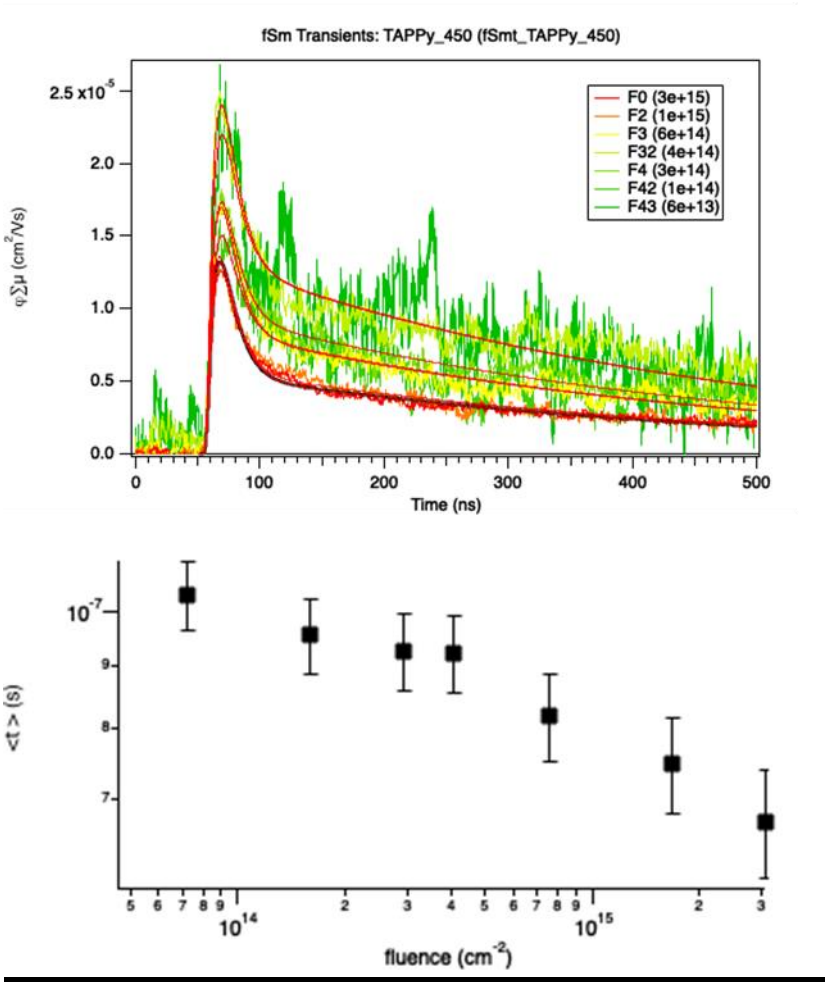

Figure 11.35 Fluence-dependent TRMC response

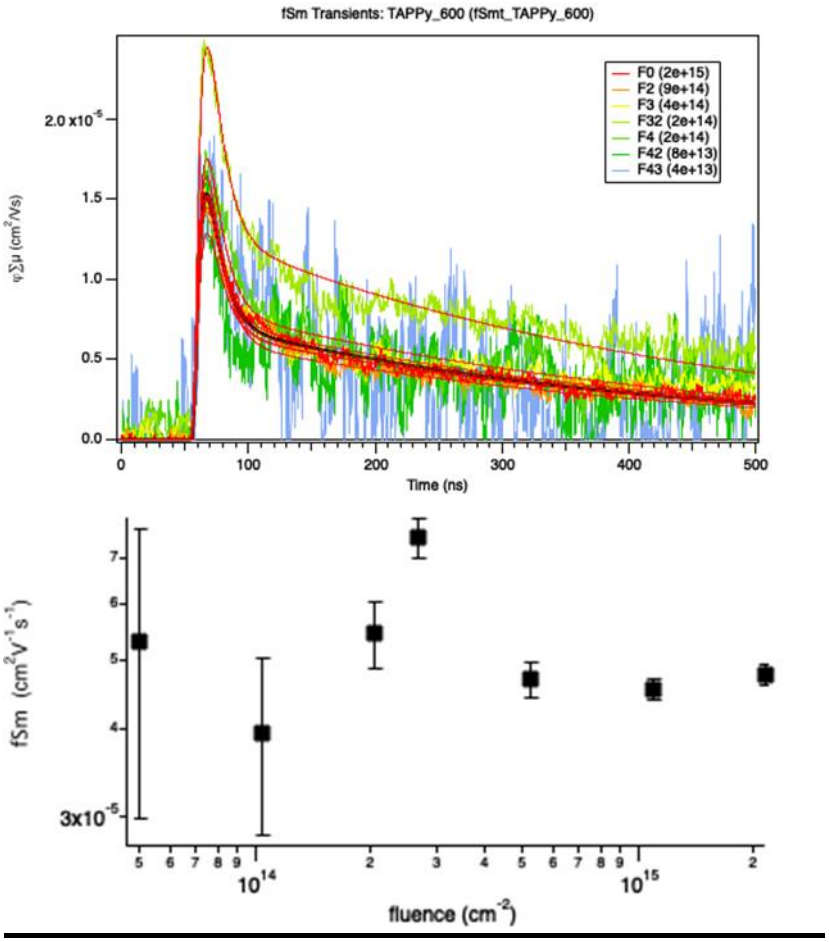

Figure 11.36 Fluence-dependent TRMC response

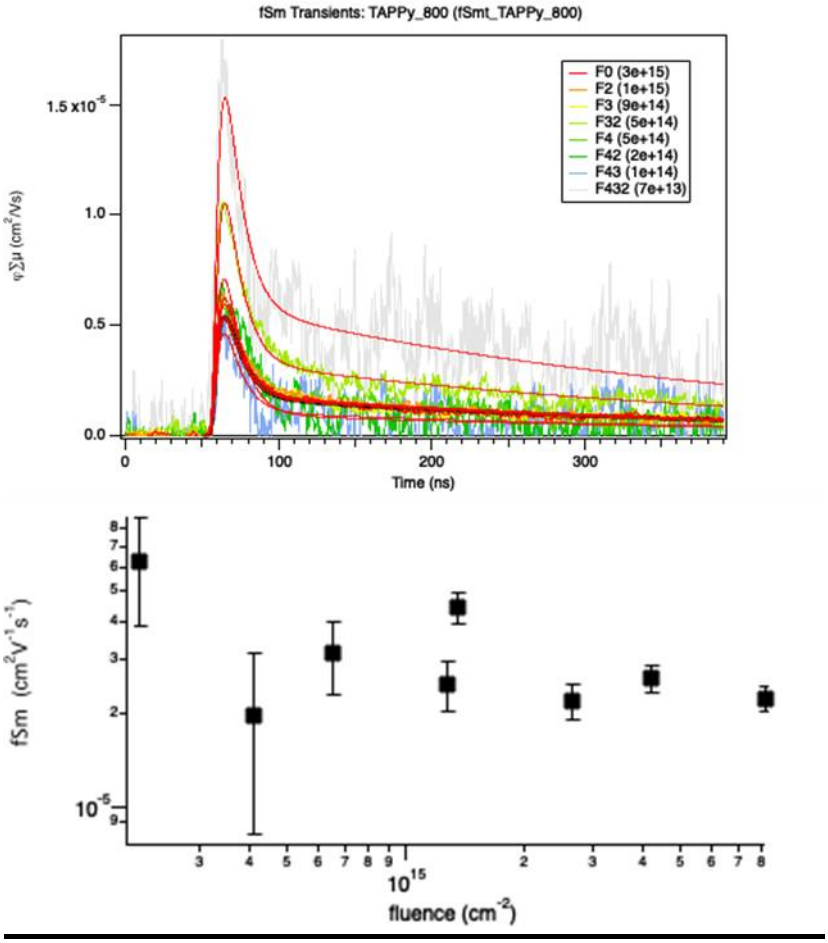

Figure 11.37 Fluence-dependent TRMC response

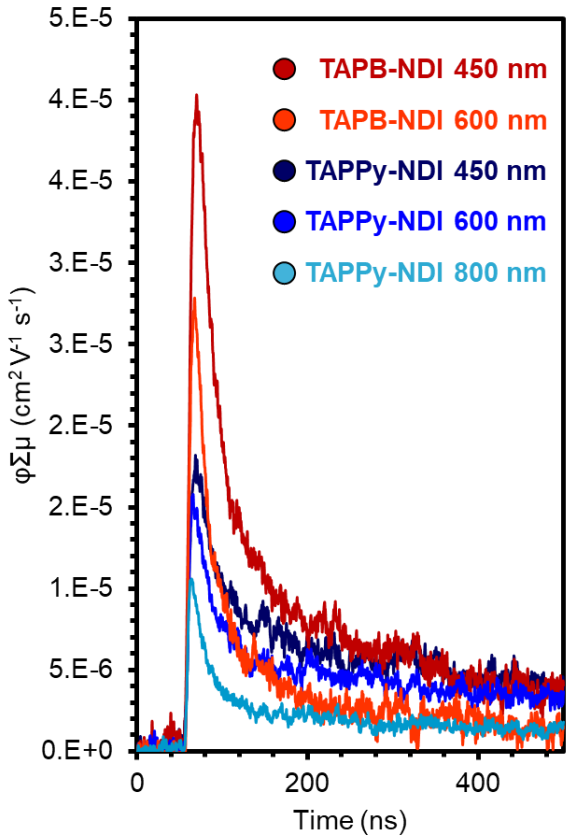

Figure 11.38 Fluence-dependent TRMC response

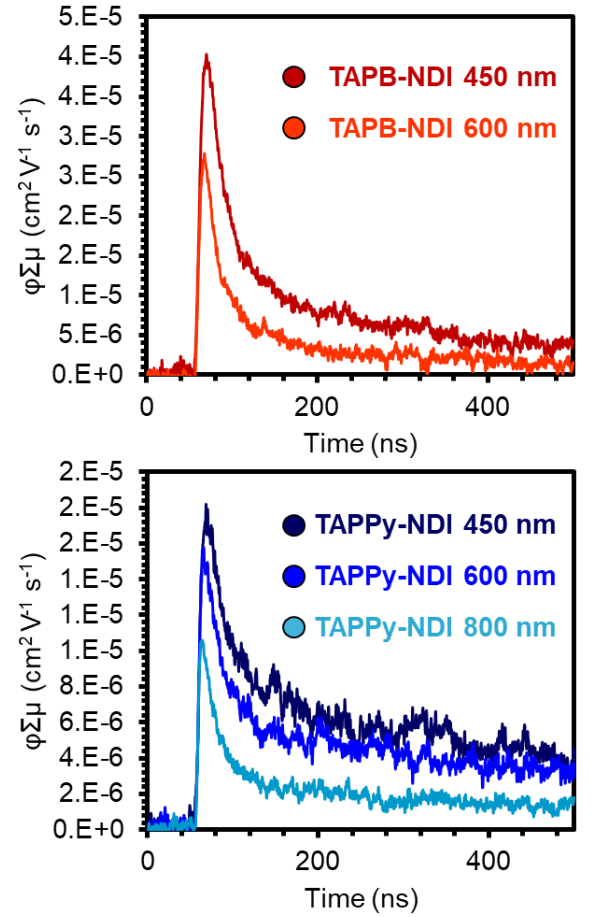

Figure 11.39 TRMC response with different energy excitations

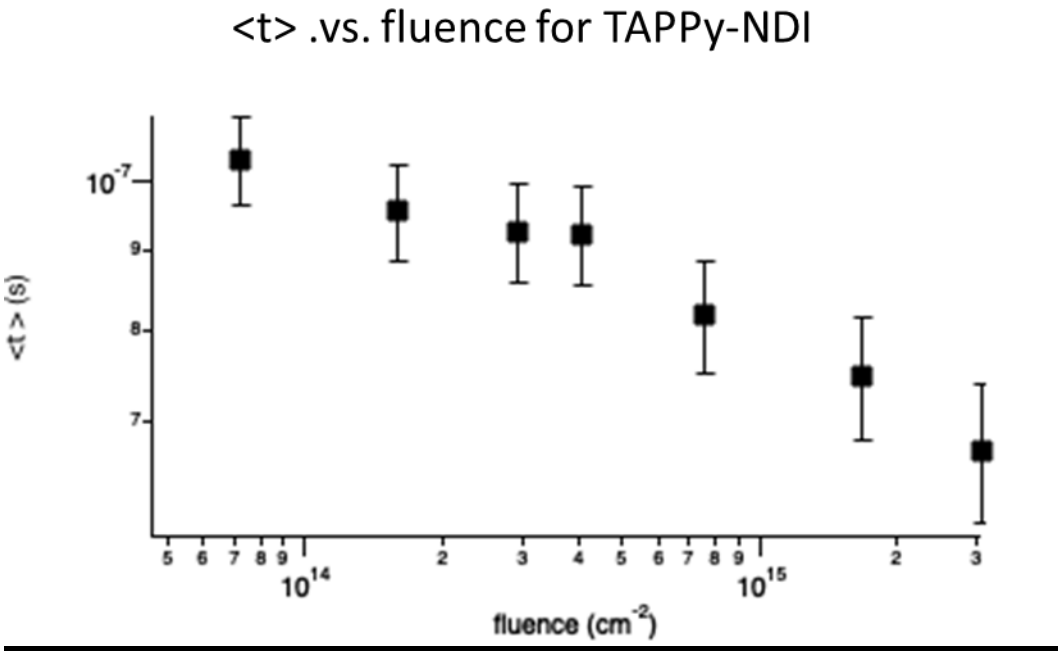

Figure 11.40 Fluence-dependent TRMC response for TAPPy-NDI COF

K. Electronic Structure Calculations

The electronic structure calculations were carried out using the Density functional theory (DFT) method. The geometry optimizations were performed at the PBE level with D3 Van der Waals (Vdw) corrections[701, 711] using the Vienna Ab initio Simulation Package (VASP)[776]. The Γ-centered Monkhorst-Pack *k*-meshes of 1 × 1 × 13 and 1 × 1 × 9 were adopted in geometry optimizations for TAPB-NDI and TAPPy-NDI COF, respectively. The energy cutoff of plane waves was 500 eV. The lattice parameters after geometry optimization of TAPB-NDI and TAPPy-NDI COFs are shown in Table SX. The electronic structures of both COFs are calculated with CRYSTAL17 package[707] at PBE0[777] level with D3 Vdw corrections[711] using POB-TZVF[710] basis set. The Γ-centered Monkhorst-Pack *k*-meshes of 2 x 2 x 28 and 2 x 2 x 14 were used in self-consistent calculations (SCF). To reduce the computational time, all hexyl side chains of TAPB-NDI and TAPPy-NDI COFs were replaced by ethyl groups.

Table 11.4. Unit cell parameters determined from geometry optimization protocol.

	a(Å)	b(Å)	c(Å)	α(°)	β(°)	γ(°)
TAPB-NDI	55.87	55.87	3.92	90.00	90.00	120.01
TAPPy-NDI	34.28	30.40	4.24	75.51	78.50	40.74

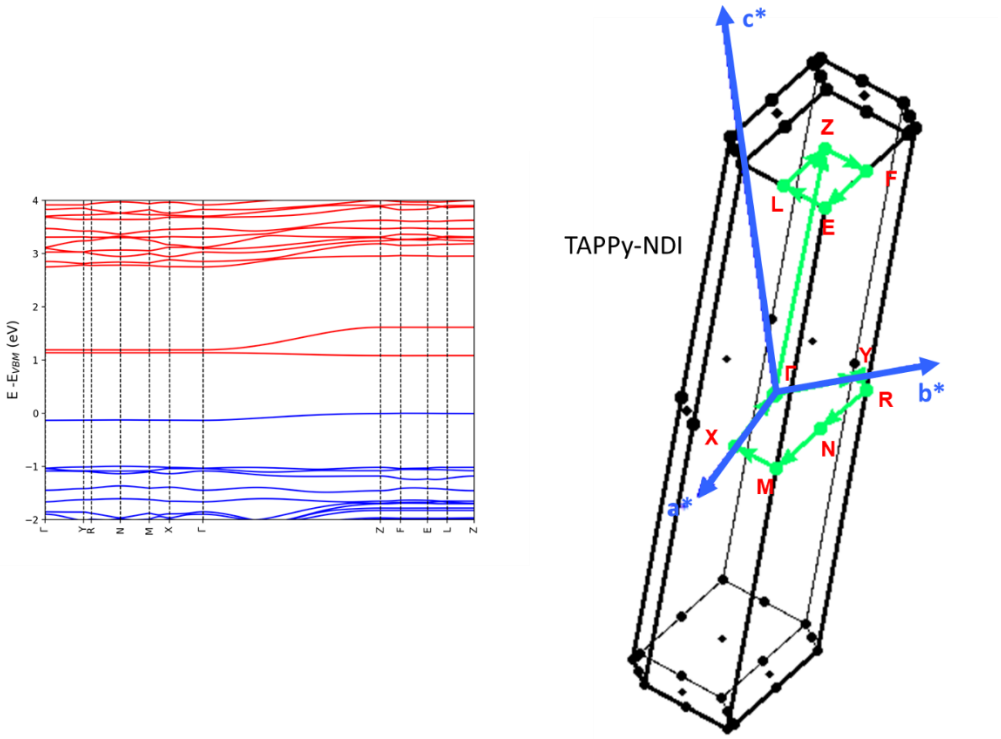

Figure 11.41 Multilayer DFT-calculated bandstructure for TAPPy-NDI COF

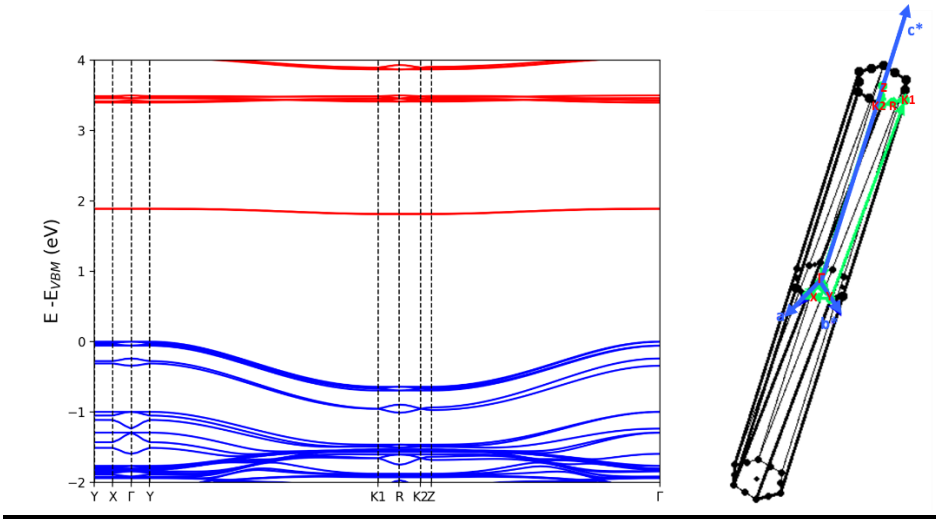

Figure 11.42 Multilayer DFT-calculated bandstructure for TAPB-NDI COF

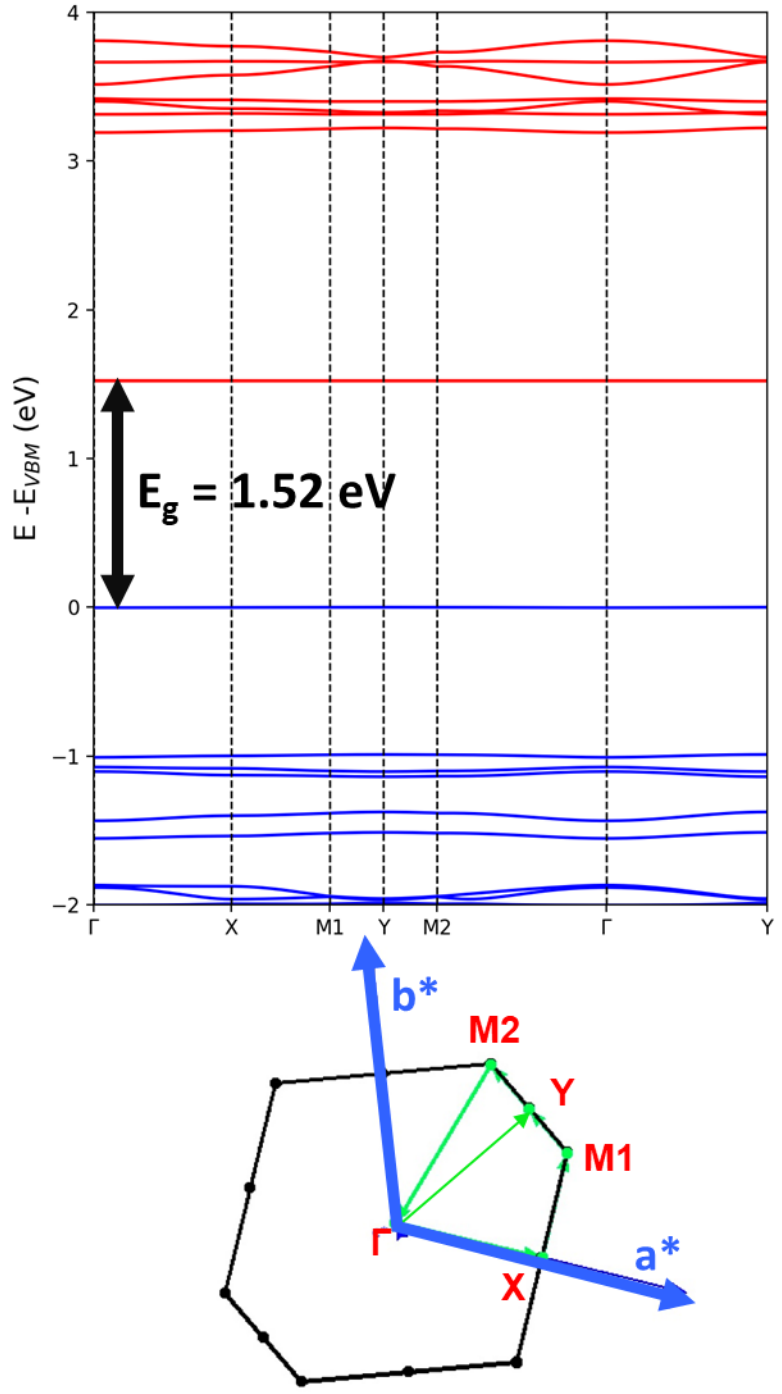

Figure 11.43 Monolayer DFT-calculated bandstructure for TAPPy-NDI COF

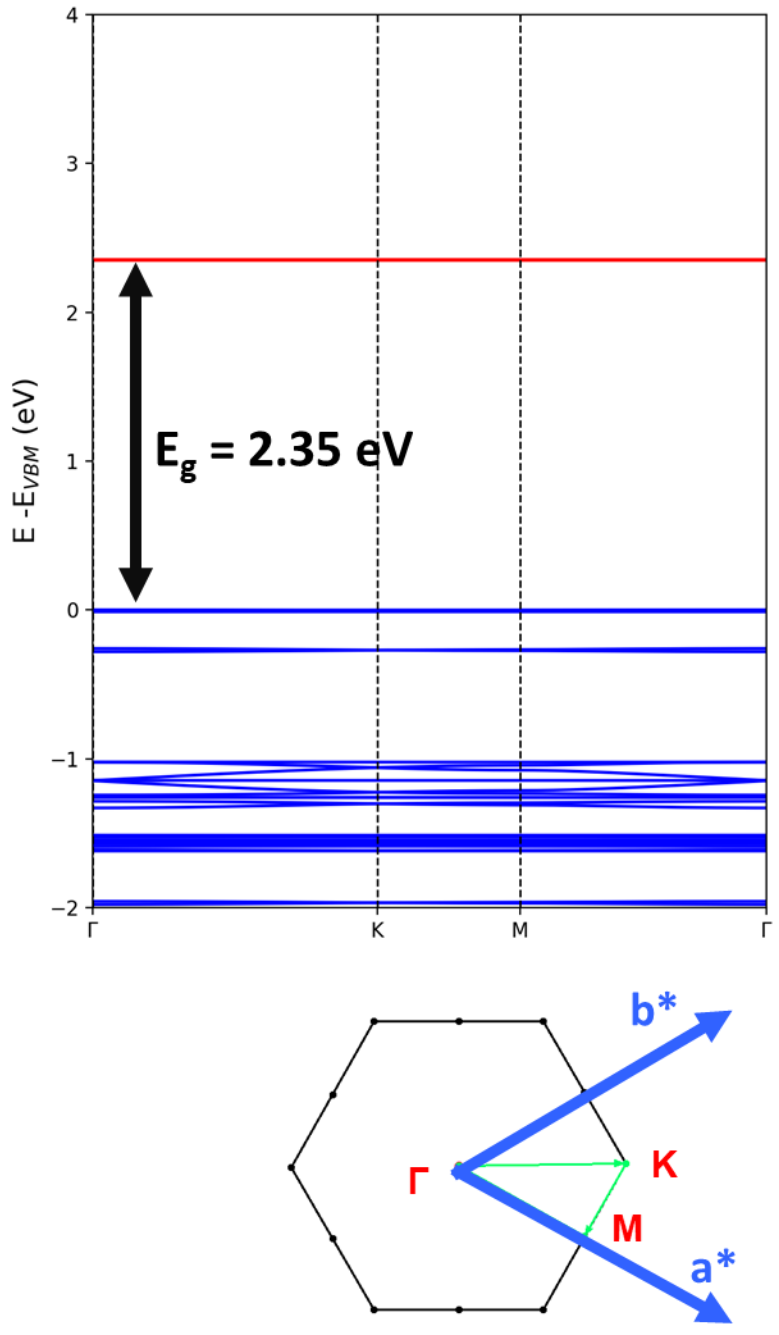

Figure 11.44 Monolayer DFT-calculated bandstructure for TAPB-NDI COF

References

1. Staudinger, H., Über Polymerization (On Polymerization). *J Ber. Dtsch. Chem. Ges.* **1920,** *53*, 1073.

2. Frey, H.; Johann, T., Celebrating 100 years of "polymer science": Hermann Staudinger's 1920 manifesto. *Polym. Chem.* **2020,** *11* (1), 8-14.

3. Abd-El-Aziz, A. S.; Antonietti, M.; Barner-Kowollik, C.; Binder, W. H.; Böker, A.; Boyer, C.; Buchmeiser, M. R.; Cheng, S. Z.; D'Agosto, F.; Floudas, G., The Next 100 Years of Polymer Science. *Macromol. Chem. Phys.* **2020**, 2000216.

4. Furukawa, Y., *Inventing polymer science: Staudinger, Carothers, and the emergence of macromolecular chemistry*. University of Pennsylvania Press: 1998.

5. Lutz, J.-F., 100th Anniversary of Macromolecular Science Viewpoint: Toward Artificial Life-Supporting Macromolecules. *ACS Macro Lett.* **2020,** *9* (2), 185-189.

6. Binder, W. H., The past 40 years of macromolecular sciences: reflections on challenges in synthetic polymer and material science. *Macromol. Rapid Commun.* **2019,** *40* (1), 1800610.

7. Marvel, C.; Carraher, C. E., Wallace Hume Carothers Innovator, Motivator, Pioneer. In *Pioneers in Polymer Science*, Springer: 1989; pp 127-143.

8. Flory, P. J., Spatial configuration of macromolecular chains. *Science* **1975,** *188* (4195), 1268-1276.

9. Cho, S. H.; White, S. R.; Braun, P. V., Self-healing polymer coatings. *Adv. Mater.* **2009,** *21* (6), 645-649.

10. Levkin, P. A.; Svec, F.; Fréchet, J. M., Porous polymer coatings: a versatile approach to superhydrophobic surfaces. *Adv. Func. Mater.* **2009,** *19* (12), 1993-1998.

11. Lopez, J.; Pei, A.; Oh, J. Y.; Wang, G.-J. N.; Cui, Y.; Bao, Z., Effects of polymer coatings on electrodeposited lithium metal. *J. Am. Chem. Soc.* **2018,** *140* (37), 11735-11744.

12. Wei, Q.; Haag, R., Universal polymer coatings and their representative biomedical applications. *Mater. Horiz.* **2015,** *2* (6), 567-577.

13. Halliwell, S., *Polymers in building and construction*. 2002; Vol. 154.

14. Mark, H. F.; Atlas, S. M., Polymers as building materials. *Annu. Rev. Mater. Res.* **1976,** *6* (1), 1-33.

15. Ray Jr, L., The role of synthetic fibers in the textile industry of the future. *Text. Res. J.* **1952,** *22* (2), 144-151.

16. Shirakawa, H., The discovery of polyacetylene film: the dawning of an era of conducting polymers (Nobel lecture). *Angew. Chem. Int. Ed.* **2001,** *40* (14), 2574-2580.

17. Heeger, A. J., Semiconducting and metallic polymers: the fourth generation of polymeric materials (Nobel lecture). *Angew. Chem. Int. Ed.* **2001,** *40* (14), 2591-2611.

18. MacDiarmid, A. G., "Synthetic metals": a novel role for organic polymers (Nobel lecture). *Angew. Chem. Int. Ed.* **2001,** *40* (14), 2581-2590.

19. Mullis, K. B., The polymerase chain reaction (Nobel Lecture). *Angew. Chem. Int. Ed.* **1994,** *33* (12), 1209-1213.

20. Walker, J. E., ATP synthesis by rotary catalysis (Nobel Lecture). *Angew. Chem. Int. Ed.* **1998,** *37* (17), 2308-2319.

21. Arnold, F. H., Innovation by evolution: bringing new chemistry to life (Nobel lecture). *Angew. Chem. Int. Ed.* **2019,** *58* (41), 14420-14426.

22. Fischer, E. H., Protein phosphorylation and cellular regulation II (Nobel lecture). *Angew. Chem. Int. Ed.* **1993,** *32* (8), 1130-1137.

23. Boyer, P. D., Energy, life, and ATP (Nobel lecture). *Angew. Chem. Int. Ed.* **1998,** *37* (17), 2296-2307.

24. Skou, J. C., The identification of the sodium–potassium pump (Nobel lecture). *Angew. Chem. Int. Ed.* **1998,** *37* (17), 2320-2328.

25. Silverman, M.; Simon, M., Flagellar rotation and the mechanism of bacterial motility. *Nature* **1974,** *249* (5452), 73-74.

26. Seo, S. E.; Hawker, C. J., The Beauty of Branching in Polymer Science. *Macromolecules* **2020**.

27. Matthews, O. A.; Shipway, A. N.; Stoddart, J. F., Dendrimers—branching out from curiosities into new technologies. *Prog. Polym. Sci.* **1998,** *23* (1), 1-56.

28. de Jesus, E.; Flores, J. C., Dendrimers: Solutions for catalyst separation and recycling–a review. *Indust. Eng. Chem. Res.* **2008,** *47* (21), 7968-7981.

29. Inoue, K., Functional dendrimers, hyperbranched and star polymers. *Prog. Polym. Sci.* **2000,** *25* (4), 453-571.

30. Khanna, K.; Varshney, S.; Kakkar, A., Miktoarm star polymers: advances in synthesis, self-assembly, and applications. *Polym. Chem.* **2010,** *1* (8), 1171-1185.

31. Laurent, B. A.; Grayson, S. M., Synthetic approaches for the preparation of cyclic polymers. *Chem. Soc. Rev.* **2009,** *38* (8), 2202-2213.

32. Endo, K., Synthesis and properties of cyclic polymers. In *New Frontiers in Polymer Synthesis*, Springer: 2008; pp 121-183.

33. Jiang, H.; Xu, F.-J., Biomolecule-functionalized polymer brushes. *Chem. Soc. Rev.* **2013,** *42* (8), 3394-3426.

34. Milner, S. T., Polymer brushes. *Science* **1991,** *251* (4996), 905-914.

35. Edmondson, S.; Osborne, V. L.; Huck, W. T., Polymer brushes via surface-initiated polymerizations. *Chem. Soc. Rev.* **2004,** *33* (1), 14-22.

36. Gee, G.; Rideal, E. K. s., Reaction in monolayers of drying oils I-The oxidation of the maleic anhydride compound of β-Elaeostearin. *Proc. Math. Phys.* **1935,** *153* (878), 116-128.

37. Bresler, S.; Judin, M.; Talmud, D., Mechanical properties of monolayers obtained by two-dimensional polymerization and condensation. *Acta Phys. Chim. URSS* **1941,** *14*, 71-84.

38. Hoffmann, R., How should chemists think? *Scientific American* **1993,** *268* (2), 66-73.

39. Manzeli, S.; Ovchinnikov, D.; Pasquier, D.; Yazyev, O. V.; Kis, A., 2D transition metal dichalcogenides. *Nat. Rev. Mater.* **2017,** *2* (8), 17033.

40. Allen, M. J.; Tung, V. C.; Kaner, R. B., Honeycomb carbon: a review of graphene. *Chem. Rev.* **2010,** *110* (1), 132-145.

41. Cote, A. P.; Benin, A. I.; Ockwig, N. W.; O'keeffe, M.; Matzger, A. J.; Yaghi, O. M., Porous, crystalline, covalent organic frameworks. *Science* **2005,** *310* (5751), 1166-1170.

42. Lehn, J.-M.; Eliseev, A. V., Dynamic combinatorial chemistry. *Science* **2001,** *291* (5512), 2331-2332.

43. Lehn, J. M., Dynamic combinatorial chemistry and virtual combinatorial libraries. *Chem. Eur. J.* **1999,** *5* (9), 2455-2463.

44. Lutz, J.-F.; Lehn, J.-M.; Meijer, E.; Matyjaszewski, K., From precision polymers to complex materials and systems. *Nat. Rev. Mater.* **2016,** *1* (5), 1-14.

45. Lehn, J.-M., From supramolecular chemistry towards constitutional dynamic chemistry and adaptive chemistry. *Chem. Soc. Rev.* **2007,** *36* (2), 151-160.

46. Rowan, S. J.; Cantrill, S. J.; Cousins, G. R. L.; Sanders, J. K. M.; Stoddart, J. F., Dynamic Covalent Chemistry. *Angew. Chem. Int. Ed.* **2002,** *41* (6), 898-952.

47. Fyfe, M. C.; Stoddart, J. F., Synthetic supramolecular chemistry. *Acc. Chem. Res.* **1997,** *30* (10), 393-401.

48. Fujita, M., *Molecular self-assembly: organic versus inorganic approaches*. Springer: 2003; Vol. 96.

49. Fujita, M., Metal-directed self-assembly of two-and three-dimensional synthetic receptors. *Chem. Soc. Rev.* **1998,** *27* (6), 417-425.

50. Tashiro, K.; Aida, T., Metalloporphyrin hosts for supramolecular chemistry of fullerenes. *Chem. Soc. Rev.* **2007,** *36* (2), 189-197.

51. Aida, T., On Supramolecular Polymerization: Interview with Takuzo Aida. *Adv. Mater.* **2020,** *32* (20), 1905445.

52. Hoeben, F. J.; Jonkheijm, P.; Meijer, E.; Schenning, A. P., About supramolecular assemblies of π-conjugated systems. *Chem. Rev.* **2005,** *105* (4), 1491-1546.

53. De Greef, T. F.; Smulders, M. M.; Wolffs, M.; Schenning, A. P.; Sijbesma, R. P.; Meijer, E., Supramolecular polymerization. *Chem. Rev.* **2009,** *109* (11), 5687-5754.

54. Brunsveld, L.; Folmer, B.; Meijer, E. W.; Sijbesma, R., Supramolecular polymers. *Chem. Rev.* **2001,** *101* (12), 4071-4098.

55. Diercks, C. S.; Yaghi, O. M., The atom, the molecule, and the covalent organic framework. *Science* **2017,** *355* (6328), 923.

56. O'Keeffe, M.; Yaghi, O. M., Deconstructing the crystal structures of metal–organic frameworks and related materials into their underlying nets. *Chem. Rev.* **2012,** *112* (2), 675-702.

57. Liu, Y.; O'Keeffe, M.; Treacy, M. M.; Yaghi, O. M., The geometry of periodic knots, polycatenanes and weaving from a chemical perspective: a library for reticular chemistry. *Chem. Soc. Rev.* **2018,** *47* (12), 4642-4664.

58. Zhou, H.-C.; Long, J. R.; Yaghi, O. M., Introduction to metal–organic frameworks. *Chem. Rev.* **2012**.

59. Long, J. R.; Yaghi, O. M., The pervasive chemistry of metal–organic frameworks. *Chem. Soc. Rev.* **2009,** *38* (5), 1213-1214.

60. Ockwig, N. W.; Delgado-Friedrichs, O.; O'Keeffe, M.; Yaghi, O. M., Reticular chemistry: occurrence and taxonomy of nets and grammar for the design of frameworks. *Acc. Chem. Res.* **2005,** *38* (3), 176-182.

61. Tranchemontagne, D. J.; Mendoza-Cortés, J. L.; O'Keeffe, M.; Yaghi, O. M., Secondary building units, nets and bonding in the chemistry of metal–organic frameworks. *Chem. Soc. Rev.* **2009,** *38* (5), 1257-1283.

62. Robson, R.; Abrahams, B. F.; Batten, S. R.; Gable, R. W.; Hoskins, B. F.; Liu, J., Crystal engineering of novel materials composed of infinite two-and three-dimensional frameworks. ACS Publications: 1992.

63. Robson, R., A net-based approach to coordination polymers. *Dalton Trans.* **2000,** (21), 3735-3744.

64. Abrahams, B. F.; Hoskins, B. F.; Robson, R., A new type of infinite 3D polymeric network containing 4-connected, peripherally-linked metalloporphyrin building blocks. *J. Am. Chem. Soc.* **1991,** *113* (9), 3606-3607.

65. Dresselhaus, M. S.; Araujo, P. T., Perspectives on the 2010 nobel prize in physics for graphene. ACS Publications: 2010.

66. Novoselov, K.; Mishchenko, A.; Carvalho, A.; Neto, A. C., 2D materials and van der Waals heterostructures. *Science*

2016, *353* (6298), aac9439.

67. Novoselov, K., Nobel lecture: Graphene: Materials in the flatland. *Rev. Mod. Phys.* **2011,** *83* (3), 837.

68. Geim, A. K., Random walk to graphene (Nobel Lecture). *Angew. Chem. Int. Ed.* **2011,** *50* (31), 6966-6985.

69. Zhang, H.; Cheng, H.-M.; Ye, P., 2D nanomaterials: beyond graphene and transition metal dichalcogenides. *Chem. Soc. Rev.* **2018,** *47* (16), 6009-6012.

70. Li, H.; Li, Y.; Aljarb, A.; Shi, Y.; Li, L.-J., Epitaxial growth of two-dimensional layered transition-metal dichalcogenides: growth mechanism, controllability, and scalability. *Chem. Rev.* **2017,** *118* (13), 6134-6150.

71. Ma, Y.; Li, B.; Yang, S., Ultrathin two-dimensional metallic nanomaterials. *Mater. Chem. Front.* **2018,** *2* (3), 456-467.

72. Han, G. H.; Duong, D. L.; Keum, D. H.; Yun, S. J.; Lee, Y. H., Van der Waals metallic transition metal dichalcogenides. *Chem. Rev.* **2018,** *118* (13), 6297-6336.

73. Zhu, Y.; Ji, H.; Cheng, H.-M.; Ruoff, R. S., Mass production and industrial applications of graphene materials. *Nat. Sci. Rev.* **2018,** *5* (1), 90-101.

74. Zhao, G.; Li, X.; Huang, M.; Zhen, Z.; Zhong, Y.; Chen, Q.; Zhao, X.; He, Y.; Hu, R.; Yang, T.; Ruoff, R., The physics and chemistry of graphene-on-surfaces. *Chem. Soc. Rev.* **2017,** *46* (15), 4417-4449.

75. Custelcean, R., Anions in crystal engineering. *Chem. Soc. Rev.* **2010,** *39* (10), 3675-3685.

76. Biradha, K.; Santra, R., Crystal engineering of topochemical solid state reactions. *Chem. Soc. Rev.* **2013,** *42* (3), 950-967.

77. Krishnamohan Sharma, C., Crystal engineering− where do we go from here? *Cryst. Growth Des.* **2002,** *2* (6), 465-474.

78. Desiraju, G., Crystal engineering: a holistic view. *Chem. Soc. Rev.* **2007,** *46* (44), 8342-8356.

79. Reichenbächer, K.; Süss, H. I.; Hulliger, J., Fluorine in crystal engineering—"the little atom that could". *Chem. Soc. Rev.* **2005,** *34* (1), 22-30.

80. Moulton, B.; Zaworotko, M. J., From molecules to crystal engineering: supramolecular isomerism and polymorphism in network solids. *Chem. Rev.* **2001,** *101* (6), 1629-1658.

81. Aakeröy, C. B.; Seddon, K. R., The hydrogen bond and crystal engineering. *Chem. Soc. Rev.* **1993,** *22* (6), 397-407.

82. Desiraju, G. R., Supramolecular synthons in crystal engineering—a new organic synthesis. *Angew. Chem. Int. Ed.* **1995,** *34* (21), 2311-2327.

83. Chen, X.; Geng, K.; Liu, R.; Tan, K. T.; Gong, Y.; Li, Z.; Tao, S.; Jiang, Q.; Jiang, D., Covalent Organic Frameworks: Chemical Approaches to Designer Structures and Built-In Functions. *Angew. Chem. Int. Ed.* **2020,** *59* (13), 5050-5091.

84. Geng, K.; He, T.; Liu, R.; Dalapati, S.; Tan, K. T.; Li, Z.; Tao, S.; Gong, Y.; Jiang, Q.; Jiang, D., Covalent Organic Frameworks: Design, Synthesis, and Functions. *Chem. Rev.* **2020**.

85. Li, Y.; Chen, W.; Xing, G.; Jiang, D.; Chen, L., New synthetic strategies toward covalent organic frameworks. *Chem. Soc. Rev.* **2020**.

86. Jin, E.; Asada, M.; Xu, Q.; Dalapati, S.; Addicoat, M. A.; Brady, M. A.; Xu, H.; Nakamura, T.; Heine, T.; Chen, Q.; Jiang, D., Two-dimensional sp2 carbon-conjugated covalent organic frameworks. *Science* **2017,** *357* (6352), 673-676.

87. Müller, V.; Hinaut, A.; Moradi, M.; Baljozovic, M.; Jung, T. A.; Shahgaldian, P.; Möhwald, H.; Hofer, G.; Kröger, M.; King, B. T., A two-dimensional polymer synthesized at the air/water interface. *Angew. Chem. Int. Ed.* **2018,** *57* (33), 10584-10588.

88. Spitzer, S.; Rastgoo-Lahrood, A.; Macknapp, K.; Ritter, V.; Sotier, S.; Heckl, W. M.; Lackinger, M., Solvent-free on-surface synthesis of boroxine COF monolayers. *Chem. Commun.* **2017,** *53* (37), 5147-5150.

89. Lackinger, M., Surface-assisted Ullmann coupling. *Chem. Comm.* **2017,** *53* (56), 7872-7885.

90. Grill, L.; Hecht, S., Covalent on-surface polymerization. *Nat. Chem.* **2020,** *12* (2), 115-130.

91. Kory, M. J.; Wörle, M.; Weber, T.; Payamyar, P.; Van De Poll, S. W.; Dshemuchadse, J.; Trapp, N.; Schlüter, A. D., Gram-scale synthesis of two-dimensional polymer crystals and their structure analysis by X-ray diffraction. *Nat. Chem.* **2014,** *6* (9), 779-784.

92. Kissel, P.; Erni, R.; Schweizer, W. B.; Rossell, M. D.; King, B. T.; Bauer, T.; Götzinger, S.; Schlüter, A. D.; Sakamoto, J., A two-dimensional polymer prepared by organic synthesis. *Nat. Chem.* **2012,** *4* (4), 287-291.

93. Sakamoto, J.; van Heijst, J.; Lukin, O.; Schlüter, A. D., Two-dimensional polymers: just a dream of synthetic chemists? *Angew. Chem. Int. Ed.* **2009,** *48* (6), 1030-1069.

94. Schlüter, A. D.; Weber, T.; Hofer, G., How to use X-ray diffraction to elucidate 2D polymerization propagation in single crystals. *Chem. Soc. Rev.* **2020**.

95. Yokozawa, T.; Ohta, Y., Transformation of step-growth polymerization into living chain-growth polymerization. *Chem. Rev.* **2016,** *116* (4), 1950-1968.

96. Sancar, A., Mechanisms of DNA repair by photolyase and excision nuclease (Nobel Lecture). *Angew. Chem. Int. Ed.* **2016,** *55* (30), 8502-8527.

97. Modrich, P., Mechanisms in E. coli and human mismatch repair (Nobel Lecture). *Angew. Chem. Int. Ed.* **2016,** *55* (30), 8490-8501.

98. Payamyar, P.; King, B. T.; Öttinger, H. C.; Schlüter, A. D., Two-dimensional polymers: concepts and perspectives. *Chem. Commun.* **2016,** *52* (1), 18-34.

99. Zhao, M.; Huang, Y.; Peng, Y.; Huang, Z.; Ma, Q.; Zhang, H., Two-dimensional metal–organic framework nanosheets: synthesis and applications. *Chem. Soc. Rev.* **2018,** *47* (16), 6267-6295.

100. Liu, Y.; Ma, Y.; Zhao, Y.; Sun, X.; Gandara, F.; Furukawa, H.; Liu, Z.; Zhu, H.; Zhu, C.; Suenaga, K.; Oleynikov, P.; Alshammari, A. S.; Zhang, X.; Terasaki, O.; Yaghi, O. M., Weaving of organic threads into a crystalline covalent organic framework. *Science* **2016,** *351* (6271), 365-369.

101. Miro, P.; Audiffred, M.; Heine, T., An atlas of two-dimensional materials. *Chem. Soc. Rev.* **2014,** *43* (18), 6537-6554.

102. Zhao, W.; Xia, L.; Liu, X., Covalent Organic Frameworks (COFs): Perspectives of Industrialization. *CrystEngComm* **2018**, Ahead of Print.

103. Yang, F.; Cheng, S.; Zhang, X.; Ren, X.; Li, R.; Dong, H.; Hu, W., 2D Organic Materials for Optoelectronic Applications. *Adv. Mater.* **2018,** *30* (2), n/a.

104. Li, L.-l.; Liu, S.; Zhang, Q.; Hu, N.-t.; Wei, L.-m.; Yang, Z.; Wei, H., Advances in covalent organic frameworks. *Wuli Huaxue Xuebao* **2017,** *33* (10), 1960-1977.

105. Jin, Y. H.; Hu, Y. M.; Zhang, W., Tessellated multiporous two-dimensional covalent organic frameworks. *Nat Rev Chem* **2017,** *1* (7).

106. Bisbey, R. P.; Dichtel, W. R., Covalent Organic Frameworks as a Platform for Multidimensional Polymerization. *ACS Cent. Sci.* **2017,** *3* (6), 533-543.

107. Yaghi, O. M., Reticular Chemistry in All Dimensions. *ACS Cent. Sci.* **2019**.

108. Zhao, Y.; Guo, L.; Gandara, F.; Ma, Y.; Liu, Z.; Zhu, C.; Lyu, H.; Trickett, C. A.; Kapustin, E. A.; Terasaki, O.; Yaghi, O. M., A Synthetic Route for Crystals of Woven Structures, Uniform Nanocrystals, and Thin Films of Imine Covalent Organic Frameworks. *J. Am. Chem. Soc.* **2017,** *139* (37), 13166-13172.

109. Diercks, C. S.; Kalmutzki, M. J.; Yaghi, O. M., Covalent organic frameworks-organic chemistry beyond the molecule. *Molecules* **2017,** *22* (9), 1575/1-1575/6.

110. Waller, P. J.; Gandara, F.; Yaghi, O. M., Chemistry of Covalent Organic Frameworks. *Acc. Chem. Res.* **2015,** *48* (12), 3053-3063.

111. Ji, Q.; Lirag, R. C.; Miljanic, O. S., Kinetically controlled phenomena in dynamic combinatorial libraries. *Chem. Soc. Rev.* **2014,** *43* (6), 1873-1884.

112. Cougnon, F. B.; Sanders, J. K., Evolution of dynamic combinatorial chemistry. *Acc. Chem. Res.* **2012,** *45* (12), 2211-2221.

113. Hunt, R. A.; Otto, S., Dynamic combinatorial libraries: new opportunities in systems chemistry. *Chem. Commun.* **2011,** *47* (3), 847-858.

114. Black, S. P.; Sanders, J. K.; Stefankiewicz, A. R., Disulfide exchange: exposing supramolecular reactivity through dynamic covalent chemistry. *Chem. Soc. Rev.* **2014,** *43* (6), 1861-1872.

115. Jin, Y.; Wang, Q.; Taynton, P.; Zhang, W., Dynamic covalent chemistry approaches toward macrocycles, molecular cages, and polymers. *Acc. Chem. Res.* **2014,** *47* (5), 1575-1586.

116. Jin, Y.; Yu, C.; Denman, R. J.; Zhang, W. J. C. S. R., Recent advances in dynamic covalent chemistry. *Chem. Soc. Rev.* **2013,** *42* (16), 6634-6654.

117. Nguyen, V.; Grunwald, M., Microscopic Origins of Poor Crystallinity in the Synthesis of Covalent Organic Framework COF-5. *J. Am. Chem. Soc.* **2018,** *140* (9), 3306-3311.

118. Li, H.; Chavez, A. D.; Li, H.; Li, H.; Dichtel, W. R.; Bredas, J. L., Nucleation and Growth of Covalent Organic Frameworks from Solution: The Example of COF-5. *J. Am. Chem. Soc.* **2017,** *139* (45), 16310-16318.

119. Koo, B. T.; Heden, R. F.; Clancy, P., Nucleation and growth of 2D covalent organic frameworks: polymerization and crystallization of COF monomers. *Phys. Chem. Chem. Phys.* **2017,** *19* (15), 9745-9754.

120. Smith, B. J.; Hwang, N.; Chavez, A. D.; Novotney, J. L.; Dichtel, W. R., Growth rates and water stability of 2D boronate ester covalent organic frameworks. *Chem. Commun.* **2015,** *51* (35), 7532-7535.

121. Smith, B. J.; Dichtel, W. R., Mechanistic Studies of Two-Dimensional Covalent Organic Frameworks Rapidly Polymerized from Initially Homogeneous Conditions. *J. Am. Chem. Soc.* **2014,** *136* (24), 8783-8789.

122. Dogru, M.; Sonnauer, A.; Zimdars, S.; Doeblinger, M.; Knochel, P.; Bein, T., Facile synthesis of a mesoporous benzothiadiazole-COF based on a transesterification process. *CrystEngComm* **2013,** *15* (8), 1500-1502.

123. Calik, M.; Sick, T.; Dogru, M.; Doeblinger, M.; Datz, S.; Budde, H.; Hartschuh, A.; Auras, F.; Bein, T., From Highly Crystalline to Outer Surface-Functionalized Covalent Organic Frameworks-A Modulation Approach. *J. Am. Chem. Soc.* **2016,** *138* (4), 1234-1239.

124. Vitaku, E.; Dichtel, W. R., Synthesis of 2D Imine-Linked Covalent Organic Frameworks through Formal Transimination Reactions. *J. Am. Chem. Soc.* **2017,** *139* (37), 12911-12914.

125. Smith, B. J.; Parent, L. R.; Overholts, A. C.; Beaucage, P. A.; Bisbey, R. P.; Chavez, A. D.; Hwang, N.; Park, C.; Evans, A. M.; Gianneschi, N. C.; Dichtel, W. R., Colloidal Covalent Organic Frameworks. *ACS Cent. Sci.* **2017,** *3* (1), 58-65.

126. Evans, A.; Parent, L. R.; Flanders, N. C.; Bisbey, R. P.; Vitaku, E.; Chen, L. X.; Gianneschi, N. C.; Dichtel, W. R., Seeded Growth of Single-Crystal Two-Dimensional Covalent Organic Frameworks. *Science* **2018**.

127. Castano, I.; Evans, A. M.; Li, H.; Vitaku, E.; Strauss, M. J.; Brédas, J.-L.; Gianneschi, N. C.; Dichtel, W. R., Chemical Control over Nucleation and Anisotropic Growth of Two-Dimensional Covalent Organic Frameworks. *ACS Cent. Sci.* **2019,** *5* (11), 1892-1899.

128. Huang, N.; Zhai, L.; Coupry, D. E.; Addicoat, M. A.; Okushita, K.; Nishimura, K.; Heine, T.; Jiang, D., Multiple-component covalent organic frameworks. *Nat. Commun.* **2016,** *7*, 12325pp.

129. Qian, H.-L.; Li, Y.; Yan, X.-P., A building block exchange strategy for the rational fabrication of de novo unreachable amino-functionalized imine-linked covalent organic frameworks. *J. Chem. Mater. A* **2018,** *6* (36), 17307-17311.

130. Daugherty, M. C.; Vitaku, E.; Li, R. L.; Evans, A. M.; Chavez, A. D.; Dichtel, W. R., Improved synthesis of β-ketoenamine-linked covalent organic frameworks via monomer exchange reactions. *Chem. Commun.* **2019,** *55* (18), 2680-2683.

131. Li, Z.; Ding, X.; Feng, Y.; Feng, W.; Han, B.-H., Structural and dimensional transformations between covalent organic frameworks via linker exchange. *Macromolecules* **2019,** *52* (3), 1257-1265.

132. Qian, C.; Qi, Q.-Y.; Jiang, G.-F.; Cui, F.-Z.; Tian, Y.; Zhao, X., Toward Covalent Organic Frameworks Bearing Three Different Kinds of Pores: The Strategy for Construction and COF-to-COF Transformation via Heterogeneous Linker Exchange. *J. Am. Chem. Soc.* **2017,** *139* (19), 6736-6743.

133. Boissonnault, J. A.; Wong-Foy, A. G.; Matzger, A. J., Core–Shell Structures Arise Naturally During Ligand Exchange in Metal–Organic Frameworks. *J. Am. Chem. Soc.* **2017,** *139* (42), 14841-14844.

134. Liu, C.; Zeng, C.; Luo, T.-Y.; Merg, A. D.; Jin, R.; Rosi, N. L., Establishing porosity gradients within metal–organic frameworks using partial postsynthetic ligand exchange. *J. Am. Chem. Soc.* **2016,** *138* (37), 12045-12048.

135. Kim, M.; Cahill, J. F.; Fei, H.; Prather, K. A.; Cohen, S. M., Postsynthetic ligand and cation exchange in robust metal–organic frameworks. *J. Am. Chem. Soc.* **2012,** *134* (43), 18082-18088.

136. Taddei, M.; Wakeham, R. J.; Koutsianos, A.; Andreoli, E.; Barron, A. R., Post-Synthetic Ligand Exchange in Zirconium-Based Metal–Organic Frameworks: Beware of The Defects! *Angew. Chem. Int. Ed.* **2018,** *57* (36), 11706-11710.

137. Yu, D.; Shao, Q.; Song, Q.; Cui, J.; Zhang, Y.; Wu, B.; Ge, L.; Wang, Y.; Zhang, Y.; Qin, Y., A solvent-assisted ligand exchange approach enables metal-organic frameworks with diverse and complex architectures. *Nat. Commun.* **2020,** *11* (1), 1-10.

138. Fei, H.; Cahill, J. F.; Prather, K. A.; Cohen, S. M., Tandem postsynthetic metal ion and ligand exchange in zeolitic imidazolate frameworks. *Inorg. Chem.* **2013,** *52* (7), 4011-4016.

139. González Miera, G.; Bermejo Gómez, A.; Chupas, P. J.; Martín-Matute, B.; Chapman, K. W.; Platero-Prats, A. E., Topological transformation of a metal–organic framework triggered by ligand exchange. *Inorg. Chem.* **2017,** *56* (8), 4576-4583.

140. Nguyen, H. L.; Gropp, C.; Yaghi, O. M., Reticulating 1D ribbons into 2D covalent organic frameworks by imine and imide linkages. *J. Am. Chem. Soc.* **2020,** *142* (6), 2771-2776.

141. Yuan, X.; Wang, Y.; Deng, G.; Zong, X.; Zhang, C.; Xue, S., Mixed matrix membrane comprising polyimide with crystalline porous imide-linked covalent organic framework for N2/O2 separation. *Polymers for Mixed Membrane Technologies* **2019,** *30* (2), 417-424.

142. Dong, J.; Wang, Y.; Liu, G.; Cheng, Y.; Zhao, D., Isoreticular covalent organic frameworks for hydrocarbon uptake and separation: the important role of monomer planarity. *CrystEngComm* **2017,** *19* (33), 4899-4904.

143. Fang, Q.; Zhuang, Z.; Gu, S.; Kaspar, R. B.; Zheng, J.; Wang, J.; Qiu, S.; Yan, Y., Designed synthesis of large-pore crystalline polyimide covalent organic frameworks. *Nat. Commun.* **2014,** *5* (1), 1-8.

144. Li, H.; Evans, A. M.; Castano, I.; Strauss, M. J.; Dichtel, W. R.; Brédas, J.-L., Nucleation-Elongation Dynamics of Two-Dimensional Covalent Organic Frameworks. *J. Am. Chem. Soc.* **2019**.

145. Chavez, A. D.; Smith, B. J.; Smith, M. K.; Beaucage, P. A.; Northrop, B. H.; Dichtel, W. R., Discrete, Hexagonal Boronate Ester-Linked Macrocycles Related to Two-Dimensional Covalent Organic Frameworks. *Chem. Mater.* **2016,** *28* (14), 4884-4888.

146. Smith, B. J.; Overholts, A. C.; Hwang, N.; Dichtel, W. R., Insight into the crystallization of amorphous imine-linked polymer networks to 2D covalent organic frameworks. *Chem. Commun.* **2016,** *52* (18), 3690-3693.

147. Corcos, A. R.; Levato, G. A.; Jiang, Z.; Evans, A. M.; Livingston, A. G.; Mariñas, B. J.; Dichtel, W. R., Reducing the Pore Size of Covalent Organic Frameworks in Thin-Film Composite Membranes Enhances Solute Rejection. *ACS Mater. Lett.* **2019,** *1* (4), 440-446.

148. Matsumoto, M.; Valentino, L.; Stiehl, G. M.; Balch, H. B.; Corcos, A. R.; Wang, F.; Ralph, D. C.; Marinas, B. J.; Dichtel, W. R., Lewis-Acid-Catalyzed Interfacial Polymerization of Covalent Organic Framework Films. *Chem.* **2018,** *4* (2), 308-317.

149. Matsumoto, M.; Dasari, R. R.; Ji, W.; Feriante, C. H.; Parker, T. C.; Marder, S. R.; Dichtel, W. R., Rapid, Low Temperature Formation of Imine-Linked Covalent Organic Frameworks Catalyzed by Metal Triflates. *J. Am. Chem. Soc.* **2017,** *139* (14), 4999-5002.

150. Chavez, A. D.; Evans, A. M.; Flanders, N. C.; Bisbey, R. P.; Vitaku, E.; Chen, L. X.; Dichtel, W. R., Equilibration of Imine-Linked Polymers to Hexagonal Macrocycles Driven by Self-Assembly. *Chem. - Eur. J.* **2018,** *24* (16), 3989-3993.

151. Li, R. L.; Flanders, N. C.; Evans, A. M.; Ji, W.; Castano, I.; Chen, L. X.; Gianneschi, N. C.; Dichtel, W. R., Controlled growth of imine-linked two-dimensional covalent organic framework nanoparticles. *Chem. Sci.* **2019,** *10* (13), 3796-3801.

152. Stewart, D.; Antypov, D.; Dyer, M. S.; Pitcher, M. J.; Katsoulidis, A. P.; Blanc, F.; Rosseinsky, M. J.; Chater, P. A.; Blanc, F., Stable and ordered amide frameworks synthesised under reversible conditions which facilitate error checking. *Nat. Commun.* **2017,** *8* (1), 1102.

153. Tan, J.; Namuangruk, S.; Kong, W.; Kungwan, N.; Guo, J.; Wang, C., Manipulation of Amorphous-to-Crystalline Transformation: Towards the Construction of Covalent Organic Framework Hybrid Microspheres with NIR Photothermal Conversion Ability. *Angew. Chem. Int. Ed.* **2016,** *55* (45), 13979-13984.

154. Brus, J.; Kobera, L.; Urbanova, M.; Dousova, B.; Lhotka, M.; Kolousek, D.; Kotek, J.; Cuba, P.; Czernek, J.; Dedecek, J., Interface Induced Growth and Transformation of Polymer-

Conjugated Proto-Crystalline Phases in Aluminosilicate Hybrids: A Multiple-Quantum 23Na-23Na MAS NMR Correlation Spectroscopy Study. *Langmuir* **2016,** *32* (11), 2787-2797.

155. Kuecken, S.; Schmidt, J.; Zhi, L.; Thomas, A., Conversion of amorphous polymer networks to covalent organic frameworks under ionothermal conditions: a facile synthesis route for covalent triazine frameworks. *J. Mater. Chem. A* **2015,** *3* (48), 24422-24427.

156. Rambo, B. M.; Tilford, R. W.; Lanni, L. M.; Liu, J.; Lavigne, J. J., Boronate-linked materials: ranging from amorphous assemblies to highly structured networks. *Macromol. Containing Met. Met.-Like Elem.* **2009,** *9* (Supramolecular and Self-Assembled Metal-Containing Materials), 255-294.

157. Zhang, G.; Tsujimoto, M.; Packwood, D.; Duong, N. T.; Nishiyama, Y.; Kadota, K.; Kitagawa, S.; Horike, S., Construction of a Hierarchical Architecture of Covalent Organic Frameworks via a Postsynthetic Approach. *J. Am. Chem. Soc.* **2018,** *140* (7), 2602-2609.

158. Wang, H.; He, B.; Liu, F.; Stevens, C.; Brady, M. A.; Cai, S.; Wang, C.; Russell, T. P.; Tan, T. W.; Liu, Y., Orientation transitions during the growth of imine covalent organic framework thin films. *J. Mater. Chem. C* **2017,** *5* (21), 5090-5095.

159. Sick, T.; Rotter, J. M.; Reuter, S.; Kandambeth, S.; Bach, N. N.; Döblinger, M.; Merz, J.; Clark, T.; Marder, T. B.; Bein, T., Switching on and off Interlayer Correlations and Porosity in 2D Covalent Organic Frameworks. *J. Am. Chem. Soc.* **2019,** *141* (32), 12570-12581.

160. Feriante, C. H.; Jhulki, S.; Evans, A. M.; Dasari, R. R.; Slicker, K.; Dichtel, W. R.; Marder, S. R., Rapid Synthesis of High Surface Area Imine-Linked 2D Covalent Organic Frameworks by Avoiding Pore Collapse During Isolation. *Adv. Mater.* **2019**, 1905776.

161. Auras, F.; Ascherl, L.; Hakimioun, A. H.; Margraf, J. T.; Hanusch, F. C.; Reuter, S.; Bessinger, D.; Doeblinger, M.; Hettstedt, C.; Karaghiosoff, K.; Herbert, S.; Knochel, P.; Clark, T.; Bein, T., Synchronized Offset Stacking: A Concept for Growing Large-Domain and Highly Crystalline 2D Covalent Organic Frameworks. *J. Am. Chem. Soc.* **2016,** *138* (51), 16703-16710.

162. Ascherl, L.; Sick, T.; Margraf, J. T.; Lapidus, S. H.; Calik, M.; Hettstedt, C.; Karaghiosoff, K.; Doeblinger, M.; Clark, T.; Chapman, K. W.; Auras, F.; Bein, T., Molecular docking sites designed for the generation of highly crystalline covalent organic frameworks. *Nat. Chem.* **2016,** *8* (4), 310-316.

163. Keller, N.; Sick, T.; Bach, N. N.; Koszalkowski, A.; Rotter, J. M.; Medina, D. D.; Bein, T., Dibenzochrysene enables tightly controlled docking and stabilizes photoexcited states in dual-pore covalent organic frameworks. *Nanoscale* **2019,** *11* (48), 23338-23345.

164. Salonen, L. M.; Medina, D. D.; Carbo-Argibay, E.; Goesten, M. G.; Mafra, L.; Guldris, N.; Rotter, J. M.; Stroppa, D. G.; Rodriguez-Abreu, C., A supramolecular strategy based on molecular dipole moments for high-quality covalent organic frameworks. *Chem. Commun.* **2016,** *52* (51), 7986-7989.

165. Salonen, L. M.; Medina, D. D.; Carbó-Argibay, E.; Goesten, M. G.; Mafra, L.; Guldris, N.; Rotter, J. M.; Stroppa, D. G.; Rodríguez-Abreu, C., A supramolecular strategy based on molecular dipole moments for high-quality covalent organic frameworks. *Chem. Commun.* **2016,** *52* (51), 7986-7989.

166. Halder, A.; Karak, S.; Addicoat, M.; Bera, S.; Chakraborty, A.; Kunjattu, S. H.; Pachfule, P.; Heine, T.; Banerjee, R., Ultrastable imine-based covalent organic frameworks for

sulfuric acid recovery: an effect of interlayer hydrogen bonding. *Angew. Chem. Int. Ed.* **2018,** *57* (20), 5797-5802.

167. Haase, F.; Gottschling, K.; Stegbauer, L.; Germann, L. S.; Gutzler, R.; Duppel, V.; Vyas, V. S.; Kern, K.; Dinnebier, R. E.; Lotsch, B. V., Tuning the stacking behaviour of a 2D covalent organic framework through non-covalent interactions. *Mater. Chem. Front.* **2017,** *1* (7), 1354-1361.

168. Fan, Y.; Wen, Q.; Zhan, T.-G.; Qi, Q.-Y.; Xu, J.-Q.; Zhao, X., A Case Study on the Influence of Substitutes on Interlayer Stacking of 2D Covalent Organic Frameworks. *Chem. - Eur. J.* **2017,** *23* (24), 5668-5672.

169. Hisaki, I.; Emilya Affendy, N. Q.; Tohnai, N., Precise elucidations of stacking manners of hydrogen-bonded two-dimensional organic frameworks composed of X-shaped π-conjugated systems. *CrystEngComm* **2017,** *19* (33), 4892-4898.

170. Chen, X.; Addicoat, M.; Irle, S.; Nagai, A.; Jiang, D., Control of crystallinity and porosity of covalent organic frameworks by managing interlayer interactions based on self-complementary π-electronic force. *J. AM. Chem. Soc.* **2013,** *135* (2), 546-549.

171. Braunecker, W. A.; Hurst, K. E.; Ray, K. G.; Owczarczyk, Z. R.; Martinez, M. B.; Leick, N.; Keuhlen, A.; Sellinger, A.; Johnson, J. C., Phenyl/perfluorophenyl stacking interactions enhance structural order in two-dimensional covalent organic frameworks. *Cryst. Growth Des.* **2018,** *18* (7), 4160-4166.

172. Jin, S.; Supur, M.; Addicoat, M.; Furukawa, K.; Chen, L.; Nakamura, T.; Fukuzumi, S.; Irle, S.; Jiang, D., Creation of Superheterojunction Polymers via Direct Polycondensation:

Segregated and Bicontinuous Donor-Acceptor π-Columnar Arrays in Covalent Organic Frameworks for Long-Lived Charge Separation. *J. Am. Chem. Soc.* **2015,** *137* (24), 7817-7827.

173. Koo, B. T.; Dichtel, W. R.; Clancy, P., A classification scheme for the stacking of two-dimensional boronate ester-linked covalent organic frameworks. *J. Mater. Chem.* **2012,** *22* (34), 17460-17469.

174. Spitler, E. L.; Koo, B. T.; Novotney, J. L.; Colson, J. W.; Uribe-Romo, F. J.; Gutierrez, G. D.; Clancy, P.; Dichtel, W. R., A 2D covalent organic framework with 4.7-nm pores and insight into its interlayer stacking. *J. Am. Chem. Soc.* **2011,** *133* (48), 19416-19421.

175. Strauss, M. J.; Asheghali, D.; Evans, A. M.; Li, R. L.; Chavez, A. D.; Sun, C.; Becker, M. L.; Dichtel, W. R., Cooperative Self-Assembly of Pyridine-2, 6-Diimine-Linked Macrocycles into Mechanically Robust Nanotubes. *Angew. Chem. Int. Ed.* **2019,** *58* (41), 14708-14714.

176. Strauss, M. J.; Evans, A. M.; Castano, I.; Li, R. L.; Dichtel, W., Supramolecular Polymerization Provides Non-Equilibrium Product Distributions of Imine-Linked Macrocycles. *Chem. Sci.* **2020**.

177. Sun, C.; Shen, M.; Chavez, A. D.; Evans, A. M.; Liu, X.; Harutyunyan, B.; Flanders, N. C.; Hersam, M. C.; Bedzyk, M. J.; de la Cruz, M. O., High aspect ratio nanotubes assembled from macrocyclic iminium salts. *Proc. Nat. Acad. Sci.* **2018,** *115* (36), 8883-8888.

178. Alahakoon, S. B.; Diwakara, S. D.; Thompson, C. M.; Smaldone, R. A., Supramolecular design in 2D covalent organic frameworks. *Chem. Soc. Rev.* **2020,** *49* (5), 1344-1356.

179. Hao, Q.; Zhao, C.; Sun, B.; Lu, C.; Liu, J.; Liu, M.; Wan, L.-J.; Wang, D., Confined synthesis of two-dimensional covalent organic framework thin films within superspreading water layer. *J. Am. Chem. Soc.* **2018,** *140* (38), 12152-12158.

180. Dai, W.; Shao, F.; Szczerbiński, J.; McCaffrey, R.; Zenobi, R.; Jin, Y.; Schlüter, A. D.; Zhang, W., Synthesis of a Two-Dimensional Covalent Organic Monolayer through Dynamic Imine Chemistry at the Air/Water Interface. *Angew. Chem. Int. Ed.* **2016,** *55* (1), 213-217.

181. Dey, K.; Pal, M.; Rout, K. C.; Kunjattu H, S.; Das, A.; Mukherjee, R.; Kharul, U. K.; Banerjee, R., Selective Molecular Separation by Interfacially Crystallized Covalent Organic Framework Thin Films. *J. Am. Chem. Soc.* **2017,** *139* (37), 13083-13091.

182. Dey, K.; Pal, M.; Rout, K. C.; Kunjattu H, S.; Das, A.; Mukherjee, R.; Kharul, U. K.; Banerjee, R. J. J. o. t. A. C. S., Selective molecular separation by interfacially crystallized covalent organic framework thin films. *J. Am. Chem. Soc.* **2017,** *139* (37), 13083-13091.

183. Wang, C.; Li, Z.; Chen, J.; Li, Z.; Yin, Y.; Cao, L.; Zhong, Y.; Wu, H., Covalent organic framework modified polyamide nanofiltration membrane with enhanced performance for desalination. *J. Membr. Sci.* **2017,** *523*, 273-281.

184. Colson, J. W.; Mann, J. A.; De Blase, C. R.; Dichtel, W. R., Patterned growth of oriented 2D covalent organic framework thin films on single-layer graphene. *J. Polym. Sci., Part A: Polym. Chem.* **2015,** *53* (2), 378-384.

185. Spitler, E. L.; Colson, J. W.; Uribe-Romo, F. J.; Woll, A. R.; Giovino, M. R.; Saldivar, A.; Dichtel, W. R., Lattice Expansion of Highly Oriented 2D Phthalocyanine Covalent Organic Framework Films. *Angew. Chem. Int. Ed.* **2012,** *51* (11), 2623-2627, S2623/1-S2623/41.

186. Colson, J. W.; Woll, A. R.; Mukherjee, A.; Levendorf, M. P.; Spitler, E. L.; Shields, V. B.; Spencer, M. G.; Park, J.; Dichtel, W. R., Oriented 2D Covalent Organic Framework Thin Films on Single-Layer Graphene. *Science* **2011,** *332* (6026), 228-231.

187. Diercks, C. S.; Lin, S.; Kornienko, N.; Kapustin, E. A.; Nichols, E. M.; Zhu, C.; Zhao, Y.; Chang, C. J.; Yaghi, O. M., Reticular Electronic Tuning of Porphyrin Active Sites in Covalent Organic Frameworks for Electrocatalytic Carbon Dioxide Reduction. *J. Am. Chem. Soc.* **2018,** *140* (3), 1116-1122.

188. Sick, T.; Hufnagel, A. G.; Kampmann, J.; Kondofersky, I.; Calik, M.; Rotter, J. M.; Evans, A.; Doeblinger, M.; Herbert, S.; Peters, K.; Boehm, D.; Knochel, P.; Medina, D. D.; Fattakhova-Rohlfing, D.; Bein, T., Oriented Films of Conjugated 2D Covalent Organic Frameworks as Photocathodes for Water Splitting. *J. Am. Chem. Soc.* **2018,** *140* (6), 2085-2092.

189. Sun, B.; Zhu, C.-H.; Liu, Y.; Wang, C.; Wan, L.-J.; Wang, D., Oriented Covalent Organic Framework Film on Graphene for Robust Ambipolar Vertical Organic Field-Effect Transistor. *Chem. Mater.* **2017,** *29* (10), 4367-4374.

190. Medina, D. D.; Petrus, M. L.; Jumabekov, A. N.; Margraf, J. T.; Weinberger, S.; Rotter, J. M.; Clark, T.; Bein, T., Directional charge-carrier transport in oriented benzodithiophene covalent organic framework thin films. *ACS Nano* **2017,** *11* (3), 2706-2713.

191. Bisbey, R. P.; DeBlase, C. R.; Smith, B. J.; Dichtel, W. R., Two-dimensional covalent organic framework thin films grown in flow. *J. Am. Chem. Soc.* **2016,** *138* (36), 11433-11436.

192. Gou, X.; Zhang, Q.; Wu, Y.; Zhao, Y.; Shi, X.; Fan, X.; Huang, L.; Lu, G., Preparation and engineering of oriented 2D covalent organic framework thin films. *RSC Adv.* **2016,** *6* (45), 39198-39203.

193. Yang, H.; Zhang, S.; Han, L.; Zhang, Z.; Xue, Z.; Gao, J.; Li, Y.; Huang, C.; Yi, Y.; Liu, H.; Li, Y., High Conductive Two-Dimensional Covalent Organic Framework for Lithium Storage with Large Capacity. *ACS Appl. Mater. Interfaces* **2016,** *8* (8), 5366-5375.

194. Feldblyum, J. I.; McCreery, C. H.; Andrews, S. C.; Kurosawa, T.; Santos, E. J. G.; Duong, V.; Fang, L.; Ayzner, A. L.; Bao, Z., Few-layer, large-area, 2D covalent organic framework semiconductor thin films. *Chem. Commun.* **2015,** *51* (73), 13894-13897.

195. Calik, M.; Auras, F.; Salonen, L. M.; Bader, K.; Grill, I.; Handloser, M.; Medina, D. D.; Dogru, M.; Loebermann, F.; Trauner, D.; Hartschuh, A.; Bein, T., Extraction of Photogenerated Electrons and Holes from a Covalent Organic Framework Integrated Heterojunction. *J. Am. Chem. Soc.* **2014,** *136* (51), 17802-17807.

196. Cai, S.-L.; Zhang, Y.-B.; Pun, A. B.; He, B.; Yang, J.; Toma, F. M.; Sharp, I. D.; Yaghi, O. M.; Fan, J.; Zheng, S.-R.; Zhang, W.-G.; Liu, Y., Tunable electrical conductivity in oriented thin films of tetrathiafulvalene-based covalent organic framework. *Chem. Sci.* **2014,** *5* (12), 4693-4700.

197. Valentino, L.; Matsumoto, M.; Dichtel, W. R.; Marinas, B. J., Development and Performance Characterization of a Polyimine Covalent Organic Framework Thin-Film Composite Nanofiltration Membrane. *Environ Sci Technol* **2017,** *51* (24), 14352-14359.

198. Khayum, M. A.; Kandambeth, S.; Mitra, S.; Nair, S. B.; Das, A.; Nagane, S. S.; Mukherjee, R.; Banerjee, R., Chemically Delaminated Free-Standing Ultrathin Covalent Organic Nanosheets. *Angew. Chem. Int. Ed.* **2016,** *55* (50), 15604-15608.

199. Kandambeth, S.; Biswal, B. P.; Chaudhari, H. D.; Rout, K. C.; Kunjattu H, S.; Mitra, S.; Karak, S.; Das, A.; Mukherjee, R.; Kharul, U. K.; Banerjee, R., Selective Molecular Sieving in Self-Standing Porous Covalent-Organic-Framework Membranes. *Adv. Mater.* **2017,** *29* (2), n/a.

200. Sasmal, H. S.; Aiyappa, H. B.; Bhange, S. N.; Karak, S.; Halder, A.; Kurungot, S.; Banerjee, R., Superprotonic conductivity in flexible porous covalent organic framework membranes. *Angew. Chem. Int. Ed.* **2018,** *130* (34), 11060-11064.

201. Dey, K.; Kunjattu H, S.; Chahande, A. M.; Banerjee, R., Nanoparticle Size-Fractionation through Self-Standing Porous Covalent Organic Framework Films. *Angew. Chem. Int. Ed.* **2020,** *132* (3), 1177-1181.

202. Müller, V.; Shao, F.; Baljozovic, M.; Moradi, M.; Zhang, Y.; Jung, T.; Thompson, W. B.; King, B. T.; Zenobi, R.; Schlüter, A. D., Structural characterization of a covalent monolayer sheet obtained by two-dimensional polymerization at an air/water interface. *Angew. Chem. Int. Ed.* **2017,** *56* (48), 15262-15266.

203. Zhong, Y.; Cheng, B.; Park, C.; Ray, A.; Brown, S.; Mujid, F.; Lee, J.-U.; Zhou, H.; Suh, J.; Lee, K.-H., Wafer-scale synthesis of monolayer two-dimensional porphyrin polymers for hybrid superlattices. *Science*

2019, *366* (6471), 1379-1384.

204. Park, S.; Liao, Z.; Ibarlucea, B.; Qi, H.; Lin, H. H.; Becker, D.; Melidonie, J.; Zhang, T.; Sahabudeen, H.; Baraban, L., Two-Dimensional Boronate Ester Covalent Organic Framework Thin Films with Large Single Crystalline Domains for a Neuromorphic Memory Device. *Angew. Chem. Int. Ed.* **2020,** *59* (21), 8218-8224.

205. Kandambeth, S.; Dey, K.; Banerjee, R., Covalent organic frameworks: chemistry beyond the structure. *J. Am. Chem. Soc.* **2018,** *141* (5), 1807-1822.

206. Wang, H.; Zeng, Z.; Xu, P.; Li, L.; Zeng, G.; Xiao, R.; Tang, Z.; Huang, D.; Tang, L.; Lai, C., Recent progress in covalent organic framework thin films: fabrications, applications and perspectives. *Chem. Soc. Rev.* **2019,** *48* (2), 488-516.

207. Zhang, B.; Wei, M.; Mao, H.; Pei, X.; Alshmimri, S. A.; Reimer, J. A.; Yaghi, O. M., Crystalline dioxin-linked covalent organic frameworks from irreversible reactions. *J. Am. Chem. Soc.* **2018,** *140* (40), 12715-12719.

208. Jin, E.; Lan, Z.; Jiang, Q.; Geng, K.; Li, G.; Wang, X.; Jiang, D., 2D sp2 Carbon-Conjugated Covalent Organic Frameworks for Photocatalytic Hydrogen Production from Water. *Chem* **2019,** *5* (6), 1632-1647.

209. Zhuang, X.; Zhao, W.; Zhang, F.; Cao, Y.; Liu, F.; Bi, S.; Feng, X., A two-dimensional conjugated polymer framework with fully sp2-bonded carbon skeleton. *Polym. Chem.* **2016,** *7* (25), 4176-4181.

210. Lyu, H.; Diercks, C. S.; Zhu, C.; Yaghi, O. M., Porous Crystalline Olefin-Linked Covalent Organic Frameworks. *J. Am. Chem. Soc.* **2019,** *141* (17), 6848-6852.

211. Lyle, S. J.; Waller, P. J.; Yaghi, O. M., Covalent organic frameworks: organic chemistry extended into two and three dimensions. *Trends in Chemistry* **2019**.

212. Waller, P. J.; Lyle, S. J.; Osborn Popp, T. M.; Diercks, C. S.; Reimer, J. A.; Yaghi, O. M., Chemical Conversion of Linkages in Covalent Organic Frameworks. *J. Am. Chem. Soc.* **2016,** *138* (48), 15519-15522.

213. El-Kaderi, H. M.; Hunt, J. R.; Mendoza-Cortes, J. L.; Cote, A. P.; Taylor, R. E.; O'Keeffe, M.; Yaghi, O. M., Designed synthesis of 3D covalent organic frameworks. *Science* **2007,** *316* (5822), 268-72.

214. Wan, S.; Guo, J.; Kim, J.; Ihee, H.; Jiang, D., A photoconductive covalent organic framework: self-condensed arene cubes composed of eclipsed 2D polypyrene sheets for photocurrent generation. *Angew Chem Int Ed* **2009,** *48* (30), 5439-42.

215. Bunck, D. N.; Dichtel, W. R., Internal functionalization of three-dimensional covalent organic frameworks. *Angew Chem Int Ed* **2012,** *51* (8), 1885-9.

216. Bunck, D. N.; Dichtel, W. R., Postsynthetic functionalization of 3D covalent organic frameworks. *Chem Commun* **2013,** *49* (24), 2457-9.

217. Brucks, S. D.; Bunck, D. N.; Dichtel, W. R., Functionalization of 3D covalent organic frameworks using monofunctional boronic acids. *Polymer* **2014,** *55* (1), 330-334.

218. Du, Y.; Calabro, D.; Wooler, B.; Kortunov, P.; Li, Q. C.; Cundy, S.; Mao, K. M., One Step Facile Synthesis of Amine-Functionalized COF-1 with Enhanced Hydrostability. *Chem Mater* **2015,** *27* (5), 1445-1447.

219. Toffoli, D.; Stredansky, M.; Feng, Z.; Balducci, G.; Furlan, S.; Stener, M.; Ustunel, H.; Cvetko, D.; Kladnik, G.; Morgante, A.; Verdini, A.; Dri, C.; Comelli, G.; Fronzoni, G.; Cossaro, A., Electronic properties of the boroxine-gold interface: evidence of ultra-fast charge delocalization. *Chem. Sci.* **2017,** *8* (5), 3789-3798.

220. Yue, J.-Y.; Mo, Y.-P.; Li, S.-Y.; Dong, W.-L.; Chen, T.; Wang, D., Simultaneous construction of two linkages for the on-surface synthesis of imine-boroxine hybrid covalent organic frameworks. *Chem. Sci.* **2017,** *8* (3), 2169-2174.

221. Wang, R.-N.; Zhang, X.-R.; Wang, S.-F.; Fu, G.-S.; Wang, J.-L., Flatbands in 2D boroxine-linked covalent organic frameworks. *Phys. Chem. Chem. Phys.* **2016,** *18* (2), 1258-1264.

222. Wu, Y.; Liu, L.; Su, J.; Yan, K.; Zhu, J.; Zhao, Y., Synthesis of digermylene-stabilized linear tetraboronate and boroxine. *Chem. Commun.* **2016,** *52* (8), 1582-1585.

223. Plas, J.; Ivasenko, O.; Martsinovich, N.; Lackinger, M.; De Feyter, S., Nanopatterning of a covalent organic framework host-guest system. *Chem. Commun.* **2016,** *52* (1), 68-71.

224. Du, Y.; Calabro, D.; Wooler, B.; Kortunov, P.; Li, Q.; Cundy, S.; Mao, K., One Step Facile Synthesis of Amine-Functionalized COF-1 with Enhanced Hydrostability. *Chem. Mater.* **2015,** *27* (5), 1445-1447.

225. Smith, M. K.; Northrop, B. H., Vibrational Properties of Boroxine Anhydride and Boronate Ester Materials: Model Systems for the Diagnostic Characterization of Covalent Organic Frameworks. *Chem. Mater.* **2014,** *26* (12), 3781-3795.

226. Faury, T.; Clair, S.; Abel, M.; Dumur, F.; Gigmes, D.; Porte, L., Sequential Linking To Control Growth of a Surface Covalent Organic Framework. *J. Phys. Chem. C* **2012,** *116* (7), 4819-4823.

227. Schlögl, S.; Sirtl, T.; Eichhorn, J.; Heckl, W. M.; Lackinger, M., Synthesis of two-dimensional phenylene–boroxine networks through in vacuo condensation and on-surface radical addition. *Chem. Commun.* **2011,** *47* (45), 12355-12357.

228. Korich, A. L.; Iovine, P. M., Boroxine chemistry and applications: A perspective. *Dalton Trans.* **2010,** *39* (6), 1423-1431.

229. Zwaneveld, N. A. A.; Pawlak, R.; Abel, M.; Catalin, D.; Gigmes, D.; Bertin, D.; Porte, L., Organized Formation of 2D Extended Covalent Organic Frameworks at Surfaces. *J. Am. Chem. Soc.* **2008,** *130* (21), 6678-6679.

230. Liu, J.; Lavigne, J. J. In *Boronic acids in materials chemistry*, Wiley-VCH Verlag GmbH & Co. KGaA: 2011; pp 621-676.

231. Lanni, L. M.; Tilford, R. W.; Bharathy, M.; Lavigne, J. J., Enhanced Hydrolytic Stability of Self-Assembling Alkylated Two-Dimensional Covalent Organic Frameworks. *J. Am. Chem. Soc.* **2011,** *133* (35), 13975-13983.

232. Tilford, R. W.; Mugavero, S. J., III; Pellechia, P. J.; Lavigne, J. J., Tailoring microporosity in covalent organic frameworks. *Adv. Mater.* **2008,** *20* (14), 2741-2746.

233. Han, S. S.; Furukawa, H.; Yaghi, O. M.; Goddard, W. A., III, Covalent Organic Frameworks as Exceptional Hydrogen Storage Materials. *J. Am. Chem. Soc.* **2008,** *130* (35), 11580-11581.

234. Cote, A. P.; El-Kaderi, H. M.; Furukawa, H.; Hunt, J. R.; Yaghi, O. M., Reticular Synthesis of Microporous and Mesoporous 2D Covalent Organic Frameworks. *J. Am. Chem. Soc.* **2007,** *129* (43), 12914-12915.

235. Doonan, C. J.; Tranchemontagne, D. J.; Glover, T. G.; Hunt, J. R.; Yaghi, O. M., Exceptional ammonia uptake by a covalent organic framework. *Nat. Chem.* **2010,** *2* (3), 235-238.

236. Medina, D. D.; Rotter, J. M.; Hu, Y.; Dogru, M.; Werner, V.; Auras, F.; Markiewicz, J. T.; Knochel, P.; Bein, T., Room Temperature Synthesis of Covalent-Organic Framework Films through Vapor-Assisted Conversion. *J. Am. Chem. Soc.* **2015,** *137* (3), 1016-1019.

237. Bertrand, G. H. V.; Michaelis, V. K.; Ong, T.-C.; Griffin, R. G.; Mircea, D., Thiophene-based covalent organic frameworks. *Proc. Natl. Acad. Sci.* **2013,** (Mar. 11 2013), 1-6, 6 pp.

238. Dogru, M.; Handloser, M.; Auras, F.; Kunz, T.; Medina, D.; Hartschuh, A.; Knochel, P.; Bein, T., A Photoconductive Thienothiophene-Based Covalent Organic Framework Showing Charge Transfer Towards Included Fullerene. *Angew. Chem. Int. Ed.* **2013,** *52* (10), 2920-2924.

239. Huang, N.; Ding, X.; Kim, J.; Ihee, H.; Jiang, D., A Photoresponsive Smart Covalent Organic Framework. *Angew. Chem. Int. Ed.* **2015,** *54* (30), 8704-8707.

240. Singh, H.; Tomer, V. K.; Jena, N.; Bala, I.; Sharma, N.; Nepak, D.; De Sarkar, A.; Kailasam, K.; Pal, S. K., A porous, crystalline truxene-based covalent organic framework and its application in humidity sensing. *J. Mater. Chem. A* **2017,** *5* (41), 21820-21827.

241. Dalapati, S.; Jin, E.; Addicoat, M.; Heine, T.; Jiang, D., Highly Emissive Covalent Organic Frameworks. *J. Am. Chem. Soc.* **2016,** *138* (18), 5797-5800.

242. Ding, X.; Chen, L.; Honsho, Y.; Feng, X.; Saengsawang, O.; Guo, J.; Saeki, A.; Seki, S.; Irle, S.; Nagase, S.; Parasuk, V.; Jiang, D., An n-channel two-dimensional covalent organic framework. *J. Am. Chem. Soc.* **2011,** *133* (37), 14510-14513.

243. Feng, X.; Liu, L.; Honsho, Y.; Saeki, A.; Seki, S.; Irle, S.; Dong, Y.; Nagai, A.; Jiang, D., High-Rate Charge-Carrier Transport in Porphyrin Covalent Organic Frameworks: Switching from Hole to Electron to Ambipolar Conduction. *Angew. Chem. Int. Ed.* **2012,** *51* (11), 2618-2622, S2618/1-S2618/91.

244. Liu, C.; Zhang, W.; Zeng, Q.; Lei, S., A Photoresponsive Surface Covalent Organic Framework: Surface-Confined Synthesis, Isomerization, and Controlled Guest Capture and Release. *Chem. - Eur. J.* **2016,** *22* (20), 6768-6773.

245. Neti, V. S. P. K.; Wu, X.; Hosseini, M.; Bernal, R. A.; Deng, S.; Echegoyen, L., Synthesis of a phthalocyanine 2D covalent organic framework. *CrystEngComm* **2013,** *15* (36), 7157-7160.

246. Ding, X.; Feng, X.; Saeki, A.; Seki, S.; Nagai, A.; Jiang, D., Conducting metallophthalocyanine 2D covalent organic frameworks: the role of central metals in controlling π-electronic functions. *Chem. Commun.* **2012,** *48* (71), 8952-8954.

247. Spitler, E. L.; Giovino, M. R.; White, S. L.; Dichtel, W. R., A mechanistic study of Lewis acid-catalyzed covalent organic framework formation. *Chem. Sci.* **2011,** *2* (8), 1588-1593.

248. Ding, X.; Guo, J.; Feng, X.; Honsho, Y.; Guo, J.; Seki, S.; Maitarad, P.; Saeki, A.; Nagase, S.; Jiang, D., Synthesis of Metallophthalocyanine Covalent Organic Frameworks That Exhibit High Carrier Mobility and Photoconductivity. *Angew. Chem. Int. Ed.* **2011,** *50* (6), 1289-1293, S1289/1-S1289/19.

249. Spitler, E. L.; Dichtel, W. R., Lewis acid-catalysed formation of two-dimensional phthalocyanine covalent organic frameworks. *Nat. Chem.* **2010,** *2* (8), 672-677.

250. Jackson, K. T.; Reich, T. E.; El-Kaderi, H. M., Targeted synthesis of a porous borazine-linked covalent organic framework. *Chem. Commun.* **2012,** *48* (70), 8823-8825.

251. Zhang, Y.; Duan, J.; Ma, D.; Li, P.; Li, S.; Li, H.; Zhou, J.; Ma, X.; Feng, X.; Wang, B., Three-Dimensional Anionic Cyclodextrin-Based Covalent Organic Frameworks. *Angew Chem Int Ed* **2017,** *56* (51), 16313-16317.

252. Du, Y.; Yang, H.; Whiteley, J. M.; Wan, S.; Jin, Y.; Lee, S. H.; Zhang, W., Ionic Covalent Organic Frameworks with Spiroborate Linkage. *Angew Chem Int Ed* **2016,** *55* (5), 1737-41.

253. Hunt, J. R.; Doonan, C. J.; LeVangie, J. D.; Cote, A. P.; Yaghi, O. M., Reticular synthesis of covalent organic borosilicate frameworks. *J Am Chem Soc* **2008,** *130* (36), 11872-3.

254. Segura, J. L.; Mancheno, M. J.; Zamora, F., Covalent organic frameworks based on Schiff-base chemistry: synthesis, properties and potential applications. *Chem. Soc. Rev.* **2016,** *45* (20), 5635-5671.

255. Segura, J. L.; Mancheno, M. J.; Zamora, F., Covalent organic frameworks based on Schiff-base chemistry: synthesis, properties and potential applications. *Chem Soc Rev* **2016,** *45* (20), 5635-5671.

256. Banerjee, R.; Champness, N. R., Covalent organic frameworks and organic cage structures. *CrystEngComm* **2017,** *19* (33), 4866-4867.

257. Ding, S.-Y.; Gao, J.; Wang, Q.; Zhang, Y.; Song, W.-G.; Su, C.-Y.; Wang, W., Construction of Covalent Organic Framework for Catalysis: Pd/COF-LZU1 in Suzuki-Miyaura Coupling Reaction. *J. Am. Chem. Soc.* **2011,** *133* (49), 19816-19822.

258. Romero-Muñiz, I.; Mavrandonakis, A.; Albacete, P.; Vega, A.; Briois, V.; Zamora, F.; Platero-Prats, A. E., Unveiling the Local Structure of Palladium Loaded into Imine-Linked Layered Covalent Organic Frameworks for Cross-Coupling Catalysis. *Angew. Chem. Int. Ed.* **2020**.

259. Uribe-Romo, F. J.; Hunt, J. R.; Furukawa, H.; Klöck, C.; O'Keeffe, M.; Yaghi, O. M., A Crystalline Imine-Linked 3-D Porous Covalent Organic Framework. *Journal of the American Chemical Society* **2009,** *131* (13), 4570-4571.

260. Kaleeswaran, D.; Vishnoi, P.; Murugavel, R., [3+3] Imine and β-ketoenamine tethered fluorescent covalent-organic frameworks for CO2 uptake and nitroaromatic sensing. *J. Mater. Chem. C* **2015,** *3* (27), 7159-7171.

261. Chen, X.; Addicoat, M.; Jin, E.; Zhai, L.; Xu, H.; Huang, N.; Guo, Z.; Liu, L.; Irle, S.; Jiang, D., Locking Covalent Organic Frameworks with Hydrogen Bonds: General and Remarkable Effects on Crystalline Structure, Physical Properties, and Photochemical Activity. *J. Am. Chem. Soc.* **2015,** *137* (9), 3241-3247.

262. Wang, P.; Kang, M.; Sun, S.; Liu, Q.; Zhang, Z.; Fang, S., Imine-Linked Covalent Organic Framework on Surface for Biosensor. *Chin. J. Chem.* **2014,** *32* (9), 838-843.

263. Zhang, Y.-B.; Su, J.; Furukawa, H.; Yun, Y.; Gandara, F.; Duong, A.; Zou, X.; Yaghi, O. M., Single-Crystal Structure of a Covalent Organic Framework. *J. Am. Chem. Soc.* **2013,** *135* (44), 16336-16339.

264. Huang, W.; Jiang, Y.; Li, X.; Li, X.; Wang, J.; Wu, Q.; Liu, X., Solvothermal Synthesis of Microporous, Crystalline Covalent Organic Framework Nanofibers and Their Colorimetric Nanohybrid Structures. *ACS Appl. Mater. Interfaces* **2013,** *5* (18), 8845-8849.

265. Rabbani, M. G.; Sekizkardes, A. K.; Kahveci, Z.; Reich, T. E.; Ding, R.; El-Kaderi, H. M., A 2D mesoporous imine-linked covalent organic framework for high pressure gas storage applications. *Chem. - Eur. J.* **2013,** *19* (10), 3324-3328.

266. de la Pena Ruigomez, A.; Rodriguez-San-Miguel, D.; Stylianou, K. C.; Cavallini, M.; Gentili, D.; Liscio, F.; Milita, S.; Roscioni, O. M.; Ruiz-Gonzalez, M. L.; Carbonell, C.; Maspoch, D.; Mas-Balleste, R.; Segura, J. L.; Zamora, F., Direct On-Surface Patterning of a Crystalline Laminar Covalent Organic Framework Synthesized at Room Temperature. *Chem. - Eur. J.* **2015,** *21* (30), 10666-10670.

267. Liu, X.-H.; Guan, C.-Z.; Ding, S.-Y.; Wang, W.; Yan, H.-J.; Wang, D.; Wan, L.-J., On-Surface Synthesis of Single-Layered Two-Dimensional Covalent Organic Frameworks via Solid-Vapor Interface Reactions. *J. Am. Chem. Soc.* **2013,** *135* (28), 10470-10474.

268. Wu, Y.; Xu, H.; Chen, X.; Gao, J.; Jiang, D., A π-electronic covalent organic framework catalyst: π-walls as catalytic beds for Diels-Alder reactions under ambient conditions. *Chem. Commun.* **2015,** *51* (50), 10096-10098.

269. Liu, T.; Hu, X.; Wang, Y.; Meng, L.; Zhou, Y.; Zhang, J.; Chen, M.; Zhang, X., Triazine-based covalent organic frameworks for photodynamic inactivation of bacteria as type-II photosensitizers. *J. Photochem. Photobiol., B* **2017,** *175*, 156-162.

270. Dong, W.-l.; Wang, L.; Ding, H.-m.; Zhao, L.; Wang, D.; Wang, C.; Wan, L.-J., Substrate Orientation Effect in the On-Surface Synthesis of Tetrathiafulvalene-Integrated Single-Layer Covalent Organic Frameworks. *Langmuir* **2015,** *31* (43), 11755-11759.

271. Dalapati, S.; Addicoat, M.; Jin, S.; Sakurai, T.; Gao, J.; Xu, H.; Irle, S.; Seki, S.; Jiang, D., Rational design of crystalline supermicroporous covalent organic frameworks with triangular topologies. *Nat. Commun.* **2015,** *6*, 7786.

272. Banerjee, T.; Haase, F.; Savasci, G.; Gottschling, K.; Ochsenfeld, C.; Lotsch, B. V., Single Site Photocatalytic H2 Evolution from Covalent Organic Frameworks with Molecular Cobaloxime Co-catalysts. *J. Am. Chem. Soc.* **2017**, Ahead of Print.

273. Sun, Q.; Aguila, B.; Ma, S., A bifunctional covalent organic framework as an efficient platform for cascade catalysis. *Mater. Chem. Front.* **2017,** *1* (7), 1310-1316.

274. Rozhko, E.; Bavykina, A.; Osadchii, D.; Makkee, M.; Gascon, J., Covalent organic frameworks as supports for a molecular Ni based ethylene oligomerization catalyst for the synthesis of long chain olefins. *J. Catal.* **2017,** *345*, 270-280.

275. Khattak, A. M.; Ali Ghazi, Z.; Liang, B.; Ali Khan, N.; Iqbal, A.; Li, L.; Tang, Z., A redox-active 2D covalent organic framework with pyridine moieties capable of faradaic energy storage. *J. Mater. Chem. A* **2016,** *4* (42), 16312-16317.

276. Aiyappa, H. B.; Thote, J.; Shinde, D. B.; Banerjee, R.; Kurungot, S., Cobalt-Modified Covalent Organic Framework as a Robust Water Oxidation Electrocatalyst. *Chem. Mater.* **2016,** *28* (12), 4375-4379.

277. Leng, W.; Peng, Y.; Zhang, J.; Lu, H.; Feng, X.; Ge, R.; Dong, B.; Wang, B.; Hu, X.; Gao, Y., Sophisticated Design of Covalent Organic Frameworks with Controllable Bimetallic Docking for a Cascade Reaction. *Chem. - Eur. J.* **2016,** *22* (27), 9087-9091.

278. Xu, S.-Q.; Zhan, T.-G.; Wen, Q.; Pang, Z.-F.; Zhao, X., Diversity of Covalent Organic Frameworks (COFs): A 2D COF Containing Two Kinds of Triangular Micropores of Different Sizes. *ACS Macro Lett.* **2016,** *5* (1), 99-102.

279. Zhou, T.-Y.; Xu, S.-Q.; Wen, Q.; Pang, Z.-F.; Zhao, X., One-Step Construction of Two Different Kinds of Pores in a 2D Covalent Organic Framework. *J. Am. Chem. Soc.* **2014,** *136* (45), 15885-15888.

280. Huang, W.; Ma, B. C.; Lu, H.; Li, R.; Wang, L.; Landfester, K.; Zhang, K. A. I., Visible-Light-Promoted Selective Oxidation of Alcohols Using a Covalent Triazine Framework. *ACS Catal.* **2017,** *7* (8), 5438-5442.

281. Keller, N.; Bessinger, D.; Reuter, S.; Calik, M.; Ascherl, L.; Hanusch, F. C.; Auras, F.; Bein, T., Oligothiophene-Bridged Conjugated Covalent Organic Frameworks. *J. Am. Chem. Soc.* **2017,** *139* (24), 8194-8199.

282. Chen, Y.; Cui, H.; Zhang, J.; Zhao, K.; Ding, D.; Guo, J.; Li, L.; Tian, Z.; Tang, Z., Surface growth of highly oriented covalent organic framework thin film with enhanced photoresponse speed. *RSC Adv.* **2015,** *5* (112), 92573-92576.

283. Hynek, J.; Zelenka, J.; Rathousky, J.; Kubat, P.; Ruml, T.; Demel, J.; Lang, K., Designing Porphyrinic Covalent Organic Frameworks for the Photodynamic Inactivation of Bacteria. *ACS Appl. Mater. Interfaces* **2018,** *10* (10), 8527-8535.

284. Gole, B.; Stepanenko, V.; Rager, S.; Gruene, M.; Medina, D. D.; Bein, T.; Wuerthner, F.; Beuerle, F., Microtubular Self-Assembly of Covalent Organic Frameworks. *Angew. Chem. Int. Ed.* **2018,** *57* (3), 846-850.

285. Wang, K.; Qi, D.; Li, Y.; Wang, T.; Liu, H.; Jiang, J., Tetrapyrrole macrocycle based conjugated two-dimensional mesoporous polymers and covalent organic frameworks: From synthesis to material applications. *Coord. Chem. Rev.* **2017**, Ahead of Print.

286. Xu, K.; Dai, Y.; Ye, B.; Wang, H., Two dimensional covalent organic framework materials for chemical fixation of carbon dioxide: excellent repeatability and high selectivity. *Dalton Trans.* **2017,** *46* (33), 10780-10785.

287. Bhunia, S.; Das, S. K.; Jana, R.; Peter, S. C.; Bhattacharya, S.; Addicoat, M.; Bhaumik, A.; Pradhan, A., Electrochemical Stimuli-Driven Facile Metal-Free Hydrogen Evolution from Pyrene-Porphyrin-Based Crystalline Covalent Organic Framework. *ACS Appl. Mater. Interfaces* **2017,** *9* (28), 23843-23851.

288. Hou, Y.; Zhang, X.; Wang, C.; Qi, D.; Gu, Y.; Wang, Z.; Jiang, J., Novel imine-linked porphyrin covalent organic frameworks with good adsorption removing properties of RhB. *New J. Chem.* **2017,** *41* (14), 6145-6151.

289. Fan, X.; Kong, F.; Kong, A.; Chen, A.; Zhou, Z.; Shan, Y., Covalent Porphyrin Framework-Derived Fe2P@Fe4N-Coupled Nanoparticles Embedded in N-Doped Carbons as Efficient Trifunctional Electrocatalysts. *ACS Appl. Mater. Interfaces* **2017,** *9* (38), 32840-32850.

290. Li, Z.-J.; Ding, S.-Y.; Xue, H.-D.; Cao, W.; Wang, W., Synthesis of -C=N- linked covalent organic frameworks via the direct condensation of acetals and amines. *Chem. Commun.* **2016,** *52* (45), 7217-7220.

291. Uribe-Romo, F. J.; Doonan, C. J.; Furukawa, H.; Oisaki, K.; Yaghi, O. M., Crystalline covalent organic frameworks with hydrazone linkages. *J Am Chem Soc* **2011,** *133* (30), 11478-81.

292. Bunck, D. N.; Dichtel, W. R., Bulk synthesis of exfoliated two-dimensional polymers using hydrazone-linked covalent organic frameworks. *J Am Chem Soc* **2013,** *135* (40), 14952-5.

293. Stegbauer, L.; Schwinghammer, K.; Lotsch, B. V., A hydrazone-based covalent organic framework for photocatalytic hydrogen production. *Chem Sci* **2014,** *5* (7), 2789-2793.

294. Li, X.; Qiao, J.; Chee, S. W.; Xu, H.-S.; Zhao, X.; Choi, H. S.; Yu, W.; Quek, S. Y.; Mirsaidov, U.; Loh, K. P., Rapid, Scalable Construction of Highly Crystalline Acylhydrazone Two-Dimensional Covalent Organic Frameworks via Dipole-Induced Antiparallel Stacking. *J. Am. Chem. Soc.* **2020,** *142* (10), 4932-4943.

295. Chen, G.-J.; Li, X.-B.; Zhao, C.-C.; Ma, H.-C.; Kan, J.; Xin, Y.-B.; Chen, C.-X.; Dong, Y.-B., Ru NPs-Loaded Covalent Organic Framework for Solvent-Free One-Pot Tandem Reactions in Air. *Inorg. Chem.* **2018**, Ahead of Print.

296. Zhang, K.; Cai, S.-L.; Yan, Y.-L.; He, Z.-H.; Lin, H.-M.; Huang, X.-L.; Zheng, S.-R.; Fan, J.; Zhang, W.-G., Construction of a new hydrazone-linked chiral covalent organic framework-silica composite as the stationary phase for high performance liquid chromatography. *J. Chromatogr. A* **2017,** *1519*, 100-109.

297. Liu, W.; Su, Q.; Ju, P.; Guo, B.; Zhou, H.; Li, G.; Wu, Q., A Hydrazone-Based Covalent Organic Framework as an Efficient and Reusable Photocatalyst for the Cross-Dehydrogenative Coupling Reaction of N-Aryltetrahydroisoquinolines. *ChemSusChem* **2017,** *10* (4), 664-669.

298. Wu, M.; Chen, G.; Ma, J.; Liu, P.; Jia, Q., Fabrication of cross-linked hydrazone covalent organic frameworks by click chemistry and application to solid phase microextraction. *Talanta* **2016,** *161*, 350-358.

299. Chakravarty, C.; Mandal, B.; Sarkar, P., Multifunctionalities of an Azine-Linked Covalent Organic Framework: From Nanoelectronics to Nitroexplosive Detection and Conductance Switching. *J Phys Chem C* **2018,** *122* (6), 3245-3255.

300. Dalapati, S.; Jin, S.; Gao, J.; Xu, Y.; Nagai, A.; Jiang, D., An azine-linked covalent organic framework. *J Am Chem Soc* **2013,** *135* (46), 17310-3.

301. Chen, W.; Huang, L.; Yi, X.; Zheng, A., Lithium doping on 2D squaraine-bridged covalent organic polymers for enhancing adsorption properties: a theoretical study. *Phys Chem Chem Phys* **2018,** *20* (9), 6487-6499.

302. Huang, L.; Cao, G., 2D Squaraine-Linked Polymers with High Lithium Storage Capacity Using the First Principle Methods. *Chemistryselect* **2017,** *2* (4), 1728-1733.

303. Huang, L.; Cao, G., 2D Squaraine-Bridged Covalent Organic Polymers with Promising CO2Storage and Separation Properties. *Chemistryselect* **2016,** *1* (3), 533-538.

304. Chen, X.; Addicoat, M.; Irle, S.; Nagai, A.; Jiang, D.-e., Control of Crystallinity and Porosity of Covalent Organic Frameworks by Managing Interlayer Interactions Based on Self-Complimentary Pi-Electronic Force. *J. Am. Chem. Soc.* **2013,** *135*, 546-549.

305. Han, X.; Xia, Q.; Huang, J.; Liu, Y.; Tan, C.; Cui, Y., Chiral Covalent Organic Frameworks with High Chemical Stability for Heterogeneous Asymmetric Catalysis. *J. Am. Chem. Soc.* **2017,** *139* (25), 8693-8697.

306. Wang, R.; Chen, Z., A covalent organic framework-based magnetic sorbent for solid phase extraction of polycyclic aromatic hydrocarbons, and its hyphenation to HPLC for quantitation. *Microchim. Acta* **2017,** *184* (10), 3867-3874.

307. Huang, L.; Cao, G., Two dimensional Squaraine-Bridged Covalent Organic Polymers with Promising CO2 Storage and Separation Properties. *Chemistryselect* **2016,** *1* (3), 533-538.

308. Nagai, A.; Chen, X.; Feng, X.; Ding, X.; Guo, Z.; Jiang, D., A Squaraine-Linked Mesoporous Covalent Organic Framework. *Angew. Chem. Int. Ed.* **2013,** *52* (13), 3770-3774.

309. Kandambeth, S.; Mallick, A.; Lukose, B.; Mane, M. V.; Heine, T.; Banerjee, R., Construction of Crystalline 2D Covalent Organic Frameworks with Remarkable Chemical (Acid/Base) Stability via a Combined Reversible and Irreversible Route. *J. Am. Chem. Soc.* **2012,** *134* (48), 19524-19527.

310. Banerjee, T.; Gottschling, K.; Savasci, G.; Ochsenfeld, C.; Lotsch, B. V., H2 Evolution with Covalent Organic Framework Photocatalysts. *ACS Energy Lett.* **2018,** *3* (2), 400-409.

311. Chandra, S.; Kundu, T.; Dey, K.; Addicoat, M.; Heine, T.; Banerjee, R., Interplaying Intrinsic and Extrinsic Proton Conductivities in Covalent Organic Frameworks. *Chem. Mater.* **2016,** *28* (5), 1489-1494.

312. Shinde, D. B.; Aiyappa, H. B.; Bhadra, M.; Biswal, B. P.; Wadge, P.; Kandambeth, S.; Garai, B.; Kundu, T.; Kurungot, S.; Banerjee, R., A mechanochemically synthesized covalent organic framework as a proton-conducting solid electrolyte. *J. Mater. Chem. A* **2016,** *4* (7), 2682-2690.

313. Thote, J.; Balaji, S. D.; Barike, A. H.; Kandambeth, S.; Biswal, B. P.; Banerjee, R.; Rahul, K. R.; Chaki, R. N., Constructing covalent organic frameworks in water via dynamic covalent bonding. *IUCrJ* **2016,** *3* (Pt 6), 402-407.

314. Biswal, B. P.; Kandambeth, S.; Chandra, S.; Shinde, D. B.; Bera, S.; Karak, S.; Garai, B.; Kharul, U. K.; Banerjee, R., Pore surface engineering in porous, chemically stable covalent organic frameworks for water adsorption. *J. Mater. Chem. A* **2015,** *3* (47), 23664-23669.

315. Das, G.; Balaji Shinde, D.; Kandambeth, S.; Biswal, B. P.; Banerjee, R., Mechanosynthesis of imine, β-ketoenamine, and hydrogen-bonded imine-linked covalent organic frameworks using liquid-assisted grinding. *Chem. Commun.* **2014,** *50* (84), 12615-12618.

316. Pachfule, P.; Kandambeth, S.; Diaz Diaz, D.; Banerjee, R., Highly stable covalent organic framework-Au nanoparticles hybrids for enhanced activity for nitrophenol reduction. *Chem. Commun.* **2014,** *50* (24), 3169-3172.

317. Chandra, S.; Kundu, T.; Kandambeth, S.; Babarao, R.; Marathe, Y.; Kunjir, S. M.; Banerjee, R., Phosphoric Acid Loaded Azo Based Covalent Organic Framework for Proton Conduction. *J. Am. Chem. Soc.* **2014,** *136* (18), 6570-6573.

318. Chandra, S.; Kandambeth, S.; Biswal, B. P.; Lukose, B.; Kunjir, S. M.; Chaudhary, M.; Babarao, R.; Heine, T.; Banerjee, R., Chemically Stable Multilayered Covalent Organic

Nanosheets from Covalent Organic Frameworks via Mechanical Delamination. *J. Am. Chem. Soc.* **2013,** *135* (47), 17853-17861.

319. Biswal, B. P.; Chandra, S.; Kandambeth, S.; Lukose, B.; Heine, T.; Banerjee, R., Mechanochemical Synthesis of Chemically Stable Isoreticular Covalent Organic Frameworks. *J. Am. Chem. Soc.* **2013,** *135* (14), 5328-5331.

320. Pachfule, P.; Acharjya, A.; Roeser, J.; Langenhahn, T.; Schwarze, M.; Schomaecker, R.; Thomas, A.; Schmidt, J., Diacetylene Functionalized Covalent Organic Framework (COF) for Photocatalytic Hydrogen Generation. *J. Am. Chem. Soc.* **2018,** *140* (4), 1423-1427.

321. Zhang, Y.; Shen, X.; Feng, X.; Xia, H.; Mu, Y.; Liu, X., Covalent organic frameworks as pH responsive signaling scaffolds. *Chem. Commun.* **2016,** *52* (74), 11088-11091.

322. Lohse, M. S.; Stassin, T.; Naudin, G.; Wuttke, S.; Ameloot, R.; De Vos, D.; Medina, D. D.; Bein, T., Sequential Pore Wall Modification in a Covalent Organic Framework for Application in Lactic Acid Adsorption. *Chem. Mater.* **2016,** *28* (2), 626-631.

323. Mulzer, C. R.; Shen, L.; Bisbey, R. P.; McKone, J. R.; Zhang, N.; Abruna, H. D.; Dichtel, W. R., Superior Charge Storage and Power Density of a Conducting Polymer-Modified Covalent Organic Framework. *ACS Cent. Sci.* **2016,** *2* (9), 667-673.

324. DeBlase, C. R.; Hernandez-Burgos, K.; Silberstein, K. E.; Rodriguez-Calero, G. G.; Bisbey, R. P.; Abruna, H. D.; Dichtel, W. R., Rapid and Efficient Redox Processes within 2D Covalent Organic Framework Thin Films. *ACS Nano* **2015,** *9* (3), 3178-3183.

325. Vitaku, E.; Gannett, C. N.; Carpenter, K. L.; Shen, L.; Abruña, H. D.; Dichtel, W. R., Phenazine–Based Covalent Organic Framework Cathode Materials with High Energy and Power Densities. *J. Am. Chem. Soc.* **2019**.

326. Fang, Q.; Zhuang, Z.; Gu, S.; Kaspar, R. B.; Zheng, J.; Wang, J.; Qiu, S.; Yan, Y., Designed synthesis of large-pore crystalline polyimide covalent organic frameworks. *Nat. Commun.* **2014,** *5*, 4503pp.

327. Zhang, C.; Zhang, S.; Yan, Y.; Xia, F.; Huang, A.; Xian, Y., Highly Fluorescent Polyimide Covalent Organic Nanosheets as Sensing Probes for the Detection of 2,4,6-Trinitrophenol. *ACS Appl. Mater. Interfaces* **2017,** *9* (15), 13415-13421.

328. Jin, S.; Furukawa, K.; Addicoat, M.; Chen, L.; Takahashi, S.; Irle, S.; Nakamura, T.; Jiang, D., Large pore donor-acceptor covalent organic frameworks. *Chem. Sci.* **2013,** *4* (12), 4505-4511.

329. Zhang, J.; Hou, S.-e.; Jin, H., Progress on porous covalent organic frameworks based on polyimide. *Huagong Xinxing Cailiao* **2013,** *41* (3), 17-19.

330. Das, G.; Skorjanc, T.; Sharma, S. K.; Gandara, F.; Lusi, M.; Shankar Rao, D. S.; Vimala, S.; Krishna Prasad, S.; Raya, J.; Han, D. S.; Jagannathan, R.; Olsen, J. C.; Trabolsi, A., Viologen-Based Conjugated Covalent Organic Networks via Zincke Reaction. *J Am Chem Soc* **2017,** *139* (28), 9558-9565.

331. Guo, J.; Xu, Y.; Jin, S.; Chen, L.; Kaji, T.; Honsho, Y.; Addicoat, M. A.; Kim, J.; Saeki, A.; Ihee, H.; Seki, S.; Irle, S.; Hiramoto, M.; Gao, J.; Jiang, D., Conjugated organic framework with three-dimensionally ordered stable structure and delocalized π clouds. *Nat. Commun.* **2013,** *4*, 3736/1-3736/8.

332. Liu, M.; Guo, L.; Jin, S.; Tan, B., Covalent triazine frameworks: synthesis and applications. *J. Mater. Chem. A* **2019,** *7* (10), 5153-5172.

333. Bhunia, A.; Vasylyeva, V.; Janiak, C., From a supramolecular tetranitrile to a porous covalent triazine-based framework with high gas uptake capacities. *Chem Commun* **2013,** *49* (38), 3961-3.

334. Bojdys, M. J.; Wohlgemuth, S. A.; Thomas, A.; Antonietti, M., Ionothermal Route to Layered Two-Dimensional Polymer-Frameworks Based on Heptazine Linkers. *Macromolecules* **2010,** *43* (16), 6639-6645.

335. Kuhn, P.; Antonietti, M.; Thomas, A., Porous, Covalent Triazine-Based Frameworks Prepared by Ionothermal Synthesis. *Angew Chem Int Ed* **2008,** *47* (18), 3450-3453.

336. Zhao, L.; Shi, S.; Liu, M.; Zhu, G.; Wang, M.; Du, W.; Gao, J.; Xu, J., Covalent Triazine Frameworks Catalytically Oxidative Cleavage of Lignin Models and Organosolv Lignin. *Green Chem.* **2018**, Ahead of Print.

337. Ren, J.-Y.; Wang, X.-L.; Li, X.-L.; Wang, M.-L.; Zhao, R.-S.; Lin, J.-M., Magnetic covalent triazine-based frameworks as magnetic solid-phase extraction adsorbents for sensitive determination of perfluorinated compounds in environmental water samples. *Anal. Bioanal. Chem.* **2018,** *410* (6), 1657-1665.

338. Zhu, S.-R.; Qi, Q.; Fang, Y.; Zhao, W.-N.; Wu, M.-K.; Han, L., Covalent Triazine Framework Modified BiOBr Nanoflake with Enhanced Photocatalytic Activity for Antibiotic Removal. *Cryst. Growth Des.* **2018,** *18* (2), 883-891.

339. Zhi, Y.; Shao, P.; Feng, X.; Xia, H.; Zhang, Y.; Shi, Z.; Mu, Y.; Liu, X., Covalent organic frameworks: efficient, metal-free, heterogeneous organocatalysts for chemical fixation of CO2 under mild conditions. *J. Mater. Chem. A* **2018,** *6* (2), 374-382.

340. Zhao, L.; Shi, S.; Liu, M.; Zhu, G.; Wang, M.; Du, W.; Gao, J.; Xu, J., Covalent triazine framework catalytic oxidative cleavage of lignin models and organosolv lignin. *Green Chem.* **2018**, Ahead of Print.

341. Pakhira, S.; Lucht, K. P.; Mendoza-Cortes, J. L., Iron Intercalation in Covalent-Organic Frameworks: A Promising Approach for Semiconductors. *J. Phys. Chem. C* **2017,** *121* (39), 21160-21170.

342. Gontarczyk, K.; Bury, W.; Serwatowski, J.; Wiecinski, P.; Wozniak, K.; Durka, K.; Lulinski, S., Hybrid Triazine-Boron Two-Dimensional Covalent Organic Frameworks: Synthesis, Characterization, and DFT Approach to Layer Interaction Energies. *ACS Appl. Mater. Interfaces* **2017,** *9* (36), 31129-31141.

343. Gunasekar, G. H.; Park, K.; Ganesan, V.; Lee, K.; Kim, N.-K.; Jung, K.-D.; Yoon, S., A Covalent Triazine Framework, Functionalized with Ir/N-Heterocyclic Carbene Sites, for the Efficient Hydrogenation of CO2 to Formate. *Chem. Mater.* **2017,** *29* (16), 6740-6748.

344. Qian, H.-L.; Dai, C.; Yang, C.-X.; Yan, X.-P., High-Crystallinity Covalent Organic Framework with Dual Fluorescence Emissions and Its Ratiometric Sensing Application. *ACS Appl. Mater. Interfaces* **2017,** *9* (29), 24999-25005.

345. Mu, X.; Zhan, J.; Feng, X.; Yuan, B.; Qiu, S.; Song, L.; Hu, Y., Novel Melamine/o-Phthalaldehyde Covalent Organic Frameworks Nanosheets: Enhancement Flame Retardant and Mechanical Performances of Thermoplastic Polyurethanes. *ACS Appl. Mater. Interfaces* **2017,** *9* (27), 23017-23026.

346. Troschke, E.; Graetz, S.; Luebken, T.; Borchardt, L., Mechanochemical Friedel-Crafts Alkylation-A Sustainable Pathway Towards Porous Organic Polymers. *Angew. Chem. Int. Ed.* **2017,** *56* (24), 6859-6863.

347. Meier, C. B.; Sprick, R. S.; Monti, A.; Guiglion, P.; Lee, J.-S. M.; Zwijnenburg, M. A.; Cooper, A. I., Structure-property relationships for covalent triazine-based frameworks: The effect of spacer length on photocatalytic hydrogen evolution from water. *Polymer* **2017,** *126*, 283-290.

348. Zhu, Y.; Qiao, M.; Peng, W.; Li, Y.; Zhang, G.; Zhang, F.; Li, Y.; Fan, X., Rapid exfoliation of layered covalent triazine-based frameworks into N-doped quantum dots for the selective detection of Hg2+ ions. *J. Mater. Chem. A* **2017,** *5* (19), 9272-9278.

349. Wen, P.; Zhang, C.; Yang, Z.; Dong, R.; Wang, D.; Fan, M.; Wang, J., Triazine-based covalent-organic frameworks: A novel lubricant additive with excellent tribological performances. *Tribol. Int.* **2017,** *111*, 57-65.

350. Sadhasivam, V.; Balasaravanan, R.; Chithiraikumar, C.; Siva, A., Incorporating Pd(OAc)2 on Imine Functionalized Microporous Covalent Organic Frameworks: A Stable and Efficient Heterogeneous Catalyst for Suzuki-Miyaura Coupling in Aqueous Medium. *Chemistryselect* **2017,** *2* (3), 1063-1070.

351. Troschke, E.; Graetz, S.; Borchardt, L.; Haubold, D.; Senkovska, I.; Eychmueller, A.; Kaskel, S., Salt templated synthesis of hierarchical covalent triazine frameworks. *Microporous Mesoporous Mater.* **2017,** *239*, 190-194.

352. Roy, S.; Kim, J.; Kotal, M.; Kim, K. J.; Oh, I.-K., Electroionic Antagonistic Muscles Based on Nitrogen-Doped Carbons Derived from Poly(Triazine-Triptycene). *Adv. Sci. (Weinheim, Ger.)* **2017,** *4* (12), n/a.

353. Li, Y.; Zheng, S.; Liu, X.; Li, P.; Sun, L.; Yang, R.; Wang, S.; Wu, Z.-S.; Bao, X.; Deng, W.-Q., Conductive Microporous Covalent Triazine-Based Framework for High-Performance Electrochemical Capacitive Energy Storage. *Angew. Chem. Int. Ed.* **2017**, Ahead of Print.

354. Osadchii, D. Y.; Olivos-Suarez, A. I.; Bavykina, A. V.; Gascon, J., Revisiting Nitrogen Species in Covalent Triazine Frameworks. *Langmuir* **2017,** *33* (50), 14278-14285.

355. Kaleeswaran, D.; Antony, R.; Sharma, A.; Malani, A.; Murugavel, R., Catalysis and CO2 Capture by Palladium-Incorporated Covalent Organic Frameworks. *ChemPlusChem* **2017,** *82* (10), 1253-1265.

356. Jiao, L.; Hu, Y.; Ju, H.; Wang, C.; Gao, M.-R.; Yang, Q.; Zhu, J.; Yu, S.-H.; Jiang, H.-L., From covalent triazine-based frameworks to N-doped porous carbon/reduced graphene oxide nanosheets: efficient electrocatalysts for oxygen reduction. *J. Mater. Chem. A* **2017,** *5* (44), 23170-23178.

357. Xu, F.; Yang, S.; Jiang, G.; Ye, Q.; Wei, B.; Wang, H., Fluorinated, Sulfur-Rich, Covalent Triazine Frameworks for Enhanced Confinement of Polysulfides in Lithium-Sulfur Batteries. *ACS Appl. Mater. Interfaces* **2017,** *9* (43), 37731-37738.

358. Lin, L.; Ou, H.; Zhang, Y.; Wang, X., Tri-s-triazine-Based Crystalline Graphitic Carbon Nitrides for Highly Efficient Hydrogen Evolution Photocatalysis. *ACS Catal.* **2016,** *6* (6), 3921-3931.

359. Yadav, R. K.; Kumar, A.; Park, N.-J.; Kong, K.-J.; Baeg, J.-O., A highly efficient covalent organic framework film photocatalyst for selective solar fuel production from CO2. *J. Mater. Chem. A* **2016,** *4* (24), 9413-9418.

360. Wang, K.; Huang, H.; Liu, D.; Wang, C.; Li, J.; Zhong, C., Covalent Triazine-Based Frameworks with Ultramicropores and High Nitrogen Contents for Highly Selective CO2 Capture. *Environ. Sci. Technol.* **2016,** *50* (9), 4869-4876.

361. Pilaski, M.; Artz, J.; Islam, H.-U.; Beale, A. M.; Palkovits, R., N-containing covalent organic frameworks as supports for rhodium as transition-metal catalysts in hydroformylation reactions. *Microporous Mesoporous Mater.* **2016,** *227*, 219-227.

362. Wang, Y.; Li, J.; Yang, Q.; Zhong, C., Two-Dimensional Covalent Triazine Framework Membrane for Helium Separation and Hydrogen Purification. *ACS Appl. Mater. Interfaces* **2016,** *8* (13), 8694-8701.

363. Zeng, Y.; Zou, R.; Zhao, Y., Covalent Organic Frameworks for CO2 Capture. *Adv. Mater.* **2016,** *28* (15), 2855-2873.

364. Gu, C.; Liu, D.; Huang, W.; Liu, J.; Yang, R., Synthesis of covalent triazine-based frameworks with high CO2 adsorption and selectivity. *Polym. Chem.* **2015,** *6* (42), 7410-7417.

365. Sakaushi, K.; Antonietti, M., Carbon- and Nitrogen-Based Organic Frameworks. *Acc. Chem. Res.* **2015,** *48* (6), 1591-1600.

366. Zhang, Y.; Ying, J. Y., Main-Chain Organic Frameworks with Advanced Catalytic Functionalities. *ACS Catal.* **2015,** *5* (4), 2681-2691.

367. Wu, S.; Gu, S.; Zhang, A.; Yu, G.; Wang, Z.; Jian, J.; Pan, C., A rational construction of microporous imide-bridged covalent-organic polytriazines for high-enthalpy small gas absorption. *J. Mater. Chem. A* **2015,** *3* (2), 878-885.

368. Stegbauer, L.; Schwinghammer, K.; Lotsch, B. V., A hydrazone-based covalent organic framework for photocatalytic hydrogen production. *Chem. Sci.* **2014,** *5* (7), 2789-2793.

369. Roeser, J.; Kailasam, K.; Thomas, A., Covalent Triazine Frameworks as Heterogeneous Catalysts for the Synthesis of Cyclic and Linear Carbonates from Carbon Dioxide and Epoxides. *ChemSusChem* **2012,** *5* (9), 1793-1799, S1793/1-S1793/6.

370. Hug, S.; Tauchert, M. E.; Li, S.; Pachmayr, U. E.; Lotsch, B. V., A functional triazine framework based on N-heterocyclic building blocks. *J. Mater. Chem.* **2012,** *22* (28), 13956-13964.

371. Liu, J.; Zong, E.; Fu, H.; Zheng, S.; Xu, Z.; Zhu, D., Adsorption of aromatic compounds on porous covalent triazine-based framework. *J. Colloid Interface Sci.* **2012,** *372* (1), 99-107.

372. Kuhn, P.; Antonietti, M.; Thomas, A., Porous, Covalent Triazine-Based Frameworks Prepared by Ionothermal Synthesis. *Angew. Chem. Int. Ed.* **2008,** *47*, 3450-3453.

373. Zhu, X.; Tian, C.; Mahurin, S. M.; Chai, S.-H.; Wang, C.; Brown, S.; Veith, G. M.; Luo, H.; Liu, H.; Dai, S., A Superacid-Catalyzed Synthesis of Porous Membranes Based on Triazine Frameworks for CO2 Separation. *J Am Chem Soc* **2012,** *134* (25), 10478-10484.

374. Zhang, W.; Qiu, L.-G.; Yuan, Y.-P.; Xie, A.-J.; Shen, Y.-H.; Zhu, J.-F., Microwave-assisted synthesis of highly fluorescent nanoparticles of a melamine-based porous covalent organic framework for trace-level detection of nitroaromatic explosives. *J. Hazard. Mater.* **2012,** *221-222*, 147-154.

375. Yu, S. Y.; Mahmood, J.; Noh, H. J.; Seo, J. M.; Jung, S. M.; Shin, S. H.; Im, Y. K.; Jeon, I. Y.; Baek, J. B., Direct Synthesis of a Covalent Triazine-Based Framework from Aromatic Amides. *Angew. Chem. Int. Ed.* **2018,** *57* (28), 8438-8442.

376. Zhu, X.; Tian, C.; Mahurin, S. M.; Chai, S.-H.; Wang, C.; Brown, S.; Veith, G. M.; Luo, H.; Liu, H.; Dai, S., A Superacid-Catalyzed Synthesis of Porous Membranes Based on Triazine Frameworks for CO2 Separation. *J. Am. Chem. Soc.* **2012,** *134* (25), 10478-10484.

377. Wang, K.; Yang, L. M.; Wang, X.; Guo, L.; Cheng, G.; Zhang, C.; Jin, S.; Tan, B.; Cooper, A., Covalent Triazine Frameworks via a Low-Temperature Polycondensation Approach. *Angew. Chem. Int. Ed.* **2017,** *56* (45), 14149-14153.

378. Jin, E.; Asada, M.; Xu, Q.; Dalapati, S.; Addicoat, M. A.; Brady, M. A.; Xu, H.; Nakamura, T.; Heine, T.; Chen, Q.; Jiang, D., Two-dimensional sp(2) carbon-conjugated covalent organic frameworks. *Science* **2017,** *357* (6352), 673-676.

379. Jin, E.; Li, J.; Geng, K.; Jiang, Q.; Xu, H.; Xu, Q.; Jiang, D., Designed synthesis of stable light-emitting two-dimensional sp2 carbon-conjugated covalent organic frameworks. *Nature Communications* **2018,** *9* (1), 4143.

380. He, T.; Geng, K.; Jiang, D., Engineering Covalent Organic Frameworks for Light-Driven Hydrogen Production from Water. *ACS Mater. Lett.* **2019**, Ahead of Print.

381. Whangbo, M.-H.; Hoffmann, R.; Woodward, R. B., Conjugated one and two dimensional polymers. *Proc. Royal Soc.* **1979,** *366* (1724), 23-46.

382. Ong, W. J.; Swager, T. M., Dynamic self-correcting nucleophilic aromatic substitution. *Nat. Chem.* **2018,** *10* (10), 1023-1030.

383. Segura, J. L.; Royuela, S.; Ramos, M. M., Post-synthetic modification of covalent organic frameworks. *Chem. Soc. Rev.* **2019,** *48* (14), 3903-3945.

384. Wei, P.-F.; Qi, M.-Z.; Wang, Z.-P.; Ding, S.-Y.; Yu, W.; Liu, Q.; Wang, L.-K.; Wang, H.-Z.; An, W.-K.; Wang, W., Benzoxazole-linked ultrastable covalent organic frameworks for photocatalysis. *J. Am. Chem. Soc.* **2018,** *140* (13), 4623-4631.

385. Seo, J.-M.; Noh, H.-J.; Jeong, H. Y.; Baek, J.-B., Converting Unstable Imine-Linked Network into Stable Aromatic Benzoxazole-Linked One via Post-oxidative Cyclization. *J. Am. Chem. Soc.* **2019,** *141* (30), 11786-11790.

386. Pyles, D. A.; Coldren, W. H.; Eder, G. M.; Hadad, C. M.; McGrier, P. L., Mechanistic investigations into the cyclization and crystallization of benzobisoxazole-linked two-dimensional covalent organic frameworks. *Chem. Sci.* **2018,** *9* (30), 6417-6423.

387. Waller, P. J.; AlFaraj, Y. S.; Diercks, C. S.; Jarenwattananon, N. N.; Yaghi, O. M., Conversion of imine to oxazole and thiazole linkages in covalent organic frameworks. *J. Am. Chem. Soc.* **2018,** *140* (29), 9099-9103.

388. Pyles, D. A.; Crowe, J. W.; Baldwin, L. A.; McGrier, P. L., Synthesis of Benzobisoxazole-Linked Two-Dimensional Covalent Organic Frameworks and Their Carbon Dioxide Capture Properties. *ACS Macro Lett.* **2016,** *5* (9), 1055-1058.

389. Li, X.; Zhang, C.; Cai, S.; Lei, X.; Altoe, V.; Hong, F.; Urban, J. J.; Ciston, J.; Chan, E. M.; Liu, Y., Facile transformation of imine covalent organic frameworks into ultrastable crystalline porous aromatic frameworks. *Nat. Commun.* **2018,** *9* (1), 1-8.

390. Wang, P.-L.; Ding, S.-Y.; Zhang, Z.-C.; Wang, Z.-P.; Wang, W., Constructing Robust Covalent Organic Frameworks via Multicomponent Reactions. *J. Am. Chem. Soc.* **2019,** *141* (45), 18004-18008.

391. Liu, H.; Chu, J.; Yin, Z.; Cai, X.; Zhuang, L.; Deng, H., Covalent organic frameworks linked by amine bonding for concerted electrochemical reduction of CO2. *Chem.* **2018,** *4* (7), 1696-1709.

392. Lyle, S. J.; Osborn Popp, T. M.; Waller, P. J.; Pei, X.; Reimer, J. A.; Yaghi, O. M., Multistep Solid-State Organic Synthesis of Carbamate-Linked Covalent Organic Frameworks. *J. Am. Chem. Soc.* **2019,** *141* (28), 11253-11258.

393. Haase, F.; Troschke, E.; Savasci, G.; Banerjee, T.; Duppel, V.; Dörfler, S.; Grundei, M. M.; Burow, A. M.; Ochsenfeld, C.; Kaskel, S.; Lotsch, B., Topochemical conversion of an imine-into a thiazole-linked covalent organic framework enabling real structure analysis. *Nat. Commun.* **2018,** *9* (1), 1-10.

394. Ji, W.; Xiao, L.; Ling, Y.; Ching, C.; Matsumoto, M.; Bisbey, R. P.; Helbling, D. E.; Dichtel, W. R., Removal of GenX and perfluorinated alkyl substances from water by amine-functionalized covalent organic frameworks. *J. Am. Chem. Soc.* **2018,** *140* (40), 12677-12681.

395. Chen, L.; Furukawa, K.; Gao, J.; Nagai, A.; Nakamura, T.; Dong, Y.; Jiang, D., Photoelectric covalent organic frameworks: converting open lattices into ordered donor-acceptor heterojunctions. *J. Am. Chem. Soc.* **2014,** *136* (28), 9806-9809.

396. Sakamoto, J.; van Heijst, J.; Lukin, O.; Schlüter, A. D., Two-Dimensional Polymers: Just a Dream of Synthetic Chemists? *Angewandte Chemie International Edition* **2009,** *48* (6), 1030-1069.

397. Diercks, C. S.; Yaghi, O. M., The atom, the molecule, and the covalent organic framework. *Science* **2017,** *355* (6328), eaal1585.

398. Colson, J. W.; Dichtel, W. R., Rationally Synthesized Two-Dimensional Polymers. *Nature Chem.* **2013,** *5* (6), 453-465.

399. Bisbey, R. P.; Dichtel, W. R., Covalent organic frameworks as a platform for multidimensional polymerization. *Acs Central Science* **2017,** *3* (6), 533-543.

400. Servalli, M.; Schlüter, A. D., Synthetic Two-Dimensional Polymers. *Annual Review of Materials Research* **2017,** *47*, 361-389.

401. Bhola, R.; Payamyar, P.; Murray, D. J.; Kumar, B.; Teator, A. J.; Schmidt, M. U.; Hammer, S. M.; Saha, A.; Sakamoto, J.; Schlüter, A. D., A two-dimensional polymer from the anthracene dimer and triptycene motifs. *Journal of the American Chemical Society* **2013,** *135* (38), 14134-14141.

402. Kissel, P.; Murray, D. J.; Wulftange, W. J.; Catalano, V. J.; King, B. T., A nanoporous two-dimensional polymer by single-crystal-to-single-crystal photopolymerization. *Nature chemistry* **2014,** *6* (9), 774-778.

403. Kory, M. J.; Wörle, M.; Weber, T.; Payamyar, P.; Van De Poll, S. W.; Dshemuchadse, J.; Trapp, N.; Schlüter, A. D., Gram-scale synthesis of two-dimensional polymer crystals and their structure analysis by X-ray diffraction. *Nature chemistry* **2014,** *6* (9), 779-784.

404. Doonan, C. J.; Tranchemontagne, D. J.; Glover, T. G.; Hunt, J. R.; Yaghi, O. M., Exceptional ammonia uptake by a covalent organic framework. *Nature chemistry* **2010,** *2* (3), 235-238.

405. Ding, H.; Li, Y.; Hu, H.; Sun, Y.; Wang, J.; Wang, C.; Wang, C.; Zhang, G.; Wang, B.; Xu, W., A Tetrathiafulvalene-Based Electroactive Covalent Organic Framework. *Chemistry-A European Journal* **2014,** *20* (45), 14614-14618.

406. Feng, X.; Liu, L.; Honsho, Y.; Saeki, A.; Seki, S.; Irle, S.; Dong, Y.; Nagai, A.; Jiang, D., High-Rate Charge-Carrier Transport in Porphyrin Covalent Organic Frameworks: Switching from Hole to Electron to Ambipolar Conduction. *Angewandte Chemie International Edition* **2012,** *51* (11), 2618-2622.

407. Ding, X.; Guo, J.; Feng, X.; Honsho, Y.; Guo, J.; Seki, S.; Maitarad, P.; Saeki, A.; Nagase, S.; Jiang, D., Synthesis of metallophthalocyanine covalent organic frameworks that exhibit high carrier mobility and photoconductivity. *Angewandte Chemie International Edition* **2011,** *50* (6), 1289-1293.

408. Wan, S.; Guo, J.; Kim, J.; Ihee, H.; Jiang, D., A Photoconductive Covalent Organic Framework: Self-Condensed Arene Cubes Composed of Eclipsed 2D Polypyrene Sheets for Photocurrent Generation. *Angewandte Chemie International Edition* **2009,** *48* (30), 5439-5442.

409. Wan, S.; Guo, J.; Kim, J.; Ihee, H.; Jiang, D., A Belt-Shaped, Blue Luminescent, and Semiconducting Covalent Organic Framework. *Angewandte Chemie International Edition* **2008,** *47* (46), 8826-8830.

410. Bessinger, D.; Ascherl, L.; Auras, F.; Bein, T., Spectrally Switchable Photodetection with Near-Infrared-Absorbing Covalent Organic Frameworks. *Journal of the American Chemical Society* **2017,** *139* (34), 12035-12042.

411. Vitaku, E.; Dichtel, W. R., Synthesis of 2D Imine-Linked Covalent Organic Frameworks through Formal Transimination Reactions. *Journal of the American Chemical Society* **2017,** *139* (37), 12911-12914.

412. Li, H.; Chavez, A. D.; Li, H.; Li, H.; Dichtel, W. R.; Bredas, J.-L., Nucleation and Growth of Covalent Organic Frameworks from Solution: The Example of COF-5. *Journal of the American Chemical Society* **2017**.

413. Smith, B. J.; Parent, L. R.; Overholts, A. C.; Beaucage, P. A.; Bisbey, R. P.; Chavez, A. D.; Hwang, N.; Park, C.; Evans, A. M.; Gianneschi, N. C., Colloidal Covalent Organic Frameworks. *ACS central science* **2017,** *3* (1), 58-65.

414. Calik, M.; Sick, T.; Dogru, M.; Döblinger, M.; Datz, S.; Budde, H.; Hartschuh, A.; Auras, F.; Bein, T., From highly crystalline to outer surface-functionalized covalent organic frameworks—a modulation approach. *J. Am. Chem. Soc* **2016,** *138* (4), 1234-1239.

415. Zeng, Y.; Zou, R.; Luo, Z.; Zhang, H.; Yao, X.; Ma, X.; Zou, R.; Zhao, Y., Covalent organic frameworks formed with two types of covalent bonds based on orthogonal reactions. *Journal of the American Chemical Society* **2015,** *137* (3), 1020-1023.

416. Medina, D. D.; Rotter, J. M.; Hu, Y.; Dogru, M.; Werner, V.; Auras, F.; Markiewicz, J. T.; Knochel, P.; Bein, T., Room temperature synthesis of covalent–organic framework films through vapor-assisted conversion. *Journal of the American Chemical Society* **2015,** *137* (3), 1016-1019.

417. Smith, B. J.; Hwang, N.; Chavez, A. D.; Novotney, J. L.; Dichtel, W. R., Growth rates and water stability of 2D boronate ester covalent organic frameworks. *Chemical Communications* **2015,** *51* (35), 7532-7535.

418. Colson, J. W.; Mann, J. A.; DeBlase, C. R.; Dichtel, W. R., Patterned growth of oriented 2D covalent organic framework thin films on single-layer graphene. *Journal of Polymer Science Part A: Polymer Chemistry* **2015,** *53* (2), 378-384.

419. Chandra, S.; Kundu, T.; Kandambeth, S.; BabaRao, R.; Marathe, Y.; Kunjir, S. M.; Banerjee, R., Phosphoric Acid Loaded Azo Based Covalent Organic Framework for Proton Conduction. *Journal of the American Chemical Society* **2014,** *136* (18), 6570-6573.

420. Smith, B. J.; Dichtel, W. R., Mechanistic Studies of Two-Dimensional Covalent Organic Frameworks Rapidly Polymerized from Initially Homogenous Conditions. *J. Am. Chem. Soc.* **2014,** *136* (24), 8783-8789.

421. Kandambeth, S.; Shinde, D. B.; Panda, M. K.; Lukose, B.; Heine, T.; Banerjee, R., Enhancement of Chemical Stability and Crystallinity in Porphyrin-Containing Covalent Organic Frameworks by Intramolecular Hydrogen Bonds. *Angewandte Chemie* **2013,** *125* (49), 13290-13294.

422. Dogru, M.; Handloser, M.; Auras, F.; Kunz, T.; Medina, D.; Hartschuh, A.; Knochel, P.; Bein, T., A Photoconductive Thienothiophene-Based Covalent Organic Framework Showing Charge Transfer Towards Included Fullerene. *Angewandte Chemie International Edition* **2013,** *52* (10), 2920-2924.

423. DeBlase, C. R.; Silberstein, K. E.; Truong, T.-T.; Abruña, H. D.; Dichtel, W. R., β-Ketoenamine-linked covalent organic frameworks capable of pseudocapacitive energy storage. *Journal of the American Chemical Society* **2013,** *135* (45), 16821-16824.

424. Ding, S.-Y.; Gao, J.; Wang, Q.; Zhang, Y.; Song, W.-G.; Su, C.-Y.; Wang, W., Construction of covalent organic framework for catalysis: Pd/COF-LZU1 in Suzuki–Miyaura coupling reaction. *Journal of the American Chemical Society* **2011,** *133* (49), 19816-19822.

425. Colson, J. W.; Woll, A. R.; Mukherjee, A.; Levendorf, M. P.; Spitler, E. L.; Shields, V. B.; Spencer, M. G.; Park, J.; Dichtel, W. R. J. S., Oriented 2D covalent organic framework thin films on single-layer graphene. *Science* **2011,** *332* (6026), 228-231.

426. Beaudoin, D.; Maris, T.; Wuest, J. D., Constructing monocrystalline covalent organic networks by polymerization. *Nat. Chem.* **2013,** *5* (10), 830-834.

427. Fiori, G.; Bonaccorso, F.; Iannaccone, G.; Palacios, T.; Neumaier, D.; Seabaugh, A.; Banerjee, S. K.; Colombo, L., Electronics based on two-dimensional materials. *Nat. Nanotechnol.* **2014,** *9* (10), 768.

428. Xu, M.; Liang, T.; Shi, M.; Chen, H., Graphene-like two-dimensional materials. *Chem. Rev.* **2013,** *113* (5), 3766-3798.

429. Kissel, P.; Murray, D. J.; Wulftange, W. J.; Catalano, V. J.; King, B. T., A nanoporous two-dimensional polymer by single-crystal-to-single-crystal photopolymerization. *Nat. Chem.* **2014,** *6* (9), 774.

430. Evans, A.; Ryder, M. R.; Flanders, N. C.; Vitaku, E.; Chen, L.; Dichtel, W., Buckling of Two-Dimensional Covalent Organic Frameworks Under Thermal Stress. *Ind. Eng. Chem. Res.* **2019,** *58* (23), 9883-9887.

431. Feng, X.; Ding, X.; Jiang, D., Covalent organic frameworks. *Chem. Soc. Rev.* **2012,** *41* (18), 6010-6022.

432. Lyle, S. J.; Waller, P. J.; Yaghi, O. M., Covalent Organic Frameworks: Organic Chemistry Extended into Two and Three Dimensions. *Trends Chem.* **2019**.

433. Jin, Y.; Hu, Y.; Zhang, W., Tessellated multiporous two-dimensional covalent organic frameworks. *Nat Rev Chem* **2017,** *1* (7), 0056.

434. Sick, T.; Hufnagel, A. G.; Kampmann, J.; Kondofersky, I.; Calik, M.; Rotter, J. M.; Evans, A.; Döblinger, M.; Herbert, S.; Peters, K., Oriented films of conjugated 2D covalent organic frameworks as photocathodes for water splitting. *J. Am. Chem. Soc.* **2018,** *140* (6), 2085-2092.

435. Thomas, S.; Li, H.; Dasari, R.; Evans, A. M.; Castano, I.; Allen, T.; Reid, O.; Rumbles, G.; Dichtel, W.; Gianneschi, N. C.; Marder, S., Design and synthesis of two-dimensional covalent organic frameworks with four-arm cores: prediction of remarkable ambipolar charge-transport properties. *Mater. Horizons* **2019**.

436. Corcos, A.; Levato, G.; Jiang, Z.; Evans, A.; Livingston, A.; Mariñas, B.; Dichtel, W., Reducing the Pore Size of Covalent Organic Frameworks in Thin-Film Composite Membranes Enhances Solute Rejection. *ChemRxiv* **2019**.

437. Ma, T.; Kapustin, E. A.; Yin, S. X.; Liang, L.; Zhou, Z.; Niu, J.; Li, L.-H.; Wang, Y.; Su, J.; Li, J., Single-crystal x-ray diffraction structures of covalent organic frameworks. *Science* **2018,** *361* (6397), 48-52.

438. Nguyen, V.; Grünwald, M., Microscopic origins of poor crystallinity in the synthesis of covalent organic framework COF-5. *J. Am. Chem. Soc.* **2018,** *140* (9), 3306-3311.

439. Smith, B. J.; Hwang, N.; Chavez, A. D.; Novotney, J. L.; Dichtel, W. R., Growth rates and water stability of 2D boronate ester covalent organic frameworks. *Chem. Comm.* **2015,** *51* (35), 7532-7535.

440. Evans, A. M.; Parent, L. R.; Flanders, N. C.; Bisbey, R. P.; Vitaku, E.; Kirschner, M. S.; Schaller, R. D.; Chen, L. X.; Gianneschi, N. C.; Dichtel, W. R., Seeded Growth of Single-Crystal Two-Dimensional Covalent Organic Frameworks. *Science* **2018,** *361* (6397), 52-57.

441. Smith, B. J.; Parent, L. R.; Overholts, A. C.; Beaucage, P. A.; Bisbey, R. P.; Chavez, A. D.; Hwang, N.; Park, C.; Evans, A. M.; Gianneschi, N. C., Colloidal covalent organic frameworks. *ACS Cent. Sci.* **2017,** *3* (1), 58-65.

442. Körzdörfer, T.; Bredas, J.-L., Organic electronic materials: recent advances in the DFT description of the ground and excited states using tuned range-separated hybrid functionals. *Acc. Chem. Res.* **2014,** *47* (11), 3284-3291.

443. Cornil, J.; Lemaur, V.; Calbert, J. P.; Brédas, J. L., Charge transport in discotic liquid crystals: a molecular scale description. *Adv. Mater.* **2002,** *14* (10), 726-729.

444. Ding, S.-Y.; Dong, M.; Wang, Y.-W.; Chen, Y.-T.; Wang, H.-Z.; Su, C.-Y.; Wang, W., Thioether-based fluorescent covalent organic framework for selective detection and facile removal of mercury (II). *Journal of the American Chemical Society* **2016,** *138* (9), 3031-3037.

445. Xie, Y.-F.; Ding, S.-Y.; Liu, J.-M.; Wang, W.; Zheng, Q.-Y., Triazatruxene based covalent organic framework and its quick-response fluorescence-on nature towards electron rich arenes. *Journal of Materials Chemistry C* **2015,** *3* (39), 10066-10069.

446. Dalapati, S.; Jin, E.; Addicoat, M.; Heine, T.; Jiang, D., Highly emissive covalent organic frameworks. *Journal of the American Chemical Society* **2016,** *138* (18), 5797-5800.

447. Fischer, A.; Galloway, W.; Vaughan, J., 695. Structure and reactivity in the pyridine series. Part I. Acid dissociation constants of pyridinium ions. *J. Am. Chem. Soc.* **1964**, 3591-3596.

448. Du, Y.; Mao, K.; Kamakoti, P.; Wooler, B.; Cundy, S.; Li, Q.; Ravikovitch, P.; Calabro, D., The effects of pyridine on the structure of B-COFs and the underlying mechanism. *J. Mater. Chem. A* **2013,** *1* (42), 13171-13178.

449. Du, Y.; Mao, K.; Kamakoti, P.; Ravikovitch, P.; Paur, C.; Cundy, S.; Li, Q.; Calabro, D., Experimental and computational studies of pyridine-assisted post-synthesis modified air stable covalent–organic frameworks. *Chem. Comm.* **2012,** *48* (38), 4606-4608.

450. Mayoral, A.; Barron, H.; Estrada-Salas, R.; Vazquez-Duran, A.; José-Yacamán, M., Nanoparticle stability from the nano to the meso interval. *Nanoscale* **2010,** *2* (3), 335-342.

451. Li, H.; Evans, A.; Castano, I.; Strauss, M.; Dichtel, W.; Bredas, J.-L., Nucleation-Elongation Dynamics of Two-Dimensional Covalent Organic Frameworks. *ChemRxiv* **2019**.

452. Berne, B. J.; Pecora, R., *Dynamic light scattering: with applications to chemistry, biology, and physics*. Courier Corporation: 2000.

453. Flory, P. J., Fundamental principles of condensation polymerization. *Chem. Rev.* **1946,** *39* (1), 137-197.

454. Heller, W.; Klevens, H.; Oppenheimer, H., The determination of particle sizes from Tyndall spectra. *J. Chem. Phys.* **1946,** *14* (9), 566-567.

455. Daugherty, M. C.; Vitaku, E.; Li, R. L.; Evans, A. M.; Chavez, A. D.; Dichtel, W. R., Improved synthesis of β-ketoenamine-linked covalent organic frameworks via monomer exchange reactions. *Chem. Comm.* **2019,** *55* (18), 2680-2683.

456. El-Kaderi, H. M.; Hunt, J. R.; Mendoza-Cortés, J. L.; Côté, A. P.; Taylor, R. E.; O'keeffe, M.; Yaghi, O. M., Designed synthesis of 3D covalent organic frameworks. *Science* **2007,** *316* (5822), 268-272.

457. Haase, F.; Troschke, E.; Savasci, G.; Banerjee, T.; Duppel, V.; Dörfler, S.; Grundei, M. M.; Burow, A. M.; Ochsenfeld, C.; Kaskel, S., Topochemical conversion of an imine-into a thiazole-linked covalent organic framework enabling real structure analysis. *Nat. Comm.* **2018,** *9*.

458. Auras, F.; Ascherl, L.; Hakimioun, A. H.; Margraf, J. T.; Hanusch, F. C.; Reuter, S.; Bessinger, D.; Döblinger, M.; Hettstedt, C.; Karaghiosoff, K., Synchronized offset stacking: A concept for growing large-domain and highly crystalline 2d covalent organic frameworks. *J. Am. Chem. Soc.* **2016,** *138* (51), 16703-16710.

459. Chavez, A. D.; Evans, A. M.; Flanders, N. C.; Bisbey, R. P.; Vitaku, E.; Chen, L. X.; Dichtel, W. R., Equilibration of Imine-Linked Polymers to Hexagonal Macrocycles Driven by Self-Assembly. *Chem.: Eur. J.* **2018,** *24* (16), 3989-3993.

460. Sun, C.; Shen, M.; Chavez, A. D.; Evans, A. M.; Liu, X.; Harutyunyan, B.; Flanders, N. C.; Hersam, M. C.; Bedzyk, M. J.; de la Cruz, M. O.; Dichtel, W., High aspect ratio nanotubes

assembled from macrocyclic iminium salts. *Proc. Natl. Acad. Sci. U.S.A* **2018,** *115* (36), 8883-8888.

461. Wu, X.; Han, X.; Liu, Y.; Liu, Y.; Cui, Y., Control interlayer stacking and chemical stability of two-dimensional covalent organic frameworks via steric tuning. *J. Am. Chem. Soc.* **2018,** *140* (47), 16124-16133.

462. Novoselov, K.; Mishchenko, A.; Carvalho, A.; Neto, A. C., 2D materials and van der Waals heterostructures. *Science* **2016,** *353* (6298), aac9439.

463. Kim, T. W.; Jun, S.; Ha, Y.; Yadav, R. K.; Kumar, A.; Yoo, C.-Y.; Oh, I.; Lim, H.-K.; Shin, J. W.; Ryoo, R., Ultrafast charge transfer coupled with lattice phonons in two-dimensional covalent organic frameworks. *Nat. Comm.* **2019,** *10* (1), 1873.

464. Pati, A. K.; Jana, R.; Gharpure, S. J.; Mishra, A. K., Photophysics of Diphenylbutadiynes in Water, Acetonitrile–Water, and Acetonitrile Solvent Systems: Application to Single Component White Light Emission. *J. Phys. Chem. A* **2016,** *120* (29), 5826-5837.

465. Pati, A. K.; Gharpure, S. J.; Mishra, A. K., Contrasting Solid-state fluorescence of diynes with small and large aryl substituents: crystal packing dependence and stimuli-responsive fluorescence switching. *J. Phys. Chem. A* **2015,** *119* (42), 10481-10493.

466. Kasha, M.; Rawls, H. R.; El-Bayoumi, M. A., The exciton model in molecular spectroscopy. *Pure Appl. Chem.* **1965,** *11* (3-4), 371-392.

467. Spano, F. C.; Silva, C., H-and J-aggregate behavior in polymeric semiconductors. *Annu. Rev. Phys. Chem.* **2014,** *65*, 477-500.

468. Gai, L.; Chen, H.; Zou, B.; Lu, H.; Lai, G.; Li, Z.; Shen, Z., Ratiometric fluorescence chemodosimeters for fluoride anion based on pyrene excimer/monomer transformation. *Chem. Comm.* **2012,** *48* (87), 10721-10723.

469. Monahan, N.; Zhu, X.-Y., Charge transfer–mediated singlet fission. *Annu. Rev. Phys. Chem.* **2015,** *66*, 601-618.

470. Goldschmidt, J. C.; Fischer, S., Upconversion for photovoltaics–a review of materials, devices and concepts for performance enhancement. *Adv. Opt. Mater.* **2015,** *3* (4), 510-535.

471. Liu, X.; Yan, C.-H.; Capobianco, J. A., Photon upconversion nanomaterials. *Chem. Soc. Rev.* **2015,** *44* (6), 1299-1301.

472. Jiang, Z., GIXSGUI: a MATLAB toolbox for grazing-incidence X-ray scattering data visualization and reduction, and indexing of buried three-dimensional periodic nanostructured films. *J. Appl. Cryst.* **2015,** *48* (3), 917-926.

473. Studio, D., Accelrys Inc. *San Diego, CA, USA* **2013**.

474. Schorb, M.; Haberbosch, I.; Hagen, W. J.; Schwab, Y.; Mastronarde, D. N., Software tools for automated transmission electron microscopy. *Nature methods* **2019**, 1.

475. Suloway, C.; Pulokas, J.; Fellmann, D.; Cheng, A.; Guerra, F.; Quispe, J.; Stagg, S.; Potter, C. S.; Carragher, B., Automated molecular microscopy: the new Leginon system. *Journal of structural biology* **2005,** *151* (1), 41-60.

476. Spitler, E. L.; Koo, B. T.; Novotney, J. L.; Colson, J. W.; Uribe-Romo, F. J.; Gutierrez, G. D.; Clancy, P.; Dichtel, W. R., A 2D covalent organic framework with 4.7-nm pores and insight into its interlayer stacking. *Journal of the American Chemical Society* **2011,** *133* (48), 19416-19421.

477. **!!! INVALID CITATION !!! {}**.

478. Ng, M. C.; Harper, J. B.; Stampfl, A. P.; Kearley, G. J.; Rols, S.; Stride, J. A., Central-Atom Size Effects on the Methyl Torsions of Group XIV Tetratolyls. *Chemistry–A European Journal* **2012,** *18* (41), 13018-13024.

479. Fournier, J.-H.; Maris, T.; Wuest, J. D.; Guo, W.; Galoppini, E., Molecular tectonics. Use of the hydrogen bonding of boronic acids to direct supramolecular construction. *Journal of the American Chemical Society* **2003,** *125* (4), 1002-1006.

480. Sakamoto, J.; van Heijst, J.; Lukin, O.; Schlüter, A. D., Two-Dimensional Polymers: Just a Dream of Synthetic Chemists? *Angewandte Chemie International Edition* **2009,** *48* (6), 1030-1069.

481. Feng, X.; Ding, X. S.; Jiang, D. L., Covalent Organic Frameworks. *Chem Soc Rev* **2012,** *41* (18), 6010-6022.

482. Wu, D. C.; Xu, F.; Sun, B.; Fu, R. W.; He, H. K.; Matyjaszewski, K., Design and Preparation of Porous Polymers. *Chem Rev* **2012,** *112* (7), 3959-4015.

483. Ding, S. Y.; Wang, W., Covalent Organic Frameworks (COFs): From Design to Applications. *Chem Soc Rev* **2013,** *42* (2), 548-568.

484. Bertrand, G. H. V.; Michaelis, V. K.; Ong, T.-C.; Griffin, R. G.; Dincă, M., Thiophene-Based Covalent Organic Frameworks. *Proceedings of the National Academy of Sciences* **2013,** *110* (13), 4923-4928.

485. Xu, H.; Gao, J.; Jiang, D., Stable, Crystalline, Porous, Covalent Organic Frameworks as a Platform for Chiral Organocatalysts. *Nature Chemistry* **2015,** *7*, 905.

486. Waller, P. J.; Gandara, F.; Yaghi, O. M., Chemistry of Covalent Organic Frameworks. *Acc. Chem. Res.* **2015,** *48* (12), 3053-3063.

487. Huang, N.; Wang, P.; Jiang, D., Covalent Organic Frameworks: A Materials Platform for Structural and Functional Designs. *Nature Reviews Materials* **2016,** *1*, 16068.

488. Ascherl, L.; Sick, T.; Margraf, J. T.; Lapidus, S. H.; Calik, M.; Hettstedt, C.; Karaghiosoff, K.; Döblinger, M.; Clark, T.; Chapman, K. W.; Auras, F.; Bein, T., Molecular Docking Sites Designed for the Generation of Highly Crystalline Covalent Organic Frameworks. *Nature Chemistry* **2016,** *8*, 310.

489. Beuerle, F.; Gole, B., Covalent Organic Frameworks and Cage Compounds: Design and Applications of Polymeric and Discrete Organic Scaffolds. *Angewandte Chemie International Edition* **2018,** *57* (18), 4850-4878.

490. Lohse, M. S.; Bein, T., Covalent Organic Frameworks: Structures, Synthesis, and Applications. *Advanced Functional Materials* **2018,** *28* (33), 1705553.

491. DeBlase, C. R.; Silberstein, K. E.; Truong, T. T.; Abruna, H. D.; Dichtel, W. R., *β*-Ketoenamine-linked covalent organic frameworks capable of pseudocapacitive energy storage. *Journal of the American Chemical Society* **2013,** *135* (45), 16821-16824.

492. Sun, B.; Zhu, C. H.; Liu, Y.; Wang, C.; Wan, L. J.; Wang, D., Oriented Covalent Organic Framework Film on Graphene for Robust Ambipolar Vertical Organic Field-Effect Transistor. *Chemistry of Materials* **2017,** *29* (10), 4367-4374.

493. Miao, J.; Xu, Z.; Li, Q.; Bowman, A.; Zhang, S.; Hu, W.; Zhou, Z.; Wang, C., Vertically Stacked and Self-Encapsulated van der Waals Heterojunction Diodes Using Two-Dimensional Layered Semiconductors. *ACS Nano* **2017,** *11* (10), 10472-10479.

494. Dey, K.; Pal, M.; Rout, K. C.; Kunjattu H, S.; Das, A.; Mukherjee, R.; Kharul, U. K.; Banerjee, R., Selective Molecular Separation by Interfacially Crystallized Covalent Organic Framework Thin Films. *J. Am. Chem. Soc.* **2017,** *139* (37), 13083-13091.

495. Medina, D. D.; Sick, T.; Bein, T., Photoactive and Conducting Covalent Organic Frameworks. *Advanced Energy Materials* **2017,** *7* (16).

496. Xiang, Z. H.; Cao, D. P.; Dai, L. M., Well-defined two dimensional covalent organic polymers: rational design, controlled syntheses, and potential applications. *Polym Chem-Uk* **2015,** *6* (11), 1896-1911.

497. Pyles, D. A.; Crowe, J. W.; Baldwin, L. A.; McGrier, P. L., Synthesis of Benzobisoxazole-Linked Two-Dimensional Covalent Organic Frameworks and Their Carbon Dioxide Capture Properties. *ACS Macro Lett.* **2016,** *5* (9), 1055-1058.

498. Xu, Q.; Tao, S.; Jiang, Q.; Jiang, D., Ion Conduction in Polyelectrolyte Covalent Organic Frameworks. *Journal of the American Chemical Society* **2018,** *140* (24), 7429-7432.

499. Zhao, F.; Liu, H.; Mathe, S.; Dong, A.; Zhang, J., Covalent Organic Frameworks: From Materials Design to Biomedical Application. *Nanomaterials* **2018,** *8* (1), 15.

500. Zhao, W.; Xia, L.; Liu, X., Covalent organic frameworks (COFs): perspectives of industrialization. *CrystEngComm* **2018,** *20* (12), 1613-1634.

501. Wan, S.; Guo, J.; Kim, J.; Ihee, H.; Jiang, D., A Belt-Shaped, Blue Luminescent, and Semiconducting Covalent Organic Framework. *Angewandte Chemie International Edition* **2008,** *47* (46), 8826-8830.

502. Wan, S.; Gándara, F.; Asano, A.; Furukawa, H.; Saeki, A.; Dey, S. K.; Liao, L.; Ambrogio, M. W.; Botros, Y. Y.; Duan, X.; Seki, S.; Stoddart, J. F.; Yaghi, O. M., Covalent

Organic Frameworks with High Charge Carrier Mobility. *Chemistry of Materials* **2011,** *23* (18), 4094-4097.

503. Duhović, S.; Dincă, M., Synthesis and Electrical Properties of Covalent Organic Frameworks with Heavy Chalcogens. *Chemistry of Materials* **2015,** *27* (16), 5487-5490.

504. Crowe, J. W.; Baldwin, L. A.; McGrier, P. L., Luminescent Covalent Organic Frameworks Containing a Homogeneous and Heterogeneous Distribution of Dehydrobenzoannulene Vertex Units. *Journal of the American Chemical Society* **2016,** *138* (32), 10120-10123.

505. Jin, E.; Asada, M.; Xu, Q.; Dalapati, S.; Addicoat, M. A.; Brady, M. A.; Xu, H.; Nakamura, T.; Heine, T.; Chen, Q.; Jiang, D., Two-dimensional sp2 carbon–conjugated covalent organic frameworks. *Science* **2017,** *357* (6352), 673-676.

506. Haldar, S.; Chakraborty, D.; Roy, B.; Banappanavar, G.; Rinku, K.; Mullangi, D.; Hazra, P.; Kabra, D.; Vaidhyanathan, R., Anthracene-Resorcinol Derived Covalent Organic Framework as Flexible White Light Emitter. *Journal of the American Chemical Society* **2018,** *140* (41), 13367-13374.

507. Albacete, P.; Martínez, J. I.; Li, X.; López-Moreno, A.; Mena-Hernando, S. a.; Platero-Prats, A. E.; Montoro, C.; Loh, K. P.; Pérez, E. M.; Zamora, F., Layer-Stacking-Driven Fluorescence in a Two-Dimensional Imine-Linked Covalent Organic Framework. *Journal of the American Chemical Society* **2018,** *140* (40), 12922-12929.

508. Wan, S.; Guo, J.; Kim, J.; Ihee, H.; Jiang, D. L., A Belt-Shaped, Blue Luminescent, and Semiconducting Covalent Organic Framework. *Angew Chem Int Edit* **2008,** *47* (46), 8826-8830.

509. Sick, T.; Hufnagel, A. G.; Kampmann, J.; Kondofersky, I.; Calik, M.; Rotter, J. M.; Evans, A.; Döblinger, M.; Herbert, S.; Peters, K.; Böhm, D.; Knochel, P.; Medina, D. D.;

Fattakhova-Rohlfing, D.; Bein, T., Oriented Films of Conjugated 2D Covalent Organic Frameworks as Photocathodes for Water Splitting. *Journal of the American Chemical Society* **2018,** *140* (6), 2085-2092.

510. Gonçalves, R. S. B.; de Oliveira, A. B. V.; Sindra, H. C.; Archanjo, B. S.; Mendoza, M. E.; Carneiro, L. S. A.; Buarque, C. D.; Esteves, P. M., Heterogeneous Catalysis by Covalent Organic Frameworks (COF): $Pd(OAc)_2$@COF-300 in Cross-Coupling Reactions. *ChemCatChem* **2016,** *8* (4), 743-750.

511. Li, H. Y.; Chavez, A. D.; Li, H. F.; Li, H.; Dichtel, W. R.; Brédas, J.-L., Nucleation and Growth of Covalent Organic Frameworks from Solution: The Example of COF-5. *Journal of the American Chemical Society* **2017,** *139* (45), 16310-16318.

512. Schwartz, D. K., Mechanisms and Kinetics of Self-Assembled Monolayer Formation. *Annual Review of Physical Chemistry* **2001,** *52* (1), 107-137.

513. Van Vleet, M. J.; Weng, T.; Li, X.; Schmidt, J. R., In Situ, Time-Resolved, and Mechanistic Studies of Metal–Organic Framework Nucleation and Growth. *Chem Rev* **2018,** *118* (7), 3681-3721.

514. Chen, J.; Zhu, E.; Liu, J.; Zhang, S.; Lin, Z.; Duan, X.; Heinz, H.; Huang, Y.; De Yoreo, J. J., Building two-dimensional materials one row at a time: Avoiding the nucleation barrier. *Science* **2018,** *362* (6419), 1135-1139.

515. Dong, J.; Zhang, L.; Ding, F., Kinetics of Graphene and 2D Materials Growth. *Advanced Materials* **2019,** *31* (9).

516. Lee, S.; Teich, E. G.; Engel, M.; Glotzer, S. C., Entropic colloidal crystallization pathways via fluid–fluid transitions and multidimensional prenucleation motifs. *Proceedings of the National Academy of Sciences* **2019,** *116* (30), 14843-14851.

517. De Yoreo, J. J.; Gilbert, P. U. P. A.; Sommerdijk, N. A. J. M.; Penn, R. L.; Whitelam, S.; Joester, D.; Zhang, H. Z.; Rimer, J. D.; Navrotsky, A.; Banfield, J. F.; Wallace, A. F.; Michel, F. M.; Meldrum, F. C.; Colfen, H.; Dove, P. M., Crystallization by particle attachment in synthetic, biogenic, and geologic environments. *Science* **2015,** *349* (6247), aaa6760.

518. Sosso, G. C.; Chen, J.; Cox, S. J.; Fitzner, M.; Pedevilla, P.; Zen, A.; Michaelides, A., Crystal nucleation in liquids: Open questions and future challenges in molecular dynamics simulations. *Chem Rev* **2016,** *116* (12), 7078-7116.

519. Smith, B. J.; Parent, L. R.; Overholts, A. C.; Beaucage, P. A.; Bisbey, R. P.; Chavez, A. D.; Hwang, N.; Park, C.; Evans, A. M.; Gianneschi, N. C.; Dichtel, W. R., Colloidal Covalent Organic Frameworks. *ACS Central Science* **2017,** *3* (1), 58-65.

520. Smith, B. J.; Overholts, A. C.; Hwang, N.; Dichtel, W. R., Insight into the Crystallization of Amorphous Imine-Linked Polymer Networks to 2D Covalent Organic Frameworks. *Chem. Commun.* **2016,** *52* (18), 3690-3693.

521. Sick, T.; Rotter, J. M.; Reuter, S.; Kandambeth, S.; Bach, N. N.; Döblinger, M.; Merz, J.; Clark, T.; Marder, T. B.; Bein, T.; Medina, D. D., Switching on and off Interlayer Correlations and Porosity in 2D Covalent Organic Frameworks. *Journal of the American Chemical Society* **2019,** *141* (32), 12570-12581.

522. Feriante, C. H.; Jhulki, S.; Evans, A. M.; Dasari, R. R.; Slicker, K.; Dichtel, W. R.; Marder, S. R., Rapid Synthesis of High Surface Area Imine-Linked 2D Covalent Organic Frameworks by Avoiding Pore Collapse During Isolation. *Advanced Materials* **2019**, 1905776.

523. Li, H. F.; Li, H. Y.; Dai, Q. Q.; Li, H.; Brédas, J. L., Hydrolytic Stability of Boronate Ester-Linked Covalent Organic Frameworks. *Advanced Theory and Simulations* **2018,** *1* (2), 1700015.

524. Li, H. Y.; Brédas, J.-L., Large Out-of-Plane Deformations of Two-Dimensional Covalent Organic Framework (COF) Sheets. *The Journal of Physical Chemistry Letters* **2018,** *9*, 4215-4220.

525. Li, H. Y.; Brédas, J.-L., Nanoscrolls Formed from Two-Dimensional Covalent Organic Frameworks. *Chemistry of Materials* **2019,** *31* (9), 3265-3273.

526. Lukose, B.; Kuc, A.; Frenzel, J.; Heine, T., On the reticular construction concept of covalent organic frameworks. *Beilstein Journal of Nanotechnology* **2010,** *1*, 60-70.

527. Lukose, B.; Kuc, A.; Heine, T., The Structure of Layered Covalent-Organic Frameworks. *Chemistry – A European Journal* **2011,** *17* (8), 2388-2392.

528. Mullin, J. W., 5 - Nucleation. In *Crystallization (Fourth Edition)*, Mullin, J. W., Ed. Butterworth-Heinemann: Oxford, 2001; pp 181-215.

529. Kashchiev, D.; van Rosmalen, G. M., Review: Nucleation in solutions revisited. *Crystal Research and Technology* **2003,** *38* (7-8), 555-574.

530. Li, Rebecca L.; Flanders, N. C.; Evans, A. M.; Ji, W.; Castano, I.; Chen, L. X.; Gianneschi, N. C.; Dichtel, W. R., Controlled growth of imine-linked two-dimensional covalent organic framework nanoparticles. *Chem. Sci.* **2019,** *10* (13), 3796-3801.

531. Vitaku, E.; Dichtel, W. R., Synthesis of 2D Imine-Linked Covalent Organic Frameworks through Formal Transimination Reactions. *J. Am. Chem. Soc.* **2017**.

532. Daugherty, M. C.; Vitaku, E.; Li, R. L.; Evans, A. M.; Chavez, A. D.; Dichtel, W. R., Improved synthesis of β-ketoenamine-linked covalent organic frameworks via monomer exchange reactions. *Chem. Commun.* **2019,** *55* (18), 2680-2683.

533. Rubio-Martinez, M.; Avci-Camur, C.; Thornton, A. W.; Imaz, I.; Maspoch, D.; Hill, M. R., New synthetic routes towards MOF production at scale. *Chem Soc Rev* **2017,** *46* (11), 3453-3480.

534. Huang, N.; Wang, P.; Jiang, D., Covalent organic frameworks: a materials platform for structural and functional designs. *Nature Reviews Materials* **2016,** *1* (10), 16068.

535. Feng, X.; Ding, X.; Jiang, D., Covalent organic frameworks. *Chemical Society Reviews* **2012,** *41* (18), 6010-6022.

536. Mulzer, C. R.; Shen, L.; Bisbey, R. P.; McKone, J. R.; Zhang, N.; Abruña, H. c. D.; Dichtel, W. R., Superior charge storage and power density of a conducting polymer-modified covalent organic framework. *ACS central science* **2016,** *2* (9), 667-673.

537. DeBlase, C. R.; Silberstein, K. E.; Truong, T.-T.; Abruña, H. c. D.; Dichtel, W. R., β-Ketoenamine-linked covalent organic frameworks capable of pseudocapacitive energy storage. *Journal of the American Chemical Society* **2013,** *135* (45), 16821-16824.

538. Wang, X.; Han, X.; Zhang, J.; Wu, X.; Liu, Y.; Cui, Y., Homochiral 2D porous covalent organic frameworks for heterogeneous asymmetric catalysis. *Journal of the American Chemical Society* **2016,** *138* (38), 12332-12335.

539. Xu, H.; Gao, J.; Jiang, D., Stable, crystalline, porous, covalent organic frameworks as a platform for chiral organocatalysts. *Nature chemistry* **2015,** *7* (11), 905.

540. Rabbani, M. G.; Sekizkardes, A. K.; Kahveci, Z.; Reich, T. E.; Ding, R.; El-Kaderi, H. M., A 2D Mesoporous Imine-Linked Covalent Organic Framework for High Pressure Gas Storage Applications. *Chemistry–A European Journal* **2013,** *19* (10), 3324-3328.

541. Doonan, C. J.; Tranchemontagne, D. J.; Glover, T. G.; Hunt, J. R.; Yaghi, O. M., Exceptional ammonia uptake by a covalent organic framework. *Nature chemistry* **2010,** *2* (3), 235.

542. Sick, T.; Hufnagel, A. G.; Kampmann, J.; Kondofersky, I.; Calik, M.; Rotter, J. M.; Evans, A.; Döblinger, M.; Herbert, S.; Peters, K., Oriented films of conjugated 2D covalent organic frameworks as photocathodes for water splitting. *Journal of the American Chemical Society* **2018,** *140* (6), 2085-2092.

543. Evans, A. M.; Parent, L. R.; Flanders, N. C.; Bisbey, R. P.; Vitaku, E.; Kirschner, M. S.; Schaller, R. D.; Chen, L. X.; Gianneschi, N. C.; Dichtel, W. R., Seeded growth of single-crystal two-dimensional covalent organic frameworks. *Science* **2018**, eaar7883.

544. Song, J.-R.; Sun, J.; Liu, J.; Huang, Z.-T.; Zheng, Q.-Y., Thermally/hydrolytically stable covalent organic frameworks from a rigid macrocyclic host. *Chemical Communications* **2014,** *50* (7), 788-791.

545. DeBlase, C. R.; Dichtel, W. R., Moving beyond boron: the emergence of new linkage chemistries in covalent organic frameworks. *Macromolecules* **2016,** *49* (15), 5297-5305.

546. Dubbeldam, D.; Walton, K. S.; Ellis, D. E.; Snurr, R. Q., Exceptional negative thermal expansion in isoreticular metal–organic frameworks. *Angewandte Chemie* **2007,** *119* (24), 4580-4583.

547. Furukawa, H.; Yaghi, O. M., Storage of hydrogen, methane, and carbon dioxide in highly porous covalent organic frameworks for clean energy applications. *Journal of the American Chemical Society* **2009,** *131* (25), 8875-8883.

548. Daugherty, M. C.; Vitaku, E.; Li, R. L.; Evans, A. M.; Chavez, A.; Dichtel, W., Improved Synthesis of β-Ketoenamine-Linked Covalent Organic Frameworks via Monomer Exchange Reactions. *Chemical Communications* **2019**.

549. Patterson, A., The Scherrer formula for X-ray particle size determination. *Physical review* **1939,** *56* (10), 978.

550. Gałka, P.; Kowalonek, J.; Kaczmarek, H., Thermogravimetric analysis of thermal stability of poly (methyl methacrylate) films modified with photoinitiators. *Journal of Thermal Analysis and Calorimetry* **2014,** *115* (2), 1387-1394.

551. Kandambeth, S.; Shinde, D. B.; Panda, M. K.; Lukose, B.; Heine, T.; Banerjee, R., Enhancement of Chemical Stability and Crystallinity in Porphyrin-Containing Covalent Organic Frameworks by Intramolecular Hydrogen Bonds. *Angewandte Chemie International Edition* **2013,** *52* (49), 13052-13056.

552. Kandambeth, S.; Mallick, A.; Lukose, B.; Mane, M. V.; Heine, T.; Banerjee, R., Construction of crystalline 2D covalent organic frameworks with remarkable chemical (acid/base) stability via a combined reversible and irreversible route. *Journal of the American Chemical Society* **2012,** *134* (48), 19524-19527.

553. Wu, Y.; Kobayashi, A.; Halder, G. J.; Peterson, V. K.; Chapman, K. W.; Lock, N.; Southon, P. D.; Kepert, C. J., Negative Thermal Expansion in the Metal–Organic Framework

Material Cu3 (1, 3, 5-benzenetricarboxylate) 2. *Angewandte Chemie International Edition* **2008,** *47* (46), 8929-8932.

554. Czaja, A. U.; Trukhan, N.; Müller, U., Industrial applications of metal–organic frameworks. *Chem Soc Rev* **2009,** *38* (5), 1284-1293.

555. Davis, M. E., Zeolites and molecular sieves: not just ordinary catalysts. *Industrial & engineering chemistry research* **1991,** *30* (8), 1675-1683.

556. Chong, J. H.; Sauer, M.; Patrick, B. O.; MacLachlan, M. J., Highly stable keto-enamine salicylideneanilines. *Organic letters* **2003,** *5* (21), 3823-3826.

557. Dovesi, R.; Saunders, V. R.; Roetti, C.; Orlando, R.; Zicovich-Wilson, C. M.; Pascale, F.; Civalleri, B.; Doll, K.; Harrison, N. M.; Bush, I. J.; D'Arco, P.; Llunell, M.; Causà, M.; Noël, Y.; Maschio, L.; Erba, A.; Rerat, M.; Casassa, S., CRYSTAL17 User's Manual (University of Torino). *CRYSTAL17 User's Manual (University of Torino)* **2017**.

558. Dovesi, R.; Erba, A.; Orlando, R.; Zicovich-Wilson, C. M.; Civalleri, B.; Maschio, L.; Rerat, M.; Casassa, S.; Baima, J.; Salustro, S.; Kirtman, B., Quantum-mechanical condensed matter simulations with CRYSTAL. *Wires Comput Mol Sci* **2018,** *8* (4), e1360.

559. Perdew, J. P.; Burke, K.; Ernzerhof, M., Generalized Gradient Approximation Made Simple. *Phys. Rev. Lett.* **1996,** *77* (18), 3865-3868.

560. Grimme, S.; Antony, J.; Ehrlich, S.; Krieg, H., A consistent and accurate ab initio parametrization of density functional dispersion correction (DFT-D) for the 94 elements H-Pu. *J Chem Phys* **2010,** *132* (15), 154104.

561. Ryder, M. R.; Donà, L.; Vitillo, J. G.; Civalleri, B., Understanding and Controlling the Dielectric Response of Metal-Organic Frameworks. *ChemPlusChem* **2018,** *83* (4), 308-316.

562. Broyden, C. G., The Convergence of a Class of Double-rank Minimization Algorithms 1. General Considerations. *IMA Journal of Applied Mathematics* **1970,** *6* (1), 76-90.

563. Broyden, C. G., The Convergence of a Class of Double-rank Minimization Algorithms: 2. The New Algorithm. *IMA Journal of Applied Mathematics* **1970,** *6* (3), 222-231.

564. Fletcher, R., A New Approach to Variable Metric Algorithms. *Comput J* **1970,** *13* (3), 317-322.

565. Goldfarb, D., A Family of Variable-Metric Methods Derived by Variational Means. *Math Comput* **1970,** *24* (109), 23-26.

566. Shanno, D. F., Conditioning of Quasi-Newton Methods for Function Minimization. *Math Comput* **1970,** *24* (111), 647-656.

567. Ryder, M. R., et al., *Submitted*.

568. Erba, A.; Mahmoud, A.; Belmonte, D.; Dovesi, R., High pressure elastic properties of minerals from ab initio simulations: the case of pyrope, grossular and andradite silicate garnets. *J Chem Phys* **2014,** *140* (12), 124703.

569. Birch, F., Elasticity and constitution of the Earth's interior. *Journal of Geophysical Research* **1952,** *57* (2), 227-286.

570. Noel, Y.; Zicovich-Wilson, C. M.; Civalleri, B.; D'Arco, P.; Dovesi, R., Polarization properties of ZnO and BeO:Anab initiostudy through the Berry phase and Wannier functions approaches. *Physical Review B* **2001,** *65* (1).

571. Dovesi, R.; Orlando, R.; Erba, A.; Zicovich-Wilson, C. M.; Civalleri, B.; Casassa, S.; Maschio, L.; Ferrabone, M.; De La Pierre, M.; D'Arco, P.; Noel, Y.; Causa, M.; Rerat, M.;

Kirtman, B., CRYSTAL14: A Program for the Ab Initio Investigation of Crystalline Solids. *Int J Quantum Chem* **2014,** *114* (19), 1287-1317.

572. Ryder, M. Physical phenomena in metal-organic frameworks: mechanical, vibrational, and dielectric response. University of Oxford, 2017.

573. Ding, S.-Y.; Wang, W. J. C. S. R., Covalent organic frameworks (COFs): from design to applications. *Chem. Soc. Rev.* **2013,** *42* (2), 548-568.

574. Feng, X.; Ding, X.; Jiang, D. J. C. S. R., Covalent organic frameworks. *Chem. Soc. Rev.* **2012,** *41* (18), 6010-6022.

575. Jhulki, S.; Evans, A. M.; Hao, X.-L.; Cooper, M. W.; Feriante, C. H.; Leisen, J.; Li, H.; Lam, D.; Hersam, M. C.; Barlow, S.; Dichtel, W. R.; Marder, S. R., Humidity Sensing through Reversible Isomerization of a Covalent Organic Framework. *J. Am. Chem. Soc.* **2020**.

576. Kulkarni, R.; Noda, Y.; Barange, D. K.; Kochergin, Y. S.; Lyu, P.; Balcarova, B.; Nachtigall, P.; Bojdys, M. J., Real-time optical and electronic sensing with a β-amino enone linked, triazine-containing 2D covalent organic framework. *Nat. Comm.* **2019,** *10* (1), 1-8.

577. Li, H.; Brédas, J.-L., Nanoscrolls Formed from Two-Dimensional Covalent Organic Frameworks. *Chem. Mater.* **2019,** *31* (9), 3265-3273.

578. Wu, X.; Han, X.; Xu, Q.; Liu, Y.; Yuan, C.; Yang, S.; Liu, Y.; Jiang, J.; Cui, Y., Chiral BINOL-based covalent organic frameworks for enantioselective sensing. *J. Am. Chem. Soc.* **2019,** *141* (17), 7081-7089.

579. Jin, E.; Lan, Z.; Jiang, Q.; Geng, K.; Li, G.; Wang, X.; Jiang, D. J. C., 2D sp2 carbon-conjugated covalent organic frameworks for photocatalytic hydrogen production from water. *Chem.* **2019,** *5* (6), 1632-1647.

580. Wang, X.; Han, X.; Zhang, J.; Wu, X.; Liu, Y.; Cui, Y., Homochiral 2D porous covalent organic frameworks for heterogeneous asymmetric catalysis. *J. Am. Chem. Soc.* **2016,** *138* (38), 12332-12335.

581. Mandal, A. K.; Mahmood, J.; Baek, J. B. J. C., Two-Dimensional Covalent Organic Frameworks for Optoelectronics and Energy Storage. *Chem. Nano. Mat.* **2017,** *3* (6), 373-391.

582. Evans, A. M.; Castano, I.; Brumberg, A.; Parent, L. R.; Corcos, A. R.; Li, R. L.; Flanders, N. C.; Gosztola, D. J.; Gianneschi, N. C.; Schaller, R. D.; Dichtel, W. R., Emissive Single-Crystalline Boroxine-Linked Colloidal Covalent Organic Frameworks. *J. Am. Chem. Soc.* **2019,** *141* (50), 19728-19735.

583. Sick, T.; Hufnagel, A. G.; Kampmann, J.; Kondofersky, I.; Calik, M.; Rotter, J. M.; Evans, A.; Döblinger, M.; Herbert, S.; Peters, K.; Bein, T., Oriented films of conjugated 2D covalent organic frameworks as photocathodes for water splitting. *J. Am. Chem. Soc.* **2017,** *140* (6), 2085-2092.

584. DeBlase, C. R.; Silberstein, K. E.; Truong, T.-T.; Abruña, H. c. D.; Dichtel, W. R., β-Ketoenamine-linked covalent organic frameworks capable of pseudocapacitive energy storage. *J. Am. Chem. Soc.* **2013,** *135* (45), 16821-16824.

585. Fan, H.; Peng, M.; Strauss, I.; Mundstock, A.; Meng, H.; Caro, J., High-Flux Vertically Aligned 2D Covalent Organic Framework Membrane with Enhanced Hydrogen Separation. *J. Am. Chem. Soc.* **2020**.

586. Yuan, S.; Li, X.; Zhu, J.; Zhang, G.; Van Puyvelde, P.; Van der Bruggen, B. J. C. S. R., Covalent organic frameworks for membrane separation. *Chem. Soc. Rev.* **2019,** *48* (10), 2665-2681.

587. Evans, A. M.; Ryder, M. R.; Flanders, N. C.; Vitaku, E.; Chen, L. X.; Dichtel, W. R., Buckling of Two-Dimensional Covalent Organic Frameworks under Thermal Stress. *Ind. Eng. Chem. Res.* **2019,** *58* (23), 9883-9887.

588. Bunck, D. N.; Dichtel, W. R., Bulk synthesis of exfoliated two-dimensional polymers using hydrazone-linked covalent organic frameworks. *J. Am. Chem. Soc.* **2013,** *135* (40), 14952-14955.

589. Gole, B.; Stepanenko, V.; Rager, S.; Grüne, M.; Medina, D. D.; Bein, T.; Würthner, F.; Beuerle, F., Microtubular Self-Assembly of Covalent Organic Frameworks. *Angew. Chem. Int. Ed.* **2018,** *57* (3), 846-850.

590. Jacobsen, J. L.; Kondev, J., Transition from the compact to the dense phase of two-dimensional polymers. *J. Stat. Phys.* **1999,** *96* (1-2), 21-48.

591. Payamyar, P.; King, B. T.; Öttinger, H. C.; Schlüter, A. D., Two-dimensional polymers: concepts and perspectives. *Chem. Comm.* **2016,** *52* (1), 18-34.

592. Vernier, E.; Jacobsen, J. L.; Saleur, H. J. J. o. S. M. T.; Experiment, A new look at the collapse of two-dimensional polymers. *J. Stat. Mech.* **2015,** *2015* (9), P09001.

593. Nagle, J., Statistical mechanics of the melting transition in lattice models of polymers. *P. Roy. Soc. A-Math. Phy.* **1974,** *337* (1611), 569-589.

594. Doonan, C. J.; Tranchemontagne, D. J.; Glover, T. G.; Hunt, J. R.; Yaghi, O. M. J. N. c., Exceptional ammonia uptake by a covalent organic framework. *Nat. Chem.* **2010,** *2* (3), 235-238.

595. Vitaku, E.; Dichtel, W. R. J. J. o. t. A. C. S., Synthesis of 2D imine-linked covalent organic frameworks through formal transimination reactions. *J. Am. Chem. Soc.* **2017,** *139* (37), 12911-12914.

596. Mokhtari, N.; Khataei, M. M.; Dinari, M.; Monjezi, B. H.; Yamini, Y. J. M. L., Imine-based covalent triazine framework: Synthesis, characterization, and evaluation its adsorption. *Mater. Lett.* **2020,** *263*, 127221.

597. Rabbani, M. G.; Sekizkardes, A. K.; Kahveci, Z.; Reich, T. E.; Ding, R.; El-Kaderi, H. M., A 2D mesoporous imine-linked covalent organic framework for high pressure gas storage applications. *Eur. J. Chem.* **2013,** *19* (10), 3324-3328.

598. Uribe-Romo, F. J.; Hunt, J. R.; Furukawa, H.; Klock, C.; O'Keeffe, M.; Yaghi, O. M. J. J. o. t. A. C. S., A crystalline imine-linked 3-D porous covalent organic framework. *J. Am. Chem. Soc.* **2009,** *131* (13), 4570-4571.

599. Luo, Y.-R., *Comprehensive handbook of chemical bond energies*. CRC press: 2007.

600. Burke, D. W.; Sun, C.; Castano, I.; Flanders, N. C.; Evans, A. M.; Vitaku, E.; McLeod, D. C.; Lambeth, R. H.; Chen, L. X.; Gianneschi, N. C.; Dichtel, W. R., Acid Exfoliation of Imine-linked Covalent Organic Frameworks Enables Solution Processing into Crystalline Thin Films. *Angew. Chem. Int. Ed.* **2019**.

601. Howarth, A. J.; Liu, Y.; Li, P.; Li, Z.; Wang, T. C.; Hupp, J. T.; Farha, O. K. J. N. R. M., Chemical, thermal and mechanical stabilities of metal–organic frameworks. *Nat. Rev. Mater.* **2016,** *1* (3), 1-15.

602. Nagai, A.; Guo, Z.; Feng, X.; Jin, S.; Chen, X.; Ding, X.; Jiang, D. J. N. c., Pore surface engineering in covalent organic frameworks. *Nat. Comm.* **2011,** *2* (1), 1-8.

603. Gedde, U., *Polymer physics*. Springer Science & Business Media: 1995.

604. Alahakoon, S. B.; McCandless, G. T.; Karunathilake, A. A.; Thompson, C. M.; Smaldone, R. A. J. C. A. E. J., Enhanced structural organization in covalent organic frameworks through fluorination. **2017,** *23* (18), 4255-4259.

605. Ryder, M. R.; Maul, J.; Civalleri, B.; Erba, A., Quasi-Harmonic Lattice Dynamics of a Prototypical Metal–Organic Framework. *Advanced Theory and Simulations* **2019,** *2* (11), 1900093.

606. Ryder, M. R.; Van de Voorde, B.; Civalleri, B.; Bennett, T. D.; Mukhopadhyay, S.; Cinque, G.; Fernandez-Alonso, F.; De Vos, D.; Rudic, S.; Tan, J. C., Detecting Molecular Rotational Dynamics Complementing the Low-Frequency Terahertz Vibrations in a Zirconium-Based Metal-Organic Framework. *Phys. Rev. Lett.* **2017,** *118* (25), 255502.

607. Ryder, M. R.; Civalleri, B.; Bennett, T. D.; Henke, S.; Rudic, S.; Cinque, G.; Fernandez-Alonso, F.; Tan, J. C., Identifying the role of terahertz vibrations in metal-organic frameworks: from gate-opening phenomenon to shear-driven structural destabilization. *Phys. Rev. Lett.* **2014,** *113* (21), 215502.

608. Abellán-Flos, M.; Tanç, M.; Supuran, C. T.; Vincent, S. P., Exploring carbonic anhydrase inhibition with multimeric coumarins displayed on a fullerene scaffold. *Org Biomol Chem* **2015,** *13* (27), 7445-7451.

609. Ji, W.; Xiao, L.; Ling, Y.; Ching, C.; Matsumoto, M.; Bisbey, R. P.; Helbling, D. E.; Dichtel, W. R., Removal of GenX and Perfluorinated Alkyl Substances from Water by Amine-Functionalized Covalent Organic Frameworks. *Journal of the American Chemical Society* **2018,** *140* (40), 12677-12681.

610. Okada, Y.; Sugai, M.; Chiba, K., Hydrogen-Bonding-Induced Fluorescence: Water-Soluble and Polarity-Independent Solvatochromic Fluorophores. *The Journal of Organic Chemistry* **2016,** *81* (22), 10922-10929.

611. Xie, Z.; Yang, B.; Liu, L.; Li, M.; Lin, D.; Ma, Y.; Cheng, G.; Liu, S., Experimental and theoretical studies of 2,5-diphenyl-1,4-distyrylbenzenes with all-cis- and all-trans double bonds: chemical structure determination and optical properties. *Journal of Physical Organic Chemistry* **2005,** *18* (9), 962-973.

612. Corcos, A. R.; Levato, G. A.; Jiang, Z.; Evans, A. M.; Livingston, A. G.; Mariñas, B. J.; Dichtel, W. R., Reducing the Pore Size of Covalent Organic Frameworks in Thin-Film Composite Membranes Enhances Solute Rejection. *ACS Materials Letters* **2019,** *1* (4), 440-446.

613. Wessig, P.; Gerngroß, M.; Freyse, D.; Bruhns, P.; Przezdziak, M.; Schilde, U.; Kelling, A., Molecular Rods Based on Oligo-spiro-thioketals. *The Journal of Organic Chemistry* **2016,** *81* (3), 1125-1136.

614. Yamamoto, T.; Nishimura, T.; Mori, T.; Miyazaki, E.; Osaka, I.; Takimiya, K., Largely π-Extended Thienoacenes with Internal Thieno[3,2-b]thiophene Substructures: Synthesis, Characterization, and Organic Field-Effect Transistor Applications. *Organic Letters* **2012,** *14* (18), 4914-4917.

615. Côté, A. P.; Benin, A. I.; Ockwig, N. W.; O'Keeffe, M.; Matzger, A. J.; Yaghi, O. M., Porous, Crystalline, Covalent Organic Frameworks. *Science* **2005,** *310* (5751), 1166-1170.

616. Matsumoto, M.; Dasari, R. R.; Ji, W.; Feriante, C. H.; Parker, T. C.; Marder, S. R.; Dichtel, W. R., Rapid, Low Temperature Formation of Imine-Linked Covalent Organic

Frameworks Catalyzed by Metal Triflates. *Journal of the American Chemical Society* **2017,** *139* (14), 4999-5002.

617. Xu, H.; Gao, J.; Jiang, D., Stable, crystalline, porous, covalent organic frameworks as a platform for chiral organocatalysts. *Nature Chemistry* **2015,** *7* (11), 905-912.

618. Antonov, L.; Deneva, V.; Simeonov, S.; Kurteva, V.; Nedeltcheva, D.; Wirz, J., Exploiting tautomerism for switching and signaling. *Angew. Chem., Int. Ed.* **2009,** *48* (42), 7875-7878.

619. Colson, J. W.; Dichtel, W. R., Rationally synthesized two-dimensional polymers. *Nat. Chem.* **2013,** *5* (6), 453-65.

620. Huang, N.; Wang, P.; Jiang, D., Covalent organic frameworks: a materials platform for structural and functional designs. *Nat. Rev. Mat.* **2016,** *1* (10), 16068.

621. Evans, A. M.; Ryder, M. R.; Flanders, N. C.; Vitaku, E.; Chen, L. X.; Dichtel, W. R., Buckling of Two-Dimensional Covalent Organic Frameworks under Thermal Stress. *Ind. Eng. Chem. Res.* **2019,** *58* (23), 9883-9887.

622. Lohse, M. S.; Bein, T., Covalent organic frameworks: Structures, synthesis, and applications. *Adv. Func. Mater.* **2018,** *28* (33), 1705553.

623. Ascherl, L.; Evans, E. W.; Hennemann, M.; Di Nuzzo, D.; Hufnagel, A. G.; Beetz, M.; Friend, R. H.; Clark, T.; Bein, T.; Auras, F., Solvatochromic covalent organic frameworks. *Nat. Comm.* **2018,** *9* (1), 3802.

624. Chong, J. H.; Sauer, M.; Patrick, B. O.; MacLachlan, M. J., Highly stable keto-enamine salicylideneanilines. *Org. Lett.* **2003,** *5* (21), 3823-3826.

625. DeBlase, C. R.; Silberstein, K. E.; Truong, T.-T.; Abruña, H. D.; Dichtel, W. R., β-Ketoenamine-linked covalent organic frameworks capable of pseudocapacitive energy storage. *J. Am. Chem. Soc.* **2013,** *135* (45), 16821-16824.

626. Kandambeth, S.; Mallick, A.; Lukose, B.; Mane, M. V.; Heine, T.; Banerjee, R., Construction of crystalline 2D covalent organic frameworks with remarkable chemical (acid/base) stability via a combined reversible and irreversible route. *J. Am. Chem. Soc.* **2012,** *134* (48), 19524-7.

627. Ning, G. H.; Chen, Z. X.; Gao, Q.; Tang, W.; Chen, Z. X.; Liu, C. B.; Tian, B. B.; Li, X.; Loh, K. P., Salicylideneanilines-Based Covalent Organic Frameworks as Chemoselective Molecular Sieves. *J. Am. Chem. Soc.* **2017,** *139* (26), 8897-8904.

628. Kandambeth, S.; Venkatesh, V.; Shinde, D. B.; Kumari, S.; Halder, A.; Verma, S.; Banerjee, R., Self-templated chemically stable hollow spherical covalent organic framework. *Nat. Comm.* **2015,** *6*, 6786.

629. Reference 13 reports that IR spectra and X-ray diffraction patterns for TAPB-PDA-OH COF are unchanged after exposure to water, consistent with our observations of this material's stability, however color or UV-vis spectral changes were not discussed.

630. Shao, P.; Li, J.; Chen, F.; Ma, L.; Li, Q.; Zhang, M.; Zhou, J.; Yin, A.; Feng, X.; Wang, B., Flexible Films of Covalent Organic Frameworks with Ultralow Dielectric Constants under High Humidity. *Angewandte Chemie* **2018,** *130* (50), 16739-16743.

631. Smith, B. J.; Overholts, A. C.; Hwang, N.; Dichtel, W. R., Insight into the crystallization of amorphous imine-linked polymer networks to 2D covalent organic frameworks. *Chem Commun* **2016,** *52* (18), 3690-3693.

632. Le Bail, A.; Jouanneaux, A., A qualitative account for anisotropic broadening in whole-powder-diffraction-pattern fitting by second-rank tensors. *J. Appl. Crystallogr.* **1997,** *30* (3), 265-271.

633. Sing, K., The Use of Nitrogen Adsorption for the Characterization of Porous Materials: Review. *Colloids and Surf., A 187*, 188.

634. Connolly, M. L., Analytical Molecular-Surface Calculation. *J. Appl. Crystallogr.* **1983,** *16* (Oct), 548-558.

635. Landers, J.; Gor, G. Y.; Neimark, A. V., Density functional theory methods for characterization of porous materials. *Colloids Surf., A* **2013,** *437*, 3-32.

636. Ascherl, L.; Evans, E. W.; Hennemann, M.; Di Nuzzo, D.; Hufnagel, A. G.; Beetz, M.; Friend, R. H.; Clark, T.; Bein, T.; Auras, F., Solvatochromic covalent organic frameworks. *Nature communications* **2018,** *9* (1), 3802.

637. Nekoeinia, M.; Yousefinejad, S.; Abdollahi-Dezaki, A., Prediction of E TN Polarity Scale of Ionic Liquids Using a QSPR Approach. *Ind. Eng. Chem. Res.* **2015,** *54* (50), 12682-12689.

638. Filipczak, K.; Karolczak, J.; Ziółek, M., Temperature influence on deactivation paths and tautomeric equilibrium of some photochromic Schiff bases studied by time-resolved and stationary spectroscopy. *Photochemical & Photobiological Sciences* **2009,** *8* (11), 1603-1610.

639. Reichardt, C., Solvatochromic Dyes as Solvent Polarity Indicators. *Chem. Rev.* **1994,** *94* (8), 2319-2358.

640. Lustig, W. P.; Mukherjee, S.; Rudd, N. D.; Desai, A. V.; Li, J.; Ghosh, S. K., Metal–organic frameworks: functional luminescent and photonic materials for sensing applications. *Chem. Soc. Rev.* **2017,** *46* (11), 3242-3285.

641. A 13C resonance corresponding to the “keto” group would provide additional evidence for tautomerization, but no such resonance is observed. Although DFT simulations indicate somewhat downfield shift for the monomer peaks compared to our observation in the COF, the DFT simulations indicate that the corresponding resonance in the imine/ketonenamine form of BPH is expected at ca. 158 ppm; this is a low chemical shift for a C=O, reflecting the importance of the zwitterionic resonance form (Figure S9). Indeed, the DFT-optimized structure of BPH indicates a C—O bond length of 1.26 Å in the single cis-ketoenamine form (Figure S17), between those of a typical C—O (1.4 Å) and C=O (1.2 Å) bonds, and the “C=O” stretching frequency is rather low (Figure S19). Our failure to observe this resonance is likely due to its intrinsic weakness (CP-MAS does not efficiently transfer magnetization to quaternary 13C nuclei) and the incomplete transformation to the imine/ketonenamine tautomer. Broadening due to structural inhomogeneity and perhaps to dynamic processes, as well as overlap with the tail of the imine resonance, may further complicate observation of this feature.

642. Wei, Y. S.; Chen, K. J.; Liao, P. Q.; Zhu, B. Y.; Lin, R. B.; Zhou, H. L.; Wang, B. Y.; Xue, W.; Zhang, J. P.; Chen, X. M., Turning on the flexibility of isoreticular porous coordination frameworks for drastically tunable framework breathing and thermal expansion. *Chem. Sci.* **2013,** *4* (4), 1539-1546.

643. Finsy, V.; Kirschhock, C. E.; Vedts, G.; Maes, M.; Alaerts, L.; De Vos, D. E.; Baron, G. V.; Denayer, J. F., Framework breathing in the vapour-phase adsorption and separation of xylene isomers with the metal–organic framework MIL-53. *Chem. - Eur. J.* **2009,** *15* (31), 7724-7731.

644. Serre, C.; Bourrelly, S.; Vimont, A.; Ramsahye, N. A.; Maurin, G.; Llewellyn, P. L.; Daturi, M.; Filinchuk, Y.; Leynaud, O.; Barnes, P., An explanation for the very large breathing effect of a metal–organic framework during CO2 adsorption. *Adv. Mater.* **2007,** *19* (17), 2246-2251.

645. Kandambeth, S.; Shinde, D. B.; Panda, M. K.; Lukose, B.; Heine, T.; Banerjee, R., Enhancement of chemical stability and crystallinity in porphyrin-containing covalent organic frameworks by intramolecular hydrogen bonds. *Angew. Chem., Int. Ed.* **2013,** *52* (49), 13052-13056.

646. Miorandi, D.; Sicari, S.; De Pellegrini, F.; Chlamtac, I., Internet of things: Vision, applications and research challenges. *Ad hoc Netw.* **2012,** *10* (7), 1497-1516.

647. Jiang, Z., GIXSGUI: a MATLAB toolbox for grazing-incidence X-ray scattering data visualization and reduction, and indexing of buried three-dimensional periodic nanostructured films. *J. Appl. Crystallogr.* **2015,** *48* (3), 917-926.

648. Lyle, S. J.; Waller, P. J.; Yaghi, O. M., Covalent Organic Frameworks: Organic Chemistry Extended into Two and Three Dimensions. *Trends in Chemistry* **2019,** *1* (2), 172-184.

649. Greenspan, L., Humidity fixed points of binary saturated aqueous solutions. *Journal of research of the national bureau of standards* **1977,** *81* (1), 89-96.

650. Chen, X.; Geng, K.; Liu, R.; Tan, K. T.; Gong, Y.; Li, Z.; Tao, S.; Jiang, Q.; Jiang, D., Covalent Organic Frameworks: Chemical Approaches to Designer Structures and Built-In Functions. *Angew. Chem. Int. Ed.* **2019,** *59* (13), 5050-5091.

651. Fan, H.; Peng, M.; Strauss, I.; Mundstock, A.; Meng, H.; Caro, J., High-Flux Vertically Aligned 2D Covalent Organic Framework Membrane with Enhanced Hydrogen Separation. *J. Am. Chem. Soc.* **2020,** *142* (15), 6872-6877.

652. Yuan, S.; Li, X.; Zhu, J.; Zhang, G.; Van Puyvelde, P.; Van der Bruggen, B., Covalent organic frameworks for membrane separation. *Chem. Soc. Rev.* **2019,** *48* (10), 2665-2681.

653. Cao, S.; Li, B.; Zhu, R.; Pang, H. J. C. E. J., Design and synthesis of covalent organic frameworks towards energy and environment fields. *Chem. Eng. J.* **2019,** *355*, 602-623.

654. Albacete, P.; López-Moreno, A.; Mena-Hernando, S.; Platero-Prats, A. E.; Pérez, E. M.; Zamora, F., Chemical sensing of water contaminants by a colloid of a fluorescent imine-linked covalent organic framework. *Chem. Comm.* **2019,** *55* (10), 1382-1385.

655. Jhulki, S.; Evans, A. M.; Hao, X.-L.; Cooper, M. W.; Feriante, C. H.; Leisen, J.; Li, H.; Lam, D.; Hersam, M. C.; Barlow, S.; Dichtel, W. R.; Marder, S. R., Humidity Sensing through Reversible Isomerization of a Covalent Organic Framework. *J. Am. Chem. Soc.* **2020,** *142* (2), 783-791.

656. Liu, X.; Huang, D.; Lai, C.; Zeng, G.; Qin, L.; Wang, H.; Yi, H.; Li, B.; Liu, S.; Zhang, M., Recent advances in covalent organic frameworks (COFs) as a smart sensing material. *Chem. Soc. Rev.* **2019,** *48* (20), 5266-5302.

657. Gao, Q.; Li, X.; Ning, G.-H.; Leng, K.; Tian, B.; Liu, C.; Tang, W.; Xu, H.-S.; Loh, K. P., Highly photoluminescent two-dimensional imine-based covalent organic frameworks for chemical sensing. *Chem. Comm.* **2018,** *54* (19), 2349-2352.

658. Das, G.; Biswal, B. P.; Kandambeth, S.; Venkatesh, V.; Kaur, G.; Addicoat, M.; Heine, T.; Verma, S.; Banerjee, R., Chemical sensing in two dimensional porous covalent organic nanosheets. *Chem. Sci.* **2015,** *6* (7), 3931-3939.

659. Rodríguez-San-Miguel, D.; Zamora, F., Processing of covalent organic frameworks: an ingredient for a material to succeed. *Chem. Soc. Rev.* **2019,** *48* (16), 4375-4386.

660. Lohse, M. S.; Bein, T., Covalent organic frameworks: structures, synthesis, and applications. *Adv. Func. Mater.* **2018,** *28* (33), 1705553.

661. Colson, J. W.; Mann, J. A.; DeBlase, C. R.; Dichtel, W. R., Patterned growth of oriented 2 D covalent organic framework thin films on single-layer graphene. *J. Polym. Sci. Pol. Chem.* **2015,** *53* (2), 378-384.

662. Peng, Y.; Wong, W. K.; Hu, Z.; Cheng, Y.; Yuan, D.; Khan, S. A.; Zhao, D., Room temperature batch and continuous flow synthesis of water-stable covalent organic frameworks (COFs). *Chem. Mater.* **2016,** *28* (14), 5095-5101.

663. Ratsch, M.; Ye, C.; Yang, Y.; Zhang, A.; Evans, A. M.; Börjesson, K., All Carbon-Linked Continuous 3D Porous Aromatic Framework Films with Nanometer Precise Controllable Thickness. *J. Am. Chem. Soc.* **2020,** *142* (14), 6548-6553.

664. Rotter, J. M.; Weinberger, S.; Kampmann, J.; Sick, T.; Shalom, M.; Bein, T.; Medina, D. D., Covalent Organic Framework Films through Electrophoretic Deposition—Creating Efficient Morphologies for Catalysis. *Chem. Mater.* **2019,** *31* (24), 10008-10016.

665. Evans, A. M.; Parent, L. R.; Flanders, N. C.; Bisbey, R. P.; Vitaku, E.; Kirschner, M. S.; Schaller, R. D.; Chen, L. X.; Gianneschi, N. C.; Dichtel, W. R. J. S., Seeded growth of single-crystal two-dimensional covalent organic frameworks. *Science* **2018,** *361* (6397), 52-57.

666. Li, H.; Evans, A. M.; Castano, I.; Strauss, M. J.; Dichtel, W. R.; Brédas, J.-L., Nucleation-Elongation Dynamics of Two-Dimensional Covalent Organic Frameworks. *J. Am. Chem. Soc.* **2020,** *142* (3), 1367-1374.

667. Torad, N. L.; Zhang, S.; Amer, W. A.; Ayad, M. M.; Kim, M.; Kim, J.; Ding, B.; Zhang, X.; Kimura, T.; Yamauchi, Y., Advanced Nanoporous Material–Based QCM Devices: A New Horizon of Interfacial Mass Sensing Technology. *Adv. Mater. Interfaces* **2019,** *6* (20), 1900849.

668. Boutamine, M.; Lezzar, O.; Bellel, A.; Aguir, K.; Sahli, S.; Raynaud, P., Determination of Volatile Organic Compounds Using Quartz Crystal Microbalances Coated with Hexamethyldisiloxane. *Anal. Lett.* **2018,** *51* (3), 387-400.

669. Chang, L.-Y.; Chuang, M.-Y.; Zan, H.-W.; Meng, H.-F.; Lu, C.-J.; Yeh, P.-H.; Chen, J.-N., One-minute fish freshness evaluation by testing the volatile amine gas with an ultrasensitive porous-electrode-capped organic gas sensor system. *ACS Sens.* **2017,** *2* (4), 531-539.

670. Pacquit, A.; Lau, K. T.; McLaughlin, H.; Frisby, J.; Quilty, B.; Diamond, D., Development of a volatile amine sensor for the monitoring of fish spoilage. *Talanta* **2006,** *69* (2), 515-520.

671. Evans, A. M.; Ryder, M. R.; Ji, W.; Strauss, M. J.; Corcos, A.; Vitaku, E.; Flanders, N. C.; Bisbey, R. P.; Dichtel, W. R., Trends in the Thermal Stability of Two-Dimensional Covalent Organic Frameworks. *Farad. Discuss.* **2020**.

672. Secor, E. B.; Gao, T. Z.; Islam, A. E.; Rao, R.; Wallace, S. G.; Zhu, J.; Putz, K. W.; Maruyama, B.; Hersam, M. C., Enhanced conductivity, adhesion, and environmental stability of printed graphene inks with nitrocellulose. *Chem. Mater.* **2017,** *29* (5), 2332-2340.

673. Krishtab, M.; Stassen, I.; Stassin, T.; Cruz, A. J.; Okudur, O. O.; Armini, S.; Wilson, C.; De Gendt, S.; Ameloot, R., Vapor-deposited zeolitic imidazolate frameworks as gap-filling ultra-low-k dielectrics. *Nat. Commun.* **2019,** *10* (1), 1-9.

674. Volksen, W.; Miller, R. D.; Dubois, G. J. C. r., Low dielectric constant materials. *Chem. Rev.* **2010,** *110* (1), 56-110.

675. Maex, K.; Baklanov, M.; Shamiryan, D.; Lacopi, F.; Brongersma, S.; Yanovitskaya, Z. S. J. J. o. A. P., Low dielectric constant materials for microelectronics. *Int. J. Appl. Phys.* **2003,** *93* (11), 8793-8841.

676. Badaroglu, M. *International Roadmap for Devices and Systems*; Semiconductor Industry Association 2017.

677. Arden, W. M., The international technology roadmap for semiconductors—perspectives and challenges for the next 15 years. *Curr. Opin. Solid State Mater. Sci.* **2002,** *6* (5), 371-377.

678. Miller, R. D., In search of low-k dielectrics. *Science* **1999,** *286* (5439), 421-423.

679. Veres, J.; Ogier, S. D.; Leeming, S. W.; Cupertino, D. C.; Mohialdin Khaffaf, S., Low-k insulators as the choice of dielectrics in organic field-effect transistors. *Adv. Func. Mater.* **2003,** *13* (3), 199-204.

680. Hopkins, P. E.; Kaehr, B.; Piekos, E. S.; Dunphy, D.; Jeffrey Brinker, C., Minimum thermal conductivity considerations in aerogel thin films. *J. Appl. Phys.* **2012,** *111* (11), 113532.

681. Erickson, K. J.; Léonard, F.; Stavila, V.; Foster, M. E.; Spataru, C. D.; Jones, R. E.; Foley, B. M.; Hopkins, P. E.; Allendorf, M. D.; Talin, A. A., Thin film thermoelectric metal–organic framework with high Seebeck coefficient and low thermal conductivity. *Adv. Mater.* **2015,** *27* (22), 3453-3459.

682. Xie, X.; Li, D.; Tsai, T.-H.; Liu, J.; Braun, P. V.; Cahill, D. G., Thermal conductivity, heat capacity, and elastic constants of water-soluble polymers and polymer blends. *Macromolecules* **2016,** *49* (3), 972-978.

683. Kim, G.-H.; Lee, D.; Shanker, A.; Shao, L.; Kwon, M. S.; Gidley, D.; Kim, J.; Pipe, K. P., High thermal conductivity in amorphous polymer blends by engineered interchain interactions. *Nat. Mater.* **2015,** *14* (3), 295-300.

684. Evans, A. M.; Ryder, M. R.; Flanders, N. C.; Vitaku, E.; Chen, L. X.; Dichtel, W. R. J. I.; Research, E. C., Buckling of Two-Dimensional Covalent Organic Frameworks under Thermal Stress. *Ind. Eng. Chem.* **2019,** *58* (23), 9883-9887.

685. Burke, D. W.; Sun, C.; Castano, I.; Flanders, N. C.; Evans, A. M.; Vitaku, E.; McLeod, D. C.; Lambeth, R. H.; Chen, L. X.; Gianneschi, N. C. J. A. C. I. E., Acid Exfoliation of Imine-linked Covalent Organic Frameworks Enables Solution Processing into Crystalline Thin Films. *Angew. Chem. Int. Ed.* **2019**.

686. Chen, X.; Li, Y.; Wang, L.; Xu, Y.; Nie, A.; Li, Q.; Wu, F.; Sun, W.; Zhang, X.; Vajtai, R. J. A. M., High-Lithium-Affinity Chemically Exfoliated 2D Covalent Organic Frameworks. *Adv. Mater.* **2019,** *31* (29), 1901640.

687. Sasmal, H. S.; Halder, A.; Kunjattu H, S.; Dey, K.; Nadol, A.; Ajithkumar, T. G.; Ravindra Bedadur, P.; Banerjee, R. J. J. o. t. A. C. S., Covalent Self-Assembly in Two Dimensions: Connecting Covalent Organic Framework Nanospheres into Crystalline and Porous Thin Films. *J. Am. Chem. Soc.* **2019,** *141* (51), 20371-20379.

688. Shao, P.; Li, J.; Chen, F.; Ma, L.; Li, Q.; Zhang, M.; Zhou, J.; Yin, A.; Feng, X.; Wang, B., Flexible films of covalent organic frameworks with ultralow dielectric constants under high humidity. *Angew. Chem. Int. Ed.* **2018,** *57* (50), 16501-16505.

689. Cao, S.; Li, B.; Zhu, R.; Pang, H., Design and synthesis of covalent organic frameworks towards energy and environment fields. *Chem. Eng. J.* **2019,** *355*, 602-623.

690. Ikeda, M.; Takeuchi, M.; Shinkai, S. J. C. c., Unusual emission properties of a triphenylene-based organogel system. *Chem. Comm.* **2003,** (12), 1354-1355.

691. Huang, B.; McGaughey, A.; Kaviany, M., Thermal conductivity of metal-organic framework 5 (MOF-5): Part I. Molecular dynamics simulations. *Int. J. Heat Mass Transf.* **2007,** *50* (3-4), 393-404.

692. Wang, X.; Liman, C. D.; Treat, N. D.; Chabinyc, M. L.; Cahill, D. G., Ultralow thermal conductivity of fullerene derivatives. *Phys. Rev. B* **2013,** *88* (7), 075310.

693. Klemens, P., The scattering of low-frequency lattice waves by static imperfections. *Proceed. Phys. Soc. A* **1955,** *68* (12), 1113.

694. Gaskins, J. T.; Hopkins, P. E.; Merrill, D. R.; Bauers, S. R.; Hadland, E.; Johnson, D. C.; Koh, D.; Yum, J. H.; Banerjee, S.; Nordell, B. J., Investigation and review of the thermal, mechanical, electrical, optical, and structural properties of atomic layer deposited high-k dielectrics: Beryllium oxide, aluminum oxide, hafnium oxide, and aluminum nitride. *ECS J. Solid State Sci. Technol* **2017,** *6* (10), N189.

695. Scott, E. A.; Gaskins, J. T.; King, S. W.; Hopkins, P. E., Thermal conductivity and thermal boundary resistance of atomic layer deposited high-k dielectric aluminum oxide, hafnium oxide, and titanium oxide thin films on silicon. *APL Mater.* **2018,** *6* (5), 058302.

696. Giri, A.; Tomko, J.; Gaskins, J. T.; Hopkins, P. E. J. N., Large tunability in the mechanical and thermal properties of carbon nanotube-fullerene hierarchical monoliths. *Nanoscale* **2018,** *10* (47), 22166-22172.

697. McGaughey, A.; Kaviany, M., Thermal conductivity decomposition and analysis using molecular dynamics simulations: Part II. Complex silica structures. *Int. J. Heat Mass Transf.* **2004,** *47* (8-9), 1799-1816.

698. Ilavsky, J., Nika: software for two-dimensional data reduction. *J. Appl. Crystallogr.* **2012,** *45* (2), 324-328.

699. Nelson, A., Co-refinement of multiple-contrast neutron/X-ray reflectivity data using MOTOFIT. *J. Appl. Crystallogr.* **2006,** *39* (2), 273-276.

700. Gajdoš, M.; Hummer, K.; Kresse, G.; Furthmüller, J.; Bechstedt, F., Linear optical properties in the projector-augmented wave methodology. *Physical Review B* **2006,** *73* (4), 045112.

701. Perdew, J. P.; Burke, K.; Ernzerhof, M., Generalized Gradient Approximation Made Simple. *Physical Review Letters* **1996,** *77* (18), 3865-3868.

702. Plimpton, S. *Fast parallel algorithms for short-range molecular dynamics*; Sandia National Labs., Albuquerque, NM (United States): 1993.

703. Stuart, S. J.; Tutein, A. B.; Harrison, J. A., A reactive potential for hydrocarbons with intermolecular interactions. *J. Chem. Phys.* **2000,** *112* (14), 6472-6486.

704. Hoover, W. G.; Posch, H. A., Direct measurement of Lyapunov exponents. *Phys. Lett. A* **1985,** *113* (2), 82-84.

705. Wan, S.; Guo, J.; Kim, J.; Ihee, H.; Jiang, D., A belt-shaped, blue luminescent, and semiconducting covalent organic framework. *Angew. Chem. Int. Ed.* **2008,** *47* (46), 8826-8830.

706. Dharmapurikar, S. S.; Arulkashmir, A.; Das, C.; Muddellu, P.; Krishnamoorthy, K., Enhanced hole carrier transport due to increased intermolecular contacts in small molecule based field effect transistors. *ACS Appl. Mater. Inter.* **2013,** *5* (15), 7086-7093.

707. Dovesi, R.; Erba, A.; Orlando, R.; Zicovich-Wilson, C. M.; Civalleri, B.; Maschio, L.; Rérat, M.; Casassa, S.; Baima, J.; Salustro, S.; Kirtman, B., Quantum-mechanical condensed matter simulations with CRYSTAL. *WIREs Computational Molecular Science* **2018,** *8* (4), e1360.

708. R. Dovesi, V. R. S., C. Roetti, R. Orlando, C. M. Zicovich-Wilson, F. Pascale, B. Civalleri, K. Doll, N. M. Harrison, I. J. Bush, P. D'Arco, M. Llunell, M. Causà, Y. Noël, L. Maschio, A. Erba, M. Rerat, S. Casassa, *CRYSTAL17 User's Manual (University of Torino, Torino, 2017)*.

709. Adamo, C.; Barone, V., Toward reliable density functional methods without adjustable parameters: The PBE0 model. *The Journal of Chemical Physics* **1999,** *110* (13), 6158-6170.

710. Peintinger, M. F.; Oliveira, D. V.; Bredow, T., Consistent Gaussian basis sets of triple-zeta valence with polarization quality for solid-state calculations. *Journal of Computational Chemistry* **2013,** *34* (6), 451-459.

711. Grimme, S.; Ehrlich, S.; Goerigk, L., Effect of the damping function in dispersion corrected density functional theory. *Journal of Computational Chemistry* **2011,** *32* (7), 1456-1465.

712. Gonze, X., Adiabatic density-functional perturbation theory. *Physical Review A* **1995,** *52* (2), 1096-1114.

713. Costescu, R. M.; Wall, M. A.; Cahill, D. G., Thermal conductance of epitaxial interfaces. *Phys. Rev. B* **2003,** *67* (5), 054302.

714. Giri, A.; Niemelä, J.-P.; Szwejkowski, C. J.; Karppinen, M.; Hopkins, P. E., Reduction in thermal conductivity and tunable heat capacity of inorganic/organic hybrid superlattices. *Phys. Rev. B.* **2016,** *93* (2), 024201.

715. Wang, X.; Liman, C. D.; Treat, N. D.; Chabinyc, M. L.; Cahill, D. G. J. P. R. B., Ultralow thermal conductivity of fullerene derivatives. *Phys. Rev. B* **2013,** *88* (7), 075310.

716. Schmidt, A. J.; Cheaito, R.; Chiesa, M., A frequency-domain thermoreflectance method for the characterization of thermal properties. *Rev. Sci. Instrum.* **2009,** *80* (9), 094901.

717. Malen, J. A.; Baheti, K.; Tong, T.; Zhao, Y.; Hudgings, J. A.; Majumdar, A., Optical measurement of thermal conductivity using fiber aligned frequency domain thermoreflectance. *J. Heat Trans.* **2011,** *133* (8).

718. Koh, Y. K.; Bae, M.-H.; Cahill, D. G.; Pop, E., Heat conduction across monolayer and few-layer graphenes. *Nano Lett.* **2010,** *10* (11), 4363-4368.

719. Plimpton, S., *J. Comp. Phys.* **1995,** *117* (1), 1-19.

720. Hoover, W. G.; Posch, H. A., Direct measurement of Lyapunov exponents. *Phys. Let. A* **1985,** *113* (2), 82-84.

721. Giri, A.; Hopkins, P. E., Resonant phonon modes in fullerene functionalized graphene lead to large tunability of thermal conductivity without impacting the mechanical properties. *J. Appl. Phys.* **2019,** *125* (20), 205102.

722. Salaway, R. N.; Zhigilei, L. V., Molecular dynamics simulations of thermal conductivity of carbon nanotubes: Resolving the effects of computational parameters. *Int. J. Heat Mass Transf.* **2014,** *70*, 954-964.

723. Lukes, J. R.; Zhong, H., Thermal conductivity of individual single-wall carbon nanotubes. *J. Heat Trans.* **2007**.

724. Allen, M. P.; Tildesley, D. J., *Computer simulation of liquids*. Oxford university press: 2017.

725. Schelling, P. K.; Phillpot, S. R.; Keblinski, P., Comparison of atomic-level simulation methods for computing thermal conductivity. *Phys. Rev. B* **2002,** *65* (14), 144306.

726. McGaughey, A.; Kaviany, M., Thermal conductivity decomposition and analysis using molecular dynamics simulations. Part I. Lennard-Jones argon. *Int. J. Heat Mass Transf.* **2004,** *47* (8-9), 1783-1798.

727. McGaughey, A.; Kaviany, M. J. I. J. o. H.; Transfer, M., Thermal conductivity decomposition and analysis using molecular dynamics simulations: Part II. Complex silica structures. *Int. J. Heat Mass Transf.* **2004,** *47* (8-9), 1799-1816.

728. Henry, A. S.; Chen, G., Spectral phonon transport properties of silicon based on molecular dynamics simulations and lattice dynamics. *J. Comput. Theor. Nanos.* **2008,** *5* (2), 141-152.

729. Wang, Z.; Safarkhani, S.; Lin, G.; Ruan, X., Uncertainty quantification of thermal conductivities from equilibrium molecular dynamics simulations. *Int. J. Heat Mass Transf.* **2017,** *112*, 267-278.

730. Lv, W.; Henry, A., Direct calculation of modal contributions to thermal conductivity via Green–Kubo modal analysis. *New. J. Phys.* **2016,** *18* (1), 013028.

731. Chalopin, Y.; Esfarjani, K.; Henry, A.; Volz, S.; Chen, G., Thermal interface conductance in Si/Ge superlattices by equilibrium molecular dynamics. *Phys. Rev. B* **2012,** *85* (19), 195302.

732. Che, J. Ç. a. T., Deng W and Goddard, Thermal conductivity of diamond and related materials from molecular dynamics simulations. *J. Chem. Phys.* **2000,** *113*, 6888.

733. Chen, J.; Zhang, G.; Li, B., How to improve the accuracy of equilibrium molecular dynamics for computation of thermal conductivity? *Phys. Let. A* **2010,** *374* (23), 2392-2396.

734. Volz, S. G.; Chen, G., Molecular-dynamics simulation of thermal conductivity of silicon crystals. *Phys. Rev. B* **2000,** *61* (4), 2651.

735. Dong, H.; Fan, Z.; Shi, L.; Harju, A.; Ala-Nissila, T., Equivalence of the equilibrium and the nonequilibrium molecular dynamics methods for thermal conductivity calculations: From bulk to nanowire silicon. *Phys. Rev. B* **2018,** *97* (9), 094305.

736. Sun, L.; Murthy, J. Y., Domain size effects in molecular dynamics simulation of phonon transport in silicon. *Appl. Phys. Let.* **2006,** *89* (17), 171919.

737. Fan, Z.; Pereira, L. F. C.; Wang, H.-Q.; Zheng, J.-C.; Donadio, D.; Harju, A., Force and heat current formulas for many-body potentials in molecular dynamics simulations with applications to thermal conductivity calculations. *Phys. rev. B* **2015,** *92* (9), 094301.

738. Boone, P.; Babaei, H.; Wilmer, C. E. J. J. o. c. t.; computation, Heat flux for many-body interactions: Corrections to LAMMPS. *J. Chem. Theory Comp.* **2019,** *15* (10), 5579-5587.

739. Sellan, D. P.; Landry, E. S.; Turney, J.; McGaughey, A. J.; Amon, C. H., Size effects in molecular dynamics thermal conductivity predictions. *Phys. Rev. B* **2010,** *81* (21), 214305.

740. Yusran, Y.; Fang, Q.; Valtchev, V., Electroactive Covalent Organic Frameworks: Design, Synthesis, and Applications. *Adv. Mater.* **2020**, 2002038.

741. Dogru, M.; Bein, T., On the road towards electroactive covalent organic frameworks. *Chem. Comm.* **2014,** *50* (42), 5531-5546.

742. Jin, S.; Ding, X.; Feng, X.; Supur, M.; Furukawa, K.; Takahashi, S.; Addicoat, M.; El-Khouly, M. E.; Nakamura, T.; Irle, S.; Fukuzumi, S.; Nagai, A.; Jiang, D., Charge dynamics in a donor–acceptor covalent organic framework with periodically ordered bicontinuous heterojunctions. *Angew. Chem. Int. Ed.* **2013,** *125* (7), 2071-2075.

743. Wan, S.; Guo, J.; Kim, J.; Ihee, H.; Jiang, D., A photoconductive covalent organic framework: self-condensed arene cubes composed of eclipsed 2D polypyrene sheets for photocurrent generation. *Angew. Chem. Int. Ed.* **2009,** *48* (30), 5439-5442.

744. Sick, T.; Hufnagel, A. G.; Kampmann, J.; Kondofersky, I.; Calik, M.; Rotter, J. M.; Evans, A.; Döblinger, M.; Herbert, S.; Peters, K.; Böhm, D.; Knochel, P.; Medina, D. D.; Fattakhova-Rohlfing, D.; Bein, T., Oriented films of conjugated 2D covalent organic frameworks as photocathodes for water splitting. *J. Am. Chem. Soc.* **2017,** *140* (6), 2085-2092.

745. Dogru, M.; Handloser, M.; Auras, F.; Kunz, T.; Medina, D.; Hartschuh, A.; Knochel, P.; Bein, T., A photoconductive thienothiophene-based covalent organic framework showing charge transfer towards included fullerene. *Angew. Chem. Int. Ed.* **2013,** *125* (10), 2992-2996.

746. Bessinger, D.; Ascherl, L.; Auras, F.; Bein, T., Spectrally switchable photodetection with near-infrared-absorbing covalent organic frameworks. *J. Am. Chem. Soc.* **2017,** *139* (34), 12035-12042.

747. Bertrand, G. H.; Michaelis, V. K.; Ong, T.-C.; Griffin, R. G.; Dincă, M., Thiophene-based covalent organic frameworks. *Proc. Nat. Acad. Sci.* **2013,** *110* (13), 4923-4928.

748. Lakshmi, V.; Liu, C.-H.; Rajeswara Rao, M.; Chen, Y.; Fang, Y.; Dadvand, A.; Hamzehpoor, E.; Sakai-Otsuka, Y.; Stein, R. S.; Perepichka, D. F., A Two-Dimensional Poly

(azatriangulene) Covalent Organic Framework with Semiconducting and Paramagnetic States. *J. Am. Chem. Soc.* **2020,** *142* (5), 2155-2160.

749. Li, T.; Zhang, W.-D.; Liu, Y.; Li, Y.; Cheng, C.; Zhu, H.; Yan, X.; Li, Z.; Gu, Z.-G., A two-dimensional semiconducting covalent organic framework with nickel (ii) coordination for high capacitive performance. *J. Mat. Chem. A* **2019,** *7* (34), 19676-19681.

750. Fratini, S.; Nikolka, M.; Salleo, A.; Schweicher, G.; Sirringhaus, H., Charge transport in high-mobility conjugated polymers and molecular semiconductors. *Nat. Mater.* **2020**.

751. Lussem, B.; Keum, C.-M.; Kasemann, D.; Naab, B.; Bao, Z.; Leo, K., Doped organic transistors. *Chem. Rev.* **2016,** *116* (22), 13714-13751.

752. Devkota, J.; Geng, R.; Subedi, R. C.; Nguyen, T. D., Organic spin valves: a review. *Adv. Func. Mater.* **2016,** *26* (22), 3881-3898.

753. Russ, B.; Glaudell, A.; Urban, J. J.; Chabinyc, M. L.; Segalman, R. A., Organic thermoelectric materials for energy harvesting and temperature control. *Nat. Rev. Mater.* **2016,** *1* (10), 1-14.

754. Walzer, K.; Maennig, B.; Pfeiffer, M.; Leo, K., Highly efficient organic devices based on electrically doped transport layers. *Chem. Rev.* **2007,** *107* (4), 1233-1271.

755. Jacobs, I. E.; Moulé, A. J., Controlling molecular doping in organic semiconductors. *Adv. Mater.* **2017,** *29* (42), 1703063.

756. Salzmann, I.; Heimel, G.; Oehzelt, M.; Winkler, S.; Koch, N., Molecular electrical doping of organic semiconductors: fundamental mechanisms and emerging dopant design rules. *Acc. Chem Res.* **2016,** *49* (3), 370-378.

757. Barlow, S.; Marder, S. R.; Lin, X.; Zhang, F.; Kahn, A., Electrical Doping of Organic Semiconductors with Molecular Oxidants and Reductants. In *Conjugated Polymers: Properties, Processing, and Applications*, 2019.

758. Yamashita, Y.; Tsurumi, J.; Ohno, M.; Fujimoto, R.; Kumagai, S.; Kurosawa, T.; Okamoto, T.; Takeya, J.; Watanabe, S., Efficient molecular doping of polymeric semiconductors driven by anion exchange. *Nature* **2019,** *572* (7771), 634-638.

759. I2 is a not an ideal dopant because it is challenging to introduce in controlled amounts, has an oxidation potential not well-matched with most aromatic systems, is volatile and desorbs over time, and produces an I3- counterion that is itself electronically conductive. These factors complicate understanding of the electronic properties of 2D COFs doped with iodine.

760. Al Kobaisi, M.; Bhosale, S. V.; Latham, K.; Raynor, A. M.; Bhosale, S. V., Functional naphthalene diimides: synthesis, properties, and applications. *Chem. Rev.* **2016,** *116* (19), 11685-11796.

761. Xie, L. S.; Skorupskii, G.; Dincă, M., Electrically Conductive Metal–Organic Frameworks. *Chem. Rev.* **2020**.

762. Feriante, C. H.; Jhulki, S.; Evans, A. M.; Dasari, R. R.; Slicker, K.; Dichtel, W. R.; Marder, S. R., Rapid Synthesis of High Surface Area Imine-Linked 2D Covalent Organic Frameworks by Avoiding Pore Collapse During Isolation. *Adv. Mater.* **2020,** *32* (2), 1905776.

763. Although the signal at 1710 cm–1, corresponding to the aldehyde C=O stretching mode, does not completely disappear, this is attributable to overlap with a carbonyl stretching mode of the NDI core

764. Pawley, G., Unit-cell refinement from powder diffraction scans. *J. Appl. Crystallogr.* **1981,** *14* (6), 357-361.

765. Sakai, N.; Mareda, J.; Vauthey, E.; Matile, S., Core-substituted naphthalenediimides. *Chem. Commun.* **2010,** *46* (24), 4225-4237.

766. Connelly, N. G.; Geiger, W. E., Chemical redox agents for organometallic chemistry. *Chem. Rev.* **1996,** *96* (2), 877-910.

767. Cobaltecinium is weakly absorbing in the visible, with a peak at 405 nm and an extinction coefficient of only 200 M^-1 cm^-1. This highlights an advantage of CoCp2 for systematic studies of controlled doping in NDI systems.

768. Andric, G.; Boas, J. F.; Bond, A. M.; Fallon, G. D.; Ghiggino, K. P.; Hogan, C. F.; Hutchison, J. A.; Lee, M. A.-P.; Langford, S. J.; Pilbrow, J. R., Spectroscopy of naphthalene diimides and their anion radicals. *Aust. J. Chem.* **2004,** *57* (10), 1011-1019.

769. Un, H. I.; Gregory, S. A.; Mohapatra, S. K.; Xiong, M.; Longhi, E.; Lu, Y.; Rigin, S.; Jhulki, S.; Yang, C. Y.; Timofeeva, T. V., Understanding the Effects of Molecular Dopant on n-Type Organic Thermoelectric Properties. *Adv. Energy Mater.* **2019,** *9* (24), 1900817.

770. Guo, S.; Kim, S. B.; Mohapatra, S. K.; Qi, Y.; Sajoto, T.; Kahn, A.; Marder, S. R.; Barlow, S., n-Doping of organic electronic materials using air-stable organometallics. *Adv. Mater.* **2012,** *24* (5), 699-703.

771. Liu, J.; Qiu, L.; Alessandri, R.; Qiu, X.; Portale, G.; Dong, J.; Talsma, W.; Ye, G.; Sengrian, A. A.; Souza, P. C., Enhancing Molecular n-Type Doping of Donor–Acceptor Copolymers by Tailoring Side Chains. *Adv. Mater.* **2018,** *30* (7), 1704630.

772. Kang, K.; Watanabe, S.; Broch, K.; Sepe, A.; Brown, A.; Nasrallah, I.; Nikolka, M.; Fei, Z.; Heeney, M.; Matsumoto, D., 2D coherent charge transport in highly ordered conducting polymers doped by solid state diffusion. *Nat. Mater.* **2016,** *15* (8), 896-902.

773. Vijayakumar, V.; Zhong, Y.; Untilova, V.; Bahri, M.; Herrmann, L.; Biniek, L.; Leclerc, N.; Brinkmann, M., Bringing conducting polymers to high order: Toward conductivities beyond 105 s cm− 1 and thermoelectric power factors of 2 mw m− 1 k− 2. *Adv. Energy Mater.* **2019,** *9* (24), 1900266.

774. Lu, Y.; Wang, J.-Y.; Pei, J., Strategies to enhance the conductivity of n-type polymer thermoelectric materials. *Chem. Mater.* **2019,** *31* (17), 6412-6423.

775. Auras, F.; Ascherl, L.; Hakimioun, A. H.; Margraf, J. T.; Hanusch, F. C.; Reuter, S.; Bessinger, D.; Döblinger, M.; Hettstedt, C.; Karaghiosoff, K.; Herbert, S.; Knochel, P.; Clark, T.; Bein, T., Synchronized offset stacking: a concept for growing large-domain and highly crystalline 2D covalent organic frameworks. *J. Am. Chem. Soc.* **2016,** *138* (51), 16703-16710.

776. Kresse, G.; Furthmüller, J., Efficiency of ab-initio total energy calculations for metals and semiconductors using a plane-wave basis set. *Computational Materials Science* **1996,** *6* (1), 15-50.

777. Adamo, C.; Scuseria, G. E.; Barone, V., Accurate excitation energies from time-dependent density functional theory: Assessing the PBE0 model. *The Journal of Chemical Physics* **1999,** *111* (7), 2889-2899.

Appendix: Polycyclic Aromatic Arrays for Quantum Operation and Transduction

Austin M. Evans

To realize the promise of quantum computation, quantum bits (i.e. qubits) must be fabricated reliably, in large numbers, and in a manner that allows them to be initialized, addressed, and read. Though many quantum bit technologies have been proposed as promising for quantum computation, none have addressed the parameters necessary for their successful deployment in medium- and large-scale computation. Here, I propose a new type of plexcitonic qubit, which combines the advantages of light- and matter-based approaches. These plexcitonic qubits will be produced by the on-surface synthesis of graphene nanoribbons with single photon emitting polycyclic aromatic hydrocarbons. By systematically controlling the electronic coupling and spatial arrangement of these emitters, entangled excited states between two chromophores will be produced. As such synthetic design will generate a defined two-state quantum system. As a consequence of their on-surface synthesis, these graphene nanoribbons will be well-adhered to their underlying metallic substrate, which leads to strong coupling of entangled electronic excitations to surface plasmons. Due to the low effective mass of these plexcitonic species, the quantum information contained in these excited states can be transduced over distances much larger than what is possible with molecular excitations alone. The long-range nature of these interactions will enable the quantum state to be read using far-field couplers (i.e. gratings) and well-established optical techniques. Collectively, plexcitonic single-photon emitters will lead to well defined many qubit systems in an on-chip photonic architecture, which would represent a substantial advance over existing quantum computation technologies.

Background, Previous Work, and Significance of the Research

The next generation of scientific innovation will be driven by the second quantum revolution.[1-2] When fully realized, quantum information science (QIS) will resolve complex problems in medicine,[3] communications,[4] environmental sustainability,[5] and many other disciplines. Already, first-generation quantum computers are being deployed to solve multidimensional problems that would not be feasible to address with conventional computation.[6] These quantum computers utilize quantum bits, known as a qubits which are two-state quantum-mechanical systems, to carry out quantum logic operations. Existing qubit technologies suffer from limited control, scalability, and demanding operating conditions, all of which restrict the potential of this QIS technologies.[7-10] Here, I propose a new type of qubit that addresses these challenges by combining the advantages of light-[11] and matter-based[12] qubits. The qubits proposed here will be produced by producing arrays of well-defined quantized emitters onto graphene nanoribbons (GNRs, **Figure 45A**), which allows for complete control of their spatial arrangement and electronic coupling. By coupling excited states of the GNRs to the plasmon modes of their underlying metallic substrates, a plexcitonic QIS platform will be developed. This will represent a substantial advance in controllably fabricated qubits that can be easily addressed and interrogated using well-established optical techniques.

Single-photon emitters (SPEs) are a broad class of materials that hold substantial promise for quantum information systems.[8, 13-14] The most prevalent example of these optically addressable qubits are diamond nitrogen-vacancy centers. However, these color-centers occur randomly, have limited emission windows, and cannot be controllably fabricated, all of which reduce their application potential in QIS systems. In contrast, chemically synthesized SPEs are entirely

identical and have tunable optical manifolds (**Figure 46B**). One such class of chemically produced SPEs are polycyclic aromatic hydrocarbons (PAHs), which are the focus of this proposal.[15-16] Basché and Moerner showed how perylene molecules, a prototypical PAH, embedded within a matrix at low temperatures served as SPEs.[16-17] More recently, Sandoghdar and coworkers showed how when perylene molecules in close proximity within a matrix can electronically couple, thereby generating entangled excited states.[18] The observation that coupled two-level excited states can exist between SPEs suggests that they may be promising as optically addressable qubits. However, the SPEs produced through this method cannot have their relative locations or electronic couplings systematically varied. This limitation motivates the proposed study to controllably array SPEs along the backbone of GNRs, which will enable the control over the relative spacing, electronic coupling, and optical manifolds of these SPE-based qubits.

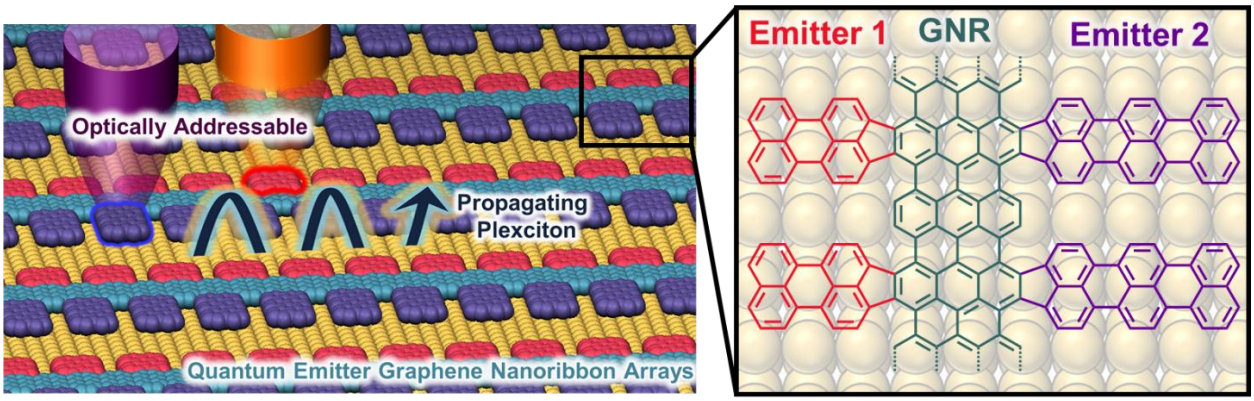

Figure 45| Schematic of PAH-functionalized graphene nanoribbons and their plexcitonic behavior.

Using established on-surface synthetic techniques, pre-designed SPEs will be reliably arrayed on graphene nanoribbons as a template to control their relative spacing and electronic coupling.[19-20] Generally, GNRs synthesized on-surface suffer from their strong adhesion to their

host substrate, which typically prevents post-synthetic manipulation.[21] However, in the context of excited-state qubits, this strong coupling is advantageous because it will generate coupled exciton-plasmon (plexciton) behavior.[22-26] One salient feature of plasmons and plexcitons is that they have a much lower effective mass than that of molecular electronic transitions. As such, while electronic transitions generally do not propagate, plasmons can carry information along extended lengths. So, by exploiting strong light-matter interactions, plexcitons can be used to transport the information encoded in electronic transitions over significantly longer distances than is possible with excitons alone. This suggests that it is possible to measure excited state qubits using conventional optical techniques, such as by collecting the quantum information at gratings that are positioned away from the quantized emitters. Ultimately, strongly coupled light-matter processes will enable low-dimensional quantum photonics in an on-chip architecture, which is a fundamental advance towards highly integrated QIS systems.

Scientific Objectives

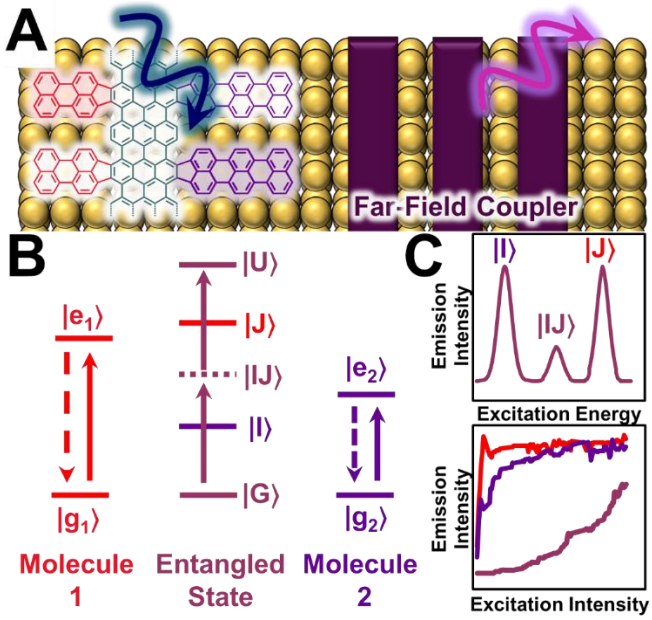

Figure 46| A. Schematic of measurement where excitation and emission are spatially resolved as a result of plexcitonic transduction and far-field reading at optical gratings. **B.** A two molecule, two level electronic system with ground, |g⟩, and excited, |e⟩, states. The entangled state can be treated as a four-level system where excitation to |IJ⟩ leads to a superposition of |I⟩ and |J⟩. **C.** Expected spectra from this dipolar coupled two molecule system.

Overall Aim: Fabricate a plexcitonic multiqubit system using polycyclic aromatic hydrocarbons arrayed on graphene nanoribbons.

Specific Aim 1: Design and Synthesis of Functionalized Quantum Emitter GNR Arrays. GNRs with pendant PAH functionalities will be synthesized through a two-stage Ullman-coupling followed by oxidative aromatization of molecular precursors. This bottom-up synthesis of GNRs

from molecular precursors will yield unparalleled control over the electronic couplings, spatial distributions, and optical profiles of excited-state qubits.

Specific Aim 2: GNR Arrays and Molecular Precursor Characterization. For GNR arrays to be used as QIS materials a wholistic portrait of electronic and light-matter couplings must be developed. Specifically, X-ray photoelectron spectroscopy, scanning tunneling spectroscopy, static and time-resolved spectroscopy, and scanning tunneling microscopy will be used to uncover the electronic- and exciton-plasmon couplings in GNR arrays.

Specific Aim 3: Plexcitonic Transduction and Readout from GNR Quantum Emitter Arrays. Nanoprobe fluorescence measurements will be used to measure the propagation lengths and coherence times of plexcitonic systems. By coupling electronic excited-states to surface plasmons of metal substrates, long-range transport, and efficient read out of quantum information will be evaluated.

Proposed Research

To investigate plexcitonic quantum operations and transduction, well-defined GNR quantum emitter arrays will be synthesized, their electronic couplings determined, and their plexcitonic device potential evaluated.

Design and Synthesis of Functionalized Quantum Emitter GNR Arrays. To prepare GNR quantum emitter arrays that are strongly coupled to metal surface plasmons, on-surface syntheses that allow for complete control of the shape, chemical functionality, and electronic structure will be used.[19, 21, 27-32] A two-stage on-surface synthesis is proposed where an on surface-mediated Ullman-coupling is followed by an oxidative aromatization.[28] This versatile strategy enables the

synthesis of a diverse range of chemical structures by deposition and subsequent polymerization of designed molecular precursors (**Figure 47**). Through this control, the emission energy, electronic coupling, spatial arrangement, and surface-GNR coupling can be systematically varied.

As a first target, a single-chromophore halogenated-anthracene derivative will be synthesized, Ullman coupled on-surface, and subsequently aromatized to form a GNR quantum emitter array. Focusing on a single-chromophore GNR will allow for the investigation of emergent electronic transitions and coupled plexcitonic phenomena in a more synthetically accessible system. More advanced systems will focus on the controlled integration and electronic coupling of multichromophore systems. To synthesize the molecular precursor the component that will lead to the GNR backbone and the PAH component will be coupled together (**Figure 47A**).[33] This will be achieved by first Suzuki coupling these two aromatic components, then conducting a Pd-catalyzed intramolecular ring-closing, and finally brominating the GNR component. This molecular precursor will be thoroughly characterized via single-crystal X-ray diffraction, nuclear magnetic resonance, and vibrational spectroscopy (**Figure 48**).

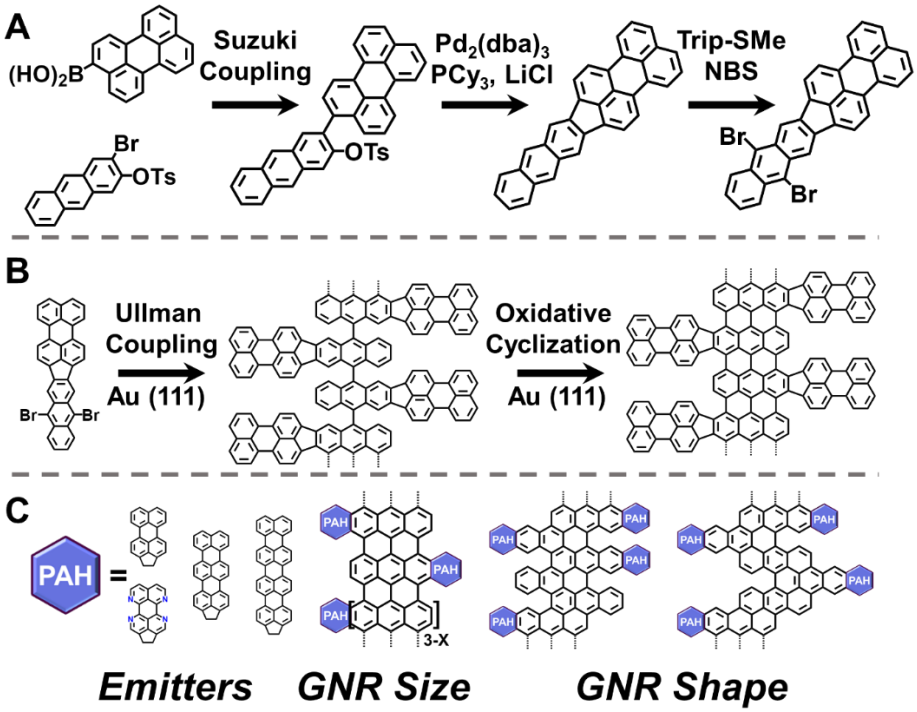

Figure 47| A. Representative synthesis of a PAH-functionalized GNR precursor. **B.** Representative on-surface synthetic approach to produce a PAH functionalized GNR. **C.** Representative modifications that could be made to GNR quantum emitter arrays.

This molecular precursor will then be Ullman-coupled and subsequently oxidatively aromatized using established on-surface ultra-high vaccum synthetic techniques on a Au(111) surface (**Figure 47B**).[34] These two processes are highly temperature dependent, with Ullman coupling proceeding at lower temperatures than aromatization. Therefore, these two processes can be controllably performed by increasing the temperature in a step-wise fashion. Successful on-surface polymerization will be characterized via X-ray photoelectron spectroscopy (XPS), Raman spectroscopy, and direct imaging via scanning tunneling microscopy (STM).[34-36] Specifically,

variable-temperature XPS will be performed to track the polymerization and subsequent aromatization of our molecular precursors (**Figure 48**). These *in situ* techniques are well-developed to track and quantify on-surface reactions, however the proposed work represents the first use of these techniques to monitor the formation of GNRs functionalized with quantum emitters. If the PAH-functionalized GNR is unable to be synthesized, the first contingency plan would be too attempt this on-surface synthesis on other metallic substrates and crystalline faces. It is well-understood that a balance of reactivity and mobility is required for successful on-surface synthesis and this balance is known to be highly surface dependent.[34] Because all metallic substrates will host plasmonic behavior, which is discussed later in the proposal, successful synthesis on virtually any substrate will work for the next steps of this proposal. The synthetic and characterization approach proposed here is highly versatile, where small changes to the molecular precursor can be used to prepare a large number of resultant PAH-functionalized GNRs (**Figure 47C**)

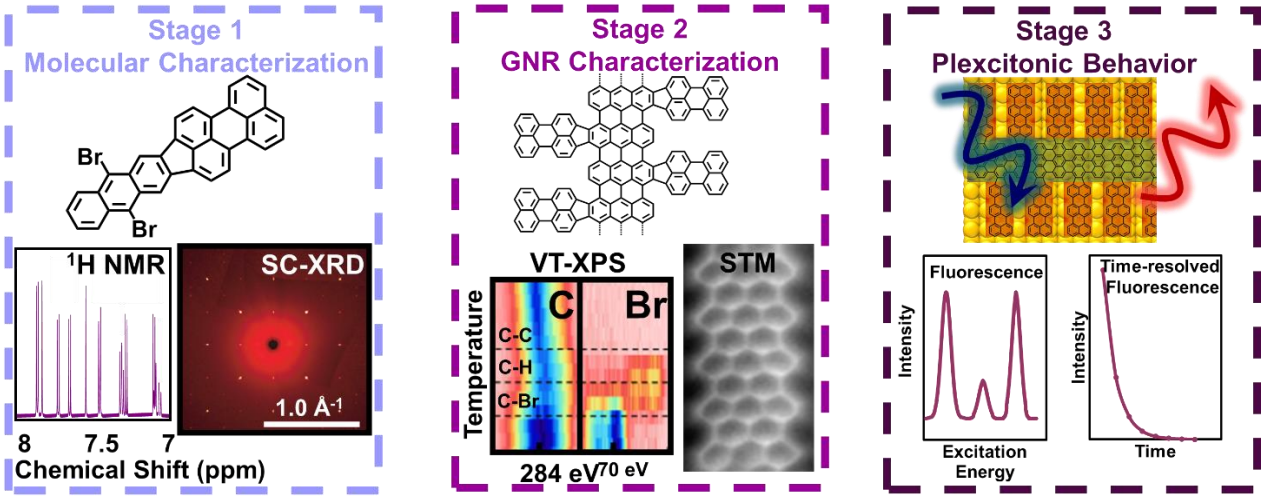

Figure 48| Planned characterization of molecular precusors (left), PAH-functionalized GNRs (middle), and electronic and plexcitonic coupling (right).

GNR Arrays and Molecular Precursor Electronic Characterization. A robust understanding of the electronic- and excitonic-plasmon couplings in GNR arrays is necessary for their development as plexcitonic quantum materials. To this end, a variety of spectroscopies will be used to characterize the electronic structure of GNRs produced on Au substrates. For instance, characterization by near-edge X-ray absorption fine structure and resonant photoemission spectroscopy will be used to characterize the bulk electronic coupling of the chromophores and the GNR to the Au surface and the charge transfer dynamics across that interface.[37] Together, these measurements will yield important insights about plexciton experimental design by informing the extent of energy transfer between the optically addressable GNRs and the underlying metallic substrate and its plasmon modes. To complement bulk spectroscopic measurements, I will also characterize these GNR quantum emitter arrays with scanning tunneling microscopy (STM) and spectroscopy (STS).[38-39] Using these techniques, the physical and electronic structure will be visualized at the atomic limit, which will resolve the spatial relationship and electronic coupling of quantum emitters of GNRs on the nanoscale. Likewise, these techniques will enable the direct mapping of the electronic bandstructures of PAH-functionalized GNRs. This is critical to properly understand the interchromophore electronic coupling and the coupling of the GNR to the underlying metallic substrate. Using recently developed techniques, optical spectroscopy will be performed within nanoscale junctions produced between the STM tip and the Au surface. Electroluminescence and voltage-dependent optical absorption in these junctions will provide a direct measure of molecular electronic coupling to the electrodes' plasmonic modes.[40] Ultimately, the collective findings of these experiments will reveal the extent of electronic coupling between chromophores and between electronic excitations and plasmon modes in plexcitonic systems. If

we observe that the PAH-functionalized GNRs do not sufficiently couple to their underlying substrate, we will modify out PAH-precursor to include N- and S-heteroatoms, which are known to give rise to stronger metal-molecule couplings. However, the single-photon emission and on-surface synthesis of these molecules are less well-understood and so this will be reserved as a secondary strategy for the preparation of these materials.

Plexcitonic Transduction and Readout. Proper plexcitonic characterization requires the identification of strongly coupled phenomena (i.e. Rabi splitting) that emerges from the GNR quantum emitters.[14, 41] Using a multidimensional approach, the coupling of these systems will be studied on the length and time-scales most relevant to their implementation as photonic QIS technologies. First, static and time-resolved fluorescence spectroscopy will inform the photostability, optical addressability, excited-state lifetimes, and the coupling strength of our GNR quantum emitters. Here, photoexcited PAH chromophores will not emit light but rather couple to plasmonic states of the surface. Therefore, far-field output couplers (i.e. gratings) will be used to collect and monitor the emission of single-photon emitters.[42] In principle, well-coupled plexcitonic systems will be highly photostable (due to the energetic dispersion into plasmon modes) and highly emissive at the far-field electronic couplers (if the plasmon and electronic excitations are well coupled).[43] By comparing the spectroscopic behavior of PAH molecular precursors, linear polymers, and GNRs, the effect of spatial arrangement and electronic coupling through the GNR will be directly interrogated. One would expect that individual molecules will likely not couple to one another at all, weakly through the linear polymer, and highly through the graphene nanoribbon. By monitoring these behaviors as a function of GNR density and optical fluence, inter- and intra-

GNR coupling will also be explored, with decreased excited-state lifetimes at higher fluences and higher densities being suggestive of cooperative behavior within and between chromophore arrays, as has recently been seen in diamond nitrogen-vacancy centers.[44]

Figure 49| Representative nano-optical mapping of plexcitonic standing waves, which allows for systematic interrogation and far-field measurement of plexcitonic qubits.

A critical feature of plexcitons is that they have a lighter effective mass than molecular excitons because of their strong coupling to surface plasmon modes.[45-46] This makes it possible for plexcitons to be used for transmitting quantum information over length scales not possible in purely molecular electronic transitions. This means that when plexcitonic qubits can be addressed and read at separate spatial location, which greatly simplifies quantum computer operation. To

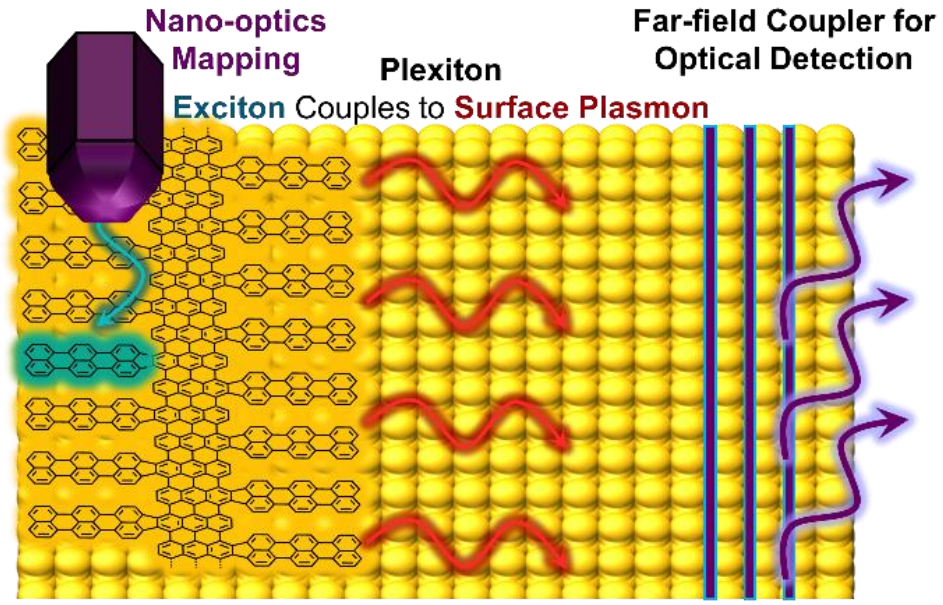

investigate this possibility, nano-probe spectroscopies based on optical antennas will be used (**Figure 49**), which have recently been used to study other materials. These optical measurements

will reveal the *k*-vectors and distances that plexcitons can efficiently propagate and maintain coherence, which are the most critical features for quantum transduction. These measurements will enable the complete mapping of plexcitonic dispersion and propagation in our GNR quantum emitters. Collectively, these measurements will be used to determine the best device configuration to address and read plexcitonic qubits without loss of their stored quantum state. With this information, it will be possible to modify the relative spacings between the excited region and the optical coupler to maximize the efficient transduction of the quantum state.

Summary and Conclusions

Here, we have proposed a new type of qubit based on plexcitonic single-photon emitters. In this design, polycyclic aromatic hydrocarbon chromophores are reliably arrayed onto graphene nanoribbons. By controlling the electronic coupling and spatial arrangement of these chromophores, it is possible to engineer their dipolar coupling and resultant entangled states. To fabricate polycyclic aromatic hydrocarbon arrays, molecular precursors will be designed, synthesized and reacted on-surface to produce graphene nanoribbons. As a result of their on-surface fabrication, these polycyclic aromatic hydrocarbon arrays will be well-interfaced to their underlying metallic substrate. This is advantageous because it will lead to coupling of the molecular electronic transitions to the plasmon modes of the metal substrate. This plexcitonic behavior will enable efficient harvesting oh the quantum information contained within molecular electronic transitions at far-field couplers. When realized, this new qubit design will enable low-dimensional quantum information science systems in an on-chip architecture, which lead to

improvements in the scalability and application potential of quantum information science based on these materials.

References

1. Cho, A., Google claims quantum computing milestone. American Association for the Advancement of Science: 2019.
2. Bruss, D.; Leuchs, G., *Quantum Information: From Foundations to Quantum Technology Applications*. John Wiley & Sons: 2019.
3. Solenov, D.; Brieler, J.; Scherrer, J. F., The potential of quantum computing and machine learning to advance clinical research and change the practice of medicine. *The Lancet* **2018,** *115* (5), 463.
4. Steane, A. M.; Rieffel, E. G., Beyond bits: The future of quantum information processing. *Computer* **2000,** *33* (1), 38-45.
5. Childs, A. M.; Maslov, D.; Nam, Y.; Ross, N. J.; Su, Y., Toward the first quantum simulation with quantum speedup. *Proc. Nat. Acad. Sci.* **2018,** *115* (38), 9456-9461.
6. Arute, F.; Arya, K.; Babbush, R.; Bacon, D.; Bardin, J. C.; Barends, R.; Biswas, R.; Boixo, S.; Brandao, F. G.; Buell, D. A., Quantum supremacy using a programmable superconducting processor. *Nature* **2019,** *574* (7779), 505-510.
7. Wendin, G., Quantum information processing with superconducting circuits: a review. *Reports Prog. Phys.* **2017,** *80* (10), 106001.
8. Chen, Y.-C.; Salter, P. S.; Knauer, S.; Weng, L.; Frangeskou, A. C.; Stephen, C. J.; Ishmael, S. N.; Dolan, P. R.; Johnson, S.; Green, B. L., Laser writing of coherent colour centres in diamond. *Nat. Photon.* **2017,** *11* (2), 77-80.
9. Stephen, C.; Green, B.; Lekhai, Y.; Weng, L.; Hill, P.; Johnson, S.; Frangeskou, A.; Diggle, P.; Chen, Y.-C.; Strain, M. J. P. R. A., Deep three-dimensional solid-state qubit arrays with long-lived spin coherence. *Phys. Rev. Appl.* **2019,** *12* (6), 064005.
10. Gaita-Ariño, A.; Luis, F.; Hill, S.; Coronado, E., Molecular spins for quantum computation. *Nat. Chem.* **2019,** *11* (4), 301-309.
11. Slussarenko, S.; Pryde, G., Photonic quantum information processing: A concise review. *Appl. Phys. Rev.* **2019,** *6* (4), 041303.
12. Krantz, P.; Kjaergaard, M.; Yan, F.; Orlando, T. P.; Gustavsson, S.; Oliver, W. D., A quantum engineer's guide to superconducting qubits. *Appl. Phys. Rev.* **2019,** *6* (2), 021318.
13. Zhao, S.; Lavie, J.; Rondin, L.; Orcin-Chaix, L.; Diederichs, C.; Roussignol, P.; Chassagneux, Y.; Voisin, C.; Müllen, K.; Narita, A., Single photon emission from graphene quantum dots at room temperature. *Nat. Commun.* **2018,** *9* (1), 1-5.
14. Yoshie, T.; Scherer, A.; Hendrickson, J.; Khitrova, G.; Gibbs, H.; Rupper, G.; Ell, C.; Shchekin, O.; Deppe, D., Vacuum Rabi splitting with a single quantum dot in a photonic crystal nanocavity. *Nature* **2004,** *432* (7014), 200-203.

15. Pazzagli, S.; Lombardi, P.; Martella, D.; Colautti, M.; Tiribilli, B.; Cataliotti, F. S.; Toninelli, C., Self-assembled nanocrystals of polycyclic aromatic hydrocarbons show photostable single-photon emission. *ACS Nano* **2018,** *12* (5), 4295-4303.
16. Lounis, B.; Moerner, W. E., Single photons on demand from a single molecule at room temperature. *Nature* **2000,** *407* (6803), 491-493.
17. Basché, T.; Moerner, W., Optical modification of a single impurity molecule in a solid. *Nature* **1992,** *355* (6358), 335-337.
18. Hettich, C.; Schmitt, C.; Zitzmann, J.; Kühn, S.; Gerhardt, I.; Sandoghdar, V., Nanometer resolution and coherent optical dipole coupling of two individual molecules. *Science* **2002,** *298* (5592), 385-389.
19. Allen, M. J.; Tung, V. C.; Kaner, R. B., Honeycomb carbon: a review of graphene. *Chem. Rev.* **2010,** *110* (1), 132-145.
20. Sun, Q.; Zhang, R.; Qiu, J.; Liu, R.; Xu, W., On-Surface Synthesis of Carbon Nanostructures. *Adv. Mater.* **2018,** *30* (17), 1705630.
21. Ma, L.; Wang, J.; Ding, F., Recent progress and challenges in graphene nanoribbon synthesis. *ChemPhysChem* **2013,** *14* (1), 47-54.
22. Ahmadivand, A.; Gerislioglu, B.; Ramezani, Z.; Ghoreishi, S. A., Demonstration of Robust Plexcitonic Coupling in Organic Molecules-Mediated Toroidal Meta-Atoms. *Adv. Opt. Mater.* **2019,** *7* (24), 1901248.
23. Marinica, D. C.; Lourenço-Martins, H.; Aizpurua, J.; Borisov, A. G., Plexciton quenching by resonant electron transfer from quantum emitter to metallic nanoantenna. *Nano Lett.* **2013,** *13* (12), 5972-5978.
24. Fofang, N. T.; Park, T.-H.; Neumann, O.; Mirin, N. A.; Nordlander, P.; Halas, N. J., Plexcitonic nanoparticles: plasmon− exciton coupling in nanoshell− J-aggregate complexes. *Nano Lett.* **2008,** *8* (10), 3481-3487.
25. Manuel, A. P.; Kirkey, A.; Mahdi, N.; Shankar, K., Plexcitonics–fundamental principles and optoelectronic applications. *J. Mater. Chem. C* **2019,** *7* (7), 1821-1853.
26. Thomas, R.; Thomas, A.; Pullanchery, S.; Joseph, L.; Somasundaran, S. M.; Swathi, R. S.; Gray, S. K.; Thomas, K. G., Plexcitons: the role of oscillator strengths and spectral widths in determining strong coupling. *ACS Nano* **2018,** *12* (1), 402-415.
27. Cai, J.; Ruffieux, P.; Jaafar, R.; Bieri, M.; Braun, T.; Blankenburg, S.; Muoth, M.; Seitsonen, A. P.; Saleh, M.; Feng, X., Atomically precise bottom-up fabrication of graphene nanoribbons. *Nature* **2010,** *466* (7305), 470-473.
28. James, D. K.; Tour, J. M., The chemical synthesis of graphene nanoribbons—a tutorial review. *Macromol. Chem. Phys.* **2012,** *213* (10-11), 1033-1050.
29. Li, X.; Wang, X.; Zhang, L.; Lee, S.; Dai, H., Chemically derived, ultrasmooth graphene nanoribbon semiconductors. *Science* **2008,** *319* (5867), 1229-1232.
30. Chen, L.; Hernandez, Y.; Feng, X.; Müllen, K., From nanographene and graphene nanoribbons to graphene sheets: chemical synthesis. *Angew. Chem. Int. Ed.* **2012,** *51* (31), 7640-7654.
31. Chen, Y.-C.; Cao, T.; Chen, C.; Pedramrazi, Z.; Haberer, D.; De Oteyza, D. G.; Fischer, F. R.; Louie, S. G.; Crommie, M. F., Molecular bandgap engineering of bottom-up synthesized graphene nanoribbon heterojunctions. *Nat. Nanotechnol.* **2015,** *10* (2), 156-160.

32. Dutta, S.; Pati, S. K., Novel properties of graphene nanoribbons: a review. *J. Mater. Chem.* **2010,** *20* (38), 8207-8223.
33. Mohammad-Pour, G. S.; Ly, R. T.; Fairchild, D. C.; Burnstine-Townley, A.; Vazquez-Molina, D. A.; Trieu, K. D.; Campiglia, A. D.; Harper, J. K.; Uribe-Romo, F. J., Modular design of fluorescent dibenzo-and naphtho-fluoranthenes: structural rearrangements and electronic properties. *J. Org. Chem.* **2018,** *83* (15), 8036-8053.
34. Grill, L.; Hecht, S., Covalent on-surface polymerization. *Nat. Chem.* **2020,** *12* (2), 115-130.
35. Lafferentz, L.; Eberhardt, V.; Dri, C.; Africh, C.; Comelli, G.; Esch, F.; Hecht, S.; Grill, L., Controlling on-surface polymerization by hierarchical and substrate-directed growth. *Nat. Chem.* **2012,** *4* (3), 215-220.
36. Grill, L.; Dyer, M.; Lafferentz, L.; Persson, M.; Peters, M. V.; Hecht, S., Nano-architectures by covalent assembly of molecular building blocks. *Nat. Nanotechnol.* **2007,** *2* (11), 687-691.
37. Hähner, G., Near edge X-ray absorption fine structure spectroscopy as a tool to probe electronic and structural properties of thin organic films and liquids. *Chem. Soc. Rev.* **2006,** *35* (12), 1244-1255.
38. Söde, H.; Talirz, L.; Gröning, O.; Pignedoli, C. A.; Berger, R.; Feng, X.; Müllen, K.; Fasel, R.; Ruffieux, P., Electronic band dispersion of graphene nanoribbons via Fourier-transformed scanning tunneling spectroscopy. *Phys. Rev. B* **2015,** *91* (4), 045429.
39. Chen, Y.-C.; De Oteyza, D. G.; Pedramrazi, Z.; Chen, C.; Fischer, F. R.; Crommie, M. F., Tuning the band gap of graphene nanoribbons synthesized from molecular precursors. *ACS Nano* **2013,** *7* (7), 6123-6128.
40. Aradhya, S. V.; Venkataraman, L., Single-molecule junctions beyond electronic transport. *Nat. Nanotechnol.* **2013,** *8* (6), 399.
41. Khitrova, G.; Gibbs, H.; Kira, M.; Koch, S. W.; Scherer, A., Vacuum Rabi splitting in semiconductors. *Nat. Phys.* **2006,** *2* (2), 81-90.
42. Heeres, R. W.; Dorenbos, S. N.; Koene, B.; Solomon, G. S.; Kouwenhoven, L. P.; Zwiller, V., On-chip single plasmon detection. *Nano Lett.* **2010,** *10* (2), 661-664.
43. Donehue, J. E.; Wertz, E.; Talicska, C. N.; Biteen, J. S., Plasmon-enhanced brightness and photostability from single fluorescent proteins coupled to gold nanorods. *J. Phys. Chem. C* **2014,** *118* (27), 15027-15035.
44. Bradac, C.; Johnsson, M. T.; van Breugel, M.; Baragiola, B. Q.; Martin, R.; Juan, M. L.; Brennen, G. K.; Volz, T., Room-temperature spontaneous superradiance from single diamond nanocrystals. *Nat. Commun.* **2017,** *8* (1), 1-6.
45. Zakharko, Y.; Rother, M.; Graf, A.; Hähnlein, B.; Brohmann, M.; Pezoldt, J. r.; Zaumseil, J., Radiative pumping and propagation of plexcitons in diffractive plasmonic crystals. *Nano Lett.* **2018,** *18* (8), 4927-4933.
46. Gómez, D. E.; Giessen, H.; Davis, T. J., Semiclassical plexcitonics: Simple approach for designing plexcitonic nanostructures. *J. Phys. Chem. C* **2014,** *118* (41), 23963-23969.